Proceedings of the
26th Seismic Research Review:
Trends in Nuclear Explosion Monitoring

September 21-23, 2004

Orlando, Florida

Volume I

Theme Paper
Seismic Regional Characterization and Wave Propagation
Seismic Event Detection and Location
Seismic Identification and Source Characterization

Approved for Public Release; further dissemination unlimited.

National Nuclear Security Administration

LA-UR-04-5801

AIR FORCE RESEARCH LABORATORY

2004

Proceedings of the 26th Seismic Research Review:
Trends in Nuclear Explosion Monitoring

Vol. I

To view these Proceedings online, visit
https://www.nemre.nnsa.doe.gov/review2004

Acknowledgements

The National Nuclear Security Administration (NNSA) and the Air Force Research Laboratory (AFRL) gratefully acknowledge the important contributions of the following people for their work to produce the ***Proceedings of the 26th Seismic Research Review – Trends in Nuclear Explosion Monitoring*****.**

Authors of papers for excellent research, good technical content and willing cooperation in electronic submission.

Dr. Anton M. Dainty, Mr. Robert J. Raistrick, Dr. Frederick R. Schult, AFRL/VSBYE, and ***Ms. Connie E. Rankin***, AFRL/VSOT, for review and clearance of abstracts and papers related to AFRL contracts.

Dr. Mark T. Woods, Air Force Technical Applicaions Center (AFTAC)/TTR, for review and clearance of abstracts and papers related to AFTAC contracts.

Mr. John J. Dwyer, AFTAC/CTI, for review of abstracts and papers related to AFTAC contracts.

Dr. Stanley D. Ruppert, Lawrence Livermore National Laboratory (LLNL), for assistance in ensuring that the CDs could be read on a variety of platforms.

Ms. Jody Benson, Ms. Stephanie Hanson, Ms. Carol Mark and Mr. Marvin A. Wetovsky, Los Alamos National Laboratory (LANL), for supplementary technical editing of papers.

Ms. Francesca C. Chavez, LANL, for overall coordination of the proceedings development and for technical editing of abstracts and papers.

Mr. Thomas W. Lyttle, LANL, for classification review of compiled papers.

Information Management Group, LANL, for burning, labeling, and jacketing the CDs, and for the color printing and binding of the hard copies.

Ms. Ruth N. Robichaud, LANL, for design and artwork of the CD label.

Ms. Leslie A. Casey, NNSA, for review and clearance of abstracts and papers related to NNSA contracts and for NNSA managerial and financial support of the Proceedings.

Dr. Joseph C. Wehlburg, NNSA/SNL, for technical review of abstracts and papers.

Dr. Raymond J. Willemann, NNSA/GEM, for technical review of abstracts and papers.

Mr. William L. Andre, Space and Missile Defense Command (SMDC), for review and clearance of abstracts and papers related to SMDC contracts.

Ms. Mary L. Girven, Sandia National Laboratories (SNL), for making everyone's job easier with web-based technology for abstract and paper submission, on-line review and approval tools, and creation of the master files for the hardcopy and CD versions of the Proceedings.

Ms. Guadalupe (Lupe) Massoth, SNL, for providing assistance to Mary Girven on troubleshooting web related problems.

Dr. David B. Harris, LLNL; ***Dr. John J. Zucca,*** LLNL; ***Mr. Julio Aguilar-Chang,*** LANL; ***Dr. CL Edwards,*** LANL; ***Dr. Dale N. Anderson***, Pacific Northwest National Laboratory (PNNL); ***Dr. Harry S. Miley,*** PNNL; ***Mr. J. Mark Harris,*** SNL; ***Mr. Preston B. Herrington,*** SNL; and ***Dr. Christopher J. Young***, SNL, for a myriad of internal management and technical reviews of NNSA abstracts and papers.

Table of Contents - Volume I

1. Theme Paper 1

1-01 **Anderson, D., R. Willemann, H. Miley, C. Edwards, P. Herrington, J. Harris, J. Wehlburg, D. Harris, J. Zucca, and L. Casey**
Trends in Nuclear Explosion Monitoring 3

2. Seismic Regional Characterization and Wave Propagation 15

2-01 **Ammon, C., M. Kosarian, R. Herrmann, M. Pasyanos, W. Walter, and H. Tkalcic**
Simultaneous Inversion of Receiver Functions, Multi-mode Dispersion, and Travel-time Tomography for Lithospheric Structure Beneath the Middle East and North Africa 17

2-02 **Ammon, C., W. Sevilla, R. Herrmann, and G. Randall**
Systematic Inversion of Receiver Functions and Surface Wave Dispersion for Crustal Structure in Central Asia 29

2-03 **Brown, W., T. VanDeMark, D. Doser, and A. Velasco**
An Integrated Geophysical Study of the Lithospheric Structure Beneath Libya 39

2-04 **Bungum, H., O. Ritzmann, J. Faleide, N. Maercklin, J. Schweitzer, W. Mooney, S. Detweiler, and W. Leith**
Development of a Three-dimensional Velocity Model for the Crust and Upper Mantle in the Barents Sea, Novaya Zemlya, Kara Sea and Kola-Karelia Regions 50

2-05 **Gitterman, Y., V. Pinsky, K. Solomi, A. Hofstetter, C. Gurbuz, and M. Ergin**
Using Ground Truth Events for Travel Time Calibration and Studying Seismic Energy Generation and Partitioning into Various Regional Phases 61

2-06 **Harris, D., F. Ringdal, E. Kremenetskaya, S. Mykkeltveit, D. Rock, J. Schweitzer, T. Hauk, and J. Lewis**
Ground Truth Collection for Mining Explosions in Northern Fennoscandia and Russia 73

2-07 **Li, H., I. Morozov, and S. Smithson**
Lg Amplitude Ratios from Peaceful Nuclear Explosions and Crustal Structure in Northern Eurasia 83

2-08 **Mackey, K., K. Fujita, H. Hartse, and L. Steck**
Seismic Regionalization Research in Northeast Russia 92

2-09 **Martin, R., M. Krasovec, M. Toksoz, H. Kuleli, and E. Vergino**
Caucasus Seismic Information Network 102

2-10 **Mayeda, K., W. Phillips, L. Malagnini, and D. Dreger**
Evolution of the Regional Coda Methodology 108

2-11 **Morozov, I., E. Morozova, and S. Smithson**
Nuclear-Explosion Profiles for Seismic Calibration of Northern Eurasia 117

2-12 **Myers, S., L. Preston, J. Wagoner, S. Larsen, K. Smith, and W. Walter**
Simulation of Regional Explosion S-phases (SiRES) Project 124

2-13 **Pasyanos, M., W. Walter, H. Tkalcic, G. Franz, and M. Flanagan**
Geophysical Model Research and Results 134

2-14 **Pulliam, J. and M. Sen**
Waveform Modeling of the Crust and Upper Mantle Using S, Sp, SsPmP, and Shear-Coupled PL Waves for Improved Event Location, Focal Depth Determination, and Uncertainty Estimation 142

2-15 **Rodgers, A. and A. Al-Amri**
Seismic Data for Nuclear Explosion Monitoring in the Arabian Peninsula 153

2-16 **Sandvol, E., J. Xie, and B. Mitchell**
High-Resolution Tomographic Mapping of Regional Phase Q in the Middle East 161

2-17 **Stevens, J., D. Adams, G. Baker, M. Eneva, and H. Xu**
Improved Surface Wave-Dispersion Models, Amplitude Measurements, and Azimuth Estimates 170

2-18 **Toksoz, M., H. Kuleli, C. Gurbuz, D. Kalafat, T. Bekler, C. Schultz, R. Gok, and D. Harris**
Calibration of Regional Seismic Stations in the Middle East with Shots in Turkey 181

2-19 **Wu, R., X. Xie, Z. Ge, and T. Lay**
Quantifying Source Excitation and Path Effects for High Frequency Regional Waves 191

2-20 **Xie, J.**
Tomographic Mapping of Regional Wave Q in Eastern Eurasia 202

3. Seismic Event Detection and Location 209

3-01 **Ballard, S., M. Chang, J. Hipp, L. Jensen, R. Simons, and L. Wilkening**
The 2004 Knowledge Base Parametric Grid Data Software Suite 211

3-02 **Bodin, P., A. Akinci, L. Malagnini, K. Mayeda, and A. Rodgers**
Seismic Sources and Wave Propagation in Western India 221

3-03 **Brazier, R., Y. Park, A. Nyblade, and M. Pasyanos**
Ground Truth Events from Regional Seismic Networks in Northeastern Africa 227

3-04 **Brooks, B., L. Frazer, F. Gomez, and E. Sandvol**
Ground Truth of African and Eastern Mediterranean Shallow Seismicity Using SAR Interferometry and Gibbs Sampling Inversion 237

3-05 **Buckley, S., P. Vincent, and K. Gudipati**
Next-Generation InSAR Ground-Truth Data and Techniques: Initial Results 247

3-06 **Engdahl, E., E. Bergman, S. Myers, and F. Ryall**
Improved Ground Truth in Southern Asia Using In-Country Data, Analyst Waveform Review and Advanced Algorithms 257

3-07 **Flanagan, M. and S. Myers**
Regional Travel-Time Prediction, Uncertainty, and Location Improvement 267

3-08 **Kim, W., D. Schaff, J. Zhang, F. Waldhauser, and P. Richards**
Evaluation of Cross-Correlation Methods on a Massive Scale for Accurate Relocation of Seismic Events 277

3-09 **Reiter, D., J. Bonner, and R. Shumway**
Development of Innovative Filtering Techniques for Improved Depth Phase Detection at Regional Distances 287

3-10 **Ringdal, F., T. Kvaerna, E. Kremenetskaya, V. Asming, S. Kozyrev, S. Mykkeltveit, S. Gibbons, and J. Schweitzer**
Research in Regional Seismic Monitoring 297

3-11 **Rodi, W.**
Error Analysis in the Joint Event Location/Seismic Calibration Inverse Problem 307

3-12 **Saikia, C., G. Ichinose, H. Thio, D. Helmberger, and M. Simons**
Ground Truth Locations Using Synergy Between Remote Sensing and Seismic Methods - Application to Earthquakes in Iran and Indian Subcontinent 317

3-13 **Saikia, C., J. Chen, G. Ichinose, D. Helmberger, A. Konca, and M. Simons**
Ground Truth Locations Using Synergy Between Remote Sensing and Seismic Methods - Application to Chinese Earthquakes 328

3-14 **Sheehan, A., G. Monsalve, C. Rowe, and M. Begnaud**
Ground Truth in Central Asia from In-Country Networks 338

3-15 **Steck, L., C. Rowe, M. Begnaud, W. Phillips, V. Gee, and A. Velasco**
Advancing Seismic Event Location Through Difference Constraints and Three-Dimensional Models 346

3-16 **Thurber, C. and H. Zhang**
Methods for Improving Seismic Event Location Processing 356

3-17 **Tibuleac, I., D. Harris, J. Britton, T. Hauk, H. Hooper, and J. Bonner**
Detection Methods for Mining Explosions in Southern Asia 366

4. Seismic Identification and Source Characterization 375

4-01 **Bonner, J., D. Reiter, D. Harkrider, and S. Russell**
Development of a Time Domain, Variable-Period Surface Wave Magnitude Measurement Procedure for Application at Regional Distances 377

4-02 **Bungum, H., T. Kvaerna, S. Mykkeltveit, M. Roth, V. Oye, K. Aastebol, D. Harris, and S. Larsen**
Energy Partitioning for Seismic Events in Fennoscandia and NW Russia 387

4-03 **Gupta, I., S. Taylor, R. Wagner, and W. Rivers**
A Seismic Event Discrimination System Based on Improved Understanding of Lg from Explosions - Preliminary Results 397

4-04 **Hedlin, M., B. Stump, S. Arrowsmith, and M. Renwald**
A Comparative Test of Seismic Discriminants for Mining Explosions 407

4-05 **Hooper, H., H. Patton, J. Bonner, and M. Leidig**
Using Short-Period Surface Waves to Model Source Phenomena 417

4-06 **Leidig, M., B. Stump, J. Bonner, C. Hayward, A. Velasco, D. Baker, H. Hooper, W. Walter, X. Yang, R. Zhou, C. Edwards, M. Renwald, and J. Lewkowicz**
Source Phenomenology Experiments in Arizona 427

4-07 **Mooney, W., S. Schulte, and S. Detweiler**
Intraplate Seismicity and the Discrimination of Nuclear Test Events Using an Updated Global Earthquake Catalog 439

4-08 **Phillips, W., H. Patton, S. Taylor, H. Hartse, and G. Randall**
Calibration for Coda Based Magnitude and Yield 449

4-09 **Rautian, T., V. Khalturin, W. Phillips, and P. Richards**
Explosion Source Phenomena Using Soviet Test Era Waveform Data 457

4-10 **Richardson, E., A. Nyblade, W. Walter, and A. Rodgers**
Seismic Source Characterization and Energy Partitioning from In-Mine and Regional Broadband Data in South Africa 467

4-11 **Sammis, C. and R. Biegel**
Mechanics of Strengthening in Crystalline Rock at Low Temperatures: A Preliminary Assessment 475

4-12 **Stevens, J., G. Baker, H. Xu, T. Bennett, N. Rimer, and S. Day**
The Physical Basis of Lg Generation by Explosion Sources 485

4-13 **Stevens, J., N. Rimer, H. Xu, J. Murphy, B. Barker, S. Gibbons, C. Lindholm, F. Ringdal, T. Kvaerna, and I. Kitov**
Analysis and Simulation of Cavity-Decoupled Chemical Explosions 495

4-14 **Toksoz, M., X. Li, M. Krasovec, and S. Chi**
Characterization of an Explosion Source in a Complex Medium by Modeling and Wavelet Domain Inversion 503

4-15 **Walter, W., K. Mayeda, A. Rodgers, S. Taylor, D. Dodge, E. Matzel, and M. Ganzberger**
Regional Seismic Identification Research: Processing, Transportability and Source Models 513

4-16 **Xie, J., A. Li, J. Zhang, and T. Hong**
A Study of Regional Wave Excitation by Clustered Underground Explosions Using a Reciprocal Theorem 523

4-17 **Yang, X., S. Taylor, M. Maceira, H. Patton, J. Rutledge, G. Randall, and M. Renwald**
Regional Event Identification Research in Eastern Asia 531

4-18 **Zhou, R., B. Stump, and C. Hayward**
Ms:Mb Discrimination Study of Mining Explosions in Wyoming, USA and Qianan, China 541

Theme Paper

TRENDS IN NUCLEAR EXPLOSION MONITORING

Dale N. Anderson[1], Raymond J. Willemann[5], Harry S. Miley[1], C. L. Edwards[2], Preston B. Herrington[3], J. Mark Harris[3], Joseph C. Wehlburg[3], David B. Harris[4], John J. Zucca[4], and Leslie A. Casey[5]

Pacific Northwest National Laboratory[1], Los Alamos National Laboratory[2], Sandia National Laboratories[3], Lawrence Livermore National Laboratory[4], and National Nuclear Security Administration[5]

Sponsored by National Nuclear Security Administration
Office of Nonproliferation Research and Engineering
Office of Defense Nuclear Nonproliferation

Contract No. DE-AC06-76RLO18304, W-7405-ENG-36, W-7405-ENG-48, DE-AC04-94AL85000

ABSTRACT

Nuclear explosion monitoring is as important today as it was at the dawn of the atomic age. Over the past several decades the scientific understanding and technological sophistication that underpin monitoring have advanced tremendously. We still face challenges, however, because the United States (U.S.) needs to monitor a growing range of events, from earthquakes to mining explosions that can cause confusion in detecting and identifying nuclear explosions.

Trends in nuclear test ban monitoring agreements reflect the challenge of global consensus building. We have seen the most pressing need change from monitoring large atmospheric tests to monitoring moratoria. Existing test ban agreements comprise bilateral and multilateral treaties in addition to declarations of moratoria.

As we grapple with real world realities, we benefit from science that has evolved and taken advantage of the data and processing capability provided by improved instrumentation and technology. Whereas once we modeled explosions as isotropic point sources, now we are developing ever more realistic distributed source models. Our understanding of radionuclide plume migration and infrasonic wave propagation was once based on ad hoc climate models, but now we have near-real-time weather models and realistic seasonal models of the upper atmosphere. As our science has matured, we have moved from investigating a broad range of topics with perhaps only an indirect monitoring connection to focused research with plans laid well in advance for integration into the monitoring system.

We have harvested the best of the revolution in communications. Data communication in the early 20th century consisted of manually prepared and typeset bulletins, or telexes for the most urgent transmissions. Today, we have real-time automated seismic alerts that soon will be transmitted over a global wireless broadband infrastructure. Data storage has moved from smoked paper or microfiche to random access memory (RAM) disks, sophisticated database systems, and disk arrays. Data processing has moved from slide rules and other types of analog computers, to mainframe computers, desktop workstations, and Linux clusters. The ways that we control digital data processing have evolved from coding in assembly language, to programming “high-level” languages such as Fortran, to integrating applications with platform independent web technology.

Trends in instrumentation are providing us with progressively more and better data, and at lower cost. Sensors have evolved from narrow band analog systems with limited dynamic range to high-fidelity, wideband, digital instruments with more than 120 decibels of dynamic range. Advancing technology has allowed us, in some cases, to replace custom-engineered components with commercial off-the-shelf products. Whereas observation stations were once manpower-demanding facilities, sensors now are progressively more autonomous, and the electrical power required by the stations can be provided by more compact facilities.

26th Seismic Research Review - Trends in Nuclear Explosion Monitoring

Introduction

The purpose of this paper is to state the obvious trends impacting nuclear explosion monitoring. While the overall mission of nuclear explosion monitoring has not changed since the beginning of the atomic age, what is being monitored has changed, as well as the technology used. Such an exposition of trends will hopefully provide insight and interesting context for this year's program review.

Monitoring Agreement Trends

From monitoring large atmospheric tests to monitoring moratoria – a monitoring agreement trend
The first test ban treaty, the Limited Test Ban Treaty (LTBT), initially signed by the U.S., the United Kingdom (U.K.) and the Soviet Union, and entered into force in 1963, was a multilateral treaty of profound impact. Prohibiting nuclear weapons tests in the atmosphere, in outer space, and under water was intended to achieve "an end to the contamination of man's environment by radioactive substances." Restricting nuclear tests to the underground environment also was instrumental in advancing seismology as a major field of science.

In anticipation of negotiations toward a comprehensive test ban treaty, the U.S. declared and entered a moratorium on any further nuclear testing in 1992, and other nuclear weapons states have made similar declarations. With the moratoria in effect, the drive to distinguish possible nuclear explosions from natural phenomena, and other explosions, represents a tremendous technical challenge.

From bilateral to multilateral test ban treaties – a monitoring agreement trend
The Threshold Test Ban Treaty (TTBT) is a bilateral treaty signed by the U.S. and the Soviet Union in 1974. The U.S and the Soviet Union agreed to verification provisions in 1990, and the treaty went into force that year. The TTBT limits weapon testing to specific designated test sites to assist verification and includes a protocol on technical data to be exchanged. The data to be exchanged – including rock density, water saturation, and depth of the water table – are useful in verifying test yields because the seismic signal produced by a given underground nuclear explosion varies with these factors at the test location. After an actual test has taken place, the geographic coordinates of the test location are to be furnished to the other party. This helps to place the test in the proper geological setting and therefore, in assessing the yield and thus determining that the 150 kT threshold, specified as the upper limit allowed, under the treaty, has not been exceeded.

The Comprehensive Nuclear-Test- Ban Treaty (CTBT) is a multilateral treaty that opened for signature in 1996 and has been signed by 172 member states as of August 2004 (http://www.ctbto.org/). The CTBT would ban all nuclear explosions for any purpose and in any environment. However, entry into force is unlikely in the foreseeable future because of opposition by several key countries, which are required to sign and ratify the treaty, but have stated that they will not sign. In the mean time, the Provisional Technical Secretariat is installing monitoring stations called for by the treaty, and data sharing amongst treaty signatories is ongoing. Even without the CTBT entering into force, in order to support the U.S. policy, there is a need to monitor for any nuclear testing occurring anywhere in the world.

Science Trends

From an isotropic point source to realistic source models – a science trend
Many measurements made at a sufficiently large distance from a source can be interpreted as if the source existed at a single point in space and time. Seismologists, for example, made great advances by treating earthquakes as point sources. These advances are locating earthquakes from the initial onset times of arrivals, discovering the existence and sizes of major parts of the earth, and measuring relative sizes of earthquakes from maximum amplitudes. As seismologists know, even the determination of seismic moment tensors, to learn the "shape" and orientation of the stresses related to a fault slip, represents an earthquake as a point in space and time.

Therefore, it is hardly surprising that the seismic study of underground explosions began with the assumption that an explosion might be quite well approximated as point sources, with a purely isotropic moment tensor to represent their force system. This representation provides a physical basis for understanding many of the methods for distinguishing explosions from earthquakes, including the predominance of P wave energy over S wave energy and the absence of a simple spatial pattern in the polarity and amplitude of P wave amplitudes.

For a variety of reasons, some of which we still only partly understand, seismic observations do not completely match predictions based on an isotropic point source model. Some of the likely causes, such as tectonic release and spall, are well known and might be represented by including nonisotropic (double-couple and CLVD) terms in a point source moment tensor. Scattering from topography and internal structure may play a role in generating S waves larger than we would otherwise suspect. Nevertheless, transverse S wave amplitudes are sometimes inexplicably large in the absence of other evidence for tectonic release. The Murphy-Mueller source model has come to be widely used, but also has its limitations. New models that better represent the frequency-dependence and source-size scaling of S wave amplitudes are being developed. It remains to be seen how best to evaluate these new models in the absence of further very large underground explosions.

Source models in other monitoring domains are also inadequate. In the ocean, the source of laterally propagating hydroacoustic waves from under-sea earthquakes is still not completely solved. In the atmosphere, further small explosions at different altitudes may be necessary to develop a good infrasonic source model.

From simple, homogeneous earth models to more realistic heterogeneous stochastic models – a science trend
Seismic monitoring of nuclear explosions began as a principally teleseismic discipline. At great range, seismic wave propagation paths dive deep into the interior of the earth, traveling predominantly through relatively simple, homogeneous portions of the planet. To predict travel times and other seismic wave characteristics, monitoring groups turned to the models of the earth devised from teleseismic observations – principally constructed as a series of homogeneous concentric spherical shells. This level of earth model sophistication sufficed for monitoring compliance with the LTBT and TTBT treaties.

In the last two decades, monitoring practice has been shifting from teleseismic to regional scales, especially with the advent of the CTBT. The propagation paths for the relevant seismic waves are in the relatively heterogeneous upper mantle and crust, leading to far more significant variations in waveforms, and waveform parameters such as phase arrival times and amplitudes. The simple models of the past are inadequate to predict regional observations. Higher resolution models estimated tomographically with the many millions of regional observations are one of the principal trends, and are needed to detect, locate and identify the very small events likely to be of current or future monitoring interest. Higher resolution models are one of the principal motivations and justifications for large-scale database development and the use of massively parallel computing resources (Linux clusters) alluded to earlier.

No matter how many observations are available, there will always be a limit to the resolution of geophysical models of the earth. Earth models will be uncertain at all scales, with the degree of uncertainty increasing at smaller and smaller scales. An alternative to the deterministic models of the past is the representation of the earth with stochastic geophysical models. These and the radically different tomographic algorithms required to develop them offer the possibility of properly accounting for model and observational uncertainties, incorporating prior constraints and using disparate data types simultaneously to constrain geophysical structure. Stochastic models offer an even greater justification for the use of strategic computing, now becoming widely available.

From linear extrapolation to kriging – a science trend
High-resolution seismic velocity models, real-time weather models, and empirical travel times, from events with ground truth locations, self-evidently have the potential to improve locations of seismic or infrasonic events. But in attempting to use these models, and empirical data, we are faced with the question of how to compute a new location using signals that may have propagated outside of the model or in the vicinity of several empirically calibrated paths. Simple-minded interpolation or extrapolation is not the best solution, since we already have background velocity models. Ground-based nuclear explosion monitoring (GNEM) has been in the forefront of implementing kriging in order to best take advantage of the empirical travel times, the best regional velocity models, and background models. Kriging will continue to be an important tool as we collect more ground truth locations and develop better regional models for more areas.

From maximum intensity to MDAC – a science trend
An frequently repeated remark, in historical seismology and seismic hazard analysis, is that the sizes of earthquakes that occurred before the 20th century are less certain because there were no seismograph stations to record them. The work of Charles Richter and other seismologists, in creating a means to compare the sizes of different earthquakes, is well known to all seismologists and is perhaps the seismological accomplishment that is most widely known among the general public. Defining different magnitude scales for earthquakes that were reliably observed

only as long-period surface waves, teleseismic body waves, or as a particular regional phase was another important success, even if it sometimes confused non-seismologists. A logarithmic magnitude scale has come to be so widely used and understood that magnitudes of historical earthquakes now are estimated retrospectively by analyzing intensity reports. Even physically based, absolute measures of earthquake size, such as seismic moment and radiated seismic energy, are often expressed using magnitude scales (M_W and M_E) that are designed to be as consistent as possible with established magnitudes.

Several of the most sophisticated ways of analyzing seismic amplitudes have been developed to support nuclear explosion monitoring. One of these is maximum likelihood magnitude, based on the absence of measurable amplitudes at some stations, or upper bound magnitude, if no appropriate amplitude can be measured at any station. Another is local and regional coda magnitude, which is important for small events recorded at just a few stations because it takes advantage of scattering so that each station can represent an average, of a significant portion, of the focal sphere. Use of magnitude-distance-amplitude-corrections (MDAC) replaces the classical use of teleseismic m_b:M_S ratios in explosion monitoring, instead basing event identification directly on amplitudes that have been corrected for event size or yield.

Coda magnitudes and MDAC analysis are each part of a broader trend to tie event location and identification closer to the waveform data. As we move forward, we are likely to place far less emphasis on making simple measurements from waveforms, computing source parameters from the measurements, and making inferences about the event from the source parameters. Instead, source parameters are likely to be computed directly from waveforms. Eventually, we may make inferences about events by comparing new waveforms with libraries of observed waveforms from previous events, and with synthetic waveforms computed from realistic source models and stochastic earth models.

From ad hoc climate models to near-real-time weather models – a science trend
Seismology, as a GNEM science, fundamentally requires numerical measurements of seismic phase travel times. The numerical knowledge of how a seismic phase travels though the interior of the earth provides the capability to detect, associate/locate, and identify events. An equivalent capability is necessary to fully realize the power of radionuclide signatures. Observation of certain radionuclides indicates with physical certainty that a nuclear weapon test has occurred; what is missing is a technically sound assertion of the source location of the radionuclides. Understanding the pathways from source to sensor, that a nuclear particle can traverse, will provide a location estimation capability. Initially, this capability may serve as confirmatory to a seismic location estimate. However, climate and weather model research is an active scientific field and it is fully expected that this research will be leveraged into GNEM capabilities. As the integration of regional weather models and real-time observations increases in maturity, detection of radionuclides could become a principal indicator that a nuclear test has occurred.

Because the signals for infrasound and radionuclide systems are often transmitted through the air, one of the main sources of errors in location for these techniques has been modeling the effects of weather. In the past, data from weather balloons and ground stations was collected by hand and would be used to retrace what the weather conditions were. The improvements in data acquisition systems and networking allows almost real-time data to be inserted into vastly improved numerical modeling codes to predict what the weather patterns were at the time of the event and the changes in them after the event. As satellite data becomes more available many of the models now also incorporate higher resolution, National Oceanic and Atmospheric Administration (NOAA) and Defense Meteorological Satellite Program (DMSP), data.

From ray theory to spectral elements – a science trend
The “infinite frequency” approximation of the ray theory has, like point source models, been a useful tool for many of the fundamental discoveries in seismology. The ray theory was used to compute accurate depths of boundaries between major parts of the earth, and is still used today in many tomographic inversions for three-dimensional earth structure. Ray theory is used to compute derivatives of travel times when locating seismic events and to compute “take-off” angles when determining fault plane solutions from P wave first motions, pP/P amplitude ratios, and S wave polarizations.

But interpreting information in seismograms beyond the initial motion of arrivals requires more complete solutions of the wave equation. Modal theory serves seismologists well in interpreting surface waves and free oscillations, and the WKBJ approximation is useful in many situations requiring synthetic seismograms computed from one-

dimensional earth models. In regional seismology, however, we require wave equation solutions for earth models that depart significantly from laterally homogeneous, isotropic and/or perfectly linearly elastic. This requirement leads us to undertake computationally intensive numerical modeling of propagation, even if only to develop simpler yet reliable ways of monitoring earthquake and explosion monitoring.

Among the computationally-intensive methods for solving the full wave equation, finite differences is appealing because of its conceptual simplicity, straightforward implementation, and proven utility in a wide range of engineering and scientific applications. Unfortunately, finite difference solutions to the wave equation introduce nonphysical artifacts that grow to be significant if used to simulate propagation to the distances that we require. This problem has been worked around in a variety of ingenious approaches to coupling finite difference calculations in small regions with more analytical methods for simulating propagation over typical distances to stations. We may be in the midst of yet another revolution in numerical simulation of propagation. The spectral element method eliminates the artifacts inherent in finite difference simulation of wave propagation and computers, which we can expect within approximately ten years, should be capable of spectral element calculations at the frequencies and distances that we require for almost all applications.

From research reports to integrated research products – a science trend
To successfully monitor for nuclear explosions, access to large quantities of detailed technical and contextual information is needed. The smaller, regional distance events, expected in the emerging monitoring environment, require a significant increase in the amount, type, and detail of information provided to both automated systems and human analysts. The interdependences among research products contributed to the operational user are a challenge that cannot be met without diverting limited resources away from operations. Therefore, it is necessary to integrate the research products prior to delivery to the user. The National Nuclear Security Administration (NNSA) Knowledge Base aims to provide this mass of information in a form that is ordered, consistent, easily accessed, well documented, reproducible, accurate, and relevant. The integration process is published (Gallegos, et al. 2003) along with a contributor's guide (Carr, 2003) so that less iteration is required and broad participation in the integration process is possible.

Technology Trends

From manual bulletins to real-time automated alerts – a technology trend
After inventing one of the first seismometers that could be readily replicated, transported, and installed in many remote locations, in the first decade of the 20th century, John Milne began to routinely compile locations and times of earthquakes around the world. Milne's data collection was facilitated by the existence of the British Empire, but in an era when printed reports of arrival times were manually typeset and transported by ship publication was, nevertheless, delayed until years after the earthquakes. Even with this delay, many of the epicenters were not computed from arrival times at all because of tedious manual computations that were abandoned if Milne or his assistant recognized that the pattern of arrival time differences was not significantly different than the pattern of another earthquake.

Milne's compilation evolved into the International Seismological Summary (ISS), published originally by the British Association for the Advancement of Science and later by the British Geological Survey. Like other summaries prepared during the first half of the 20th century, the ISS was published years after the earthquakes. Computations were greatly aided by the use of an analog computer that consisted of a large globe inscribed with the locations of important seismological observatories, and a brace with a slider and a pencil for tracing arcs around the stations and distance inferred from S minus P times. Thus, even epicenters far from major cities could be given to an accuracy of one-half or even one-quarter degree of longitude and latitude.

The ISS and several other global summaries were superseded by the more standardized and comprehensive "Bulletin of the International Seismological Centre". The ISC granted free use, at night, of new-fangled digital computers in the banks of Edinburgh. The ISC staff finally implemented routine use of the already venerable "Geiger's method" for iteratively solving the nonlinear equations, leading to epicenters with unreasonable precision and wildly optimistic uncertainties.

Since then, the U.S. National Earthquake Information Center (NEIC) has been among the agencies producing ever more timely global earthquake bulletins. Today NEIC produces its daily global report, "Quick Epicenter

Determinations", one week after the earthquakes. Global earthquake bulletins were produced within a day for a very short time, during the Group of Scientific Experts Technical Test 2 (GSETT-2), and continuously, since January 1, 1995 for GSETT-3 and later by the CTBTO International Data Centre (IDC). Completeness of the GSETT-3 and IDC bulletins depends partly on automatically generating an event list within one hour and then retrieving waveform segments from auxiliary stations near the preliminary event locations.

Automated alerts for significant earthquakes around the world are now available within an hour from several sources, including the NEIC and the European-Mediterranean Seismological Centre (EMSC). The NEIC and EMSC alerts both depend on real-time international exchange of seismic data, which is now widespread. Automation has facilitated distributing alerts minutes after moderate earthquakes within many regional seismic networks, and initiating emergency responses seconds after citywide dense networks of accelerometers detect dangerous seismic shaking. The U.S. Advanced National Seismic System is planned to provide a range of different types of information products for significant earthquakes in the U.S., beginning with location information within tens of seconds to minutes and shake maps within tens of minutes.

From telexes to global wireless broadband – a technology trend

For almost any type of earth observation, what can be learned from a network vastly exceeds the sum of what can be learned from each station in isolation. Thus, to a greater degree than laboratory sciences, earth sciences require prompt and effective data exchange. This requirement has engendered a history of cooperation among most earth scientists and prompted early and continued development of effective data exchange infrastructure.

The earliest international exchanges of seismic data involved shipping typeset reports of arrival picks to other seismological observatories. As transoceanic cables became more common, telex came to be widely used to exchange seismic data promptly. The 1979 edition of the Manual of Seismic Observatory Practice (Wilmore, 1979) describes a standardized format for telexing seismic arrival times and amplitudes. Telexes were expensive and charged by the character, so seismic telex format compromises completeness (e.g., the year of the arrivals is not required) in favor of brevity. While reports of arrivals times are no longer exchanged in telexes, this history echoes into our time in the form of e-mails formatted in seismic telex format.

Exchanging waveforms was difficult early in the 20th century, when data were recorded as ink on paper or as traces in smoked paper. Xerox machines made it easier to exchange waveforms, and dispatching Xeroxes of waveforms requested by professional seismologists became an important responsibility of seismic observatories. WWSSN waveforms were recorded on microfilm, which was reproduced and distributed to several archives. Even seismologists as young as the authors of this paper have spent time in WWSSN film archives extracting data for their early projects.

Digital recording revolutionized our ability to exchange data. More than a decade before the music industry realized the implications of all but perfect reproduction of digital data, seismologists eagerly established digital waveform centers to make waveforms widely available. Long before web users complained about slow downloads, seismologists saw the limitations of the Internet and resorted to exchanging computer tapes. In the 1990's AutoDRM servers came to be a common means of offering automated responses to e-mail data requests. Today, many stations and networks maintain web sites with routinely updated images of their most recent data as well as web browser-based interfaces for retrieving waveform segments.

Seismologists have been transmitting continuous waveforms, at least over short distances, using radio-frequency analog signals for 30 years. For the past 10 years, at stations with sufficient infrastructure, the Internet has been used to re-transmit 24-bit, 40 s.p.s. 3-component continuous waveforms around the world, and the Albuquerque Seismic Laboratory's Live Internet Seismic Server (LISS) has helped us to avoid collectively overwhelming links to individual stations. Nevertheless, transmitting data with absolute security and reliability still requires expensive installation of a dedicated system, as is being pursued by the Comprehensive Nuclear Test Ban Treaty Organization with its Global Communications Infrastructure. In the future, with the establishment of global wireless broadband communications, multicasting technology may eliminate the need for discipline-specific tools such as LISS, we look forward to more readily starting transmission of data from newly installed stations such as PASSCAL deployments, and we hope to transmit continuous authenticated digital waveforms in near-real-time from remote sites almost anywhere in the world, even without reliable and plentiful electrical power. Widespread deployment of the

available advances in communications technology bodes well for monitoring ease and reliability, and the technology is still advancing rapidly.

From microfiche to RAM disks – a technology trend
The early data generated by GNEM monitoring systems was very likely to be waveforms on paper rolls or film. This demanded a large group of well-trained analysts to evaluate the data by hand. Data was only collected when the roll of paper needed to be replaced and there was a much greater risk of failure from complex mechanical systems. The trend from analog data to digital data has permitted individual stations to not only store an almost unlimited amount of data, but has also increased reliability. Now a single analyst can download data from many of the different GNEM stations in real-time to allow one-person access to data from a large number of stations simultaneously. This allows a smaller number of analysts to bring together all the resources that are needed to solve a problem. The reduced cost of on-site storage has also provided a large buffer against data loss by allowing a longer period of time for network repairs to be made before any data will be lost.

From slide rules to Linux clusters – a technology trend
CPU power and memory size has historically followed Moore's Law – a doubling every 18 months. All of 25 years ago, the calculation time for the inverse of a 15 by 15 matrix was measured in tens of minutes. Today that same inverse can be calculated in fractions of a second. Dual processor workstations are readily available today, while 25 years ago the desktop computing environment was rare.

Present computing possibilities also include super-computers that are constructed by gluing together (with wires and software) desktop computers. Users on a super-computer "LAN" can use all available CPU cycles from idle desktop systems. The future of research computation will include "LAN" type super-computers with mostly open source operating systems (e.g. Linux) and abundant technical software that is constructed from open source code. Recently, for example, a Linux cluster version of the Community Climate System Model (CCSM) was released that achieves 80% of the performance of the CCSM on a supercomputer using processors that are 10 times less expensive (Renold, 2004).

The scientific research environment of the future may be limited only by the sophistication of software and the efficiency of the human-computer interface. The gap between analysis speed and human thought will be reduced dramatically as computer input evolves to include voice and finger-touch interaction.

From hand-coded assembly language to platform independent web technology – a technology trend
No one would disagree that the common language of science is mathematics. However as the computer became a research tool, other scientific languages emerged. Mathematics was translated to assembler code in the early days of the computer and through the evolution of the computer the research and business world has seen FORTRAN, BASIC, PASCAL, COBOL, C++ and many other languages, each with their claim as "the" language of the future. No less is true of operating systems. As with all modern scientific endeavors, GNEM is a mission filled with diverse computer platforms, operating systems and analysis codes. In the context of scientific computation, efficient communication of analysis results to a broader audience is becoming very important. This is driven to a great degree by the cross-disciplinary nature of GNEM. The broad communication expectations on the GNEM community will become sharpened in the future and will fully utilize the World Wide Web. Platform independent web tools will, in the future, provide the capability to seamlessly link operating systems and analysis codes. From a web tool, a scientist will be able to access and run a diverse suite of analysis codes and distribute the analysis to colleagues around the globe in a fraction of a second.

The earliest computer programmers using assembly language had to write sequences of instructions that explicitly copied values to input registers, executed multiplication instructions, and saved values from output registers. Subsequently, "high-level" languages, such as C and Fortran allowed, programmers to concentrate on aspects of an algorithm that are closely related to the original problem and to trust the compiler to create the machine-level instructions. This great advance allowed several generations of seismologists to write ever more complex programs, often with little help from professional programmers. These programs helped to advance our science tremendously, based on acceptable, if sometimes quirky, implementations of wide ranges of algorithms for locating earthquakes and computing synthetic seismograms, among many other tasks.

These user-written computer programs also created their own problems. Despite the use of high-level languages, programs written for one computer often would work on no other computer. Subroutines that performed reliably in one program produced nonsense when used in another program. When one program needed results from another, it sometimes seemed as if the only way to communicate the results was for a person to read the first results and manually type them into the other program. Modifying a program to produce a slightly different result, or to store the result in a different data system, seemed to take longer than it took to write the program originally. Effectively monitoring even the smallest nuclear explosions requires us to deal with pervasive clutter that includes earthquakes, mining explosions and bolides. Thus, monitoring requires an efficient interactive decision-support system that integrates data from different sensor types, uses a wide variety of background or historical information, and carries out routine processing reliably. The complex requirements for the complete system require several cross-disciplinary teams, who may use different types of computer hardware, programming languages, and data systems. Assembling their diverse components into a reliable and efficient system requires us to take advantage of the latest and best tools, including object-oriented programming and web technology for interprocess communication.

From file cabinets to databases with sophisticated search engines – a technology trend
Seismology often is at its best when comparing the differences between related seismic events (interpreting relative observations) and when extracting patterns from large numbers of observations. For these reasons the discipline is concerned more than most with record keeping, and assembling long-term, large-scale, permanent archives. In the early years records were kept in file cabinets and libraries of permanent paper catalogs of seismic events. These were difficult to search when seeking past events for comparison with new events and expensive to maintain. Catalogs devised by many individual observatories around the planet were inconsistent in format and difficult to collate and reconcile manually.

Electronic databases developed for the business sector were adapted to the seismological archival task in the 80's and 90's. These reduced the cost of maintaining archives and made possible efficient, large-scale searches for events and observations needed to carry out monitoring research and development. Database holdings on the scale of a few million events and many tens of millions of event parameters and waveforms are becoming the standard for cutting-edge research in this empirical discipline. Seismology is in a transition from ad hoc analysis of small collections of events to large-scale systematic searches for patterns.

Databases increasingly are the engines for integration of many scientific results. Automatic catalog reconciliation is now a reality for scores of formats. Databases are used to integrate and index waveform observations from thousands of stations in many formats into structured collections of uniform data amenable to sophisticated data mining approaches. Increasingly the construction of databases will be automated with autonomous agents scouring the Web for new catalog results and waveform data collected across the Internet in continuous streams. The convergence of communication technology, storage technology, sophisticated software tool development and database technology will put terabytes of organized information in the hands of researchers through largely automated processes.

Instrumentation Trends

From sensors as filters to high-fidelity instruments – an instrumentation trend
The expected seismic, hydroacoustic or infrasonic record of an event can be written as a convolution of a source function with several filters that represent the response of the earth and the seismic sensing and recording system. The objective of sensor engineering is to design a system that represents earth motion as truly as possible, thus minimizing information filtered out of the record by the instrumentation

Many seismometers from the very early 20th century produced signals for earth vibrations only in a narrow frequency band, and sometimes in a band that was not especially useful. Due to limited engineering, in addition, some early seismometers were under damped and consequently suffered resonances that might obscure all information other than the initial arrival time. Instruments of the World Wide Standardized Seismograph Network (WWSSN) were deliberately designed with non-overlapping passbands to exclude microseisms induced by atmospheric storms over ocean. Many instruments had frequency-dependent phase delays and a dynamic range that prevented them from recording either the smallest detectable signals or signals from the largest earthquakes.

Seismometers in the 21st century have overcome most of the previous limitations. The use of force-balance accelerometers (FBAs) has expanded the dynamic range of sensors to the point that very few applications cannot be met. Further development of the electronics in FBAs has expanded the passband so that now seismologists anticipate sensors that are effective from several tens of Hz to the fundamental periods of lunar and solar tides. Digital recording, with its wide dynamic range and its potential for subsequent digital filtering when necessary, has obviated the need to avoid sensing microseism frequencies. For all but the most demanding applications, moderately broadband sensors are affordable and can be readily installed and maintained. Thus, quite rapidly now, broadband stations are being much more widely deployed in both permanent and temporary networks.

From custom-engineering to COTS – an instrumentation trend
At the start of the ground-based nuclear explosion monitoring (GNEM) program, systems were typically constructed as one-of-a-kind custom designed systems that could accomplish the tasks, but were expensive and difficult to maintain or upgrade. As a general push in engineering to save money and to leverage previous design work, the GNEM program has moved in the direction of COTS equipment whenever possible. Using COTS equipment has resulted in teaming with industry to promote development of off-the-shelf equipment that meets or exceeds the requirements for many of the computational and data acquisition subsystems being used by the current monitoring technologies.

Radionuclide sensors have come to rely on commercial production of several components. For the Automated Radioxenon Sampler/Analyzer (ARSA), which has hundreds of valves in each unit, commercial production provides us with affordable very low temperature valves that are sufficiently small to avoid unacceptable product losses. The ARSA data acquisition system also depends on commercial products, in this case laboratory electronic building blocks known as Nuclear Instrumentation Method (NIM) modules. The electronic coincidence system for future Radionuclide Aerosol Sampler Analyzer (RASA) devices is also based on commercial electronics components.

From manpower-demanding monitoring stations to autonomous stations – an instrumentation trend
Teams of seismologists, engineers and technicians often operated the earliest seismic stations. Installing a seismometer sometimes resulted in the development of an entire Observatory Institute. Seismologists at the Observatory Institute were responsible for overseeing a variety of maintenance tasks, for interpreting the records of the seismometers, and for communicating their interpretations (but often not the original records) to the world. The Observatory Institute seismologists developed skills that were unique to their particular site that might enable them, for example, to recognize the seismogenic zone from which a signal originated from a mere glance at the data.

The early days of operating a global network for teleseismic monitoring of large nuclear explosions involved deploying large detachments of personnel. Even if the sensors themselves could operate unattended, the associated gear to transmit data from array elements and record it at a central site required regular maintenance and daily operational work. Detachment personnel again developed skills that were unique to their particular site.

Single-site stations and arrays now are expected to operate without maintenance for months at a time, recording data locally or transmitting it to an analysis center that might be located anywhere in the world. Near-ground radio transmission of data, especially from array elements where power may be very limited to a central recording or transmission-relay site, remains less reliable than other aspects of station operations, requiring a mobile maintenance staff for station repairs. Staff members at the analysis center develop network-wide skills that enable them to recognize correlations and inconsistencies among the data from different stations.

In the future, a common point of failure represented by an array's central site will be eliminated. Even within the power requirements at array elements, communication within arrays using global wireless communication technology may be used for preliminary processing. If bandwidth limitations delay transmission of continuous data, then data segments may be transmitted to a remote analysis center based on evaluation from the preliminary processing or demands from the analysis center.

From car batteries to fuel cells – an instrumentation trend
In a typical modern station, an external source of electrical power is required for the digitizer, the data logger, the clock, and (since we no longer use passive pendulum seismometers for many applications) the sensor. A permanent station must be connected to the electric power grid but still requires a backup battery for reliable operations, and the

battery unit is probably an Uninterruptible Power Supply (UPS) that executes a controlled shutdown if power is lost for so long that the battery runs low.

Temporary stations deployed far from any infrastructure will have the same types of electrical gear as a permanent station, and perhaps a transmitter as well. Thirty years ago, many field systems that integrated the digitizer, clock and data logger (such as the Sprengnether DR-100) could run on 12-volt DC power. This was a convenient standard, since the power requirements were substantial and 12-volt car batteries are readily available almost anywhere in the U.S.. A fully charged car battery could operate a DR-100 for about one week. A motel with a door to the outside was preferable to one with a door to an interior hallway, so that a battery could be left charging outside the door each night. Typical field gear included several pairs of jeans with holes where battery acid had spilled on them during previous deployments. Using a common "COTS" power source had a downside: battery theft was a significant cause for station down time, and sometimes necessitated moving a station.

Today, low-power active sensors, digitizers and recorders require approximately 1 Watt of power each for a 3-component system. A transmitter may require substantially more power, depending on the distance to the receiver and the transmission technology. Solar panel-charged batteries allow such systems to operate for months at a time, but the visibility of the solar panels increases risks to the station, including vandalism and theft. Further reduction in power consumption is being actively pursued, and within several years we might expect to require less than 1 Watt in total for all of the systems required at a station. Fuel cells with external fuel tanks (which could be buried) probably can replace solar panels in the near future. At current best efficiency, 1 liter of methanol drives a 1Watt system for 100 days. The Defense Advanced Research Projects Agency (DARPA) foresees a doubling of usable energy density by 2008, and a further re-doubling by 2018 to 2025 (Nowak, 2000).

Summary

As we look ahead, it is useful to see how far we have come in monitoring nuclear explosions. True global consensus on banning nuclear tests remains elusive in spite of significant agreement: from monitoring large atmospheric tests to monitoring moratoria; and from bilateral to multilateral test ban treaties.

Science understanding continues to grow: from an isotropic point source to realistic source models; from homogeneous earth models to heterogeneous stochastic models; from linear extrapolation to kriging; from maximum intensity to MDAC; from ad hoc climate models to near-real-time weather models; from ray theory to spectral elements; and from delivering research reports to integrating research products for operational usefulness prior to delivery.

Technology has dramatically changed how the monitoring data is recorded and analyzed: from manual bulletins to real-time automated alerts; from telexes to global wireless broadband; from microfiche to RAM disks; from slide rules to Linux clusters; and from hand-coded assembly language to platform independent web technology; and from file cabinets to databases.

Instrumentation improvements have provided for the collection of more and better data: from sensors as filters to high-fidelity instruments; from custom-engineering to COTS; from manpower-demanding monitoring stations to autonomous sensors; and from car batteries to fuel cells.

These trends suggest that a next generation monitoring system should integrate the best of the science, technology and instrumentation trends to further monitoring and global consensus on test bans. Such a system would clearly move toward more autonomous sensors, advanced event characterization and improved understanding of what is being monitored.

Acknowledgements

We are grateful to Dr. Gerald P. Kiernan for a constructive review of this paper. This paper describes only a selection of many trends in nuclear explosion monitoring; it is limited to ground-based methods and emphasizes seismology among those ground-based methods. Numerous positive trends in nuclear explosion monitoring, in seismology, in other ground-based methods, and in satellite-based methods, have been possible due to contributions

over many years from a broad community of researchers. Those of us with the privilege of working in the GNEM R&E Program thank the research community for their outstanding work.

References

Carr, D. (2003), *National Nuclear Security Administration Knowledge Base Contributor's Guide*, (Sandia National Laboratories, SAND2002-2771 Revised August 2003), 22pp.

Gallegos, D.P., D.B. Carr, C.J. Young, P.B. Herrington, J.M. Harris, C.L. Edwards, S.R. Taylor, J.C. Aguilar-Chang, J.J. Zucca, D.B. Harris, D.N. Anderson and L.A. Casey (2003), *The Integration Process for Incorporating Nuclear Explosion Monitoring Research Results into the National Nuclear Security Administration Knowledge Base*, (SAND2002-2772 Revised).

Nowak, R. J. (2000), DARPA's Advanced Energy Technologies, *DARPATech2000* (http://www.darpa.mil/DARPATech2000/Presentations/dso_pdf/4NowakAdvancedEnergyB&W.pdf).

Renold, M., U. Beyerle, C.C. Raible, R. Knutti and T.E. Stocker and T. Craig (2004), Climate modeling on a Linux cluster, *Eos, v85*, p290.

Willmore, P. L. (1979), *Manual of Seismological Observatory Practice*, (National Oceanic and Atmospheric Administration, Boulder, CO).

Seismic Regional Characterization and Wave Propagation

SIMULTANEOUS INVERSION OF RECEIVER FUNCTIONS, MULTI-MODE DISPERSION, AND TRAVEL-TIME TOMOGRAPHY FOR LITHOSPHERIC STRUCTURE BENEATH THE MIDDLE EAST AND NORTH AFRICA

Charles J. Ammon[1], Minoo Kosarian[1], Robert B. Herrmann[2], Michael E. Pasyanos[3], William R. Walter[3], and Hrvoje Tkalcic[3]

Penn State University[1], Saint Louis University[2], Lawrence Livermore National Laboratory[3]

Sponsored by Air Force Research Laboratory
and
National Nuclear Security Administration
Office of Nonproliferation Research and Engineering
Office of Defense Nuclear Nonproliferation

Contract No. DE-FC03-02SF22498[1], DTRA01-02-C-0038[2], W-7405-ENG-48[3]

ABSTRACT

This paper reports on the initial investigations into the seismic structure of the lithosphere in the Middle East and North Africa (MENA) using surface waves and receiver functions. Collections of prior work in the region and computing receiver functions, for use in the joint inversion, has been initiated. Critical to the joint inversion is surface-wave dispersion information localized to approximately the same region sampled by receiver functions. We continue to improve our surface-wave dispersion model of western Eurasia and North Africa and have developed group velocity maps at two-degree resolution for both Love and Rayleigh waves from 10 to 100 seconds period. The model shows an excellent relationship to tectonic structure and group velocity variations correlate well with orogenic zones, cratons, sedimentary basins, and rift zones. We have recently implemented a variable-resolution tomography and have pushed the resolution of the model down to one-degree in areas with sufficient density sampling. Our paper presents information on the complexity of the receiver structure at many permanent sites in the region and several illustrative inversions for the lithospheric structure. We have examined receiver functions at over 70 stations in western Eurasia and North Africa and have inverted a number using dispersion measurement from global and regional tomographic models. A comparison of the crustal thickness and Poisson's ratio estimates for the crust beneath these stations will be presented. Other work on the combination of additional observations (body-wave travel times, higher-mode observations, surface-wave polarization information) is planned for future stages of the project, however we include illustrations outlining our ideas for the use of these data to help further constrain the seismic structure of the lithosphere. Access information to on-line information (results, earth models, etc.) will also be provided.

OBJECTIVES

Our objectives are the construction of shear-velocity profiles for regions surrounding broad-band seismic stations throughout the Middle East, central and north Africa, and parts of western Europe. Application of the technique in the MENA region provides an opportunity to revise models of the crust and upper mantle structure throughout the region and to exploit the global and regional work of previous seismic verification research (e.g. Pasyanos *et al.*, 2001; Ritzwoller & Levshin, 1998, Larson *et al.*, 2001). The resulting shear-velocity models provide a single structure consistent with a range of observations and that can be tested as a tool for the construction of mode isolation filters that can help improve the surface-wave magnitude estimate. We also plan to explore the possibility of adding additional data to our inversions of receiver functions and surface-wave dispersion. The diverse seismic activity throughout the region will facilitate cross-validation of the mode isolation filters with simple empirical filters constructed using larger events with adequate signal-to-noise ratios (SNR).

Background

Much of the background for this project is identical to that found in “Simultaneous Inversion of Receiver Functions, Multi-Mode Dispersion, and Travel-Time Tomography for Lithospheric Structure Beneath the Middle East and North Africa”, by Ammon *et al.*, which appears elsewhere in these proceedings. We refer the reader to this other work for additional background information.

RESEARCH ACCOMPLISHED

Receiver Function Computation

The first step in this project is the selection of target stations and the computation of receiver functions at those stations. To begin, we have a selected a subset of permanent stations that have relatively long recording histories and thus will have substantial data already available. More recently installed stations and temporary operating stations will be added later in the project. The data processed at the time this report was written are shown in Figure 1. We plan to include all available temporary and permanent stations within central and northern Africa, the Middle East, and parts of Europe. Sixty-nine stations, to date, have been investigated; 36 in Africa, 34 in the Middle East, and 24 stations in southern Europe.

Poisson’s Ratio and Crustal Thickness Estimation

As a first step in the receiver function analysis the receiver function stacking method of Zhu and Kanamori [2000] is used to estimate the crustal thickness and Vp/Vs velocity ratio (or Poisson’s ratio). The stacking method makes a rather limiting assumption of a uniform crust but the analysis provides good estimates of these quantities when the structure is relatively simple. The estimated values of Poisson’s ratios can be used in subsequent inversions that require some assumed value of bulk crustal Poisson’s ratio. The current results are summarized in Figure 2. If a station appears twice, that indicates that a significant azimuthal variation was observed (which may indicate a likely failure of this simple imaging approach). Crustal thickness estimates agree on average with the global crustal model 2.0, but at times the differences are significant (greater than 5 km). The mean difference between our results and Crust 2.0 is about 1 km and the standard deviation of the differences is about 7 km, which is larger than the resolution we have on stations with stable receiver functions (probably between, 2.5 to 5 km). The numbers agree more closely when we rank our estimates using the complexity of the observed receiver functions. The estimated Vp/Vs values for each station are shown at the bottom of Figure 2. The shaded region shows a liberal range that is typical for the continental crust. For the most part, our results are showing up lower than average (Zandt and Ammon, 1995). More analysis and the incorporation of quality factors is needed to assess the significance of this observation.

Tomographic Imaging of Group-Velocity Variations

A large-scale study of surface-wave group velocity dispersion across western Eurasia and north Africa (Pasyanos, 2002) has been carried out. This study expands the coverage area northwards relative to previous work (Pasyanos *et al.*, 2001), which covered only north Africa and the Middle East. As a result, we have increased, by about 50%, the

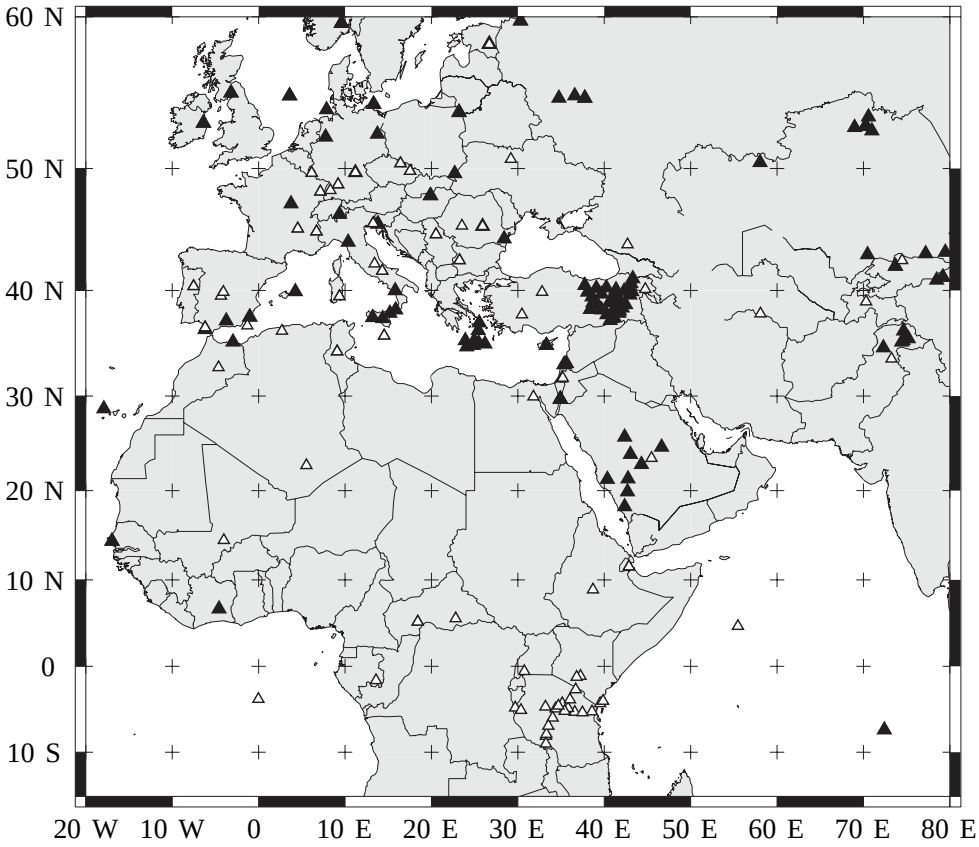


Figure 1. Available permanent and temporary three-component seismic stations in the research area. Shear-wave velocity inversions have been computed for the stations with white triangles. Shaded symbol indicate stations for which we have data, but have not yet completed our analyses.

number of seismograms examined and group velocity measurements made. Good quality dispersion measurements for about 10,000 Rayleigh wave and 6,000 Love wave paths have been made into this study, incorporating measurements from several other researchers. A conjugate gradient method to perform a group velocity tomography was used. We have improved our inversion from the previous study by adopting a variable smoothness (Pasyanos, 2002). This technique allows us to go to higher resolutions, where the data allow, without producing artifacts. Our current results include both Love and Rayleigh wave inversions across the region for periods from 10 to 100 seconds. Figure 3 shows the inversion results for Rayleigh waves at periods of 20 and 50 seconds. Short period group velocities are sensitive to slow velocities associated with large sedimentary features such as the Russian Platform, Mediterranean Sea, and the Persian Gulf. Intermediate periods are sensitive to differences in crustal thickness, such as those between oceanic and continental crust or along orogenic zones. At longer periods, we find fast velocities beneath cratons and slow upper mantle velocities along rift systems and the Tethys Belt.

The Joint Inversion of Receiver Functions and Surface-Wave Dispersion Curves

The receiver function is sensitive to velocity transitions and vertical travel times, surface-wave dispersion measurements are sensitive to aver-ages of the velocities, and relatively insensitive to sharp velocity contrasts. The complementary nature of the signals makes them ideal selections for joint study because they can fill in resolution gaps of each data set. Ammon and Zandt (1993) pointed this out in a study of the Landers region of southern California (although for their specific case, available observations were unsuitable to resolve subtle features in the lower crust) and Özalaybey et al. (1997) and Last et al. (1997) have performed complementary analyses of surface-wave disper-

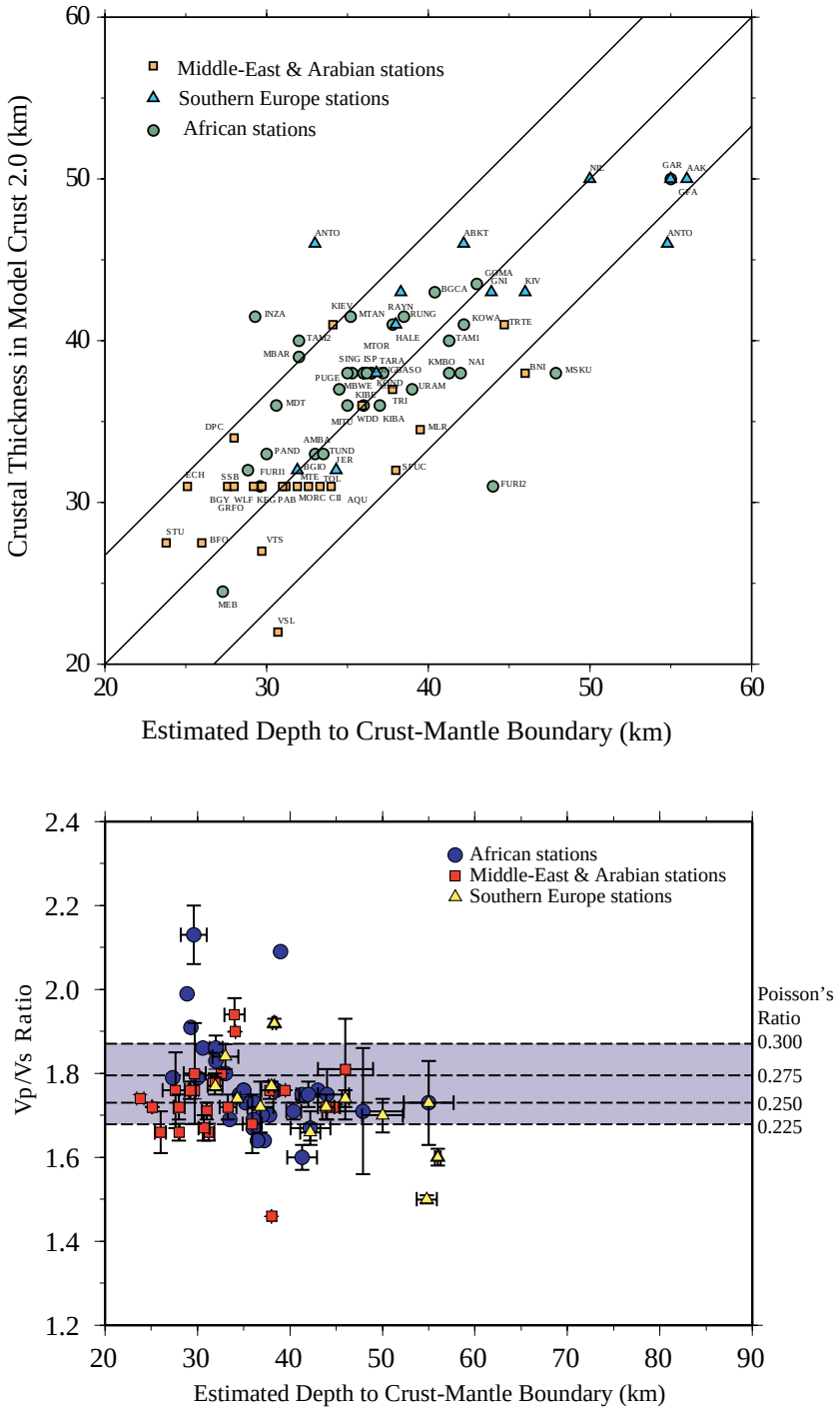


Figure 2. (Top) Comparison of crustal thickness estimated with receiver functions versus values from crustal model 2.0. Stations located in Africa in agreement more with crust 2.0, rather than stations located in Europe and Middle East. It maybe because of heterogeneity and more complicated structure in those regions. (Bottom) Variation of Vp/Vs ratio with crustal thickness, overall trend suggests a decrease in Poisson's ratio with increasing crustal thickness. The depth scale is extended to allow comparison with our results in Asia [Ammon et al., this volume].

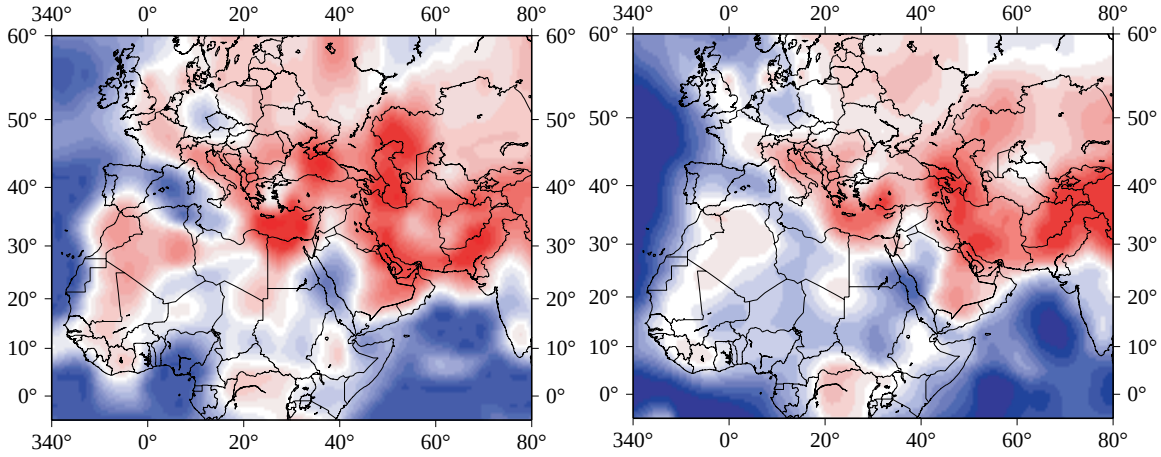


Figure 3. Tomographic imaging results for the Middle East, north Africa, and western Europe. The left diagram shows the lateral group velocity variations in 35-second period Love waves, the map on the right shows the corresponding variations in 35-second period Rayleigh waves. Color scales are relative, blue is fast, red is slow.

sion and receiver functions and Du and Foulger (1999) and Julia *et al*. (2000) implemented joint inversions of these data types. The mechanics of the inversion are relatively simple since partial derivatives of dispersion observations (Herrmann, 1995) and receiver functions waveforms (e.g., Randall, 1989, Ammon *et. al*, 1990) can be calculated quickly and accurately. For more details on the method, we refer the reader to Ammon *et al.* (located elsewhere in these proceedings).

An Example Combined Inversion, Station PUGE, Tanzania

We illustrate the ideas with an example. The results of the inversion of PUGE receiver functions with the Rayleigh-wave group-velocity dispersion values from Pasyanos and Walter [2002] combined with phase velocities digitized from Weeraratne et al [2003] are shown in Figure 4. The fit to the Pasyanos and Walter [2002] dispersion curve is very good and the general fit to the phase-velocities is good. The phase velocities are slightly under-predicted for the shorter periods and over-predicted for the longest periods. The long-period over-prediction is a result of our constraints that the deepest part of the model match that of PREM. Relaxing that assumption would allow the low velocities to extend deeper that 220 km and reduce the deepest average shear-velocity to match the phase velocity. The difference at the shorter periods represents a fundamental difference between the group and phase-velocities. One explanation may be the smoothing of the group velocities has resulted in an artificially lower estimate - very slightly inconsistent with the phase velocities. The receiver functions are very well modeled and produce the relatively smooth crust-mantle transition and crustal thickness (provided with the absolute velocity information from the surface-wave information).The model has a relatively simple crust, consistent with earlier results, and the crust-mantle transition about 7.5 km thick (this could be an intermediate layer at the base of the crust). The mantle structure includes a lid with a thickness of approximately 100 km underlain by a region of low velocities. These velocities are low compared with other shields - consistent with the results of Weeraratne *et al.* [2003]. Although the lid is fast at shallow depths, consistent with regional propagation [e.g. Nyblade and Brazier, 2002; Langston *et al.*, 2002] the model lid is also thinner than usual for an Archean shield.

An Example Combined Inversion, Station KOWA, Mali

In Figure 5 we present the results of the inversion of KOWA receiver functions with the Rayleigh- and Love-wave group-velocity values from Pasyanos and Walter [2002]. The fit to the Pasyanos and Walter [2002] dispersion curve is reasonable, but the complexity in the tomographic dispersion curves is difficult to fit with a lateral homogeneous isotropic earth model. The Love and Rayleigh values appear to be incompatible at the shortest and longest periods (where the tomography has the largest uncertainties).

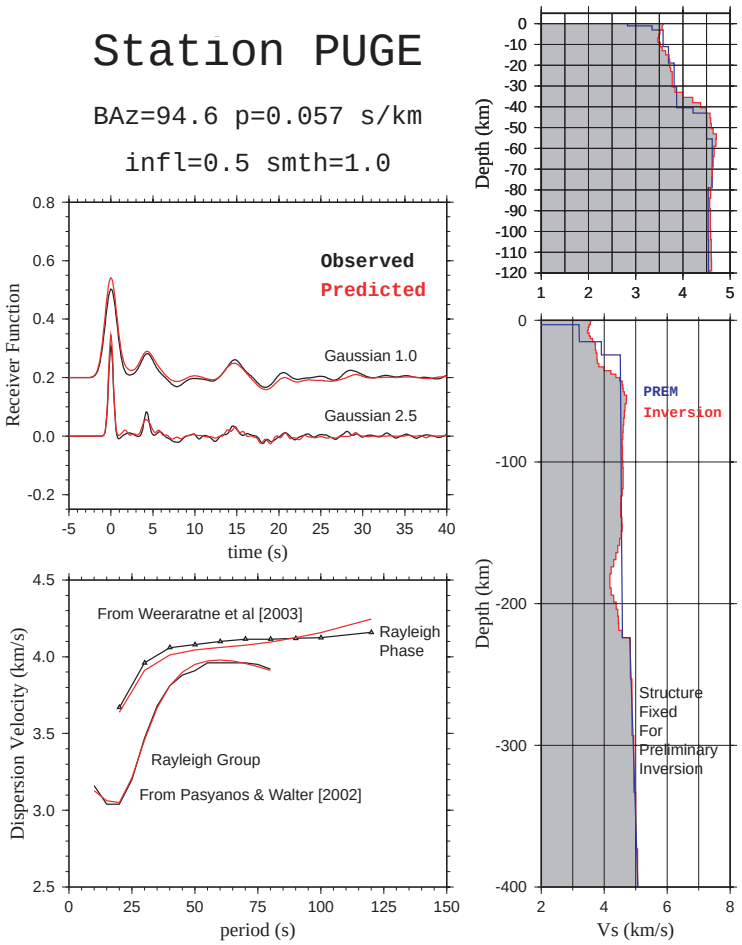


Figure 4. Inversion results for station PUGE using dispersion curves from Pasyanos and Walter [2002] & Weeeratne *et al.*, [2003]. The back-azimuth and ray parameter of the incoming P-wave are shown at the top. The influence parameter was 0.5, which balances the weight between the receiver functions and dispersion values, and the smoothness weight was 1.0. The observed and predicted receiver functions in two bandwidths are shown in the upper left, the observed and predicted dispersion curves in the lower left, and the resulting models are shown on the right. The deep structure is constrained to transition smoothly into the PREM - the data have little sensitivity for detailed absolute velocities below approximately 100-150 km. These velocities are earth-flattened by default since we use flat-earth codes to perform the analyses.

The estimated velocity structure has an unusually fast surface layer. This features is to a large part the result of limited resolution in the upper kilometer, and can be removed with increased smoothing near of the shallowest layers with little penalty in the fit to the observations. The mantle lid is faster than PREM, with P-velocities approaching 8.5 km/s at a depth of about 80 km. The lower crust and uppermost mantle have a strong gradient, which could have a large affect on waves turning in that depth such as *Pn* and *Sn*. The low-velocity zone beneath the lid is intriguing. We can remove the structure by increasing smoothing at that depth; the fit to the surface waves degrades marginally, the fit to the arrival at about 233 seconds in the receiver function is worse. To evaluate the structure more carefully will require more data from the station. Despite a rather long formal operation time for KOWA, the number of data useful for receiver functions is limited by frequent gaps in data availability.

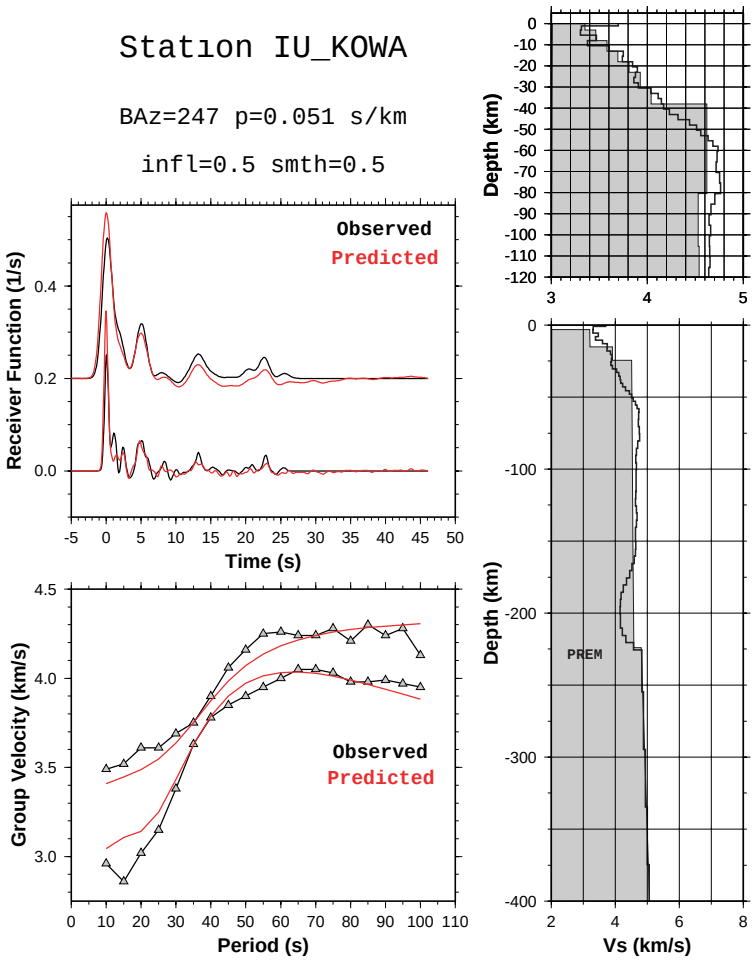


Figure 5. Joint-Inversion result for station KOWA, located in northern Africa. The receiver functions from back-azimuth 247 both in low frequency (0.5 Hz) and high frequency bandwidth of (1.2 Hz) are shown in upper left along with their predictions. Smoothed group velocities from Pasyanos and Walter [2002] with corresponding fit are shown on the lower left. The original and estimated earth models are shown in the upper right. The models have 74 layers with a total thickness of 532 km and the inversion is allowed to vary the upper 225 km. H-K stacking estimated crustal thickness is 42.2±2.15 km with a Vp/Vs = 1.67±0.04. These values calculated from 10 receiver functions, which obtained from 39 available events in the period of 1998-1999 and 2001. For the joint-inversion, smoothness and influence parameters were both 0.5.

An Example Combined Inversion, Station ISP, Isparta, Turkey

Resultsof the inversion of ISP receiver functions with the Rayleigh- and Love-wave group-velocity values from Pasyanos and Walter [2002] are presented in Figure 6 . The observed Love and Rayleigh group velocities are very low, looking almost oceanic at the shorter periods. No short-period Airy phase is evident as the curves plummet to very low velocities at the shortest periods. The fit to the Pasyanos and Walter [2002] dispersion curve is very good. The two receiver functions are the stacks of data from all azimuths and last only about 25 seconds (much of the scattered energy at later times is incoherent and removed by averaging). The early part of the receiver function is complicated in the higher-frequency signal, but relatively simple in the longer period signal. Velocities in the earth model are unusually low, as dictated by the low group velocities. The upper crust is bounded below by a layer with an equivalent P-velocity of about 6.2 km/s. The lower crust begins with a decrease in velocity to an equivalent P-velocity of

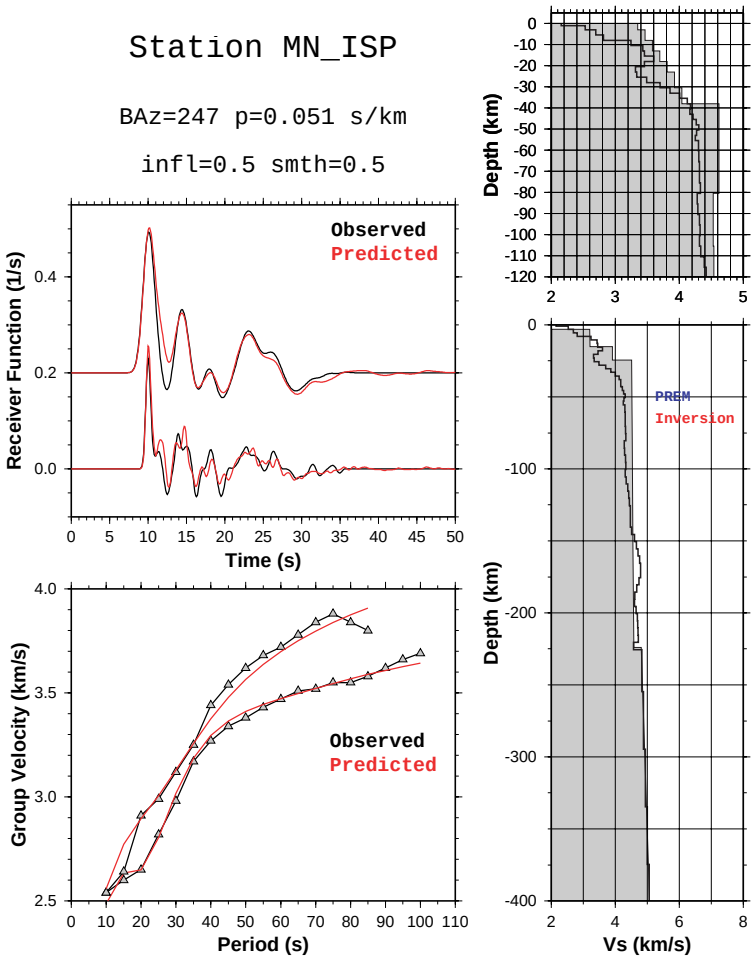


Figure 6. Inversion results for station ISP, located in east-central Turkey. Stacks of 50 receiver functions from all back-azimuth both in low frequency (0.5 Hz) and high frequency bandwidth of (1.2 Hz) are shown in upper left with their predicted ones. Smoothed group velocities from Pasyanos and Walter [2002] with corresponding fit are shown on the lower left. The original and estimated earth models are shown on the right. The model extends to 532 km, but only the upper 225 km are included in the inversion. The H-K stacking crustal thickness estimates is 36.8±1.4 km with a Vp/ Vs = 1.72 ± 0.06. These values calculated from 50 receiver functions which obtained from 500 events in the period of 1996-2003.

5.7 km/s, which is underlain by a strong positive velocity gradient. An apparent crust-mantle boundary at a depth of about 30-35 km is very slow - velocities in this depth range are just above 7 km/s. Typical upper mantle velocities of 7.8 and greater are not reached until a depth of 80-90 km.

An Example Combined Inversion, Station HIT, Jordan

In Figure 7 we present the results of the inversion of station HIT receiver functions with the Rayleigh- and Love-wave group-velocity dispersion values from Pasyanos and Walter [2002]. Initial inversions indicated that fitting both Love and Rayleigh dispersion simultaneously was not possible. Separate inversions with the receiver function and Love waves and the receiver function and Rayleigh waves were performed. A similar observation was made for data from station EIL.

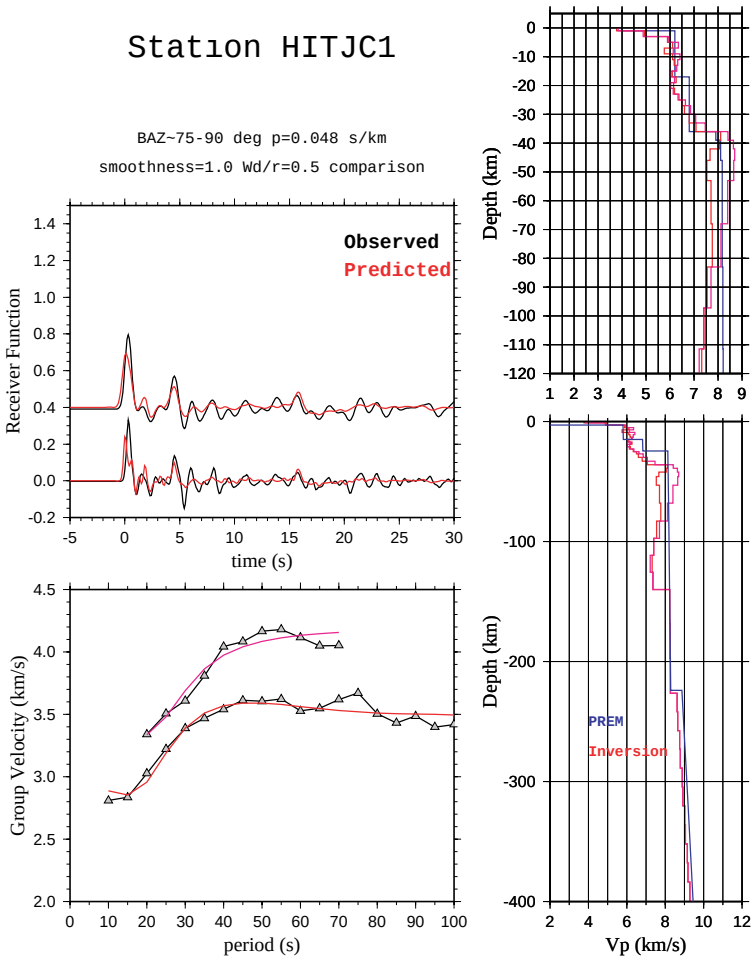


Figure 7. Inversion results for station HIT, Jordan using dispersion curves from Pasyanos and Walter [2002]. Format is similar to earlier presentations except that separate inversions were performed for the Love and Rayleigh wave dispersion curves. The results of the independent inversions are compatible in the crust, but substantially different in the uppermost mantle. Shear velocities have been converted to P-velocities using a standard estimate for Poisson's ratio.

An Example Combined Inversion, Station KBS, Kuwait

The results of the inversion of KBS receiver functions with the Rayleigh- and Love- wave group-velocity dispersion values from Pasyanos and Walter [2002] are presented in Figure 8. The results for three different back-azimuths produce similar fits in all directions. The model in the direction of the Zagros Mountains is approximately 5 km thicker than the results in other directions.

CONCLUSIONS AND RECOMMENDATIONS

Our work is proceeding nicely and most of the permanent stations have been imaged. We are also working with other groups to secure and image structures beneath several more sites in northeastern Africa. We have a few more permanent stations to analyze. We are moving from the initial data collection and preliminary analysis phase into a more expansive interpretation and assessment stage.

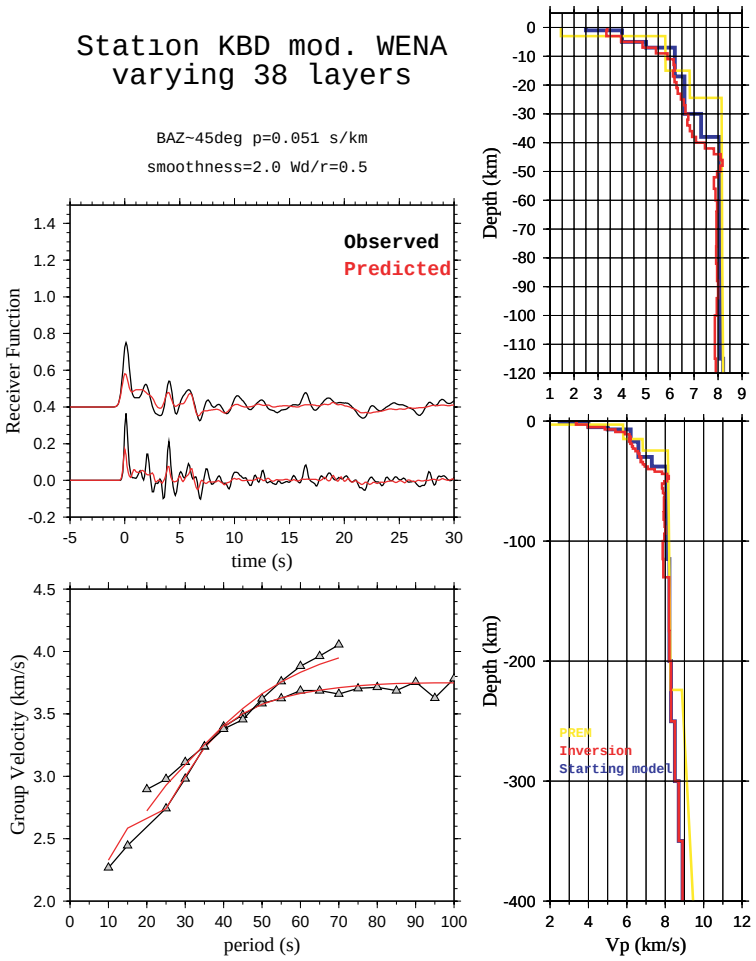


Figure 8. Inversion results for station KBD using dispersion curves from Pasyanos and Walter [2002]. The figure format is similar to earlier examples. Shear velocities have been converted to P-velocities using a standard estimate for Poisson's ratio.

ACKNOWLEDGEMENTS

We thank the P. Wessel and W. H. F. Smith (1990), the authors of GMT for producing easy-to-use, quality software for making maps and charts.

REFERENCES

Ammon, C.J., G.E. Randall, and G. Zandt (1990), On the non-uniqueness of receiver function inversions, *J. Geophys. Res.*, 95, 15303-15318.

Ammon, C.J. (1991), The isolation of receiver effects from teleseismic P waveforms, *Bull. Seism. Soc. Am.*, 81, 2504-2510.

Ammon, C. J., and G. Zandt (1993), The receiver structure beneath the southern Mojave Block, *Bull. Seism. Soc. Am.*, 83, 737-755.

Cassidy, J.F., Numerical experiments in broadband receiver function analysis, *Bull. Seismol. Soc. Am.*, 82, 1453-1474, 1992.

Chevrot, S., and N. Girardin (2000), On the detection and identification of converted and reflected phases from receiver functions, *Geophys. J. Int.*, 141 (3), 801-808.

Clitheroe, G., O. Gudmundsson, and B.L.N. Kennett (2000), Sedimentary and upper crustal structure of Australia from receiver functions, *Australian Journal of Earth Sciences*, 47 (2), 209-216.

Constable, S.C., R.L. Parker, and C.G. Constable (1987), Occam's inversion: A practical algorithm for generating smooth models from electromagnetic sounding data, *Geophysics*, 52, 289-300.

Du, Z.J. and G.R. Foulger (1999), The crustal structure beneath the northwest fjords, Iceland, from receiver functions and surface waves, *Geophys. J. Int.*, 139, 419-432.

Julia, J., C. J. Ammon, R. B. Herrmann, and A. M. Correig (2000), Joint Inversion of receiver function and surface-wave dispersion observations, *Geophys. J. Int.* 143, 99-112.

Kikuchi, M., and H. Kanamori, Inversion of complex body waves (1982), *Bull. Seism. Soc. Am.*, 72, 491-506, 1982.

Langston, C.A. (1979), Structure under Mount Rainier, Washington, inferred from teleseismic body waves, *J. Geophys. Res.*, 84, 4749-4762.

Larson, E. W. F. and G. Ekström (2001), Global Models of Group Velocity, *Pure and Applied Geophys.*, 158, 1377-1399.

Levin, V., and J. Park (1997), Crustal anisotropy in the Ural Mountains from teleseismic receiver functions, *Geophysical Research Letters*, 24 (11), 1283-1286.

Ligorría, J.P. (2000), An Investigation of the Crust-Mantle Transition Beneath North America and the Bulk Composition of the North American Crust, *Ph.D. Thesis, Saint Louis University*, 261 pages.

Ligorría, J.P. and C. J. Ammon (1999), Iterative deconvolution and receiver function estimation, *Bull. Seismol. Soc. Am.*, 89, 1395-1400.

Myers, S.C., and S.L. Beck (1994), Evidence for a local crustal root beneath the Santa Catalina metamorphic core complex, Arizona, *Geology*, 22, 223-226.

Owens, T.J., G. Zandt, and S.R. Taylor (1984), Seismic evidence for an ancient rift beneath the Cumberland Plateau, Tennessee: A detailed analysis of broadband teleseismic P waveforms, *J. Geophys. Res.*, 89, 7783-7795.

Özalaybey, S., M.K. Savage, A.F. Sheehan, J.N. Louie, and J.N. Brune (1997), Shear-wave velocity structure in the northern Basin and Range Province from the combined analysis of receiver functions and surface waves, *Bull. Seismol. Soc. Am.*, 87, 183-199.

Park, J., and V. Levin (2000), Receiver functions from multiple-taper spectral correlation estimates, *Bull. Seismol. Soc. Am.*, 90 (6), 1507-1520.

Pasyanos, M.E., W.R. Walter, and S.E. Hazler (2001), A Surface wave dispersion study of the Middle East and North Africa for Monitoring the Comprehensive Nuclear-Test-Ban Treaty, *Pure and Applied Geophys*, 158, 1445-1474.

Pasyanos, M.E., and W.R. Walter, Crust and upper-mantle structure of North Africa, Europe and the Middle East from inversion of surface waves, Geophys. J. Int., 149, 463-481, 2002.

Pasyanos, M.E. (2002), A Variable-resolution Surface Wave Dispersion Study of Western Eurasia and North Africa, submitted to *Journal of Geophysical Research*.

Ritzwoller, M. H. and A. L. Levshin (1998), Eurasian surface wave tomography: Group velocities, *J. Geophys. Res., 103*, 1839-1878.

Ryberg, T., and M. Weber (2000), Receiver function arrays; a reflection seismic approach, *Geophys. J. Int.*, 141 (1), 1-11.

Sandvol, E., D. Seber, A. Calvert, M. Barazangi (1998), Grid search modeling of receiver functions: Implications for crustal structure in the Middle East and North Africa, *J. Geophys. Res.*,103, 26,899-26,917.

Savage, M.K. (1998), Lower crustal anisotropy or dipping boundaries? Effects on receiver functions and a case study in New Zealand, *J. Geophys. Res.*, 103 (7), 15,069-15,087, 1998.

Stevens, J. L. and K. L. McLaughlin (2001), Optimization of Surface Wave Identification and Measurement, *Pure and Applied Geophys*., 158, 1547-1582

Su, W., R. L. Woodward, and A. M. Dziewonski (1994), Degree 12 model of shear velocity heterogeneity in the mantle, *Nature*, 99, 6945-6980.

Weeraratne, D.S., D.W. Forsyth, K.M. Fischer, and A.A. Nyblade, Evidence for an upper mantle plume beneath the Tanzanian craton from Rayleigh wave tomography, J. Geophys. Res., 2002JB002273R, 2003.

Zandt, G., and C. J. Ammon (1995), Continental Crustal composition constrained by measurements of crustal Poisson's ratio, *Nature*, 374, 152-154.

Zandt, G., S.C. Myers, and T.C. Wallace (1995), Crust and mantle structure across the Basin and Range-Colorado Plateau boundary at 37 degrees N latitude and implications for Cenozoic extensional mechanism, *J. Geophys. Res.*, 100 (6), 10,529-10,548.

Zhu, L., and H. Kanamori (2000), Moho depth variation in Southern California from teleseismic receiver functions, *J. Geophys. Res.*, 105 (2), 2969-2980.

SYSTEMATIC INVERSION OF RECEIVER FUNCTIONS AND SURFACE WAVE DISPERSION FOR CRUSTAL STRUCTURE IN CENTRAL ASIA

Charles J. Ammon[1], Winchelle Sevilla[1], Robert B. Herrmann[2], and George E. Randall[3]

Penn State University[1], Saint Louis University[2], and Los Alamos National Laboratory[3]

Sponsored by National Nuclear Security Administration
Office of Nonproliferation Research and Engineering
Office of Defense Nuclear Nonproliferation

Contract No. DE-FC03-02SF22498[1,2] and W-7405-ENG-36[3]

ABSTRACT

We report on our investigations into the seismic structure of the lithosphere in central Asia using surface waves and receiver functions. We rely on global and regional tomographic analyses for long-period surface wave dispersion constraints on the structure that are supplemented with short-period observations measured directly from regional signals (when available). This paper is an overview of receiver function complexity across the region using results from previous studies and receiver functions from many of the permanent stations. We have completed short-period tomographic imaging of the central and eastern Tibetan Plateau using Love and Rayleigh waves with periods between 10 and 40 seconds. The short period information is critical to tight constraints on shallow shear-wave velocity structure, but the measurements are sensitive to source location and origin time uncertainties. We have also surveyed receiver functions from the INDEPTH III, northeast China, and Tien-Shan Continental Dynamics temporary deployments. We illustrate the combined inversion of surface waves and receiver functions using a variety of model constraints focusing on select stations and provide information to access on-line results (earth models, etc.).

OBJECTIVES

Our objectives are the construction of station-centric shear-velocity profiles for regions surrounding broadband seismic stations throughout central Asia. Application of the technique in the region provides an opportunity to revise models of the crust and upper mantle structure throughout the region and to exploit the global and regional work of previous seismic verification research (e.g. Pasyanos et al., 2001; Ritzwoller & Levshin, 1998, Larson and Ekstrom, 2001, Stevens and McLaughlin, 2001). The resulting shear-velocity models provide a single structure consistent with a range of observations and which can be tested as a tool for the construction of mode isolation filters that can help improve surface wave magnitude estimates. We also plan to explore the possibility of adding additional data to our inversions of receiver functions and surface wave dispersion. The diverse seismic activity throughout the region will facilitate cross-validation of the mode isolation filters with simple empirical filters constructed using larger events with adequate signal-to-noise ratios.

Estimating Subsurface Shear Velocities

Subsurface geology generally has a broad “wavenumber” spectrum containing sharp, or high-wavenumber, changes in velocity near the Earth’s major geologic boundaries and smooth low-wavenumber variations in regions of relatively uniform geologic structure. Access to the full spectrum of earth structure requires that we exploit signals that span a wide frequency range and that are sensitive to the entire spectrum of heterogeneity. Surface waves, travel times, and direct-wave amplitudes, for example, are sensitive to smooth variations in earth structure; reflected and converted waves are sensitive to velocity contrasts. Combining seismic data in joint inversions is an obvious approach to improve estimates of earth structure. To successfully combine data in an inversion, we must insure that all the data are sensitive to the same (or related) physical quantities and that they sample or average structure over comparable length scales. Recent advances in surface wave tomography have provided an opportunity to combine localized surface wave dispersion estimates with other data such as P- and S-wave receiver functions. Ammon and Zandt (1993) used surface wave dispersion observations to try and distinguish between competing models of the Mojave desert, but Özalaybey et al., (1997) pioneered a formal, joint inversion of these data. They nicely illustrated the value of even a limited band of dispersion values to help reduce the trade-off between crustal thickness and velocity inherent in receiver function analyses. Specifically, they used Rayleigh wave phase velocities in the 20–25 second period range to help produce stable estimates of crustal thickness in the northern and central Basin & Range. The limited bandwidth did not permit resolution of details in the crust and they limited their inversion (or at least their interpretation) to depths above 40 km. More recent authors have exercised the approach and combined the data with additional a priori model constraints (Du and Foulger, 1999; Julia et al., 2000). Recent accomplishments in global and regional tomography now provide a more complete band of dispersion measurements to combine with receiver functions that allow us to improve the resolution of earlier works.

Surface wave dispersion measurements are sensitive to broad averages, or low wavenumber components of the earth structure. They provide valuable information on the absolute seismic shear velocity but are relatively insensitive to sharp, high-wavenumber velocity changes. Generally surface wave inversions must be constrained using a particular layer parameterization (e.g. near-surface, upper-crust, lower crust, mantle lid, deep mantle), resemble an a priori model, or substantially smoothed to stabilize earth-structure estimation. Despite these drawbacks, surface wave dispersion values contain important constraints on the subsurface structure, and the general increase in depth sensitivity with depth allows an intuitive understanding of their constraints on structure. Additionally, modeling dispersion values facilitates a broadband inversion by reducing the dominance of Airy phases, which pose problems when constructing broadband misfit norms to model seismograms directly. Perhaps most important for our application is the ability to localize Earth’s dispersion properties using seismic tomography. The idea is now well established and global dispersion models exist for a broad range of frequencies (e.g. Larson and Ekström, 2001; Stevens et al., 2001). The localization of dispersion allows us to isolate the variations in properties spatially and global models of surface wave dispersion exist and are readily available for application to other studies such as the proposed work.

Receiver functions are time series computed from three-component body-wave seismograms that show the relative response of the Earth structure near the receiver (e.g. Langston, 1979). Source, near-source structure, and mantle propagation effects are removed from the seismograms using a deconvolution that sacrifices P-wave information for the isolation of near-receiver effects (Langston, 1979; Owens et al., 1984; Ammon, 1991; Cassidy, 1992). Receiver

function waveforms are a composite of P-to-S (or S-to-P) converted waves that reverberate within the structure near the seismometer. Modeling the amplitude and timing of those reverberating waves can supply valuable constraints on the underlying geology. In general, the receiver functions sample the structure over a range of ten's of kilometers from the station in the direction of wave approach (the specific sample width depends on the depth of the deepest contrast). Stations sited near geologic boundaries can produce different responses for different directions. Recent innovations in receiver function analysis include more detailed modeling of receiver function arrivals from sedimentary basin structures (e.g. Clitheroe et al., 2000), anisotropic structures (e.g. Levin and Park, 1997; Savage 1998), estimation of Poisson's ratio (e.g., Zandt et al., 1995; Zandt and Ammon, 1995; Zhu and Kanamori, 2000, Ligorría, 2000), reflection-like processing of array receiver functions (e.g., Chevrot and Girardin, 2000; Ryberg and Weber, 2000) and joint inversions (e.g., Özalaybey et al., 1997; Du and Foulger, 1999; Julia et al., 2000).

Our joint inversion method is similar to that of Özalaybey et al. (1997) except that we use jumping, smoothness, and constraints to include as much *a priori* information into the inversion as is available. We combine the receiver function and surface wave observations into a single algebraic equation and account for their different physical units and equalize their importance in the misfit norm by weighting each data set by an estimate of the uncertainty in the observations and the number of data. We also append smoothness constraints and *a priori* model constraints on the deepest part of the model. Although we cannot resolve fine details in the deep upper mantle, these regions can impact our results since surface wave dispersion values at intermediate and longer periods are somewhat sensitive to this deeper structure. We believe that it is important to have a reasonable basement structure so that our results are more consistent with global models. We extend our models to about 500–700 *km* to insure this consistency. The resulting inversion equations are

$$\begin{bmatrix} \sqrt{\frac{\mathbf{p}}{\mathbf{w}_s^2}}\mathbf{D}_s \\ \sqrt{\frac{\mathbf{q}}{\mathbf{w}_r^2}}\mathbf{D}_r \\ \sigma\Delta \\ \mathbf{W} \end{bmatrix} \cdot \mathbf{m}_{i+1} = \begin{bmatrix} \sqrt{\frac{\mathbf{p}}{\mathbf{w}_s^2}}\mathbf{r}_s \\ \sqrt{\frac{\mathbf{q}}{\mathbf{w}_r^2}}\mathbf{r}_r \\ 0 \\ 0 \end{bmatrix} + \begin{bmatrix} \sqrt{\frac{\mathbf{p}}{\mathbf{w}_s^2}}\mathbf{D}_s \\ \sqrt{\frac{\mathbf{q}}{\mathbf{w}_r^2}}\mathbf{D}_r \\ 0 \\ 0 \end{bmatrix} \cdot \mathbf{m}_i + \begin{bmatrix} 0 \\ 0 \\ 0 \\ \mathbf{W} \end{bmatrix} \cdot \mathbf{m}_a \qquad (1)$$

where $\mathbf{p}$, $\mathbf{q} = 1 - \mathbf{p}$, σ, and $\mathbf{W}$ are weights that control the relative importance of receiver functions, dispersion values, smoothness, and *a priori* model constraints in the norm minimized during the inversion. The data comprise the vectors $\mathbf{r}_s$ and $\mathbf{r}_r$, and the partial derivatives fill the matrices $\mathbf{D}_r$ and $\mathbf{Ds}$. The matrix Δ is a finite-difference stencil that "computes" model roughness, and the matrix $\mathbf{W}$ is a layer-dependent weight that is used to insure the model blends smoothly into the *a priori* model, $\mathbf{m}_a$, at depth. The values of $\mathbf{w}_s$ and $\mathbf{w}_r$ are equal to the product of the number of points in the dispersion curve and receiver functions and the variance of the observations. The second term on the right is added to create the "jumping" inversion scheme (e.g. Constable et al., 1987; Ammon et al., 1990) and allows us to solve for (and constrain) the shear-velocity models as opposed to shear-velocity correction vectors. Equation (1) is solved in a least-squares sense for the model, $\mathbf{m}_{i+1}$, starting with an initial model $\mathbf{m}_0$. The procedure generally converges in a few iterations.

Estimating Receiver Functions

When the data are high-quality and the receiver structure is not too complex, the choice of a deconvolution procedure does not make much difference. However, when the noise in the seismograms is substantial, or the receiver structure is complex, different deconvolution approaches have strengths and weaknesses. We will compute receiver functions using the iterative time-domain deconvolution procedure described by Ligorría and Ammon (1999). We prefer the iterative approach, which is based on the Kikuchi and Kanamori (1982) source-time function estimation algorithm, for several reasons. First, in the iterative approach the receiver function is constructed by a sum of Gaussian pulses which produces a flat spectrum at the longest periods. The flat long-period spectrum can be viewed as *a priori* information that helps reduce side-lobes that may result of spectral or singular-value truncation stabilization procedures. The reduction of side-lobes eases the interpretation and helps stabilize "low-frequency" receiver functions. Second, the iterative approach constructs a causal receiver function, which is what we expect in all cases of reasonable earth structure. This is a subtle difference from spectral techniques (e.g. Langston, 1979; Park and Levin, 2000) which can

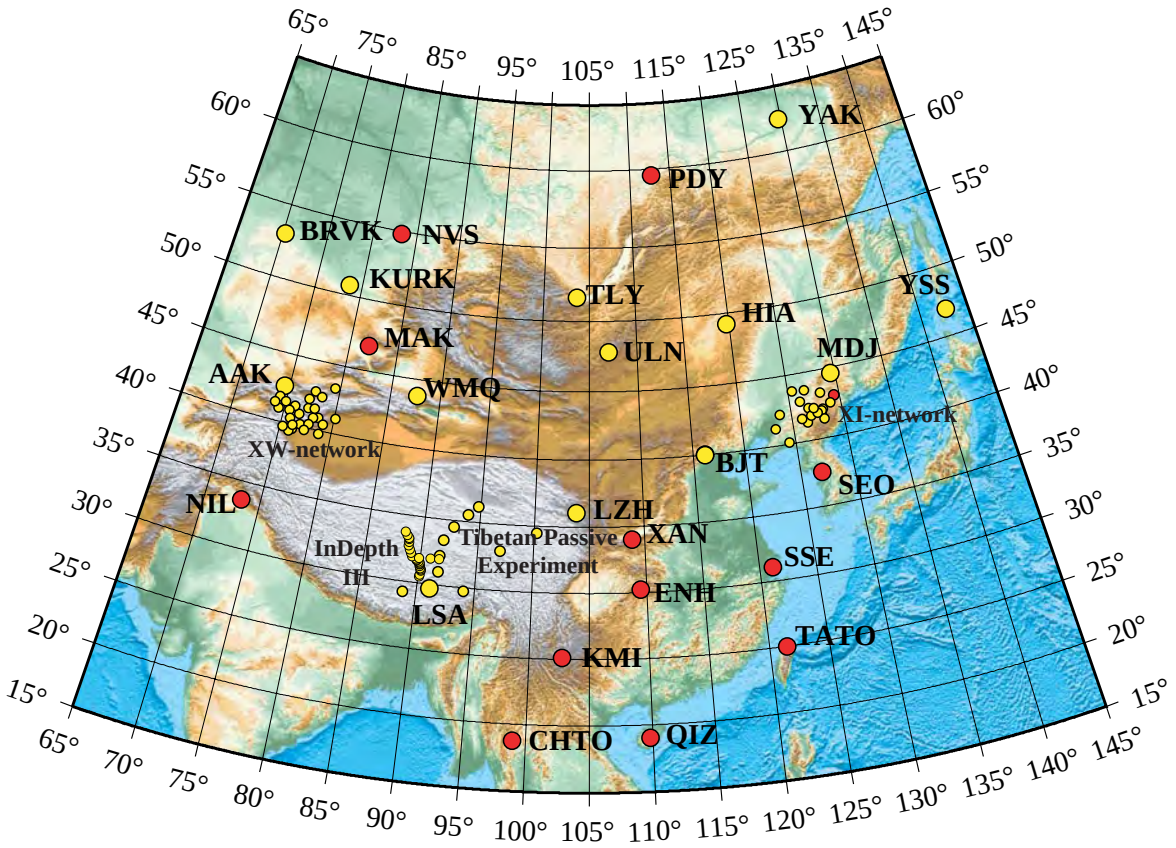


Figure 1. Location of stations that we have analyzed so far in this project. Large and small circles represent GSN and the temporary network stations respectively. Yellow symbols identify stations for which we have computed receiver functions (and performed Poisson's Ratio analyses). Stations currently being processed are identified by red symbols.

always introduce a component to the signal before the P-wave. The acausal component of the spectral signal may be small, but still important to the satisfaction of the convolutional model that defines a receiver function, i.e.,

$$\mathbf{R}(t) = \mathbf{Z}(t) * \mathbf{E_R}(t)\,. \qquad (2)$$

In equation (2), $\mathbf{R}(t)$ and $\mathbf{Z}(t)$ are the radial and vertical seismograms, and $\mathbf{E_R}(t)$ is the radial receiver function (a similar equation holds for the transverse component). The point is that even when the receiver function estimation is unstable, spectral deconvolutions may satisfy (2) quite well. The iterative time-domain approach, which can be restricted to produce the best *causal* solution, may not always satisfy (2). Experienced modelers have always been able to identify failed receiver functions, but the misfit to (2) available from iterative deconvolutions provides quantitative information that can be used when stacking signals, or in extreme cases, to discard obviously failed deconvolutions. In our case we find using a threshold cut-off of 80-90% of the radial power fit allows us to quickly discard poorly constrained deconvolution results, enabling an efficient and objective select of the data to include in further analysis.

RESEARCH ACCOMPLISHED

Receiver Function Computation

We have processed 13 of the 26 GSN stations and 44 stations from temporary networks in central and eastern Asia, which includes 18 stations from the XI-network and 26 stations from the XW-network shown in Figure 1. Computation of the receiver functions follows a simple approach by gathering first teleseismic P-waveforms of events greater

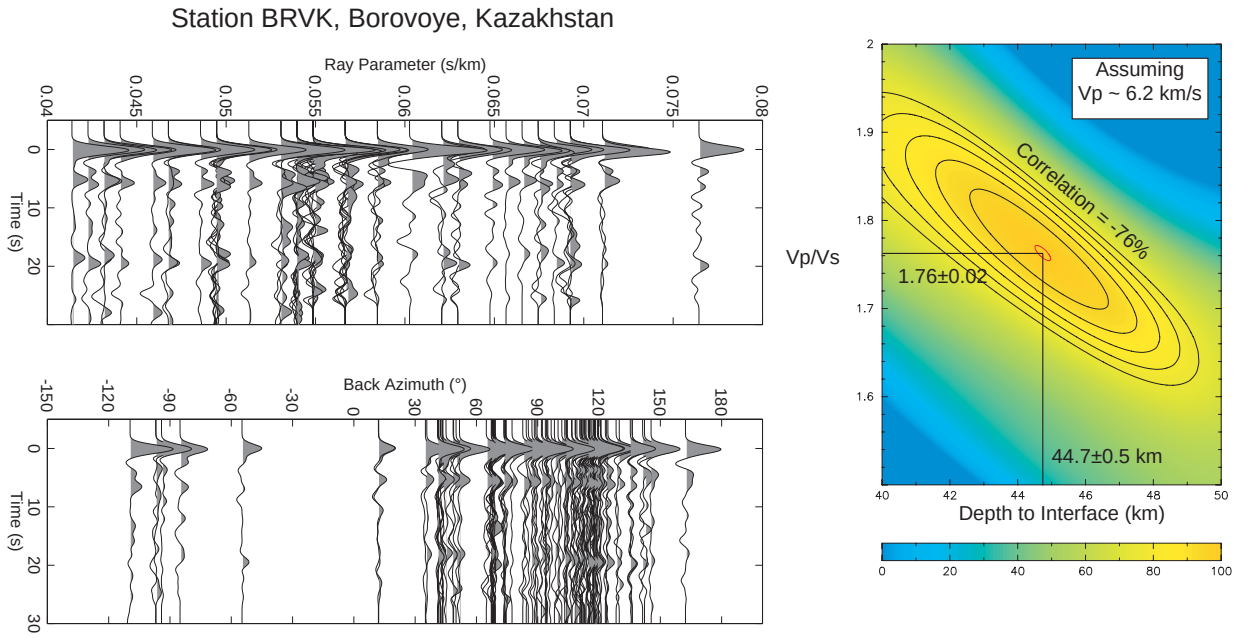


Figure 2. Sample receiver function observations and a limited analysis of Poisson's ratio and crustal thickness (assuming Vp ~ 6.2 km/s). The observed receiver functions are shown as a function of ray parameters (sin of the P-wave incident angle) and as a function of back azimuth. The data do not sample the azimuthal structure uniformly as teleseisms are predominantly observed from western-Pacific subduction zones. The ray parameter sampling is good, and identifiable conversions and multiples are seen clearly for a range of incident angles. The image on the right shows the results of stacking all waveforms to identify the crust-mantle transition. Uncertainties were estimated using a jack-knifing technique. These uncertainties are conservative since they also depend on the assumed P-velocity of the crust. As a result of azimuthal sampling, the results are most reflective of the structure to the east of the station.

than Mw 5.5 for a given station. Then, we use the iterative time-domain deconvolution of Ligorria and Ammon (1999) to do the computation and select the best receiver functions for analysis. We cluster the receiver functions as a function of back azimuth and ray parameter (the amount of data determines the feasibility of this approach). Our analysis usually begins with a relatively simple stacking procedure that allows the estimation of the Vp/Vs ratio (or Poisson's ratio) and crustal thickness (Zhu and Kanamori, 2000). The analysis produces relatively good estimates when the simple assumptions (relatively flat crust-mantle boundary) are satisfied. Then the radial receiver functions are combined with the surface wave dispersions for joint shear-velocity inversions. As had been mentioned earlier, the receiver functions may exhibit different patterns as a function of back azimuths such that we assigned a narrow range of back azimuths to be used in the inversions. The simplicity and the similarity in the forms of the receiver functions primarily dictate the criteria we used for the bounds. After choosing the bounds, we stacked the receiver functions and use this stack for the joint inversions.

An Example Analysis, Station BRVK, Borovoye, Kazakhstan

Example receiver functions for station BRVK in central Asia are shown in Figure 2. BRVK is a station of IRIS/IDA - GSN network located at coordinates 53.05810 N and 70.28280 E and is situated on top of a granitic pluton (Richards et al., 1992). Seismograms recorded at this station are high quality because of the very low microseisms on the site (e.g. Kim et al., 1993; Kim and Ekstrom, 1996) making it a well suited for a receiver function analysis. Previous receiver function studies of BRVK (Kim et al., 1993) estimated a 45 km thick crust along the direction 87° from north. Since the receiver functions vary with azimuth and ray parameter we summarize our observations in two profiles, one for azimuth and one for ray parameter. As a first order approximation of the structure, we've ignored azimuthal variation and performed a stacking procedure to use the waveforms to estimate the thickness and Poisson's ratio of the crust (assuming that Vp ~ 6.2 km/s) using the method of Zhu and Kanamori (2000). The resulting fits are

reasonable, with a thickness value of about 45 km and a Poisson's ratio of 0.26. We will perform similar analyses and inversions for each station with suitable data.

We show the results of an example joint inversion in Figure 3. The receiver functions are shown at the upper left panel, and correspond to averages from five events with similar ray parameter and back azimuth. The lower left panel shows the group velocities, which are from the Pasyanos et al. (2001) surface wave group velocity model. The panels along the right show the initial and estimated velocity profiles in a direction roughly east of the station. The fit to both receiver functions and surface wave dispersion curves in Figure 3 is very good, which may reflect the simplicity of the crustal structure underlying the station. The resulting shear-velocity model is quite simple, with a PREM-like mantle and the crustal thickness and poisson's ratio that you would expect in a platform (Zandt and Ammon, 1995). The only unusual feature is low shear-velocity zone between 20 and 30 km depth (~10% slower than the "typical" continental crust used at the top of the initial model). This zone corresponds to the prominent trough at around three seconds on the stacked receiver functions. The crust-mantle transition is relatively sharp, indicated by the strong converted phases at around 18 seconds on both stacks, which is consistent with previous observations (Kim et al., 1993). The crustal thickness is about 48 km for the joint inversion result.

Bulk Crustal Structure Comparisons

We plot the crustal thicknesses of our results together with the estimated thickness under the Tibetan passive-source experiment (Mejia, 2001) and INDEPTH III experiment (Diehl, 2003) with the Crust 2.0 model (global crustal model at 2x2 degrees) of Bassin et al. (2000) (Figure 4). We don't accept the values of Crust 2.0 in all places, but it is a useful reference for comparison. The results show good agreement; the mean difference between the our results and Crust 2.0 is less than one *km*, the standard deviation of the differences is between 5 and 6 *km*. Median crustal thicknesses for the XI- and XW-networks (eastern and central Asia, respectively) are 32 *km* and 53 *km*. We also examined variations of the bulk crustal *Vp/Vs* ratio and show them as a function of crustal thickness (Figure 4). The plot can help us to identify which stations produce *Vp/Vs* values that plot outside the *Vp/Vs* bounds appropriate for the crustal materials. These unrealistic values are a result of crustal complexity which is not included in the simple *Vp/Vs* ratio estimation procedure.

CONCLUSIONS AND RECOMMENDATIONS

The future thrust of this project is to finish computing the receiver functions of the remaining stations and complete the joint inversion processes to estimate the shear velocity structure beneath all available broadband three-component seismic stations in central Asia. The next year will also include assessment of the potential applications of the velocity models to seismic waveform modeling and seismic event location.

ACKNOWLEDGEMENTS

We thank P. Wessel and W. H. F. Smith, the authors of GMT, for producing easy-to-use, quality software for making maps and charts.

REFERENCES

Ammon, C.J., G.E. Randall, and G. Zandt (1990), On the non-uniqueness of receiver function inversions, *J. Geophys. Res.*, 95, 15303-15318.

Ammon, C.J. (1991), The isolation of receiver effects from teleseismic P waveforms, *Bull. Seism. Soc. Am.*, 81, 2504-2510.

Ammon, C. J., and G. Zandt (1993), The receiver structure beneath the southern Mojave Block, *Bull. Seism. Soc. Am.*, 83, 737-755.

Bassin, C., Laske, G., and G. Masters (2000), The current limits of resolution for Surface Wave Tomography in North America, *EOS Trans AGU*, 81, F897.

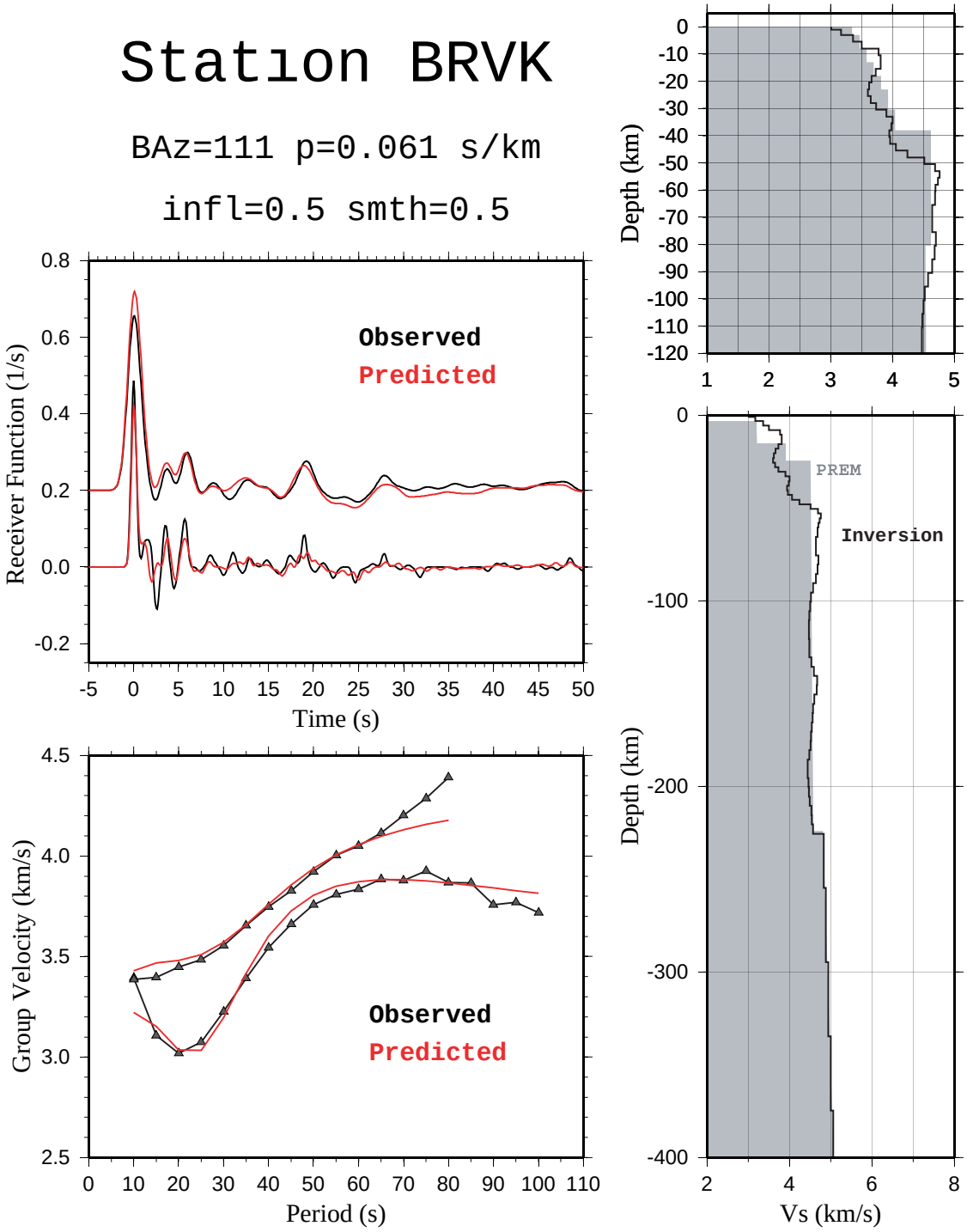


Figure 3. Simultaneous inversion results for the station BRVK using Pasyanos et al., (2001) surface wave dispersion model (lower left panel) and stacked receiver functions (upper left panel) that sample the structure roughly east of the station. A Gaussian width factors of 1.0 (top stacked) and 2.5 (bottom stacked) were used to generate the receiver functions. BAz is the average back azimuth and p is the average ray parameter of the incoming P-waves. The influence parameter, "infl", balances the weight between the receiver functions and dispersion during the inversion. "smth" is the smoothness weight. On the right panels are the initial model (a modified version of PREM) (shaded in gray) and the estimated shear-wave velocity models.

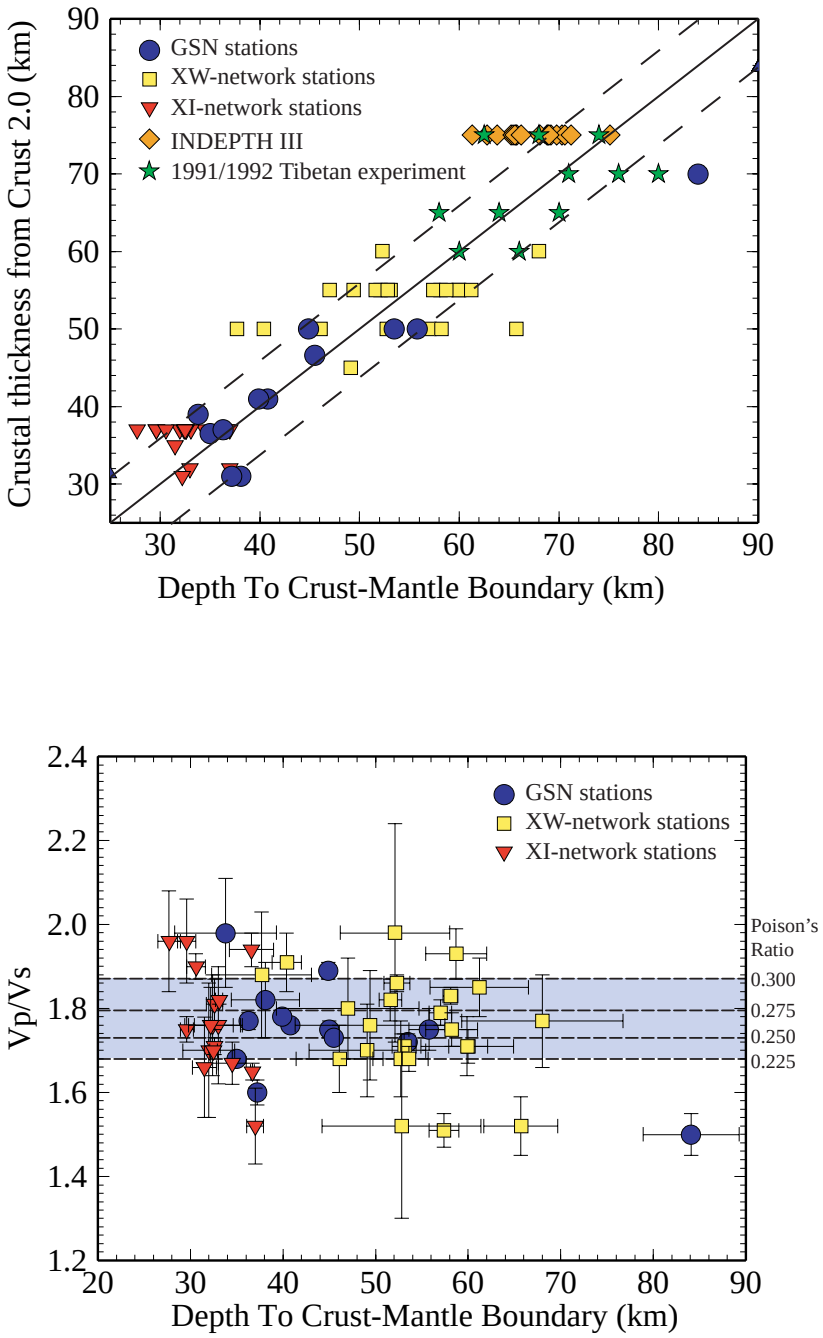


Figure 4. (Top) Plot showing the correlation between the crustal thickness obtained by this study (horizontal axis) and the Crust 2.0 model. Different symbols represent different networks, but all data have been processes the same way. GSN stations generally have much larger data sets than the temporary networks. The dashed lines represent ±1 standard deviation in the model differences. (Bottom) Estimated Vp/Vs ratio variation with crustal thickness. The error bars are uncertainties on the results from the bootstrap method of Julia and Mejia (2004). Dashed horizontal lines are Poison's ratio used as a reference for determining which station is underlain by complicated crustal structure, which are characterized by having a very high or very low

Cassidy, J.F., Numerical experiments in broadband receiver function analysis, *Bull. Seismol. Soc. Am.*, 82, 1453-1474, 1992.

Chevrot, S., and N. Girardin (2000), On the detection and identification of converted and reflected phases from receiver functions, *Geophys. J. Int.*, 141 (3), 801-808.

Clitheroe, G., O. Gudmundsson, and B.L.N. Kennett (2000), Sedimentary and upper crustal structure of Australia from receiver functions, *Australian Journal of Earth Sciences*, 47 (2), 209-216.

Diehl, T. M., Determining crustal Structure Beneath the Tibetan Plateau Using Receiver Functions, *B. S. Thesis*, Penn State University, University Park, PA, 2003.

Du, Z.J. and G.R. Foulger (1999), The crustal structure beneath the northwest fjords, Iceland, from receiver functions and surface waves, *Geophys. J. Int.*, 139, 419-432.

Herrmann, R. B., *Computer Programs in Seismology, 1995*, Saint Louis University, St. Louis, MO, USA.

Jackson, D.D., Interpretation of inaccurate, insufficient, and inconsistent data (1972), *Geophys. J. R. Astron. Soc.*, 28, 97-109.

Julia, J., C. J. Ammon, R. B. Herrmann, and A. M. Correig (2000), Joint Inversion of receiver function and surface-wave dispersion observations, *Geophys. J. Int.* 143, 99-112.

Julia, J., and J. Mejia (2004), Thickness and Vp/Vs ratio variations in the Iberian crust, *Geophys. J. Int.*, 156, 59-72.

Kim, W. Y., and G. Ekstrom, (1996) Instrument responses of digital seismographs at Borovoye, Kazakhstan, by inversion of transient calibration pulses, *Bull. Seism. Soc. Am.*, 86, 191-203.

Kim, W. Y., L. Gao, and P. Richards, (1993) Crust and upper mantle seismic velocity structure beneath Borovoye Observatory, northern Kazakhstan, EOS, Trans., AGU, 74, Suppl., 433.

Kind, R., J. Yuan, J. Saul, D. Nelson, S.V. Sobolev, J. Mechie, W. Zhao, G. Kosarev, J. Ni, U. Achauer, and M. Jiang, Seismic Images of Crust and Upper Mantle Beneath Tibet: Evidence for Eurasian Plate Subduction, *Science*, 298, 1219-1221, 2002.

Langston, C.A. (1979), Structure under Mount Rainier, Washington, inferred from teleseismic body waves, *J. Geophys. Res.*, 84, 4749-4762.

Larson, E. W. F. and G. Ekström (2001), Global Models of Group Velocity, *Pure and Applied Geophys.*, 158, 1377-1399.

Last, R. J., A. A. Nyblade, C. A. Langston and T. J. Owens (1997), Crustal structure of the East African Plateau from receiver functions and Rayleigh wave phase velocities, *J. Geophys. Res.*, 102, 24,469-24,483.

Levin, V., and J. Park (1997), Crustal anisotropy in the Ural Mountains from teleseismic receiver functions, *Geophysical Research Letters*, 24 (11), 1283-1286.

Ligorria, J.P., and C.J. Ammon, Iterative deconvolution of teleseismic seismograms and receiver function estimation, *Bull. Seism. Soc. Am.*, 89, 1395-1400, 1999.

Mejia, J. (2001), Lithospheric structure beneath the Tibetan Plateau using simultaneous inversion of surface wave dispersion and receiver function, *Ph.D. thesis, St. Louis University.*

Owens, T.J., G. Zandt, and S.R. Taylor (1984), Seismic evidence for an ancient rift beneath the Cumberland Plateau, Tennessee: A detailed analysis of broadband teleseismic P waveforms, *J. Geophys. Res.*, 89, 7783-7795.

Özalaybey, S., M.K. Savage, A.F. Sheehan, J.N. Louie, and J.N. Brune (1997), Shear-wave velocity structure in the northern Basin and Range Province from the combined analysis of receiver functions and surface waves, *Bull. Seismol. Soc. Am.*, 87, 183-199.

Pasyanos, M.E., W.R. Walter, and S.E. Hazler (2001), A Surface wave dispersion study of the Middle East and North Africa for Monitoring the Comprehensive Nuclear-Test-Ban Treaty, *Pure and Applied Geophys*, 158, 1445-1474.

Randall, G. E. (1989), Efficient calculation of differential seismograms for lithospheric receiver functions, *Geophys. J. Int.*, 99, 469-481.

Richards, P., K. Won-Young, and G. Ekström (1992), Borovoye Geophysical Observatory, Kazakhstan, *EOS Trans AGU*, 73, 201--206.

Ritzwoller, M. H. and A. L. Levshin (1998), Eurasian surface wave tomography: Group velocities, *J. Geophys. Res., 103*, 1839-1878.

Ryberg, T., and M. Weber (2000), Receiver function arrays; a reflection seismic approach, *Geophys. J. Int.*, 141 (1), 1-11.

Savage, M.K. (1998), Lower crustal anisotropy or dipping boundaries? Effects on receiver functions and a case study in New Zealand, *J. Geophys. Res.*, 103 (7), 15,069-15,087, 1998.

Stevens, J. L. and K. L. McLaughlin (2001), Optimization of Surface Wave Identification and Measurement, *Pure and Applied Geophys*., 158, 1547-1582

Zandt, G., and C. J. Ammon (1995), Continental Crustal composition constrained by measurements of crustal Poisson's ratio, *Nature*, 374, 152-154.

Zandt, G., S.C. Myers, and T.C. Wallace (1995), Crust and mantle structure across the Basin and Range-Colorado Plateau boundary at 37 degrees N latitude and implications for Cenozoic extensional mechanism, *J. Geophys. Res.*, 100 (6), 10,529-10,548.

Zhu, L., and H. Kanamori (2000), Moho depth variation in Southern California from teleseismic receiver functions, *J. Geophys. Res.*, 105 (2), 2969-2980.

AN INTEGRATED GEOPHYSICAL STUDY OF THE LITHOSPHERIC STRUCTURE BENEATH LIBYA

Wesley A. Brown, Thomas F. VanDeMark, Diane I. Doser, and Aaron A. Velasco

University of Texas at El Paso

Sponsored by Air Force Research Laboratory

Contract No. DTRA01-01-C-0058

ABSTRACT

We have used over 6,000 gravity measurements, in conjunction with other geophysical and geological data obtained from oil exploration, published research, and other academic institutions to develop a three-dimensional (3-D) density model for the Libya region. Next we derived a preliminary 3-D velocity model (called LIBYA3D) based on this density model. Our resulting 1-D approximation of the 3-D velocity model was found to compare favorably with the standard 1-D IASPEI91 (International Association of Seismology and Physics of the Earth's Interior) velocity model. We verified our velocity model by deriving individual velocity models along specific source receiver paths traversing our study area (1.5-D). Only earthquakes of 4.7m_b or greater occurring in Libya were found to be suitable sources for this analysis. Our velocity models were then used to generate synthetic waveforms for waveform modeling. Analysis of the preliminary results from the waveform modeling indicates that our 1-D velocity model is valid for frequencies greater than 20 s. We are confident that our velocity model of subsurface Libya has improved our understanding of the regional wave propagation and will be useful to the nuclear testing community and to anyone interested in a better understanding of the seismicity of the area.

We also utilize this model in the context of regional discrimination to investigate small to moderate size natural events (m_b 3.7 – 5.7) in the Libyan region occurring from May 1990 to May 2000. Observations of Pn and Sn energy at varying frequency ranges (0.5 – 8 Hz) and propagation paths recorded by broadband instrumentation lead us to investigate the attenuation affects the geologic structure of the Libyan region and the adjacent Mediterranean Sea. We perform multi-frequency analysis to discern which frequencies have the optimum signal-to-noise ratio (SNR) for these regional phases. Pn and Sn show stronger amplitudes at higher frequencies (4 – 8 Hz) along propagation paths where continental crust is limited. Conversely, we only observe strong Pn and Sn amplitudes at lower frequencies (0.5 – 4 Hz) along propagation paths where continental crust is prevalent. We utilize LIBYA3D to develop trends in our data as a function of crustal path and volume. These empirical observations could be used to aid future clandestine explosion discrimination work in the Libyan region if the need arises.

OBJECTIVE

To monitor a zero yield nuclear explosion treaty, we must be able to analyze events of all magnitudes that occur throughout the world. Furthermore, it is difficult to analyze the effectiveness of discriminating between earthquakes and explosions when there are a small amount of events to analyze. Compounding problems arise with small magnitude events recorded at regional distances, since path effects can lead to complex regional seismograms causing misclassification of events (e.g., Velasco et al., 2003). The Libyan region exhibits many of these difficulties, where there are few events, and those that occur are generally small in magnitude. One approach to overcome some of these difficulties is to develop velocity models utilizing auxiliary data, and build a model from which we can build confidence in discrimination at regional distances. We develop a 3-D velocity/density model (LIBYA3D) of a portion of subsurface Libya from over 6,000 gravity data points available for the region. We validate the model with regional waveforms, and then apply this model for a discrimination analysis in the region.

RESEARCH ACCOMPLISHED

3-D Model Development & Validation

Our model consists of five lithospheric layers and an extra layer accounting for the Mediterranean Sea is added as necessary. We calculated the dimensions of the Mediterranean Sea within the study area by writing a small Microsoft excel script that assigns an elevation of 0 km depth to areas of the DEM with elevation less than 0 km. The difference between the newly calculated body (i.e. Mediterranean body excluded) and the original DEM defines the expanse of the Mediterranean Sea. The standard density of sea water 1.1g/cc was assigned to this water layer. The Cenozoic and Mesozoic units were treated as a single layer. The base of the Mesozoic and the top of the Precambrian Basement were digitized from a 1:2,000,000 structure contour map of the Libyan Arab Republic and adjacent areas; compiled by G. H. Goudarzi, U.S. Geological Survey with J. P. Smith as consulting Geologist, 1978. Both sets of contours were drawn at intervals of 250m. The top of the Precambrian Basement and the bottom of the Mesozoic layer sandwiches the Paleozoic layer which is assigned a density of 2.55g/cc. The top of the lower crust was set at a depth of 19 km (Dial 1998) and the surface of the Moho was digitized from Dial (1998). The various densities assigned were obtained from Dial 1998 and Carmichael 1989. We call our model “LIBYA3D”.

Resulting 3-D velocity model

Figure 1 is the average velocity/density model resulting from the study compared to the standard IASPEI91 model. The velocities used in this model were derived using the Nafe-Drake method in conjunction with previous studies from Dial (1998). Overall the resulting velocity/density model showed a good correlation with the IASPEI91 model in all three quantities. The values for the *P*-wave and *S*- wave velocities for the IASPEI91 model are generally slightly too low for subsurface Libya. For the Moho both models returned identical values for *P*- and *S*-wave velocities; however, a density of 3.3 g/cc was assigned to our model as opposed to 3.396 g/cc in the IASPEI91 model. Again our LIBYA3D model consistently showed slightly higher values than the IASPEI91 for density. The widest margin of disparity occurred within the lower crust where the *P*-wave velocity estimation for the lower crust according to the IASPEI91 model is 6.5 km/s while other studies (Seber et al 1996, McNamara et al. 1996) showed that a higher *P*-wave velocity exists. Dial’s study led him to conclude that a value of 7.16 is the most reliable *P*-wave velocity for the lower crust in the region. For the Precambrian layer the general trend remained the same, slightly too low on the part of the IASPEI91 model. Above the Precambrian basement layer the IASPEI91 model did not differentiate for any of the divisions and assigned a uniform value of 5.8 km/s, 3.46 km/s, and 2.449g/cc to the *P*-wave velocity, *S*-wave velocity and density, respectively. For our model however, having digitized the surface of the top of the Precambrian Basement rock and the base of the Mesozoic surface, we were able to assign values to each. The top of the lower crust is set to a depth of 19 km in our model instead of 20 km as in the IASPEI91 model, since there are better regional seismic constrains in the area. In the Libya region, the crust thins towards the north and so it is inaccurate to assign a single value for the depth to the Moho. Since we have a 1-D model, we used the average value of 35 km (Figure 2), which is the same as the value used in the IASPEI91 model. The small overall differences between the IASPEI91 model and our LIBYA3D model may be subtle, but on a localized scale, we can expect to see a difference in the effect on seismic waves.

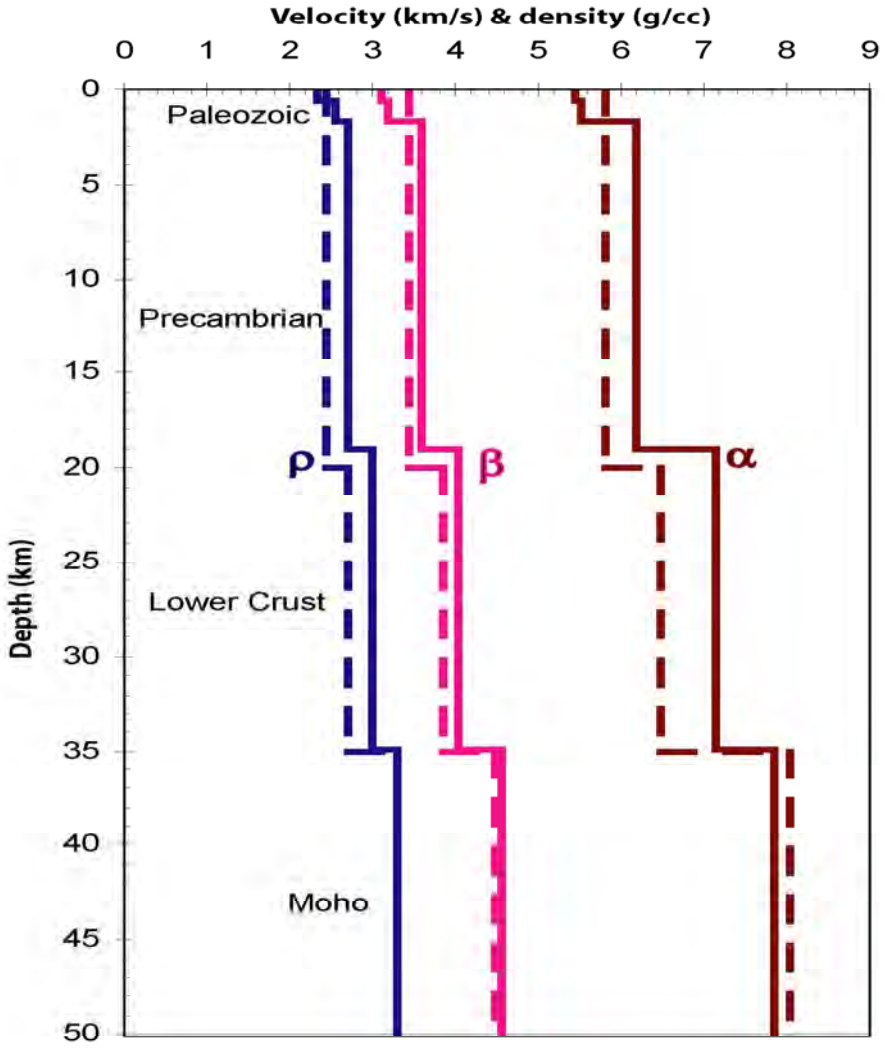


Figure 1: Velocity/density model as derived from our investigation compared with the standard IASPEI91 global velocity model. The broken lines represent the IASPEI91 model and the solid lines show results from our model. Blue lines show density values, magenta lines show S-wave velocity values, and the brown lines show the P-wave velocity values.

Validation of 3-D Velocity Model

We carried out a preliminary seismic evaluation on the average 1-D velocity model. Event 910808 (YYMMDD) is of magnitude 4.7m_b located at 35.65N and 11.64E and was chosen since it sampled a significant portion of the study area and a part of the Mediterranean Sea. The waveform collected for this event was also good enough for seismic analysis to be carried out. We computed a predicted travel time for the event to station KEG in Egypt using our 1-D model and compared the results to the actual waveform recorded in KEG and visually inspect for a match. The results were satisfactory.

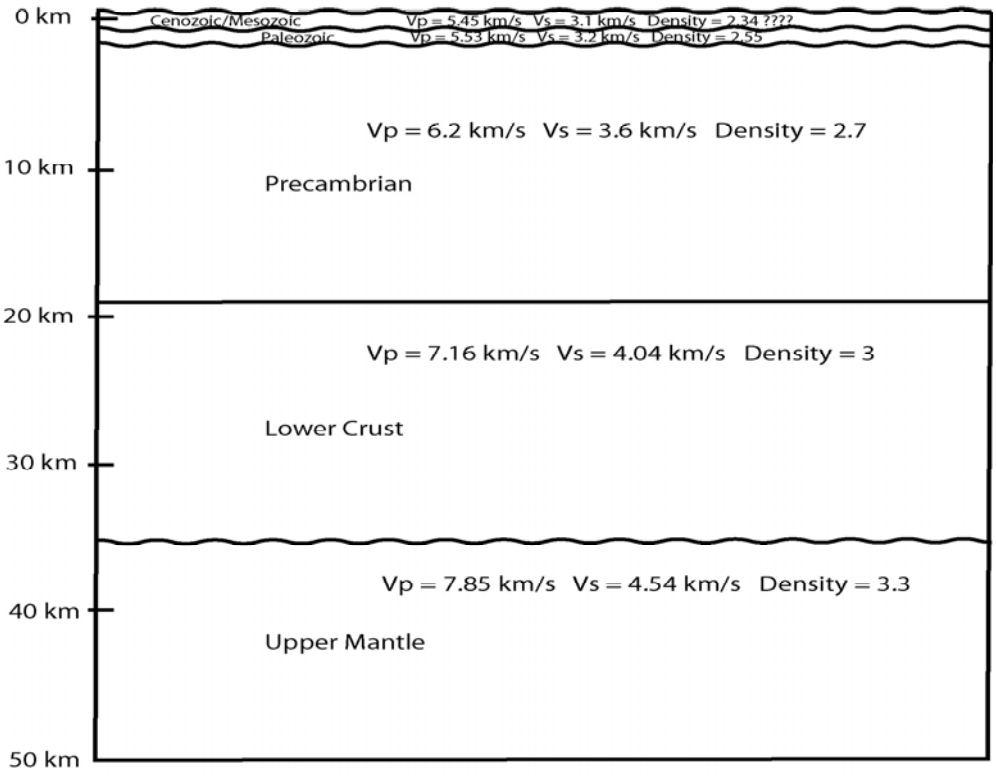


Figure 2: Shows the average 1-D velocity and density model beneath Libya. The wavy lines show surfaces that were digitized from data. A uniform depth of 19 km was assumed for the top of the lower crust.

Next we calculated individual path specific velocity models for two other events in order to do a 1.5D velocity model. Events 980528 and 921012 (Figure 3, Table 1) were chosen as the source-receiver path traversed the Libyan lithosphere and was not greatly affected by lithospheric structure at distances beyond the study area. Special care had to be taken when choosing source-receiver pathways since the border between the African plate and the Eurasian plate is situated to the north of Libya. In this area there is considerable thinning of the crust and a velocity gradient exists.

An unfiltered seismogram of event 910808 (Figure 4) is tested against the averaged 1-D model. The red line shows the predicted P-wave arrival time (T_0) for the event generated from our model. We used SAC to carry out the seismic analysis for this portion of the study. The predicted arrival time accurately coincides with the arrival time of the *P*-wave. Other similar tests carried out further validated our 1-D model. The preliminary results of the modeling of the two events are shown in Figure 5. The seismograms are filtered using a low pass Butterworth filter of 0.05Hz. For event 921012 we observed a close correlation between the synthetic and the recorded seismogram on the vertical and transverse components while we did not receive a good fit on the radial component. For event 980528 we again observed favorable correlation on the vertical component but were off on the radial and transverse components. This could be due to the presence of sedimentary basins that are not accounted for.

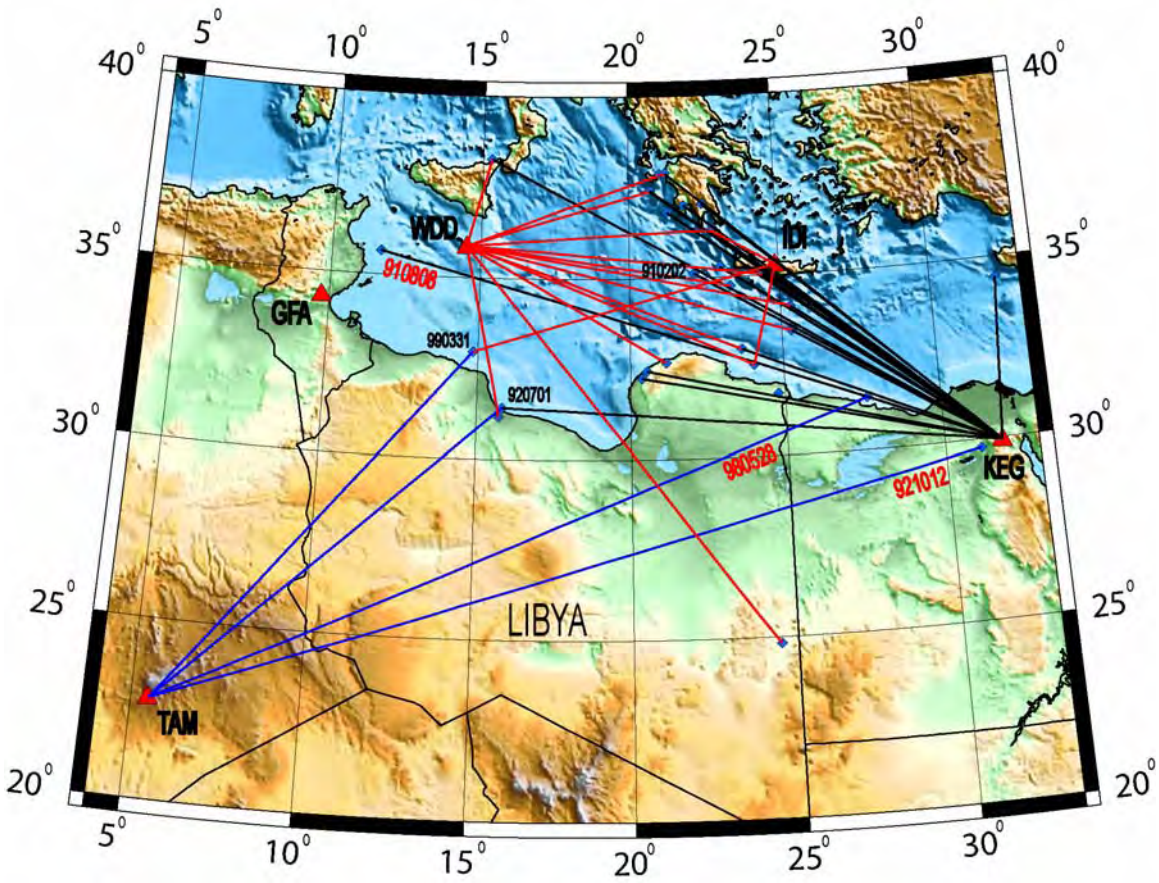


Figure 3: Map of study shows earthquakes as blue diamonds, stations as red triangles, and multi-colored great circle arcs represent source-receiver paths.

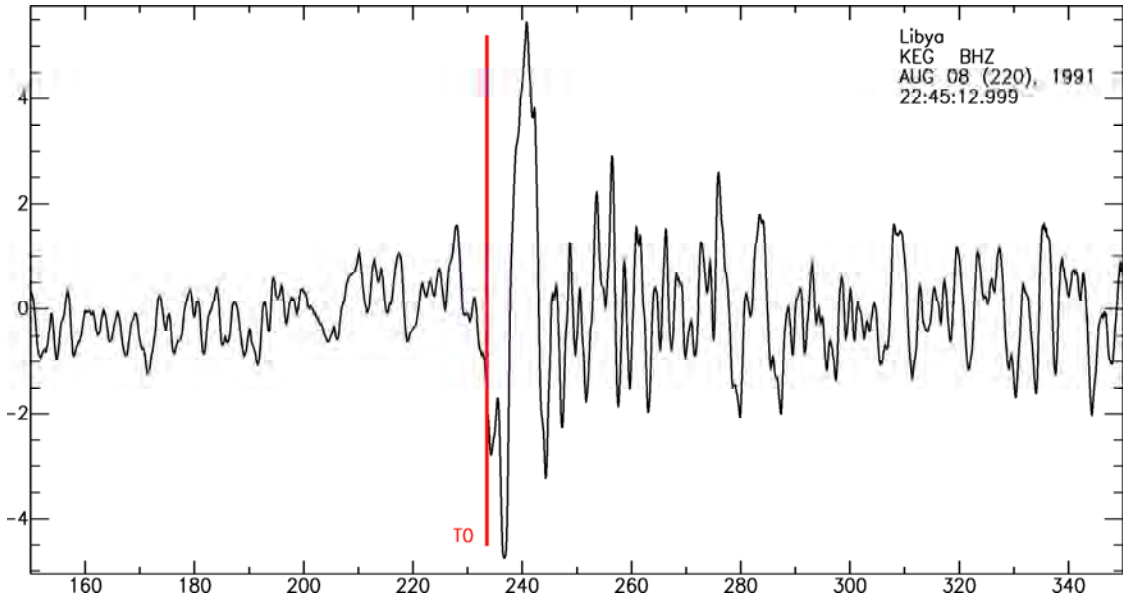


Figure 4: Unfiltered seismogram of event 910808. The red line (T0) shows the predicted *P*-wave arrival time using our derived model.

Table 1: List of earthquakes used for research project. Times and locations are provided by the International Seismic Centre (ISC).

Date	Time	Lat.	Lon.	Depth	Mag.
2000/05/21	22:45:38.3	31.1570	15.7340	23.6	mb 3.8
1990/05/18	18:27:51.2	31.7130	24.7960	10.0	MD 4.3
1990/05/25	15:44:45.9	37.8702	21.0578	1.0	mb 3.8
1990/07/30	17:52:37.9	34.4845	25.5438	45.8	mb 4.4
1991/02/02	05:34:47.3	35.1190	22.1571	10.0	mb 3.7
1991/02/08	13:50:40.1	35.2852	23.0458	63.8	mb 4.4
1991/05/28	18:58:46.6	37.0235	22.4817	20.8	mb 4.5
1991/08/08	22:46:10.9	35.6467	11.6387	22.0	mb 4.7
1992/07/01	15:13:32.8	31.4246	15.8143	10.0	mb 4.2
1992/10/12	13:09:55.4	29.7566	31.1360	21.5	mb 5.8
1993/09/09	00:32:35.5	32.2394	20.3859	10.0	mb 4.8
1995/07/22	06:24:45.5	34.7502	23.3754	72.2	mb 4.1
1995/08/02	01:42:20.6	33.4384	25.3153	33.0	mb 3.4
1995/08/27	19:42:14.7	38.2610	15.2912	25.2	mb 3.6
1995/11/25	14:10:46.0	28.8123	34.9227	14.0	mb 3.8
1996/01/06	10:38:23.9	32.9867	23.6555	1.0	
1996/03/23	20:40:46.9	36.9910	21.8653	30.3	mb 3.5
1996/05/19	14:15:14.2	34.1160	25.3398	37.6	mb 4.0
1996/06/21	13:03:38.5	37.8847	21.2394	91.1	mb 3.5
1996/10/09	16:57:40.1	36.8145	21.2931	13.6	mb 4.0
1996/10/09	17:01:49.0	34.4148	32.1809	50.2	mb 4.1
1996/10/30	10:43:02.9	32.4343	20.5326	10.0	mb 4.6
1997/02/01	23:08:36.0	35.0318	24.4391	10.0	mb 3.9
1997/05/10	14:03:03.6	24.8180	24.4750	0.0	mb 3.9
1998/01/13	12:34:21.1	37.3992	20.7101	15.1	mb 3.6
1998/04/12	22:06:31.0	37.4186	20.7159	10.0	mb 4.4
1998/05/28	18:33:28.4	31.4459	27.6426	10.0	mb 5.5
1998/08/08	16:39:28.7	36.2939	22.7695	5.0	mb 3.5
1999/03/31	09:42:16.1	32.9550	14.8380	32.2	mb 4.3
1999/06/17	10:18:02.2	32.5410	24.0530	10.0	mb 4.3
1999/11/07	14:43:36.0	32.6600	21.1740	10.0	mb 4.4

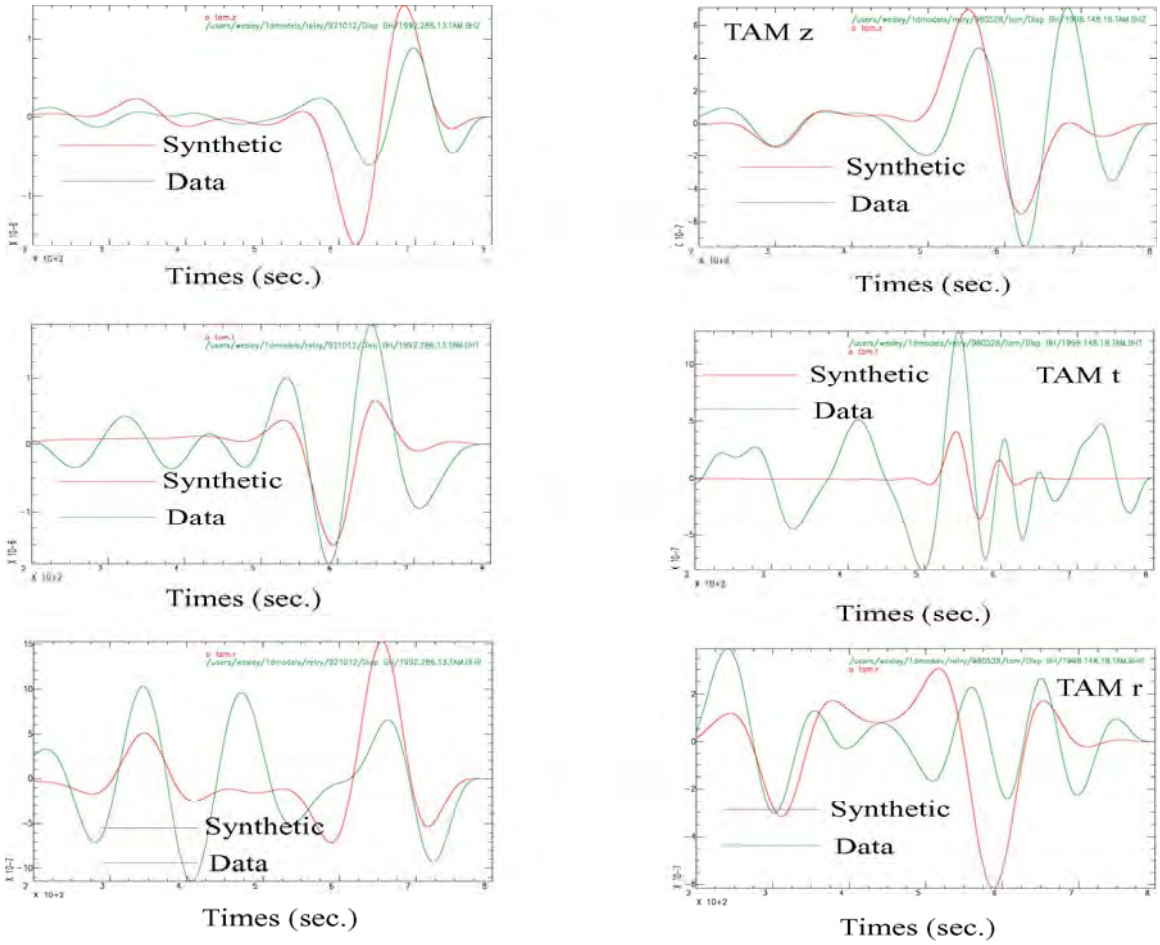


Figure 5: Waveform comparison between synthetic and data for events 980528 and 921012 (Table 1) used in validation study.

Application for Regional Discrimination

We investigate events in and around Libya (Figure 3, Table 1). Problems arise because there is no explosion data for Libya, and we are limited by the small number of reliable stations at regional distances. However, we apply our LIBYA3D model for discrimination purposes. We gather seismic data for events that occurred from 18 May 1990 to 21 May 2000 in the Libyan region and the adjacent Mediterranean Sea. Event times and locations were obtained from the International Seismic Centre (ISC). We have data consisting of 31 natural events, 7 located in Libya, 1 located in Egypt, with the remainder located in the adjacent area of the Mediterranean Sea. Magnitudes range from (m_b) 3.7 to 5.7. The stations used in this research effort are Kottamia, Egypt (KEG), Wield Dalam, Malta (WDD), Tamanrasset, Algeria (TAM), Anoyia, Crete (IDI), and Gafsa, Tunisia (GFA), all with broadband instrumentation (Figure 3). Initial multi-frequency analysis of events (e.g., Walter et al., 1995) showed consistent high frequency propagation of Pn and Sn energy at KEG and low frequency propagation of Pn and Sn energy at TAM. We show the 02 February 1991 (910202) event (see Figure 6) recorded at KEG ($\Delta = 9.67^o$; AZ = 120), which leads us to investigate attenuation affects of source-receiver paths as related to their orientation across the varying topography and bathymetry of Libya and the Mediterranean Sea. We use the 3-D model to investigate path effects associated with signal-to-noise ratio. We also identify path dependent cross spectral ratios (Walter et al., 1995) which show the elevated SNR frequency ranges at specific stations as solid parameters for future verification work.

Two events of particular interest, due to have being recorded at two receivers are the 31 March 1999 (990331) event recorded at IDI ($\Delta = 8.66^o$; AZ = 71.9^o) and TAM ($\Delta = 13.1^o$; AZ = 221^o), and the 01 July 1992 (920701) event recorded at KEG ($\Delta = 13.9^o$; AZ = 92.0^o) and TAM ($\Delta = 12.6^o$; AZ = 229^o) (see Figure 3)

Signal-to-Noise and Amplitude Ratios

Waveform data was acquired from the Incorporated Research Institutions for Seismology's (IRIS) Data Management Center (DMC). We remove instrument response and set origin times for each event. Waveform data is then cut and rotated to its radial and transverse components, and finally, we apply a Butterworth filter to view the waveform at several frequency ranges (0.5-1, 1-2, 2-4, 4-6, and 6-8 Hz) (Figure 6).

We pick regional phases Pn and Sn manually and mark the header for each waveform. We calculate phase amplitude and SNR by measuring the maximum displacement in a ten second pre-phase and phase window. By comparing the SNR of Pn against frequency at a specific station (Figures 7A-C) we observe trends in station-frequency dependence. These trends were normalized by dividing each point by the SNR at the lowest frequency range for each event (0.5-1.0 Hz). This highlights the difference in high frequency propagation. We also calculate cross-spectral ratio values (1-2 / 6-8 Hz) (Walter *et al.*, 1995) by using both displacement and SNR measurements. In this way we can define the events with high-frequency propagation by there low cross-spectral value.

As expected the SNR for both events at TAM is low from 4 to 8 Hz; however at IDI and KEG the SNR is still large if not dominant from 4 to 8 Hz. Note the receiver distance to KEG is greater than the receiver distance to TAM for 920701, but the SNR is still strong enough to be seen at KEG in the high frequency ranges. This shows us that receiver distance is not the primary controlling parameter for signal attenuation. As seen in the SNR-Frequency diagrams, (Figures 7A-C) KEG conveys the most dramatic results with the SNR peaking at 6-8 Hz in 10 of the 14 events recorded there. IDI and WDD show a trend similar to KEG with good SNR at 4 to 8 Hz, but actually peak at 3 Hz for most of these Intra-Mediterranean events. We combine their results due to their similar trends, as well as their receiver environments are the same topographically. TAM shows expected high frequency attenuation of Pn energy.

Using LIBYA3D and a 0.5 degree wide swath, we calculate the crustal volume for each source-receiver path. We also use a simple, but accurate map measurement to determine the percentage of continental crust in each source-receiver path. We also calculate cross-spectral amplitude and cross-spectral SNR values and X-Y diagrams are made by plotting these topographic statistics against the cross-spectral values and correlations are sought (Figures 8A, B) (e.g., Zhang & Lay, 1994). At KEG we find a strong correlation between high frequency propagation and the percentage of continental crust in the source-receiver path when compared to cross-spectral amplitude (Figures 8A, B) and a weak correlation between high frequency propagation and crustal volume. We see similar results for KEG when compared to cross-spectral SNR. There is a correlation for percentage of continental crust, and a weak trend when compared to crustal volume. For IDI, WDD, and TAM there is some correlation when comparing percentage of continental crust and crustal volume to cross-spectral SNR. However, these correlations break down when compared to cross-spectral amplitude.

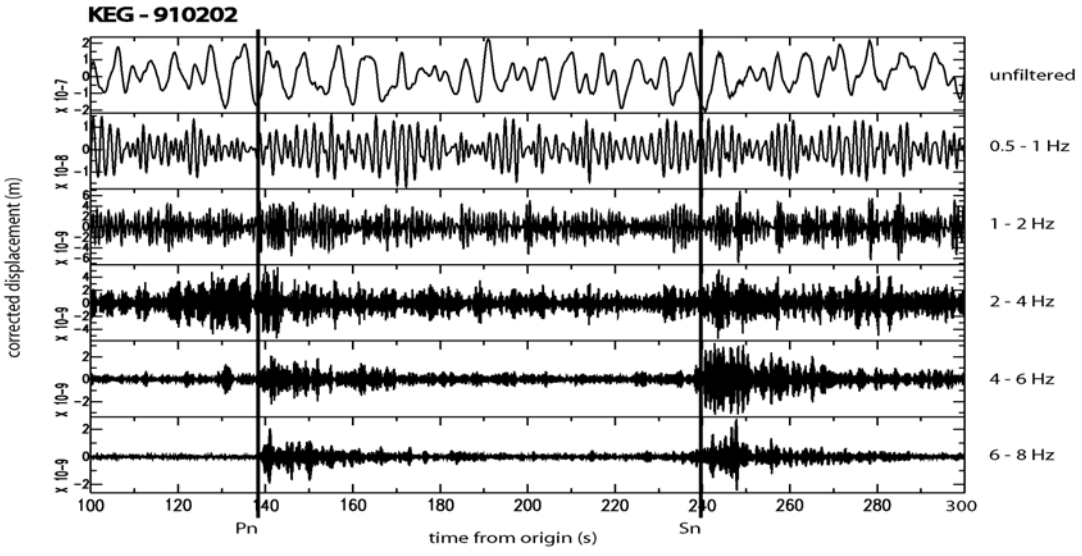


Figure 6: Multi-frequency bandpassed seismogram of the 01 July 1992 event recorded at KEG. Note that SNR increases at the higher frequency ranges. This is a good example that led us to question what path effects were responsible for high frequency propagation such as this.

Finally, we compare cross-spectral values of regional Libyan earthquakes against values of Nevada Test Site (NTS) earthquakes and explosions to show certain frequency ranges at specific stations as solid verification parameters (Figure 9). The figure shows two distinct populations; one of NTS events and one of Libyan events. We note the good separation of the two populations through the entire range of magnitude.

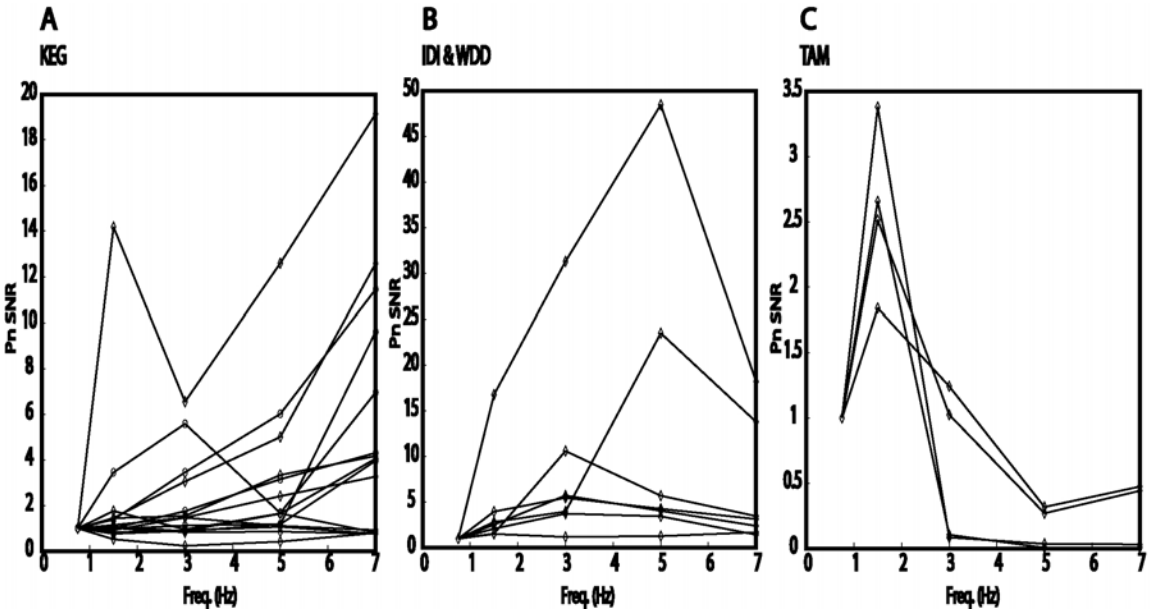


Figure 7: SNR-Frequency diagrams show trends in station-frequency dependence, note the unusual high frequency propagation displayed at KEG accompanied by the expected high frequency attenuation at TAM.

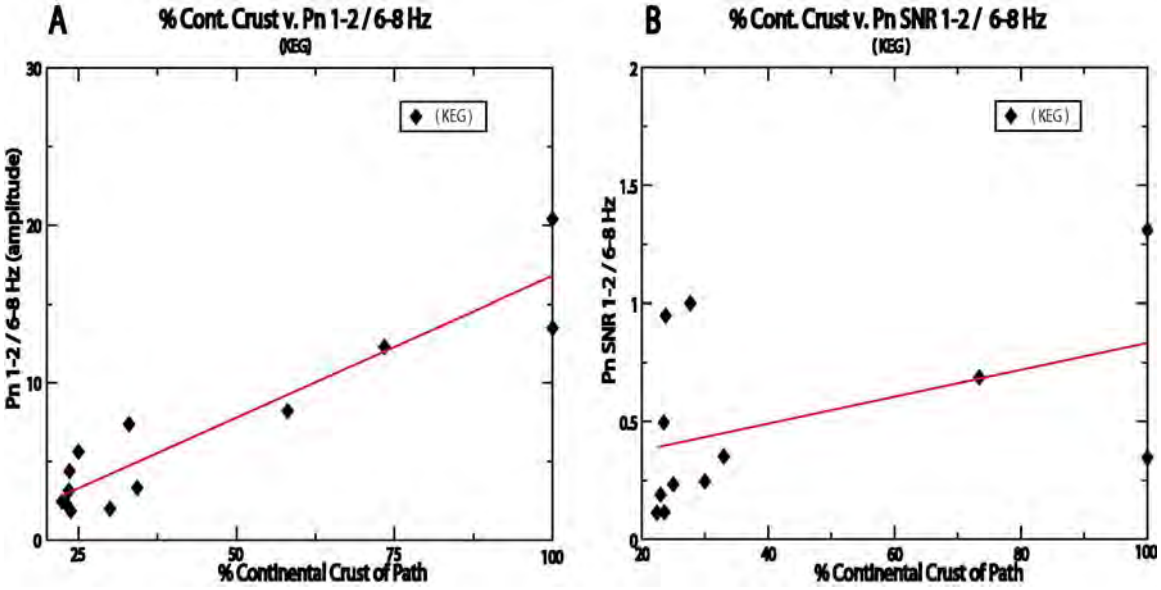


Figure 8: Shows a good correlation between the percentage of continental crust in the source-receiver path and cross-spectral values. Note the lower the cross-spectral value the better the high frequency propagation.

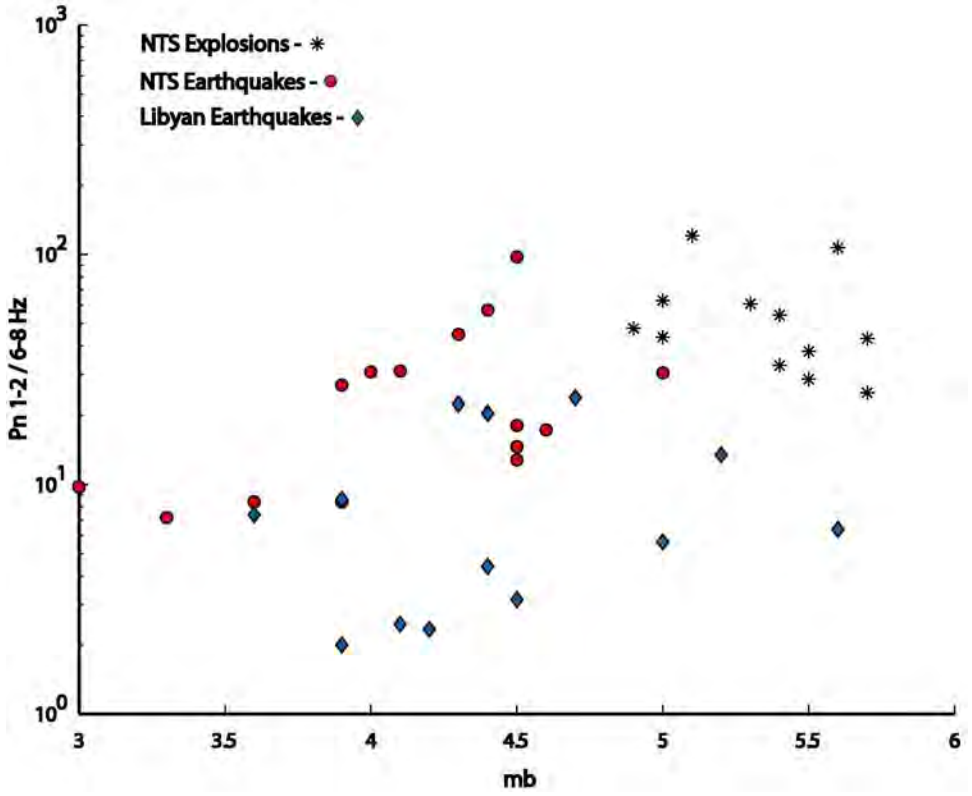


Figure 9: Cross-Spectral ratio comparison of regional Libyan earthquakes and Nevada Test Site (NTS) explosion and earthquake events. All Libyan events were recorded at KEG; note the good separation of the Libyan and NTS populations through the entire magnitude range.

CONCLUSIONS AND RECOMMENDATIONS

Our average 1-D velocity model for Libya worked well in predicting the *P*-wave arrival time for seismic events, but could not produce surface wave synthetics that matched the seismic data at frequencies less than 20 s. This could be due to the fact that we are close to the plate margin and an average 1-D velocity model may not work suitably because of the thinning of the crust. We obtained better results when we developed path specific 1-D velocity models (1.5D approach). In this case, there was a significant increase in the correlation of the synthetic seismogram and the data. At this stage, we do not have enough data to completely validate our model, but as more events occur with a significant portion of the source receiver path traversing Libya, we expect to further update and test LIBYA3D.

For regional station KEG, we see a strong correlation between percentage of continental crust and signal propagation in the high frequency ranges; however, this relationship does not persist for IDI, WDD, and TAM, where there is a lack of data. Most of the paths for IDI and WDD are purely oceanic, since they are island stations, while the paths for TAM are purely continental, which skews the results. We feel that given a full range of data that this parameter will consistently predict high frequency propagation events that would aid in verification work in regions of mixed crusts. Using LIBYA3D, we found weak correlations for all four stations when comparing crustal volumes to cross-spectral values. We feel more data is needed before drawing any solid conclusions on the relationship between crustal volume and high frequency propagation.

REFERENCES

Carmicheal R. S., 1989, Practical handbook of Physical Properties of Rocks and Minerals, CRC Press, Inc. 2000, 741 pp.

Dial, P., 1998, An integrated geophysical study of North Africa and Mediterranean lithospheric structure, *PhD. Dissertation*, University of Texas at El Paso 207 pp.

Goudarzi, G.H, and Smith J.P., 1978, Preliminary-structure contour map of the Libyan Arab Republic and other adjacent areas, *USGS.*

Hearn, P. Jr., et Al, 2001, Global GIS Database: Digital Atlas of Africa, *USGS. Digital Data Series (DDS-62-B).*

McNamara, D.E., Walter, W.R., Shultz, C. and Goldstein P., 1996, Regional phase propagation in northern Africa and the Mediterranean (abstract), *Seism. Res. Lett.*, 67, p 47.

Nafe, J.E. & Drake, C.L., 1957. Variation with depth in shallow and deep water marine sediment of porosity, density and the velocities of compressional and shear waves, *Geophysics*, 22, 523-553.

Seber, D.E., Sandoval E., Vallve, M., Brew, G. And Barazangi, 1996, Development of a geological and geophysical information system and seismological studies in the Middle East and north Africa, *Proceedings of the 18th Annual Seismic Research Symposium on Monitoring a CTBT*, 4-6 September 19996, pp. 1026-1035, PL-TR-96-2153, ADA313692.

Velasco, A.A., Hartse, H.E., Randall, G.E. (2003) Propagation or Source? Analysis of a Moderate-Magnitude Seismic Event in the Qinghai Province, China, *Bull. Seism. Soc. Am.* 93, 2281-2288.

Walter, W.R., Mayeda, K.M., Patton, H.J. (1995) Phase and Spectral Ratio Discrimination between NTS Earthquakes and Explosions. Part I: Empirical Observations, *Bull. Seism. Soc. Am.* 85, 1050-1067.

Zhang, T. & Lay, T. (1994) Analysis of Short-Period Regional Phase Path Effects Associated with Topography in Eurasia, *Bull. Seism. Soc. Am.* 84, 119-132.

DEVELOPMENT OF A THREE-DIMENSIONAL VELOCITY MODEL FOR THE CRUST AND UPPER MANTLE IN THE BARENTS SEA, NOVAYA ZEMLYA, KARA SEA AND KOLA-KARELIA REGIONS

Hilmar Bungum[1], Oliver Ritzmann[2], Jan. I. Faleide[2], Nils Maercklin[1], Johannes Schweitzer[1], Walter D. Mooney[3], Shane T. Detweiler[3], and William S. Leith[3]

NORSAR[1], University of Oslo[2], United States Geological Survey[3]

Sponsored by National Nuclear Security Administration
Office of Nonproliferation Research and Engineering
Office of Defense Nuclear Nonproliferation

Contract No. DE-FC52-03NA99508[1], DE-FC52-03NA99509[2], DE-FC52-03NA99531[3]

ABSTRACT

The principal objective of the present study is to compile a three-dimensional (3D) seismic velocity model of the crust and upper mantle for the larger Barents Sea region, at a spatial resolution of nominally 50x50 km. The main accomplishments so far have been concerned with compilation, collation and review of primary existing geophysical data, including first of all deep seismic wide-angle profiles (OBS and ESP - two-ship expanded spread profiles), deep multi-channel seismic reflection (MCS) profiles, and shallower 1D velocity profiles. The main source of data has been a database compiled over many years at the University of Oslo (UiO), supplemented by data compiled at the United States Geological Survey (USGS) and from collaboration partners in Norway and in Russia. Subsequently, detailed comparisons of data and models between the UiO and USGS have been performed, and unified criteria for quality assessment have been developed. The result is a full integration of the underlying data, and a common unified model.

The 50x50 km grid tiles in the target region have been defined in an optimum way such that the tiles form a fully equi-distant grid. The filling of the grid tiles so far shows a very good coverage in the western Barents Sea, a reasonable coverage also in the Novaya Zemlya region, but is less-constrained in the northern and northeastern parts of the target region. The results show that the depths to Moho vary from about 10 km in the oceanic crustal domain to more than 40 km in coastal regions of Norway and Russia and in the Kara Sea, while sediment thicknesses are 15-20 km in the southwestern and eastern parts of the Barents Sea. Following the USGS methodology each grid tile is represented with layers for ice, water, soft sediments, hard sediments, and crystalline upper, middle and lower crust. Finally there is a layer describing the seismic velocity and density of the uppermost mantle, which is controlling Pn and Sn travel times.

We have also acquired an upper mantle model (Shapiro and Ritzwoller, 2002) that eventually may be integrated with our new crustal model and tested for a ground truth (GT) database of about 50 events that also has been established as a part of this study. Since some large regional distances also will be used when comparing observed GT travel times with computed travel times through the established model, a mantle velocity model down to about 400 km is needed. To facilitate this travel time testing a number of 2D profiles have been established through the regions that are well covered with initially sampled 1D velocity functions, followed by different smoothing and interpolating techniques, dependent on which modelling method that will be applied. So far 2D ray tracing and finite difference methods have been used here, with preliminary testing also of 3D methods.

Since the grid tiles filled with primary data are unevenly distributed it has been necessary also to develop and to test methodologies for interpolation and extrapolation, in order to have all tiles filled. In regions where the data coverage is not dense, geological provinces are defined which are supposed to hold similar tectonic histories. In this case a method is being tested in which the velocity profiles have been used to calculate the crystalline crustal thickness as a function of sediment thickness. Since the crustal rock velocity distribution for a particular geological province is known, a regional depth-to-basement map can used to calculate representative 1D velocity-depth functions for the entire crust. This technique looks promising as a means for providing an equally sampled crustal model, as is required for seismological purposes.

OBJECTIVE

The principal objective of this study has been to compile a three-dimensional seismic velocity model of the crust and upper mantle for a region including the Barents Sea, Novaya Zemlya, Kara Sea and Kola-Karelia regions, at a spatial resolution of nominally 50x50 kilometers. Using existing seismic profiling data compiled by the University of Oslo, USGS and the Russian institutes, we are in the process of constructing a high resolution, regional lithospheric model based on a comprehensive compilation of all available seismological, geophysical and (where available) drill hole data. The resulting regional lithospheric model will consist of seven crustal layers: (1) ice, (2) water, (3) soft sediments, (4) hard sediments, (5) crystalline upper, (6) middle, and (7) lower crust. An eighth layer describes the seismic velocity and density of the uppermost mantle (with P_n and S_n velocities). Both P- and S-wave velocities and density are specified in each layer.

The purpose of making higher-resolution crust models is to improve seismic event locations and event discrimination for nuclear test monitoring. The goal is to develop a model useful both for further research on the detection, location and identification of small events in the study region and for operational use in locating and characterizing seismic events in the region. Along with the development of the model, a calibration and validation program will be executed, aimed both at quality controlling the model through comparisons between observed and synthetic travel times, and at investigating the potential improvements in terms of event locations.

RESEARCH ACCOMPLISHED

The target area for this study is shown in Figure 1, where a 50x50 km sampling grid has been defined as shown by hexagons. The chosen tiling provides the best conditions for the calculation of transects for subsequent travel time modeling (ray tracing). The grid should also be easy to use as it will be relatively straight forward to assign the nearest tile to whatever coordinates that someone may want to use, and it also optimizes the number of individual 1D models that must be constructed for the model while still maintaining the basic resolution.

The western part of the target region shown in Figure 1 is extensively covered by Norwegian seismic reflection data that largely is available at UiO, where also a large database of 1D velocity profiles has been established. The eastern areas are covered, albeit not so densely, by Russian studies. Most of these studies are, however, too shallow for the purposes of the present study, and what remains of primary interest are the wide-angle profiles shown in Figure 1. The data are mostly based on continuous seismic refraction profiles that are sampled every 25 km (~560 points). These data were achieved by gathering digital profiles (ray-tracing models of newer experiments) and by digitizing published velocity-depth profiles (the complete reference list comprises a large number of entries and will be published elsewhere). The majority of these seismic profiles was acquired with receiver spacings of less than 30 km so that a sampling interval of 25 km seems appropriate. About 120 velocity-depth functions were derived by depth-migration of deep-seismic multi-channel profiles with nearby ESP-information and subsequent gravity modeling (velocity-density conversion). Moreover, about 20 single-location velocity-depth functions complete the database (expanding spread profiles, surface-wave analysis). Approximately 90% of the database constrains the crust-mantle transition based on observed Pn and/or PmP phases.

Figure 1 also illustrates the inhomogeneity in data input distribution for the wide-angle and deep seismic reflection data. Whereas the western Barents Sea is well covered with seismic profiles, the eastern part shows larger gaps up to several hundred kilometers in the data coverage (6-8 tiles). Regarding the geological main provinces this disparity gets tempered since the eastern Barents Sea shows broader, more homogeneous extended geological units compared to the western part (Johansen *et al.*, 1992; Grogan *et al.*, 1998).

Model setup and results

The target region is covered by 1,490 tiles as shown in Figure 1, where the average distance between the tiles does not deviate from 50 km by more than about 300 m. For every tile a P-wave velocity (later to be extended with S-wave velocity and density) profile is gathered. The velocity-depth functions of the final model will follow an eight-layer model: water (ice), soft- and hard sediments (with a threshold at 3 km/s), upper-, middle- and lower igneous crust (variable velocity thresholds), and upper mantle.

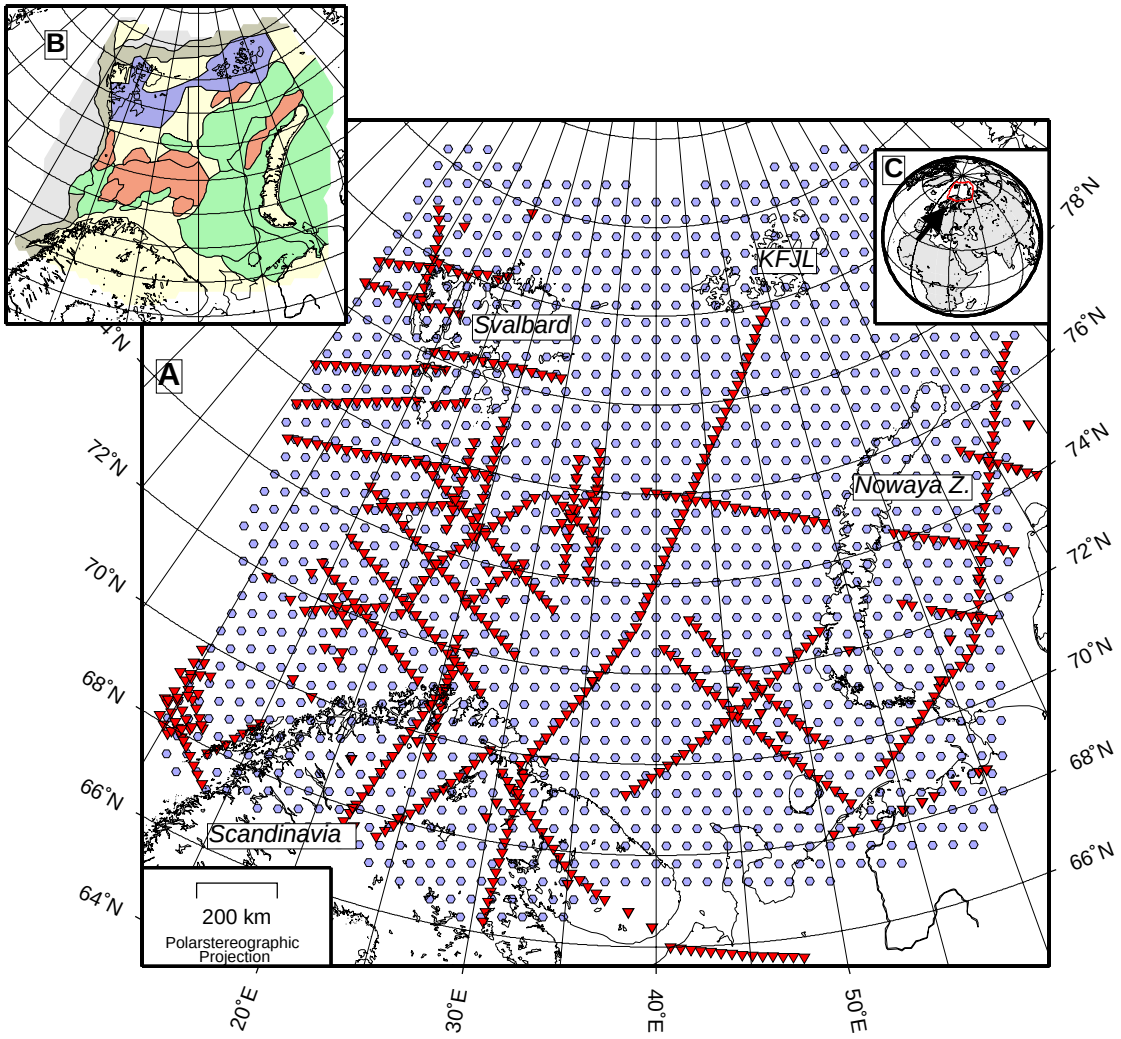


Figure 1. Target area for the present study (A). The sampling grid is shown by blue hexagons, defined so as to satisfy a 50x50 km spacing requirement, disconnected from the latitude-longitude grid. The red inverted triangles show the positions of sampled 1D velocity columns, largely reflecting available wide-angle and deep seismic reflection transects. The insert map (B) is showing the geological provinces within the target region: Onshore regions, platforms (yellow); offshore sedimentary basins (green); offshore basement highs (red); Cretaceous volcanic province (purple); continent-ocean boundary (brown); oceanic crust (grey). The insert map in the upper-right corner (C) shows the general location.

Figure 2 shows the depth-to-Moho at the locations of the sampled 1D velocity functions (triangles) where depth is color coded by the rainbow palette. The depth range varies between 4.5 km off western Svalbard, within very thin oceanic crust (2 km water depth), and 54 km within the cratonic region of northern Scandinavia. P-wave velocities below the Moho range between 7.4 km/s (serpentinized peridotites at fracture zones along Knipovich Ridge) and 8.35 km/s below Scandinavia. Initially, the work on developing this model was done in parallel at UiO/NORSAR and at USGS, both of which having extensive databases for the target region.

As expected, there was a considerable overlap between the databases employed by UiO and USGS, and the nature and details of this overlap have been fully resolved through a recent workshop in Oslo. The databases have now been completely coordinated and integrated, resulting in a common model, albeit preliminary, based on joint efforts within

the project. The final model, with optimal resolution and quality, will be constructed on the basis of original and project reviewed data which are clearly identified and documented, emphasizing transparency.

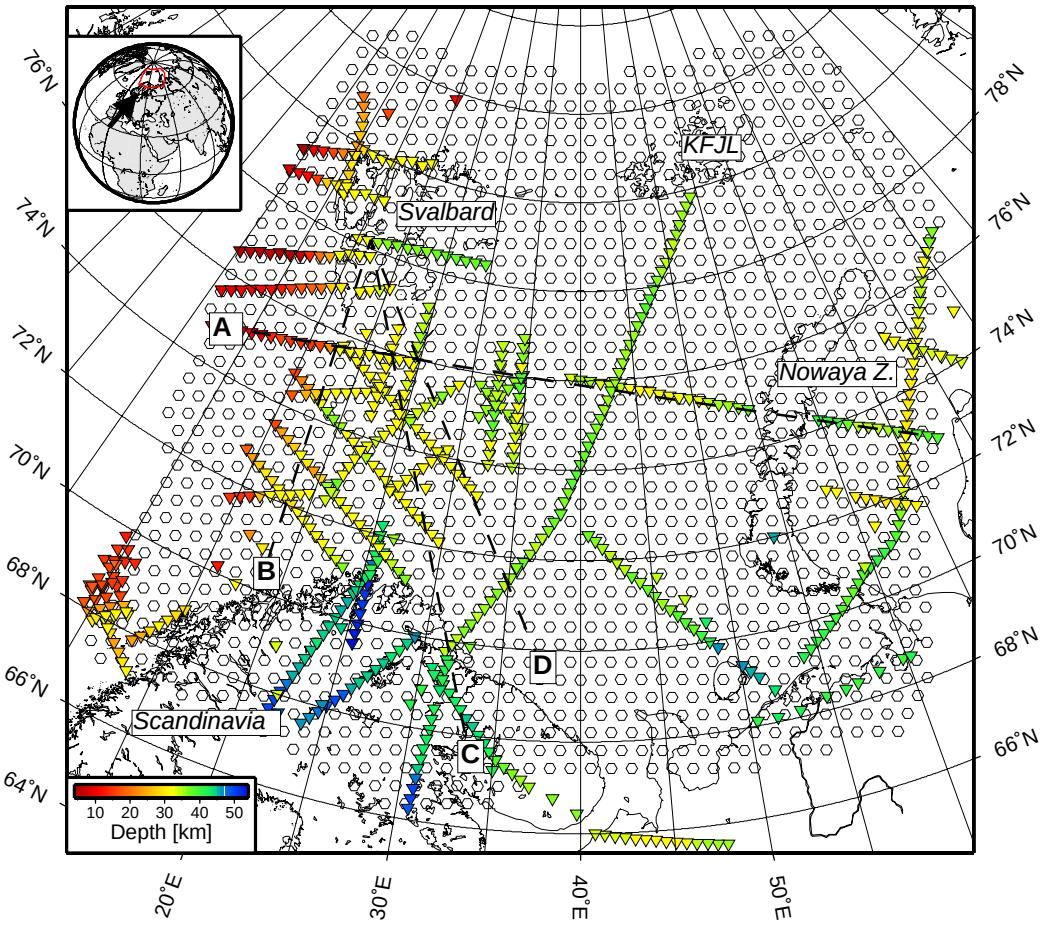


Figure 2. Map showing the depth-to-Moho at all sampling coordinates that directly constrain the crust-mantle boundary (color-coded, inverted triangles). The hexagons show the 50 km-equal spaced grid-construction of the final model. The dashed lines mark the location of the transects A (running W-E in the middle of the map) and B-D (running southwards from Svalbard), to be used in subsequent figures.

In order to illustrate some of the contents of the velocity database (the sampled 1D velocity functions) in Figure 2, we have constructed a transect (A) running west-east between 73 and 75^{o}N (shown in Figure 3). Generally, only sampled velocity functions (see triangles in Figure 2 for location) with a maximum distance of 25 km to the transect line are used for the profile construction.

The seismic velocities in Figure 3 are shown by the color palette in columns, where each column refers to a particular location, depicted by triangles, in Figure 2. In addition the sediment, basement and Moho boundaries are shown. This west-east profile (A) across the entire western Barents Sea identifies clearly the very particular structures in this region, with very thick sediment layers and a strongly varying depth-to-Moho discontinuity.

Since the constraints on the upper-mantle velocity structure are limited throughout the database, a homogeneous upper-mantle model is used initially, below the Moho velocities that are taken from the experiments. This will later, however, be replaced by an upper mantle model derived from Shapiro and Ritzwoller (2002), sampled down to a depth (~400 km) needed for modeling of far-regional P phases (Figure 4). The Moho depths from this model have

been demonstrated to be reasonably consistent with the model from the present study. Later, we hope to replace the Shapiro and Ritzwoller (2002) model by an updated model based on new inversions in which more regional surface wave (including higher mode) data are also included, in conjunction with Pn and Sn data.

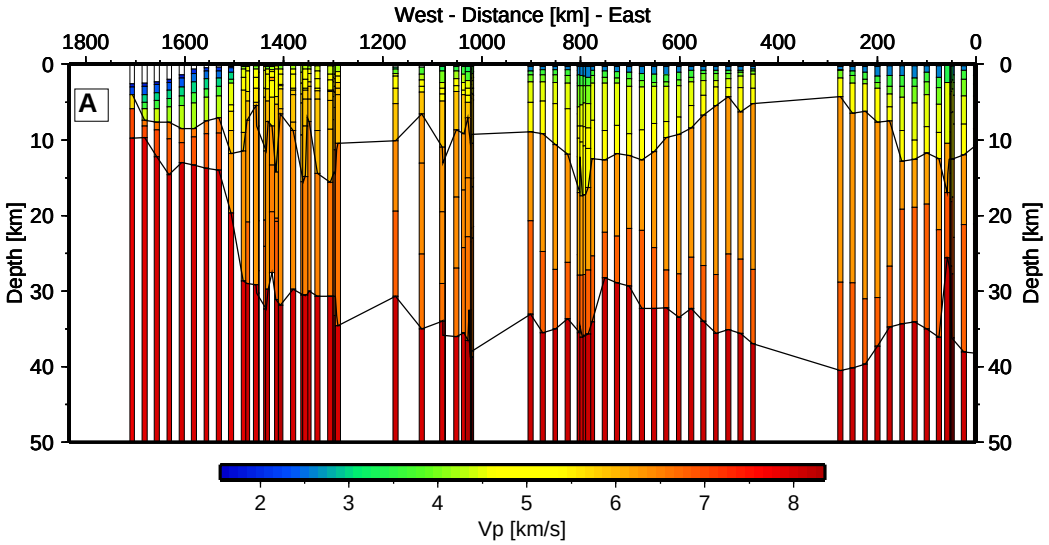


Figure 3. 1D-velocity functions along the EW-oriented transect A in Figure 2. The thick lines crossing the velocity columns mark the top of the crystalline basement and the Moho discontinuity, respectively.

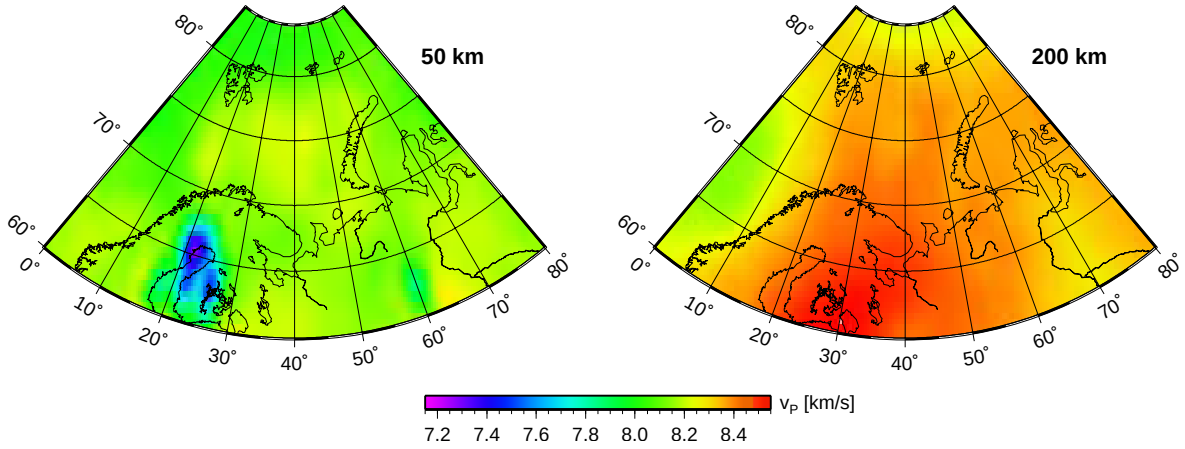


Figure 4. Mantle P-wave velocities at two depths (50 and 200 km), based on the model of Shapiro and Ritzwoller (2002). This model will be used initially in conjunction with the crustal and Pn velocity model established in this project. Courtesy of A. Levshin, Univ. of Colorado-Boulder.

Model interpolation, method and results

More than 40% of the 1,490 model tiles (Figure 1A) are directly constrained by one (or more) sampled velocity-depth function(s). According to the sampled seismic profiles some functions contain more detailed (geological) information than it is required for the suggested final 8-layer structure. To enable a homogeneous construction of constrained and unconstrained tiles of the final 3D model the following 'interpolation' method was tested and is now being considered to be used for filling the remaining tiles.

The provinces shown in Figure 1B bear in general a nearly similar geological history, hence a similar basin architecture can be assumed to be present throughout the entire province. It is reasonable to assume that this is due to a common setting in a broader tectonic regime and a common physical behavior of the deeper igneous crust and its isostatic response. An extensional regime would therefore result in increasing sediment thickness with decreasing igneous crustal thickness, while strong compression might lead to crustal thickening and subsequent erosion of sedimentary strata.

This assumption gains substantial support from an observed strong correlation between the sediment thickness and the remaining igneous crustal thickness. Three examples of this are shown in Figure 5a, where data are taken from the sampled velocity functions that appear as inverted triangles in Figure 5b. If we ignore some outlying observations (which should be expected), we find reasonably well constrained linear relations throughout most provinces, and we also find that these relations are significantly different from each other.

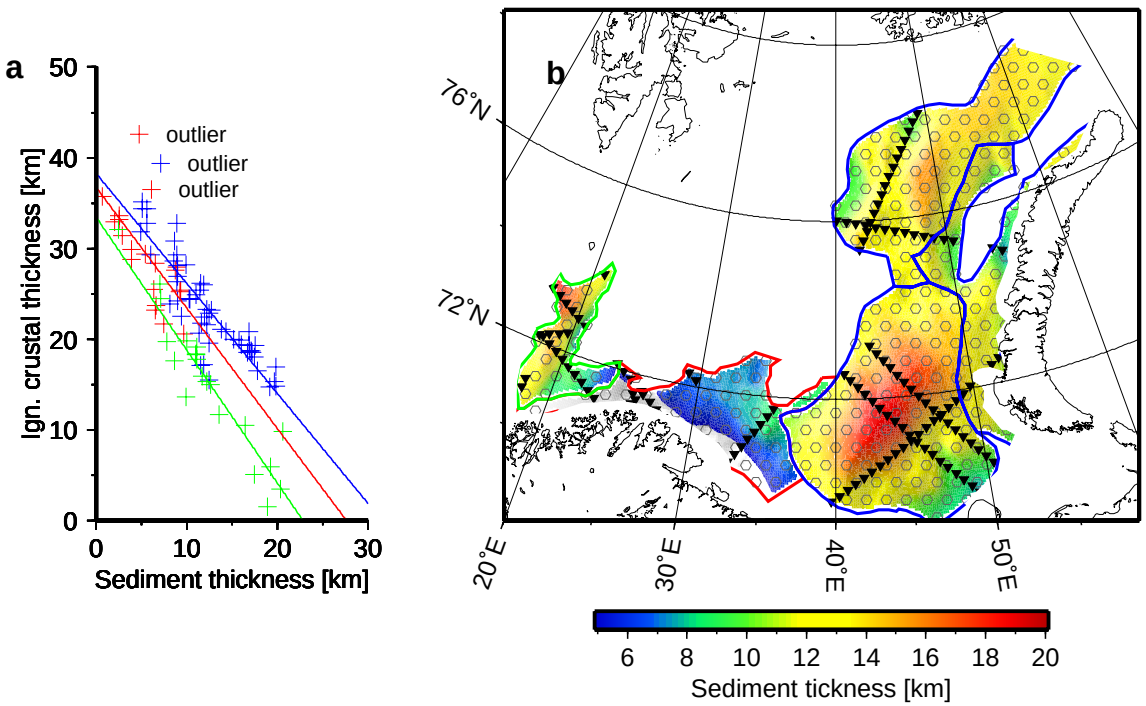


Figure 5. A. Relations between sediment thickness (abscissa) and igneous crustal thickness (ordinate) in three example regions: SW Sedimentary Basins (green); Finnmark Platform (red); and E-Barents Sea Basin (blue). For location see enclosed regions on map B. Relationships are taken from the sampled velocity functions, locations are marked by inverted black triangles in B. Green, red and blue thick lines in A are linear regressions that can be used for calculation of the igneous crustal thickness where only sedimentary thickness is known (Myklebust, 1994).

On this basis, area-wide sediment thickness data as taken from the so-called Magnetic Mapping of the Barents Sea (MMBS) project (Myklebust, 1994), based on potential field, seismic reflection/refraction, and borehole data, can potentially be used to calculate the igneous crustal thickness for those provinces that hold sufficient sampled profiles to manifest a relationship, as demonstrated in Figure 6. Tiles that are constrained by sampled profiles are equipped with the exact measured depth-to-basement and depth-to-Moho (hexagons in the vicinity of black inverted triangles). Unconstrained tiles are in this setup assigned a sediment thickness taken from area-wide data and an igneous crustal thickness inferred from manifested relationships. Mean seismic velocities for all six crustal and mantle layers are calculated from the sampled velocity-depth functions and are used for the entire province.

For the spread of the sediment thickness data of the MMBS-project (Myklebust, 1994) we calculated the respective total crustal thickness using 15 different regression lines, based on the methodology described above. Figure 6 illus-

trates well that occasionally, at province boundaries, the different regression parameters result in unintended stepping (e.g. 35°E, 72.5°N). Further it appears that prominent high and lows are aligned along sampled profiles (e.g. 40°E, 74°N). The latter effect is due to systematic deviations in the sedimentary thickness along these sampled profiles from the sediment thickness database (MMBS). In order to avoid these artefacts future steps will probably incorporate: (i) Initial adjustment of the sediment thickness data to the velocity database gathered within this project (merging), (ii) a final filtering/smoothing within and across geological provinces, (iii) adjustments of the province boundaries.

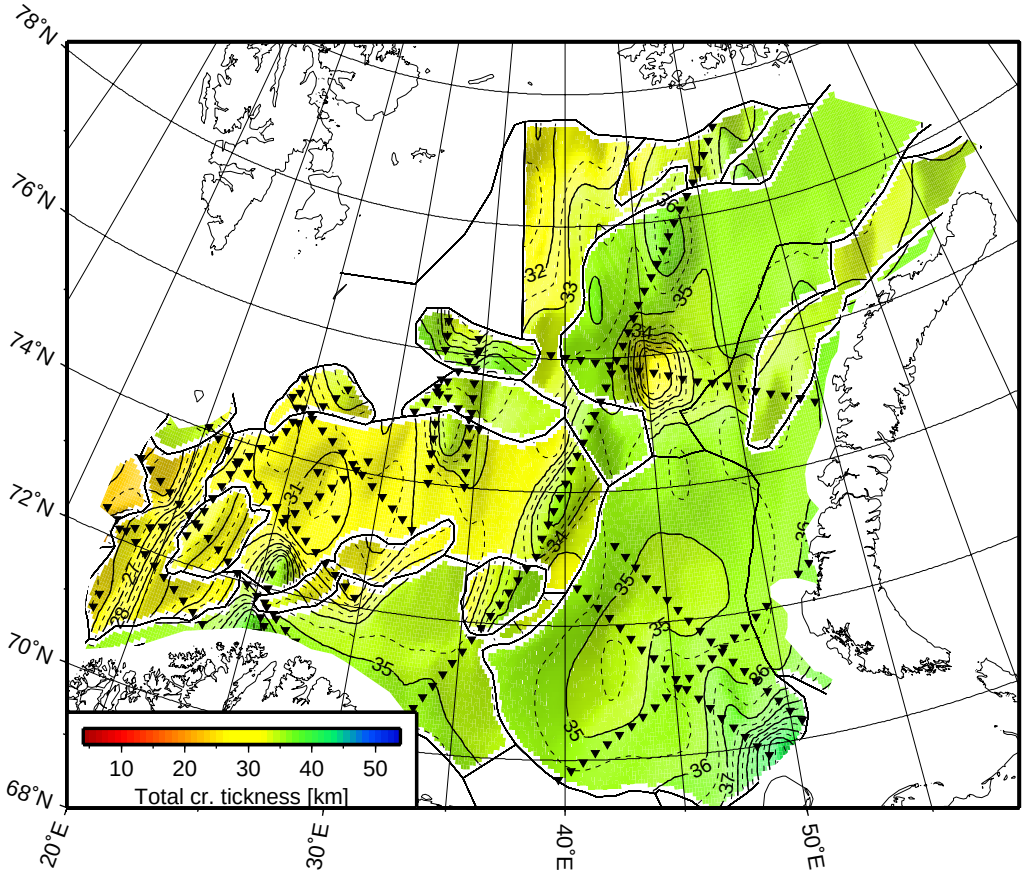


Figure 6. Map showing the inferred (interpolated) total crustal thickness for 15 geologic provinces within the target region, covering most of our target area. Black inverted triangles mark the position of sampled velocity functions. Solid isolines at 1 km, dashed lines at 0.5 km. The total crustal thickness is nearly similar to the Moho depth, since the water depths are not higher than 400 m within the displayed region.

The thickness of the igneous oceanic crust is independent from sediment thickness, rather it is a function of other factors such as spreading rate or asthenospheric temperatures. Therefore the method described above is not applicable for this domain. The sedimentary thickness data are used to constrain the thickness of the sedimentary layers of the velocity models. The igneous crustal thickness within the oceanic provinces therefore have to be derived basically by lateral interpolation, since regional seismic profiles show no indications for broad thickness undulations, i.e. basement ridges or extensive fractures.

Ground truth data; validation

A database of around 50 potential ground truth (GT) events has been established for this project, to a large extent based on work done under earlier Defense Threat Reduction Agency (DTRA) and Department of Energy (DOE) con-

tracts. The events are all relocated based on the available travel time data, and initial GT levels have been assigned based on the formal uncertainties. These GT assignments will be re-evaluated at a later time.

Figure 7 shows the travel paths for these GT events. Seismic stations are indicated by blue triangles while the events are plotted as open circles, color coded based on formal location uncertainties. For all of these travel paths, seismic data are archived and available at NORSAR, constituting an excellent basis for subsequent model validation and refinement, based on ray tracing through 2D and 3D models. It is seen from Figure 7 that large parts of the target region, notably the eastern Barents Sea and even more so the Kara Sea and the areas southeast of Kaiser-Franz-Josef Land, are not well covered in terms of travel paths, related to low seismicity and poor station coverage. The aims of this study are to determine what is available and compile it into a working database, which we believe we have done, and it seems there is no information available for this region of our study area.

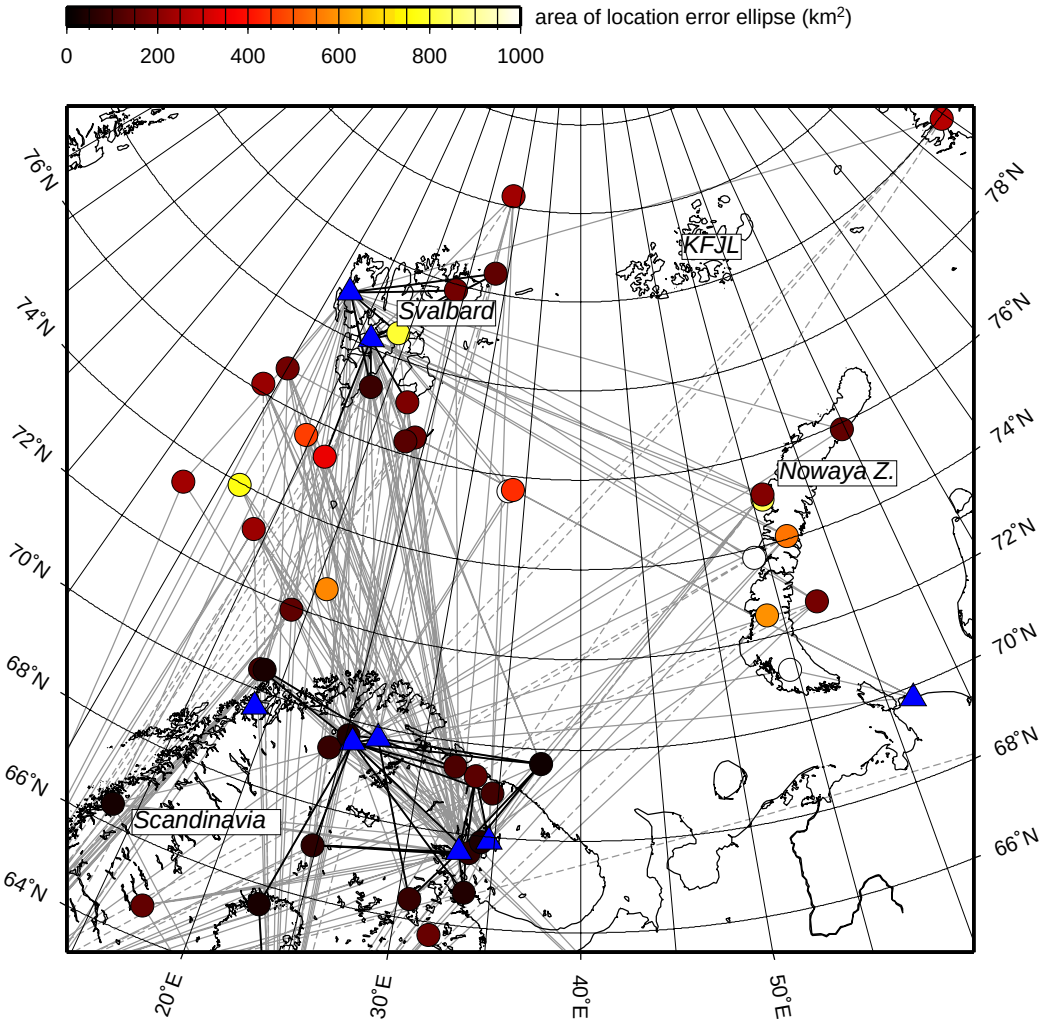


Figure 7. Ground truth travel paths in the target region, where the lines indicate Pn and the dashed lines longer-distance P phases. For most of the Pn data there are also Sn data. The events are color coded with respect to the formal uncertainty (area in km^2).

Figure 2 also shows the location of three additional crustal transects (B, C, D) in the western Barents Sea between northern Fennoscandia and Svalbard (the SPITS array). Transect C stretches from the Kola peninsula to SPITS, and transect D from the location of the Kursk accident to SPITS. Whereas these two transects are in a region of a rather simple, layered crustal structure, the westernmost transect B crosses deep sedimentary basins.

For these three profiles, 2D models comparable to the one in Figure 3 (for transect A) have been established. To calculate synthetic travel times, gaps in the velocity structure have to be filled by interpolation, the model has to be extended downwards, and the model parameterization must be adapted to the specific modelling algorithm used. Figure 8 (bottom panels) shows the 2D velocity structure along the three transects B, C, and D on a regular grid. Crustal and uppermost mantle velocities are taken from the 1D velocity-depth functions, and gaps were filled by Delauney triangulation between 1D functions. Here, the model is extended downward by the 1D BAREY model for the Barents Sea (Schweitzer and Kennett, 2002).

Wave fronts and synthetic travel times were then calculated using a 2-D finite-difference (FD) scheme with a grid node spacing of 0.5 km in both directions. Since the FD scheme assumes a Cartesian grid, an Earth-flattening transformation has been applied to each of the velocity models to account for the spherical Earth. Wave fronts are shown every 5 seconds (dashed lines) and 10 seconds (solid lines). Corresponding ray paths reach depths of about 100 km, depending on the velocity gradient and maximum profile distance. Synthetic first arrival travel times for the three transects are shown in the top panel of Fig. 8. Although corresponding rays travel mostly in the upper mantle, the laterally variable crust significantly affects the resulting travel time curves.

The three transects shown here will be updated continuously and used as test cases for various model parameterizations and modelling algorithms.

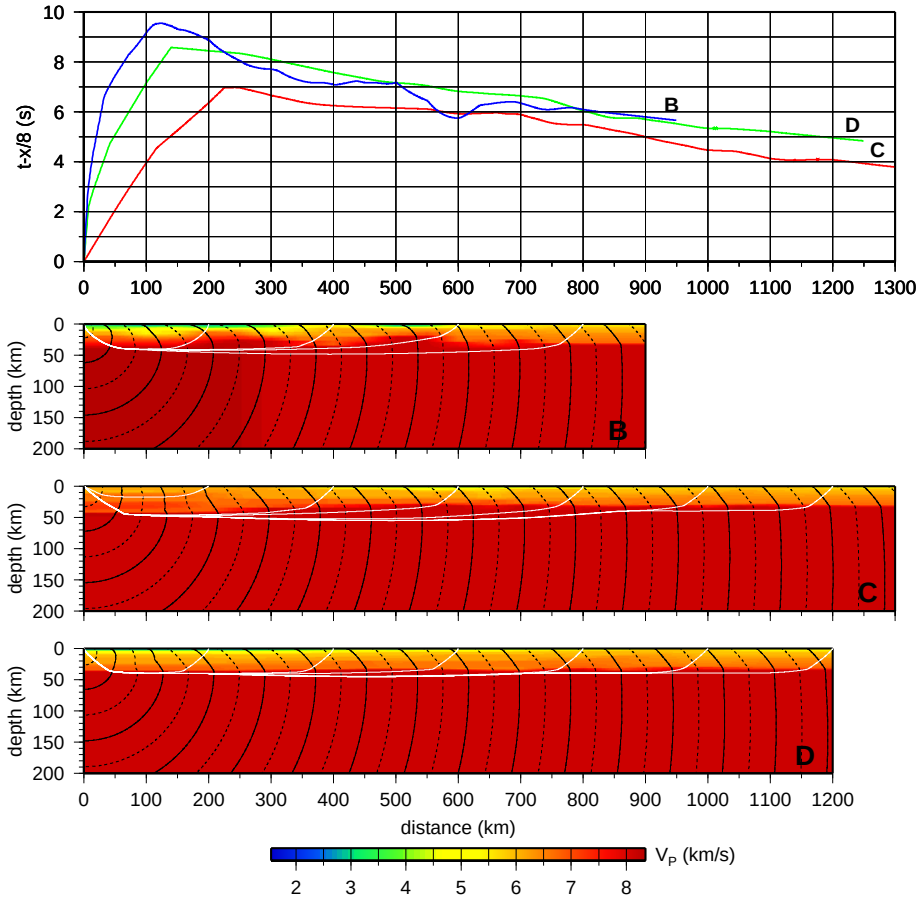


Figure 8. Wave fronts, ray paths and first arrival travel times for the transects in Figure 2, based on a FD algorithm (Cohen and Stockwell, 2003). A reduction velocity of 8 km/s has been applied. The ray paths reflect the small gradient in the upper mantle velocities down to about 200 km. For distances up to 2500 km the rays will penetrate down to about 400 km.

CONCLUSIONS AND RECOMMENDATIONS

After the first year of this two-year study we have come a long way in that the UiO and USGS databases have been fully integrated, done in part in two Oslo workshops, followed by the filling of all of the tiles that can be tied directly to primary observed data. The amount of data that have been collected and reviewed is extensive, with emphasis given to unification, quality assessment and transparency. So far only P-wave velocities have been filled in, but this will be extended with S-wave velocities and densities later. The results show that the depths to Moho vary from about 10 km in the oceanic crustal domain to more than 40 km in coastal regions of Norway and Russia and in the Kara Sea, while sediment thicknesses are 15-20 km in the southwestern and eastern parts of the Barents Sea.

The data coverage is quite good in the western Barents Sea, but weaker in other parts of the target region. Because of this it has been necessary to develop a methodology for filling in the rest of the tiles. The approach which is being tested now and which appears to be quite promising, is based on separating each tile into a geologic province or unit, supposed to hold similar tectonic histories. The key here is the fact that we find a strong correlation between the sediment thickness and the remaining igneous crustal thickness, calculated from the available velocity profiles. Since the crustal rock velocity distribution for a particular geological province is known, a regional depth-to-basement map can therefore be used to calculate representative 1D velocity-depth functions. Using this methodology we have been able to fill most of the tiles in the continental crust not covered by primary data. For the oceanic crust we expect to use a procedure based essentially on lateral interpolation.

The work will continue into the second year with the acquisition of primary data in parallel with the continued filling of the 1,490 grid points (tiles), including S-velocities and densities. A close cooperation with Russian institutions are essential to this end, including Sevmorgeo and VNIIOkeangeologia of the Russian Academy of Science. Both of these have contributed to updates on Russian data/results in our regional compilation. There are also plans for acquisition of new deep seismic data as part of a current Norwegian-Russian research program.

The primary wide-angle data used in the present study provides only Moho (Pn) velocities, while some of the distances to be used in the travel time testing will have rays traversing down to 400 km. Because of this we have initially replaced a homogeneous upper mantle model with the one of Shapiro and Ritzwoller (2001). In cooperation with Dr. Anatoli Levshin, we are planning to combine the data behind this model with more regional surface wave, and Pn and Sn data (e.g., Levshin *et al.*, 2001), thereby developing an updated model also for the upper mantle.

A soon as the first version of a complete model has been established, the validation work will be intensified, essentially based on comparisons between observed and calculated travel times. The GT database already established will have to be further refined, tested and classified in terms of GT levels, and possibly also extended with more events and phase readings. For travel time modelling along transects we use 2D ray tracing in Cartesian and spherical coordinates as well as FD eikonal solvers. Case studies in 3D will follow during the second year of this study.

REFERENCES

Grogan, P., K. Nyberg, B. Fotland, R. Myklebust, S. Dahlgren, and F. Riis (1998), Cretaceous magmatism south and east of Svalbard: evidence from seismic reflections and magnetic data, International Conference on Arctic Margins III, Polarforschung 68, 25-34.

Cohen, J. K. and J.W. Stockwell (2003), CWP/SU: Seismic Unix Release 37: a free package for seismic research and processing, Center for Wave Phenomena, Colorado School of Mines.

Johansen, S.E., B.K. Ostisty, Ø. Birkeland, Y.F. Fedorovsky, V.N. Martirosjan, O. Bruun Christensen, S.I. Cheredeev, A.A. Ignatenko, and L.S. Margulis (1992), Hydrocarbon potential in the Barents Sea region: play distribution and potential, in: Vorren, T.O., E. Bergsaker, Ø.A. Dahl-Stamnes, E. Holter, B. Johansen, E. Lie, and T.N. Lund, Arctic geology and petroleum potential, NPF Special Publication 2, 273-320.

Levshin, A.L., M.H. Ritzwoller, M.P. Barmin, A. Villaseñor, and C.A. Padgett (2001), New constraints on the arctic crust and uppermost mantle: surface wave group velocities, P_n, and S_n, *Phys. Earth Planet. Int*., 123, 185-204.

Myklebust, R. (1994), Magnetic mapping of the Barents Sea (MMBS) Interpretation report, Amarok A.S., Oslo, Norway.

Schweitzer, J. and B.L.N. Kennett, (2002), Comparison of Location Procedures - the Kara sea Event 16 August 1997, Semiannual Technical Summary, NORSAR Sci. Rep. 2-2001/2002, Kjeller, Norway.

Shapiro, N. M., and M. H. Ritzwoller (2002), Monte-Carlo inversion for a global shear velocity model of the crust and upper mantle, *Geophys. J. Int.*, 151, 88-105.

USING GROUND TRUTH EVENTS FOR TRAVEL TIME CALIBRATION AND STUDYING SEISMIC ENERGY GENERATION AND PARTITIONING INTO VARIOUS REGIONAL PHASES

Yefim Gitterman[1], Vladimir Pinsky[1], Kyriakos Solomi[2], Rami Hofstetter[1], Cemil Gurbuz[3], and Mehmet Ergin[4]

Geophysical Institute of Israel[1], Geological Survey Department of Cyprus[2], Bogazici University[3], Kandilli Observatory and Earthquake Research Institute[4], and TUBITAK Marmara Research Center[5]

Sponsored by Defense Threat Reduction Agency and Air Force Research Laboratory

Contract No. DTRAOI-01-C-0119[1] and FI962 -03-C-0I24[2]

ABSTRACT

On-land seismic calibration explosions were recently conducted in Cyprus complementary to a previous calibration series at Rotem quarry, Israel. The experiment's goal was to improve our models for calculating travel times of seismic waves to local and regional seismic stations, and to contribute to the study of explosion source phenomenology in specific geological settings. A preliminary shot of 300 kg and the subsequent main calibration shot of 2,000 kg were conducted in the same deep (~200 m) borehole full of water located in the diabase massif in the Macheras Forest. Both explosions were accompanied by a series of water fountains and gas emissions in the air of more than 100 m in height for 10-30 seconds. The explosions produced much higher frequency seismic energy than the Dead Sea and Rotem calibration shots, which resulted in rapid signal attenuation with distance. Strong seismic signals with prominent P first arrivals dominant over weak S waves were observed at the close broadband (BB) station CSS (~20Hz at distance ~10 km). Peak frequencies and spectral shape were nearly identical for both calibration shots, only amplitudes increased for the larger shot (4-5 times). The relatively low seismic strength and the invariance of spectral content with charge size were due to the placement in a deep borehole in diabase filled with water. High-frequency P-signals can be still found after narrow-band filtration at some remote (up to 300 km) portable stations deployed by TUBITAK and KOERI in Turkey. The explosions, the first conducted for calibration of Cypriot stations, contributed to the improvement of the crustal velocity model in the Eastern Mediterranean and the characterization of seismic signal attributes of this unique source for nuclear monitoring identification.

Spectral ratios of Pg and Lg waveforms were used to investigate source-scaling relations for different pairs of explosions in Cyprus and Israel (Rotem quarry), and to estimate the source corner-frequency dependence on yield. We complemented the ground truth (GT) database by new GT0-GT5 events which occurred before and during the project, and also by GT10 cluster events, and verified newly computed source-specific station corrections (SSSCs) using this additional data. The database was enriched by GT5 events from east Turkey, Lebanon, southern and eastern Iran and Israel. New event clusters, from aftershocks of the Bingol, Turkey (M=6.4, May 1, 2003), and Dead Sea (ML=5.2; February 11, 2004) earthquakes, were collected and characterized.

The series of aftershocks from the Dead Sea earthquake were relocated using the AUTOLOC non-linear algorithm, and used for validation of the local travel time model obtained from calibration explosions in the Dead Sea in 1999 and for establishing empirical travel time corrections (ETTCs) for the Israel Seismic Network and the International Monitoring System (IMS) array AS049 on Mt. Meron. A subset of 10 aftershocks together with a number of regional earthquakes, recorded by the array, was used for tuning the newly designed ROBBEAM algorithm. The algorithm showed considerably better performance than conventional beamforming.

We computed 3D CUB1.0 model-based SSSCs for the IMS stations EIL, MRNI, KEG and BRAR and compared these SSSCs with ETTC from the relocation experiment and raw waveform pickings for different seismic phases. For a subset of the source-station travel time corrections the model based SSSCs were in good agreement with ETTCs, however large discrepancies were also observed. We then digitized the regionalization map of Sweeney and Walter (1998) and utilized the new Global Moho model of Barazangi and Sandvol (2001) to construct a modified model MCUB1. The new model shows less discrepancy between the ETTCs and SSSCs and was used as a starting point in a trial and error process for construction of the best-fit GCUB1 model. This model has been validated by travel time computations from the two large GT5 Izmit (August 17, 1999) and Bingol earthquakes in Turkey.

OBJECTIVE

The main objectives of the projects are: 1) determination and verification of empirical source scaling relationships, estimation of seismic efficiency and comparison of different calibration explosions; 2) quantifying the coupling and specific seismic source features, including energy generation analysis and energy partitioning into various regional phases; 3) collection of regional Ground Truth data GT0-GT5; 4) improvement and automation of event monitoring by development and application of advanced methods; 5) calibration of seismic travel times at local and regional distances in the Middle East and East Mediterranean region.

RESEARCH ACCOMPLISHED

Cyprus calibration experiment

GSD and GII conducted two experimental explosions in a deep borehole in the nature reserve of Macheras Forest, Cyprus (Figure 1). The borehole was placed in a diabase hard rock massif and filled with water, providing good stemming, and favorable factors for good coupling and a strong seismic signal. Ground Truth parameters and charge design of the explosions are presented in Table 1 and Figure 2.

First, we conducted a test explosion of 300 kg of dynamite. During this test we checked all logistics, timing, and explosive downloading operations. We measured ground vibrations at close distances and estimated that the ground vibration level during the main calibration explosion would be safe for nearby churches and monasteries (see Figure 1).

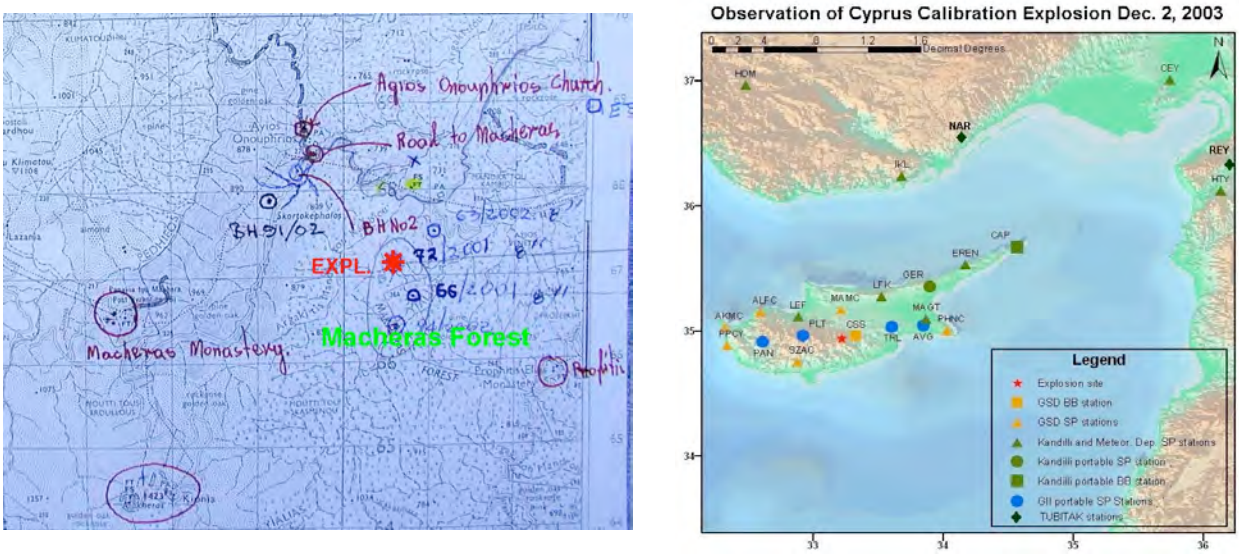


Figure 1. Location of Cyprus experimental explosions (left) and recording stations (right).

Table 1. Ground truth parameters of Cyprus explosions

Date	Borehole #	Coordinates Latit. Long.	Origin Time, GMT	Charge, kg	Hole depth, m	Water level, m	Charge length, m
17.11.03	BH72/01 203 mm	34.94604°N 33.22509°E	13:17:23.17	300	213	9.5	8
2.12.03			13:00:00.92	2000	208		26

The test shot did not damage the borehole, so the main calibration explosion of 2000 kg of dynamite was detonated in the same borehole refilled with ground water. The charge length (26 m) was less than expected (53 m), possibly due to a cavity created during the test shot (see Figure 2).

Video-record analysis showed that the explosion was followed by three water fountains separated by 7-8 sec, and gas emission into the air (total duration ~2 min) to a height of more than 100 m (Figure 3).

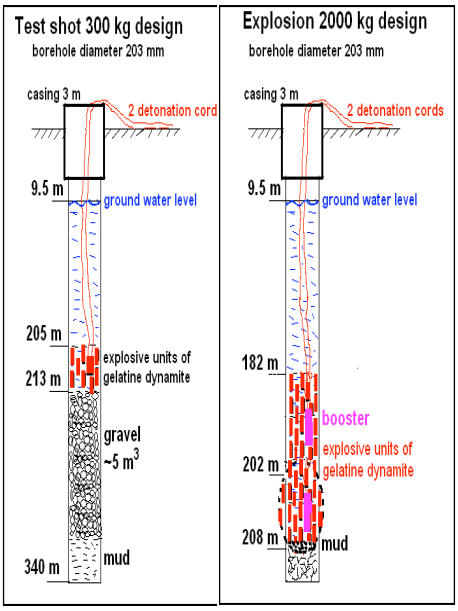


Figure 2. Charge design for the explosions (in the same borehole). For the 2-ton explosion the charge length (26 m) was less than expected (53 m), due to a cavity created during the test shot.



Figure 3. Water fountains during the test shot (left) and the 2-ton explosion (right), snapshots from a remote video-camera placed at the top of a nearby hill in Macheras forest.

For the explosions GSD and GII deployed a number of strong motion instruments at close range: 3 vibration sensors (at the same sites for both shots) and 3 accelerometers, to provide high-quality records of seismic radiation (Figure 4) for characterization of the specific source phenomenology.

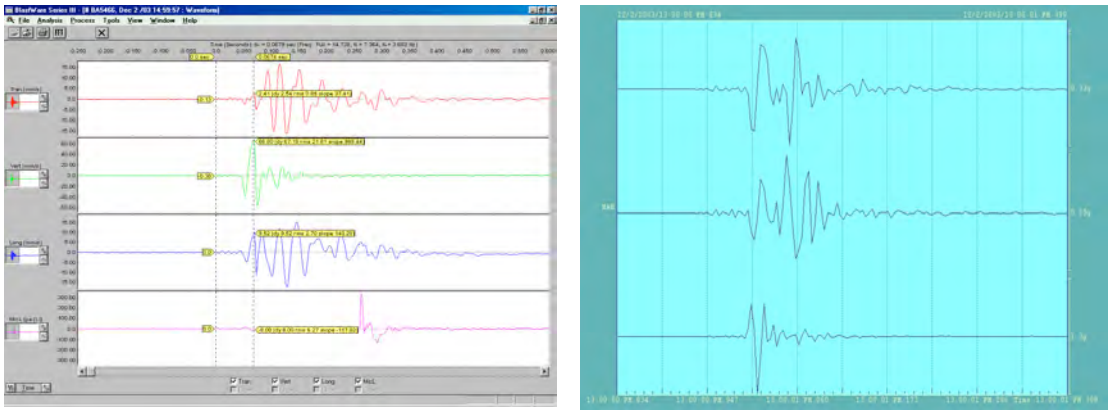


Figure 4. Records of radiated signals from the 2-ton shot at the closest epicentral distances: BlastMate III velocity sensors at ~100 m (left); and accelerometer at ~90 m, maximal vertical acceleration 1.3g (right).

Ground vibration records at close distances revealed large peak particle velocities, 2-3 times more than the values measured for calibration explosions at Rotem quarry, Israel (Gitterman et al, 2002), but at much higher frequencies (40-60 Hz). A maximal vertical peak velocity of 67 mm/sec was observed from the 2-ton explosion, ~1.7 times larger than for the test shot. Three accelerometers with GPS timing located at epicentral distances of 90-1900 m supplied good signals in the range 0.006-1.3g (Figure 4). These close-in records and impressive video observations suggest that the explosives detonated completely, resulting in increased amplitudes.

Strong high-frequency (~20 Hz) seismic signals, observed at the close BB station CSS, with prominent first P-arrivals, dominant over weak S waves, are similar for both explosions (see Figure 5). For the almost 8-times larger 2

ton charge the dominant frequency f_0 should decrease at least a factor of 2 times according to theoretical considerations: $f_0 \sim k/W^{1/3}$. Surprisingly, waveform, spectral shape and peak frequencies did not change for the larger shot as estimated; only amplitudes were increased (~5 times) as expected.

We hypothesize that the system "dynamite charge in deep borehole filled water + strong hard rock diabase massif" behaved like a resonator tuned to a specific high frequency, independent of power of excitation.

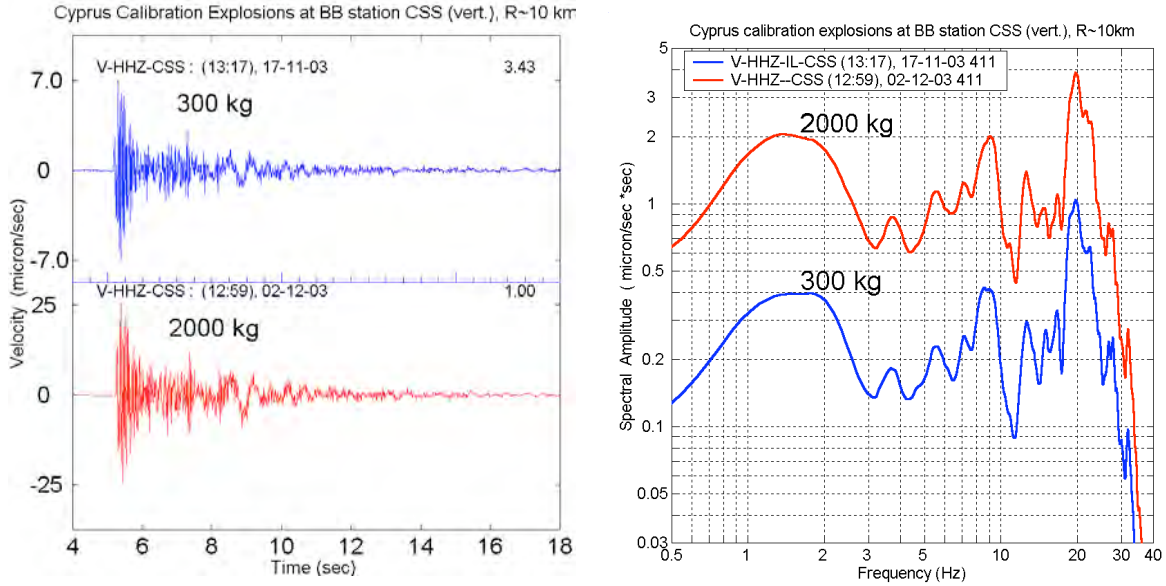


Figure 5. Comparison of waveforms and spectra of the whole signal (~ 10 sec) for the test and calibration explosions at CSS station.

GII, Kandilli Observatory and TUBITAK installed a number of portable short-period stations in Cyprus and Southern Turkey (see map in Figure 1). The large explosion was recorded by most of the Cyprus Seismic Network stations and several portable instruments, including a few stations in Turkey. At many stations the signal-to-noise ratio is low and signal can be found only after narrow band-pass filtration. The local magnitude of the explosion was estimated as $M_L \leq 2$, lower than predicted (M_L~2.3-2.5) from the high-coupling factors (fully-contained, explosives in water, hard rocks). However, it is known that deeper burial of a charge can result in decreasing seismic strength (e.g. Leith and Kluchko, 1998). The rapid attenuation of seismic energy with distance can be related to the unexpected very high-frequencies of the radiated signal, much higher than for the Dead Sea and Rotem calibration shots (Gitterman et al. 2002).

Construction of 1D velocity model for Cyprus.

The first Pg and Pn arrivals from the 2-ton explosion to the stations deployed in Cyprus and Turkey have been used to upgrade the existing velocity model by the modified Marquardt-Levenberg optimization procedure. An initial residual RMS=0.9 s for the routine GSD velocity model was reduced to RMS=0.48 as a result of the procedure. The station distribution, P travel time curves before and after the data fitting, and the initial and final P waves velocity models are shown in Figure 6. The new model differs from the previous one by essentially higher velocities in the upper crust, which changed from 4.3 to 5 km/s at H < 3 km range and from 5.5 to 6.3 km/s in the depth range 4–10 km. The early P arrivals to the stations AVG and ALFC on opposite sides of Cyprus and the higher velocity model agree with the overthrusted ophiolite structure of Cyprus, with its gravity anomaly (Makris & Wang, 1994).

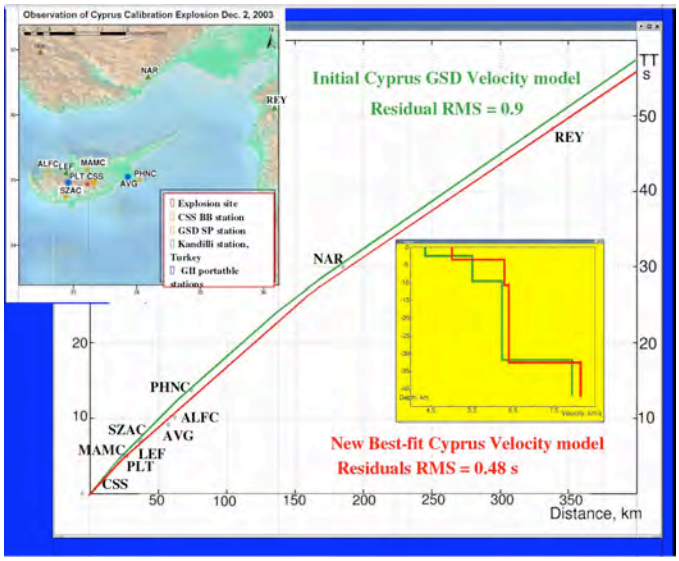


Figure 6. Velocity model construction for Cyprus.

Source Scaling

Amplitude spectra of P and S waveforms were used to investigate source scaling relations for the pair of Cyprus explosions, ideally placed at the same point, recorded at BB station CSS (Figure 7). We used the procedure based on spectral ratios of a pair of explosions of different yield to estimate source corner frequencies (Stump et al., 2003); we extracted also corner frequency estimates from the results presented in this paper for nearly contained blasts in a mine in Wyoming, recorded at the Pinedale array.

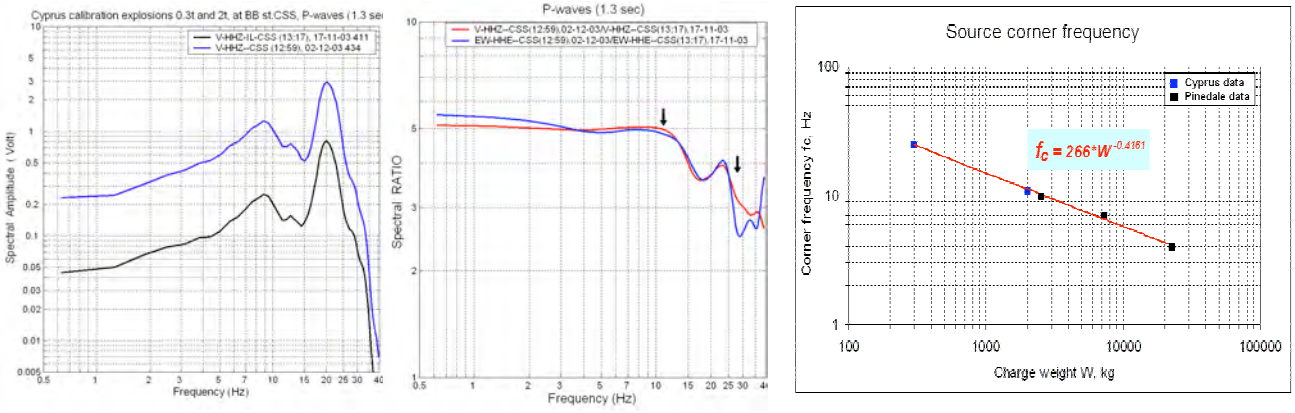


Figure 7. Smoothed amplitude spectra of P-wave portion for the pair of Cyprus explosions (left) were used to calculate spectral ratios for vertical and radial components and estimate corner frequencies from the ratios (middle); these estimates together with values from Stump et al. (2003) were used to compute a regression curve (right).

The Cyprus explosions can be undoubtedly considered fully contained despite impressive external effects. Both datasets showed consistency in spite of the different conditions: charge design, scaled depth, geological settings, distances. This leads to a good fit for the empirical corner frequency-yield relation:

$$f_c = 266*W^{-0.4161}$$

Sayarim experiment

Experimental explosions of 0.3, 2 and 32.5 ton of ANFO were conducted recently in Sayarim Valley near Eilat, Israel, providing a series for yield-dependent analysis of regional waveforms (Figures 8, 9). The large shot,

considered as a calibration explosion, was mostly supported by the MERC program of the U.S. AID. Explosives were placed in boreholes of large diameter (0.6-0.8 m) with depth of 17-21 m, drilled in dry Quaternary alluvial conglomerates. A seismic refraction survey was conducted before the experiment on the site; P-velocity ~1670 m/sec was found for the layer that accommodated the charges.

Good waveform records were obtained for the explosion series in the near-source region by accelerometers at distances 100-500 m, and numerous portable and network seismic SP and BB stations, up to ~400 km. Significant seismic excitation was achieved (M_L~2 for 2 ton and M_L~3 for 32.5 ton) in spite of the non-consolidated sediment shot medium - dry alluvium, commonly considered a low-coupling material (e.g., US Congress, 1988). Comparison with the Rotem experiment results (Gitterman, 2002) does not show any significant magnitude drop (Figure 10). All available regional data (Jordan, Saudi Arabia) will be collected and analyzed jointly with the close-in records.



Figure 8. Ground uplift for the 2-ton explosion (video snapshot ~1 sec after detonation).



Figure 9. View of the largest explosion.

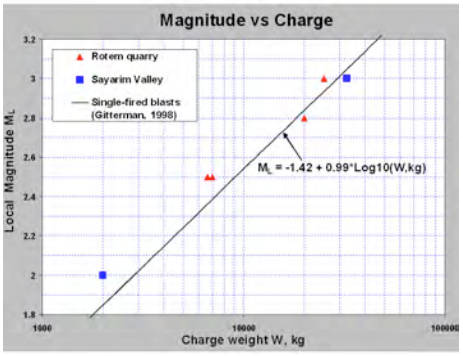


Figure 10. Local magnitude vs charge weight dependence for simultaneous explosions.

5. GT5–Ground Truth Database.

This database was enriched by one candidate GT5 event from East Turkey, and three from Israel. The GT data for these four events is presented in Table 2. The main shock and aftershocks around Bingol, Turkey (M=6.4, May 1, 2003) (see Figure 11, Table 2, event 2), were collected and characterized, using data from the Kandilli observatory network and two portable networks deployed promptly after the large event: 10 stations of the joint deployment of GFZ (Potsdam) and ERD (Ankara) and 6 temporary stations of the TUBITAK deployment (see Figure 12). The event has a good coverage by the Kandilli network, which together with the temporary deployments delivers 90% GT5 criterion certification to the event. Unfortunately both portable deployments do not close an azimuthal gap to the North of the event.

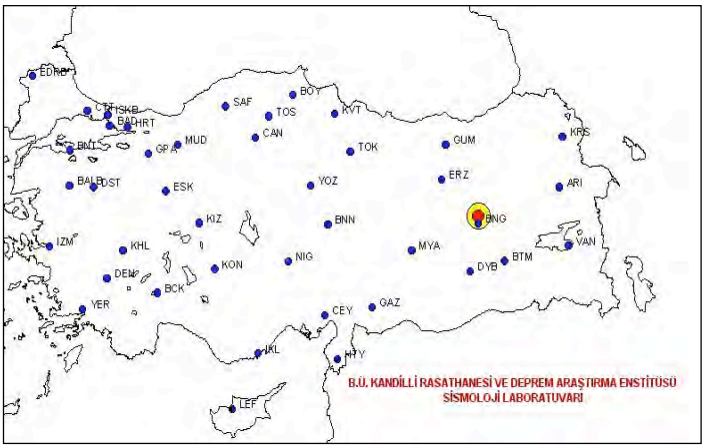


Figure 11. Distribution of Kandilli observatory stations, reporting Bingol main shock.

Table 2. New candidate GT5 event collection.

Event number	yy mm dd	hh:mn:sd	M	Lat	Lon	dx	dy	H km	Min R, km	Gap1	Gap2
1	94 08 16	03:18:57.2	4.0	32.046	35.5.00	3.3	2.1	18.0±8.1	19	79º	88º
2	03 05 01	00:27:04.5	6.4	39.004	40.435	2.6	2.2	6.0	10	100º	170º
3	04 02 11	08:15:03.2	5.2	31.706	35.550	2.0	0.9	16.0±1.6	14	68º	98º
4	04 07 07	14:35:08.7	4.7	31.979	35.546	4.0	0.3	14.0±2.9	30	72º	94º

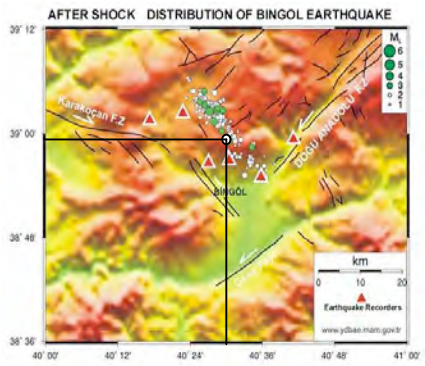


Table 3. Aftershocks list M > 4.

Event number	M D H M Sc	Lat Lon	Dep M_L
1	05/10 23 41 40.6	39.065 40.469	4.8 4.0
2	05/08 01 44 19.2	39.095 40.437	5.4 4.6
3	05/10 15 44 49.4	39.079 40.442	3.8 4.4
4	05/05 06 05 27.5	38.987 40.505	6.9 4.3
5	05/12 04 10 08.9	39.022 40.497	5.3 4.0
6	05/04 02 09 56.4	39.043 40.453	5.5 4.0

Figure 12. Aftershocks of the Bingol earthquake M=6.4, recorded by the TUBITAK portable network

A set of the relatively strong aftershocks has been recorded in the close vicinity of the temporary network stations. For example, event 3 (Table 3) was recorded by station SUD with Ts-Tp=0.6 sec, giving distance to the hypocenter within 5 km (see Pinsky et al., 2003a). The event was also registered by the TUBITAK portable network, by the Kandilli network, reported to the EMSC and also by the IDC. TUBITAK reports about six events M>4 in the area (see Figure 12 and Table 3), particularly, event 4 occurred very close to stations B06 and B03 of the TUBITAK portable network. The Bingol cluster candidate GT5 events may be very useful for site specific station calibration.

Two recent significant earthquakes within the Israel and Jordan seismic networks were collected: the M_L=5.2 Dead Sea earthquake (Figure 13, Table 2, event 3) and the M_L=4.7 Jordan Valley earthquake (Table 2, event 4). Both of them satisfy the GT5 candidate event selection criteria at the 95% confidence level.

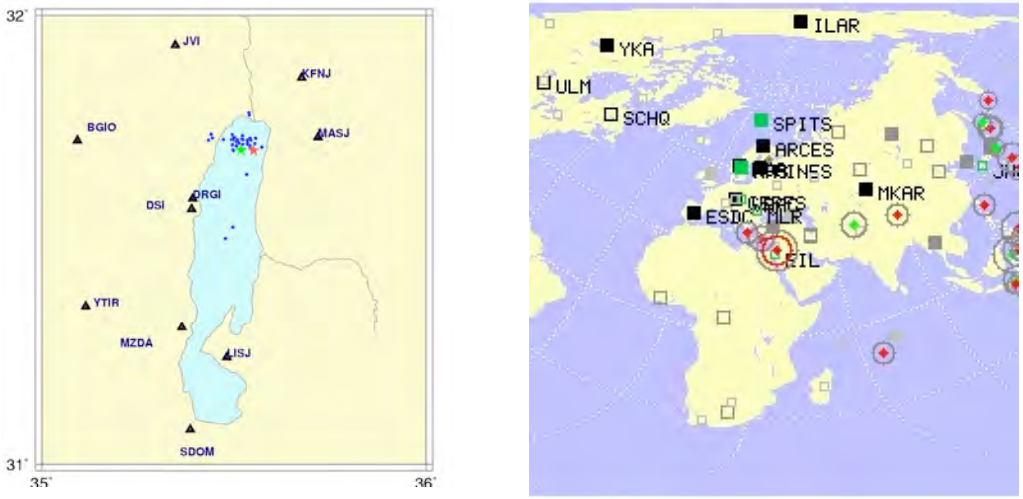


Figure 13. The Dead Sea, Israel (M_L=5.2, December 11, 2004) earthquake, located at the 95% level of the GT5 selection criteria (left) was detected at large distance, providing useful calibration information to a number of IMS stations (right, from the IDC Website). The Dead Sea earthquake (★) was followed by a swarm of aftershocks (●), shifted slightly to the north-west (left). The green star (★) indicates location of the earthquake, using the AUTOLOC procedure.

The earthquake location has been tested using the relocation approach (Pinsky et al, 2003a) and P and S arrival times to the ISN, JSN and IMS stations within 2500 km (including the new AS049 array and the ASF station). The P and S travel times have been calculated according to the ISAPEI91 model and compared to the measured times for computation of Empirical Travel Time Corrections (ETTCs). Theoretical reciprocal SSSCs according to the CUB1 and CUB2 models (Barmin et al, 2001) and the newly designed NCUB1 and MCUB1 (Pinsky et al, 2003a) have been calculated for SSSC and ETTC comparison. For the earthquake calibration information, contact vlad@mni.gov.energy.il.

The Shomron Region (Israel) earthquake, M_L=4.1, 1994/09/16 03:18:57 was located during the Joint Seismic Observation Period Experiment (JSOP-1) carried out during September-November, 1994 by several Eastern Mediterranean networks. The minimum distance of 19 km, primary gap Gap1=79º and secondary gap Gap2=88º attribute this event to the 95% GT5 class.

IMS station KEG calibration due to the GT5 events.

We analyzed the GT5 reference event list (McLaughlin, 2003) for calibration of KEG. The P arrivals were picked at GII using the BB KEG seismograms. From the initial list of 55 events, only 18 have been chosen (Pinsky et al, 2003a), because of poor SNR or large time misfit. The data consists of the two main clusters and two separate events (see Figure 14).

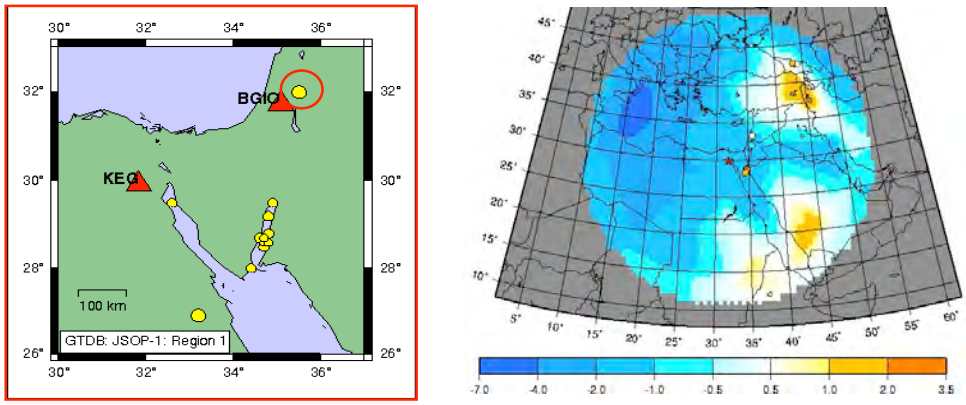


Figure 14. KEG calibration reference events from the JSOP-1 experiment (left) and CUB1.0 model SSSCs (contours) compared to empirical TT corrections (points), obtained from the set of GT5 events (right).

One cluster around Lat=42.4, Lon=43.7 comprises Caucasus events, the second (Lat=28.5, Lon=34.6) is the Gulf of Aqaba set. Two separate earthquakes: north of the Dead Sea, and Golan Heights, show satisfactory fit between ETTCs and the SSSCs of CUB1.0. The Caucasus events are in average in satisfactory agreement with the model. But the Gulf of Aqaba clusters deviate far from the model and even from each other.

CUB1.0 upgrading within the Middle East, Eastern Mediterranean Region.

The map of Sweeney and Walter, (1998, Figure 15) was taken for construction of a digitized 1° x 1° grid 1D crust model within the given boundaries. A new global model NCUB1 (Pinsky et al, 2003a) was determined by substitution of this new digital crust for the CUB1.0 crust. SSSCs for the given regional IMS stations EIL, MRNI, BRAR, KEG, KVAR, MLR have been calculated using the Barmin 2D raytracer utility and compared to the empirical ETTCs, obtained via thorough seismogram analysis, re-picking and relocation of the collected regional GT events (Pinsky et al, 2003a). An additional modified model MCUB1 was constructed by introduction of Global Moho depth information (Barazangi and Sandvol, 2001). Empirical travel times are assumed fitting a model, if |ETTC-SSSC| < 1 sec. The number of fitted ETTCs versus the total number of existing GT5 events for the IMS stations is presented in Table 4.

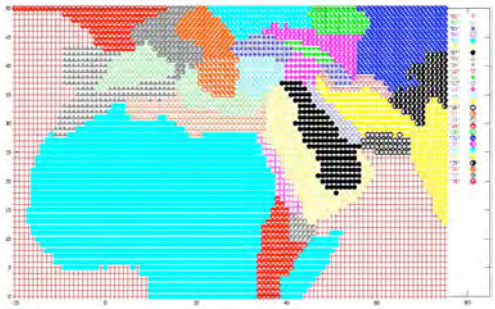


Figure 15. Digital regionalization map, computed according Sweeney and Walter, 1998

Table 4. Pn Model Travel Time Corrections versus Empirical Travel Time Corrections.

STATION NAME /MODEL	EIL	MRNI	BRAR	MLR	KVAR	DAVOS	GERESS	OBN	Σ
CUB1	4/8	3/5	2/4	3/5	3/5	0/2	1/4	3/3	18/35
NCUB1	6/8	5/5	4/4	5/5	4/5	1/2	4/4	3/3	32/35
MCUB1	5/8	4/5	4/4	3/5	4/5	1/2	4/4	3/3	28/35

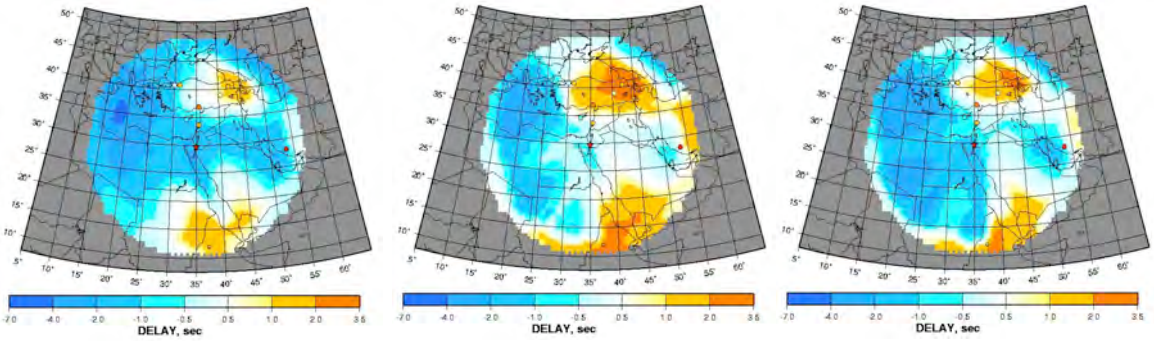


Figure 16. Pn SSSCs and ETTCs for depth H=10 km for station EIL using the CUB1.0 model (left), NCUB1 (centre) and MCUB1 (right).

Figure 16 demonstrates the computation results for station EIL. Map color indicates (Tmodel –Tiaspei91) residuals, circles show the GT5 event locations and their color corresponds to the ETTCs. Table 4 and Figure 16 show that by application of NCUB1 and MCUB1 we generally improve the fit between the model SSSCs and ETTCs. For example, the EIL observations of Duzce, Izmit, S. Iran and Lebanon events better fit NCUB1 and MCUB1 than CUB1.0. The fitting is significantly improved for the stations BRAR and MLR (see Pinsky et al, 2003a) for all available observations. However, several cases of discrepancy between SSSCs and ETTCs are still present.

Travel time improvements by NCUB1 are demonstrated in Figure 17, where (Tobs-Tcalc) histograms for the IMS stations are shown for the GT5 Izmit earthquake of August 17, 1999, M=7.1. Due to the station configuration and location results the earthquake is a candidate GT5 event at 95% confidence level. The NCUB1 model removes the bias of 0.91 sec provided by the CUB1.0 model with almost the same standard deviation.

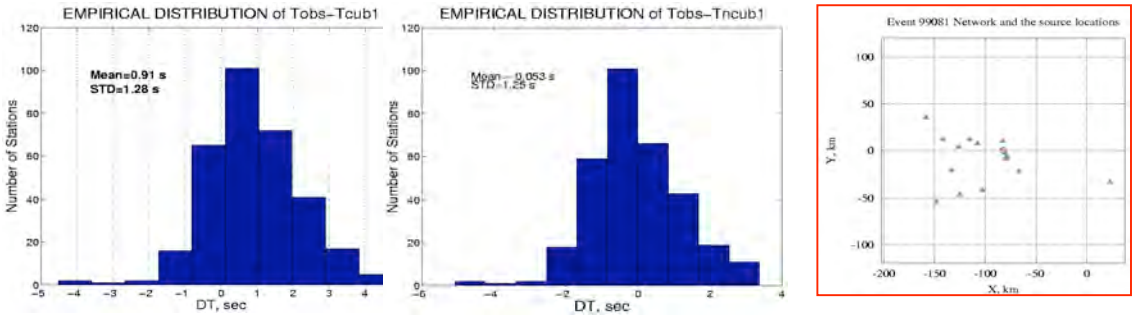


Figure 17. Empirical distributions of Tobs-Tcalc (P first arrival) for the Izmit earthquake, calculated for all relevant regional stations using CUB1.0 (left) and NCUB1 (center) models. Local Network configuration (right) provides 95% confidence level (GT5) for the event.



Figure 18. Aftershock location by the AUTOLOC (•) and analyst solutions (•).

Dead Sea Earthquake Series Advanced Location Study.

The February 11, 2004 earthquake of M_L=5.2 was followed by a series of aftershocks with magnitudes M_L=2 and less. The earthquake swarm was utilized for testing and calibration of advanced location procedures AUTOLOC and RBEAM (Pinsky et al, 2003b), being developed at GII. AUTOLOC (Pinsky, 2000) is a sophisticated procedure, based on automatic P and S phase picking and robust non-linear grid-search location. The algorithm provides automatic weighting of the pick data: enhancing good fit data and eliminating outliers for location. Persistently deviating first arrivals are accumulated for following station corrections. Figure 18 shows that 10 of 12 earthquakes have been located automatically by the AUTOLOC procedure within 3 km of the GII analyst solutions. For two events the error is somewhat greater, due to poor network configuration and low SNR at first arrivals for these events.

Waveforms of the earthquake series were also used for source location by the new 16 element seismic array on Mt. Meron and its calibration. The new robust beamforming algorithm RBEAM (Pinsky et al, 2003b) was tested using this data, showing advantages over the conventional beamforming and F-K analysis (see Figure 19 and Table 5).

Table 5. Comparison between RBEAM and Beam Azimuth estimations for 6 aftershocks.

Event N	1		2		3		4		5		6		Standard deviation
	Az	Err	Az	Err	Az	Err	Az	Err	Az	Err	Az	Err	
Beam	161º	12.7º	185º	11.4º	189º	15.2º	171º	-3.4º	168º	-6.6º	163º	-11.5º	10.8º
Rbeam	172º	-1.7º	174.5º	-0.1º	171º	-3.8º	174º	-0.4º	176º	2.4º	175º	0.5º	1.98º
"True Az"	173.7º		174.6º		174.8º		174.4º		174.6º		174.5º		

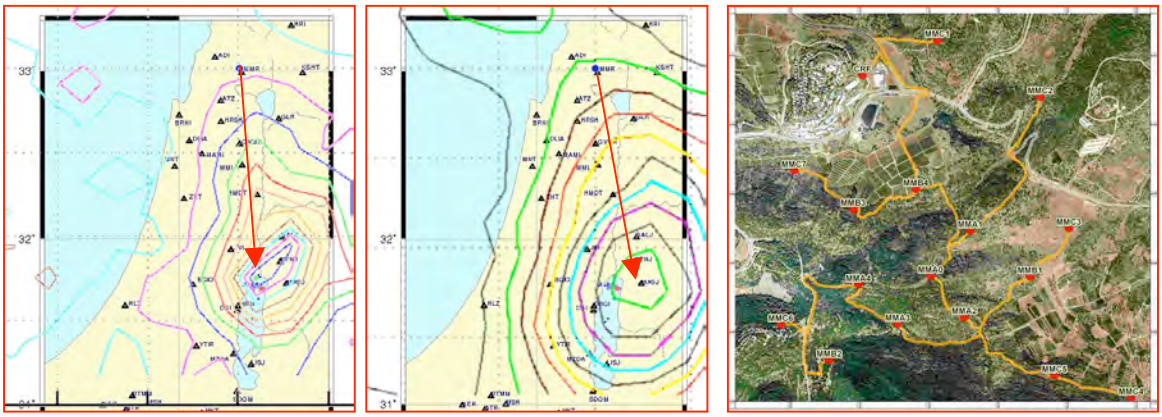


Figure 19. Wavenumber K_x, K_y domain solution, using RBEAM (left) and conventional beamforming (central) for the Dead Sea main shock recorded by AS049 array (right).

CONCLUSIONS AND RECOMMENDATIONS

GII jointly with GSD successfully conducted an on-land seismic calibration explosion series in Cyprus. The unique source parameters (two shots of different charge in the same deep borehole filled with water in a diabase massif) supplied valuable close-in and regional observations. The data were used for a source scaling study, including estimations of corner frequency by the spectral ratio procedure and determination of a simple empirical corner frequency-charge relationship. To check the potential of this analysis for yield estimation it is necessary to accumulate appropriate data from other experimental series of contained explosions. The calibration explosion helped to obtain an improved velocity model for the Cyprus area.

GII conducted a yield-dependent series in Sayarim Valley, Israel, to study energy generation from regional phases. Significant seismic excitation was achieved in spite of non-consolidated sediment media - dry alluvium, commonly considered a low-coupling material, and the shallow burial, far from fully-contained, conditions. All available regional data (Jordan, Saudi Arabia) will be collected and analyzed jointly with close-in accelerometer records.

We have supplemented the reference events data base by a number of GT5 candidates from new sites, evaluated ETTCs for the regional IMS stations and compared them to SSSCs from the CUB1.0 and two new models NCUB1 and MCUB1, demonstrating higher regional accuracy. The new models will be further developed and validated using reliable GT data including recent reference events within the Israel and Jordan Networks.

The new robust beamforming technique RBEAM showed significant advantages over conventional beamforming, using aftershock data from the large event in the Dead Sea in February, 2004. Further investigation is necessary for calibration of the new IMS array AS049, using the RBEAM technique, including a large statistical experiment to estimate the effectiveness of the new approach in various conditions.

The Dead Sea swarm was advantageous for an AUTOLOC procedure test. The algorithm is a non-linear grid-search location routine providing separation of well fitting data and outliers carrying information useful for station calibration.

REFERENCES

Barazangi M. & Sandvol E. (2001), Calibration of the Selected IMS stations in the Middle East to Improve Seismic Event Location, (contract 00/20/5019 CTBTO/IDC Calibration Programme – Phase 1).

Barmin, M.P., M.H. Ritzwoller, and A.L. Levshin (2001), A fast and reliable method for surface wave tomography, Pure Appl. Geophys., 158(8), 1351 - 1375.

Gitterman, Y. (1998), Magnitude-yield correlation and amplitude attenuation of chemical explosions in the Middle East, Proceedings of the 20th Annual Seismic Research Symposium on Monitoring a Comprehensive Nuclear Test Ban Treaty, Santa Fe, Sept.21-23, 1998, 302-311.

Gitterman, Y., V. Pinsky, A. Shapira, M. Ergin, D. Kalafat, G. Gurbuz, K. Solomi (2002), Improvement in detection, location and identification of small events through joint data analysis by seismic stations in the Middle East/Eastern Mediterranean region, Proceedings of the 24th Seismic Research Review, Ponte Vedra Beach, Sept. 17-19, 2002.

Leith, W. and L. Kluchko (1998), Seismic Experiments, Nuclear Dismantlement Go Hand in Hand in Kazakhstan, *Eos Trans. Am. Geophys. Union*, 79, 437, 433-444.

Makris J. and J. Wang (1994), Bougier gravity anomalies of the Eastern Mediterranean Sea. In Geological Structure of the Eastern Mediterranean, Historical Productions-Hall Ltd 1994.

McLaughlin (Editor) (2003), Source Specific Station Corrections (SSSCs) for Monitoring Seismic Stations in North Africa, Middle East and Western Asia, Group 2. Final Report - Contract DTRA01-00C-0013.

Pinsky V, Y. Gitterman, V. Goldshmidt, A. Shapira (2003a), Collection of regional calibration data within the area around the Israel Seismic Network. CTBTO Calibration Program - Phase 1, Final Report- Contract 00/20/5024.

Pinsky V., Y. Gitterman, A. Shapira, M. Ergin, C. Gurbuz. (2003b), Improvements in Monitoring of Small Regional Events Based on Ground Truth Data in Turkey and Israel. Proceedings of the 25th Seismic Research Review, Tucson, Arizona, September 23-25, 2003.

Pinsky, V. (2000), Prototype autonomous earthquake locator for regional networks, Geophysical Research Letters, Vol. 27, No. 21, 3549-3552.

Stump, B., D.C. Pearson and V. Hsu (2003), Source scaling of contained chemical explosions as constrained by regional seismograms, BSSA, 93, 1212-1225.

Sweeney J.J, W.R. Walter (1998), Preliminary Definition of Geophysical Regions for the Middle East and North Africa. LLNL report. UCRL-ID-132899.

U.S. Congress (1988), Office of Technology Assessment, Seismic Verification of Nuclear Testing Treaties, OTA-ISC-361 (Washington, DC: U.S. Government Printing Office, Chapter 6, May 1988).

GROUND TRUTH COLLECTION FOR MINING EXPLOSIONS IN NORTHERN FENNOSCANDIA AND RUSSIA

David B. Harris[1], Frode Ringdal[2], Elena O. Kremenetskaya[3], Svein Mykkeltveit[2], Donald W. Rock[1], Johannes Schweitzer[2], Teresa F. Hauk[1], and Jon P. Lewis[1]

Lawrence Livermore National Laboratory[1], NORSAR[2], Kola Regional Seismological Centre[3]

Sponsored by National Nuclear Security Administration
Office of Nonproliferation Research and Engineering
Office of Defense Nuclear Nonproliferation

Contract No. W-7405-Eng-48[1] and DE-FC03-01SF22420[2,3]

ABSTRACT

An analysis of data from our deployments and ground truth collection in northern Fennoscandia and northwestern Russia shows systematic variations in the P/S ratios of different types of explosions. The fact that this fundamental discriminant varies with firing practice is not in itself surprising—such variations probably contribute to the spread in P/S ratios normally observed for ripple-fired explosions. However, the nature of the variations is sometimes counterintuitive. Last year (Harris, 2003), we found that the P/S ratios of small compact underground explosions in mines of the Khibiny Massif are systematically lower than the P/S ratios of large ripple-fired surface explosions. We had anticipated that smaller underground shots would be more like single well-coupled explosions, thus having higher P/S ratios than large ripple-fired explosions.

We are now performing a more extensive analysis of the data, including compact and large ripple-fired explosions at additional mines and different types of explosions: small surfaces shots and large ripple-fired underground explosions. Our data are more complete as a result of an additional year of collection and allow a more complete sampling of the signals in range from the source. As of this writing, we have measured Pn/Lg ratios on a larger number of explosions of three types: compact underground explosions, surface ripple-fired explosions, and now underground ripple-fired explosions. We find that both types of underground explosions have systematically lower P/S ratios than surface ripple-fired shots; this effect is most pronounced in the 4–8 Hz frequency band. This result appears to be due to relatively diminished shear-wave excitation by the surface explosions. We speculate that the relatively large shear phases in underground explosions may be caused by large amounts of rockfall in these events, which are designed to collapse the ceilings of tunnels.

We have continued comprehensive ground truth collection at the Khibiny, Olenegorsk, Kovdor, and Zapolyarnyi mines, and now have basic information on 2,052 explosions. In addition, we have more detailed information for select surface and underground ripple-fired explosions and underground compact explosions. This information ultimately may help the community understand the observed P/S ratio offsets. We also are continuing the compilation of ground truth and associated regional waveform data into a database as a prelude to further analysis.

We have operated two lines of stations extending from the Khibiny Massif to the ARCES array and to the north of the ARCES array for a second year. This deployment provides the principal data for measuring the range-dependence of near-regional phase amplitudes. Data collection has been more robust in this second season of the deployment. Preparations are now underway for concluding the line deployment in late August or early September 2004 and for redeploying the stations to the Kiruna, Malmberget, and Aitik mines in northern Sweden. Like the Khibiny mines, these mines provide an interesting natural laboratory for examining questions about the phase characteristics of mining explosions because they include both underground and surface operations.

OBJECTIVES

This year the project had the following 5 principal objectives:

1. Collect ground truth information for a large number of explosions in a diverse set of mines in the Kola Peninsula, including more detailed ground truth for a select set of representative explosions.

2. Assemble a database of waveform observations of these events from principal monitoring stations of the region.

3. Continue the operation of temporary stations deployed to fill gaps in the set of observations.

4. Plan the redeployment of these same temporary stations to frequently observed mines in northern Sweden.

5. Continue a preliminary analysis of the variation of regional discriminants with source-receiver range and source type.

RESEARCH ACCOMPLISHED

Ground Truth Collection

We have begun collection of detailed ground truth information for selected events. We seek more detailed ground truth information to assist the interpretation of differences in regional observations of different types of explosions. An example of the kind of ground truth information we have been able to obtain is shown in Figure 1 below. This explosion in the Nyurkpakh quarry of the Vostochny mine (Khibiny Massif) occurred at 7.08:03 GMT on August 28, 2003. The total weight of the explosive was 138,346 kg detonated in 34 phases with typical delays between phases of 20 milliseconds, although 3 delays were 40 milliseconds. The total explosion time was 740 milliseconds. The figure depicts the sequence in which phases (connected dots) were detonated. The weights of explosives in each phase are shown in Table 1. The 40-ms delays were between phases 0 and 1, 4 and 5, 20, and 21.

Database Assembly

Waveforms from permanent and temporary stations in the region and ground truth information are being assembled into an NNSA schema database for subsequent convenient analysis. To date, ground truth information on 2,052 events have been loaded into the database, including the following events from the Khibiny Massif mines:

Table 1. Sample numbers and types of explosions available in the database for Khibiny Massif mines

Mine	Explosion Type	Yield Range (tons)	Number Available
Kirovsk	Underground Compact	1–7	619
Kirovsk	Open-pit ripple-fired	1–16	43
Kirovsk	Underground ripple-fired	10–278	41
Rasvumchorr	Underground compact	1–7	335
Rasvumchorr	Underground ripple-fired	14–257	5
Central	Open-pit ripple-fired	10–396	174
Koashva	Open-pit ripple-fired	21–249	111

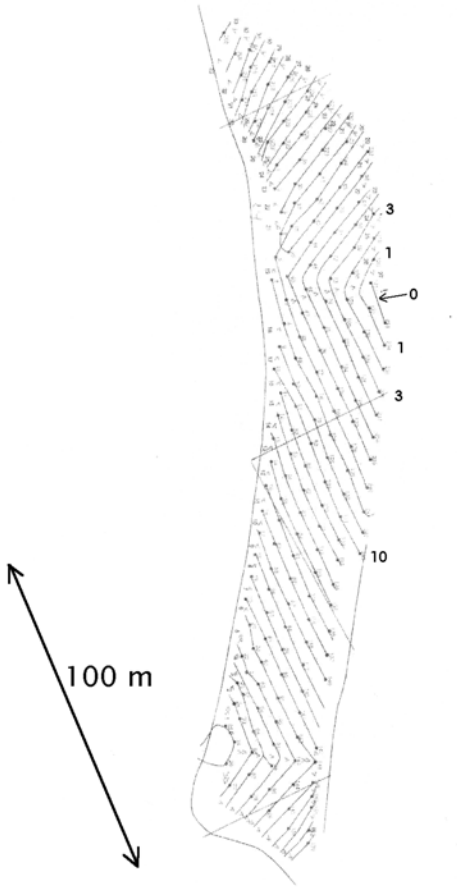


Figure 1. Plan of the August 28, 2003, Nyurkpakh explosion. Explosion phases are denoted by the lines connecting the dots; the dots denote holes with explosives. The numbers to the right of the plan indicate the sequencing of the phases. The explosion began with the phase denoted 0, which consisted of two holes.

Table 2. Weight of explosives per delay for the Nyurkpakh explosion of August 28, 2003

Phase	Weight (kg)	Phase	Weight (kg)	Phase	Weight (kg)
0	2,016	12	2,929	24	5,520
1	2,540	13	4,176	25	5,410
2	3,336	14	3,661	26	2,484
3	2,484	15	3,788	27	2,622
4	4,817	16	4,689	28	1,380
5	5,740	17	5,228	29	828
6	5,238	18	6,117	30	621
7	5,045	19	7,249	31	1242
8	4,907	20	5,694	32	621
9	5,422	21	9,347	33	621
10	4,249	22	8,040		
11	3,901	23	6,384		
				Total	138,346

Operation of Temporary Stations to Improve Observational Coverage of Mining Explosions

Lawrence Liveremore National Laboratory (LLNL) and NORSAR installed six Reftek recorders provided by LLNL along two profile lines in Finland and Norway (Figure 2) during late August/early September 2002. These units record data in continuous mode. A local NORSAR representative in Karasjok, northern Norway, travels to the six sites at appropriate intervals to retrieve data. These data are then forwarded to NORSAR for reformatting, archiving, and distribution to the other project participants. KRSC has deployed two stations to provide close-in observations of the same explosions.

As of July 10, 2004, the following data from these six profile stations are available in NORSAR's data archives:

IVL: 2002: days 239–293, days 314–365. 2003: days 001–017, day 044, days 049–365. 2004: days 001–115.

KMM: 2003: days 048–157, days 176–224, days 274–282, days 316–365. 2004: days 001–016, 020, 039–047, 056.

SKV: 2002: days 245–365. 2003: days 001–041, days 061–066, days 069–172, days 241–297, days 315–365. 2004: days 001–023.

SKF: 2002: days 241–245, days 248–320, days 323–365. 2003: days 001–038, days 053–197.

NDN: 2002: days 241–243. 2003: days 097–240, days 340–352, days 355–357, days 360–365. 2004: days 001–002, days 005–007, days 010–020, days 028–081.

VGB: 2002: days 242–314. 2003: days 097–164, day 168, days 177–244, days 248–316, days 340–365. 2004: days 001–030, days 035–107.

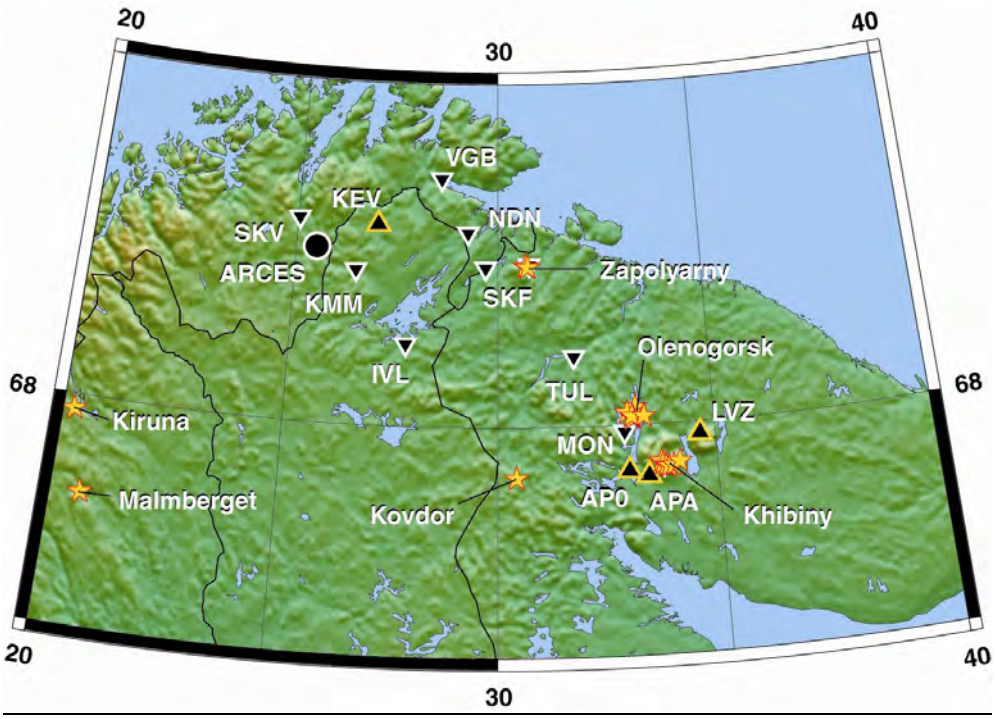


Figure 2. Locations of the temporary stations (inverted triangles) deployed by LLNL, NORSAR and KRSC (TUL, MON).

Preparation for Field Instrument Redeployment to Mines in Northern Sweden

The six Reftek field recorders that have been collecting data along two profile lines in northern Norway and Finland since the fall of 2002 will be redeployed to northern Sweden in early September 2004. The target for the redeployment is an area of active iron and copper ore mining. The LKAB company is operating the largest underground iron mine in the world at Kiruna and is also exploiting underground iron ore deposits at Malmberget, some 75 km SSE of Kiruna. The Boliden Company is operating the largest open-pit mine in northern Europe at Aitik, approximately 17 km SE of Malmberget. Each of these three mines arrange blasts on a very active and also fairly regular schedule, and this area thus offers an excellent opportunity to collect data for detailed studies of different kinds of mining explosions.

A visit to these three mines was carried out in late April 2004, to establish relations with personnel involved in the blasting operations, to obtain information on their respective blasting practices, to discuss prospects for obtaining ground truth information, and to survey for suitable locations for the six field recorders. With regard to mining operations and blasting practices in particular, the following information has been derived from openly available sources, and from contacts during the visit.

The large ore body exploited at Kiruna (Figure 3) is descending below the surface at an angle of 60 degrees from horizontal, is 4 km long, extends to a depth of 2 km, and is averaging 80 m wide. The mining method used is called large-scale sublevel caving. The current production level is at a depth of about 800 meters below the surface. Horizontal drifts (Figure 4) are driven through the 80-m-wide ore body, and fans of 7–12 holes, typically 40–45 m long, are drilled upwards into the ore at 3-m intervals in the drifts. Fans are charged with up to 500 kg of explosive in each hole. The explosives in a fan are detonated with delays between the various holes, so that the detonation time for a fan typically is of the order of 1.5 seconds. A single blast at the Kiruna mine is usually composed of a number of fans, located in drifts that are separated laterally along the ore body by as much as 3 kilometers. A number of such blasts are conducted every day, at around midnight, local time (23:00 GMT). LKAB has been operating a four-element, three-component, in-mine seismic network of the ISS (Integrated Seismic System) type in the Kiruna mine since December 2003.

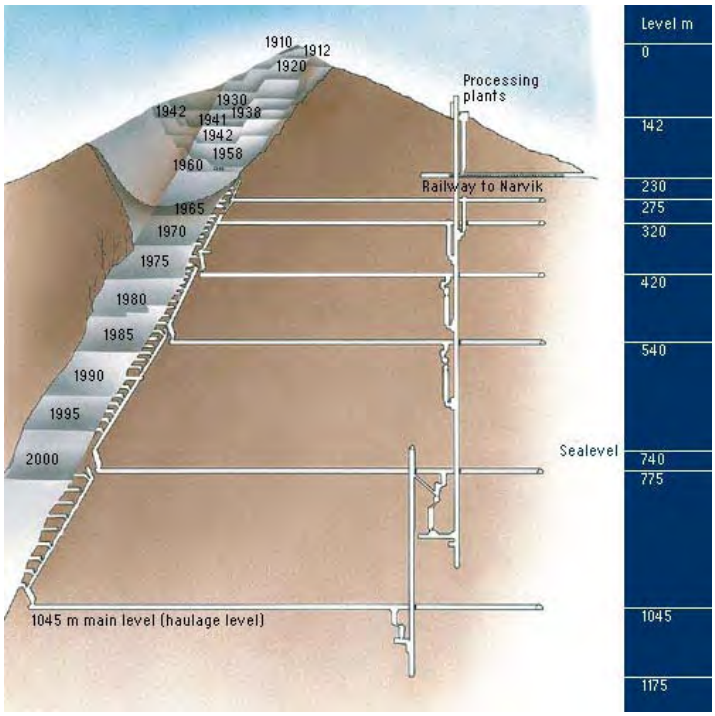


Figure 3. **Exploitation of the ore body at Kiruna, Sweden**.

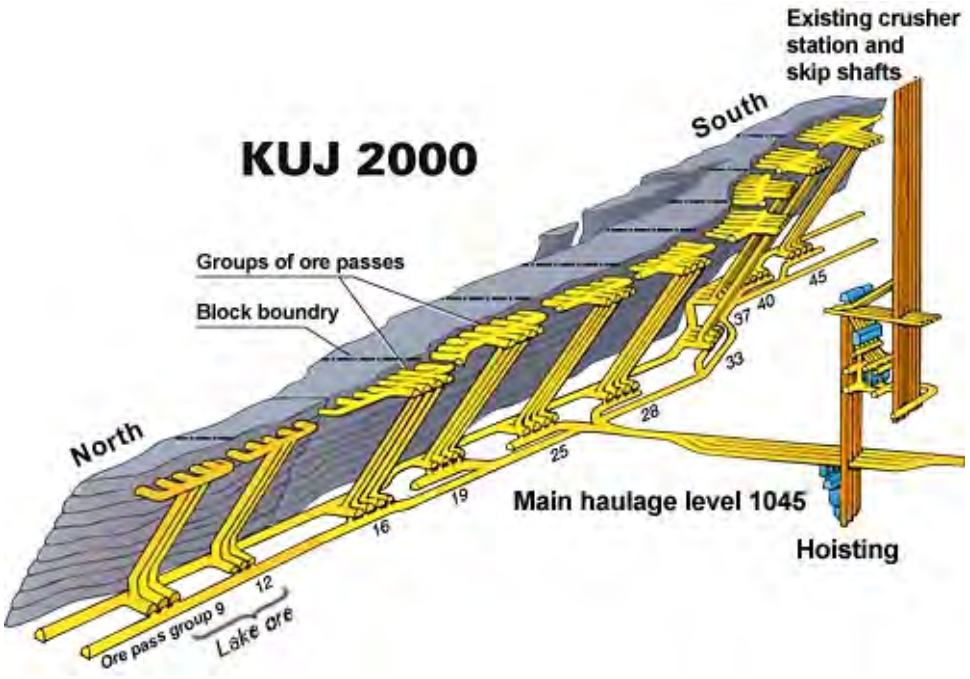


Figure 4. Groups of drifts (ore passes) in the Kiruna mine.

The iron deposits at Malmberget consist of about 20 separate ore bodies (Figure 5), 8 of which are currently mined. The mining method is the same as in Kiruna, and the main activity is currently at a depth of about 1,000 meters. There are, on average, four blasts per day, each consisting of detonation of up to 3 adjacent fans in the same drift, and blasting is confined to the time window 00:00–01:00 (23:00–24:00 GMT). LKAB plans to install an in-mine ISS network in Malmberget during the summer of 2004. The plans call for installation of an 18-element network of three-component sensors, possibly grouped in 3 subnetworks of 6 stations each.



Figure 5. Multiple ore bodies at Malmberget.

The single open-pit mine at Aitik (Figure 5) exploits a low-grade copper deposit. The depth of the mine currently is 300 meters, and the mining is proceeding towards an ultimate depth of 400 meters by the year 2012. Extraction of

the ore is based on so-called Nonel blasting, with explosives loaded in 17-m-deep boreholes of a 311-mm diameter. One blast is composed of detonations in up to 300 boreholes for a typical total shot duration of 8–10 seconds. Total yield in one blast ranges up to 500 tons. Figure 6 shows the drilling of holes for a blast that totaled 266,800 kg of explosives a few days after the photograph was taken. The event was recorded by ARCES at a distance of 333 km with a very high signal-to-noise ratio (SNR) (423). There is, on average, one explosion per week in the Aitik mine. All explosions are conducted at around 5:30 pm, local time (16:30 GMT).



Figure 6. Drilling holes for explosives at the Aitik open pit.

The exact plans for the deployment of the six Reftek recorders in and around these three mines have not been worked out as of the submission date of this paper. We expect to concentrate the resources directly on the mines, with surface deployments of two recorders at each mine. For the Aitik open-pit mine, there are possibilities of deployment on the rim of the pit. Whereas, deployment at Kiruna and Malmberget will be considered in light of the positions occupied by the sensors of the in-mine networks.

Regional Discriminant Analysis

With the collection of a large number of observations of mining explosions of different types and corresponding ground truth information, it is possible to begin examining the dependence of regional discriminants on source type as well as frequency and range. The large number of explosions collected (Table 1) allows distributions of discriminants to be developed. Figure 7 shows histograms of the Pn/Lg ratio in four different frequency bands for three types of mining explosions: compact underground shots (in Rasvumchorr), ripple-fired underground explosions (in Kirovsk) and surface (open-pit) ripple-fired shots (in Central). These mines are all within 10–15 kilometers of each other and are observed in these data by the ARCES central vertical element (ARA0 SHZ) at a range of about 410 kilometers (Figure 2). The data were screened to exclude superimposed seismograms from multiple shots (a frequent occurrence at the Central mine) and to ensure an (amplitude) SNR of at least 2 on both Pn and Lg measurements.

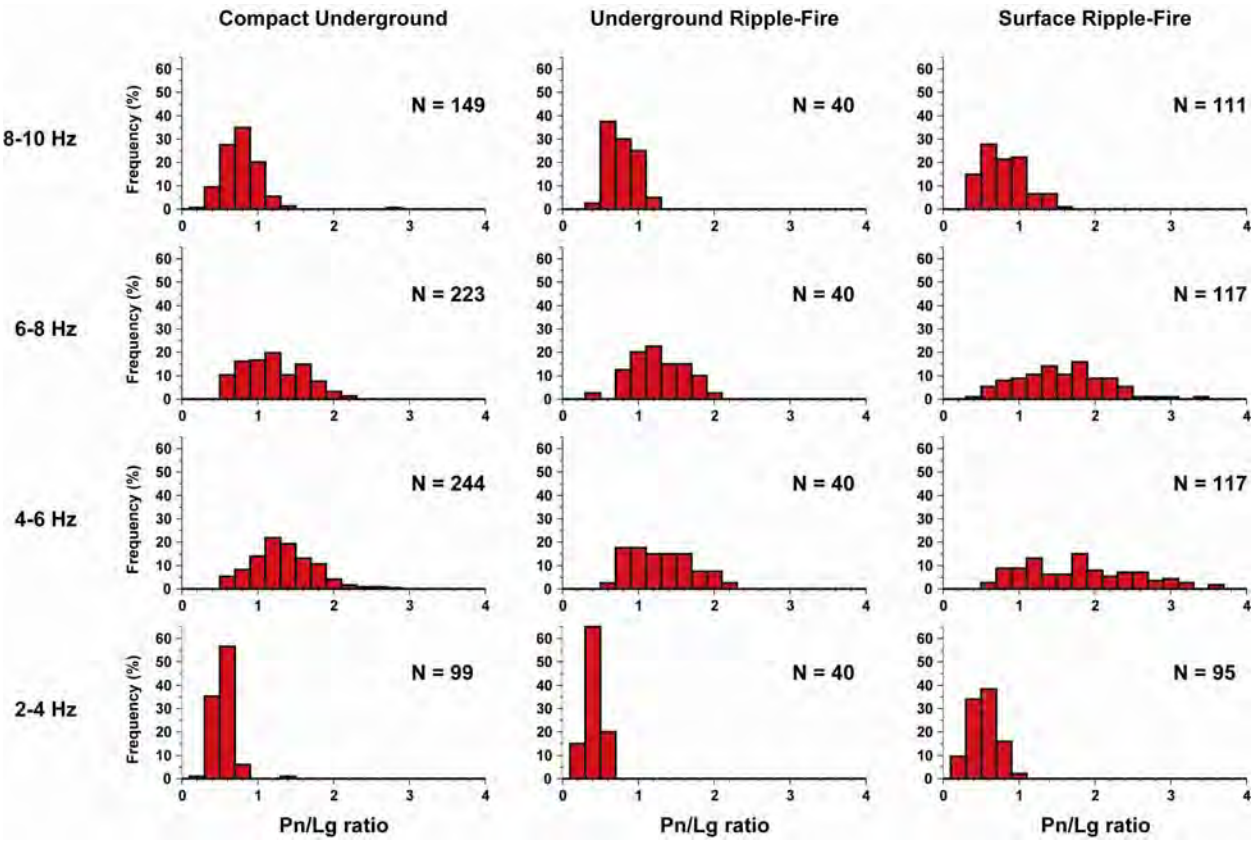


Figure 7. Histograms of P/S (Pn/Lg) ratios for three types of explosions at mines of the Khibiny Massif recorded at ARCES. The numbers in the upper-right corners of the plots indicate the number of measurements contributing to the distributions.

Several significant features and differences among the explosion types stand out. The Pn/Lg ratios for all three types of explosions are very low (below 1) in the lowest frequency band (2–4 Hz), increase markedly in the midbands (4–6 and 6–8 Hz), then decrease again in the highest band (8–10 Hz). Among the three event types, the surface ripple-fired explosions typically have the highest Pn/Lg ratios and the greatest scatter.

Figure 8 shows waveforms for three representative events (one for each explosion type) filtered by a bank of filters to bring out frequency content. The most noticeable features are the small amplitude of P waves in the (particularly) low band (2–4 Hz) and high band (8–10 Hz), consistent with the low Pn/Lg ratios across the board in those bands, and the relative lack of shear energy in the surface ripple-fired explosions, consistent with the high Pn/Lg ratios of the surface explosions in the 2–6 Hz band. This latter feature is particularly pronounced and might be explained by the nature of the underground explosions. These underground explosions, particularly the compact underground explosions, are designed to drop large quantities of ore from the ceiling of a drift or drifts (Figure 9). As in the Kiruna mine, fans of holes are drilled into the ceiling and walls of a drift, filled with explosive and detonated to drop and rubbelize the ore. It may be that the falling rock contributes the bulk of the shear energy to the source. Surface explosions also move quantities of overburden and ore, but not with the same efficiency (tons of rock dropped per kilogram of explosive) as the underground explosions where released gravitational potential energy can be expected to be a significant if not dominant fraction of the total energy released in the explosive event.

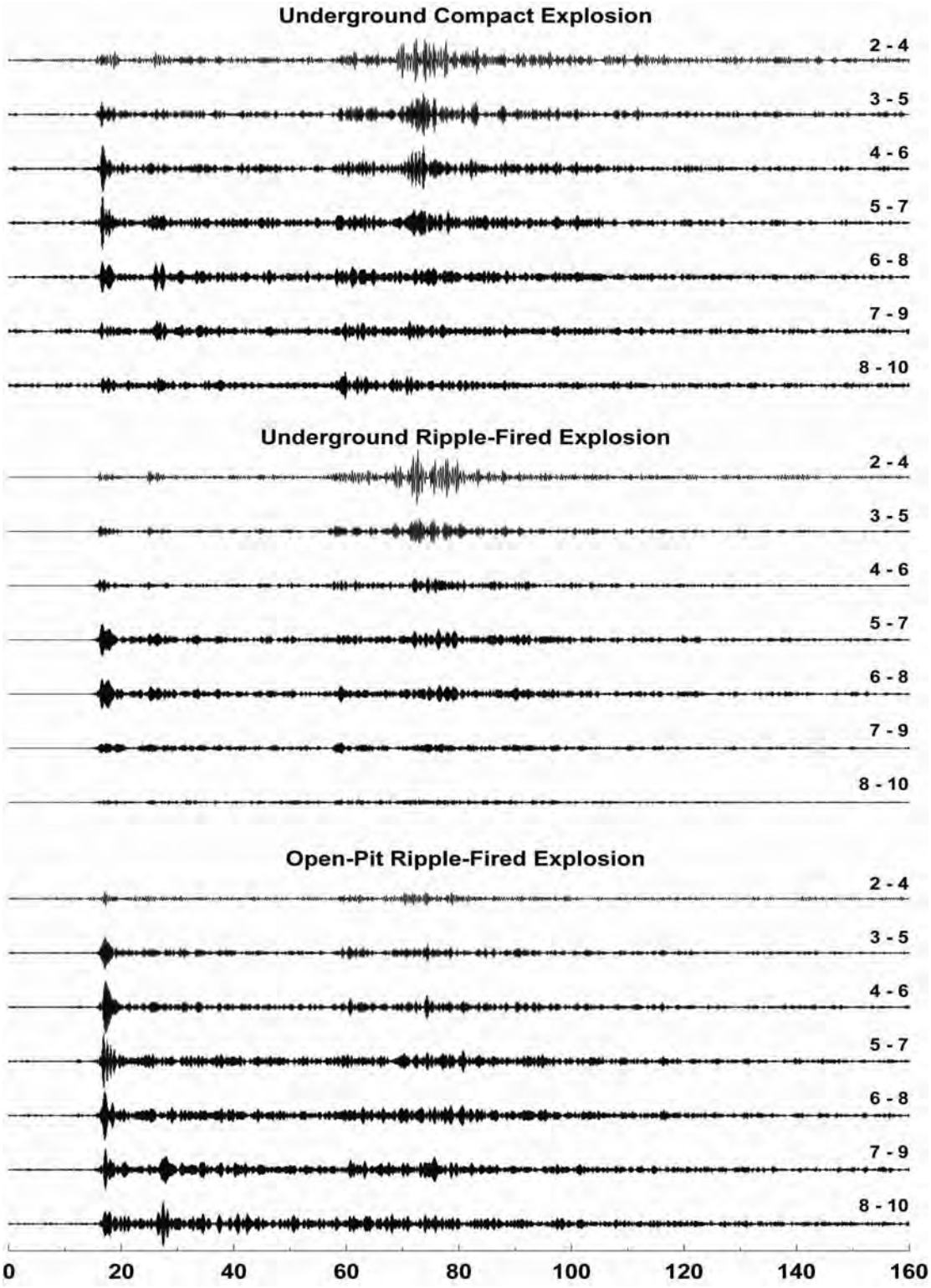


Figure 8. Sample waveforms of three different types of Khibiny mining explosions. The three signals are broken into seven frequency bands (2 Hz wide, annotated at right) to show spectral content. The underground shots have more shear energy than the surface shot.

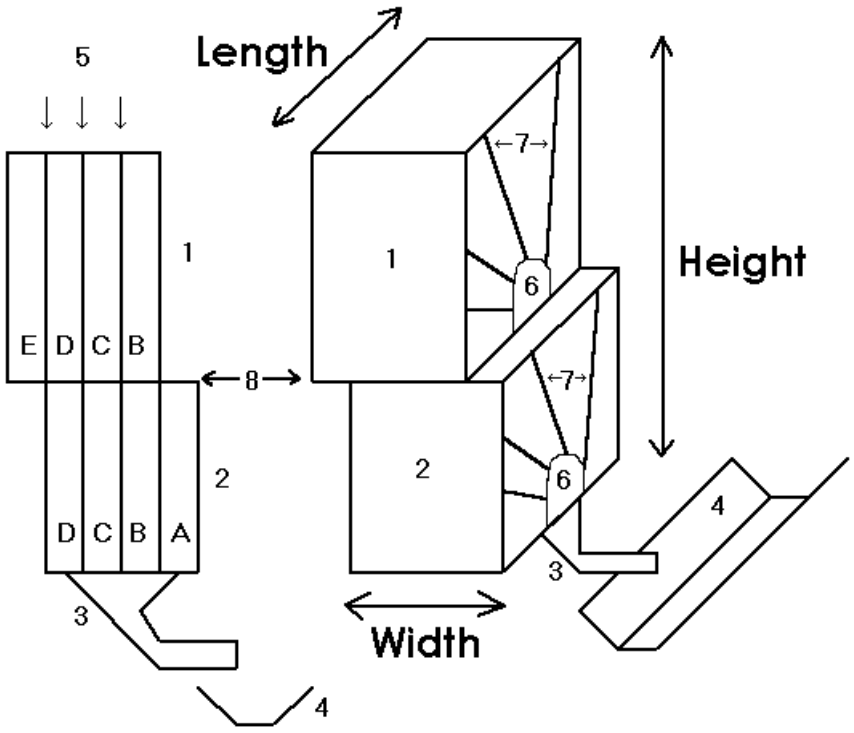


Figure 9. Simplified scheme of a typical underground explosion. 1,2 ore sub-blocks; 3 finger-like funnels; 4 haulage ore with trolleys; 5 parallel planes with charges; 6 horizontal drifts used to drill "fans" of holes and insert explosive; 7 "fans" of holes with charges arranged on parallel planes (5); A-E delayed phases, 8 intermediate horizon-separating ore blocks. Dimensions can be on the order of 100 m in length, 70 m in height, and 20 m in width.

CONCLUSIONS AND RECOMMENDATIONS

We conclude that we have assembled and continue to assemble a valuable data set for examining the relative excitation of different seismic phases by several types of mining explosions. Initial examination of the data has revealed significant offsets in P/S ratios for three types of mining explosions conducted in the Khibiny mine group, which may be linked to the different ways that ore is moved by the explosions in surface and underground mines. We recommend that the following additional analyses be conducted on the data:

- Compare explosion P/S discriminants with similar discriminants for the few earthquakes that we have in the area.
- Perform a thorough study of discriminant range dependence and seek corrections, perhaps similar to the Magnitude and Distance Amplitude (MDAC) correction for earthquakes, to remove range dependence. It may be possible to use the dataset assembled by this project to optimize an MDAC-like correction empirically.
- Compare Aitik surface explosions to Malmberget underground explosions to ascertain if the diminished P/S ratio for underground explosions observed in the Khibiny events is transportable to these Swedish mines.
- Examine additional discriminants, such as Pn/Sn.

REFERENCE

Harris, D., F. Ringdal, E. Kremenetskaya, S. Mykkeltveit, J. Schweitzer, T. Hauk, V. Asming, D. Rock and J. Lewis (2003), "Ground-Truth Collection for Mining Explosions in Northern Fennoscandia and Russia," in *Proceedings of the 25th Seismic Research Review - Nuclear Explosion Monitoring: Building the Knowledge Base*, LA-UR-03-6029, Vol. I,, pp. 54–62.

Lg AMPLITUDE RATIOS FROM PEACEFUL NUCLEAR EXPLOSIONS AND CRUSTAL STRUCTURE IN NORTHERN EURASIA

Hongyan Li[1], Igor B. Morozov[1, 2], and Scott B. Smithson[1]

University of Wyoming[1], University of Saskatchewan[2]

Sponsored by Air Force Research Laboratory

Contract No. DTRA01-01-C-0057

ABSTRACT

The *Lg* phase is widely used in Comprehensive Nuclear-Test-Ban Treaty (CTBT) monitoring since it is usually the strongest at regional distances. However, studies of its amplitude variability have revealed that the *Lg* phase can be attenuated or even blocked in some continental areas. Consequently, it is important to study the key factors that affect the *Lg* phase propagation across tectonic and geological boundaries. For Northern Eurasia, an unparalleled dataset for such analysis is the historic Peaceful Nuclear Explosion Deep Seismic Sounding (PNE DSS) program. Dense (10-20-km spacing), short-period (0.5-20 Hz), three-component PNE recordings of the regional phases have recently become available. In this study, data from 17 PNEs are analyzed for variability of the *Lg*/*Sn* and *Lg*/*Pg* amplitude ratios and their relation to tectonics and crustal structure.

The recorded *Lg* phase energy is mainly concentrated at 0.5-3 Hz, and this band appears to be optimal for calibration. In our PNE datasets, the *Lg* phase is not always the strongest phase, which could be due to the differences in source magnitudes and conditions.

The high density of PNE recordings allowed careful and detailed picking of the phase time windows (*P*, *Pg*, *Sn*, and *Lg*), by contrast with group velocity-based windowing usually employed, and measurement of their amplitudes using several techniques, with measurement uncertainties statistically determined. Further, differential slopes of the phase amplitude ratios were estimated and decomposed into the regional trends and effects of crustal variability.

Lg amplitude ratios along the reversed and crossing PNE profiles show that the *Lg* phase can be strongly attenuated (blocked) by rapid variations in the crustal thickness, such as the Patom Vilyuy Basin with more than 15 km of sediments and over10 km of Moho uplift. Smaller variations of the crustal thickness (e.g., Ural Mountains and Mezenskaya Depression) lead to moderate decay of *Lg* amplitudes. Within sedimentary basins (West Siberian, Timan-Pechora, Low Angara, and Tunguss), the *Lg*/*Sn* ratios decrease with the source-receiver offset. The corresponding decay rates are ~0.001km^{-1} within the Tunguss Basin, ~0.002 km^{-1} within the West Siberian Basin, ~0.002 km^{-1} to ~0.003 km^{-1} within the West Siberian Rift (Ob-Tasovsk Depression) and the Yenisei-Hantanga Basin. By contrast, within cratons with thinner sedimentary covers (East European and Siberian), the ratios increase or stay constant with offset. In addition to correlation with the sediment thickness, *Lg* phase propagation efficiency appears to be affected by the age of the sediments. Younger sediments appear to attenuate the *Lg* phase more strongly than older ones. These correlations are particularly pronounced in the 0.5-3 Hz frequency band, indicating that this band would benefit most from calibration.

OBJECTIVES

The *Lg* phase is usually observed as the strongest of the regional phases and is widely used for nuclear discrimination and studying crustal structure variations. However, the *Lg* phase is totally or partially blocked in some areas. Therefore, studying the characteristics of *Lg*-phase propagation and its main factors are critical for its use in nuclear-test monitoring.

This study analyzes the spectrum characteristics of the *Lg* and *Sn* phases to find the best frequency band for calibration; then computes the *Lg*/*Sn* and *Lg*/*Pgcoda* amplitude ratios with the optimal frequency band to study the variations of the ratios in different geologic areas of Northern Eurasia, in order to constrain the main factors affecting *Lg* propagation.

RESEARCH ACCOMPLISHED

Of all the regional phases, the *Lg* is usually the most prominent and robust in continental regions, and therefore it is widely used to determine regional variations of crustal structure and discriminate nuclear explosions from earthquakes. However, the *Lg* phase can also be highly attenuated or even blocked by abrupt changes in crustal structure; understanding the main factors that affect *Lg* in different crustal structures is crucial to the use of the *Lg* phase in nuclear test monitoring.

Northern Eurasia represents a large and complex geologic area, and therefore is ideal for studying the main factors influencing *Lg* phase propagation in contrasting tectonic areas. However, the means for traditional calibration of this region based on natural sources are limited. Northern Eurasia is largely aseismic, and regional recordings of natural sources are relatively scarce. Also, path calibration of regional seismic phases is strongly dependent on the accuracy of hypo-central locations of calibration events (Saikia et al, 2001), and for earthquakes, especially for small events, this information can be difficult to obtain.

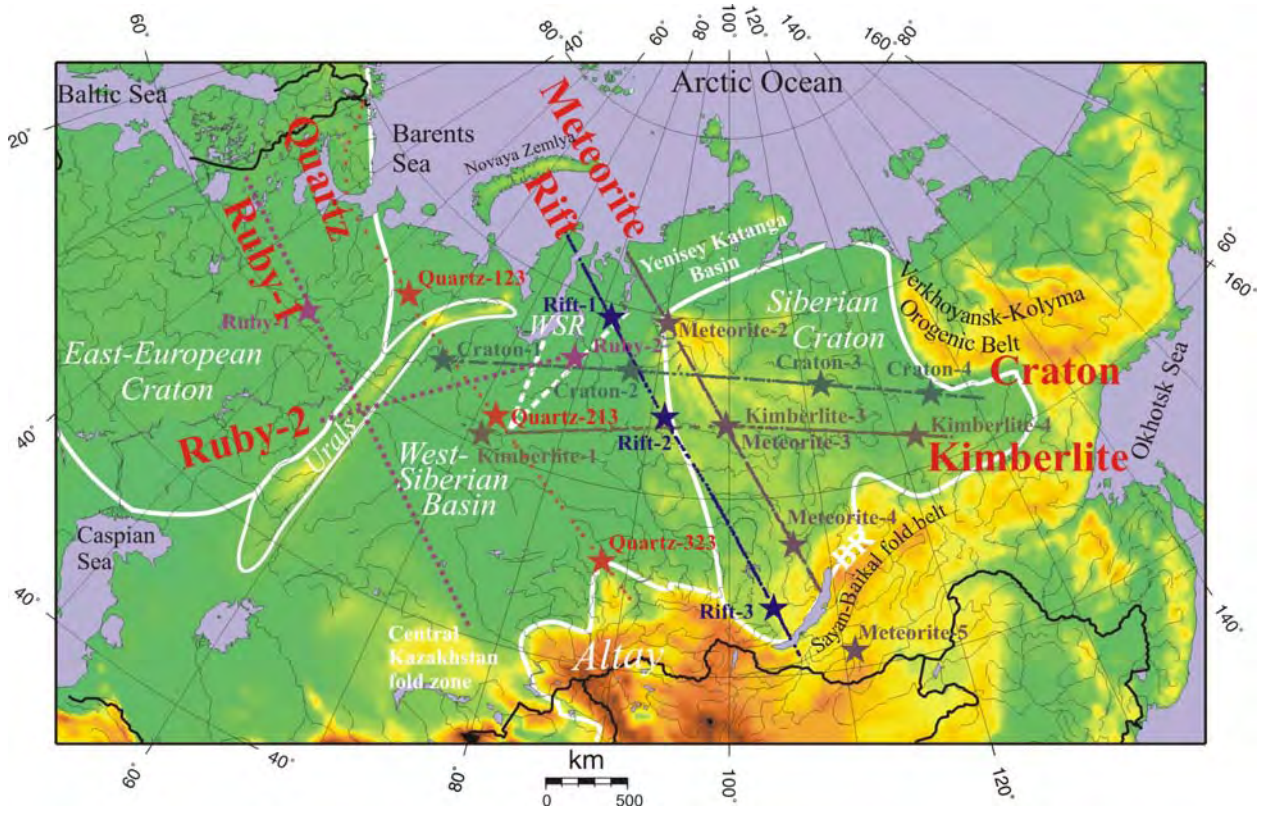


Figure 1. Six DSS projects that recorded 19 PNEs of this study. Large stars indicate the PNEs, and white shows the major tectonic boundaries (WSR – West Siberian Rift; BR – Baikal Rift) (Zonenshain, 1990). Color represents the surface elevation.

However, Northern Eurasia is also arguably the world's best-covered region with crustal and mantle-scale controlled-source seismic profiles. From the 1960s to the 1980s, the Soviet Union acquired a network of dense,

linear, long range, three-component Deep Seismic Sounding (DSS) profiles using conventional and Peaceful Nuclear Explosions (PNEs) over almost all of Northern Eurasia. In ongoing cooperation with Russian scientists, several research groups (Karlsruhe, Copenhagen, and Wyoming) have contributed to the preservation and analysis of the unique PNE datasets. At the University of Wyoming, our particular emphasis is on application of the PNE waveform recordings to nuclear test monitoring. We have obtained from Russia seven ultra-long-range profiles including 19 PNEs (Figure 1), which contribute greatly to the ground truth of the region and to the development of techniques of seismic nuclear test monitoring.

Because site effects cause strong variability of the absolute recorded amplitudes, particularly with the portable deployments of the DSS program, relative amplitudes are preferable for correlation with crustal structures. From previous studies, the *Lg* amplitude ratios, such as *Lg*/*Sn* (Sandvol et al., 2001), *Pg*/*Lg* (Philips et al., 2001), or *Lg*/*Pgcoda* (McNamara and Walter, 2001) were found to be effective in correlating with variations of crustal structure. In addition, recent studies have concentrated on studying the spectral characteristics of all the regional phases, and calibrating the sensitivity of different ratios to the variations of the crustal structure. In this work, we utilize our PNE waveform database to determine the main factors affecting *Lg* phase propagation and correlate the variations of the crustal structure in Northern Eurasia with the more sensitive amplitude ratios (*Lg*/*Sn* and *Lg*/*Pgcoda*) within the optimal frequency band.

An important advantage of PNE DSS interpretation over the traditionally used single-station recording is the ability to correlate the seismic phases over short distances of 10-20 km and within continuous offset gathers of up to 0-3800 km. In particular, in the analysis of the amplitude and spectral characteristics below, this dense recording allows us to identify and chose *P*, *S*, and *Lg* event time windows straddling the particular phases rather then rely on the

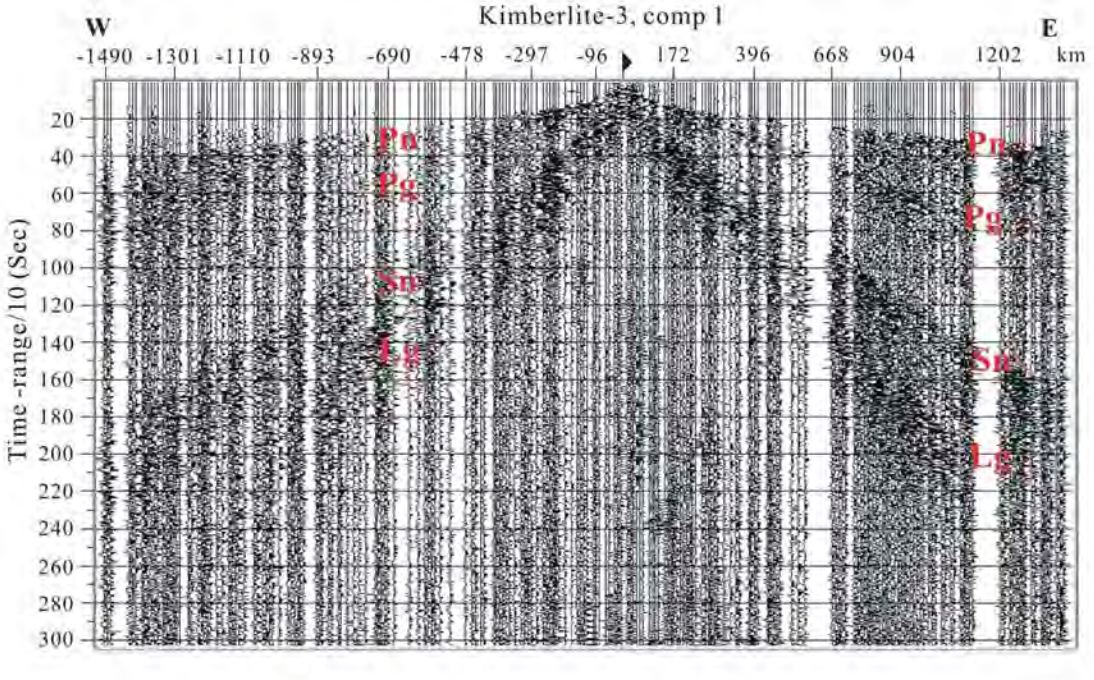


Figure 2. Inline-component seismic records from PNE Kimberlite-3 within 0.5-10-Hz frequency band. All the regional phases (*Pn*, *Sn*, *Lg*, *Pg*) are clear and propagate to 1000-1500-km offsets. Note the asymmetry of the phase amplitude pattern in two directions from the shot.

average group velocities as is commonly done in *Lg* studies. In the following, the event time gates are based on such carefully picked arrival onset times extended by 10-20 sec, as required by the analysis.

Spectral characteristics of regional phases

In the radial-component seismic records of Kimberlite-3 all the regional phases, *Pn*, *Pg*, *Sn* and *Lg* are clear within the recording offset range (Figure 2). To compare the *Lg* and *Sn* spectra at different offsets, we averaged the Fourier spectra of traces within 50 km around the 500- and 1000-km offsets from several PNEs (Figure 3). The *Lg* phase is mainly strong at low frequencies (<3Hz), and the *Sn* phase is strong at higher frequencies (>3Hz). Therefore, the *Lg*/*Sn* amplitude ratio is highest within the frequency band of 0.5-3 Hz, and this frequency band is used in our study.

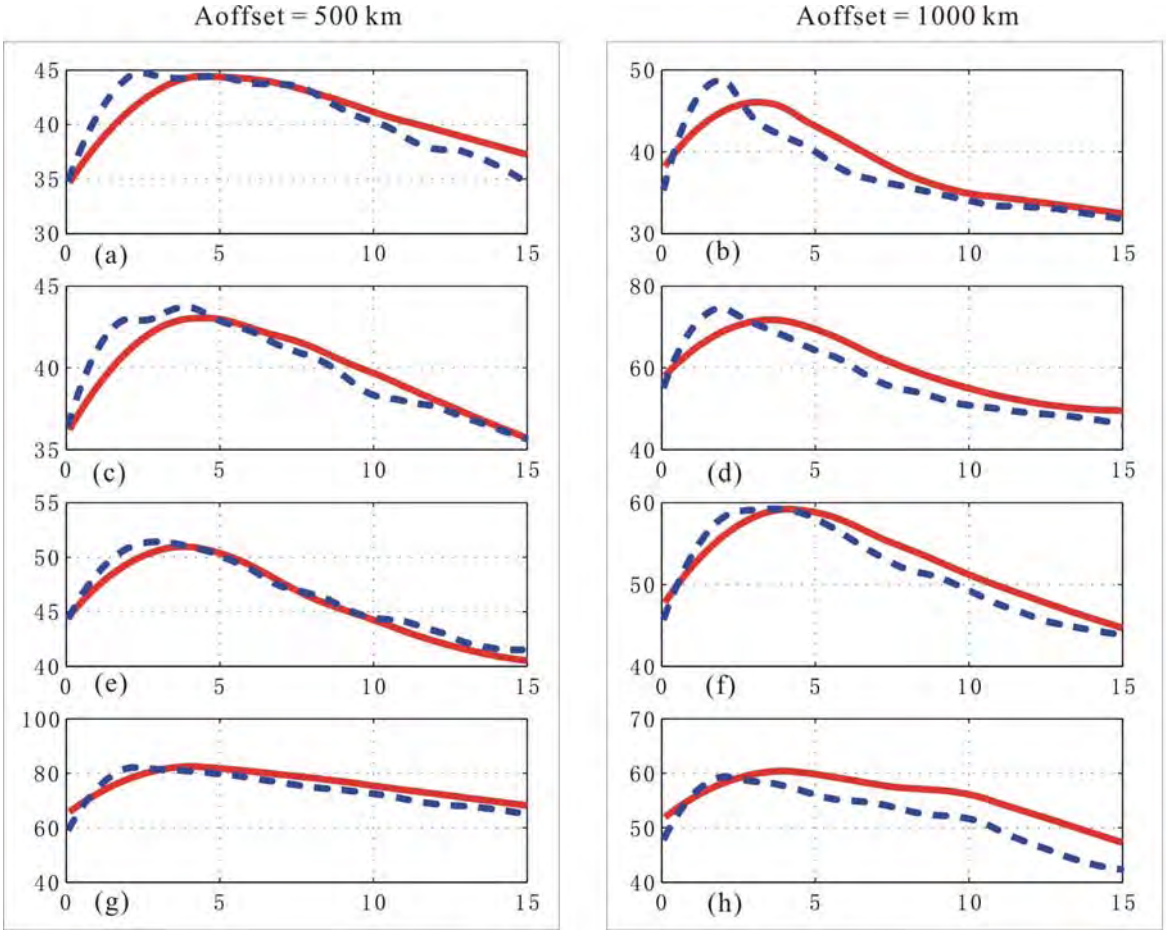


Figure 3. *Sn* (solid line) and *Lg* (dashed line) spectra at 500- and 1000-km offsets from several PNEs: a-b) Craton-3; c-d) Kimberlite-3; e-f) Meteorite-3; g-h) Kimberlite-4. Note that the peak *Lg* energy is concentrated below 3 Hz whereas the *Sn* peaks between about 3-5 Hz. Consequently, in our analysis of spatial variability of the amplitude ratios, we use the 0.5-3 Hz band in which the *Lg*/*Sn* ratios are higher.

Stability of amplitude ratios and comparison of different amplitude ratios

After picking the onset times of all the regional phases, arrival amplitudes were computed within the phase time windows. In this study, we chose the *Lg* window length to be 20 s and the *Sn* window length as 10 s. For the coda of *Pg*, we used the 10-sec window immediately before the picked onset of the *Sn* phase. For each phase, we computed amplitudes of each of the three components and combined them into a RMS vector measure, i.e., Amp = $(amp1^2 + amp2^2 + amp3^2)^{1/2}$.

Since *Lg* and *Pg* are guided waves trapped in the crust, they form only after ~300 km offset in Northern Eurasia. Therefore, the regional phases become separated after the offset of ~300 km (Figure 2), and we used only these

offsets in our analysis. By comparing the amplitude ratios obtained using different mathematical methods (RMS, median, peak, and bootstrapping) (Figure 4), we found that the resulting amplitude ratios are quite consistent, and the error from the bootstrapping method is small. The amplitude measurements and the ratios are stable and depend only on shot size, shot conditions, and travel path. By comparing the amplitude ratios (*Lg*/*Sn*, *Lg*/*Pgcoda*, *Lg*/*Pg*) (Figure 4) with the variations of the crustal structure, we found the *Lg*/*Sn* and *Lg*/*Pgcoda* were better for correlating with variations of the crustal structure and thus constraining the main factors affecting *Lg* propagation.

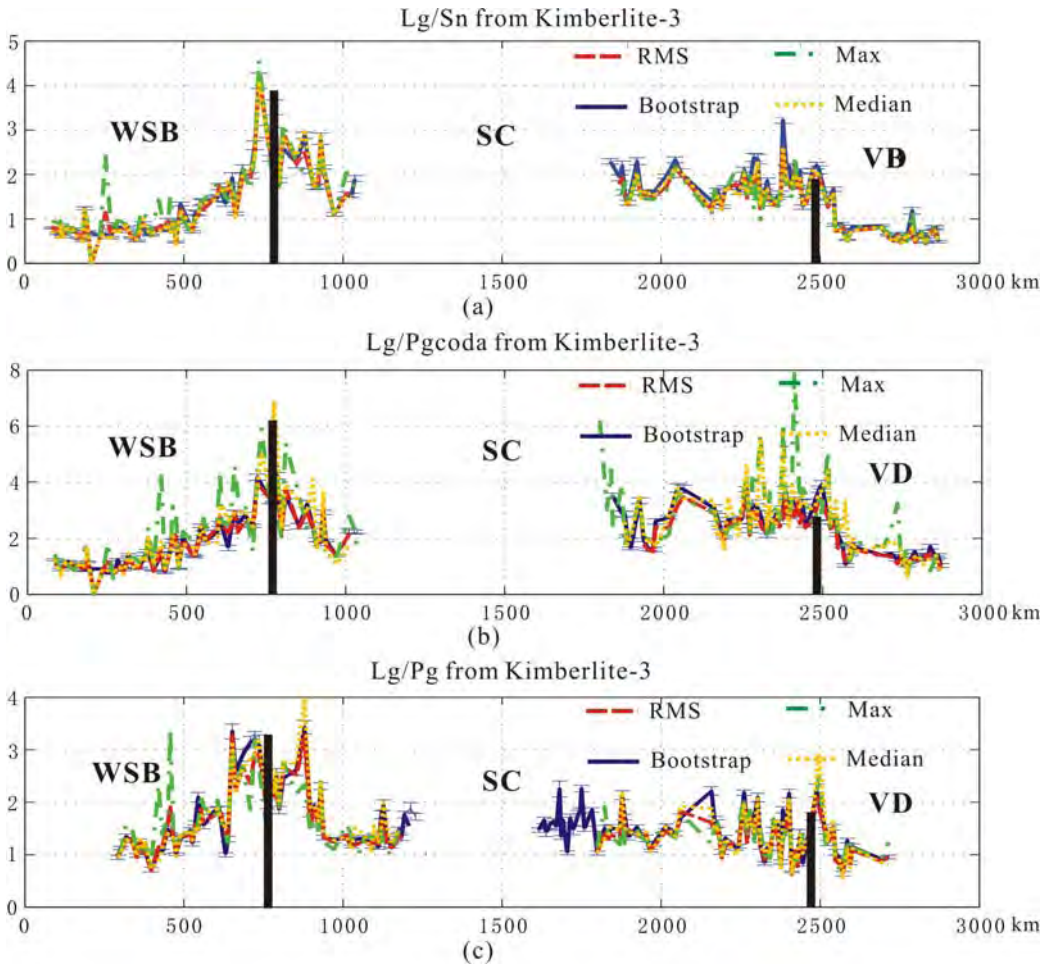


Figure 4. Comparison of several amplitude measures applied to several amplitude ratios: a) *Lg*/*Sn*, b) *Lg*/*Pgcoda*, and c) *Lg*/*Pg*. All measures produce similar results, with the exception of a somewhat less stable peak amplitude estimator (labeled as Max). Among the three amplitude ratios, the *Lg*/*Pg* is different from the other two and is less consistent with the variations of the crustal structure. Black bars are the major tectonic boundaries; WSB denotes the West Siberian Basin, SC- Siberian Craton, VD – Viluy Depression (Figure 1).

Comparison of the variations of amplitude ratios with crustal structure along profile CRATON

The Craton profile starts from the Preural High in the west, crosses the Ob-Tasovsk Depression, Yenisey Ridge, Tungass Basin, Mirninsk-Aihalsk High, and Vilui Depression, and ends in the Aldan Shield in the East (Figure 1). The complicated crustal structure provides an excellent chance to study the main factors to affect the *Lg* propagation and calibrate the amplitude ratios with the variations of crustal structure.

The *Lg*/*Sn* and *Lg*/*Pgcoda* along the Craton profile from the different PNEs (Craton-1, 2, 3, and 4) have very different amplitudes, which could be due to the source size and shot conditions (Sultanov et al., 1999). The source

spectra are different from shot to shot and different phases peak within different frequency bands. However, the spatial variations of the amplitude ratios are consistent between the different shots. We distinguish two constituents in these spatial variations: 1) regional offset dependence, and 2) local variations due to the local crustal structure. These components can potentially be separated where multiple coverage by reversed PNEs is available.

Along the profile, the amplitude ratios show systematic variations that are likely correlated with the local crustal structure. In general, it appears that the crustal thickness could be the primary factor affecting the *Lg* amplitude ratios (Figure 5). At profile distances < 900 km, both ratios decrease with offset at a rate of ~0.002/km; between ~1200 and 1500 km, the rate of their decrease becomes lower, < 0.001 /km, which could be due to a slow variation of crustal thickness. Between ~1500 to 2000 km both ratios increase with offset, in contradiction to what would be expected from the effect of the increased sediment thickness (up to 8 km, Figure 5a). This could be due to the high-velocity (4.5-5.5 km/s) and presumably low-attenuation sediments in the Tunguss Basin. Between kilometers ~2000 to ~2500 of the profile, the amplitude ratios stay constant or increase with offset, which could correspond to a thin sediment cover of the craton. At the eastern end of the profile (> 2500 km in Figure 5), the *Lg*/*Sn* and *Lg*/*Pgcoda* decrease rate is ~0.005/km, corresponding to the thick (up to 13 km), young (2.5-4.5 km/s *P*-wave velocities) sediments and pronounced Moho uplift (more than 10 km).

Note that between the profile positions of ~1000 and 1200 km, the amplitude ratios from the reversed Craton-1, Craton-3, Craton-4 PNEs are quite different. This difference can be explained if the effects of crustal thickening on *Lg* propagation are different from those of crustal thinning. A similar observation can be made between offsets ~2500 and ~2700 km (Figure 5). These preliminary observations would need to be tested and supported by further inversion and modeling.

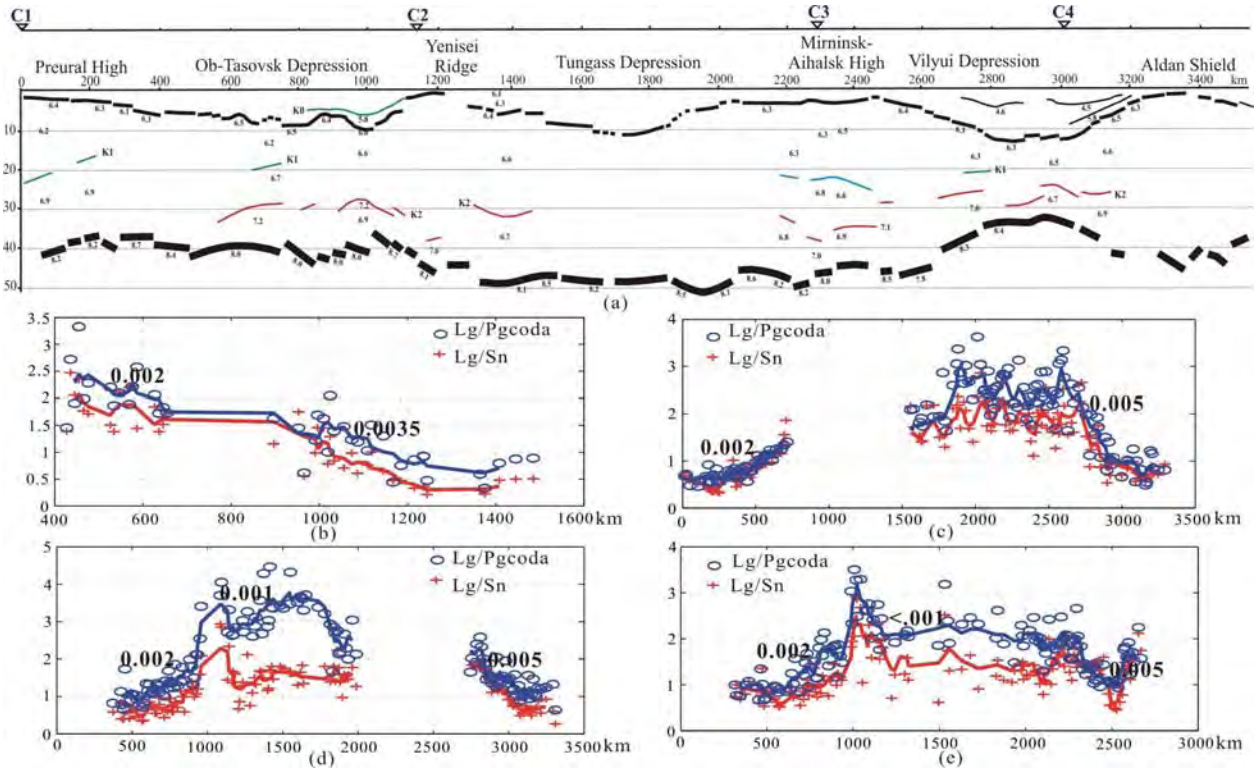


Figure 5. a) Crustal cross-section from profile Craton (Egorkin et al., 1987; Figure 1) and b-e) *Lg*/*Sn* and *Lg*/*Pgcoda* ratios from its four PNEs: Craton-1 (b), Craton-2 (c) , Craton-3 (d) , and Craton-4 (e). In cross-section a), thick black lines indicate the mapped reflecting Moho segments, red and blue lines – crustal reflections. The top of the basement is shown in black, and some reflections within the sedimentary cover are also indicated. In all plots, horizontal scales correspond to profile distance. Note the consistent variations of the amplitude ratios along the profile.

In the eastern part of the Ob'-Tasovsk Depression, a remarkable increase in the relative *Lg* amplitudes is located between kilometers 1000-1100 of the Craton profile (Figure 5). This feature still remains enigmatic; however, it could potentially be related to the complex crustal structure identified in this area, with a localized basin and a suggestion of deep crustal faulting extending to the Moho (Figure 5a). With a less consolidated crust, its response at lower (below 3-Hz) frequencies could be increased, resulting in increased relative *Lg* amplitudes. After the *Lg* waves pass this region, their amplitudes resume the "regional" trend (Figure 5d).

Variations of amplitude ratios in Northern Eurasia from seven PNE profiles

By computing the *Lg*/*Sn* and *Lg*/*Pgcoda* amplitude ratios for the 19 PNEs and correlating the ratios from the different reversed shots along the same profile, the variations of amplitude ratios in Northern Eurasia were determined along the seven profiles and summarized in Figure 6.

In the East-European Craton, along the Ruby-1 profile and Quartz profile in the Baltic Shield, the thickness of the sediments is <2 km, and the crustal thickness is ~40 km; both *Lg*/*Sn* and *Lg*/*Pgcoda* along the Ruby-1 (Ruby-1) and

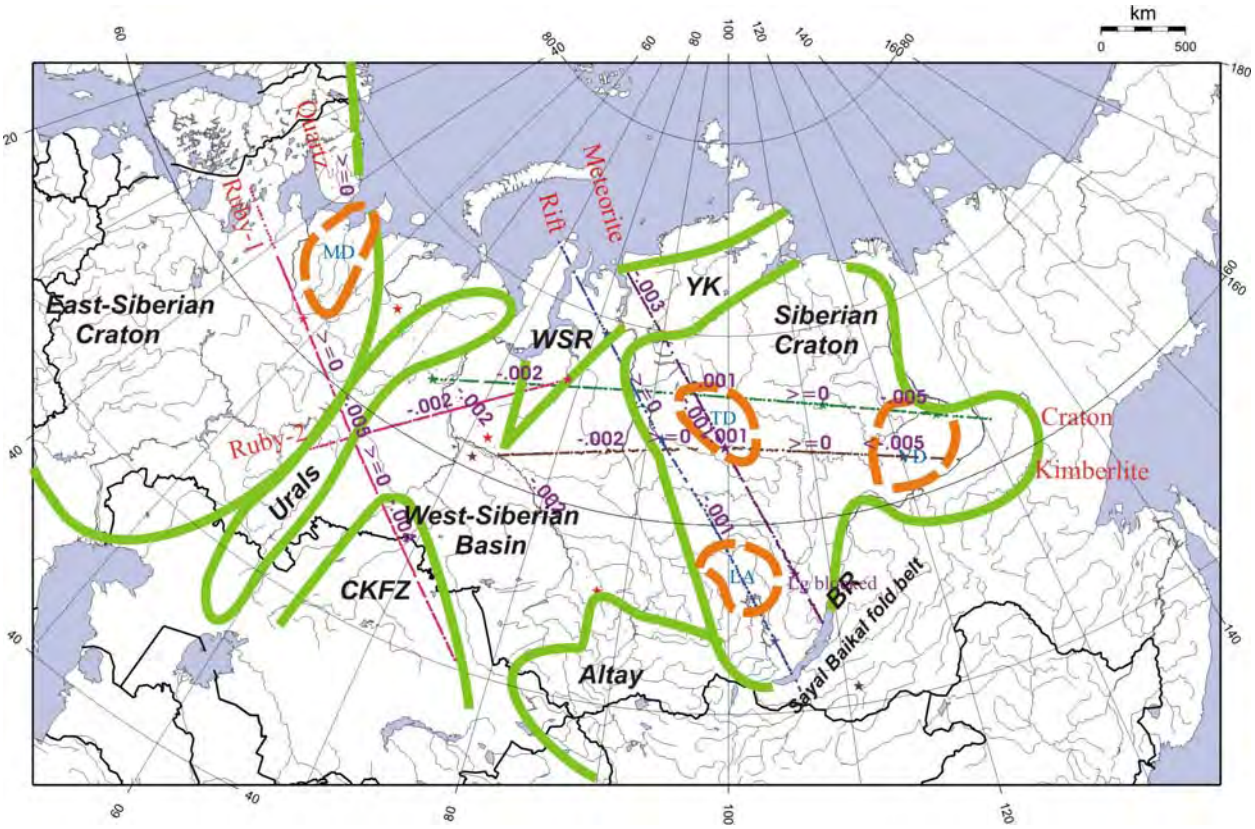


Figure 6. Sketch of tectonic boundaries (green lines) of Northern Eurasia and distribution of the observed *Lg* coda Q and *Lg* amplitude ratio-offset slopes (purple numbers). Orange contours show the areas where *Lg* appears to be blocked or highly attenuated. Labels indicate the key crustal structural features: WSR – West Siberian Rift; BR – Baikal Rift; CKFZ – Central Kazakhstan Folded Zone; YK – Yenisey-Khatanga Basin (up to 10 km of sediments); TD – Tunguss Depression (8-km sediments); LA – Low-Angara Depression (10 km of sedimentary rocks); VD – Viluy Depression (6-13 km of sediments); MD – Mezen Depression (2-5 km of sedimentary cover).

Quartz (Quartz-2, also often referred to as Quartz-123) profiles increase or are constant with offset. Under the Mezen' Depression between the Baltic Shield and the Timan Belt, the Moho is uplifted about 5 km and the sediments are ~2-5 km thick (Morozova et al., 1999); the observed *Lg/Sn* and *Lg/Pgcoda* along Quartz profile decrease with offset and the slope is ~0.002 km/s.

Three deep depressions (Viluy, Tungass, and Low-Angara) are present in the Siberian Craton. The Tungass Basin is filled with thick sediments (up to 8 km) composed of metamorphosed Paleozoic rocks mixed with plateau-basalts, and their velocities are high (~4.5-5.5 km/s) (Egorkin et al., 1987; Pavlenkova, 1996). Although the sedimentary rocks are thick in the Tungass Basin, no strong Moho uplift is observed and the crustal thickness is up to ~48 km. From Craton (Craton-2, Craton-3, Craton-4), Kimberlite (Kimberlite-3, Kimberlite-4), and Meteorite (Meteorite-4) profiles, both amplitude ratios decrease very slowly (<0.001km/s), which could correspond to the high sediment velocity and slow variations of crustal thickness. The sedimentary rocks and crust in the Low-Angara Basin have lower velocities than those in Tungass Bain, and the sedimentary rocks are up to 10 km thick. Moreover, the Moho is uplifted under this basin by ~3 km (Pavlenkova, 1996; Pavlemkova et al., 2002). From Rift PNEs (Rift-1, Rift-2, and Rift-3), both ratios in Low-Angara Basin decrease with offset and the slope is higher (~0.0015/km). The slopes of the amplitude ratios are ~0.005/km (Craton-2, Craton-3, and Kimberlite-3) in Viluy Depression, corresponding to abrupt crustal thinning (>10 km) and thick (up to 13 km), low-velocity (2.5-4.5 km/s), sediments.

Although the heat flow is high (~120mW/m^2) in the Baikal Rift Zone, no clear amplitude ratio variations are observed along the Meteorite profile (PNEs Meteorite-3 and Meteorite-5). However, for Meteorite-4 and Meteorite-5, which are near the Baikal Rift Zone, both *Lg* and especially *Sn* amplitudes are low while the *Pg* is strong; this could be due to the crustal heterogeneity that could be associated with the high heat flow region. From Craton (Craton-2, Craton-3, and Craton-4), Kimberlite (Kimberlite-3 and Kimberlite-4), and Meteorite (Meteorite-3 and Meteorite-4), along paths with thin sediments in the Siberian Craton, both ratios increase or are constant with offset.

The West-Siberian Basin is filled with young (post-Cretaceous), low-velocity (2.5-5 km/s) sediments, and the sediments are ~2-5 km thick. Steep subsidence of the basement is found in the northern part in the West-Siberian Rift (or Ob-Tanskov Depression) (up to 10 km), Yenisey-Khatanga Depression, and particularly in the Pur-Geden Basin (~13 km). The negative ratio-offset slope in the West-Siberian Basin is ~0.002/km, and ~0.003/km in the Yenisey-Khatanga Basin with its thick sediments (>10 km) and crustal thinning (~ 5 km).

The ratios decrease quickly at the Ural Mountains (~0.005/km) due to rapid crustal thickening (>10 km) and at the Central Kazakhstan folded zone (~0.004/km) with more than 5 km crustal thickening. Both ratios also decrease (~ 0.002/km) at the Mezen Depression between the Russian Plate and the Baltic Shield, which could be due to crustal thickening (< 5 km) and attenuation by the sediments.

More importantly, for the travel paths from the East-European Craton to the West-Siberian Basin across the Ural Mountains (Ruby-1 profile), and from the Siberian Craton to the West-Siberian Basin (Craton and Kimberlite profiles), both ratios increase with offset rapidly at the tectonic boundaries, and then drop quickly, perhaps because the *Lg* phase is partially blocked due to abrupt variations of crustal thickness at the tectonic boundaries.

CONCLUSIONS

The *Lg*/*Sn* and *Lg*/*Pgcoda* amplitude ratios are useful for calibration of the characteristics of *Lg* propagation with variations of crustal structure and to constrain the main factors affecting *Lg* propagation. In the DSS Peaceful Nuclear Explosion datasets in Northern Eurasia, both ratios increase or are constant with offset within the Siberian Craton and the East-European Craton, covered with thin sediments, and decrease with offset within regions with thick sedimentary covers (the Tungass Basin and Low-Angara Basin of the Siberian Craton, West-Siberian Basin, and Yenisey-Hantanga Basin). The slope of the amplitude ratios' decrease (< 0.001/km in the Tungass Basin, ~0.0015/km in the Low-Angara Basin, ~0.002/km in the West-Siberian Basin, and ~0.003km/s in the Yenisey-Hantanga Basin) could depend on both the thickness and the age of the sediments. Both ratios drop quickly where *Lg* is totally (Patom-Viluy Basin) or partially (Ural Mountains, Mezen Depression, and Central Kazakhstan folded zone) blocked, apparently by rapid variations of the crustal thickness. The *Lg* phase is mainly concentrated at low frequencies (<3 Hz), and therefore this frequency band is promising in *Lg*-based nuclear-test calibration.

REFERENCES

Baumgardt, D. R. 2001. Sedimentary basins and the blockage of Lg wave propagation in the continents. Pure and Applied Geophysics, Vol. 158, 1207-1250.

Belousov, V.V., Pavlenkova, N.I., and Kvyatkovskaya, G.N., 1992. Structure of the crust and upper mantle of the [Former] USSR. Part I, Integrated geophysical models of the major geostructures of the USSR. Vol. 34, 213-343.

Belousov, V.V., Pavlenkova, N.I., and Kvyatkovskaya, G.N., 1992. Structure of the crust and upper mantle of the [Former] USSR. Part II, Generalized geophysical data on the structure of the tectonosphere of the USSR. International Geology Review, Vol. 34, 345-444.

Egorkin, A.V., Zuganov, S.K., Pavlenkova, N.A., and Chernyshev, N.M., 1987. Results of lithospheric studies from long-range profiles in Siberia. Tectonophysics, Vol. 140, 29-47.

Kim, W.Y., et al., 1997. Discrimination of earthquakes and explosions in Southern Russia using regional high-frequency three-component data from IRIS/JSP. Bulletin of the Seismological Society of America, Vol. 87, 569-588.

McNamara, D. E., and Walter, W.R. 2001. Mapping crustal heterogeneity using Lg propagation efficiency throughout the Middle East, Mediterranean, Southern Europe. Pure and Applied Geophysics 158, 1165-1188.

Morozova, E. A., I. B. Morozov, S. B. Smithson, and L. N. Solodilov, 1999. Heterogeneity of the uppermost mantle beneath the ultra-long range profile “Quartz,” Russian Eurasia, J. Geophys. Res., 104 (B9), 20,329-20,348.

Pavlenkova, N. I., 1996. Crust and upper mantle structure in Northern Eurasia from seismic data. Advances in Geophysics, Vol. 37, 1-133.

Pavlenkova, G.A., Priestley, K., and Cipar, J., 2002. 2D model of the crust and uppermost mantle along rift profile, Siberian Craton. Tectonophysics, Vol. 355, 171-186.

Philips, W. S., et al. 2001. Application of regional phase amplitude tomography to seismic verification. Pure and Applied Geophysics, Vol. 158, 1189-1206.

Papine, R.R., and Ni, J.F., 2003. Propagation characteristics of Sn and Lg in Northern China and Mongolia. Bulletin of the Seismological Society of America. Vol. 93, 939-945.

Saikia, C. K., Woods, B.B., and Thio, H.K. 2001. Calibration of the regional crustal waveguide and the retrieval of source parameters using waveform modeling. Pure and Applied Geophysics, Vol. 158, 1301-1338.

Sandvol, E., et al. 2001. Tomographic imaging of Lg and Sn propagation in the Middle East. Pure and Applied Geophysics, Vol. 158, 1121-1163.

Sultanov, D. D., J. R. Murphy, and Kh. D. Rubinstein (1999). A seismic source summary for Soviet Peaceful Nuclear Explosions, Bull. Seism. Soc. Am., 89, 640-647.

Walter, W.R., Mayeda, K.M., and Patton, H.J., 1995. Phase and spectral discrimination between NTS earthquakes and explosions. Part I: empirical observations. Bulletin of the Seismological Society of America, Vol. 85, no.4, 1050-1067.

Volkov V.M., et al. 1984. Geology of the USSR. Publishing Office "Nauka", Moscow, 1984.

Zonenshain L.P., Kuzmin, M.I., and Natapov. B.M., 1990. Geology of the USSR: a plate tectonic synthesis. American Geophysical Union, Washington, D.C.

SEISMIC REGIONALIZATION RESEARCH IN NORTHEAST RUSSIA

Kevin G. Mackey[1], Kazuya Fujita[1], Hans E. Hartse[2], and Lee K. Steck[2]

Michigan State University[1], Los Alamos National Laboratory[2]

Sponsored by National Nuclear Security Administration
Office of Nonproliferation Research and Engineering
Office of Defense Nuclear Nonproliferation

Contract No. DE-FC03-02SF22490[1], W-7405-ENG-36[2]

ABSTRACT

In an effort to characterize seismicity in support of nuclear explosion monitoring for the continental regions of northeast Russia, we have continued field deployments in eastern Russia to acquire seismic ground-truth and waveform data. Recent fieldwork includes a ground-truth derived travel-time curve in the central Magadan region, as well as a seismic aftershock study in eastern Chukotka. We also continue to develop and make use of an extensive database of historic seismic bulletins covering all of northeastern Russia. To this end, we have parsed and merged six separate Siberian bulletins into standard database tables and from those tables produced a comprehensive map of Siberian seismicity covering the years 1960 to 2003.

We conducted an experiment in the Susuman gold mining region in northeastern Russia where many large explosions occur each spring. In this study, we used five explosions having ground-truth origin times and locations (+/- 150 m), and nine temporary seismic station deployment sites to construct a general travel-time curve for the region extending east from Susuman to the seismic station at Seymchan, a maximum distance of approximately 240 km. Using these ground-truth explosions, we determined that along this profile Pg velocity is 5.96 km/s and Sg velocity is 3.51 km/s. Additional phase arrivals are also noted which may correspond to PmP, P*, and/or other phases, although Pn and Sn arrivals are not clearly visible. A qualitative analysis of data recorded at Seymchan show that high noise levels obscure the majority of events that are clearly recorded at sites only a few kilometers out of town. This applies to the Susuman explosions we recorded, which are not visible in the Seymchan Station data without filtering, while they are clear at nearby but remote sites. This is important to note because the Comprehensive Nuclear-Test-Ban Treaty Organization (CTBTO) will soon open Seymchan as an International Monitoring System (IMS) auxiliary station.

In December 2002 a magnitude 4.2 earthquake occurred in eastern Chukotka. This began an extensive aftershock sequence/seismic swarm of small but felt events that continue to the present (June 2004). In September 2003, we deployed one permanent and two temporary seismic stations in and around the village of Neshkan. As a result of events located in this deployment, we were able to determine a fault trace that runs essentially under the town. With the use of additional data from western Alaska, we find that teleseismically recorded events located in this area are likely to have calculated epicenters approximately 5─10 km too far west.

Our bulletin parsing and merging efforts have produced database tables holding information from about 210,000 event locations ranging from around 105 degrees east longitude to across the Bering Strait into western Alaska. Also included are locations from Sakhalin Island and the Kamchatka Peninsula. We hold arrival times for about 80,000 of these events. The original sources for this information varies from published, Siberia-wide Russian earthquake bulletins to unpublished bulletins of regional network operators. We are currently working on a new-site table of consistent station names and locations, and we are parsing pre-1960 historic bulletins and mining explosion catalogs, with plans to insert this information into our Siberia database.

OBJECTIVE

The objective of our research is to improve event location and identification capability in eastern Russia in support of nuclear explosion monitoring.

RESEARCH ACCOMPLISHED

Ground Truth Velocities in the Susuman Region

The Susuman region in Northeastern Russia is an active gold mining region in which many large explosions occur each spring. In April 2004, we recorded five mine explosions (three from Kholodnie mine, two from Teekhee mine) ranging in size from 45 to 72 tons to construct a seismic profile. Ground truth origin times and locations (+/- 150 m) were obtained for all explosions by deploying a seismic station at the mine. These explosions were used to construct a general travel-time curve for the region extending east from Susuman to the seismic station at Seymchan, a maximum distance of approximately 240 km (Figures 1 and 2A). For each explosion, two field stations were deployed, and moved progressively farther along the profile prior to the next blast. In total, nine temporary seismic stations were deployed between Susuman and Seymchan. Each deployed station was 3-component, using SM3 seismometers, and was digitally recorded at 100 sps on a 24 bit A/D with a GPS clock. As this work was conducted in late winter in a remote region, all stations were deployed via snowmobile. We found that the most practical place for station deployment to be on small frozen streams (Figure 2B). As the region is generally permafrost, small streams are frozen solid completely through and thus provide a ready-made hard flat surface. Bedrock outcroppings were essentially impossible to find given the snow cover.

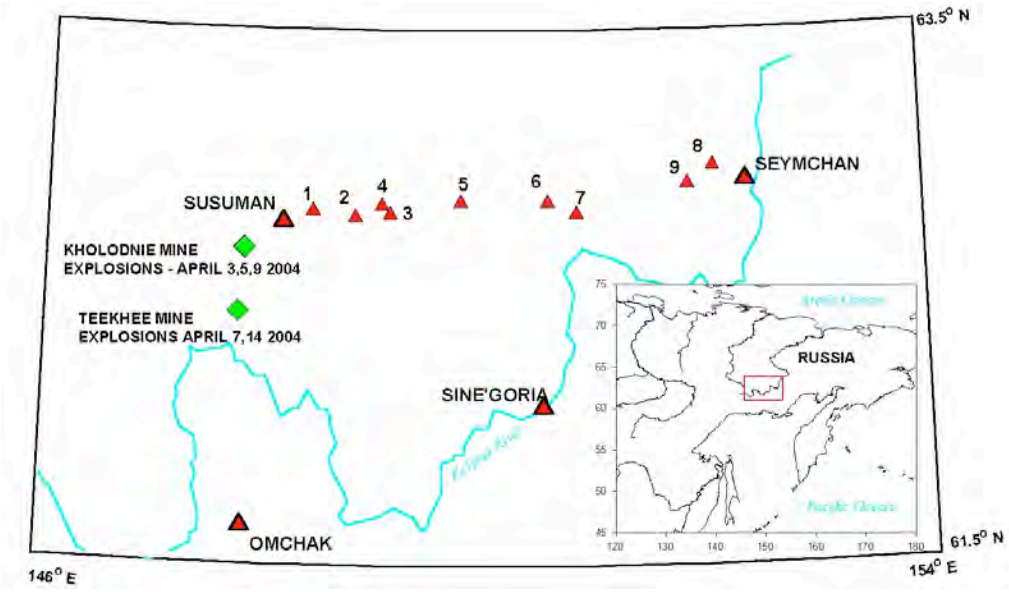


Figure 1. Seismic stations (numbered) deployed between seismic stations at Susuman and Seymchan for a seismic profile to determination ground-truth velocities in the region. Explosions originated from the Kholodnie and Teekhee mines. Other permanent regional seismic stations are also shown. Additional stations off the map also recorded some of the explosions.

In addition to stations directly along the profile route, other permanent seismic stations also recorded the explosions, contributing arrivals at distances up to 470km. Using these ground-truth explosions, we observed that the crustal seismic velocities increase slightly with distance. Velocities at about 25 km from the source are 5.798 km/s for Pg, and 3.490 km/s for Sg. At 230 km, these velocities are increased to 6.113 km/s and 3.5239 km/s for Pg and Sg respectively. Sg velocities to the north of Susuman increase only slightly more to 3.565 km/s at a distance of 470 km. Although Pg and Sg arrivals are clearly observed out to several hundred kilometers, Pn and Sn arrivals were not clearly observed at any distance. The Pg and Sg velocities determined are very close to the crustal velocity model developed by Mackey *et al*., 2003a, where velocities for this region were found to be 6.025–6.075 km/s for Pg and

3.51–3.53 km/s for Sg. The close match of the ground truth velocities imparts a strong degree of validation to the crustal model. Sample explosion seismograms at varying distances recorded during this fieldwork are shown in Figure 4.

a. b.



Figure 2. 2.a. 47,775 kg explosion at the Teekhee placer gold mine on April 14, 2004. 2.b. typical station setup used for temporary stations deployed along the profile. The SM3 short period sensors are sitting on a small frozen stream, which was determined to be the best deployment option given field conditions and logistics. The small streams are completely solid, thus there is no hydroacoustic noise produced. As the streams are very shallow (5–20 cm) there are no problems with acoustic impedance between the ice and underlying rock. This is Station Site #2 in Figure 1.

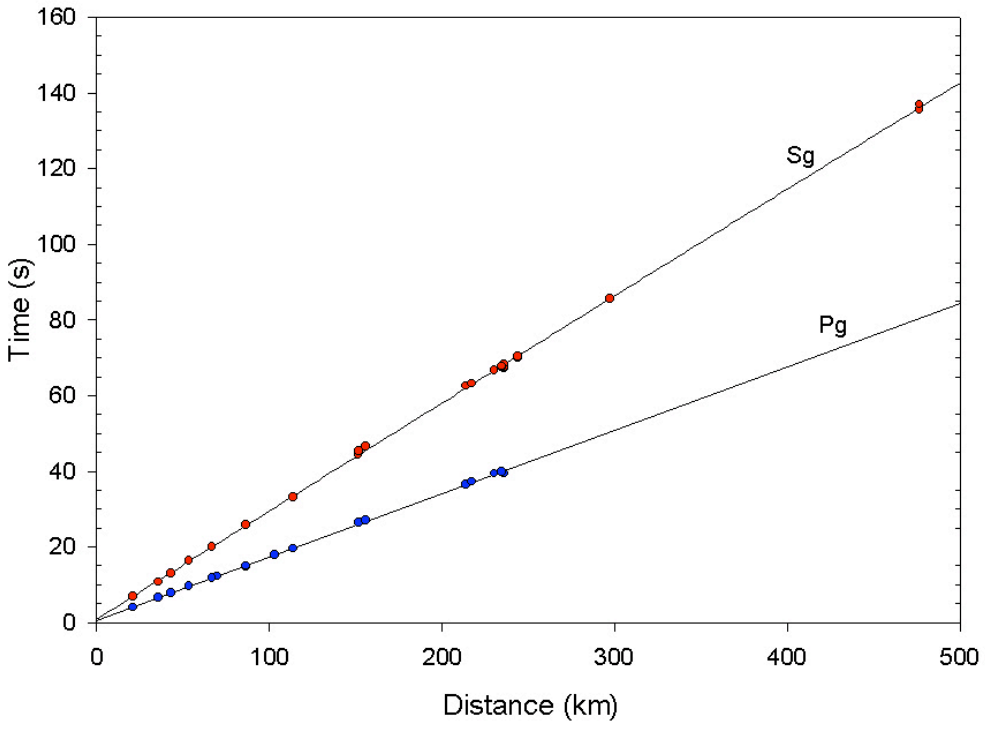


Figure 3. Ground-truth crustal travel-time curve derived from mine explosions. There were no Pn or Sn arrivals that were sufficiently clear to pick times with any degree of confidence. Data points are fit with a second-order regression curve.

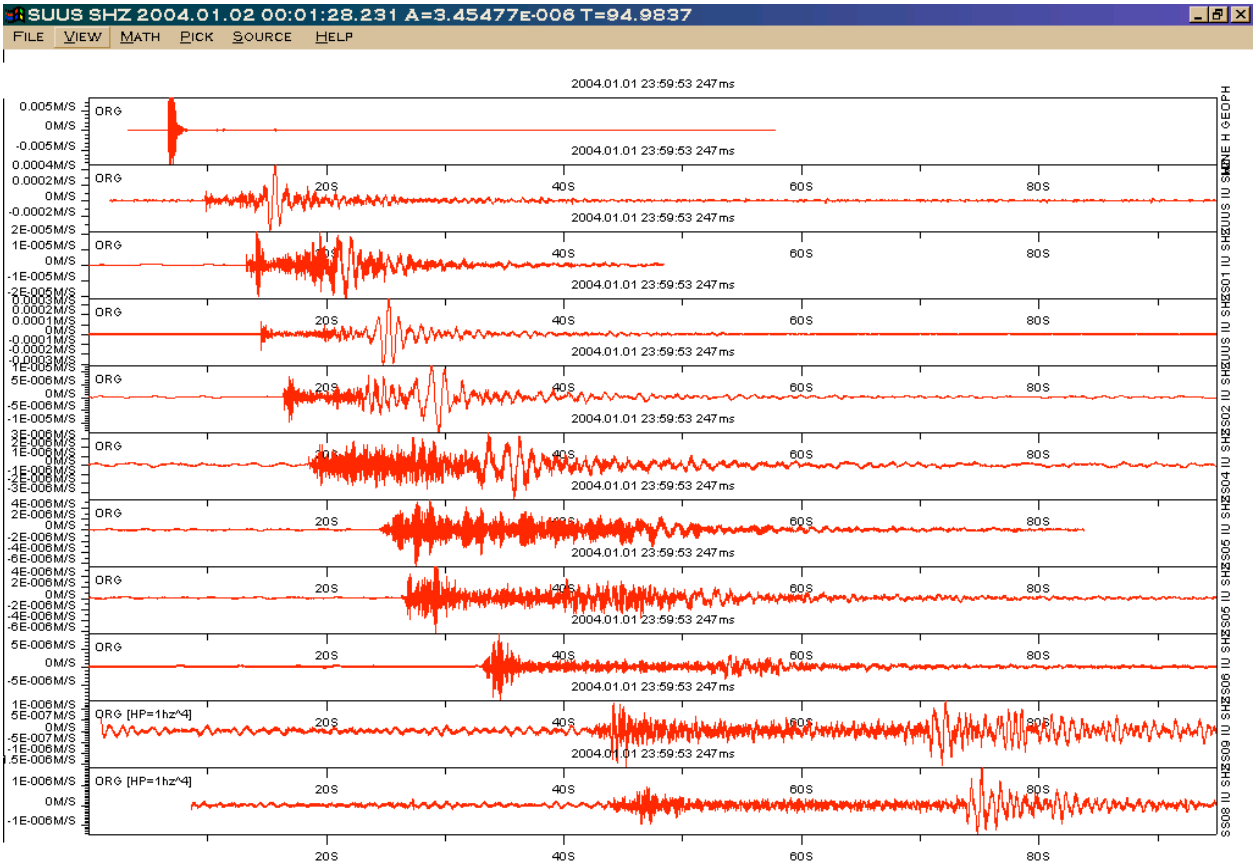


Figure 4. Sample explosion seismograms of mine explosions used to derive ground truth velocities. These records vary in distance from 0-230 km. All traces are unfiltered except the bottom two traces, to which a 1-Hz-high pass filter was applied.

Quality of Future CBTBO Recordings at Seymchan

A qualitative analysis of data recorded at Seymchan shows that high noise levels obscure the majority of events that are clearly recorded at sites only a few kilometers out of town. For instance, the Susuman explosions recorded here, are not visible in the Seymchan Station data without filtering, while they are clear at nearby but remote sites. The situation is easily illustrated by comparing seismograms from the April 14 explosion as recorded at Station 8 and Seymchan (Figures 1 and 5). In this case raw, unfiltered data from Station 8 shows a clear seismogram with a lot of information, while the same raw, unfiltered data from Seymchan does not show any obvious event. It is possible to see the event at Seymchan by filtering the data in a narrow frequency range, though it is not possible to obtain a clear seismogram (Figure 5). Horizontal components of Seymchan are even noisier than the vertical component shown. In comparing these seismograms it is important to note the differences in both stations. Station 8 used short period SM3 seismometers, while Seymchan records STS-1 Streckheisen seismometers. Station 8 was a hastily prepared site on a frozen stream and not thermally isolated, while the sensors at Seymchan are situated on a buried concrete pier in a thermally controlled underground vault. For this explosion, Station 8 was 13 km closer to the explosion (230 km) than Seymchan (243 km). A similar recording situation exists for earthquakes. Station 8 operated continuously for four days and recorded over 50 local and near-regional earthquakes. Of those events, only a few are visible at Seymchan. The problem in Seymchan is that the station is situated only one block from the center of the town, and more importantly, a coal fired heating plant is situated about 100 m from the station. The heating plant operates grinders for processing coal, which produces a large amount of anthropogenic noise on the seismograms. The situation is somewhat better during the summer months (mid May to mid September) when the heating plant is not in operation. This discussion on Seymchan is important to note because CTBTO will soon open Seymchan as an IMS auxiliary station. The CTBTO instruments will reside in the same seismic vault as the current STS-1 instruments shown here, and thus subject to the same levels of anthropogenic noise.

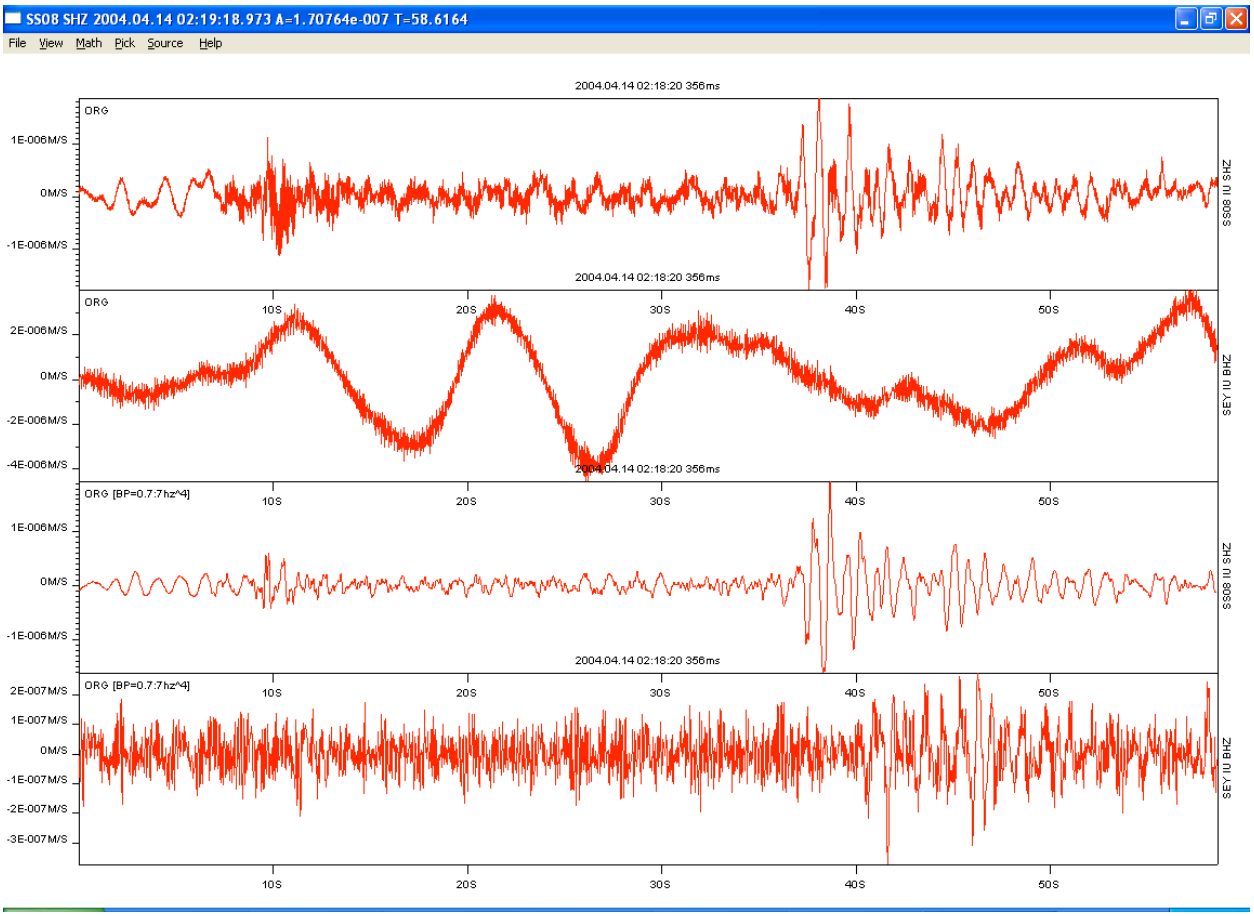


Figure 5. Seismograms from the 47,775 kg April 14, 2004 mine explosion. The top trace is unfiltered data from Station 8 (230 km distant), while the second unfiltered trace was recorded at Seymchan (243 km distant). The bottom two traces are the same data bandpass filtered from 0.7–7 Hz.

Neshkan Aftershock Study

The village of Neshkan, located along the Arctic coast of Chukotka in northeastern Russia, has been experiencing felt earthquakes almost daily since a M_L 4.2 (4.1 m_b) earthquake occurred on December 9, 2002 (Figure 6). The mainshock and several aftershocks over several months were large enough to be included in the Reviewed Event Bulletin (REB). The continuing aftershock sequence allowed us to deploy temporary stations in the region and determine the extent of the aftershock zone, and compare it with teleseismically determined hypocenters.

The tectonic setting of the area is poorly understood, but recent cooperative work with our Russian colleagues, combining teleseismic and regional seismic data, have suggested that the area is in an extensional setting, which is contiguous with rift systems proposed in Seward Peninsula, Alaska (Mackey *et al*., 1997; Fujita et al., 2002).

For the 2003 Neshkan experiment, three seismic stations were deployed. The main station, Neshkan (NSH), is a three component short period station deployed in the village of Neshkan. Two temporary stations were also deployed in the tundra (Table 1). Both temporary stations were single-component using a short period vertical seismometer. Station NSH1 failed shortly after installation due to an instrument problem.

Over approximately 18 days of operation, the Neshkan temporary deployment recorded approximately 150 earthquakes, most at Station NSH. The largest event recorded during the experiment had a K-class of 9.4, which corresponds approximately to M_L 3.4. Most events recorded were considerably smaller. Only events with clear Pg and Sg arrivals recorded at both operating stations were located. For these locations, first motions at the three

component Station NSH were determined to constrain the approximate location of the source. Considering that the closest events have an S-P time of only 0.6 seconds, we obtain a maximum possible depth for many events near Neshkan of only 5 – 7 km, assuming the event is directly below the station. By assuming a shallow hypocenter depth (5 km), an approximate epicenter based on first motion polarities, and using Pg and Sg times from both stations, we are able to locate the earthquakes. A sample seismogram is shown in Figure 7.

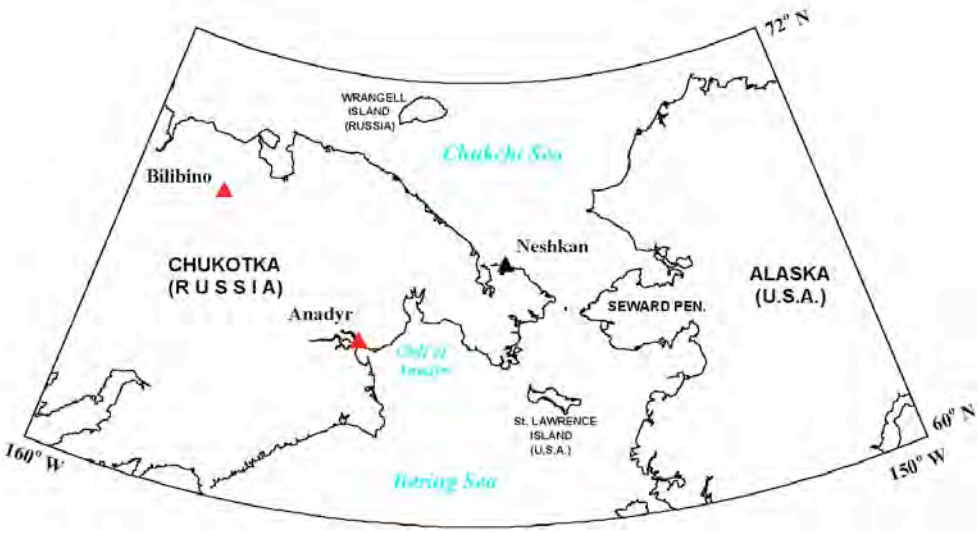


Figure 6. Neshkan is located on the north coast of Chukotka, near the Bering Strait Red triangles indicate the open seismic stations in Chukotka during the first nine months of the aftershock sequence.

Results from 18 locatable events fall in a linear zone extending from Neshkan to approximately 20 km to the south-southwest (Figure 8). We suggest that this linear trend of earthquakes represents a specific but previously unknown active fault in close proximity to the village. Located epicenters indicate that this fault may be within 1 km of the town, to the west. In addition, a small pond located approximately 1 km west of the village had drained for the first time in people's memory by spring, 2003, suggesting that there may have been some surface deformation over the course of the earthquake sequence. Approximately 500 m west of the village, there is an extensive region of rapidly eroding permafrost sand deposits. The erosion is facilitated by extensive cracks in the permafrost, allowing water to penetrate and melt the permafrost in the warmer summer months, causing the crack to expand as material is washed out. It is the recollection of the village administrator that the cracks may have first appeared in 1997. This would be consistent with a small amount of surface deformation resulting from the Magnitude 6.0 Neshkan earthquake in October 1996. It should be noted that the exact date or year this erosion began might not be recalled exactly correctly. No other similar fractured erosional areas were observed in approximately 15 km of walking along the beach to the west of Neshkan.

Following the end of active fieldwork in the Neshkan region, the main seismic station (NSH), was left in place as a permanent station site. Analysis of data from September 12 through early 2004 show over 1500 earthquakes recorded, with the sequence still active as of June, 2004.

Table 1. Seismic station parameters

Station	Latitude	Longitude	Elevation (m)	Date Open — Close
NSH	67.036	-172.960	5	12/9/2003 –
NSH1	66.263	-173.328	29	Did Not Operate
NSH2	67.107	-173.635	65	12/9/2003–30/9/2003

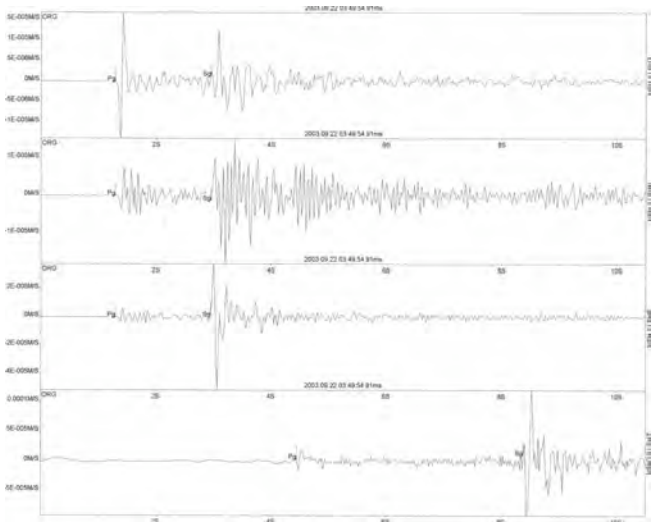


Figure 7. Event with dilatational arrivals at Station NSH. Components are, top to bottom, Z, N-S, and E-W. The bottom trace is the vertical from Station NSH2.

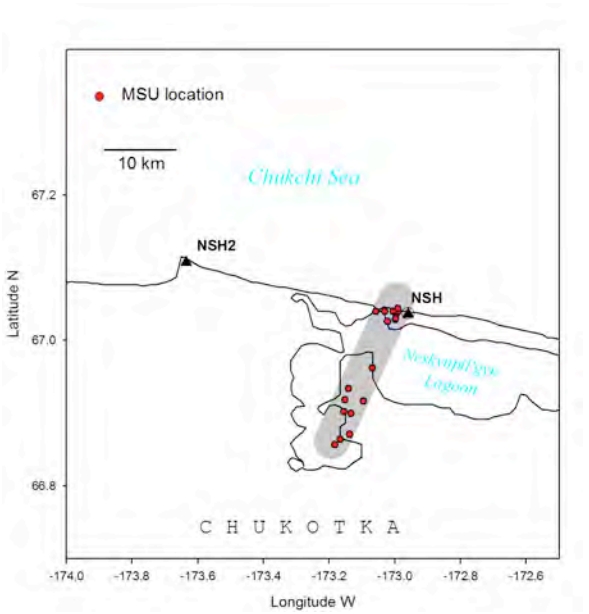


Figure 8. Earthquakes located near Neshkan from our deployment in September 2003.

Location Quality of Recent Teleseismically Recorded Events

We can compare the seismic trend defined from the recently located events of this study to earlier teleseismically located events. The most recent large earthquake near Neshkan was the magnitude 6.0 Chukotka event of 1996, which was followed by an aftershock sequence (Figure 9). Several of the aftershocks ranging is size from magnitude 3.0–5.0 were also recorded and located teleseismically. There are no locations or data on small events in the aftershock sequence as there were no local stations. The mainshock from this sequence is teleseismically located approximately 5 km west of the center portion of the trend defined in this study. The larger aftershocks are generally within 10 km, while smaller aftershocks are located up to 30 km from our currently observed trend. Considering the proximity of the 1996 mainshock, distribution of aftershocks, and realistic epicentral errors, we suggest that the 1996 sequence occurred on the same fault segment. Unfortunately, it is not currently possible to greatly improve the locations of these teleseismic events as no local data are available.

The current swarm of earthquakes near Neshkan began with a M_L 4.2 on 9 December 2002. Other magnitude estimates for this event range from 3.9–4.7, depending on magnitude type and source. Several teleseismically recorded aftershocks also occurred, primarily reported in the REB. The REB teleseismically determined mainshock epicenter appears to be mislocated approximately 10 km too far west, similar to events of the 1996 sequence, relative to our newly defined trend. Through October 2003 the REB reports six additional events, having magnitudes between 3 and 4, which may be aftershocks occurring in this sequence (There is also one possible foreshock on 22 June, 2002; See below). The REB locations for these events vary considerably, thus it is not initially clear which of them are actually associated with mainshock (Figure 10.a.). Of the six possible aftershocks, 5 were felt strongly in Neshkan (Mackey *et al*., 2003b). For the events reported in the REB, we obtained additional seismograms from four stations operated by the Alaska Earthquake Information Center (AEIC). Arrival times at the Alaska stations were used in conjunction with teleseismically reported arrivals to relocate the events. The relocations were computed using calibrated Pg and Sg velocities for the region using the model and methodology as described in Mackey (1999) and Mackey *et al*. (2003a).

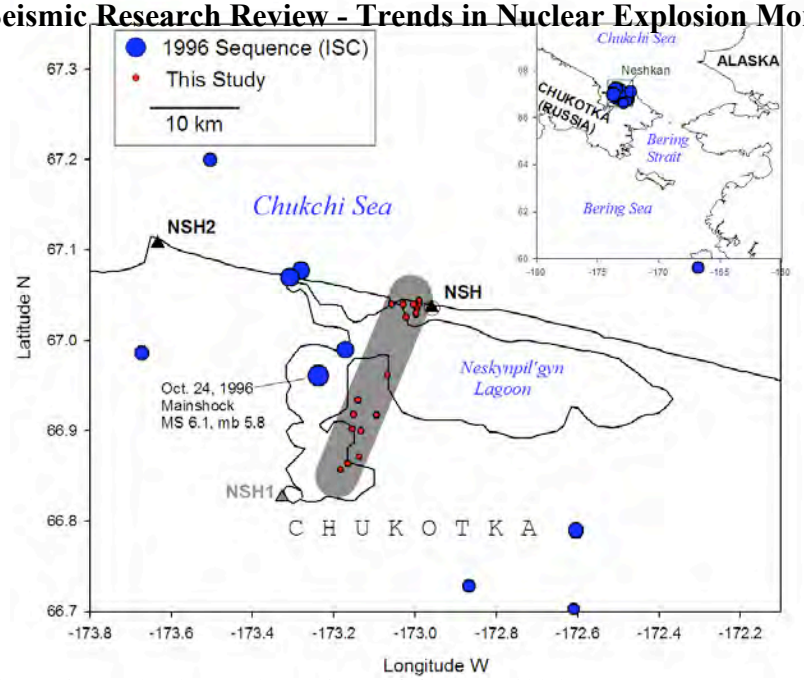
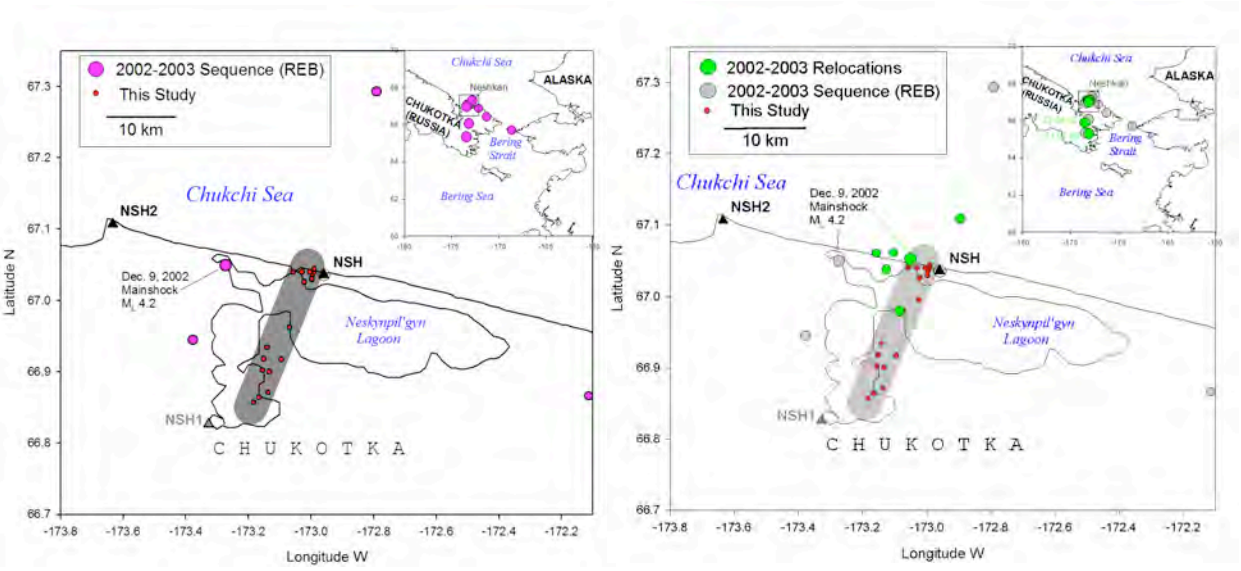


Figure 9. Comparison of teleseismic locations of the 24 October 1996 earthquake and associated aftershocks to the currently active aftershock zone. The 1996 sequence may fall on the same fault segment, with location differences being due to epicenter calculation errors. In general, the larger event teleseismic locations appear to be 5–10 km systematically to the west of our aftershock zone



a **b**

Figure 10.a. Comparison of REB determined epicenters to the aftershock zone determined here. Note that several events are only located on the map inset, while the mainshock locates west of our defined trend. Figure 10b. Relocations of the REB reported events, using supplemental arrivals from Alaska stations and using the crustal velocity model of Mackey *et al.*, 2003a. The relocated mainshock plots within the aftershock zone and other aftershocks cluster close. Two other events reported in the REB locate far to the south of, which also consistent with felt reports from Neshkan.

Relocation of the 9 December 2002 mainshock moved the epicenter approximately 10 km east, placing it on the west edge of the northern, and most active, portion of our defined trend (Figure 10b). All other REB-reported epicenters following the 9 December 2002 event except one are also found to cluster on or near our fault trend. The 31 January 2003 event reported in the REB was found to locate approximately 150 km south of Neshkan. Of the possible REB-reported aftershocks, this was also the only earthquake not reported as felt in Neshkan. Another event, occurring on

22 June 2002, was evaluated to see if it might have been a foreshock of the Neshkan events. Relocation of this event using Alaska data shows this event also to be located approximately 100 km south of Neshkan. Both of the non-Neshkan events are associated with other trends in the historic seismicity. Overall, the relocations are a significant improvement over the REB-determined epicenters, with two events moving more than 100 km. In the relocation process, depths were allowed to vary freely. The depths for all events converged between 2 and 16 km. Showing conclusively that the mainshock, and five of the six possible REB aftershocks, are associated with the northern end of the defined trend allows us to use, with a reasonable degree of certainty, these events to improve future teleseismic locations in the region by providing travel-time residuals and source specific station corrections (SSSC's) for eastern Chukotka. Unfortunately the events were not large enough to provide useful corrections to many teleseismically-reporting stations. It may be possible to obtain reasonable SSSC's for several of the seismic arrays that may have recorded the events. The events will also be useful to improve locations of future events in the area with the available local and near regional stations. In conclusion of the Neshkan study, teleseismic locations (REB, ISC) of moderate- to well recorded events in this area appear to be mislocated 5–10 km west of the true epicenters. Based on the relocated teleseismic events association with the determined aftershock region, the location methodology and crustal-seismic velocities in Mackey *et al*., 2003a appear to be valid for the region.

Database Improvements

Michigan State University (MSU) has accumulated a large volume of catalog and bulletin information (both electronic and paper) from several Russian sources. One of our main efforts has been to merge all of this information into one common source. To accomplish this, we have parsed, merged, and inserted many catalogs and bulletins into SQL-style database tables following the NNSA schema. The database consists of event, origin, origerr, arrival, assoc, amplitude, stamag, netmag, remark, and site tables. Many data files provided by MSU covered specific network bulletins and catalogs and other files had already been merged by MSU into Siberia-wide bulletins. Initially, each file was parsed and inserted into an appropriate, individual suite of database tables keyed to network. Table suites included data from (1) Kamchatka, (2) Irkutsk, (3), Sakhalin, (4) merged bulletins (primarily from Magadan and Yakutsk), and (5) region-wide catalogs from other Russian sources. Once all data files were parsed and inserted into database tables, we merged origins from the five suites of tables into a final set of tables. We refer to these final tables as the "Siberia database." We merged events by ranking origin authors and defining maximum-allowable time and distance separations between origins based on origin author. In total, 66 origin authors were used to insert 209,982 events into the Siberia database. About 72,000 of these events have additional origins reported by more than one source.

The Siberia database spans from pre-instrument times (1725 to the early 1900's) to sparse-instrument times (1900 to 1960) and on through the era of analog, and then digital, regional instruments to 2003. We hold over 1.31 million arrival times and 590,000 amplitude measurements beginning in 1970, and ranging up through the present. Many of these amplitudes contributed to Russian "k-class" event-size estimates, and nearly all events have a k-class measure stored in our netmag table. We have also accumulated information on over 11,000 industrial explosions from throughout the Magadan region (1977 to 2003). The catalog lists the approximate parameters of the explosions. Arrival times from Magadan network stations are included for explosions occurring in 2002 and 2003.

Summarizing the database work, we have made substantial progress in gathering a complete set of digital Siberian seismic information available to MSU under a single set of well-defined SQL-style database tables. While building the tables we have done quality-control work as the data were inserted, and we have developed tools based on the Perl scripting language and the Perl Database Interface modules (DBI) for adding even more information to the Siberian database in the future. Most importantly, we have now been able to exploit the database for research purposes, the first product of which was to produce the most complete seismicity map of eastern Russia (Figure 11).

CONCLUSIONS

In an effort to improve nuclear explosion monitoring for the continental regions of northeast Russia, we have continued field deployments to acquire seismic ground-truth and waveform data. Recent fieldwork includes a seismic aftershock study in eastern Chukotka and a ground-truth derived travel-time curve in the central Magadan region. We have also continued development of an extensive database of historic seismic bulletins covering all of northeastern Russia from which we produced a comprehensive map of Siberian seismicity covering the years 1960 to 2003.

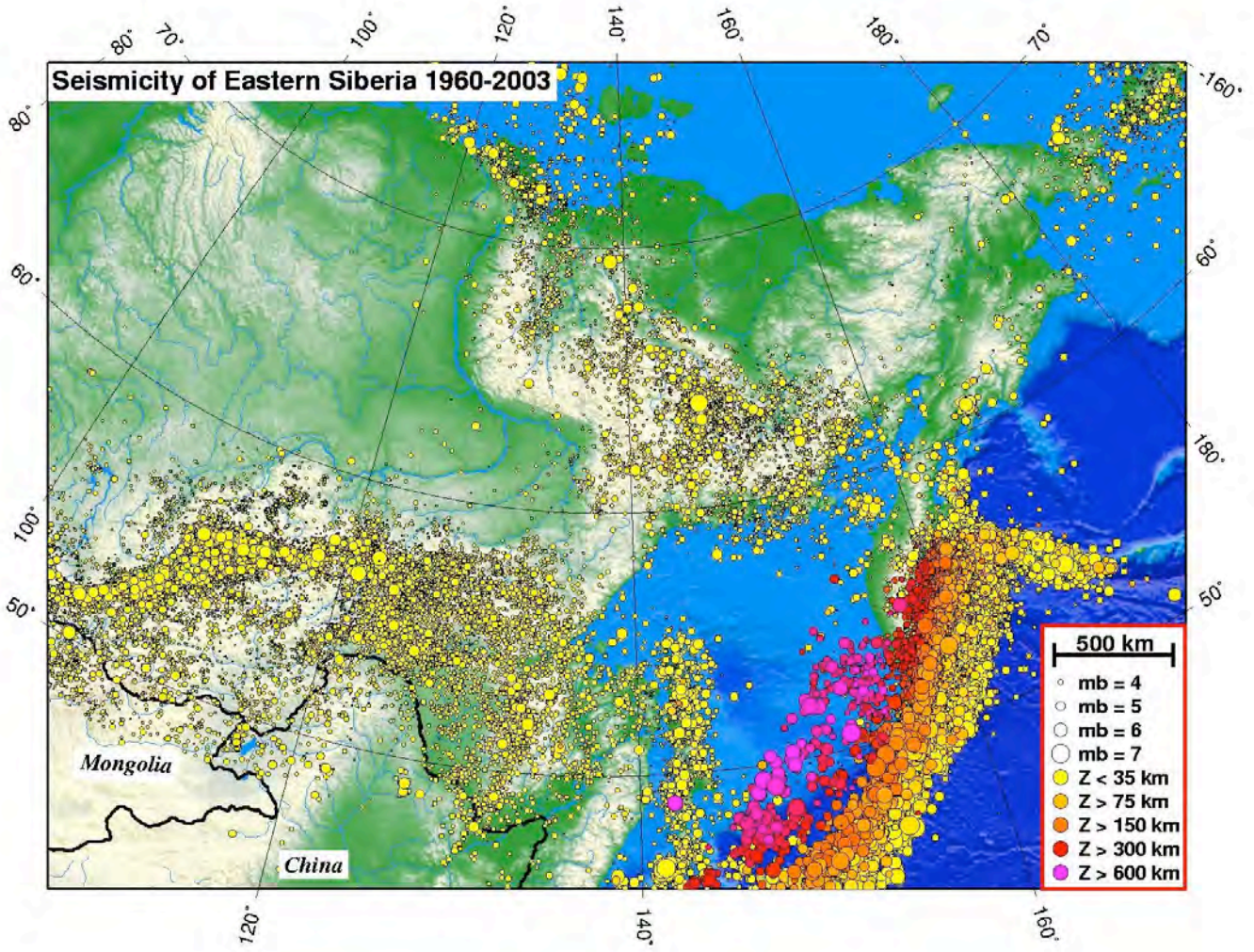


Figure 11. Seismicity map of eastern Russia

REFERENCES CITED

Fujita, K., Mackey, K. G., McCaleb, R. C., Gunbina, L. V., Kovalev, V. N., Imaev, V. S., and Smirnov, V. N., (2002), Seismicity of Chukotka, northeastern Russia: *Geol. Soc. of Amer., Special Paper 360*, 259-272.

Mackey, K. G., Fujita, K., Gunbina, L. V., Kovalev, V. N., Imaev, V. S., Koz'min, B. M., and Imaeva, L. P., (1997), Seismicity of the Bering Strait region: Evidence for a Bering block: *Geology*, 25, 979-982.

Mackey (1999), *Seismological studies in northeast Russia*, Ph.D. Dissertation, Michigan State University, East Lansing, xxiii + 346 pp.

Mackey, K. G., Fujita, K., Hartse, H. E., and Steck, L. K. (2003a), Seismic Regionalization in Eastern Russia, in *25th Seismic Research Review–Nuclear Explosion Monitoring: Building the Knowledge Base*, 1, 73-82.

Mackey, K. G., Fujita, K., Sedov, B.M., Gounbina, L.V., Leyshuk, N., and Kurtkin, S. (2003b), *A Seismic Aftershock Deployment and Analysis of Seismicity of the Neshkan Region, Chukotka, Russia*, NERSP #10, Department of Geological Sciences, Michigan State University, East Lansing, 85 pp.

CAUCASUS SEISMIC INFORMATION NETWORK

Randolph J. Martin[1], Mary L. Krasovec[1], M. Nafi Toksöz[2], H. Sadi Kuleli[2], and Eileen S. Vergino[3]

New England Research[1], Massachusetts Institute of Technology[2], Lawrence Livermore National Laboratory[3]

Sponsored by National Nuclear Security Administration
Office of Nonproliferation Research and Engineering
Office of Defense Nuclear Nonproliferation

Contract No. DE-AC-52-03NA99600[1], NNSA-03-2S[2], W-7405-ENG-48[3]

ABSTRACT

The geology and tectonics of the Caucasus region is highly variable. Generating a structural model and characterizing seismic-wave propagation and attenuation in the region requires data from local seismic networks. Such data were not available until recently due to the absence of dense seismic networks. However, in the last two years the Republic of Georgia, Armenia, and Azerbaijan have installed modern seismic networks with the assistance of the International Science and Technology Center (ISTC).

The Caucasus Seismic Information Network (CauSIN) project is developing a unified, coherent database of the geology and active tectonics of the Caucasus region, and the database includes historical data as well as data from the new networks. This database will be used to obtain a detailed crust/upper mantle structure in the Caucasus, eastern Turkey, and northwestern Iran. Current models have been obtained from long pathways and do not have adequate spatial resolution. Availability of data from more than two-dozen new seismic stations in the region, in conjunction with extensive geophysical data (e.g., surface-seismic reflection profiles, gravity maps, and geological maps) will improve the model resolution and correlation with tectonic units.

Progress to date of the CauSIN project includes the collection of geological, geophysical, and earthquake data that exist at national data centers of participating countries. At a meeting held in May 2004 in Strasbourg, France, participants from Armenia, Azerbaijan, and Georgia agreed on standardized formats for a unified database of the historical and current geological and seismic data. A June 2004 meeting in Vermont addressed issues such as improved seismic-event location, further standardization of formats and techniques, and improved cohesion of the unified database. Preliminary results of these efforts will be presented.

OBJECTIVE

The primary goal of this project is to develop a database of geology and active tectonics in the Caucasus region. Data will include the localized, shallow crustal structure obtained from geophysical surveys for oil exploration.

With this new database, we will be able to improve the identification of earthquake locations and identify potential "ground truth" (GT) events. The dense network, calibration events (mining and quarry blasts), improved models, and better location algorithms (including multiple-event grid search, and double difference) will improve the event locations. Scientists in collaborating countries are eager to assist with this task since improved locations will aid in the identification of active faults.

With the ground truth events serving as validation, we will obtain a detailed crust/upper mantle structure in the Caucasus, eastern Turkey, and northwestern Iran, using data from newly installed seismic stations as well as ground station networks (GSNs) and other stations operated as part of the national networks. The model will incorporate extensive geological and geophysical data (e.g., surface seismic-reflection profiles, and gravity maps) and seismic data.

RESEARCH ACCOMPLISHED

Thus far, our primary effort has been to improve communication between the research groups in the collaborating countries and to collect station and event-epicenter locations for the local networks in the Caucuses region. Figure 1 shows the locations of stations in the local network. The GSN stations are also shown, in blue.

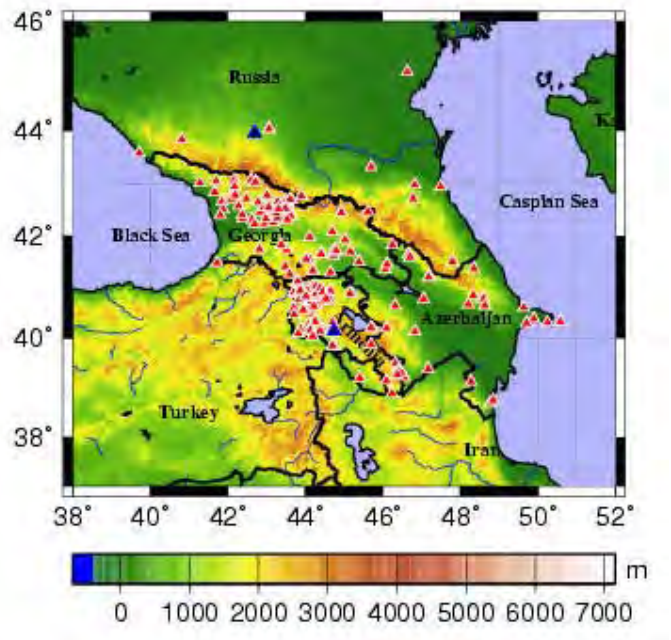


Figure 1. Stations in the local network, shown as red and white triangles. The two blue triangles are GSN stations.

An event database has been compiled at the Institute of Geophysics in Georgia from the event catalogues of Armenia, Azerbaijan, and Georgia. The database includes events dated as far back as 50 AD. A total of 300 events in the database are dated before 1900, which will be helpful in understanding the historical seismicity of the region and characterizing major faults. The database also includes over 25,000 events that occurred between 1900 and 1980. Many of these events have analogue recordings, which have been in storage for years, and some of them have

been lost to water damage and fires. Scientists in Georgia have begun to convert these recordings to digital records before they are irretrievably lost.

Figure 2 shows the seismicity of the study area. This is a subset of the event catalogue and includes only events from 1980 to 1997. Many of these events are digitally recorded, and we have begun to add both strong motion and regional digital records to our database.

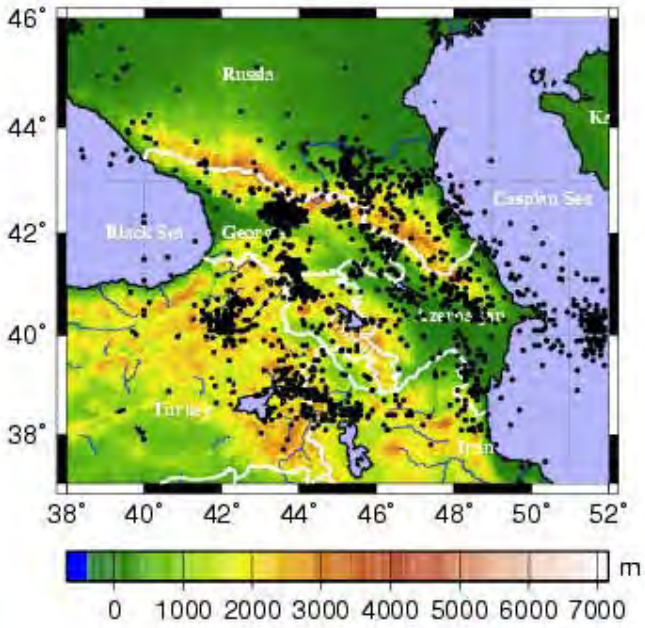


Figure 2. Earthquake epicenters from local stations for events of magnitude 3 or greater and for dates spanning 1980 to 1997.

Meetings held in Strasburg, France, in May 2004and Burlington, Vermont, in June 2004 have yielded agreement as to a common digital data file format, so that in the future data will be easily and quickly available to all collaborators. Figure 3 shows an example of such an opportunity. This record of the M_w = 5 Agri earthquake of July 1, 2004 in eastern Turkey was made at the MDTA station in the Georgian local network.

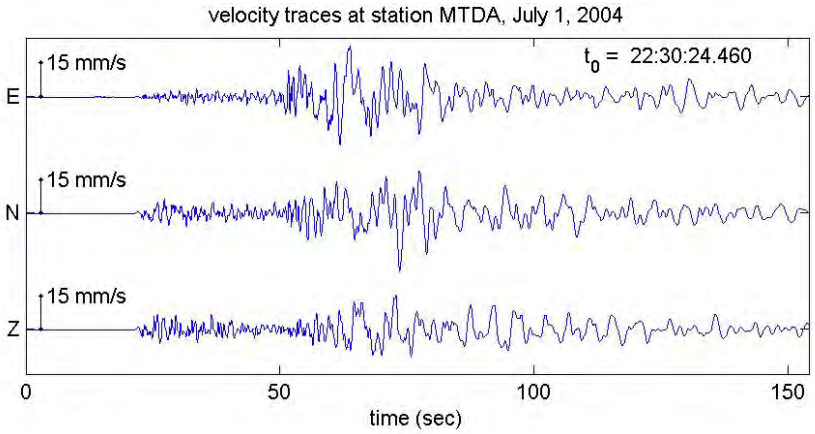


Figure 3. July 1 2004, Agri earthquake recorded at a station in the local network in Georgia.

HISTORICAL PERSPECTIVE

The following summary focuses on several tectonic features and problems of a complex major segment of the Alpine-Himalayan Belt, the segment that extends from the Caucasus and South Caspian Sea southward across the East Anatolian-Iranian Plateau, down into the collision zone with the Arabian plate.

This segment has become of prime political and scientific importance in recent years. Several of its principal features to be discussed are (1) the Bitlis-Zagros suture zone of continental-continental collision between the Arabian and Eurasian plates, (2) some basic problems and tectonics in the Zagros and Caucasus regions, (3) the question of whether subduction is being initiated beneath the South Caspian Basin, (4) some peculiar features of the seismically active Alborz and Talysh mountain belts that appear to wrap around the south and southwest border of the South Caspian Basin, and (5) tectonic implications of seismic-wave attenuation observed in the Turkish-Iranian Plateau.

Included in this summary are published results of our collaboration with Georgian colleagues at the Department of Geology and Paleontology, Tbilisi State University, and the Geological Institute of the Georgian Academy of Sciences.

Continental Collision, the Bitlis-Zagros Suture Zone, and the Zagros:

Figure 4 illustrates a schematic stage of continental collision between the Anatolian microplate and the Arabian and Eurasian plates. This continental collision usually is considered to be one of the youngest on Earth, initiated only 10–12 million years ago (e.g., Sandvol et al., 2003). However, Hempton (1985, 1987) has presented evidence that initial suturing began near the west end of the Bitlis suture (shown in Figure 4) around the mid-to-late Eocene (45–36 million years ago). It pre-dated the opening of the Red Sea and the development of the Dead Sea Transform Fault (DSF in Figure 4). Lateral closure apparently progressed gradually, completing the length of the Bitlis suture (shown in Figure 4) almost 5 million years ago.

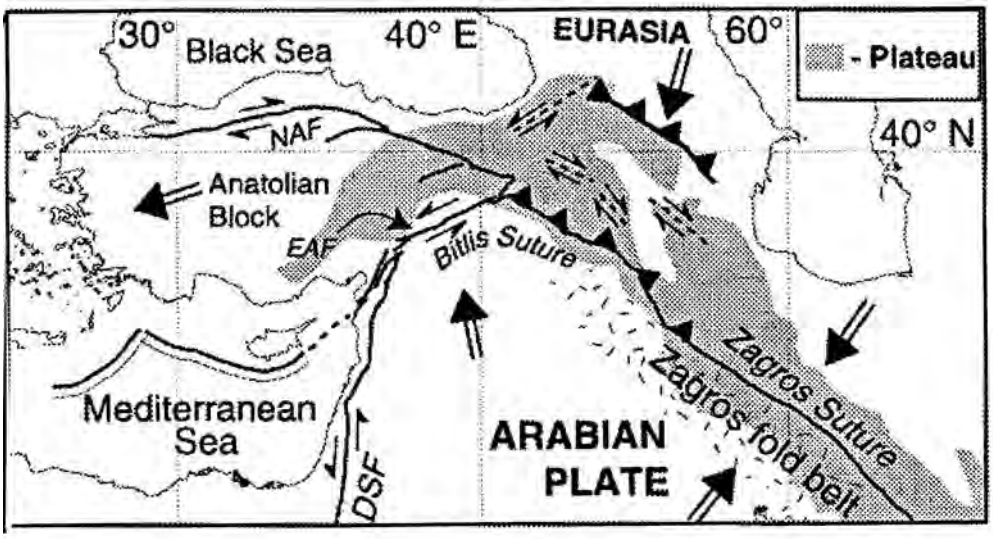


Figure 4. A schematic stage of continental collision between the Anatolian microplate and the Arabian and Eurasian plates.

Dewey et al. (1986) interpreted the East Anatolian plateau as undergoing a thickening to 52 km, which had begun in the Medial Miocene and transmits deformation to surrounding regions, such as the Lesser Caucasus. As will be seen, re-interpretation here is necessary. For example, the modern Caucasus extends east-southeast from the Black Sea to the Caspian Sea (Figure 4). A huge amount of stratigraphic data, mostly not published in the western literature, has been collected in the Caucasus over many years by our Georgian colleagues. These data contain the first stratigraphic evidence of a relatively late stage of Tethys subduction critical for the Caucasus' subsequent growth.

This stage began at the turn between the late Eocene and Oligocene, about 37–38 million years ago, when the single Ocean Tethys was transformed into the enclosed and semi-enclosed sea basins of Paratethys. Shallowing of these basins began gradually. Then, dramatically, a complete inversion of these basins, with the formation of the Greater and Lesser Caucasus, began in late Miocene time, 10–12 million years ago, with inversion proceeding at a higher rate (not less than 1.6 mm/yr average) during Pliocene-Quaternary times. The amount of vertical displacement of relevant key marker beds, measured with respect to their subsidence and uplift, is approximately 10 km (Adamia et al., 2002a, 2002b).

The front of the Zagros fold belt in Figure 4 extends over the Arabian platform. This belt also is considered to be young (Pliocene). Jackson and McKenzie (1984, 1988) and their colleagues (e.g., Berberian, 1995) interpret the Zagros to be an active basement-involved fold-and-thrust belt undergoing possibly 20 mm/yr northeast shortening, modified by local zones of strike-slip faulting, such as the Main Recent Fault located along the northwest portion of the Zagros suture (Figure 4). Many of their well-constrained focal mechanisms are interpreted to occur on reverse with thrust faults dipping 40°–50° NE within the continental basement at 8–12 km depth, and with no hypocenters detected deeper than 20 km. Deformation of the sedimentary cover, ranging in thickness from some 6 to 15 km, appears to be predominantly aseismic above the Lower Cambrian Hormuz salt horizon. Spectacular fold trains are presumably detached from the underlying Hormuz Salt and other salt horizons. Recent balanced cross sections across the Zagros, however, have been interpreted to indicate that the earthquakes described above might be originating in some of the sedimentary strata above the Hormuz (McQuarrie, 2004).

A major problem here is the rarity of exposed thrusts, deep wells, and published seismic sections across the Zagros fold belt. This makes structural and tectonic interpretation difficult (e.g., Blanc et al., 2003). As a result, the correlation of specific earthquakes with specific faults is questionable in most cases (Berberian, 1995). To partially circumvent these difficulties, Berberian has utilized a wealth of supplementary data for many years in his analyses of the Zagros. He and most students of the Zagros identify the Zagros suture in Figure 4 with a major regional fault, the Main Zagros Reverse Fault. If this is correct, it supports a Pliocene age for the Zagros. But a potentially critical factor in this case is whether a parallel, complexly deformed belt, the Sanandaj-Sirjan Belt, on the NE side of the designated suture in Figure 4, is an integral part of the Zagros, as maintained by Alavi (1994). If so, then the Zagros suture would lie further NE in Iran, possibly between the Sanandaj-Sirjan belt and the remnants of a parallel interpretive magmatic arc, the Urumiah-Dokhtar Arc, an Andean-type arc of possibly Upper Cretaceous age.

CONCLUSIONS AND RECOMMENDATIONS

Efforts at improving communication and increasing the availability of seismic data among the countries of the Caucuses have met with success. We have begun to build a database, which can be used toward the final goal of improving crustal models of the region.

REFERENCES

Adamia, S. A., V.S. Alphaidze, E.G. Bombolakis, A.O. Chabukiani, S.I. Kuloshvili, G.M. Majsuradze, and R.J. Martin (2002a), “Late Neogene-Quaternary Chronology, Volcanic and Geodynamic Activities of the Caucasus,” in *Proceedings of the XVII Congress of Carpathian-Balkan Geological Association*, Vol. 53 (Special Issue), Bratislava.

Adamia, S. A., E.G. Bombolakis, A. Chabukiani, S. Kuloshivili, R.J. Martin, and L. Tatarashvili (2002b), “Deep Structure and Seismotectonics of the Oil-and-Gas Bearing Regions of Georgia,” *International Conference on Assessment of Seismic Risk in the Oil-Gas Bearing Areas*, Geology Institute of Azerbaijan National Academy of Sciences and United Institute of Earth Physics of Russian Academy of Science, Baku (Oct. 28–30, 2002).

Alavi, M. (1994), “Tectonics of the Zagros Orogenic Belt of Iran: New Data and Interpretations,” *Tectonophysics* 229, 211–238.

Berberian, M. (1995), "Master 'Blind' Thrust Faults Hidden under the Zagros Folds: Active Basement Tectonics and Surface Morphotectonics," *Tectonophysics* 241, 193–224.

Blanc, E. J. P., M.B. Allen, S. Inger, and H. Hassani (2003), "Structural Styles in the Zagros Simple Folded Zone, Iran," *J. Geol. Soc. London* 160, 401–412.

Dewey, J.F., M.R. Hempton, W.S.F. Kidd, F. Saroglu and A.M.C. Sengör (1986), "Shortening of Continental Lithosphere: the Neotectonics of Eastern Anatolia – a Young Collision Zone," in "Collision Tectonics," *Geological Society Special Publication* 19, 3–36.

Hempton, M.R. (1987), "Constraints on Arabian Plate Motion and Extensional History of the Red Sea," *Tectonics*, 6, 687–705.

Hempton, M.R. (1985), "Structure and Deformation History of the Bitlis Suture near Lake Hazar, Southeastern Turkey," *GSA Bulletin* 96, 233–243.

Jackson, J. and D. McKenzie (1988), "The Relationship between Plate Motions and Seismic Moment Tensors, and the Rates of Active Deformation in the Mediterranean and Middle East," *Geophys. Journal* 93, 45–73.

Jackson, J. and D. McKenzie (1984), "Active Tectonics of the Alpine-Himalayan Belt between Western Turkey and Pakistan," *Geophys. J.R. Astr. Soc*. 77, 185–264.

McQuarrie, N. (2004), "Crustal Scale Geometry of the Zagros Fold-Thrust Belt," Iran, *J. Struct. Geol*. 26, 519–535.

Sandvol, E., N. Turkelli, and M. Barazangi: (2003), "The Eastern Turkey Seismic Experiment: the Study of a Young Continent-Continent Collision," *Geophys. Res. Letters* 30, (24), pp. 1-1 and 1-2.

EVOLUTION OF THE REGIONAL CODA METHODOLOGY

Kevin M. Mayeda[1], W. Scott Phillips[2], Luca Malagnini[3], and Douglas S. Dreger[4]

Lawrence Livermore National Laboratory[1], Los Alamos National Laboratory[2],
Istituto Nazionale di Geofisica e Vulcanolgia[3], and University of California at Berkeley[4]

Sponsored by National Nuclear Security Administration
Office of Nonproliferation Research and Engineering
Office of Defense Nuclear Nonproliferation

Contract No. W-7405-ENG-48, W-7405-ENG-36

ABSTRACT

For the past decade, Lawrence Livermore National Laboratory (LLNL) and Los Alamos National Laboratory (LANL), have been developing and testing a stable, regional coda magnitude methodology for the determination of magnitude and yield. The motivation behind this research was to take advantage of the averaging nature of coda waves in support of monitoring small seismic events from a sparse regional seismic network (*e.g.*, International Monitoring System (IMS) network). The methodology as described in Mayeda et al., (2003) has been successfully applied in a variety of tectonic settings where the assumption of a one-dimensional (1-D), radially symmetric path correction was sufficient. In general, this resulted in interstation amplitude scatter that was 3 to 4 times smaller than the traditional approach using direct *S*, *Lg,* and surface waves ($0.02 < f < 8.0$-Hz). However, in more laterally complex regions there is a need to extend this approach to account for smaller-scale 2-D variations in structure, especially at frequencies above ~1 Hz. Recently, Phillips et al., (2003) have applied a 2-D approach to data in central Asia by assuming that the coda-envelope amplitude could be idealized as if it were a direct wave. They performed a tomography to invert for *Q* along the path and through the choice of damping parameter and geometrical spreading, they in effect distributed the attenuation over an area, not unlike what has been previously assumed in the single-scattering model of Aki (1969) where the attenuation is attributed to an ellipsoidal volume.

As a test of the two methods, we chose over 100 well-located earthquakes ($3.5 < Mw < 6.5$) distributed throughout the northern California region recorded on high-quality broadband stations of the Berkeley Digital Seismic Network (BDSN). The complicated tectonics of the region coupled with this high-quality data, provide for an ideal situation to test the two approaches. We found that source spectra derived from the 2-D approach were essentially identical to those from the 1-D approach for frequencies less than ~0.7 Hz; however, for the high frequencies ($0.7 < f < 8.0$-Hz), the 2-D approach resulted in interstation scatter that was generally 30% smaller. Since our main objective is to improve moment-magnitude estimation for small regional events, the 30% improvement is significant in helping to meet the United States (U.S.) monitoring goals.

OBJECTIVES

The purpose of this study is several fold. First and foremost, the accurate determination of M_o, E_R, and derived stress drop is important in understanding the scaling of earthquakes, which is a key component in the estimation of seismic hazards in a region. Second, magnitudes that are presently determined for events in Northern California come in a variety of forms, which include duration magnitudes (M_D), local magnitudes (M_L), and moment magnitude (M_w) for events $M_L > \sim 3.5$. By using the method of Mayeda et al., (2003) a new M_w(coda) scale was developed that is continuously defined for all earthquakes between $\sim 1 < M_w < 7+$. Over the past several years, the empirically derived coda methodology has provided unprecedented stability in source-spectral estimates for earthquakes and underground nuclear explosions (UNE's) recorded at local and regional distances. For example, the coda-derived source spectra have provided the most stable estimates of magnitude and yield for Nevada Test Site (NTS) explosions (*e.g.*, single-station F-values are less than 1.7) and were successfully transported to foreign test sites such as Lop Nor, Novaya Zemlya, and Semipalitinsk. More recently, the methodology has been successfully applied to earthquakes recorded by small local networks in the Eastern Alps (Malagnini et al., 2004), Western Alps (Morasca et al., 2004), as well as the Dead Sea rift in the Middle East (Mayeda et al., 2003). For the broader regions, Eken et al., (2004) found that the standard 1-D path correction of Mayeda et al., (2003) for the region in and around Turkey was valid between 0.02 and 2.0 Hz, but not for higher frequencies. The success of the coda methodology is commonly believed to come from the volume averaging of the coda waves that sample the entire focal sphere and renders them virtually insensitive to any source radiation pattern effect and path heterogeneity (e.g., Aki, 1969; Aki and Chouet, 1975; Rautian and Khalturin, 1978). Both the observational and theoretical studies of the past several decades are reviewed thoroughly by Sato and Fehler (1998). In the current study, we compare performance between coda and direct waves using both 1-D and 2-D formulations for the path effect using the same events and stations. Our final results (source spectra) are validated against ground-truth moment estimates as well as network-averaged direct wave spectra corrected for path and site effects using both 1-D and 2-D path corrections.

RESEARCH ACCOMPLISHED

Our findings are as follows: (1) 2-D path corrections for the direct waves significantly reduces the scatter over 1-D corrections; however, interstation scatter remains large, ranging between ~0.18 and 0.3 for $0.1 < f < 8.0$-Hz; (2) 1-D coda path corrections result in scatter that is roughly 50% smaller than the 2-D direct-wave results; (3) 2-D coda path corrections result in data scatter that is ~10 to 30% smaller than the 1-D coda results.

Geologic Setting and Data

In the simplest terms, Northern California has a pronounced thickening of the crust from west to east, from 25 km on average in the San Francisco region to more than 40 km beneath the Sierra Nevada. Average crustal velocity and near-surface velocity gradients differ significantly between the Coast Ranges and the Sierra Nevada (Dreger and Romanowicz, 1994). The San Joaquin Valley, a sedimentary basin with thicknesses as great as 4 km, produces complicated surface waves. The northern part of the state is influenced by the southern reaches of the Cascade volcanic arc. Observed broadband waveforms (e.g., Dreger and Romanowicz, 1994, and surface wave-group velocity variations (Pasyanos et al., 1996) reflect the geologic complexity.

The U.C. Berkeley moment tensor catalog and broadband waveform dataset is ideal for testing and applying the regional coda envelope method because of the high level of ground truth. Seismic moment tensors have been routinely computed from both complete three-component waveforms, surface wave amplitude, and phase spectra since 1993 (Romanowicz et al., 1993; Pasyanos et al., 1996). These codes are fully automated at the Berkeley Seismological Laboratory (BSL) and have been applied successfully in other regions of the world (e.g., Fukuyama et al., 1998; Fukuyama and Dreger, 2000; Örgülü and Aktar, 2001), and has been tested for near-realtime, continuous operation (Tajima et al., 2002). The complete waveform method has been recently expanded to allow for the investigation of full moment tensors (Dreger et al., 2000), and a double-couple plus isotropic model (e.g., Dreger and Woods, 2002), which is useful for studying volcanic and geothermal-related events as well as man-made explosions. The seismic moment tensors are routinely determined for events with $M_L > \sim 3.4$ ranging in magnitude from M_w 3.5 to 7.0. Currently, the broadband BDSN has expanded to 20 stations providing excellent regional coverage of the distributed seismicity of northern and central California (Figure 1).

We selected 144 events distributed throughout northern California of which approximately 100 of these had moment tensor solutions derived from multiple station inversions ranging between $3.5 < M_w < 6.5$ (see Figure 1). In total, we calibrated 16 BDSN broadband stations in this study, but as will be shown later, we used a subset of these stations to derive the calibration parameters. The point of this was to show the robustness of the calibration procedure and the ease to which calibration parameters could be applied to new stations.

Coda Method

The 1-D coda methodology is described in detail by Mayeda et al., (2003) so we give only a short, qualitative review here. In contrast to direct-wave measurements, the coda method is based upon narrowband amplitude measurements taken simultaneously from the envelope ranging from several tens of seconds up to hours depending on the frequency band and event magnitude (e.g., Mayeda and Walter, 1996). In the simplest terms, a coda envelope amplitude measurement significantly reduces the variance associated with 3-D path heterogeneity, random interference, and source heterogeneity, which strongly affect the direct waves. The codas we use are composed of local *S*-waves, regional L_g, and long-period surface waves. In spite of these various wave types, which travel at different velocities and sample different parts of the focal sphere, our empirically derived corrections produce very stable *S*-wave source spectra from as few as one station.

The coda envelopes for each frequency band can be idealized with the following equation,

$$\mathrm{A_c}(f,t,r) = W_o(f)\cdot S(f)\cdot T(f)\cdot P(r,f)\cdot H(t-t_s)\cdot(t-t_s)^{-\gamma(r)}\exp\left[-b(r)\cdot(t-t_s)\right] \quad , \tag{1}$$

where f is the center frequency, r is the epicentral distance in kilometers, t is the time in seconds from the origin time, t_s is the *S*-wave travel time in seconds, W_o represents the *S*-wave source, S is the site effect, T represents the *S*-to-coda transfer function effect, P includes the distant-dependent effects of geometrical spreading and attenuation, H is the Heaviside step function, $\gamma(r)$ and $b(r)$ are the distance-dependent coda shape factors that controls the coda envelope shape. For simplicity, we have set $\gamma = 0.2$ noting that this parameter only controls the early part of the coda immediately following the direct arrival which is more influenced by source radiation pattern. Because we are fitting the coda over large amounts of time, the exponential term $b(r)$ is the most important parameter because it controls the majority of the coda envelope shape. However, for the purpose of generating synthetics we set *W, S, T,* and *P* to unity. Following the methodology outlined in Mayeda et al., (2003), the coda shape parameters and velocity of the peak S/L_g-wave arrival were fit as a function of distance using the form of a hyperbola.

1-D Coda Path Corrections

In the following, we briefly review how we derived 1-D path corrections. For each narrowband envelope in our dataset, raw coda amplitudes were determined by generating synthetics at the appropriate distance and using a source of unity then DC shifting using an L-1 norm to fit the observed envelope. The amount of the DC shift is the nondimensional raw coda amplitude. Next, we use the following empirical equation for the coda path correction of Mayeda et al., (2003).

$$P(r,f) = \left[1 + \left(\frac{r}{p_2}\right)^{p_1}\right]^{-1} \tag{2}$$

We used common recordings using 6 station pairs and then grid-searched over p_1 and p_2 and tabulated the interstation scatter for each frequency band. The 6 pairs were chosen such that there was good geographic sampling and are shown in Figure 1. The choice of a frequency-dependent path correction for the entire region was based upon the path parameters p_1 and p_2 that gave the lowest average interstation standard deviation between our six station pairs. To test the robustness of the method, we compared path parameters using completely different station combinations, and the results were virtually unchanged. With path parameters determined, we can transform our synthetics to path-corrected envelopes. Finally, we applied the path corrections to all the data, including the other 10 stations that were not part of the path-calibration procedure. In the following, we consider the direct waves so that we can compare directly, one-to-one, the coda results.

1-D Direct Waves Path Corrections

For every coda amplitude that was measured, we also measured the corresponding peak amplitude of the direct wave (e.g., *S*, L_g or surface waves). As done previously with the coda, we applied a grid search using the same events and stations to estimate the best value of *Q* using the formulation of Street *et al*., (1975), where the direct wave amplitude at distance *r* and frequency *f* is,

if $r < r_c$

$$A(r,f) = A_0 \cdot S(f) \cdot \frac{1}{r} \cdot e^{-\left[\frac{\pi f}{\beta Q_\beta}\right]}$$

and if $r \geq r_c$

$$A(r,f) = A_0 \cdot S(f) \cdot \frac{1}{r_c} \cdot \left(\frac{r_c}{r}\right)^{\gamma} \cdot e^{-\left[\frac{\pi f}{\beta Q_\beta}\right]} \quad (3)$$

where A_0 is the source term, *S* is the site effect, r_c is the critical distance (fixed at 100 km), γ is the spreading coefficient (set to 0.5), β is the *S*-wave velocity, and Q_β is the *S*-wave quality factor. We chose this formulation because it accounts for both local *S*-wave geometrical spreading, ($1/r$) at distances less than r_c, and transitions smoothly to L_g spreading, ($1/r^{0.5}$) when *r* is greater than r_c. We then solved for the best value of *Q* that minimized the scatter between the same six station pairs that were used for the coda path corrections. The averaged *Q* follows the form, $Q(f) = 90 f^{0.64}$ for frequencies between 0.3 and 8.0 Hz. As found with the coda, a different choice of station pairs had little to no effect on the resulting *Q* values.

2-D Direct and Coda Path Corrections

For both the direct waves and coda waves, we assumed the same formulation as that shown in Equation 3. However, for the case of the coda, we set the geometrical spreading parameter to 0 and just inverted for $1/Q$ only. The inversion we chose is a least-squares algorithm (LSQR) that inverts for $1/Q$ using a grid size of 0.1 degree. As done previously, we performed a tomography to invert for $1/Q$ along the path and through the choice of damping parameter and geometrical spreading, and in effect distributed the attenuation over an area, not unlike what has been previously assumed in the single-scattering model of Aki (1969) where the attenuation is attributed to an ellipsoidal volume. Figure 2a and 2b show maps of *Q* for both direct waves and coda for the case of 3.0–4.0 Hz. Notice that the two figures are remarkably similar even though the wave types are completely different. In general, comparisons with other frequency bands were similar, all showing higher *Q* in the Sierra Nevada and lower *Q* in the Cascade ranges extending down into the Franciscan formation, including the Geysers geothermal field.

Comparison Between Coda and Direct Waves

For frequencies ranging between 0.1 and 8.0 Hz, Figure 3 summarizes the average interstation standard deviation derived from up to 45 station pairs for distance-corrected coda and direct waves. In general, the average interstation standard deviation for all measures (e.g., 1-D *S*-wave, 2-D *S*-wave, 1-D coda, 2-D coda) increases with increasing frequency. First, we observe that the 2-D path corrections for the direct waves significantly reduce the scatter over 1-D corrections; however, the interstation scatter remains large, ranging between ~0.18 and 0.3. Second, the 1-D coda path corrections result in scatter that is roughly 50% smaller than the 2-D direct wave results, generally less than 0.15 for frequencies less than 2.0 Hz, similar to results in Turkey from Eken et al., (2004). Third, 2-D coda path corrections result in data scatter that is ~10% to 30% smaller than the 1-D coda results.

Although the coda amplitudes are corrected for frequency-dependent path effects, they still carry the *S*-to-coda transfer function as well as site effects and must be removed in order to obtain a moment-rate spectrum that has absolute units (*e.g.*, newton-meter). We note that the *S*-to-coda transfer function is likely not station dependent and is therefore assumed to be common to all events in this region. Practically speaking, however, we have no way of differentiating this effect from the station site effect. Therefore we simply lump $S(f)$ and $T(f)$ together and call it the "moment-rate" correction term. We used the moment calibration and empirical Green's function procedure outlined in Mayeda et al. (2003), which uses a handful of independently derived seismic moments to tie the low-frequency (*f*

< ~1.0 Hz) coda amplitudes to an absolute scale and smaller events as empirical Green's functions to derive corrections for the higher frequencies (f > ~1.0 Hz). In our case, we chose 10 events from the BSL's moment-tensor catalog with magnitudes ranging between M_W 3.6 to 5.5. Assuming that the smallest of our calibration events has a corner frequency around 1 Hz, we can find the frequency-dependent corrections that, in a least-squares sense, match our 10 independent moments, thereby giving us the corrections between $0.05 \leq f \leq 1.0$ Hz. For frequencies above 1 Hz we use small empirical Green's function events noting that the these events are around M_W ~2 to 2.5 based on their 1-Hz amplitudes, and we assume that on average, these small events have flat-source spectra of at least up to 8.0 Hz, the highest frequency that we are considering. The procedure to derive moment-rate corrections was done station-by-station. Using the average of the two lowest frequency values, we computed M_W from the coda-derived spectra. The same procedure was applied to the direct-wave amplitudes to correct for the site effect. We find excellent agreement between our coda-derived moment magnitudes and the BSL's. Figure 4a shows an example of 1-D, coda-derived source spectra for the M_W 5.3 Napa earthquake of September 3, 2000, and Figure 4b shows the corresponding *S*-wave source spectra using all 16 stations. (We note that the 2-D coda results exhibit a tighter distribution especially at frequencies above 2.0 Hz). Though more scattered, the average of the direct wave spectra is very similar to the individual coda spectra, thus proving the point that a single-station coda spectra is roughly equivalent to a 9-station average using direct waves. The stability of the coda-derived spectra is remarkable, considering that they are derived from different azimuths and distances, mixing local *S*-wave, regional L_g, and surface wave codas.

CONCLUSIONS

As a test of the two methods, we chosen over 140 well-located earthquakes ($3.5 < Mw < 6.5$) distributed throughout the northern California region recorded on high-quality broadband stations of the Berkeley Digital Seismic Network (BDSN). The complicated tectonics of the region coupled with these high-quality data, provides for an ideal situation to test the two approaches. We found that source spectra derived from the 2-D approach were essentially identical to those from the 1-D approach for frequencies less than ~0.7-Hz; however, for the high frequencies ($0.7 < f < 8.0$ Hz), the 2-D approach resulted in interstation scatter that was generally 30% smaller. Because our main objective is to improve moment-magnitude estimation for small regional events, the 30% improvement is significant in helping to meet the U.S.'s monitoring goals. Our findings are as follows: (1) 2-D path corrections for the direct waves significantly reduce the scatter over 1-D corrections; however, interstation scatter remains large, ranging between ~0.2 and 0.3 for $0.05 < f < 8.0$-Hz; (2) 1-D coda path corrections result in scatter that is roughly 50% smaller than the 2-D direct wave results; (3) 2-D coda path corrections result in data scatter that is ~10 to 30% smaller than the 1-D coda results.

REFERENCES

Aki, K. (1969), Analysis of Seismic Coda of Local Earthquakes as Scattered Waves, *J. Geophys. Res*., 74, 615-631.

Aki, K. and B. Chouet (1975), Origin of Coda Waves: Source, Attenuation and Scattering Effects, *J. Geophys. Res*. 80, 3322-3342.

Dreger, D. S. and D. V. Helmberger (1993), Determination of Source Parameters at Regional Distances with Single Station or Sparse Network Data, *J. Geophys. Res*. 98, 8107-8125.

Dreger, D. and B. Romanowicz (1994), Source Characteristics of Events in the San Francisco Bay Region, *USGS Open-file report, 94-176*, 301-309.

Dreger D. and B. Woods (2002), Regional Distance Seismic Moment Tensors of Nuclear Explosions, *Tectonophysics*, in press.

Dreger, D. S., D. Oglesby, R. Harris, N. Ratchkovski, and R. Hansen (2003), Kinematic and Dynamic Rupture Models of the November 3, 2002 *M*w7.9 Denali, Alaska Earthquake, submitted to *Geophys. Res. Lett*.

Eken, T., K. Mayeda, A. Hofstetter, R. Gök, G. Örgülü and N. Turkelli (2004), An Application of the Coda Methodology for Moment-rate Spectra Using Broadband Stations in Turkey, *Geophys. Res. Lett*. 31.

Fukuyama, E., M. Ishida, D. Dreger, and H. Kawai (1998), Automated Seismic Moment Tensor Determination by Using on-line Broadband Seismic Waveforms, *Jishin, 51*, 149-156.

Fukuyama, E. and D. Dreger (2000), Performance Test of an Automated Moment Tensor Determination System, *Earth Planets Space, 52*, 383-392.

Kaverina, A., D. Dreger, and E. Price (2002), The Combined Inversion of Seismic and Geodetic Data for the Source Process of the 16 October 1999 Mw 7.1 Hector Mine, California, Earthquake, *Bull. Seism. Soc. Am.* 92, 1266-1280.

Malagnini, L., K. Mayeda, A. Akinci, and P.L. Bragato (2004), Estimating Absolute Site Effects, *Bull. Seismol. Soc. Am*., in press.

Mayeda, K., A. Hofstetter J. L. O'Boyle, and W. R Walter (2003), Stable and Transportable Regional Magnitudes Based on Coda-derived Moment-rate Spectra. *Bull. Seismol. Soc. Am.,* 93, 224-239.

Mayeda, K. and W.R. Walter (1996), Moment, Energy, Stress Drop, and Source Spectra of Western United States Earthquakes from Regional Coda Envelopes. *J. Geophys. Res.* 101, 11, 195-11,208.

Morasca, P., L. Malagnini, A. Akinci, and D. Spallarossa (2004), Ground-motion Scaling in the Western Alps. *Bull. Seism. Soc. Am. (submitted)*.

Örgülü, G., and M. Aktar (2001), Regional Moment Tensor Inversion for Strong Aftershocks of the August 17, 1999 Izmit Earthquake (MW-7.4), *Geophys. Res. Lett*., 28, 371-374.

Pasyanos, M. E., D. S. Dreger, and B. Romanowicz (1996), Towards Real-Time Determination of Regional Moment Tensors, Bull. Seism. Soc. Am., 86, 1255-1269.

Rautian, T. G. and V. I. Khalturin (1978), The Use of the Coda for the Determination of the Earthquake Source Spectra, *Bull. Seism. Soc. Am*. 68, 923-948.

Romanowicz, B., M. Pasyanos, D. Dreger, and R. Uhrhammer (1993), Monitoring of Strain Release in Central and Northern California Using Broadband Data, *Geophys. Res. Lett. 20*, 1643-1646.

Sato, H. and Fehler (1998), M, Seismic Wave Propagation and Scattering in the Heterogeneous Earth. *AIP Press, Modern Acoustic and Signal Processing*.

Street, R. L., R. Herrmann, and O. Nuttli (1975), Spectral Characteristics of the Lg Wave Generated by Central United States Earthquakes, *Geophys. J. R. Astr. Soc.,* 41, 51-63.

Tajima, F., C. Mégnin, D. Dreger, and B. Romanowicz (2002), Feasibility of Real-time Broadband Waveform Inversion for Simultaneous Moment tensor and Centroid Location Determination, *BSSA, 92, 739-750*.

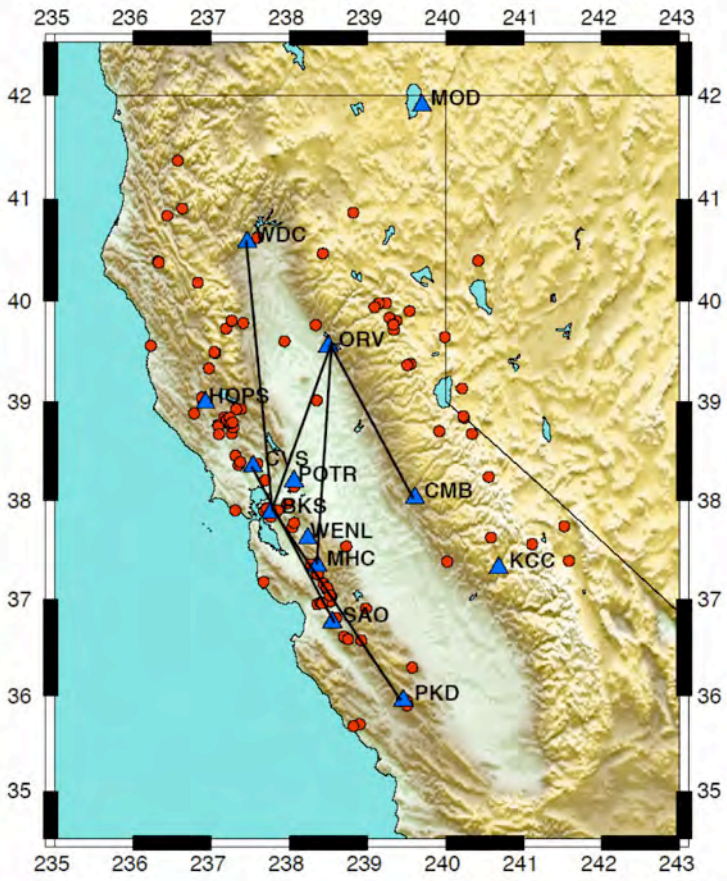


Figure 1 Map of events and stations used in this study. Lines show station pairs that were used in the 1-D coda and 1-D direct wave path corrections.

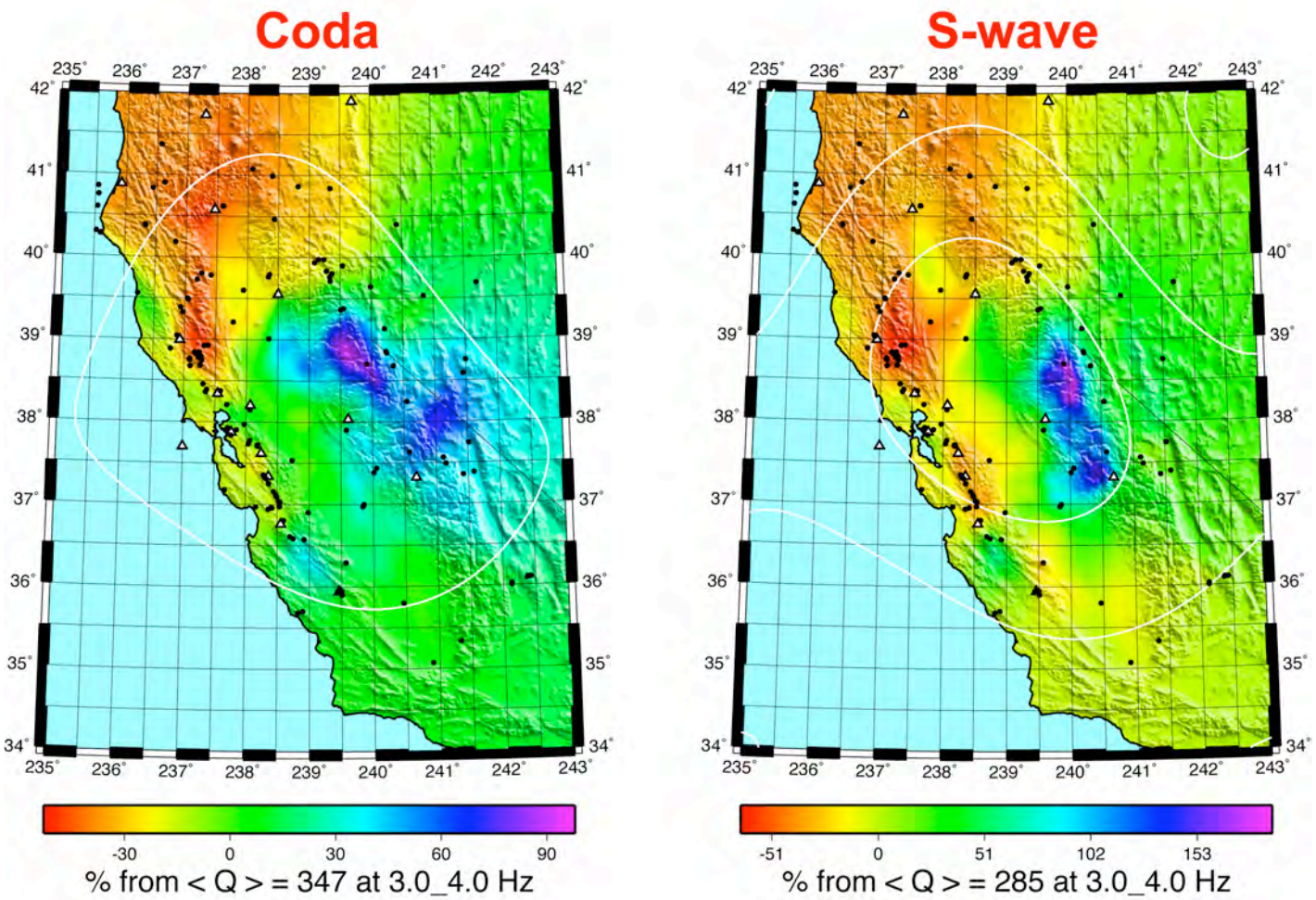


Figure 2 Maps of Q from coda wave and S-wave inversion using the same station and event distribution.

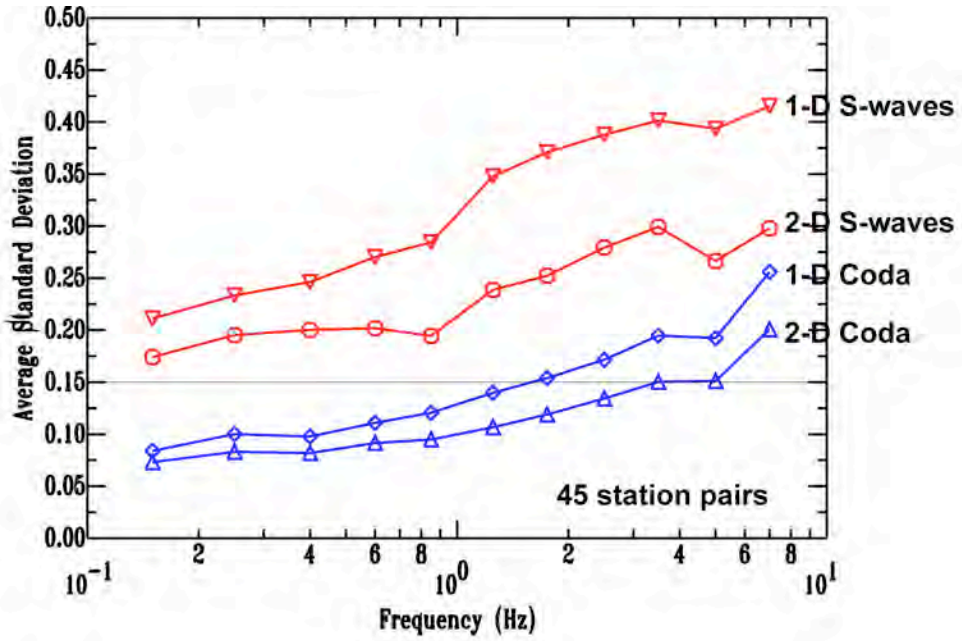


Figure 3 Average interstation data standard deviation for all four methods using the same events and stations. Notice that even the 1-D coda is far better than a 2-D inversion using direct waves. The 2-D coda allows for even more improvement by up to 30%.

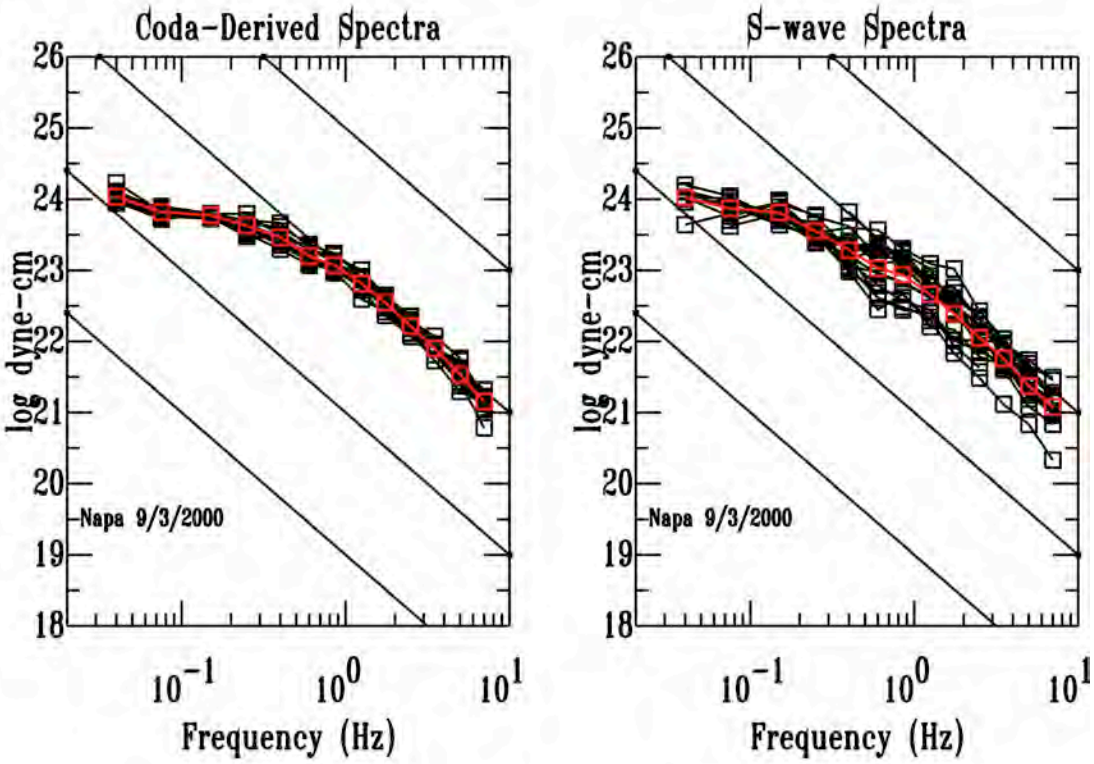


Figure 4 Moment-rate spectra for the September 3, 2000 Napa earthquake using 1-D coda and 1-D direct waves. Notice that a single coda-derived spectra is nearly equivalent to the average direct wave spectra.

NUCLEAR-EXPLOSION PROFILES FOR SEISMIC CALIBRATION OF NORTHERN EURASIA

Igor B. Morozov[1, 2], Elena Morozova[2], and Scott B. Smithson[2]

University of Saskatchewan[1, 2], University of Wyoming[2]

Sponsored by Air Force Research Laboratory

Contract No. DTRA01-01-C-0081

ABSTRACT

In a four-year project sponsored by the Air Force Research Laboratory (AFRL) (75% of funding) and the National Science Foundation (NSF) (25%), the University of Wyoming and Center GEON (Moscow, Russia) are collaborating on restoration, digitizing, and delivery to Incorporated Research Institutes in Seismology (IRIS) and AFRL several long-range Deep Seismic Sounding (DSS) profiles. These datasets include nine major Soviet DSS projects using 22 Peaceful Nuclear Explosions (PNEs), and several hundred of chemical explosions. Data acquisition was performed by Center GEON (the Special Geophysical Expedition at the time) using ~400 specially designed three-component instruments recording on analogue magnetic tapes. These records are being digitized at GEON, verified, edited, and transformed into standard formats at the University of Wyoming, and delivered to seismological data repositories on compact disks (CDs).

PNE profiles recorded between the early 1970's and late 1980's represent sources of seismological and calibration information unparalleled anywhere in the world. Two to four reversed PNEs and several dozens of chemical explosions were recorded at 10-20-km spacing in each 2,000-3,800-km long profiles that formed a regular grid covering most of the former Union of Soviet Socialist Republic (USSR). Long listening times (up to ~600 sec after the first arrivals) allowed recording of the secondary phases (*S*, *Lg*, *Pg*, *Rg*) that are critical for nuclear test monitoring. The energies of the PNEs (7-22 kton, resulting in m_b >5) were sufficient for reliable recordings beyond 3,000-4,000 km. Interpretations of the data from these projects inspired most of the recent high-resolution models of the uppermost mantle, and are still being actively discussed at present.

To date, digital seismic records from projects QUARTZ, CRATON, RIFT, KIMBERLITE, RUBY, and AGATE were delivered to IRIS and AFRL. Profiles BATHOLITH, BAZALT, and METEORITE are currently being processed and will be delivered next year. When this work is completed, most of recoverable data from the PNE projects will be preserved and made available to the nuclear test monitoring, as well as the broader seismological communities.

OBJECTIVES

From the 1970's to the late 80's, Russian scientists acquired a network of dense, linear, long-range, three-component Deep Seismic Sounding (DSS) profiles using conventional and Peaceful Nuclear Explosions (PNEs) over a large territory of Northern Eurasia. These historic datasets, and in particular, their unique PNE components, provide unique opportunities to calibrate existing seismic nuclear discrimination techniques by studying regional wave propagation through complex lithospheric structures.

The objective of this research is to complete digitization, verify, edit and make broadly available through IRIS the key part of the collection of DSS PNE datasets currently stored at Center GEON. The data from nine major projects including 22 PNEs will be processed and transferred to IRIS over the four years of this research (Figure 1). As a result of this effort, we will deliver to the seismic monitoring, and also to the broad seismological community, a set of unparalleled recordings of a large number of nuclear explosions recorded across a variety of propagation paths to the distances of ~3000 km in Northern Eurasia.

RESEARCH ACCOMPLISHED

DSS PNE data have been widely recognized as an unparalleled source of seismic information about the detailed structure of the upper mantle down to 400- to 800-km depth and even to the Earth's core that is practically impossible to obtain by other means. The core PNE data sets of the DSS program cover an intermediate distance range between 0 – 3200 km bridging the gap between conventional controlled source, earthquake, and nuclear–

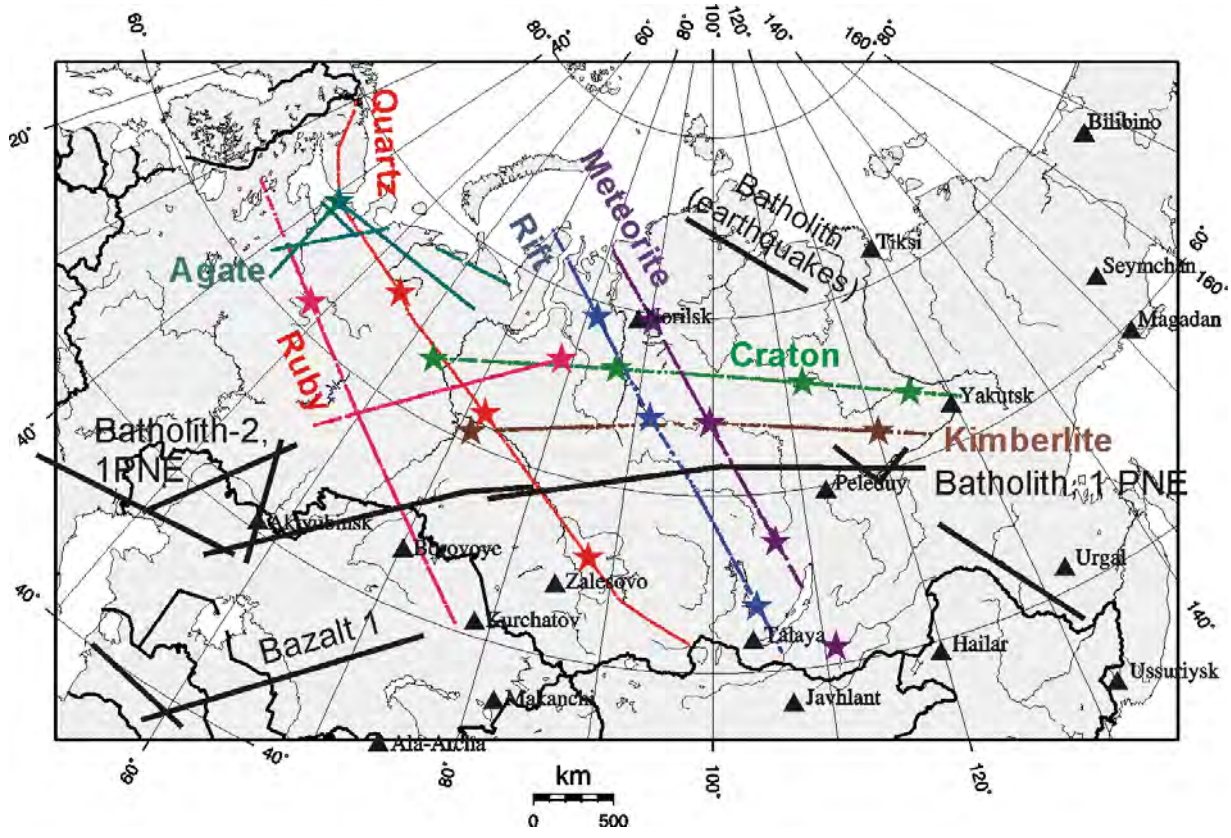


Figure 1 Nine DSS PNE projects of this project. Colored lines show the profiles that were delivered to IRIS and AFRL. Large stars are the PNEs, small triangles are recording sites. Black lines indicate the approximate locations of the profiles that will be delivered in 2004-2005. Note the extent of systematic, continuous profiling, with PNEs detonated at the nodes of a 2-D recording grid. Note that the profiles cover a vast aseismic area that would be difficult to calibrate by other means. IMS stations are also shown (black triangles).

explosion-monitoring seismology (Figure 1). The dense, linear systems of PNEs and chemical explosions allow determination of unusually detailed models of the crust and uppermost mantle over 4000-km long geotraverses. These datasets provide virtually the only dense three-component recordings of regional phases in aseismic regions of Northern Eurasia.

Analogue data are stored on magnetic tapes and digitized at Center GEON, Moscow (Figures 2 and 3), and pre-processed and edited at the University of Wyoming. PNE yields were 7 – 23 kton, providing reliable seismic recording throughout the full recording ranges (Figure 1). Continuous and often reversed PNE recordings allow observations of seismic phases diving to depths of ~800 km (e.g., Egorkin et al, 1987; Ryaboy, 1989; Kozlovsky, 1990; Morozova et al., 1999). On a typical PNE profile, 3 – 4 nuclear explosions were recorded at up to 400 three-component seismograph stations with a nominal spacing of 10 to 15 km. About 50 – 80 chemical explosions (typically, each 3000 – 5000 kg) per profile were also recorded to enable interpretation of crustal and uppermost mantle structures. The locations, depths, yields, and times of the PNEs, and characterizations of the source conditions were recently reported by Sultanov et al. (1999).

DSS profiles cross a variety of contrasting tectonic structures in Northern Eurasia and their analysis has resulted in detailed images of the crust and uppermost mantle (Yegorkin, 1992). Some of the recent interpretations were performed by Egorkin and Mikhaltsev (1990), Mechie et al. (1993, 1997), Cipar et al. (1993), Priestley et al., (1994), Ryberg et. al. (1995, 1996), Schueller et al., (1997), Lorenz et al. (1997), Morozov et al. (1998a), and Morozova et al. (1999). The interpretations of the profile QUARTZ (**Figure**) by the University of Wyoming utilized the full spectrum of seismic data, including refractions and reflections from all 51 explosions of the dataset, lithospheric multiples, crustal-guided phases, seismic attenuation (Morozov et al., 1998b), coda amplitude decay (Morozov and



Figure 2. Analogue magnetic tapes from DSS project in GEON's basement in Moscow.



Figure 3. Digitization system for magnetic tapes from portable seismograph "Taiga."

Smithson, 2000), receiver functions (Morozov et al, in press), and empirical travel-time regionalization (Morozov et al., in review). Using travel-time, amplitude, and attenuation data, this study resulted in unusually well constrained images of crustal and mantle heterogeneity (Schueller et al., 1997; Morozov et al. 1998a, 1998b; Morozova et al., 1999).

Without doubt, PNE datasets still remain a source of the most detailed seismic information about the upper mantle (down to ~700 km) that is not likely to be surpassed even by the USArray and its satellite projects in Canada and Europe. As an example, PNE data from profiles QUARTZ and RUBY (Figure 4) served as a basis for a new class of stochastic models of the uppermost mantle (e.g., Ryberg et al., 1995; Enderle et al., 1997), which, however, also resulted in a significant controversy (Morozov et al., 1998a; Morozov, 2001) which is being actively debated at present. The datasets contain spectacular and unusually continuous, 3-component recordings of regional phases (Figure 4), and still hold great potential for nuclear test monitoring research (for more detail, see our reports to previous SRR symposia).

According to the project schedule to date, we have delivered to IRIS digitized seismic data from six profiles: QUARTZ, CRATON, RIFT, KIMBERLITE, RUBY, and AGATE (Figure 1). GEON has also digitized and transferred to the University of Wyoming records from projects BATHOLITH-1, 2, and BAZALT-1 (Table 1). The schedule for further planned data deliveries is given in Table 1.

Table 1. Revised planned and actual data delivery schedule as of September 2003.

#	Data set	Raw data delivery from GEON to UWyo (months)		Edited and reduced data delivered to IRIS DMS (months)	
		planned	*actual*	*planned*	*actual*
1	QUARTZ	-	1995	12/2001	12/2002
2	CRATON	02/2002	10/2002	08/2002	11/2002
3	KIMBERLITE	05/2002	11/2002	11/2002	11/2002,10/2003(chem)
4	RIFT	08/2002	11/2002	05/2003	10/2003
5	RUBY	02/2003	02/2003	10/2003	02/2004
6	AGATE (5 profiles)	08/2003	07/2003	05/2004	06/2004
7	BATHOLITH-1	10/2003	12/2003	11/2004	
8	BATHOLITH-2	03/2004	12/2003	11/2004	
9	BAZALT-1	06/2004	01/2004	06/2005	
10	BAZALT-2	10/2004		06/2005	
11	METEORITE	03/2005*		11/2005	

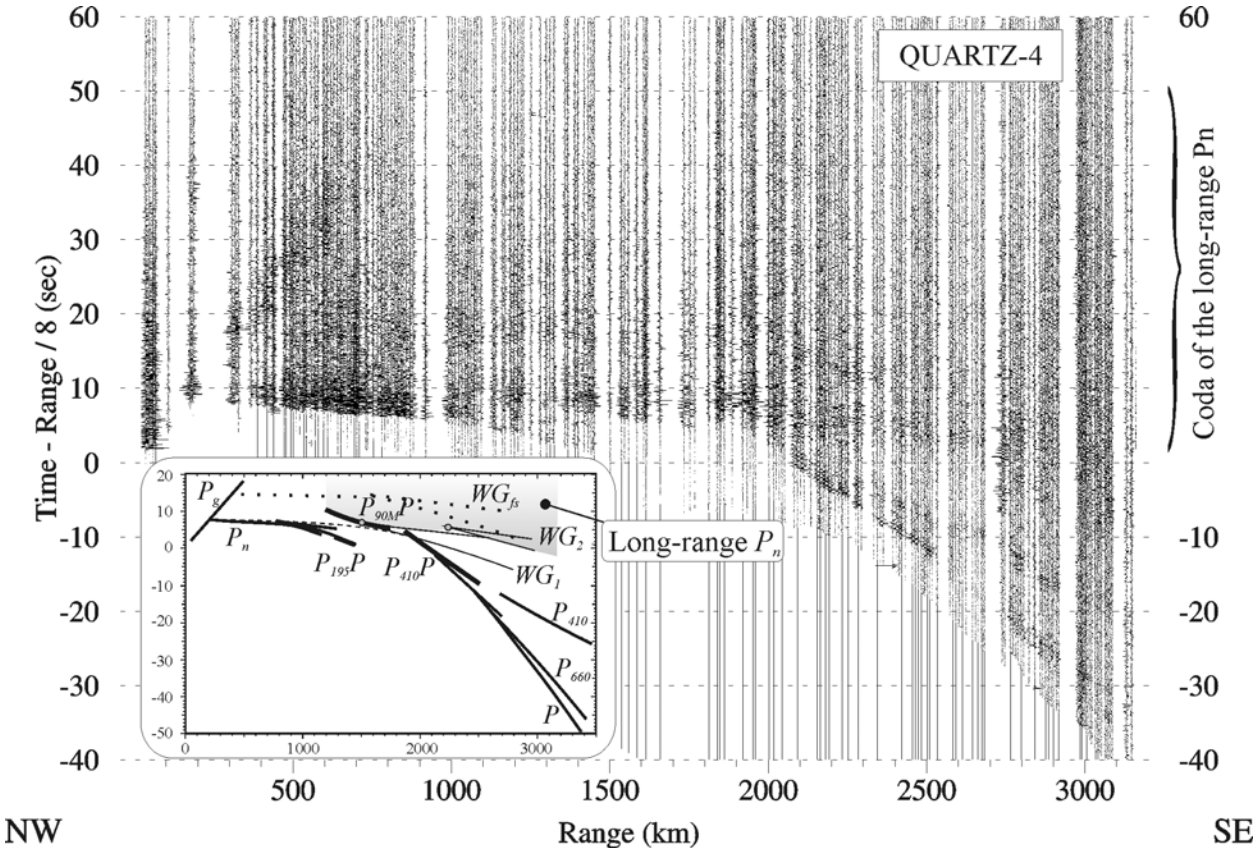


Figure 4. Vertical component record from PNE QUARTZ-4 (at the southeastern end of profile QUARTZ; Figure 1). Inset shows a sketch of seismic phases identified in the wavefield. Note the free-surface and Moho *P*-wave multiples (PP, or whispering-gallery modes) labeled WG_{fs} and WG, respectively. These phases were interpreted as caused by strong scattering within the uppermost mantle (Ryberg et al., 1995); however, in another interpretation, they may be due to a strong velocity gradient and mantle layering beneath the East European platform and the southern part of the West Siberian Basin (Morozov, 2001). Both of these inferences might have significant implications for nuclear test monitoring along the critical NW-SE paths across the East European Platform.

CONCLUSIONS AND RECOMMENDATIONS

Preliminary examination of the newly obtained Russian PNE records from the Siberian DSS PNE profiles demonstrates that the data provide valuable information for the analysis of the propagation of L_g and other regional phases for their use in nuclear test monitoring and calibration studies. When made broadly accessible for nuclear test monitoring research, the datasets will boost research on seismic calibration of the region and on transportable seismic discriminants in Northern Eurasia. Availability of the unique PNE recordings should foster current research on several DoD-sponsored projects and facilitate extension of such research in the future. In addition, from a broader scientific perspective, the digitized DSS recordings and models of the upper mantle could also provide ideal reference and calibration data sets for the detailed structure of the upper mantle, and particularly for USArray.

REFERENCES

Cipar., J., K. F. Priestley, A. V. Egorkin, and N. I. Pavlenkova (1993). The Yamal Peninsula-Lake Baikal deep seismic sounding profile, Geophys. Res. Lett., 20 (15), 1631-1634.

Egorkin, A. V. and A. V. Mikhaltsev (1990). The Results of Seismic Investigations along Geotraverses, in Super-Deep Continental Drilling and Deep Geophysical Sounding, K. Fuchs, Y. A. Kozlovsky, A. I. Krivtsov and M. D. Zoback (Editors), Super-Deep Continental Drilling and Deep Geophysical Sounding, Springer, Berlin, 111-119.

Enderle, U., M. Tittgemeyer, M. Itzin, C. Prodehl, and K. Fuchs (1997). Scales of structure in the lithosphere - Images of processes, Tectonophysics, 275, 165-198.

Kozlovsky, Y. A. (1990). The USSR Integrated Program of Continental Crust Investigations and Studies of the Earth's Deep Structure under the Globus Project, in Super-Deep Continental Drilling and Deep Geophysical Sounding, Fuchs K., Kozlovsky Y. A., Krivtsov A. I. and Zoback M. D. (Editors), Springer, Berlin, 90-103.

Lorenz, F., F. Wenzel, and J. Mechie (1997). Lateral heterogeneity implications from 2-D nuclear-seismic travel-time inversion, in: Fuchs, K. (Ed.) Upper mantle heterogeneities from active and passive seismology, pp. 237-248, Kluwer Academic Publ., Dordrecht.

Mechie, J., A. V. Egorkin, K. Fuchs, T. Ryberg, L. Solodilov, and F. Wenzel (1993). P-wave velocity structure beneath northern Eurasia from long-range recordings along the profile Quartz, Phys. Earth Planet Inter., 79, 269-286.

Mechie, J., A. V. Egorkin, L. Solodilov, K. Fuchs, F. Lorenz, and F. Wenzel (1997). Major features of the mantle velocity structure beneath northern Eurasia from long-range seismic recordings of peaceful nuclear explosions, in: Fuchs, K. (Ed.) Upper mantle heterogeneities from active and passive seismology, pp. 33-50, Kluwer Academic Publ., Dordrecht.

Morozov I. B, E. A. Morozova, S. B. Smithson, P. G. Richards, V. I. Khalturin, A. Stroikova, V. Cormier, and L. N. Solodilov, Regional travel time model of Northern Eurasia using Deep Seismic Sounding data sets, Bull. Seism. Soc. Am, in final preparation.

Morozov, I. B., and S. B. Smithson (2000). Coda of long-range arrivals from nuclear explosions, Bull. Seism. Soc. Am., 90, 929-939.

Morozov, I. B., E. A. Morozova, and S. B. Smithson, (1998a). On the nature of the teleseismic Pn phase observed in the recordings from the ultra-long range profile “Quartz”, Russia, Bull. Seism. Soc. Am, 88 (1), 62-73.

Morozov, I. B., E. A. Morozova, S. B. Smithson, and L. N. Solodilov. (1998b). 2-D image of seismic attenuation beneath the Deep Seismic Sounding profile “Quartz”, Russia, Pure and Applied Geoph., 153, 311-348.

Morozov, I. B., S. B. Smithson, and L. N. Solodilov, Imaging crustal structure along refraction profiles using multicomponent recordings of first-arrival coda, Bull. Seism. Soc. Am., in press.

Morozova, E. A., I. B. Morozov, S. B. Smithson, and L. N Solodilov (1999). Heterogeneity of the uppermost mantle beneath the ultra-long range profile “Quartz,” Russian Eurasia, *J. Geophys. Res.*, 104 (B9), 20,329-20,348.

Priestley, K. F., J. Cipar, A. Egorkin, and N. I. Pavlenkova (1994). Upper-mantle velocity structure beneath the Siberian Platform, Geophysical Journal International, 118 (2), 369-378.

Ryaboy, V. (1989). Upper mantle structure studies by explosion seismology in the USSR, Delphic Associates, 138 pp.

Ryberg, T., F. Wenzel, J. Mechie, A. Egorkin, K. Fuchs, and L. Solodilov (1996). Two-dimensional velocity structure beneath Northern Eurasia derived from the super long-range seismic profile Quartz, Bull. Seismol. Soc. Am., 86, 857-867.

Ryberg, T., K. Fuchs, A. V. Egorkin, and L. Solodilov (1995). Observations of high-frequency teleseismic Pn on the long-range Quartz profile across northern Eurasia, J. Geophys. Res., 100, 18151-18163.

Schueller, W., I. B. Morozov, and S. B. Smithson (1997). Crustal and uppermost mantle velocity structure of northern Eurasia along the profile Quartz, Bull. Seismol. Soc. Am., 87, 414-426.

Sultanov, D. D., J. R. Murphy, and Kh. D. Rubinstein (1999). A seismic source summary for Soviet Peaceful Nuclear Explosions, Bull. Seism. Soc. Am., 89, 640-647.

Yegorkin, A. V. (1992). Crustal structure along seismic geotraverses, International Geology Review, 34 (4), 345-362.

SIMULATION OF REGIONAL EXPLOSION S-PHASES (SIRES) PROJECT

Stephen C. Myers[1], Leiph Preston[2], Jeffrey L. Wagoner[1], Shawn C. Larsen[1], Kenneth D. Smith[2], and William R. Walter[1]

Lawrence Livermore National Laboratory[1], University of Nevada, Reno[2]

Sponsored by National Nuclear Security Administration
Office of Nonproliferation Research and Engineering
Office of Defense Nuclear Nonproliferation

Contract No. W-7405-ENG-48[1] and DE-FC03-02SF22656[2]

ABSTRACT

Generation of S-waves from explosion sources continues to be an intriguing area of seismological research. Empirical studies document a general decrease in regional S-phase amplitudes (compared to P-phases) for explosion sources. Although decreased S-phase amplitude for explosive (compressional) sources is intuitive, a comprehensive physical understanding of the many mechanisms that contribute to S-phase excitation does not currently exist. Despite the success of many regional discriminant and magnitude methods that rely on decreased S-phase amplitude for explosion sources, instances remain where explosions produce anomalous S-phase amplitudes that confound regional methods.

Scattering of the Rg phase is forwarded in several studies as an important mechanism for the generation of explosion S-waves. In this study, we construct a three-dimensional (3D) model of the Nevada Test Site (NTS) and the surrounding region. Extensive databases of geologic information, including existing 3D models developed under past and ongoing NTS programs, are used in the construction of a local model. The detailed local model is merged into a regional model that extends several hundred kilometers from the NTS. In addition to deterministic geologic structure and topography, we introduce stochastic variability along geologic contacts and within geologic units. Model roughness made possible by the stochastic perturbations enhances scattering, allowing realistic simulation of the local and regional wavefield. In this phase of the project, we report on version 1 of the NTS model and on preliminary validation tests. Validation simulations use E3D, a fully elastic, finite-difference computer code. This code allows us to introduce 3D topographic effects, as well as 3D geologic variability. Simulations are compared to recordings of the 1993 Non-Proliferation Experiment (NPE). The validation data set consists of local and regional distance seismograms and provides a rigorous test of the distance and time evolution of the wavefield.

OBJECTIVE

Regional monitoring relies heavily on S-phases. Discriminants commonly use P- and S-wave amplitude ratios (Pomeroy et al., 1982; Walter et al., 1995). Widely used methods of determining magnitude make use of Lg and Lg coda amplitudes (e.g., Nuttli, 1986; Mayeda and Walter, 1996; Patton, 2001), and regional S-phases often add important arrival-time observations to limited, small-magnitude datasets used for location (Mayeda and Walter 1996; Myers et al., 1999).

Most investigators agree that appreciable energy from the explosions is converted to S-waves near the source, but the dominant P-to-S transfer mechanism is not agreed upon. Several physically reasonable transfer mechanisms are proposed, including P-to-S conversion at the free surface, spall, scattering of short-period surface waves, tectonic release, and rock-damage (e.g., Vogfjord, 1997; Day and Mclaughlin, 1991; Gupta et al., 1992; Johnson and Sammis, 2001). Each mechanism fits a subset of observations, and each mechanism, with the exception of surface-wave scattering, is understood from first principles. Currently the Rg-to-S mechanism is represented by an empirical transfer function (e.g., Gupta et al., 1992; Patton, 2001). Notwithstanding the ultimate goal of deriving the transfer function from first principles, application of the empirical transfer function would be bolstered if the Rg-to-S mechanism could be simulated. This study aims to conduct full simulations in realistic geology of the explosion source. The simulations focus near the source to see if Rg is converted to higher-mode S-wave. If Rg-to-S is observed in local simulations, we further characterized the propagation of S-waves to regional distance.

RESEARCH ACCOMPLISHED

NPE Case Study

We fashion seismic simulations around the 1993 NPE (see reference in Denny and Stull, 1994). The NPE was a chemical explosion with nominal yield of 1 kiloton. Knowledge of the source location, origin time, emplacement conditions, and near source geology are unparalleled, providing an excellent data set for modeling.

Geological Modeling

One of this project's goals is to produce a realistic model that can be used in seismic simulations. Because of our focus on the generation of S-waves near the source, we have built a highly accurate, 20 km–20 km–8 km model that is centered on the NPE shot. This local model is imbedded in a 3-D, lithospheric-scale model that extends several hundred kilometers from the NPE. Throughout the model we implement stochastic perturbations of the geologic structure. These perturbations introduce heterogeneity to parts of the model where resolution is limited.

Local Model

A detailed geologic model near the source is needed to produce a realistic simulation of Rg scattering. The local model is based on surface mapping and an extensive borehole database at Lawrence Livermore National Laboratory (LLNL) (Figure 1). The detailed model extends 10 km from the NPE shot and to a depth of 8 km. A digital elevation model (DEM) with 10-m resolution is used in the local model, and the following stratigraphic units are specified: Quaternary alluvium, welded tuff, unwelded tuff, Tertiary volcanics, Mesozoic intrusives, Paleozoic sedimentary and metasedimentary rocks, and upper-crustal crystalline rocks. Each of these stratagraphic units has distinct seismic properties, and significant scattering of seismic waves can occur at the contacts between these units. As an example, we show the top of the Paleozoic (Figure 1), which is constrained by numerous borehole data points. Two other examples are the intrusive granites (Gold Meadows stock and Climax stock; green in Figure 1), which are locally exposed at the surface, penetrated by several boreholes, and further constrained by gravity modeling (Healey and Miller, 1963; USGS OFR, 1983).

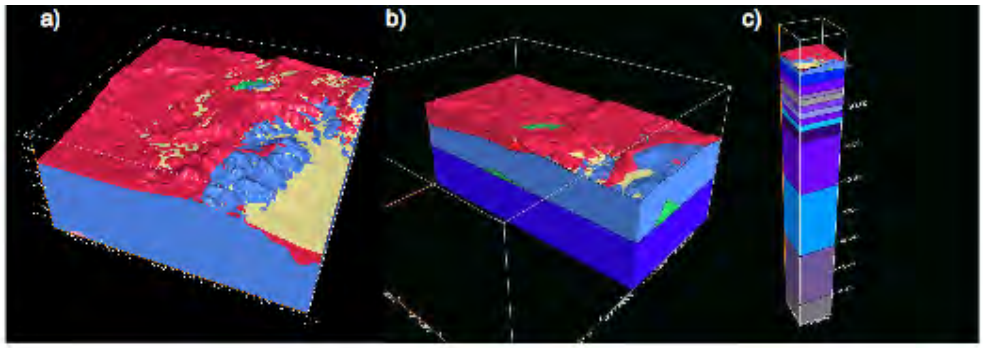


Figure 1. Local model around NPE shot determined from detailed geologic and geophysical studies. a) The entire local model. b) Cross section through the NPE shot. c) Local model merged into a lithospheric velocity stack.

Regional Model

The regional model is based on a slightly modified version of the 1-dimensional Patton and Taylor (1984) model. The Patton and Taylor model is constrained by surface-wave modeling, giving us confidence that our model will predict longer-period seismic data. A minor adjustment in Moho depth (Myers et al., 2003) improves prediction of regional body phase arrival times. We add topography, basin structures, variable Moho depth, and lateral velocity variations to the 1-dimensional model. Figure 2 is an example of the geologic information that we have compiled to constrain the upper crust of the regional model.

Our seismic simulations suggest that topography significantly effects regional wave propagation. We have compiled several DEMs that, taken together, cover our modeling area. Significant effort was required to merge these models into a seamless DEM with 80-m resolution (Figure 2). The high-resolution DEM enables us to push simulations to higher frequency, with confidence that topographic effects are adequately modeled.

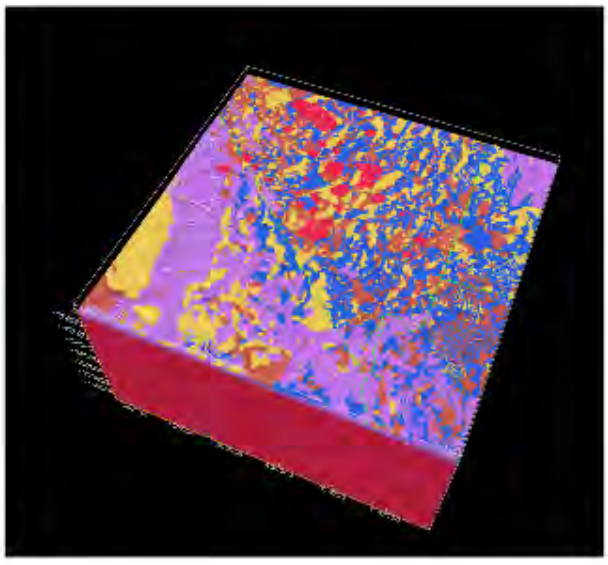


Figure 2. Compilation of geologic information spanning the states of Nevada, California, Utah, and Arizona. The geologic information is used to constrain the upper crust for our geophysical model. In this preliminary compilation, some of the geologic features are not properly merged, causing crystalline units to appear at the surface instead of basins. Reconciliation of these details is required before model finalization.

Inclusion of sedimentary basins in the model is needed if synthetics are to match the coda durations of Pg, Lg, and longer-period surface waves (Preston et al., 2004). Blakely et al. (1999) produced a detailed basement map in the Death Valley region from gravity data and found that large basins may contain numerous hidden sub-basins of varying depth and extent. We adopt Blakely's basin structure for the southwest portion of our model, and we use a simplified methodology to characterize basins elsewhere. Our simple characterization utilizes geologic mapping (Figure 2), mapped faults to bound basin edges, and the relative variations in local gravity data as a proxy for sub-basin structures. Where gravity constraints do not exist, we estimate basin depth based on regional averages.

Lateral variations in model boundaries (e.g. Moho depth) and seismic velocity are based on published studies (http://quake.wr.usgs.gov/research/structure/CrustalStructure/database/index.html). These profiles and point measurements suggest that the depth to Moho within the Basin and range can vary between 28 and 35 km. Our study extends into the Colorado Plateau and Sierra Nevada Mountains, where the crustal thickness exceeds 40 km. These changes in Moho depth focus and defocus energy and cause considerable variability in regional-phase amplitude (Zandt et al., 1995). Bulk seismic properties also vary within the study area (www.quake.wr.usgs.gov/research/structure/CrustStructure/crust), and we include these variations in order to produce the most realistic simulations possible.

Stochastic roughening of boundaries and media
Although we are taking great measures to incorporate as much deterministic structure as possible, it is impossible to construct a model with sufficient detail without a major 3-D imaging campaign. In order to better simulate the earth, we are using geostatistical simulation techniques to perturb geologic boundaries and elastic parameters within geologic units. Statistical characteristics are gleaned from densely sampled data sets, and these characteristics are then used to "roughen" the model in areas with few data constraints.

Figure 3 is an example of a conditional simulation of the upper contact of Paleozoic (Pz) sedimentary rocks near Rainier Mesa. The top of the Pz is one of the first major seismic contrasts encountered by the NPE wavefield. Therefore, proper simulation of this contact is critical for realistic evaluation of seismic scattering. Numerous boreholes and surface exposures define the Pz contact in the southeast portion of the local model. Elsewhere, only the general dip and depth of the Pz contact are constrained. If conventional interpolation is used to construct the Pz surface, then the surface is quite smooth in areas with sparse borehole sampling (Figure 3a,b). Figure 3c,d shows that a more realistic Pz surface can be constructed through conditional simulation. The new surface will scatter high-frequency energy more readily than a smooth surface and may help to explain the frequency dependence of Rg attenuation.

Validation Data

Most of the local and regional recordings of the NPE have been well studied, and these data were bundled soon after the shot. Stations included in the NPE data bundle are shown in Figure 4a and 4b. At distances less than a few kilometers, accelerometers were deployed on the surface and in nearby tunnels, providing important constraints on the early development of the wavefield. Many short period instruments were deployed on the surface within 20 km of the shot. These recordings provide further constraint on the early evolution of the wavefield, particularly the evolution of short-period surface waves. LLNL and the University of Arizona broadband deployments cover near-regional distances (out to ~300 km) with linear arrays towards the northwest and east, respectively. These deployments record the complexity of regional wave propagation from the NPE. A number of permanent stations provide further constrain on regional wave propagation.

The University of Nevada, Reno (UNR) recoded the NPE on nearly 50 stations that extend southwest of Rainier Mesa (Figure 4c). The UNR data set provides unique coverage in the 6 km to ~100 km distance range. This data set was not included in the NPE data bundle, and it has not been widely distributed. Therefore, we briefly describe the waveform characteristics here. The majority of the instruments deployed were short-period, 3-component seismometers (Geotech S-13), and a limited number of broadband instruments were deployed in Death Valley. Most records closer than 16km were clipped, but the previously discussed recordings (from the data bundle) cover that distance range. The UNR recordings contain significant Sg energy between 20 km and 95 km (Figure 5). The distinct Sg energy is consistent with previous observations that suggest generation of S-energy soon after the shot.

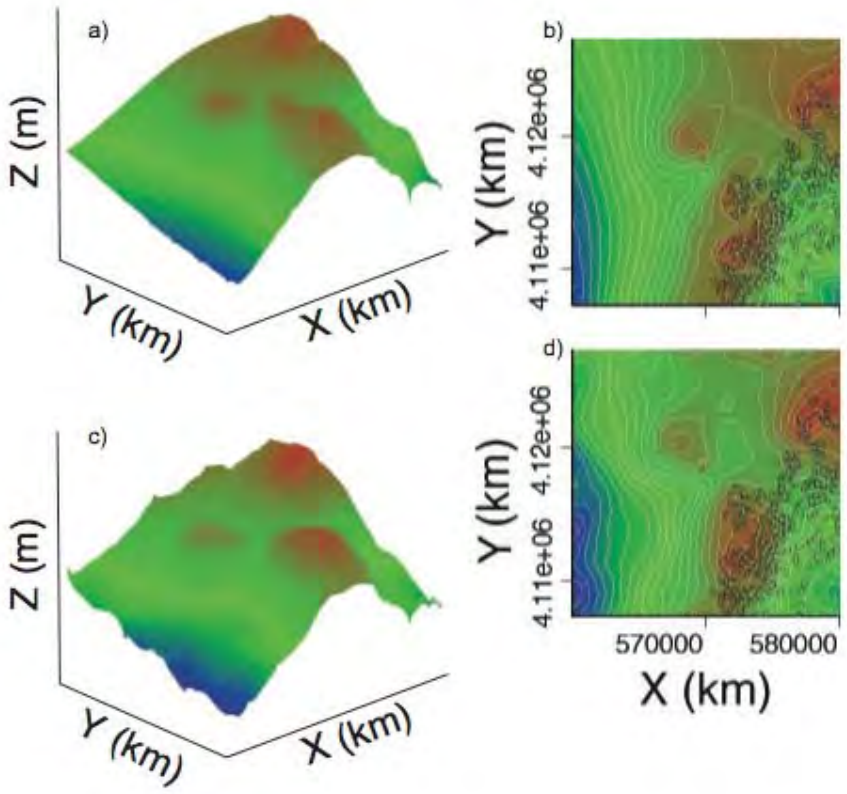


Figure 3. Conditional simulation of the upper contact for Paleozoic (Pz) rocks. a) Surface determined using borehole data, which are concentrated in the southeast portion of the model area, and a simple interpolation algorithm. b) plan view of a) showing borehole data (circles colored in accordance with borehole observation). Note the difference in the roughness of the surface between areas with and without borehole data. c) Conditional simulation of upper Pz surface using statistical characterization of surface roughness and constraints from borehole observations. d) Plan view of c) showing borehole observations and consistent surface roughness in areas with and without observations.

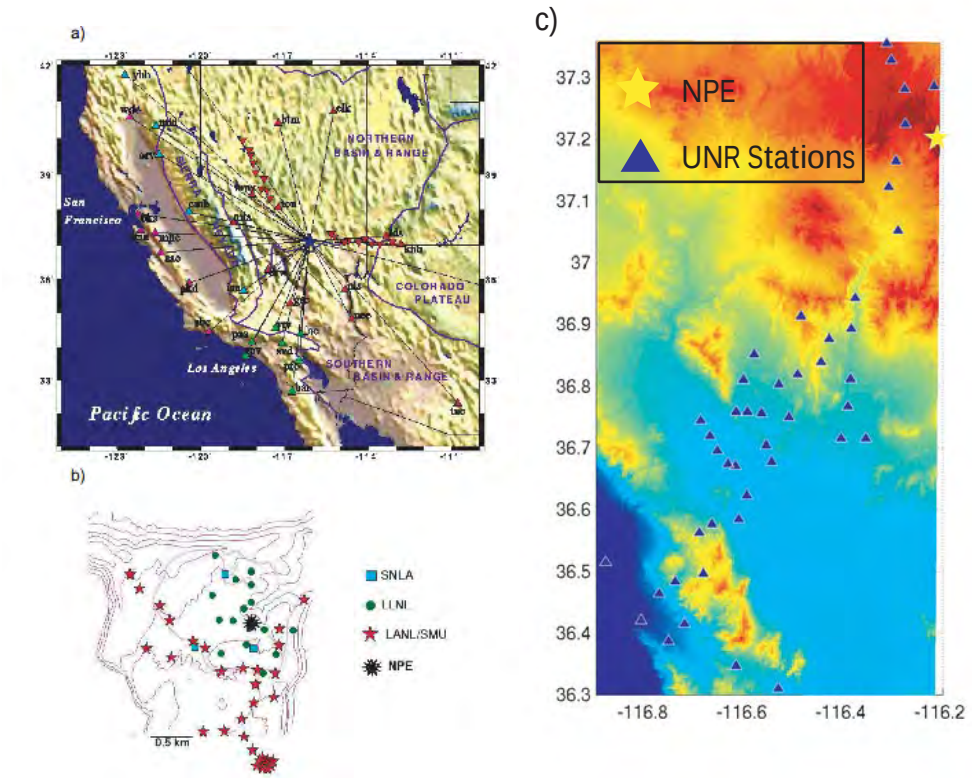


Figure 4. a) Regional and b) local networks recording the NPE shot. c) UNR stations provide unique distance and azimuth coverage. The local and regional recordings of the NPE provide validation data for simulations.

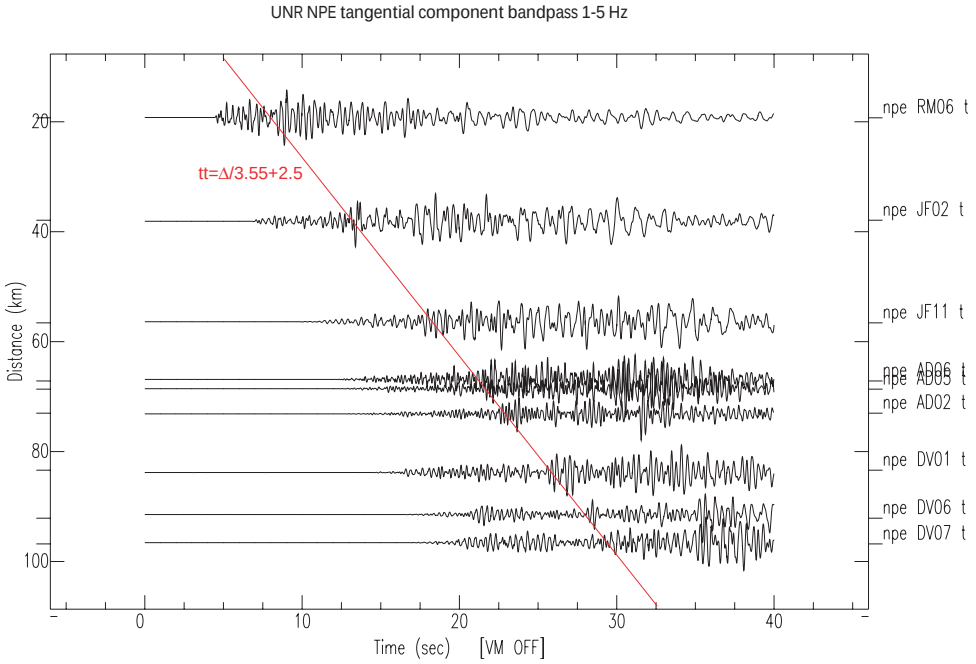


Figure 5. Development of Sg is documented on tangential recording of the NPE on the UNR stations. Sg velocity is consistent with basin and range models, but the arrival is delayed by ~2.5 seconds.

Seismic Simulation

E3D Finite-Difference Computer Code

We are beginning to run simulations with early versions of our geologic model. The simulations are performed with E3D, a state-of-the-art finite-difference seismic wave propagation code developed at LLNL (e.g., Larsen and Schultz, 1995; Larsen and Grieger, 1998). A preliminary simulation along the University of Arizona line is shown in Figure 6. Model grid spacing for this simulation is 40 m. Incorporation of Moho topography and a crude estimate of topography produce considerable S-energy (green). The snapshot is taken at approximately 9 seconds after shot detonation, when Pn is emerging as the first arrival.

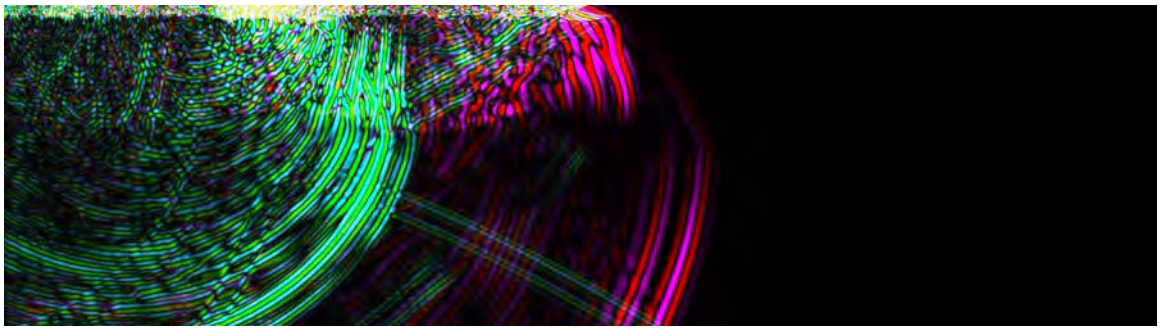


Figure 6. Snap shot of a preliminary NPE simulation. This simulation is 300 km in length and 80 km in depth. P-wave energy is shown in red, and S-wave energy is shown in green.

Validation of a simulation along the LLNL line is shown in Figures 7 and 8 (from Preston et al., 2004). The simulation includes topography, preliminary basin models, and Q. Model grid spacing in this instance is 250 m, enabling simulation at periods greater than 1 second. Figure 7 shows Pn and Pg phases at station BHR5 (LLNL line). Travel-times for Pn and Pg are well predicted, and initial (first swing) amplitudes are also in approximate agreement with the simulations. However, Figures 7 and 8 show that Pg complexity is not well predicted. Figure 8 shows that Lg is produced in the simulation and the arrival time is in reasonable agreement with the validation data. However, Lg amplitudes are severely under-predicted. While Lg amplitudes are under predicted, the simulations contain large surface waves that are not present in the data. Our preliminary models contain minimal complexity, and we believe that agreement between simulations and the validation data set will improve as model complexity is added.

CONCLUSIONS AND RECOMMENDATIONS

We review the first year of progress on the SIRES project. During this period, we made use of geologic and geophysical studies at NTS to construct a detailed earth model within 10 km of the NPE shot. Geologic and geophysical studies are being used to construct a regional model out to several hundred kilometers from the NPE. Further, we are incorporating geostatistical simulation to perturb geologic contacts and elastic parameters within geologic units to made the model as realistic as possible.

We have compiled all regional recordings of the NPE, including a temporary UNR deployment that has not been widely distributed. The UNR data set provides unique distance coverage in the range from 6 km to approximately 100 km. In the UNR data set, the Sg phase is evident from 10 km to 100 km (closer seismograms are clipped in this data set), but the arrivals are delayed by ~2.5 seconds from predictions. These observations are consistent with previous observations, which have been interpreted as resulting from conversion of Rg to higher-mode S-energy at some distance from the source.

We are nearing finalization of the NPE local model. Construction of the regional model is well underway, and we are starting to conduct simulations to test the effect of topography, basins, Moho topography, and lateral variations in velocity structure. Although simulations to date are preliminary in nature, we are finding that model heterogeneity is crucial for simulating the complexity of regional seismograms. Other important findings are as follows:

- Relatively simple models predict Pn and Pg travel-times.
- Inclusion of topography, basins, and Q reasonably predicts first-swing amplitudes for Pn and Pg.

- Complexity of Pg is not well-simulated with the current model.
- A model with topography, basins, and Q produces an Lg phase with arrival-times that are in good agreement with the validation data.
- Simulated Lg amplitudes are far smaller than observed, but we note that this simulation does not include the complex local model.

Our next step is to conduct 3-D simulations using our detailed local model and to validate these simulations with the local data set. We will continue to compile geologic and geophysical studies to complete the regional model. After the local model is imbedded in the regional model, we will test the model via regional two-dimensional simulations. The project will culminate in a tera-scale, 3-D simulation.

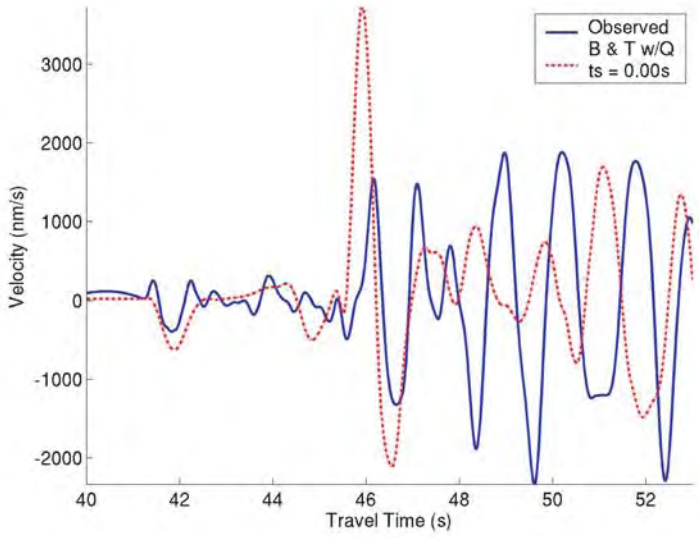


Figure 7. Simulation of station BHR5 on the LLNL line. Simulation includes topography, basins, and Q. Pn and Pg timing and the first swings are well characterized.

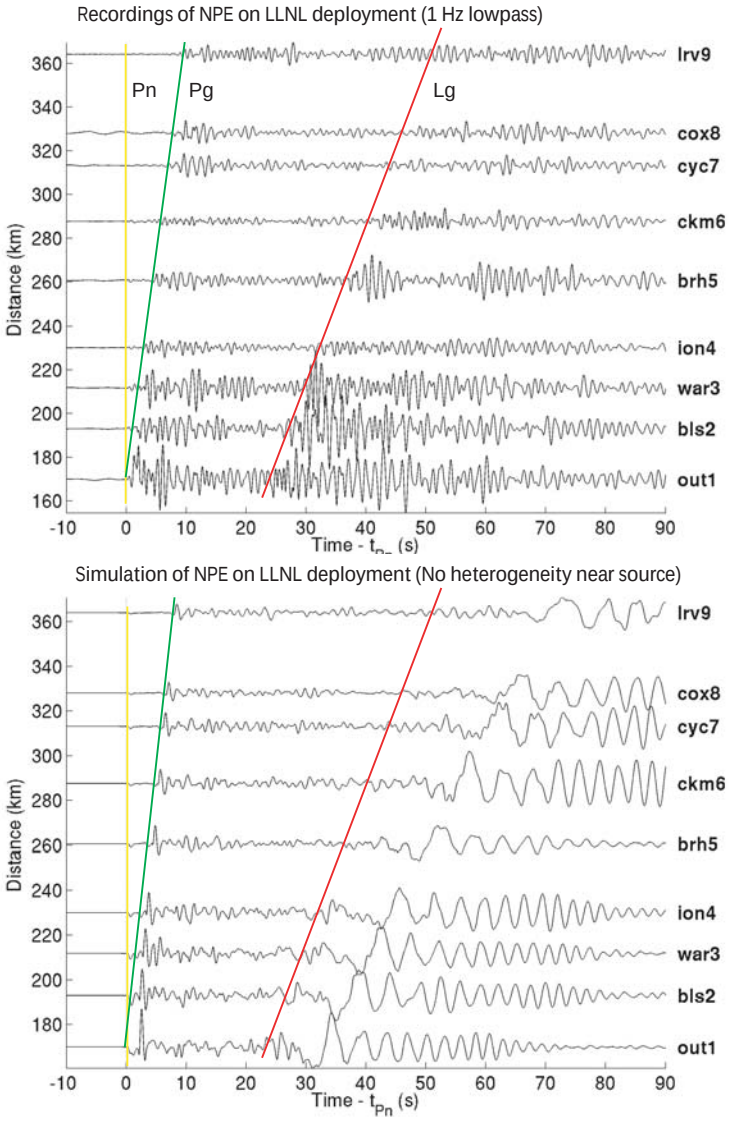


Figure 8. Observations (above) of NPE observed along LLNL (northwest) line. Two-dimensional NPE simulation along LLNL line. Simulations includes topography, basins and Q. Simulations of Pn, Pg, and Lg arrival times are good. Pn is well-characterized. Pg complexity is not predicted, and the amplitude and complexity of Lg are not predicted. Surface waves are predicted but not observed.

REFERENCES

Blakely, R. J., R. C. Jachens, J.P. Calzia, and V.E. Langenheim (1999), Cenozoic Basins of the Death Valley Extended Terrain as Reflected in Regional-Scale Gravity Anomalies in Wright, L.A. and B.W. Troxel, Eds., Cenozoic Basins of the Death Valley Region: Boudler, CO, *Geol. Soc. Am. Special Paper 333*.

Day, S. and K. Mclaughlin (1991), Seismic Source Representations for Spall, *Bull. Seismol. Soc. Am.* 81, 191-201.

Denny, M. D. and S. P. Stull (1994), Proceedings of the Symposium on The Non-Proliferation Experiment (NPE): Results and Implications for Test Ban Treaties, Rockville MD; Lawrence Livermore National Laboratory.

Gupta, I. N., W. W. Chan, and R. A. Wagner (1992), A Comparison of Regional Phases from Underground Nuclear Explosions at East Kazakh and Nevada Test Sites, *Bull. Seismol. Soc. Am.* 82, 352-382.

Healey, D. L. and Miller, C. H., (1963), Gravity Survey of the Gold Meadows Stock, Nevada Test Site, Nye County, Nevada, *USGS Technical Letter NTS-40*.

Johnson, L. R. and C. G. Sammis (2001), Effects of Rock Damage on Seismic Waves Generated by Explosions, *Pageoph* 158, 1869-1908.

Larsen, S. C. and C. A. Schultz (1995), ELAS3D: 2D/3D elastic finite-difference wave propagation code, LLNL, 18 P.

Larsen, S., and J. Grieger (1998), Elastic Modeling Initiative, Part III: 3-D Computational Modeling, *Soc. Expl. Geophys. Confer. Proceed*. 68, 1803-1806.

Mayeda, K. and W. Walter (1996), Moment, Energy, Stress Drop, and Source Spectra of Western United States Earthquakes from Regional Coda Envelopes, *Jour. Geophys. Res*. 101, 11, 195-11, 208.

Myers, S. C., W. R. Walter, K. Mayeda, and L. Glenn (1999), Observations in Support of Rg Scattering as a Source for Explosion S Waves: Regional and Local Recordings of the 1997 Kazakhstan Depth of Burial Experiment, *Bull. Seismol. Soc. Am*. 89, 544-549.

Myers, S. C., D. B. Harris, M. L. Anderson, W. L. Rodi, W. R. Walter, M. P. Flanagan, and Flori Ryall (2003), "Relative Location Accuracy and Waveform Subspace Detector", in *Proceedings of the 25th Seismic Research Review - Nuclear Explosion Monitoring: Building the Knowledge Base*, LA-UR-03-6029, Vol. 1, pp. 259-268.

Nuttli, O. W. (1986), Yield Estimates of Nevada Test Site Explosions Obtained from Seismic Lg waves, *J. Geophys. Res*. 91, 2137-2151.

Patton, H. J. (2001), Regional Magnitude Scaling, Transportability, and Ms:mb Discrimination at Small Magnitudes, *Pageoph*, 158, 1951-2015.

Patton, H. J., and S. R. Taylor (1984), Q-Structure of the Basin and Range from Surface Waves, *J. Geophys. Res*. 89 (NB8): 6929-6940.

Pomeroy, P., W. Best, and T. McEvilly (1982), Test Ban Treaty Verification with Regional Data - a Review, *Bull. Seismol. Soc. Am*. 72, S89-S129.

Preston, L., K. Smith, and S.C. Myers (2004), Near-Source Structural Effects on Regional P and Lg Waveforms, *Seismo. Soc. Am. Spring meeting*, http://209.249.56.185/abstracts/RMPro.

USGS, 1983. Geologic and Geophysical Investigations of Climax Stock Intrusive, Nevada. USGS Open-File Report 83-377.

Vogfjord, K. (1997). Effect of Explosion Depth and Earth Structure on the Excitation of Lg Waves: S* Revisited, *Bull. Seismol. Soc. Am*. 87, 1100-1114.

Walter, W., K, Mayeda, and H. Patton (1995), Phase and Spectral Ratio Discrimination between NTS Earthquakes and Explosions: Part I: Empirical Observations, *Bull. Seismol. Soc. Am*. 85, 1050-1067.

GEOPHYSICAL MODEL RESEARCH AND RESULTS

Michael E. Pasyanos, William R. Walter, Hrvoje Tkalcic, Gregory A. Franz, and Megan P. Flanagan

Lawrence Livermore National Laboratory

Sponsored by National Nuclear Security Administration
Office of Nonproliferation Research and Engineering
Office of Defense Nuclear Nonproliferation

Contract No. W-7405-ENG-48

ABSTRACT

Geophysical models constitute an important component of calibration for nuclear explosion monitoring. We will focus on four major topics: 1) *a priori* geophysical models, 2) surface wave models, 3) receiver function derived profiles, and 4) stochastic geophysical models. The first, *a priori* models, can be used to predict a host of geophysical measurements, such as body wave travel times, and can be derived from direct regional studies or even by geophysical analogy. Use of these models is particularly important in aseismic regions or regions without seismic stations, where data of direct measurements might not exist. Lawrence Livermore National Laboratory (LLNL) has developed the Western Eurasia and North Africa (WENA) model which has been evaluated using a number of datasets, including travel times, surface waves, receiver functions, and waveform analysis (Pasyanos *et al.*, 2004). We have joined this model with our Yellow Sea – Korean Peninsula (YSKP) model and the Los Alamos National Laboratory (LANL) East Asia model to construct a model for all of Eurasia and North Africa. In addition, we continue to improve upon our surface wave model by adding more paths. This has allowed us to expand the region to all of Eurasia and into Africa, increase the resolution of our model, and extend results to even shorter periods (7s). High-resolution models exist for the Middle East and the YSKP region. The surface wave results can be inverted either alone, or in conjunction with other data, to derive models of the crust and upper mantle structure. We are also using receiver functions, in joint inversions with the surface waves, to produce profiles directly under seismic stations throughout the region. A collaborative project (Ammon, et al.) has been focusing on stations throughout western Eurasia and North Africa, while we have been focusing on LLNL deployments in the Middle East, including Kuwait, Jordan, and the United Arab Emirates. Finally, we have been exploring methodologies such as Markov Chain Monte Carlo (MCMC) to generate data-driven stochastic models. We have applied this technique to the YSKP region using surface wave dispersion data, body wave travel time data, and receiver functions.

OBJECTIVE

The objective of regional-scale geophysical models is to improve predictions for the location and identification of regional seismic events by improving the resolution in comparison to global-scale models. As such, we wish to provide models of the highest possible resolution that can used to reliably derive parameters such as body wave travel times, group velocity dispersion, waveforms, etc. In addition, the models should also convey proper uncertainty estimates which can be mapped into uncertainties in the derived products.

Geophysical models can take a number of forms. We consider several types here. The first are *a priori* geophysical models. These can serve as background values for travel time correction surfaces and other derived parameters. This can be particularly important in aseismic regions, which might only have a limited number of empirical measurements. These models can also serve as an integrated geophysical repository for research community results. The second type are surface wave models. By themselves, these stand-alone models can be used to construct phase-matched filters, which can improve weak surface wave signal and calculate regionally determined M_S. In addition, they can be used either alone or in conjunction with other data to construct 3-D velocity models of the lithosphere. They can also be a method to evaluate *a priori* geophysical models.

Receiver functions are a reliable way of obtaining the local velocity structure near a station from teleseismic events. While the results are only applicable to the limited portions of our model area covered by seismic stations, they are important to constrain precisely because they represent the structure at the station locations. Improvements in the model at the location of the seismic stations will improve the results of all recordings made at that station. Finally, we present some of the first results from data-driven models generated using a “stochastic engine” inversion technique. This method combines *a priori* information with geophysical data from multiple sources (and varying sensitivities) to produce models that are most consistent with the constraints.

RESEARCH ACCOMPLISHED

Geophysical Models

Geophysical models, such as *a priori* models, can be used to predict a host of geophysical measurements, such as body wave travel times, and can be derived from direct regional studies or even by geophysical analogy. Use of these models is particularly important in aseismic regions or regions without seismic stations, where data of direct measurements might not exist. LLNL has developed the WENA model, an *a priori* model for Western Eurasia and North Africa.

Details of the construction and validation of the model can be found in Pasyanos et al., 2004. Briefly, the WENA model is constructed from separate sediment, crust, and upper mantle models. Sediments are taken from Laske and Masters (1997), a 1º 3-layer sediment model based on the 1985 Exxon map. Crustal regionalizations and velocity profiles are taken from a series of LLNL reports (Walter et al., 2000; Bhattacharyya et al., 2000; Sweeney et al., 1998) and based on Exxon, the global crustal model CRUST 5.1, and many published studies. Overall, we have subdivided the region into 45 base models, each representing a different tectonic region (i.e. Russian Platform, Zagros Mts., etc.). Our regionalizations are shown in Figure 1. The crustal regionalizations also include velocities in the uppermost mantle layer. The 3-Dimensional Seismological Model *A Priori* Constrained (3SMAC) (Nataf and Ricard, 1996) is an *a priori* model based on tectonics, heat flow, and geophysical knowledge, and is used for the remainder of the upper mantle extending down to 660 km depth.

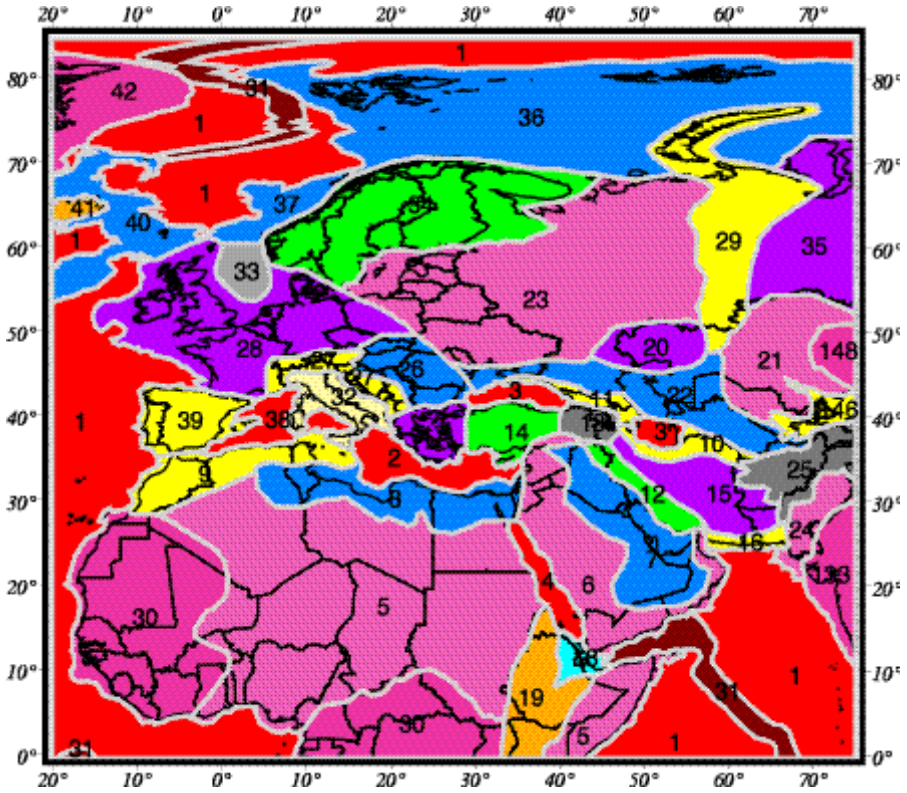


Figure 1. Crustal regionalization used in the WENA geophysical model. There are about 45 base models for the region.

The WENA model has been extensively evaluated using a number of datasets, including body wave travel times, surface wave dispersion measurements, teleseismic receiver functions, gravity, and waveform analysis (Pasyanos et al., 2004). It has been shown to significantly improve the fit to these datasets with respect to global models. Furthermore, it has been shown to improve travel time correction surfaces by reducing the overall amplitude of the corrections and accounting for the non-stationary component of travel times.

There are a number of other geophysical models that have been developed in the context of improved regional monitoring. Los Alamos National Laboratory (LANL) has created the Commissariat à l'Energie Atomique (CEA) model that covers China and East Asia. This effort has paralleled some of LLNL's work on geophysical models in Western Eurasia and North Africa. We have worked with LANL to ensure that the regionalizations of the two individual models are consistent, allowing us join the models. The result is a Unified Geophysical Model for all of Eurasia. WINPAK3D is a model for India and Pakistan that was developed by Weston Geophysical (Johnson and Vincent, 2002). We have recently worked with Weston to convert this model into a format consistent with tools developed to access geophysical models.

Working with Sandia National Laboratories (SNL), we have created a utility designed to view and extract geophysical models. VEXtool (or Viewing and EXtraction tool) allows users to extract 1-D profiles (boreholes), 2-D profiles (cross-sections), and 3-D profiles (volumes) from the models. These portions of the model can either be viewed graphically or exported into a series of export formats, including those for the TauP travel time generator (Crotwell et al., 1999), Randall's reflectivity codes (based on Kennett, 1985), or several input formats for Herrmann's Computer Programs in Seismology and surface wave package SURF (based on Russell, 1988). Most recently, we have added the capability of outputting 1-D and 2-D portions of the model to Xgbm (Davis and Henson, 1993), a travel time predictor that uses a Gaussian beam method.

Surface Wave Models

Over the past several years, LLNL has been developing surface wave models in Eurasia for nuclear explosion monitoring (Pasyanos et al., 2001). Dispersion measurements are made using multiple narrow-band filters on deconvolved displacement data from the LLNL SRKB. We continue to improve upon our surface wave model by adding more paths, generally by taking advantage of new datasets, but also by revisiting stations with more recent events. Most recently, we have added measurements from stations in Central Asia and central and southern Africa, as well as from PASSCAL deployments in Eastern Turkey, Ethiopia/Kenya, China, and South Africa.

To date, over 55,000 seismograms have been analyzed to determine the individual group velocities of 7 – 150s Rayleigh and Love waves. Overall, we have made good quality dispersion measurements for 23,000 Rayleigh and 13,500 Love wave paths. We then tomographically invert these measurements to produce group velocity maps for Love and Rayleigh waves. A conjugate gradient method is used for the tomography. Accurate group velocity maps can be used to construct phase-matched filters, which can improve weak surface wave signal and calculate regionally determined M_S.

The group velocity models continue to improve in several ways. First, with more measurements, we have been able to expand the region of coverage to all of Eurasia and into Africa. By increasing the density of coverage in existing regions, we have increased the resolution of our model. Finally, we have been able to provide more reliable maps at short periods, expanding the frequency coverage down to 7s period. With the group velocities, we are able to resolve structural features associated with the tectonics of the region. Short period surface waves correspond well to sedimentary basins. At intermediate periods, we find a good correspondence to crustal thickness, but still see the effect of the deepest sedimentary basins. At long periods, we are primarily sensitive to upper mantle structure with fast cratons, slow convergence zones, and very slow ridges.

We have created high-resolution models for the Middle East and the YSKP region. Figure 2 shows an example of our results from the Middle East for 15s Rayleigh waves, which are sensitive to relatively-shallow crustal structure. Here, we compare the results to a sediment thickness map and the results are excellent. Details like the extent of basins in the eastern Mediterranean, Persian Gulf, Mesopotamian Foredeep, and Caspian Sea are well resolved, as is the thin oceanic crust in the Red Sea.

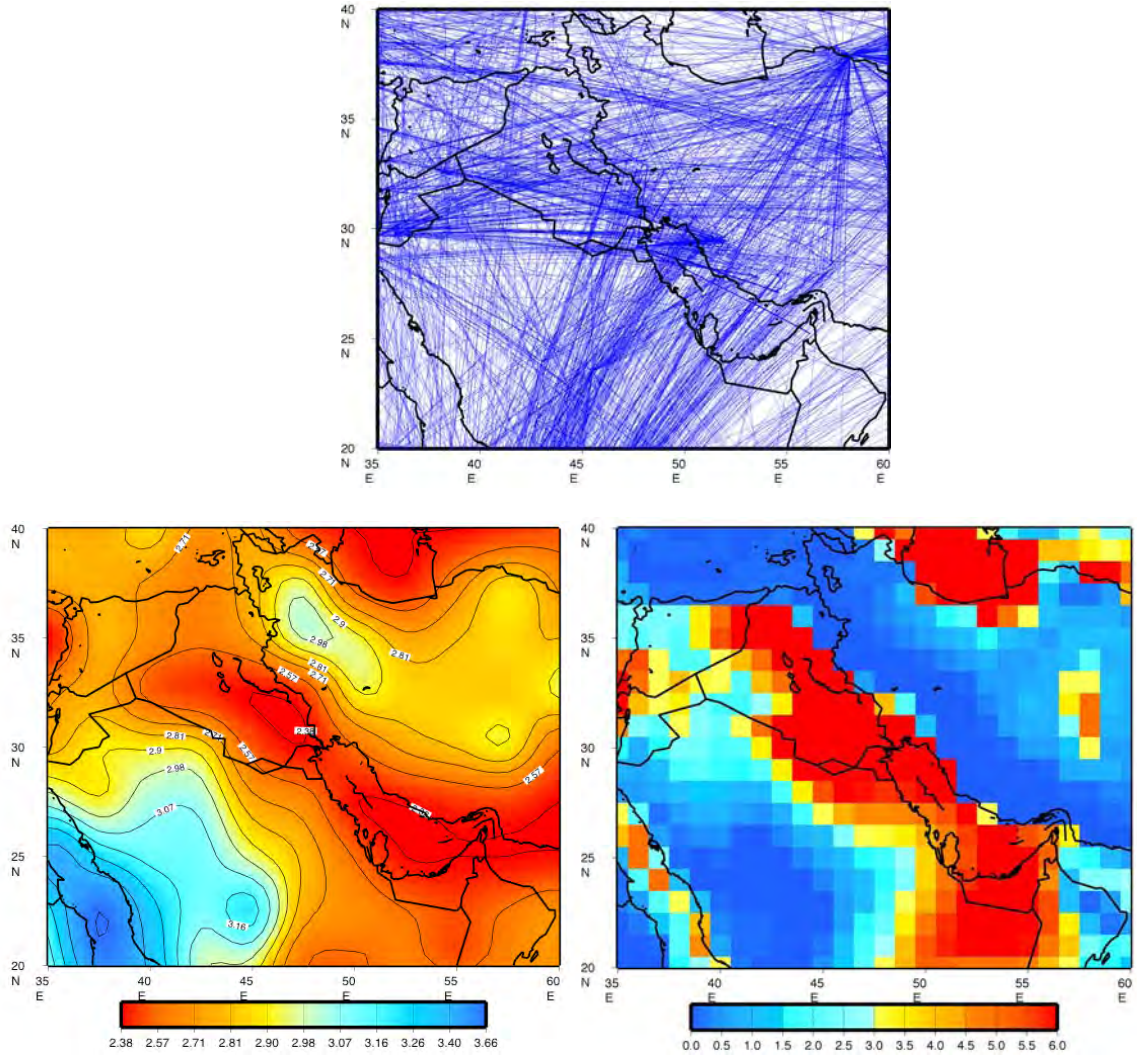


Figure 2. A path map of 15s Rayleigh wave group velocities for the Middle East, followed by a tomographic model of 15s Rayleigh waves and a comparison of the results to a sediment thickness map of the region.

The surface wave results can be inverted either alone, or in conjunction with other data, to derive models of the local crust and upper mantle structure. By combining the surface wave data with other data, we can reduce the non-uniqueness inherent in the profile inversions performed using only surface wave data. In the next section, for example, we will be using the surface wave data in combination with teleseismic receiver functions.

Receiver Function Profiles

We are also using receiver functions, in joint inversions with the surface waves, to produce profiles directly under seismic stations throughout the region. These two data types are complementary since receiver functions are sensitive to velocity contrasts and surface waves are sensitive to depth-averaged velocity. In a collaborative ROA with Pennsylvania State University, Ammon et al., have been focusing on stations throughout Western Eurasia and North Africa, while we have been focusing on LLNL deployments in the Middle East, including Kuwait, Jordan, and the United Arab Emirates.

Figure 3 shows an example of a joint inversion for station KBD in Kuwait. We were able to fit the surface waves without significantly degrading the fit to the receiver functions. The resulting models were similar between various ray parameters and back azimuths, giving us confidence in our results. The profiles were also consistent with the tectonic setting of the region. In Kuwait, we find the thick sediments that would be expected for the Arabian Platform. We also find a crustal thickness of 45 km, which is thicker than models of the region that have looked at the western portions of the platform. The thicker crust that we find, however, is consistent with the general trend of increasing thickness to the northeast and the thick crustal root from the nearby Zagros Mountains. orogenic zone.

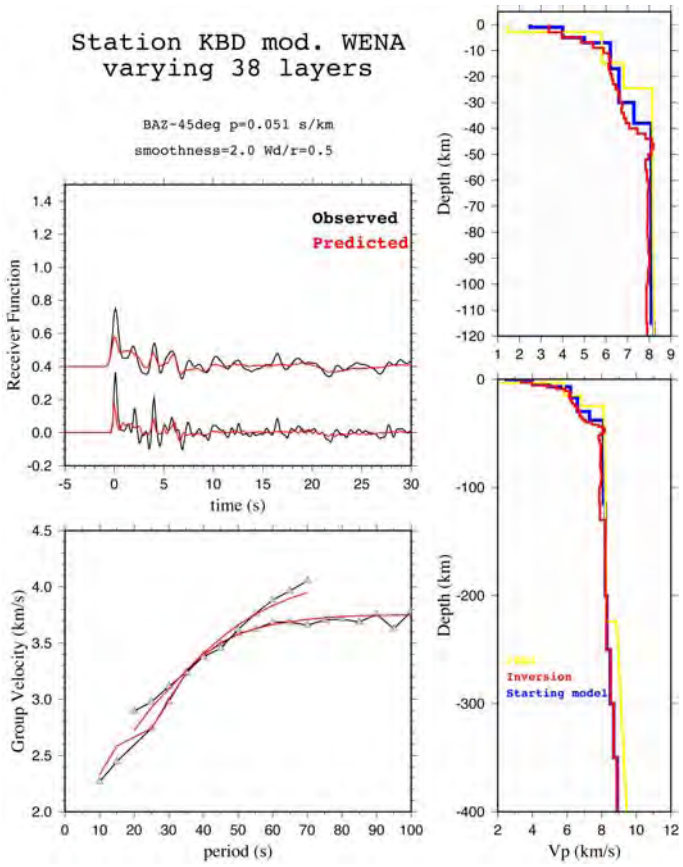


Figure 3. Joint inversion of receiver functions and surface waves to produce a velocity profile for Kuwait. On the left, the black lines are observed data and red lines data predicted from the model. On the right, blue and red lines indicate the starting model and the inversion.

Stochastic Geophysical Models

We have been exploring methodologies such as MCMC to generate data-driven stochastic models. In an effort to build seismic models that are most consistent with multiple seismic datasets, we have applied a new method known as the Stochastic Engine (SE). The SE uses MCMC to sample models from a prior distribution and to test them against multiple data types in a staged approach to generate a posterior distribution of models.

While computationally expensive, this approach has several advantages over a single deterministic model. First, we are able to easily incorporate prior information on the model, such as the *a priori* geophysical models that we considered earlier. Secondly, with this technique, we are able to reconcile different data types that can be used to constrain the model. We can also estimate the uncertainties of model parameters, properly migrating data uncertainties into model uncertainties. The method does not constrain models to be normally distributed, but instead allows non-Gaussian or multi-modal distributions. Finally, we can estimate uncertainties on predicted observable signals, such as would be required to apply this model as a correction surface.

We use this method to determine the crust and upper mantle structure of the YSKP region using surface wave dispersion data, body wave travel time data, and receiver functions. We have had great success using this approach. Where little or no data exist, the posterior model simply reflects the prior distribution. Where data exists, however, the model is driven by the data. Figure 4 shows a crustal thickness map and corresponding uncertainties, taken by calculating the mean and standard deviation of the posterior distribution. One can see the thinning associated with the oceanic crust of the Pacific Ocean and Sea of Japan. One can also see crustal thickening in the westernmost portion of our study area. In the future, we aim to improve the model by incorporating more datasets (i.e., amplitude information, waveforms, etc.) and increasing the resolution.

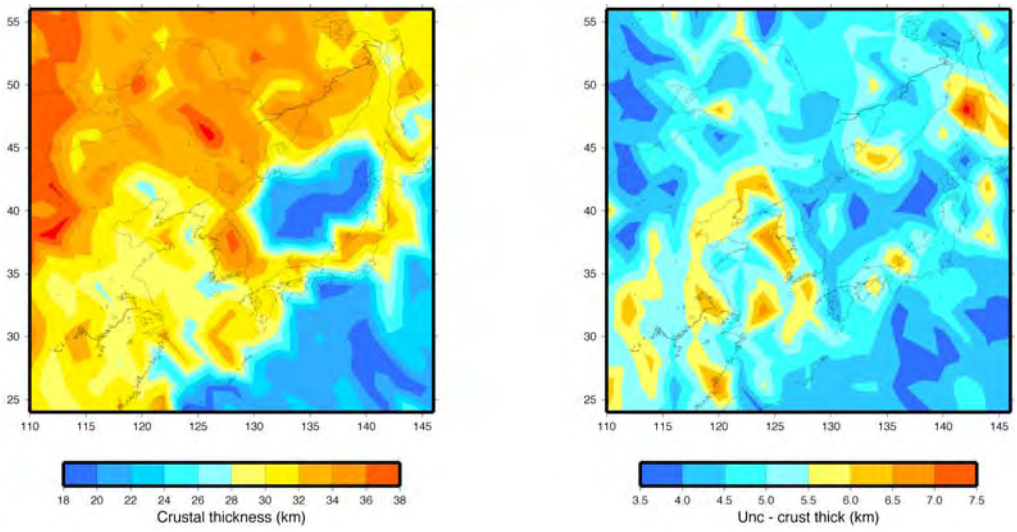


Figure 4. A crustal thickness map of the YSKP region determined using stochastic inversion methods, along with its associated uncertainties.

In short, stochastic methods are an innovative technique for producing next-generation data-driven models. Geophysical models shown in the first section can be used as starting models for the inversion. Other model information such as surface wave dispersion measurements and teleseismic receiver functions (shown in the second and third sections) can be included as additional constraints. Stochastic models have a number of advantages compared to traditional models, such as the ability to reconcile different types of geophysical data. An important component of this is the ability to predict new observables with proper uncertainties.

CONCLUSIONS AND RECOMMENDATIONS

Geophysical models are an important way of calibrating regions in the absence of direct measurements. Models can be a repository for a vast array of geological and geophysical datasets of all types—receiver functions, refraction profiles, tomographic inversions, travel-time models, amplitude measurements, etc. This product integrates results from many sources and can be used to incorporate future results from current research.

Geophysical model research at LLNL has developed along a number of lines. We have developed a 3-D geophysical model for Western Eurasia and North Africa, along with sophisticated access tools, which are directly usable for generating a number of geophysical parameters of interest. The surface wave measurements and model for greater Eurasia and receiver functions throughout the region provide additional model constraints. We are now moving toward developing data-driven geophysical models that can use all of these results to produce reliable geophysical models.

ACKNOWLEDGMENTS

We wish to thank Lee Jensen and Chris Young at SNL for their work on VEXtool, Charlotte Rowe from LANL for her efforts in preparing the Unified Geophysical Model for Eurasia, Shelly Johnson and Carolyn Vincent from Weston Geophysical for their help in converting the WINPAK3D model, Jordi Julia from Duke University for use of his receiver function codes, and Flori Ryall from Lawrence Livermore National Laboratory for the use of her travel time picks.

REFERENCES

Bhattacharyya, J., W. Walter, M. Flanagan, J. O'Boyle and M. Pasyanos (2000), Preliminary Definition of Geophysical Regions in Western Eurasia, UCRL-ID-138402, LLNL (http://www.llnl.gov/tid/lof/documents/pdf/237980.pdf).

Crotwell, H. P., T. J. Owens, and J. Ritsema (1999), The TauP ToolKit: Flexible Seismic Travel-Time and Raypath Utilities, *Seism. Res. Lett.* 70, 154-160.

Davis, J. P. and I. H. Henson (1993), Development of an X-Windows Tool to Compute Gaussian Beam Synthetic Seismograms, TGAL-93-03, Phillips Laboratory, Kirtland AFB, NM, 23pp.

Davis. J. P. and I. H. Henson (1993), *User's Guide to Xgbm: An X-Windows System to compute Gaussian beam synthetic seismograms*, Teledyne Geotech Alexandria Laboratories, Alexandria, VA, 1.1 edition.

Johnson, M. and C. Vincent (2002), Development and Testing of a 3-D Velocity Model for Improved Event Location: a Case Study for the India-Pakistan Region, *Bull. Seism. Soc. Amer*. 92, 2893-2910.

Kennett, B. L. N. (1985), *Seismic wave propagation in stratified media*, 342 pp., Cambridge University Press, Cambridge, England.

Laske, G. and T. G. Masters (1997), A Global Digital Map of Sediment Thickness, *EOS Trans. AGU* 78, F483.

Nataf, H. C., and Y. Ricard (1996), 3SMAC: an a priori Tomographic Model of the Upper Mantle based on Geophysical Modeling, *Phys of Earth & Plan. Int.* 95, 101-122.

Pasyanos, M. E., W. R. Walter, S. E. Hazler (2001), A Surface Wave Dispersion Study of the Middle East and North Africa for Monitoring the Comprehensive Nuclear-Test-Ban Treaty, *Pure & Appl Geophys.* 158, 1445-1474.

Pasyanos, M. E., W. R. Walter, M. P. Flanagan, P. Goldstein and J. Bhattacharyya (2004), Building and Testing an a priori Geophysical Model for Western Eurasia and North Africa, *Pure & Appl. Geophys.* 161, 235-281.

Russell, D. R. (1988), Multichannel Processing of Dispersed Surface Waves, Ph.D. Dissertation, St. Louis University, St. Louis, MO.

Sweeney, J. and W. R. Walter (1998), Preliminary definition of geophysical regions for the Middle East and North Africa, UCRL-ID-132899, LLNL (http://www.llnl.gov/tid/lof/documents/pdf/235042.pdf).

Walter, W. R., M. E. Pasyanos, J. Bhattacharyya and J. O'Boyle (2000), MENA 1.1 - An Updated Geophysical Regionalization of the Middle East and North Africa, UCRL-ID-138079, LLNL (http://www.llnl.gov/tid/lof/documents/pdf/237521.pdf).

WAVEFORM MODELING OF THE CRUST AND UPPER MANTLE USING S, SP, SSPMP, AND SHEAR-COUPLED PL WAVES FOR IMPROVED EVENT LOCATION, FOCAL DEPTH DETERMINATION, AND UNCERTAINTY ESTIMATION

Jay Pulliam and Mrinal K. Sen

University of Texas at Austin

Sponsored by Air Force Research Laboratory

Contract No. FA8718-04-C-0014

ABSTRACT

During this contract's performance period (1 October 2004-30 September 2007) we intend to complete the development of a method for determining crust and upper mantle structure in aseismic regions and evaluate its capacity to produce sufficiently accurate models for locating hypocenters of small-to-moderate seismic events. Specifically, we will

- complete development of a waveform modeling approach to determine the structure of the crust and upper mantle in a broad region surrounding a broadband seismographic station;
- validate the method through careful comparison between models produced with our method and models produced by higher resolution active-source experiments, as well as models produced by surface wave inversion and receiver function methods;
- apply and validate methods for computing uncertainty statistics from the products of global optimization searches; and
- refine, apply, and evaluate waveform correlation methods to ground-truth data from regional events and explosions with well-constrained focal depths, using crust/upper mantle models produced with our method;
- apply the modeling method to teleseismic data recorded at stations in China, Africa, and the Middle East;
- apply and evaluate waveform correlation methods to determine focal depths for small- and moderate-magnitude regional events recorded at stations in China, Africa, and the Middle East using crust/upper mantle models determined in this study.

The high frequencies and long time-series required for phases that arrive near the direct SV phase, including Sp, SsPmP, and shear-coupled PL waves, their deep penetration into the Earth and observation at teleseismic distances make the computation of synthetic seismograms time-consuming. We have parallelized and optimized a synthetic seismogram code based on the reflectivity method and are now able to compute complete seismograms up to 0.5 Hz in just over one minute using eight AMD Opteron processors. This has allowed us to produce the best-fitting waveform matches that result from searches of many thousands of models, yet searching the model space comprehensively multiple times, as is required to estimate posterior covariance, correlation, and posterior probability distribution functions is still prohibitive. However, the speed-up in computation time is nearly linear with the number of processors used, so a massively parallel computer installed recently at the University of Texas at Austin should allow us to compute posterior probability density function (PPD) estimates readily. We intend to explore the utility of PPD estimates for estimating the reliability of our crustal models for the purposes of estimating hypocenters of small- to moderate-sized regional seismic events.

OBJECTIVES

Our research focuses on developing and testing methods for determining event locations at regional distances (100-1,000 km) using one or a few three-component, broadband seismographic stations. To be useful for discriminating explosions from earthquakes, focal depths must be determined accurately to within a few kilometers, yet the structure of the crust and upper mantle between the source and station strongly influences the arrival times and amplitudes of regional phases. Our first task, therefore, is to determine this structure. We will attempt to obtain a sufficiently accurate model of crustal structure beneath a given station by searching over a wide variety of crustal models to find the one whose synthetics best match the amplitudes and travel times of phases that arrive in the time window around the direct S phase, and which appear most strongly on the radial component seismogram. We use data from large-magnitude (6<Mb<7) deep events located at teleseismic distances for this purpose, for reasons discussed in detail below.

After structural models are in hand we propose to find focal depths by means of a waveform correlation technique. We will compute suites of synthetic seismograms for the candidate model corresponding to a given broadband station and, given data from small-magnitude regional events recorded at the same station, compute correlations between the suites of synthetic seismograms generated for a variety of distances and focal depths.

Case studies around the world, including application to "ground-truth" data in which focal depths are well-constrained, are required in order to determine the range of applicability and usefulness of our event location strategy. Small magnitude events (2<mb<4) are rarely recorded at more than a few stations in many parts of the world, yet identifying these events is essential to monitoring nuclear explosions effectively. Our objective, therefore, is to develop and test methods for distinguishing between explosions and natural events in sparsely-instrumented parts of the world. Our strategy is to estimate hypocenter locations for small- and moderate-magnitude events using one or a few single broadband, three-component stations. Focal depth is a particularly helpful discriminating characteristic, if determined reliably.

HISTORICAL PERSPECTIVE

The problem of finding earthquake locations using only a single three-component station, or a very sparse network of stations, has received a great deal of attention. Some authors, recognizing the greater difficulty in constraining focal depths, have focused on estimating event epicenters and origin times (e.g., Magotra et al., 1987; Roberts et al., 1989; Kedrov and Ovtchinnikov, 1990; Kim and Wu, 1997). Others have attempted to estimate not only focal depths but focal mechanisms, as well, via waveform modeling of regional events (Jimenez et al., 1989; Fan and Wallace, 1991; Zhao and Helmberger, 1994; Walter, 1993; Zhu and Helmberger, 1996). Frohlich and Pulliam (1999) review efforts to locate earthquakes using a single three-component station in detail. In contrast, the problem of determining earthquake focal depths with one or a few stations has received far less attention, yet obtaining accurate estimates of focal depths is important to tectonic interpretations of seismicity, to understanding seismic hazard, and to seismic monitoring of underground nuclear tests (National Research Council, 1997). If a seismic event were known reliably to have occurred at a depth greater than a few kilometers, one could confidently categorize that event as an earthquake rather than an explosion.

The most common approaches to determining focal depths utilize travel times (e.g., Douglas, 1967), which must be picked for the major seismic phases and then back-projected by a nonlinear or bootstrapped linear algorithm. A great deal of effort has been devoted to methods for picking arrival times automatically (Roberts et al., 1989; Saari, 1991). While these methods have proven useful for moderate to large magnitude events at far-regional and teleseismic distances, particularly for events that are deeper than a few tens of kilometers, they are prone to picking errors. These picking errors become relatively more important and more problematic for location procedures when dealing with small magnitude and shallow events. Furthermore, shallow events have little time separation between the downgoing, direct body wave phases and the upgoing, reflected ("depth") phases that are most useful for constraining focal depth. One must use high-frequency data to have any hope of identifying and picking distinct arrivals for these phases, which again complicates the picking process and increases the likelihood that errors will contaminate the location process. In some parts of the world, small-magnitude and relatively shallow events observed at regional distances typically have emergent rather than impulsive first arrivals, which renders travel time picking even more prone to errors. Lastly, reliable estimates of both epicenters and focal depths using travel times require redundancy, i.e., at least several and preferably many recordings from stations that are well-distributed with respect to azimuth around the event. But the great majority of earthquakes are small-magnitude, shallow events, which are much more likely than large events to be recorded by just one or a few seismographic stations. Locating

these small events accurately can be most useful for discriminating between nuclear explosions and earthquakes and can contribute a great deal to understanding regional tectonics.

Waveform modeling offers the best hope for constraining small-magnitude, shallow seismic events at regional distances with sparse observations. Ideally one would be able to match, and thereby determine the origin of, the time and amplitude of each arriving wave. Such a match is an unrealistic goal, in general, due to approximations required for tractability in modeling algorithms, to an incorrect or inadequately precise understanding of the crust and upper mantle in most regions, and to poor constraints on focal mechanisms and source time functions. While approaches such as finite difference methods offer hope for accurate and computationally feasible three-dimensional (3D) modeling in the relatively near future, to be useful they will require far more precise and accurate velocity models than are currently available. Assuming that accurate 3D, or even 2D, modeling is currently out of reach, the question that arises is whether 1D modeling methods can be used in a strategy that minimizes the effects of laterally-varying structure and focal mechanism to constrain the focal depths of seismic events. Presenting and evaluating such a strategy are the goals of our research. Rather than matching direct and reflected pulse shapes, as do Goldstein and Dodge (1999) for larger-magnitude (mb>=4.5) and more distant events, we seek to match some gross characteristics, such as the relative arrival times of a series of waves, as well as possible.

A strategy for producing 1D models that are sufficiently accurate to constrain focal depths of small events

Phases that arrive near the direct SV phase, including Sp (converted at the base of the Moho), SsPmP, and shear-coupled PL (SPL) waves, collectively sample the Earth's crust and upper mantle at oblique angles and therefore have the potential to produce an accurate lateral average of structural properties than teleseismic P waves. SPL waves essentially mimic the propagation characteristics of regional PL phases, with the important difference that the number of events available for modeling is often greater for relatively aseismic regions, since sources are located at teleseismic distances. SPL waves are sensitive to crust and upper mantle structure, including seismic velocity gradients, Vp/Vs, impedance contrast across the Moho, and layer thicknesses.

The conventional S phase (Figure 1) is the initial, relatively sharp and pulse-like arrival that signals the beginning of a wavetrain with generally longer periods and normal dispersion. The particle motion associated with the S phase is rectilinear and all three components of motion are in phase. The dispersive wavetrain, that follows S, exhibits prograde elliptical particle motion that is confined to the vertical plane. Oliver (1961) named this wavetrain "shear-coupled PL" because it is analogous to the PL wavetrain, which appears between P and S arrivals at regional distances. Oliver (1961) presented a theory, based on the observed group and phase velocity of SPL that explained the phase as coupling between S and the fundamental leaking mode of Rayleigh waves in the crustal waveguide. According to this theory, shear energy generated by an earthquake (or explosion) travels through the Earth's mantle as a body wave, whereupon it impinges upon the Moho. Afterward a portion travels through the crustal waveguide as trapped P-waves and leaky SV-waves (Figure 2). The only difference between a PL phase, which is observed at regional distances from a source, and SPL phases, which are observed at teleseismic distances, is that SPL is generated by a shear wave impinging upon the Moho at regional distances from the observing station. In addition to producing SPL as it impinges on the Moho, a portion of the incident S wave converts to P as well, which then travels through the crust to arrive at the station as a precursor to S (Figures 1 and 3). This phase is called Sp, and it has been used to model the crust by Jordan and Frazer (1975). Its sampling is much more localized to the station than is SPL's, making its sensitivity less representative of the broader region and more similar to that of P-coda receiver functions. SsPmP arrives at the base of the crust as a shear wave, travels upward through the crust as a shear wave, converts to a P wave at its surface reflection and bounces once off the Moho as a P wave. Langston (1996), while demonstrating that it can be highly useful for regional crustal modeling, showed that SsPmP can arrive before or after direct S, with either larger or smaller amplitude, and can also distort the S arrival pulse. We will attempt to simultaneously model S, Sp, and SsPmP that essentially isolates differences to the P structure of the crust, for data collected for SPL modeling. Because receiver function methods typically deconvolve the vertical seismogram, which is most sensitive to compressional wave energy, from the radial seismogram, constraints on P velocity are essentially sacrificed in order to obtain clean records of shear phases. The

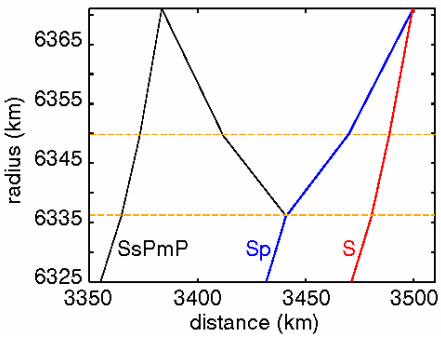
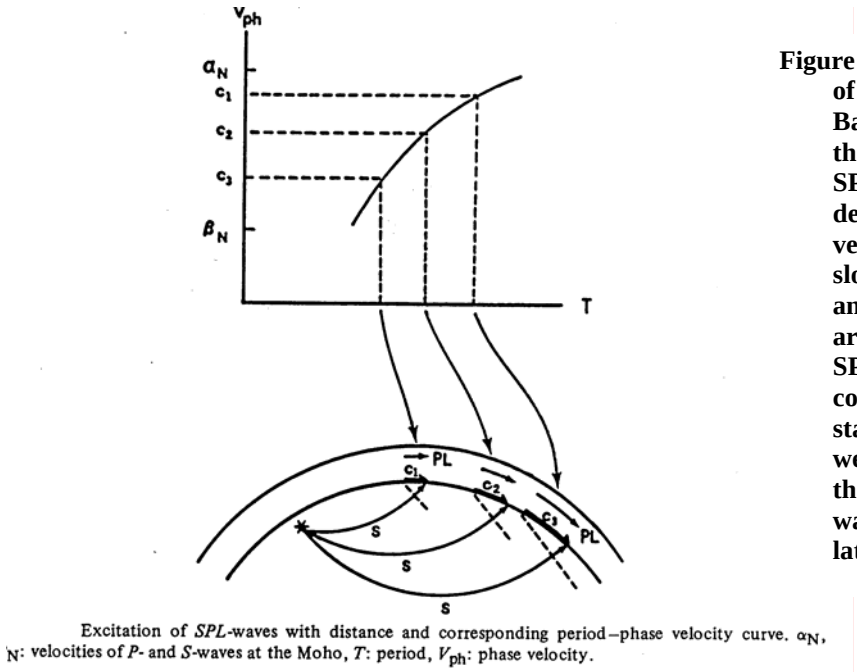


Figure 1. Typical raypaths for S, Sp, and SsPmP. These body wave phases provide constraints on crustal thickness, P and S velocities near the station.

data we propose to model will provide a valuable check of receiver functions, in that they constrain the bulk properties of the crust—average P velocity and crustal thickness (Sp and SsPmP)—and upper mantle (SPL). If the broad model search turns out to be too time-consuming or impractical, a fall-back strategy would be to first obtain a basic starting model by modeling Sp and SsPmP, then automating the SPL modeling using the Sp/SsPmP model as a starting point. Since reflectivity is a full-waveform method, there is no need to specify which phases should be included (nor need we identify or "pick" specific arrivals) in the waveform fitting procedure. While the waveform fitting itself will be automated, a great deal of exploration will be required to determine optimal window lengths, frequency content, and, perhaps, variable weighting functions for different portions of the seismograms.



Excitation of *SPL*-waves with distance and corresponding period–phase velocity curve. α_N, β_N: velocities of *P*- and *S*-waves at the Moho, *T*: period, V_{ph}: phase velocity.

Figure 2. Propagation characteristics of shear-coupled PL phases (from Baag and Langston, 1985). Note that the distance of propagation of SPL, and therefore its sampling, depends on characteristics of the velocity structure, including the slope of velocities below the Moho and attenuation. The earliest-arriving and largest-amplitude SPL waves are those that have converted from S nearest to the station, so our modeling will weight local sampling more highly than distant sampling but the wavefield still averages structure laterally.

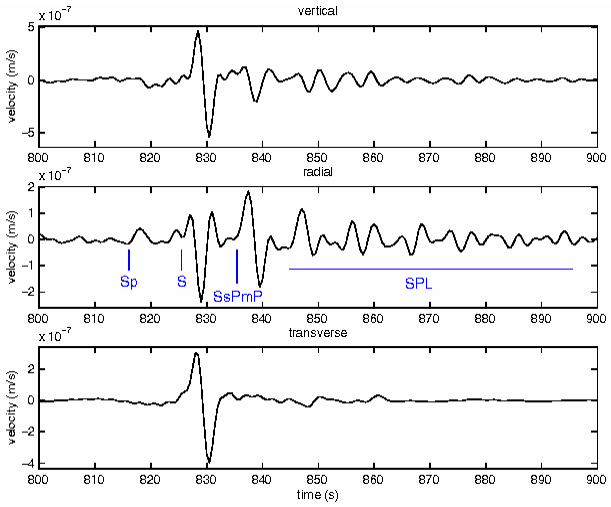


Figure 3. Depending on Earth structure and an earthquake's radiation pattern, the phases Sp, S, SsPmP, and SPL may appear prominently on the radial component seismogram at distances between 30° and 75°.

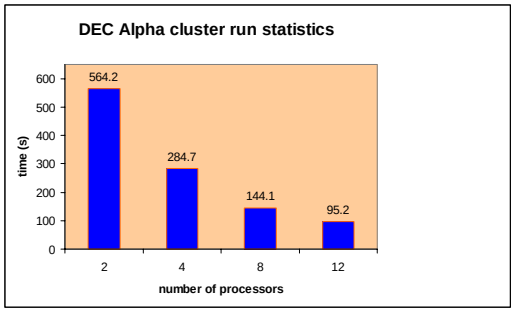


Figure 4. Statistics of an example run to compute complete seismograms for frequencies from 0 to 0.5 Hz (number of frequencies = 2000, number of layers=192, number of ray-parameters=1000) on the DEC Alpha cluster. Note the near linear speedup of the algorithm with the increase in the number of processors.

We are evaluating the usefulness of S, Sp, SsPmP (Figures 1 and 3), and shear-coupled PL (SPL) phases (Figures 2 and 3) for modeling crustal and upper mantle structure using real and synthetic data, developing a waveform inversion technique based on a novel implementation of the reflectivity method and global optimization algorithms, and applying this method to data recorded in China. We have made substantial progress in speeding up the synthetic seismogram computations to the point where a global optimization is feasible. The reflectivity calculation involves computation of reflectivity matrices for a stack of layers as a function of ray parameter (or wavenumber) and frequency. The computation of reflectivity responses for different ray parameters and frequencies are completely independent of each other. We took advantage of this independence to develop a reflectivity code that runs on parallel computer architectures. Our code loops over ray parameters, i.e., to each node we assign a certain number of ray parameters to compute. At the end, the master node assembles the partial responses and performs the inverse transformation to generate synthetic seismograms at the required azimuths and distances. We used MPI for message passing and ran our code on a PC cluster consisting of 16 nodes; each node is a 660MHz alpha processor with 8MB cache and 1GB of RAM. A Myrinet interconnect is used to communicate between nodes.

Figure 3 shows synthetic seismograms computed using our parallelized reflectivity code for a distance of 50° and an earthquake at 600 km focal depth. Since the reflectivity algorithm is "embarrassingly parallel" in that the response for each frequency or ray parameter can be computed on independent processors, without communication between processors, on a parallel machine computation speed increases nearly linearly with the number of processors (Figure 4). In a side-by-side comparison for various distances, source depths, and model complexity, our code matched results of the Fuchs-Muller code very well.

Our modeling method retains the time and cost advantages of P-coda receiver function methods but which uses types of data that are more appropriate for nuclear monitoring purposes: Shear-coupled PL phases (SPL), Sp phases converted at the Moho, and SsPmP. SPL samples the crust and upper mantle in the vicinity of a station most broadly compared to Sp, SsPmP and P and it emulates the propagation of regional phases, which reflect at more oblique angles (or are refracted by these layers) than are the more steeply arriving body phases typically used in receiver function modeling. In short, because of the data they use, the models produced by receiver function methods may be inadequate for the purposes of nuclear monitoring. These latter phases sample only a narrow cone beneath the station (e.g., Zhao and Frohlich, 1996). Modeled simultaneously (where they exist), SPL, Sp, and SsPmP offer the potential for producing azimuthally-dependent structural models.

We are pursuing this strategy because efforts to determine the locations of small, regional seismic events are hampered, in most parts of the world, by insufficient knowledge of the crust and upper mantle. Also, while focal depths are often a highly useful discriminant between explosions and earthquakes, their determination is quite sensitive to crustal structure. The most encouraging approaches to determining focal depths require precise modeling of seismic waveforms, particularly for small-magnitude events, in which travel time picks are relatively more prone to errors than for larger events. Yet, a precise modeling of waveforms at regional distances requires an accurate model of the crust and upper mantle along the propagation path between source and receiver.

RESEARCH ACCOMPLISHED

Forward Modeling

In order to explore the sensitivity of each phase we computed synthetics for a variety of distances using different crust and upper mantle models, including PREM (Dziewonski and Anderson, 1981), SNA (Grand and Helmberger, 1986), TNA (Grand and Helmberger, 1986), ECH (Zhao et al., 1991), and WCH (Beckers et al., 1999). Differences between these results point to sensitivity on the parts of these phases to distinct parts of the models' structure. Figure 5 shows an expanded comparison of waveforms produced using the different models for a single epicentral distance.

Figure 6 shows differences in waveform features to be expected from structural variations within China alone. The models at upper right were produced by Mangino et al. (1999) by modeling receiver functions for structure beneath stations of the China Digital Seismographic Network. The models differ primarily in the lower crust. One can see from the synthetics at left that these model differences are reflected by differences in the S coda, largely in SsPmP and SPL, for the distance range 30°-50°. These synthetics were produced for a 600-km deep event. This suggests that the relative timing of SsPmP-S and the phase and amplitudes of SPL phases are sensitive to the lower crust.

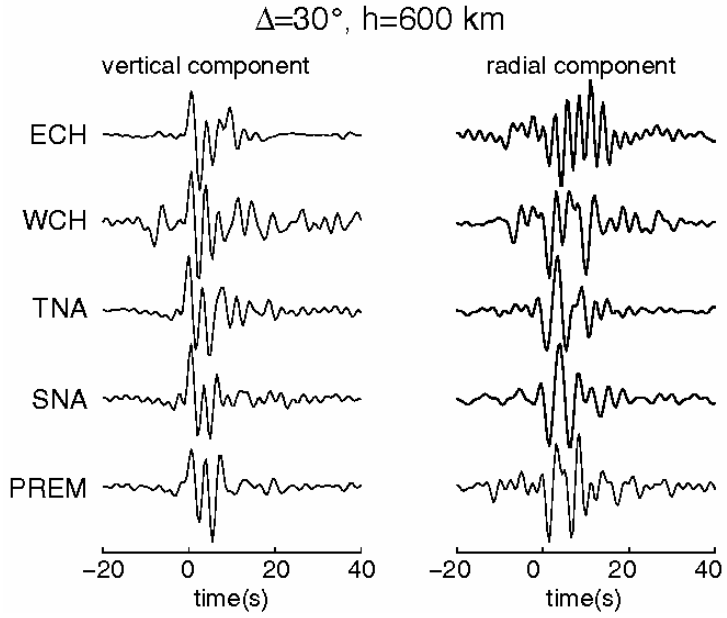
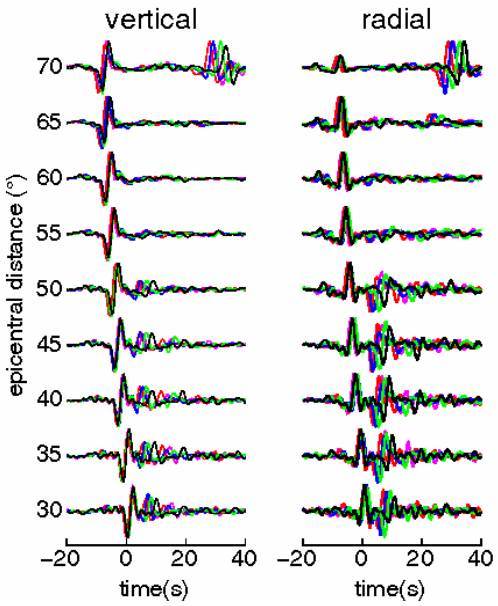


Figure 5. Comparison of synthetic seismograms computed using various Earth models for the same deep, double-couple source at an epicentral distance of 30°. Differences in the arrival times and amplitudes of S, Sp, SsPmP and SPL indicate those phases' sensitivity to structure near the receiver.

Inverse Modeling

Our modeling process is controlled by a global optimization algorithm called Very Fast Simulated Annealing (VFSA) (e.g., Sen and Stoffa, 1995). Simulated annealing (SA) is analogous to the natural process of crystal annealing when a liquid gradually cools to a solid state. The SA technique starts with an initial model m_0, with associated error or energy $E(m_0)$. It draws a new model m_{new} from a flat distribution of models within the predefined limits. The associated energy $E(m_{new})$ is then computed and compared against $E(m_0)$. If the energy of the new state is less than the energy of the initial state, the new model is accepted and it replaces the initial model. However, if the energy of the new state is higher than the initial state, m_{new} is accepted with the probability of $\exp\left(\left(E(\mathbf{m}_{new})-E(\mathbf{m}_0)\right)/T\right)$, where T is a control parameter called temperature. This rule of probabilistic acceptance (called the Metropolis rule) allows SA to escape local minima. The process of model generation and acceptance is repeated a large number of times with the annealing temperature gradually decreasing according to a predefined cooling schedule. A variant of SA, called Very Fast Simulated Annealing (VFSA) speeds up the annealing process by drawing new models from a temperature dependent Cauchy-like distribution centered on the current model. This change with respect to SA has two fundamental effects. First, it allows for larger sampling of the model space at the early stages of the inversion (when "temperature" is high), and much narrower sampling in the model space as the inversion converges and the temperature decreases, while still allowing the search to escape from local minima. Second, each model parameter can have its own cooling schedule and model-space sampling scheme. VFSA therefore allows for individual control of each parameter and the incorporation of a priori information. The model is parameterized in terms of layers, in which Vp, Vs, density, and layer thickness are free parameters.



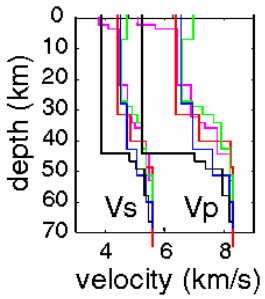


Figure 6. Synthetic seismograms computed for various receiver function models of the crust and upper mantle beneath China (models from Mangino et al., 1999). The primary differences between the seismograms are in the S coda, including SsPmP and SPL, which indicates these phases are highly sensitive to distinguishing structural details of these models.

In seismic inversion, more than one model can often explain the observed data equally well and trade-offs between different model parameters are common. It is therefore important not only to find a single, best-fitting solution but also to find the uncertainty and level of uniqueness of that solution. A convenient way to address these issues is to cast the inverse problem in a Bayesian framework (e.g., Tarantola, 1987; Sen and Stoffa, 1995) in which the posterior probability density function (PPD) is the answer to the inverse problem. "Importance sampling" based on a Gibbs sampler or a Metropolis rule (Sen and Stoffa, 1998) can be used effectively to evaluate the necessary multi-dimensional integrals and to estimate PPD, posterior mean, covariance and correlation matrices. The posterior covariance and correlation matrices quantify the trade-off between different model parameters. Sen and Stoffa (1995) showed that multiple VFSA runs with different random starting models could be used to sample models from the most significant parts of the model space. This "poor man's" importance sampling, which is computationally efficient, results in estimates that are fairly close to the values obtained by theoretically-correct Gibbs sampling.

Example of an Application to Data from the China Digital Seismographic Network

Figure 7 shows the result of modeling radial and vertical records from station BJT of the 9/28/1994 event in Indonesian. Subjective choices must be made in the modeling about which parts of the seismogram to try to fit. In regions with strong lateral variations or anisotropy, it may be that no single 1D model will predict all the phases adequately. Requiring the modeling to try to fit each phase similarly will result in a model that does not predict any single phase well. Given the sampling produced by the various phases, we tried to prioritize fits in the following order: SPL, SsPmP, SV, and Sp. Given the broad sampling and lateral averaging performed by SPL we believe that the single 1D model that fits SPL best will be the most useful for locating earthquakes regionally. SsPmP also has a broad sample and constrains Vp, so it's second in priority. This priority order reflects a starting point—an initial preference—and will be evaluated as a strategy.

To implement this strategy we successively try to fit broader time windows of the data waveforms. 8 15 shows the results of 600 iterations in which only the window between 815 s and 860 s is evaluated for correlation at each iteration. The BJT receiver function model of Mangino et al. (1999) is shown for comparison, although it is not a "reference" or "starting" model in any sense. In our procedure we specify the search limits (also shown in Figure 8) and the first candidate model is chosen randomly. Figure 9 shows an attempt to fit a broader window that includes SV and Sp. Differences between the two final models shown in Figures 7 and 8 are again concentrated in the lower crust, between 30 and 50 km depth. Figure 9 shows the result of a 600-iteration run to model records from BJT of the 11/15/1994 Indonesia event, in which the time interval fit is restricted to include SsPmP and SPL. Figure 10 shows the results of a 600-iteration run to fit a broader window, as in Figure 8. Figure 11 shows results for a third event, also recorded at BJT. Figure 12 compares the models produced for the region containing BJT with Mangino et al.'s (1999) receiver function model, in the context of the imposed search limits.

CONCLUSIONS AND RECOMMENDATIONS

For the optimization example shown in Figure 8, depth zones A, B, and C in Figure 13 correspond to parameter correlations indicated by the same labels in Figure 14. Note that the thin, shallow layers in A are characterized by significant off-diagonal cross-correlations (trade-offs) with other parameters. This indicates that the data do not constrain these layers well. Also, the symmetric "variances" about the mean (actually 1 standard deviation) do not contain the best-fitting model at this depth, pointing to the non-linearity of the inverse problem. We defined the prior to be Gaussian, so the computed (posterior) variances are also symmetric, but the fact that the best-fitting model lies outside this distribution suggests that the true distribution is skewed. Zone B, in contrast, contains a low-velocity zone in Vs that appears to be well-constrained (Figure 13). There is no corresponding Vp low-velocity zone.

Results for Zone C suggest that the data do not place strong constraints on the model parameters at these depths, on the one hand. However, since the best-fitting model is pegged against the search limits for both Vp and Vs, we will widen the search limits and perform a greater number of VFSA iterations to explore this zone further.

REFERENCES

Baag, C.-E. and C.A. Langston, Shear-coupled PL, *Geophys. J. R. Astr. Soc.*, 80, 363-385, 1985.

Beckers, J., S. Schwartz, and T. Lay, *Geophys. J. Int.*, 119, 574-594, 1994

Douglas, A. (1967). Joint hypocentral determination, *Nature*, 214, 47-48.

Dziewonski, A. M., Anderson, D. L., Preliminary reference Earth model, *Phys. Earth. Planet. Int.*, 25, p. 297-356, 1981.

Fan, G. and T. Wallace (1991). The determination of source parameters for small earthquakes from a single, very broadband seismic station, *Geophys. Res. Lett.*, 18, 1385-1388.

Frazer, L.N., Synthesis of shear coupled PL. *Ph.D. thesis*, Princeton University, 54 pp., 1977.

Frohlich, C., and J. Pulliam (1999). Single-station location of seismic events: A review, and a plea for more research, *Phys. Earth Planet. Int.*, 113, 277-291.

Goldstein, P., and D. Dodge (1999). Fast and accurate depth and source mechanism estimation using P-waveform modeling: A tool for special event analysis, event screening, and regional calibration, *Geophys. Res. Lett.*, 26, 2569-2572.

Grand, S.P., and D. Helmberger, Upper mantle shear structure of North America, Geophys. *J. R. Astr. Soc.*, 76, 399-438, 1984

Jimenez, E., M. Cara, and D. Rouland (1989). Focal mechanisms of moderate-size earthquakes from the analysis of single-station three-component surface-wave records, *Bull. Seism. Am.*, 79, 955-972.

Jordan, T.H., and L.N. Frazer, Crustal and upper mantle structure from Sp phases, J. Geophys. Res., 80, 1504-1518, 1975.

Kedrov, O.K., and V.M Ovtchinnikov (1990). An on-line analysis system for three-component seismic data: Method and preliminary results, *Bull. Seism. Am.*, 80, 2053-2071.

Kim, S. G. and Z. Wu (1997). Uncertainties of seismic source determination using a 3-component single station, *J. Phys. Earth*, 45, 1-11.

Langston, C.A., The SsPmP phase in regional wave propagation, *Bull. Seism. Soc. Am*., 86, 133-143, 1996.

Magotra, N., N. Ahmed and E. Chael (1987). Seismic event detection and source location using single-station (three-component) data, *Bull. Seism. Soc. Am.*, 77, 958-971.

Mangino, S., K. Priestley, and J. Ebel, The receiver structure beneath the China Digital Seismograph Network Station, *Bull. Seism. Soc. Am.*, 89, 1053-1076, 1999

National Research Council (1997). Research Required to Support Comprehensive Nuclear Test Ban Treaty Monitoring, National Academy Press, Washington, D. C., 139 pp.

Oliver, J., On the long period character of shear waves, *Bull. Seism. Soc. Am.*, 51, 1-12,1961.

Roberts, R. G., A. Christoffersson and F. Cassidy (1989). Real-time event detection, phase identification and source location estimation using single-station three-component seismic data, *Geophys. J.*, 97, 471-480.

Saari, J. (1991). Automated phase picker and source location algorithm for local distances using a single three-component seismic station, *Tectonophysics*, 189, 307-315.

Sen, M., and P. L. Stoffa, 1995, Global Optimization Methods in Geophysical Inversion, Elsevier Science Publishing Company, The Netherlands.

Tarantola, A., Inverse Problem Theory: Methods for Data Fitting and Model Parameter Estimation, 613 pp., Elsevier, Amsterdam, 1987.

Walter, W. R. (1993). Source parameters of the June 29, 1992 Little Skull Mountain earthquake from complete regional waveforms at a single station, *Geophys. Res. Lett*., 20, p. 403-406.

Zhao, L.-S., D. Helmberger, and D.V. Harkrider, *Geophys. J. Int.*, 105, 713-730, 1991.

Zhao, L.-S. and C. Frohlich. Teleseismic body waveforms and receiver structures beneath seismic stations, *Geophys. J. Int.*, 124, 525-540, 1996.

Zhu, L. and D.V. Helmberger (1996). Advancement in source estimation techniques using broadband regional seismograms, *Bull. Seism. Soc. Am.*, 86, 1634-1641.

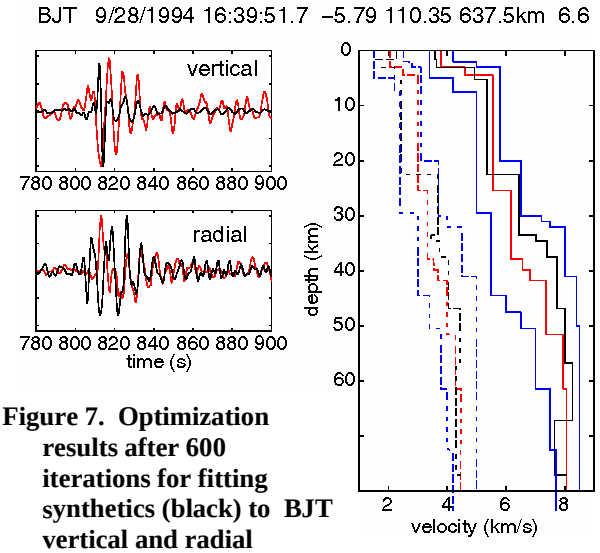


Figure 7. Optimization results after 600 iterations for fitting synthetics (black) to BJT vertical and radial records (red) of the 9/28/1994 event, using the time interval 815-860 s. Best-fitting model (black), search bounds (blue), and receiver function model by Mangino et al. (1999)

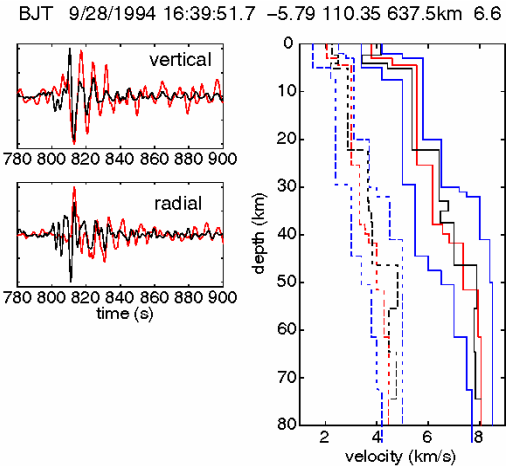


Figure 8. Same as in Figure 7 except that the interval 800-860 s was used in the waveform fitting.

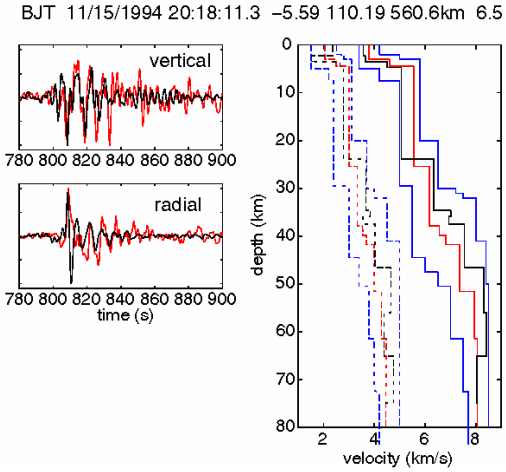


Figure 10. Same as in Figure 9 except that the interval 800-860 s was used in the waveform fitting.

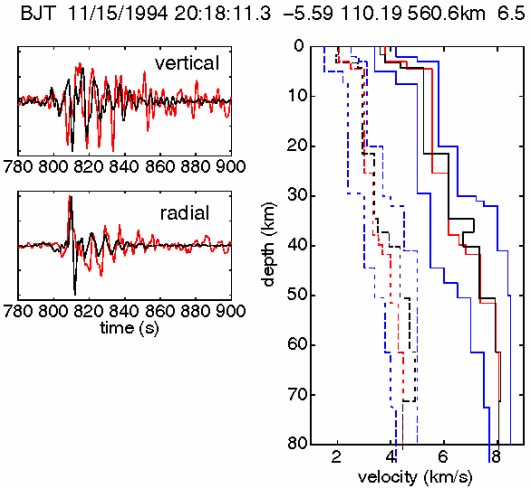


Figure 9. Optimization results after 600 iterations for fitting synthetics (black) to BJT vertical and radial records (red) of the 11/15/1994 event, using the time interval 815-860 s. Best-fitting model (black), search bounds (blue), and receiver function model by Mangino et al. (1999) (red).

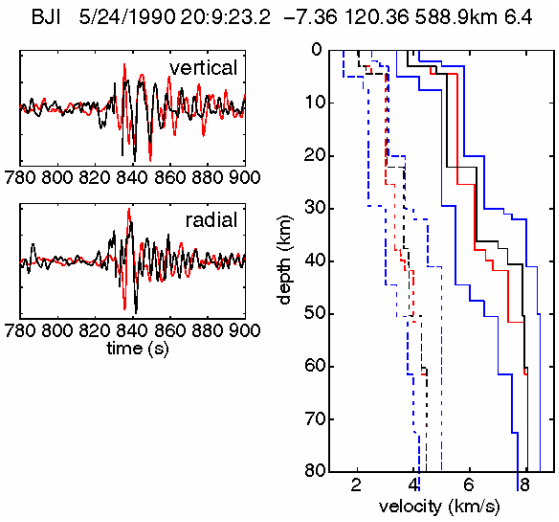


Figure 11. Optimization results after 400 iterations for fitting synthetics (black) to BJT vertical and radial records (red) of the 5/24/1994 event, using the time interval 835-870 s. See Figure 9 for other details.

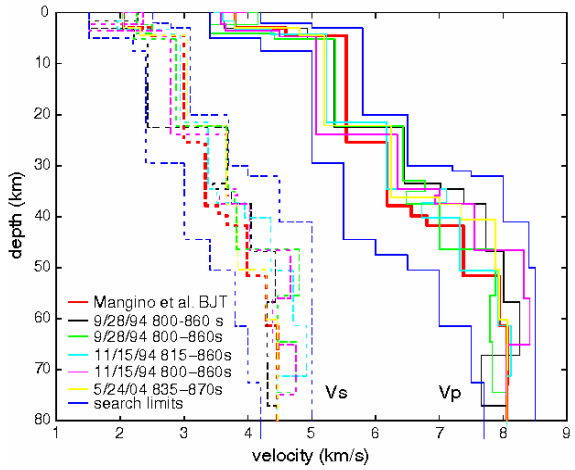


Figure 12. Comparison of models for the crust and upper mantle in the vicinity of station BJT resulting from waveform fits to various data (see legend), Mangino et al.'s (1999) receiver function model (red), and the simulated annealing search limits (blue).

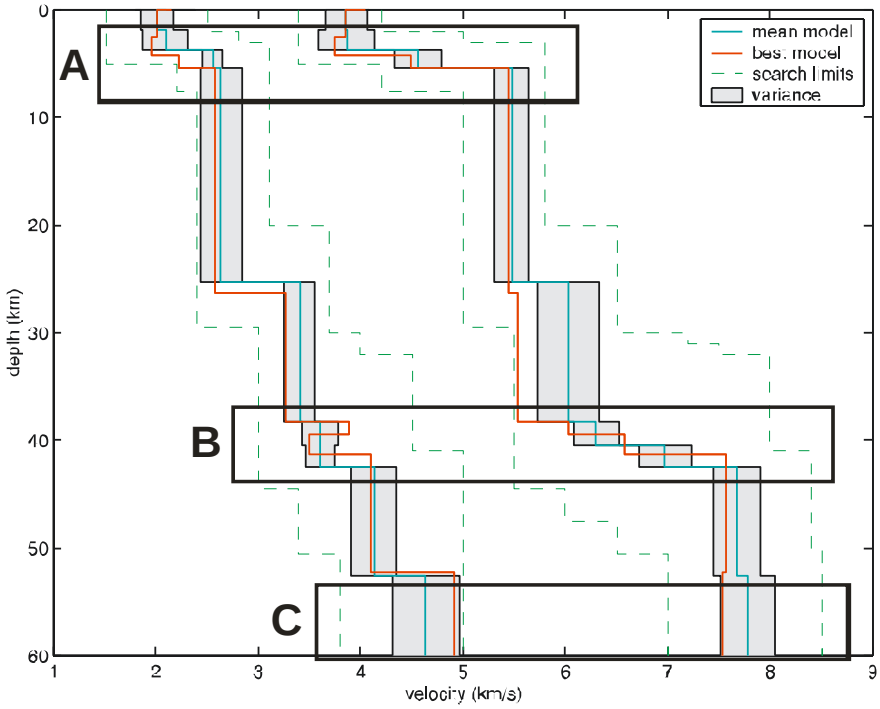


Figure 13. Mean (cyan) and best-fitting (red) models and variance of the optimization run shown in Figure 8. Search limits imposed by the operator at the outset are shown in green. Variances are only shown for Vs (left) and Vp (right).

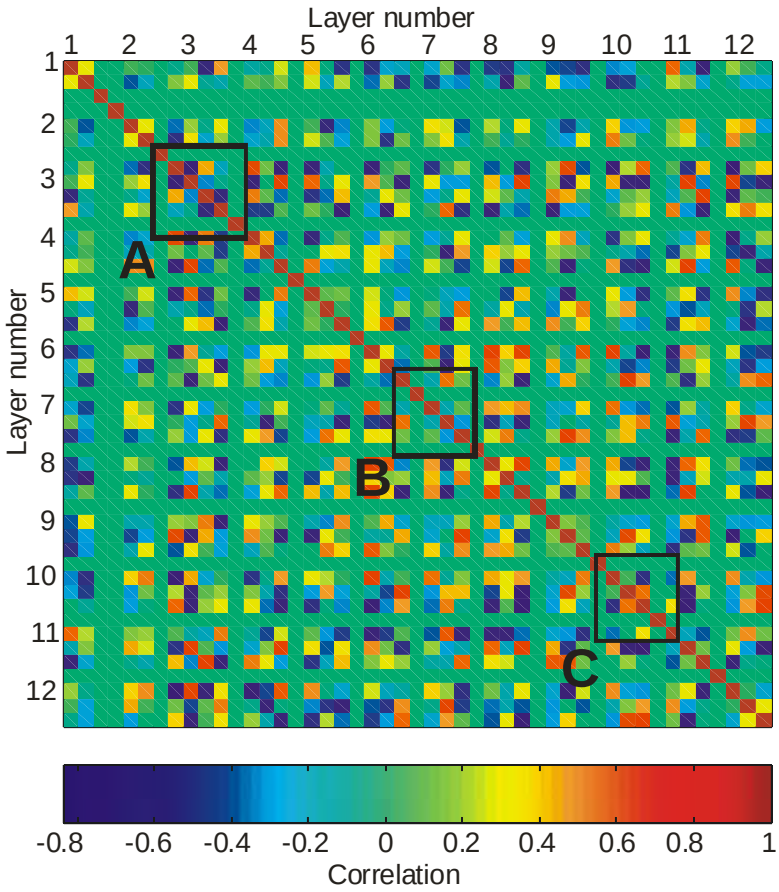


Figure 14. Parameter correlations computed for the optimization run shown in Figure 15. There are four independent parameters: Vp, Vs, layer thickness, and density, repeated in that order for 12 layers. The total of 48 parameters is shown here in color (left) and with a modified grayscale, in which zero correlation is white and perfect positive and negative correlations are both black (right).

SEISMIC DATA FOR NUCLEAR EXPLOSION MONITORING IN THE ARABIAN PENINSULA

Arthur J. Rodgers[1] and Abdullah M. S. Al-Amri[2]

Lawrence Livermore National Laboratory[1] and King Saud University[2]

Sponsored by National Nuclear Security Administration
Office of Nonproliferation Research and Engineering, and
Office of Nonproliferation and International Security
Office of Defense Nuclear Nonproliferation

Contract No. W-7405-ENG-48[1], DE-FC03-01SF22418[2]

ABSTRACT

Results from the third and final year of our project (ROA01-35) to collect seismic event and waveform data recorded in and around the Arabian Peninsula are reported in this paper. This effort involved several elements. We installed two temporary broadband stations in the United Arab Emirates, funded by the National Nuclear Security Administration (NNSA), Office of Nonproliferation and International Security (NA-24). Working with King Abdulaziz City for Science and Technology and King Saud University data was collected and analyzed from the Saudi Arabia National Seismic Network, which consists of 38 digital three-component stations (27 broadband and 11 short-period). Ongoing collaboration with the Kuwait Institute for Scientific Research, which runs the Kuwait National Seismic Network, has also helped this project.

We will present the data collected under these efforts including integration of raw data into the Seismic Research Database, operated by Lawrence Livermore National Laboratory (LLNL), and preliminary analysis of event locations and source parameters, and inference of earth structure.

OBJECTIVES

The objective of this project was to gather seismic event, arrival and waveform data for nuclear explosion monitoring calibration purposes in the Arabian Peninsula. Over the past three years we have worked with institutions in the region to gain access to unique data sets from permanent and temporary deployments of seismic instrumentation.

Data was collected and loaded into the LLNL Seismic Research Database. Organization and archival of these data facilitates analysis for nuclear explosion monitoring calibration research, such as station siting, noise studies, regional phase signal propagation and detection modeling, event source parameters (e.g., depth, moment and focal mechanism) and Earth structure estimates (e.g. travel times, surface wave group velocities, receiver functions, full waveforms).

RESEARCH ACCOMPLISHED

This project provided support to collect data in the Arabian Peninsula for nuclear explosion monitoring calibration purposes. Data was archived at LLNL and loaded into the Seismic Research Database. This is an ORACLE database containing waveform and parameter data, based on the NNSA schema. In the following sections we describe the various data sets we have collected.

Saudi Arabia

The Saudi Arabian National Digital Seismic Network (SANDSN) is operated by King Abdulaziz City for Science and Technology (KACST). The network consists of 38 stations (27 broadband and 11 short-period) and is described by Al-Amri and Al-Amri (1999). Figure 1 shows the configuration of the SANDSN stations. The network began operation in May 1998 and records continuous waveform data. Data is collected and events are detected and located with the Boulder Real Time Technologies (BRTT) Antelope software. Data are digitized at the stations and telemetered to KACST. All data is recorded at 100 samples/sec.

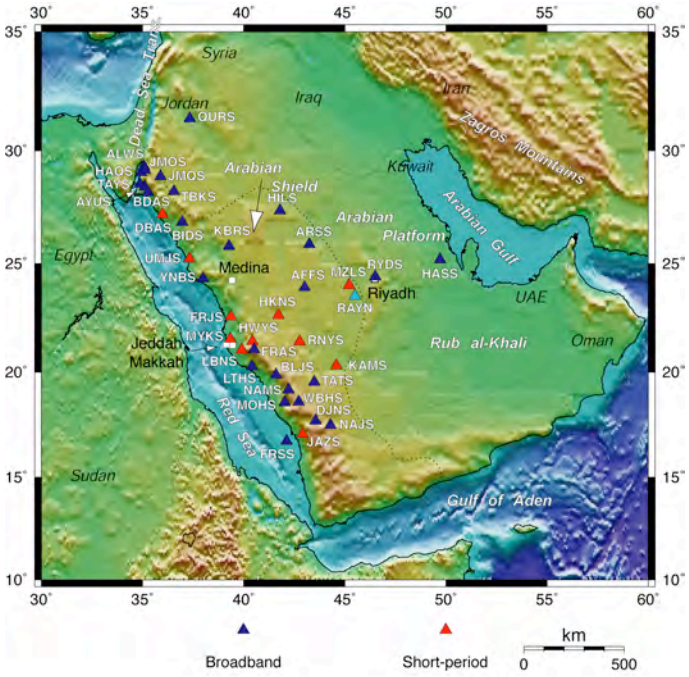


Figure 1. Stations of the Saudi Arabian National Digital Seismic Network: broadband (blue) and short-period (red) sites.

We obtained event segmented waveform data for local, regional and teleseismic events. Figure 2 shows the distributions of events.

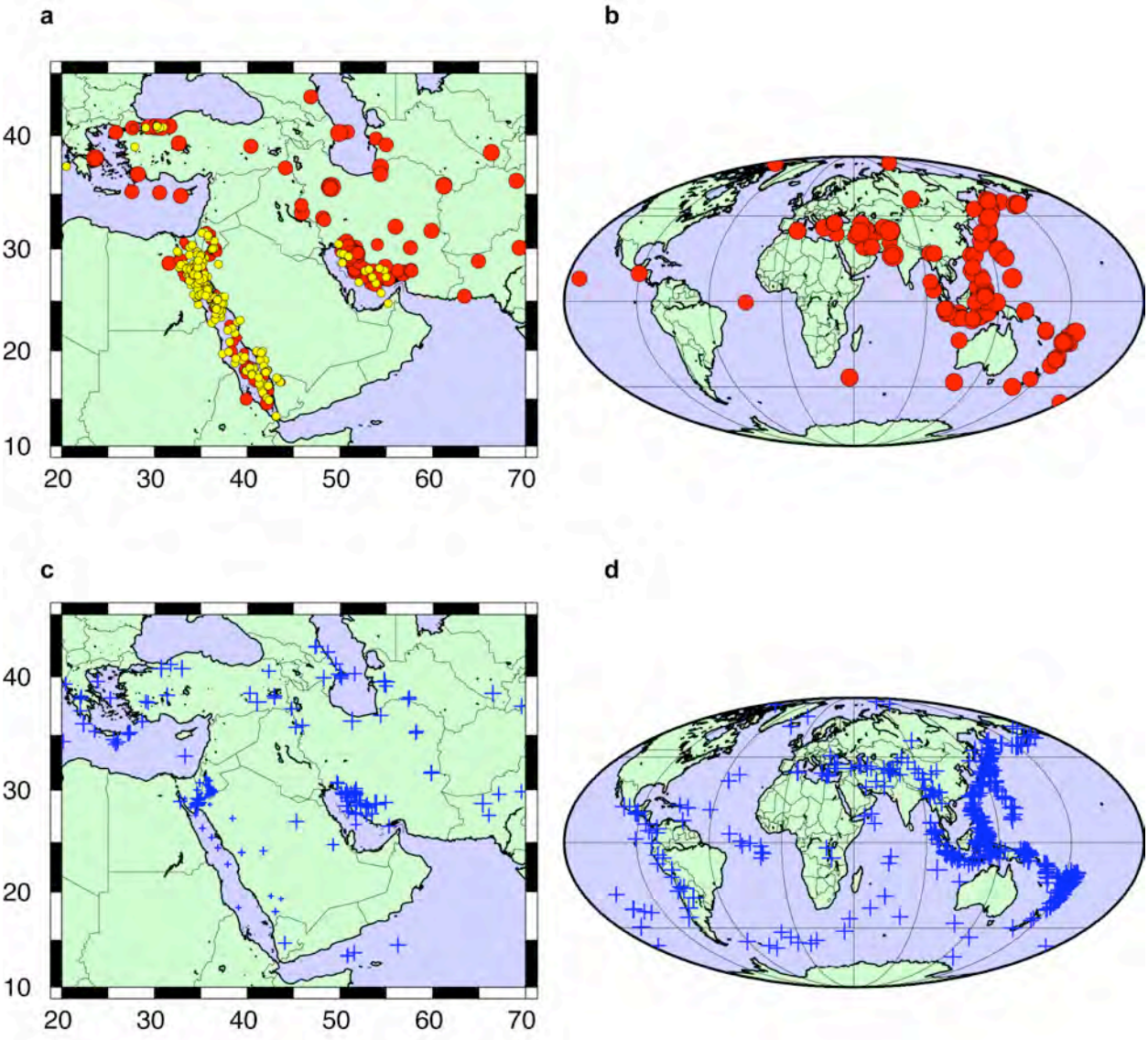


Figure 2. Events collected from the Saudi Arabian National Digital Seismic Network: (a) regional and (b) large global (M≥5) events loaded into the LLNL Seismic Research Database; (c) regional and (d) large global (M≥5) not yet loaded. Red circles and blue crosses are scaled to event magnitude, yellow circles indicate events with only a KACST local magnitude.

The SANDSN records very high-quality waveform data. Figure 3 shows waveforms we've obtained for station HILS and the associated regional events. For simplicity, we're only showing the events with body-wave magnitude, m_b, greater than or equal to 5.0. Note the extended dispersed surface waves for these paths crossing the deep sediments of the Arabian/Persian Gulf and Arabian Platform.

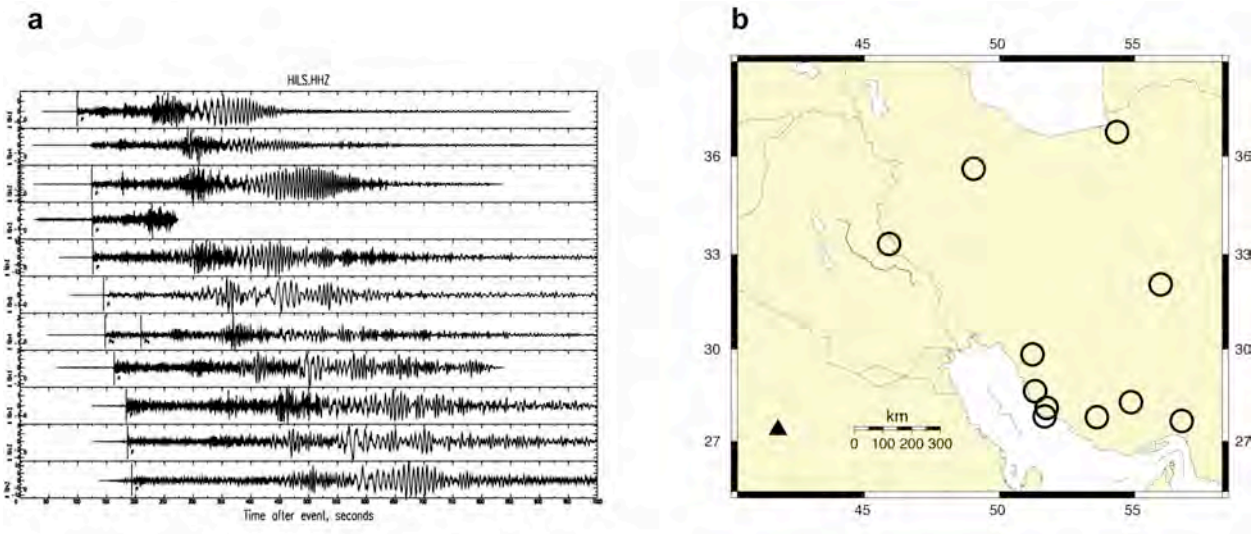


Figure 3. (a) Vertical component broadband (unfiltered) waveforms recorded at station HILS for (b) events in the Iranian Plateau.

Kuwait

The Kuwait Institute for Scientific Research (KISR) operates the Kuwait National Seismic Network (KNSN). This network consists of eight three-component stations (one broadband and seven short-period; see Al-Awadhi and Midzi, 2001), shown in Figure 4. The KNSN began operating in March 1997. The stations operate in triggered mode and transmit data when short/long term average levels exceed a pre-set threshold of six. Data are sampled at 100 samples/second with 24-bit digitization and communicated to KISR in Kuwait City via radio telemetry. An event is declared when three stations trigger within 30 seconds. The data for declared events are transferred to a PC and analyzed with the SEISAN software package, including location and magnitude estimation.

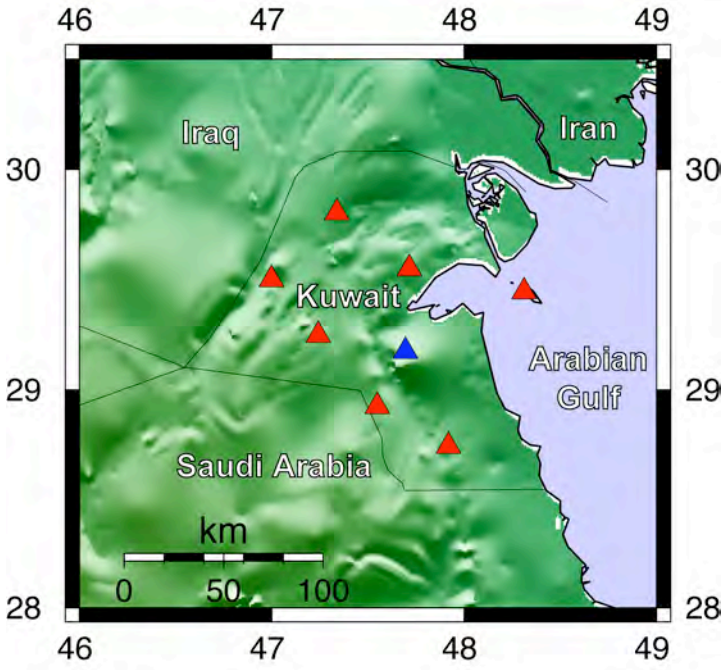


Figure 4. Stations of the Kuwait National Seismic Network: broadband (blue) and short-period (red) sites.

We obtained event segmented waveform data for local, regional and teleseismic events. Figure 5 shows the distributions of events. Seismic events in Kuwait are clustered near some, however not all, oil production regions. The nature of these events remains to be determined in more detail. It is important to note that events in Kuwait can approach magnitude 4.0 and can be observed at regional distances.

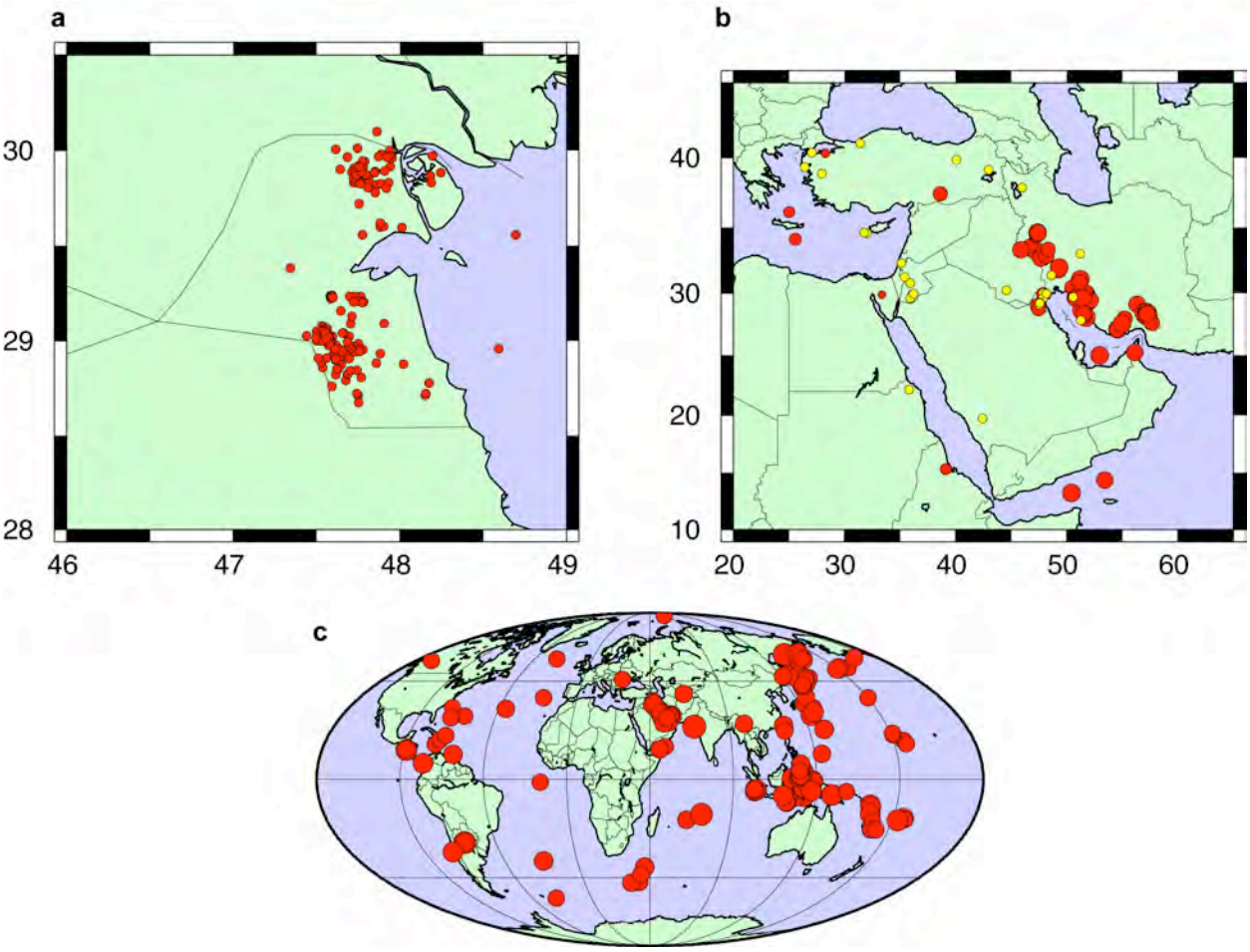


Figure 5. Events collected from the Kuwait National Seismic Network: (a) local; (b) regional and (c) teleseismic. Yellow circles in (b) indicate KISR locations.

United Arab Emirates (UAE)

In May 2003, LLNL in cooperation with United Arab Emirates University (UAEU) deployed two broadband stations in the UAE. The deployment specifics are detailed in Rodgers et al. (2003a). A team from the Geology Department serviced the stations. Figure 6 shows the site locations. These stations recorded continuously from May 2003 – April 2004. Event segments were extracted and loaded into the LLNL database. These stations were located within near-regional distances of the seismically active Zagros Mountains. Figure 7a shows regional and teleseismic events recorded at the stations.

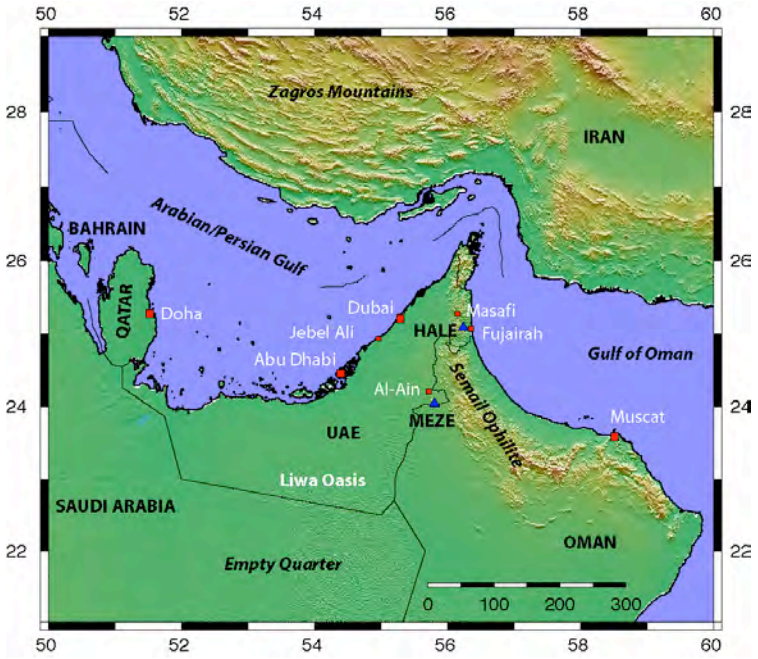


Figure 6. Map of the UAE showing the locations of two LLNL-UAEU seismic stations: MEZE and HALE.

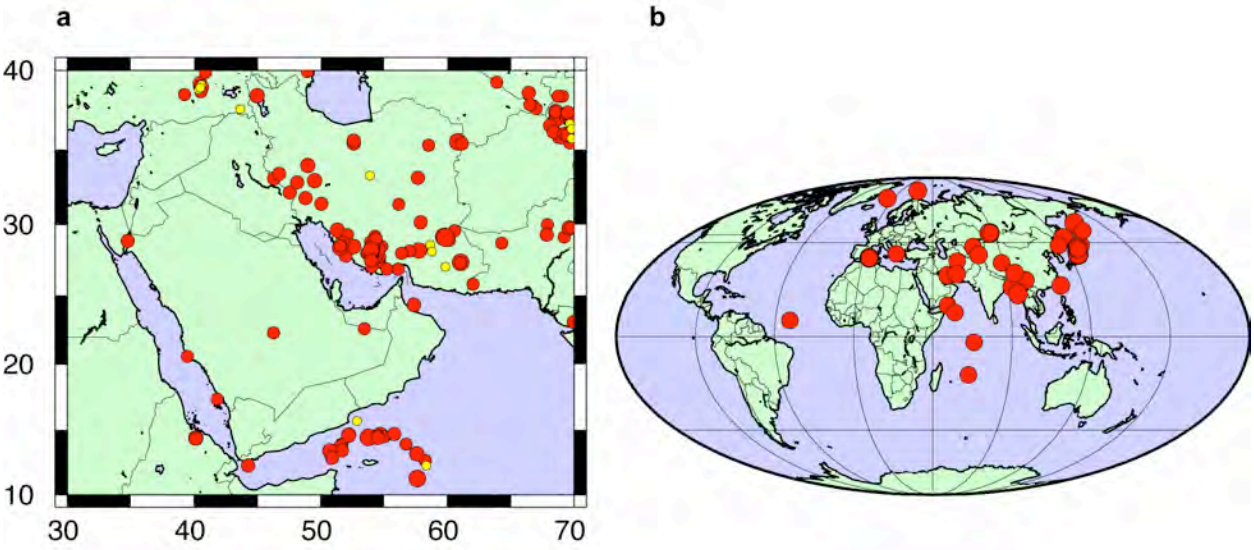


Figure 7. Events collected from the LLNL-UAEU stations: (a) regional and (b) teleseismic. Yellow circles in (b) indicate events with only local magnitudes.

The LLNL-UAEU stations provide a unique opportunity to sample local seismicity in the Musadam Peninsula. These stations were the first broadband systems to be deployed in the UAE. We will use these data to search for local events. Preliminary investigations found a local event, shown in Figure 8. Also shown in the Figure 8 is the focal mechanism of the March 11, 2002 Masafi earthquake. This event had a moment magnitude, M_W of 4.85 and was widely felt in the northern Emirates.

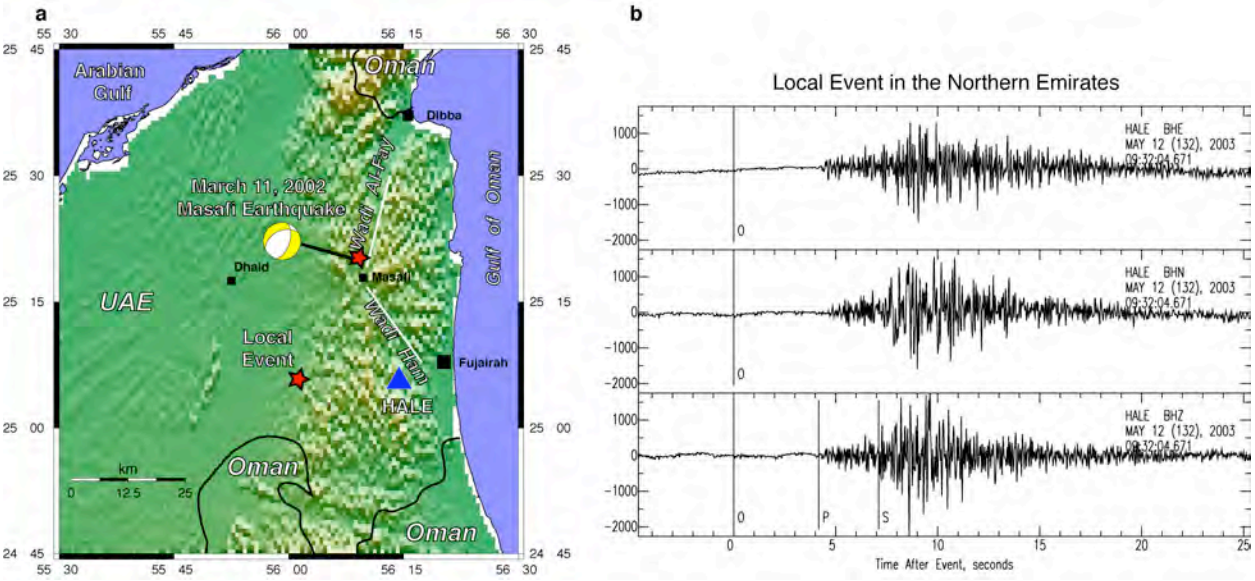


Figure 8. (a) Map of the northern Emirates showing our station HALE (blue triangle) and the estimated location of a local event (red star). Also shown is the focal mechanism of the March 11, 2002 Masafi Earthquake (M_W 4.85) and the two major faults cutting through the region. (b) The waveforms from the May 12, 2003 local event.

Regional Crustal Structure

We used data collected by this project to estimate crustal structure in the region. These efforts involve Pnl waveform modeling and joint inversions of surface wave dispersion and receiver function. Figure 9 compares estimates of crustal structure from various studies. We are able to resolve the deep sediments of the Arabian Gulf, as well as the bulk crustal velocities and thickness (e.g. Pnl waveform modeling and receiver function results). These models are compared to previous results for the Arabian Platform (Rodgers et al., 1999, 2003b) and a recent result for the Zagros Mountains (Hatzfeld et al., 2003).

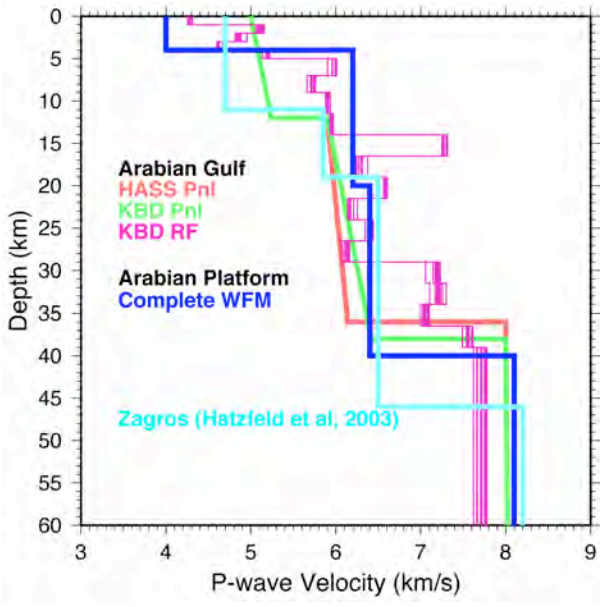


Figure 9. Comparison of crustal structure in the Arabian Gulf, Arabian Platform and Zagros Mountains (Hatzfeld et al., 2003).

CONCLUSIONS AND RECOMMENDATIONS

The data collected under this effort is valuable for calibrating wave propagation in the Arabian Peninsula and adjacent regions. When data are loaded into the LLNL database, they are automatically associated with other origins and waveforms from the same event. This allows for data collected from all sources to be accessible to the researcher (e.g. GSN, PASSCAL, IMS, national networks, other deployments).

ACKNOWLEDGEMENTS

This project benefited from several key individuals at various institutions. Pat Lewis and Don Rock facilitated installations of seismic equipment in Jordan, Saudi Arabia and the UAE. Stan Ruppert, Doug Dodge and Terri Hauk maintain the LLNL Seismic Research Database, greatly facilitating the use of the data collected by this and other projects.

We are grateful to Dr. Tariq Al-Khalifah of KACST for facilitating access to SANDSN data through KACST projects. Dr. Abdullah Al-Enezi of KISR provided access to KNSN data. Dr. Abdel-Rahman Fowler and colleagues at UAEU provided valuable assistance for the UAEU deployment.

REFERENCE(S)

Al-Amri, M. S. and A. M. Al-Amri (1999). Configuration of the Seismographic networks in Saudi Arabia, *Seism. Res. Lett.*, 70, 322-331.

Al-Awadhi, J., and V. Midzi (2001). The Seismicity of the Kuwaiti Subregion, *Seismo. Res. Lett.,* 72, 462-473.

Hatzfeld, D., M. Tartar, K. Priestley and M. Ghafory-Astinany (2003). Seismological constraints on the crustal structure beneath the Zagros Mountain belt (Iran), *Geophys. J. Int.,* 155, 403-410.

Rodgers, A., W. Walter, R. Mellors, A. M. S. Al-Amri and Y.-S. Zhang (1999). Lithospheric structure of the Arabian Shield and Platform from complete regional waveform modeling and surface wave group velocities, *Geophys. J Int*., 138, 871-878.

Rodgers, A., J. P. Lewis and A. R. Fowler (2003a). A Broadband Seismic Deployment in the United Arab Emirates, Lawrence Livermore National Laboratory Informal Document, UCRL-ID-153713.

Rodgers, A., D. Harris, S. Ruppert, J. P. Lewis, J. O'Boyle, M. Pasyanos, A. Q. Fandi Abdallah, T. Al-Yazjeen and A. Al-Gazo (2003b). A broadband seismic deployment in Jordan, *Seism. Res. Lett.*, 74, 374-381.

HIGH-RESOLUTION TOMOGRAPHIC MAPPING OF REGIONAL PHASE Q IN THE MIDDLE EAST

Eric A. Sandvol[1], Jiakang Xie[2], Brian J. Mitchell[3]

University of Missouri[1], Columbia University[2], and St. Louis University[3]

Sponsored by National Nuclear Security Administration
Office of Nonproliferation Research and Engineering
Office of Defense Nuclear Nonproliferation

Contract No. DE-FC52-03NA99518[1], DE-FC52-03NA99519[2], DE-FC52-03NA99520[3]

ABSTRACT

To develop reliable discriminants for a given region, it is essential that source, station, and path effects be isolated. This is even more critical for paths through a region such as the Middle East, where both crustal and uppermost mantle attenuation are very high. The most efficient method for developing path corrections for potential discriminants is to construct a frequency dependent Q model for the corresponding regional seismic phases Pn, Pg, Sn, and Lg. We have collected waveform data from a wide variety of sources in the Middle East. A large number of digital seismograms (approximately 8,000) yield dense path coverage for all four regional seismic phases throughout most of the northern portion of the Arabian plate as well as the Antolian and Iranian plateau regions. These waveform data are collected from PASSCAL experiments in Turkey, Saudi Arabia, and the Caspian Sea region and from national networks, ground station network (GSN) stations, and various other permanent and temporary sites. This dense coverage should dramatically improve the resolution of the Q tomography. Moreover, it allows the bias in Q measurements to be minimized by using methods that are more reliable, but require restrictive path geometries. The tomography will yield high-resolution maps of laterally varying Lg Q_0 and h (Lg Q at 1 Hz and its power-law frequency dependence, respectively) as well as Q_{Pg} in the Middle East. This study will also yield regionalized Q models for Pn and Sn.

Our strategy is to begin in regions where we have very dense two station ray paths; therefore, we have chosen to begin our focus on the eastern Anatolian plateau and northern Arabian plate where we have data from the Kandilli Observatory and Earthquake Research Institute (KOERI), Jordanian Seismic Observatory, and from the temporary PASSCAL network in eastern Turkey (ETSE). This region has been shown to be a region of anomalously high Lg and Sn attenuation and blockage. Our Q-models will be used to quantify the level of attenuation within the Anatolian plateau.

OBJECTIVE

The objective of this study is to obtain laterally varying Q models for multiple regional waves, including Lg, Pg, Pn and Sn, for the Middle East. We are developing Q models that have the highest possible lateral resolution. For some waves such as Lg and Pg, the resulting Q model will be in the form of a tomographic Q map; for other waves such as Sn, the resulting Q models may be region-specific--we will divide the Middle East into several sub-regions of constant Q. Blockage effects will be represented by low effective Q values in the models.

The difficulty associated with Q measurements

It is well known that the attenuation rate of regional waves, including the high-frequency Lg, Pg, Sn and Pn and the lower-frequency surface waves, is highly variable over major continents. Reliable knowledge of the lateral variation in regional wave attenuation rate, or its inverse, Q, is extremely important for event detection and identification in the nuclear monitoring program. The preferred way to acquire this knowledge is to conduct tomographic mapping of regional wave Q. However, in contrast to the wide success in seismic velocity tomography since the 1970s, there has been relatively little progress in Q tomography. The main obstacle is the difficulty in obtaining reliable measurements of Q: the observed amplitude of high-frequency waveforms is affected by a number of factors, including (1) possible non-isotropic source radiation patterns, (2) source spectra that may be grossly described by a seismic moment and a corner frequency; (3) geometrical spreading terms caused by the wave front expansion which, in complex 3D Earth structures, may cause focusing and defocusing; and (4) potential site responses caused by local structural complications under the seismic stations. Effects of these factors are difficult to correct, causing biases in Q measurement.

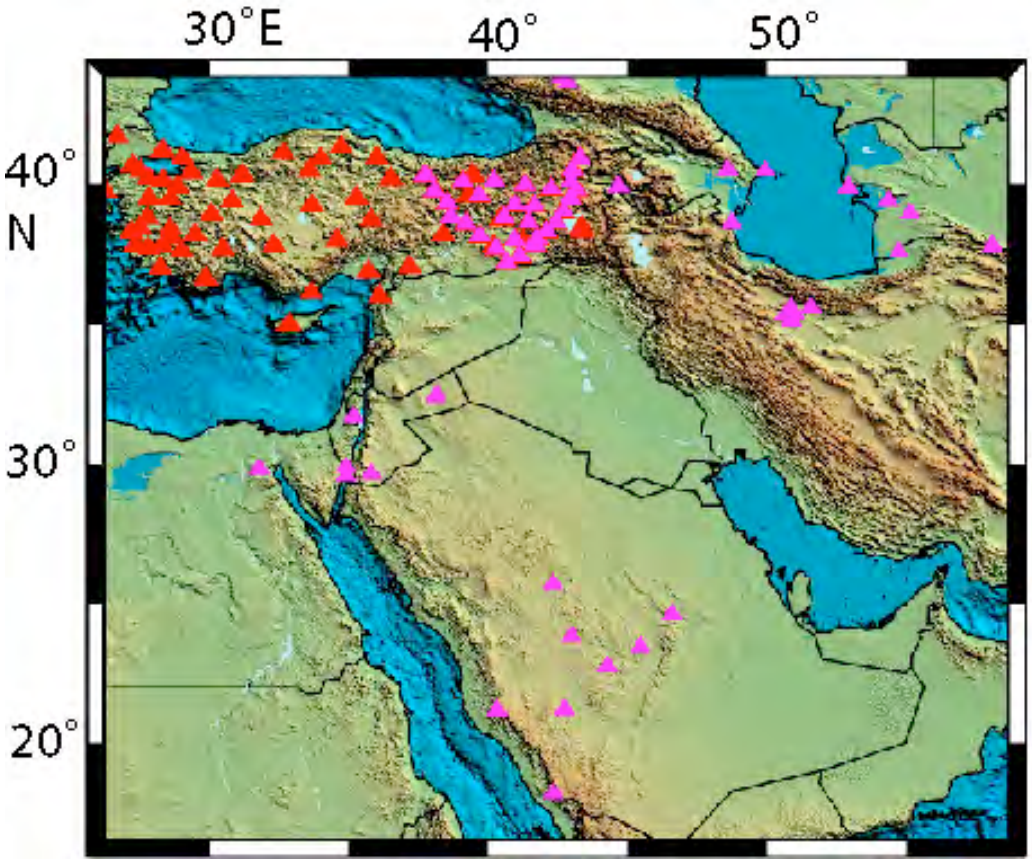


Figure 1. Stations for which we will have waveform data in the Middle East. Red triangles are stations for which we plan to acquire data; magenta triangles are those for which we already have waveform data.

The difficulty of precise Q measurement is clearly demonstrated by two examples involving the Lg phase. This first is given by Xie and Mitchell (1990), who lists eight published Lg Q models for the Basin and Range Province. The 1 Hz Lg Q (Q0) values in these models vary between 139 and 774, despite the area's being one of the best studied. The second is given by Fan and Lay (2003b), who list a number of previously and recently published models in Tibet. In these models, the Q0 for the same sub-region (i.e., southern or eastern Tibet) ranges between 60 and 400. Despite the difficulties, the problem of measuring Q using regional waves has been a rapidly evolving research topic. Recently, progress has been made on mapping laterally varying regional wave Q structure, particularly through Q tomography. There are two reasons for this progress: first, there is high demand from the scientific and nuclear monitoring community to acquire realistic Q models. Second, the digital seismic database has grown rapidly, permitting the use of methods for measuring Q that are more precise but require abundant data and/or a specific pattern of path geometries. In the following sections, we will briefly summarize the work of various researchers, including both the co-principal investigator's, on regional wave Q tomography.

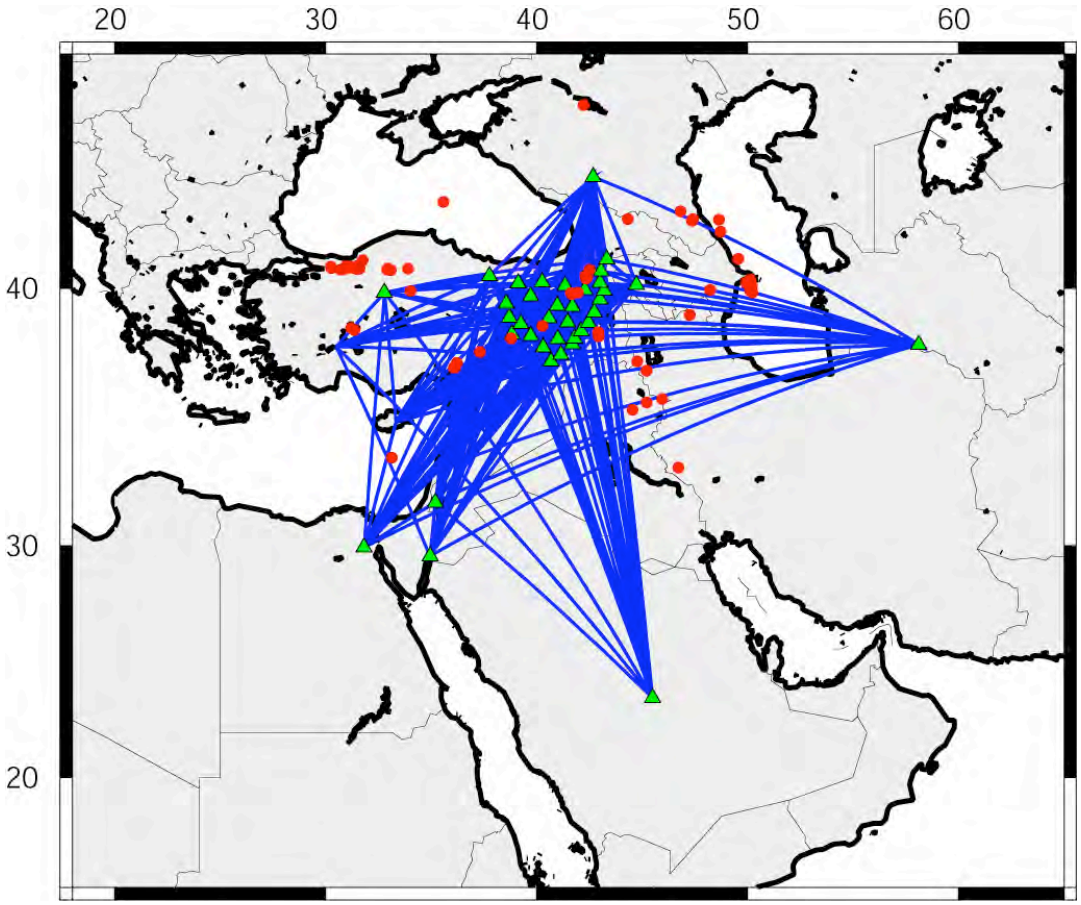


Figure 2. All existing two station paths for in the Middle East between 1999 and 2001. Given the excellent coverage in eastern Turkey we are beginning to calculate inter-station Q values for all of these paths except for those events with blocked Lg.

RESEARCH ACCOMPLISHED

Data Collection

A major component of this proposal is the acquisition and processing of new waveform data in the region. In order to successfully formulate a robust Q model for the four fundamental regional phases we need to collect and construct a large waveform database for the Middle East. Given the large regions within the Middle East that are not accessible for a variety of reasons, this will continue to be an ongoing problem that we will address.

We have made agreements with scientists in several countries for them to share data for the Middle East. These new databases will greatly improve the existing ray coverage, especially the two station path coverage**.** Most significantly, we have reached a collaborative agreement with Kandilli Observatory and Earthquake Research Institute (KOERI) to exchange software and waveform data for Turkey. The KOERI national network combined with the temporary PASSCAL networks give us dense and rather uniform data coverage for all of Anatolia and many of the surrounding regions (see Figure 1). This network is composed of 16 broadband stations and another 32 short period stations. These data will be combined to give excellent ray path coverage for the all of the Anatolian plateau and a large portion of the Eastern Mediterranean and northern Arabian plate. The data have all been digitized by either 16 or 24 bit digitizers and a substantial portion of the data has been visually inspected to confirm the existence or absence of the primary regional phases as a part of the Ph.D. thesis work of Rengin Gok.

Furthermore, we have made an agreement with Prof. Eid Tarazi to collaborate on analyzing waveform data from the Jordanian Seismological Observatory (JSO). The JSO consists entirely of short period single component instruments that are distributed throughout Jordan. We have begun to select waveforms for key events and analyze them during Professor Tarazi's visit to the University of Missouri. We are also continuing to work to establish a collaborative agreement with Syrian National Seismic Network (SNSN).

We are also collecting waveform data from a number of temporary seismic networks in the Middle East, including the St. Louis University western Turkey array. This array consisted of 4 broadband and 4 short period instruments running continuously for about a year starting in the fall of 2002. We are also utilizing the large waveform database from the 29-station ETSE broadband seismic network that ran from late 1999 to August 2001 and spanned much of Eastern Anatolia.

Methodology

We are using a number of methodologies to isolate the regional wave path attenuation (Q_0 and η) in the Middle East. In the following sections we outline each of the planned methods. Due to the rather non-uniform ray path coverage, we will need to apply different techniques depending upon the regional data availability. Figure 2 shows the two station paths that we have analyzed or plan to analyze in the near future. These paths were selected from data that was recorded during the operation of the ETSE array.

Methods of inversion for path-variable regional wave Q
Over the years the P.I.'s have developed and/or implemented several methods for measuring regional wave Q. These methods are briefly described in the following sections.

(1) *The standard two-station method for measuring inter-station Q*. This method cancels the source effect in Q measurement by using station pairs aligned with the source. Xie and Mitchell (1990) and Xie (2002a) used this method for measuring Lg Q, and presented rigorous error analyses.

(2) *The reversed two-station, two-event spectral ratio method*. This method was developed by Chun et al. (1987) and requires that regional waves (e.g., Lg) be recorded at two stations from two events; all must be located approximately on the same great circle. If this very restrictive recording condition can be met, then the method can simultaneously determine inter-station Q and the station site response (factor (4) in §1.1)).

(3) *The event-based, Bayesian method that simultaneously determines source* M_0 and fc *and path-variable* Q_0 *and* h *by Xie (1993, 1998).* This method is based on Tarantola's Bayesian inverse scheme (Tarantola, 1987). With a priori information on path obtained using methods (1) and (2), and on source obtained using method (5) below, this method is robust and capable of reducing or eliminating the trade-off between source and path parameters.

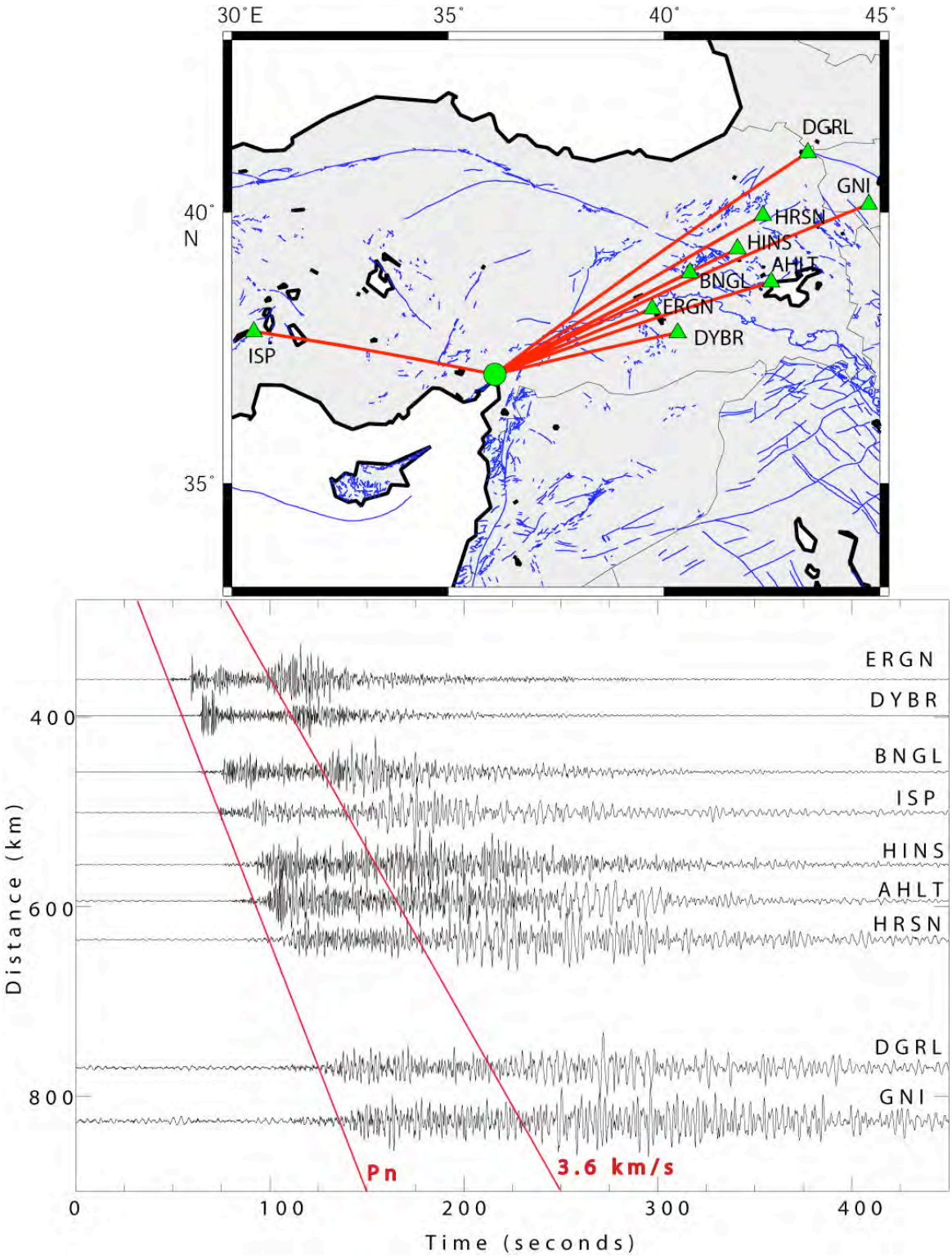


Figure 3. Record section from an earthquake along the east Anatolian Fault Zone (06/25/2001; Mb = 5. 0; located at 40.693°N, 32.993°E). The seismograms are collected from ETSE temporary array and GSN stations in the region. Station code is shown to the right of each trace.

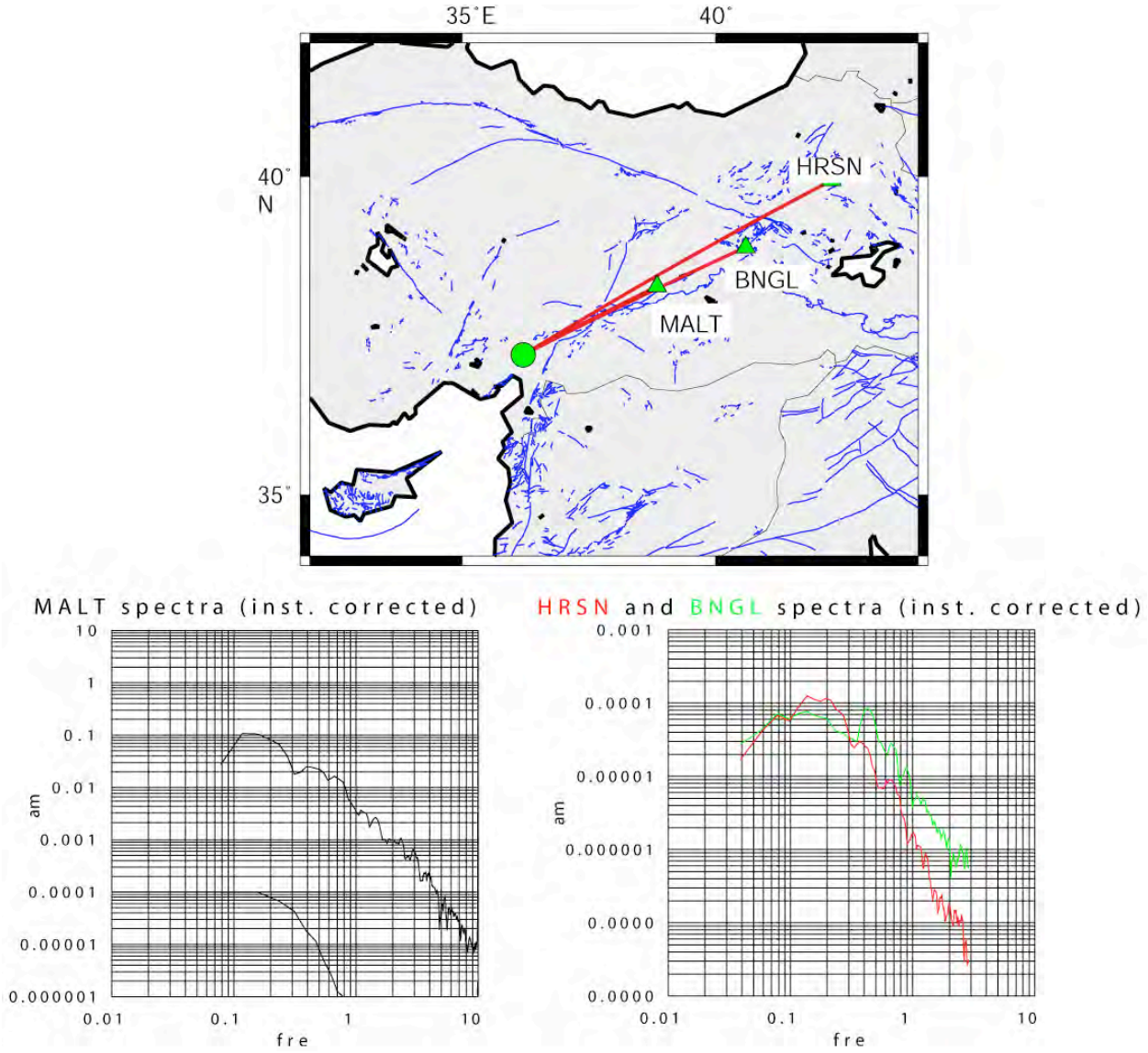


Figure 4. Instrument corrected Lg spectra for an earthquake along the East Anatolian Fault Zone (06/25/2001; $M_b = 5.0$; located at 40.693°N, 32.993°E). The seismograms are collected from ETSE temporary array and GSN stations in the region. Note the change in the spectral character with increasing distance across the east Anatolian plateau. In general, Lg is eliminated past 500 km within the plateau.

Method for establishing the geometrical spreading terms

Of the various regional waves, long-period surface waves and high-frequency Lg have well known geometrical spreading terms (G.S.T.). For other high-frequency regional waves, the G.S.T. can be established using synthetic seismograms in one dimensional structures that are developed for the geographic region of interest. Sometimes the G.S.T. are also directly fit simultaneously with Q models (Zhu et al., 1991; Taylor et al., 2000, Walter and Taylor, 2002). We will also need to determine the G.S.T. for Pn phases in the Middle East given that little work has been done there. For Pg, Xie (2002b) fit synthetic seismograms (Saikia, 1994) in three 1D models for central Asia and obtained G.S.T. that are generally similar to that of Pn. The G.S.T. of Sn is probably the most difficult to estimate precisely because the upper mantle in sub-regions of the Middle East probably has abnormal Poisson ratios and Vp/Vs ratios (McNamara et al., 1995; Owens and Zandt, 1997; Rapine et al., 1997; Rodgers and Schwartz, 1998).

The estimated G.S.T. for Sn using synthetic seismograms will thus be less reliable. If the G.S.T. is biased, the estimated Q will not faithfully reflect the true Q of the crust or upper mantle. However, for the users of our research products, errors in the G.S.T. will have virtually no effect on event detection and identification because the Q models, when used in conjunction with the specified G.S.T., will adequately predict the frequency-dependent amplitude decay of various regional waves.

Lg Q tomography for the Middle East

We anticipate that Lg Q over about 900 paths can be measured with the two-station methods (methods 1 and 2 in the last section) or the Newton-like non-linear method for inversion with multiple co-located events (method 4). We may also use the Bayesian method (method 3) or the EGF method (method 5) which both take advantage of our extensive regional ray path coverage for regions where we do not have good 2 station coverage. Lg Q_0 and η values measured using these methods are of very high quality since they are not subject to the trade-off between source and path parameters. Therefore in the tomographic inversion of laterally varying Q_0 and η values, the input Q_0 and η values along approximately 900 paths will be used to derive a long-wavelength Q map for those regions of the Middle East with good 2 station path coverage. This model will be subsequently used as *a priori* knowledge when Q over the rest of 8,000+ paths is inverted for (for the detailed methodology to achieve this, see Appendix A). Figure 4 shows a subset (about 900) of the 1,500 anticipated paths over which Q_0 and η values can be measured with methods (1), (2), (3 with (5)), and (4). We anticipate that the initial Q_0 and η maps will be available near the end of September, 2004.

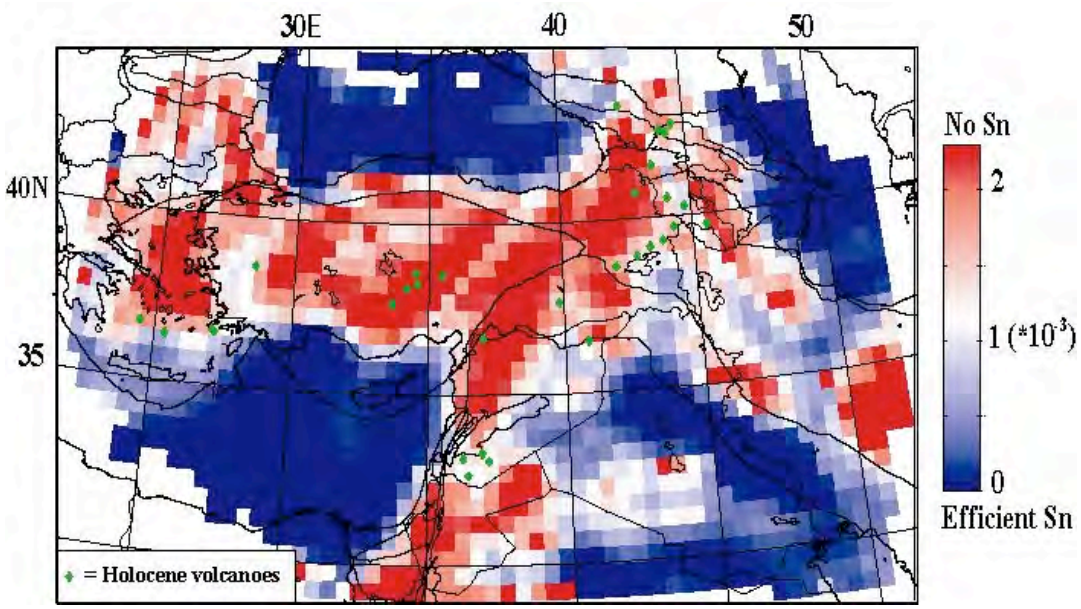


Figure 5. Our most recent Sn efficiency map for the Middle East and surrounding regions (Gok et al., 2003). Red areas denote regions of Sn blockage.

Upper Mantle Attenuation

Laterally varying Pn Q models are more difficult to develop than Lg Q models because Pn is observed only in a limited distance range (between 2°-14°), thus reducing the number of Pn paths available. We are not certain that high resolution tomographic mapping is viable for Pn Q_0 and η. However, at the very minimum we can develop representative Pn Q_0 and models for sub-regions of Anatolia and for portions of the Arabian plate. Sn Q determination will be the most difficult due to the large amount of blockage that occurs for Sn paths in the Middle East. We will create blockage maps for Sn (e.g. Sandvol et al., 2001) and then use these to estimate a maximum allowable Q for those regions with Sn blockage.

CONCLUSIONS AND RECOMMENDATIONS

We have found that in order to achieve sufficiently dense two station paths to cover the majority of the middle east, it is necessary to integrate data from a variety of temporary and permanent, short period and broadband seismic stations within the Middle East. Using these large data sets it is possible to construct a reliable model for Lg Q throughout the northern portions of the Middle East and Dead Sea Fault System. We are currently in the process of calculating Q models for Pn, Pg, and Lg.

Clearly one of the most challenging aspects of calculating Lg and especially Sn Q in the Middle East is the large number of blocked paths. Therefore it is critical to accumulate a large number of waveforms at local and near-regional distances in order to better constrain the Q in the very high attenuation zones such as the Eastern Anatolian plateau. Prior work has established the blockage zones, and these blocked paths will also be used to help create a robust attenuation model for the majority of the Middle East.

ACKNOWLEDGMENTS

We would like to acknowledge Prof. Dr. Niyazi Turkelli for his helping processing Eastern Turkey Seismic Data. Dr. Turkelli will both provide data from the KOERI network and assist in the analysis of portions of the data. We would also like to thank Professor Eid Tarazi and Randa Mohamad of Hashemite University and the Syrian National Seismic Network, respectively.

REFERENCES

Fan, G.-W., and T. Lay, 2003b. Strong Lg Attenuation in the Tibetan Plateau, *Bull. Seism. Soc. Am.*,, in press.

Gok, R., N. Turkelli, E. Sandvol, D. Saber and M. Brazing, Regional wave propagation in Turkey and surrounding regions, *Geophys. Res. Lett.*, 27, No 3, 429-432, 2000

Hartse, H.E., S.R. Taylor, W. S. Phillips and G.E. Randall, 1997. A preliminary study of regional seismic discrimination in central Asia with emphasis on western China, *Bull. Seism. Soc. Am.*, *87*, 551-568.

McNamara, D.T., T. Owens and W. Walter, 1995. Observations of regional phase propagation across the Tibetan Plateau, *J. Zephyrs. Res.* 100, 22,215-22,229.

Mitchell, B.J., Y. Pan, J. Xie and L. Cong, 1997. Lg coda Q variation across Eurasia and its relation to crustal evolution, *J. Geophys. Res.*, 102, 22767-22780.

Owens, T.J., and G. Zandt, 1997. Implications of crustal property variations for models of Tibetan plateau evolution, *Nature*, 387, 37-43.

Patton, H.J., 2001. Regional magnitude scaling, transportability, and S-m discrimination at small magnitudes. *Pure Appl. Geophys.*, 158, 1951-2015.

Phillips, W.S., G.E. Randall and S.R. Taylor, Path correction using interpolated amplitude residuals: An example from central China, *Geophys. Res. Lett.*, 2 5, 2729-2732, 1998.

Phillips, W.S., Empirical path corrections for regional phase amplitudes, *Bull. Seism. Soc. Am.*, 89, 384-393, 1999.

Phillips, W.S., H. E. Hartse, S. R. Taylor, and G. E. Randall, 2000. 1 Hz Lg Q Tomography in Central Asia, *Geophys. Res. Lett.*, 27, 3425-3428.

Rapine, R., J. Ni, J. Wu, and T. Hearn, 1997. Wave propagation in China and surrounding regions, Bull. Seism. Soc. Am., 87, 87, 1622-1636.

Rodgers, A., and S. Schwartz (1998). Lithospheric structure of the Qiangtang Terrane, northern Tibetan Plateau, from complete regional waveform modeling: evidence for partial melt, *J. Geophys. Res.,* 103, 7137-7152.

Sandvol, E., K. Al-Damegh, A. Calvert, D. Seber, M. Barazangi, R. Mohamad, R. Gok, N. Turkelli and C. Gurbuz

C, 2001. Tomographic imaging of Lg and Sn propagation in the Middle East, *Pure Appl Geophys.*, 158, 1121-1163.

Sereno, T.J., 1989, Numerical modeling of Pn geometric spreading and empirically determination attenuation of Pn and Lg phases recorded in eastern Kazakhstan, Technical Report of Science Application International Corporation, SAIC 89//1555, San Diego.

Shin, T.C. and R.B. Herrmann, 1987, Lg attenuation and source studies using 1982 Miramichi Data, *Bull. Seism. Soc. Amer.* , 77(2) April, p. 366-383.

Tarantola, A., Inverse problem theory : methods for data fitting and model parameter estimation, Elsevier ; New York, NY, U.S.A.,1987

Taylor, S., Velasco, A., X. Yang, M. Maceria and W.S. Phillips, 2000. Bayesian tomography applied to seismic event identification problems. *Proc. 23rd. Seismic Res. Rev.: Worldwide Monitoring of Nuclear Explosions, Oct. 2-5, 2001*, 440-447. (URL: http://www.nemre.nn.doe.gov/review2001/CD/Print/02-33.pdf).

Taylor, S.R., Velasco, A.A., Hartse, H.E., Phillips, W.S., Walter, W.R. and A.J. Rodgers, 2002. Amplitude corrections for regional seismic discriminants, *Pure Appl. Geophys.*, 159, 623-650.

Toiran, B.M., 2002. The New Cuban Seismograph Network, *Seism. Res. Lett.,* 73, No. 4, 504-532.

Walter, W. R. and S. Taylor, 2002. A revised magnitude and distance correction (MDAC2) procedure for regional seismic discriminants, Lawrence Livermore National Laboratory UCRL-ID-246882.

Xie, J., 1993. Simultaneous inversion of source spectra and path Q using Lg with applications to three Semipalatinsk explosions, *Bull. Seismol. Soc. Am.*, *83*, 1547-1562.

Xie, J., 1998. Spectral inversion using Lg from earthquakes: Improvement of the method with applications to the 1995, western Texas earthquake sequence, *Bull. Seismol. Soc. Am*., 88, 1525-1537.

Xie, J., 1999. Excitation and attenuation of regional waves from recent seismic events in China, *Proc. 19th Ann. Seismic Symp. on Monitoring a Comprehensive Test Ban Treaty, 21-24 Sep. 1999, Las Vegas,*, Edited by U.S. DoD and U.S. DOE., Vol. 1, 323-332.

Xie, J., 2002a. Lg Q in the Eastern Tibetan Plateau, *Bull. Seism. Soc. Am*, 92, 871-876.

Xie, J., 2002b. The physical basis and improved criteria for the phase spectral ratio discriminants, *DTRA Final Report*, in review.

Xie, J. and B.J. Mitchell, 1990. Attenuation of multiphase surface waves in the Basin and Range Province, part I: Lg and Lg coda, *Geophys. J. Int.*, 102, 121-137.

Zhu, T.F., K.Y. Chun and G.F. West, 1991. Geometrical spreading and Q of Pn waves: An investigative study in eastern Canada. *Bull. Seism. Soc. Am.*, 81, 882-896.

IMPROVED SURFACE-WAVE DISPERSION MODELS, AMPLITUDE MEASUREMENTS, AND AZIMUTH ESTIMATES

Jeffry L. Stevens, David A. Adams, G. Eli Baker, Mariana G. Eneva and Heming Xu

Science Applications International Corporation

Sponsored by Air Force Research Laboratory

Contract No. DTRA01-01-C-0082

ABSTRACT

Surface waves are of primary importance for nuclear monitoring because the Ms:mb discriminant and its regional variants are among the most reliable means of determining whether an event is an earthquake or an explosion. The primary goal of this project is to reduce the magnitude threshold for which surface waves can be identified and measured reliably and to improve the accuracy of surface wave measurement, using phase-matched filtering and global regionalized earth and dispersion models.

This is the final year of a three-year project. Following are the most significant products and results of this work:

(1) Assembled a dataset of dispersion measurements of over one million data points. Some of this dataset came from our own measurements, but most came from other research studies, and we thank all of those scientists who have contributed to this effort. This dataset is one of the largest dispersion datasets ever assembled and is particularly unique in its coverage for a broad range of frequencies.

(2) Developed and have continuously improved a set of global earth models and dispersion models defined on a one-degree grid. These models were developed by simultaneously inverting the entire dataset for a set of earth structures, which in turn allow surface wave dispersion to be calculated between any two points on the earth at any set of frequencies, with the dispersion models constrained by the large dataset. These global earth and dispersion models are available on request to other researchers working in this program.

(3) Implemented the azimuth-estimation technique developed by Selby using Chael's algorithm, tested it on a large dataset of the International Monitoring System (IMS) data, and demonstrated that it is a major improvement over other commonly used azimuth-estimation techniques. This azimuth-estimation technique can be used together with the existing detection test based on consistency of measurement with surface-wave-dispersion maps, to reduce the detection threshold for which surface waves can be reliably identified and measured.

(4) Implemented and tested a path-corrected spectral magnitude, developed procedures for optimizing it and evaluated the discrimination capability of this and other types of surface wave measurements. Two particularly important results of this work are (a) the path-corrected spectral magnitude is independent of distance and unaffected by dispersion and therefore can be measured at any distance, including very close to the source, and it will have the same value as a measurement made at a greater distance. The path-corrected spectral magnitude is therefore a "regional Ms" which has been a long-term goal of this program (b) for discrimination purposes, surface waves should be measured at periods greater than 10 seconds. Periods of 10 seconds and longer can be measured even at very close range, and there is only a small S/N improvement, if any, at shorter periods. Any benefit from measurement at higher frequencies is lost due to the decrease in earthquake spectral amplitude relative to explosions at higher frequencies.

(5) Performed a study of "problem cases," where surface wave dispersion and/or amplitudes are inconsistent with model predictions. Typically, these cases occur where there are strong heterogeneities in earth structure along the path, particularly for grazing incidence along large changes in material properties. Ray theory predicts that surface waves will take the minimum time path between the source and receiver in such cases, but the observed waveforms are considerably more complex than this. In cases of large-velocity contrast such as the Tarim Basin region, there are multiple surface wave arrivals with a distinct arrival passing through the basin and another traveling around it. The arrivals merge at longer periods. Special care is required for construction and use of dispersion and attenuation models in such cases.

OBJECTIVE

The goal of this project is to reduce the magnitude threshold for which surface waves can be identified and measured reliably and to improve the accuracy of surface wave measurement, using phase-matched filtering, development of global regionalized earth and dispersion models, and other techniques.

RESEARCH ACCOMPLISHED

Overview

The importance of long period (>~10 second) surface waves for nuclear monitoring is in the discrimination capability of the M_s:m_b discriminant and its variants (Marshall and Basham, 1972; Stevens and Day, 1985). In general, contained underground explosions generate larger m_b relative to M_s than earthquakes of comparable size. This is one of the most reliable discriminants, but it has a few limitations:

1. Body waves can be measured for significantly smaller events than surface waves, so the discriminant is not useful for very small events. In this project we have addressed this issue by investigating methods to reduce the threshold for which surface waves can be reliably identified and measured, including the development of improved dispersion maps constrained by a very large data set to facilitate phase-matched filtering.

2. Although the strongest surface wave signals are at the closest distances, M_s is an unreliable amplitude measure at regional and local distances because of differences in dispersion and variations in the frequency content of the signal. We have addressed this issue by developing surface wave measurement techniques that can be used at local and regional distances, even very close to the source, which are consistent with measurements made at greater distances.

3. The discrimination capability of surface waves decreases with increasing frequency because the spectral difference between earthquakes and explosions declines. We have addressed this issue by analyzing surface wave and noise measurements to define the optimum frequency bands for discrimination.

4. Incorrect association of surface waves with the wrong event is a problem that can potentially lead to misclassification of an explosion as an earthquake. We have addressed this issue in two ways: first, by improving dispersion models that are used in the dispersion test for surface wave identification; and second by implementing and testing an improved azimuth estimation technique that can be used to improve association of surface waves with the corresponding event.

5. In general, surface waves can be modeled quite well using path-averaged dispersion and attenuation calculated from discrete plane-layered earth models and great circle propagation; however, there are some complex cases where standard methods of measuring surface wave dispersion and amplitude measurement do not work well. We have investigated some problem cases and made some suggestions for techniques to handle these situations.

Dispersion data set

We have been developing global, regionalized dispersion models that allow the phase and group velocity to be calculated between any two points on the earth. We have done this by accumulating a very large data set of dispersion measurements derived by a number of researchers, and then inverting this data set to determine earth structure, which in turn is used to generate phase and group velocity maps at all frequencies. The data set now contains more than one million data points. The dispersion data set has been derived from a variety of regional and global studies, including the following: global surface wave-group velocities from earthquakes derived using IMS data (Stevens and McLaughlin, 1996), as well as our own measurements derived from IMS data and several other data sets; surface-wave phase and group-velocity dispersion curves from underground nuclear test sites (Stevens, 1986; Stevens and McLaughlin, 1988), calculated from earth models for 270 paths (test site—station combinations) at 10 frequencies between 0.015 and 0.06 Hz; phase and group-velocity measurements for western Asia and Saudi Arabia from Mitchell et al.(1996) for 12 paths at 17 frequencies between 0.012 and 0.14 Hz; the global phase-velocity model of Ekstrom et al. (1996) for 9 periods between 35 and 150 seconds calculated for each grid block from a spherical harmonic expansion of order l = 40; group velocity measurements for Eurasia from Ritzwoller et al.

(1996) and Levshin et al.(1996) for 20 frequencies between 0.004 and 0.1 Hz with 500 to 5,000 paths per frequency; Antarctic and South American group velocity measurements from the University of Colorado (Vdovin et al., 1999; Ritzwoller et al., 1999); high-frequency Eurasian dispersion measurements from the University of Colorado (Levshin et al. 2003), a large set of dispersion measurements from Saudi Arabia provided by Herrmann and Mokhtar at St. Louis University; a data set from Los Alamos National Laboratory (Yang et al. 2002) for 2000 individual paths from Central Asia ranging between 0.05 Hz and 0.23 Hz, and a data set developed by Huang et al. (2003) for 9,730 paths from China. Considerable quality control was performed on the data set, and questionable data were removed or downweighed. Some of the data were improved substantially by relocating events from their original locations to the improved locations of Engdahl et al. (1998). The distribution of the group velocity data set at periods of 50, 20, and 10 seconds is illustrated in Figure 1.

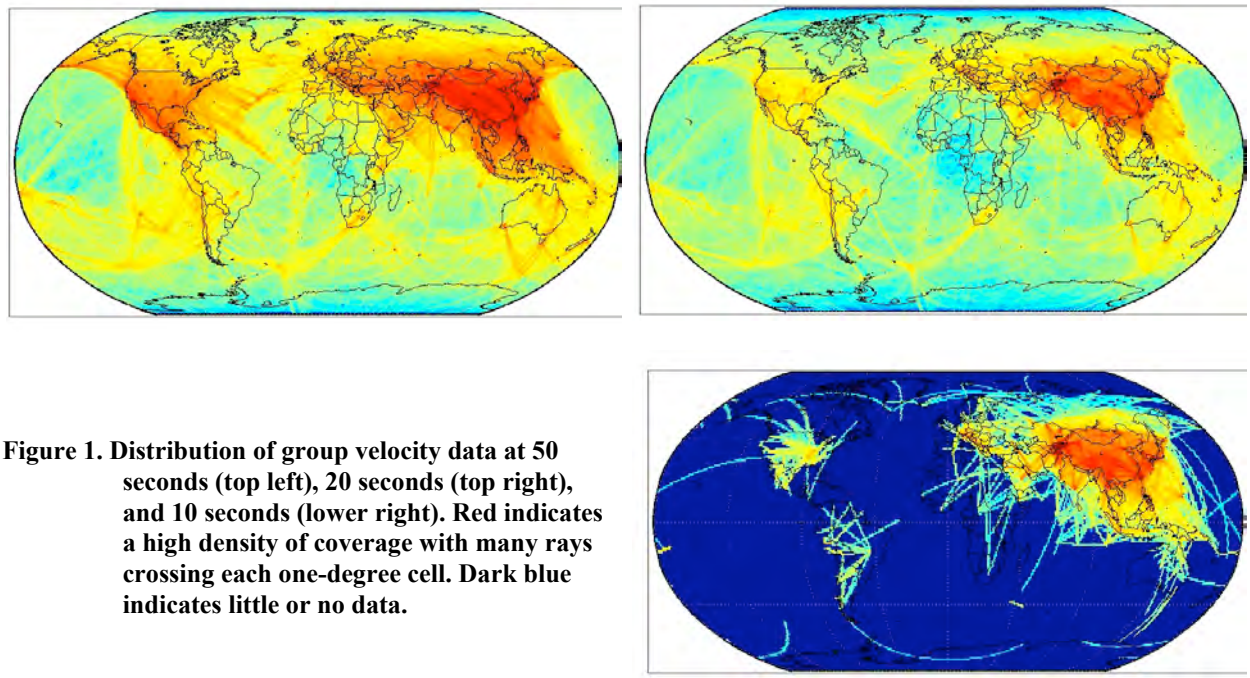


Figure 1. Distribution of group velocity data at 50 seconds (top left), 20 seconds (top right), and 10 seconds (lower right). Red indicates a high density of coverage with many rays crossing each one-degree cell. Dark blue indicates little or no data.

Global earth models and dispersion models

By developing dispersion maps based on earth models, we are able to invert all relevant data in a single inversion. The data include phase-velocity and group-velocity measurements measured along specific paths at all frequencies, as well as some phase and group velocity data points derived from models (e.g., the Harvard-phase velocity models). Developing dispersion maps based on earth models has some additional advantages relative to the more common technique of performing tomographic inversions separately for each frequency. In particular, we can easily include information from other studies leading to physically reasonable constraints on dispersion. For our earth models this information consists of the boundaries between geologic zones, bathymetry of oceans, thicknesses of sediments and ice, Moho depths, and previous estimates of seismic velocities derived from existing earth models. The regionalized earth model consists of 1º x 1º blocks and is made up of layers of ice, water, sediments, crust, and upper mantle. Currently this model depends on 9,008 free parameters that are adjusted by a damped least-squares fit to Rayleigh wave-dispersion data. The free parameters are the S-wave velocities of layers of 577 different model types. Other constrained parameters in the model are P-wave velocities, densities, and Q. The model types are based on the Crust 2.0 2º x 2º crustal types (Bassin et al., 2000 and Laske et al. 2001) and also on ocean ages (Stevens and Adams, 2000). The top few km of the model (consisting of water, ice and/or sediments) are fixed and match data from one degree bathymetry maps made by averaging Etopo5 five-minute measurements of topography, and Laske and Masters (1997) one-degree maps of sediments. There is an explicit discontinuity between the bottom of the sediments and the crust. There are three or more crustal layers. The Crust 2.0 models, which were the starting point for these structures, have three crustal layers, but we found it necessary to add more layers in regions of thick crust.

There is another explicit discontinuity at the Crust/Mantle boundary. The Moho depth is derived from Crust 2.0 and varies on a 2º grid. The mantle starting model is derived from AK135 (Kennett, et al, 1995). With these constraints, the inversion is performed for the shear velocity of the crust and upper mantle to a depth of 300 km. Below 300 km the earth structure is fixed, and the inversion model is required to be continuous with the mantle structure at the base of the inversion. In broad ocean areas, we replace the Crust 2.0 model with models distinct for each ocean and subdivided by ocean age. We also separate into distinct models Crust 2.0 models that are geographically separated. So, for example, if Crust 2.0 has the same model type in North America and in Asia, we use the same starting model for each, but treat them as separate models in the inversion.

The inversion procedure for the 3D earth model

The relationship between dispersion and the shear wave velocities of the layers in the earth model is nonlinear, so the shear velocities are estimated by an iterative least-squares inversion procedure. At each step a system of tomographic equations is formed, augmented by additional equations of constraint, and then solved by the LSQR algorithm. The equations solved are

$$\begin{bmatrix} A \\ sH \\ \lambda I \end{bmatrix} \vec{\Delta x} = \begin{bmatrix} \vec{\Delta d} \\ -sH\vec{x} \\ \lambda\left(\vec{x}_C - \vec{x}\right) \end{bmatrix} + \vec{\varepsilon}\,, \tag{1}$$

where Δx is the vector of adjustments to the shear wave slownesses of layers in each of the 577 model types. Δd is the vector of slowness differences between predicted and observed dispersion measurements. ε is the vector of residuals that remain after inversion (the inversion minimizes $|\varepsilon|$). x is the vector of slownesses estimated in the previous iteration. The elements of the matrix A consist of partial derivatives of dispersion predictions with respect to shear wave slownesses in each layer. H is a difference operator that applies to vertically neighboring layers and has the effect of constraining the vertical smoothness of velocity profile. H applies to layers in the crust and upper mantle, but has explicit discontinuities at the crust/mantle boundary and at the base of surface sediments. s is the weighting of the smoothness constraint and can be a diagonal matrix (for variably weighted smoothing) or a scalar (constant smoothing). A different smoothing parameter can be selected for each model type. Lateral smoothing, which is usually applied in tomography studies, is executed indirectly in our study through the selection of the model types. I is the identity matrix and λ weighs the damping, which constrains the norm of the difference between final slownesses and constraining model slownesses x_c (in this case, a variant of the Crust 2.0 values). The variable λ can be a scalar for constant damping, or a diagonal matrix for variable damping. As with smoothing, variable damping is implemented so that a different parameter can be selected for each model type.

The Selby/Chael algorithm for azimuth estimation

This section summarizes work done under this project that is described in more detail by Baker and Stevens (2004).

As part of its responsibilities under the Comprehensive Nuclear-Test-Ban Treaty (CTBT), the International Data Center (IDC) automatically processes seismic data recorded at IMS stations, identifying surface waves and measuring surface wave amplitude and M_s (Stevens and McLaughlin, 2001). Three-component backazimuth estimates derived using the current, spectral methods are recorded but are too inaccurate to use for association. That method is based on an algorithm originally proposed (Smart, 1978) as part of a surface wave detector, rather than as a means of estimating the backazimuth. Selby (2001) suggested that another detection technique (Chael, 1997), based on cross-correlation of the vertical and Hilbert transformed radial component Rayleigh wave records, could be used for backazimuth estimation and would improve IDC processing.

To compare the performance of the algorithms, we incorporated the Chael/Selby (CS) algorithm into the automatic surface-wave processing software that uses the current IDC method (CM). Under current IDC procedures, for an event location and time based on body-wave arrivals, a surface wave is considered detected if it passes a dispersion test in the group velocity window predicted for the event. We tested both algorithms on 2,599 records that passed the dispersion test and 2,363 generally poorer S/N records that failed, all from events that had at least four surface-wave detections. We assessed the performance of each algorithm for different passbands and group velocity windows.

Figure 2 shows histograms of backazimuth residuals for the CM and one implementation of the CS algorithm for a frequency band of 0.3–0.5 Hz. The CS algorithm performs better in two ways. First, the CM applied as it is currently used in the automatic processing, has errors of 180° for a significant number of events. This is due to the 180-degree ambiguity in Love wave polarization, which causes large Love wave amplitudes to increase the likelihood of a 180-degree error in backazimuth. Second, the histograms reveal many more outliers for the CM than for the CS algorithm.

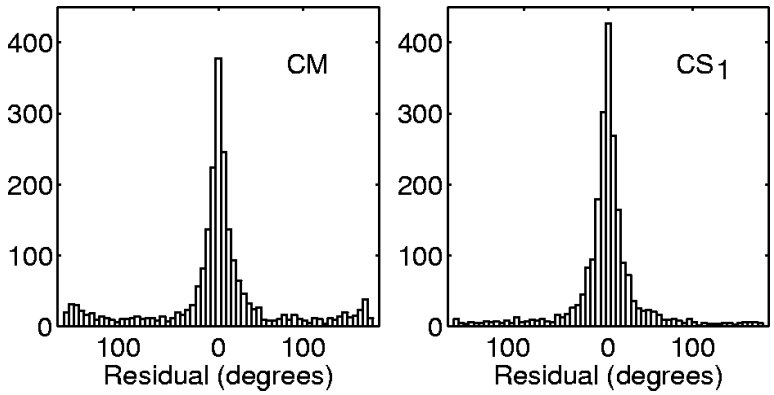


Figure 2. Backazimuth residuals for 0.03–0.05 Hz using the current method (left) and the Chael/ Selby algorithm.

Figure 3 shows the backazimuth residuals for each of the algorithms vs event size, which serves as a proxy for the signal-to-noise ratio. For large events, the CM's performance is almost comparable to the CS algorithms, except for a large number of sign errors. The greatest advantage of the CS algorithm is in estimating backazimuth of smaller events, especially at lower frequency, where the CM fails badly. We use the scaled-median absolute deviation (SMAD), the one-norm measure of the central tendency, to provide a measure of the spread of data about the central value that is less biased by outliers than the STD in heavy-tailed data such as these.

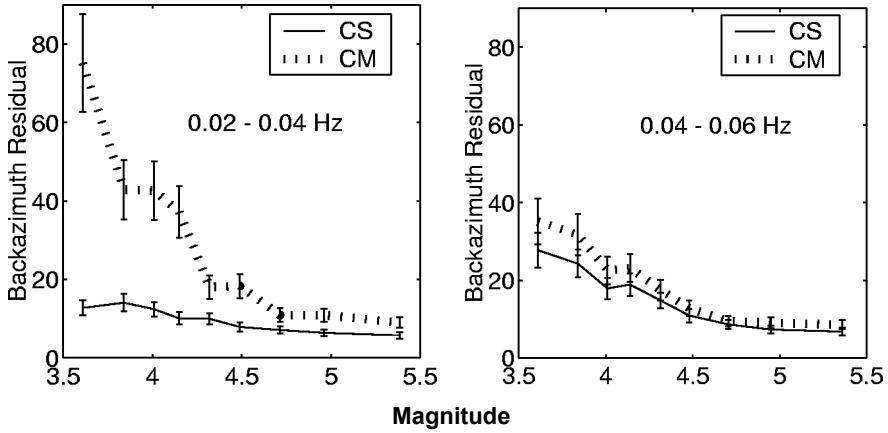


Figure 3. Median ±2 SMAD confidence intervals of backazimuth residuals binned by M_s values for the CM (dotted) and CS_1 algorithm (solid). Each bin has 250 backazimuth residuals. Results at 0.03–0.05 Hz are intermediate between those shown.

The cross correlation of the Hilbert transformed vertical component with the radial predicts the accuracy of the backazimuth estimate. Figure 4 shows backazimuth residuals vs the cross correlation for the best implementation of the CS algorithm applied to data that pass the dispersion test. This ability to predict backazimuth estimate accuracy can aid association with known events. In particular, the strict dispersion criteria for detection at the IDC could be relaxed in cases where the backazimuth is consistent with the theoretical backazimuth and the cross-correlation value is high.

Figure 5 shows the results of the CS method applied to the poorer S/N records that did not pass the dispersion test. This method extracts accurate backazimuth estimates for many of these data, and the more accurate estimates can be

identified by their cross-correlation value. The middle plot shows histograms just for data with a cross-correlation ≥ 0.8, which comprise 14.7% of the data. Their backazimuth residual has a SMAD of 14.8°. The F-statistic of the CM does not provide similar predictive capabilities.

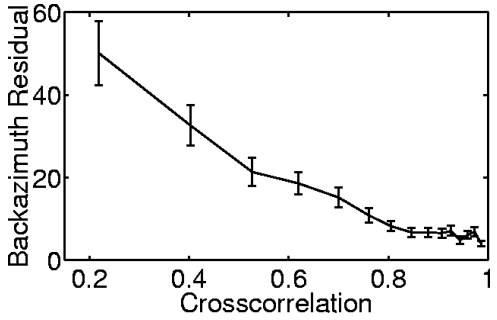


Figure 4: Median backazimuth residuals ±2 SMAD confidence intervals at 0.03–0.05 Hz vs the median cross correlation of the radial and Hilbert transformed vertical Rayleigh waves, for bins of 171 measurements. Results are similar for the other passbands.

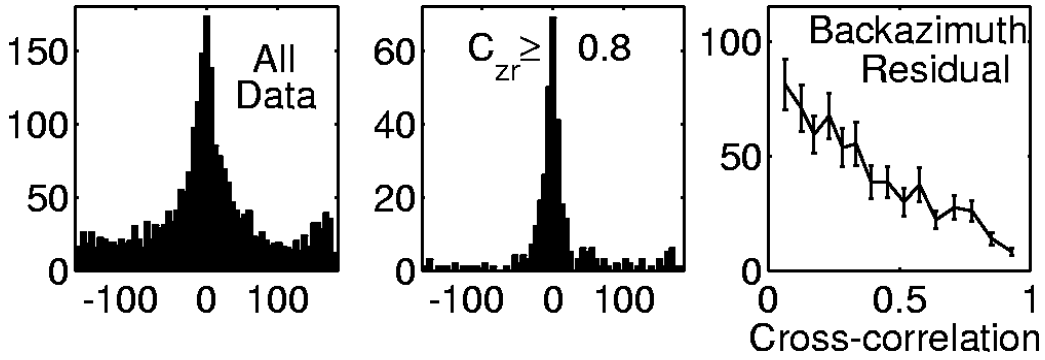


Figure 5. Backazimuth residuals at 0.02–0.04 Hz for the CS algorithm, applied to data not passing the dispersion test. Histograms of backazimuth residuals for all the data (left column) and for the 14.7% of the data with cross correlation ≥ 0.8 (middle). The right-hand plot shows median backazimuth residual ±2 SMAD confidence intervals vs cross correlation, as in Figure 4.

Optimized surface wave amplitude measurements

Surface wave measurements traditionally are accomplished by measuring a time-domain amplitude at a period near 20 seconds and then calculating a surface wave magnitude M_s. This procedure is problematic at regional distances because the surface wave is not well dispersed and a distinct 20-second arrival may not be present. It is possible to measure time-domain amplitudes at higher frequencies with corrections (e.g., Marshall and Basham, 1972), however measurements may be inaccurate due to differences in dispersion caused by differences in earth structure. Stevens and McLaughlin (2001) suggested as an alternative replacing time-domain measurements with a path-corrected spectral magnitude. The path corrected spectral magnitude, $\log M_0$, is calculated by dividing the observed surface wave spectrum by the Green's function for an explosion of unit moment and taking the logarithm of this ratio, averaged over any desired frequency band. Stevens et al. (2003) performed a study to determine the optimum procedures and optimum frequency band for measuring $\log M_0$. This is necessary because there are a number of factors that can affect $\log M_0$, including noise levels, spectral dips and peaks, and the shape of the source spectrum.

The path-corrected spectral magnitude is defined as the logarithm of

$$M_0^{'} = \left| U(\omega, r, \theta) \Big/ \left(\frac{S_1^x(\omega, h_x) S_2(\omega) \exp\left[-\gamma_p(\omega) r\right]}{\sqrt{a_e \sin(r/a_e)}} \right) \right| \qquad (2)$$

where U is the observed surface wave spectrum, S_1^x depends on the source region elastic structure and the explosion source depth, S_2 depends on the receiver-region elastic structure. γ_p is the attenuation coefficient that depends on the attenuation integrated over the path between the source and receiver. a_e is the radius of the earth, and $M_0^{'} = \frac{3\beta^2}{\alpha^2} M_0$ where M_0 is the explosion isotropic moment, defined this way so that the function S_1^x does not depend explicitly on the material properties at the source depth. All of the functions in equation 2 are easily derived from plane-layered earth models, allow the measurement to be regionalized to account for differences in earth structure at the source and receiver, and are due to attenuation along the path.

The advantages of using logM_0 instead of the traditional surface wave magnitude M_s are that logM_0 is insensitive to dispersion, independent of distance, works well at regional distances, and can be regionalized. Regionalized path-corrected spectral magnitudes incorporate geographic variations in source excitation and attenuation. Some limitations are shared by M_s and logM_0 : spectra from earthquakes vary because of source mechanisms and depth, and errors can occur if the measurement is made in a spectral dip or at high frequencies for a deep event (Figure 6). Azimuthal variations in amplitude caused by focal mechanism also affect the amplitudes of both logM_0 and M_s.

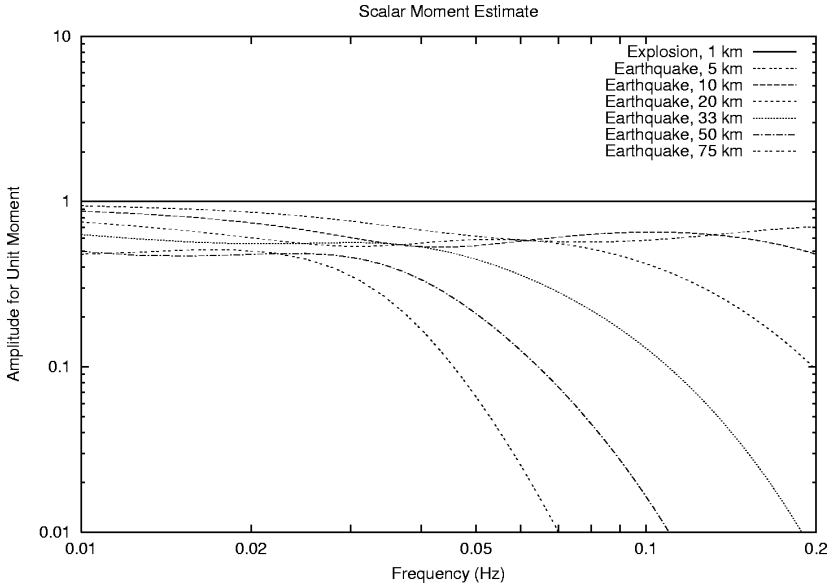


Figure 6. Path-corrected spectra for an explosion and for earthquakes calculated for several depths. The path-corrected explosion spectrum is flat over the entire frequency band (for perfect data and path correction), but the path-corrected earthquake spectrum is flattened and has some variation as a result of source mechanism and source depth.

While a path-corrected spectral magnitude can be measured over any frequency band, it is subject to the following constraints:

1. Earthquake spectra decrease at high frequencies, depending on depth (see Figure 6); therefore, the high end of the frequency band should be low enough that discrimination is not degraded by this effect.
2. At high frequencies, attenuation is higher and the dispersion more variable; therefore the path correction is likely to be less well determined and the signal may be lower than at lower frequencies, particularly at longer distances.
3. Noise increases at low frequency; therefore the low end of the frequency band should be high enough to be above the noise level.

In order to quantify these effects, we created some "path-corrected noise spectra" using path corrections appropriate for the Lop Nor test site. These are simply noise spectra measured at the station that have been divided by an explosion Green's function in the same manner as would be done for a signal. Because the signal spectra are

approximately flat over most of the frequency band, the path-corrected noise spectra are a measure of the minimum path corrected signal that could be measured at each station.

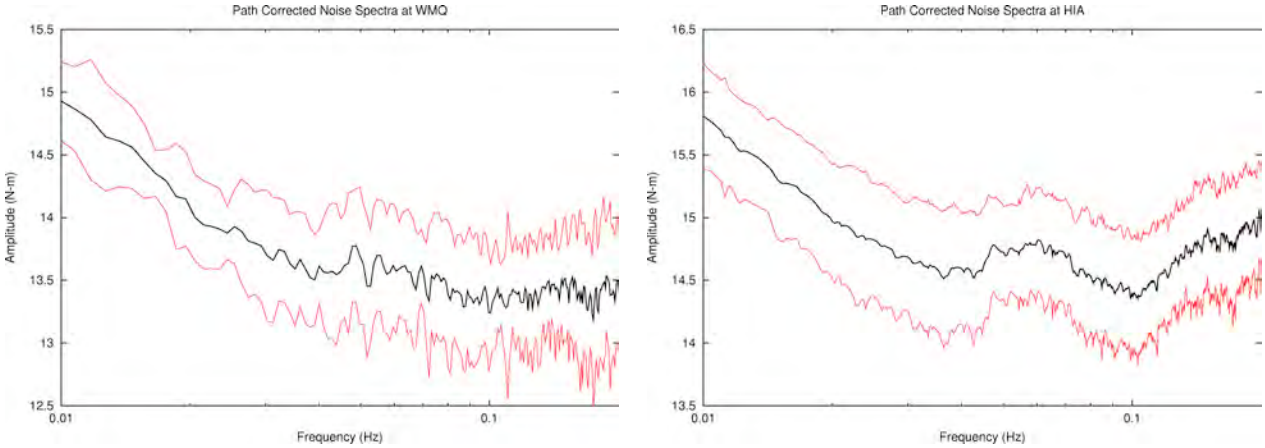


Figure 7. Average path-corrected noise measurement and ±1 standard deviation curves for 13 time segments at WMQ (left) and for 54 time segments at HIA (right). Note that the predicted path-corrected explosion spectrum is flat over this frequency band, and the predicted path-corrected earthquake spectra *decrease* with increasing frequency.

Figure 7 shows the path-corrected noise measurements for two stations: WMQ, located an average of 2 degrees from each event, and HIA, located an average of 27-degrees from each event. At HIA, the noise spectrum has minima at 0.04 and 0.1 Hz, either side of the 0.06 Hz primary microseism peak. Noise amplitudes increase substantially below about 0.04 Hz. Noise levels at WMQ are similar, but are flatter from 0.04 to 0.2 Hz with a less-prominent microseism peak and lower (path corrected) noise at the highest frequencies because of the close distance. Figure 7 shows that there is also considerable variability in the noise level, so that although the average noise level is about 13.5 at WMQ and 14.5 at HIA (corresponding approximately to M_s 1.7 and 2.7, respectively), the minimum spectral magnitude that could be measured may be substantially lower or higher depending on the noise level at the time the measurement is made. These results suggest that in general it is best to measure surface wave spectra at frequencies above 0.03 Hz and below 0.1 Hz. Although noise levels remain fairly low in the 0.1–0.2 Hz frequency band at the closest stations, factors #1 and #2 mentioned above make measurement in this band risky. Based on a number of empirical tests, we recommend measuring surface waves at frequencies between 0.03 and 0.08 Hz for this region. The optimum frequency band may be different in other regions where there are structures that cause large amplitude changes, such as along paths that cross oceanic regions.

Performance of algorithms and analysis of "problem cases"

In many respects surface waves are well behaved and straightforward to model. Two characteristics in particular are helpful (1) because the surface wave always follows a minimum time path, any path other than the great circle path is necessarily longer, which reduces the error in the travel time (in inversions, the main effect of this is to make low-velocity regions appear somewhat smaller than they actually are); and (2) along most continental paths at the regional distances of greatest interest today, and at the periods greater than 10 seconds that are recommended for discrimination, amplitude differences resulting from variations in attenuation are small. Only regions of unusually high attenuation cause significant errors in amplitude predictions along short paths. For most surface wave studies, uncertainties in event location and measurement error are responsible for more of the unmodelable error than actual differences because of complexities in the earth. There are some exceptions to this, however. In cases where surface waves travel along grazing paths near large changes in earth structure, surface waves can be much more complex and difficult to model. Multiple interfering or distinct surface wave arrivals can be observed that take different paths through or around a low-velocity region. The Tarim Basin in western China is a particularly strong example of this effect. In this case, dispersion models can at best predict the dominant surface-wave arrival, and the amplitude may not be predictable without detailed analysis of the data and the earth structure that causes the variations. One technique that we found to help for achieving consistency of measurement and reliability of the inversion is to review the data and order (select) the arrivals so that the dispersion picks change from fast to slow to fast smoothly as the azimuth changes across the basin. Although this doesn't completely resolve the multiple arrival problem, it

selects the arrivals in a manner consistent with waves traveling on a continuous set of paths across the complex earth structure. We plan to investigate this further using numerical modeling of surface waves.

CONCLUSIONS AND RECOMMENDATIONS

The dispersion models developed in this study can be used to find the phase and group velocities between any two points on the earth at any frequency. These models are available to all researchers on request, and have been provided for use in a number of other research projects. The dispersion models depend on dispersion data for accuracy, and so can be improved as more dispersion data become available. We therefore recommend continuation of this iterative process. As more data become available, particularly from regions or in frequency bands currently sparsely covered, we can improve the models and in turn provide these predictions for comparison with and as a starting point for new surface wave studies in regions of interest.

The azimuth estimation algorithm currently used at the International Data Center should be replaced with the Selby/Chael algorithm that was implemented and tested in this project. The procedure can be used together with the dispersion test to reduce the detection threshold for automatic surface wave processing by relaxing the requirements of the dispersion test when the azimuth estimate is consistent with an event hypothesis with a high-correlation value.

The path-corrected spectral magnitude provides a "regional Ms" which has been a long-term goal of this program. The path-corrected spectral magnitude can be measured over any frequency band; however, for discrimination purposes, surface waves should be measured at periods greater than 10 seconds. Periods of 10 seconds and longer can be measured even at very close range, and there is only a small S/N improvement, if any, at shorter periods. Measurement at higher frequencies risks error in discrimination because of the decrease in earthquake spectral amplitude relative to explosions at higher frequencies, particularly for events for which shallow depth is uncertain.

Additional work is needed regarding how to model and invert surface wave amplitude and dispersion in regions of complex earth structure. In particular, surface waves traveling at near-grazing incidence to strong heterogeneities may exhibit amplitude variations not only as a result of focusing/defocusing, but also because of interference of arrivals taking multiple paths through the medium. Similarly, dispersion measurements are complicated by the presence of distinct, multiple arrivals at short periods and interfering arrivals that cannot be separated at longer periods.

ACKNOWLEDGEMENTS

We would like to thank Mike Ritzwoller, Anatoli Levshin and Nikolai Shapiro of the University of Colorado, Bob Herrmann of St. Louis University, and other researchers who have allowed us to use their data in this project.

REFERENCES

Baker, G. Eli and Jeffry L. Stevens (2004), "Backazimuth Estimation Reliability Using Surface Wave Polarization," Geophysical Research Letters, v. 31, L09611, doi:10.1029/2004GL019510.

Bassin, C., G. Laske, and G. Masters (2000), The Current Limits of Resolution for Surface Wave Tomography in North America, *EOS Trans AGU* 81, F897.

Chael, E. (1997), An Automated Rayleigh-Wave Detection Algorithm, *B.S.S.A*., 87, 157-163.

Ekstrom, G., A. M. Dziewonski, G. P. Smith, and W. Su (1996), Elastic and Inelastic Structure Beneath Eurasia, in *Proceedings of the 18th Annual Seismic Research Symposium on Monitoring a Comprehensive Test Ban Treaty, 4-6 September, 1996*, Phillips Laboratory Report PL-TR-96-2153, July, ADA313692, 309-318.

Engdahl, E. R., R. van der Hilst, and R. Buland (1998), Global Teleseismic Earthquake Relocation with Improved Travel Time and Procedures for Depth Determination, *Bull. Seismol. Soc. Am.* 88, 722-743.

Huang, Z., W. Su, Y. Peng, Y. Zheng, and H. Li (2003), Rayleigh Wave Tomography of China and Adjacent Regions. *J. Geophys. Res.* 108(B3), 2073, doi: 10.1029/2001JB001696.

Kennett, B. L. N. E. R. Engdahl, and R. Buland (1995), Constraints on Seismic Velocities in the Earth from Travel Times, *Geophys. J. Int*. 122, 108-124.

Laske, G. and G. Masters (1997), A Global Digital Map of Sediment Thickness, *EOS Trans. AGU* 78, F483.

Laske, G., G. Masters, and C. Reif, Crust 2.0 (2001): A New Global Crustal Model at 2x2 Degrees, http://mahi.ucsd.edu/Gabi/rem.html.

Levshin, Anatoli L., Jeffry L. Stevens, Michael H. Ritzwoller, David A. Adams, and G. Eli Baker (2003), "Improvement of Detection and Discrimination Using Short Period (7s-15s) Surface Waves in W. China, N. India, Pakistan and Environs," Final report submitted to Defense Threat Reduction Agency, SAIC Report No. 03/2008, CU Project No. 1532378, April.

Levshin, A. L., M. H. Ritzwoller, and S. S. Smith (1996), "Group Velocity Variations Across Eurasia," in *Proceedings of the 18th Annual Seismic Research Symposium on Monitoring A Comprehensive Test Ban Treaty,* Phillips Laboratory Report PL-TR-96-2153.

Marshall, P. D. and P. W. Basham (1972), Discrimination Between Earthquakes and Underground Nuclear Explosions Employing an Improved Ms Scale, *Geophys. J. R. astr. Soc*. 28, 431-458.

Mitchell, B. J., L. Cong and J. Xie, (1996), "Seismic Attenuation Studies in the Middle East and Southern Asia", St. Louis University Scientific Report No. 1, PL-TR-96-2154, ADA317387.

Ritzwoller, M. H., A. L. Levshin, L. I. Ratnikova, and D. M. Tremblay (1996), "High Resolution Group Velocity Variations Across Central Asia, "*Proceedings of the 18th Annual Seismic Research Symposium on Monitoring A Comprehensive Test Ban Treaty"*.

Ritzwoller, M.H., O.Y Vdovin, and A.L. Levshin (1999), "Surface Wave Dispersion Across Antarctica: A First Look", Antarctic J. U.S., in press.

Selby, N.D. (2001), Association of Rayleigh Waves Using Backazimuth Measurements: Application to Test Ban Verification. *Bull. Seism. Soc. Am*., 91, 580-593.

Smart, E. (1978), A three-component, single-station, maximum-likelihood surface wave processor, *Geotech Report No*. SDAC-TR-77-14.

Stevens, J. L. (1986), "Estimation of Scalar Moments From Explosion-Generated Surface Waves," *Bull. Seism. Soc. Am.*, v. 76, pp. 123-151.

Stevens, J. L. and S. M. Day (1985), "The Physical Basis of the mb:Ms and Variable Frequency Magnitude Methods for Earthquake/Explosion Discrimination," *Journal of Geophysical Research*, v. 90, pp. 3009-3020.

Stevens, J. L. and D.A. Adams (2000), Improved Surface Wave Detection and Measurement Using Phase-Matched Filtering and Improved Regionalized Models, in *Proceedings of the 22nd Annual DOD/DOE Seismic Research Symposium: Planning for Verification of and Compliance with the Comprehensive Nuclear-Test-Ban Treaty (CTBT), 12-15 September 2000*, 145-154.

Stevens, J. L., D. A. Adams, and E. Baker (2001), *Surface Wave Detection and Measurement Using a One Degree Global Dispersion Grid*, SAIC Final Report to Defense Threat Reduction Agency, SAIC-01/1084, December.

Stevens, J. L. and K. L. McLaughlin (1996), "Regionalized Maximum Likelihood Surface Wave Analysis," Maxwell Technologies Technical Report PL-TR-96-2273, SSS-DTR-96-15562, September.

Stevens, J. L., and K. L. McLaughlin (1988), "Analysis of surface waves from the Novaya Zemlya, Mururoa, and Amchitka test sites, and maximum likelihood estimation of scalar moments from earthquakes and explosions," S-CUBED technical report SSS-TR-89-9953, September.

Stevens, J. L. and K. L. McLaughlin (2001), Optimization of Surface Wave Identification and Measurement, *Pure Appl. Geophs.* 158, 1547-1582.

Stevens, J. L., D. A. Adams, and M. G. Eneva (2003), "Improved Surface Wave Dispersion Models and Amplitude Measurements," *Proceedings of the 25th Annual Seismic Research Review - Nuclear Explosion Monitoring: Building the Knowledge Base*, Tucson, AZ, 23-25 September, 2003.

Vdovin, O. Y., J. A. Rial, M. H. Ritzwoller, and A. L. Levshin (1999), "Group-velocity tomography of South America and the surrounding oceans", *Geophys. J. Int.*, 136, 324-330.

Yang, X., S. R. Taylor, H. J. Patton, M. Maceira, and A. A. Velasco (2002), Evaluation of Intermediate-Period (10- to 30-sec) Rayleigh-Wave Group Velocity Maps for Central Asia, in *Proceedings of the24th Seismic Research Review - Nuclear Explosion Monitoring: Innovation and Integration,* 17-19 September 2002*,* 609-617.

CALIBRATION OF REGIONAL SEISMIC STATIONS IN THE MIDDLE EAST WITH SHOTS IN TURKEY

M. Nafi Toksöz[1], Sadi Kuleli[1], Cemil Gurbüz[3], Dogan Kalafat[3], Tolga Bekler[3], Craig A. Schultz[2], Rengin Gok[2], and David B. Harris[2]

Massachusetts Institute of Technology[1], Lawrence Livermore National Laboratory[2], Bogazici University[3]

Sponsored by National Nuclear Security Administration
Office of Nonproliferation Research and Engineering
Office of Defense Nuclear Nonproliferation

Contract No. DE-FC03-01SF22398[1,3] and W-7405-ENG-48[2]

ABSTRACT

The objective of this project is to calibrate regional travel times and propagation characteristics of seismic waves in Turkey and surrounding areas in order to enhance detection and location capabilities in the region. Important data for the project are obtained by large calibration shots in central and southeastern Turkey. The first, a two-ton shot, was fired in boreholes near Keskin in central Anatolia on 23 November 2002. The explosives were placed in 14 holes, each 80 m deep, arranged in concentric circular arrays. Ninety temporary seismic stations were deployed within a 300 km radius around the shot. These and the permanent stations of the Turkish National Seismic Network provided good azimuthal coverage as well as three radial traverses. Most stations within a radius of 200 km recorded the shot. A second shot on 17 July 2003 (1.4 ton ANFO) located 55 km southeast of the first and directly on one of the profiles provided a reversal of the southeast profile. This explosion provides reciprocal calibration data for the first shot near the Keskin short-period array.

A third shot on 12 April 2004 (one ton dynamite in seven holes) was detonated near Gaziantep, at the northeast edge of the Arabian Plate, and recorded along a northwest profile crossing the Arabian-Anatolian Plate boundary.

All obtained travel-time and waveform data are analyzed to obtain a three-dimensional (3-D) crust and upper mantle velocity model. The crustal thickness under Keskin is 38 km and the P_n velocity is 7.9 km/s. In the crust, P velocity increases from 6.1 km/s below the first layer to 6.8 km/s at the lower crust. In central Anatolia, crustal thickness varies between 36 and 38 km.

OBJECTIVES

The primary objectives of the project are to: (1) calibrate the regional travel-times and propagation characteristics of seismic waves across the Middle East and eastern Mediterranean region; (2) calibrate local and regional models for specific International Monitoring System (IMS) stations in Turkey; (3) conduct a reciprocity experiment to provide dense local and near regional calibration of the Keskin-Belbasi IMS array in Turkey; and (4) provide data to enhance IMS detection, location, and discrimination capabilities.

Several shots have been fired in boreholes near, or at regional distances to, the Keskin array in central Anatolia. Data are interpreted to obtain a crust/uppermost mantle in Central Anatolia. Combined with data from other explosions in eastern and western Turkey, a comprehensive database is generated for a 3-D crust/upper mantle velocity model for the region.

RESEARCH ACCOMPLISHED

The first calibration shot was fired in central Turkey near Keskin in November 2002. The detailed technical information and preliminary earth structure was given in a previous SRR paper (Toksöz et al., 2003). Two more explosions were recorded in 2003 and 2004. In addition, available seismic data from various other seismic explosions in Turkey are collected (Bekler, 2001). Locations of the shots and seismic profiles are shown in Figure 1. Information about the shots is listed in Table 1.

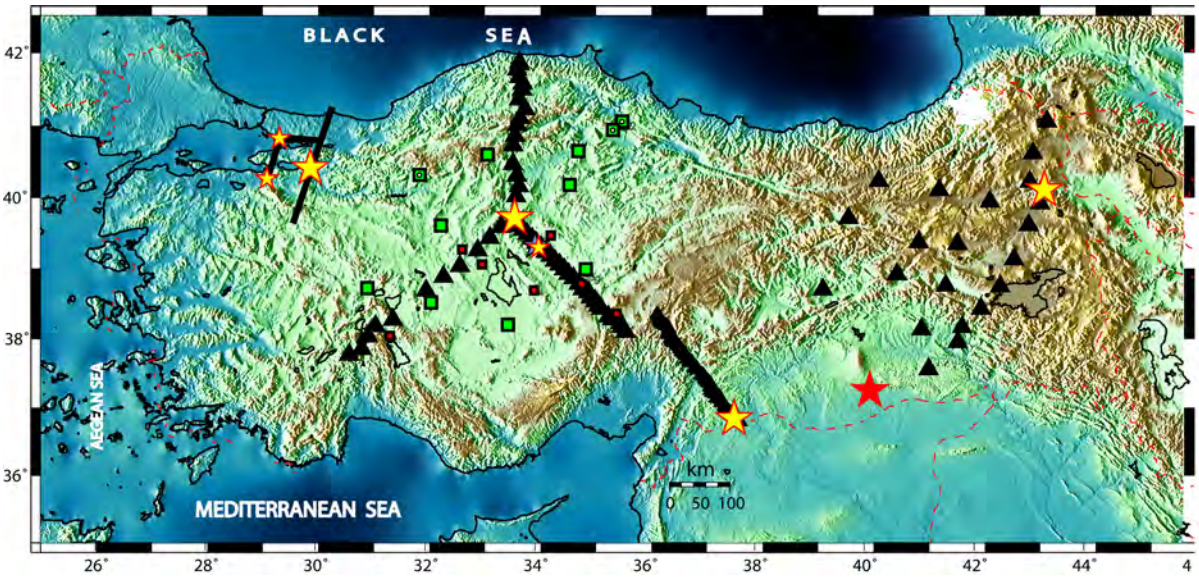


Figure 1. Location of several seismic calibration experiments carried out with active sources in Turkey. Yellow stars show the shot (or explosion) points. Black triangles are seismic recording profiles or stations. Red star is the proposed shot location on the northern edge of the Arabian Plate.

Table 1.

	DATE	LOCATION	O.T.	EXPLOSIVE (T)
Keskin 1	23 November 2002	39.7242 N 33.6355 E	22:47:33:40 UT	Dynamite, 0.280 T
Keskin 2	23 November 2002	39.7242 N 33.6355 E	21:10:04:80 UT	Dynamite, 1.220 T
Agri	5 June 2001	39.803 N 43.167 E	14:10:58:80 UT	Ammonium Nitrate, 12 T
Kaman	17 July 2003	39.326 N 34.001 E	13:48:35:376 UT	Quarry
Gaziantep	12 April 2004	36.800 N 37.730 E		Dynamite, 1 T
Sakarya 1	19 November 2000	40.768 N 29.4587 E	23:30:30:43 UT	Dynamite, 0.3 T
Sakarya 2	23 July 1998	40.1723 N 29.2313 E	12:48:29.5 UT	Dynamite, 6 T

Keskin Calibration Shot

Two calibration shots were fired near Keskin in Central Anatolia on 23 and 24 November 2002. The first shot was 280 kg dynamite in two boreholes. The main shot was 1,720 kg dynamite in twelve 100 m deep holes in granite. This shot was recorded along three profiles of temporary seismic stations, as well as the stations of the Turkish National Seismic network. Locations of the shot and the profiles are shown in Figure 1. Details of the experiment and initial crustal models were given in earlier papers (Toksöz et al., 2002, 2003). Here, we present more detailed crustal velocity models.

Seismic records of the Keskin shot along the three profiles (north, west, and south) are shown in Figure 2. Two-dimensional (2-D) velocity models are obtained for the north and south profiles using travel-time inversions and ray-based synthetic seismograms (Cerveny and Psencik, 1984; Zelt and Smith, 1992). The observed seismic section, matching synthetic seismograms and travel-times for direct, reflected, and refracted phases are shown in Figures 3a and 3b. The 2-D crustal velocity models are also shown. The models incorporate discrete layers and velocity gradients in each layer. The crustal thickness under those shot point is 38 km, and the P_n velocity is 7.9 km. The crustal thickness decreases to the north, and thickness changes are observed where the profile crosses the major fault zones. Along the southern profile, crustal thickness increases to 40 km and P_n velocity to 8.0 km/s.

Kaman Quarry Blast

The Kaman quarry is located along the southern profile 55 km from the Keskin shot point (Figure 4). During the Keskin experiment, one station (n973) was placed at the quarry site. In July 2003, we recorded the quarry blast with an array of 14 stations to the north (including the Keskin shot point) and 11 stations to the south. Seismograms, shown in Figure 4, have good signal-to-noise ratio. Data from the northerly profile of the quarry blast and the southerly profile of the Keskin shot provide an opportunity for a reciprocity test. The Keskin to quarry and quarry to Keskin travel-times agree within 0.04 second. The sampling interval of the seismic data is 0.01 second, and potential errors of picking first arrivals are ± 0.01 second. Since the shots were timed with seismometers near the shot point, the observed 0.04-second difference is within the potential reading errors. Currently, we are looking at waveforms, corrected for instrument response, to determine differences between source functions.

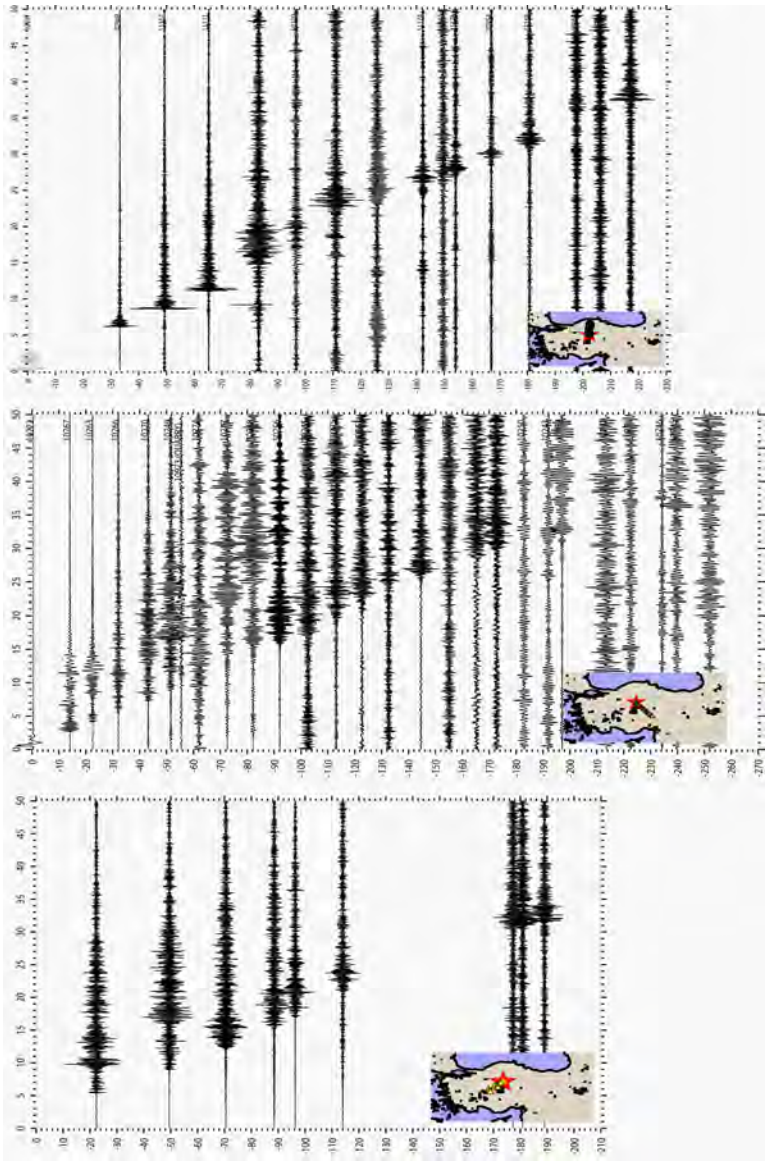
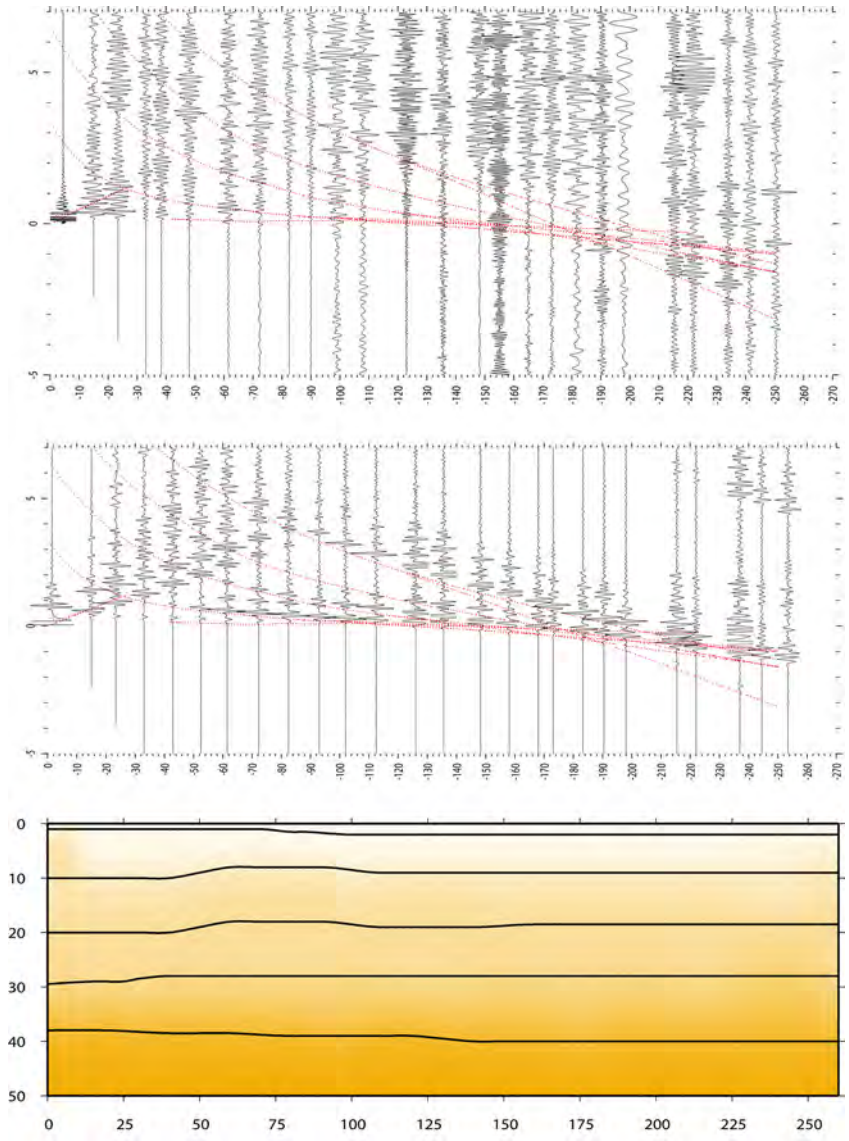
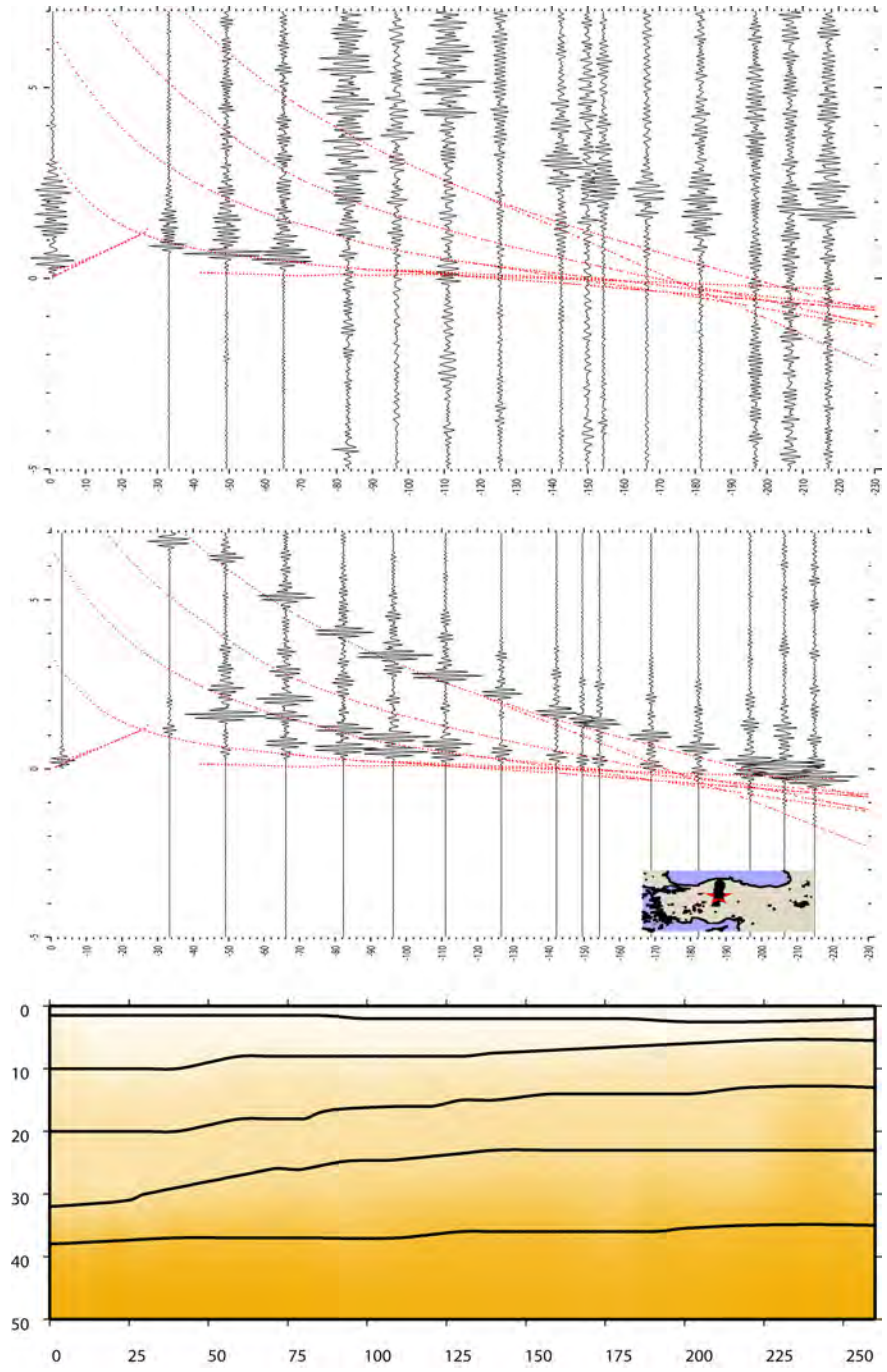


Figure 2. Seismic data recorded along three profiles from the Keskin shot. Insets show the locations of the shot and the profiles.



(a)

Figure 3a. Observed seismograms from the southern profile of the Keskin shot, and synthetic seismograms, travel-time curves based on the crustal structure and velocities. Reduced travel-time scale (t – Δ/6 km/s) is used.



(b)

Figure 3b. Observed seismograms from the northern profile of the Keskin shot, and synthetic seismograms, travel-time curves based on the crustal structure and velocities. Reduced travel-time scale (t – Δ/6 km/s) is used.

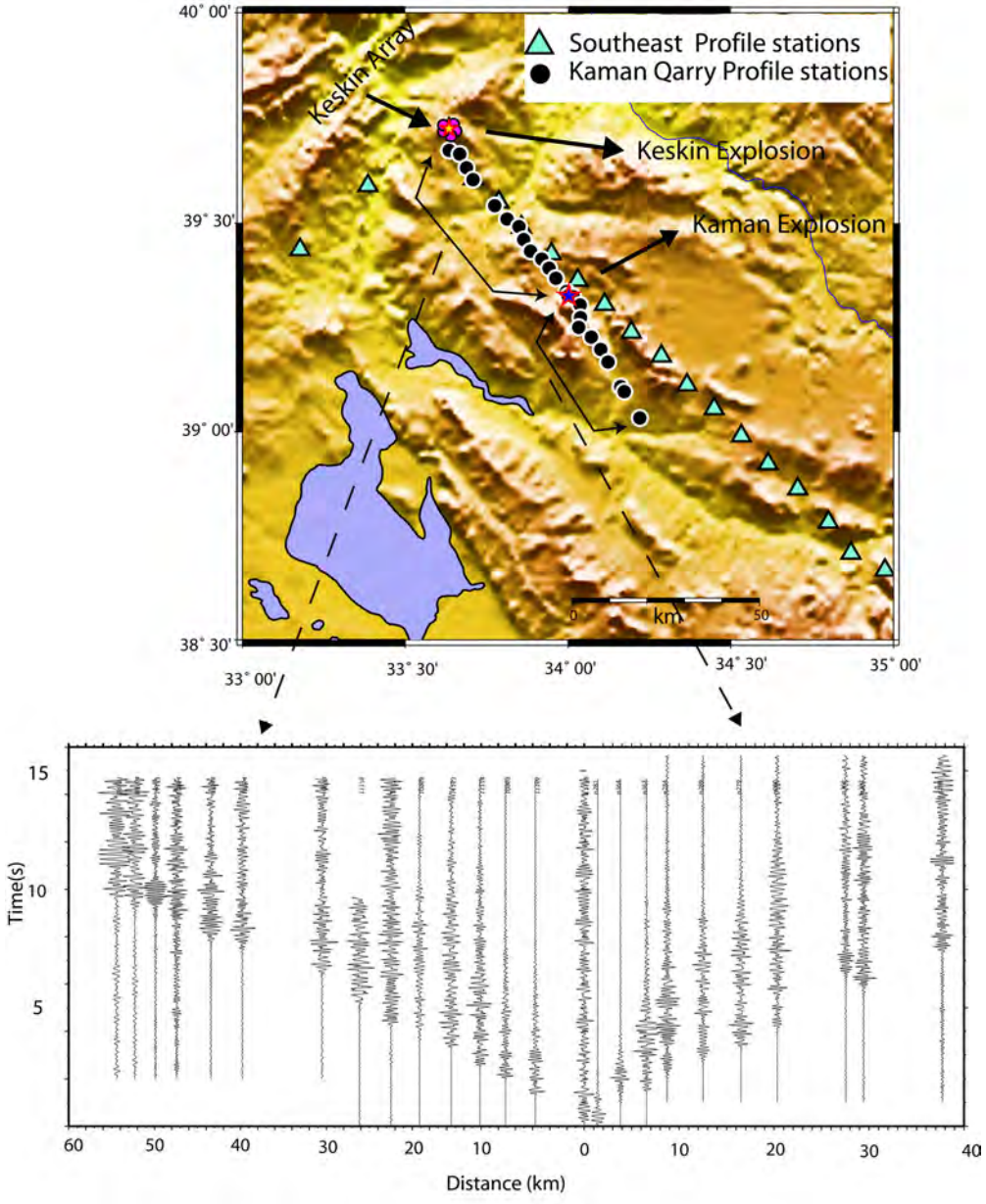


Figure 4. Seismic data from the quarry blast to the south of Keskin array. Locations of the quarry blast, Keskin, and seismic stations are shown at the top of the figure. Triangles are stations that recorded the 2002 Keskin shot, and circles are stations that recorded the quarry blast. Seismograms are shown at the bottom of the figure.

Gaziantep Shot

A one-ton (dynamite) shot was detonated (on 12 April 2004) in southeastern Turkey, at the northern tip of the Arabian Plate. Sixty-one seismic stations were deployed along a linear array oriented northwest toward Keskin. The shot location, recording array, and seismograms are shown in Figure 5. The array crosses the boundary between the Arabian and Anatolian Plates, and the extension of the Dead Sea rift zone near the Maras triple junction. As

seen in the data in Figure 4, the attenuation of the crustal seismic phases across the rift zone is dramatic. Yet the P_n propagation is not affected by the rift structure.

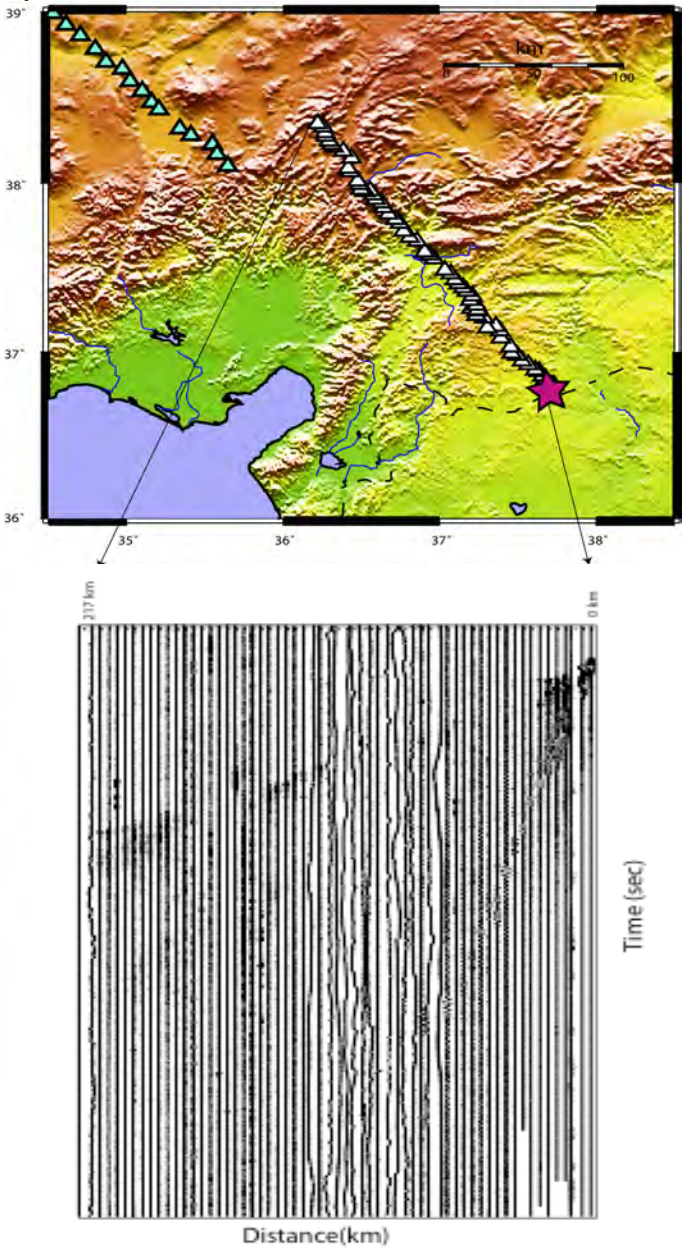


Figure 5. Location of the Gaziantep profile and the seismic data. The shot location is shown by a purple star. The profile crosses the extension of the Dead Sea rift zone, near the Maras triple junction. Note the strong attenuation of seismic crustal phases by the rift. The P_n arrivals are attenuated less.

Other Active Source Seismic Studies

Other refraction experiments in Turkey complemented those carried out as part of this project, the majority of which were carried out by the Kandilli Observatory and Earthquake Research Institute (Bekler, 2001). The two significant ones were in the Sakarya region of western Turkey and the Agri Province of eastern Turkey. Data from these shots are collected and being integrated with the data from Keskin and other shots conducted under this project.

Sakarya Refraction Experiment. A refraction experiment was conducted in November 2000 in the eastern Marmara Sea (Figure 6). A 180 km long profile, oriented in the north-south direction across the North Anatolian

Fault Zone, was used. Three shots were fired along the profile, one at each end and one in the middle. Charge sizes were 350 kg at the end shots and 325 kg in the middle shot point. Explosives were loaded into 50-meter deep holes. Data were collected with instrumentations similar to those used in our explosion studies (Figure 6a).

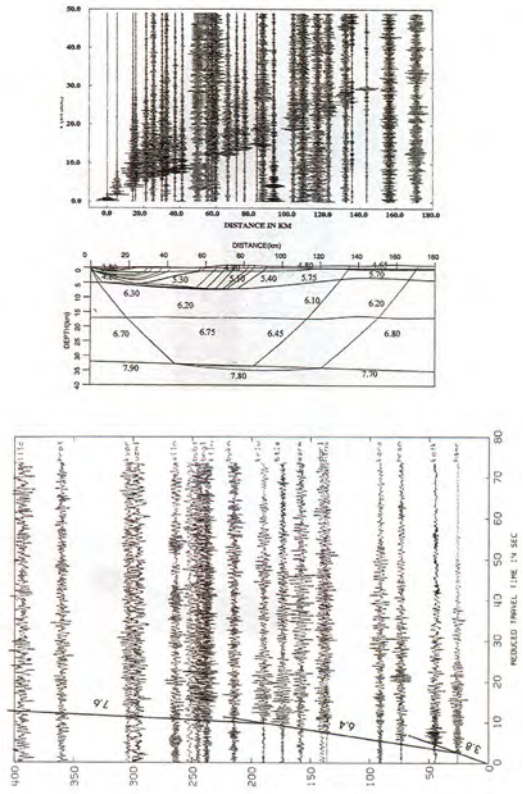


Figure 6. (a) Seismic refraction profiles from Sakarya shot. (b) Seismograms from Agri Dam Gallery explosions. Locations of explosions and stations are shown in Figure 1.

The calculation of P wave velocity structure was obtained using 2-D raytracing (SEIS83 package, Cerveny and Psencik, 1984), and inversion (RAYINVR program of Zelt and Smith, 1992). A 2-D crustal velocity structure beneath the profile was obtained. The P wave velocities at the top layer vary from 3.8 km/s to 4.8 km/s along the profile. The part shallow crust has high velocity gradients. Below the top layer seismic velocities vary between 6.2 km/s and 6.8 km/s with variable velocity gradients between 7 to 17 km depth. Clear P_n arrivals were not observed, and depth could not be determined.

Agri Dam Explosion. Two explosions were conducted as a part of the Agri Dam construction work. One was a ripple fire consisting of 20 holes which were filled with a total of three tons of Ammonium Nitrate. The second explosion was in a T-shaped gallery 100 meters away from the first shot point. This gallery shot (with 12 tons of explosives) was recorded by 18 stations of the Eastern Turkey Seismic Experiment (ETSE) PASSCAL broadband array (Gurbüz et al., 2004; Turkelli et al., 2003). The preliminary results show very high Lg and Sn attenuation in eastern Turkey. The shot was observed out to a maximum distance of about 300 km. (Figures 6b). The crust was characterized by three velocities of 3.8, 6.4, and 7.6 km/s. The thickness of the crust at the shot point was found to be 34 km (Gurbüz et al., 2004), much thinner than anticipated.

CONCLUSIONS AND RECOMMENDATIONS

Seismic recordings from calibration shots, a quarry blast, and Agri Dam construction explosions, obtained under this project increased by tenfold the amount of deep crustal sounding data in Turkey. Analysis of these data gives a

crustal thickness of 38 km under Keskin. Crust thins to the north and northwest, and is about 32 km thick to the east of the Sea of Marmara. South of Keskin, crustal thickness increases to 40 km.

In eastern Turkey, crustal thickness obtains from refraction (Gurbüz et al., 2004) and receiver function studies (Zor et al., 2004) are between 34 and 40 km, much less than 50 to 55 km some previous studies had suggested. The P_n velocities vary between 7.9 and 8.0 km/s.

Attenuation of seismic waves in the Anatolian Plate is variable. Attenuation is higher in Eastern Anatolia than the central plateau. Along one profile crossing the Arabian-Anatolian Plate boundary and the northern extension of the Dead Sea rift, a dramatic extinction of P-wave crustal phases was observed. Yet the P_n propagation along the same profiles was not affected.

For future work, we recommend the study of seismic wave propagation and attenuation across the Anatolian-Arabian continental collision zone and the Bitlis Suture. A broadband seismic network deployment and a calibration shot of about 10 tons in southeastern Turkey at the northern tip of the Arabian Plate would provide much needed data for the study.

REFERENCES

Bekler, T. (2001). Crustal evaluation of eastern Marmara region using seismic refraction experiments and earthquake data, Ph.D. thesis, Bogazici University.

Cerveny, V. and I Psencik (1984). SEIS83- Numerical modeling of seismic wave fields in 2-Dlaterally varying layered structures by the ray method, in *Documentation of earthquake algorithms. Report SE-35*, E.R. Engdahl (ed.), 36-40, Boulder: WDC A for SEG

Gurbüz, C., N. Turkelli, T. Bekler R. Gok, E. Sandvol, D. Seber, and M. Barazangi (2004). Seismic event location calibration using the Eastern Turkey broadband seismic network: Analysis of the Agri Dam explosion, Bull. Seism. Soc. Am., 94, 1166-1171.

Toksoz, M.N., S. Kuleli, C.A. Schultz, D.B. Harris, C. Gurbuz, D. Kalafat, and A.M. Isikara (2002). Calibration of regional seismic stations in the Middle East with shots in Turkey, *Proceedings, 24th Seismic Research Review*, Florida, 2002.

Toksöz, M.N., S. Kuleli, C. Gurbuz, D. Kalafat, T. Bekler, E. Zor, M. Yilmazer, Z. Ogutcu, C.A. Schultz, and D.B. Harris (2003). Calibration of regional seismic stations in the Middle East with shots in Turkey, *Proceedings, 25th Annual DoD/DOE Seismic Research Review*, Arizona.

Turkelli, N.,E. Sandvol, E. Zor, R. Gok, Tolga Bekler, A. Al-Lazki, H. Karabulut, S. Kuleli, T. Eken, C. Gurbuz, S., Bayraktutan, D. Seber, and M. Barazangi (2003). Seismogenic zones in Eastern Turkey, *Geophys. Res. Lett.*, 30, 8039.

Zelt, C.A. and R.B. Smith (1992). Seismic travel-time inversion for 2-D crustal velocity structure, *Geophys. J. Int.*, *108*, 16-34.

Zor, E., E. Sandvol, C. Gurbuz, N. Turkelli, D. Seber, and M. Barazangi (2003). The crustal structure of the East Anatolian plateau (Turkey) from receiver functions, *Geophys. Res. Lett.*, *30*, 8044.

QUANTIFYING SOURCE EXCITATION AND PATH EFFECTS FOR HIGH FREQUENCY REGIONAL WAVES

Ru-Shan Wu, Xiao-Bi Xie, Zengxi Ge, and Thorne Lay

University of California, Santa Cruz

Sponsored by Air Force Research Laboratory

Contract No. DTRA01-01-C-0076

ABSTRACT

For the purpose of monitoring nuclear testing, the range of interest for Lg-wave simulations spans a broad frequency band and long propagation distance, while factors that control the source energy partitioning depend on the detailed source model and multi-scale near source velocity structures. We use the finite-difference (FD) modeling plus slowness analysis method developed in this project to solve this problem and investigate the near source Lg-wave excitation and energy partitioning. Our approach is to separate the problem into consideration of near-source energy partitioning effects apart from long-range propagation effects. This method allows a very fine near source model to be used to investigate the near-source processes. A slowness analysis is used for tracking where energy will be partitioned into the long-range propagation regime. The high efficiency of the method is the major advantage, as it allows us to examine a broad source/model space using numerical simulations. To verify the validity of the method, we calculated a suite of full-scale two-dimensional (2D) FD simulations. The trapped energy measured in the waveguide at short distance is compared with the Lg energy obtained from the surface seismograms at long distance. The consistency of these measurements confirms the validity of our approach.

Several preliminary results have been obtained from the numerical simulation and the ensuing slowness analysis. The near source P-to-S conversion in the presence of small-scale lateral heterogeneities is tested as a mechanism for generating the near source S-wave energy from an explosive source. The numerical results reveal that the depth of the source and the depth of the scattering region have strong effects on the P-to-S conversion and the partitioning of energy into trapped and leaking signal. The excitation spectrum for the trapped energy from the S*-wave is also investigated. The modeling shows that the excitation is generally favorable for lower frequencies and shallow source depth. The frequency dependence of these excitation spectra can provide the basis for evaluating the dominant mechanisms for Lg-wave excitation. It also provides the relationship between the observations and the characteristics of the source and near source structure. The amplitude ratios between the P- and S-phases (e.g., Pn/Lg, Pg/Lg, Pn/Sn and Pg/Sn) are widely used as discriminants. We simulate the amplitude ratio between the P-wave and trapped modes for a relatively broad frequency range using velocity models with and without lateral velocity variations. For a typical explosion source and a shallow earthquake source, the results show a general feature similar to that in the observations. At the low frequency end, the earthquakes and explosions have similar ratios but at higher frequencies, the explosive source generates less S-energy.

OBJECTIVE

With the current emphasis on global monitoring for low-yield nuclear tests, regional seismic phases such as Lg and Lg coda have become very important for magnitude and yield estimation of underground nuclear tests. (e.g., Nuttli, 1986; Xie, et al., 1996; Patton, 2001). In addition, various P/S-type amplitude ratios for high frequency regional phases (e.g., Pn/Sn, Pn/Lg, Pg/Lg, Pg/Sn) have become important for event discrimination (e.g., Taylor et al., 1989; Kim et al., 1993, 1997; Walter et al., 1995; Fisk et al., 1996; Taylor, 1996; Taylor and Hartse, 1997; Hartse et al., 1997; Fan and Lay, 1998a-c, Xie and Patton, 1999). Several possible near source energy transfer mechanisms have been proposed, including P- Lg scattering, pS-Lg conversion at the free surface, Rg-to-Lg coupling, S*-Lg conversion, spall excitation of S, tectonic release and rock-damage (e.g., Day and Mclaughlin, 1991; Gupta et al., 1992, 1997; Walter, et al., 1995; Wallace, 1991; Gutowski, et al., 1984; Vogfjord, 1997; Johnson and Sammis, 2001). There is continuing controversy about which mechanism(s) dominate the explosion source energy partitioning processes. Another unsolved puzzle is the frequency dependence observed for regional P/S discriminants. Numerous studies (e.g., Walter et al., 1995; Fisk et al., 1996; Taylor, 1996; Taylor and Hartse, 1997; Hartse et al., 1997; Fan et al., 2002) have demonstrated that regional P/S measurements (Pn/Lg, Pg/Lg, Pn/Sn, Pg/Sn) provide useful discrimination of earthquakes and explosions at frequencies above about 3 Hz, but the discrimination performance is much lower at low frequencies. There is very incomplete theoretical understanding of this strong frequency-dependent phenomenon.

Due to the complex excitation and energy partitioning processes associated with regional phases, it is difficult to separate the contribution of individual energy partitioning mechanisms from the observed data empirically. Numerical modeling approaches are thus of great importance for investigating the excitation and propagation of regional phases. Early research investigated various propagation properties of the Lg phase using 1D models and the results were very limited. A one-way wave equation based method (Wu, et al., 2000a,b) has been used to investigate the path effect of the Lg wave propagation but it is not suited for the excitation issue. Full wave numerical techniques such as finite-difference (FD) are also widely used for investigating Lg-wave excitation and propagation in complicated crustal waveguides (Xie and Lay, 1994; Jih, 1995, 1996; Bonner, et al., 2003; Stevens et al., 2003). The main disadvantages of these numerical methods that provide complete synthetic seismograms are the low computation efficiency and huge computer memory requirement, especially when applied to long distance Lg propagation.

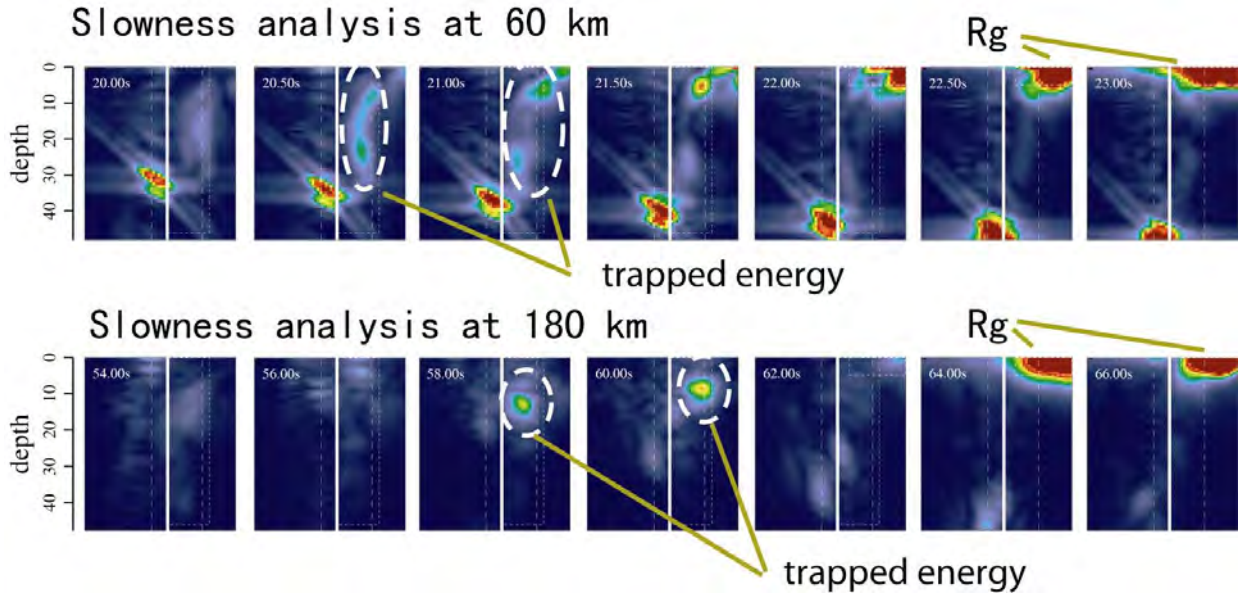


Figure 1. Examples showing the slowness analyses at distances of 60 km (upper panel) and 180 km (lower panel). In all slowness diagrams the range of slowness is 0–0.4 s/km and the thick white vertical line is the upper mantle S wave slowness (0.22 s/km). The energy that can be trapped is indicated in the figure. The wavefields show quite different features at these distances but give consistent predictions for the trapped energy fluxes.

Most investigators agree that appreciable energy from explosion sources is converted to S-waves in the near-source region (Myers, 2003). Following this perspective, we developed a "finite-difference modeling plus slowness analysis method" (FDSA). Using this approach, the wave propagation process can be investigated in a joint time-frequency-space-slowness domain. Very detailed near-source structures and high frequencies can be used to investigate the underlying physical process of Lg excitation and energy partitioning. The frequency dependent properties of the energy partitioning can also be investigated.

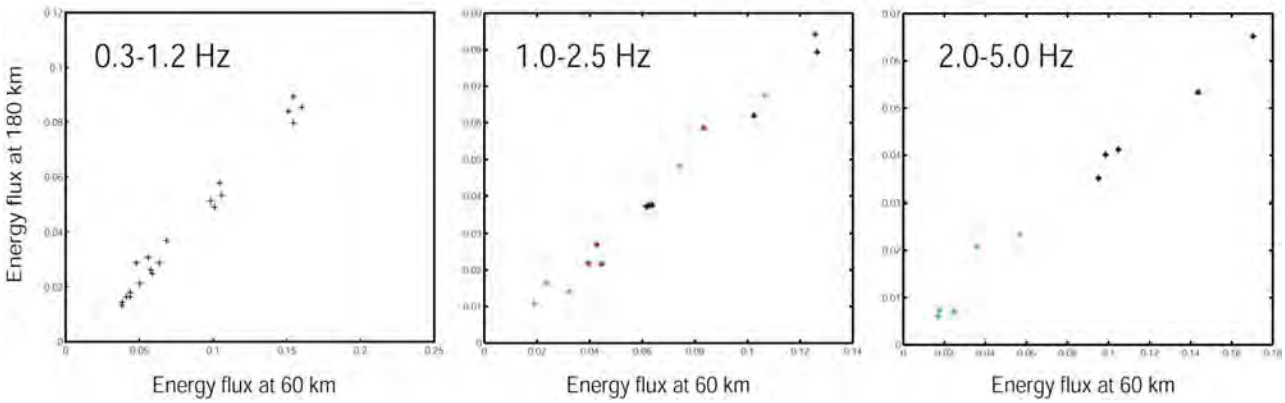


Figure 2. Comparison between trapped waveguide energy measured at 60 km (horizontal coordinate) and 180 km (vertical coordinate) for frequency bands 0.3-1.2 Hz, 1.0-2.5 Hz and 2.0-5.0 Hz. The results are from different velocity models and source depths. Different colors represent different velocity models. The results show a general linear relationship for all frequency bands.

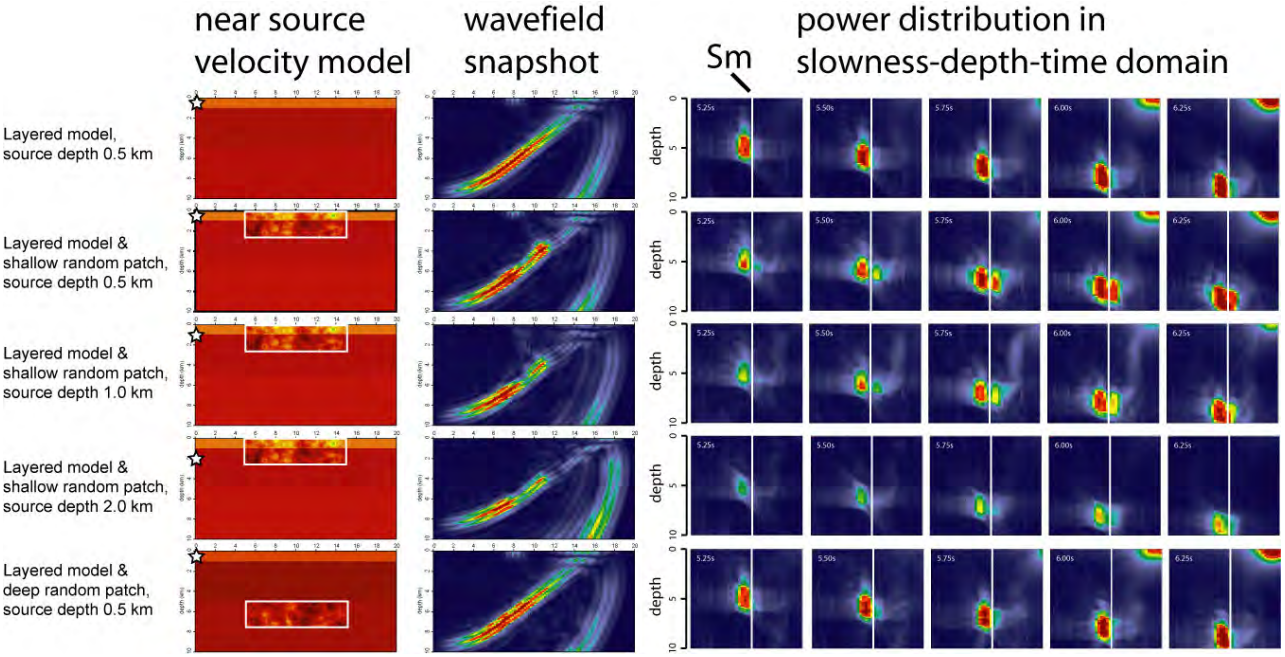


Figure 3. Summary of the P-pS-Lg wave coupling. From left to right are velocity models, wavefield snapshots and energy distributions in the slowness-depth domain. For details see text.

RESEARCH ACCOMPLISHED

Numerical test of the method

The "finite-difference modeling plus slowness analysis method" (FDSA) is described in Xie and Lay (1994) and Wu, et al., (2002, 2003). For verifying the method, the waveguide energy flux at short distance is compared to the surface Lg-wave energy (Wu, et al., 2003). To examine the energy flux measurements obtained at even shorter distances, we compared the slowness analysis measurements at 60 km with measurements at 180 km distance. For all numerical examples calculated in this report, we use the EK (Eastern Kazakh) model (Priestley et al., 1988) as the background and modify it by adding different laterally varying structures. A range of sources and near source structures was used in the simulations. Figure 1 gives examples for energy with different slowness (phase velocities) at these two distances. The wave fields at these distances show quite different features in the slowness-depth domain but give consistent predictions for the wave field energy fluxes. Figure 2 compares the corresponding wave guide energy measured at 60 km and 180 km distances. Although a wide range of near-source structures and source depths are used to generate these measurements, they show very good linear relationships. This further verifies that we can use a small model to predict the energy distribution at greater distances.

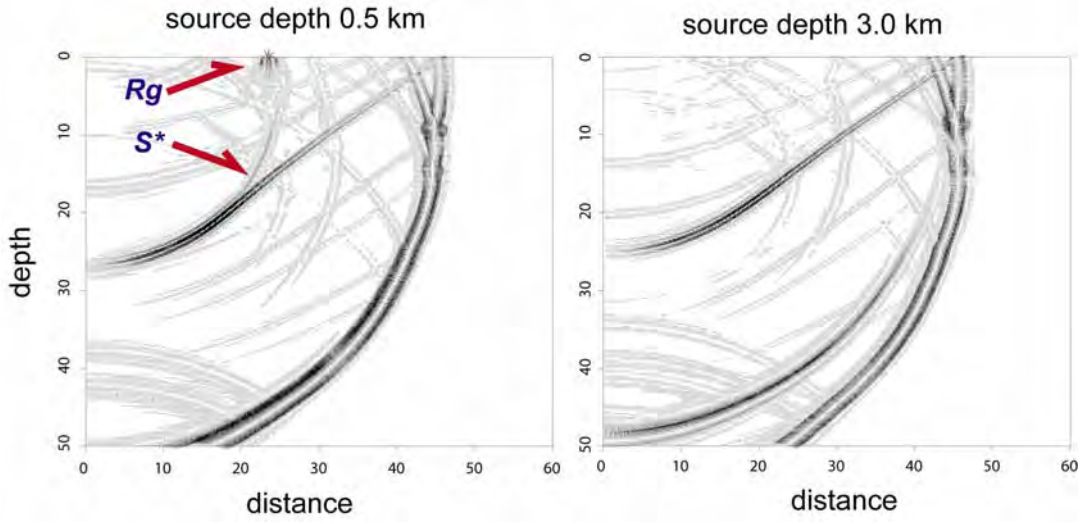


Figure 4. Wavefield snapshots for explosion sources at different depths. The source depths for left and right panels are 0.5 km and 3.0 km, respectively. A shallower explosion is a more efficient source for S* and Rg-waves.

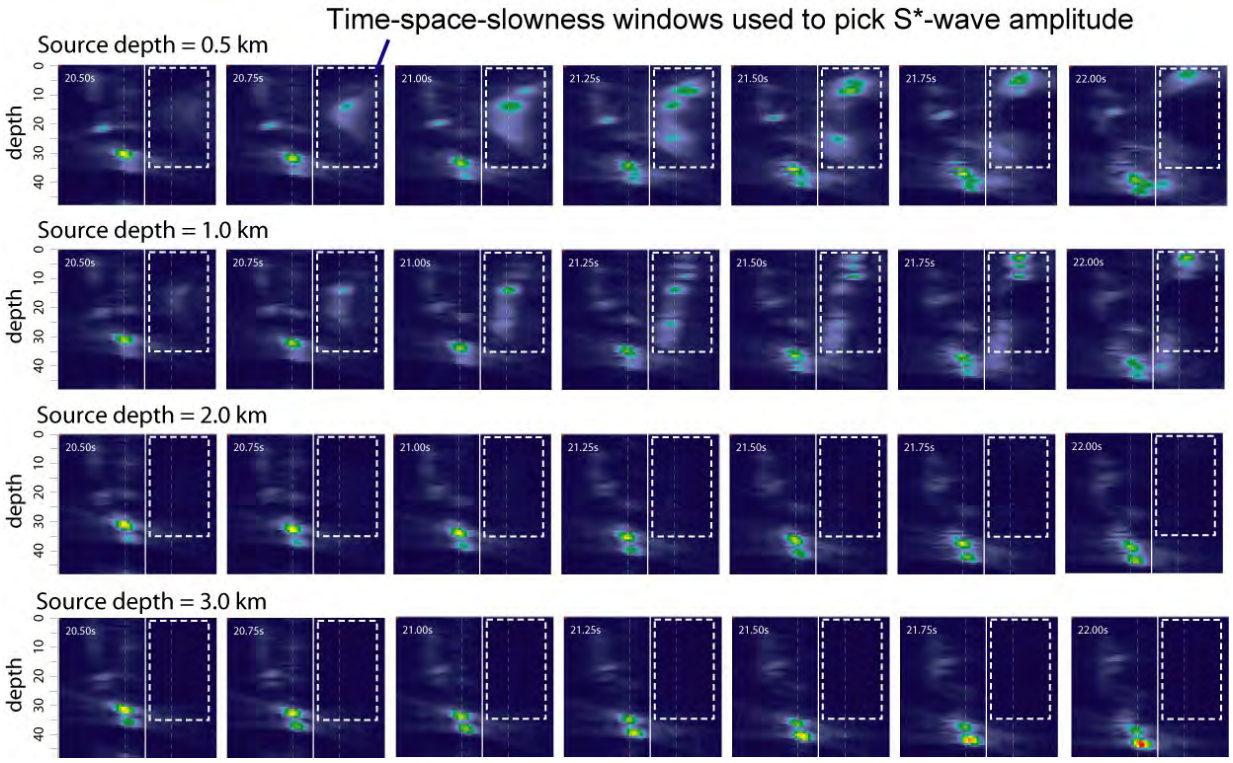


Figure 5. Slowness analysis for investigating the S*-wave energy contributing to the Lg-wave. Different rows are for different source depths. Dash line rectangles indicate the time-space-slowness windows used to pick the S* energy.

Investigating P-Lg and pS-Lg conversion

Figure 3 summarizes how the near-source lateral velocity variations affect the explosion P-to-S energy conversion. From left to right are velocity models, wave field snapshots and energy distributions in the slowness domain. Slowness analysis is used at a distance of 16 km and depth 0-10 km. We use different source/model combinations in the simulations and test their effects on the P-to-S conversion. This example shows that without the lateral velocity heterogeneity, the energy of the free-surface reflected pS wave falls to the left of the upper mantle S-wave slowness and therefore cannot form trapped energy at regional distance. With a random velocity layer added to the model, the pS-wave front becomes distorted and its slowness content crosses the upper mantle S-slowness. Assessing the energy that builds to the right of the upper mantle S-slowness allows us to predict the Lg-wave component associated with P-to-S conversion. As can be seen from the numerical simulation, the depth of the source and the depth of the scattering region have strong effects on the P-to-S conversion and the partitioning of energy into trapped and leaking signal.

Contributions from S*-wave

For shallow spherical explosions, depending on the situation, the S*-wave may become a significant contributor to Lg (Gutowski, et al., 1984; Xie and Lay, 1994; Vogfjord, 1997). The amplitude of S* can be large as long as the source depth is within a fraction of a wave length from an interface. This makes its excitation highly dependent on the source depth and frequency. Figure 4 shows snapshots for explosion sources at 0.5 km and 3.0 km, respectively. This clearly shows that a shallow source generates larger S*- and Rg-waves. Figure 5 gives slowness analysis at 60 km distance for explosions at different depths. The S* energy is marked using dash line rectangles located to the right of the upper mantle S-wave slowness. With the FDSA method, we can isolate and quantify the S* energy even within the complicated near source region, e.g., separate the S* from the pS-wave. Using a band pass filter, the excitation function of the S*-wave can be easily obtained. This can be used to compare with various observations such as the spectral content of Sn and Lg, and various types of P/S amplitude ratios.

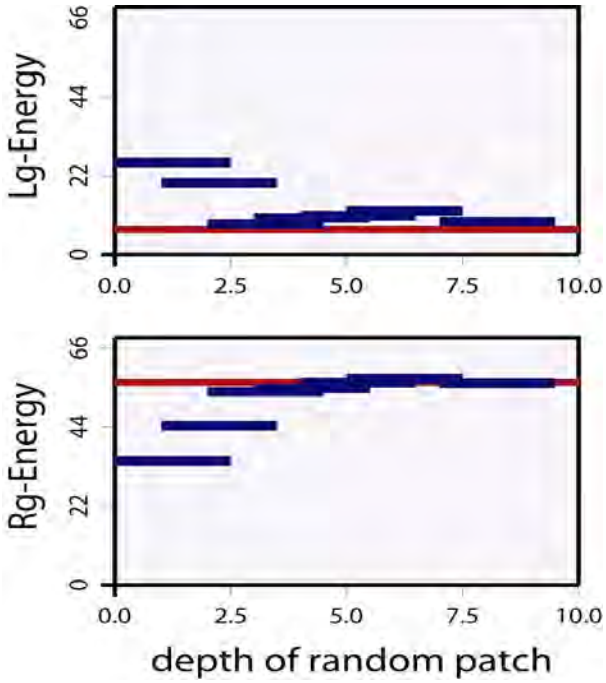


Figure 6. Apparent relationship between the Lg- and Rg-wave energy at 180 km in the waveguide vs. the depth of near source random scattering. Frequency range is 0.3-1.2 Hz. Red lines are for the background layered model. Blue bars are for models with near source random patches at different depths.

Possible Rg-to-Lg coupling

Rg-to-Lg coupling has long been proposed as a potential mechanism for low frequency Lg-wave excitation. However, there is disagreement as to whether this is a dominant mechanism or not. This is mainly due to the lack of knowledge about the actual mechanism of this process. Although it is generally agreed that Rg-to-Lg coupling is caused by scattering in the near-surface environment, systematic investigation of this process is still lacking. We have conducted two types of tests: a) for a shallow explosion source, we locate scattering regions at different depths; and b) for a shallow scattering region, sources are located at different depths. Figure 6 shows the waveguide energy fluxes for Lg and Rg versus the depth of near-source heterogeneities. The frequency range is 0.3-1.2 Hz. For models with shallow scattering, Rg loses energy while Lg gains energy. Figure 7 gives the apparent relationship between the source depth and the Rg and Lg energy. The three frequency bands are 0.3-1.5, 1.0-2.0 and 2.0-5.0 Hz, respectively. The sources are located at different depths and scattering is provided by adding a near source random patch at the top of the crust. A shallower source raises both Rg and Lg energy while shallow scattering increases the Lg energy but decreases the Rg energy. The apparent Rg-Lg coupling occurs in the low frequency band and Pg-Lg coupling occurs in the high frequency band. Although these preliminary results provide an apparent relationship similar to some observations, they do not yet provide robust evidence that the energy lost from Rg necessarily transferred to the Lg, since the S*-wave also has a similar excitation function. To solve this problem, further investigations which can reveal direct energy exchange between Rg and Lg at the near source region are required.

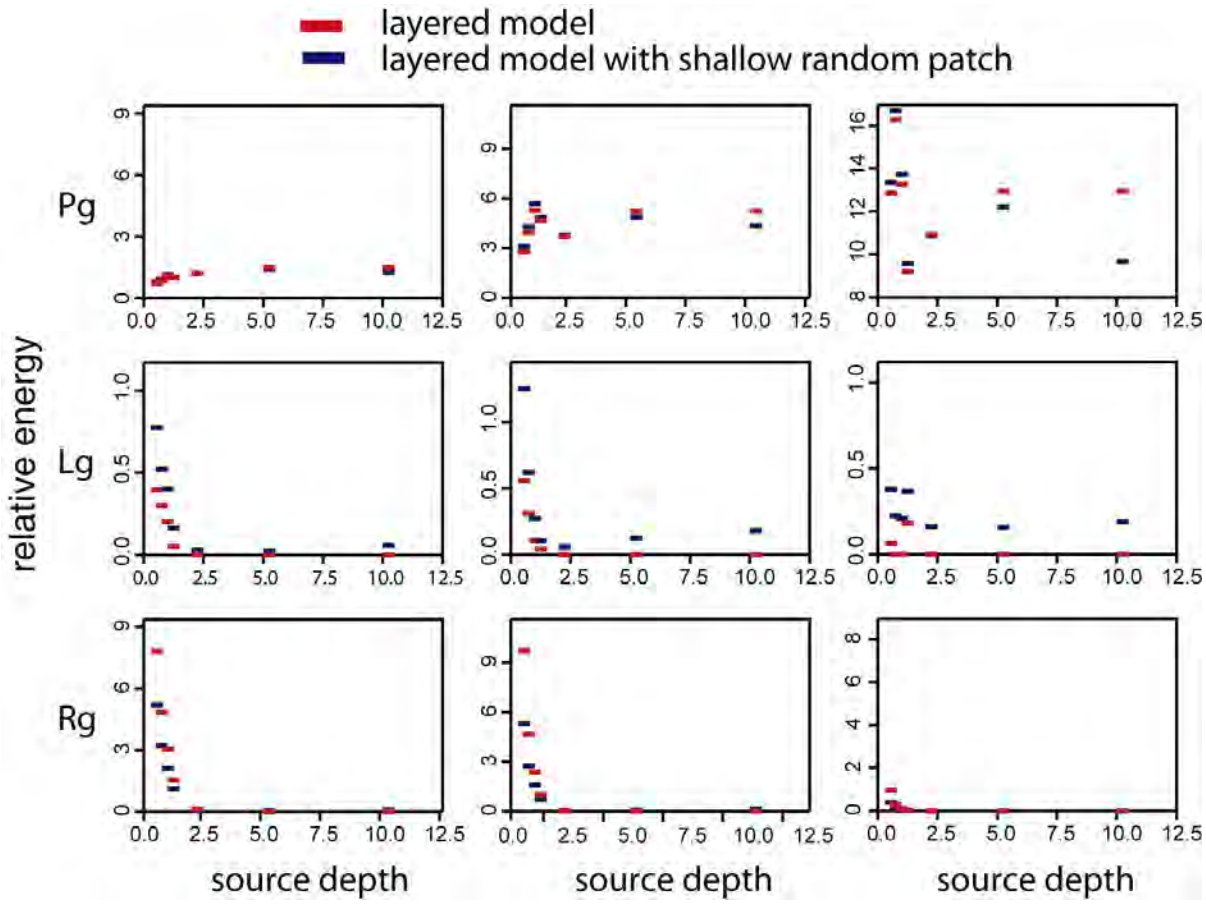


Figure 7. Effects of shallow near source scattering on the energy partitioning of Pg-, Lg- and Rg-waves. Sources located at different depths between 0.5 and 10 km. Results for background model are shown with red bars and results for models with random patches are shown with blue bars.

Frequency dependent excitation spectra and P/S ratios

We emphasize simulating the observed frequency dependent attributes of P and S partitioning. These frequency variations are rooted in the underlying physical processes and are usually controlled by different characteristic scales. For example, the excitation of Lg by S*, Rg-to-S scattering and spall are all highly source-depth dependent. The excitation spectra of specific phases depict the frequency dependence of these processes. Frequency-dependent P/S ratios will depend on the excitation functions of multiple phases. Figure 8 gives the excitation spectrum for the trapped energy from the S*-wave (without calibration using the source spectrum). The result clearly shows that the excitation is generally favorable to lower frequency and shallow source depth. Although the maximum amplitude usually appears at the low frequency end, the spectrum of a 1 km deep source has a maximum at around 3 Hz. This may result from that the particular velocity model used, which has an interface at 1 km depth. The frequency dependence of these excitation spectra can provide a basis for evaluating the dominant mechanisms for Lg-wave excitation, or for down-weighting particular mechanisms as being less significant. It can also provide a relationship between the observations and the characteristics of the source and near source structure.

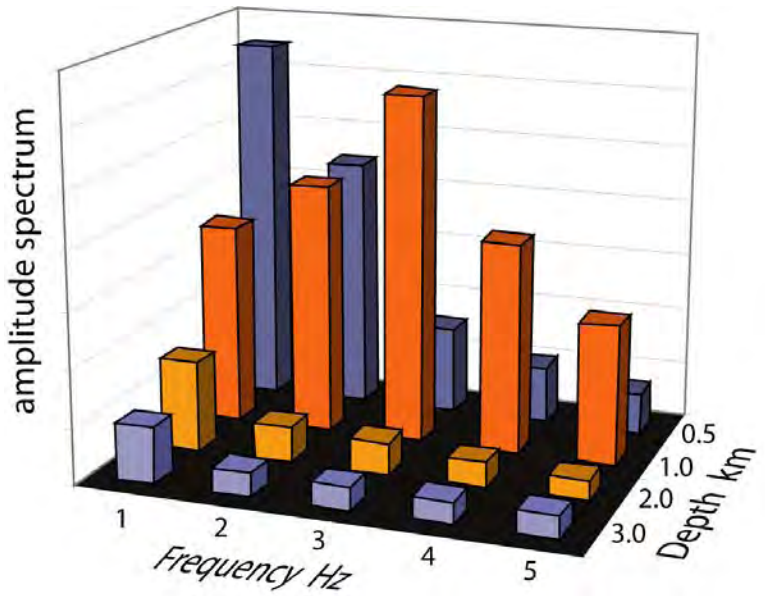


Figure 8. S*-to-Lg excitation spectra for sources at different depths. Note that the power is mostly concentrated at lower frequencies and for shallower sources.

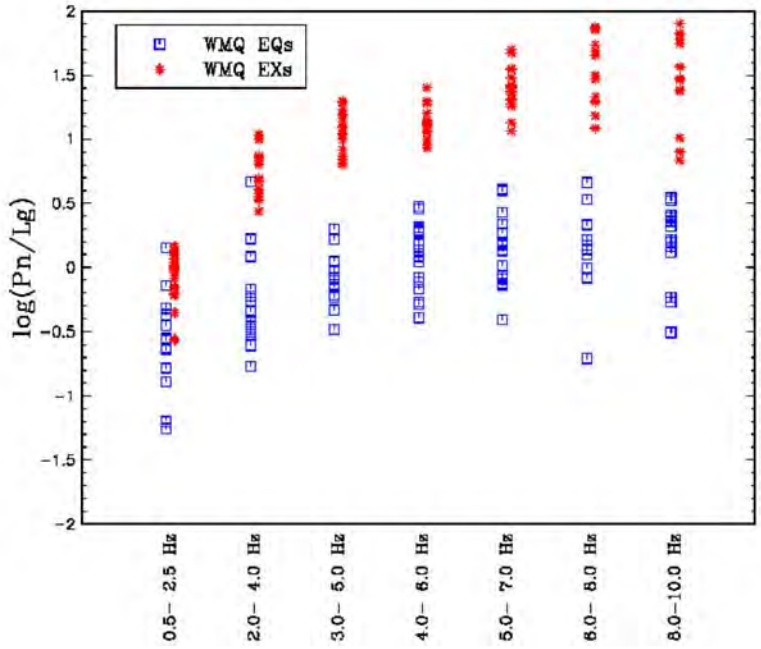


Figure 9. Log Pn/Lg amplitude ratios in frequency bands from 0.5 to 10.0 Hz for 20 Balapan nuclear explosions (asterisks) and 24 earthquakes (squares) recorded by WMQ (Fisk, 2003). The two populations exhibit poor separation below about 2 to 3 Hz and good separation at higher frequencies. SNRs for three of the nuclear explosions are marginal at frequencies above ~8 Hz.

Figure 9 shows observed Log (Pn/Lg) amplitude ratios in the frequency band between 0.5 and 10.0 Hz for explosions and earthquakes (Fisk, 2003). The two populations exhibit poor separation below about 2 to 3 Hz and good separation at higher frequencies. Figure 10 gives a simple simulation of the Log(P/Lg) amplitude ratio in the frequency band 0.2 to 5.2 Hz. Two types of sources are used, an isotropic explosive source at 0.5 km depth representing a typical "explosion", and a 45-degree dip-slip dislocation source at 3.0 km depth representing a typical "shallow earthquake". Two velocity models are used in the calculation, EK and EK plus a shallow near source random layer (depth 0-2.5 km, distance 5-25 km). The slowness analysis is conducted at a distance of 60 km. For the

explosive source in the EK model, the Lg energy mainly comes from the S* phase. For the EK plus random layer model, it is expected that S*, P-to-Lg and Rg-to-Lg couplings will jointly contribute to the Lg energy. Compared with the explosive source, the somewhat deeper dislocation source is less affected by the shallow random layer. The general features of the simulation are similar to the observations (Figure 9): at the low frequency end, the earthquakes and explosions have similar P/Lg ratios but at higher frequencies, the explosive source generates less S energy.

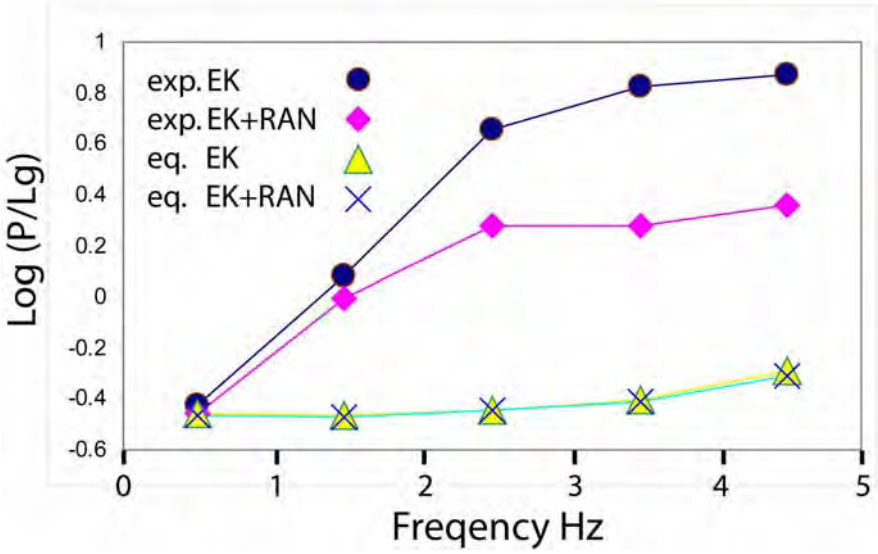


Figure 10. Simulated Log (P/Lg) amplitude ratios in frequency domain. The circle, diamond, triangle and cross represent explosion source in the EK model, explosion source in the EK model with shallow random patch, dislocation source in the EK model and dislocation source in the EK model with shallow random patch. The explosion source is located at depth 0.5 km and the dislocation source is located at depth 3.0 km.

CONCLUSIONS AND RECOMMENDATIONS

The "finite-difference modeling plus slowness analysis method" is used to investigate the excitation and near source energy partitioning for crustal guided waves. The method has two major advantages. First, it allows us to study the wavefield property in multiple domains including space, time, slowness and frequency, which gives a better opportunity to isolate different mechanisms within the complicated near source region. Second, the method can be applied at close range, well before Lg is actually formed. This makes the method very efficient. It allows us to use very fine near source velocity models, calculate a broader frequency band and test a large quantity of source/model combinations. Using this method, several excitation and partition mechanisms, e.g., P-Lg, pS-Lg, Rg-Lg and S*-Lg, are separately investigated. The results are preliminary.

Since the FDSA is an efficient method, we suggest using this method to systematically assess the relationship between the near-source velocity structure, source parameters and the resulting Lg energy. The relative importance of different excitation mechanisms can be evaluated. The statistical features of the velocity structure, RMS value and correlation length, along with the depth of the scattering region and the source depth will control the frequency-dependent transfer functions. It is expected that with more complexities being added to the model (CLVD, different overburden structures and scattering models, source depth changes, different source time functions, etc.), these frequency dependent features will be complicated, but can be systematically mapped out. This is an essential undertaking for placing regional phase energy partitioning on a sound physical basis. The numerical modeling will set up a link between the physical model and observable frequency dependent features, which can provide guidelines for improving the empirical discrimination relations. Feedback from the observations will guide the simulations towards the correct physical models as well.

Although most Lg observations are taken from the vertical component of seismograms, the tangential component often has as much energy as the vertical component. Some researchers reported that in the near field strong motion

records, clear SH energy comparable to that from SV component can be observed and they must be generated in the source region. Any Lg-wave excitation theory must provide an explanation for these observations. Since 2D geometry decouples the P-SV problem and the SH problem, it does not provide any information on the coupling between the source and SH component. We propose to extend the FDSA method from 2D to 3D case to address this problem.

ACKNOWLEDGEMENTS

This research is supported by the Air Force Research Laboratory under the Contract No. DTRA01-01-C-0076. Facility support from the W.M. Keck Foundation is also acknowledged.

REFERENCES

Bonner, J.B., H.J. Patton, A.C. Rosca, H. Hooper, J. Orrey, M. Leidig and I. Gupta, (2003), Aspects of Rg and Lg generation from the Shagan depth of burial explosions, *Proceedings of the 25th Seismic Research Review, Muclear Explosion Monitoring: Building the Knowledge Base*, LA-UR-03-6029, Vol. I, pp. 384-394.

Day, S.M. and K.L. McLaughlin, 1990, Seismic source representations for spall, *Bull. Seism. Soc. Am.*, 81, 191-201.

Fan, G.W. and T. Lay, 1998a, Statistical analysis of irregular waveguide influences on regional seismic discriminants in China, *Bull. Seismol. Soc. Am*., 88, 74-88.

Fan, G.W. and T. Lay, 1998b, Regionalized versus single-station wave-guide effects on seismic discriminants in western China, *Bull. Seismol. Soc. Am*., 88, 1260-1274.

Fan, G.W. and T. Lay, 1998c, Statistical analysis of irregular waveguide influences on regional seismic discriminants in China: additional results for Pn/Sn, Pn/Lg and Pg/Sn, *Bull. Seismol. Soc. Am*., 88, 1504-1510.

Fisk, M. D., H. L. Gray and G. D. McCartor 1996, Regional discrimination without transporting thresholds, *Bull. Seism. Soc. Am*., 86, 1545-1558.

Gupta, I.N., W. Chan, and R. Wagner, 1992, A comparison of regional phases from underground nuclear explosions at East Kazakh and Nevada Test Sites, Bull. Seism. Soc, Am., 82, 352-382.

Gupta, I. N., T. Zhang, and R. A. Wagner 1997, Low-frequency Lg from NTS and Kazakh nuclear explosions: observations and interpretations, *Bull. Seism. Soc. Am*., 87, 1115-1125.

Gutowski, P.R., Hron, F., Wagner, D.E. and Treitel, S., 1984, S*, Bull. Seism. Soc. Am. 74, 61-78.

Hartse, H.E., S.R., Taylor, W.S., Phillips, and G.E., Randall, 1997, A preliminary study of regional seismic discrimination in central Asia with emphasis on western China, *Bull. Seism. Soc. Am*., 87, 551-568.

Jih, R.S., 1995, Numerical investigation of relative contribution of Rg scattering and incomplete dissipation to Lg excitation, *Proceedings of the 17th Seismic Research Symposium on Monitoring a CTBT, PL-TR-95-2108*.

Jih, R.S., 1996, Waveguide Effects of large-scale structural variation, anelastic attenuation, and random heterogeneity on SV Lg propagation: a finite-difference modeling study, 182-194, *Proceedings of the 18th Annual Seismic Research Smposium on Monitoring a CTBT, 4-6 September 1996.*

Johnson, L.R., and C.G. Sammis, 2001, Effects of rock damage on seismic waves generated by explosions, *Pageoph*, 158, 1869-1908.

Kim, W. Y., V. Aharonian, A. L. Lerner-Lam and P. G. Richards 1997. Discrimination of earthquakes and explosions in southern Russia using regional high-frequency three-component data from IRIS/JSP Caucasus Network, *Bull. Seism. Soc. Am*., 87, 569-588.

Kim, W. Y., D. W. Simpson and P. G. Richards 1993. Discrimination of earthquakes and explosions in the eastern United States using regional high-frequency data, *Geophys. Res. Lett*., 20, 1507-1510.

Myers, S.C., J. Wagoner, S. Larsen, A. Rodgers, K. Mayeda, K. Smith, and W. Walter, 2003, Simulation of regional explosion S-phases (SIRES) project, *Proceedings of the 25th Seismic Research Review, Muclear Explosion Monitoring: Building the Knowledge Base*, LA-UR-03-6029, Vol. I, pp. 117-124.

Nuttli, O.W., 1986, Yield estimates of Nevada Test Site explosions obtained from Lg waves, *J. Geophys. Res*., 91, 2137-2151.

Priestley, K. F., G. Zandt, and G. E. Randall, 1988, Crustal structure in Eastern Kazakh, USSR from teleseismic receiver functions, *Geophys. Res. Lett*., 15, 613-616.

Patton, H.J., 2001, Regional magnitude scaling, transportability, and Ms:mb discrimination at small magnitudes, *Pageoph*, 158, 1951—2015.

Stevens, J.L., G.E. Baker, H. Xu, T.J. Bennett, N. Rimer, S.M. Day, 2003, The physical basis of Lg generation by explosion sources, *Proceedings of the 25th Seismic Research Review, Muclear Explosion Monitoring: Building the Knowledge Base*, LA-UR-03-6029, Vol. I, pp. 456-465.

Taylor, S.R., 1996, Analysis of high frequency Pn/Lg ratios from NTS explosions and western U.S. earthquakes, *Bull. Seism. Soc. Am*., 86, 1042-1053.

Taylor, S. R., M. D. Denny, E. S. Vergino, and R. E. Glaser 1989, Regional discrimination between NTS explosions and western U.S. earthquakes, *Bull. Seism. Soc. Am*., 79, 1142-1176.

Taylor, S. R., and H. E. Hartse (1997). An evaluation of generalized likelihood ratio outlier detection to identification of seismic events in western China, *Bull. Seism. Soc. Am*., 87, 824-831.

Vogfjord, K.S., 1997, Effects of explosion depth and earth structure on the excitation of Lg waves: S* revisited, *Bull. Seism. Soc. Am*., 87, 1100-1114.

Wallace, T.C., 1991, Body wave observations of tectonic release, in: S.R. Taylor, H.J. Patton and P.G. Richards (editors), *Explosion Source Phenomenology*, pp 161-170, American Geophysical Union.

Walter, W.R., K.M., Mayeda, and H. Patton, 1995, Phase and spectral ratio discrimination between NTS earthquakes and explosions. Part I: Empirical observations, Bull. Seism. Soc. Am., 85, 1050-1067.

Wu, R.S., S. Jin and X.B. Xie, 2000a, Seismic wave propagation and scattering in heterogeneous crustal waveguides using screen propagators: I SH waves, *Bull. Seism. Soc. Am*., 90, 401-413.

Wu, R.S., S. Jin and X.B. Xie, 2000b, Energy partition and attenuation of Lg waves by numerical simulations using screen propagators, *Phys. Earth and Planet. Inter*., 120, 227-243.

Wu, R.S., X.B. Xie, X. Wu and T. Lay, 2003, Quantifying source excitation and path effects for high frequency regional waves, *Proceedings of the 25th Seismic Research Review, Muclear Explosion Monitoring: Building the Knowledge Base*, LA-UR-03-6029, Vol. I, pp. 173-181.

Xie, J.K., Cong, L.L., and Mitchell, B.J., 1996, Spectral characteristics of the excitation and propagation of Lg from underground nuclear explosions in central Asia, *J. Geophys. Res*., 101, 5813-5822.

Xie, J.K. and Patton, H.J., 1999, Regional phase excitation and propagation in the Lop Nor region of central Asia and implications for P/Lg discriminations, *J. Geophys. Res*., 104, 941-954.

Xie, X.B. and Lay, T., 1994, The excitation of Lg waves by explosions: A finite-difference investigation, *Bull. Seism. Soc. Am*., 84, 324-342.

TOMOGRAPHIC MAPPING OF REGIONAL WAVE Q IN EASTERN EURASIA

Jiakang Xie

Columbia University

Sponsored by Air Force Research Laboratory

Contract No. F19628-03-C-0122

ABSTRACT

In the past several months of research we have achieved the following: (a) nearly fully automated the processing of Fourier spectra of regional waves, including Lg, Pn and Pg on SUN workstations; (b) have collected a large set of new regional wave spectra from eastern Eurasia, which include about 1,000 Lg spectra from recent moderate seismic events (to year 2004), and hundreds of spectra of Pn and Pg; (c) have largely completed the implementation of the two-step procedure of tomographic regional wave Q inversion, which we proposed in January 2003. In the first step of the procedure, path-variable Q are measured using the most reliable, two-station methods. Since this method requires pairs of two recording stations to be aligned with the seismic sources, fewer Q measurements can be obtained in this step, leading to a low-resolution tomographic Q map. In the second step of the procedure, an event-based method that simultaneously measures source spectrum and path-variable Q is used. Using the low-resolution Q map, we can obtain an *a priori* knowledge on path-averaged Q for multiple stations that record a single event. This *a priori* knowledge can be used to remove the trade-off between source spectral level and path averaged Q, which may otherwise cause an uncertainty in both Q and source measurements. We estimate that for Lg Q inversion in eastern Eurasia, less than 10% of the total 2,500 spectra can be used in the first step, whereas all spectra can be used in the second step. The tomographic Q map obtained at the end of the second step will have a high resolution. We are currently in the process of completing the Lg Q map in eastern Eurasia.

OBJECTIVE

The objective of this research is to map lateral variations of regional wave Q in eastern Eurasia using data from various sources, including the Incorporated Research Institutions for Seismology Data Management Center (IRIS DMC) and other data centers. The regional waves to be used include Lg, Pg, Pn, Sn and long-period Rayleigh waves. The target is to develop regionalized Q models that have lateral resolutions as high as the data and methods permit. For some waves such as Lg and Pg, the resulting Q model will be in the form of a tomographic Q map; for other waves such as Sn, the resulting Q models may be region-specific, dividing eastern Eurasia into several (or more) subregions. The resulting Q models can be used for (a) estimating seismic source spectra, source energy radiation and seismic moments, (b) inferring source spectral scaling, stress drops and apparent stresses; (c) inferring fundamental properties of the crust and upper mantle such as their temperature fields, and (d) evaluating the magnitude threshold of seismic events that can be recorded and studied using any set of seismic stations.

Because the Q models are of such fundamental and practical importance for scientific research and earthquake hazard mitigation, and because the new Chinese National Digital Seismic Network (CNDSN) has a large number of stations providing data to Chinese seismologists, the Lamont-Doherty Earth Observatory (LDEO) established a mutually beneficial collaboration with the Data Management Center of the Chinese National Digital Seismic Network (DMC/CNDSN) to generate high-quality Q models. An LDEO seismologist (Jiakang Xie) installs software on the DMC/CNDSN computers and trains the local personnel to collect and process regional wave spectra. Eventually the large number of regional wave spectra collected at the IRIS DMC by LDEO, and at DMC/CNDSN by Chinese seismologists, will be merged and the seismologists from both LDEO and China will jointly invert these spectra to obtain Q models and source spectral scaling using high-frequency regional waves and long-period Rayleigh waves from eastern Eurasia.

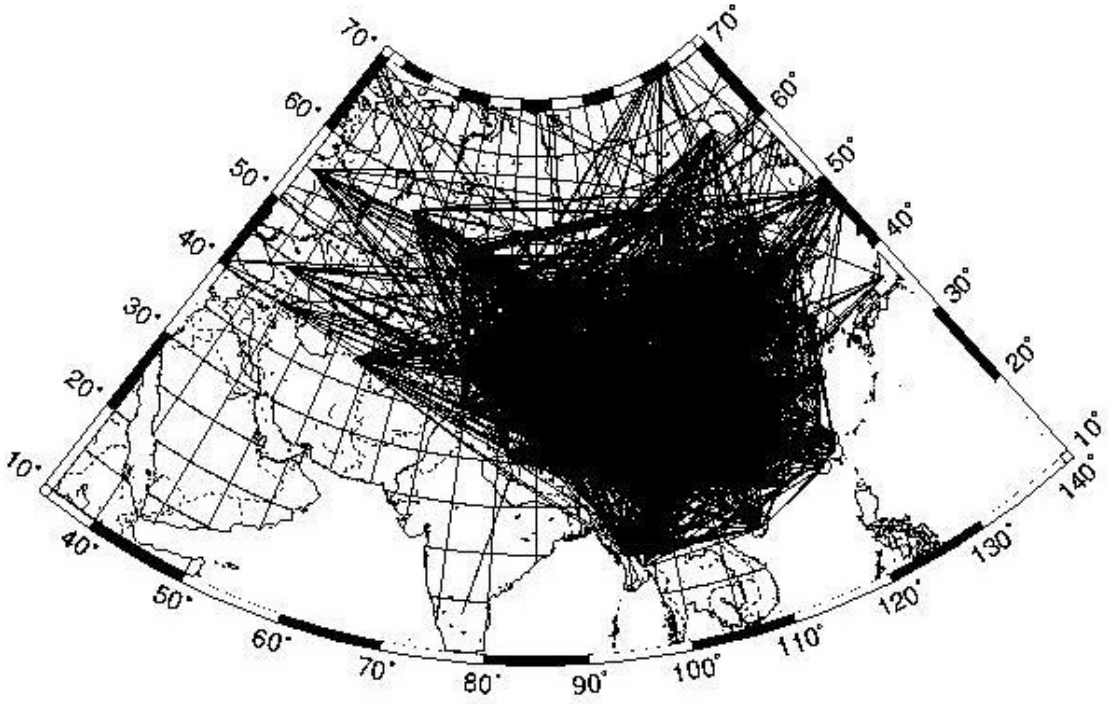


Figure 1. Path-coverage for eastern Eurasia currently available for tomographic inversions of Lg Q_0 and η. So far, Lg spectra have been collected over more than 3,000 paths, from numerous events and stations. Lg spectra over most (about 70%) paths have been collected by LDEO from the Incorporated Research Institutes for Seismology Data Management Center (IRIS DMC). The rest (about 30%) spectra have been collected by the Data Management Center of the Chinese National Seismic Network (DMC/CNDSN). This figure was produced by the DMC/CNDSN.

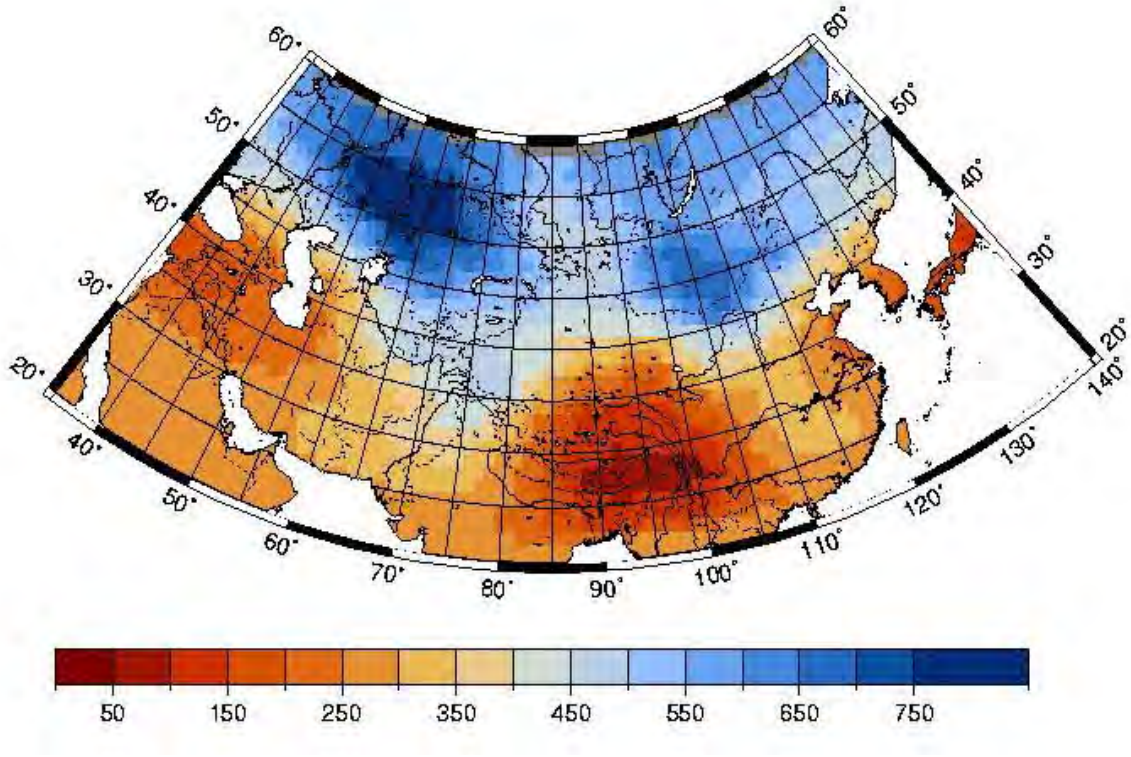


Figure 2. A low-resolution tomographic Lg Q_0 map in eastern Eurasia obtained in a "pilot" inversion, in which only about 100 path-variable Lg Q_0 measurements are input into the tomographic algorithm. Only long-wavelength features for the central portion are retrieved in this map. We anticipate that a total of more than 3,000 Lg Q measurements (Figure 1) will soon be input into our two-stage inversion algorithm to obtain a final tomographic Lg Q_0 model.

We plan to develop regionalized Q models using the Lg waves first (within the next few months). We will then develop Q models for Pg, Pn, Sn and Rayleigh waves, in the second and third phases of this research.

RESEARCH ACCOMPLISHED

This is a multi-year research project that only started several months ago. In the following sections, we summarize the research conducted so far.

Implementation of a two-stage tomographic Q inversion method

In January, 2003, we proposed to invert for a tomographic Q model using a two-stage procedure. The procedure is designed to maximize the resolution of tomographic Q inversions while avoiding bias resulting from the parameter trade-off between source spectra and path Q. The latter trade-off is often difficult to remove unless a priori knowledge exits prior to the Q measurements (Xie, 1998). We illustrate this procedure using the map showing paths that are currently available for a tomographic Lg Q inversion in eastern Eurasia (Figure 1). The map contains over 3,000 paths over which Lg spectra are processed. We anticipate that Lg Q over a significant number of inter-station paths (more than 300) can be measured with the two-station method (e.g., Xie, 2002). Lg Q_0 and η (Lg Q at 1 Hz and its power-law frequency dependence) values measured using the two-station method are reliable since they are not subject to the trade-off between source and path parameters. In the first stage of the tomographic inversion, the Q_0 and η values along these 300 or more paths will be used to derive a long-wavelength Q map. This map is of lower spatial resolution but is reliable in the sense that it is not affected by the source-path parameter trade-off.

In the second stage we shall measure path-variable Q for all of the 3,000+ paths using an event-based algorithm that simultaneously determines the source seismic moment (M_0), corner frequency (f_c) and path-variable Lg Q_0 and η values, using *a priori* knowledge of path-averaged Q_0 and η (Xie, 1998). Such *a priori* knowledge is obtained using the results from the first stage using the following procedure: for each event with multiple-station Lg recordings, we ray-trace the respective paths through the low-resolution Q_0 and η maps obtained in the first stage, and predict path-averaged Q_0 and η values. These path-averaged Q_0 and η values are then used as *a priori* knowledge to constrain the simultaneous determination of the source M_0, f_c and path-variable Lg Q_0 and η values. Applying this procedure to all events, Lg Q_0 and η values along all the 3,000+ paths can be measured free of the parameter trade-off between source spectra and path Q. At the end of the second stage, the resulting Q_0 and η for all of the 3000+ paths will be input to a new tomographic inversion of Q_0 and η maps, which will be of much higher spatial resolution than the first maps derived using only the 300+ inter-station paths in the first stage.

We have implemented virtually the entire two-stage algorithm on SUN workstations. Figure 2 shows a low-resolution Lg Q_0 model obtained by a "pilot" application of the algorithm. For this model, only about 100 path-variable Lg Q_0 measurements are used as against the anticipated 3,000+ paths. We are currently in the final stages of completing the measurement of Lg Q values along these 3,000+ paths.

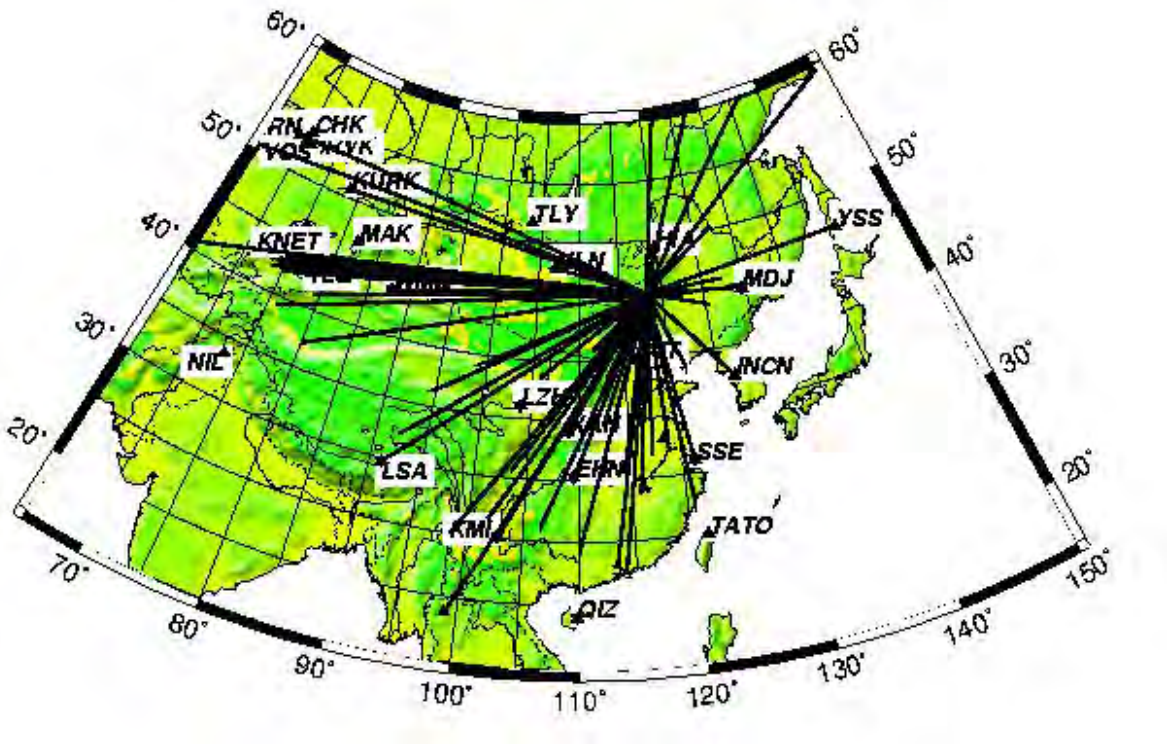


Figure 3. Paths over which regional waves from the March 24, 2004, Inner Mongolia earthquake (M_W = 5.4, 01:53:49.3 UT) were recorded. The paths connect the source to more than 60 recording stations belonging to the Global Seismic Network (GSN), and various national networks in eastern Eurasia. This figure is generated using software package GMT. Courtesy of the Data Management Center of the Chinese National Digital Seismic Network.

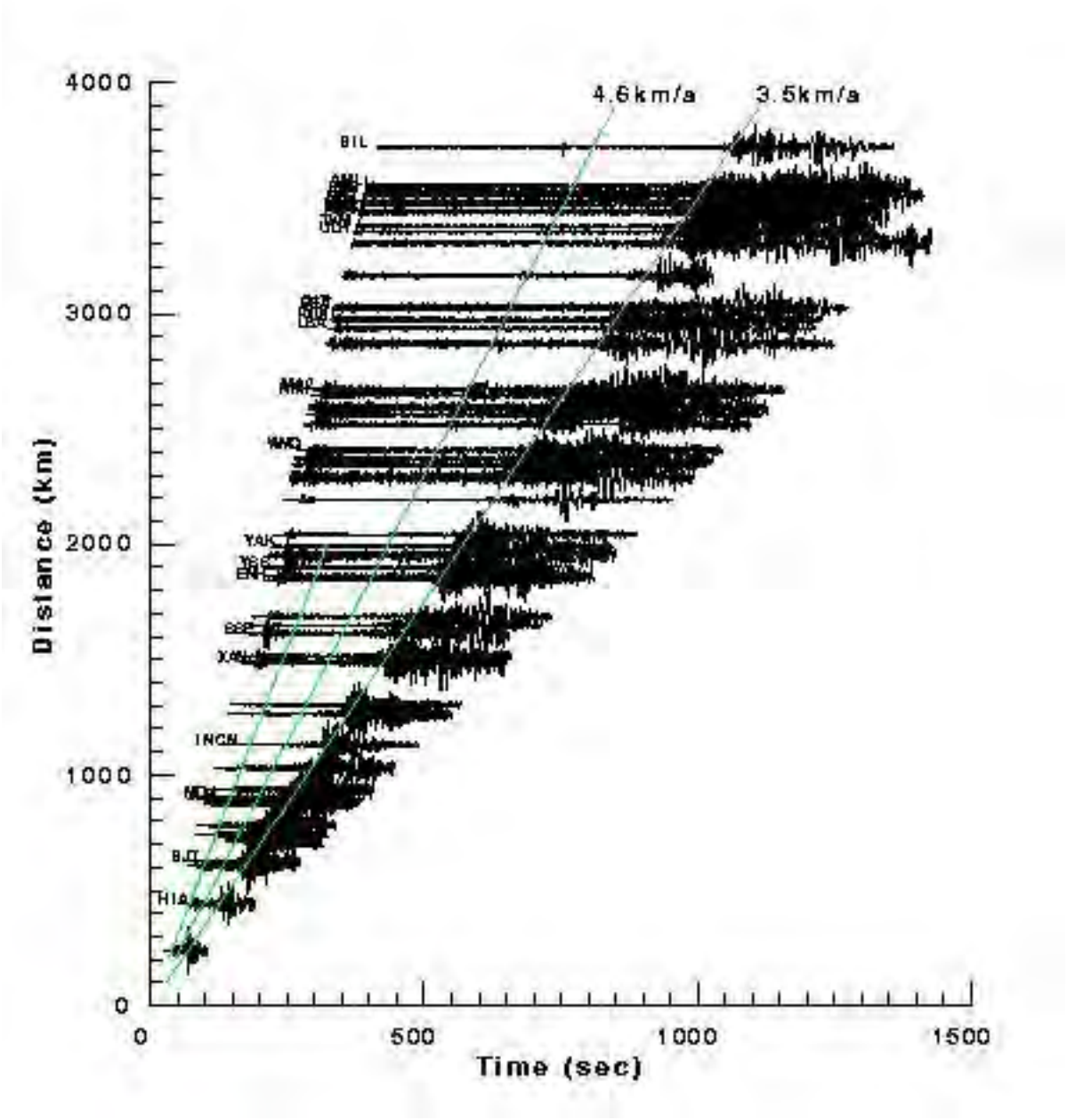


Figure 4. Record section showing over 60 seismograms from the March 24, 2004 (M_W= 5.4) earthquake in Inner Mongolia (Figure 3). The seismograms are collected from stations of the Global Seismic Network (GSN), and various national networks in continental Eurasia. Straight lines indicate arrivals with typical regional wave group velocities (e.g., 4.6 and 3.5 km/s for Sn and Lg, respectively). Courtesy of the Data Management Center of the Chinese National Digital Seismic Network.

Data processing

In the past several months, we have retrieved and processed regional wave spectra from various stations, including IRIS, GSN, Kyrgyzstan, Kazakhstan and Chinese Digital Seismic Network stations. A substantial computer programming effort was carried out for processing Pn and Pg spectra, and for automating much of the regional wave processing (we did not fully automate the processing because we wished to use certain steps for manual quality

controls, and for precise phase picking). These data processing and programming efforts were carried out simultaneously on SUN workstations at LDEO and DMC/CNDSN.

The collection of Lg spectra is much ahead of other phases because we have collected over 1,500 sets of Lg spectra in past work prior to this project. In the past several months, marking the beginning phase of this project, we wrapped up the Lg spectra collection from earthquakes as recent as 2004, and started to collect Pn and Pg spectra. In this time period at LDEO we have retrieved over 2,500 Lg, Pg and Pn spectra from the IRIS DMC. At the DMC/CNDSN, our Chinese colleagues have processed a similar quantity of spectra. Figure 3 shows paths from a recent event in Inner Mongolia that provided Lg, Pg and Pn spectra. Figure 4 shows the record section. Data accumulation rate is very high in Eastern Eurasia owing to the high seismicity and increasingly large number of broad-band stations. As mentioned above, we will soon complete tomographic maps of Lg Q_0 and η. Maps of Q_0 and η developed using other regional waves will be obtained in the later phases of this research.

CONCLUSIONS AND RECOMMENDATION

We have been collecting a large number of regional wave spectra from Eastern Eurasia. Multiple-source data that are archived at the IRIS DMC are collected at LDEO, while data archived at the DMC/CNSDN are collected by colleagues in China using LDEO software. We are currently completing Lg Q_0 and η measurements over more than 3,000 paths. These measurements will be input to the two-stage method that we proposed in 2003 for generating high-quality tomographic Lg Q maps. The final inversion will soon be jointly conducted by LDEO and DMC/CNDSN.

We have collected over 1,000 Pg spectra so far, and several hundred Pn spectra. We shall continue collecting Pn, Pg and Sn spectra in the next year so that regionalized Q models can be derived in a later phase of this research, probably in the next year.

REFERENCES

Xie, J. (1998), Spectral inversion using Lg from earthquakes: Improvement of the method with applications to the 1995, western Texas earthquake sequence, *Bull. Seism. Soc. Am.*, 88, 1525-1537.

Xie, J. (2002), Lg Q in the Eastern Tibetan Plateau, *Bull. Seism. Soc. Am*, 92, 871-876.

Seismic Event Detection and Location

THE 2004 KNOWLEDGE BASE PARAMETRIC GRID DATA SOFTWARE SUITE

Sandy Ballard, Marcus C. Chang, James R. Hipp, Lee A. Jensen, Randall W. Simons, and Lisa K. Wilkening

Sandia National Laboratories

Sponsored by National Nuclear Security Administration
Office of Nonproliferation Research and Engineering
Office of Defense Nuclear Nonproliferation

Contract No. DE-AC04-94AL85000

ABSTRACT

One of the most important types of data in the National Nuclear Security Administration (NNSA) Ground-Based Nuclear Explosion Monitoring Research and Engineering (GNEM R&E) Knowledge Base (KB) is parametric grid (PG) data. PG data can be used to improve signal detection, signal association, and event discrimination, but so far their greatest use has been for improving event location by providing ground-truth-based corrections to travel-time base models. In this presentation we discuss the latest versions of the complete suite of Knowledge Base PG tools developed by NNSA to create, access, manage, and view PG data.

The primary PG population tool is the Knowledge Base calibration integration tool (KBCIT). KBCIT is an interactive computer application to produce interpolated calibration-based information that can be used to improve monitoring performance by improving precision of model predictions and by providing proper characterizations of uncertainty. It is used to analyze raw data and produce kriged correction surfaces that can be included in the Knowledge Base. KBCIT not only produces the surfaces but also records all steps in the analysis for later review and possible revision. New features in KBCIT include a new variogram autofit algorithm; the storage of database identifiers with a surface; the ability to merge surfaces; and improved surface-smoothing algorithms.

The Parametric Grid Library (PGL) provides the interface to access the data and models stored in a PGL file database. The PGL represents the core software library used by all the GNEM R&E tools that read or write PGL data (e.g., KBCIT and LocOO). The library provides data representations and software models to support accurate and efficient seismic phase association and event location. Recent improvements include conversion of the flat-file database (FDB) to an Oracle database representation; automatic access of station/phase tagged models from the FDB during location; modification of the core geometric data representations; a new multimodel representation for combining separate seismic data models that partially overlap; and a port of PGL to the Microsoft Windows platform.

The Data Manager (DM) tool provides access to PG data for purposes of managing the organization of the generated PGL file database, or for perusing the data for visualization and informational purposes. It is written as a graphical user interface (GUI) that can directly access objects stored in any PGL file database and display it in an easily interpreted textual or visual format. New features include enhanced station object processing; low-level conversion to a new core graphics visualization library, the visualization toolkit (VTK); additional visualization support for most of the PGL geometric objects; and support for the Environmental Systems Research Institute (ESRI) shape files (which are used to enhance the geographical context during visualization).

The Location Object-Oriented (LocOO) tool computes seismic event locations and associated uncertainty based on travel time, azimuth, and slowness observations. It uses a linearized least-squares inversion algorithm (the Geiger method), enhanced with Levenberg-Marquardt damping to improve performance in highly nonlinear regions of model space. LocOO relies on PGL for all predicted quantities and is designed to fully exploit all the capabilities of PGL that are relevant to seismic event location. New features in LocOO include a redesigned internal architecture implemented to enhance flexibility and to support simultaneous multiple event location. Database communication has been rewritten using new object-relational features available in Oracle 9i.

OBJECTIVE

Monitoring sensor data for possible nuclear explosions involves four fundamental tasks: signal detection, signal association, event location, and event identification. For all but the first of these, the task is accomplished by minimizing the misfit between observations and theoretical predictions, which in turn depend on the model of the Earth used. Thus, improving the quality of the earth model used for monitoring, is of critical importance, and is the primary focus of the GNEM R&E efforts.

Having a better earth model is not enough, however; if the model is to be maintained and used for operational monitoring, we need a cohesive set of software tools to leverage the improved model benefits. Population tools are needed to make it easy to process the data into the proper format, and to update the model when new data become available. The earth model must be designed and defined into an integrated and extensible software system. An interface is needed around the model to serve predictions to various applications. An efficient, extensible storage format is needed to archive the model on disk. Finally, some sort of data management and viewing utility is needed to easily allow users to browse through the model to better understand it, and to make simple edits, such as deletions and insertions, as needed. Once the models are thoroughly integrated into a software system, they must be used by the seismic event analysis tools such as Sandia National Laboratories (SNL) LocOO code that computes event locations and associated uncertainty based on travel time, azimuth, and horizontal slowness observations (Ballard, 2002).

Researchers at SNL have been working to meet these needs by developing an integrated suite of tools collectively expressed as the Parametric Grid Software Suite (PGSS).

RESEARCH ACCOMPLISHED

The PGSS presently consists of the primary data population tool KBCIT, the low-level storage, representation, and model library PGL; the database management tool, DM; and a seismic location tool, LocOO. We briefly describe each tool below accompanied by a discussion of the new enhancements incorporated over the previous year. See Hipp et al. (2002) for more information concerning the basic operation of each tool.

Knowledge Base Calibration Integration Tool

The Knowledge Base Calibration Integration Tool (KBCIT) is an interactive computer application whose goal is to produce interpolated calibration-based information that can be used to improve monitoring performance by improving precision of model predictions and by providing proper characterizations of uncertainty. It is used to analyze raw data and produce kriged correction surfaces that can be included in the KB. The KB calibration integration tool not only produces the surfaces, but also records every step in the analysis for later review and possible revision.

KBCIT allows the user to define the boundaries of regions, where the data in each region can be treated differently, including using different base models, trend removals, outlier limits, and variograms in each region (Figure 1). KBCIT allows the user to set parameters for blending functions to apply across region boundaries to avoid discontinuities. A declustering operation is available to reduce dataset size by removing redundancy, and stabilize kriging by averaging values close to one another.

KBCIT uses the PGL, described below, to implement both stationary and nonstationary Bayesian kriging for interpolation of empirical data with uncertainties (Figure 2). The results of kriging can be cross validated by comparing empirical values with interpolated predictions based on a kriged surface formed using all but the values to be compared.

To provide a faster alternative to interpolating a kriged surface, the user can specify a tessellation on which KBCIT will precompute kriged values. Any combination of kriged and tessellated surfaces can be summed or differenced and viewed with an interactive three-dimensional (3D) viewer. Kriged and tessellated surfaces can be saved in a Parametric Grid database for use by other programs, such as those doing event location.

New features added to KBCIT this year (2004) include the following:

1. New variogram autofit algorithm – added a new algorithm to fit a curve to variogram data, allowing multiple degrees of freedom (nugget, sill, range, and fraction of curve used) using a simplex optimization method.

2. Storage of database identifiers with a surface – Origin ID, Event ID, and Arrival ID from the NNSA schema database can now be input with the observation data, and will be stored with the kriged surface in the file database.

3. Ability to merge surfaces – added support for merging multiple kriged surfaces, specifying boundaries for where each surface applies, and specifying how to smooth between surfaces. This capability is expected to be useful for merging results from two or more researchers producing correction surfaces for the same station/phase.

4. Improved surface-smoothing algorithms – better algorithms for smoothing between regions to avoid discontinuities in the resulting surface.

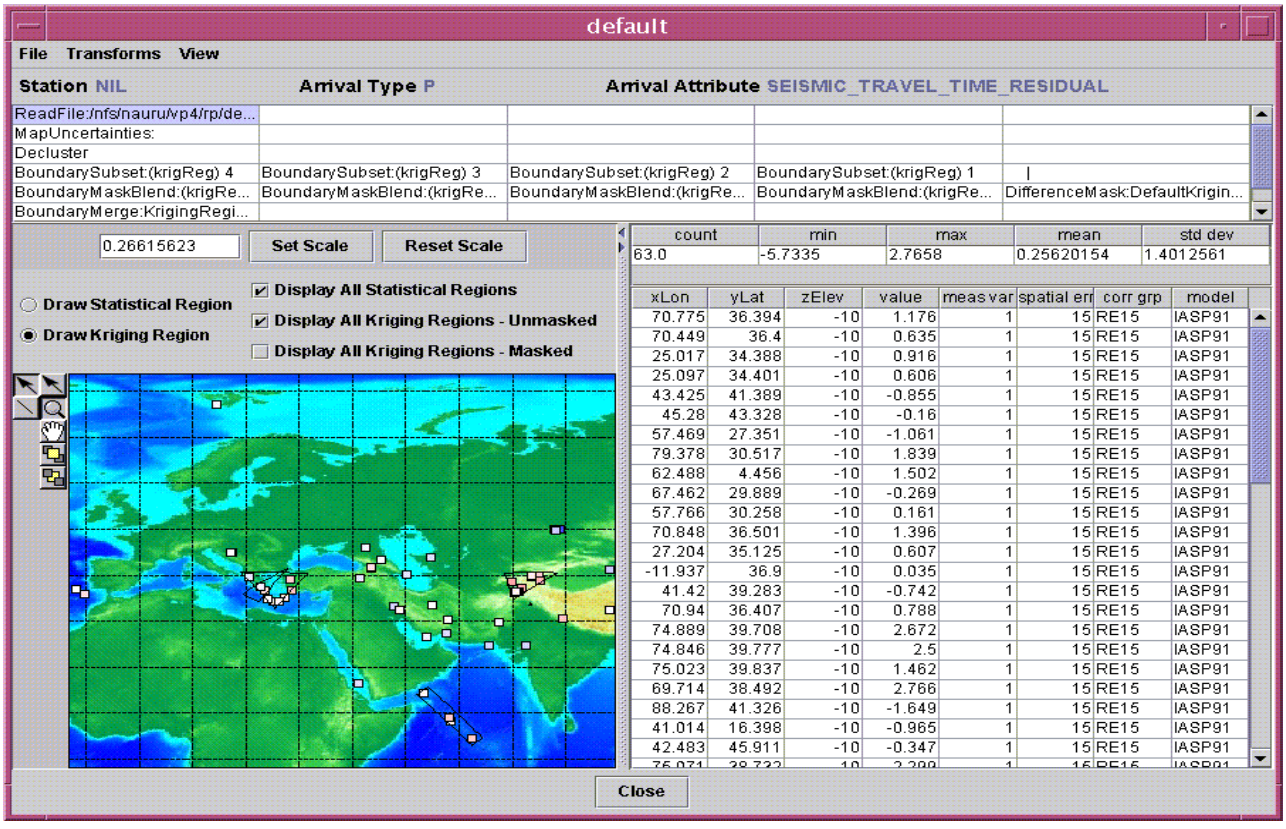


Figure 1. Kriging set window in KBCIT.

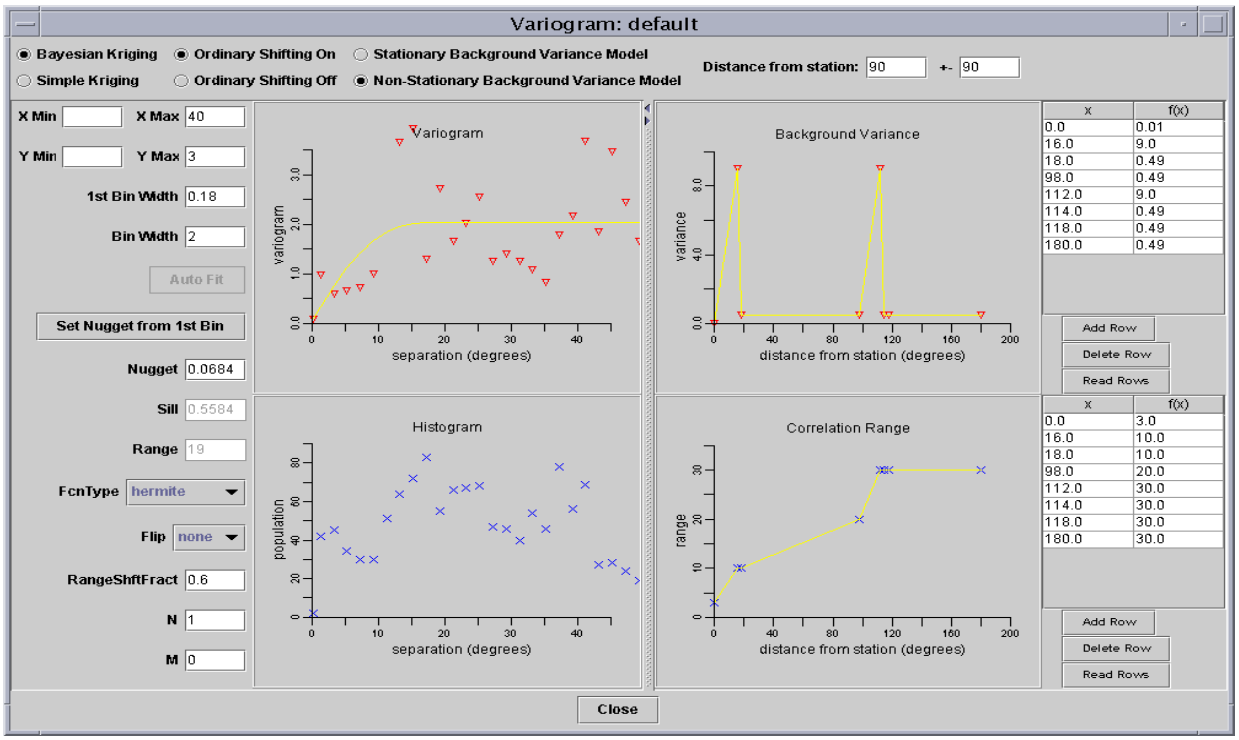


Figure 2. Variogram window in KBCIT.

Parametric Grid Library

The parametric grid library (PGL) provides the internal representation and client interfaces to access the data and models used by all the GNEM R&E tools. This library includes tools that provide a means of populating the PGL (e.g., KBCIT described above) and those that require access to its data or models (e.g., LocOO).

Several improvements were made to the 2004 version of PGL including:

1. The addition of a new PGL Oracle database (ODB) storage mechanism. Previously, a flat-file database stored all of the PGL data files directly into the file system. Now, an ODB can be used to store the PGL data files in an Oracle 9i database. Because the code utilizes the new Oracle C++ call interface (OCCI) Oracle 9i is required. Each PGL object is stored as a binary large object (BLOB) in the database, with the MD5 key string set as its primary key. Translation functionality has been implemented to allow the users to translate from an FDB to an ODB, and vice-versa. With the new ODB, station data from the site table is used to create station objects in the ODB. When merging stations from an FDB into an ODB, the translation utility will attempt to resolve conflicts (stations with identical names) by using the existing ODB station instead; this is done if the two stations have matching data, or if there are no dependencies on the FDB station. However, if other FDB objects are dependent on the conflicting FDB station, errors describing the conflicts will be output to a log file indicating that those FDB objects were not added to the ODB. The user, as a result, has the option of forcing a switch of dependencies on an FDB station to an ODB station, thus enabling those FDB objects to be added to the ODB.

2. Extensive modifications were made to the internal data structure of an FDB, and automatic translation functionality is provided to update an existing FDB to the latest version. FDB versions were introduced to solve several user issues including (a) a simplified and cleaner FDB file structure, (b) forcing the MD5 hash key to depend only on an object's binary data and its dependencies (objects required for instantiation) instead of its metadata attributes, which do not guarantee uniqueness, and (c) ensuring MD5 key cross-platform compatibility, with little-endian architectures (Intel x86, etc., see 7 below).

3. We began a major design renovation that collects the set of mid-level PGL data representation objects into a single interface object called a *DataModel*. The *DataModel* object uses a consistent collection of objects with which any generic geometric data-set representation can be described. The objects include (1) an abstract *Grid* object that defines the geometric position, dimensionality, and topology of the data, (2) a set of point and cell attributes, stored in new data-array objects, that are defined at each point or cell of the grid (3) an *Interpolator* object that is used to interpolate the attributes over the grid using an arbitrary user defined order, and (4) a *Polygon* object that is used to constrain the influence of the *DataModel* to a region that may be more restrictive than the *DataModel* grid. The concrete implementations of the *Grid* object account for dimensionality (1-, 2-, or 3-dimensional curves, surfaces, or volumes), and various geometry/topology portrayals, including structured, unstructured, layered, and polygonal data representations.

4. New “Merged-Model” support was added to PGL to handle cases where several geophysical models are developed for the same station/phase by two or more research organizations resulting in regions where the models overlap. This approach simply uses the new *Polygon* object, defined above, to define regions where interpolation results from each regional model are used exclusively. Transition boundaries assigned to the *Polygons* guarantee a smooth transition from one region to the next.

5. A new *StationRow* object was added that works in conjunction with the *Station* object to track the input rows provided from the NDC database site table. The information includes station on- and off-dates, position, an array flag (true implies an array while false implies a stand-alone station), a reference station vector of strings, a description, a north/east component vector, and load date attributes. All attributes are accessible using corresponding "get" functions. This object was added to properly track station information in a manner consistent with the NDC database site-table. Recently, errors inherent in the site table have been a cause for concern as algorithms increasingly use the site table data, and require logical consistency from their representations in order to behave as intended.

6. We provided significant enhancements to the locator/PGL interface to improve its capability to assemble ad hoc geophysical models on the fly and to minimize the pre-input interaction required by users connected to the interface through location algorithms. These enhancements and features include the following (1) a new optional model configuration file that replaces the required master file — this file uses a simple arbitrarily formatted keyword approach to easily and effectively define the input data, (2) an automatic lookup of path corrected models within the FDB without the need for their specification in the model configuration file (i.e., no master file), (3) an automatic generation of path corrected models from array siblings that already possess a path corrected definition — if a path corrected model is not found for a client requested station/phase then the PGL locator interface will attempt to find a related array station (another element or the array itself) for which a defined path correction exists in the database. If one is found a new model is constructed on the fly that uses the requested station (for which no model was found) and the discovered related model path correction components to construct a new model, which can be used for the requested station/phase. If more than one related model is discovered, the one closest to the requested station is used to construct the new model, (4) if the first two attempts (described in steps 2 and 3 above) fail to find a path corrected model then a standard default base model for the requested station/phase will be constructed, and (5) a new log file (pglli.log) is automatically generated in the execution directory that contains information about the input file parse, and about all models that are (a) loaded from the database, (b) constructed from a related sister array that has an FDB definition, or (c) constructed as a standard base model definition.. All issued alerts, warnings, and errors are output to the log file.

7. Finally, The PGL code was successfully migrated from a Unix/Sun Solaris port to a Microsoft Windows VC++ 7.0 .Net platform. This migration was accomplished to partially satisfy some of our customers needs to run the GNEM software on platforms other than a Sun Solaris. In the future, ports to MAC OS X and LINUX will be migrated.

Data Manager Tool

The Data Manager tool (DM) provides access to the PG data for purposes of managing the organization of the generated PG database, and for perusing the data for visualization and information purposes. The tool is written in Java providing a GUI front end and a Java native interface into the PGL. The low-level visualization support component is primarily handled by the visualization toolkit library, which is described below.

The database management facilities of the data manager include a means for inspecting the entire object reference and dependency hierarchy for any object in multiple databases simultaneously. These facilities provide mechanisms to copy or move objects and their dependents from one database to another or to simply remove them from their containing database entirely. These services allow a user to construct new databases from existing databases that use a subset of the objects contained in any of the existing databases. This functionality provides a means for users to build databases that are tailored for spatially interesting regions or that contain objects that are specific for certain types of problems (e.g., seismic location). Figure 3 below illustrates a typical hierarchical dependency view of a database including object meta data key listings and their dependents.

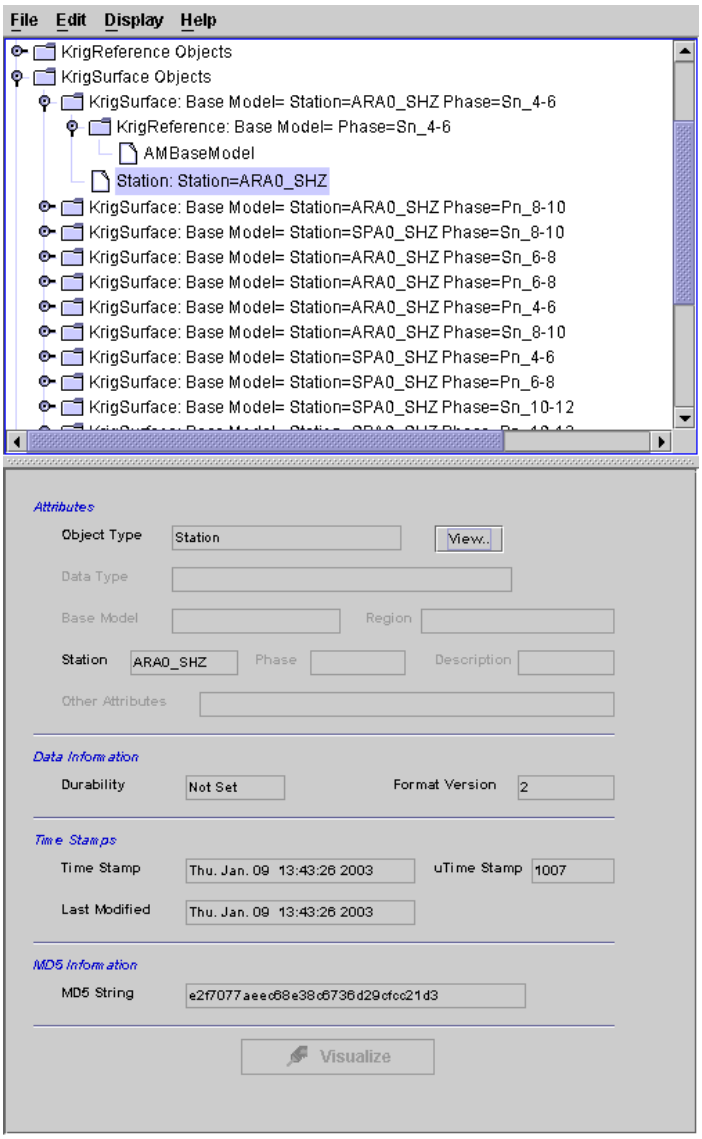


Figure 3. A typical screen shot of the DM GUI displaying a hierarchical view of the database objects and their dependents.

Aside from standard overhead management facilities, the DM was improved this year with the addition of the following features.

1. DM was updated to support PG *Station*, station row, and station data classes. These modifications allow for the creation of *Station* objects that more closely resemble stations in the NNSA schema site table. A user can import dumps from the site table (using a SQL script provided with DM to customize the format of the file) that now includes all fields in the site table and not just the positional information that provided for in the previous years. The import function contains complex error checking that attempts to resolve outstanding discrepancies in the site table data, such as incorrect or differing spatial and temporal positional information or invalid use of reference stations. Few assumptions are made about the data as they are read, however, multiple detailed messages are output regarding the state of the data as they are processed and fed into an FDB.
2. The station editor table was corrected and expanded to utilize the underlying PGL station classes and the error checking described above, and to improve visualization of the data and editing capabilities of the table itself. Stations may be input individually, rows added or deleted, and information altered, given proper permissions and object reference limitations.
3. A small class was added to employ some of the functionality of the PGL FDB_Query command line tool in the DM. The functions of this class allow the user to select a database, or an object within that database, and return information about it, which is dumped to a separate text pane. This capability is part of an ongoing effort to consolidate PG object management tasks into DM.

Besides these new input/output and object information enhancements, several global improvements involving the DM visualization system are also underway. Some of these major improvements include the following.

1. The low-level visualization library was converted to the VTK. This conversion involved significant modifications to the underlying DM interface to eliminate old functionality and replace it with the new calls to the VTK application programmer interface.
2. The old geophysical volume viewer was converted to utilize the new VTK interface, preserving most of the original functionality. In the future, new capabilities will be added that access features found in VTK that were not available in the old visualization system.
3. We provided the beginnings of a general-purpose visualization system that can depict any objects found in a PGL FDB. The new interface currently visualizes all PGL model and base-model objects. In the future polygon, tessellation, and parametric grid objects will be added.
4. An ESRI shape file to VTK data file translator was created so that the many ESRI shape files used by the Air Force Technical Applications Center (AFTAC) can easily be converted to the new VTK format for subsequent visualization. The shape file objects are used as contextual backdrops when visualizing PGL data objects.

Figures 4 and 5 illustrate an example VTK screen shot of the geophysical model and the base-model component of a travel-time model, respectively.

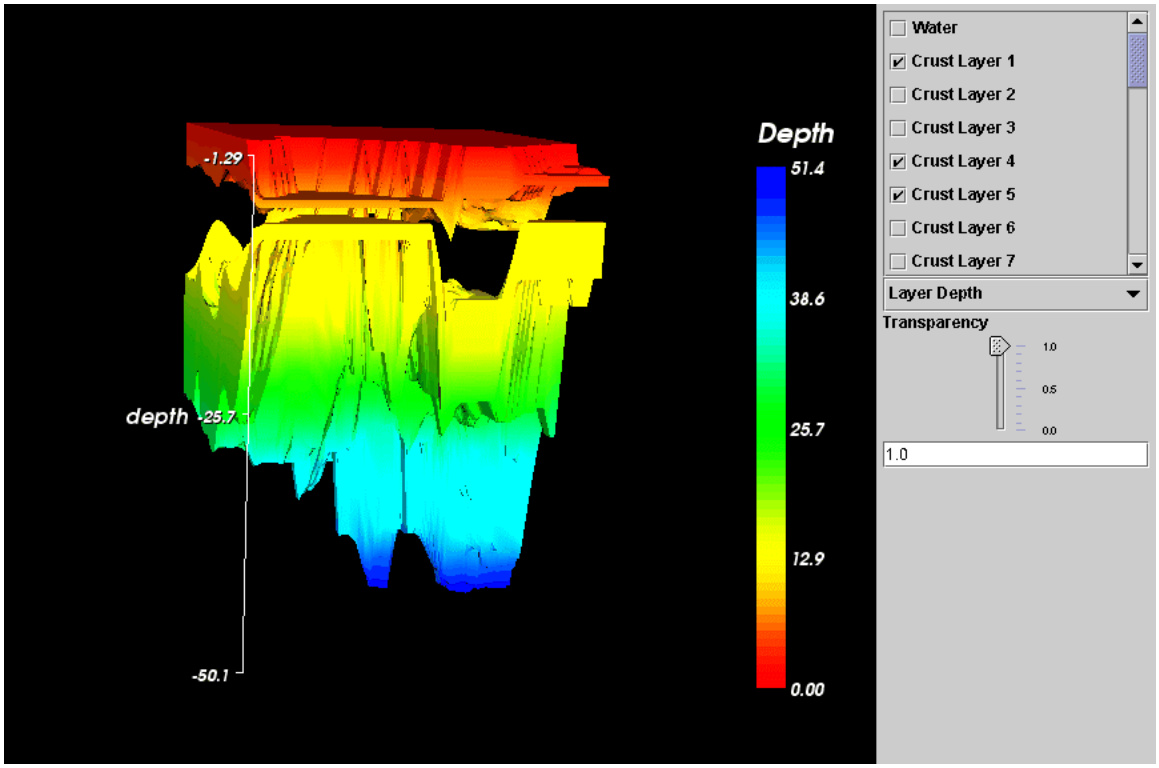


Figure 4. A typical screen shot of the DM geophysical model view.

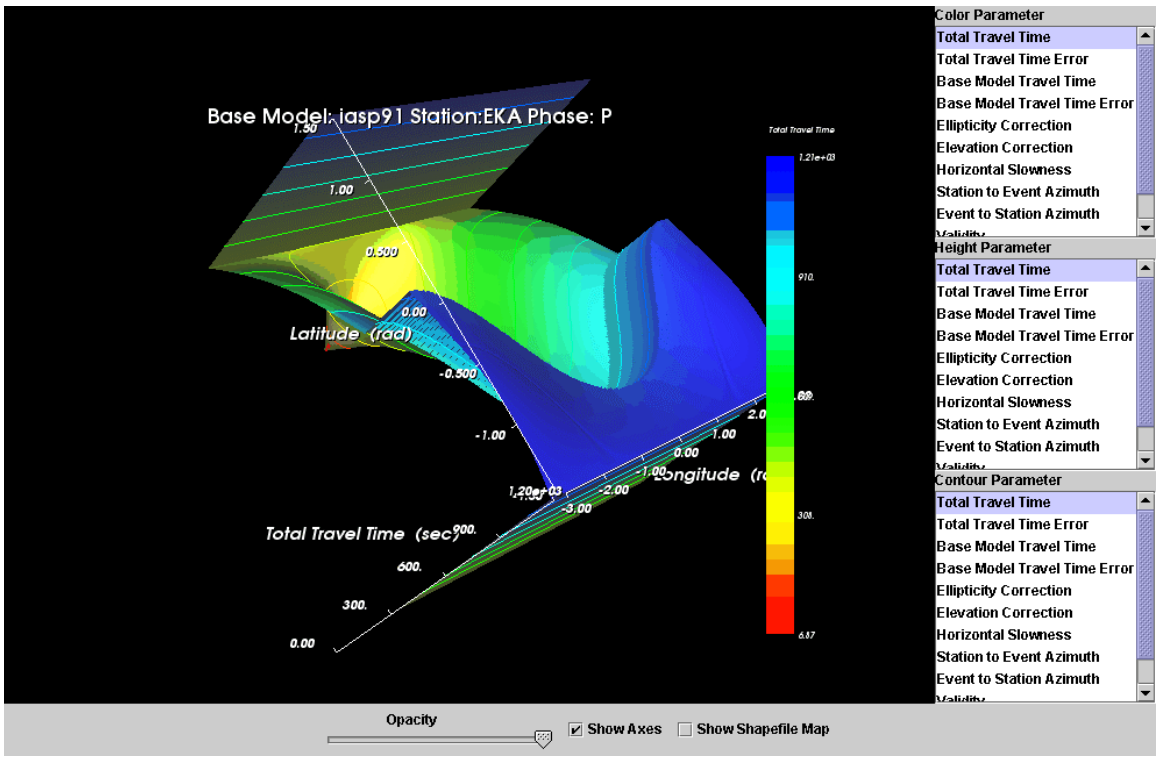


Figure 5. A typical screen shot of the DM travel-time model view displaying the base model component.

Seismic Event Location Tool

The Seismic Event Location Tool (LocOO) is a seismic event location code that computes event locations and associated uncertainty based on travel time, azimuth, and horizontal slowness observations (Ballard, 2002). LocOO was written using an object-oriented approach. It is fundamentally an infrastructure for a seismic event locator. This code relies on four modules to actually implement seismic event location, (1) a data input module, (2) a seismic observation prediction module, (3) a location algorithm module, and (4) a results output module. Currently, the only location algorithm implemented is a linearized least-squares inversion algorithm (Geiger, 1910; Bratt and Bache, 1988), enhanced with Levenberg-Marquardt damping (Levenberg, 1944; Marquardt, 1963) to improve the performance in highly nonlinear regions of model space. The location algorithm also computes multidimensional uncertainty estimates regarding the best-fit event location (Jordan and Sverdrup, 1981), including non-linear uncertainty bounds that are not necessarily elliptical in shape (Wilcock and Toomey, 1971; Ballard, 2003). The only prediction module currently implemented is the Parametric Grid Library (Hipp et al., 1999). LocOO was developed in parallel with PGL and continues to keep up with all of its new features and capabilities, including utilization of complex data models and elimination of master files. In short, any capability that is implemented in PGL, and that can affect seismic event location, can be accessed with LocOO.

The most important improvement in LocOO version 2.0, released in July 2004, is that the architecture of the code was redesigned to allow simultaneous, multiple event location algorithms to be implemented. To date, no such algorithms have been incorporated into LocOO, but the internal data structures in the code are now in place to handle such algorithms and we expect to add one more multiple event location algorithm in the coming year. In addition, the internal structures of the code were streamlined to simplify future incorporation of new location algorithms.

Another improvement in the code was the replacement of the NNSA schema database access modules used in version 1 with two new database access modules. The first is implemented on top of the new OCCI features available in Oracle 9i, and the second uses DBToolBox functions (Ballard and Lewis, 2004) for input and output to database flat-files and XML data sources.

While these features are not readily apparent to the everyday users of LocOO, they should significantly enhance the stability and robustness of the code, and facilitate future modifications and enhancements.

CONCLUSIONS AND RECOMMENDATIONS

In this paper, we have described the enhancements, made in 2004, to the integrated set of NNSA software known as PGSS. Parametric Grid Software Suite tools were developed to take advantage of the improvements, in the ongoing development, of the GNEM R&E earth model, and the tools' uses span data population and storage, data management and viewing, and seismic event location.

Future versions of the PGSS will be developed to support new enhancements to the GNEM R&E earth model. Some of the planned improvements are as follows.

1. Continued transition of the PGL mid-level geometry representation toward the new *DataModel* paradigm described above.
2. Additional DM GUI improvements include the following:
   - Enforcement of the correct tree structure text and alphabetization of entries.
   - Layout and content restructuring of the attribute panel to hold table displays of object attributes.
   - Additional right-click menu items updated to access commonly used functions, such as searching, visualization, etc.
   - Expanded error/alert/warning notifications using enhanced font and color-coding techniques.
   - Incorporation of a separate tree node pane displaying navigable FDB object references and dependencies for the selected object.
   - Provisions for generic FDB object creation functionality that will allow a user to define any FDB supported object as a keyword based text input file. This capability will provide another population input path when there are no tools able to provide a specific required flavor of a requested object.

- Capability to support point interpolation in the GUI allowing a user to enter a set of geographic interpolation coordinates to perform object interpolation and subsequently output the results to a table.

3. Integration of selected DM functionality directly into the Sandia National Laboratories KB Navigator tool.
4. Addition of one or more multiple event location algorithms to LocOO.

REFERENCES

Ballard, S. (2002), Seismic Event Location Using Levenberg-Marquardt Least Squares Inversion, Sandia National Laboratories, SAND2002-3083.

Ballard, S. (2003), "Seismic Event Location: Dealing with Multi-dimensional Uncertainty, Model Non-Linearity and Local Minima", in *Proceedings of the 25th Seismic Research Review – Nuclear Explosion Monitoring: Building the Knowledge Base*, LA-UR-03-6029, Vol. 3, pp. 193-202.

Ballard, S. and J. E. Lewis (2004), "DBTools: A Suite of Tools for Manipulating Information in a Relational Database", in *Proceedings of the 26th Seismic Research Review: Trends in Nuclear Explosion Monitoring*, Orlando, FL (Sept. 21-23, 2004).

Bassin, C., Laske, G. and Masters, G., (2000), The Current Limits of Resolution for Surface Wave Tomography in North America, EOS Trans AGU, 81, F897, 2000.

Bratt, S. R. and T. C. Bache (1988), Locating Events with a Sparse Network of Regional Arrays, *Bull. Seis. Soc. Am.*, v. 78, pp. 780-798.

Geiger, L. (1910), Herdbestimmung bei erdbeden ans den ankunftzeiten, K. Gessel. Wiss. Goett. v. 4, pp. 331-349.

Hipp, J.R., Young, C. J., Moore, S. G., Shepherd E. R., Schultz C. A, Myers S. C., (1999), Parametric Grid Information in the DOE Knowledge Base: Data Preparation, Storage, and Access, Sandia National Laboratories, SAND99-2277.

Hipp, J.R., Simons, R.W., Jensen, L.A., (2002), "The GNEM R&E Parametric Grid Data Software Suite: Tools for Creation, Access, Management, Viewing, and Export", in *Proceedings of the 24th Seismic Research Review - Nuclear Explosion Monitoring: Innovation and Integration*, LA-UR-02-5048, Vol. 1, pp. 283-291.

Jordan, T. H. and K. A. Sverdrup (1981), Teleseismic Location Techniques and their Application to Earthquake Clusters in the South-Central Pacific, Bull. Seis. Soc. Am., v. 71, pp. 1105-1130.

Levenberg, K. (1944), A method for the solution of certain non-linear problems in least squares, *Quart. Appl. Math*., v. 2, pp. 164-168.

Marquardt, D. W. (1963), Journal of the Society for Industrial and Applied Mathematics, v. 11, pp. 431-441.

Schroeder, W., Martin, K., Lorensen B., (2003), The Visualization Toolkit, 3rd Edition, Kitware, Inc., February 2003, ISBN: 1930934076

Wilcock, W. S. D. and D. R. Toomey (1971), Estimating Hypocentral Uncertainties for Marine Microearthquake Surveys: A Comparison of generalized inverse and grid search methods, Marine Geophysical Researches, v. 13, 161-171.

SEISMIC SOURCES AND WAVE PROPAGATION IN WESTERN INDIA

Paul Bodin[1], Aybige Akinci[2], Luca Malagnini[2], Kevin Mayeda[3], Arthur Rodgers[3]

University of Memphis,[1] Istituto Nazionale di Geofisica e Vulcanologia,[2] Lawrence Livermore National Laboratory[3]

Sponsored by National Nuclear Security Administration
Office of Nonproliferation Research and Engineering
Office of Defense Nuclear Nonproliferation

Contract No. DE-FC52-03NA99512,[1] W-7405-ENG-48[3]

ABSTRACT

We recorded more than 2500 aftershocks of the 2001 Mw7.6 Bhuj, India, earthquake on a network of 9 portable seismographs. We are augmenting this dataset with waveforms acquired by other temporary networks operated by other investigators, and that covers different times, propagation paths, and distance ranges than our data. Taken together, these data form excellent ground truth calibrations for regional and teleseismic determinations of locations and source amplitudes for seismic sources in the western India region. The uniqueness of these data derive from the fact that the region is relatively aseismic and that it has historically been difficult to obtain ground motion recordings from the earthquakes that do occur there. The Bhuj aftershock data would permit the testing of the effect of varying focal mechanisms, source depths, and magnitudes on commonly used teleseismic and regional seismic discriminants. The events (with magnitudes between ~2 and ~5.5) are being carefully relocated as precisely as possible. Using the re-located aftershock catalog derived from the local network(s), we are extracting waveforms for stations at region and upper mantle distances. Using methods developed at Lawrence Livermore National Laboratory (LLNL) these data are being analyzed to calibrate highly accurate coda moment magnitudes. We are measuring frequency dependent phase amplitudes to study the effect of depth and focal mechanism on P/S discriminants. Regional detection threshold curves will be computed for the regional phases in this region. Our preliminary results indicate that we will be able to provide several solid waveform-constrained focal-mechanisms, depths and moments. We have also constrained local frequency-dependent attenuation properties based on a subset of the dataset.

OBJECTIVE(S)

Our study of aftershocks of the Bhuj, India, earthquake of 26 January 2001 has several objectives, with the overall goals of improving our ability to locate and characterize seismic sources and to improve our understanding of wave propagation in western India. The first objective is to incorporate aftershock data that we have taken ourselves with that from colleagues at other institutions, and to use this combined dataset to improve our location quality. We also wish to calculate coda-derived seismic source spectra and include waveform modeling of the largest aftershocks. With these stable moment-rate spectra we further plan to achieve an absolutely calibrated dataset, from source, through attenuation/spreading to the near-site effects. Our final objective is to estimate regional structure/propagation from surface wave dispersion and waveform model regional broadband data.

RESEARCH ACCOMPLISHED

Bodin and Horton (2004) located about 1200 events using a subset of the data we are assembling. Figure 1 shows the highest-quality locations (887 events), based on data from 8 University of Memphis temporarily-deployed (12-27 Feb., 2001) seismographs. The events shown on the figure all have rms values of 0.02 s or less. To date we have combined the University of Memphis data with recordings from the National Geophysical Research Institute (NGRI) in Hyderabad, India. We have used these combined data to relocate with the improved station coverage the 1200 earthquakes.

We have also used the ~800 events located well by the University of Memphis network to constrain the frequency-dependent attenuation in the region, and to model the scalar seismic moments of earthquakes in our dataset. Figure 2 illustrates our methods—showing the decay of peak amplitudes with distance for data in narrow passbands around a set of center frequencies. (Bodin et al., in press, 2004). Because the earthquakes that yielded the observations span a wide range of depths (from 5-35 km), we divided the data into 2 overlapping subsets, Shallow (H<25 km) and Deep (H>20 km). We interpreted the spatial decay of amplitudes observed in Figure 1 in terms of a frequency dependent attenuation operator, Q(f), and a distance dependent spreading term (g(r)), and assigned site amplification factors relative to an average of the stations. The results are summarized as.

Deep:

$$Q(f) = 790\left(\frac{f}{f_{ref}}\right)^{0.22} \quad ; \quad f_{ref} = 1.0hz \tag{1}$$

$$g(r) = \begin{Bmatrix} r^{-1}; r \le 40km \\ r^{-0.3}; 40 \le r \le 50km \\ r^{-0.9}; 50 \le r \le 60km \\ r^{-0.4}; 60 \le r \le 80km \\ r^{-0.55}; r \ge 80km \end{Bmatrix} \tag{2}$$

Shallow:

$$Q(f) = 790\left(\frac{f}{f_{ref}}\right)^{0.35} \quad ; \quad f_{ref} = 1.0hz \tag{3}$$

$$g(r) = \begin{Bmatrix} r^{-1}; r \le 40km \\ r^{-0.5}; 40 \le r \le 50km \\ r^{-1.0}; 50 \le r \le 60km \\ r^{-0.5}; 60 \le r \le 80km \\ r^{-0.55}; r \ge 80km \end{Bmatrix} \tag{4}$$

We are starting to perform a similar analysis on the dataset that includes the “new” NGRI sites, and on the additional earthquakes the combined dataset permits.

We have made a catalog of larger events (M~4+), which may have been recorded both locally and at regional and/or teleseismic distances. Our combined dataset extends the time for which we have useful local data (both earlier in

time, to 7 Feb, 2001, and later in time, to 6 March), and thus represents a significant increase in earthquakes that might have been detected more remotely.

We have initiated waveform modeling to obtain well-constrained moment tensors for the largest events in our catalog. To date we have used only the University of Memphis data. We have applied both surface wave techniques (Herrmann), and a full-waveform technique (e.g. Zhao and Helmberger, 1994). An example of the surface waveform modeling is shown in Figure 3 and Figure 4. Waveform modeling revealed the earthquake to have been Mw 4.6, at a focal depth of 6 km. Figure 5 shows an example of a full waveform technique. Our preliminary work reveals that our earth model needs to be improved, and that additional constrains provided by the increased station density we will achieve from NGRI data will strengthen our results.

CONCLUSIONS AND RECOMMENDATIONS

This study is still in its early stages. We are progressing on all objectives. Our work to date has demonstrated the capability of the data to provide very well determined locations for many events. The number of events recorded both locally and remotely remains unknown, but with the inclusion of the data from other sources, should be increased significantly from our earlier estimates. The moment tensors we derive from waveform modeling will "tie down" the proposed stable coda-derived moment-rate spectra, to facilitate comparison with global data.

ACKNOWLEDGEMENTS

We thank Bob Herrmann and Lupei Zhu, respectively, for help with the surface wave and full-waveform source inversions.

REFERENCES

Bodin, P., and S. Horton (2004) Source Parameters and Tectonic Implications of Aftershocks of the Mw 7.6 Bhuj Earthquake of January 26, 2001. *Bull. Seism. Soc. Am.*94, 818, 827.

Bodin, P., L. Malagnini, and A. Akinci (2004) Ground motion scaling in the Kachchh basin, India, deduced from aftershocks of the 2001 Mw 7.6 Bhuj earthquake. *Bull. Seism. Soc. Am.* (in press).

Herrmann, R. B. (2004) Personal communication, available at: http://mnw.eas.slu.edu/People/RBHerrmann/BHUJ/20010500824/

Mayeda, K., Hofstetter, A., O'Boyle, J.L., Walter, W.R., 2003, Stable and transportable regional magnitudes based on coda-derived moment-rate spectra , *Bull. Seismol. Soc. Am*., 2003

Zhao, L. S., and D. V. Helmberger, (1994) Source estimation from broadband regional seismograms, Bull. Seismol. Soc. Am., 84 , 91–104, 1994.

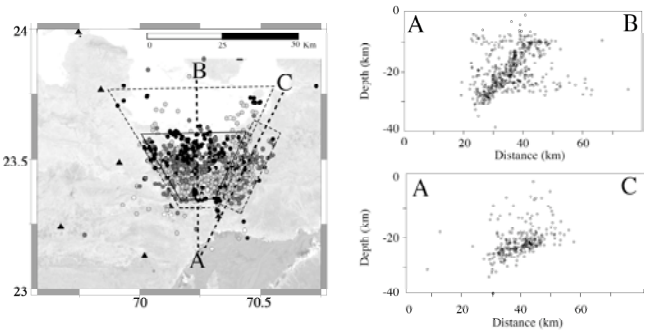


Figure 1. Bhuj aftershock locations. On the map at the left we plot 887 aftershock epicenters over a satellite image. These locations represent events with depth errors less than ±3 km, horizontal uncertainties less than ±2 km. Mean RMS travel-time uncertainty for these data is 0.0036 s., and the greatest RMS uncertainty is .01 s. Epicenters are shaded by depth, with white = >30 km, light grey = 20 to 30 km, dark grey = 10 to 20 km, and black = < 10 km. Small black triangles are seismograph sites. Dashed quadrilaterals show spatial regions for events shown in cross-sections at right. Solid trapezoid is surface projection of rupture model discussed in text.

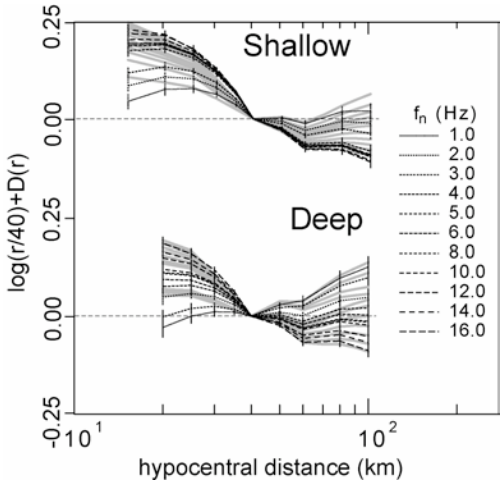


Figure 2. Decay of peak amplitudes of ground motion as a function of distance and frequency for the Bhuj aftershock data. Each dashed curve is the average peak amplitude, referred to the average peak amplitude of signals at 40 km, within a narrow passband with each dash pattern representing a particular central frequency, as shown on the right. Error bars are two standard deviations. Uncertainties for periods greater than 1 Hz were large, and these frequencies were not used in the modeling. The curves are plotted such that a horizontal line represents a spatial decay of r^{-1}, which is expected for body waves in a homogeneous crust. Equations (9-12) lead to models of the observed decay curves shown as family of grey curves underlying the brightly dashed curves..

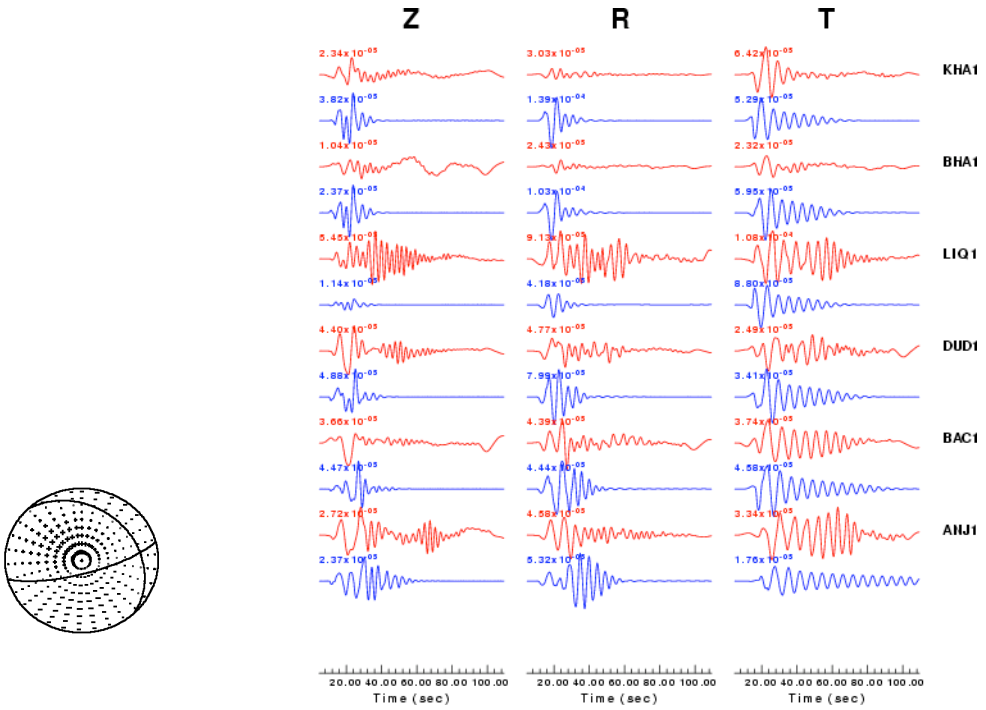


Figure 3. The focal mechanism shown at the left was produced by modeling surface waveforms. The waveform data (red) and synthetics (blue) are shown at the right.

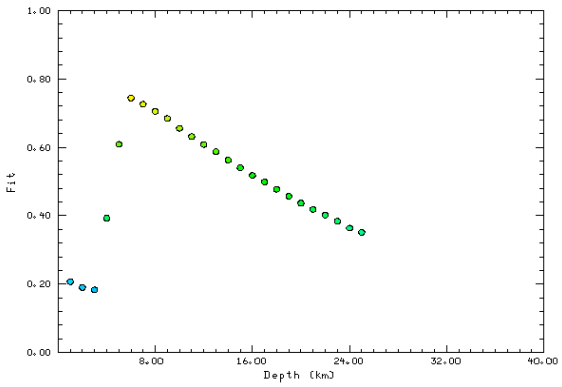


Figure 4. Depth sensitivity of the focal mechanism solution quality, for the event shown in Figure 3.

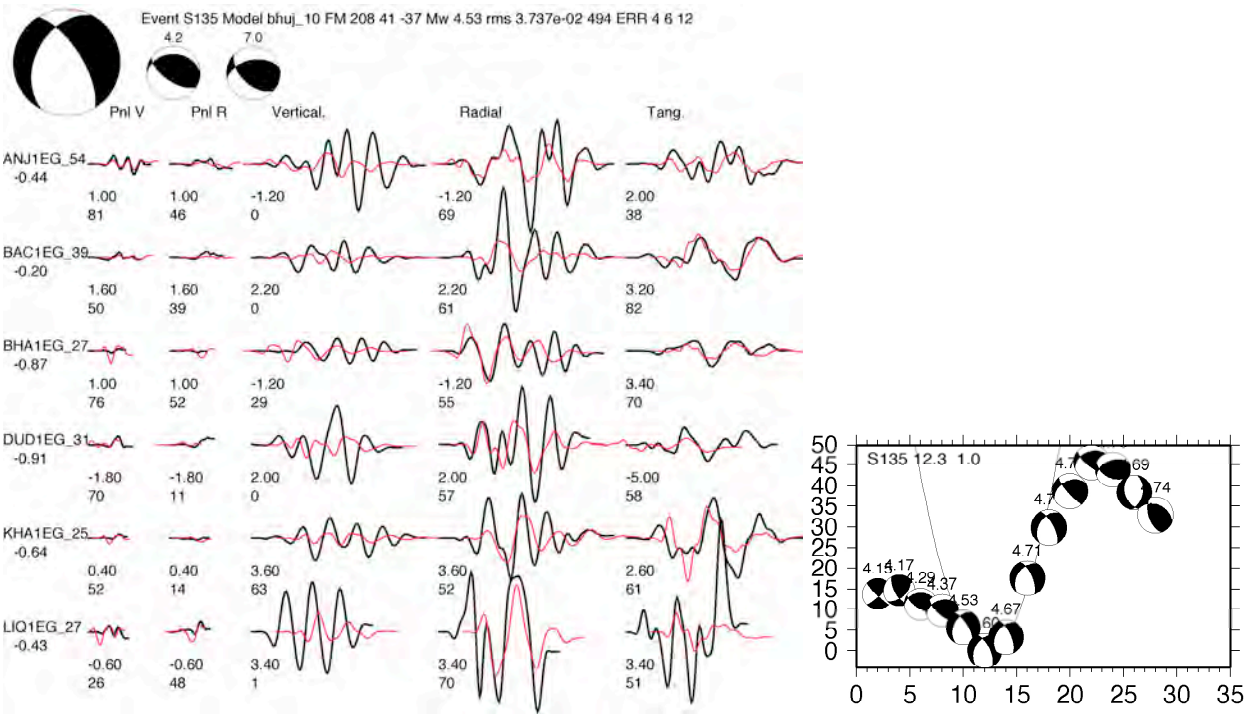


Figure 5. Preliminary modeling results for the earthquake of 2001:050:08:23. At right is depth sensitivity and variability of the focal mechanism. Station LIQ1, for example, exhibits clear site effects in the tangential component from many earthquakes, but have not yet been accounted for.

GROUND TRUTH EVENTS FROM REGIONAL SEISMIC NETWORKS IN NORTHEASTERN AFRICA

Richard A. Brazier[1], Yongcheol Park[1], Andrew A. Nyblade[1], and Michael E. Pasyanos[2]

Penn State University[1] and Lawrence Livermore National Laboratory[2]

Sponsored by National Nuclear Security Administration
Office of Nonproliferation Research and Engineering
Office of Defense Nuclear Nonproliferation

Contract No. DE-FC03-02SF22500[1] and W-7405-ENG-36[2]

ABSTRACT

Determining accurate seismic locations, with representative uncertainty estimates, is of fundamental importance to ground-based nuclear explosion monitoring. This project is developing a catalog of reference events (ground truth (GT)), in the northeast African area of interest, where reference event coverage is exceptionally poor because of the limited station coverage by historic networks. The results of this project will enable the seismic monitoring community to enhance their operational capability to monitor for nuclear tests in north Africa and the Middle East by increasing their ability to accurately locate and identify seismic events in these regions.

The collection of ground truth events for northeastern Africa is being achieved using state-of-the-art event location methods applied to broadband seismic data from regional PASSCAL networks in Ethiopia, Kenya and Tanzania, as well as to broadband data from primary and auxiliary International Monitoring System (IMS) stations in the region. The ground truth catalog is being assembled by determining origin time, focal mechanism and hypocenters for many events that lie within close proximity of recording stations or else are well recorded teleseismically.

Accurate event locations for fourteen M>3.5 events, in northeastern Africa, have been obtained thus far using data from the Tanzania Broadband Seismic Experiment and the Ethiopia Broadband Seismic Experiment. Focal mechanisms for most of these events have been obtained by modeling P and SH polarities and amplitude ratios in a grid search method. Epicenters have been constrained by using P and S arrival times. Focal depths have been constrained by waveform modeling of regional and local depth phases. Most of the earthquakes occur on either the western or eastern branch of the East African Rift, and the mechanisms obtained are all normal or strike-slip. Preliminary epicentral locations for several hundred additional local and near-regional earthquakes have been obtained for Ethiopia using P arrival times.

The Bayesian kriging method is being used with the well located events to construct regional travel-time correction surfaces for northern Africa. To improve further our capabilities to accurately locate events in this part of the world, we are also using surface wave data to construct new velocity models of the crust and upper mantle. Group velocity measurements from many thousand station event pairs ranging from 15-60 second periods for Rayleigh and Love waves have been measured, and these measurements have been inverted to produce group velocity maps of eastern Africa.

OBJECTIVE

Introduction

Determining accurate seismic locations with representative uncertainty estimates is of fundamental importance to ground-based nuclear explosion monitoring. In this project, we are developing a catalog of reference events (GT) in the northeast Africa where reference event coverage is exceptionally poor due to the limited station coverage by historic networks. We are developing a catalog of accurately located hypocenters within a range of GT levels, origin times, and focal mechanisms for several tens of earthquakes with magnitudes > 3. The catalog will enable the seismic monitoring community to enhance their operational capability to monitor for nuclear tests in North Africa and the Middle East by increasing their ability to accurately locate and identify seismic events in these regions.

Earthquakes in northeastern Africa provide a principal source of ground truth for north Africa and the Middle East. The earthquakes of interest are associated with the northern and central portions of the East African Rift System (Figure 1). Since there are very few earthquakes within North Africa proper or within large parts of the Middle East that can be used to develop a set of ground truth, naturally occurring events in northeastern Africa take on an added importance for improving monitoring capabilities in the region for the Comprehensive Nuclear-Test-Ban Treaty (CTBT).

The development of GT for north Africa and the Middle East has in the past been limited not only by the lack of appreciable seismicity but also by a dearth of seismic stations throughout most of Africa. This situation is now changing. We operated regional seismic networks in Ethiopia and Kenya comprised of 27 and 11 broadband stations, respectively, between 2000 and 2002, and several years ago (1994-1995) we operated a similar network of 20 broadband seismic stations in Tanzania. The broadband waveforms recorded by these networks, together with waveforms from primary and auxiliary IMS stations in the region, provide a rich data set that can be used to accurately locate earthquakes and determine their origin times and source mechanisms.

The GT catalog is being assembled by (1) determining origin time, focal mechanism and hypocenters for many events that lie within close proximity of recording stations or else are well recorded teleseismically; (2) using these events to construct regional travel time correction surfaces using a Bayesian kriging technique, and (3) using the travel time correction surfaces to obtain origin times and epicenters for numerous other events. Robust estimates of the uncertainties in the locations and origin times will also be determined.

Here we present improved locations for 11 events within Tanzania with M>4 and 3 events from Ethiopia with M >3.5 constrained by P and S arrival times and pPn, sPn, and Pmp depth phases recorded by the regional broadband networks in Tanzania and Ethiopia. We begin by providing background information about the geology of the region and on the broadband seismic experiments. This is followed by a discussion of our ongoing work of our event locations and uncertainties including a group velocity tomography for eastern Africa and travel time correction surfaces to improve locations and determine new locations.

Background Information

The locations of the broadband seismic experiments, together with the geology and topography of east Africa, are shown in Figure 1. The geology of the region is comprised of an Archean craton (the Tanzania craton, Figure 1) surrounded by Proterozoic mobile belts. The rift faults of the Cenozoic East African Rift System have developed mainly within the Proterozoic mobile belts, forming a rift system that begins with the Main Ethiopian Rift intersecting the Red Sea and the Gulf of Aden at the Afar triple junction continuing southwest through Kenya and splitting into two branches (western rift and eastern rift) around the Tanzanian craton.

The broadband seismic experiment in Tanzania was conducted in 1994 and 1995 and consisted of 20 seismic stations deployed for a year in two skewed arrays; one oriented more or less east-west, and the other northeast-southwest. The experiment was designed so that structure beneath the Archean Tanzania craton and the terminus of the eastern rift in northern Tanzania could be imaged with seismic data from local, regional and teleseismic earthquakes. Information about the station configuration, recording parameters and other details of the field deployment has been reported by Nyblade et al. (1996).

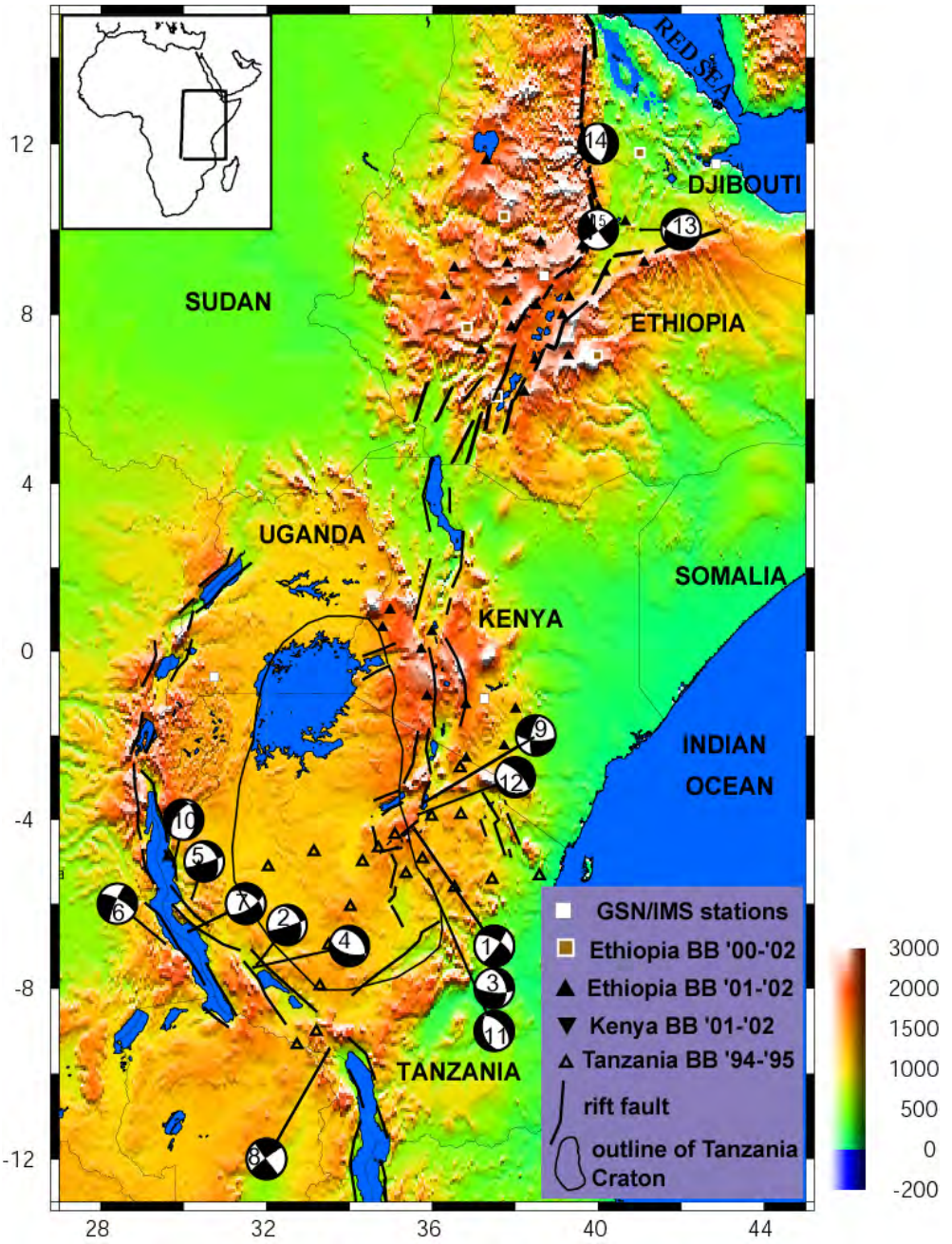


Figure 1. Topographic map of east Africa showing the Ethiopian and east African plateaus (regions with >1,000 m elevation), the outline of the Archean Tanzania craton, the major rift faults of the East African Rift System, focal mechanisms for our events, and the location of broadband seismic stations.

In the other broadband seismic experiments, seismic stations consisting of broadband sensors, 24-bit data loggers, 4 Gbyte hard disks, and GPS clocks were deployed in regions of Ethiopia and Kenya safe for traveling (Figure 1). The stations were spaced 50 to 200 km apart and were located to optimize the recording of teleseismic body and surface waves that sample upper mantle structure beneath the eastern rift. For east Africa, the major source regions for teleseismic earthquakes are the Hindu Kush/Pamir region to the northeast and the Fiji/Tonga subduction zones to the east. Additional criteria used for site selection included access to bedrock, security, and year-round road conditions.

Installation of the Ethiopian stations was completed in two phases. During March 2000, five stations were installed around the periphery of the network, and then one year later (March 2001) an additional 20 stations were installed to densify the

network (Figure 1). All 25 stations were removed from the field in March 2002. Installation of the Kenyan stations took place during July and August 2001, and all 10 of the stations were removed in July 2002. Two data streams were recorded, a 1 sample/sec continuous stream and a 20 sample/sec continuous stream, yielding a data volume of 21 Mbytes per station per day. Data recovery for the Ethiopian stations was nearly 90%, and it was about 70% for the Kenyan stations.

EVENT LOCATIONS

Event locations have been obtained for several events in Tanzania with magnitudes $\geq$ 4 and in Ethiopia with magnitudes > 3.5 that were well recorded by the Tanzania and Ethiopia regional networks. The locations were obtained using P and S arrival times, a regional velocity model for the crust and upper mantle constrained by a number of previous studies, and the event location code HYPOELLIPSE (Lahr, 1993). The P and S onset times were individually handpicked to within 0.1 seconds. The velocity models in Table 1 were used in the event location code for each respective region. Crust and uppermost mantle in east Africa has been studied in detail by many authors using refraction surveys, receiver functions, surface waves, regional waveforms and Pn tomography. From these studies, it is clear that Tanzania's crustal and uppermost mantle structure is fairly uniform in the Precambrian terrains away from the rift valleys proper (Last et al., 1997; Brazier et al., 2000; Nyblade, 2002; Langston et al., 2002; Fuchs et al. 1997 and references therein). Only minor differences in crustal thickness (2-5 km), mean crustal velocity (0.1-0.2 km/s), and uppermost mantle P velocities (0.1 – 0.2 km/s) are found between the various stations of the Tanzania network, and these differences introduce very small uncertainties in the event locations.

Table 1. Crust and uppermost mantle seismic structure for Tanzania and Ethiopia, east Africa.

	V1 (km/s)	V2 (km/s)	Poisson's Ratio	Moho Depth (km)	Mean crustal Vp (km/s)	Pn (km/s)
Tanzania	5.84	7.09	0.25	38	6.5	8.3
Ethiopia	6.2	6.99	0.25	44	6.4	8.0

V1= uppermost crustal velocity; V2=lowermost crustal velocity

Table 2 summarizes the event origin times and locations, and the uncertainties associated with the locations. All of the events are well recorded on at least 11 stations in Tanzania 6 in Ethiopia. A number of the events are within a few tens of kilometers of a station and none are more than a few hundred kilometers from a station. The magnitude estimates for these events comes from using the maximum P wave amplitude within the first five seconds and the local magnitude scale for east Africa determined by Langston et al. (1998). Standard statistical measures at the 68% confidence interval in the error ellipse indicate that the hypocenters appear to be constrained to within a few kilometers. However, a detailed study of several of these events using regional waveform modeling (Langston et al., 2002) indicates that while the P and S arrival times do a fairly good job at constraining epicentral location, they do not provide tight constraints on source depth. Source depth for the events studied by Langston et al. (2002) is shown in Table 2. The source depth obtained from the P and S arrival times for these events differed from the source depths in Table 2 by ten or more kilometers.

Focal mechanisms have been determined using polarities and amplitude ratios of local and regional P and S phases using the grid-search technique by Snoke (1984) and are plotted in Figure 1 and are listed in Table 3. The focal mechanisms are then used with a wavenumber integration algorithm (Kennett, 1983) to compute full synthetic seismograms for several stations at several depths. The synthetics are compared against the data and regional depth phases such as pPn, sPn and PmP can be used to constrain the source depths. In Figure 2 we show the P wave train from the vertical component for an event from Tanzania. These traces are reduced to the Pn velocity. Focal depth is determined by finding the depth at which the best alignment occurs between the data and synthetics. Fixing this depth and relocating using hypoellipse gives a more accurate location overall.

For comparison, we also show in Table 2 the locations and origin times for several of the events taken from the International Seismological Centre (ISC) catalog, our earlier results without depth determination, and two locations including stations outside the networks. The comparison shows discrepancies in origin times of several seconds in most cases, and differences in event location of many tens of kilometers for some events. In addition, no catalog listings were found for several of the events.

Table 2. Locations for earthquakes in east Africa with M > 4 from July 94 June 95 recorded by the Tanzania Broadband Seismic Experiment and the Ethiopia Regional Network from April 2000 to March 2002.

Event:source	yr:mo:day:hr:min:sec	Lat.	Lon.	Dep	M	N	Gap	RMS	Smaj	Az	Smin	Sez
1:Traveltimes	94:07:20:11:32:04.30	-4.080	35.440	42	4.5	19	141	0.44	0.25	-106	0.45	1.7
1:ISC	94:07:20:11:31:58.49	-4.171	35.185	0	3.8			1.26	10.4	90	6.6	
1:Fixed Depth	94:07:20:11:32:04.09	-4.225	35.585	29+	4.5	19	133	1.52	0.25	-106	0.40	0.47
2: Traveltimes	94:08:17:03:23:34.98	-4.513	35.277	17	3.7	20	76	0.70	0.22	-104	0.33	.42
2: Fixed Depth	94:08:17:03:23:32.68	-4.448	35.585	13	3.7	20	18	4.05	0.22	-105	0.31	.52
3: Fixed Depth	94:08:18:00:45:48.80	-7.440	31.770	25*	5.9+	17	167	1.77	0.35	-34	0.48	2*
3: ISC	94:08:18:00:45:52.70	-7.650	31.830	25	5.9			0.69	2.20	90	2.20	
4: Traveltimes	94:09:05:04:08:56.04	-7.508	31.700	?	4.1	15	174	0.43	0.41	-59	0.70	?
4: ISC	94:09:05:04:08:50.41	-7.738	30.882	4	4.6			1.38	10.9	90	6.3	
4: Fixed Depth	94:09:05:04:08:54.83	-7.502	31.700	15+	4.1	18	174	0.54	0.38	-50	0.55	2*
5: Traveltimes	94:09:30:01:36:53.14	-5.920	29.890	26	4.5	16	229	1.13	0.55	-40	1.18	1.4
5: ISC	94:09:30:01:36:47.62	-8.426	37.261	0	4.4			1.78	15.6	90	8.6	
6: Traveltimes	94:11:12:12:18:00.00	-6.950	29.920	30*	5.3	16	179	0.55	0.42	-24	0.89	2*
6: ISC	94:11:12:12:18:01.33	-6.777	29.821	22	4.6			1.05	6.3	90	4.5	
6: Fixed Depth	94:11:12:12:18:00.88	-6.708	30.111	18+	5.3	16	179	0.95	0.39	-26	0.74	2+
6: Fixed Depth +	94:11:12:12:17:57.73	-6.939	29.552	18+	5.3	23	94	2.13	0.31	-40	0.36	2+
7: Traveltimes	94:11:12:20:16:59.37	-6.617	30.016	?	4.7	17	223	0.88	0.45	-33	0.96	?
7: ISC	94:11:12:20:16:49.66	-6.834	29.946	0	4.6			1.15	8.4	90	5.5	
7: Traveltimes	94:11:12:20:16:58.19	-6.652	30.135	8	4.7	17	211	1.29	0.39	-26	0.73	2*
8: Traveltimes	94:11:16:01:08:11.20	-9.070	33.330	8*	4.5	17	193	0.80	0.48	-129	0.66	2*
8: ISC	94:11:16:01:08:09.07	-9.179	33.273	10	5.0			1.64	7.8	90	6.8	
8: Fixed Depth	94:11:16:01:08:10:21	-9.145	33.454	7+	4.5	17	204	0.86	0.51	-112	0.73	2+
8: Fixed Depth +	94:11:16:01:08:05.78	-9.424	33.513	7+	4.5	20	150	3.6	0.29	-52	0.54	0.97
9: Traveltimes	94:11:27:04:20:51.65	-3.568	35.827	30	4.0	15	213	0.51	0.36	-93	0.95	0.7
9: ISC	94:11:27:04:20:44.27	-3.954	35.722	10	4.0			0.12	22.4	90	10.1	
9: Fixed Depth	94:11:27:04:20:53.71	-4.084	35.828	11	4.0	15	146	2.28	0.29	-112	0.48	0.7
10: Traveltimes	94:12:25:04:25:27.44	-5.113	29.752	21	4.2	11	301	0.59	0.81	19	6.42	1.9
10: Fixed Depth	94:12:25:04:25:35.97	-5.173	30.580	29	4.2	11	150	1.48	0.67	22	4.98	2*
11: Traveltimes	95:01:29:00:23:35.02	-5.419	35.909	13	4.1	11	128	0.37	0.34	-107	0.51	1.0
11: Fixed Depth	95:01:29:00:23:33.29	-5.033	35.923	9	4.1	11	111	3.51	0.31	-111	0.53	1.04
12: Traveltimes	95:02:12:16:37:30.00	-3.960	35.830	32*	4.5	20	?					2*
12: Fixed Depth	95:02:12:16:37:33.85	-3.879	35.670	34+	4.5	13	215	0.56	0.36		0.96	2+
13: ISC	00:05:16:20:47:51.93	10.10	41.23	10	4.4							
13: Fixed Depth	00:05:16:20:47:51.27	10.17	41.95	7+	4.4	6	166	1.72	0.49	-120	1.25	3.45
14: Traveltimes	01:04:06:16:36:30.99	11.403	39.659	62	3.6	23	82	2.06	2.10	-51	0.72	4.97
14: Fixed Depth	01:04:06:16:36:29.10	11.492	39.445	5+	3.6	8	171	1.53	0.7	-51	0.7	0.8
15: Traveltimes	01:05:12:01:44:16.07	9.508	39.691		3.6	11	123	2.32	0.46	-34	0.35	0.86
15: Traveltimes	01:05:12:01:44:14.22	9.541	39.658		3.6	10	84	1.44	0.4	-34	0.4	0.7

D = depth in km. * = depth was determined from regional depth phases (Langston et al., 2002). Otherwise depths were determined from only P and S arrival times. M = magnitude. Magnitudes in this study are based on the ML scale from Langston et al. (1998). ISC magnitudes are a mixture of different types. N = number of stations used in the event location. Gap = azimuth range in stations. RMS = Rms error in arrival times. Smaj, Smin, Sez, Az = dimensions (in kms) and orientation of the error ellipse. For this study, the numbers in the table are for a 68% confidence level. * on Sez numbers indicates that the depth uncertainty was obtained from modeling regional depth phases (Langston et al., 2002).

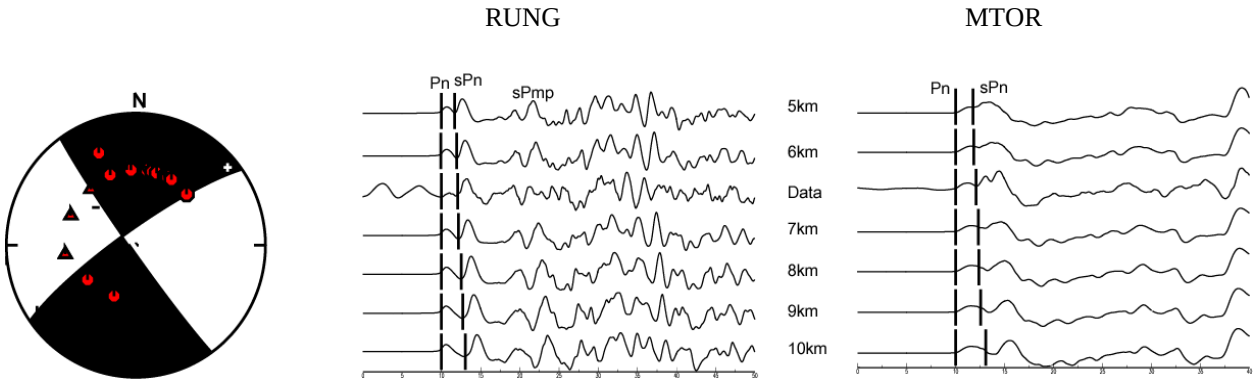


Figure 2. Waveforms and focal mechanisms from the 16 November 1994 Mbeya event (8: in Table 2) recorded at RUNG ($\Delta = 248$ km) and MTOR ($\Delta = 480$ km) and synthetics for source depths between 5-10 km.

TABLE 3. Focal mechanisms for events in Table 2.

	Strike (deg)	Dip (deg)	Rake (deg)
Event 1	301	64	-11
Event 2	335	35	-10
Event 3	345	43	-26
Event 4	318	36	-63
Event 5	335	36	-10
Event 6	204	80	-20
Event 7	303	46	-35
Event 8	143	88	-5
Event 9	93	69	-22
Event 10	215	55	-65
Event 11	162	43	-71
Event 12	316	68	-77
Event 13	105	64	-63
Event 14	54	85	-4
Event 15	3	53	-71

Ongoing Work

In all of these steps it is crucial to have good velocity models for the crust and upper mantle. We are using analyses of receiver functions, surface waves, and seismic refraction profiles to provide independent estimates of crustal and mantle velocities. In addition, we are in the process of making surface wave dispersion measurements of data from the three regional networks in the area. We are measuring both Love and Rayleigh surface wave group velocities using a multiple narrow-band filter technique. Combined with thousands of other measurement made in the broader regional area (Pasyanos et al., 2001), we are conducting a high resolution group velocity tomography of northeastern Africa. Preliminary surface wave tomography results can be seen for eastern Africa in Figure 3 for 20 and 60 second period Rayleigh waves. These maps will be inverted for crustal and upper mantle structure. Using near-regional data will enable us to make more accurate short-period (5-15 seconds) measurements, which will allow us to constrain velocities in the uppermost crust. We will use the surface wave analysis, with receiver functions and other data, to improve the velocity model of the crust and upper mantle, which will in turn improve the event locations.

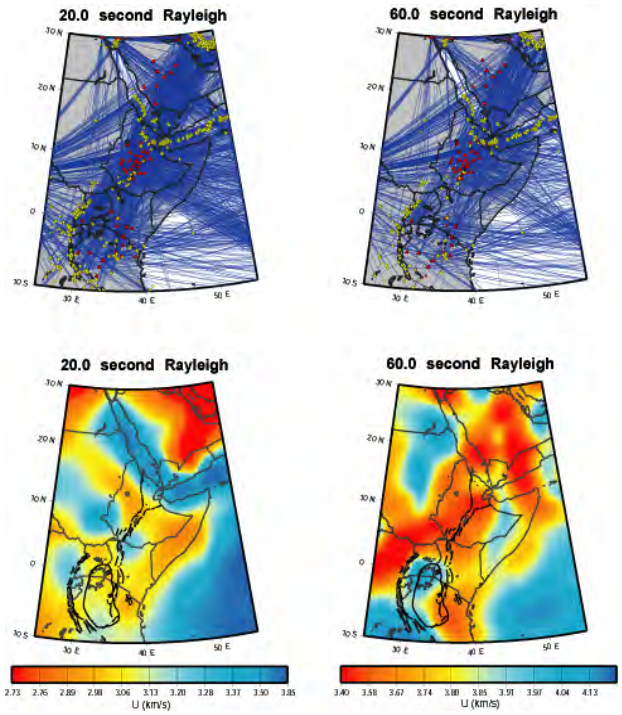


Figure 3. Path locations and preliminary results of the tomography for 20 and 60 second Rayleigh waves

To expand the catalog of events in northeastern Africa, we are taking events located using the approach described above and using them along with teleseismic GT15-25 events (Engdahl, et. al., 1998) as calibration events to construct travel-time correction surfaces using the kriging method of Schultz et al., (1998, 1999) and Myers and Schultz (2000). The travel-time correction surfaces will be used together with local and regional P arrivals to determine epicenters and origin times for numerous other events in the Ethiopia, Kenya, and Tanzania data sets.

The travel-time correction surfaces are constructed following the approach outlined by Myers and Schultz (2000). For the regional networks, we calculate travel-time residuals for the calibration events relative to a regional velocity model, IASPI91 (Kennett et. al. 1991) for the teleseismic events and the Tanzania velocity structure from Table 1 for the regional events. The travel-time residuals will be assigned to the respective calibration epicenter, forming a set of spatially varying travel-time correction points. This set of points will then be declustered to reduce the dimensions of the observations, reducing singularities, and this refined set of calibration points is then modeled with a variogram (variance as a function of spatial separation). The variogram *-----is used with non-stationary Bayesian kriging to form continuous travel-time surface that will provide source-specific corrections for each station in the regional networks. In locating epicenters, a standard location algorithm will be used with the kriging corrections applied. A conservative uncertainty estimate for the kriging correction is used to characterize the travel-time-prediction error, according to the procedure followed by Myers and Schultz (2000). This conservative estimate will be developed using rigorous statistical modeling with available seismic data. Cross-validations will be provided to ensure that the estimates are accurate. In general, these statistics will be used as input to generate chi-squared distribution for robustly determining the final reference event error ellipses.

Preliminary P –wave results for station BGCA can be seen in Figure 4. P and S correction surfaces are being developed for stations DBIC, BOSA, LBTB, and TAM.

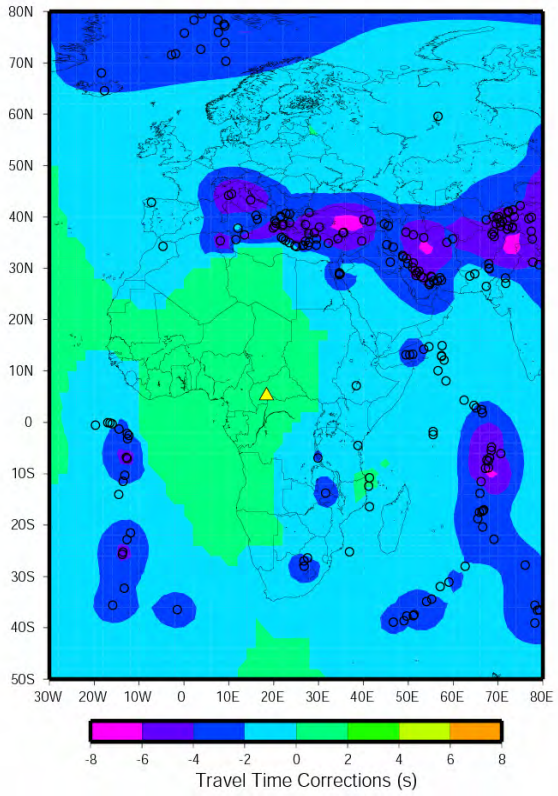


Figure 4. P wave traveltime correction surface for BGCA in the Central African Republic.

Future work will focus on obtaining accurate hypocenters for many additional regionally recorded events in Ethiopia. Figure 5 shows the distribution of events recorded in Ethiopia between April 2000 and March 2002. Accurate locations will be obtained for many of these events with M>3.5 using a combination of the modeling techniques discussed above.

CONCLUSIONS

Accurate event locations for fourteen M>3.5 events in northeastern Africa have been obtained so far using data from the Tanzania Broadband Seismic Experiment and the Ethiopia Broadband Seismic Experiment. Focal mechanisms for most of these events have been obtained by modeling P and SH polarities and amplitude ratios in a grid search method. Epicenters have been constrained by using P and S arrival times. Focal depths have been constrained by waveform modeling of regional and local depth phases. Most of the earthquakes occur on either the western or eastern branch of the East African Rift System, and the mechanisms obtained are all normal or strike-slip. Preliminary epicentral locations for several hundred additional local and near-regional earthquakes have been obtained for Ethiopia using P arrival times.

The Bayesian kriging method is being used with the well located events to construct regional travel-time correction surfaces for northern Africa. To improve further our capabilities to accurately locate events in this part of the world, we are also using surface wave data to construct new velocity models of the crust and upper mantle. Group velocity measurements from many thousand station event pairs ranging from 15-60 second periods for Rayleigh and Love waves have been measured, and these measurements have been inverted to produce group velocity maps of eastern Africa.

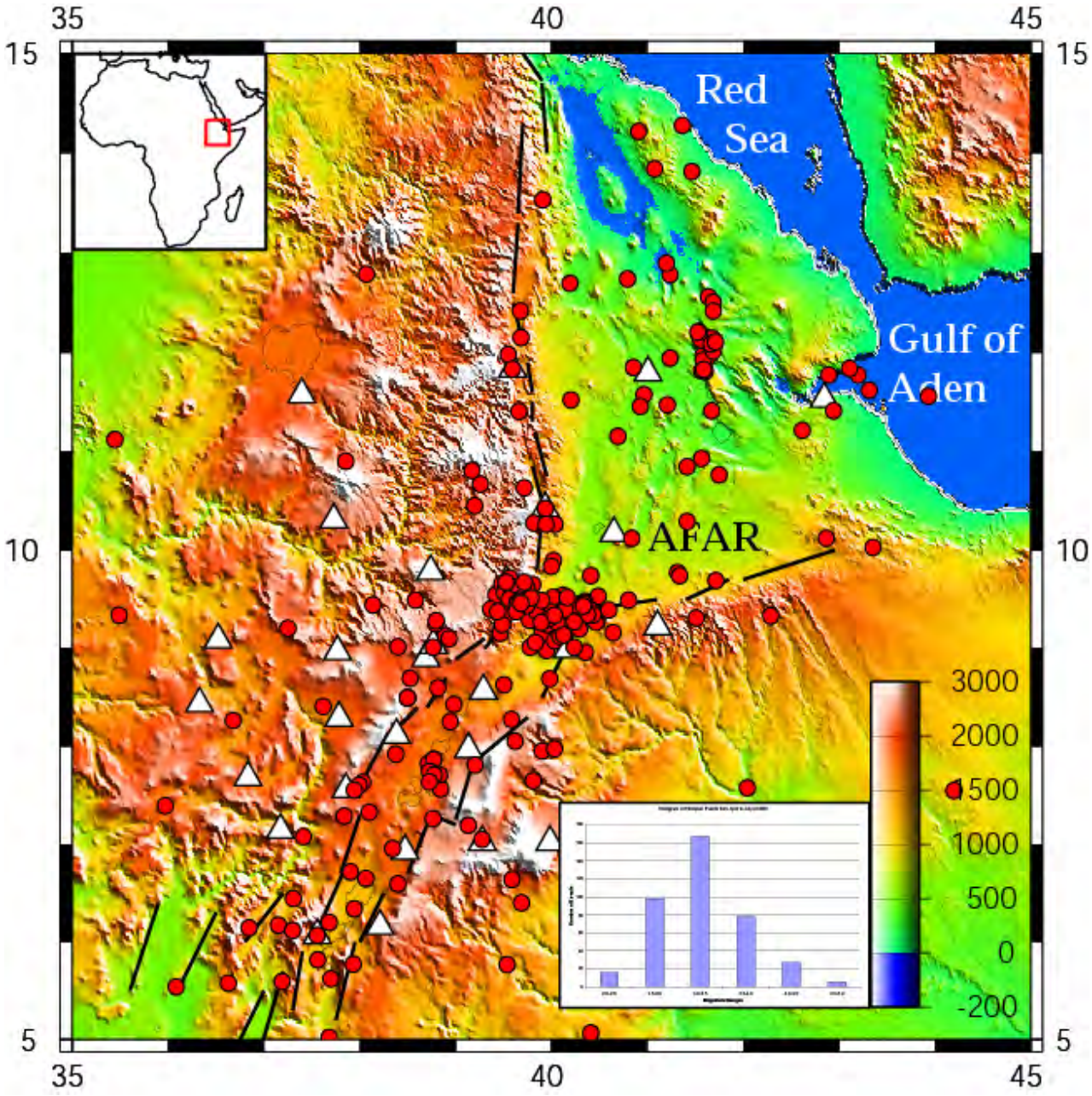


Figure 5. Seismicity (red circles) in Ethiopia with M > 2 from April 2000 to March 2002. Inset histogram of magnitude of events (20 + events M > 4). Seismic stations are shown by white triangles.

REFERENCES

Brazier, R., A.A. Nyblade, C. A. Langston, and T.J. Owens, Pn velocities beneath the Tanzania Craton and adjacent rifted mobile belts, East Africa, *Geophys. Res. Lett.*, 27, 2365-2368, 2000.

Engdahl, E. R., R. D. Van der Hilst and R.P. Buland, Global teleseismic earthquake relocation with improved travel times and procedures for depth determination. *Bull. Seis. Soc. Am., 88*, 722-743, 1998.

Fuchs, K., Altherr, B., Muller, B., and Prodehl, C., Structure and dynamic processes in the lithosphere of the Afro-Arabian rift system: *Tectonophysics, 278*, 1-352, 1997.

Kennett, B.N.L., and E. R. Engdahl, Travel Times for global earthquake location and phase identification, *Geophys. J. Int.* , 105, 429-465, 1991.

Kennett, B.N.L., Seismic wave propagation in stratified media, *Cambridge University Press*, 1983.

Lahr, J.C., Hypoellipse, a computer program for determining local earthquake hypocentral parameters, magnitude and first motion pattern, U.S. Geological Survey Open File Report 89-116, 1993.

Langston, C.A., R. Brazier, A.A. Nyblade and T. J. Owens, Local magnitude scale and seismicity rate for Tanzania, East Africa, *Bull. Seis. Soc. Am., 88*, 712-721, 1998.

Langston, C.A., A.A. Nyblade, and T.J. Owens, Regional wave propagation in Tanzania, East Africa, *J. Geophys. Res.*, 107, 10.1029, 2002.

Last, R., A.A. Nyblade, C.A. Langston, and T.J. Owens, Crustal structure of the East African plateau from receiver functions and Rayleigh wave phase velocities, *J. Geophys. Res., 102*, 24469-24483, 1997.

Myers, S., and C. Schultz, Improving sparse network seismic location with Bayesian kriging and teleseismically constrained calibration events, *Bull. Seis. Soc. Am., 90*, 199-211, 2000.

Nyblade, A.A., C. Birt, C. A. Langston, T.J. Owens, and R. J. Last, Seismic experiment reveals rifting of craton in Tanzania, *Eos Trans. AGU, 77*, 517-521, 1996.

Nyblade, A.A., Crust and upper mantle structure in East Africa and the origin of Cenozoic extension, magmatism and plateau uplift, in *Magmatic Rifted Margins*, edited by M. Menzies, C. Ebinger and S. Klemperer, Geological Society of America special paper 362-0, in press, 2002.

Pasyanos, M.E., W.R. Walter, and S.E. Hazler, A surface wave dispersion study of the Middle East and North for monitoring the Comprehensive Nuclear-Test-Ban Treaty, *Pure and Applied Geophysics*, 2001.

Schultz, C., S. Myers, J. Hipp, and C. Young, Nonstationary Bayesian kriging: a predictive technique to generate spatial corrections for seismic detection, location and identification, *Phys. Earth. Planet. Int., 113*, 321-338, 1999.

Schultz, C., S. Myers, J. Hipp, and C. Young, Nonstationary Bayesian kriging: a predictive technique to generate spatial corrections for seismic detection, location and identification, *Bull. Seis. Soc. Am., 88*, 1275-1288, 1998.

Snoke, J.A., Munsey, J W; Teague, Alan G; Bollinger, G A. A program for focal mechanism determination by combined use of polarity and SV-P amplitude ratio data, *Seismological Society of America, Eastern Section, 56th annual meeting, Earthquake Notes, vol.55, no.3, pp.15, Sep* 1984.

GROUND TRUTH OF AFRICAN AND EASTERN MEDITERRANEAN SHALLOW SEISMICITY USING SAR INTERFEROMETRY AND GIBBS SAMPLING INVERSION

Benjamin A. Brooks[1], Neil Frazer[1], Francisco Gomez[2], and Eric A. Sandvol[2]

University of Hawaii[1] and University of Missouri[2]

Sponsored by Air Force Research Laboratory

Contract No. F19628-03-C-0107

ABSTRACT

Comprehensive Nuclear-Test-Ban Treaty (CTBT) verification is dependent on the ability to locate and determine source parameters of small (< M 5.5) and shallow seismic events that have been recorded by sparse seismic networks. Many studies have demonstrated that event calibration significantly improves the location capability of a sparse seismic network; thus, collecting ground truth data for calibration purposes is essential to the operational adequacy of the International Monitoring System (IMS) network.

In our study, we are using InSAR to provide much-needed ground truth (GT) events for a large region currently covered by a very small number of GT5 or better events. Additionally, by applying Gibbs Sampling, a powerful non-linear inversion technique, to the problem of inverting InSAR data for earthquake parameters, we specifically address uncertainties in the GT events and introduce a methodology that should be of use to the entire monitoring community.

In general our work is focusing on shallow earthquakes with moderate magnitudes (M > 5.0). Existing seismic networks and location algorithms can provide adequate epicenter and magnitude estimates but focal depth and mechanism are often poorly constrained. For example, we have measured the co-seismic displacement field for the December 26, 2003 Bam earthquake in central Iran. Using this displacement field we have inverted for the hypocentral location. We plan to invert for the origin time using available seismic phase data. During the past decade, there have been a number of moderate, shallow earthquakes in North Africa and central/east Africa, as well as parts of the eastern Mediterranean region, for which InSAR data may be available to help fill in gaps in calibration seismic events.

In addition to our analysis of specific GT events, we are refining the coupled InSAR/Gibbs Sampling method so that it may be more widely used by the monitoring community. Recent algorithmic advances include: (1) development of a more robust technique for determining sampling temperature, an important Gibbs Sampling control parameter; and (2) development of a parallel processing approach to the entire problem that will decrease computational cost and increase robustness of results.

OBJECTIVES

Our research focuses on delivering 5-km ground truth (GT5) or better locations for seismic events in North and East Africa and the Eastern Mediterranean region using Synthetic Aperture Radar Interferometry (InSAR) geodesy. InSAR, combined with elastic dislocation modeling, is an emerging tool for acquiring GT information in remote areas (Begnaud et al., 2000; Lohmann et al., 2002). Our work will provide much-needed GT events for a large region currently covered by a very small number of GT5 events. Additionally, by applying Gibbs Sampling (GS), a powerful non-linear inversion method, to the problem of inverting InSAR data for earthquake characteristics, the posterior probability distributions for our estimated source parameters will reflect accurate treatment of data variance. This will allow GT event parameters to be compared quantitatively with one another and to be used, for instance, as prior distributions for kriging-based interpolation efforts (Schultz et al., 1998). The general methodology is one that will be of use to the entire monitoring community engaged in regional calibration.

RESEARCH ACCOMPLISHED

At this stage, we divide our accomplished research into two main arenas: (1) algorithm development for earthquake source parameters from InSAR data inversion and (2) delivery of GT events for North and East Africa and the Eastern Mediterranean regions. Below, we describe the general algorithm and illustrate its use for GT-based calibration efforts with an example from the Bam (Iran), 26 December 2003 earthquake.

Algorithm Development

Ground displacements from InSAR deformation maps can be used to invert for earthquake source parameters in a general class of problems called the coseismic geodetic inverse problem. This is written in the standard form, $Gm = d$ where d is a vector of the measured displacements, m is a vector of the source parameters to be inverted for, and G is a matrix of Green's functions which contain the physics relating the two. For a double-couple earthquake source, elastic dislocation Green's functions (Okada,1985) are usually employed and m has 9 components describing the location, orientation and amount of slip for the dislocation. When auxiliary data exist, such as surface traces of coseismic ground rupture or dense seismologic networks, some of these parameters may be eliminated and the general problem can be formulated with fewer free parameters or even linearized allowing for the details of the earthquake slip distribution process to be investigated (Price and Burgmann, 2002).

For the smaller, more remote events that are the focus of this work, however, the full 9-parameter problem must be solved and so the method used to address this multidimensional, non-linear inverse problem becomes important. For instance, gradient-based methods are susceptible to getting stuck in local minima and so more advanced methods are necessary (Murray et al., 1996). Monte Carlo methods (Mosegaard and Sambridge, 2002) such as Gibbs sampling (GS) are particularly powerful tools for multidimensional non-linear inversion and this is the primary routine we will employ for our analysis of the North African seismic events. Although GS has been used in other geophysical problems (Basu and Frazer, 1990; Jaschke, 1997) it has not been explicitly applied to the coseismic geodetic problem to the best of our knowledge.

The Heat Bath (HB) algorithm (Basu and Frazer, 1990; Chapman and Jaschke, 2001; Creutz, 1980; Rebbi, 1984) is an algorithm for Gibbs sampling (GS): it samples from the Gibbs-Boltzmann probability distribution

$$p_j(m) = \frac{e^{-E_j/T}}{\sum_{j=1}^{N_S} e^{-E_j/T}} \quad , \tag{1}$$

where m, referred to here as the model, is a vector of unknown parameters, E_j is the free energy of the j^{th} of N_S states, and T is temperature. In the HB algorithm sampling begins at a high temperature and each parameter, m_j, is visited in sequence. During a visit to the *jth* parameter, the values for the other parameters are held fixed and the system energy, E_j is calculated for each allowed value of m_j. These energies are used to generate a Gibbs-Boltzmann distribution for parameter j, from which a new state for that parameter is chosen by sampling once. After each parameter in the system has been visited once (a cycle called a 'sweep'), the temperature T is lowered by a

small amount and each parameter is visited again. When the desired sampling temperature is reached, samples are collected for later use, but samples obtained during the cooling process are not used.

Ideally, to sample from an arbitrary $\sigma(m)$ one simply defines E in equation (1) by $E(m) = -\ln \sigma(m)$, then samples at $T = 1$; as the number of sweeps becomes infinite the system's equilibrium distribution becomes the Gibbs-Boltzmann distribution (Geman and Geman, 1984; Rothman, 1986) for $T=1$. It is this theoretical underpinning which makes the GS technique so attractive for GT-based calibration efforts: when properly implemented, GS-estimated parameter distributions from different GT events can be quantitatively compared with one another. Although other authors have used Monte Carlo-based inversion techniques for estimating earthquake source parameters from InSAR and other geodetic data (Cervelli et al., 2001; Lohmann et al., 2002; Wright et al., 2003), it is not clear how inversion results from independent events may be related to one another using these other techniques.

In practice, before beginning to sample at $T = 1$, GS moves to the sampling temperature via a cooling schedule whose characteristics affect the performance of the associated inversion method (Rothman, 1985). If cooled too rapidly, the system will not be in equilibrium, and sampling will be biased, but cooling too slowly is computationally inefficient. A common practice is to cool very slowly from a high temperature to T^*, the critical temperature at which a phase change occurs (Basu and Frazer, 1990). At T^*, low-E models are preferred, but the system is still warm enough for the sampler to escape from local energy minima. Below T^* the system is at least partly frozen, and successive samples tend to have the same value. If $T^* < 1$, it is straightforward to sample at $T = 1$; however, it is practically impossible to sample at $T = 1$ if $T^* > 1$. Moreover, it follows from equation (1) that sampling at T^* gives samples from $\sigma(m)^{1/T^*}$ which is a much broader distribution than $\sigma(m)$ if $T^* > 1$. As $\sigma(m)$ is multidimensional, correcting for this T-scaling is difficult and so has been neglected in previous GS implementations. In our recent work (Brooks and Frazer, in review), we derive an effective correction for the T-scaling in GS results that allows unbiased sampling from an arbitrary $\sigma(m)$, even if $T^* > 1$.

For a given inverse problem, how likely is it that T^* is greater than unity? The answer is rooted in the relationship between T^* and data variance, ν^2. Consider a thought experiment in which data from an event are measured simultaneously by less precise and more precise equipment. The more precise measurements will yield data with variances ν^2 / k^2 where $k > 1$. If the squared residual, $(d - G(m))^T C^{-1}(d - G(m))$ is used for $E(m)$ in equation (1), then a factor k^2 will enter the numerator of the exponent. The physics of the 'melt' hasn't changed, so when k increases (data variance decreases), T^* will increase. This reveals an interesting irony associated with GS-based inversion: when signal-to-noise ratio (SNR) is higher (i.e., the data variances are smaller and the data are qualitatively 'better') T^* is more likely to be greater than unity, and the uncorrected GS procedure is less likely to be sampling from the true distribution, $\sigma(m)$.

We build upon our recent advances and delineate a general method of inverting InSAR data for earthquake source parameters and GT-based calibration efforts. Important aspects include determination of realistic data variance values for InSAR data and, because of the large number of parameters in the inversion (typically >= 9) and the large number of data points (typically tens of thousands for InSAR data sets), data decimation issues. Additionally, we address the possibilities of increasing performance through parallel processing.

We implement our algorithm as follows:

1) Data preparation.
   a) Form interferograms for the GT event (Begnaud et al., 2000), see below, Figure 1a. Our InSAR processing strategy is standard with a small number of exceptions. We process the SAR data using the Gamma Remote Sensing suite of processing tools. In the Middle East region, we have used these tools to construct high-resolution (20 meter pixel) DEM data for regions in Northern Syria and Lebanon (Gomez et al., in review). To remove the signal of the surface topography, we use either: 1) DTED level-1 data; 2) Shuttle Radar Topographic Mission (SRTM) data; 3) existing DEM data (if resolution is 100 meter/pixel or better); or, 4) we construct a high-resolution DEM data using ERS1/2 tandem data. We employ recently developed methods involving minimum-cost-flow algorithms weighted by interferometric coherence to better unwrap patchy interferograms (Chen and Zebker, 2000; Constantini, 1998).

b) Convert radar line of sight (LOS) phase values to range change values with length units (Figure 1b).
c) Crop the image so that it contains most pertinent earthquake related ground motions (Figure 1c).
d) Mask out the near-field signal and, for the whole scene (including the area that was excluded during cropping) determine the data variance, ν^2 , in the far field from the co-seismic deformation (Figure 1c). To the extent that atmospheric conditions are consistent across an image, ν^2 is an empirical measure of the likely atmospheric contribution to measured phase in the coseismic interferogram. If multiple interferograms are available, then variance can be determined on a pixel-by-pixel basis; if not, then ν^2 will be used for each measurement point in the data set and will represent a conservative estimate of variance.
e) Because typical InSAR data sets may comprise thousands of pixels, computational restrictions require that the data be decimated (Figure 1d). Currently we employ the quadtree method (Jónsson et al., 2002), a decimation technique that divides a data block if differences between maximum and minimum values in the block are greater than some threshold value.

2) Data analysis.
a) On one CPU, run a series of 'Short-Runs' (Basu and Frazer, 1990) to determine a range of sampling temperatures, T_s (Figure 2). The T_s range is determined with a series of fixed-temperature 'short runs' for five starting models. A short run consists of 25 sweeps over the parameter space, far fewer sweeps than for an actual inversion. The energy of the final model from each short run is thus a function of short-run starting model and short-run temperature: $E(m_s,T)$. $E(m_s,T)$, is averaged over the starting model, and the T_s range is taken to be the temperature that minimizes the averaged E, or, if there is no minimum, the temperature at which averaged E begins to increase.
b) On as many CPUs as possible, synchronously run the GS algorithm, with each CPU using a different T_s from the narrowed range determined from the short-runs. Here, it is important to note the slight change in nomenclature from T^* to T_s. Previous GS implementation focused on sampling at only one value, T^* . By sampling over a range of values, however, we evaluate various choices for T_s and iteratively approach an optimal value. Additionally, because the parameter value from the previous sweep is used in the sampling of the current sweep, the GS algorithm is not easily parallelizable in the sense of passing multiple computations from one GS run to multiple CPUs. Thus, the limiting factor for parallelizing the GS routine is the objective function itself, in this case, Okada's solutions for surface displacements due to a dislocation embedded in an elastic half-space. For these routines, the computational cost of message passing is greater than the cost of simply continuing the routine on one processor.
c) Construct a plot of T_s vs. E_s, where E_s is the median E values obtained from all of the samples at T_s (Figure 2b). If the plot shows an obvious minimum, then the posterior distributions corresponding to this minimum is the preferred solution. If there is no minimum, then, most likely, the T_s range determined from the short-runs is too narrow and more GS runs should be performed at a wider range of temperature values.
d) Inspect the posterior distributions from the GS runs, using the $T_s > 1$ correction if necessary (Brooks and Frazer, in review) (Figure 3). Posterior distributions usually will converge towards a solution as the most appropriate T_s is approached.

In our experience with InSAR datasets of ~250 surface measurements the entire process, including non-automated aspects (data masking, etc.) should take ~ 2-3 days with an array of 10 modern computers

GT Example: The Bam earthquake

The M_w 6.5 Bam, Iran, earthquake of 26 December, 2003 did not exhibit major macroscopic ground rupture features, but rather it was associated with small-scale surface fissuring (Talebian et al,2004). Focal mechanisms from 3 independent sources (Harvard CMT, NEIC, and Talebian et al (2003)) agree roughly on epicentral location and that the earthquake occurred on a sub-vertical north-south (or east-west) striking plane.

The event was imaged first with descending, then with ascending orbital passes of the Advanced Synthetic Aperture Radar (ASAR) on the European Space Agency's (ESA) Envisat space vehicle. Using the descending data, we created a differential interferogram by differencing a preseismic interferogram (6/11/03 and 12/03/03 acquisition dates, 480 meter perpendicular baseline) and a coseismic interferogram (12/03/03 and 1/07/04 acquisition dates, 540 meter perpendicular baseline). We removed the topographic phase from these data by subtracting a synthetic interferogram created from SRTM data. The results, shown as a map of fringes representing changes in phase values

along the radar's LOS (Figure 1a), yield an especially complete representation of ground motion due to the earthquake. It is important to keep in mind, however, that this image represents only the LOS component of ground deformation and not full 3-d displacements (Wright et al., 2004).

We followed our data preparation and analysis algorithm described above and present the preliminary results in Figures 1-3. The standard deviation of far-field data (ν) was 14.1 mm (Figure 1c) and after cropping and quadtree decimation (Figure 1c) with a threshold of 15cm we performed the GS analysis on 257 data points (Figure 1d). Short-run analysis (Figure 2a) indicated a candidate region of T_s values between 0 and 500. On 8 CPUs we simultaneously ran the full GS algorithm, cooling for 3500 iterations and sampling for 5000 iterations once the cooling schedule reached the particular T_s value. In total, well over 10 million function evaluations were performed on each CPU. The results of plotting median E value versus T_s shows that a value of T_s = 60 yields the lowest median energies, and so it is the most appropriate value of T_s to use when constructing posterior distributions (Figure 3).

Mean values from the preliminary GS results indicate that the earthquake accommodated ~ 2.75 meters of right-lateral strike-slip and negligible dip-slip on a north-south striking, 60° east-dipping fault with dimensions of ~10 x 10 km and an upper edge at ~2500 meters depth. Standard deviations of location parameters (dx, dy, the upper left corner of the dislocation) are of the order of 400 meters. Because $T_s > 1$ in all of our sampling, our correction (Brooks and Frazer, in review) is necessary to tighten the distributions which are sampled from $\sigma(m)^{1/T_s}$ (Figure 3, see discussion above). Although the corrected distributions (red histograms, Figure 3) significantly tighten the sampled distribution (black histograms, Figure 3) it is likely that the 'peakiness' of the correction is an artifact from insufficient number of samples collected. In our tests on synthetic datasets, upon further sampling, the corrected values will converge towards an intermediate distribution shape.

The values determined from this preliminary GS analysis are similar to, though somewhat different than the recently published study of Talebian et al. (2004). The differences are largely due to the inclusion of a secondary thrust fault to the east of the principal strike-slip fault, warranted by consideration of teleseismic P- and SH- bodywaves and strong motion records (Talebian et al,2004). It is possible that the relatively shallow mean dip (Figure 3) of our preliminary solution reflects an averaging of the displacement fields due to two distinct fault slip patches. This discrepancy reflects the possible complications introduced by source complexity if relatively larger earthquakes are to be used for InSAR based GT efforts. Our future work on this earthquake will include inclusion of the ascending interferogram's data and joint inversion with waveform data.

CONCLUSIONS AND RECOMMENDATIONS

1. The Gibbs sampling technique has associated theoretical properties of convergence that make it very attractive for addressing uncertainly issues which arise in inversion of InSAR coseismic data sets for GT efforts. Here, we have developed and presented a general algorithm for implementing GS in GT studies.

2. We give a preliminary test of the GS algorithm on the 2003 Bam (Iran) earthquake and find that it yields results similar to a recently published study, though source complexity may bias the results somewhat. Further sampling is required to provide properly scaled posterior distributions.

3. The apparent source complexity of the Bam earthquake is a good example of why earthquakes smaller than M_w 6 are likely the best candidates for InSAR-based GT studies.

4. There are many different nonlinear inversion/optimization techniques that have been recently implemented to solve for earthquake source parameters from InSAR data (Brooks and Frazer, in review; Cervelli et al., 2001; Lohmann et al., 2002; Sambridge, 1998a; Sambridge,1998b; Wright et al., 2003). The monitoring community's needs for addressing location uncertainties, however, are typically more, well defined and stringent than the usual criteria for a scientific publication. Thus, to best determine which methods are acceptable for GT studies, we recommend that a thorough comparison (empirical and/or theoretical) between inversion techniques be undertaken.

REFERENCES

Basu, A. and L. N. Frazer (1990) Rapid Determination of the Critical Temperature in Simulated Annealing Inversion, *Science*, *249*, 1409-12

Begnaud, M. L., A. A. Velasco and L. K. Steck (2000) Utilizing results from InSAR to develop seismic location benchmarks and implications for seismic source studies, in *22nd Annual DOD/DOE Seismic Research Symposium*, New Orleans, LA

Brooks, B. and L. N. Frazer (in review) Gibbs sampling from an arbitrary distribution, inversion and a test for multimodality, with an application to the coseismic geodetic problem, *Geophys. J Int.*

Cervelli, P., T. Kato, M. H. Murray, P. Segall and Y. Aoki (2001) Estimating source parameters from deformation data, with an application to the March 1997 earthquake swarm off the Izu Peninsula, Japan, *Journal of Geophysical Research B: Solid Earth*, *106* (6), 11217-37

Chapman, N. R. and L. Jaschke (2001) Freeze Bath Inversion for Estimation of Geoacoustic Parameters, in *Inverse Problems in Underwater Acoustics*, edited by M. I. Taroudakis and G. Makrakis, pp. 15-35, Springer-Verlag, New York

Chen, C. and H. Zebker (2000) Network approaches to two-dimensional phase unwrapping: intractability and two new algorithms, *Journal of the Optical Society of America*, *17*, 401-14

Constantini, M. (1998) A novel phase unwrapping method based on network programming, *IEEE Transactions on Geoscience and Remote Sensing*, *36*, 813-21

Creutz, M. (1980) Monte-Carlo study of quantized SU(2) gauge theory, *Phys. Rev. D*, *21*, 2308

Geman, S. and D. Geman (1984) Stochastic relaxation, Gibbs distributions and the Bayesian restoration of images, *IEEE Trans. Patt. Analysis Mach. Int.*, *6*, 721-41

Gomez, F., M. Khawlie, C. Tabet, K. Khair, A. N. Darkal and M. Barazangi (in review) Neotectonics of the northern Dead Sea fault system in Lebanon and Syria based on SAR imagery and high resolution DEM data, *Earth and Planetary Science Letters*

Jaschke, L. (1997) Geophysical Inversion by the Freeze Bath Method with an Application to Geoacoustic Ocean Bottom parameter Estimation, Ph.D. thesis, University of Victoria

Jónsson, S., H. Zebker, P. Segall and F. Amelung (2002) Fault slip distribution of the 1999 Mw 7.1 Hector Mine, California, earthquake, estimated from satellite radar and GPS measurements, *Bull. Seism. Soc. Am.*, *92* (4), 1377-89

Lohmann, R. B., M. Simons and B. Savage (2002) Location and mechanism of the Little Skull Mountain earthquake as constrained by satellite radar interferometry and seismic waveform modeling, *J. Geophys. Res.*, *107* (6)

Mosegaard, K. and M. Sambridge (2002) Monte Carlo analysis of inverse problems, *Inverse Problems*, *18*, 29-54

Murray, M. H., G. A. Marshall, M. Lisowski and R. S. Stein (1996) The 1992 M=7 Cape Mendocino, California, earthquake: Coseismic deformation at the south end of the Cascadia megathrust, *J. Geophys. Res.*, *101* (8), 17,707-17,25

Okada, Y. (1985) Surface deformation due to shear and tensile faults in a half-space, *Bull. Seism. Soc. Am.*, *75*, 1135-54

Price, E. J. and R. Burgmann (2002) Interactions Between the Landers and Hector Mine, California, Earthquakes from Space Geodesy, Boundary Element Modeling, and Time-dependent Friction, *BSSA*, *92* (4), 1450-69

Rebbi, C. (1984), in *Applications of the Monte Carlo Method*, edited by K. Binder, pp. 277-98, Springer-Verlag, New York

Rothman, D. H. (1985) Nonlinear inversion, statistical mechanics, and residual statics estimation, *Geophysics*, *50*, 2784-96

Rothman, D. H. (1986) Automatic estimation of large residual statics corrections, *Geophysics*, *51*, 332-46

Sambridge, M. (1998) Geophysical inversion with a neighborhood algorithm, 1, Searching a parameter space, *Geophys. J. Int.*, *138*, 479-94

Sambridge, M. (1998) Geophysical inversion with a neighborhood algorithm, 2, Appraising the ensemble, *Geophys. J. Int.*, *138*, 727-46

Schultz, C., S. Myers, J. Hipp and C. Young (1998) Nonstationary Bayesian kriging: application of spatial corrections to improve seismic detection, location and identification, *Bull. Seism. Soc. Am.*, *88*, 1,275-1,88

Talebian, M., E. J. Fielding, G. J. Funning, M. Ghorashi, J. Jackson, H. Nazari, B. Parsons, K. Priestly, P. A. Rosen, R. W. Walker and T. J. Wright (2004) The 2003 Bam (Iran) earthquake - rupture of a blind strike-slip fault, *Geophys. Res. Lett.*

Wright, T. J., Z. Lu and C. Wicks (2003) Source model for the Mw 6.7, 23 October 2002, Nenana Mountain Earthquake (Alaska) from InSAR, *Geophys. Res. Lett.*, *30* (18), 1974

Wright, T. J., B. Parsons and Z. Lu (2004) Toward mapping surface deformation in three dimensions using InSAR, *Geophys. Res. Lett.*, *31*, 1607

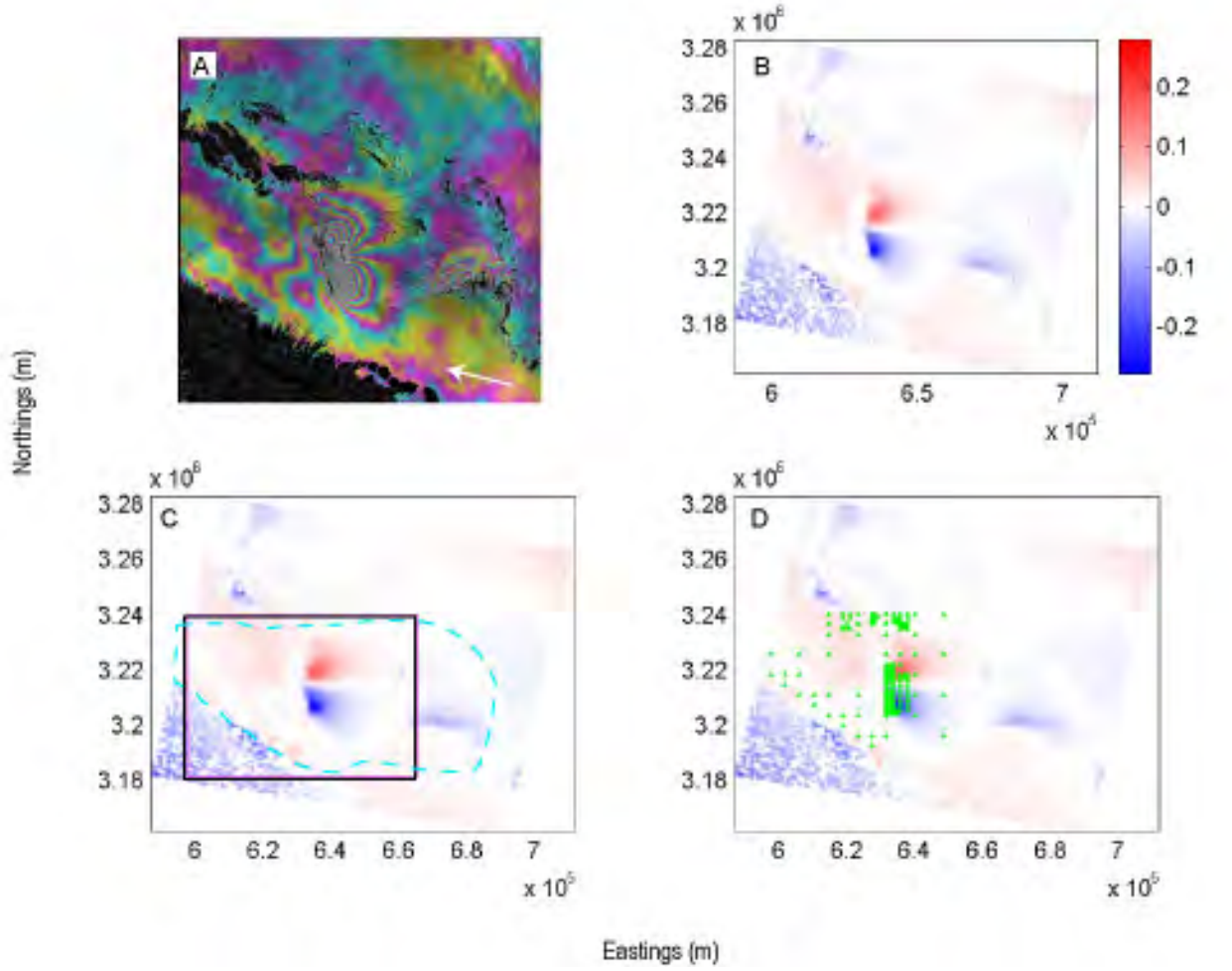


Figure 1. A) Envisat descending differential interferogram showing line of sight (LOS) phase changes (one color cycle represents 28 mm range change) for the Bam 2003 earthquake. White arrow represents look direction of the satellite. B) LOS range change contour map of the data in A, placed in UTM projection. C) Same as B. Black box shows the zone of cropping for GS analysis. Dashed blue line is the mask for calculation of far-field data variance. Only values outside of the mask are included in the calculation. D) Same as C. Green dots show the points retained from quadtree decomposition of the cropped data set.

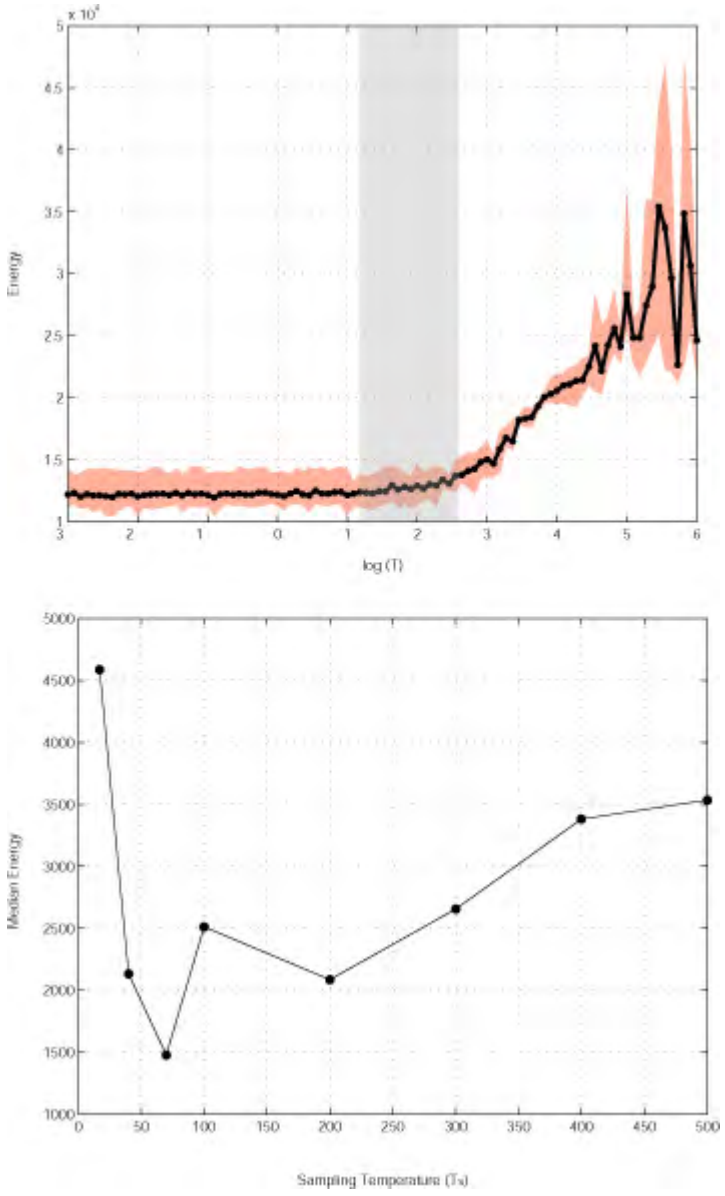


Figure 2. A) Results of Gibbs sampling 'short-run' analysis. The thick black line is the mean energy value of each short run, the pink envelope represents the minimum and maximum energy values of the short run. The grey shaded area indicates the most appropriate range of sampling temperatures. B) Plot of sampling temperature vs. median energy values from full Gibbs sampling runs at a variety of temperatures in the range defined in A. The sampling temperature corresponding to the lowest median energy value is the most appropriate for construction of posterior distributions.

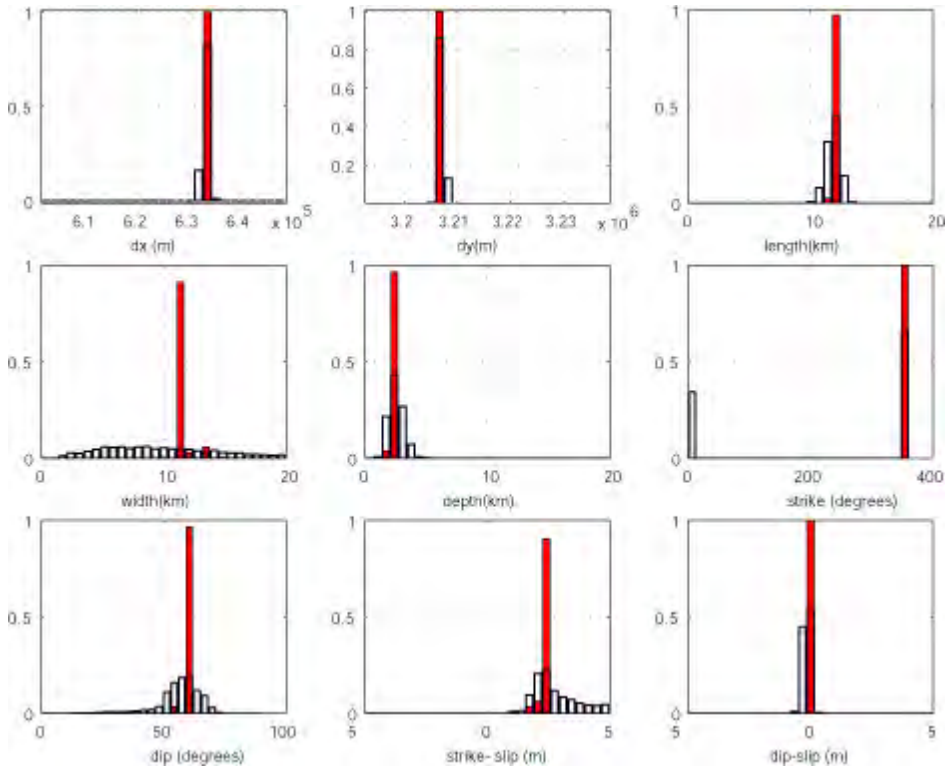


Figure 3. Posterior distributions constructed from full GS run at a sampling temperature of 60. Dx, dislocation east offset; Dy, dislocation north offset; length, dislocation length; width, dislocation width; depth, dislocation upper edge depth; strike, dislocation strike; dip, dislocation dip (using right hand rule with strike); strike-slip, dislocation strike-slip; dip-slip, dislocation dip-slip. The black histograms are from samples collected at T_s. The red histograms represent the correction when sampling occurs at values of $T_s > 1$.

NEXT-GENERATION INSAR GROUND-TRUTH DATA AND TECHNIQUES: INITIAL RESULTS

Sean M. Buckley[1], Paul Vincent[2], and Krishnavikas Gudipati[1]

University of Texas at Austin[1], Lawrence Livermore National Laboratory[2]

Sponsored by National Nuclear Security Administration
Office of Nonproliferation Research and Engineering
Office of Defense Nuclear Nonproliferation

Contract No. DE-FC52-03NA99566[1], W-7405-ENG-48[2]

ABSTRACT

The purpose of this study is to assess the capability of next-generation interferometric synthetic aperture radar (InSAR) satellite data and processing techniques to improve remotely-sensed ground truth associated with seismic source location, depth, and characterization. Initial project work has focused on the implementation of InSAR time series algorithms and their application to European Remote Sensing (ERS) synthetic aperture radar (SAR) data already in-hand. In an approach utilizing an ensemble of interferograms and singular value decomposition solution methods, a set of interferograms is used to construct a history of time-varying deformation, e.g., seasonal centimeter-scale subsidence variations superimposed on long-term constant subsidence rates. In addition, a coherent scatterer technique may be used to separate undesirable phase contributions from sub-centimeter deformation signatures on isolated coherent InSAR pixels. These time series approaches show promise in improving the signal-to-noise (SNR) ratio in data sets with atmospheric and decorrelation noise sources. The new Envisat satellite, with its increased number of operating modes as compared with ERS, is also providing SAR data over regions of interest to this study. These new processing approaches and data will be applied to several nuclear test sites as well as to moderate earthquakes used as calibration events; and their improvements documented.

OBJECTIVES

The goal of this study is to assess new satellite SAR data and InSAR processing techniques for improvements to current remotely-sensed ground truth (GT) collection capability for determining seismic source location, depth and characterization. Specifically, we are (a) applying InSAR time series analysis to sets of ERS and Envisat radar interferograms, (b) evaluating SAR data from several new acquisition modes offered by the European Envisat satellite, and (c) using InSAR results to constrain geophysical source modeling to improve determinations of seismic source location, depth, and mechanism.

RESEARCH ACCOMPLISHED

This paper presents results derived as part of initial development of two InSAR time series techniques: a linear inversion of a database of interferograms and InSAR processing of isolated coherent scatterers. Although results are shown for Phoenix, Arizona, our ongoing work involves the application of these techniques to several target seismic source regions throughout the world for which we possess ERS SAR data. In addition, we will make use of several new imaging modes available from the Envisat SAR satellite.

Linear Inversion of a Set of Interferograms

Recent InSAR research has focused on extracting time-variable deformation from a set of interferograms spanning overlapping periods of times. The result of these techniques is a history of deformation relative to a given reference image date, at each of the subsequent SAR acquisition dates, and broadly applied to areas of generally good coherence.

In developing a linear inversion solution based on least squares and singular value decomposition approach [Usai, 2001; Schmidt and Bürgmann, 2003], we invert 28 interferograms spanning 17 SAR acquisition dates (Figure 1, refer to Gudipati, Buckley and Wilson [2004] for additional details). The resulting 7-year time series (Figure 2 and Figure 3) reveals seasonal variations believed to be related to groundwater fluctuations. These subtle variations in deformation over time reveal important geophysical information not readily accessible through comparison of individual interferograms.

As part of ongoing work, 120 interferograms corresponding to 16 SAR acquisitions over the Nevada Test Site are being reduced for use in the time series and coherent scatterer InSAR assessment. A preliminary time series result shows cumulative displacement over the Nevada Test Site from June 11, 1995, to June 16, 1997, (Figure 4). The synthetic interferogram was derived from 15 interferograms spanning six SAR acquisition dates.

InSAR Processing of Isolated Coherent Scatterers

In assessing InSAR time series techniques, we decided that developing a coherent scatterer InSAR processing capability is important to the success of the project. For the general application of InSAR, the variation of the atmosphere over time and space results in artifacts masking deformation features. In addition, the presence of vegetation results in widespread decorrelation over time for C-band InSAR. The purpose of coherent scatterer InSAR analysis is to use several interferograms spanning different time spans to separate atmospheric delays from surface deformation [Ferretti et al., 2001; Ferretti et al., 2000]. We utilize Phoenix data already in hand to create full-resolution InSAR results for use in coherent scatterer algorithm development and application.

Coherent scatterer InSAR processing is performed on an irregular grid of interferogram pixels that remain coherent over long periods of time. A sequence of differential interferograms is created, each relative to the same reference date. In general, these interferograms cannot be unwrapped due to temporal decorrelation and large interferometric baselines. However, there remains a subset of sparse useable phase data associated with coherent subpixel scatterers.

An initial set of coherent scatterers is identified from pixels with low radar backscatter dispersion over the stack of SAR images (Figure 5). For each initial coherent scatterer pixel, phase differences are formed with neighboring coherent scatterers. Relative (differences in) displacement velocities and height errors are estimated between pairs of coherent scatterers by maximizing the single-pixel multi-interferogram correlation. With the gradients estimated,

the relative velocities, height errors and phases can be unwrapped (Figure 6). Various high and low pass filters are applied in time and space to separate atmospheric artifacts from nonlinear deformation. The process is then repeated to find additional coherent scatterers.

The benefit of coherent scatterer analysis is that it might have success in regions where conventional InSAR fails due to temporal decorrelation. The success of coherent scatterer InSAR depends, in part, on the density of coherent scatterers in the area of interest. Because of the determination and removal of the atmospheric phase contribution, coherent scatterer InSAR has the potential to detect millimeter per year deformation rates.

New SAR Modes of Operation

As the successor to ERS, Envisat was launched in March 2002 with SAR data acquisitions available from September 2002. Envisat SAR characteristics include the following:

- spatial and radiometric resolution, sensitivity and ambiguity suppression similar to ERS
- improved orbits due to DORIS microwave tracking instrument (more accurate orbits will result in more accurate and automated InSAR data processing relative to ERS)
- multiple polarizations, including an Alternating Polarization Mode, as compared with fixed polarization for ERS (using an alternative polarization may provide improved InSAR coherence in certain locations due to different scattering mechanisms)
- seven swaths ranging in incidence angles from 15 to 45 degrees

InSAR data from multiple satellite passes can be combined to constrain, reveal the spatial extent, and determine more than the line-of-sight displacement associated with a deformation event captured in a set of interferograms. For example, Fialko et al. [2001] reveal the three-dimensional coseismic displacement field of the October 1999 Hector Mine earthquake through the use of InSAR from descending and ascending satellite passes as well as from the azimuth offsets determined as part of the registration of the SAR images used to form the descending pass interferogram. Peltzer et al. [1999] utilized the InSAR offsets and data from three adjacent satellite tracks to capture the 170-km-long surface rupture associated with the November 1997 Manyi, Tibet earthquake.

Acquisitions from multiple SAR swaths can also provide valuable additional data for identifying subtle deformation features or deformation rates that vary over time. The overlap of adjacent SAR swaths affords the opportunity to image a deformation feature at additional times. The amount of overlap is determined by the SAR operating mode, latitude of study site and how the SAR processing is implemented. For example, for the fixed viewing geometry of ERS, adjacent SAR swaths over Phoenix overlap by approximately one-third when processed to the full extent possible in slant range. More overlap occurs as satellite tracks converge at the poles. In contrast, Envisat provides flexible swath positioning at different incidence angles. This is a powerful new capability relative to ERS, which assures that a deformation feature of interest can be imaged by two adjacent tracks as well as on both descending and ascending satellite passes.

A sample of Envisat SAR data over Hokkaido, Japan was used for developing and testing Envisat SAR and InSAR processing capability (Figure 7). We intend to use Envisat swath positioning to image deformation features of interest from multiple satellite tracks. This will greatly increase the amount of InSAR data available for use with advanced InSAR processing techniques. A detailed comparison will be made between previous ERS InSAR results and new Envisat results to quantify the anticipated improvements to seismic event location and source mechanism determination capabilities.

HISTORICAL PERSPECTIVE

It was recently demonstrated that InSAR can play a significant role in providing accurate GT for both seismic event location calibration and discrimination purposes, and is especially valuable in denied or difficult-access regions. For example, InSAR has been applied to nuclear explosion monitoring efforts at LLNL by creating deformation maps of the NTS and other nuclear test sites, as well as mine collapses and moderate earthquakes in the Middle East [Vincent, et al., 1999; Vincent, et al., 2000; Swenson, et al., 2001; Vincent, et al., 2001; Walter, et al., 2001; Myers, et al., 2002; Vincent et al, 2002; Walter, et al., 2002]. A review of InSAR and its technical challenges follows.

Differential Interferometry

SAR is an active microwave coherent (phase preserving) imaging remote sensing instrument. Typical satellite SAR can collect data along ~100 km imaging swaths on both ascending and descending satellite passes. In differential InSAR studies, the difference in the phases of nearly-coincident SAR images collected at different times are related to surface topography as well as any deformation that may have occurred along the radar line-of-sight. The deformation signature is isolated by removing the phase due to topography using either another interferogram that contains only topographic phase information, or by using an independent digital elevation model to simulate the topographic phase.

Differential InSAR has developed into a viable and valuable tool for measurement of earth-surface deformation associated with natural and anthropogenic hazards such as seismic activity [Peltzer et al., 2001a; Sandwell et al., 2000; Bürgmann et al., 1998; Zebker et al., 1994] and subsidence associated with subsurface fluid withdrawal [Bawden et al., 2001; Hoffmann et al., 2001; Galloway et al., 1998; Fielding et al., 1998]. InSAR scientific studies have progressed from single interferogram investigations of line-of-sight deformation over a given time period [Massonnet et al., 1993] to multi-interferogram reconstructions of three-dimensional displacements [Fialko et al., 2001] and InSAR time series of continuous but variable deformation [Berardino et al., 2001].

InSAR Technical Challenges

The primary limitations of repeat-pass InSAR are temporal and geometric decorrelation, artifacts in the interferogram as the result of atmospheric variations between acquisitions, and to a lesser degree, imprecise knowledge of the interferometric baseline [Table 1, Sandwell and Sichoix, 2000]. Temporal decorrelation occurs when individual scatterers within a pixel are rearranged or move incoherently by a distance on the order of the radar wavelength or greater between acquisitions. At the ERS C-band 6-cm wavelength, urban areas are generally well-correlated but widespread decorrelation is observed in vegetated areas. At longer wavelengths, e.g., L-band, vegetation penetration is possible and results in more coherence in lightly vegetation areas, although cultivated agricultural fields still decorrelate over time. Geometric decorrelation is a result of the direct relationship between the interferometric baseline and the maximum correlation between the SAR images, i.e., at the critical baseline, the maximum correlation decreases to zero. For ERS, the critical baseline is ~1100m, with a practical baseline limit of ~400m for conventional InSAR applications.

Atmospheric artifacts are associated with variations in the ionosphere and troposphere, with spatial and temporal variations in water vapor typically being the largest source of error. These variations occur on many spatial scales, from kilometer-scale artifacts that appear similar to localized subsidence features, to large-scale phase ramps spanning much of the interferogram. Imprecise knowledge of the baseline results in similar broad-scale residual phase ramps across the flattened interferogram. However, these phase ramps can be removed with a few topographic or deformation control points distributed across the image.

Differential interferograms contain the deformation signature of interest as well as several other contributions, such as residual topography and atmospheric artifacts. For differential interferogram phase signatures greater than a cycle and spatial extent less than the size of the interferogram, visual inspection of a few interferograms can be used to confirm that the signature is surface deformation. In other words, phase signatures that are persistent across several independent interferograms are likely related to deformation. For analyses of many interferograms and more subtle and complex deformation (e.g., mm- to cm-scale interseismic displacement or time-varying subsidence), these ad-hoc qualitative comparisons are neither satisfying nor tractable.

CONCLUSIONS

InSAR time series approaches have several advantages when compared with the ad-hoc consideration of individual interferograms. Shorter period interferograms in the time series analysis results in useful cumulative deformation measurements at pixels that otherwise decorrelate in a single or few longer period interferograms spanning the total period of the time series. We are working on various interferogram weighting schemes to take into consideration phase noise associated with decorrelation and height error propagation for each interferogram to better address the contribution of noisy interferograms in the solution process. The use of the coherent scatterer InSAR processing provides a means to isolate differential interferometric phase signatures (deformation, atmospheric artifacts,

topographic phase residuals due to digital elevation model height errors) on a subset of pixels in an otherwise noisy set of interferograms. This allows for the detection of millimeter-level deformation signals over time.

ACKNOWLEDGEMENTS

ERS original SAR data provided by the European Space Agency copyright 1993-2000. Additional data purchases made by the WInSAR consortium with funding from NASA, USGS, and NSF.

REFERENCES

Bawden, G., W. Thatcher, R. Stein, K. Hudnut, G. Peltzer, Tectonic contraction across Los Angeles after removal of groundwater pumping effects, Nature, 412, Aug. 23, 2001.

Berardino, P., G. Fornaro, A. Fusco, D. Galluzzo, R. Lanari, E. Sansosti, S. Usai, A new approach for analyzing the temporal evolution of Earth surface deformations based on the combination of DIFSAR interferograms, Int. Geosci. Rem. Sens. Symp., Sydney, Australia, July 9-13, 2001.

Buckley, S., Radar Interferometry Measurement of Land Subsidence, Ph.D. dissertation, The University of Texas at Austin, 2000.

Bürgmann, R., E. Fielding, J. Sukhatme, J., Slip along the Hayward fault, California, estimated from space-based synthetic aperture radar interferometry, Geology, 26(6), 559-562, 1998.

Ferretti, A., C. Prati, F. Rocca, Permanent Scatterers in SAR Interferometry, IEEE Trans. Geosci. Rem. Sens., 39(1), 2001.

Ferretti, A., C. Prati, F. Rocca, Nonlinear Subsidence Rate Estimation Using Permanent Scatterers in Differential SAR Interferometry, IEEE Trans. Geosci. Rem. Sens., 38(5), 2000.

Fialko Y., M. Simons, D. Agnew, The complete (3-D) surface displacement field in the epicentral area of the 1999, Mw 7.1, Hector Mine earthquake from space geodetic observations, Geophys. Res. Lett., 28(16), 3063–3066, 2001.

Fielding, E., R. Blom, R. Goldstein, Rapid Subsidence over Oil Fields Measured by SAR Interferometry, Geophys. Res. Lett., 25(17), 3215-3218, 1998.

Galloway, D., K. Hudnut, S. Ingebritsen, S. Philips, G. Peltzer, F. Rogez, P. Rosen, Detection of aquifer system compaction and land subsidence using interferometric synthetic aperture radar, Antelope Valley, Mojave Desert, CA, Water Resour. Res., 34(10), 2573–2586, 1998.

Goldstein, R., C. Werner, Radar Interferogram Filtering for Geophysical Applications, Geophys. Res. Lett., 25(21), 4035, 1998.

Gudipati, K., S. M. Buckley and C. R. Wilson, Temporal Variations in Phoenix, Arizona Subsidence from Radar Interferometry, submitted to Geophys. Res. Lett., 2004.

Hoffmann, J., H. Zebker, D. Galloway, F. Amelung, Seasonal subsidence and rebound in Las Vegas Valley, Nevada, observed by synthetic aperture radar interferometry, Water Resour. Res., 37(6), 1551-1566, 2001.

Lundgren, P., S. Usai, E. Sansosti, R. Lanari, M. Tesauro, G. Fornaro, P. Berardino, Modeling Surface Deformation observed with SAR Interferometry at Campi Flegrei Caldera, J. Geophys. Res., 106(B9), 19355-19367, 2001.

Massonnet, D., M. Rossi, C. Carmona, F. Adragna, G. Peltzer, K. Feigl, T. Rabaute, The Displacement Field of the Landers Earthquake Mapped by Radar Interferometry, Nature, 364, 138-142, July 8, 1993.

Myers, S.C., M. Flanagan, M. Pasyanos, W. Walter, P. Vincent, and C. Schultz, Location calibration in Western Eurasia and North Africa: ground truth, improved earth models, Bayesian kriging, regional analysis,

location algorithms, array calibration, and validation, Proceedings of the 23rd Seismic Research Review, 2002.

Peltzer, G., F. Crampé, P. Rosen, The Mw 7.1, Hector Mine, California earthquake: surface rupture, surface displacement field, and fault slip solution from ERS SAR data, Earth and Plaentary Sciences, 333, 545-555, 2001a.

Peltzer, G., F. Crampé, S. Hensley, P. Rosen, Transient strain accumulation and fault interaction in the Eastern California shear zone, Geology, 29(11), 975–978, 2001b.

Peltzer, G., F. Crampé, G. King, Evidence of Nonlinear Elasticity of the Crust from the Mw7.6 Manyi (Tibet) Earthquake, Science, 286, 272-276, Oct. 8, 1999.

Sandwell, D., L. Sichoix, D. Agnew, Y. Bock, J.-B. Minster, Near real-time radar interferometry of the Mw 7.1 Hector Mine Earthquake, Geophys. Res. Lett., 27(19), 3101-3105, 2000.

Sandwell, D. and L. Sichoix, Topographic phase recovery from stacked ERS interferometry and a low-resolution digital elevation model, J. Geophys. Res., 105(B12), 28211-28222, 2000.

Sandwell, D. and E. Price, Phase gradient approach to stacking interferograms, J. Geophys. Res., 103(B12), 30183-30204, 1998.

Schmidt, D. A. and R. Bürgmann, Time-dependent land uplift and subsidence in the Santa Clara valley, California, from a large interferometric synthetic aperture radar data set*, J. Geophys. Res., 108(B9)*, 2416, doi:10:1029/2002JB002267, 2003

Swenson, J.L., W. Foxall, W.R. Walter and P. Vincent (2000). Source characterization of the February 3, 1995 and January 30, 2000 mine collapses in the trona mining district of southwestern Wyoming from InSAR and seismic waveform modeling, EOS, Transactions 81, S8.

Usai, S., A New Approach for Long Term Monitoring of Deformations by Differential SAR Interferometry, Ph.D. Dissertation, Delft University of Technology, The Netherlands, 2001.

Vincent, P., Final Report (00-ERD-056) MEDIOS: Modeling Earth Deformation Using Interferometric Observations from Space, LLNL, UCRL-ID-146985, 2002.

Vincent, P., J. Sweeney, Utility of InSAR for Test Site Monitoring, LLNL, UCRL-ID-150194 (OUO), 2003.

Vincent, P., S. Larsen, D. Gallaway, R.J. Laczniak, W. R. Walter, B. Foxall, J. Zucca, New signatures of underground nuclear tests revealed by satellite radar interferometry, LLNL, UCRL-JC-145562, 2001.

Vincent, P., Using satellite radar interferometry to detect and characterize HDBTs, NPAC TWG R and D Conference on Detecting, Characterizing and Defeating Underground Facilities, April 3-4, 2001 (INVITED).

Vincent, P., B. Foxall, W. R. Walter, Analysis, comparison and modeling of radar interferometry data of surface deformation signals associated with underground explosions, mine collapses and earthquakes, PHASE 1: Underground explosions, Nevada Test Site, 21st Seismic Research Symposium on Monitoring a Comprehensive Test Ban Treaty, Las Vegas, NV, September 21-23, 1999.

Walter, W. R., J. Swenson, W. Foxall, P. Vincent, A. J. Rogers, J. Bhattacharyya, Complete regional waveform modeling for source and structure: A source example using the January 30, 2000 mine collapse in Wyoming, 12th Annual IRIS Workshop, Rockport, Maine, May 7-10, 2000.

Walter, W. R., P. Vincent, S. C. Meyers, Joint Seismic Waveform and InSAR Modeling of Moderate Earthquakes in Iran, EOS Transactions, AGU Fall, 2002.

Zebker, H., P. Rosen, R. Goldstein, A. Gabriel, C. Werner, On the Derivation of Coseismic Displacement Fields Using Differential Radar Interferometry: The Landers Earthquake, J. Geophys. Res., 99(B10), 19617-19634, 1994.

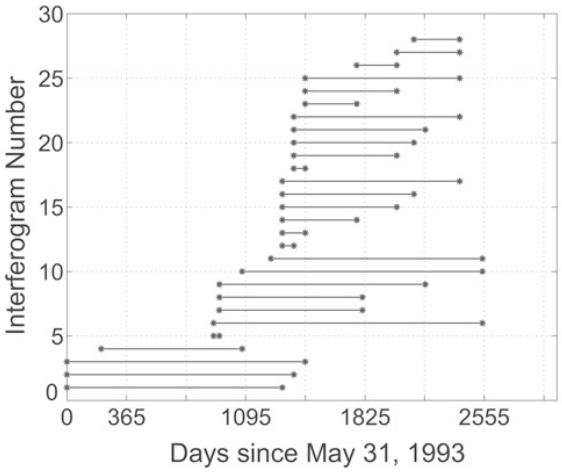


Figure 1. Distribution of Phoenix interferograms used in linear inversion [from Gudipati, Buckley and Wilson, 2004].

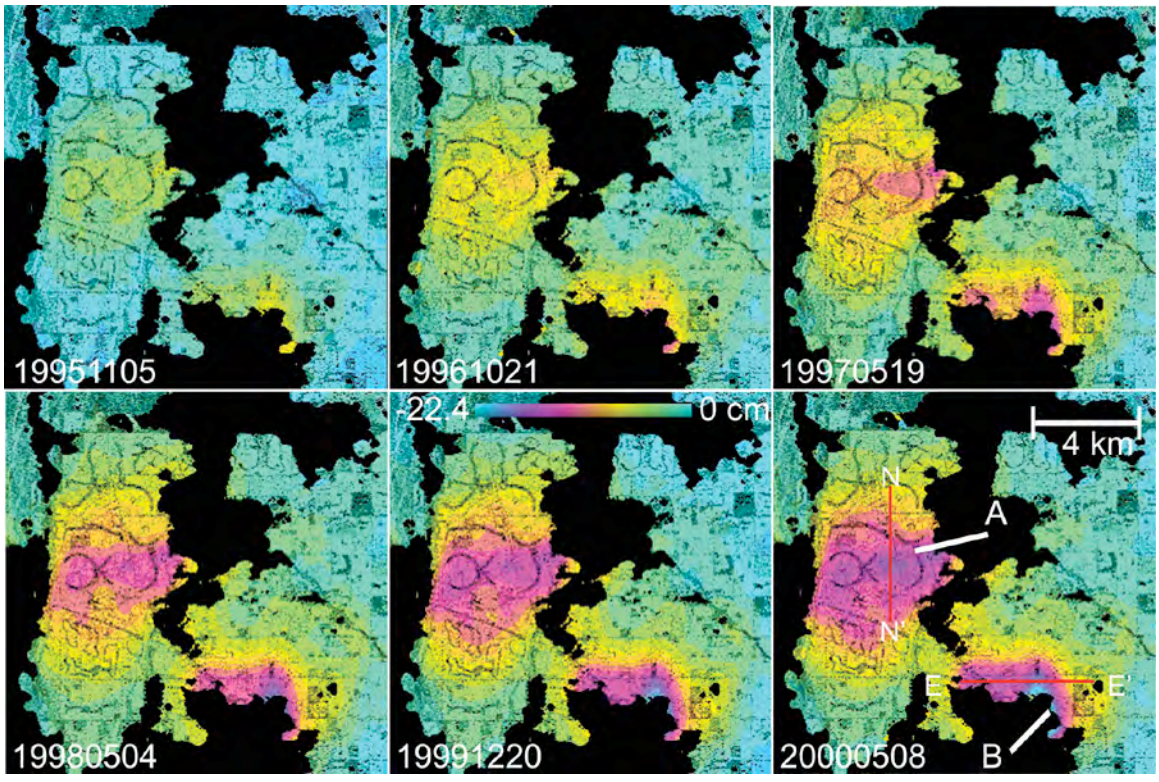


Figure 2. Cumulative subsidence since May 21, 1993 in Glendale near Phoenix. Black corresponds to areas of decorrelation. [from Gudipati, Buckley and Wilson, 2004].

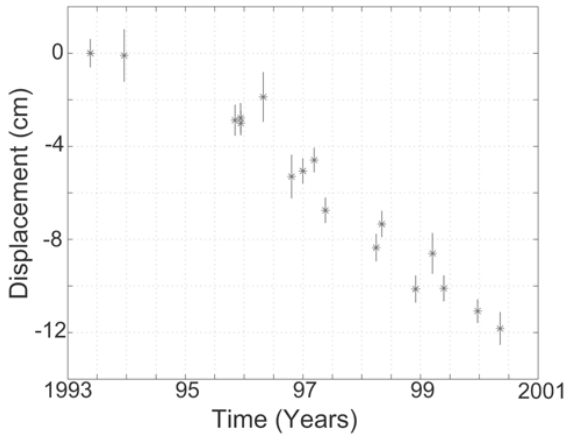


Figure 3. Mean subsidence near the maximum observed subsidence of feature B. Mean computed along profile EE' in Figure 2. Error bars correspond to one standard deviation phase error mapped from correlation and digital elevation model height error [from Gudipati, Buckley and Wilson, 2004].

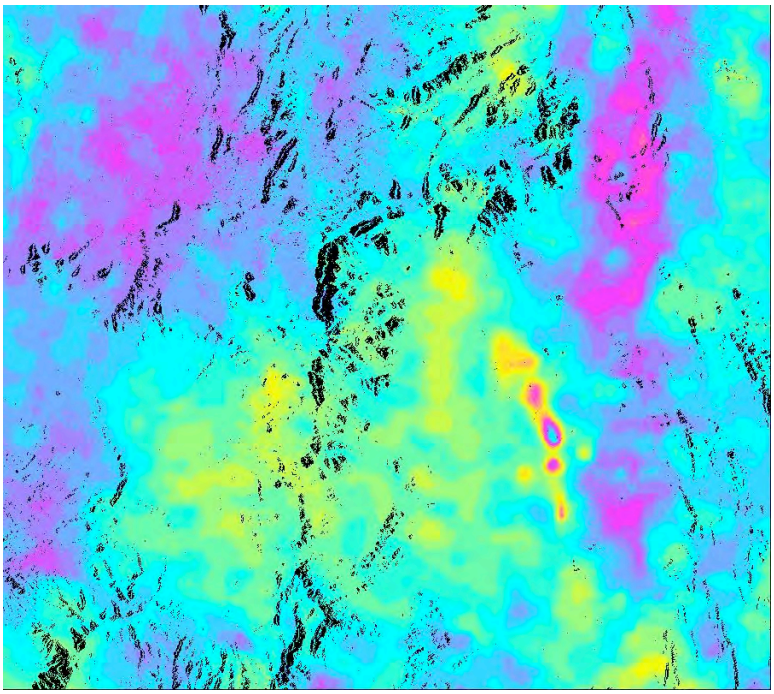


Figure 4. Preliminary time series result showing cumulative displacement over the Nevada Test Site from June 11, 1995 to June 16, 1997. One cycle through color wheel represents 5 cm of radar line-of-sight displacement.



Figure 5. Initial coherent scatterers identified in Scottsdale near Phoenix.

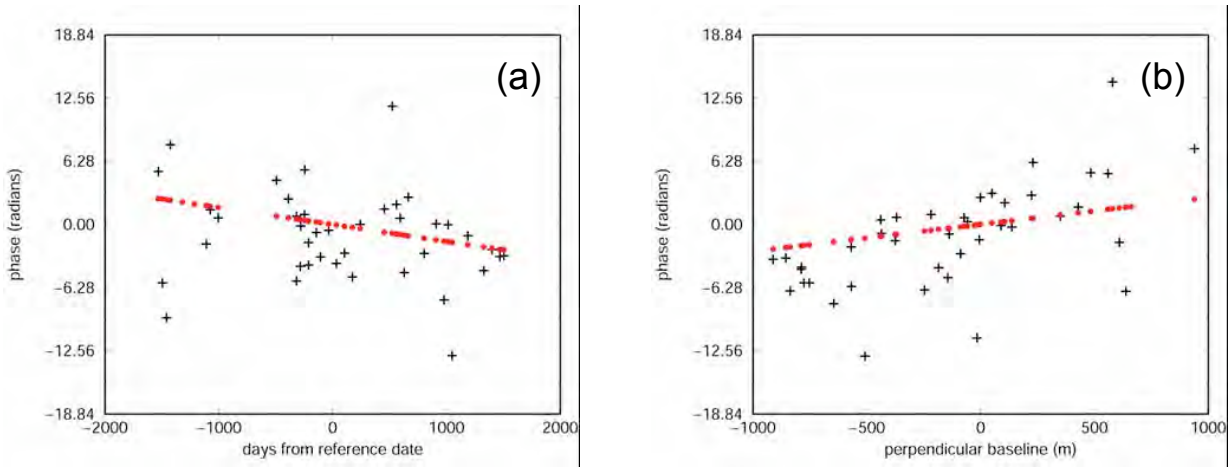


Figure 6. Sparse unwrapping result for a single coherent scatterer observed in a preliminary set of Scottsdale interferograms. Coherent scatterer velocity and height error estimated as 3 mm/yr and 3 meters, respectively. (a) Coherent target interferogram phases after removal of height error phase contribution. Red is estimated velocity phase contribution. (b) Coherent scatterer interferogram phases after removal of estimated velocity phase contribution. Red is estimated height error phase contribution. Large phase dispersion likely due to residual phase ramps in preliminary interferograms. Refinement of interferograms will lead to improved estimates and smaller phase dispersion.

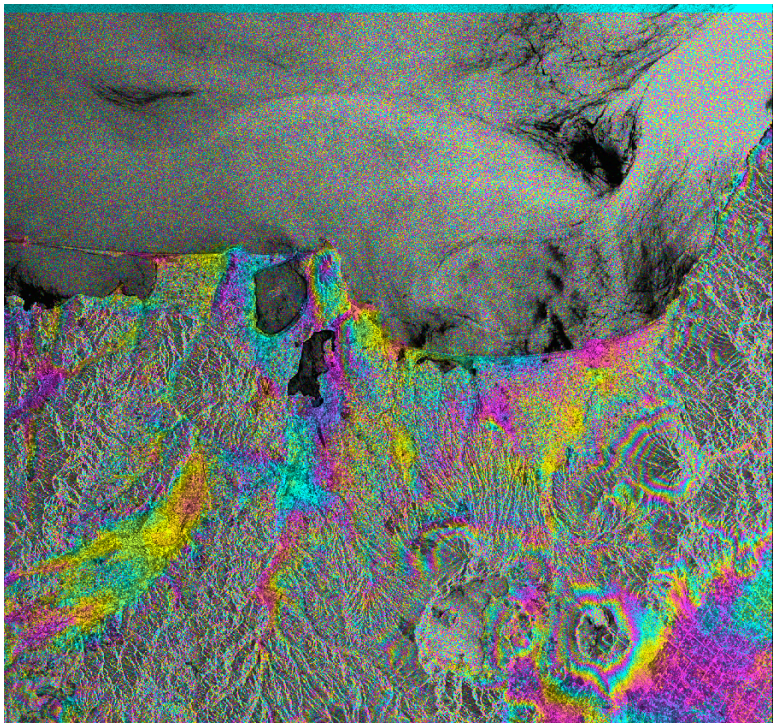


Figure 7. Hokkaido, Japan Envisat flattened interferogram spanning August 24 to September 28, 2003.

IMPROVED GROUND TRUTH IN SOUTHERN ASIA USING IN-COUNTRY DATA, ANALYST WAVEFORM REVIEW AND ADVANCED ALGORITHMS

Eric R. Engdahl[1], Eric A. Bergman[1], Stephen C. Myers[2], and Floriana Ryall[2]

University of Colorado[1], Lawrence Livermore National Laboratory[2]

Sponsored by National Nuclear Security Administration
Office of Nonproliferation Research and Engineering
Office of Defense Nuclear Nonproliferation

Contract No. DE-FC52-03NA99516[1], W-7405-ENG-48[2]

ABSTRACT

Nearly 2,000 earthquakes occurring in the Iran region during the period 1909-2002 have been relocated with special attention to focal depth, using the EHB methodology (Engdahl, *et al*., 1998). We make a careful review of starting depths, association of teleseismic depth phases, and the effects of reading errors on these phases. When available, waveforms are examined. Uncertainties in EHB locations are, owing to Earth's lateral heterogeneity, on the order of 10-15 km in the Iran region. Uncertainties of reviewed EHB focal depth estimates are on the order of 10 km, as compared to about 4 km for waveform inversions. Nevertheless, these EHB depth estimates are sufficiently accurate to resolve robust differences in focal depth distribution throughout the Iran region. Most earthquakes in the Iranian continental lithosphere occur in the upper crust. In the Zagros Mountains most earthquakes are restricted to the upper crust (depths < 20 km). However, there is some evidence for infrequent earthquakes as deep as 30 km. In southeastern Iran, where the Arabian seafloor is being subducted beneath the Makran Coast, earthquakes occur in the upper crust as well as at intermediate depths within a northward dipping subducting slab. Near the transitional Oman Line, seismicity extends to depths of up to 45 km in the crust. In central Iran, along the Alborz Mountain belt, seismic activity occurs primarily in the upper crust but with some infrequent events in the lower crust.

Starting from this new catalog of Iranian seismicity, we further improve the relative accuracy of locations for recent large earthquakes through analyzing clusters of earthquakes simultaneously. Absolute locations of such clusters are still biased by departures of the Earth's structure from the one-dimensional (1-D) model (ak135) used in the location algorithm. This problem can be solved through the use of reference (or ground truth) event information, which provides independent evidence for the absolute location of the seismic source. If one or more reference events can be located jointly with a cluster of earthquakes, then the entire cluster's absolute location can be calibrated. There are three main sources of reference event information with which to calibrate the absolute locations of earthquake clusters. The first method is to compare the pattern of relocated earthquakes with mapped fault geometry. The second method is to find situations in which a cluster event has been accurately located by a local seismic network or aftershock deployment. The third method is to use InSAR data to determine the rupture zone of shallow earthquakes. For moderate-sized events, this zone is small enough to provide useful constraints on absolute location. Examples of all three kinds of reference information in Iran are shown in this paper. When both location and origin time can be calibrated for a cluster through use of reference event information, we are able to estimate the true travel times to all reporting stations. These estimates are the basis for improved models of the crust and upper mantle, which in the future will permit far more accurate routine earthquake locations using regional seismic data in Iran.

OBJECTIVES

This research seeks to improve the database of ground truth (GT) information and velocity models useful for calibration in southern Asia with the following objectives: (1) Aggressive pursuit of in-country data acquisition, especially the collection of ground truth at GT5 level or better for events of magnitude 2.5 and larger recorded by dense local networks, including associated velocity models; (2) Expanded analyst review of relevant regional waveforms for ground truth events by the comprehensive re-picking of phase arrival times from all available waveforms, with special attention to the regional phases Pg, P*, Pn, Sg, S* and Sn; and (3) Application of advanced algorithms, such as those used for multiple event relocation, to refine and validate all available ground truth data, to achieve the optimal selection of data for analysis, to better understand the uncertainties of the results, and to handle the error budget as realistically as possible.

RESEARCH ACCOMPLISHED

Nearly 2,000 earthquakes occurring in the Iran region during the period 1909-2002 that are well-constrained (secondary teleseismic azimuth gap < 180 deg) by phase arrival times reported to the International Seismic Summary (ISS), the International Seismological Centre (ISC) and the United States Geological Survey (USGS) have been relocated with special attention to focal depth using the EHB methodology (Engdahl, et al., 1998). The new locations are shown in Figure 1, along with seismotectonic features.

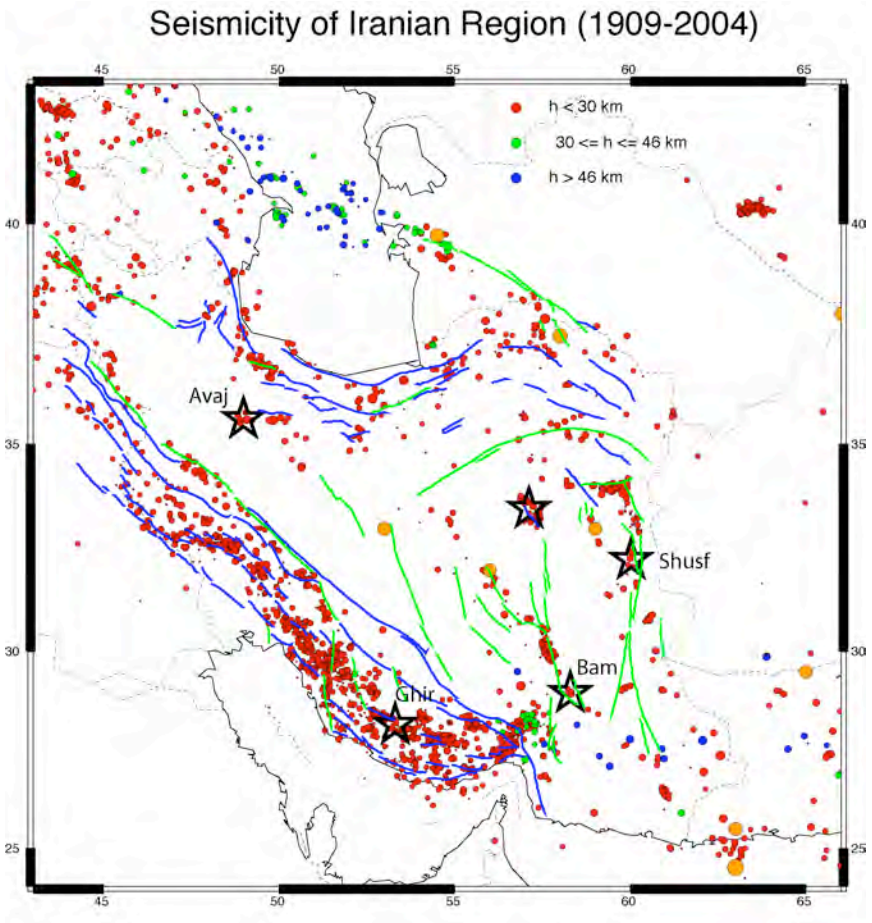


Figure 1. Seismicity in the Iran region relocated and color classified by depth. Filled yellow circles are historical earthquakes that need to be relocated. Faults are thrust (blue) and strike-slip (green). Stars are cluster locations analyzed and reported on later in this paper.

The EHB method uses the phase arrival times of P, S, PKP and depth phases (pP, sP and pwP) with a modern 1-D Earth model (ak135) to obtain improved estimates of locations and focal depths. The purpose of this study is to

expand the work of Maggi et al. (2000) who re-assessed focal depth distributions in southern Iran using synthetic seismograms to analyze P and SH body waveforms. In this study, we rely on a careful review of EHB starting depths, the EHB assignment of teleseismic depth phases, and the effects of reading errors on these phases. Uncertainties in EHB locations are, owing to Earth's lateral heterogeneity, on the order of 10-15 km in the Iran region. Uncertainties of reviewed EHB focal depth estimates are on the order of 10 km, as compared to about 4 km for waveform inversions. These EHB depth estimates are sufficiently accurate to resolve robust differences in focal depth distribution within the crust and upper mantle throughout the Iran region. For the modern period (1964-2002) the data base is complete to at least M 5.5, but includes many events of smaller magnitude that are well constrained. Preliminary results indicate that most earthquakes in the Iranian continental lithosphere occur in the upper crust. In the Zagros Mountains of southern Iran, a linear intra-continental fold and thrust belt trending NW-SE between the Arabian shield and central Iran, most earthquakes are restricted to the upper crust (depths < 20 km). However, there is some evidence from this study and that of Tatar et al. (2003) for infrequent earthquakes as deep as 30 km. In southeastern Iran, where the Arabian seafloor is being subducted beneath the Makran coast, earthquakes occur in the upper crust as well as at intermediate depths within a northward dipping subducting slab. Where there is a change from continent to ocean near 57 deg in the Zagros-Makran transition zone, a region of complicated structure known as the Oman Line, seismicity extends to depths of up to 45 km in the crust. In central Iran, along the Alborz mountain belt, seismic activity occurs primarily in the upper crust but with some infrequent events in the lower crust. These differences in the focal depth distribution of Iranian earthquakes may have important implications about variations in the strength of the crust and uppermost mantle across the region.

Reported arrival times for depth phases from larger and even some smaller events, which may have a complex rupture, are often subject to misinterpretation. Shown in Figure 2 are waveforms from an Mw 5.2 Zagros event that was originally thought to be deeper than 40 km on the basis of a phase arrival (T2) widely reported as pP. By examination of the waveforms at a broadband station in Africa, we were able to determine that the coda of the T2 signal is a very good fit to the coda of the T1 signal (right panel), indicating that this earthquake is a double event. By virtue of this forensic seismology and waveform modeling we find the depth of this event to be on the order of 4 km, suggesting that the arrival T3 in the left panel is sP.

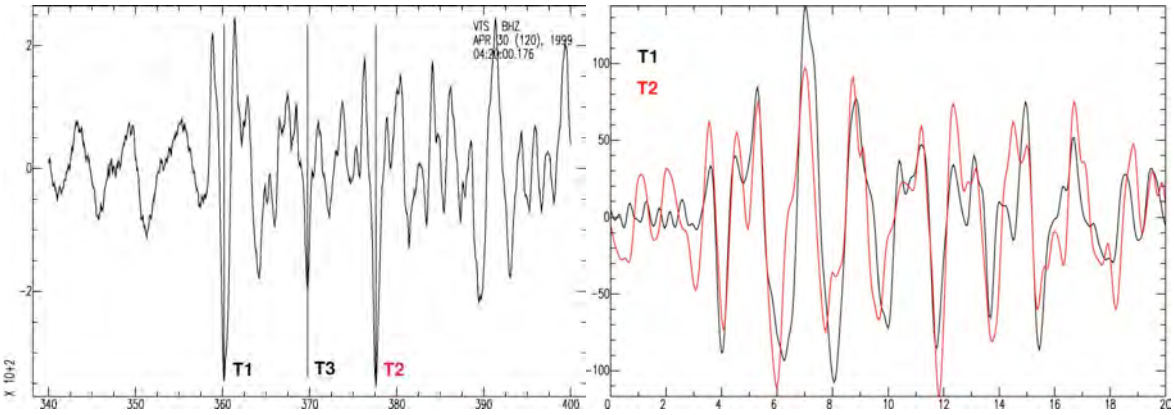


Figure 2. Left panel shows original seismogram with phase arrivals T1, T2 and T3. Right panel shows coda of T2 signal (red) overlying coda of T1 signal (black).

Waveform depths accurate to ~ 4 km for Iranian earthquakes, as determined by the Cambridge research group, were a valuable resource for this project. Waveform depths were used as EHB starting depths for over 100 events in the Iran region. For events, which had more than five phases that could be identified as pP or sP, we compare the differences in depth estimation as functions of depth and magnitude in Figure 3. The EHB depths for most events were within 10 km of the corresponding waveform depths, with a maximum difference no larger than 15 km (left panel). There does not appear to be a significant magnitude to depth dependence (right panel). EHB depths are slightly deeper than waveform depth estimates because different reference models were used (ak135 vs. Cambridge generalized source velocity model).

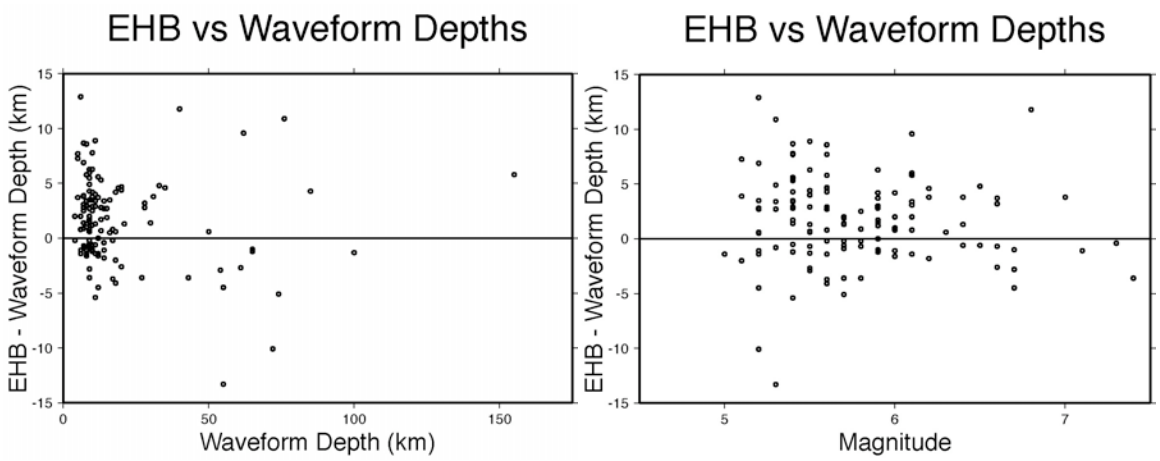


Figure 3. EHB versus waveform depth differences plotted as function of waveform depth (left panel) and magnitude (right panel).

The band of earthquakes crossing the central Caspian shown in Figure 4a is unusually deep focus, with depths ranging from about 30 to 100 km. Jackson et al. (2002) suggest that these events are related to the NE subduction of the south Caspian lithosphere or possibly to the detachment of a sinking slab.

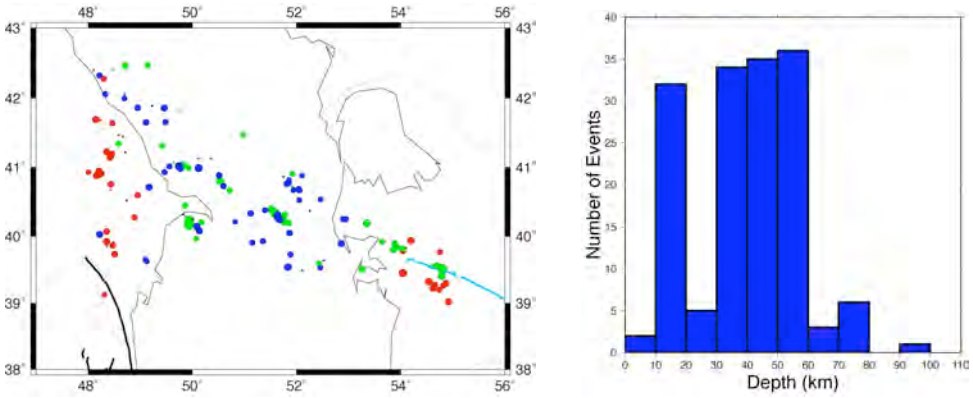


Figure 4a. Seismicity (left panel) and depth distribution (right panel) plotted for the central Caspian region. Color classification by depth as in Figure 1.

Most earthquakes along the southern Caspian Basin active border region (Figure 4b) are less than 20 km in depth. However, there are a few slightly deeper events (e.g., the filled green circle is nearly 35 km in depth).

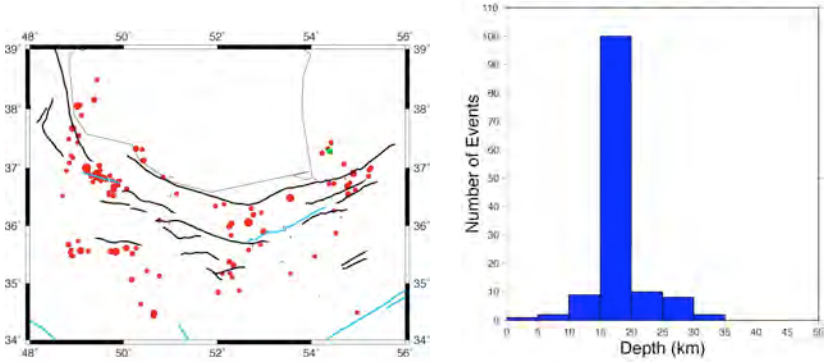


Figure 4b. Same plots as Figure 4a for the southern Caspian Basin active border region.

Nearly all earthquakes in the Zagros (Figure 4c) are less than 30 km in depth, largely confined to an upper crust with a lower boundary at about 19 km (Hatzfeld, et al., 2003). A few are deeper, but with the 10 km depth uncertainty.

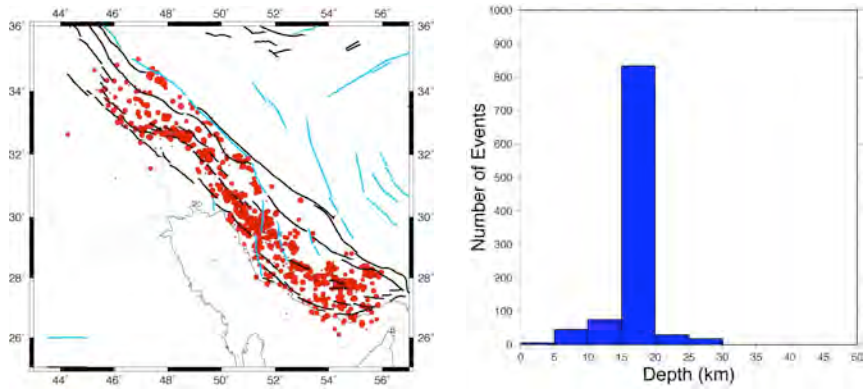


Figure 4c. Same plots as Figure 4a for the Zagros mountains region.

Near the transitional Oman line (Figure 4d) the Zagros seismicity extends to greater depths. Earthquake focal depths of more than 30 km are common, with a few quite deep that are probably related to subduction in the Makran.

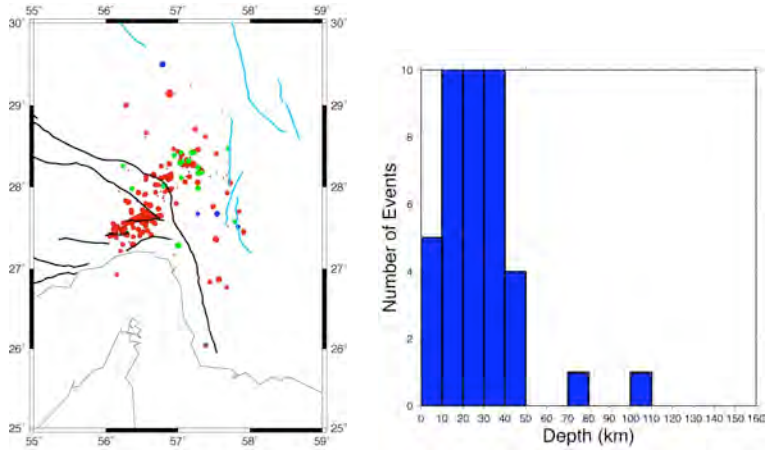


Figure 4d. Same plots as Figure 4a near the Oman Line.

The Makran region (Figure 4e) has earthquakes with depths well in excess of 40 km. These events occur within a northward shallow dipping slab, but are also accompanied by earthquakes at shallower depths in the upper crust.

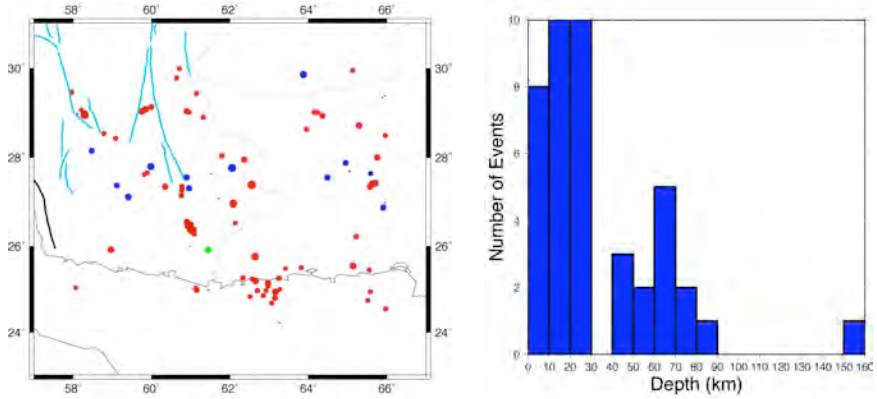


Figure 4e. Same plots as Figure 4a for the Makran region.

Multiple Event Relocations and Ground Truth Studies

We relocated several clusters of earthquakes in Iran with a recently developed technique that yields improved accuracy for both the relative and absolute locations of clustered earthquakes. The gist of the method is to use a multiple event relocation method with regional and teleseismic phase arrival times to constrain relative locations of clustered earthquakes and then to calibrate the absolute location of the cluster by obtaining independent information on the absolute location of one or more members of the cluster. For the multiple event relocation (cluster analysis) we use a version of the Hypocentroidal Decomposition (HDC) method first proposed by Jordan and Sverdrup (1981), which has been developed specifically for this kind of "ground truth" research. Further explanation of the methodology may be found in Bondar et al. (2004). For each cluster there is independent information on location that helps to calibrate the absolute locations. The clusters shown here illustrate several approaches to this important problem.

The clusters of earthquakes used in these analyses were extracted from the new catalog of Iranian seismicity presented earlier in this paper. For multiple event relocation, it is necessary to keep the dimensions of the cluster small enough (typically 50-75 km across) to avoid the effects of lateral heterogeneity in the crust and upper mantle.

The HDC analysis includes further refinement of the data set by making empirical estimates of readings errors and using these estimates to help identify outliers. These steps yield significant improvements in accuracy and resolution for the relocations. Of course, the main benefit of HDC analysis is to largely remove the biasing effects (path anomalies) of lateral heterogeneity in the Earth, which permits much better resolution of the relative locations of cluster earthquakes.

Changureh (Avaj): Calibration Using Aftershock Survey Data and Comparison with Geological Mapping and Remote Sensing Data

The cluster consists of the June 22, 2002 Mw 6.4 Changureh mainshock, aftershocks, and several earlier events, 17 events in total. The result of our HDC analysis of the Changureh earthquakes is shown in Figure 5. The relative locations of events are plotted with respect to the hypocentroid or geometrical center of the cluster vectors that describe the relative locations.

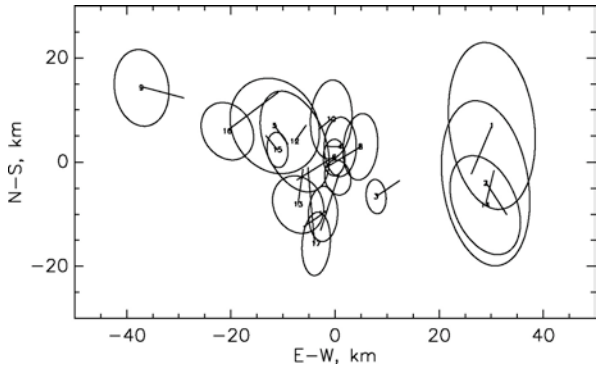


Figure 5. Relative locations of the Avaj cluster. Confidence ellipses (90%) are shown. Line to each event shows change in relative location from starting (EHB single event) location.

The Changureh mainshock (#3) is isolated from the other earthquakes. Most of the aftershocks occurred to the northwest of the mainshock. These results support a fault model in which rupture initiated in the southeast end of the rupture zone and propagated unilaterally to the northwest for 20-25 km. This would be consistent with the source time function duration of about five seconds, derived from body wave modeling by the Cambridge group.

We obtained arrival time data for one of the cluster events (#12) from an aftershock study by a group of IIEES (International Institute of Earthquake Engineering and Seismology) scientists, and also a crustal model derived from the aftershock study of Changureh (Farahbod, personal comm.). We relocated the event using the HYPOSAT code of Schweitzer (2001) and used this location to calibrate the absolute location of the HDC cluster. The mislocation

vector was among the largest we have observed, 17.3 km at an azimuth of 78°, with an origin time shift of -2.55 seconds.

After correction of the cluster event locations, we can compare them with the seismotectonic analysis of the Cambridge group (Richard Walker and James Jackson, personal comm.), summarized in Figure 6. Numbers 1-14 are the HDC cluster locations from an earlier study (before events 15-17 were added). The dashed line is an inferred "Abdarreh fault" based on mapping of surface rupture. Remote sensing data and analysis of stream offsets support a model in which the seismogenic faulting extends to the southeast, to the location of the mainshock epicenter, but did not break the surface. Most of the aftershocks would have occurred in the hanging wall of the essentially "blind" thrust event.

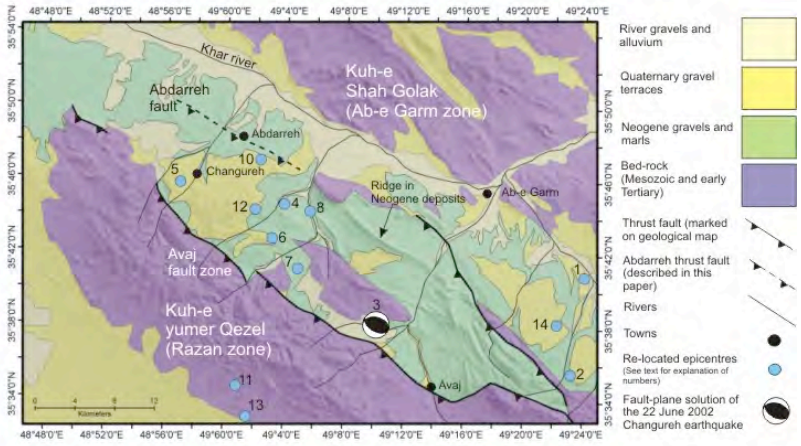


Figure 6. Seismotectonic map of the Avaj earthquake sequence

Finally, we use the calibrated cluster arrival time data to infer empirical path anomalies from the Changureh source region to seismic stations. Figure 7 shows the results for Pn and P phases at regional distances. The path anomalies are relative to the ak135 global model. There is broad consistency of longer travel times at most azimuths. The early arrivals at stations in Saudi Arabia reflect propagation across the Arabian shield. The path anomalies can be the result both of variations in bulk velocity and differences in ray paths caused by lateral heterogeneity.

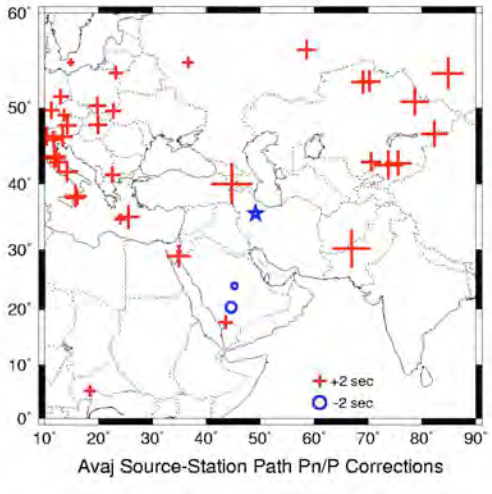


Figure 7. Empirical path anomalies for Pn and P phases from Avaj

This example illustrates the usefulness of combining carefully conducted aftershock surveys and analysis of regional and teleseismic data with geological mapping and remote sensing data.

Ghir: Calibration Using Two Types of Ground Truth Data

The Ghir cluster contains 65 events in a region of active and complex earthquake activity. Figure 8 (left panel) shows the relative locations of the Ghir cluster events.

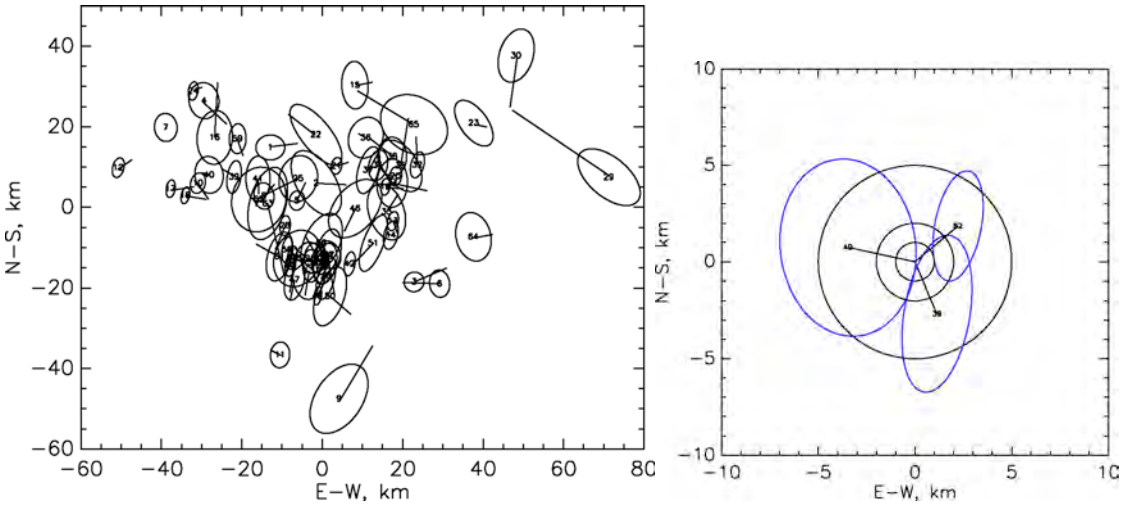


Figure 8. (left) Relative locations of the Ghir cluster. See Figure 5. (right) Consistency of estimates of mislocation vector for three reference events, after the average vector is subtracted. Confidence ellipses (90%) are shown. Concentric circles of radius 1, 2, and 5 km are shown.

For this cluster we had three reference events from two different kinds of data: two events for which good quality aftershock network data were available, and an epicentral location based on InSAR analysis. InSAR provides no constraint on origin time but a surprisingly tight constraint on depth. A moderate-sized earthquake cannot create a detectable InSAR signal unless it is quite shallow.

When we have more than one reference event for a cluster, there are separate estimates of the mislocation vector for each case. We average them to obtain a best estimate of the shift needed to calibrate the cluster location (6.2 km at 66°, -2.80 seconds in origin time), and also as an internal consistency check, both on the HDC analysis and the reference event data. In this case there is good agreement between all three reference events. Figure 8 (right panel) shows the residual mislocation vectors after the average has been removed. These results show that our calibration of this cluster is accurate at 1-2 km at a 90% confidence level. Events 39 and 40 have aftershock network locations and event 62 is the InSAR event. The origin time shift is estimated only from events 39 and 40.

Bam: Preliminary Results

The Mw 6.5 Bam earthquake on December 26, 2003 is of great interest because of the terrible loss of life and the damage that it caused. It is not a strong candidate for multiple event relocation, however, because no other earthquakes of any significance have occurred near Bam in the instrumental seismology period. Nevertheless we formed a small cluster from the mainshock and 7 of the larger aftershocks. The data available immediately from the USGS National Earthquake Information Center (NEIC) are not complete and we expect to be able to constrain relative locations more precisely in the future when more data is available. This preliminary HDC analysis provides useful improvement in resolution over the single event locations. In Figure 9 (left panel), the mainshock is event #1. The location for event #5 is rather suspect. Data coverage to the south is poor for this small event and it has the appearance of a "flyer" caused by some late readings at European stations. It is worth noting that the relative location of events 1 and 2 (and, to a lesser extent, #6) strongly suggest faulting on more than one fault strand in that area.

A shift of 5-10 km to the northeast would bring the HDC cluster into close agreement with the aftershock study. We are hopeful that it will be possible to obtain a local network solution for one or more events that we can locate with HDC, so that a full calibration of this important earthquake series can be done.

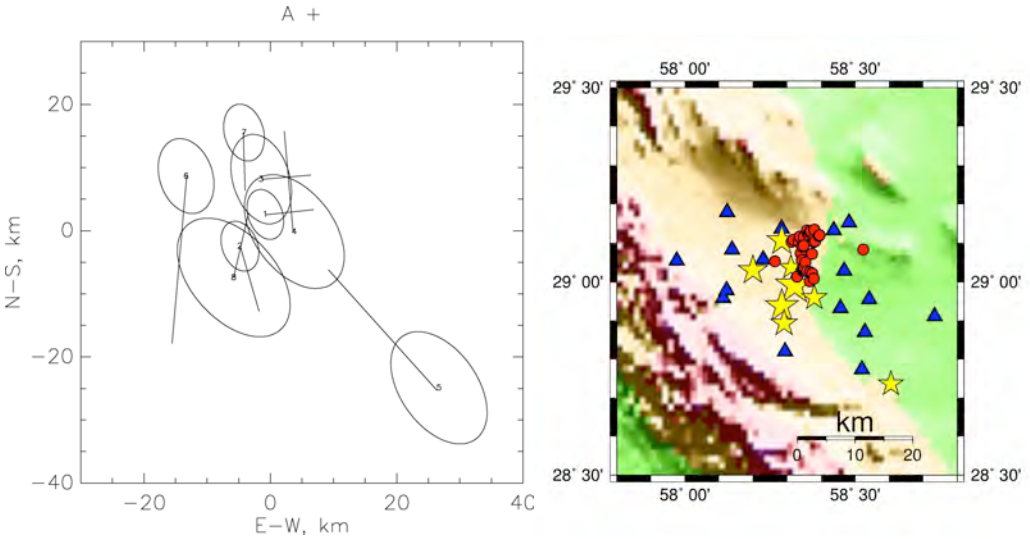


Figure 9. (Left) Relative locations of the Bam cluster. See Figure 5. (Right) Locations of aftershocks (red circles) from a temporary deployment (blue triangles). Yellow stars are the locations of the main shock and larger aftershocks from HDC analysis.

South Zirkuh (Shusf): Ambiguity in the use of InSAR Locations for Ground Truth

We formed this cluster (Figure 10) to take advantage of InSAR data that reveal deformation related to a moderate sized earthquake in the late 1990s. The situation is complicated by the fact that there are two candidate earthquakes during the InSAR time window, the Mw 5.6 "Chakhu" event on 6/20/1997 (Event 8), and the Mw 5.8 "Sahlabad" event on 4/10/1998 (Event 13). InSAR data reveal one very strong signal and a much weaker signal about 20 km north. Our calibration of this cluster is based on associating the Chakhu event with the stronger InSAR signal and the Sahlabad event with the diffuse signal to the north. We use only the Chakhu location for calibration because it is much better defined. In this case we find a mislocation vector of 5.8 km at an azimuth of 13°. Of course, no calibration of origin time is possible with InSAR data alone. Eric Fielding, Cambridge University provided us access to the preliminary results of his InSAR study of these events.

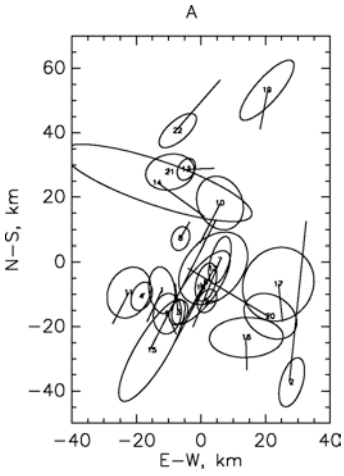


Figure 10. Relative locations of the Shusf cluster. See Figure 5.

In an initial phase of this study we associated the strongest InSAR signal with the Sahlabad event, which led to a mislocation vector of length 25 km, much larger than we have ever seen and barely credible. This emphasizes the need for caution in associating InSAR data with a particular event. When dealing with moderate-sized earthquakes, the "before-after" time window for InSAR often encompasses more than one event that could be the source.

CONCLUSIONS AND RECOMMENDATIONS

Our results for deeper earthquakes that occur beneath the central Caspian along the Apsheron- Balkhan sill support the view of Jackson et al. (2002), i.e., these events most likely "indicate the onset of subduction of the South Caspian Basin beneath the central Caspian, a process that appears to occur aseismically at shallow levels". In the earthquake belts of northern Iran (Talesh-Alborz-Kopeh Dag) surrounding the South Caspian Basin most events are less than 20 km in depth, but there is some evidence for a small number of events occurring at a greater depth (up to 35 km). In the Zagros region earthquake focal depths do not exceed 30 km. Thus, within the uncertainty of EHB depth estimates, there is no evidence (in the form of mantle earthquakes) to support active subduction of continental crust. In southeastern Iran, the continent-continent collision in the Zagros merges along strike with the subduction of the Arabian Sea floor beneath the Makran coast. The change from continent to ocean occurs in a region of complicated structure known as the Oman Line. Tomographic images confirm the existence of subducted slab. Our results support the view of Maggi et al. (2000), i.e., a "continental lithosphere in which a lower crust of relatively low strength, where aseismic ductile deformation predominates, is sandwiched between relatively strong upper crustal and uppermost mantle seismogenic regions".

We have developed several new ground truth events in Iran, based on detailed multiple event relocation and use of reference events, both from local seismic network data and from InSAR data. We have found that the use of analyst reviewed picks is extremely helpful in some circumstances, and the practice should be expanded. We are continuing to develop resources for local network data inside Iran and expect these efforts to lead to new ground truth events and resulting data on empirical path anomalies that will substantially improve location capabilities in this region.

ACKNOWLEDGEMENTS

We are grateful to Denis Hatzfeld (University of Grenoble) for providing preliminary results of the aftershock survey (Figure 9, right panel). Eric Fielding, Richard Walker and James Jackson (Cambridge University), and M. Farahbod (IIEES) for providing data, figures, and advice used in this study.

REFERENCES

Bijwaard, H., W. Spakman, and E. R. Engdahl, (1998), Closing the gap between regional and global travel time tomography: Journal of Geophysical Research, v. 103, p. 30055-30078.

Bondár, I., S.C. Myers, E.R. Engdahl and E.A. Bergman, (2003), Epicentre accuracy based on seismic network criteria, Geophys. J. Int., 156, 1-14, 2004 doi: 10.1046/j.1365-246X.2004.02070.x

Engdahl, E. R., R.D. Van der Hilst and R.P. Buland. (1998), Global teleseismic earthquake relocation with improved travel times and procedures for depth determination, Bull. Seism. Soc. Amer., v. 88, p. 722-743.

Hatzfeld, D., M. Tatar, K. Priestley, and M. Ghafory-Ashtiany, (2003), Seismological constraints on the crustal structure beneath the Zagros Mountain belt (Iran), Geophys. J. Int., v. 155, p. 403-410.

Jackson, J., K. Priestley, M. Allen, and M. Berberian, (2001), Active tectonics of the South Caspian basin. Geophys. J. Int., v. 148, p. 214-245.

Jordan, T.H. and K.A. Sverdrup, (1981), Teleseismic location techniques and their application to earthquake clusters in the south-central Pacific, Bull. Seis. Soc. Amer., 71, 1105-1130.

Maggi, A., J.A. Jackson, K. Priestley, and C. Baker, (2000), A re-assessment of focal depth distributions in southern Iran, the Tien Shan and northern India: do earthquakes really occur in the continental mantle? Geophys. J. Int., v. 143, p. 629-661.

Schweitzer, J. (2001), HYPOSAT - an enhanced routine to locate seismic events, Pure Appl. Geophys. 158, 277-289.

Tatar, M., D. Hatzfeld, and M. Ghafory-Ashtiany, (2003), Tectonics of the Central Zagros (Iran), Geophys. J. Int., in press.

REGIONAL TRAVEL-TIME PREDICTION, UNCERTAINTY, AND LOCATION IMPROVEMENT

Megan P. Flanagan and Stephen C. Myers

Lawrence Livermore National Laboratory

Sponsored by National Nuclear Security Administration
Office of Nonproliferation Research and Engineering
Office of Defense Nuclear Nonproliferation

Contract No. W-7405-ENG-48

ABSTRACT

We investigate our ability to improve regional travel-time prediction and seismic event location using an *a priori* three-dimensional (3D) velocity model of Western Eurasia and North Africa (WENA 1.0). Three principal results are presented. First, the 3D WENA 1.0 velocity model improves travel-time prediction over the IASPI91 model, as measured by variance reduction, for regional phases recorded at 22 stations throughout the modeled region, including aseismic areas. Second, a distance-dependent uncertainty model is developed and tested for the WENA 1.0 model. Third, relocation using WENA 1.0 and the associated uncertainty model provides an end-to-end validation test.

Model validation is based on a comparison of approximately 10,000 *Pg, Pn*, and *P* travel-time predictions and empirical observations from ground truth (GT) events. Ray coverage for the validation dataset provides representative, regional-distances sampling across Eurasia and North Africa. The WENA 1.0 model markedly improves travel-time predictions for most stations with an average variance reduction of 14% for all ray paths. We find that improvement is station dependent, with some stations benefiting greatly from WENA predictions (25% at OBN and 16% at BKR), some stations showing moderate improvement (12% at ARU and 17% at NIL), and some stations benefiting only slightly (7% at AAE and 8% at TOL). We further test WENA 1.0 by relocating five calibration events. Again, relocation of these events is dependent on ray paths that evenly sample WENA 1.0 and therefore provide an unbiased assessment of location performance. These results highlight the importance of accurate GT datasets in assessing regional travel-time models and demonstrate that an *a priori* 3D model can markedly improve our ability to locate small magnitude events in a regional monitoring context.

OBJECTIVE

Our objective is to improve the accuracy of seismic location estimates and to reduce the uncertainty of the estimated locations. As we focus on the geographic region of western Eurasia, the Middle East, and north Africa, we develop, test, and validate 3D model-based travel-time prediction models for about 30 stations in the study region. Improvement in travel-time prediction is quantified, and final calibrations are tested in an end-to-end relocation of five events with known location accuracy between 1 km and 5 km. Improvement in both location and uncertainty estimates are assessed.

RESEARCH ACCOMPLISHED

WENA1.0: 3D *a priori* Geophysical Model

We demonstrate improvement in travel-time prediction of P-waves and regional location performance using the WENA1.0 model (Figure 1) (Pasyanos, et al., 2004). WENA1.0 is a 3D Earth model of the crust and upper mantle that is made up of geophysically distinct regions. Each regional velocity model is determined using previous a geophysical studies and analogy with similar geologic provinces. Because the regional models are developed independently, the WENA1.0 is an *a priori* model that is not based on any one data set. Because the model is developed using geophysical analogy, it is particularly applicable to aseismic regions where calibration data are sparse. The model resolution is 1° by 1°, and the data are primarily compiled from the Exxon Map, Crust 5.1 (Mooney et al., 1998), topography, seismicity, phase blockages, *Pn* tomography, surface-waves, receiver functions, a sediment map from Laske and Masters (1997), crustal regionalizations by Bhattacharyya et al. (2000) and Walter et al. (2000), and the mantle model 3SAC by Nataf and Ricard (1996).

The WENA1.0 model has been extensively evaluated using a number of data sets, including surface wave dispersion measurements, teleseismic receiver functions, gravity, and waveform analysis (Pasyanos et al., 2004). In this study we test the improvement of P-wave travel-time prediction and location performance using a newly developed validation data set.

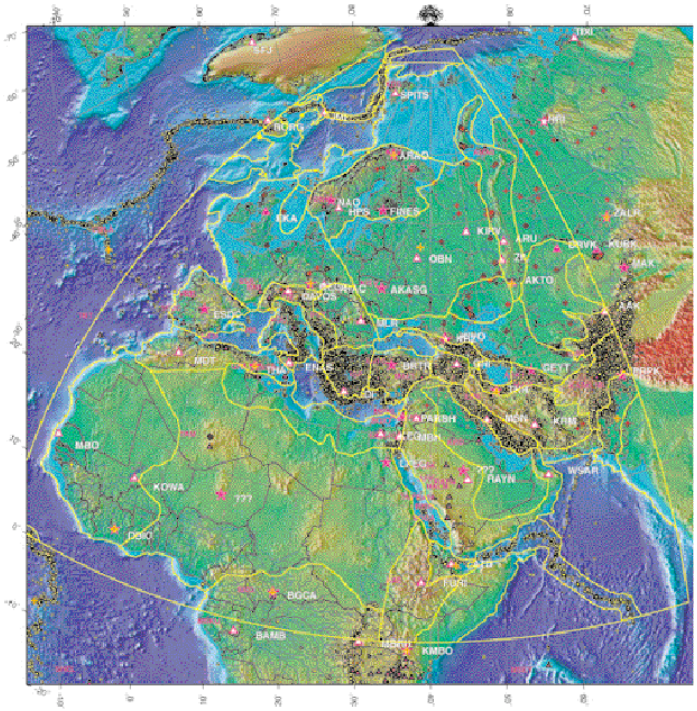


Figure 1. Crustal regionalization used in the WENA1.0 geophysical model. There are about 45 base models, outlined in yellow, which describe *P*- and *S*-wave velocities, attenuation, and density (Pasyanos et al., 2004).

Validation Data Set

We validate improvement in travel-time prediction using well-recorded events with accurate locations. Each validation event meets the network-coverage accuracy criteria of Bondar et al. (2004) or the location accuracy constrained by nonseismic means (e.g., explosions with know sources). Epicenter accuracy ranges from perfect (for known locations) to 25 km for events constrained with a teleseismic network. A procedure similar to the leave-one-out validation described in (Myers and Schulz, 2000) is used to check the consistency of each arrival-time observation. This procedure is a considerable improvement over outlier removal based on statistics of the whole population, because local trends and biases are taken into consideration. Culling based on location accuracy and arrival-time consistency produces a self-consistent data set of accurate travel-time measurements. Ray paths for the validation data set are shown in Figure 2. Raypath coverage is excellent over much of the region, and our new data set provides considerable improvement in ray coverage for aseismic regions, such as North Africa.

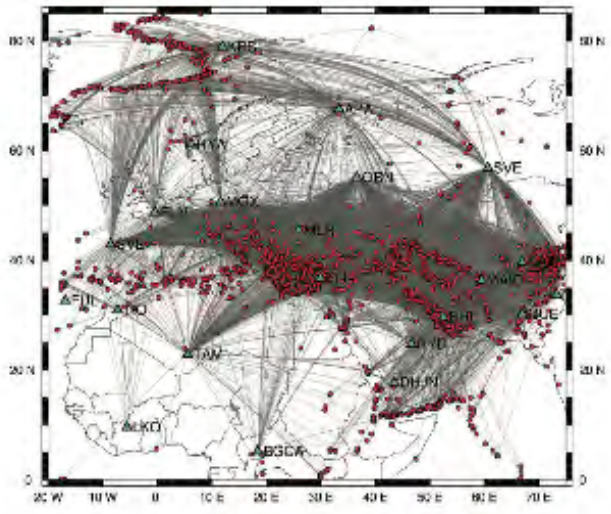


Figure 2. Map of raypath coverage for WENA region. Paths are from the GT events to 23 stations and show good coverage of the entire model region.

Our ultimate goal is to improve regional-network location accuracy. We test location performance by relocating five events with an epicenter accuracy of 5 km or better (Figure 3). Four of the events meet the local-network-coverage criteria of Bondar et al., (2004) for a 5 km epicenter accuracy at 95% confidence. One event is taken from the catalog of Soviet peaceful nuclear explosions (PNEs) reported in Sultanov et al., (1999). The PNE event is reported to have an accuracy of 1 km. These five events are well distributed geographically, and they are recorded at more regional-distance stations than other events with similar location accuracy. Therefore, the validation events provide even ray sampling over the model and an unbiased assessment of travel-time prediction accuracy and location performance.

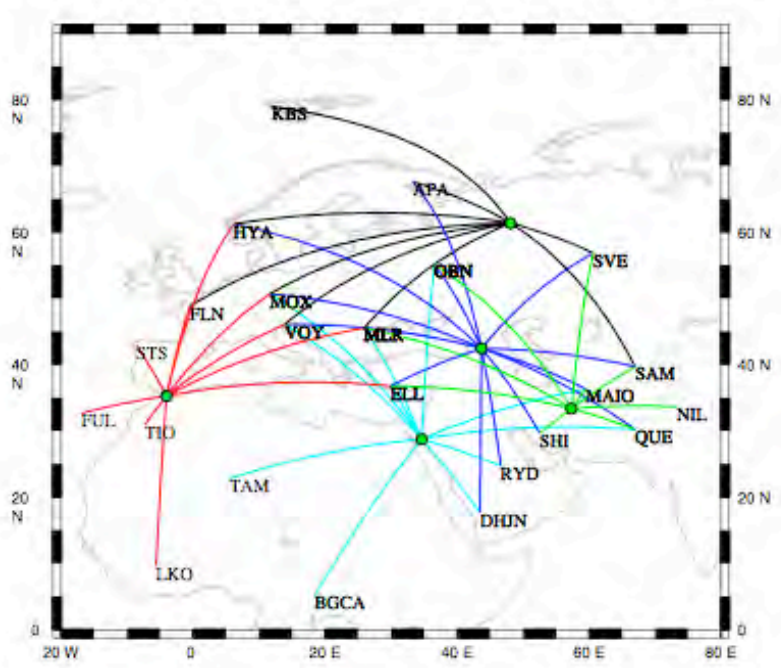


Figure 3. Five reference events used to test location accuracy and the 23-station network used for relocation.

3D Finite Difference Travel-time Calculations

We use the finite-difference method (FD) of Vidale (1988) with modifications by Hole and Zelt (1995) to compute travel times through the WENA1.0 velocity model. This technique propagates wave fronts radially outward from a point source using each grid (or time) point as a secondary source for each successive grid point. This procedure is more efficient and accurate than ray tracing because it is able to treat sharp velocity gradients that produce refracted, diffracted, or head waves in addition to direct phases. Furthermore, by taking advantage of travel-time reciprocity, we place the ray-tracing source at the station locations and calculate travel times to a 3D are estimated through interpolation of the travel-time prediction grid.

We have made two significant modifications to the finite difference code. First, we adapt it to read in 3D velocity models instead of 1D, enabling it to compute times through our WENA1.0 (or any custom 3D) model. Second, we apply a Cartesian-to-spherical coordinate transformation to the source and receiver locations that are input to the code (Flanagan et al., 2004). Therefore, instead of using an earth-flattening approach (which may not be applicable to 3D models), we literally create a spherical grid of points. This modification allows us to compute travel-times out to regional and near-teleseismic distances (~13° to 30°). The code is run in a volume of dimensions of roughly 35° by 50° laterally and 1,200 to 1,500 km deep with a grid spacing of 5 km. The grid spacing is determined empirically as a tradeoff between the accuracy of the travel-time prediction and computer memory limitations, and we find that a grid spacing of 5 km provides a reasonable accuracy (i.e., timing errors of approximately 0.25 s, see Figure 3).

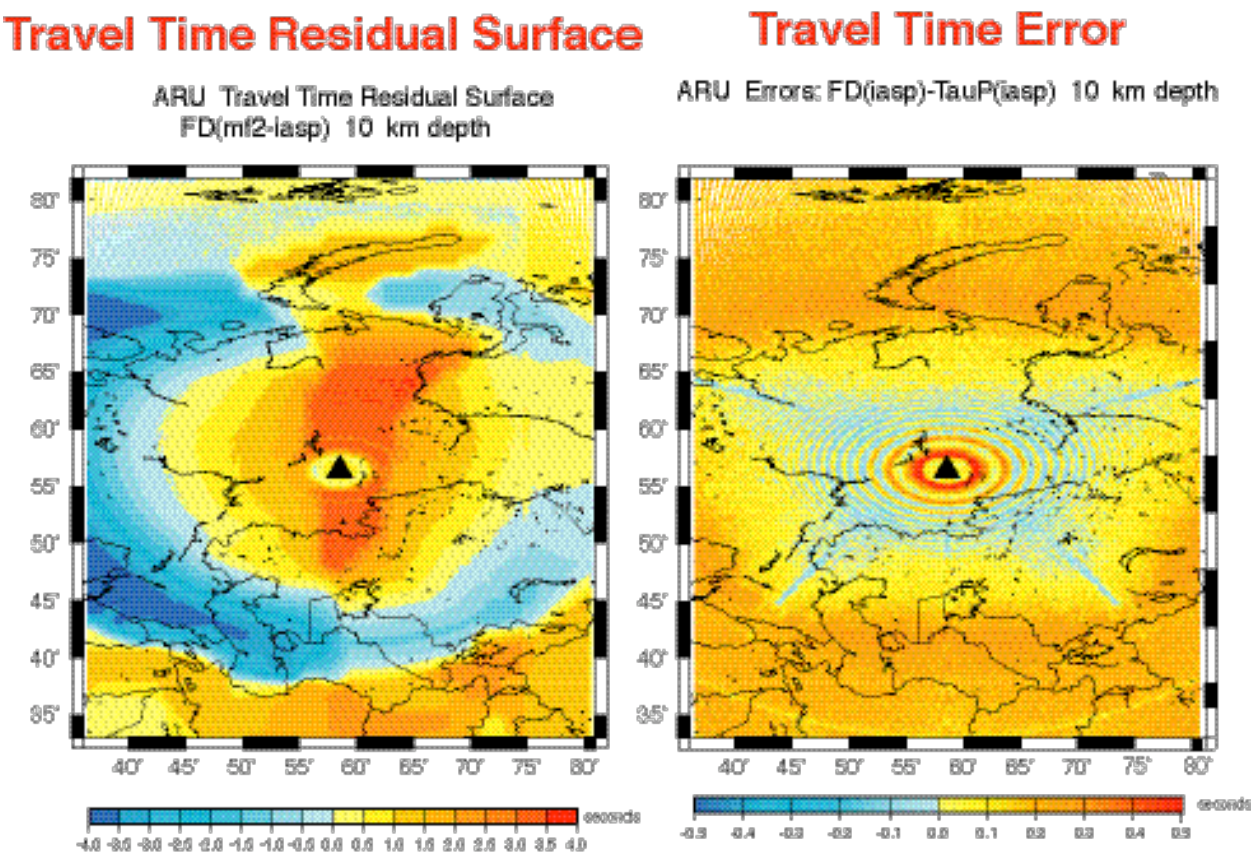


Figure 4. a) Travel-time residual surface for station ARU (black triangle); this surface shows the variations in travel-time as a result of 3D structure in the WENA1.0 model relative to the 1D IASP91 model. (b) Numerical errors in the FD code are quantified by subtracting theoretical 1D *IASP91* times computes from *TauP* (Crotwell, et al., 1999) from the IASP91 times predicted by the 3D, FD computation. Blue indicates fast regions, and red indicates slow; note the difference in the scale.

Result 1: Improvement in Travel-time Prediction

We compute 3D travel-time prediction models for first arriving *P*-wave travel-times predicted by the FD algorithm. The total predicted arrival time is computed along a regular grid in latitude, longitude grid with 25 km sampling. Depth is regularly sampled at intervals of 10 km down to 50 km. Each prediction model provides station-specific travel-times for regional to near-teleseismic distances, which can be used to locate regional-distance events. The difference between WENA1.0 and IASP91 travel-time predictions at four stations are shown in Figure 5. The example in Figure 5 is for a source depth of 10 km. We find travel-time differences of up to 6 seconds relative to IASP91. Extreme differences in travel-time prediction are generally caused by anomalous upper-mantle velocity, thick crust, and/or thick sediments. Note that the patterns in these correction surfaces correlate with the structural features in the WENA1.0 model; fast predictions are seen to the north (e.g., Russian platform) but slow anomalies are seen in the south (e.g. Turkey, Mediterranean, Iran).

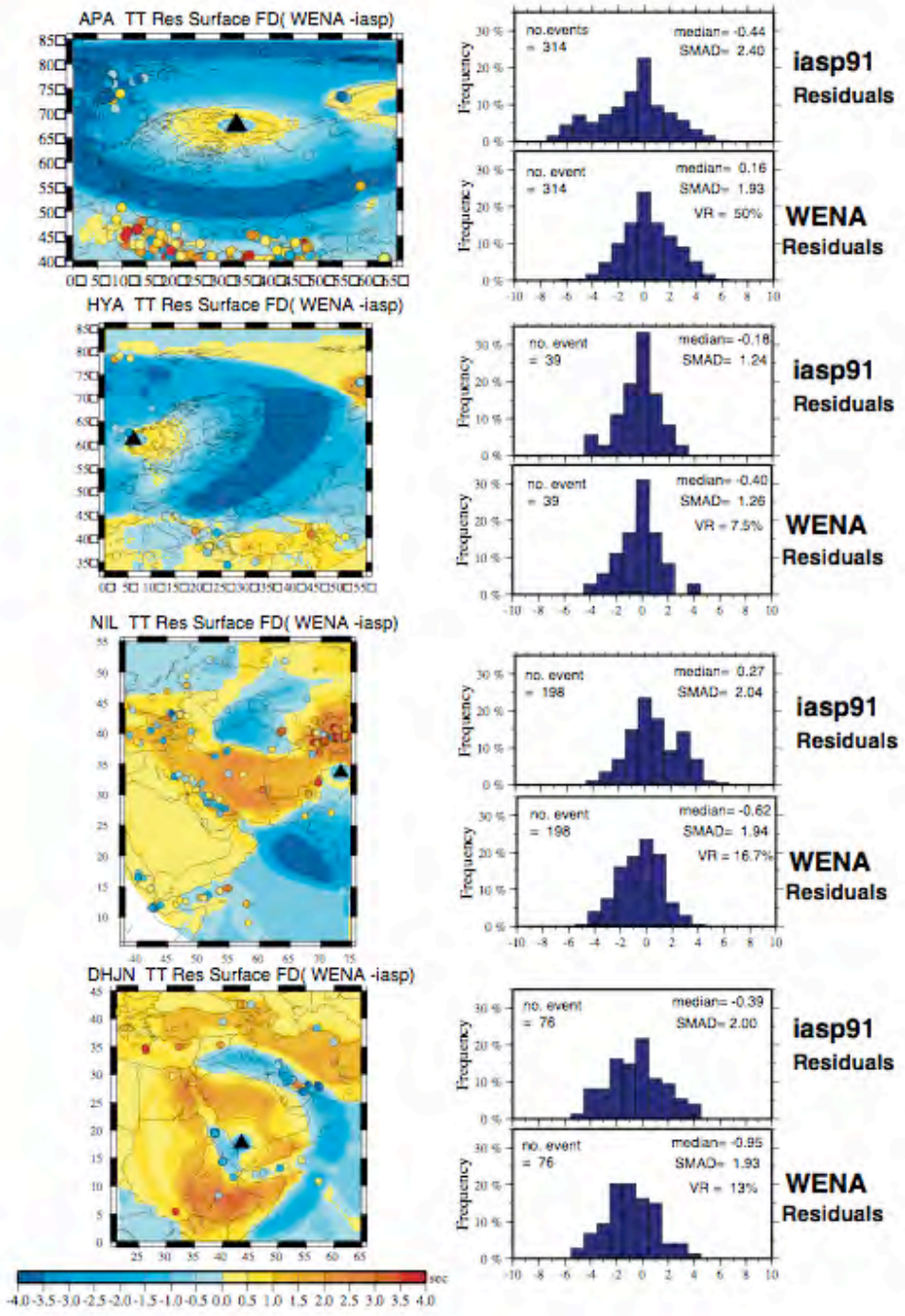


Figure 5. (left) Travel-time residual surfaces at 10 km depth; these model-based correction surfaces are computed by subtracting the IASP91 predicted time from the WENA1.0 predicted time. Blue indicates fast regions, and red indicates slow. The (GT-IASP91) residuals are plotted on top of the correction surfaces. (right) Histograms of GT-IASP91 and GT-WENA1.0 residuals showing the variance reduction for observed times at different stations. While WENA1.0 does not improve travel-time prediction in all cases, we find that overall prediction is improved by 15% to 20%.

Variation in residual variance is generally on the order of 15% to 20% for the stations we tested (e.g., Station NIL in Figure 5). The performance at any given station is quite variable, however, with improvement ranging from 50% (e.g. Station APA in Figure 5) to negligible.

Result 2: Uncertainty Model for WENA1.0

Travel-time prediction uncertainty is commonly distance dependent. Distance dependent uncertainty results from velocity-model errors that cause cumulatively more bias in travel-time prediction with distance. In this study we fit a distance-dependent uncertainty model using our validation data set. The simple fitting procedure entails calculating the mean and spread of the residual distribution in distance bins. Statistics of each bin are then used to determine the uncertainty at a given confidence in each distance bin. The distance-dependent uncertainty for WENA is shown in Figure 6. Because the uncertainty model is based on a data set that covers nearly all of the WENA model, it is applicable over the whole model.

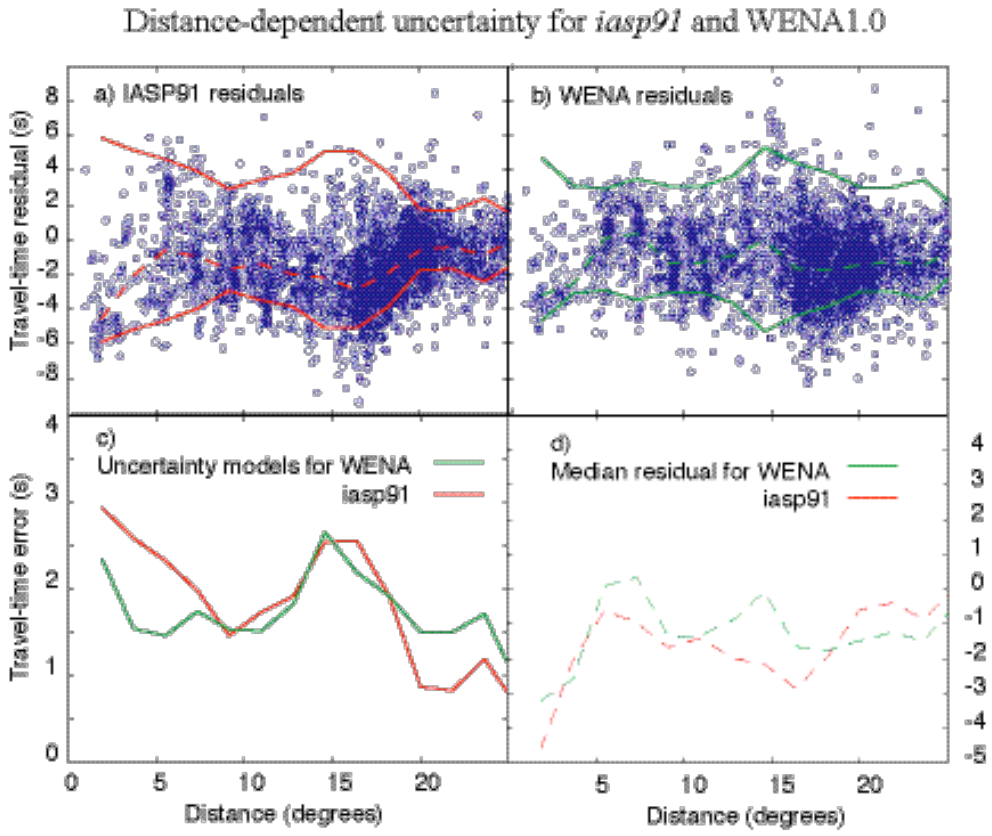


Figure 6. Distance-dependent uncertainty for IASP91 and WENA1.0. Note the nonstationarity and correlation in travel-time uncertainty between 1,000 and 2,800 km; uncertainty increases and errors are correlated (negative bias).

We use variogram modeling to assess the spatial statistic of the travel-time residuals. This approach examines the difference between residuals as a function of inter-event distance. An example of variogram analysis is shown in Figure 7. Note that the variograms do not approach zero for points that are nearly colocated (i.e., data are not perfectly correlated) because of errors associated with determining travel-time residuals. However, it is apparent that the variograms reach minima (correlation is maximum) for points close together, and the variograms increase (correlation decreases) as points become separated by greater distance. The 3D WENA1.0 model accomplishes two goals: improving the travel-time prediction by reducing the overall variance of residuals and reducing the nonstationarity of the uncertainties.

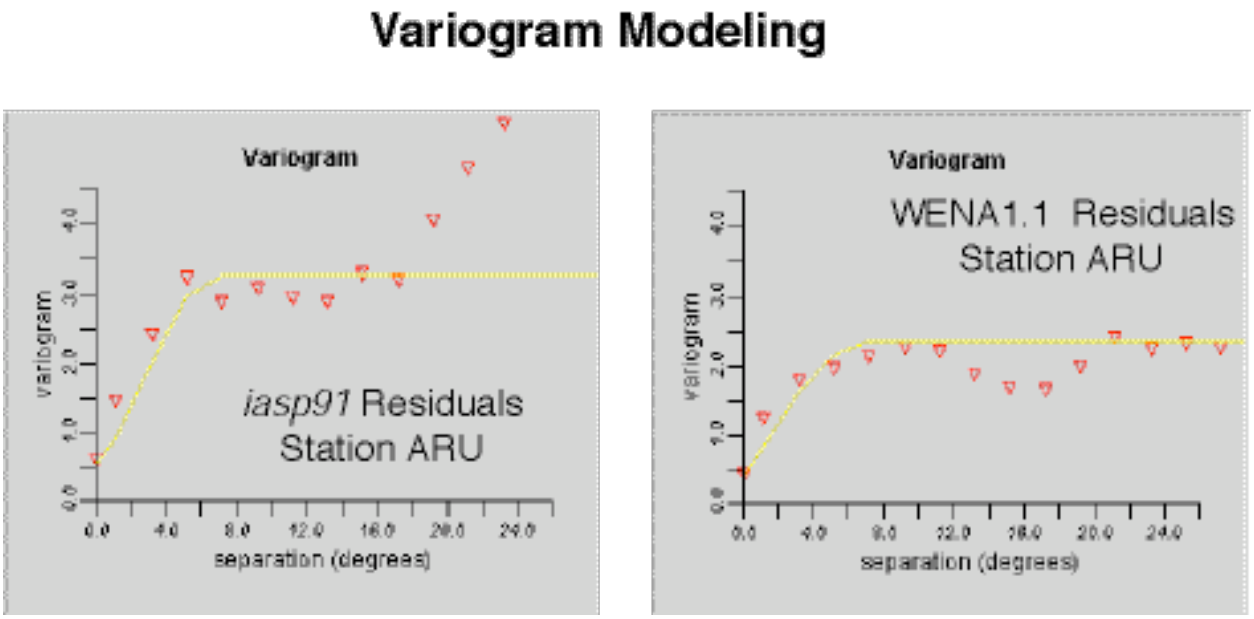


Figure 7. Variograms of travel-time residuals at station ARU for both the WENA1.0 and IASP91 velocity models. Crosses are the data variogram values in 1.0 degree bins; solid lines are the model variograms determined by curve fitting. The sill is the background variance of the data, the range is the distance at which correlation between points is zero, and the nugget is the covariance of colocated points. The IASP91 variogram is nonstationary (levels off at the sill, then increases again). The nonstationarity is caused by long-period features in the residual structure. WENA1.0 improves prediction of long-period residual features, and the variogram is relatively flat after the sill is reached.

Result 3: Improvement in Location using WENA1.0

Test events for location improvement are shown in Figure 3. Each of these events was relocated using first-arriving P-waves and either the IASP91 or WENA1.0 model. Figure 8 shows the result of these relocation tests. Average IASP91 mislocation is 19 km. WENA1.0 improves location accuracy by an average of 6.8 km to 12.2 km. This degree of improvement is similar to other calibration efforts that make use of tomographic models and GT15 calibration events.

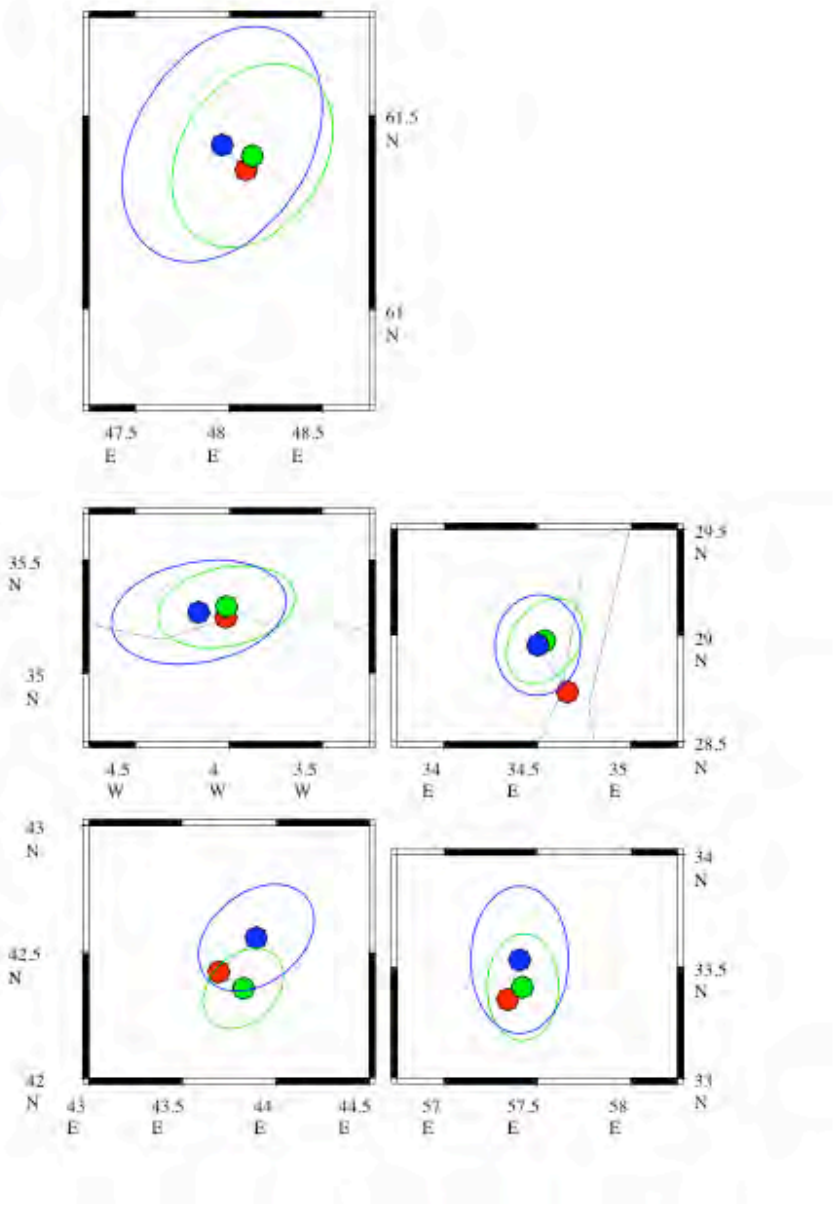


Figure 8. Results of location tests for WENA1.0 (green) and IASP91 (blue). Ground truth locations are shown in red.

The travel-time uncertainty model shown in Figure 6 is used to estimate coverage ellipses shown in Figure 8. In each instance, the coverage ellipse is smaller for the WENA1.0 model than the IASP91 model. This is consistent with our finding that WENA1.0 improves location accuracy. In most instances, the known location lies within the 95% confidence ellipse, suggesting that our error model is representative, but the known location is outside the 95% coverage ellipse in one instance. The one instance is likely to be a statistical anomaly, but further investigation is warranted.

CONCLUSIONS AND RECOMMENDATIONS

We test the applicability of the WENA1.0 model for regional seismic location. Tests include travel-time prediction performance for a large validation data set, and improvements in location accuracy for a limited, geographically distributed set of validation events. Three main findings are as follows:

- Application of WENA1.0 improves travel-time prediction by approximately 20% on average. For some stations, improvement approaches 50%, and for other stations improvement is negligible.
- Test of location improvement suggest that WENA1.0 improves epicenter accuracy in most cases, and uncertainty estimates are representative of observed mislocation.
- Improvement in WENA1.0 travel-time predictions primarily stems from the removal of long wavelength anomalies in the IASP91 predictions. These long wavelength features cause undesirable correlations in travel-time predictions that violate assumptions of most location algorithms.

REFERENCES

Bhattacharyya, J., W. Walter, M. Flanagan, J. O'Boyle and M. Pasyanos (2000), Preliminary definition of geophysical regions in Western Eurasia, UCRL-ID-138402, LLNL (http://www.llnl.gov/tid/lof/documents/pdf/237980.pdf).

Bondar, I., S.C. Myers, E. R. Engdahl and E.A. Bergman, (2004) Epicenter accuracy based on seismic network criteria, *Geophys. J. Int*, 156, 483-496, 2004.

Crotwell, H.P., T.J. Owens, and J. Ritsema (1999), The TauP ToolKit: Flexible seismic travel-time and raypath utilities, *Seism. Res. Lett.*, 70, 154-160.

Flanagan, M. P., S. C. Myers, K. D. Koper, (2004), Regional travel-time uncertainty and seismic event location improvement using 3-Dimensional *a priori* velocity models, *in preparation.*

Hole, J.A. and B.C. Zelt, (1995), 3-D Finite Difference Reflection Travel Times, *Geophys. J. Int.,* 121, 427-434.

Kennett, B.L.N. and E.R. Engdahl, (1991), Traveltimes for global Earthquake reference location and phase identification, *Geophys. J. Int, 105*, 429-465.

Laske, G. and T.G. Masters (1997), A global digital map of sediment thickness, EOS Trans. AGU, 78, F483.

Mooney, W.D., G. Laske and G. Masters, (1998) CRUST 5.1: A global crustal model at 5°x5°. *J. Geophys. Res*., 103, 727-747, 1998.

Myers, S.C. and C.A. Schultz, (2000), Improving Sparse Network Seismic Location with Bayesian Kriging and Teleseismically Constrained Calibration Events, *Bull. Seism. Soc. Am.*, 90, 199-211

Nataf, H.C., and Y. Ricard (1996), 3SMAC: an a priori tomographic model of the upper mantle based on geophysical modeling, Physics of the Earth and Planetary Interiors, 95, 101-122.

Pasyanos, M. E., W. R. Walter, M. P. Flanagan, P. Goldstein and J. Bhattacharyya (2004), Building and testing an a priori geophysical model for western Eurasia and North Africa, Pure and Applied Geophysics, 161, 235-281.

Schultz, C. A, and S. C. Myers, (1998), Nonstationary Bayesian Kriging: A predictive technique to generate spatial corrections for seismic detection, location, and identification, *Bull. Seism. Soc. Am*., 88, 1275-1288.

Sultanov, D.D., J.R. Murphy, and K.D. Rubinstein, A seismic source summary for Soviet peaceful nuclear explosions, Bull. Seismol. Soc. Am., 89, 640-647, 1999.

Vidale, J., (1988) Finite-difference Calculation of Travel Times, *Bull. Seismol. Soc. Am.,* 78, 2062-2076.

Walter, W.R., M.E. Pasyanos, J. Bhattacharyya and J. O'Boyle (2000), MENA 1.1 - An updated geophysical regionalization of the Middle East and North Africa, UCRL-ID-138079, LLNL (http://www.llnl.gov/tid/lof/documents/pdf/237521.pdf).

EVALUATION OF CROSS-CORRELATION METHODS ON A MASSIVE SCALE FOR ACCURATE RELOCATION OF SEISMIC EVENTS

Won-Young Kim, David P. Schaff, Jian Zhang, Felix Waldhauser, and Paul G. Richards

Columbia University

Sponsored by Air Force Research Laboratory

Contract No. F19628-03-C-0129

ABSTRACT

Lamont-Doherty Earth Observatory (LDEO) at Columbia University is evaluating a method of locating seismic sources (earthquakes, explosions) based on the use of waveform cross-correlation (WCC) measurements instead of using the conventional measurements of seismic wave arrival time (phase picks). WCC measurements have been demonstrated to be 10 to 100 times more accurate, where they can be used. The principal issue we are exploring is the extent to which a significant fraction of seismicity can be located using WCC measurements. We have organized the work into two projects: (1) the application of WCC methods to relocate earthquakes and explosions in China and neighboring regions, and (2) the application of WCC methods to relocate earthquakes in parts of North America.

Using a very sparse network it was discovered that about 10% of earthquakes in and near China between 1985 and 2000 with $M \geq 3$ were repeating events that generated essentially the same signals from sources which could not be more than 1 km from each other. The estimated location precision is a few 100 m. A specialized case study for the 1999 sequence of events in Xiuyan, China, found that WCC on Lg-waves combined with the double-difference technique significantly improved the epicentral locations. Several reflectivity synthetic experiments have been conducted to understand how depth, distance to the station, and mechanism influence the similarity of the Lg waveforms. In the synthetic Lg waveforms there is greater sensitivity to depth, than to epicentral distance.

In North America, we are studying the Charlevoix region in eastern Canada and the New Madrid seismic zone in the central United States. Datasets have been assembled from scratch working in conjunction with regional network operators. For Charlevoix courtesy, of the Geological Survey of Canada, we now have 2,472 events with corresponding catalog, phase, and waveform data. For New Madrid, two datasets have been acquired. The first is from the PANDA deployment between 1989 and 1992, which consists of 884 events with bulletin and waveform information. The second is from the Center for Earthquake Research and Information (CERI) network, operated by Memphis State University, which we currently have waveform data from 1995-2003, and catalog and phase data from 2000-2003 for 680 events, with catalog and phase data from 1995-1999 expected shortly. Preliminary WCC results of the PANDA network indicate that 68% (597 out of 884 events) correlate with cross-correlation coefficients above 0.7 at four or more stations. Four stations are the minimum required to obtain a location estimate. Both P- and S-waves are correlated on all three components. The window lengths are 1 s and the lags searched over are also 1 s. It appears in a few examples that similar correlations are possible over 1 to 10 kilometer inter-event separation distances due to a site resonance from soft sediments underneath certain stations. Subsequent work will continue the correlation analysis for the other regions and then perform locations using the double-difference algorithm.

OBJECTIVES

To evaluate a method of locating seismic sources (earthquakes, explosions) that is based on use of waveform cross-correlation (WCC) measurements instead of using the conventional measurements of seismic wave arrival time. WCC measurements are ten or a hundred times more accurate, where they can be used. The principal issue we shall explore is the extent to which a significant fraction of seismicity can be located using WCC measurements.

RESEARCH ACCOMPLISHED

We have organized the work into two Projects. Project 1 concerns application of WCC methods to relocate earthquakes and explosions in China and neighboring regions. Project 2 concerns application of WCC methods to relocate earthquakes in parts of North America.

Project 1

For Project 1, we studied 14,000 earthquakes in China for the years 1985 to 2000, and in particular 130,000 regional seismograms recorded at a sparse network of stations up to 20 degrees distance. We made the surprising discovery that in some cases the complex, highly scattered Lg-wave is remarkably similar for clusters of events. We analyzed in detail a subset of 28 events out of 90 from the 1999 Xiuyan sequence associated with a damaging earthquake that was successfully predicted in Liaoning Province, northeast China. Excellent relative locations could be obtained using only four or five stations 500 to 1000 km away. This approach was expanded to cover all of China and surrounding regions, and we found that about 10% of seismic events in and near China for the fifteen-year period were repeating events not more than about 1 km from each other. Specifically we found a set of 1301 seismic events with the property that any one of them wrote regional seismograms (in many cases lasting for hundreds of seconds, and using a band from 0.5 to 5 Hz) almost exactly like those from at least one other event. Among these events, 950 waveform doublets could be identified, which can used to evaluate the precision of phase picks and standard catalogs. This work has been written up and accepted for publication in two papers (Schaff and Richards, 2004a,b).

We continued a detailed study of the Xiuyan sequence of earthquakes in Liaoning Province, China. Specifically, we used a reflectivity code to generate synthetic regional waves in the passband 0.5 to 5 Hz, at a distance of 750 km (corresponding to the distance at which we have data), and found that the synthetics are far more sensitive to changes in source depth than they are to changes in epicentral distance. This is of interest in the context of interpreting event clusters that have approximately the same epicenter centroid, yet have different waveforms. We speculate that in this case the waveforms are different and do not cross-correlate well between clusters, because the clusters are centered at different depths.

Project 2

For Project 2, we are carrying out detailed studies of the seismicity of two regions in North America, namely New Madrid in the Central United States, and Charlevoix, East Canada.

Data Compilation

For New Madrid, three datasets have been acquired. The first is from the PANDA (Portable Array for Numerical Data Acquisition) network deployment from Oct. 1989 - Aug. 1991, which consists of 884 events with bulletin and waveform information. The second is from the network operated by CERI (Center for Earthquake Research and Information, University of Memphis) and we currently have waveform data from 1995 to 2003 and catalog and phase data from 2000 to 2003 for 680 events, with catalog and phase data from 1995 through 1999 expected shortly. The third data set is the Central Mississippi Valley seismic bulletin data from St. Louis University, which consists of over 60,000 phase picks from about 4,000 earthquakes that occurred during 1974-1998.
For the Charlevoix seismic zone, courtesy of the Geological Survey of Canada, we now have 2,472 events with corresponding catalog, phase, and digital waveform data.

Technique

We have experimented with a correlation detector that is able to recover lags greater than half the window length. This is a new feature and different from the correlation function which was applied in our earlier work. When dealing with finite duration signals, time-domain cross correlation is computed by fixing one window on the first seismogram and moving a sliding window over the second seismogram padded with zeros (Figure 1). An equivalent result is obtained if the cross-correlation is computed in the frequency domain. Although the cross correlation function is technically defined for lags plus and minus the window length, in practice only lags less than or equal to half the window length can be recovered (Schaff et al., 2004). The reason is that beyond this point the percentage of similar energy in the two windows is less than 50%. A related effect is that the cross correlation coefficient measurement degrades with increasing initial offset of the two seismograms (Schaff et al., 2004). If instead of padding with zeros, the original data is retained in the second seismogram, both of these negative effects with correlation functions are eliminated (Figure 1). We call such an application employing a correlation detector. Now the sliding window can align arbitrarily long offsets and perfectly capture the correct correlation coefficient.

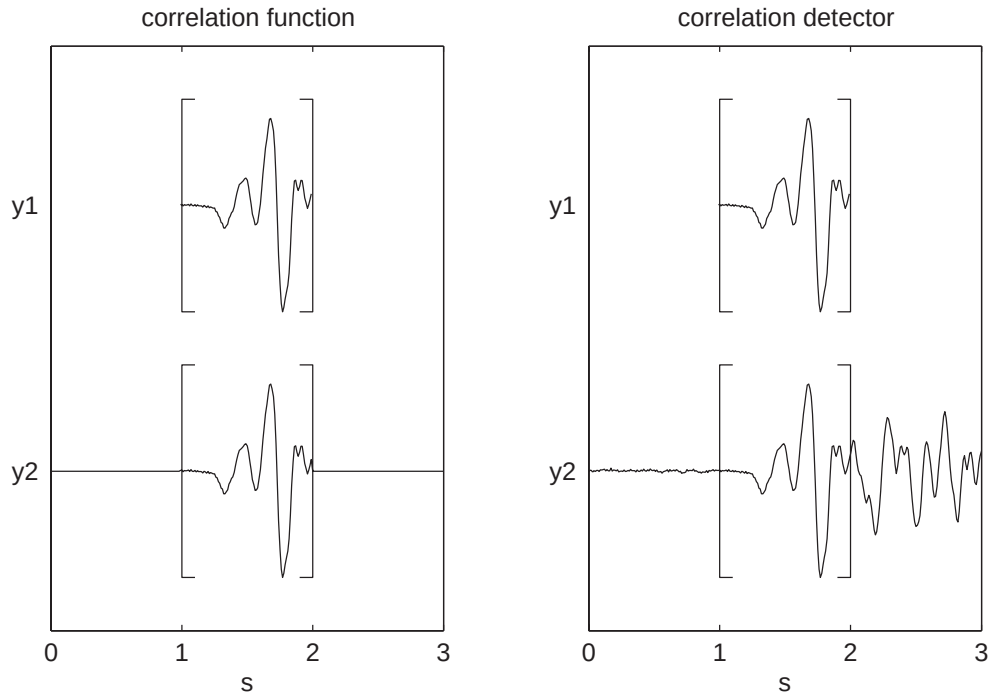


Figure 1. Illustration of the difference between a correlation function and a correlation detector. Window is fixed for seismogram y1. A sliding window for seismogram y2 runs over zeros padding for the correlation function, and over data for the detector.

Most implementations of cross correlation in the seismological literature we know of use a correlation function or the cross spectral technique, and are therefore limited by these fixed window length/finite duration records. This is a practical issue since the initial windows may be offset by substantial amounts due to mispicks or theoretical travel times. For example, if two seismograms were mispicked each by 0.5 s the total offset could range up to 1 s. A correlation function using 1 s window lengths would not be able to align these offsets.

Event pairs were selected for cross correlation computations based on distance thresholds since waveform similarity is known to decrease with increasing inter-event distance (e.g. Geller and Mueller, 1980). All event pairs with horizontal separations less than 5 km and vertical separations less than 10 km were processed. The input parameters used were window lengths of 1 s, lags searched over 1 s, and band-pass filtering from 1 to 15 Hz. All channels end components were processed where available. Measurements were made for both P- and S-waves, and phase picks listed in the bulletins were used to align windows initially. In cases where no phase picks were present, theoretical

travel times were computed using ray tracing through a 1D layered velocity model. If a P-wave pick existed but no S-wave pick existed, we used 1.732 times the P-wave travel time. Computations were performed on a Sun Blade 100 and processing time averaged on the order of a few hours.

New Madrid Seismic Zone (PANDA deployment)

Results for the 884 events recorded at the PANDA network (Figure 2) are summarized in Table 1 for correlation measurements of pairs of events that had cross-correlation coefficients CC > 0.7 at four or more common stations. This table indicates that the location of 597 events or (68%) can be improved with the more accurate differential times from waveform cross correlation. If an event pair meets the criterion of CC > 0.7 at four or more stations it is also an indication of the robustness of the measurements and quality of the data since there is less of a chance of outliers. Event pairs that have CC > 0.7 at only one station may be more suspect as potential outliers. It may however be due to weak signal-to-noise ratios, stations coverage, or radiation patterns. Therefore in a joint inversion for all the events using the double-difference method (Waldhauser and Ellsworth, 2000) it is useful to include all data with CC > 0.7 even if only recorded at one station to provide a better constraint for the whole system of equations. Figure 3a represents the distribution of correlation data graphically for event pairs with CC > 0.7. More compact clusters have event pairs that meet this criterion at more stations as expected; for example six or more stations plotted in magenta. Such a plot is useful for determining how well certain event clusters are constrained by correlation data.

Table 1: CC > 0.7 for 884 events at PANDA network*

Stations	1 or more	4 or more
Number of events	830 (94%)	597 (68%)
Number of pairs	25,030	2,285
Number of observations	47,459	10,908

*statistics for vertical component P-waves

Before proceeding with the relocation stage, it is prudent to verify that the measurements are indeed improving alignments. Based on high correlation coefficients we identify a large cluster of 26 events with similar P-wave trains (Figure 4). The signal is relatively monochromatic in nature with a period of approximately 0.1 s. Figure 5 (bottom) shows that the cross correlation coefficients are quite high for all the event pairs in the cluster. Figure 5 (top) reveals a surprising feature that these events appear to be so compact spatially, but are in fact quite spread out. Some event separation distances are greater than 10 km and yet their P-waves have high correlation coefficients (Figure 5, bottom). This explains why the later S-wave arrivals on Figure 4 did not align when the P-waves are adjusted. The explanation for this behavior is probably due to the fact that there are no hard rock sites in the central Mississippi Valley, but all the PANDA stations are situated on soft sediments. These conditions may set up a site resonance for an incoming P-wave that may be less sensitive to differences in the initial locations of the events in terms of affecting waveform similarity. Whether these correlation measurements actually provide useful data to improve earthquake locations given an assumed velocity model for first arrivals should be explored more fully.

Preliminary double-difference relocation of the largest cluster (649 events) is shown in Figure 3b (upper panel), along three northeast trending cross sections. This cluster is selected to include pairs of events with at least 8 P- and/or S-wave cross-correlation measurements, to ensure a well-conditioned system of double-difference equations. The velocity model used for relocation is from Chiu et al. (1992). Weighted RMS residuals decrease from 230 ms before relocation to 34 ms after relocation. The average horizontal error determined by a bootstrap analysis of the final residual vector at the 90% confidence level is 90 m, the vertical error is 101 m. Relocation results clearly delineate a narrow zone of active faulting, with some diffuse seismicity occurring away from the main fault. The

main seismically active fault plane dips to the southwest, with a dip of about 30° (cross section A-A´) at the northern end of northwest striking step over seismicity and about 45° at its southern end (cross section C-C´). Comparison of the double-difference results with corresponding original network locations (lower panel in Figure 3b) indicate a sharper picture of seismicity in the new locations. Additional work is necessary to ensure proper modeling of the complicated phases (Chiu et al., 1992), such as the use of 3D models to predict differential times and partial derivatives for each event.

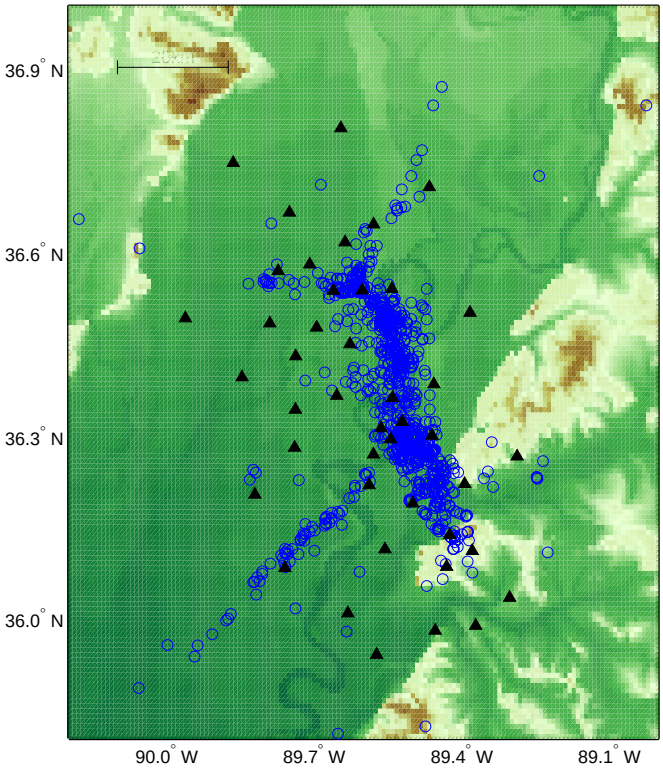


Figure 2. 918 earthquakes (circles) that occurred during 1989-1992 in the New Madrid seismic zone recorded by the PANDA network (triangles).

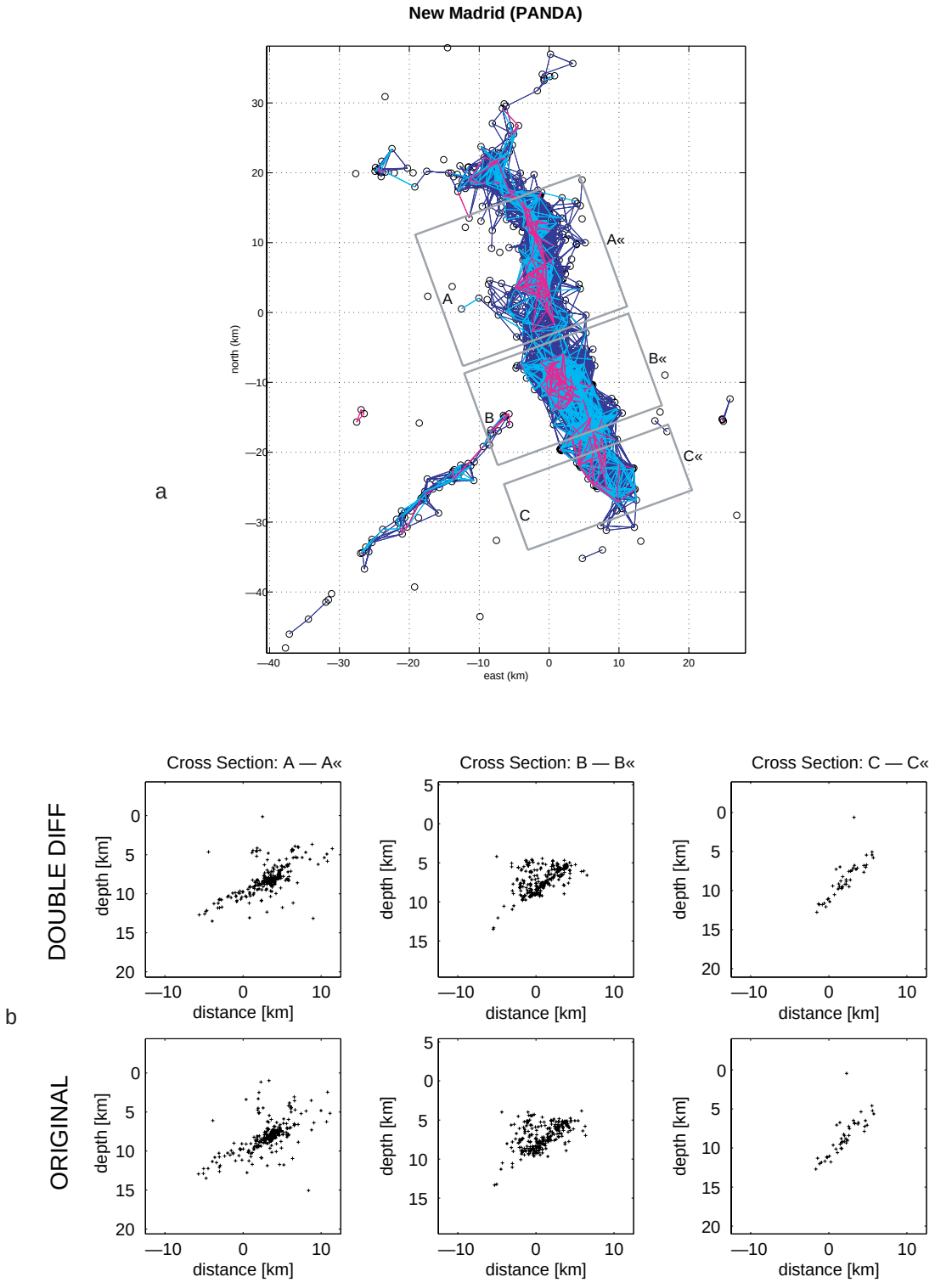


Figure 3. a) Connectivity of correlation measurements that have CC > 0.7 for event pairs at 2 (blue) or more stations, 4 (cyan), and 6 (magenta). Event locations are from the initial catalog. Boxes include events shown in (b). b) Cross sections of double-difference relocation of 649 events in the step-over zone using the cross-correlation based differential times (top row). Original locations (bottom row) are shown for comparison. Locations of cross-sections are indicated in (a).

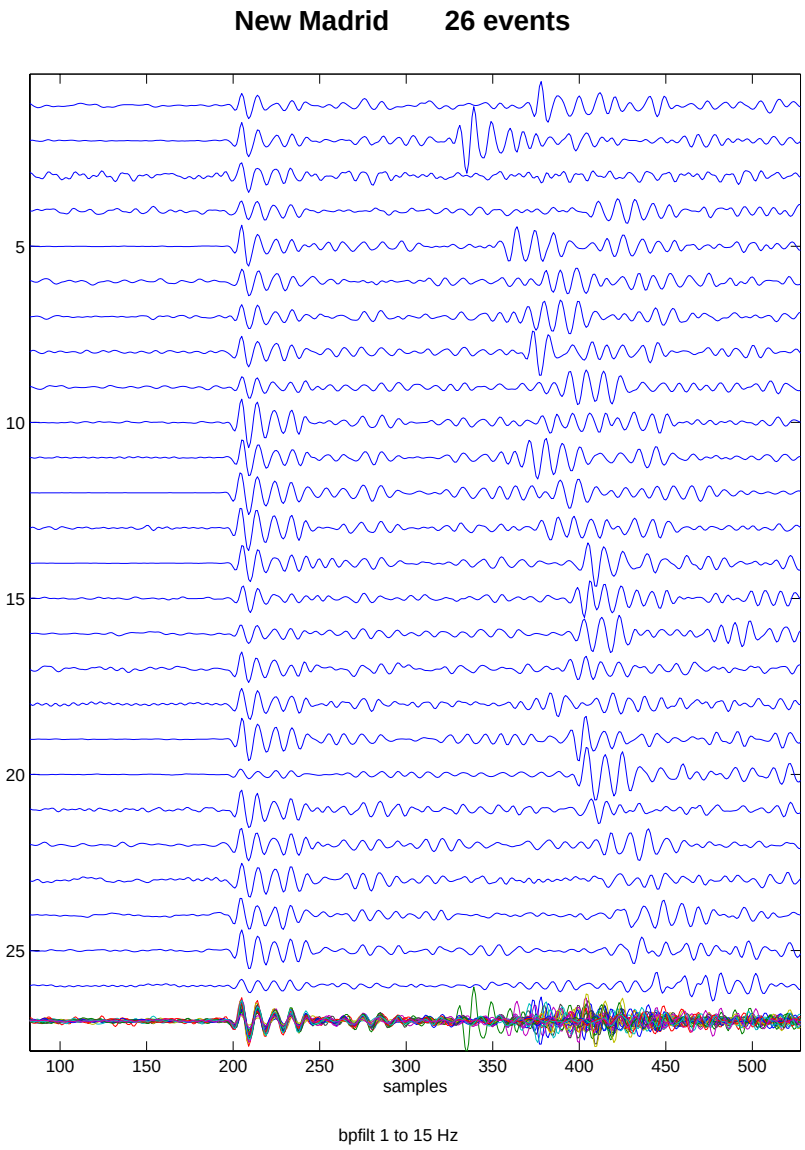


Figure 4. Seismograms for 26 events at the PANDA station, i01, band-pass filtered from 1 to 15 Hz and aligned by cross correlation on the P-wave train coming in at 200 samples (delta = 0.01 s).

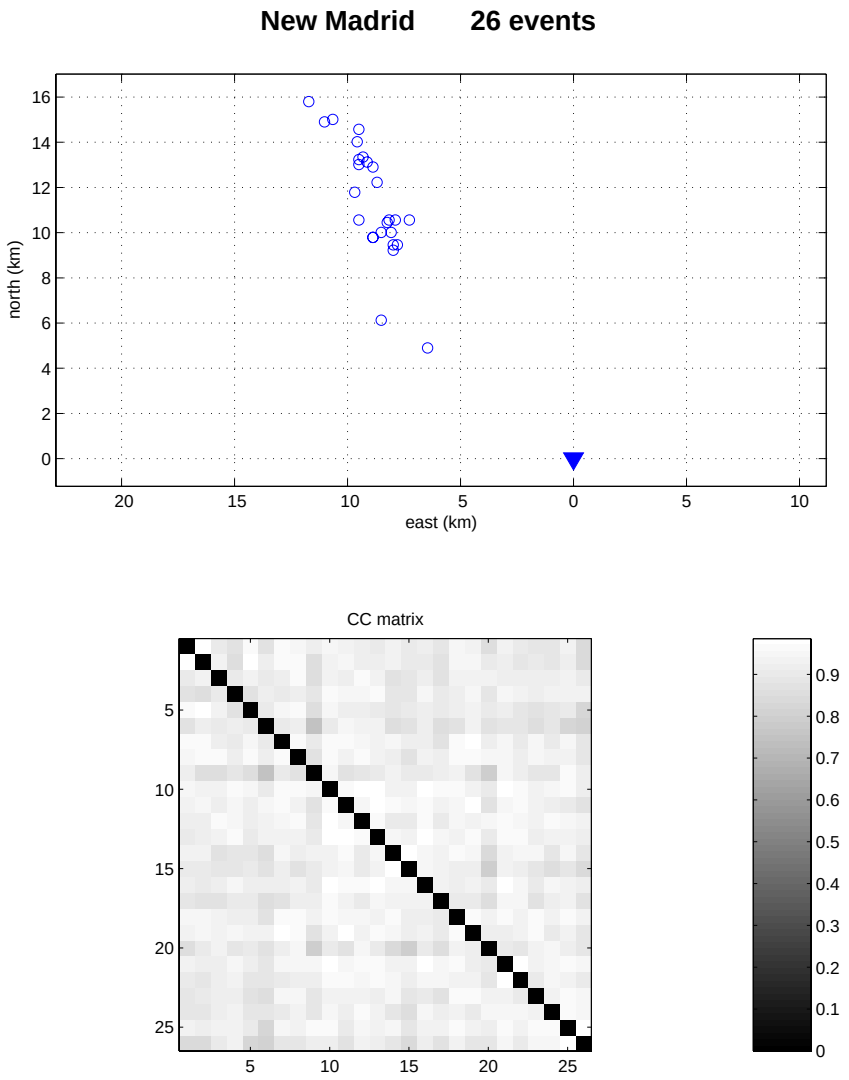


Figure 5. (top) Map view of the epicenters for the 26 event cluster along with station i01 plotted at the origin (triangle). (bottom) Cross correlation coefficient matrix for the waveforms in Figure 4.

Charlevoix seismic zone

Preliminary results from cross-correlating events in the Charlevoix seismic zone (Figure 6) are summarized in Table 2. Phase data was available for 2797 events. Waveforms were available for 2470 of those events. In this case, only 255 or (10%) of the events meet the criterion of CC > 0.7 at four or more stations. The primary reason for this is that only 8 stations are close to the majority of the seismicity as compared to the high station density of the PANDA network (see Figure 2). This affects also the number of pairs and the number of observations. To compare networks with variable station density it may be more appropriate to consider the "1 or more stations" value which is 78% for events in Charlevoix and 94% for the PANDA network (Tables 1 & 2). Figure 6 displays the connectivity plot for the correlation data and shows hardly any event pairs with 6 or more stations recording. Another reason for the relatively low "4 or more" 10% of the events that are expected to have locations improved by correlation measurements, is earthquake density. If event-pair separation distances are too great, the waveform similarity may breakdown to the point of being unusable for accurate differential time measurement. For comparison 92% of the

8000 events on the Calaveras fault in California were able to have significantly improved locations with the inclusion of correlation data (Schaff et al. 2002). These events were spread over a 35 km stretch of fault of minimal width (~75 m). In the Charlevoix seismic zone there are only 2470 events, which are distributed in two wide bands spanning 70 km in length and about 40 km in width. Estimating the difference in earthquake density for the two regions using these rough numbers is well over a factor of a thousand. Although this analysis is imperfect since denser clusters are likely to exist for both regions, it still gives an idea of overall improvement for the majority of the seismicity on a larger scale. In summary both earthquake density and station density are important for applying waveform cross correlation. A final comparison can be made with all of northern California where both earthquake density and station density are high. A recently completed project performing 26 billion correlation measurements for 225,000 events demonstrated that a remarkable 90% of the events in northern California have CC > 0.7 with at least one other event at four or more stations (Schaff and Waldhauser, in prep.).

Table 2: CC > 0.7 for 2470 events at Charlevoix*

Stations	1 or more	4 or more
Number of events	1916 (78%)	255 (10%)
Number of pairs	17,477	256
Number of observations	22,437	1,123

* statistics for vertical component P-waves

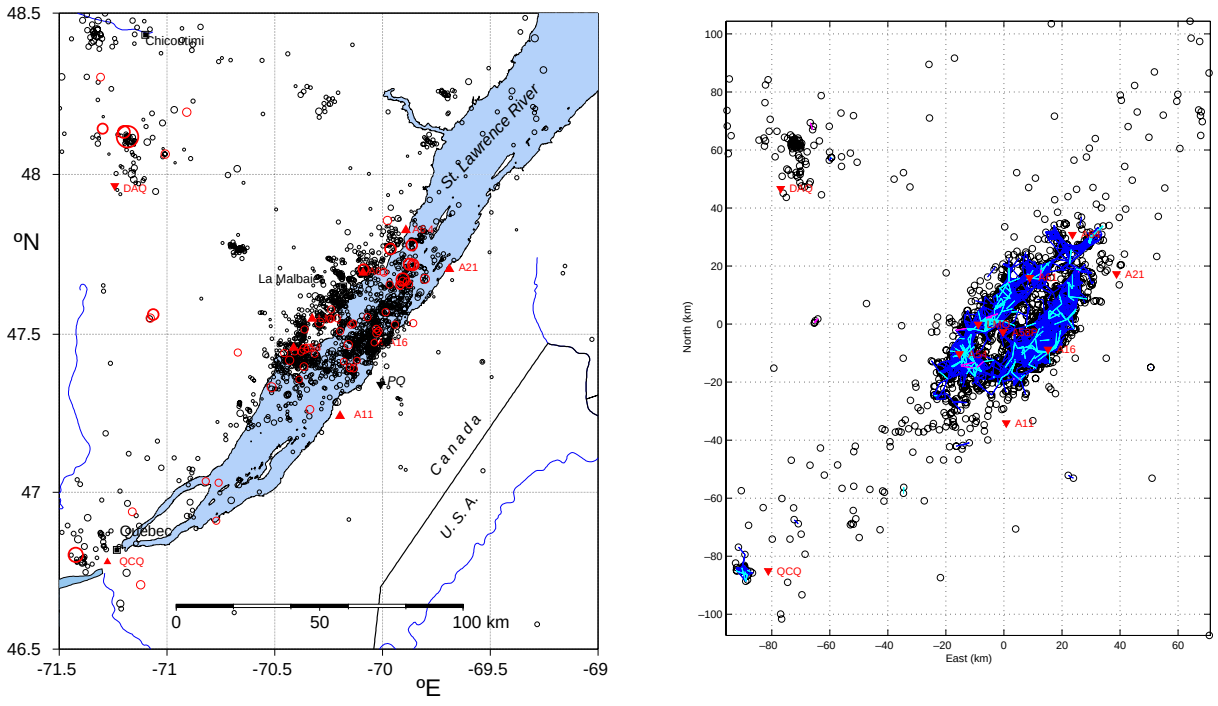


Figure 6. (left) Charlevoix seismicity and station locations. (right) Connectivity of correlation measurements that have CC > 0.7 for event pairs at 2 (blue) or more stations, 4 (cyan), and 6 (magenta). Event locations (2797) are from the initial catalog for the years 1988 to 2003. Stations plotted are those that had waveforms with correlation measurements.

CONCLUSIONS AND RECOMMENDATIONS

Cross-correlation measurements for earthquakes in the New Madrid seismic zone (NMSZ) and the Charlevoix seismic zones (CSZ) indicate that a much higher number of events (68%) correlate in the NMSZ, compared to only 10% of the events that correlate in the CSZ. The reason for this discrepancy may be due to: differences in the network geometry and number of stations; differences in the type and diversity of faulting associated with the events; the variation of geophysical properties in general; and the degree of structural heterogeneity in particular, within the areas of investigation; or a combination of all. Our observations have the potential to address important scientific questions, as well as technical questions related to the earthquake location problem. We will focus on these issues during the second half of our project.

We recommend that for regions of high seismicity within which a high percentage of events cross-correlate at enough stations to achieve precise relocations, consideration be given to a wholly different paradigm for event location — namely, a framework in which events are located using cross-correlation measurements obtained from relevant portions of the waveform, rather than using phase picks.

ACKNOWLEDGEMENTS

Network operators who agree to provide us with all their data are engaging in a highly civilized activity. The data cost millions of dollars to acquire and many man-years of work, and have been given us at no charge. It is typically a significant effort to provide the data in formats we can use. We greatly appreciate the assistance of the Geological Survey of Canada, and personnel at St. Louis University and Memphis State University. In particular we thank Drs. David McCormack and Jim Lyons at the Geological Survey of Canada, Ottawa, who helped assemble phase and waveform data from earthquakes in the Charlevoix region. We thank Drs. Jer-Ming Chiu of CERI, University of Memphis and Jiakang Xie at Lamont-Doherty who helped us to acquire phase and waveform data from the PANDA New Madrid deployment. We also thank Drs. Mitch Withers at CERI, University of Memphis and Robert Herrmann at St. Louis University for New Madrid seismic network data and Central Mississippi Valley seismic bulletin, respectively.

REFERENCES

Chiu, J.M., A.C. Johnston, and Y.T. Yang, Imaging the active faults of the central New Madrid seismic zone using PANDA array data, *Seismol. Res. Lett*., 63, 375-393, 1992.

Geller, R. J., and C. S. Mueller (1980). Four similar earthquakes in Central California, *Geophys. Res. Lett*., 7, 821-824.

Schaff, D. P., and P. G. Richards(2004a), Lg-wave cross correlation and double-difference location: application to the 1999 Xiuyan, China, sequence, *Bull. Seism. Soc. Amer*., in press.

Schaff, D. P., and P. G. Richards (2004b), Repeating seismic events in China, *SCIENCE*, 303, 1176Ð1178.

Schaff, D. P., G. H. R. Bokelmann, G. C. Beroza, F. Waldhauser, and W. L. Ellsworth (2002). High resolution image of Calaveras Fault seismicity, *J. Geophys. Res.*, 107, 2186, doi:10.1029/2001JB000633.

Schaff, D.P., G.H.R. Bokelmann, W.L. Ellsworth, E. Zanzerkia, F. Waldhauser, and G.C. Beroza (2004). Optimizing correlation techniques for improved earthquake location, *Bull. Seismol. Soc. Amer*., 94, 705-721.

Schaff, D.P., and F. Waldhauser. Improved Differential Travel Time Measurements at the Northern California Seismic Network, *Bull. Seismol. Soc. Amer*. in prep.

Waldhauser, F. and W.L. Ellsworth (2000), A double-difference earthquake location algorithm: Method and application to the northern Hayward fault, *Bull. Seism. Soc. Amer*., 90, 1353-1368.

DEVELOPMENT OF INNOVATIVE FILTERING TECHNIQUES FOR IMPROVED DEPTH PHASE DETECTION AT REGIONAL DISTANCES

Delaine T. Reiter[1], Jessie L. Bonner[1], and Robert H. Shumway[2]

Weston Geophysical Corporation[1] and University of California, Davis[2]

Sponsored by National Nuclear Security Administration
Office of Nonproliferation Research and Engineering
Office of Defense Nuclear Nonproliferation

Contract No. DE-FG02-03ER83820

ABSTRACT

Accurate determination of the focal depth of seismic events continues to be an important seismic monitoring problem. The primary objective of this research is to improve seismic depth phase detection and identification capabilities at regional distances using new filtering techniques. To accomplish this objective, we applied wavelet denoising and optimal (Wiener) filtering to the problem of depth phase detection at regional distances for synthetic and real array data. We have developed a detection routine that includes array processing to isolate the *Pn* window for analysis, Fourier filtering and wavelet denoising of the windowed data to improve the signal-to-noise ratio (SNR), and depth phase analysis using a cepstral F-statistic detection module. We applied the processing routine to synthetic regional waveforms computed for an array of similar size and geometry to the South Korean seismic array (KSAR). Gaussian white and autoregressive (AR2) noise models were used to add complexity to the synthetic data, and many different simulations with variable signal-to-noise ratios were conducted to examine the performance of the filtering and denoising techniques on data. We concluded that wavelet denoising did not offer substantially improved detection rates over standard Fourier bandpass filtering if the depth phases were buried in white noise. However, when the waveforms were contaminated with noise produced by an AR2 model or observed noise from KSAR, we noted a significant decrease in the depth phase false alarm rate when wavelet denoising or Wiener filtering were applied.

These filtering techniques were then applied to a database of test events recorded at regional distances from the KSAR array. These events had high quality depth estimates that were based on multiple teleseismic depth phases. The KSAR array data were first processed using traditional *f-k* techniques to determine the analysis window, which typically includes pre-event noise, the *Pn* arrival, and the signal prior to *Pg* or other sustained arrivals with characteristics that differ from the *Pn* phase. We determined that a *sym4* wavelet decomposed at level 6 removed noise at periods less than 1 Hz better than the level-4 decomposition found in our synthetic studies. We applied the *sym4* wavelet, together with Heursure thresholding to denoise the events in our database and compared the results to those found using both standard Fourier filtering (Butterworth BP 0.6 to 4.5 Hz) and Wiener filtering. The results of this preliminary study suggest that wavelet denoising improves our ability to detect depth phases on complicated regional seismograms. Wavelet denoising improves our ability to visually detect phase arrival onset, but additionally, and perhaps more importantly, it decreases the false alarm rates in the cepstral F-statistic analysis significantly (by factors of 2 and greater). Our results thus far indicate that wavelet denoising is a feasible method that can improve the detectability and phase arrival time estimation of regional depth phases. Further study is needed to determine the effectiveness of the method in a data center/operational setting.

OBJECTIVES

The accurate estimation of the depth of small, regionally recorded events continues to be an important and difficult monitoring research problem. In our previous studies, we have focused on the extraction of depth phases from body waves using cepstral analysis (Bonner *et al*., 2002), with varied degrees of success at regional distances. The objective of the research presented in this paper is to improve the identification of regional seismic depth phases using innovative filtering techniques applied to the data prior to cepstral F-statistic processing.

RESEARCH ACCOMPLISHED

Seismologists are very familiar with filtering schemes based on Fourier analysis, which uses sine and cosine functions to represent seismograms. While this technique is highly effective in the analysis of seismic data, it has limitations when the signal contains sharp discontinuities or transient features. In contrast, wavelet analysis relies upon other classes of mathematical functions that can be used to dissect and represent data. The wavelet transform segments data into separate frequency components, which can then each be studied independently. For example, certain frequency components may consist of a large "window" of data that provides information on gross features of the data, while other frequency components allow the examination of smaller windows and detailed waveform features. Another advantage of the wavelet transform is that it can utilize many possible basis functions, while the Fourier transform has only one set of basis functions (sines and cosines). This allows wavelet analysis to illuminate features in the data that can be obscured by other time-frequency methods such as Fourier analysis. We refer the reader to additional references by Misiti *et al.* (2000), Strang and Nguyen (1996) and Daubechies (1992) for further background information on wavelets. In the following sections, we present the results of applying a type of wavelet analysis known as *wavelet denoising* to the problem of depth phase detection.

Development of Denoising Filters for Regional Seismograms

The objective in our application is to remove noise from regional seismic data, while retaining the complex depth phase signals. In previous research, we utilized Fourier band-pass filters to reduce noise and aid in the detection of depth phases. The results were not optimal at regional distances, and many false depth phase detections were attributed to background noise, secondary arrivals, and filtering artifacts. Therefore, we have applied various methods to wavelet denoise (Misiti *et al.*, 2000; Shumway and Stoffer, 2000) regional seismograms for improved depth phase extraction. The application of wavelet denoising requires the selection of three components: a wavelet basis function, the thresholding procedure and a noise scaling option. Each of these components is discussed below.

Wavelet Selection. The first step in producing a wavelet denoising filter is to choose a wavelet basis function to be used in decomposing the seismic waveforms. In our research we have focused on the *symmlet4* (or *sym4*) and *db2* wavelets, as described by Daubechies (1992), and the *bior3.5* wavelet (Tibuleac, 2003). We chose these wavelets based on their similarities to typical *P*-wave arrivals and their success in previous studies of *P* waves (Anant and Dowla, 1997; Tibuleac, 2003; Zhang *et al*., 2003). These wavelet functions are shown in Figure 1. Note that the *bior3.5* wavelet uses two different wavelets: one for decomposition and one for reconstruction

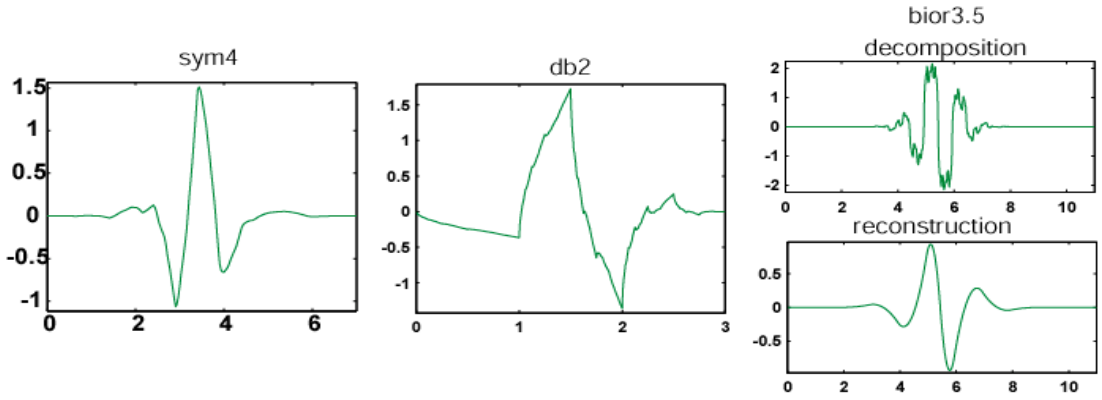


Figure 1. Wavelet basis functions used in the study.

Threshold Selection. To denoise a regional waveform, we must select a threshold that effectively removes seismic noise and increases the desired arrival (e.g., the depth phase) signal-to-noise ratio. The thresholding can be designated as either "hard" or "soft". Shumway and Stoffer (2000) provide a summary on how soft thresholding is accomplished. For example, the value of a wavelet detail coefficient, a, is set to 0 if $|a| \le \lambda$, where λ is the actual threshold. For $|a| \ge \lambda$, the coefficient is set to some other value (e.g., $sign(a)(|a| - \lambda)$). In the case of hard thresholding, the coefficient is set to a if $|a| \ge \lambda$ and 0 if $|a| \le \lambda$. Misiti *et al*. (2000) allow for several choices of thresholding, including methods known as Rigrsure, Sqtwolog, Heursure, and Minimaxi. We have compared these four methods of automatically determining a soft threshold; each is briefly described in Table 1.

Table 1. Threshold Selection Criteria (from Misiti *et al*., 2000)

Threshold Type	Comments
Minimax	Uses the Minimax principle (Mallat, 1999) to design estimators that realize the *minimum* of the *maximum* mean square error.
Rigrsure	Uses Stein's (1981) Unbiased Estimate of Risk to set a threshold that minimizes the risks.
Sqtwolog	Uses a Minimax threshold multiplied by a factor proportional to the log of the waveform length.
Heursure	Combines Sqtwolog and Rigrsure techniques.

Rescaling Options. The most basic noise model that we can consider consists of Gaussian white noise with $\sigma = 1$. However, this model is not often observed in practice, and more complex methods of rescaling the estimated noise function are necessary. We examined three different methods of scaling the noise in this study, including white noise with $\sigma = 1$ (i.e., rescaling is not performed), variable white noise, and non-white noise. They are briefly described in Table 2 and referred to throughout the study by their Misiti *et al*. (2000) descriptors.

Table 2. Noise Rescaling Options (from Misiti *et al*., 2000)

Method	Comments
ONE	No rescaling.
SLN	Rescales the noise based on coefficients in the first level of the wavelet decomposition.
MLN	Determines a rescaling factor estimated from noise at each decomposition level. Best used for non-white noise or signals where the noise changes characteristics at some time (t) in the data.

Application to Noisy Synthetics. The Herrmann (2002) wavenumber-integration code was used to generate synthetic seismograms for an array of seismometers with similar configuration to the first 11 elements of the KSAR (Wonju, South Korea) array (e.g., KS01-KS11). The IASP91 velocity model was used to generate these synthetics (Kennett and Engdahl, 1991). We simulated a double-couple earthquake at a depth of 15 km approximately 430 km from the array.

To examine the performance of wavelet denoising in different SNR conditions, we applied both Gaussian white and autoregressive noise of varying levels to the synthetic signals. For the autoregressive noise, we used observed seismic noise from the KSAR array (denoted $x(t)$) and a white noise input, $w(t)$, to calculate an autoregressive model of order 2 (AR2) with the equation (Shumway and Stoffer, 2000)

$$x(t) = x(t-1) - 0.90\ x(t-2) + w(t)\,. \qquad (1)$$

Our AR2 model estimates the current value of a time series as a scaled function of the previous two values of the series. This type of model is frequently used to model noise series in which periodic behavior is observed. Examples of both Gaussian white and AR2 noise are shown in Figure 2.

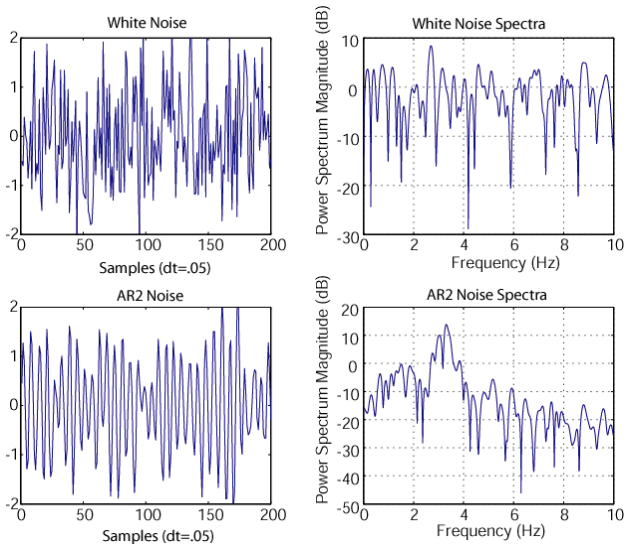


Figure 2. Examples of white and AR2 noise used in our evaluation of depth-phase denoising techniques. In practice, the amplitude of the noise was randomly scaled and added to the synthetic data.

Wavelet Denoising Results. We simulated 100 array recordings of the synthetic data using different Gaussian white or AR2 SNR levels ($0.7 < Pn$ SNR < 10). The synthetic data were windowed using traditional *f-k* techniques to determine an appropriate analysis window, which typically includes pre-event noise, the *Pn* arrival, and the signal prior to *Pg*. We then applied wavelet denoising using the wavelets shown in Figure 1, the thresholding routines listed in Table 1, and the rescaling options listed in Table 2. Figure 3 presents a comparison of wavelet denoising to standard Fourier filtering applied to a noisy regional signal containing depth phases.

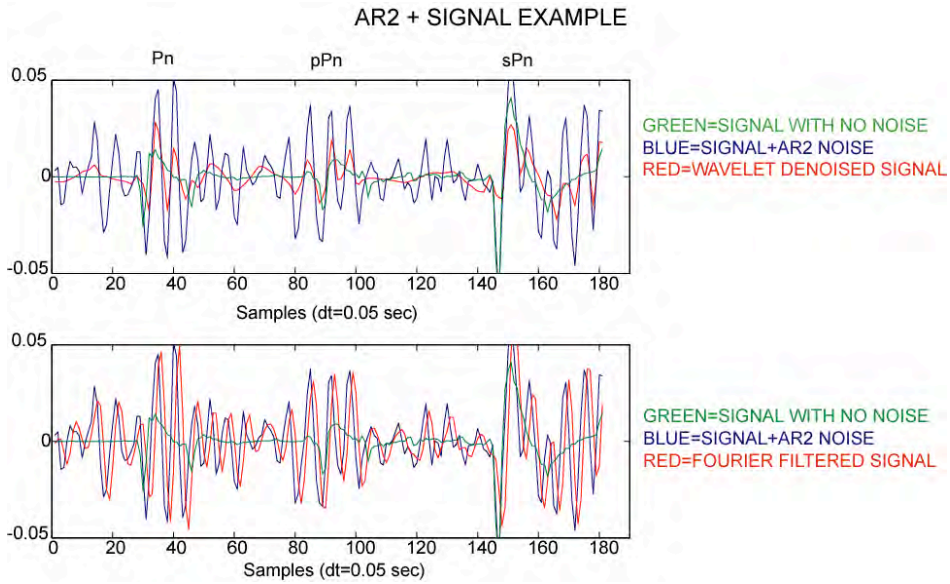


Figure 3. Comparison between wavelet denoising and Fourier filtering for synthetic *Pn*, *pPn*, and *sPn* arrivals contaminated with AR2 noise. (*Top*) Wavelet-denoised results (red), input noisy synthetic signal (blue), and noise-free synthetic signal (green). Wavelet denoising was performed using level-3 decomposition with the *sym4* wavelet, Heursure thresholding, and MLN rescaling. (*Bottom*) Fourier filtered results (red), input noisy synthetic signal (blue), and noise-free synthetic signal (green). We performed the Fourier filtering using a 3rd order band-pass filter (0.6 to 4.5 Hz).

To determine whether depth phase detection was improved by wavelet denoising compared to Fourier filtering, we input both the denoised and filtered waveforms into the cepstral F-statistic module of our depth phase processing tool (see Bonner *et al*., 2002), and potential depth phase candidates were selected. Figure 4 shows the results of the cepstral F-statistic processing for the case in which AR2 noise was added to the synthetic signals. These signals were then either Fourier filtered or wavelet denoised using all possible combinations of the processing options listed in Tables 1 and 2. The top plot in Figure 4 shows the ratio of the number of detections that were associated with the primary depth phases (hits; within ±0.25 seconds of IASP91-predicted depth phase arrival time) compared to the detections that were either artifacts of the filtering, noise-related, or multiple echoes (misses). The ratio for the Fourier filtering results is approximately 1.2 for the AR2 noise case. In contrast, the ratio for the wavelet-denoised data varies from as small as 1.2 to as high as 27 true detections per every false alarm. In the lower subplot the number of hits and misses per possible depth-phase candidate solutions is shown. The Heursure method of thresholding (see Table 1 for a description) with SLN rescaling consistently provides multiple successful hits and few misses at all decomposition levels when compared with the other results. The related Rigrsure method with SLN scaling also provides a high number of successful hits to misses. However, it is the Sqtwolog thresholding method using SLN rescaling that provides the highest success-to-failure ratios at all decomposition levels.

Although it not is shown here, we note that for white noise, the Heursure method of thresholding with SLN rescaling consistently provides the most successful hits and the least number of misses when compared with the other results. We also note, however, that the improvement offered by wavelet denoising over the Fourier filtering techniques is smaller than for the AR2 noise case.

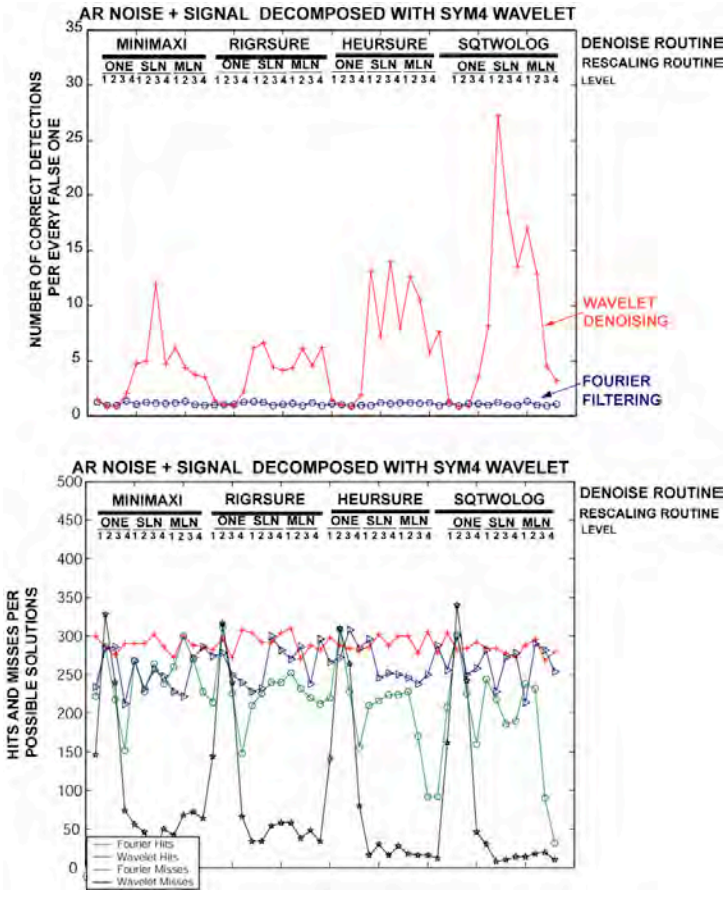


Figure 4. Cepstral F-statistic depth phase detection success to failure rates (top) and hits and misses (bottom) for standard Fourier filtering and wavelet denoising of synthetic data contaminated by AR2 noise. The denoising was accomplished using a sym4 wavelet at decomposition levels 1-4, thresholding routines including Minimax, Heursure, Rigrsure, and Sqtwolog, and rescaling models including ONE, SLN, and MLN. See Tables 1 and 2 for explanations.

Depth-Phase Detection Using Optimal (Wiener) Filtering. In the results presented thus far, we used a standard bandpass Fourier filter (0.6 to 4.5 Hz) that is frequently used in regional seismic applications. However, other types of Fourier filters are likely to be superior to the standard filtering technique. For example, we have compared the ability of wavelet denoising to find depth phases in noisy seismograms to that of an optimal (or Wiener) filter (Der and Shumway, 2000). To perform Wiener filtering, we place a 1.5-second "signal" window around the noisy synthetic *Pn* arrival and compute the Fourier transform of the signal and noise windows. We use the magnitude response for each of these windows and recursively design a filter to match these spectra. This Wiener filter is then applied to the noisy data and the result input into the cepstral F-statistic for depth phase analysis.

The results indicate that use of the Wiener filter improves success-to-failure rates for depth phase detections in white noise compared to wavelet denoising and standard Fourier filtering. This improved detection rate is a result of fewer false alarms, but comes at the expense of fewer detections. When AR2 noise is added to the signal, the Wiener filter again provides increased performance over the standard Fourier filtering. Also, wavelet denoising and Wiener filtering have similar false alarm rates for the AR2 noise case; however, the wavelet denoising results in increased detections of depth phases. Overall, these results suggest that Wiener filters can be designed that compete with wavelet denoising in terms of improved depth-phase detection capabilities.

Denoising Applied to Regional KSAR Data for Improved Depth Phase Detection

We applied the standard Fourier, wavelet denoising and Wiener filtering techniques to a small test data set of regional waveforms recorded at the South Korean seismic array (KSAR). We determined the optimum denoising parameters for these data and examined the extent to which the new filtering methods increase depth phase detection capabilities. We note that for this phase of the project, our focus was not on blind testing of the method. Our objective was to determine if the denoising procedure could improve depth phase detection, which dictated that we know *a priori* where the depth phase detections actually occurred. In the following sections, we present depth-phase detection results from two events in this waveform database. Further analysis will be completed during future research on this project.

Honshu, Japan. The first example is an event with m_b=4.7 from the Honshu region of Japan, located by the preliminary International Data Center (pIDC) at a depth of 22 km (based on multiple teleseismic depth phase arrivals). The event occurred approximately due east of KSAR at an epicentral distance of 10.2 degrees (Figure 5A). Although KSAR has 19 short-period elements, we processed a subset of the first 11 elements (Figure 5B) to imitate the number of short-period elements in prototype regional arrays that have recently been installed in important monitoring regions. The *Pn* arrival for this event at KSAR has large SNR (Figure 5C); however, the signal-generated noise is also large and may be obscuring the possible depth phases. *F-K* array processing (Figure 5D) on the first 25 seconds of data following the initial *P*-wave suggests there is no clear *Pb* or *Pg* arrival, thus the depth-phase analysis includes 25-second windows of both noise and signal.

We performed cepstral F-statistic analyses on these data following wavelet denoising (Figure 6A), standard Fourier filtering (Figure 6B), and Wiener filtering (Figure 6C). The array beam resulting from the application of these filtering/denoising techniques is presented in the upper subplot of each cepstral analysis. In the lower subplots, the cepstral F-statistic analysis is time aligned to the *P*-wave arrival. The initial 2 seconds of cepstral results are not plotted, because large amplitude peaks caused by non-varying direct current (DC) offsets that occur in the log spectra. For the wavelet denoising, we used Heursure thresholding and a *sym4* wavelet decomposed at level 6. The Fourier filtering was accomplished using a Butterworth bandpass filter between 0.6 and 4.5 Hz, and the Wiener filtering was completed by centering a 1.5-second signal window on the *Pn* arrival. The IASP91-predicted travel time arrivals for this event are shown above the top subplot in each of these analyses.

We note that wavelet denoising produces clean waveforms that highlight the regional depth phases. Additionally, cepstral F-statistic results for the denoised data shows a very large peak that corresponds to the *pPn* arrival and a smaller statistically significant peak (at a 99% significance level) for the *sPn* arrival. For the wavelet denoising results, we only note two additional peaks that do not correspond to the predicted arrival of the depth phases (i.e., false detections). The standard Fourier and Wiener filtering also detect the depth phases; however, the number of false detections is up by a factor of three over the wavelet-denoised data. The improvement in success to failure rates noted on these real data are similar to the rates observed from the analysis of the synthetic data presented earlier.

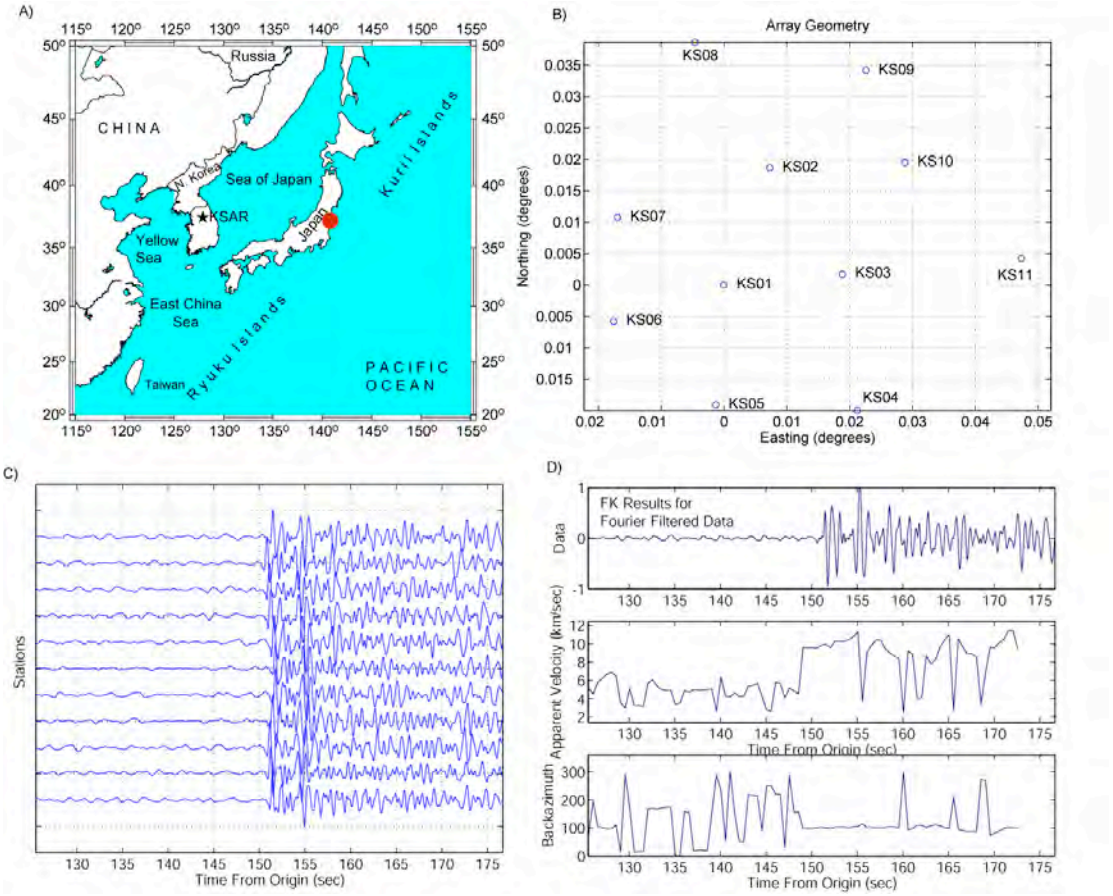


Figure 5. Array processing for Honshu, Japan event (pIDC EVID 1259474). A) Location of event and KSAR array. B) KSAR elements used in the processing. C) Unfiltered seismic records for KSAR stations shown in subplot B. D) *f-k* results showing sample data, phase velocity, and backazimuth. The *f-k* results are used to pick the analysis window.

Kuril Islands. The second example presented is an m_b=4.5 event from the Kuril Islands, located by the pIDC at a depth of 30.1 km and 16.6 degrees northeast of KSAR (Figure 7A). KS01 was not available for this event, so we show only 10 elements in Figure 7B, with KS02 as the new reference station. The *f-k* array processing (Figure 7D) reveals a slowly-propagating, off-azimuth arrival near 250 seconds and a fast arrival near 255 seconds after origin (with a 4-second window length in the *f-k* analysis). To avoid contamination from these arrivals, which may or may not be associated with the event of interest, the cepstral analysis window was ended prior to these arrivals. The results of the cepstral analysis are shown in Figure 8, and we note that wavelet denoising best highlights the regional depth phases. The cepstral F-statistic results for the wavelet-denoised data show a large peak that corresponds to the *pPn* arrival; however, the peak for the *sPn* arrival is not statistically significant at the 99% level. The Wiener filtering method also detects the *pPn* depth phase and two false detections, while standard Fourier filtering had no correct depth phase detections.

CONCLUSIONS AND RECOMMENDATIONS

Accurate estimation of the depth of small, regionally recorded events continues to be an important and difficult monitoring research problem. In our previous studies we have focused on the extraction of depth phases from body waves, with varied degrees of success at regional distances. In this paper, we demonstrated that wavelet denoising shows promise in improving depth phase detectability on complex regional seismograms. To further enhance regional focal depth estimation accuracy, we believe other technologies that utilize different features of the seismic waveform must be exploited. Therefore, the primary goal of the next stage of our project will be to develop a

synergistic tool that combines three different methods to estimate the depth of regional seismic events. These methods include 1) improved depth phase detection in the complex *Pn* coda of regional seismograms; 2) sparse-network hypocenter locations with associated Monte-Carlo confidence regions that incorporate regional primary and depth phase arrivals; and 3) surface-wave spectral amplitude inversions for depth. We will then use rigorous statistical analyses to combine these three different methods into a depth and associated confidence estimate.

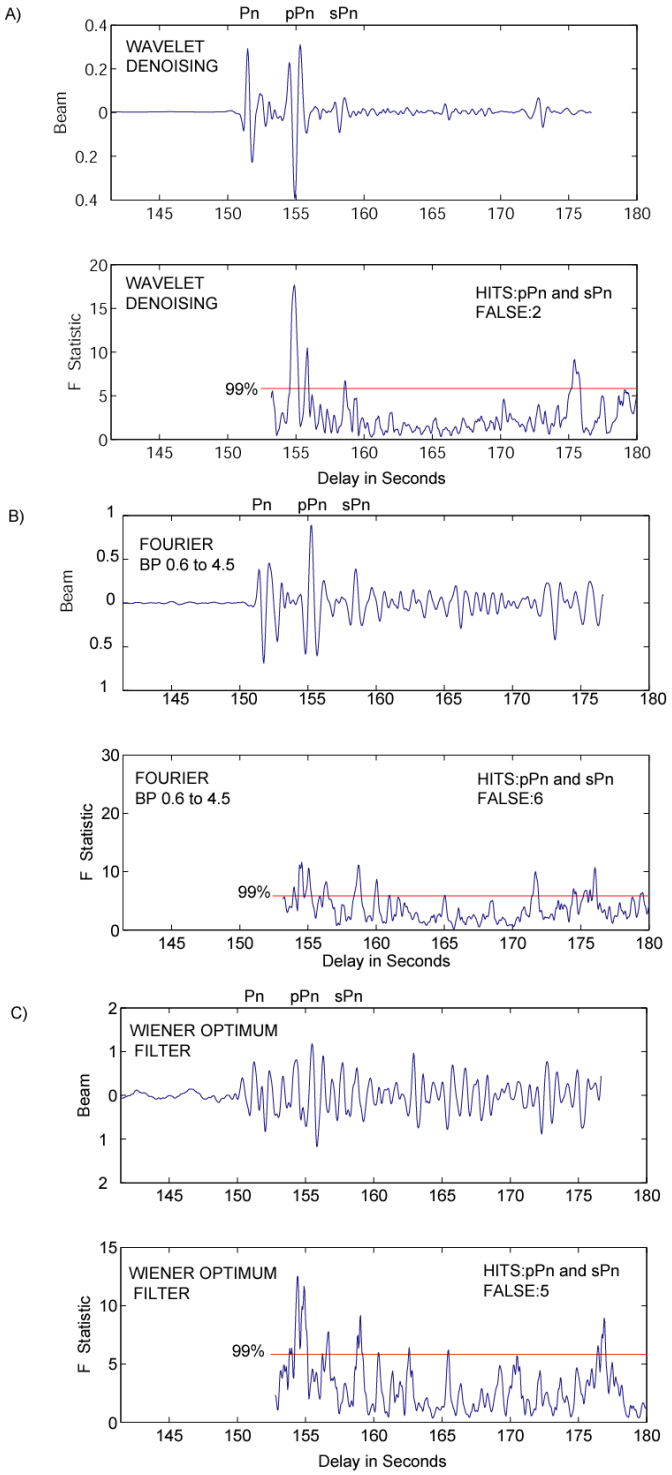


Figure 6. Cepstral F-Statistic processing for the Honshu, Japan event (pIDC EVID 1359474). A) *Top*: Array beam of wavelet-denoised data. The IASP91 predicted times of the depth phases are indicated above the top subplot. *Bottom*: Results of applying the cepstral F-statistic method to wavelet-denoised data (red line is the 99% significance level). The cepstral F-statistic is time aligned to the *P*-wave arrival; the initial 2 seconds of cepstral results are not plotted due to large amplitude peaks caused by a DC offset in the spectra. B) *Top*: Array beam of Fourier-filtered data. *Bottom*: Results of applying the cepstral F-statistic method to standard Fourier-filtered data. C) *Top*: Array beam of Wiener-filtered data. *Bottom*: Results of applying cepstral F-statistic method to Wiener-filtered data.

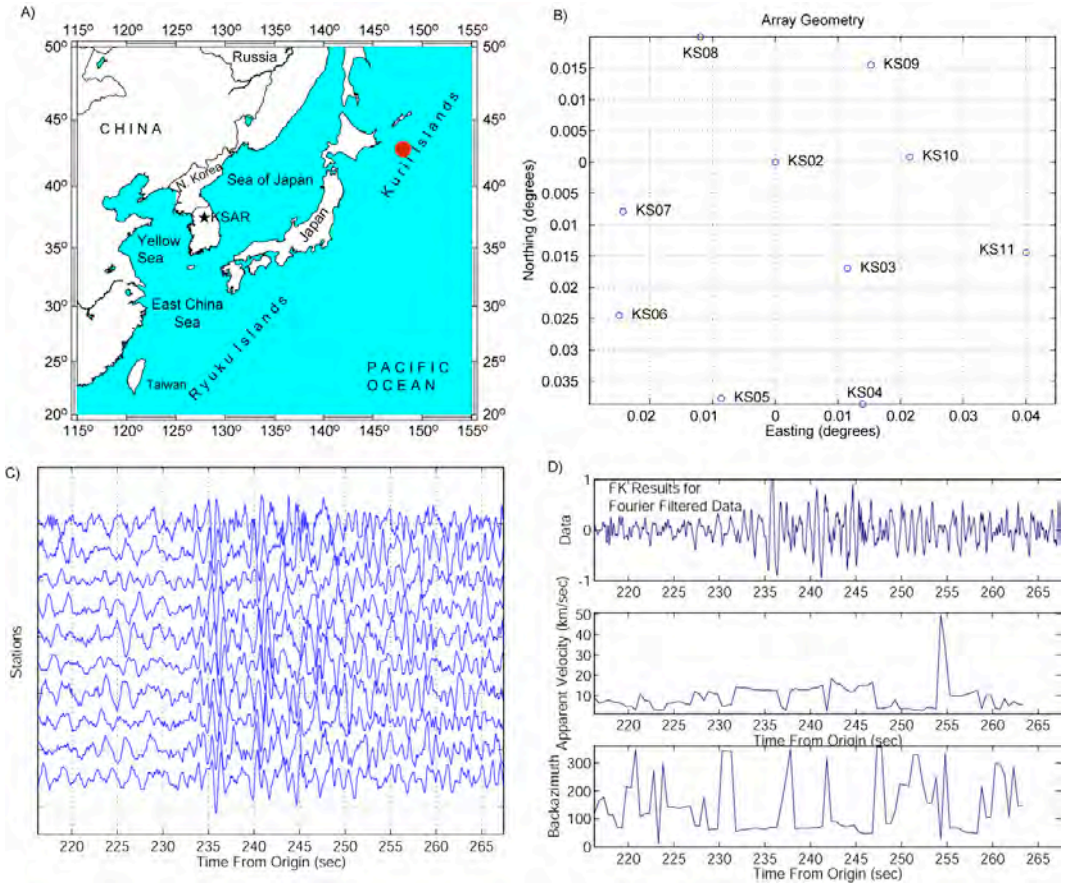


Figure 7. Array processing for Kuril Islands event (pIDC EVID 21380185). A) Location of event and KSAR array. B) KSAR elements used in the processing. C) Unfiltered seismic records for KSAR stations shown in subplot B. D) *F-K* array processing results showing sample data, phase velocity, and backazimuth.

REFERENCES

Anant, K. S. and F. U. Dowla (1997), Wavelet transform methods for phase identification in three-component seismograms, *Bull. Seis. Soc. Am.*, 87, 1598-1612.

Bonner, J. D.T. Reiter, and R. H. Shumway (2002), Application of a cepstral F statistic for improved depth estimation, *Bull. Seism. Soc. Am*, 92, 1675-1693.

Daubechies, I. (1992), Ten lectures on wavelets*, Regional Conference Series in Applied Mathematics*, Vol. 61.

Der, Z. and R. H. Shumway (2000), Automatic interpretation of regional seismic signals using the CUMSUM-SA algorithms, *Proceedings* of the 21st Annual Seismic Research Symposium on Monitoring a Comprehensive Nuclear Test Ban Treaty, 393–403.

Herrmann, R. B. (2002), Computer Programs in Seismology Version 3.15, St. Louis University.

Kennett B. L. N., and E. R. Engdahl (1991), Travel times for global earthquake location and phase identification, *Geophys. J. Int.,* 105, 429-465.

Mallat, S. (1999). A Wavelet Tour of Signal Processing. Academic, San Diego, 2nd edition.

Misiti, M., Misiti, Y., Oppenheim, G. and J. Poggi, (2000), *Wavelet Toolbox*, *ForUse with Matlab*, © Copyright 1996 by the MathWorks, Inc.

Shumway, R. H., and D. S. Stoffer (2000), Time Series Analysis and its Applications. Springer Verlag.

Strang, G., and T. Nguyen (1996), *Wavelets and Filter Banks*, Wellesley-Cambridge Press.

Tibuleac, I.M. (2003). Wavelet pre-processing for stable magnitude estimation and spectral mb magnitudes. Weston Geophysical Scientific Report

Zhang, H., C. Thurber and C. Rowe (2003), Automatic P-wave arrival detection and picking with multiscale wavelet analysis for single-component recordings, *Bull. Seism. Soc. Am.*, 93, 1904 – 1912.

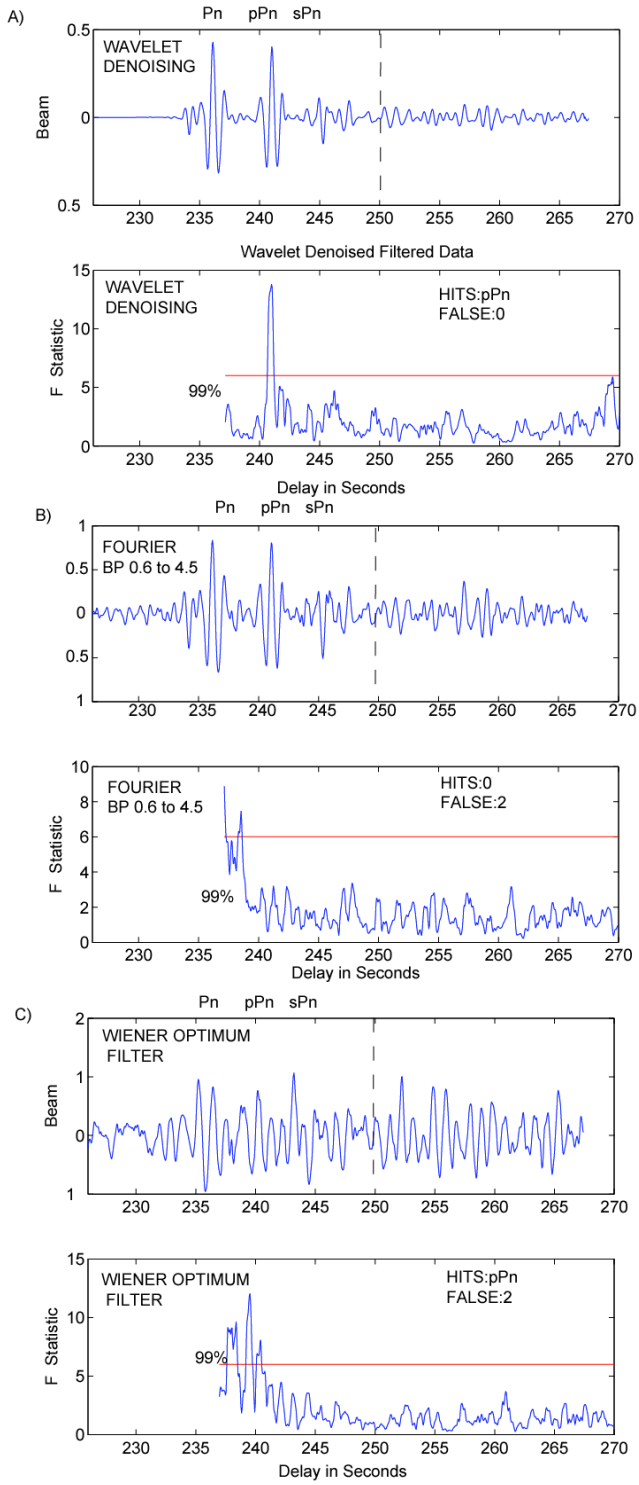


Figure 8. Cepstral F-Statistic processing for Kuril Islands event (pIDC EVID 21380185). A) *Top*: Array beam of wavelet-denoised data. The IASP91 predicted times of the depth phases are indicated above the top subplot. The dashed line shows the end of the cepstral analysis window. *Bottom*: Results of applying the cepstral F-statistic method to wavelet-denoised data (red line is the 99% significance level). The cepstral F-statistic is time aligned to the *P*-wave arrival; the initial 2 seconds of cepstral results are not plotted due to large amplitude peaks caused by a DC offset in the spectra. B) *Top*: Array beam of Fourier-filtered data. *Bottom*: Results of applying the cepstral F-statistic method to standard Fourier-filtered data. C) *Top*: Array beam of Wiener-filtered data. *Bottom*: Results of applying cepstral F-statistic method to Wiener-filtered data

RESEARCH IN REGIONAL SEISMIC MONITORING

Frode Ringdal[1], Tormod Kvaerna[1], Elena O. Kremenetskaya[2], Vladimir E. Asming[2], Sergeij Kozyrev[2], Svein Mykkeltveit[1], Steven J. Gibbons[1], and Johannes Schweitzer[1]

NORSAR[1], Kola Regional Seismological Centre[2]

Sponsored by Army Space and Missile Defense Command

Contract No. F08650-01-C-0055

ABSTRACT

This project represents a continuing research effort aimed at improving seismic monitoring tools at regional distances, with emphasis on the Barents/Kara Sea region, which includes the former Novaya Zemlya test site. The tasks comprise development and improvement of detection, location and discrimination algorithms as well as experimental on-line monitoring using tools such as regional Generalized Beamforming (GBF) and Threshold Monitoring (TM). It also includes special studies of mining events, for which detailed ground truth information is being provided by the Kola Regional Seismological Centre (KRSC).

Data from the regional networks operated by NORSAR and KRSC were used to assess the seismicity and characteristics of regional phases of the European Arctic. KRSC has for the past 10 years provided to NORSAR ground truth information for selected mining explosions in the Kola Peninsula. Since 2001, the project has been expanded in scope, and is currently carried out jointly with Lawrence Livermore National Laboratory (LLNL), in a Department of Energy (DOE) funded project. This ground truth information comprises accurate locations, charges and explosion characteristics, relating to large underground and surface ripple-fired explosions as well as smaller “compact” underground explosions. The Mining Institute of the Kola Science Centre has made a video recording of two large explosions (one surface and one underground) on 16 November 2002. This video has been made available to us, and the paper presents selected snapshots of the explosions.

Significant progress has been made in automating the detection and location of seismic events from selected areas. In particular, we have continued to improve the regional processing currently carried out at NORSAR for the European Arctic. The emphasis has been on automatic detection and association of phases for small seismic events in the Novaya Zemlya region, using the on-line Generalized Beamforming (GBF) process. The number of false associations can be reduced by 90 percent through relatively simple selection criteria, while still retaining the “real” seismic events. Furthermore, some possibilities for additional future improvements are discussed, including the development of a systematic automatic post-processing algorithm to be applied to event candidates produced by the GBF process currently in operation. Examples of recent small seismic events at Novaya Zemlya detected by the regional network are presented.

A study of location accuracy for seismic events near the Spitsbergen archipelago is illustrated. In cooperation with KRSC, more than 200 earthquakes occurring during the first half of 2003 with epicenters in Spitsbergen and adjacent areas have been relocated. We have compared our location results with those published in the Reviewed NORSAR Regional Bulletin, which makes use of the same station network. Additionally, we compared both of these interactive location results to the automatic location provided by the on-line GBF procedure at NORSAR. The Spitsbergen region is geologically far more complex than Fennoscandia, and multiple arrivals of P and S phases are quite common. Consequently, different phase interpretation by different analysts result in occasionally large deviations in location estimates, sometimes as much as 100 km for events located by the SPITS array alone. Some possibilities for future enhancements of the event location procedures are discussed.

OBJECTIVES

This work represents a continued effort in seismic monitoring, with emphasis on studying earthquakes and explosions in the Barents/Kara Sea region, which includes the former Russian nuclear test site at Novaya Zemlya. The overall objective is to characterize the seismicity of this region, to investigate the detection and location capability of regional seismic networks and to study various methods for screening and identifying seismic events in order to improve monitoring of the Comprehensive Nuclear-Test-Ban Treaty (CTBT). Another objective is to carry out special studies of mining events, for which detailed ground truth information is being provided by the Kola Regional Seismological Centre.

RESEARCH ACCOMPLISHED

Introduction

NORSAR and Kola Regional Seismological Centre of the Russian Academy of Sciences have for many years cooperated in the continuous monitoring of seismic events in northwest Russia and adjacent sea areas. The research has been based on data from a network of sensitive regional arrays which has been installed in northern Europe during the last decade in preparation for the CTBT monitoring network. This regional network, which comprises stations in Fennoscandia, Spitsbergen and NW Russia, provides detection capability for the Barents/Kara Sea region that is close to m_b = 2.5 (Ringdal, 1997).

The research carried out during this effort is documented in detail in several contributions contained in the NORSAR Semiannual Technical Summaries. In the present paper we will limit the discussions to some recent results of interest in the general context of regional monitoring of seismic events in the European Arctic. In particular our studies have focused on mining explosions in the Kola Peninsula, using data from stations shown in Figure 1. This figure also shows some of the most active mining areas.

Khibiny mine explosions

Data from the regional networks operated by NORSAR and KRSC was used to assess the seismicity and characteristics of regional phases of the European Arctic. KRSC has for the past 10 years provided to NORSAR ground truth information for selected mining explosions in the Kola Peninsula. Since 2001, the project has been expanded in scope, and is currently carried out jointly with Lawrence Livermore National Laboratory, (Harris *et. al.*, 2003). This ground truth information comprises accurate locations, charges and explosion characteristics, relating to large underground and surface ripple-fired explosions as well as smaller “compact” underground explosions.

Of particular interest are two explosions, one underground and one at the surface carried out in the Rasvumchorr mine in Khibiny on 16 November 2002. These explosions were briefly discussed in Ringdal *et al.* (2003). Additional information will be presented in this paper. As illustrated in Figures 2 and 3, the underground explosion was a ripple-fired explosion of 257 tons, whereas the open-pit explosion comprised four separate ripple-fired explosions, set off at approximately one-second intervals, from south to north. The surface and underground explosions were only 300 m apart so that differences in path effects, at the more distant stations, can be ignored. Nevertheless, the recorded signals, at the temporary station in Ivalo, Finland at 300 km distance, were remarkably different. The vertical component of these recordings is shown in Figure 4 in different filter bands. At lower frequencies (2-4 Hz), the underground explosion was stronger by a factor of 10 in amplitude, whereas above 10 Hz, the surface explosion had, by far, the stronger signals. The Mining Institute of the Kola Science Centre made a video recording of these explosions. This video was made available to us, and Figure 5 shows selected snapshots of the explosions.

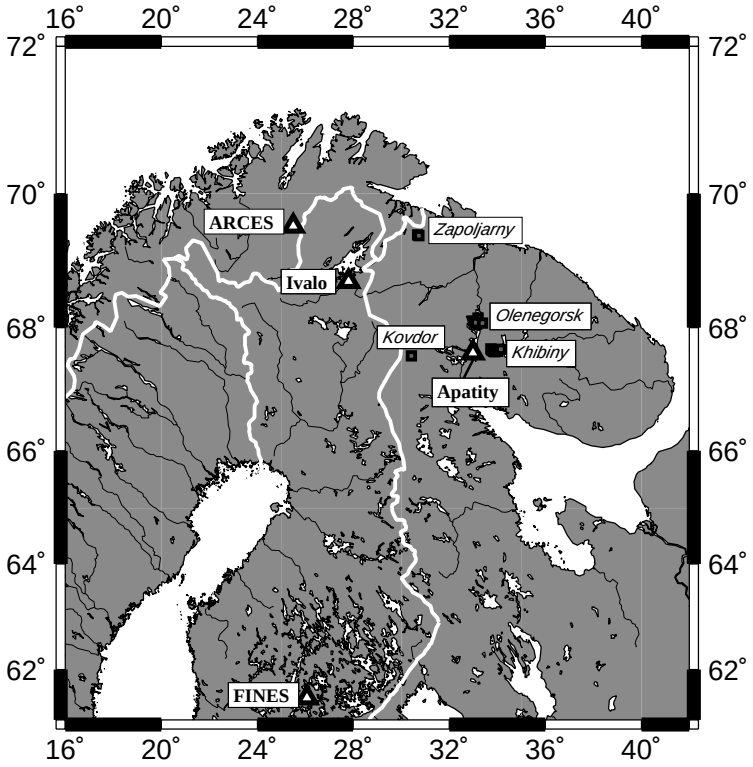


Figure 1. Seismic stations (triangles) used in our studies of mine explosions in Kola Peninsula. The main mining sites are marked as squares. The station Ivalo is one of six temporary stations established in cooperation with LLNL.

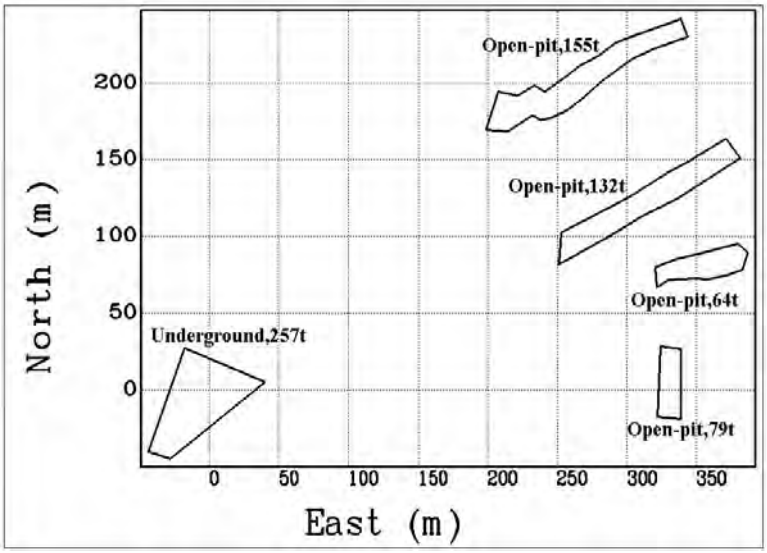


Figure 2. Schematic view of the shot configuration for the two explosions in Khibiny on 16 November 2002. Geographical coordinates of the point (0,0) are 67.6322N 33.8565E. See text for details.

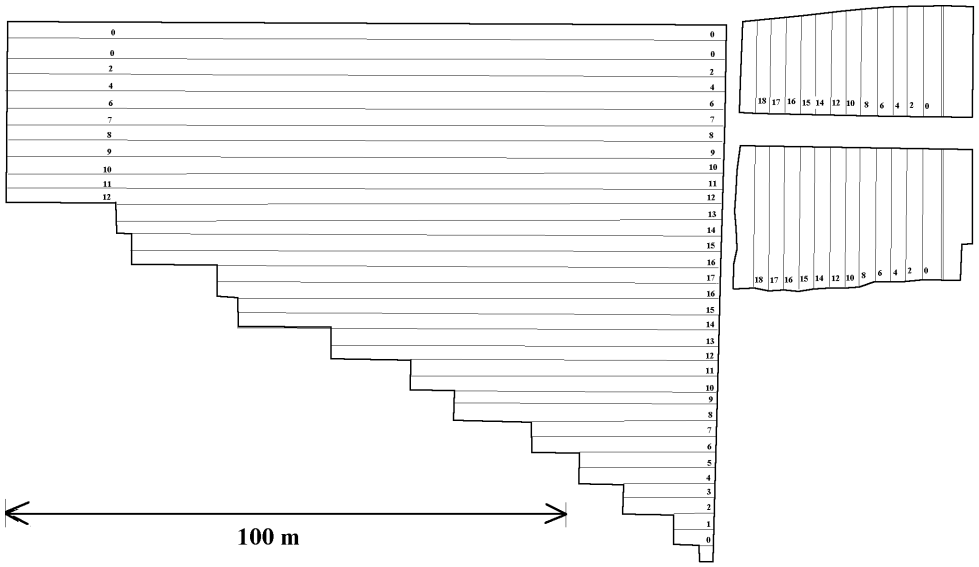


Figure 3. Geometry of the underground mining explosion in Khibiny 16 November 2002. The charges were detonated in 19 groups (delay 23 ms between each group). The sequence is indicated by the numbers, and individual charge sizes have been made available.

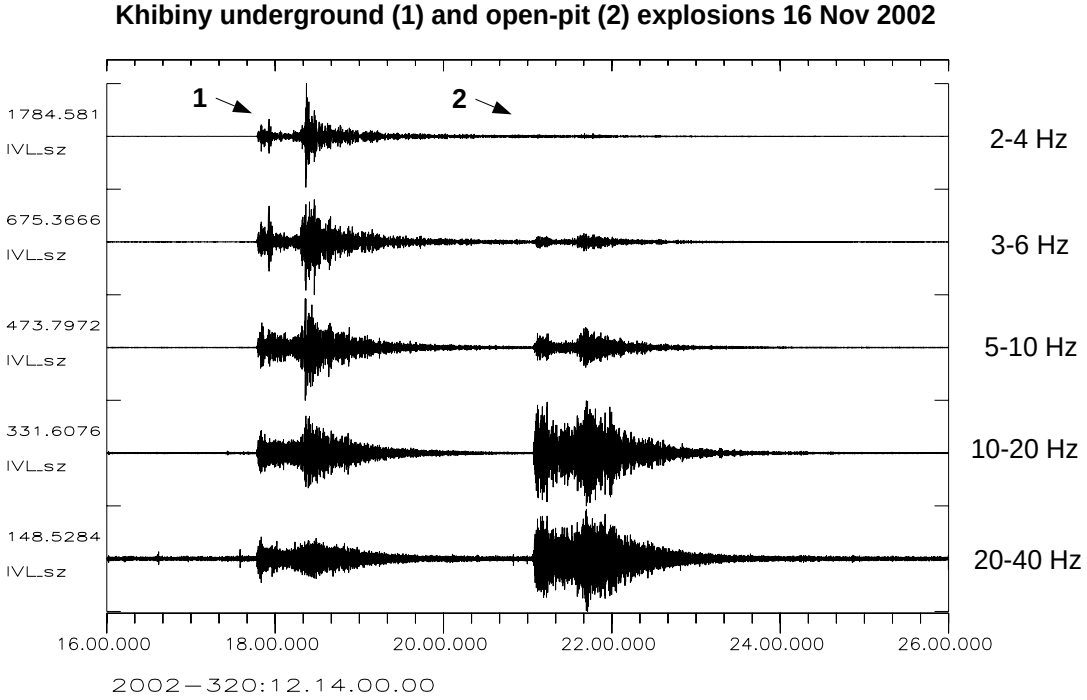
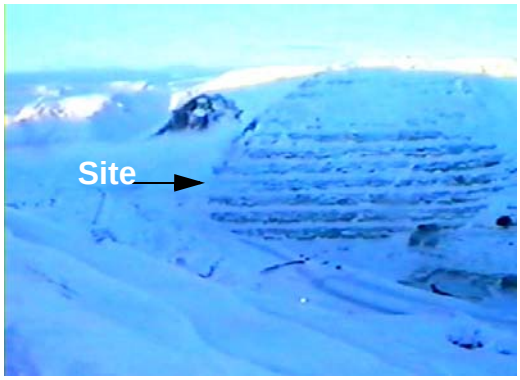
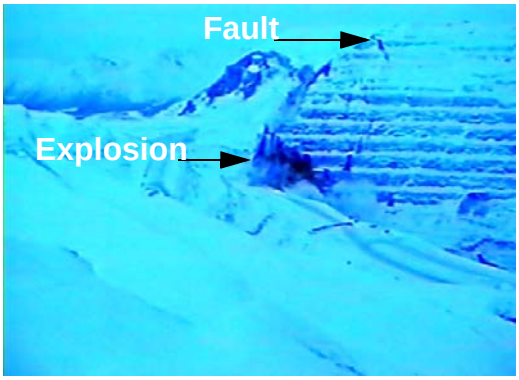


Figure 4. Recorded SPZ waveforms at station Ivalo (northern Finland) for the two explosions in Khibiny on 16 November 2002. The data have been filtered in five different frequency bands. Note the significant difference in relative size of the two events as a function of frequency.

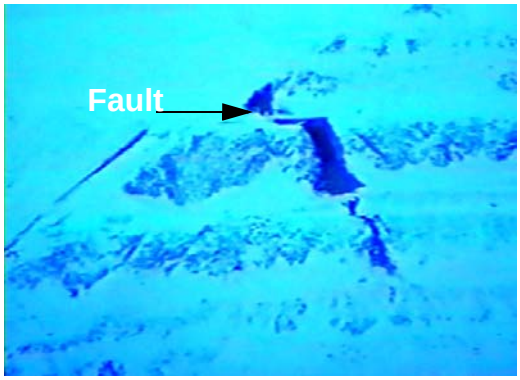
Khibiny Massif



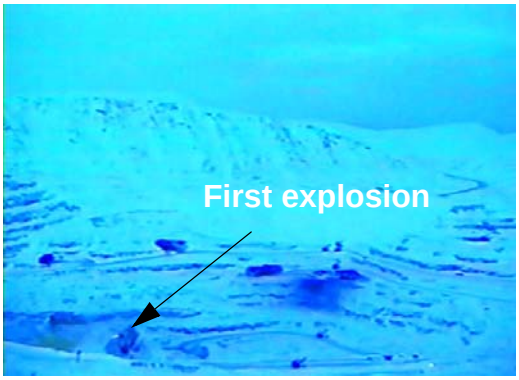
Underground explosion



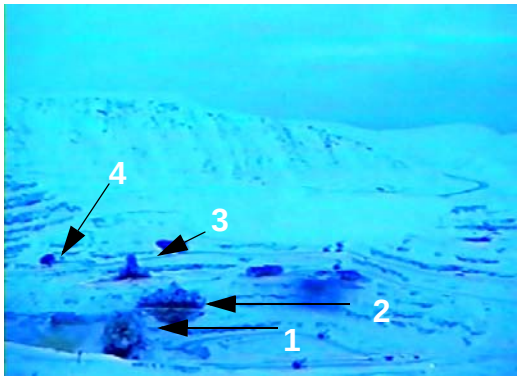
Close-in view of fault after 5 minutes



First surface explosion



The four surface explosions (1,2,3,4)



Five seconds after first surface explosion

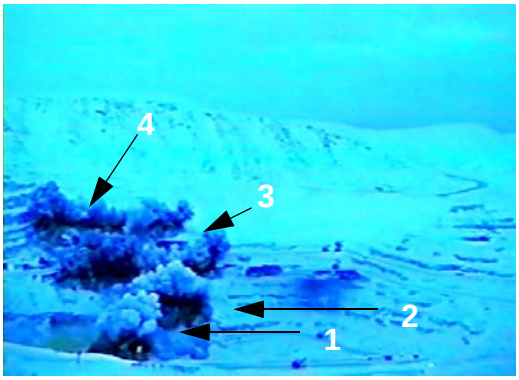


Figure 5. Snapshots of video from the sequence of Khibiny explosions on 16 November 2002. Note in particular the large crack ("fault") opening up in the mountainside at the time of the first (underground) explosion.

Developing NORSAR's regional processing system

NORSAR has for a number of years carried out processing and analysis of seismic events in the European Arctic, using the regional array network in Fennoscandia and NW Russia. The regional processing system at the NORSAR Data Center comprises the following steps:

- Automatic single array processing, using a suite of bandpass filters in parallel and a beam deployment that covers both P and S type phases for the region of interest.
- An STA/LTA detector applied independently to each beam, with broadband f-k analysis for each detected phase in order to estimate azimuth and phase velocity.
- Single-array phase association for initial location of seismic events, and also for the purpose of chaining together phases belonging to the same event, so as to prepare for the subsequent multi-array processing.
- Multi-array event detection, using the GBF approach (Ringdal and Kværna, 1989) to associate phases from all stations in the regional network and thereby provide automatic network locations for events in all of northern Europe. The resulting automatic event list is made available on the Internet (www.norsar.no).
- Interactive analysis of selected events, resulting in a reviewed regional seismic bulletin, which includes hypocentral information, magnitudes and selected waveform plots. This reviewed bulletin is also available on the Internet.

Monitoring the Novaya Zemlya region

The philosophy behind the automatic process at NORSAR is to ensure, as far as possible, that no real detectable event is lost. The penalty is that a number of false associations are generated. This problem is most significant for regions at large distances from the arrays, such as the Novaya Zemlya region. We describe below some initial steps undertaken to eliminate many of these false associations.

It is well known that the most sensitive arrays for seismic events in the Novaya Zemlya region are ARCES and SPITS. Our initial step to reduce the number of false associations is therefore to require detection by one or both of these two arrays, using a combination of the following criteria:

1. Pn and Sn detections by SPITS
2. Pn and Sn detections by ARCES
3. Pn detections by both SPITS and ARCES

In addition, we have experimented with additional constraints on Pn phase velocities for the two arrays, in order to eliminate obvious teleseismic or near-regional phases. Reasonable constraints, based on observational evidence, are:

- For ARCES: Pn velocity between 8-12 km/s
- For SPITS: Pn velocity between 7-10 km/s

Furthermore, we have considered the effects of constraining the acceptable difference in estimated azimuth for the P and S phase, by removing single-station events that have an azimuth difference (P-S) exceeding 15 degrees.

Table 1 gives an overview of the number of GBF event candidates located in the region surrounding Novaya Zemlya for the years 2002 and 2003. The geographical limits are 70-78 degrees north, 50-70 degrees east. The counts using the current on-line GBF algorithm as well as the counts requiring detection by ARCES and SPITS, and counts imposing additional constraints are given.

Table 1 GBF event candidates 70-78 deg N, 50-70 deg E

Detection criterion	ARCES Pn velocity	SPITS Pn velocity	Az. diff.	Total 2002	Total 2003	Sum
All GBF	All	All	All	683	950	1733
1 or 2 or 3	All	All	All	294	382	676

Table 1 GBF event candidates 70-78 deg N, 50-70 deg E

Detection criterion	ARCES Pn velocity	SPITS Pn velocity	Az. diff.	Total 2002	Total 2003	Sum
1 or 2 or 3	8-12 km/s	7-10 km/s	All	177	211	388
1 or 2 or 3	8-12 km/s	7-10 km/s	<15 deg	66	81	147

The criteria specified in the table are conservative in the sense that they should not eliminate any potential real seismic events occurring in this region. Nevertheless, the table above indicates that the number of event candidates is reduced by about 90 percent when applying the final (strongest) test.

We note that the significant reduction in false detections when imposing the azimuth constraint is due to a wide azimuth window currently applied in the GBF processing. The GBF algorithm allows phases to be associated to the same event if they deviate less than 30 degrees from the grid point toward which the generalized beam is steered. This implies that P and S phases associated to a given event could (in extreme cases) differ by up to 60 degrees, which is clearly excessive. There is consequently a good argument for adding a more restrictive azimuth test in the second step of the on-line GBF process.

Table 2: List of seismic events in or near Novaya Zemlya (1980-2003) located outside the test site

Date/time	Location	m_b	Comment
01.08.86/ 13.56.38	72.945 N, 56.549 E	4.3	Located by Blacknest, UK
31.12.92/ 09.29.24	73.600 N 55.200 E	2.7	Located by NORSAR
23.02.95/ 21.50.00	71.856 N, 55.685 E	2.5	Located by NORSAR
13.06.95/ 19.22.38	75.170 N, 56.740 E	3.5	Located by NORSAR
13.01.96/ 17.17.23	75.240 N, 56.660 E	2.4	Approximately co-located with preceding event
16.08.97/ 02.11.00	72.510 N, 57.550 E	3.5	Located by NORSAR
16.08.97/ 06.19.10	72.510 N, 57.550 E	2.6	Co-located with preceding event
23.02.02/ 01.21.14	74.047 N, 57.671 E	3.0	Located by NORSAR
08.10.03/ 23.07.10	75.645N, 63.345E	2.5	Located by NORSAR

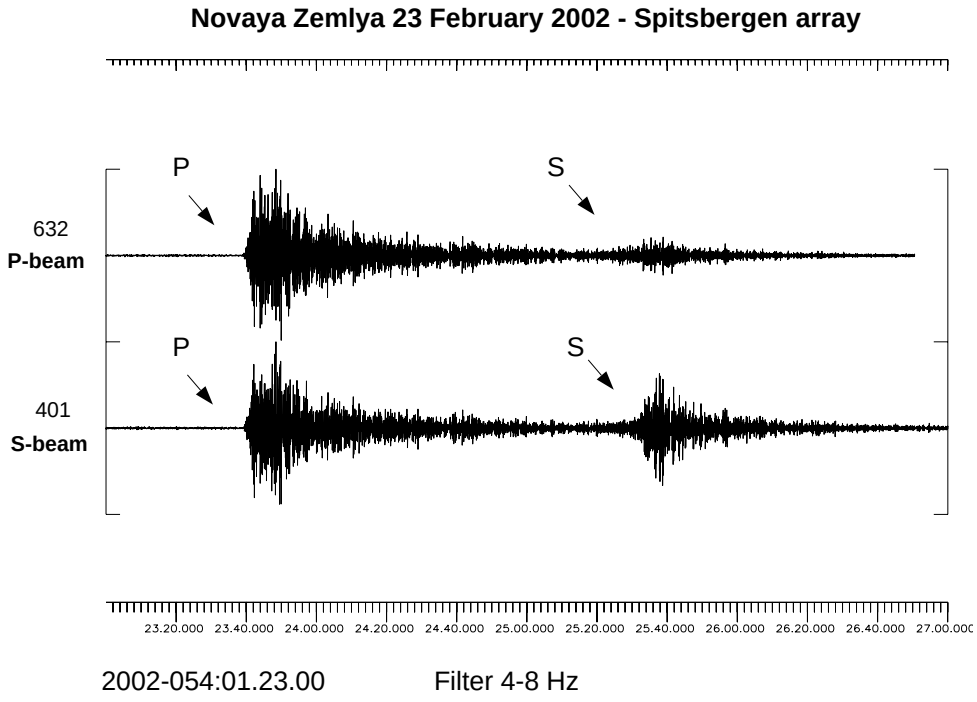


Figure 6. Spitsbergen P and S beams for the Novaya Zemlya event on 23 February 2002

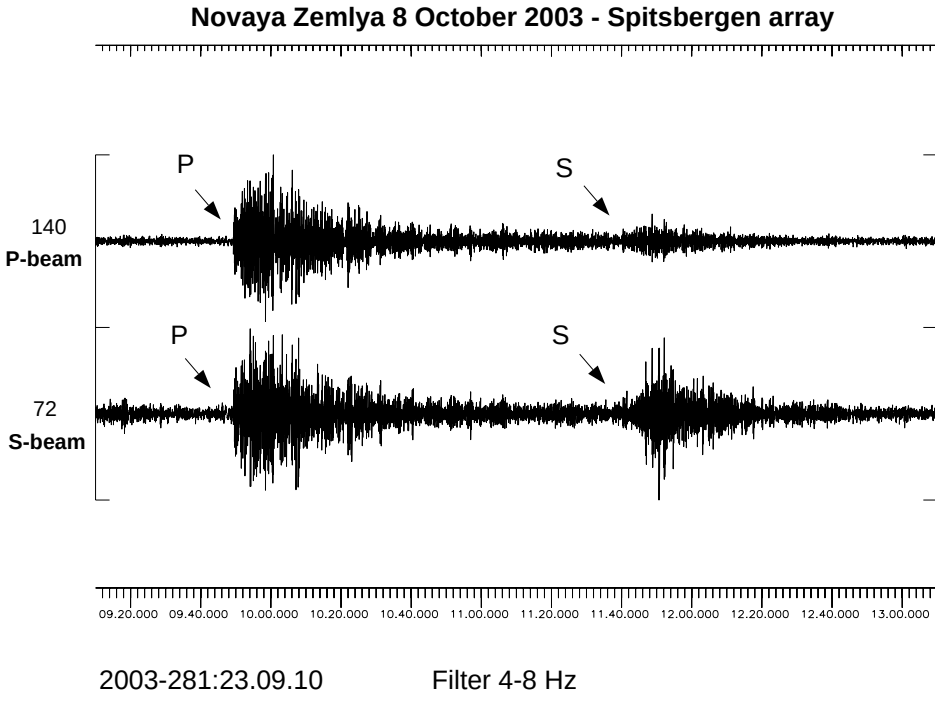


Figure 7. Spitsbergen P and S beams for the Novaya Zemlya event on 8 October 2003

Examples of recent low-magnitude events

Small events in the Novaya Zemlya region located outside the test site and detected over the years by the NORSAR regional processing are listed in Table 2. Recordings of the two most recent events are illustrated in Figures 6 and 7. The first figure shows a magnitude 3.0 event on 23 February 2002, as recorded by the SPITS array. Two filtered (4-8 Hz) array beams are displayed, corresponding to Pn and Sn velocities and directed towards the epicenter. The high signal-to-noise ratio (SNR) is noted for the P-phase and also that the S-phase is clearly detected on the S-beam. The second event (magnitude 2.5) occurred on 8 October 2003, and Figure 7 shows the SPITS Pn and Sn beams for this event. The waveforms have similar characteristics to those observed for the 23 February 2002 event. This event illustrates the importance of including, in the detection criteria, single-station detections (P and S phases detected at the same array) as well as events detected at both arrays. In fact, there was no automatic detection of this event at ARCES. However, by inspecting the ARCES waveforms visually, P and S onsets could be found, and were included in the reviewed event location in Table 2.

Locating small events near Spitsbergen

The geology of the Spitsbergen archipelago and surrounding regions is complex, and results in very complex seismograms from some areas. Multiple onsets of P and S waves are not uncommon, and can strongly increase location errors. More than 200 small earthquakes (mostly of magnitude around 2.0) occurring during the first half of 2003 with epicenters in Spitsbergen and adjacent areas were relocated. All of these events were detected by at least two stations (usually KBS and SPITS, sometimes with the addition of ARCES and other distant stations). We compared our location results with those published in the Reviewed NORSAR Regional Bulletin, which makes use of the same station network. Additionally, both of these interactive location results were compared to the automatic location provided by the on-line GBF procedure at NORSAR. Detailed results are presented in Asming *et. al.* (2004).

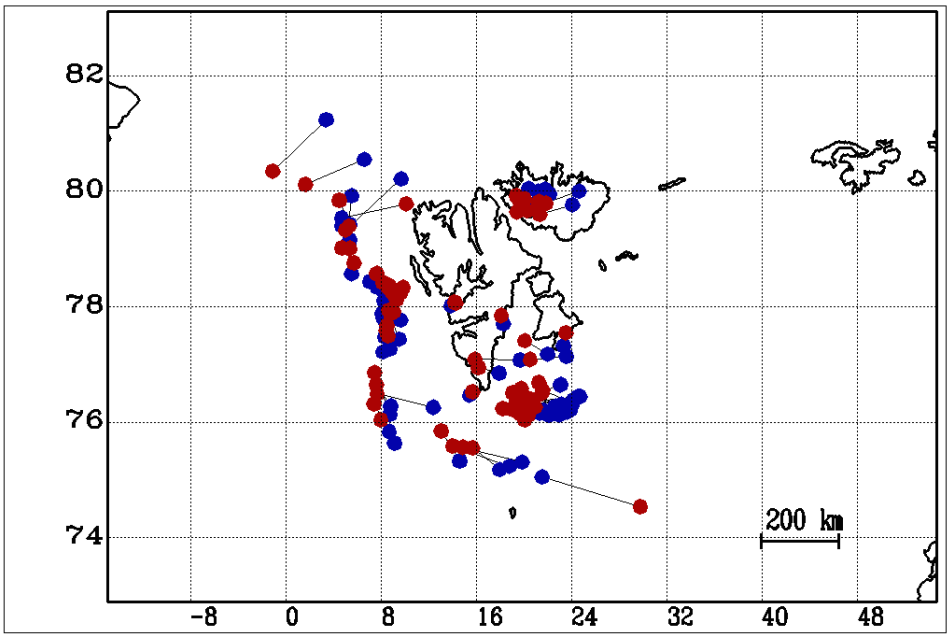


Figure 9. Location comparison: Relocated events (red) vs. NORSAR reviewed bulletin (blue)

Figure 9 compares the two sets of analyst reviewed locations (marked NORSAR for the results in the NORSAR Regional Bulletin and KRSC for the relocated solutions). In general, they are quite consistent, but a systematic shift in the locations of groups of events is noted, with the KRSC locations generally being shifted in westerly directions compared to those of the NORSAR analyst. Mostly, the location differences are small (a few tens of kilometers), but for a few events the difference exceeds 100 km, and in one case it is more than 200 km. The smaller differences can

be attributed, at least in part, to the different velocity models used at KRSC and NORSAR (KRSC uses the SPITS0 model, whereas NORSAR uses a general Fennoscandian model). The cases with large differences are a direct consequence of the difficulties in phase interpretations, and demonstrate that locations of small earthquakes in this region can be associated with significant uncertainties.

CONCLUSIONS AND RECOMMENDATIONS

The accumulation of detailed ground truth for mining explosions in the Kola Peninsula is a significant step towards improved understanding of the waveform characteristics of various types of mining explosions. Our analysis shows significant spectral differences between surface and open-pit explosions. It is our recommendation to pursue this work as more ground truth data of mining events is accumulated, and a larger database of recordings from near-field stations becomes available.

We have demonstrated that a set of relatively simple post-processing criteria can significantly reduce the number of false associations in the automatic GBF process. Nevertheless, there is still room for considerable improvement. A promising approach is to use fixed-frequency filter bands for the broad-band f-k estimation. In this way, one can obtain more stable azimuth estimates, thereby enabling a much lower tolerance than the currently used threshold of 15 degrees for the difference in P and S azimuths. Our work will continue on reducing the false alarm rate in the automatic GBF lists, while retaining as many as possible of the real seismic events. Additionally, the automatic detector algorithms could be further improved, and work towards this is continuing.

By studying a set of more than 200 earthquakes in the Spitsbergen region, we have shown that analyst reviewed locations (as processed by different analysts) can have occasional large deviations, in several cases exceeding 100 km. This is due to the complexity of the seismograms, which sometimes results in ambiguous phase identification. Detection of S-phases using the SPITS array is often problematic, and improvements in this area is a topic of current research. With the planned refurbishment of SPITS, several three-component sites will be included in the array, and this should improve the detection potential for S-phases in the future. In particular, attention should be given to high-frequency processing of data for phase identification and velocity/azimuth estimation purposes.

REFERENCES

Asming, V. E., E. O. Kremenetskaya and F. Ringdal (2004): Locating seismic events near the Spitsbergen Archipelago. *Semiannual Technical Summary 1 July - 31 December 2003*, NORSAR Sci. Rep. 1-2004, Kjeller, Norway.

Harris, D. B., F. Ringdal, E. O. Kremenetskaya, S. Mykkeltveit, J. Schweitzer, T. F. Hauk, V. E. Asming, D. W. Rock and J. P. Lewis (2003), "Ground-truth Collection for Mining Explosions in Northern Fennoscandia and Russia", in *Proceedings of the 25th Seismic Research Review - Nuclear Explosion Monitoring: Building the Knowledge Base*, *LA-UR-03-6029*, Vol. I, pp. 54-62.

Ringdal, F. (1997): Study of low-magnitude seismic events near the Novaya Zemlya nuclear test site, *Bull. Seism. Soc. Am. 87 No. 6*, 1563-1575.

Ringdal, F. and T. Kværna (1989). A multichannel processing approach to real time network detection, phase association and threshold monitoring, *Bull. Seism. Soc. Am., 79*, 1927-1940.

Ringdal, F., T. Kværna, E. O. Kremenetskaya, V. E. Asming, S. Mykkeltveit, S. J. Gibbons and J. Schweitzer (2003), "Research in Regional Seismic Monitoring", in *Proceedings of the 25th Seismic Research Review - Nuclear Explosion Monitoring: Building the Knowledge Base*, *LA-UR-03-6029*, Vol. I, pp. 291-300.

ERROR ANALYSIS IN THE JOINT EVENT LOCATION/SEISMIC CALIBRATION INVERSE PROBLEM

William L. Rodi

Massachusetts Institute of Technology

Sponsored by Air Force Research Laboratory

Contract No. F19628-03-C-0109

ABSTRACT

It is well established that errors in global travel-time models can induce large biases into event locations inferred from regional and teleseismic arrival-time observations. Conversely, the travel-time corrections to these models that are estimated from calibration arrival times are affected by errors in the locations of the ground-truth events providing the data. This project addresses the interaction between location and calibration uncertainty in the context of the joint location/calibration inverse problem, in which arrival time data from multiple events and stations are used to simultaneously determine the locations of the events and calibration parameters such as 3-D velocity models or explicit path corrections. The project builds on and integrates mathematical and computational techniques developed in previous projects, including a grid-search algorithm for multiple-event location, a Monte Carlo technique for location uncertainty analysis, and a new kriging method for empirical calibration. The ultimate goal is a procedure for computing accurate confidence regions on the locations of new events, reflecting the observational errors in their arrival-time data as well as the uncertainty inherited from incomplete and imperfect calibration data sets. This paper describes our formulation of the joint location/calibration inverse problem and the algorithm we have developed to date for performing a fully nonlinear location/calibration uncertainty analysis in the special case in which correction parameters comprise a simple time term for each seismic station and phase, as is often assumed in multiple-event location methods. We present initial applications of the algorithm to earthquake clusters in Turkey and nuclear explosions at the Nevada Test Site, for which very precise ground-truth locations are available for validation purposes. The results show the expected dependence of the location confidence region for an event on the ground-truth location constraints imposed on other events, thus confirming the concept of our new approach to event location uncertainty. The algorithm is computationally intensive, however, and we are investigating computational shortcuts and approximations that yield the same results more efficiently before extending the approach to more general parameterizations of travel-time corrections.

OBJECTIVE

The objective of this project is to develop new mathematical and computational techniques for quantifying the errors in seismic event locations, including the effects of observational errors and calibration errors, that is, errors in the travel-time forward model. Calibration errors stem from observational errors in calibration data, incomplete geographical coverage of these data, and uncertainty in the locations of the ground-truth events providing the data. Our goal is to take all of these error sources into account in determining the location uncertainty on new events.

Our approach to location uncertainty is formulated within the framework of the joint location/calibration inverse problem. In this problem, arrival time data from multiple events and stations are used to simultaneously determine the event locations and calibration parameters, such as explicit path corrections or a 3-D velocity model. We treat one of the events as a new event under investigation and the remaining events as calibration events. A complete error analysis that considers the uncertainty in all the unknown parameters—the location of the new event, the locations of non-GT0 calibration events, and the calibration parameters—accounts for the sources of location uncertainty, which are the topic of this project.

We are addressing this joint inverse problem with numerical techniques that lift key limitations in previous analytic approaches to uncertainty analysis in large inverse problems. These limitations include the restriction to Gaussian data errors, the necessity of using a linear approximation to the forward model, and restricted mechanisms for incorporating *a priori* constraints on the unknowns. Hard bounds on parameters, in particular, are not accommodated in the analytical approach and these can introduce a nonlinearity to the problem that can be more severe than the nonlinearity of the forward model. Requiring an event location to be below the Earth's surface is an example of such a constraint. The primary numerical methods we are currently using to accommodate these complexities are grid search, for finding optimal solutions for parameters, and Monte Carlo sampling, for finding confidence regions on parameters.

Given the ability to perform a rigorous analysis of event location uncertainty, the ultimate objective of this project is to achieve a more complete understanding of the main factors controlling the errors in seismic locations and to identify the new information or procedures needed to reduce these errors for the purposes of improved nuclear-event monitoring.

RESEARCH ACCOMPLISHED

Formulation of the Joint Inverse Problem

We state our formulation of the joint location/calibration inverse problem for a data set comprising the arrival times of n seismic station/phase combinations (e.g. phase Pn at station MNV) observed from a subset of m seismic events. Let d_{ij} denote the observation for the ith event and jth station/phase (i,jth path). Then the joint event location/seismic calibration inverse problem can be written as

$$d_{ij} = t_i + T_j(\mathbf{x}_i) + c_{ij} + e_{ij} \qquad (1)$$

where t_i and $\mathbf{x}_i$ are origin parameters (time and hypocenter, respectively) of the ith event; T_j is a model-based travel-time function for the jth station/phase; c_{ij} is a correction to this function; and e_{ij} is an observational error. This equation holds only for the paths i, j for which data have been observed.

The unknown parameters of this joint location/calibration inverse problem are the event hypocenters and origin times, $\mathbf{x}_i$, t_i, $i = 1,\ldots,m$, and the path travel-time corrections c_{ij}. The problem becomes one of purely calibration when the event parameters are assumed known, and one of purely location when the path corrections are known. In practice, neither set of parameters is completely known or unknown. Two difficult aspects of nuclear monitoring, in fact, fall within the general formulation. The first is how to account for uncertainty in a seismic calibration (errors in estimates of c_{ij}) when the calibration events have imperfectly known locations, i.e. ground-truth (GT) levels greater than zero. The second is how the location error of any particular event is affected by imperfect knowledge of the path corrections. These difficult questions are addressed by a complete uncertainty analysis in the joint location/calibration problem.

Parameterization of path corrections

The joint inverse problem is hopelessly ill-posed if the path corrections c_{ij} are not constrained via prior information or a parameterization that reduces the number of independent unknowns, or both. The exact nature of the inverse problem depends on how this is done.

In the "basic" multiple-event location problem, relevant to small event clusters, the path corrections are assumed to be event-independent, i.e.

$$c_{ij} = a_j. \tag{2}$$

The calibration parameters comprise a time term, a_j, for each station/phase pair in the data set. This problem has been treated by several workers (e.g. Jordan and Sverdrup, 1981; Pavlis and Booker, 1983) and it is the focus of this paper. However, our formulation pertains to other ways of parameterizing path corrections that will be addressed later in the project. One is with correction functions (or surfaces), whereby

$$c_{ij} = a_j (\mathbf{x}_i). \tag{3}$$

Here, there is an unknown function, a_j ($\mathbf{x}$), assigned to each station/phase. Another is the universal parameter function described by Rodi et al. (2003). Spatial functions contain many more degrees of freedom than simple time terms and it is necessary to provide prior information on their smoothness, such as with geo-statistical constraints (e.g. Schultz et al., 1998), to make the inverse problem well posed. Our formulation also includes the problem of earthquake tomography (joint location/velocity determination; e.g. Spencer and Gubbins, 1980) as a special case. Path corrections are then parameterized by the Earth's velocity function and the c_{ij} are integrations of this function over ray paths.

Maximum-likelihood formulation

Our approach to inverse problems and uncertainty analysis is based on likelihood functions. A likelihood function is a function of the unknown parameters whose purpose is to quantify how well any given values for the parameters agree with the observed data. An optimal estimate of the unknown parameters (the *maximum-likelihood* estimate) can be taken as those parameter values that maximize the likelihood function. A confidence region on the parameters is the collection of parameter values whose likelihood is within some tolerance of the maximum likelihood.

A given assumption about the probability distribution of the data errors defines a particular likelihood function for the parameters. In our work thus far we have assumed that the observational (picking) errors, e_{ij}, are statistically independent and that each has a *generalized Gaussian* probability distribution of order p (Billings et al., 1994). For the small-cluster problem ($c_{ij} = a_j$), this error model implies a likelihood function, L, given by

$$-\log L = \mathbf{const} + \sum_{ij} \log \sigma_{ij} + \frac{1}{p} \sum_{ij} \frac{1}{\left(\sigma_{ij}\right)^p} \left| d_{ij} - t_i - T_j\left(\mathbf{x}_i\right) - a_j \right|^p . \tag{4}$$

In this paper we will assume the data standard errors, σ_{ij}, are known *a priori*. The task of maximizing the likelihood is then equivalent to minimizing an L_p norm (to the pth power) of the data residuals, as given by the last term of equation (4). The case of Gaussian errors coincides with $p = 2$ and maximization of the likelihood function with respect to the problem unknowns (event locations and time terms) becomes a problem of nonlinear least squares.

In previous projects we have developed an algorithm called GMEL (grid-search multiple-event location) for maximizing the likelihood function in equation (4). The algorithm is described in Rodi et al. (2002). GMEL solves jointly for the location parameters of the events, $\mathbf{x}_i$ and t_i, and the travel-time correction terms of the station/phase combinations, a_j. It accepts prior constraints on all the parameters in the form of prior bounds. A prescribed lower and upper bound is allowed on each event origin time t_i, event depth z_i, and travel-time correction, a_j (e.g. $a_j^{\min} \le a_j \le a_j^{\max}$). Bounds on an event epicenter take the form of a maximum epicentral distance from a specified geographic point. The GMEL algorithm iterates over alternating loops over events, to update event locations with

station/phase terms fixed, and over station/phase pairs, to update their correction terms with the event locations fixed. Grid search is used to find the optimal event locations.

Location Confidence Regions in the Joint Inverse Problem

Our formulation of uncertainty analysis in the joint location/calibration (or multiple-event location) inverse problem extends the formulation we developed for the single-event location problem (Rodi and Toksöz, 2001). The same principles are applied, but to a problem with many more parameters.

Our approach is to address the uncertainty in a subset of the unknown parameters, which we denote as a vector **p**, considering their trade-off with the remaining "hidden" parameters, **q**. For example, **p** may be the hypocenter of one of the events, say the first event ($\mathbf{p} = \mathbf{x}_1$). In single-event location, **q** would then be simply the origin time of the event ($\mathbf{q} = (t_1)$). In the multiple-event location problem, however, **q** includes this plus all the other event locations and the travel-time corrections:

$$\mathbf{q} = (t_1, \mathbf{x}_2, t_2, \ldots, \mathbf{x}_m, t_m, a_1, a_2, \ldots, a_n). \tag{5}$$

To address the uncertainty in the *epicenter* of event 1, as another example, we would move its depth, z_i, from **p** to **q**.

For single-event location, Flinn (1965) developed the methodology for hypocentral confidence regions for the case of Gaussian data errors ($p = 2$) and no parameter constraints, and using a linear approximation to the travel-time functions, T_j. His method can be formulated in terms of hypothesis testing using a likelihood ratio as the test statistic. Doing so allows us to define confidence regions under less restrictive assumptions and for the multiple-event problem.

In the multiple-event problem, let **d** denote the vector of arrival time data (d_{ij} for the observed *ij* pairs), and write the likelihood function as $L(\mathbf{p}, \mathbf{q}; \mathbf{d})$. We will denote the prior parameter constraints as sets P and Q, which contain the admissible values of **p** and **q**, respectively (e.g., for $\mathbf{p} = \mathbf{x}_1$, the below-surface constraint yields $P = \{(\theta_1, \phi_1, z_1) \mid z_1 \geq 0\}$, where θ and ϕ are epicentral coordinates). A confidence region on **p** is defined in terms of a likelihood ratio test statistic, $\tau(\mathbf{p}, \mathbf{d})$, which compares the likelihoods that are achieved with **p** fixed to a particular value and with **p** free to vary within P. Thus

$$\tau(\mathbf{p},\mathbf{d}) = \log \max_{\substack{\mathbf{p}' \in P \\ \mathbf{q}' \in Q}} L(\mathbf{p}', \mathbf{q}; \mathbf{d}) - \log \max_{\mathbf{q} \in Q} L(\mathbf{p}, \mathbf{q}; \mathbf{d}). \tag{6}$$

Given a confidence level β, we can reject **p** at that level if $\tau(\mathbf{p}, \mathbf{d})$ is greater than some critical value, τ_β. This critical value is determined by the probability distribution of $\tau(\mathbf{p}, \mathbf{d})$, as induced by the errors in **d**. If **p** is *not* rejected, it is *inside* the confidence region for the specified confidence level. That is, the confidence region comprises the parameter vectors **p** satisfying

$$\tau(\mathbf{p}, \mathbf{d}) \leq \tau_\beta. \tag{7}$$

In Gaussian/linear inverse problems ("linear'" means the T_j are linear *and* hard parameter constraints are not used), with the additional assumption that the standard errors (σ_{ij}) are known, τ (actually 2τ) is chi-squared distributed with the number of degrees of freedom being the number of parameters in **p** (e.g., 2 for epicentral confidence regions). Thus, τ_β is easily determined from tables of the chi-squared cumulative distribution function. Furthermore, in the Gaussian/linear case, the dependence of τ on **p** is quadratic. Therefore, the locus of points **p** satisfying equation (7) fill a hyper-ellipsoid whose axis lengths and orientations are easily found. With our more general assumptions (non-Gaussian errors, or nonlinear forward model or parameter constraints), τ does not necessarily have a well-known probability distribution and the geometry of a confidence region cannot be found with analytic formulas. Therefore, we use numerical techniques to find τ_β and the values of **p** that satisfy equation (7).

Confidence Region Algorithm

Our confidence region algorithm is a two-step procedure. We describe it for the case where **p** is the hypocenter, **x**, of one of the events, and where a single value of β is of interest (e.g. $\beta = 90\%$). The steps are

1. Compute $\tau(\mathbf{x}, \mathbf{d})$ at points $\mathbf{x}$ on a dense 3-D hypocenter grid. This entails maximizing L with respect to the hidden parameters ($\mathbf{q}$) for each $\mathbf{x}$ on the grid.
2. Perform a Monte Carlo simulation to find τ_β. This entails computing $\tau(\mathbf{x}^{tru}, \mathbf{d}^{syn})$ for an assumed "true" hypocenter $\mathbf{x}^{tru}$ and true hidden parameters $\mathbf{q}^{tru}$, and many realizations of synthetic data, $\mathbf{d}^{syn}$.

In step 2, each realization $\mathbf{d}^{syn}$ is constructed by adding a realization of pseudo-random errors to arrival times calculated for ($\mathbf{x}^{tru}$, $\mathbf{q}^{tru}$):

$$\mathbf{d}^{syn} = F(\mathbf{x}^{tru}, \mathbf{q}^{tru}) + \mathbf{e}^{syn} \tag{8}$$

where F denotes the arrival time forward model and $\mathbf{e}^{syn}$ is the pseudo-random noise vector (comprising the e_{ij}). The computation of $\tau(\mathbf{x}^{tru}, \mathbf{d}^{syn})$ requires that each realization of the synthetic data be used in two likelihood maximizations: one with $\mathbf{x} = \mathbf{x}^{tru}$ and one with $\mathbf{x}$ free to vary within its admissible region (X). Both maximizations vary $\mathbf{q} \in$ Q.

In our current implementation of this algorithm, we take $\mathbf{x}^{tru}$ and $\mathbf{q}^{tru}$ to be their maximum-likelihood values for the real data. The method then coincides with a statistical method called *parametric bootstrapping* (e.g. Hall, 1992).

Both steps of this procedure maximize the likelihood function many times. In step 1 (likelihood sampling) L is maximized for all hypocenters on a 3-D grid, but only for the real data. The second step (Monte Carlo simulation) entails maximizing L twice, with $\mathbf{x}$ fixed and free, for each of many realizations of synthetic data. (We have found that ~300 realizations of synthetic data yield stable results if β is not too close to 1.) In the single-event problem, maximizing L is a fast procedure and a confidence region can be computed with a few seconds of CPU time. In multiple-event location, each maximization of L is an invocation of the GMEL algorithm to solve for multiple event and station parameters. Even for *epicentral* confidence regions, with event depths assumed known (implying a 2-D sampling grid in step 1), each step of the procedure can require on the order of one hour of CPU time (on a 2.4 GHz Xeon processor), depending on the denseness of the epicenter sampling grid and the number of Monte Carlo realizations.

Other workers in event location uncertainty (c.f. Wilcock and Toomey, 1991) have used analytical values of τ_β in calculating location confidence regions, even while sampling the likelihood function (our algorithm step 1) to avoid linearization of the forward problem. Doing so avoids step 2 of our algorithm. For single-event location, we have performed numerical experiments with real and synthetic data to test the accuracy of analytical critical statistic values, in the case of Gaussian errors. We discovered that bounds on the target parameters $\mathbf{p}$ (e.g. depth bounds when computing hypocentral confidence regions) can lead to significant errors in the analytical τ_β. However, the experiments also showed that τ_β is not sensitive to the constraints on the *hidden* parameters, $\mathbf{q}$. For example, the statistic for an epicentral confidence region did not depend on whether or how strongly the focal depth was constrained.

This fact suggests a way to tremendously speed up the Monte Carlo simulation in the multiple-event problem: by fixing the locations of the calibration events (which are parameters in $\mathbf{q}$). In effect, single-event location is performed on each realization of synthetic data. We used this approximation in the applications below. We point out that the calibration events cannot be fixed for step 1 of the procedure, for doing so would ignore important trade-offs between the parameters in $\mathbf{p}$ and $\mathbf{q}$.

Application to the Izmit Earthquake Sequence

Rodi and Toksöz (2003) presented some preliminary tests of our multiple-event uncertainty approach applied to the 17 August 1999 Izmit, Turkey, earthquake sequence. These tests demonstrated the concept of the approach but revealed its computational difficulties. Here we present updated results for this data set, using finer sampling grids and more Monte Carlo realizations. The new results employ the approximation of fixing calibration event locations in the Monte Carlo simulation, as described in the previous section.

The data set previously used contains 3484 Pn and teleseismic P arrival times from 643 stations from the National Earthquake Information Center (NEIC), which we obtained from the IASPEI Working Group on Multiple-Event

Location, courtesy of R. Engdahl and E. Bergman. For the new tests we winnowed the data set by eliminating station/phase pairs having fewer than 3 events. The winnowed data subset comprises 3083 Pn or P arrivals from 373 stations (387 station/phase combinations) from 34 events (the Izmit mainshock and 33 aftershocks).

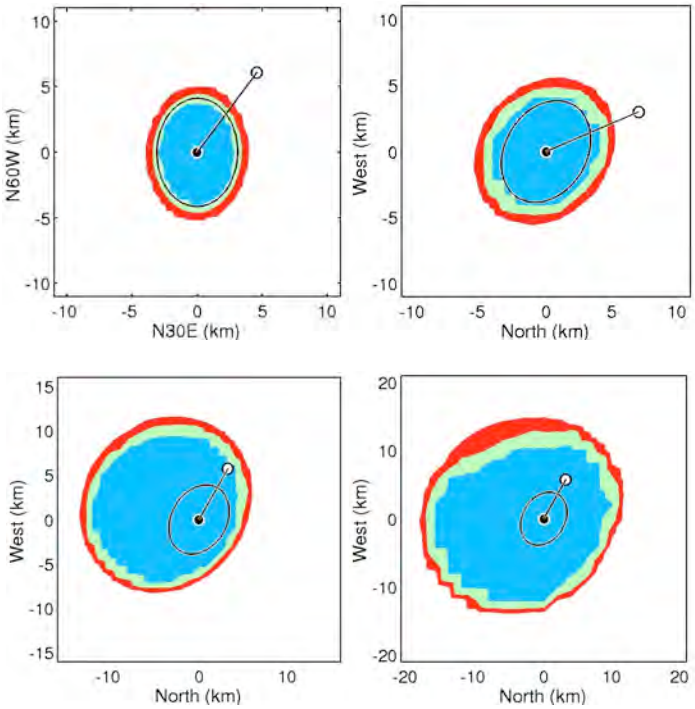


Figure 1. ***Top left*****: Single-event epicentral confidence regions (at 90, 95 and 98% confidence; blue, green and red, respectively) for a well-recorded aftershock of the 1999 Izmit Turkey earthquake (135 defining phases). Station travel-time corrections were assumed to be known.** ***Top right and bottom left/right*****: Multiple-event confidence regions for the same event.** ***Top right*****: computed with the Izmit mainshock constrained as a GT0 event.** ***Bottom left*****: with the Izmit mainshock constrained as a GT5 event.** ***Bottom right*****: with the Izmit mainshock as a GT10 event. In each frame, the black circle marks the maximum-likelihood (GMEL) solution for the aftershock and the white circle is a GT5 local network solution for the event (Engdahl and Bergman, private communication). The ellipse is the analytic, single-event 90% confidence ellipse on the aftershock.**

We show confidence regions on two of the Izmit aftershocks. One is a well-recorded aftershock occurring on 31 August 1999, and has 135 defining phases in the winnowed data set (compared to 283 defining phases for the Izmit mainshock). The other is a poorly recorded aftershock on 26 August 1999 having 17 defining phases. Only epicentral confidence regions were calculated with depths fixed to values found by Engdahl and Bergman (2001). For both aftershocks, the Izmit mainshock was treated as a ground-truth calibration event. Its prior location was set to the solution from a local seismic network and is estimated to be of GT5 accuracy. In our tests, however, we assumed various GT levels of the mainshock. The other 32 "calibration" events were unconstrained. In all cases, picking errors were assumed to be Gaussian with a standard deviation of 0.622 sec. The AK135 travel-time tables were used for the forward model in all cases.

Figure 1 shows the confidence regions for the well-recorded aftershock. The top/left frame shows single-event confidence regions (at three confidence levels) found with our numerical approach. These assume the travel-time corrections are known exactly, making the calibration events irrelevant. The other three frames show multiple-event confidence regions, i.e. the corrections are assumed to be unknown and are only constrained by the calibration events with some degree of uncertainty. The multiple-event confidence regions were computed under the assumptions, respectively, that the Izmit mainshock was a GT0 event (upper right frame), a GT5 event (lower left) and GT10 event (lower right). In each frame, the maximum-likelihood location for the aftershock is compared to a GT5 local seismic solution that was available for the aftershock. Figure 2 shows the analogous computations for the poorly recorded aftershock.

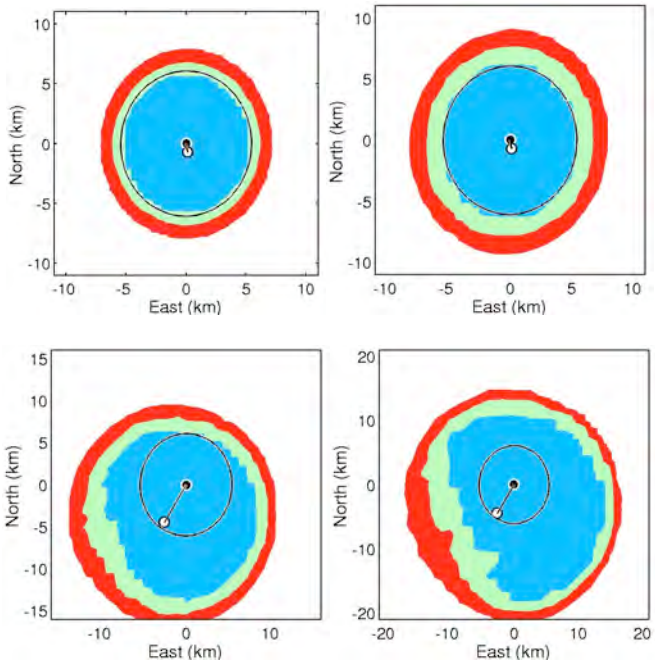


Figure 2. Same as Figure 1 but for a poorly recorded aftershock of the Izmit earthquake (17 defining phases).

The confidence regions in both figures show the behavior we expect. When the uncertainty in travel-time corrections is ignored (top left frames) the confidence regions are comparable to the confidence ellipses computed with the conventional Gaussian/linear formula (shown only for $\beta = 90\%$). When the uncertainty in corrections is accounted for (top right) the confidence regions are larger. When the GT level of the Izmit mainshock is increased (bottom frames) the regions become accordingly larger still. In the case of the well-recorded aftershock (Figure 1) only the bottom confidence regions, accounting for the location error in the one GT event, contain the local network solution.

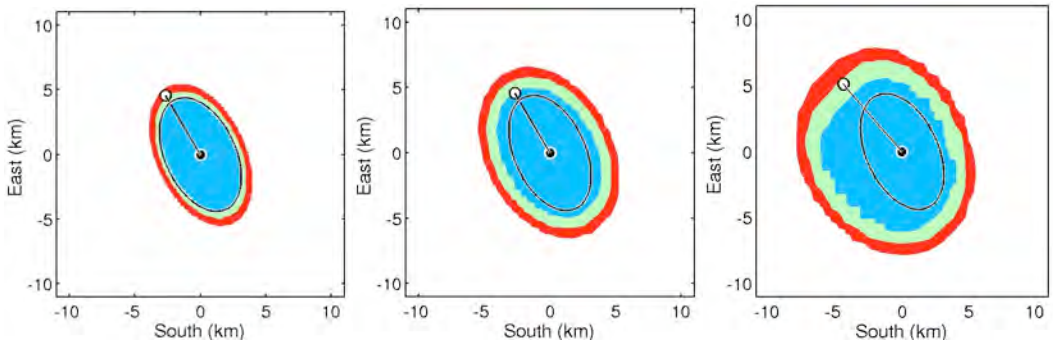


Figure 3. Epicenter confidence regions for a Rainier Mesa explosion determined from 6 Pn arrival times. *Left*: Single-event confidence regions (at 90, 95 and 98% confidence), computed with path travel-time corrections assumed known. *Center/Right*: Multiple-event confidence regions for the same event, allowing for the uncertainty in path corrections. *Center*: computed with one well-recorded Rainier Mesa explosion (22 Pn arrivals) constrained to be a GT0 event. *Right*: with the same explosion constrained as a GT2 event. All other events were unconstrained. In each frame the black circle marks the maximum-likelihood solution for the event and the white circle is its GT0 location (from Walter et al., 2003). The ellipse in each frame is the analytic, single-event 90% confidence ellipse on the event location.

Application to NTS Explosions

We have also tested our new error analysis technique on a data set from NTS explosions that has been assembled by Lawrence Livermore National Laboratory (LLNL) (Walter et al., 2003). The data set comprises 74 nuclear explosions with known locations and origin times recorded at a network of regional and local stations. The examples here use only a subset of the Pn picks from the data set, selected under the following criteria. First, arrivals from two stations (TPH and DAC) that are within 1.5° of most of the explosions were excluded, leaving only stations at greater distances. Of the remaining data set, events with fewer than 4 arrivals and stations with fewer than 2 arrivals were removed. The resulting subset comprises 548 arrivals from 71 events and 38 stations. IASP91 travel-time tables were used for the forward model. Picking errors were assumed to have a standard deviation of 0.324 sec.

The examples here follow the schema of the Izmit examples shown above. One NTS explosion was chosen as a ground-truth calibration event with finite GT level: GT0 or GT2 this time. This event was a Rainier Mesa explosion with 20 Pn arrivals. Several other events were treated, in turn, as new events to be located. The remaining 69 explosions in the winnowed data set were treated as calibration events with unconstrained locations.

Figures 3–6 show confidence regions on four of the explosions that have relatively few arrivals: one each from the Rainier Mesa and Pahute Mesa test areas and two from Yucca Flat. We see the same behavior of confidence regions as in the Izmit examples, with the regions growing as the uncertainty in travel-time corrections and the finite location accuracy of the GT calibration event are accounted for. We point out that the Rainier Mesa explosion was constrained with its GT0 location. Therefore, the confidence regions in the center frame of each figure should cover the GT0 location shown for the target event. In three of four cases, the GT0 location is near the edge of the confidence region and for one of the Yucca explosions it is decidedly outside the confidence region. Further study is needed to determine why this is the case, but a possible explanation is the inadequacy of a simple time-term parameterization of travel-time corrections.

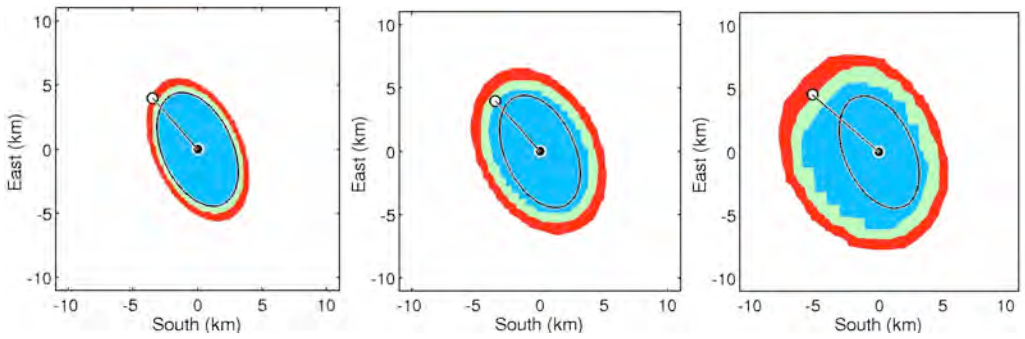


Figure 4. Epicenter confidence regions for a Pahute Mesa explosion determined from 6 Pn arrival times. See Figure 3 for explanation of the different frames and conventions.

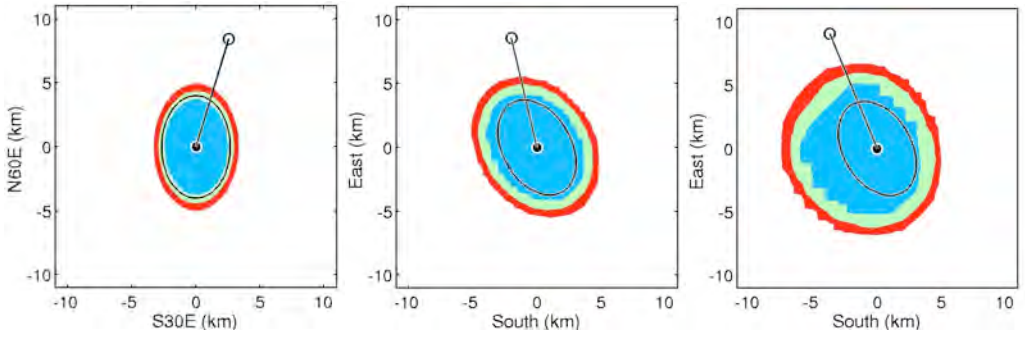


Figure 5. Epicenter confidence regions for a Yucca Flat explosion determined from 7 Pn arrival times. See Figure 3 for explanation of the different frames and conventions.

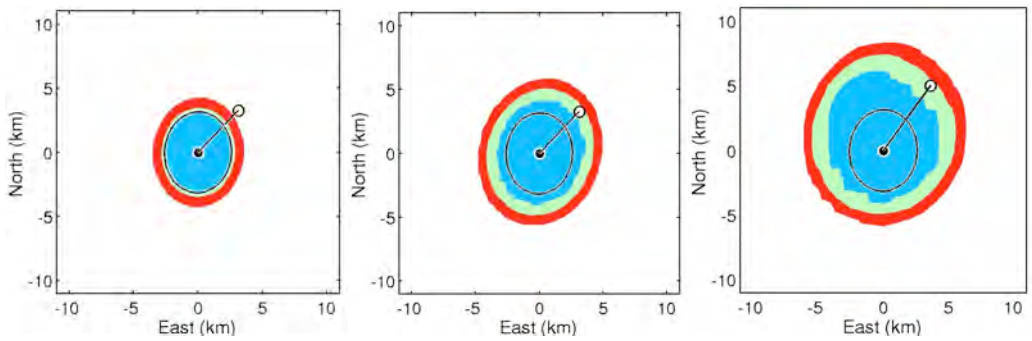


Figure 6. Epicenter confidence regions for a Yucca Flat explosion determined from 8 Pn arrival times. See Figure 3 for explanation of the different frames and conventions.

CONCLUSIONS AND RECOMMENDATIONS

We have developed a general theoretical and computational framework for characterizing the uncertainty in seismic event locations in the context of the joint inverse problem of multiple-event location and travel-time calibration. The approach accounts for complexities such as nonlinear forward models and parameter constraints and the finite accuracy of calibration event locations, which create significant difficulties for analytic methods of uncertainty analysis. We have implemented the approach for the basic multiple-event location problem with time-term corrections, and begun testing it with earthquake and explosion data sets. The results to date have validated the approach qualitatively but it awaits quantitative validation. We have made some significant inroads in improving the computational efficiency of the method. However, more improvement is needed for the method to be a tool of routine analysis, and if it is to be practical with more complex parameterizations of travel-time corrections.

ACKNOWLEDGMENTS

I wish to thank the people who provided the data used in this paper: Bob Engdahl and Eric Bergman of University of Colorado at Boulder, who provided the NEIC data for the Izmit earthquake sequence, and Steve Myers of Lawrence Livermore National Laboratory, who provided the NTS explosion data set.

REFERENCES

Billings, S.D., M.S. Sambridge and B.L.N. Kennett (1994). Errors in hypocenter location: picking, model and magnitude dependence, *Bull. Seism. Soc. Am., 84*, 1978-1990.

Engdahl, E.R. and E.A. Bergman (2001). Validation and generation of reference events by cluster analysis, *Proceedings*, 23rd Annual DoD/DOE Seismic Research Review, Jackson Hole, Wyoming.

Flinn, E.A. (1965). Confidence regions and error determinations for seismic event location, *Rev. Geophys., 3*, 157-185.

Hall, P. (1992). *The Bootstrap and Edgeworth Expansion*, Springer-Verlag, New York.

Jordan, T.H. and K.A. Sverdrup (1981). Teleseismic location techniques and their application to earthquake clusters in the south-central Pacific, *Bull. Seism. Soc. Am., 71*,1105-1130.

Myers, S.C. and C.A. Schultz (2000). Improving sparse network seismic locations with Bayesian kriging and teleseismically constrained calibration events, *Bull. Seism. Soc. Am., 90*, 199-211.

Pavlis, G.L. and J.R. Booker (1983). Progressive multiple event location (PMEL), *Bull. Seism. Soc. Am., 73*, 1753-1777.

Rodi, W. and M.N. Toksöz (2001). Uncertainty analysis in seismic event location, *Proceedings*, 23rd Annual DoD/DOE Seismic Research Review, Jackson Hole, Wyoming.

Rodi, W., E.R. Engdahl, E.A. Bergman, F. Waldhauser, G.L. Pavlis, H. Israelsson, J.W. Dewey, and M.N. Toksöz (2002). A new grid-search multiple-event location algorithm and a comparison of methods, *Proceedings*, 24th Annual Seismic Research Review, Ponte Vedra Beach, Florida, 403-411.

Rodi, W., S.C. Myers, and C.A. Schultz (2003). Grid-search location methods for ground-truth collection from local and regional seismic networks, *Proceedings*, 25th Annual Seismic Research Review, Tucson, Arizona.

Rodi, W. and M.N. Toksöz (2003). Confidence regions on seismic event locations based on multiple-event analysis, *Proceedings*, 25th Annual DoD/DOE Seismic Research Review, Tucson, Arizona, DOE NNSA.

Schultz, C.A., S.C. Myers, J. Hipp, and C.J. Young (1998). Nonstationary Bayesian kriging: a predictive technique to generate spatial corrections for seismic detection, location, and identification, *Bull. Seism. Soc. Am., 88*, 1275-1288.

Spencer, C. and D. Gubbins (1980). Travel-time inversion for simultaneous earthquake location and velocity structure determination in laterally varying media, *Geophys. J. R. Astr. Soc., 63*, 95-116.

Walter, W.R., K.D. Smith, J. L. O'Boyle, T.F. Hauk, F. Ryall, S.D. Ruppert, S.C. Myers, M. Anderson, and D.A. Dodge (2003), Improving the fundamental understanding of regional seismic signal processing with a unique western United States dataset, *Proceedings*, 25th Seismic Research Review, Tucson, Arizona.

Wilcock, W.S.D. and D.R. Toomey (1991), Estimating hypocentral uncertainties for marine microearthquake surveys: a comparison of the generalized inverse and grid search methods, *Marine Geophysical Researches, 13*, 161-171.

GROUND TRUTH LOCATIONS USING SYNERGY BETWEEN REMOTE SENSING AND SEISMIC METHODS - APPLICATION TO EARTHQUAKES IN IRAN AND INDIAN SUBCONTINENT

Chandan K. Saikia[1], Gene A. Ichinose[1], H. -K. Thio[1], Donald V. Helmberger[2], and Mark Simons[2]

URS Group, Inc.[1] and California Institute of Technology[2]

Sponsored by Defense Threat Reduction Agency

Contract No DTRA01-01-C-072

ABSTRACT

This study aims to establish ground truth locations of moderate to large magnitude earthquakes ($4.5 \leq M_w \leq 7$) occurring in Iran, and in and around the Indian subcontinent using both seismic and interferometric synthetic aperture radar methods. To this end, we analyzed seismic waveforms and InSAR (Interferometric Synthetic Aperture Radar) data for one large ($M_w \geq 6$) and two moderate ($5.3 \leq M_w \leq 5.7$) earthquakes in Iran. Similar studies were also conducted for two earthquakes in the Indian subcontinent. One occurred in the northern Himalaya on 29 March 1999 (known as the Chamoli earthquake) and the other occurred in central India on September 29, 1993 (known as the Latur earthquake). For the latter two events, we obtained high quality seismic locations, but interferograms processed using radar data from the European Remote Sensing (ERS) satellites did not produce any discernable surface displacement. Both earthquakes were followed by many aftershocks and were recorded by local temporary stations. For the Chamoli aftershock sequence, we could identify nine aftershocks for which the local network provided good azimuthal coverage and were relocated using an adaptive grid-search location algorithm. Many stations of the Chinese National Network also recorded these aftershocks. We were able to estimate reliable source specific station corrections (SSSCs). The SSSCs from the Chinese stations were, in turn, used in conjunction with other common Incorporated Research Institutes in Seismology (IRIS) and Indian broadband stations to relocate the main event, establishing its location at 30.51±0.045°N latitude and 79.24±0.045°E longitude (depth: 15±1.0 km and origin time: 19h 05m 8.26±1.274s). For the Latur earthquake, local field reports indicated a significant surface deformation, but no deformation could be observed in interferograms because of the large temporal baseline between the radar frames. Using the aftershock data, we were able to conduct a seismic study similar to the Chamoli earthquake to establish its location. For the earthquakes in Iran, the largest event investigated in this study is the Fandoqa earthquake that occurred in Kerman province on 14 March 1998 (M_w 6.6). Our teleseismic P-wave modeling established its depth at 7 km and processing of its InSAR data from the ERS satellites also produced discernable surface displacement. We also identified surface displacements in the processed interferograms for two other earthquakes that occurred in northern and central Iran on 20 June 1997 (lat: 32.254ºN and lon: 60.0278ºE, M_w=5.4) and at the margin of northern and southern Iran on 8 November 1996 (lat: 30.059ºN and lon: 51.006ºE, M_w 5.3). The seismic analysis of the recent BAM earthquake of 26 November 2003 has just been completed. The reliable locations of these events including the others previously established will now allow a reliable calibration of the International Monitoring System (IMS) and other permanent seismic stations available around the study regions.

OBJECTIVES

The goal of this on-going study is to obtain reliable locations for moderate-sized earthquakes (M_w<5.5) in parts of Asia and the Middle East. We will deliver accurate locations, associated waveforms, raw satellite synthetic radar interferometry (InSAR) images, processed InSAR phase maps and ground deformation maps to the Department of Energy Knowledge Base. The study is divided into two parts, seismic and geodetic, which are concerned with identifying ground truth (GT) locations for reference events in regions of monitoring interest. The primary objective is to improve earthquake locations to GT10 or GT5 level of accuracy (i.e., events within 10 or 5 km accuracy in their epicentral locations, respectively) when they apparently satisfy GT25 criteria (Yang and Romney, 1999). The other objective is to utilize geodetic data, including synthetic aperture radar interferometry (InSAR) to establish accurate locations for shallow and moderate-sized seismic events (M_w<5.2) to validate the ground truth (GT) results determined from seismic methods.

The final task of this study combines seismic and geodetic results to validate the GT locations (Foxall et al., 1998; Lohman et al., 2002; Meyers et al., 2002; Saikia et al., 2003; Steck et al., 2002). These locations determined from a combination of InSAR and seismic methods will be used to develop Source-Specific-Station corrections (SSSCs) for the upper-mantle P-wave phase arrivals, which in turn will be used for relocating nearby earthquakes (M_w < 4.5).

RESEARCH ACCOMPLISHED

28 March 1999 Chamoli earthquake, India (M_w 6.5)

In our previous reports, we presented results of analyzing all available seismograms recorded at regional, far-regional and teleseismic distances from this earthquake. Regional seismograms included waveforms recorded by all broadband stations from the Indian subcontinent. Far-regional seismograms included waveforms from the IRIS stations at distances within 10º<_<30º including those from the INDEPTH-III experiment. The teleseismic waveforms were from sixty-six stations and included both the vertical and radial components. Modeling of this entire data set enabled us to establish a robust focal mechanism and depth at 17 km. Theoretical surface deformation was calculated with this new depth and focal mechanism. Our calculation suggested that surface deformation from such an event should be discernable in interferograms processed from the radar data. We acquired European Radar Satellite (ERS) data for this earthquake and analyzed satellite data from both descending and ascending tracks using the Repeat Orbit Interferometry Package, but were unable to identify any discernable co-seismic signals. The epicenter of this earthquake lies in the Lesser Himalayas, a region of high relief and shadowing evident in the digital elevation model (DEM), which could be the reason for this failure.

Although we could not find surface deformation in the radar signal, we revisited P and S travel time data, including the aftershock sequence. By analyzing the local data, we identified four aftershocks; each recorded by more than twelve local stations that lie within 100 km of the epicenter and each having a maximum azimuthal gap not more than 180°. The mainshock was not recorded by any of the local stations at such close proximity. There were about 9 aftershocks, which satisfied this criterion (Figure 1). We relocated these nine events using a new adaptive grid-search algorithm in which the reported P and S waves are treated either as the direct or the Pn (or Sn) phase. Scientists in India also provided locations of these events. Considering these locations as initial locations, we defined a rectangular area (10 x 10 km^2) around them and searched for the best hypocenter. We used the minimization of the root-mean-square (RMS) error in the origin time as the selection criterion for the best location of a given event. The entire 10 x 10 km^2 area was discretized into many cells with a constant cell size (5 x 5 km^2). For each cell, the RMS error in the origin time was estimated for a suite of depths ranging from 3 to 30 km in an interval of 1 km. In Figure 1, we show two locations for each event, one determined in this study and the other determined by Indian scientists. To have a better control on the location, we included stations that are within 300 km of the epicenter.

Of the nine events, we selected four; 9904061937, 9904062046, 9904071549, and 9904071623 that were also included in the Chinese earthquake catalog published by the Bureau of Seismology, Beijing. This catalog included the P and S arrival times from the Chinese National Seismograph Network (CDSN). This study used stations that lie within 20° of the epicenter and this data base was augmented by adding arrival time data reported from regional stations that operate in India, including the station NIL (Nilore) in Pakistan and those in Nepal. All these stations provided a good network of stations that surround each event from all azimuths. For the Chinese stations, we used

the station co-ordinates determined in an earlier study by Dr. Paul G. Richards of Lamont-Doherty Earth Observatory at Columbia University. Using the locations determined in this analysis, we computed average source-specific-station-corrections (SSSCs) for all stations. Note that the first arrivals at stations lying beyond the critical distance were considered to be the classical Pn wave. The SSSCs so estimated at stations at upper-mantle distances, are, therefore, the difference in the travel times between the observed P or S waves (which are really turning rays) and the classical head waves. Thus, when the SSSCs are applied to stations at large distances, we reduce the first arrivals to become the arrival times of the head waves. Using these average corrections and the adaptive grid-search technique, we relocated the four selected events (Table 1) to within 5 km of their true locations. Epicenters are well established, but the depth estimates as indicated by poor resolution are often inferior. Epicenters always converged to the same locations irrespective of the depths.

Table 1. Relocation of four aftershocks for estimating SSSCs

Date	Origin Time hr:mn:ss	Latitude (°N)	Longitude (°E)	Depth (km)
99/04/06	19:37:25.85±0.635	30.375	79.33	21
99/04/06	20:46:42.05±0.647	30.33	79.33	19
99/04/07	15:49:14.90±0.615	30.33	79.375	17
99/04/07	16:23:28.86±0.656	30.375	79.285	19

Error in Latitude and Longitude = 0.045°
Error in depth = 1 km

Note that locations reported by the Bureau of Seismology, Beijing for the events investigated in this study have significant error and are off by 24 to 62 km from our estimated locations.

Next, we have relocated the mainshock and an aftershock (9903281936; m_b=5.2) using the same set of stations and the SSSCs. Table 2 shows the relocations of these events.

Table2. Relocation of the mainshock and its largest aftershock

Date	Origin Time hr:mn:ss	Latitude (°N)	Longitude (°E)	Depth (km)
99/03/28	19:05:08.26±1.274	30.51±0.045	79.24±0.o45	15.0±1.0
99/03/28	19:36:04.17±1.487	30.463±0.045	79.150±0.045	19.0±1.0

We have located the mainshock 15.6 km from the ISC (International Seismological Center) and 14.7 km from the Harvard CMT locations, which are at 30.512°N 79.403°E and 30.38°N 79.21°E, respectively. The ISC and HRV locations are 23 km apart. The aftershock is also mislocated by these organizations by about 27 km.

We emphasized locating the mainshock because it is a large event in the Himalayan foothills, and its accurate location can provide means to calibrate 3D models (Ritzwoller et al., 2002) for the structure of the Tibet and Indian subcontinent for future monitoring of the Comprehensive Test Ban Treaty. This new location can improve the locations of other events in the neighborhood of the Chamoli earthquake.

29 September 1993 Latur earthquake, India

This is a large earthquake that occurred 200 km northwest of Hyderbad in Peninsular, India, on 29 September 1993 (22h:25m:48.5s, 18.066ºN 76.451ºE, Mw=6.1, ISC). According to Seeber et al. (1996), this is a very shallow earthquake (h=2.6 km), occurred on a southeast dipping (46º) fault and produced significant surface deformation. Kagami et al. (1994) also indicated that this event is shallow. Based on the analysis of teleseismic waveforms, the existence of localized fractures on the surface and the depth distribution of aftershocks, they suggested that most of the seismic energy was released at very shallow depth and the rupture propagated over a very small source area in a very short time, involving a high stress drop during the rupture process. We also analyzed the teleseismic data. By integrating the high stress condition at the source, we also found, based on modeling of teleseismic P waves at 21 stations, this event to have a depth about 6 km (Figure 2a). An event of this size occurring at such shallow depth is

an ideal candidate for satellite data analysis. Additionally, its epicentral area is in the Deccan Plateau, which is nearly flat. The top and bottom left panels in Figure 3 show the line-of-sight (LOS) and total displacement field calculated for one of the nodal planes obtained by teleseismic P-wave modeling (Figure 2b). The top and bottom right panels show the LOS and total displacement field based on the second nodal plane. Based on those calculations, we expected to observed surface deformation of about ±5 cm, but surface deformation could not be identified in the processed interferogram for this event even though the DEM, which was processed from the Shuttle Radar Topography Mission (SRTM) "*.hgt" files was of adequate quality. The radar data used scenes from tracks and frames that encompass the area where the surface deformation was observed by the reconnaissance team following the earthquake (Seeber et al., 1996). One reason for failing to observe the surface deformation is probably the temporal baseline, which is 3 years. The surface deformation may have been masked by flooding of the Tirana River in the epicentral region and new vegetation. We had one pair of satellite data with a temporal baseline of 8 months, but the data were noisy. Although the satellite data could not help us, we continued further investigation using seismic data from a German task force that installed temporary stations that operated in the epicentral region from 10 October 1993 to 20 January 1994. This network included 11 analog, 5 digital and 4 strong-motion instruments. This network recorded many aftershocks of which three aftershocks were reported in the ISC bulletin (Table 3).

Table 3. Locations for three aftershocks of the Latur earthquake (ISC)

Date	Origin Time hr:mn:ss	Latitude (°N)	Longitude (°E)	Depth (km)	nsta/Az Gap
93/11/12	13:27:28.99±2.91	18.0884	76.5309	14.5	48/94º
93/11/18	14:01:32.07±1.04	18.3600	76.8755	33.0f	9/114
93/11/24	14:45:57.74±0.78	18.1818	76.3833	10.0f	8/116º
Locations based on the Local Network Data					
93/11/12	13:27:31.75	18.00083	76.5442	2.5	15/81º
93/11/18	14:01:27.38	18.00083	76.027	8.5	9/110º
93/11/24	14:46:01.71	18.03367	76.5310	5	12/95º

f=fixed, nsta=Number of Stations, Az Gap=Azimuthal Gap

Of the three aftershocks, the largest one occurred on 12 November 1993 (m_b 4.5), and was recorded by a large number of stations extending up to teleseismic distances (R<69º). We used the network location to estimate SSSCs and relocate the main earthquake.

Earthquakes in Iran

In our previous reports (Saikia et al., 2002, 2003), we presented both seismic and InSAR analyses results for several earthquakes in southern Iran. These earthquakes were of small magnitude (M_w < 5). Only one regional and a few stations at upper-mantle distances recorded these earthquakes. In this study, we have further analyzed satellite data for additional earthquakes that occurred in different parts of Iran. Of all the events for which satellite data were analyzed, we were successful in identifying surface deformation for three events. In the following, we present results of one earthquake from our previous studies and then present results for these new earthquakes.

Figure 3 shows interferograms for the 30 April 1999 earthquake (M_w 4.8) formed using radar images for track 20/frame 3051 (99/04/21-99/05-26) and for track 249,/frame 3051 (99/04/02-99/06/11). The surface deformation generated by this earthquake is observed in the upper right of the image at location of 27.87°N and 53.610°E as two circular interferometric fringes. Based on the waveform analysis, we were able to constrain its depth to 4-6 km. While the centroid depth could not be resolved to within ±10 km using the long-period data, the depth resolution improved significantly by using the broadband P waves from stations in the upper-mantle. The latter analysis yielded depth consistent with the results obtained by modeling the surface deformation observed in satellite data. We should note that the ISC and other organizations estimated its depth deeper than 30 km. The seismic depth and InSAR location were used to estimate origin time and Source Specific Station Corrections (SSSCs) for regional and teleseismic stations. These SSSCs were, in turn, used to relocate 11 other events in the proximity of this earthquake.

In order to extend this study to larger earthquakes, we analyzed both seismic and satellite data for the 13 April 1998

Fandoqa earthquake (M_w 6.6). This is a large earthquake, which produced 23 km of surface faulting with up to 3 m right-lateral strike-slip and 1 m of vertical offsets (Berberian et al., 2001). Berberian et al. also analyzed the satellite data relevant to this earthquake, primarily to understand the triggering of slip on the thrust system and the active tectonics in the associated fault zone. We are currently analyzing its seismic and satellite data together for establishing the ground truth location along with the uncertainty associated with the inferred location. We have modeled the teleseismic P waves (Figure 4, left panel) to constraint the depth at 7-km.

We have successfully processed satellite data acquired from orbits 5714 and 17738 and from track 349/frame 2961 on 24 May 1996 and 11 September 1998, respectively and identified several elliptical fringes at the geographical coordinates 32.1579°N and 59.814°E. Using this location as the focus and by searching through the ISC catalog over an 80 km x 80 km area, we found 9 earthquakes to occur during the span of the satellite data. Of these, two earthquakes that occurred on 20 June 1997 (12h57m36.22s, 32.3269°N 60.0240°E, 34.8 km, ISC, HRV M_w 5.6, M_o=4.2x10^{25} dyne-cm) and 4 April 1998 (15h00m53.00s, 32.4338°N 60.0857°E, h=33.0 km (fixed), ISC, HRV M_w=5.8, M_o=2.42x10^{25} dyne-cm) had M_w larger than 5.5. Based on the teleseismic modeling of P waves, the June event has a depth of 9 km (Figure 4, right panel). The Harvard (HRV) depth for this event is 15 km. We are now analyzing the teleseismic waveform for the April event. A comparison of the waveforms at common stations suggests that both these events are shallow. The April event, which is larger by a factor 2, is shallower based on the damage reports alone. While only 60 houses were damaged in Khorasan Province during the June event, at least 12 people were killed, 10 injured and 600 houses severely damaged in the Birjand-Gonabad area (located east of the Khorasan) during the April event. We have further collected waveforms from stations operating in upper-mantle distances with good signal-to-noise ratios. Modeling of these data has yet to be completed, following which we will be able to associate the surface deformation in satellite data with one or both of these events. Since both events are of moderate size and recorded by more than 100 stations, they will provide useful parameters for the calibration of the region.

Another event analyzed for ground truth is the 25 June 1997 (19h:38m:406s, 33.9380°N 59.4750°E, h=10km, NEIC; HRV M_w=5.9, M_o=7.4x10^{25} dyne-cm) earthquake, which occurred 100 km north of the 20 June 1997 and 10 April 1998 earthquakes. Our teleseismic modeled depth is similar to the depths reported in the NEIC and Harvard catalogs. Because of its shallow depth, we expected the surface deformation caused by this earthquake to be discernable on interferograms from the satellite data. As expected, interferograms showed some surface deformation, but the fringes appeared to have added contributions from the large M_w 7.2 Zirkuh (Qa'enant) earthquake of 10 May 1997, thus requiring further analysis toward establishing the location. In addition to these earthquakes, we processed satellite data acquired on 23 May 1996 and 10 September 1998 (frame 2997). The interferogram showed fringes at a location extending from 30.0901°N latitude/50.9873°E longitude to 30.0376°N latitude/51.0390°E longitude. Searching the NEIC earthquake catalog within a 50 x 50 km^2 area around this location, we identified 11 earthquakes with m_b ranging from 3.9 to 5.0, of which four events occurred in a single day on 11 January 1998 about 40 km away. Their m_b varies between 4.7 and 5.0 and depths between 5 km and 70 km. In our earlier study (Saikia et al., 2003), we noted that locations of such small events may be off by several tens of kilometers and the depths are often shallow compared to those presented in the catalog because of the limited access to local network data.

Our final analysis is the recent BAM earthquake of 26 December 2003 (01h:56m:58.10s) in Iran. This event has been subject to several studies (Fielding et al., 2004, Talebian et al., 2004). We have also pursued a study of its rupture process using seismic data to establish a seismic slip model (Figure 5). We intend to invert the seismic data along with the InSAR deformation to constrain the hypocenter using the method discussed in Saikia et al. (2004). We have also used the local SSSCs that were previously established by Saikia et al. (2003) to find its seismic location, this moved the location toward the location determined by the International Data Center (IDC) and away from the Harvard and our own location determined without using SSSCs

CONCLUSIONS AND RECOMMENDATIONS

Estimating accurate ground truth locations for earthquakes is difficult in areas where seismic network stations are sparse or inaccessible. The addition of InSAR data can overcome this difficulty and provide accurate ground truth locations. Earthquakes that do not produce surface rupture may still generate measurable surface deformation observed from processed radar images acquired before and after the event. However, atmospheric noise or topographical uncertainty may have a correlation length smaller than the regular coherence estimation window,

which may prevent retrieval of useful InSAR signals from processed interferograms. Nevertheless, when ground deformation is discernable in satellite data, hypocenter locations of seismic events can be reliably estimated within the error of the fault dimensions (for M 5 earthquake this is about 2-5 km).

Processing of satellite data for earthquakes occurring in the Indian subcontinent did not produce interferograms where surface deformation could be identified. Often the temporal baseline for the available radar data spans over several years during which natural phenomena seem to mask the surface deformation that may have been caused by the earthquakes. We were able to identify surface deformation on interferograms for several earthquakes in different parts of Iran with magnitude ranging from 4.8 to 7.5.

We found the previously established SSSCs based on ground truth locations using synergy between the seismic and InSAR method useful in the relocation of large earthquakes. Although moderate to large shallow earthquakes (M_w > 5.5-6) have large fault dimensions, they are the earthquakes that often produce discernable surface deformation in interferograms formed from the satellite data. Future study should focus on such earthquakes for providing reliable locations for calibration.

REFERENCES

Berberian, M., Jackson, J. A., Fielding, E., B. E. Parsons, Priestley, K., Qorashi, M., Talebia, M., Walker, R., T. J. Wright, and Baker, C. (2001). The 1998 March 14 Fandoqa earthquake (Mw 6.6) in Kerman province, southeast Iran: re-rupture of the 1981 Sirch earthquake fault, triggering of slip on adjacent thrusts and the active tectonic of the Gowk fault zone, Geophys. J.. Int., 146, 371-398.

Fielding, E. J., T. J. Wright, J. Muller, B. E. Parsons, R. Walker (2004). A seismic deformation of a fold-and-thrust belt imaged by synthetic aperture radar interferometry near Shahbad, southeast Iran, Geol. Soc. Am., V32, N7, 577-580.

Foxall, B., J. J. Sweeny, and W. R. Walter (1998). Identification of mine collapses, explosions and earthquakes using InSAR: a preliminary investigation, in Proceedings of the 20th Annual Seismic Research Symposium., Monitoring Comprehensive Test Ban Treaty (CTBT), 21-23 September, pp. 408-416.

Kagami, H., Kuge, K., Bhartia, B. K., and Sakai, S. (1994). Reconnaissance Report: On the 30 September 1993 Earthquake in the State of Maharastra, India, Research report on Natural Disaster, Japanese Ministry of Education, Science and Culture, No. B-5-4, 88p

Lohman, R. B., M. Simons and B. Savage (2002). Location and mechanism of the Little Skull Mountain earthquake as constrained by satellite radar interferometry and seismic waveform modeling, J. Geophys. Res., 107,10.1029/2001JB000627. ETG, 7-1 to 7-8.

Myers, S., M. Flanagan, M. Pasyanos, W. Walter, P. Vincent and C. Shultz (2002). "Location Calibration in Western Eurasia and North Africa: Ground Truth Improved Earth Models, Bayesian Kriging, Regional Analysis, Location Algorithms, Array Calibration and Validation", in *Proceedings of the 24th Seismic Research Review - Nuclear Explosion Monitoring: Innovation and Integration*, LA-UR-02-5048, Vol. I, pp. 351-360.

Saikia, C. K., R. Lohman, G. Ichinose, D. Helmberger, M. Simons and P. Rosen (2002). Ground truth locations - A synergy of Seismic and Synthetic Aperture Radar Interferometric Methods, 24th Seism. Res. Rev., Nuclear Explosion Monitoring: Innovation and Integration, Sept 17-19, p420-429.

Saikia, C. K., R. Lohman, G, Ichinose, and M. Simons (2003). "Ground Truth Location using a Synergy Between InSAR and Seismic Methods", in *Proceedings of the 25th Seismic Research Review, Nuclear Explosion Monitoring: Building the Knowledge Base*, LA-UR-03-6029, Vol. I, pp. 324-333.

Saikia, C. K., Chen, J., G. A. Ichininose, D. V. Helmberger and M. Simons (2004). "Ground Truth Locations using Synergy Between Remote Sensing and Seismic Method – Application to Chinese Earthquake", *26th Seismic Research Review: Trends in Nuclear Explosion Monitoring*, Orlando, FL (Sept. 21-23, 2004).

Seeber, L, Ekstrom, G., Jain S. K., Murty, C. V. R., Chandak, N., and Armsbruster, J. G. (1996). The 1993 Killary earthquake in central India: A new fault in mesozoic basalt flows, J. Geophys. Res., 101, B4, 8543-8560.

Steck, L. H. Hartse, C. Bradley, C. Aprea, A. Velesco, G. Randall, and J. Franks (2002). "Regional Location Calibration in Asia", in *Proceedings of the 24th Seismic Research Review - Nuclear Explosion Monitoring: Innovation and Integration*, LA-UR-02-5048, Vol. I, pp. 430-439.

Talebian, M., E. J. Fielding, G. J. Funning, M. Ghorashi, J. Jackson, H. Nazari, B. Parsons, K. Priestley, P. A. Rosen, R. Walker, and T. J. Wright (2004). The 2003 Bam (Iran) earthquake: Rupture of a blind nstrike-slip fault, Geophys. Res. Lett., 31, L11611-.

Yang, X. and C. Romney (1999). PIDC ground truth event (GT) database (revision 1), CMR Tech Rept, CMR-00/15.

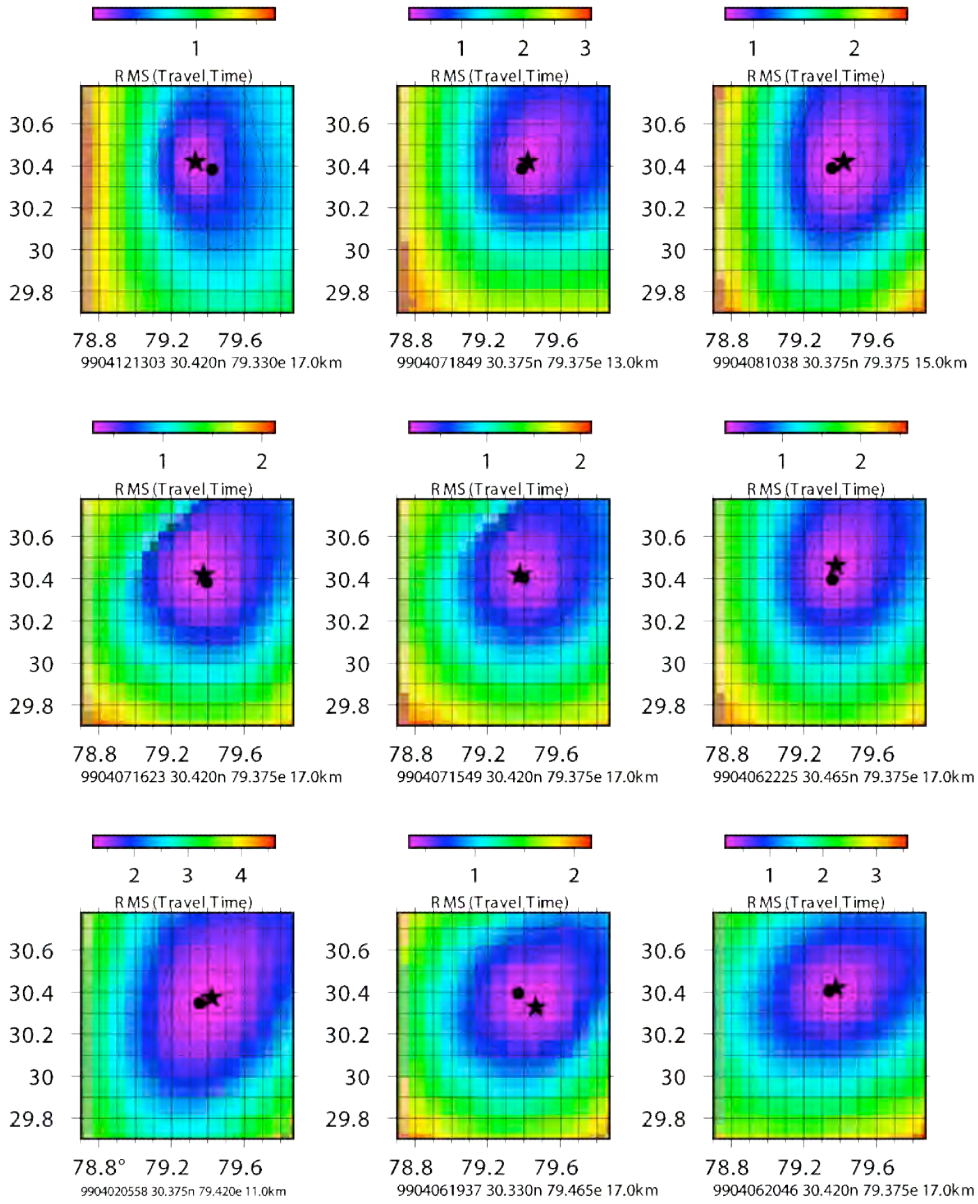


Figure 1 Relocations of nine aftershocks of the March 29, 1999 Chamoli earthquake using our adative grid search algorithm. Events identified as YYMMDDHRMM where YY stands for the year, DD for the month and MM for the day. Stars are the new locations and solid circles are the corresponding locations provided by the scientists in India. The initial contour surrounding the epicenter gives the area over which the RMS (root-mean- squares) origin time error remains same and is minimum, thus essentially corresponds to the uncertainty in the location. The other contours are plotted in an interval of 0.1s.

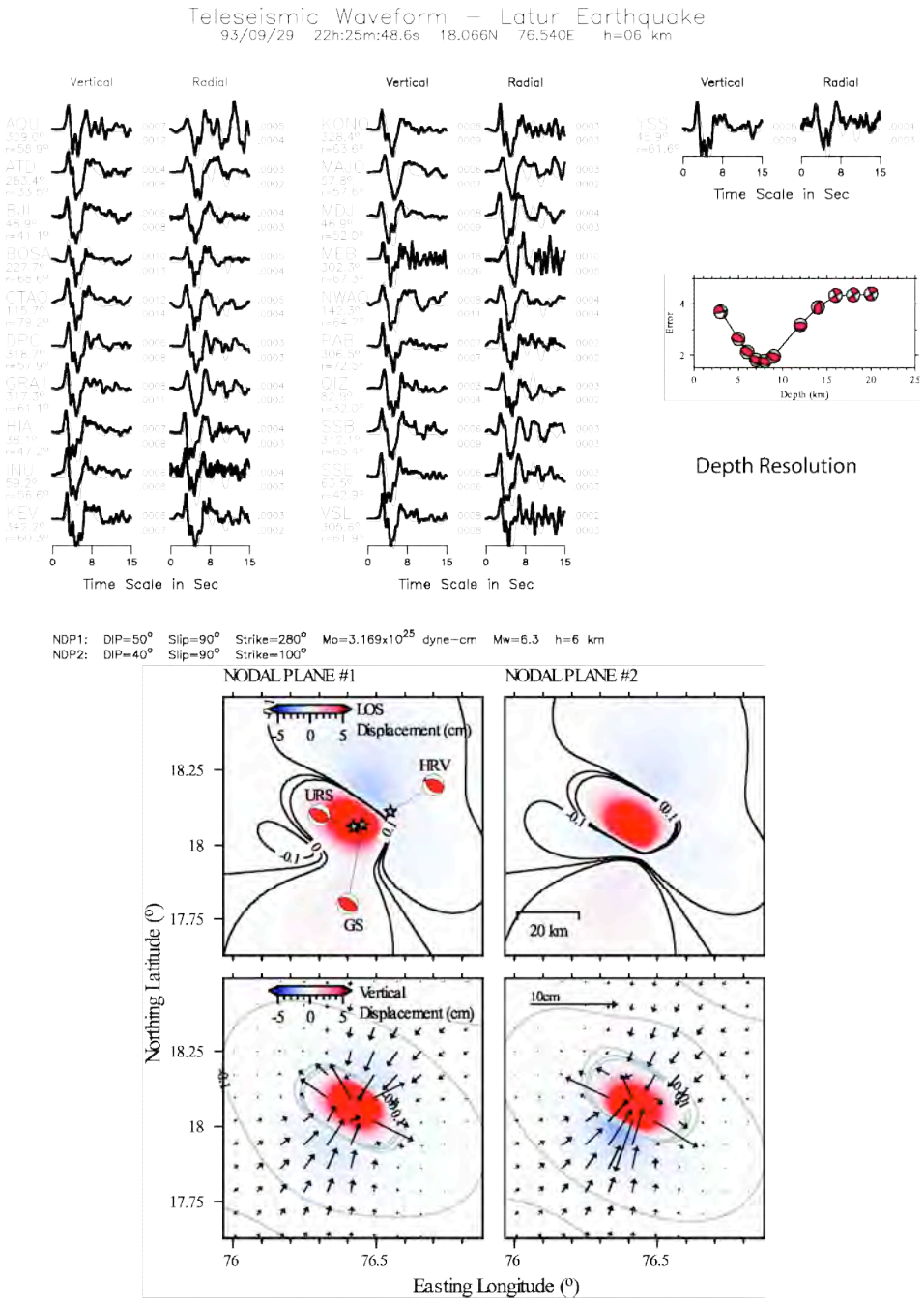


Figure 2. (a) Teleseismic modeling of vertical and radial P waves. Solid traces are the recorded waveforms with instrument response removed. Thin traces correspond to the corresponding synthetic seismograms. (b) LOS (upper) and total (bottom) displacements calculated for the nodal plane 1 (left) and nodal plane (2) right.

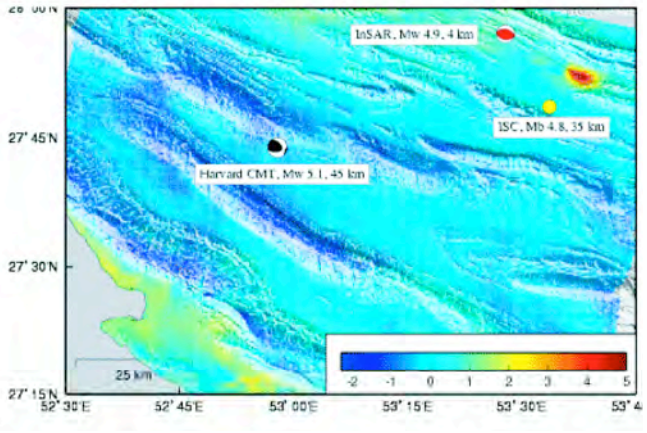


Figure 3. Example showing the seismic locations for the April 30, 1999 southern Iran (Mw 4.8) earthquake relative to the surface deformation observed from the satellite data (elliptical lobe, abot 5 cm surface deformation). Note the location error as well as its error in depth (Harvard nd ISC).

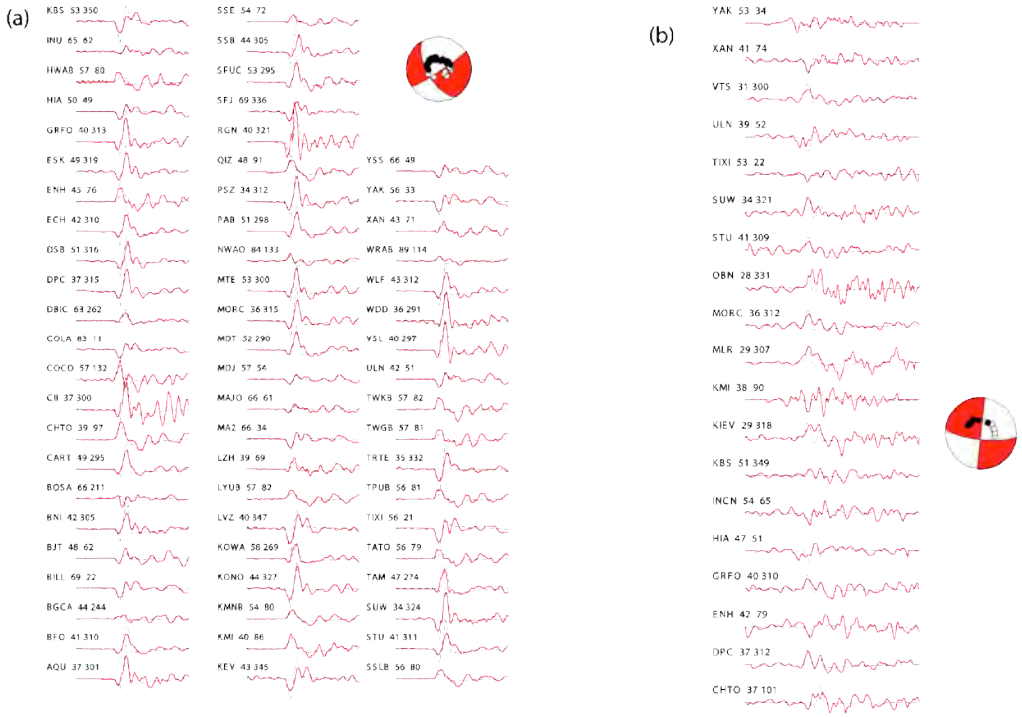


Figure 4. Modeling of teleseismic vertical P waves for (a) March 14, 1998 (Mw=6.6) and (b) June 20, 1997 (Mw=5.6) earthquakes that have occurred in northern and central Iran (red: observed data; dark: syhthetics). Modeling establishes depths of 7 km for the 1998 and 9 km for the 1997nearthquakes. Surface deformation f rom both these earthquakes are observed in satellite data.

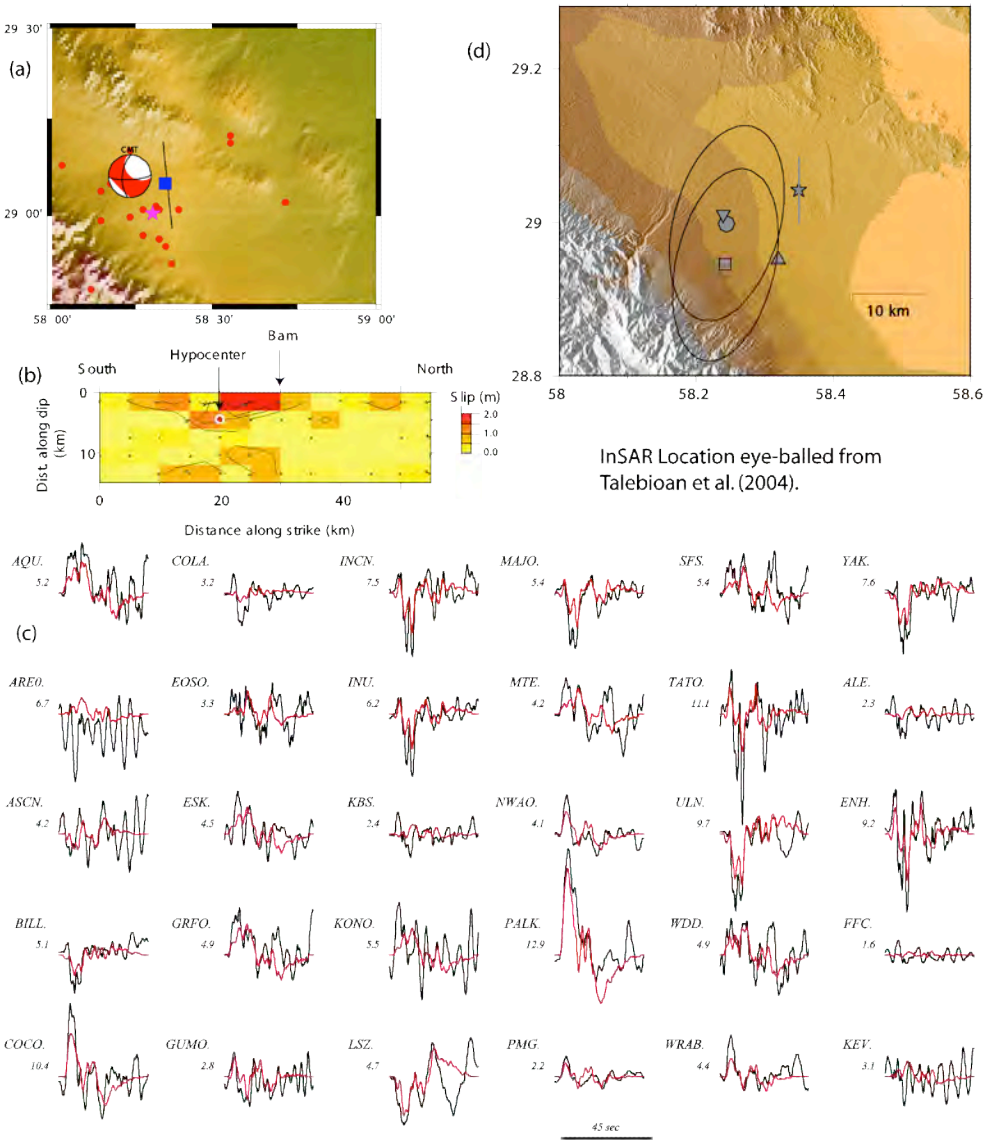


Figure 5. The 2003 Bam earthquake. a - location of the hypocenter (star) and aftershocks (red dots) simplified fault trace and CMT solution. The blue square denotes the city of Bam. b - preliminary slip distribution based on teleseismic body wave inversion. c - observed (black) and synthetic waveforms, d - comparison of different hypocenters, IDC (triangle), Harvard CMT (centroid location, inverted triangle), INSAR (star) and our locations including SSSC's (square) and without SSSC's (circle).

GROUND TRUTH LOCATIONS USING SYNERGY BETWEEN REMOTE SENSING AND SEISMIC METHODS - APPLICATION TO CHINESE EARTHQUAKES

Chandan K. Saikia[1], Ji Chen[2], Gene A. Ichinose[1], Donald V. Helmberger[2], Ali O. Konca[2], and Mark Simons[2]

URS Group, Inc[1]; California Institute of Technology[2]

Sponsored by Department of Energy
Office of Nonproliferation Research and Engineering
Office of Defense Nuclear Nonproliferation

Contract No. DE-AC52-03NA995051

ABSTRACT

The primary objective of this study is to establish ground truth locations of moderate to large magnitude earthquakes ($4.5 \leq M_w \leq 8$) occurring in China using a synergy between seismic and synthetic aperture radar interferometric methods. To this end, we have analyzed both seismic waveforms and relevant InSAR data for the Tibet (Manyi) earthquake (97/11/08, origin time: 10h02m, latitude: 35.069˚E, longitude: 87.325˚N, PDE; and M_w=7.5) and its large aftershock (01/03/05, origin time: 15h50m, latitude: 34.369˚N, longitude: 86.902˚E, and M_w=5.7). In addition to these events, we have also successfully analyzed similar data from another earthquake in northeastern China (98/01/10, origin Time: 03h50m, latitude: 41.11˚N, longitude: 114.55˚E, and M_w=5.7). For this last event, we modeled its teleseismic P waves and long-period regional waveforms separately and established a depth of 7 km, consistent with the depth estimates reported in the EHB and ISC catalogs (within ±2km). Our estimated depth is off by tens of km from other catalogs including the value reported in the Chinese catalog. We have further analyzed the radar data from frame 2772 on tracks 304 and 32, and geo-deformation from this earthquake could easily be delineated in the processed interferograms. For the 1997 M_w 7.5 Manyi earthquake, we established kinematics rupture model using teleseismic P waves (14 stations) and SH waves (9 stations). Seismic data could be modeled using a vertical fault plane striking toward 80˚N, but their complex waveform characteristics required three major sub-events. The slip in the first 4 sec from the first event was very small, which was followed primarily by a pure strike-slip sub-event and occurred east of the hypocenter rupturing for about 6 sec with a peak slip around 7m. The second sub-event occurred 40 km west of the hypocenter and ruptured following 15 to 25 seconds of the first event. The third event occurred 80 km west of the hypocenter about 45 sec later. The average rupture velocity is 2.1 km/sec, which is about 60% of the shear velocity. A slip model was also built based on the geo-deformation obtained by processing InSAR data from frame 2889 on tracks 33, 76, and 305. The major pattern of slip distribution is consistent with the seismic analysis, but the slip distribution requires about 33 km spatial shifting to 35.30˚N and 87.55˚E. This new slip model is being used to refine the hypocenter on the fault using a procedure recently developed by Chen et al. (2004). The seismic study pertaining to its aftershock has indicated that it is a shallow event and we have ordered its radar data only recently. We further completed regional and teleseismic modeling, including the prediction of the static wavefield, for a M_w 6.4 earthquake (98/08/27, 09h03m34.7s) in southern Xinjiang Province, which indicates that it must have produced surface deformation that will be discernable in satellite data. These new locations will allow a high-quality calibration of a large area around the epicenters using arrival times for various seismic phases that are available for these two events from many stations of the Chinese National Network.

OBJECTIVES

One of the most important problems in seismic monitoring is in determining ground truth (GT) locations so that the events can be used for calibration. Usually, large explosions provide the best GT location with error in the order of 1 km, but they are limited and one must rely primarily on earthquake data to extend the geographical coverage. Geodetic data, in the form of Synthetic Aperture Radar Interferometry (InSAR) measurements, provide much needed help in this process under some circumstances. The overall goal of this ongoing study to utilize geodetic data to establish high quality locations for shallow and moderate-sized earthquake in Asia and North Africa in conjunction with seismic methods to validate ground truth (GT) location results. The work concentrates on events in North Africa (Algeria, Libya, Morocco, and Egypt), southwest Asia (Iraq and Iran, including China) and the Korean Peninsula. One of the major objectives of this study is to develop schemes to ascertain the location of rupture initiation on a given fault associated with large earthquakes. In this presentation, we will discuss earthquakes occurring in China, which have potential to become candidates for such GT events.

RESEARCH ACCOMPLISHED

November 8, 1997 (M_w 7.6) Tibet (Manyi) Mainshock

Our initial thrust here is in development of schemes that integrate both seismic and satellite data in order to establish the GT locations of large earthquakes. The earthquakes of magnitude greater than 6 at shallow depths provide strong co-seismic deformation that is easily discernable in satellite data, but unfortunately are difficult for establishing their epicenters. However, co-seismic deformation can be inverted for a dislocation fault model and the seismic data can then be inverted for a dislocation fault model and the seismic data can be used to establish the time delays of these slip elements on the fault. This approach proved highly effective in the study of the Chi Chi earthquake (Ji et al., 2004).

In this study, we demonstrate the resolving power of InSAR in conjunction with seismic data for the November 8, 1997 M_w 7.6 Manyi (Tibetan) earthquake. This event occurred along the Kun Lun fault as displayed in Figure 1. The fault that ruptured has been studied by Tapponier and Molnar (1977) and portion of it ruptured earlier in 1973. Three epicenters for the main event were reported; two based on the teleseismic data (Centroid Moment Tensor, USGS) and one based on the regional travel time data as published by the Chinese Seismological Bureau (CSB), Beijing. The fault breakage outlined in Figure 1 is discussed in Peltzer et al. (1999).

Modeling of the Teleseismic Data

We used a waveform inversion procedure developed by Ji et al. (2002a,b) that uses wavelet transforms to model the P and S data. The slip model developed based on the teleseismic P waves assuming the location from the Chinese Digital Seismograph Network (CDSN) as a rupture initiation point, including the linear strike orientation (W18°N) of the inferred fault, are displayed in the top panel of Figure 2. We used P waves from 14 and SH waves from 9 teleseismic stations to establish its kinematics rupture process. Seismic data seemed consistent with a vertical fault striking toward 80˚N, but the complex waveform characteristics in observed data required three major sub-events. The slip in the first 4 sec from the first event was very small, which was followed primarily by a pure strike-slip sub-event and occurred east of the hypocenter rupturing for about 6 sec with a peak slip around 7m. The second sub-event occurred 40 km west of the hypocenter and ruptured following 15 to 25 seconds of the first event. The third event occurred 80 km west of the hypocenter about 45 sec later. The average rupture velocity is 2.1 km/sec, which is about 60% of the shear velocity. The event based only on the data shown in Figure 2 has a large asperity near the CDSN epicenter with nearly pure strike-slip vectors although a second energy release occurs to the east separated by about 50 km. Nearly all of the slip occurs above the depth of 15 km. This slip distribution is quite compatible with those of Velasco et al. (2000).

InSAR Results

The InSAR data used in conjunction with the fault breakage geometry is given in the middle panel in Figure 2. Using ROIPAC, we processed radar data from frame 2889 on tracks 33, 76, and 305 using ROIPAC jointly developed at Jet Propulsion National Laboratory and California Institute of Technology. The slip appears to be more concentrated in length, but deeper in extent; its signature appears different from the seismic model. The distributed slip occurs along six segments with slight changes in rotation as indicated in Figure 1. The slip vectors indicate some thrust motion near

the CDSN epicentral location, which appears to be associated with the rupturing of the asperity on the right. Since it is a big earthquake, we can combine this data with the seismic data to establish a better location of the epicenter.

Synergy of Seismic and InSAR Results

The combined inversion produces a very good fit to all data (discussed later) with a complex looking picture (bottom panel in Figure 2), but its major feature is similar to the slip model developed based on the InSAR data alone. The dominate motions and geodetic filed occurs over a zone of about 50 km, which appears to be well resolved. The pattern to the east seems too complicated and may be produced by forcing the seismic data to fit. Note the shallow and deep pattern, which produces some interference patterns in the waveform fits. The most important change in result in this new position of the epicenter, which moved 20 km to the west and to a depth of 16 km.

Prediction of Regional Waveforms

One of the biggest advantages of this inversion method is the simplicity of our time history, which is essentially one parameter

$$\dot{S}(t) = \frac{1-\cos(2\pi t/r)}{r} \qquad 0 < t < r$$

where $\dot{S}(t)$ is the derivative of the rise-time, after Cotton and Campillo (1995). This assumption greatly reduces the number of the parameters used in the inversion and allows predictions (Ji et al., 2004). For example, the predictions at stations situated on the Tibetan Plateau are displayed in Figure 3. These fits are based on absolute travel times and amplitudes which appear to agree very well with the crustal model of the region.

Foreshock Problem

The location in Figure 2 (bottom panel) is controlled by the main rupture and not affected by weak precursor, which has been reported in *ACTA Seismologica Sinica* (V21, No 5, Sept 1999). They conclude that a small foreshock occurred roughly 5 seconds before the main event based on the CDSN data. This small event can, also, be seen at the teleseismic distances (Figure 4). We present these panels where the beginning motions have been enhanced on the left. The middle column displays observations from several stations WRAB-YSS that start about 5 seconds early ranging in azimuth (133° to 56°). This weak motion appears to come from the same location as the mainshock and is probably a typical initiation event for many of the events that followed.

The location suggested by Velasco et al. (2000) is halfway between our preferred (Figure 1) and the CDSN (35.19°N, 87.43°E), which is in good agreement (roughly 10 km different). We plan to examine the regional data in more detail in future.

March 5, 2001 (M_w 5.7) Tibet Aftershock

The March 5, 2001 (15h:50m:07.63s, 34.258°N 86.860°E, 38.9 km, M_w=5.7) earthquake is the largest aftershock of the Tibet (Manyi) earthquake. Its depth is an unresolved parameter and is deeper than 20 km, as reported in all earthquake catalogs. To ascertain its depth, we analyzed its teleseismic P waves (often noisy at all stations) and found the event to have a complex source process, involving several sources like the mainshock. Teleseismic modeling (Figure 5) shows that its depth can be anywhere between 2 and 6 km. The focal mechanisms determined at these various depths (h<6 km) have the same strike as the mainshock (340°) and similar dip and rake angles. Modeling using the source at deeper depths resulted in focal mechanism that indicates that the earthquake was caused by movement across a tensional fault. Regional seismograms have good signal-to-noise ratios. Preliminary modeling of these regional data indicates that it is indeed a shallow earthquake. In addition, numerical calculation of the static wavefield based on the focal mechanism presented in Figure 5 suggests that its surface deformation will be discernable in satellite data. We will receive its satellite data soon from EURIMAGE and analyze both the seismic and satellite data together to establish its ground truth location.

January 10, 1998 (M_w 5.7) North East China Earthquake

Next, we examined earthquakes occurring in the northeast part of China. We have successfully examined both seismic and satellite data for the January 10, 1998 earthquake (ISC: 03h: 50m:37.88s, 41.1131°N 114.5010°E, h=4.8 km, M_w 5.7). The in-country scientists in China have also located this earthquake using the CDSN travel times and determined its epicentral location at latitude 41.14°N and longitude 114.52°E, similar to the ISC epicenter. The CDSN depth is at 17 km. We modeled its teleseismic P waves and long-period regional waveforms separately and established a depth of 7 km (Figure 6), consistent with the depth estimates reported in the EHB and ISC catalogs (within ±2km). Our estimated depth is off by tens of km from other catalogs, including the depth reported in the CDSN catalog. It is also recorded at 12 regional (R<13.5°) and 16 upper-mantle (15°<R<30°) stations with good signal-to-noise ratios. We also acquired radar data relevant to this earthquake from frame 2772 on tracks 304 and 32 acquired on 97/09/23 and 98/05/26. The interferograms have been processed where we could easily delineate four fringes associated with the surface deformation caused by this earthquake. The horizontal extent of these fringes is from 41.1209°N/114.426°E (lat/lon) to 41.14°N/114.519°E and of the vertical extent is from 41.0926°N/114.467°E to 41.1967°/114.476°E.

The next step in this analysis is to model the delineated surface deformation field together with the regional and teleseismic waveforms to conclusively establish the ground truth location of this earthquake. We collected travel-time data from 85 CDSN stations within 30° for this earthquake which will provide basis for reliable source specific station corrections (SSSCs) for the calibration of China. Additionally, many earthquakes have occurred in northeast China in the proximity of this earthquake. Hence, these SSSCs will enable us to provide reliable locations for these others events (Saikia et al., 2003).

August 27, 1998 (M_w 6.4) Southern Xinjian Province, China Earthquake

Based on the seismic data analysis, we also identified an earthquake that occurred in the southern Xinjiang Province, China on August 27, 1998 (09h03m:34.7s, 39.67°N 77.31°E, h=23 km, Ms 6.4, CDSN). Both regional and teleseismic waveforms of this earthquake were modeled and are consistent with a shallow depth (Figure 7). The top right panel shows agreement between regional data and synthetic seismograms and the bottom panel shows the same for the teleseismic P waves. Teleseismic P waves were modeled using the "Kikuchi method". Like the other earthquakes, this event is also complex and required multiple sources as shown in the top right panel to fit both regional and teleseismic observations. An initial calculation of the static deformation along the vertical line-of-sight has suggested that this earthquake must have produced surface deformation, which should be discernable in the satellite data.

CONCLUSIONS AND RECOMMENDATAIONS

The overall objective of this three-year study is to concentrate on events in North Africa (Algeria, Libya, Morocco, and Egypt), southwest Asia (Iraq and Iran, including China) and the Korean Peninsula. However, this study is primarily focused on the earthquakes occurring China because of the availability of travel-time data from the Chinese network stations. This study shows that the travel-time data from the Chinese Digital Seismograph Network (CDSN) have great promise for analyzing both the seismic and satellite data together towards establishing ground truth locations for some moderate-sized Chinese earthquakes (M_w>5.5). In areas where such seismic network stations will be sparse or inaccessible, such an effort may encounter difficulties.

We analyzed satellite data and successfully identified surface deformation for two earthquakes. Of these, one is the large November 8, 1997 Tibet (Mayni) earthquake. This is a complex earthquake and consists of several events. Several investigators have analyzed this event and the initial locations presented in these studies differ. By combining both seismic and InSAR data, we established a location that differs from Velasco et al. (2000, Figure 1). Because of this variation, we are performing a sensitivity study to establish the level of uncertainties involved in each of these locations.

Surface deformation was distinctly delineated in satellite data relevant for the January 10, 1998 northeast China earthquake.

Seismic analysis has shown that many earthquakes, which are reported to have occurred at depths, are actually shallow. In light of this observation, we need to continue modeling of both regional and teleseismic data of more earthquakes to

establish ground truth for extending the geographical coverage in China. Our next effort will be to extend these studies to earthquakes occurring in the North Africa and Korean Peninsula.

REFERENCES

Chen, Ji., Wald, D. J., and Helmberger, D. V. (2002a). Source description of the 1999 Hector Mine, California earthquake; Part I: Wavelet domain inversion theory and resolution analysis, Bull Seismol. Soc. Am., 92, 1192-1207.

Chen, Ji., Wald, D. J., and Helmberger, D. V. (2002b). Source description of the 1999 Hector Mine, California earthquake; Part II: Complexity of slip history, Bull. Seismol. Soc. Am., 92, 1208-1226.

Chen, Ji., Helmberger, D. V., Wald, D. J. and Ma, K F. (2003). Slip history and dynamic implications of the 1999 Chi-Chi Taiwan, earthquake, J. Geophys. Res., V108, NO B9, 2412, doi:10,1029.2002JB001764.

Chen Ji., Helmberger, D. V., and Saikia, C. K. (2004). Refined locations using InSAR and seismic waveforms, J. Geophys. Res. Lett. (submitted).

Cotton, F., and Campillo (1995). Frequency domain inversion of strong motions: application to 1992 Landers earthquake, J. Geophys. Res., 100 (B3), 3961-3975.

Peltzer, G., Crame, F., and King., G. (1999). Evidence of non-linear elasticity of the crust from the Mw 7.6 Manyi (Tibet) earthquake, Science, 286, 272-276.

Saikia, C. K., R. Lohman, G, Ichinose, and M. Simons (2003). Ground truth location using a synergy between InSAR and seismic methods, 25th Seism. Res. Rev., Nuclear Explosion Monitoring: Building Knowledge Base, Sept 23-25, p324-333.

Tapponier, P. and Molnar, P. (1977). Active faulting and tectonics in China, J. Geophys. Res., 82, 2905-2930.

Velasco, A. A, Ammon, C. J., and Beck, S. L. (2000). Broadband source modeling of the November 8, 1997 Tibet (Mw 7.5) earthquake and its tectonic implications, J. Geophys. Res., V105, B12, 28,065-28,080.

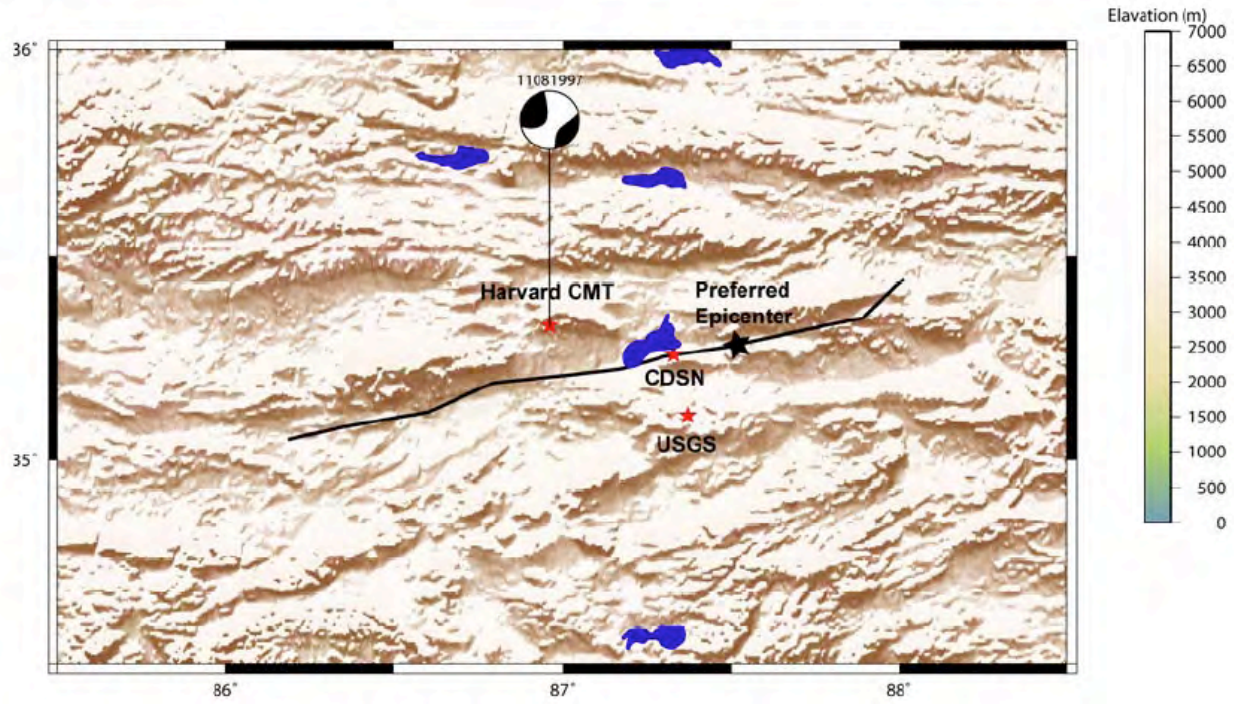


Figure 1. Map with proposed epicenters in red along with our preferred location for the November 8, 1997 Tibet (Mayni) earthquake. The fault breakage is indicated with the heavy dark line.

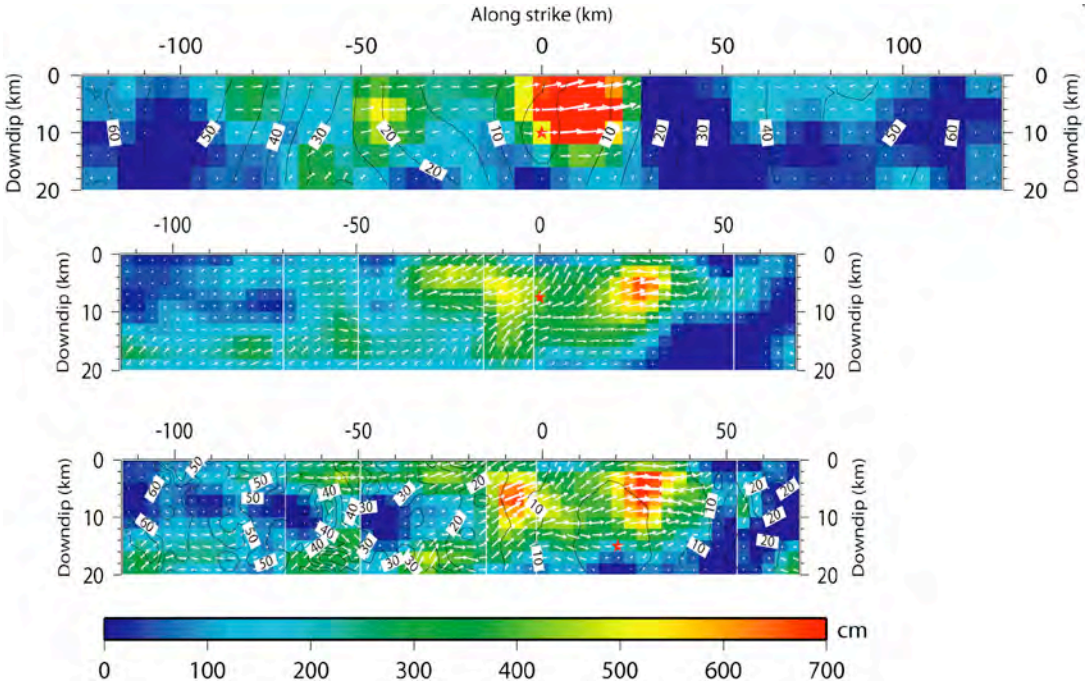


Figure 2. Three panels of slip distributions: top (teleseismic waveforms only), middle (geodetic only, InSAR), and bottom (combined teleseismic and InSAR). Contour lines are included indicating the positions of the rupture front as a function of time after onset. Note that the location of the CDSN epicenter has been shifted 20 km to the right in the bottom panel.

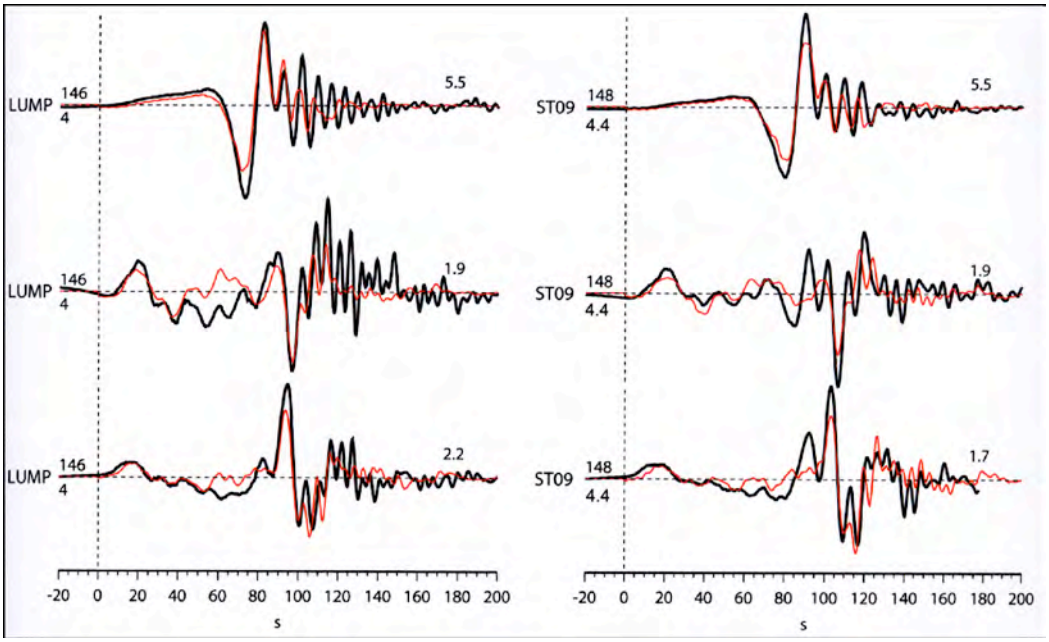


Figure 3. Predictions of synthetics using the combined slip model (InSAR and Teleseismic) along with observations at two PASSCAL stations (INDEPTH III) as given at IRIS stations. They are located about 4 degrees (lower number) and at azimuths given in the top number.

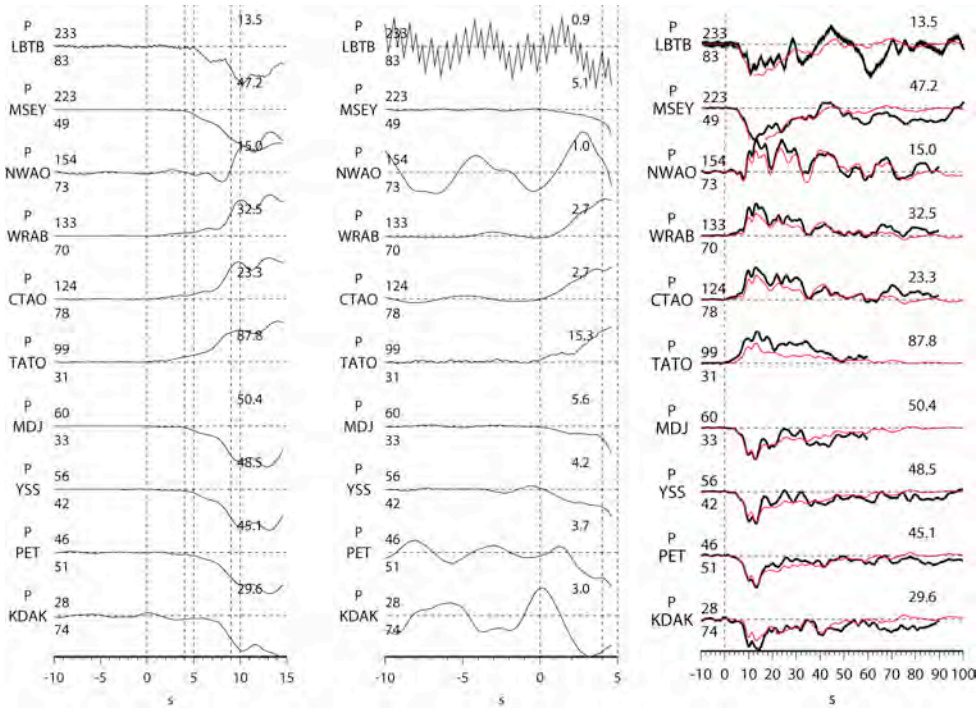


Figure 4. The fits of teleseismic P waveform with the synthetics predicted using the combined slip model (InSAR and teleseismic). Upper number gives the azimuths and lower number the distances. Columns on the left display blow-ups, all aligned on the origin time of the CDSN location. Note the weak onset starting at WRAB.

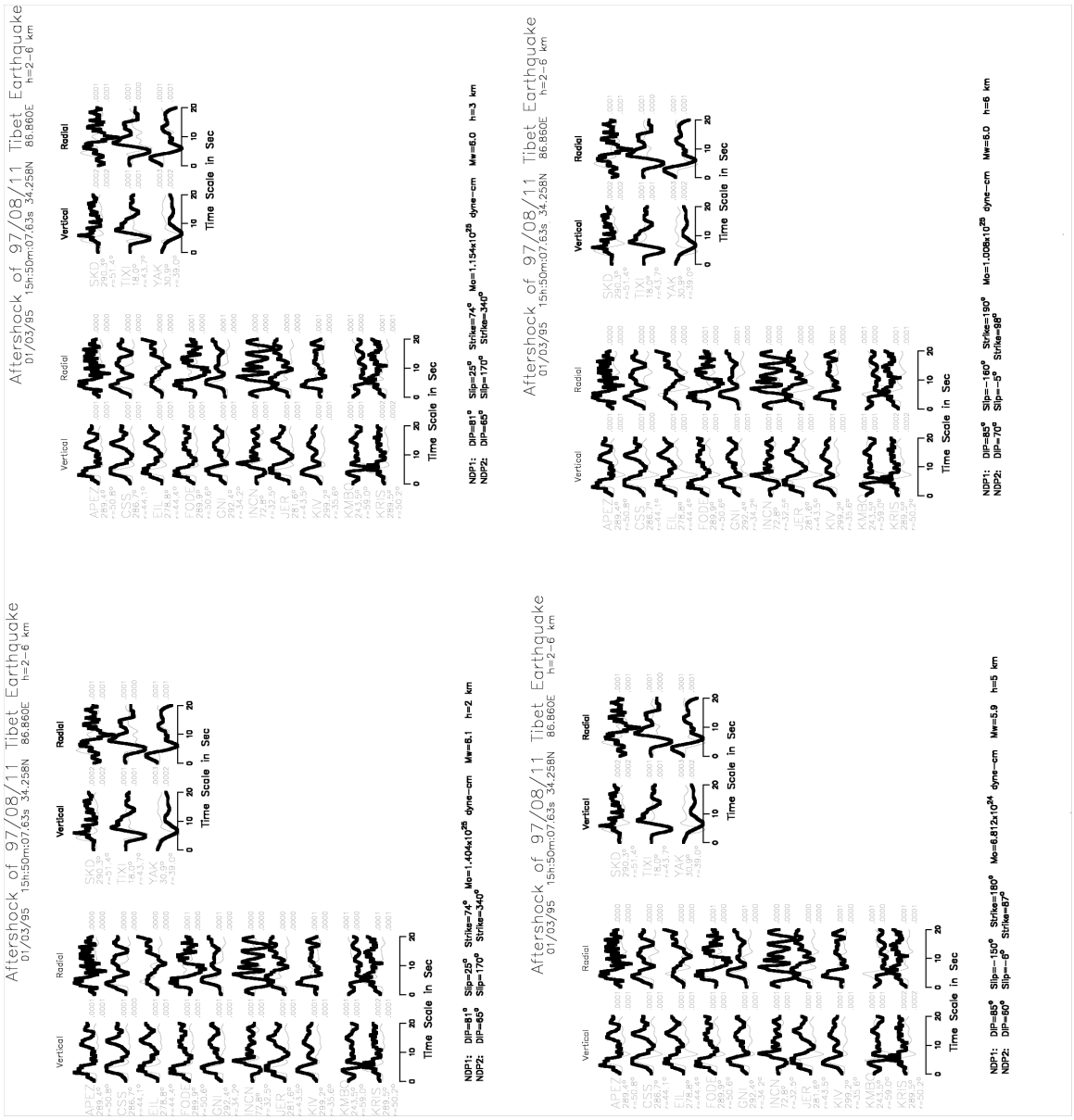


Figure 5. Modeling of teleseismic P waves recorded from the March 5, 2001 in Tibet for a suite of depths and is the largest aftershock of the 1997 Tibet (Mayni) earthquake. We have used a single point source, which is the reason for some mismatch between the synthetics and observations. Based on this modeling study, the earthquake has occurred at a depth shallower than the reported catalog depths.

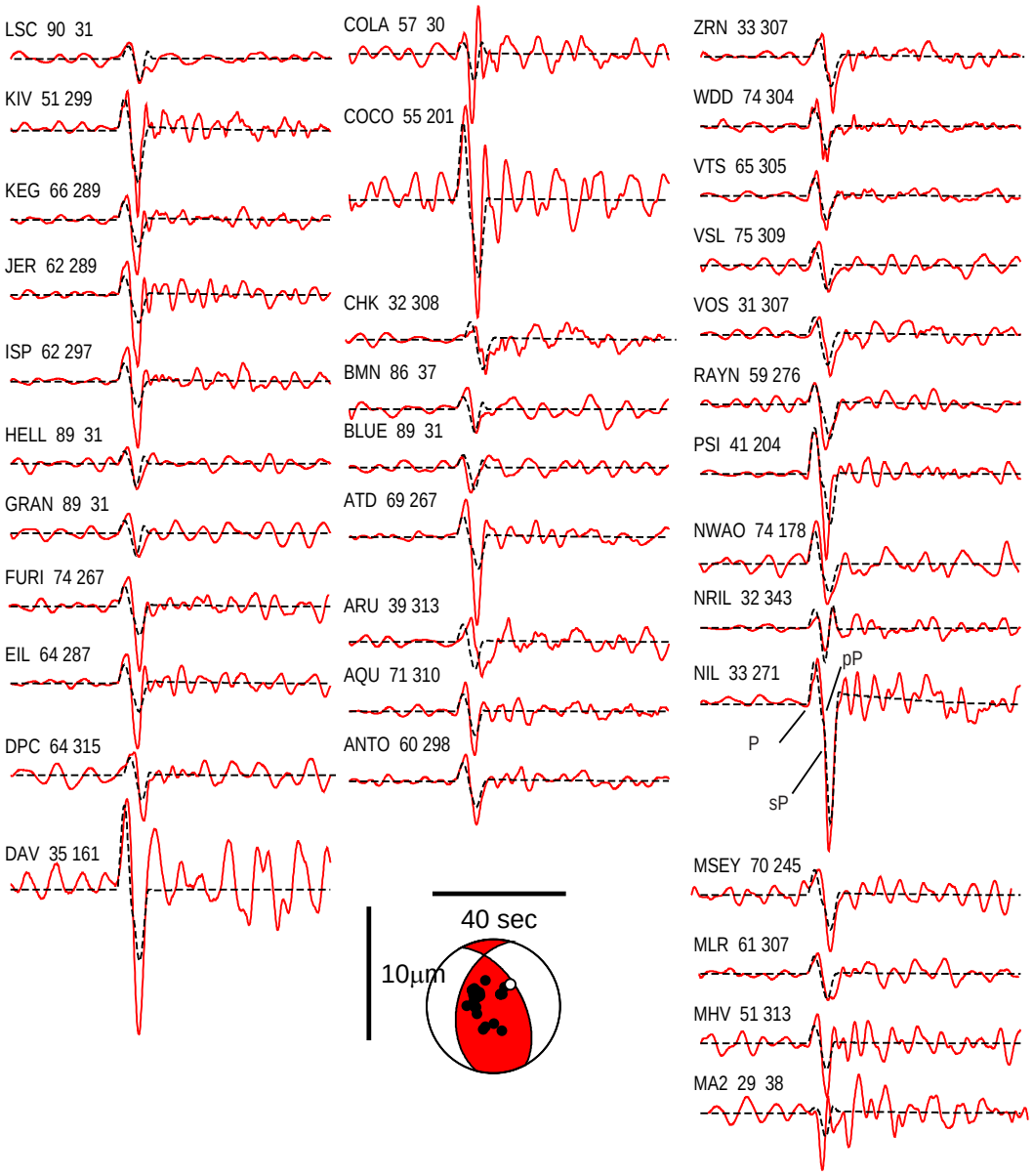


Figure 6. Modeling of teleseismic P waves recorded from the January 10, 1998 North East China earthquake using Green's functions computed for a source at 7 km depth. Also shown is the interference of depth phases (pP and sP) with the P onset.

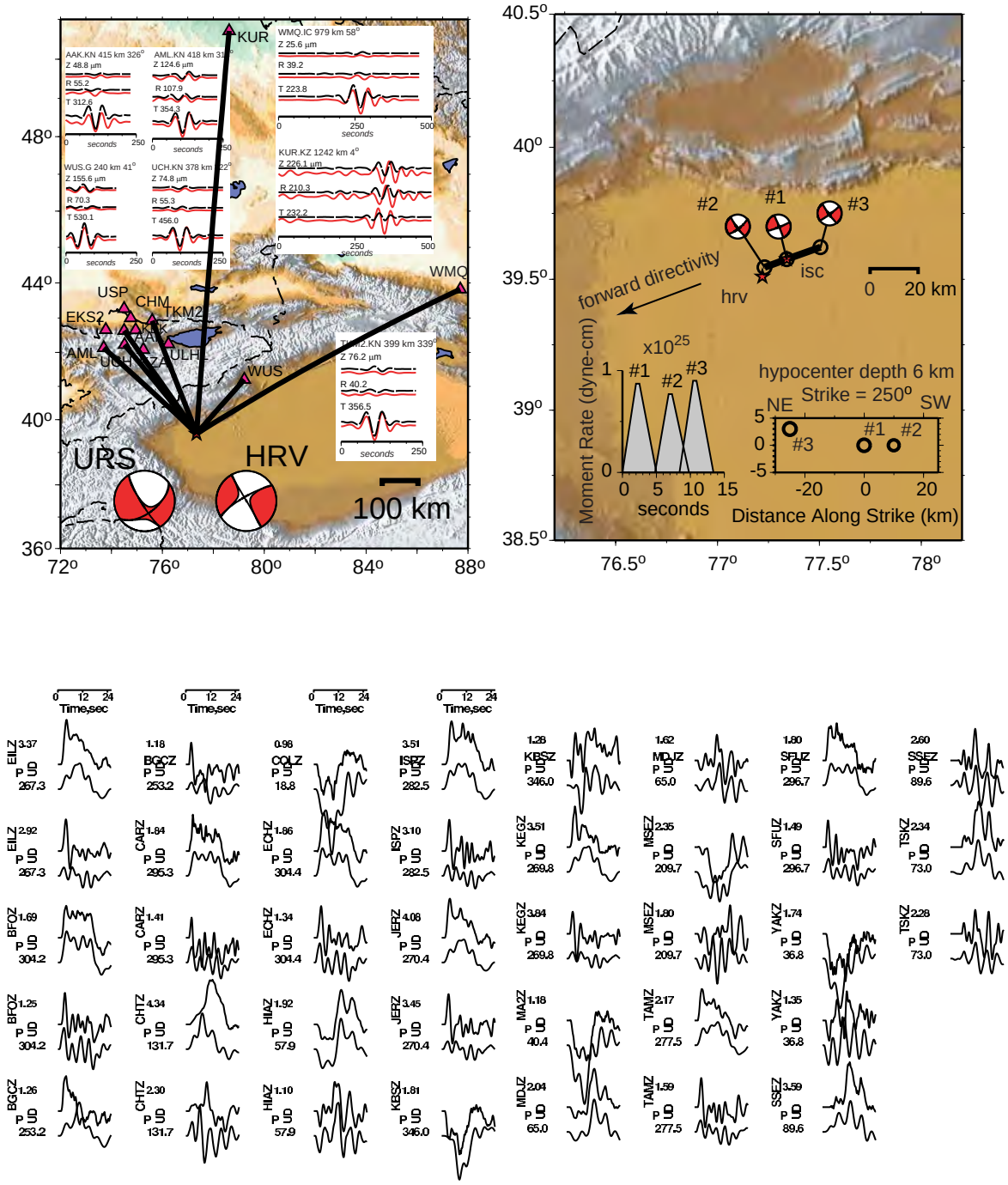


Figure 7. Top left panel shows regional moment tensor inversion (RMTI) results for the August 27, 1998 southern Xinjian Province, China earthquake. Three component long-period data from 7 regional stations were used to estimate the moment tensor solution, and its origin time and centroid depth. The top right panel shows the multiple point sources used in inversion including the results of teleseismic P wave inversion (bottom panel) using the "Kikuchi-method". This modeling is based on three point sources, a triangle shaped moment rate function and a fixed rupture velocity.

GROUND TRUTH IN CENTRAL ASIA FROM IN-COUNTRY NETWORKS

Anne F. Sheehan[1], Gaspar Monsalve[1], Charlotte Rowe[2], and Michael Begnaud[2]

University of Colorado at Boulder[1], Los Alamos National Laboratory[2]

Sponsored by National Nuclear Security Administration
Office of Nonproliferation Research and Engineering
Office of Defense Nuclear Nonproliferation

Contract No. DE-FC52-04NA25541[1], W-7405-ENG-36[2]

ABSTRACT

Our project involves improving the database of seismic event ground truth (GT) information for central and southern Asia using data from a recent broadband seismic experiment in Nepal and Tibet, supplemented by local network data and other regional data. We will develop a catalog of ground-truth events in central Asia where reference-event coverage is poor due to the limited station coverage. The GT catalog will include origin time, hypocenter, and focal mechanisms of well-recorded local events. The results of this project will enable the seismic monitoring community to enhance operational capability to monitor for nuclear tests in central Asia by calibrating station-centric correction surfaces and increasing the ability to accurately locate and identify seismic events in these regions.

The Himalayan Nepal Tibet Seismic Experiment (HIMNT) consisted of the deployment of 29 broadband STS2 seismometers throughout eastern Nepal and southern Tibet during 2001, 2002, and 2003. The network lies in a relatively unexplored but strategic position in close proximity to India, Pakistan, and parts of China. The dataset is unique with many stations in remote and difficult to access locations. Security concerns may limit future deployments in many of these regions. Ground-truth coverage in this region is sparse, and no permanent stations exist in most of the area covered by our array. To date, we have detected and located hundreds of high quality events from the HIMNT experiment using the dbloc2 and dbgenloc software of the Antelope database software. Refinement and validation of GT will be performed using advanced location algorithms (such as the National Nuclear Security Administration (NNSA) event location algorithm Loc00 and the three-dimensional (3D) nonlinear NonLinLoc algorithm), full waveforms, as well as joint inversion for earthquake location and 3D velocity structure. Given our station and event coverage, we are in a good position to determine local 3D velocity structure and to perform joint or iterative inversion for hypocenters and velocity structure. Development of the GT catalog will include supplementing the HIMNT data with that from other networks, collection of additional waveform data, picking of secondary phases, checking against teleseismically located events, and moment tensor and source parameter analysis of GT events (with particular attention to depth control).

Seismic waveforms are often difficult to obtain from sensitive areas. In this case, we have such waveforms in hand and are in a good position to apply and utilize advanced location, velocity structure, and source parameter algorithms. The high quality GT will be used to validate regional scale models for raypaths emanating from the study region, and will be used to validate and further calibrate station-centric correction surfaces that account for unmodeled travel-time variations. Although this is a small area compared to the breadth of the region of monitoring interest, results from deployments of this type may be optimal in terms of GT quality and expense. A number of efforts such as that described here will be necessary to provide high quality GT over broad areas; however, given the restrictions on data availability in the region, such an approach is of great value.

OBJECTIVE

The goal of this project is to contribute to the database of ground truth seismic events in central Asia using data from the Himalayan Nepal Tibet Seismic Experiment (HIMNT) network and other regional seismic data.

RESEARCH ACCOMPLISHED

HIMNT Deployment

The Himalayan Nepal Tibet Seismic Experiment (HIMNT) was a National Science Foundation (NSF) and Incorporated Research Institutes for Seismology (IRIS) PASSCAL (Program for Array Seismic Studies of the Continental Lithosphere) deployment in Nepal and Tibet in 2001-2003 (Figure 1). HIMNT was the first broadband seismic experiment to simultaneously cover the plains of southern Nepal, the Lesser and Greater Himalaya, and the Southern Tibetan Plateau. The HIMNT experiment included the deployment of twenty-nine three-component broadband seismic stations, which recorded continuously at a sample rate of 40 sps. Though the project primarily has tectonic objectives, the high-quality data collected is ideal for ground truth data for monitoring purposes. HIMNT stations were installed with approximately 40-50 km station spacing, covering a two-dimensional area approximately 300 km wide east-west by 300 km north-south (Table 1). This geometry is well suited for both event location and seismic velocity structure projects. Station locations were dictated strongly by logistics, with some stations only accessible by air or by a several day hike on foot. Because of the political situation in Nepal many HIMNT stations would not be safe to redeploy today. Stations from other regional networks are shown in Figure 2, including the Bhutan PASSCAL deployment (e.g. Steck et al., 2004).

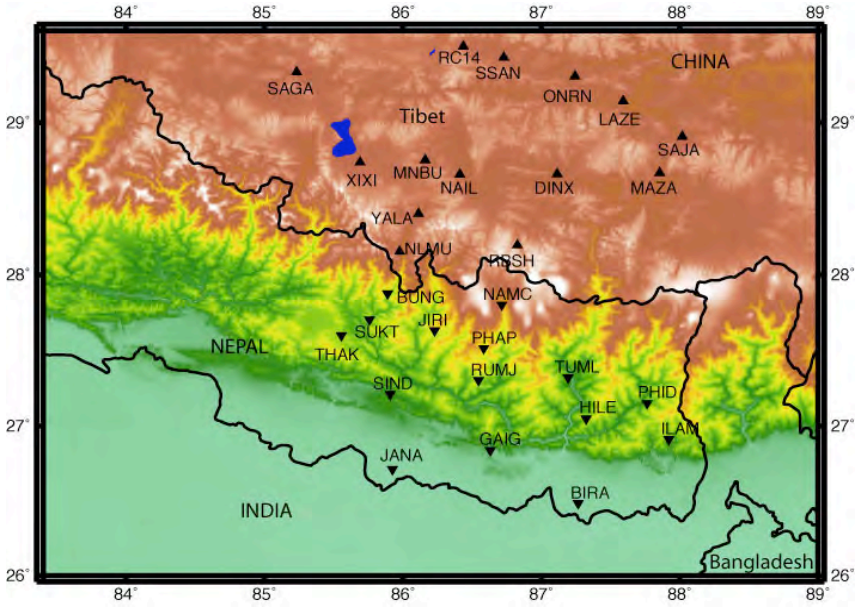


Figure 1. Topographic map with broadband seismic stations of the 2001-2003 Himalayan Nepal Tibet PASSCAL Seismic Experiment (HIMNT).

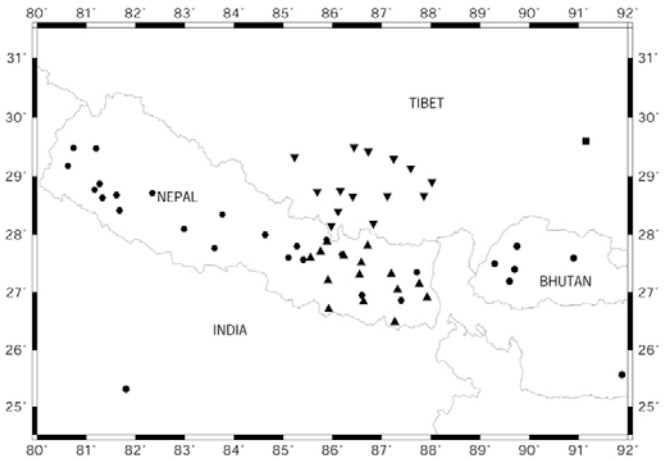


Figure 2. Seismic stations in the vicinity of the HIMNT network. HIMNT stations (triangles), Nepal DMG (circles in Nepal), Bhutan PASSCAL (circles in Bhutan), Indian IMD (circles, more stations off map), GSN station LSA (square).

Data Quality

A background noise analysis for HIMNT stations has been performed (de la Torre et al., 2003). Power spectral density (PSD) estimates of background noise were calculated for all stations and compared to the High Noise Model (HNM) and Low Noise Model (LNM) of Peterson (1993) (Figure 3). All waveforms from designated day and night local time windows for twenty-one day time periods are included in the calculation without segregating events. Moderate noise levels are found for HIMNT stations, with all but the two southernmost stations falling within the HNM and LNM bounds. The southern Nepal (Terai) stations were installed in specially constructed above ground vaults because of the high water table, and exceed the HNM at frequencies greater than 1 Hz. The time period needed for sites to stabilize was found to be short, on the order of one week.

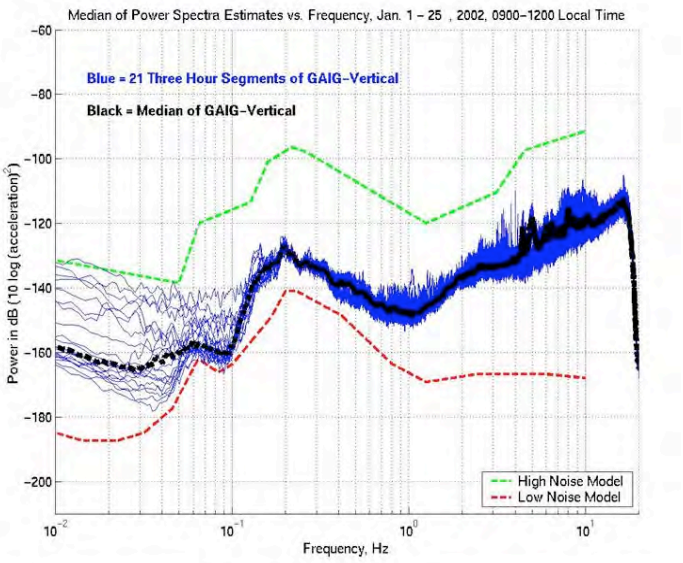


Figure 3. Noise spectra at HIMNT station GAIG, vertical component, daytime. Noise spectrum is calculated for many 3-hour segments, shown, and the median of these segments is calculated. Dashed lines represent the High and Low Noise model of Peterson (1993).

Data Management

The entire continuous HIMNT database has been organized using the Antelope software developed by Boulder Real Time Technologies (BRTT). This package includes software for waveform analysis, including picking and location algorithms. To facilitate first arrival picking, origin tables were made by merging the Nepal Department of Mines and Geology catalog, USGS NEIC catalog (with distance-magnitude criteria appropriate for our purposes), and an automatic event detection list. The automatic event detections are made by first applying STA/LTA criteria to the data to detect possible P-wave arrivals. The STA/LTAs are applied within several filter bands (0.5-1.2 Hz, 0.8-3 Hz, 3-10 Hz), with the STA/LTA window lengths and ratio varying with each filter band. Another algorithm is used to check for detections at several stations inside a given time window, and declaring a trigger if enough stations had a detection within a given time. For each trigger a preliminary location was determined using a grid search algorithm and the detection times. Our merged origin table consists of >10,000 triggers, of which approximately 20% are pickable events. For comparison, the NEIC PDE catalog for this time and area has 71 events (42 within our network footprint) (Figure 4).

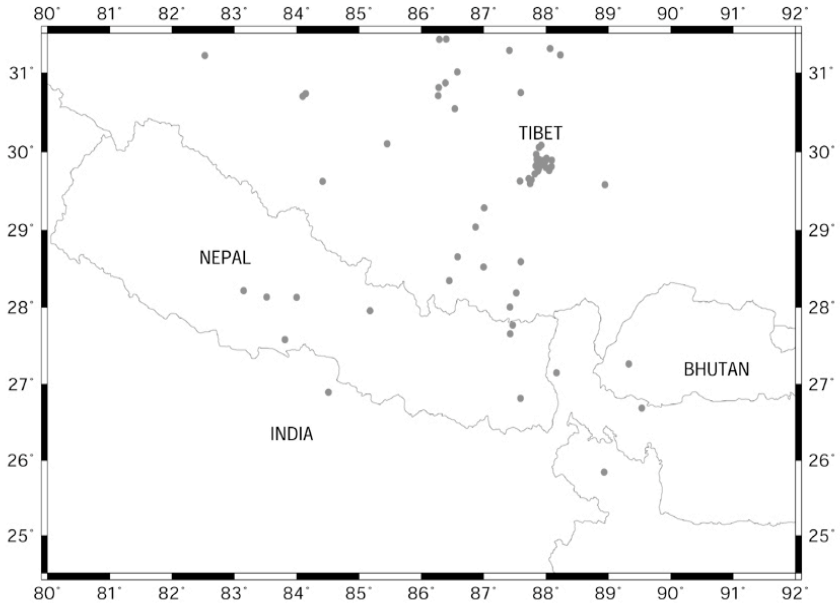


Figure 4. NEIC PDE catalog of events in vicinity of HIMNT, Nov 2001-March 2003. Events depicted by circles, magnitude > 3.5. Our local HIMNT network catalog (in progress) has hundreds more earthquakes.

Waveform Picking

For in-house processing, the data are reviewed by an analyst, with first arrival P-wave and S-wave picks made. Our database contains over 20,000 picks (P and S). Determination of preliminary event locations is underway using the dbloc2 interactive hypocenter location software. The dbloc2 software facilitates the location of hypocenters from picked trace data, while allowing interaction with the location program and the ability to edit arrival picks. The genloc event location library called from dbloc2 utilizes traditional iterative least squares inversion for event location, given station locations, phase arrival times and a velocity model. We use the Nepal velocity model of Pandey et al. (1995) and the southern Tibet velocity model of Cotte et al. (1999) depending upon earthquake location. The velocity models for Nepal and Tibet are dramatically different in terms of crustal thickness. An

important part of our project involves dealing with location uncertainty in light of large structure and velocity contrasts, and modeling of lateral velocity variations in order to obtain well-constrained locations.

Preliminary Locations

From the 700 earthquakes located so far, we find a dense alignment of seismic events along the front of the High Himalaya (Figure 5). Many earthquakes cluster at 15-25 km depth beneath the High Himalaya of northern Nepal, and earthquakes with depths between 70-85 km are found in northeastern Nepal and southern Tibet. Many of the southern Nepal earthquakes are at depths close to the crust-mantle boundary. The double-difference algorithm HypoDD (Waldhauser and Ellsworth, 2000) has been used to relocate earthquakes, improving relative locations. After relocation, the alignment of earthquakes following the front of the High Himalaya is clearer, as well as clustering with depth. As seen by comparing Figures 4 and 5, the NEIC catalog has only a fraction of the events recorded by our network. While most of the best quality ground truth events are likely to be those that were large enough to be detected and reported by the NEIC, we are finding many excellent quality events between magnitudes 3.5 – 4.1 that are not in the NEIC PDE catalog (Figure 6). The number of potential ground truth events will increase when we consider the ISC catalog and our own HIMNT catalog, as well as the expanded network made possible through inclusion of complementary data from Bhutan (e.g., Steck et al., 2004) and regional stations.

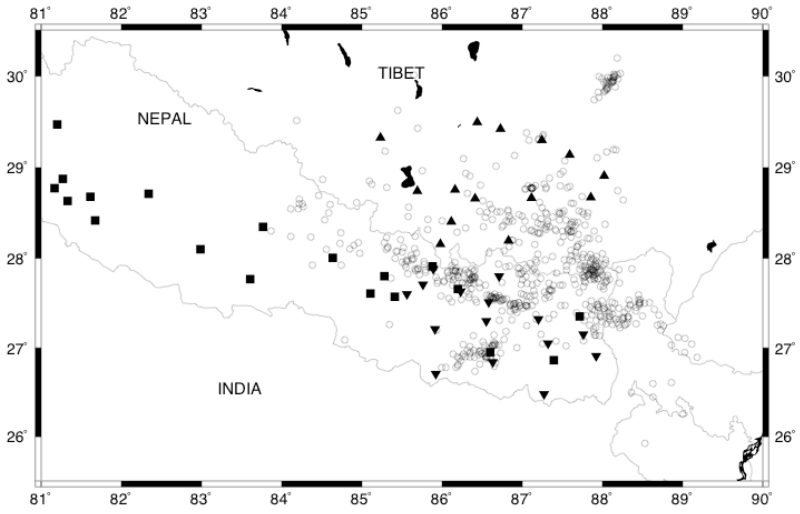


Figure 5. HIMNT preliminary event locations. Events depicted by unfilled circles, seismic stations by solid symbols. HIMNT (triangles), Nepal DMG (squares).

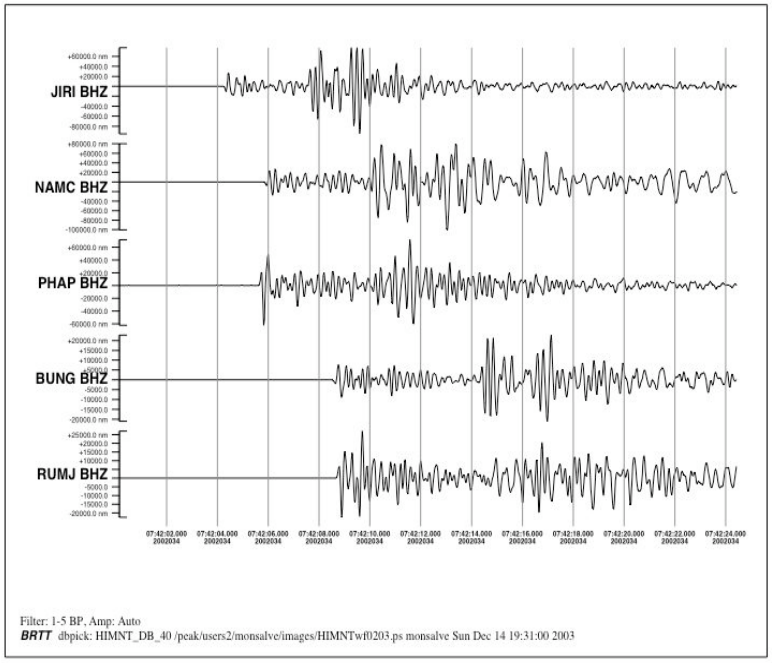


Figure 6. Sample HIMNT seismograms for magnitude 4.1 earthquake of February 3, 2002. This high quality event does not appear in the NEIC PDE catalog. Vertical component at HIMNT stations JIRI, NAMC, PHAP, BUNG, and RUMJ. Closest station is JIRI, at a distance of 30 km. Bandpass filter band 1-5 Hz. Time between tick marks is 2 seconds.

Correction Surfaces and Seismic Event Relocations

Incorporation of these new data will aid in the development and application of preliminary first-arrival P- and S-wave propagation path correction surfaces for regional stations used in seismic locations in Nepal, Tibet, or northern India. This method relies on empirical estimation of corrections that are applied to travel-time estimates in the location process; ground truth is therefore essential. The correction surface method has been shown to be successful in several studies, including those of Myers and Schultz (1998) in the Middle East, and Steck et al. (2001a and b) in Asia. Our approach will be to use the modified Bayesian kriging method currently used by the NNSA labs (Schultz et al., 1998). The method has been implemented in the NNSA kriging tool, Knowledge Base Calibration Integration Tool (KBCIT), and provides output suitable for use with EvLOC, LocOO and other NNSA location tools. GT events from this dataset will be seen at regional stations around Asia, and will be used for calibration of the correction surfaces. In a similar fashion, this GT will provide calibration for regional velocity models around Asia, not just within the study area.

Earthquake locations were initially determined assuming a velocity model with no lateral variations within the lithosphere. In order to account for this lateral heterogeneity, a joint inversion for hypocenter determination and 3D velocity structure will be performed. Given our station and hypocenter distribution, as well as the quality of the arrival time picks and waveforms, out data set is well suited for use of tomographic tools such as tomoDD (Zhang and Thurber, 2003).

CONCLUSIONS AND RECOMMENDATIONS

Use of in-country networks contributes to ground truth location determination in central Asia, important for validation of regional velocity models and correction surfaces. Examination of data from the HIMNT network indicates a wealth of high quality events not indicated in global catalogs such as the NEIC PDE. In addition to detection and location, use of in-country networks will be utilized for source parameter estimation and for event

depth determination. Such events are of utility for GT as well as for regional velocity structure, and will contribute to the NNSA Knowledge Base.

REFERENCES

Cotte, N., H. Pedersen, M. Campillo, J. Mars, J. F. Ni, R. Kind, E. Sandvol, and W. Zhao (1999), Determination of the Crustal Structure in Southern Tibet by Dispersion and Amplitude Analysis of Rayleigh Waves, *Geophysical Journal International* 138, 809 - 819.

De la Torre, T., A. Sheehan, and F. Blume (2003), Broadband Seismic Noise Analysis of the Himalayan Nepal Tibet Seismic Experiment, IRIS Annual Meeting, Fish Camp, California.

Firbas, P., K. Fuchs, and W. Mooney (1998), Calibration of Seismograph Network May Meet Test Ban Treaty's Monitoring Needs, *Eos Trans. Am. Geophys. Union* 79, 413 and 421.

Myers, S. C., and C. Schultz (1998), "Demonstrating Improvement in Seismic Source Location using Bayesian kriging: A Case Study of the 1991 Racha Aftershock Sequence," in Proceedings of the 20th Annual Seismic Research Symposium on Monitoring a Comprehensive Test Ban Treaty, Sept. 21-23, Las Vegas, NV, pp. 66-74.

Pandey, M. R., R. P. Tandukar, J. P. Avouac, J. Lave, and J. P. Massot (1995), Interseismic Strain Accumulation on the Himalayan Crustal Ramp (Nepal), *Geophys. Res. Lett*. 22, 751-754.

Peterson, J. (1993), Observations and Modeling of Background Seismic Noise, Open File report 93-322, U. S. Geological Survey, Albuquerque, New Mexico.

Schultz, C. A., S. Meyers, J. Hipp (1998), and C. J. Young, Nonstationary Bayesian Kriging: A Predictive Technique to Generate Spatial Corrections for Seismic Detections, Locations, and Identification, *Bull. Seismol. Soc. America* 88, 1275-1288.

Steck, L. K., Velasco, A. A., and Begnaud (2001), M. L., On the Use of Kriged P-Wave Travel Time Correction Surfaces: Los Alamos National Laboratory LA-UR 01-1538, 34 pp.

Steck, L. K., A. A. Velasco, A. H. Cogbill (2001), and H. J. Patton, Improving Regional Seismic Event Location in China, *Pageoph 158*, 211-240.

Steck, L. K., C.A. Rowe, M.L. Begnaud, S. Phillips (2004), V.L. Gee, and A.A. Velasco, Turning Straw into Gold: Advancing Seismic Event Location through Difference Constrains and 3-D Models, this volume.

Waldhauser, F., and W. L. Ellsworth (2000), A Double-Difference Earthquake Location Algorithm: Method and Application to the Northern Hayward Fault, California, *Bull. Seism. Soc. Am*. *90*, 1353-1368.

Zhang, H., and C.H. Thurber (2003), Double-Difference Tomography: The Method and its Application to the Hayward Fault, California, *Bull. Seism. Soc. Am*. *93*, 1875-1889.

Table 1. HIMNT Stations *

Station name	Latitude, N	Longitude, E	Elevation (km)	Start date	End date
BIRA	26.4840	87.2670	0.012	10/19/2001	11/10/2002
BUNG	27.8771	85.8909	1.191	10/13/2001	04/06/2003
GAIG	26.8380	86.6318	0.166	10/14/2001	06/03/2002
HILE	27.0482	87.3242	2.088	10/12/2001	11/06/2002
ILAM	26.9102	87.9227	1.181	10/17/2001	10/30/2002
JIRI	27.6342	86.2303	1.866	10/15/2001	10/22/2002
NAMC	27.8027	86.7146	3.523	10/21/2001	03/31/2003
PHAP	27.5150	86.5842	2.488	10/14/2001	04/01/2003
PHID	27.1501	87.7645	1.176	10/22/2001	10/31/2002
RUMJ	27.3038	86.5482	1.319	10/10/2001	04/03/2003
SIND	27.2107	85.9088	0.465	10/19/2001	04/03/2003
THAK	27.5996	85.5566	1.551	10/16/2001	11/07/2002
TUML	27.3208	87.1950	0.360	10/10/2001	04/03/2003
LAZE	29.1403	87.5922	4.011	07/21/2002	10/27/2002
SAJA	28.9093	88.0209	4.351	07/23/2002	11/07/2002
ONRN	29.3020	87.2440	4.350	07/13/2002	08/02/2002
SSAN	29.4238	86.7290	4.585	09/14/2001	09/08/2002
SAGA	29.3292	85.2321	4.524	09/16/2001	10/31/2002
DINX	28.6646	87.1157	4.374	09/26/2001	11/06/2002
RBSH	28.1955	86.8280	5.100	09/20/2001	05/21/2002
NAIL	28.6597	86.4126	4.378	06/26/2002	11/03/2002
MNBU	28.7558	86.1610	4.500	07/18/2002	11/05/2002
YALA	28.4043	86.1133	4.434	07/17/2002	11/04/2002
XIXI	28.7409	85.6904	4.660	07/15/2002	11/01/2002
RC14	29.4972	86.4373	4.756	07/14/2002	10/28/2002
MAZA	28.6713	87.8553	4.367	07/24/2002	11/07/2002
JANA	26.7106	85.9242	0.077	11/13/2001	02/05/2003
SUKT	27.7057	85.7611	0.745	03/05/2002	11/07/2002

*Station NLMU did not have usable data and is not included.

ADVANCING SEISMIC EVENT LOCATION THROUGH DIFFERENCE CONSTRAINTS AND THREE-DIMENSIONAL MODELS

Lee K. Steck[1], Charlotte A. Rowe[1], Michael L. Begnaud[1], W. Scott Phillips[1], Vicki L. Gee[2], and Aaron A. Velasco[2]

Los Alamos National Laboratory[1], University of Texas at El Paso[2]

Sponsored by National Nuclear Security Administration
Office of Nonproliferation Research and Engineering
Office of Defense Nuclear Nonproliferation

Contract No. W-7405-ENG-36

ABSTRACT

Current seismic event location based on kriged travel-time correction surfaces requires high-quality ground truth (GT) for optimal success. Unfortunately in many important regions of the world, including China, it is rare to find more than a handful of events over vast areas whose locations are known with an accuracy of 5 km (GT 5) or less. To mitigate this we are developing a technique for applying relative constraints among travel-time correction surfaces for stations within a network, in effect turning GT 15 or worse into GT 5 or better. This method is based on the hypothesis that for two stations recording the same event, the effect of the event mislocation is eliminated through residual differencing. By exploring the relative travel-time residual differences among events recorded at combinations of station pairs within a network, we can build a set of relationships among residual surfaces that can be fixed to absolute levels by incorporating ground truth information. Nonlinear inversion is used to then find the best-fit surfaces. Using the Northern California Earthquake Data Center (NCEDC) catalog to develop and test our method, we have demonstrated that for well-picked events the travel-time residual differences for events co-linear with a given station pair vary smoothly for crustal P phases. Numerical tests show that the residual relationships are usable over a broad azimuth range, allowing us to include more events than for a strictly co-linear requirement. We plan to extend the method to incorporate regional phases on a variety of available catalogs. To this end, the preliminary z-format Annual Bulletin of Chinese Earthquakes (zABCE) catalog has been relocated with IASPEI91 using our merged global database to test Asia residual data. Data are also being integrated from regional Nepal and Bhutan datasets.

A second innovation we are working on is the use of travel times from three-dimensional (3-D) velocity models in the generation of correction surfaces instead of simple one-dimensional (1-D) Earth models. The National Nuclear Security Administration (NNSA) software design allows us to build empirical correction surfaces from any set of travel-time tables. This capability enables us to better predict travel times in aseismic regions, and it should remove bias in travel times estimated in seismic regions (facilitating improved correction surfaces and reducing bias in earthquake locations). Despite the increase in processing speed and capacity, large global seismic catalogs are still produced primarily by using 1-D velocity models. 3-D velocity models, however, are improving in both resolution and reliability. Studies have demonstrated their superiority over 1-D models in terms of improved location and reduction in uncertainty. It therefore seems appropriate that routine seismic event location methods should migrate to the 3-D velocity model standard. However, we must consider the increased processing time to produce 3-D locations even when using faster computers. It is important to assess the accuracy of 3-D travel-time tables and the ray-tracing algorithms used to create them. We must weigh, in combination with the added computational burden, the merits versus costs of such a transition. Our effort will focus on performing relocation tests on a catalog scale (or at least a large subset), and on analyzing computational times to determine if using 3-D tables for regional location on a routine basis can be justified in an operational setting.

In addition to testing the operational feasibility of using 3-D models in routine location, we are building and testing 3-D models from several sources. Internally, we use LITHO3D, a Matlab-based tool developed at Los Alamos National Laboratory (LANL), to construct 3-D models from published and unpublished velocity and attenuation information.We are currently testing a number of 3-D models for Asia, including the model developed at Massachusetts Institute of Technology (MIT), the Lamont Consortium model, and the LANL model. Early results suggest that the external models perform well under circumstances for which they were designed. Limited Pn performance testing in two specific geographic locations shows similar favorable results for both the MIT and Lamont models.

OBJECTIVE

The objective of this work is to improve seismic event location throughout Asia. This will be accomplished through improving the usefulness of poor-quality ground truth data and by building and improving 3-D velocity models of the region. An essential element of the former is constrained spatial correlation of residual differences between stations, in contrast to the implementation of Rodi et al. (2003) that is based on spatial correlation of residuals between stations, as observed by Steck et al. (2001a), (2001b), and (2001c). For 3-D model building and testing, high quality ground truth is needed, as is the ability to correctly calculate regional phase travel times from 1-D, 2-D, and 3-D models.

RESEARCH ACCOMPLISHED

Correction Surface Differences

Current seismic event location based on kriged travel-time correction surfaces requires high-quality ground truth for optimal success. Unfortunately in many important regions of the world, including China, it is rare to find more than a handful of events over vast areas whose locations are known with an accuracy of 5 km (GT 5) or less. To overcome this limitation, we are developing a technique for applying relative constraints among travel-time correction surfaces for stations within a network, with the goal of in effect turning GT 15 or worse into GT 5 or better. This method is based on the premise that for two stations recording the same event and phase, the effect of the mislocation of the event is reduced through differencing the residuals. By exploring the relative travel-time residual differences among events recorded at combinations of station pairs within a network, we can build a set of relationships among residual surfaces that can be fixed to absolute levels by incorporating available GT information. This does not require high correlation between corrections, merely a stable relationship amongst the given set of events. Biases can exist between stations, possibly arising from different site geology. We have begun to implement a nonlinear inversion to find the best-fit surfaces. Using the Northern California Earthquake Data Center catalog to develop and test our method, we have demonstrated that for well-picked events the travel-time residual differences for events co-linear with a given station pair vary gradually, with little scatter, for crustal P phases. Numerical tests show that the residual relationships are usable over a broad azimuth range, allowing us to include more events than for a strictly co-linear requirement (Rowe, 2003). Our plan is to extend this method to incorporate regional phases on a variety of available catalogs. The zABCE catalog offers significant potential in Asia for this method due to its station density. We are currently relocating the zABCE with IASPEI91 and using our merged global database to assure a consistent treatment of base model and station correction. The use of our merged arrival tables may also improve some locations. Data are also being integrated from regional Nepal and Bhutan catalogs (Sheehan, et al., 2004). Figure 1 shows roughly 45,000 original zABCE event locations. Approximately three million arrivals are associated with these events after our global database merge. Figure 2 shows that stable residual difference relationships between events are present for station pairs in this dataset.

3-D Models

A second innovation we are working on is the use of travel times from 3-D velocity models in the generation of correction surfaces instead of simple 1-D Earth models. NNSA's software design allows us to build empirical correction surfaces from any set of travel-time tables. This capability enables us to better predict travel times in aseismic regions, and should remove bias in travel times estimated in seismic regions (facilitating improved correction surfaces and reducing bias in earthquake locations). Despite the increase in available processing speed and capacity, large global seismic catalogs are still produced primarily by using 1-D velocity models. 3-D velocity models, however, are improving in both resolution and reliability. Studies have demonstrated their superiority over 1-D models in terms of improved location and reduction in uncertainty. It therefore seems appropriate that routine seismic event location methods should migrate to the 3-D velocity model standard. However, we must consider the increased processing time to produce 3-D locations even when using faster computers. It is important to assess the accuracy of 3-D travel-time tables and the ray-tracing algorithms used to create them. We must weigh, in combination with the added computational burden, the merits versus costs of such a transition. Our effort focuses on performing relocation tests on a catalog scale (or at least a large subset), and on analyzing computational times to determine if using 3-D tables for regional location on a routine basis can be justified in an operational setting.

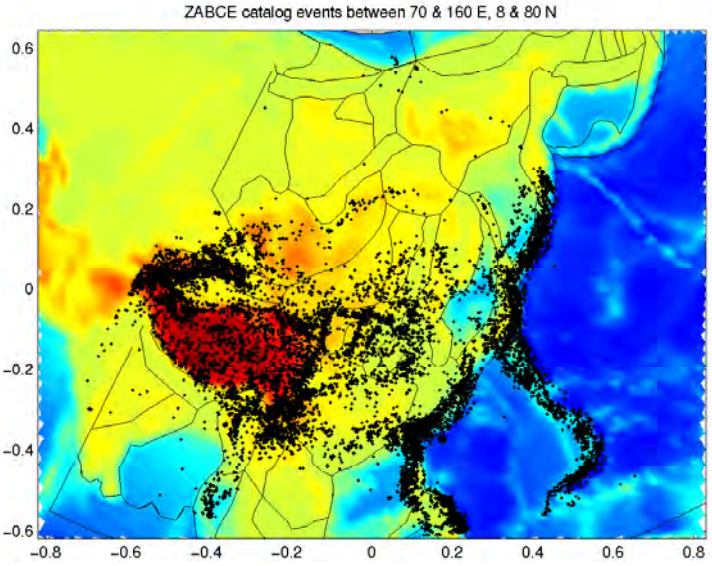


Figure 1. Seismicity plot from zABCE catalog.

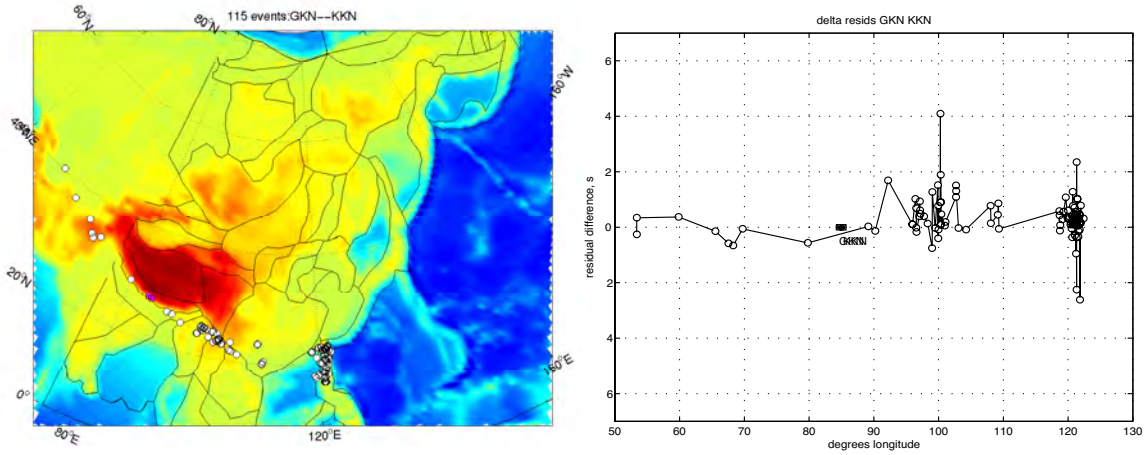


Figure 2. Co-linear seismicity for GKN-KKN station pair from zABCE (left). Residual differences plotted versus distance from stations (projected onto a line of latitude). Note that while the differences cluster around zero mean, such behavior is not required. What we are looking for is a stable relationship, not necessarily zero mean, which is to say it does not require a high correlation between residuals from the station pair.

In the examples, relocations were performed on a 750 Mhz Sun Blade 1000 with 1 Gbyte of RAM. The 3-D travel time table file, in Parametric Grid Library (PGL) format, was 65 Mbytes in size. Figure 3 shows processing times for individual origins having different numbers of associated phases and stations in the selected station list (used in parameter files to limit those stations used). Each event was run five times individually, taking the average and standard deviation. The computation times reported are a sum of the base time required by LocOO/PGL to load and execute a default set of base model station/phase pairs, plus the time required to load the 3-D information associated with the different stations needed, plus the time to perform the location once all data are read in. To show only the time required for the 3-D aspects of the relocation, we took the difference between the average 3-D time and 1-D time for the different numbers of stations available for an event. There is a clear increase in time with the number of stations needed to be loaded/processed for the 3-D relocation (Figure 4, left). Projecting to 100 stations by fitting a line (through zero) to the data (Figure 4, right), we see that the overhead for 3-D location of such an event will be about 16 seconds. The average "reported" events/day for global catalogs (ISC, EDR, and REB) are around 50-85 events/day. Of course, this is only a small portion of the actual events relocated in any given day, but the time required to use 3-D model appears manageable.

Correctly locating seismic events requires a good estimate of the geophysical parameters of the material through which the seismic energy travels. Toward this end, we are developing a geophysical model for China and East Asia (CEA). Our current model was derived as a patchwork of geologically distinct provinces, each of which is assigned a geophysical profile. The profiles are joined and a 3-D model is generated using LITHO3D (Aprea et al., 2001). Two additional geophysical models were obtained from MIT (Sun, 2004) and the Lamont-Doherty Earth Observatory (LDEO) consortium (Richards et al., 2003). We are working to compare these two models with the CEA model and may adopt one in lieu of our ad-hoc CEA parameters where warranted. Figure 5 compares the estimated depth to Moho for the MIT model and our CEA model. The MIT collection of 1-D "layercake" velocity-depth profiles (Figure 5, right) are defined through Monte Carlo perturbation of initial profiles, to minimize travel time misfit for a region near every integer latitude-longitude point, whereas the 1-D "layercake" velocity-depth profiles for the CEA model are constant within a province.

While testing these models using TauP (Crotwell et al., 1998) we see that the LDEO model does a good job of predicting the Pn arrivals, although it incorporates (and provides) no structural information such as crustal thickness or significant discontinuities. The lack of crustal and mantle discontinuities in LDEO model results in the inability to estimate arrival times for other phases that are often important in earthquake location. Unlike the CEA and MIT models, the LDEO model is characterized by velocity gradients (Figure 6) derived to fit travel times for first-arriving P-waves from mantle refractions at regional distances. Like the CEA model, it is characterized using one profile for each large, geologically distinct province. Shallow velocities for each of the LDEO provinces are shown in the map.

To test components of the various models for Asia, we have gathered GT 0-20 information for two nuclear test sites in Asia: the former Soviet test site in Kazakhstan (KTS), and the Chinese site at Lop Nor. Figure 7 (for Lop Nor) shows picks and predictions for the WH3Lc (LANL; Whitted et al., 1999), MIT, and Lamont models. The picks for MKAR and MAKZ are plotted together and suggest that nuclear tests recorded at MAKZ can be used to calibrate models for MKAR. No nuclear tests from KTS have been recorded on either station and seismicity is sparse. There have been numerous chemical shots at KTS that were recorded on MAKZ. Figure 8 shows seismograms for several of these tests, with labels indicating the shot size in tons. Two-ton shots are clearly seen at MAKZ on several occasions. Detailed investigation of high signal-to-noise-ratio (SNR) chemical tests indicates a very small amplitude Pn phase followed a few seconds later by a prominent lower crustal phase which we have tentatively identified as PmP. At low SNR, this secondary phase will be picked as the first arrival. For KTS, Figure 9 shows picks and predictions for the KZ45 (Jih and Wagner, 2000) and MIT models. All models do a decent job of predicting Pn. For our purposes it is advantageous to be able to predict all regional phases from a single model. Of the models tested, the WH3Lc and MIT models do the best job of predicting all observed regional phases for their respective regions.

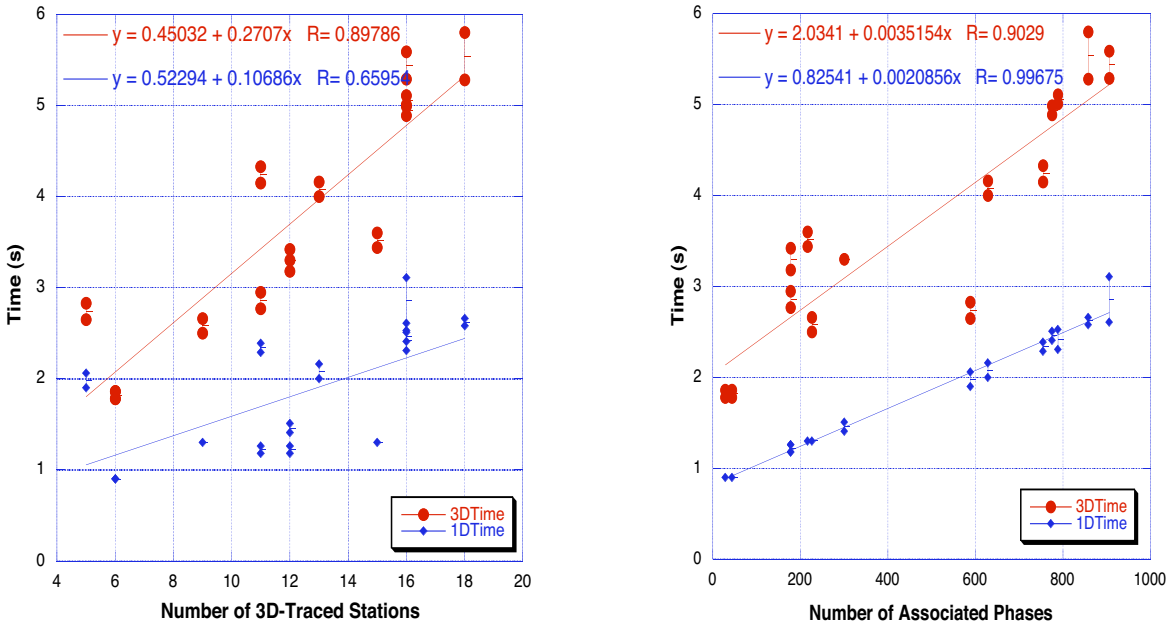


Figure 3. Computation times for 1-D and 3-D locations. Left plot shows dependence on number of 3-D ray-traced stations. Right plot indicates dependence on the number of associated phases. Note that only the stations having 3-D travel time tables built for them are used in the relocations (both 3-D and 1-D).

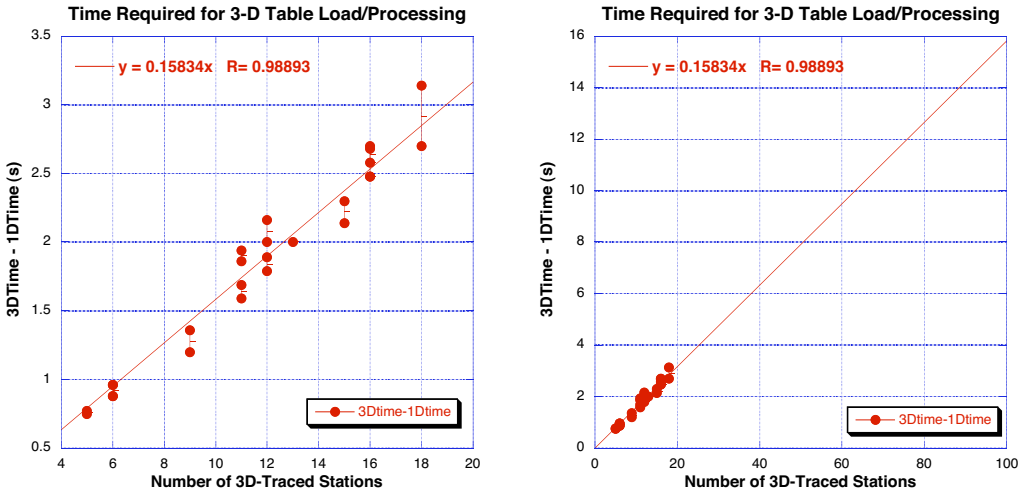


Figure 4. Differences in time between 3-D and 1-D relocations, to highlight the additional burden of 3-D travel-time table usage. The left plot shows actual tests, while the right plot shows a prediction to a 100-station location based on the tests.

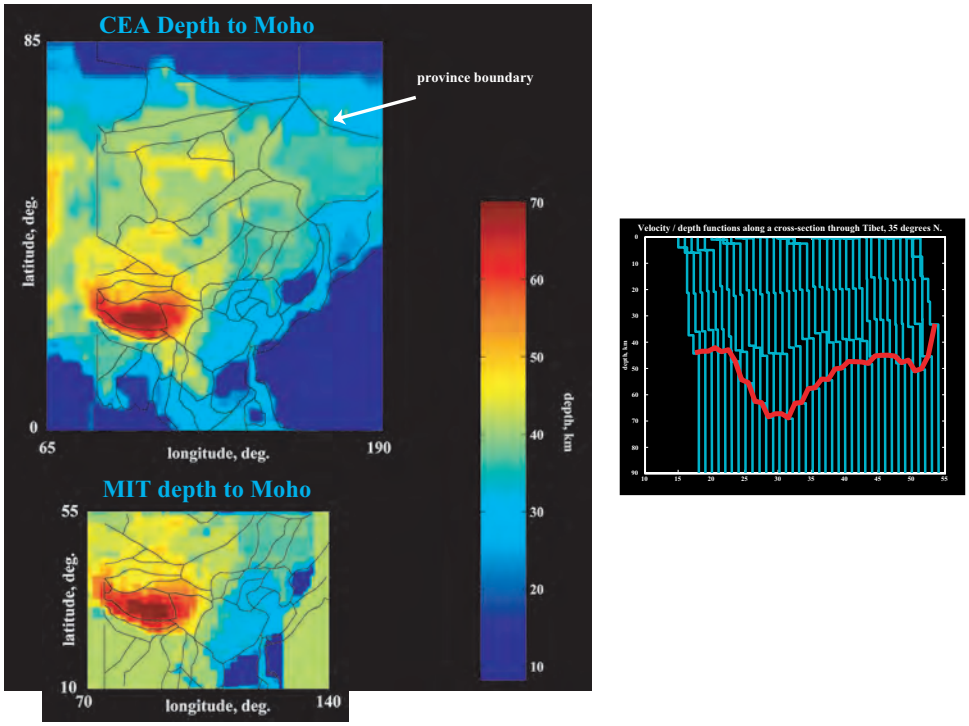


Figure 5. Comparison of Moho depths between the LANL CEA model and the MIT model. Also shown are velocity profiles along latitude 35 north for the MIT model. The red line indicates Moho.

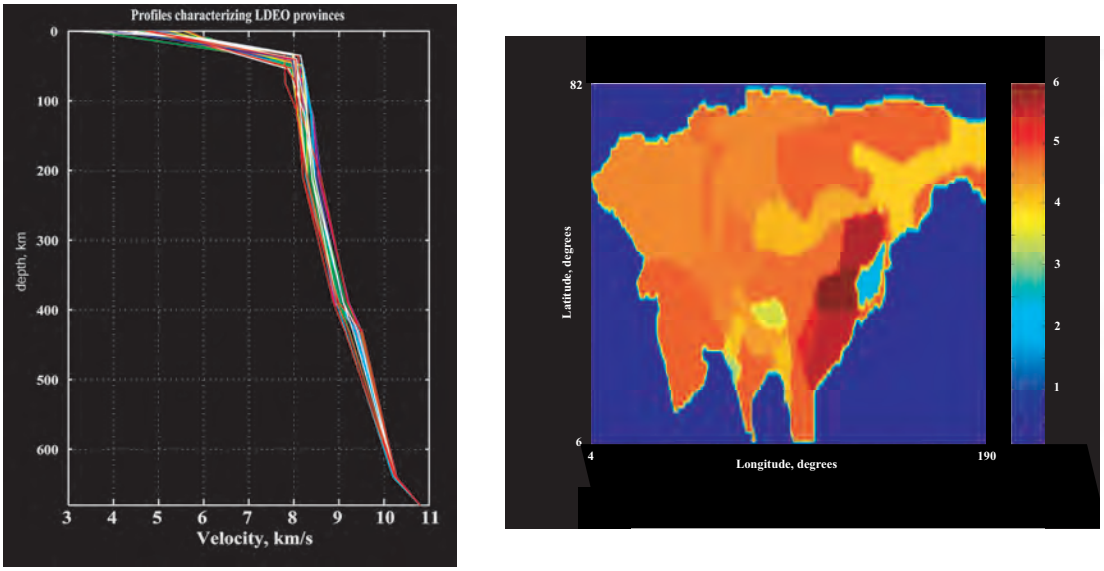


Figure 6. Plots showing some elements of the LDEO model. Left are velocity profiles with depth, right shows the LDEO provinces and shallow velocity structure.

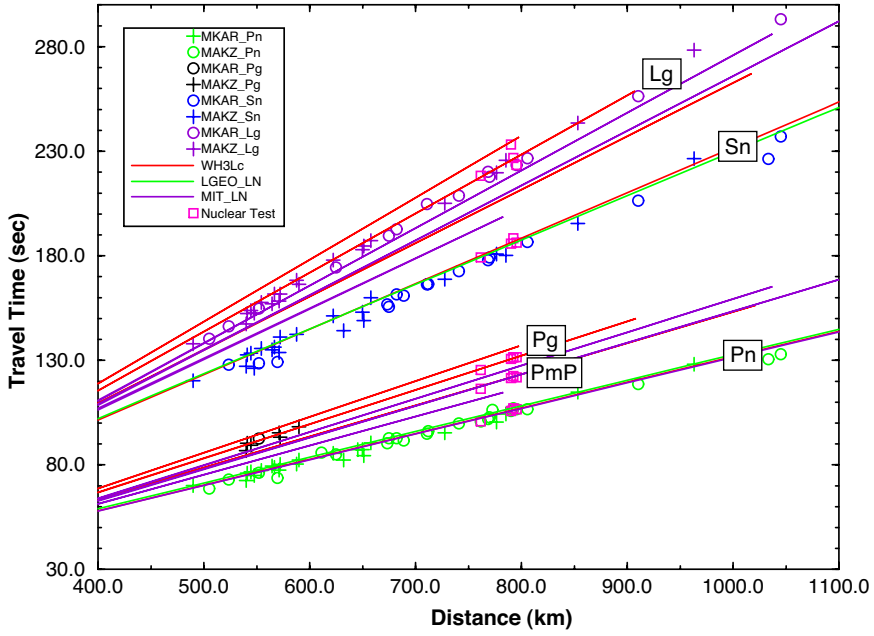


Figure 7. Travel time picks at both MKAR (circles) and MAKZ (plus signs) comparing the WH3Lc, LDEO_LN, and MIT_LN models for a surface source. Text phase labels call out picks and not necessarily model predictions.

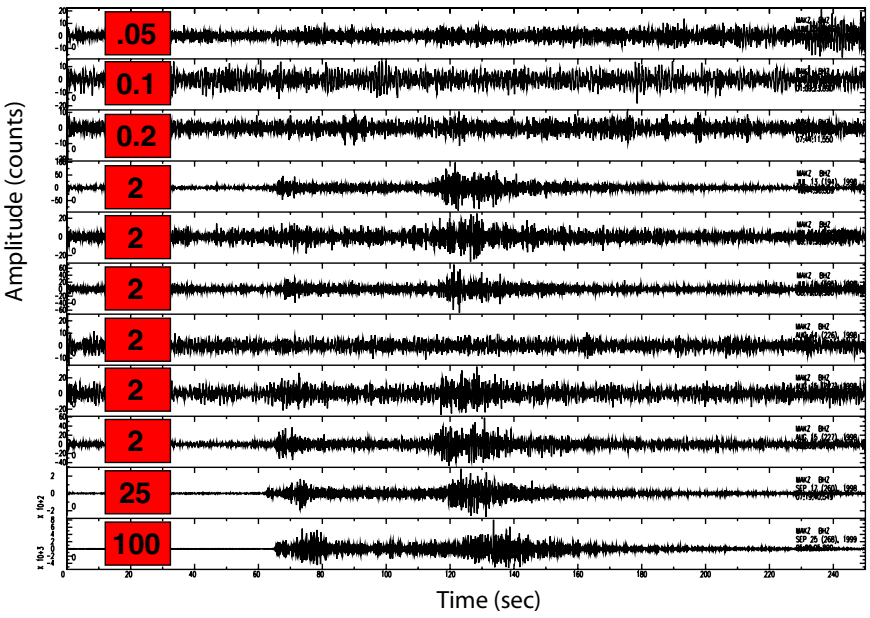


Figure 8. Selection of seismograms recorded at MAKZ for chemical shots at KTS ranging in size from .05 to 100 tons. Notice variable noise levels for the suite of 2 ton shots.

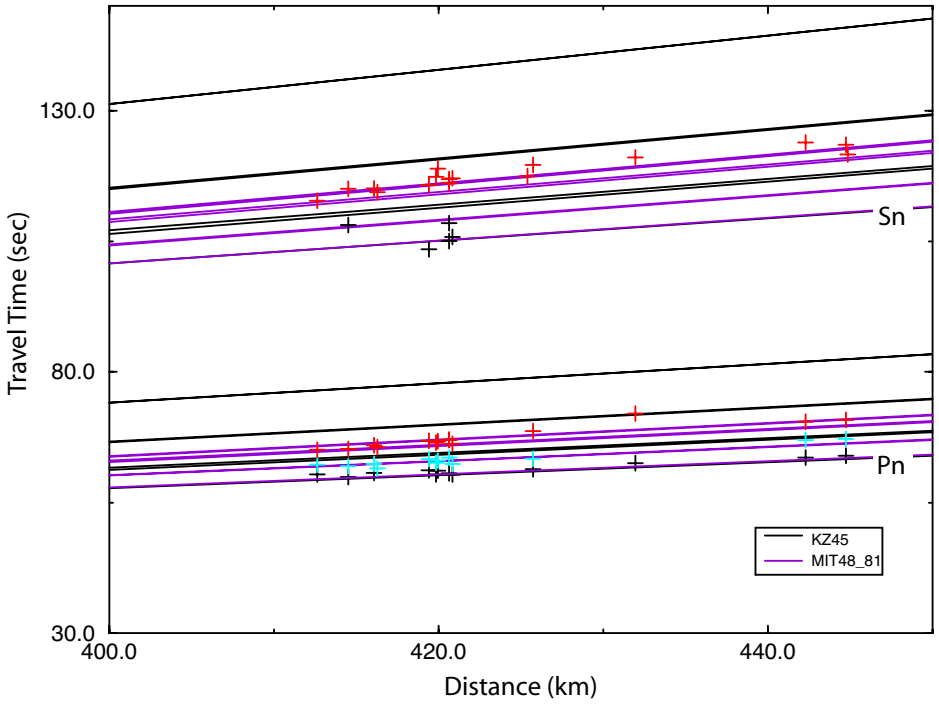


Figure 9. Comparison of KZ45 and MIT48_81 models with picks at MAKZ for the chemical shots at KTS. Arrival time symbols as in previous figure. Only Pn and Sn curves are labelled, as the travel time curves for later phases become interleaved. PmP is the second time curve for each model, Pg and Lg are the third. Picks are shown with plus signs (black = Pn and Sn; red = Pg and Lg) and squares (light blue = PmP).

CONCLUSIONS AND RECOMMENDATIONS

Initial investigations into the use of travel-time residual difference constraints for purposes of leveraging poor GT into good GT suggest that while some challenges exist, the potential payoffs are substantial. This approach extends the idea that nearby stations should show spatial correlation between their respective correction surfaces. Here, we require only that the differenced correction surfaces show some specific spatial correlation properties; the correction surfaces alone need not be correlated. We have begun exploring the usefulness of the 3-D Asia models provided by the consortium teams. For some test sites, the best-fitting models, some of which come from these Asia products, have been identified for MAKZ/MKAR. We have found also that feasibility testing of location using 3-D raytracing is favorable for catalog-scale location efforts. One recommendation coming out of this work is that better tools are needed to predict regional phases, such as Pg and Lg, from 1-D, 2-D, and 3-D models. Some research and development effort should be devoted to this goal.

ACKNOWLEDGEMENTS

Special thanks to Nafi Toksoz and Paul Richards and the myriad consortium researchers who put together the datasets and models that we are using. We appreciate the hard work that went into developing these products. Richard Stead undertook the substantial task of grooming and integrating the zABCE data into the global database at LANL.

REFERENCES

Aki, K., and P. Richards (1980), Quantitative Seismology, W.H. Freeman and Company, San Francisco.

Aprea, C., C. Bradley, and L.K. Steck, (2001), 3D Earth Models at regional and global scales, in *Proceedings of the 23rd Seismic Research Review: Worldwide Monitoringof Nuclear Explosions*, LA-UR-01-4454, Vol. I, pp. 147-155.

Crotwell, H. P., T. J. Owens, and Jeroen Ritsema (1998), The TauP Toolkit: Flexible seismic travel-time and raypath utilities, Board of Trustees of the University of South Carolina, 31 pp.
(available at http://www.geol.sc.edu/seis/software).

Hartse, H. E. (2000), The anticipated view of Lop Nor test site from array MKAR based on research using data recorded at GSN station MAKZ, Los Alamos National Laboratory LA-CP-00-204, 42 pp.

Jih, R.-S. (1998), Location calibration efforts in China, in *Proceedings of the 20th Annual Seismic Research Symposium on Monitoring a Comprehensive Test Ban Treaty (CTBT)* 12 pp.

Jih, R.-S. and R. Wagner (2000), Location calibration of Kazakhstan based on DTRA (U.S.) - NNC (RoK) joint experiments (1997-1999) in the former Semipalatinsk test site, *Proc. 22nd Annual DoD/DOE Seismic Research Symposium: Planning for Verification of and Compliance with the Comprehensive Nuclear-Test-Ban Treaty (CTBT)*, September, pp. 12-15.

Kennett, B.L.N. and E.R. Engdahl (1991), Traveltimes for global earthquake location and phase identification, *Geophys. J. Int*, 105, 429-465.

Li, S. and W. D. Mooney (1998), Crustal structure of China from deep seismic sounding profiles, *Tectonophysics*, 288, 105-113.

Richards, P., J. Armbruster, V. Burlacu, V. Cormier, M. Fisk, V. Khalturin, W. Kim, I. Morozov, E. Morozova, C. Saikia, D. Schaff, A. Stroujkova, and F. Waldhauser (2003), Seismic location calibration for 30 International Monitoring System stations in eastern Asia: Final Results, in *Proceedings of the 25th Seismic Research Review - Nuclear ExplosionMonitoring: Building the Knowledge Base*, LA-UR-03-6029, Vol. I, pp. 280-290.

Rodi, W.L., S.C. Myers, and C. A. Schultz (2003), Grid-search location methods for ground-truth collection from local and regional seismic networks, in *Proceedings of the 25th Seismic Research Review - Nuclear Explosion Monitoring: Building the Knowledge Base*, LA-UR-03-6029, Vol. I, pp. 311-319.

Rowe, C., S. Phillips, and L. Steck (2003), Relative constraints on correction surfaces for more effective use of low-order ground truth, Eos. Trans. AGU, 843(467), Fall Meet. Suppl., San Francisco, F1018.

Sheehan, A.F., G. Monsalve, C.Rowe, and M. Begnaud (2004), *Proceedings of the 26th Seismic ResearchReview: Trends in Nuclear Explosion Monitoring*, Orlando, FL (Sept. 21-23, 2004).

Steck, L.K., A. A. Velasco, A. H. Cogbill, and H. J. Patton (2001a), Improving regional seismic event location in China, *Pageoph.*, 158, 211-240.

Steck, L. K., A. A. Velasco, M. L. Begnaud (2001b), On the use of kriged P-wave travel time correction surfaces, Los Alamos National Laboratory LA-UR 01-1538, 34 pp.

Steck, L. K., A. A. Velasco, M. L. Begnaud (2001c), On the use of kriged P-wave travel time correction surfaces, in *Proceedings of the 23rd Seismic Research Review: Worldwide Monitoring of Nuclear Explosions*, LA-UR-01-4454, Vol. I, pp. 410-419.

Steck, L.K., G. Randall, M. Begnaud, C. Rowe, and A. A. Velasco (2003), Karatau, Makanchi, and location in Western China, in *Proceedings of the 25th Seismic Research Review - Nuclear Explosion Monitoring: Building the Knowledge Base*, LA-UR-03-6029, Vol. I, pp. 344-352.

Sun, Youshun (2004), A P-Velocity Model for the Crust and Uppermost Mantle of China by Monte Carlo Inversion, Massachusetts Institute of Technology *Ph.D. Dissertation*, 134 pp.

Whitted, C. A., S. R. Taylor, A. A. Velasco, H. E. Hartse, and G. Zandt (1999), A path specific crustal study in central Asia from group velocity inversions and full waveform modeling, Los Alamos National Laboratory, LA-UR-99-3040, 24pp.

METHODS FOR IMPROVING SEISMIC EVENT LOCATION PROCESSING

Clifford H. Thurber and Haijiang Zhang

University of Wisconsin-Madison

Sponsored by Air Force Research Laboratory

Contract No. DTRA01-01-C-0085

ABSTRACT

Our research program consists of four components, each involving some aspect of multiple-event analysis: (1) high-precision waveform cross-correlation (WCC) for arrival time estimation, (2) robust event clustering, (3) waveform decomposition and source wavelet deconvolution reshaping, and (4) double-difference (DD) multiple-event location and tomography. Our research focused initially on the development and testing of these seismic analysis methods using "ground-truth" (GT) datasets at different scales (local and regional), and was followed by the application of these methods to real-time and simulated real-time data streams. Here we summarize the more significant project achievements in the four research areas.

(1) Differential arrival times for pairs of seismic events observed at the same station are often calculated by WCC. Researchers often choose the differential times to use based on the associated cross-correlation (CC) values exceeding a specified threshold. When two similar time series are contaminated by significant noise, or in the case of cycle skipping, the time delay calculated with the WCC technique may not be reliable even if it exceeds the specified threshold. If the threshold is set too high, then only a limited number of very precise differential time data are available to constrain the relative positions of earthquakes. If the threshold is set too low, then many unreliable differential time estimates are used and they will negatively affect the relocation results. The bispectrum method can suppress the Gaussian or low-skewness noise sources in two similar time series and can be used to obtain a second, independent estimate of the relative time delay between them. We compute time delay estimates between the waveform pairs with the bispectrum method and use them to verify the WCC-determined one. This technique can provide quality control for the time delay estimates, and can potentially provide more differential time data for close event pairs by verifying the reliability of differential times that might not meet the threshold criterion.

(2) We have tested a two-step clustering and location technique with a California GT dataset. In Step 1, event locations are estimated via WCC of Hilbert-envelope waveforms. The Step 1 procedure located the epicenters within 20 km (approximately 1 bin) of the catalog location for 16 of the 20 test events. However, depth estimates were poorly constrained. The Step 2 refinement based on WCC of the high-frequency P arrivals followed by DD relocation improved both epicenter and depth estimates. This two-step procedure offers advantages over conventional location techniques including a Step 1 event clustering and preliminary location not dependent on the accuracy of catalog picks and a Step 2 improvement using the high-precision DD technique.

(3) We tested a variety of decomposition and filtering techniques with the multiple goals of noise reduction, waveform "homogenization" (reshaping to similar "wavelet"), and depth phase identification. Methods examined include eigenimage decomposition, KLD, CANC, and coherency filtering. A key issue is the effect of arrival misalignment between a pair of traces on the success of a given technique. We tested a two-stage process whereby the similarity and strength of a CANC-filtered trace (relative to the original and error traces, respectively) is used to align the trace to the reference signal. We also developed a wavelet-based auto-picker for detecting and picking first-P arrivals that can be used in conjunction with our location processing procedures, both for identifying waveform segments for correlation and for adjusting stack picks.

(4) We have developed the new method of DD tomography. The code tomoDD takes the DD location method (hypoDD) a step further to solve for three-dimensional (3D) velocity structure simultaneously with hypocenter locations, using both catalog picks and differential arrival times. Compared to conventional tomography, the result is a sharpening of the seismicity distribution equal in quality to hypoDD plus a sharpening of the velocity image due to removal of the majority of the location scatter. We have developed local- and regional-scale versions of tomoDD, and have applied each to synthetic and real datasets. We have also developed a version of the new location code locOO.

OBJECTIVES

Our research program consists of four components, each involving some aspect of multiple-event analysis: (1) high-precision WCC for arrival time estimation, (2) robust event clustering, (3) waveform decomposition and source wavelet deconvolution reshaping, and (4) DD multiple-event location and tomography. Our research focused initially on the development and testing of these seismic analysis methods using GT datasets at different scales (local and regional), and was followed by the application of these methods to real-time and simulated real-time data streams.

RESEARCH ACCOMPLISHED

High-precision waveform cross-correlation for arrival time estimation

When two earthquakes have close hypocenters and share similar source mechanisms, they will generate similar ground motions. It is possible to obtain very accurate differential times from waveform data for such nearby events, and use them to improve location results (e.g., Shearer, 1997; Rubin *et al*., 1999; Waldhauser and Ellsworth, 2000; Schaff *et al*., 2002, Rowe *et al*., 2002), or combine them with absolute arrival times to invert for high-quality 3D velocity structure (Zhang and Thurber, 2003). Such studies generally use a WCC technique to calculate the relative time delay between the waveforms of two events recorded at the same station. For very similar traces, some researchers obtain a time delay to the sub-sample level by a weighted linear fitting of the cross spectral phase after first aligning the two waveforms with the cross-correlation- (CC-) determined lag (Poupinet *et al*., 1984). The calculated time delay has an associated CC coefficient whose value may not be very high if the underlying signals are not time-delayed similar waveforms, or if the underlying time-delayed signals are contaminated by high levels of noise. It is hard to differentiate these two possible causes, especially when many thousands or more waveforms are being analyzed automatically. Thus researchers often choose those time delay estimates with CC coefficients above a specified threshold. For example, Schaff *et al*. (2002) only select those time delays with CC values larger than 0.70 and mean coherences above 0.70.

The selection of an optimum threshold value is important but difficult. If it is set too high, then only a limited number of very accurate differential time data are available to constrain the relative positions of earthquakes. If the threshold value is set too low, then many unreliable differential time estimates, which are used, can negatively affect the relocation results. Du *et al.* (2004) deal with this problem by computing additional estimates of the time delay with the bispectrum (BS) method. The BS method, which works in the third-order spectral domain, can suppress correlated Gaussian or low-skewness noise sources (Nikias and Raghuveer, 1987; Nikias and Pan, 1988). Du *et al.* (2004) adopt this method to calculate two additional time delay estimates with both the raw (unfiltered) and band-pass filtered waveforms, and use them to verify (select or reject) the one computed with the CC technique using the filtered waveforms. This BS verification process can reject unreliable CC time delay estimates and also can accept additional CC time delays even if their associated CC coefficients are smaller than some threshold value, if they pass the BS checking procedure. We do not claim that the BS method always obtains a better time delay estimate than the CC technique, but use it to check the reliability of the time delay estimates computed with the CC technique. By applying two different methods that work in different spectral domains (second- and third-order), we can improve the reliability of the selected time delays. The two BS time delay estimates do not always agree with each other because the characteristics of noise in the raw and filtered waveforms are different. Therefore checking the values of the CC time delay against both of them provides additional quality control.

Figure 1 shows examples of the application of the BS verification method to waveforms recorded at New Zealand stations for two pairs of relatively close events. In Figure 1a, the CC value (0.74) is above the nominal threshold (0.70), but the lag does not agree with that obtained from the bispectrum (bottom panel), so this CC value is rejected. From the seismograms, we can see that this is apparently a case of cycle skipping - the filtered waveforms coincidentally correlate slightly better at a lag of -10. In Figure 1b, both methods provide the same time delay, but the associated CC coefficient is only 0.50. Under the threshold criterion, such a time delay estimate associated with a low CC coefficient is simply discarded. Using the BS checking method we can identify the reliable time delays from these "seemingly not very similar" waveforms, such as for this pair, and as a result provide more control over the relative locations of the events. Du *et al.* (2004) apply this technique to 822 New Zealand earthquakes in the Wellington area and find that the CC time delays verified with the BS method provide improved earthquake relocation results (noticeably more clustered) compared to those selected with the standard threshold criterion. An example of the improvement of the BS-verified locations compared to original catalog locations, DD locations using differential catalog picks, and DD locations using standard threshold CC lags is shown in Figure 2 for a sub-region near Lake Wairarapa.

Robust event clustering

An adaptive, automatic phase-picking and epicenter-location program is now fully developed and is being applied to update the New Mexico microseismicity catalog. The program is built upon the MATLAB environment using MatSeis (Young, *et al.*, 2002). The package is named PLRR (Pick-Locate-Repick-Relocate). The key strategy of PLRR is to find the event from a reference database that is most similar to a new event according to the spectrogram cross-correlation, and to use the alignment with the similar reference event to assign phase picks to the new event. No preliminary pick or location information is needed for the new event.

The following are some key characteristics of the PLRR package.

(1) Data format: the seismic data format recognized by PLRR is the CSS-3.0 flatfile format.

(2) Reference database: the quality of phase-picking and epicenter-location results will ultimately depend on the coverage and quality of the reference database (Figure 3).

(3) Spectrogram cross-correlation: we find for this data set that the spectrogram is most diagnostic and discriminates events best within a limited bandwidth between 6 and 10 Hz.

(4) Waveform-pair match and event-pair match: we have explored two options in PLRR to find phases and locations for unknown events. The first, waveform-pair matching, finds the most similar waveforms in the reference database, station by station, and after alignment, assigns the corresponding phase information to the new waveforms. This technique was found to produce too many false associations. The second, event-pair matching, is more robust. This option stacks the cross-correlation coefficient curves of waveform-pairs between the new event and waveforms grouped from each event in the reference database, and finds the reference event that has the highest stacked CC coefficient value (by taking the mean/median of stacked CC coefficient curves).

(5) Database operation: several simple functions to enhance and simplify the operation of CSS-3.0 database are added into PLRR, such as the "Update monthly table," which adds a new event to a CSS-3.0 database.

PLRR was developed to process the seismic data of New Mexico, and we have not tested our code on other seismic networks Users from other areas will have to modify the PLRR code to apply it to their situation, including building travel-time tables and modifying *site* and *sitechan* tables. PLRR also defaults to a sample rate of 100 samples per second. For the New Mexico region, we use PLRR to process the seismic data generated by an Earthworm data acquisition system on a month-by-month basis. Visual checking is applied to ensure that the automatic results are valid and that events arising from new source regions are properly added to the reference database. Given enough representative seismicity, the system should progressively increase in its accuracy.

A two-step clustering and location version of PLRR was also tested with a California GT data set. In step 1the event locations are estimated using WCC of Hilbert-envelope waveforms. This procedure located the epicenters within 20 km of the catalog location for 16 of the 20 test events; however, the depth estimates were poorly constrained. The Step 2 refinement, based on WCC of the high-frequency P arrivals followed by DD relocation improved both epicenter and depth estimates. This two-step procedure offers advantages over conventional location techniques including event clustering and preliminary location not dependent on the accuracy of catalog picks and subsequent location improvement using the high-precision DD technique.

Waveform decomposition and source wavelet deconvolution reshaping

We tested a variety of decomposition and filtering techniques with the multiple goals of noise reduction, waveform "homogenization" (reshaping to similar "wavelet"), and depth phase identification. The methods examined include eigenimage decomposition, KLD, Correlated data Adaptive Noise Canceling (CANC), and coherency filtering. A key issue is the effect of arrival misalignment between a pair of traces on the success of a given technique. Some methods rely on signals being time-aligned before processing, which of course cannot be assumed for seismic data in a monitoring context. We also developed a wavelet-based auto-picker for detecting and picking first-P arrivals that can be used in conjunction with our location processing procedures, both for identifying waveform segments for correlation and for adjusting stack picks (Zhang *et al*., 2003b).

A recent paper by Ulrych *et al*. (1999) reviews several decomposition and transformation techniques that are useful for signal-noise separation in an exploration seismic context. The two most relevant to our work are eigenimage

decomposition and Karhunen-Loéve decomposition (KLD). KLD is distinguished from the more common eigenimage decomposition (essentially principal components) in that the latter extracts eigenvector-eigenvalue information from multi-channel data based on a covariance matrix computed at a single lag (zero), whereas the former carries out a decomposition for single-channel data based on a covariance matrix for multiple lags (Ulrych *et al*., 1999). In practice, to apply KLD to multi-channel data, an average covariance matrix can be computed.

The utility of the KLD method for extracting similar signals from noisy data is being tested. A synthetic example is shown in Figure 4. In this particular case, we construct initially noise-free seismograms (upper left panel) that consist of a first-arriving signal that is time-aligned and an identical second-arriving signal with substantial moveout. Gaussian noise with root mean square (RMS) amplitude, 20% of the signal amplitude, is added (upper right panel) and eigenimage decomposition (not shown) and KLD (Figure 4) are carried. The eigenimage decomposition, using eigenvalues of average value and greater, preserves the time-aligned signal but degrades the secondary arrival, leaving most of the latter's energy in the residual "noise." KLD (middle left panel), again using eigenvalues of average value and greater (bottom left panel), preserves both the time-aligned signal and the secondary arrival (middle right panel).

For a second example, we apply KLD to real data from a group of earthquakes of magnitude 3.6 to 3.8 in Long Valley, California from January 1998. In the catalog, the events are within about 1 km of each other in epicenter but have estimated depths ranging from 0.5 to 5.0 km. Relocation using hypoDD and catalog arrival times plus catalog-generated arrival time differences yields epicenters within less than 1 km and depths within 250 m of each other. The analyzed waveforms were recorded at station ORV with an epicentral distance of 314 km.

The results of the KLD analysis are shown in Figure 5. The raw data traces are relatively noisy. In this case, we recognize that the eigenvectors for the four largest eigenvalues represent long-period noise (bottom left panel), and we exclude them along with the smaller eigenvalues. The resulting KLD-processed traces (upper right panel) are quite similar and the data residue (middle left panel) contains no obvious remnant signal of interest. In contrast, the eigenimage decomposition does little if anything to improve the signal similarity, only removing some of the higher frequency noise.

An alternative approach to noise reduction by extracting common waveform signals is adaptive filtering. We have experimented with a CANC algorithm of Hattingh (1988). Input into the CANC procedure consists of a "reference signal" S1 and a "primary signal" S2, correlated to each other in some unknown way. Each signal is presumed to contain noise that is uncorrelated with the noise from the other trace. The reference signal is used as a "learning signal" to derive filter coefficients. The filter adjusts its impulse response to minimize the mean-squared error between filter output and the primary signal (in terms of power). The algorithm rapidly solves for the filter coefficients without requiring matrix inversion or a CC operation. The CANC procedure is an iterative solution, computing updated filter coefficients at each iteration.

The CANC procedure is applied to seismic data from two events in a cluster with similar catalog epicenters but different depths, recorded at UC-Berkeley network station San Andreas Observatory (SAO). The two events are from the 1994 Northridge aftershock sequence and are located within 7 km of each other in the epicenter based on catalog information. Trace 1 (Figure 6a), the reference signal, is from a shallow earthquake (2 km depth), whereas trace 2 (Figure 6b), the primary signal, is from an earthquake occurring at greater depth (12 km). Adaptive filtering to shape the windowed signal from the deeper earthquake to extract the signal common to the shallow event in an attempt to improve subsequent WCC results is applied. A 7s window containing approximately 4.5s of data following the P pick was used. The windowed signal from the deeper event (Figure 6b) was aligned relative to the shallow event signal (Figure 6a) initially by the P picks, and then fine-tuned by applying a lag search. The zero-lag CC between the primary and filtered traces (Figure 6c) and the signal-to-noise ratio of the filtered trace relative to the error trace (Figure 6d) have coincident maxima. After five iterations of the CANC algorithm, the signal from the deeper event is successfully decomposed into an estimate of the common signal (Figure 6e) and the dissimilar error signal (Figure 6f).

We can compare the estimate of common signal to individual trace output by the application of coherency filtering. Shown are the coherency-filtered traces for the shallow and deep event (Figures 6g and h). The frequency content of the two clustered events is very similar. Consequently, coherency filtering yields output traces similar to the original trace data. The adaptive filter shaping of the deep event's waveform visually yields a signal (Figure 6e) closer in appearance to the shallow event (Figure 6a). Application of adaptive filtering increases the maximum CC value for the shallow event with the CANC-filtered trace from 0.51 to 0.83. CC of the coherency-filtered data yields a

maximum value of 0.70. These CC maxima occur at the same lag. Thus the CANC approach can successfully extract a more similar waveform from the primary signal than coherency filtering while preserving timing.

Double-difference multiple-event location and tomography

We have developed the new method of double-difference (DD) tomography. The code tomoDD takes the DD location method (hypoDD) a step further to solve for 3D velocity structure simultaneously with hypocenter locations, using both catalog picks and differential arrival times. Compared to conventional tomography, the result is a sharpening of the seismicity distribution equal in quality to hypoDD plus a sharpening of the velocity image due to removal of the majority of the location scatter. We have developed local- (Zhang and Thurber, 2003a) and regional-scale (Zhang *et al*., 2004) versions of tomoDD, and have applied each to a number of synthetic and real datasets. The local-scale version of the tomoDD code, along with a users manual and sample dataset, is currently available on the web (http://www.geology.wisc.edu/~hjzhang/download.htm). We have also developed a preliminary JHD version of the new location code locOO (Ballard, 2003) as a first step towards the creation of a DD version of the code.

CONCLUSIONS AND RECOMMENDATIONS

Advances in techniques for waveform alignment, event clustering, waveform decomposition, and location and tomography have been achieved with the support of this contract. We echo the conclusion voiced by Prof. Paul Richards that a quantum change is needed in the manner in which earthquake locations are determined in the seismic monitoring environment (both nuclear and otherwise). Effective tools for event clustering, waveform alignment, and joint location/tomography are available, and a concerted effort will be required to implement these tools in "real-world" monitoring situations. Accomplishing this will probably require closer and more direct interaction between the tool developers and the users, in particular to allow for direct feedback from the users to the developers.

ACKNOWLEDGEMENTS

We thank Wayne Du, Bill Lutter, Jean Battaglia, Rick Aster, and Wenzheng Yang for their contributions to this paper, Megan Flanagan for providing the code for the spherical earth finite-difference method, Chris Young and Sandy Ballard for assistance with locOO, and Charlotte Rowe for many valuable discussions.

REFERENCES

Ballard, S. (2003), Seismic event location: dealing with multi-dimensional uncertainty, model non-linearity and local minima, *Proceedings of the 25th Seismic Research Review - Nuclear Explosion Monitoring: Building the Knowledge Base*, 193-202.

Ballard, S. (2003), Seismic event location: dealing with multi-dimensional uncertainty, model non-linearity and local minima, Proceedings of the 25th Seismic Research Review: Building the Knowledge Base (September 23-25, Tucson, Arizona, 2003), 193-202.

Du, W., C. H. Thurber, and D. Eberhart-Phillips (2004), Earthquake relocation using cross-correlation time delay estimates verified with the bispectrum method, *Bull. Seismol. Soc. Am.*, 94, 856-866.

Hattingh, M. (1988), A new data adaptive filtering program to remove noise from geophysical time- or space-series data, *Comp. Geosci.*, 14, , 467-480.

Nikias, C. L. *and* R. Pan (1988), Time delay estimation in unknown Gaussian spatially correlated noise, *IEEE Trans. Acoust. Speech Signal Processing*, 36, 1706-1714.

Nikias, C. L. *and* M. R. Raghuveer (1987), Bispectrum estimation: A digital signal processing framework, *Proc. IEEE*, 75, 869-891.

Poupinet, G., W. L. Ellsworth, and J. Fréchet (1984), Monitoring velocity variations in the crust using earthquake doublets: an application to the Calaveras fault, California, *J. Geophys. Res.*, 89, 5719-5731.

Rowe, C. A., R.C. Aster, B. Borchers and C. J. Young (2002), An automatic, adaptive algorithm for refining phase picks in large seismic data sets, *Bull. Seismol. Soc. Amer*, 92, 1660-1674.

Rubin, A., D. Gillard, and J. Got (1999), Streaks of microearthquakes along creeping faults, *Nature*, 400, 635-641.

Schaff, D. P., G. H. R. Bokelmann, G. C. Beroza, F. Waldhauser, and W. L. Ellsworth (2002), High-resolution image of Calaveras Fault seismicity, *J. Geophys. Res.*, 107, 2186, doi:10.1029/2001JB000633.

Shearer, P. M. (1997), Improving local earthquake locations using the L1 norm and waveform cross correlation: Application to the Whittier Narrows, California, aftershock sequence, *J. Geophys. Res.*, 102, 8269-8283.

Ulrych, T. J., M. D. Sacchi, and J. M. Graul (1999), Signal and noise separation: art and science, *Geophys.*, 64, 1648-1656.

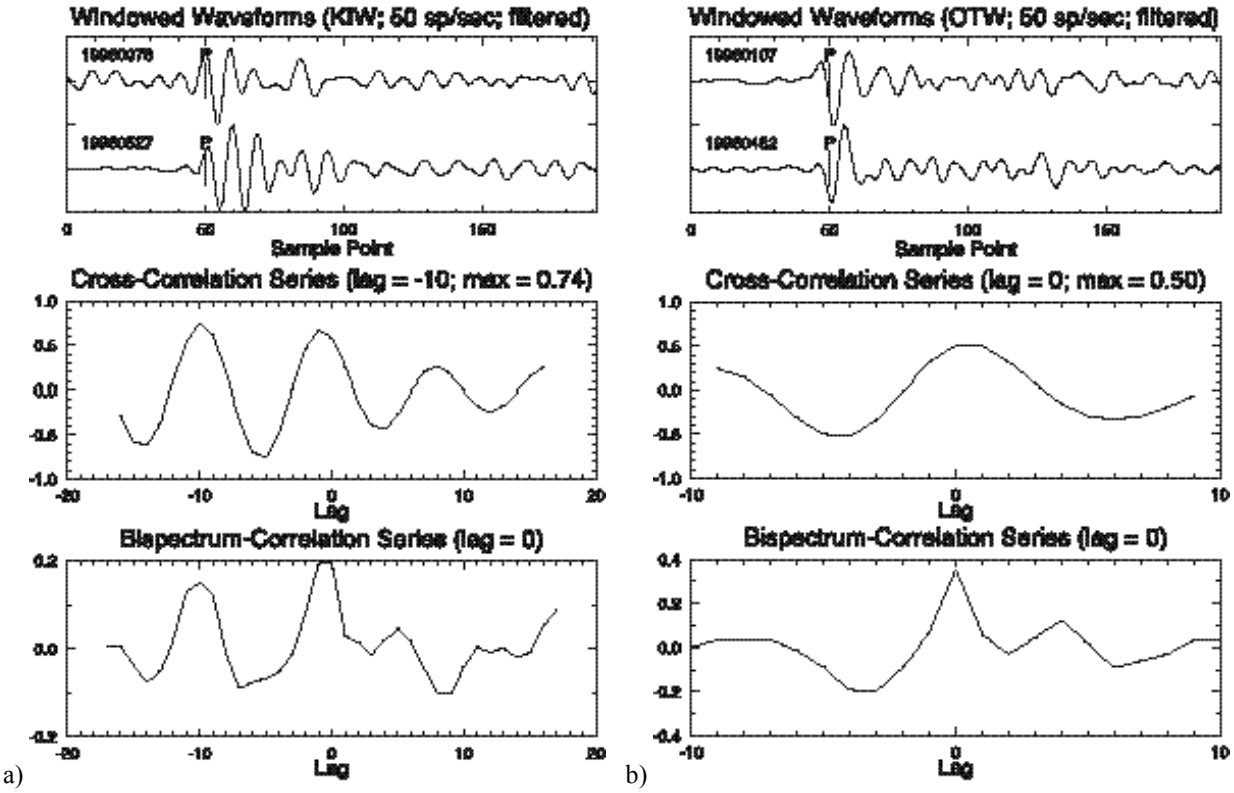
Waldhauser, F. and W.L. Ellsworth (2000), A double-difference earthquake location algorithm: Method and application to the Northern Hayward Fault, California, *Bull. Seism. Soc. Am.*, 90, 1353-1368.

Young, C. J., E. P. Chael, and B. J. Merchant (2002), Version 1.7 of MatSeis and the GNEM R&E regional seismic analysis tools, *Proc. 24th Seismic Research Review*, 915-924.

Zhang, H. *and* C. H. Thurber (2003), Double-difference tomography: The method and its application to the Hayward fault, California, *Bull. Seism. Soc. Am.*, 93, 1875-1889.

Zhang, H., C. H. Thurber, C. A. Rowe (2003), Automatic first-arrival detection and picking with multiscale wavelet analysis, *Bull. Seism. Soc. Am*., 93(5), 1904-1912.

Zhang, H., C. Thurber, D. Shelly, S. Ide, G. Beroza, and A. Hasegawa (2004), High-resolution subducting slab structure beneath N. Honshu, Japan, revealed by double-difference tomography, *Geology*, 32, 361-364.



a) b)

Figure 1. Examples of a) rejection of a high CC value due to inconsistent results between the CC and BS lags and b) acceptance of a low CC value due to consistent results between the CC and BS lags.

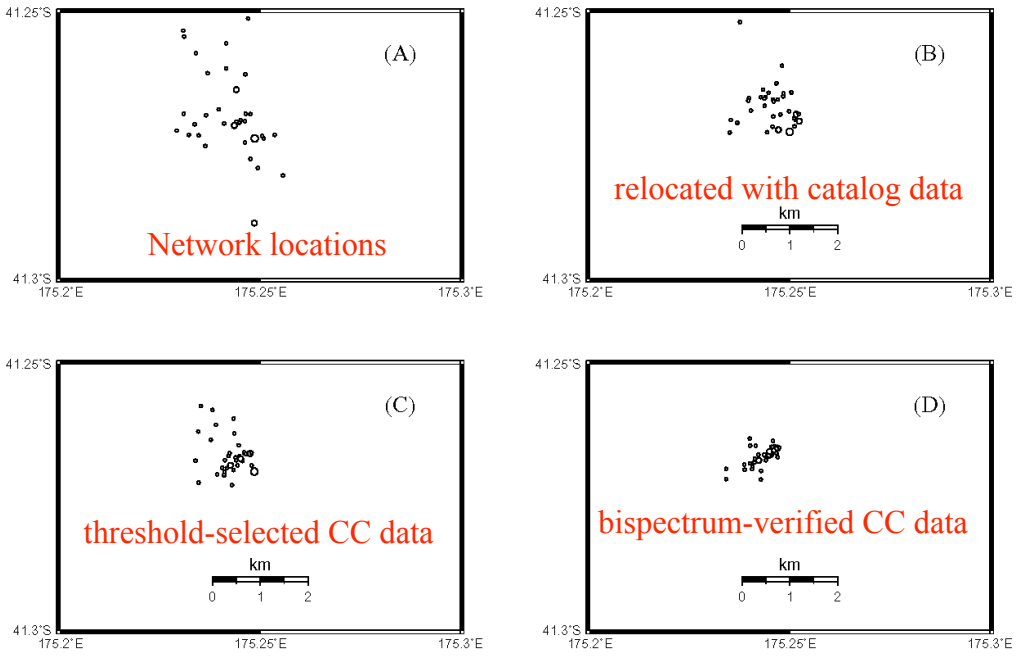


Figure 2. Example of successive improvement in location clustering of a set of earthquakes in New Zealand, comparing catalog locations to those obtained by use of DD location with catalog picks, then with threshold-selected CC data, and finally with BS-verified CC data.

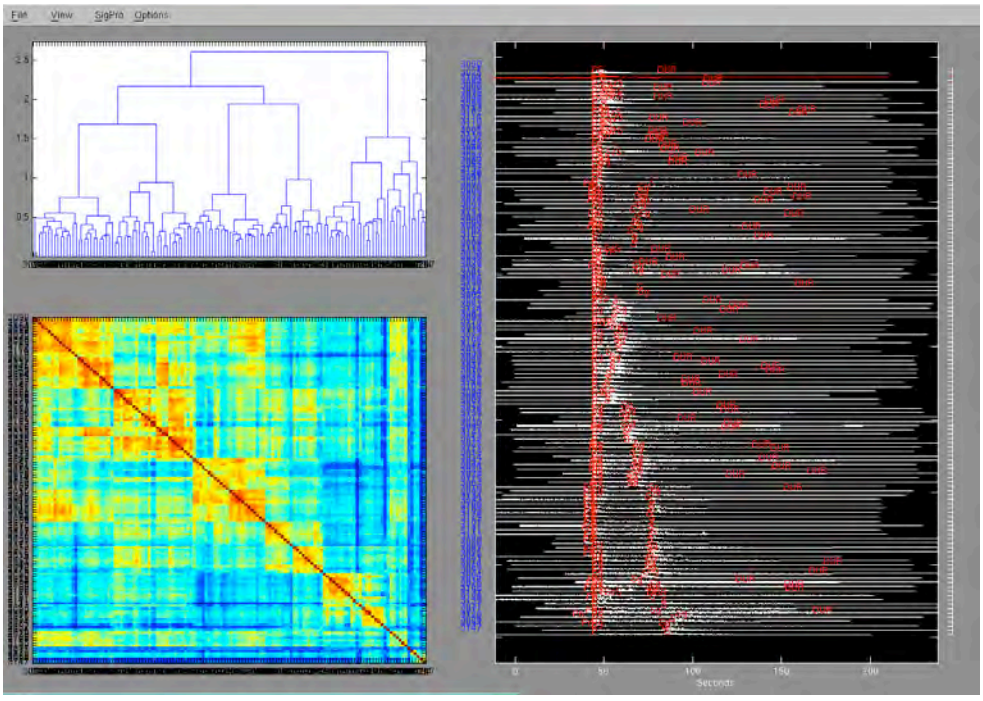


Figure 3. Reference waveforms for station CAR are shown at right, also showing the cross-correlation coefficient matrix of each waveform pair (left, bottom) and corresponding dendrogram (left, top).

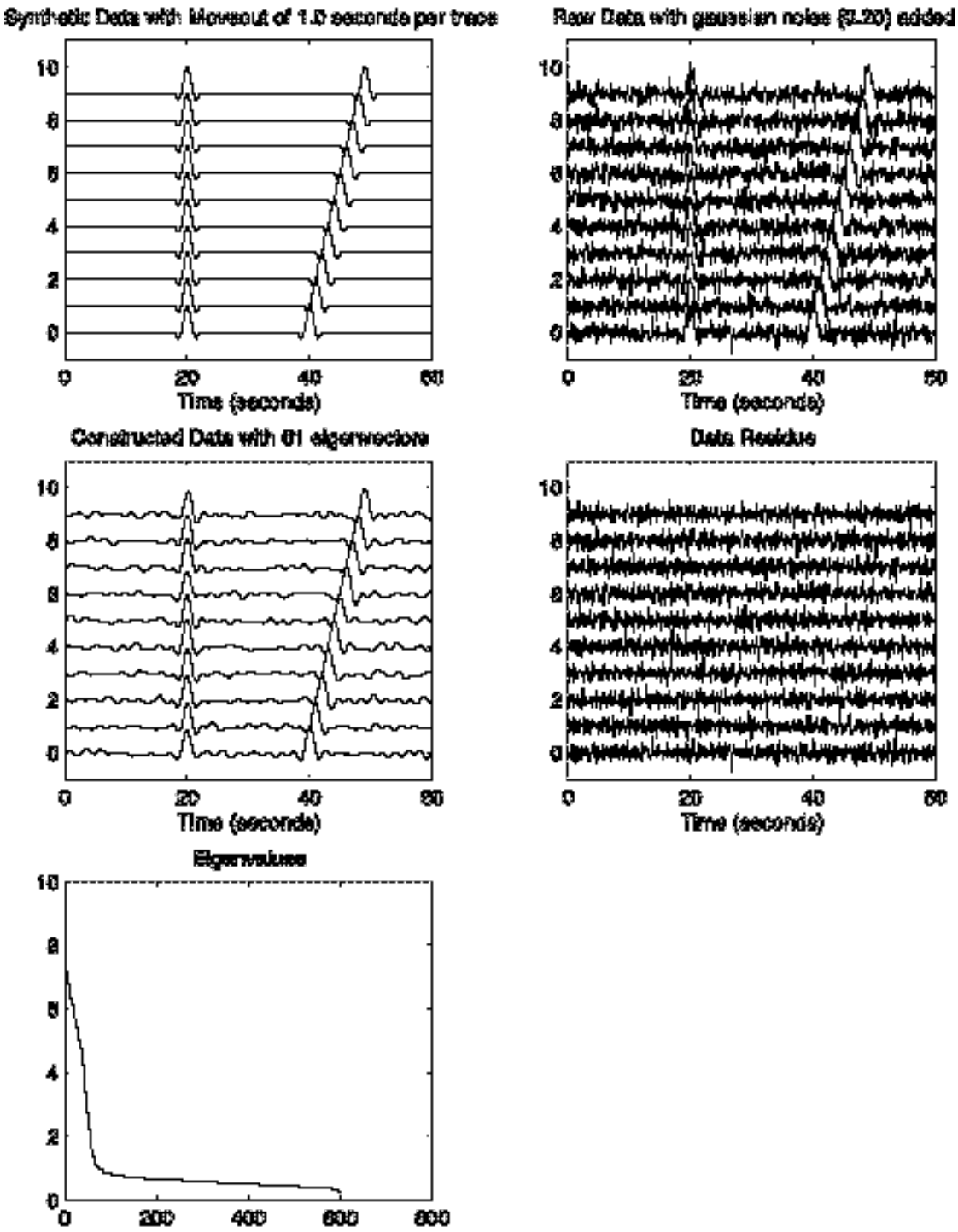


Figure 4. Example application of KLD to a set of seismograms with a pair of "arrivals" only one of which is time-aligned across the records (top left), with noise added (top right). The data reconstructed from the 61 eigenvectors with eigenvalues above average in size (bottom left) retains both the time-aligned arrival and the arrival with moveout (middle left), leaving little signal energy in the residual image (middle right). In contrast, eigenimage decomposition cannot reconstruct both arrivals adequately.

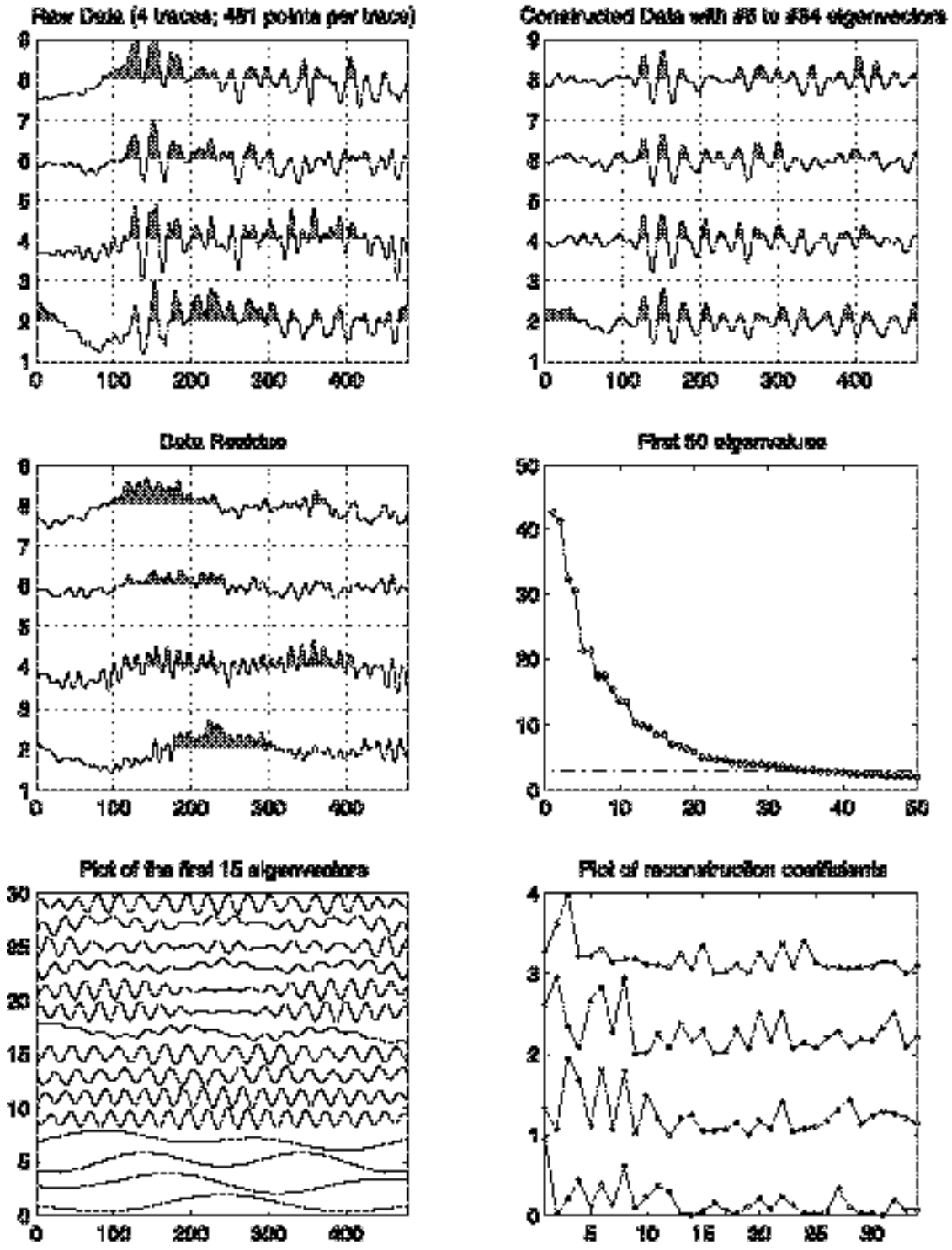


Figure 5. Example application of KLD to real data (upper left). Large and small eigenvalues were excluded in this case. The reconstructed data (upper right) from the 30 eigenvectors with eigenvalues from #5 to #34 (middle right) produces similar looking waveforms, leaving relatively little energy in the residual image (middle left). The eigenvectors for the larger eigenvalues (lower left) and their corresponding reconstructions (lower right) show the long-period noise character of the first 4 eigenvectors.

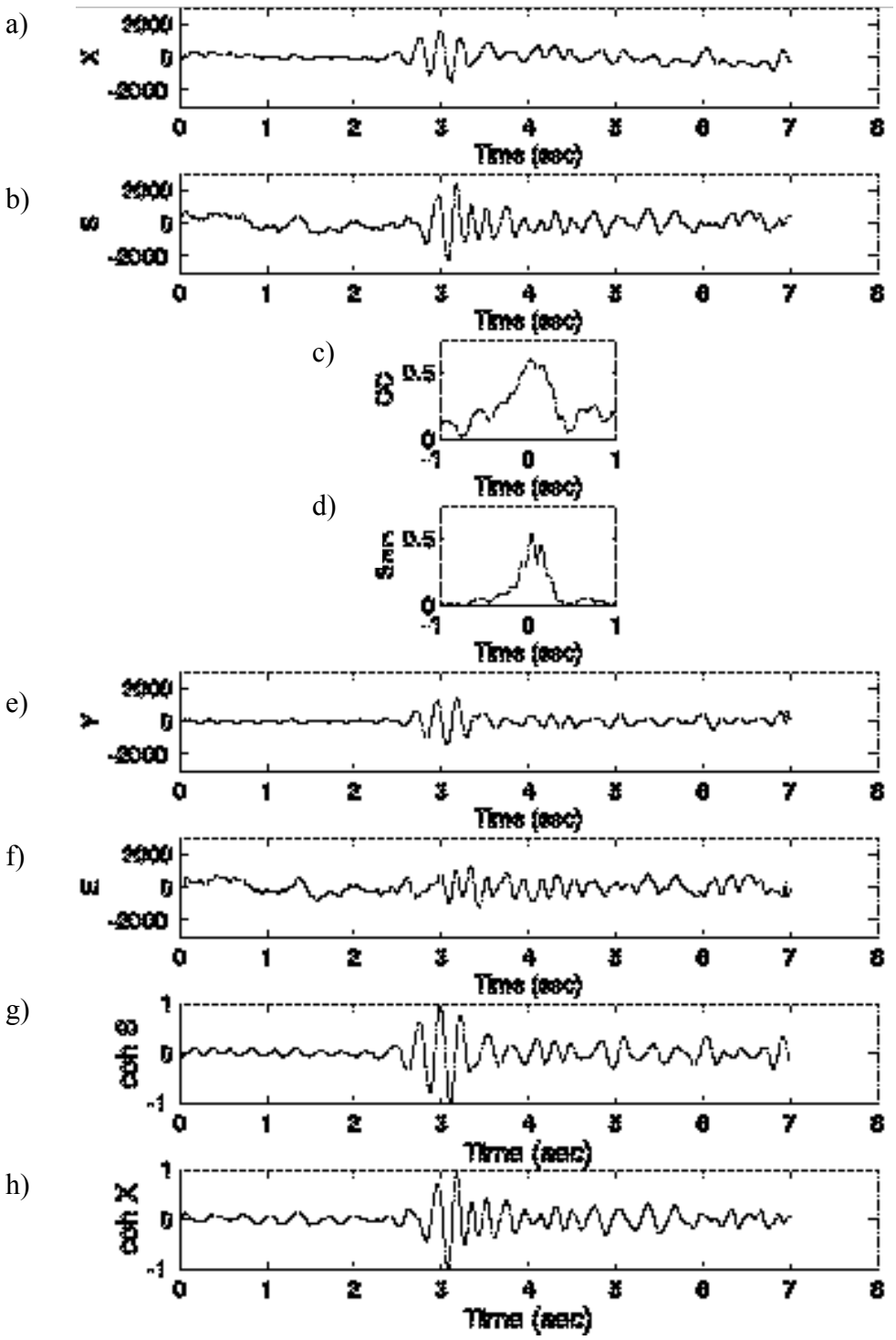


Figure 6. a,b) Seismic data windowed around the P arrival for the a) shallow (2 km) and deep (12 km) earthquakes from Northridge (S. California) cluster. The shallow event is used as the reference signal and the deeper event is used as the primary signal; noise has been added to the latter trace. c) Zero-lag cross-correlation between the primary and CANC-filtered traces for a range of signal alignments (see text). d) SNR for the CANC-filtered trace versus the error trace for a range of signal alignments. e) Common signal obtained from CANC adaptive filter. f) Error trace. Coherency filtering applied to data in a) and b) results in the signal traces displayed in g) and h), respectively.

DETECTION METHODS FOR MINING EXPLOSIONS IN SOUTHERN ASIA

Ileana M. Tibuleac[1], James Britton[1], David B. Harris[2], Terri Hauk[2], Heather Hooper[1] and Jessie L. Bonner[1]

Weston Geophysical Corporation[1] and Lawrence Livermore National Laboratory[2]

Sponsored by National Nuclear Security Administration
Office of Nonproliferation Research and Engineering
Office of Defense Nuclear Nonproliferation

Contract No. DE-FG02-01-ER83341[1] and W-7405-ENG-48[2]

ABSTRACT

Weston Geophysical maintains a high-quality seismic research database for southern Asia consisting of detailed mining information together with seismograms recorded from mine blasts in northwestern India, southern Pakistan and the surrounding regions. This digital mining database contains data on more than 260 mines and mineral deposits in southern Asia, including information on location, geology, commodities, production, mineralogy, references, operator, and mining explosion resources. The waveform data consists of seismograms from several stations in southern Asia including NIL, ABKT, HYB, and GBA, in addition to data from proprietary stations.

We have employed complementary techniques to detect probable mining explosions. First, we applied the waveform correlation method (Harris, 1991) to data recorded in 2002 at each station of interest. Six clusters of mining events were detected between May and October 2002 near stations in southern, central and northwestern India. Second, a short-period Rayleigh wave (*Rg*) detector (Tibuleac and Britton; 2004, Britton et al, 2003) was developed for quarry-blast/shallow source, near-regional events. The *Rg* detector was integrated into a semi-automatic event-detection and -location algorithm and applied on continuous data. The algorithm uses improved three-component frequency-wavenumber (*fk*3C) single-station location techniques. We obtained better detection results and back azimuth estimates using nonlinear pre-filtering. We present continuous detection results from two proprietary stations in March and April 2001.

We are in the process of obtaining satellite imagery for the areas covering the locations of the mining clusters. The imagery, event locations, station locations, and information on the mines are stored in an ArcView 8.3 geographic information system (GIS) database in which the digital seismic waveform data are linked. The database is updated as more mining clusters are detected and supplemental information (satellite imagery, mining information) is received.

OBJECTIVES

The objectives of this research are to catalog the mining resources of southern Asia and to compile mine information together with mining explosion waveforms into a single digital database.

RESEARCH ACCOMPLISHED

Mine Database

Continuous broadband waveform data were obtained from the IRIS/IDA stations ABKT, NIL, and PALK. HYB waveforms were obtained from the Geoscope Network, and GBA waveforms were obtained through the Atomic Weapons Exchange (AWE) in the United Kingdom. The locations of these stations are shown in Figure 1, with proprietary stations indicated by P1 and P2 on the map and in this paper. Table 1 shows the dates of continuous data segments obtained from these stations.

In addition to obtaining continuous waveform data, information on the mines and mining districts surrounding these stations is being compiled. Supplemental information, such as satellite imagery, is imported into the database to aid in determining ground truth for the locations of detected mine blasts.

Table 1. Stations for which continuous data have been obtained

Station	Network	Dates	Segment Length [days]	Lat (deg)	Lon (deg)
ABKT	IRIS/IDA	4/9/02 - 10/22/02	196	37.9	58.1
NIL	IRIS/IDA	7/2/98 - 3/3/99	244	33.7	73.2
HYB	GEOSCOPE	4/21/99 - 5/20/99	30	17.4	78.5
GBA	GEOSCOPE	2/1/1996 – 2/7/1996	7	13.6	77.4
P1	Proprietary	3/19/01 - 12/31/02	652	NW	India
P2	Proprietary	3/29/01 - 8/8/01	132	Southern	India

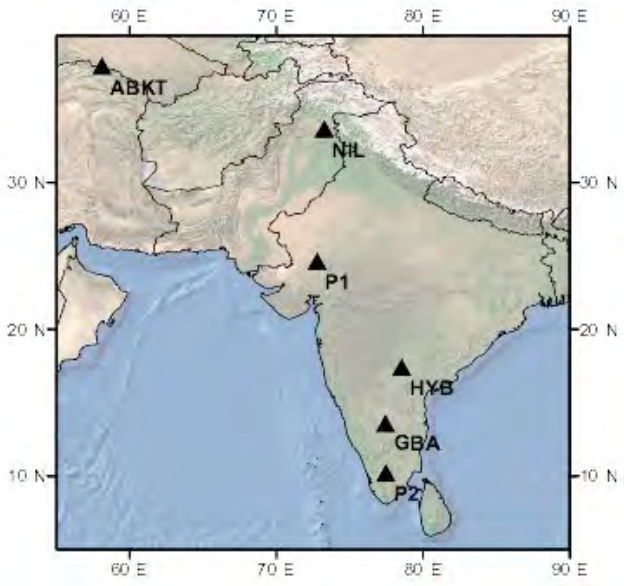


Figure 1. Location of IRIS/IDA (ABKT and NIL) stations, Geoscope station HYB, station GBA, formerly operated by the Atomic Weapons Establishment (AWE) at Blacknest, UK, and proprietary stations P1 and P2.

Detection of Mining Events from Continuous Data

Waveform correlation techniques. Two methods for detecting mine blasts are employed in this research. The first is the waveform correlation method (Harris, 1991). This method has been used on data from HYB, ABKT, GBA, NIL and the proprietary stations P1 and P2 (see also Britton *et al*., 2003 for an example of previous results at station P2). A simple STA/LTA detector was applied to twelve months of continuous data from proprietary station P1 as an initialization for the waveform correlation. Over 2000 detections were made for this period and the detected waveforms were correlated to a threshold of 0.7 into clusters of two or more events each. We developed subspace detectors for the six largest clusters (Table 2). These detectors were used to reprocess six months of the P1 dataset in order to find additional events in the six clusters. Events in these clusters are initially examined by eye, and if the events appear to be mine blasts (based on the presence of the *Rg* phase or repeated occurrence during daylight hours) then the events in the cluster are located. Figure 2 shows the locations of the clusters relative to P1. Figure 3 shows the detections, sorted by time of day, for a six-month period for each cluster. Figure 4 shows an example of events from each cluster.

Table 2. P1 cluster parameters. *P* and *Rg* back azimuth sample standard deviation was calculated only for events with detected *Rg* arrivals.

Cluster	Latitude (deg)	Longitude (deg)	Initial No. events	No. events used for cluster location	No. events with detected *Rg* arrivals	*P* back azimuth Sample Std. Dev (deg)	*Rg* back azimuth Sample Std. Dev. (deg)
2	25.1	74.9	88	39	33	11.2	11.5
3	23.5	73.6	30	14	5	10.3	6.23
4	24.4	73.8	22	16	16	7.4	7.1
5	22.9	73.5	35	16	-	14.2	-
6	24.4	73.9	12	7	4	4.1	8.7
7	24.8	73.7	21	6	4	12.3	12.2
Total events			208	98			

Only events detected by an analyst and with signal-to-noise ratio (SNR) greater than 1 were used for cluster location estimates. We calculated SNR as the ratio between the maximum *P* amplitude in a 3-sec window and twice the standard deviation of the noise (Der and Shumway, 1999) in a 10-sec window preceding the signal. The largest location outliers were discarded from each cluster. *P* and *Lg* arrival times were picked by an analyst, an *Rg* detector was applied and the events were located using semi-automatic methods similar to those described in the next section (Britton *et al.*, 2003). Median values for latitude and longitude were calculated for each cluster. A comparison between the *Rg* and *P* back azimuth residuals for 98 events with *Rg* arrivals from five clusters in northwestern India recorded at station P1 is presented in Figure 5. We observe (Table 2) that sample standard deviations of back azimuth estimates using the *Rg* detector are comparable or better than single station *P* back azimuth estimates for all clusters (except for the four events in Cluster 6). A possible explanation is that the *Rg* phase often has larger amplitude than the *P* phase.

Most of the events in Cluster 2 were recorded between 0800 and 1000 UTC (13:30 to 15:30 local time). Less than half of the events in Cluster 3 had SNR > 1. Of these, five events had *Rg* arrivals recorded at times marked by arrows in Figure 3. Further investigation of events in Cluster 3 is necessary to find whether one or several mines are operating in the area. All the events in Cluster 4 had *Rg* arrivals and occurred between 0800 and 1000 UTC (13:30 to 15:30 local time). No *Rg* arrivals were found in Cluster 5 except for an event with SNR lower than 1. The events in Cluster 5 were recorded between 04:00 and 07:00 UTC (09:30 to 12:30 local time) or 1200 and 1500 (17:30 to 20:30 local time). Cluster 5 might be composed of two sub-clusters with different occurrence times. Three events without *Rg* arrivals were located apart from the other four events in Cluster 6 with detected *Rg* phases. Given the long durations of these cluster sequences (Table 2) and the consistency of the origin times, these sources appear to be mines. The fact that events from Clusters 2, 3, 4, 6 and 7 exhibit *Rg* phases, which are consistent with shallow sources such as open-pit mine blasts, supports this interpretation.

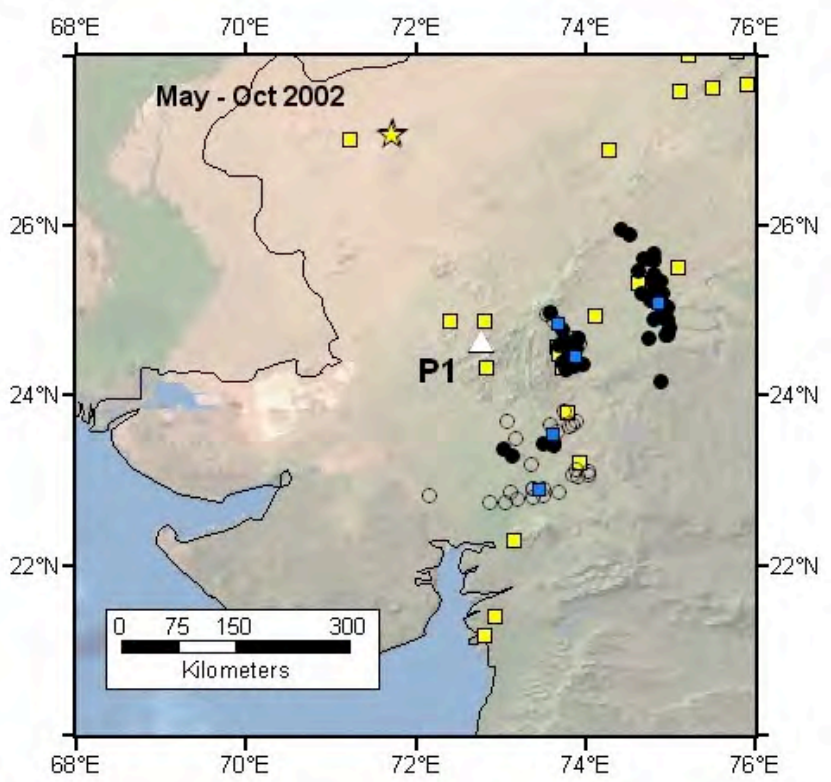


Figure 2. Single-station location of the six largest subspace detection clusters (blue squares) recorded at P1 between May and October 2002. Events for which *Rg* was detected (suspected mine blasts) are plotted as black circles. Yellow squares represent locations of open-mine pits. All the other cluster events are plotted as open circles. The yellow star is the location of the Pokhran test site.

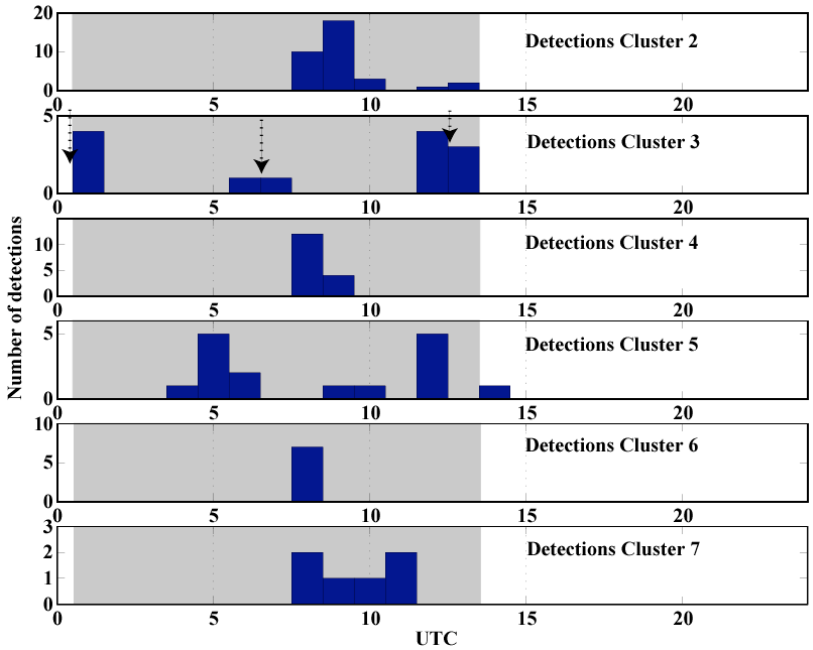


Figure 3. Clusters 2 to 7 event detections at station P1 sorted by time of day. Local time equals UTC plus 5.5 hours. Daylight hours (0600 to 1900 local time are highlighted). The arrows represent occurrence times for the Cluster 3 events with *Rg* arrivals.

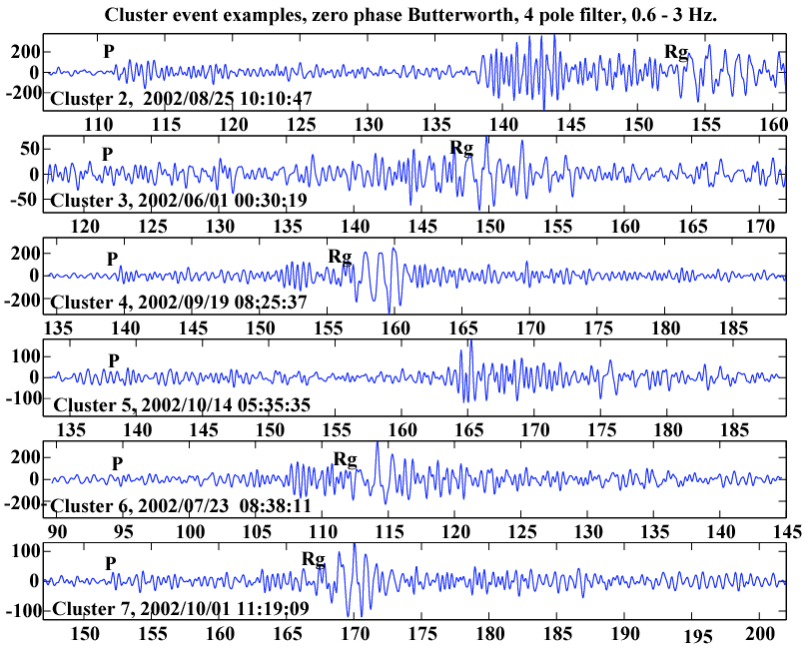


Figure 4. Examples of events from the six clusters, recorded at P1.

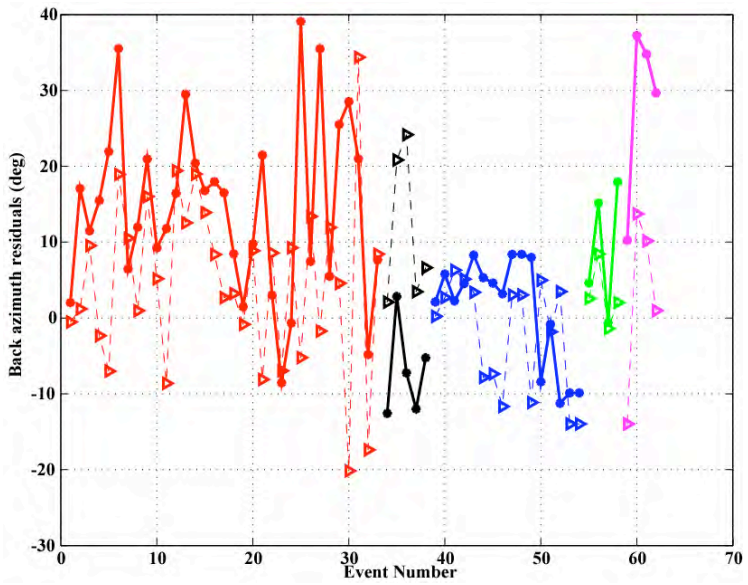


Figure 5. *P* back azimuth residuals (dotted line with triangles) and *Rg* back azimuth residuals (continuous line with stars). The residuals were calculated relative to the cluster estimated back azimuth. Events 1 to 33 are from Cluster 2 (red), events 34 to 38 are from Cluster 3 (black), events 39 to 54 are from Cluster 4 (blue), events 55 to 58 are from Cluster 6 (green) and events 59 to 62 are from Cluster 7 (magenta).

Semi-automatic detection of possible mining events from continuous data using an Rg detector. An alternate approach to the waveform correlation method is to continuously scan the station data for *Rg* arrivals without reference to known events. The presence of *Rg* on waveforms indicates shallow source depth, and when it is detected repeatedly during daytime hours, it is often an indication of mining operations. At this point we use only the *P* back azimuth in location algorithms. However, estimates of *Rg* back azimuth could be used for location of events with low SNR first arrival and large *Rg* amplitude. Thus, a complementary method used to detect small

shallow events (possible mine blasts) is the automatic *Rg* detector (Tibuleac and Britton, 2004; Britton *et al.*, 2003; Chael, 1997). When applied after non-linear pre-filtering, the *Rg* detector code, using both polarization and amplitude information, produced back azimuth estimates comparable to the frequency to wavenumber three-component (*fk*3C) single station *P* back azimuth estimates when tested on clusters of well-located events in India (see also Figure 5 in this study).

Continuous data processing algorithms. The *Rg* detector was incorporated into routines for semi-automatic analysis of continuous data. A first arrival (*P*) detector and the *Rg* detection algorithm were applied to 10-min files. The *P* detector code was designed for three-component data using an algorithm similar to the *Rg* detector, modified for first arrival detection, and using a combination of Fourier and non-linear pre-filtering techniques. So far, the *P* detector has only been used for qualitative information purposes. Based on previous studies (Britton *et al.*, 2003), we decided to use non-linear pre-filtering before *Rg* detection. The non-linearly filtered data consists of coefficients of a Continuous Wavelet Transform using the 'Meyer' wavelet. Due to its similarity to a sinc function, the Fourier transform of a Meyer wavelet is a boxcar, centered on the analyst-chosen period (1 sec for this region).

Once a detection was declared, we applied the WAVELET1.0 picker developed at Weston Geophysical by Tibuleac *et al.*, (2003), to estimate *P* and *Lg* phase arrival times. Epicentral distance was estimated from the *P* and *Lg* arrival time difference using empirical, station specific formulas for station P1, and using the SSLOC3D single-station location method (Leidig *et al.*, 2003) for station P2. The first arrival back azimuth was estimated using the *fk*3C method adapted from MatSeis (Harris and Young, 1997). Improvements to the *fk*3C method include: 1) non-linear pre-filtering using a 'bior3.7' wavelet centered on the analyst-chosen *P* period. 2) *fk* analysis in a sliding 1 sec window with a step of 0.5 sec, performed within 5 sec of the detected *P* arrival to obtain the most stable back azimuth value estimation. Starting 2 min. before the detected *P* arrival, 10 min. of waveforms were stored in the database for each event, using specific MATLAB–to–SAC conversion routines.

Detection results for proprietary station P1. The detection algorithms were applied to continuous data from station P1 recorded for 15 days in March and April 2001. The analysis resulted in 282 detected local events. Of these events, 35 had *Rg* arrivals and were classified as possible explosions (orange circles in Figure 6). All the events with detected *Rg* arrivals were located to the northeast of P1, in the direction of known local mines (yellow squares), except for five events located in the seismically active Bhuj region, near the Basantgarh Copper Mine. Examples of possible explosions recorded from northeast of station P1 are presented in Figure 7. The upper plot presents a suspected explosion, recorded on 8 April 2001, 08:31, followed by a similar, lower magnitude event, 43 sec later. Another typical event with an *Rg* arrival, recorded on 5 April 2001, 08:13, also classified as a possible explosion, is presented in Figure 7, lower plot.

Detection results for proprietary station P2. The detection algorithms were applied to continuous data from station P2 recorded for 24 days in March and April, 2001. The analysis resulted in 156 detected local events. Of these events, 40 had *Rg* arrivals and were classified as possible explosions. The majority of the events with detected *Rg* arrivals were located to the northwest, in the direction of known local mines described by Britton *et al*, (2003). An example of suspected explosion detected northeast of station P2 on 3 April 2001, 09:12, is presented in Figure 8.

GIS Database

Waveforms of mine blasts detected by the waveform correlation and *Rg* detection methods are linked through hypertext transfer protocol (http) to an ArcView 8.3 geographic information system (GIS) database containing information on event location, satellite imagery, regional geology, station information, and mine information. An example is shown in Figure 9.

Event locations are added to the mining activity tables. When the suspected mine blasts do not occur near known mines contained in the database, a literature search for mines in that area is initiated. Satellite imagery in the area of the event location aids in providing ground-truth locations for the mining events. Often, the event locations lie within 10 km of an observed pit. The images are geo-referenced and can be readily incorporated into GIS maps. The database now contains satellite imagery for four mining districts showing the locations of at least a half dozen open pit mines. We have been unable to obtain any blast confirmations from the southern Asia mines; therefore satellite imagery has become our main source of ground truth.

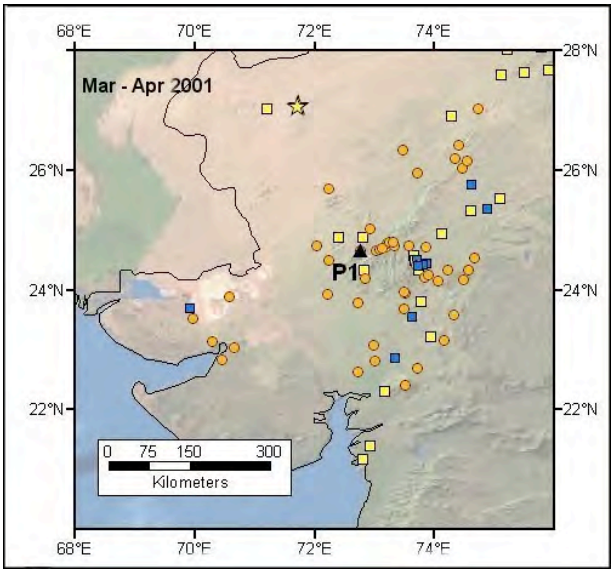


Figure 6. Location of suspected mine blasts (events with *Rg* arrivals) detected in March and April 2001 at station P1. Events for which *Rg* was detected (suspected mine blasts) are plotted as orange circles. Yellow squares represent locations of open-mine pits. Locations of event clusters estimated using waveform correlation methods are represented as blue squares.

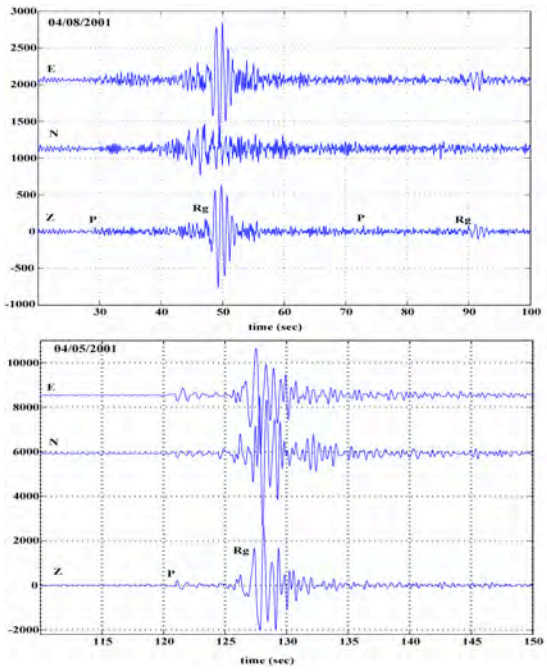


Figure 7. Upper plot: Zero-phase Butterworth 4 pole, 0.6-.5 Hz filtered waveforms for the 8 April 2001, 08:31:49 and 08:32:32 suspected explosions with *Rg* arrivals. The first event (*P* time lag 29 sec) was located 142 km east of P1. First arrival back azimuth was estimated to be 112 deg for the first event, located at 24.2 N and 74.1 E, and 109 deg for the second event, located at 24.3 N and 73.8 E. The *Rg* back azimuth was estimated to be 105 deg for both events. Lower plot: An event recorded at P1 on 5 April 2001, 08:13:12. The estimated location of this event was 24.82 N and 73.21 E, 48 km northeast of P1. First arrival back azimuth was 67 deg, while the *Rg* back azimuth was 63.4 deg.

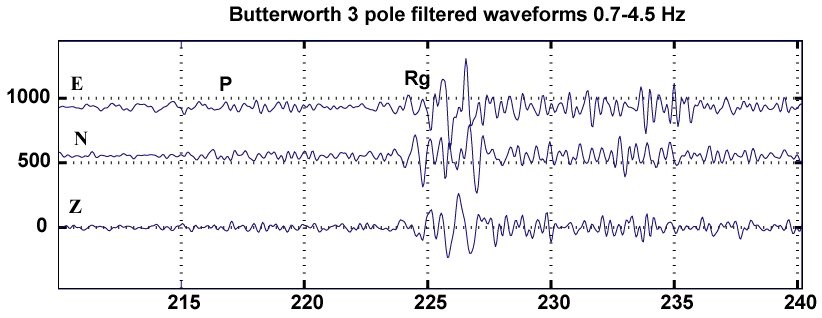


Figure 8. Suspected explosion on 2001/04/03 recorded at 09:12:34, with an estimated location of 10.4 N and 77.7 E, 40 km northeast of P2. Back azimuth was estimated as follows: 57 deg (*P*) and 58 deg (*Rg*).

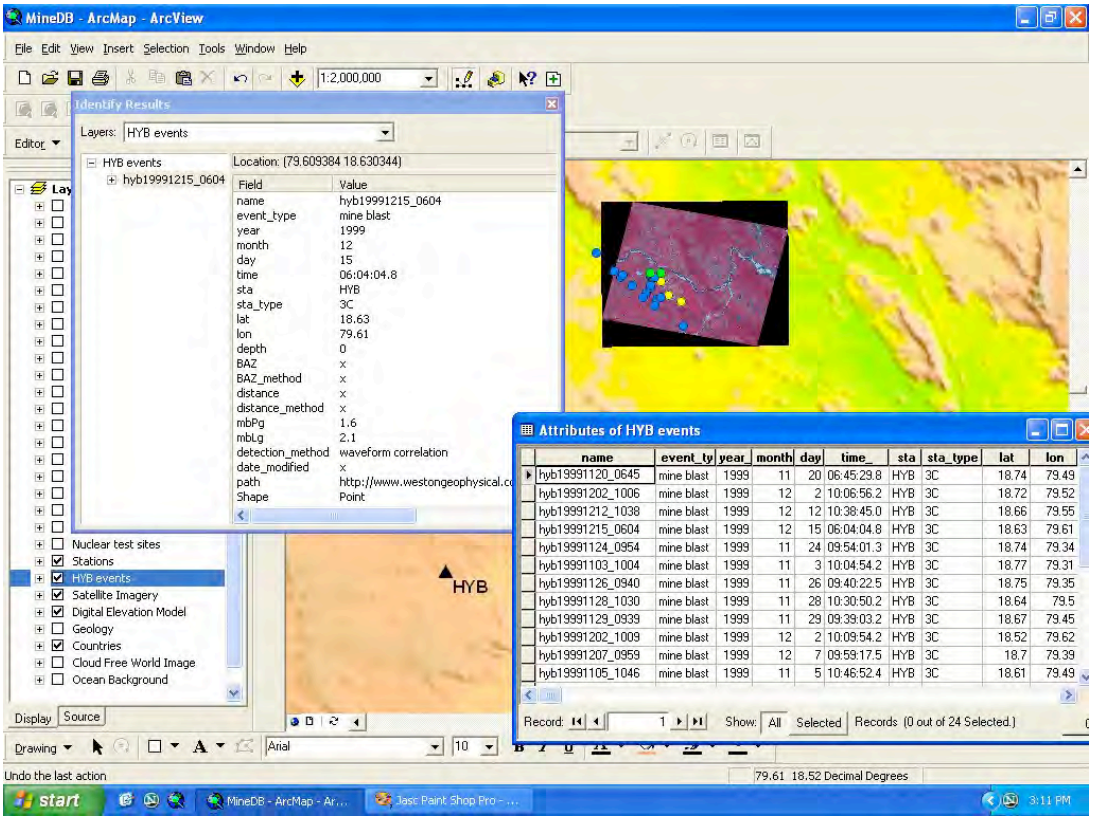


Figure 9. An ArcView interface window showing mining events detected near station HYB (blue, green and yellow circles), overlain satellite imagery and a digital elevation model. A window with event details and links to waveform data (right), and a window showing the attribute table for one of the events (left) are also shown.

CONCLUSIONS AND RECOMMENDATIONS

Information on mining activity around seismic stations in southern Asia is continually being compiled and updated. A combination of techniques, including waveform correlation and continuous data processing algorithms using single-station location methods and an *Rg* detection algorithm, was used to develop the mine database.

Continuous data have been analyzed using the waveform correlation method to detect events associated with nearby mines and mining districts. Waveforms from event clusters detected by the waveform correlation method at station P1 were spatially associated with nearby mines in the database. Additionally, the presence of *Rg* and the occurrence times during daylight hours confirm that these events are mine blasts. We observed that sample standard deviations of cluster back azimuth estimates using the *Rg* detector are comparable to *fk*3C *P* back azimuth estimates. Therefore, using the *Rg* phase back azimuth for event location is a promising alternative using small SNR first arrival back azimuth.

An *Rg* detector was integrated into a semi-automatic event-detection and -location algorithm and applied on continuous data. The algorithm uses improved *fk*3C single-station location techniques. We obtained better detection results and back azimuth estimates using non-linear pre-filtering. We presented continuous detection results at two proprietary stations in March and April 2001.

Detected waveforms are linked to an ArcView 8.3 geographic information system (GIS) database containing information on event location, satellite imagery, regional geology, station information, and mine information.

ACKNOWLEDGMENTS

We express our gratitude to Dr. Delaine Reiter and Mark Leidig for fruitful discussions and help on this project.

REFERENCES

Britton, J. M., D. Harris, I. M. Tibuleac, and J. L. Bonner (2003), Detection of Mining Explosions for a Southern Asia Seismic Database, *Proceedings of the 25th Seismic Research Review-Nuclear Explosion Monitoring: Building the Knowledge Base*, LA-UR-03-6029, Vol. 1, pp. 211-219.

Chael, E. P., (1997), An Automated Rayleigh-Wave Detection Algorithm, *Bull. Seis. Soc. Am*. 87, 157-163.

Der, Z. A. and R. H. Shumway (1999), Phase onset time estimation at regional distances using the CUMSUM algorithm, *Phys. Earth Planet. Int*. 113, 227 –246.

Harris, D.B, (1991), A Waveform Correlation Method for Identifying Quarry Explosions, *Bull. Seis. Soc. Am*. 81, 2395-2419.

Leidig, M., D.T. Reiter, J. L. Bonner, and A. Rodgers, (2004) Applicability of 3D modeling techniques in creating single-station locations: A test case in southern Asia, *Bull. Seis. Soc. Am*. 94, 753-759.

Tibuleac, I. M. and J. M. Britton (2004), An automatic Rg detection algorithm, (in preparation for *Bull. Seis. Soc. Am*).

Tibuleac, I. M., E. T. Herrin, James Britton, R. G. Shumway and A. C. Rosca (2003), Automatic of secondary phase arrivals using wavelet transforms, *Seis. Res. Lett.* 74, 884-892

Harris, M. and C. Young (1997), MatSeis: A Seismic GUI and Toolbox for MATLAB, *Seis. Res. Lett*. 68, 267-269.

Seismic Identification and Source Characterization

DEVELOPMENT OF A TIME-DOMAIN, VARIABLE-PERIOD SURFACE WAVE MAGNITUDE MEASUREMENT PROCEDURE FOR APPLICATION AT REGIONAL DISTANCES

Jessie L. Bonner, Delaine T. Reiter, David G. Harkrider, and Sara A. Russell

Weston Geophysical Corporation

Sponsored by Air Force Research Laboratory

Contract No. DTRA01-01-C-0080

ABSTRACT

We continue to examine the feasibility of using short-period surface waves for estimating magnitude at regional distances. In previous research studies, we demonstrated that calibrated surface wave magnitudes (e.g., Marshall and Basham, 1972; Rezapour and Pearce, 1998) based on 7-second surface waves provided adequate M_s-m_b discriminant performance at the Nevada Test Site (NTS). However, at the Lop Nor test site we determined that the method worked best by forming magnitudes at the period of maximum amplitude.

We have recently shifted our focus to a new surface wave magnitude scale developed by Russell (2004) that uses Butterworth-filtered seismic signals. Russell (2004) developed a zero-phase 3rd order Butterworth magnitude equation (with amplitude, a_b, measured zero-to-peak in nanometers) of:

$$M_S = \log(a_b) + \frac{1}{2}\log\left(\sin(\Delta)\right) + .0031\left(\frac{T_0}{T}\right)^{2.3}\Delta - \log(f_c) - 0.43 - 0.66\log\left(\frac{20}{T}\right)$$

where T_o is 20 seconds, Δ is distance, and f_c is the Butterworth corner frequency which is defined by

$$f_c \le \frac{G_{\min}}{T\sqrt{\Delta}}.$$

Setting G_{min}= 0.6 is appropriate for continental signals between 8 and 40 seconds and oceanic signals between 20 and 40 seconds, including mixed oceanic and continental paths.

We have developed a new processing methodology in order to use the Russell (2004) equation. Our current processing technique begins with a multiple filter analysis on the vertical component seismic data of interest. We use this trial estimate of the dispersion curve to complete phase-matched filtering by following the iterative approach of Herrin and Goforth (1977). Next we apply a filter comb to the data, using center periods at 1-second intervals between 5 and 25 seconds. The envelope function of the filtered signal is constructed, and the maximum zero-to-peak amplitude is measured. An amplitude correction based on the assumption that the event is a shallow explosion is applied to account for the larger shorter period amplitudes generated from shallow earthquakes and explosions. The final processing step is to form a network average of the maximum magnitudes between 8 and 25 seconds, dependent on pre-event noise conditions. M_s (VMAX) is the name that we have given to this combination of the Russell (2004) magnitude scale and the variable-period maximum magnitude averaging.

We have tested this M_s (VMAX) methodology on synthetic data from various earthquake fault mechanisms and depths and found the method to be an improvement over the currently employed methods of surface wave estimations at regional distances. We have also applied the processing methodology to 154 explosions and 69 earthquakes from the NTS region and have found that the new method decreases the variance from single-period estimates by 33%, thus improving the M_s-m_b discriminant performance. Extensive testing of the technique will be completed using a dataset of Eurasian explosions and earthquakes during the next two years as part of a joint project with Lawrence Livermore National Laboratory (LLNL).

OBJECTIVES

Most surface-wave magnitude (M_s) measurements determined for explosion sources consist of events with m_b greater than 4.5; thus, there is uncertainty in the performance of the M_s-m_b discriminant for explosions with yields of less than approximately 5 kilotons fully coupled. At regional distances, an important nuclear monitoring question remains as to whether variable and short-period magnitude scales can be applied successfully to lower M_s thresholds and reduce the variance in the estimates. The objective of this research is to propose and test a new methodology for measuring variable-period surface waves at both regional and teleseismic distances. These new methods take advantage of a recently developed, time-domain surface-wave magnitude formula (Russell, 2004) designed for Butterworth-filtered surface waves. These new methods also make use of a new magnitude measuring procedure that uses the maximum magnitudes at variable periods from multiple stations to form a network-averaged M_s estimate. In this paper, we present the results of applying this new formula and measurement technique to explosions at the NTS and earthquakes in the western United States.

RESEARCH ACCOMPLISHED

A New Surface Wave Magnitude Formula

Russell (2004) has developed a new time-domain surface wave magnitude formula based on a theoretical derivation for surface waves and a zero-phase 3rd order Butterworth filter (with amplitude, a_b, measured zero-to-peak in nanometers). The equation is

$$M_s = \log(a_b) + \frac{1}{2}\log\left(\sin(\Delta)\right) + .0031\left(\frac{T_0}{T}\right)^{2.3}\Delta - \log(f_c) - 0.43 - 0.66\log\left(\frac{20}{T}\right), \quad (1)$$

where T_o is 20 seconds and the filter corner frequency is given by:

$$f_c \le \frac{G_{\min}}{T\sqrt{\Delta}} \quad (2)$$

Russell (2004) notes that setting G_{min}= 0.6 should be valid for continental signals between 8 and 40 seconds and oceanic signals between 20 and 40 seconds, including mixed oceanic and continental paths. The formula is equivalent to the von Seggern (1977) magnitude formula at 20 seconds.

Variable-Period, Maximum Magnitude Estimation (VMAX)

The surface-wave magnitude estimation procedure currently employed at most data centers involves measuring the amplitude of surface waves near 20-seconds period. In previous research projects (Bonner et al), we tried to extend this technique to lower periods (e.g., 7 seconds). It was determined that shorter-period surface waves could be used for magnitude estimation for events with smaller m_bs than when only considering 20-second data. Although the 7-second magnitude scale formed a robust discriminant at NTS, it failed to provide adequate explosion/earthquake separation at other test sites, where earthquakes were deeper than the nearby NTS. This failure led to our current design of measuring the maximum magnitude at variable periods between 8 and 25 seconds. We refer to this technique as VMAX. In the following paragraphs, we describe this new magnitude estimation technique.

Phase-Matched Filtering. Our current processing technique begins with a multiple filter analysis on the vertical component of data (in displacement) for our test dataset. We use this trial estimate of the dispersion curve to complete phase-matched filtering following the iterative approach of Herrin and Goforth (1977). The phase-matched filtered and extracted surface waves are then entered into a Matlab-based surface wave magnitude program that calculates the Russell (2004) magnitude. This method is easily automated in a data center setting. We note that for events with m_b > 4.5, the phase matched filtering processing step is not needed because the surface waves have significant signal-to-noise ratio (SNR) and are easily identified. This processing step is most advantageous for smaller magnitude events, where the surface wave SNR may be approaching 1.

Butterworth Filtering. We apply a zero-phase 3rd order Butterworth filter to the data with the corner frequency determined from Equation 2. The center periods are at 1-second intervals between 5 and 25 seconds. An example of these filter "combs" applied to a nuclear explosion recorded at Mina, Nevada (MNV), is shown in Figure 1. The envelope function of the filtered signal is then constructed and the maximum zero-to-peak amplitude is measured in a group velocity window between 2.0 and 4.0 km/sec. Equation 1 is used to calculate a variable-period Butterworth

surface-wave magnitude. The advantage of the time-domain measurement is evident in Figure 1, as the technique allows the analyst to visually confirm that the correct waveform feature is being measured.

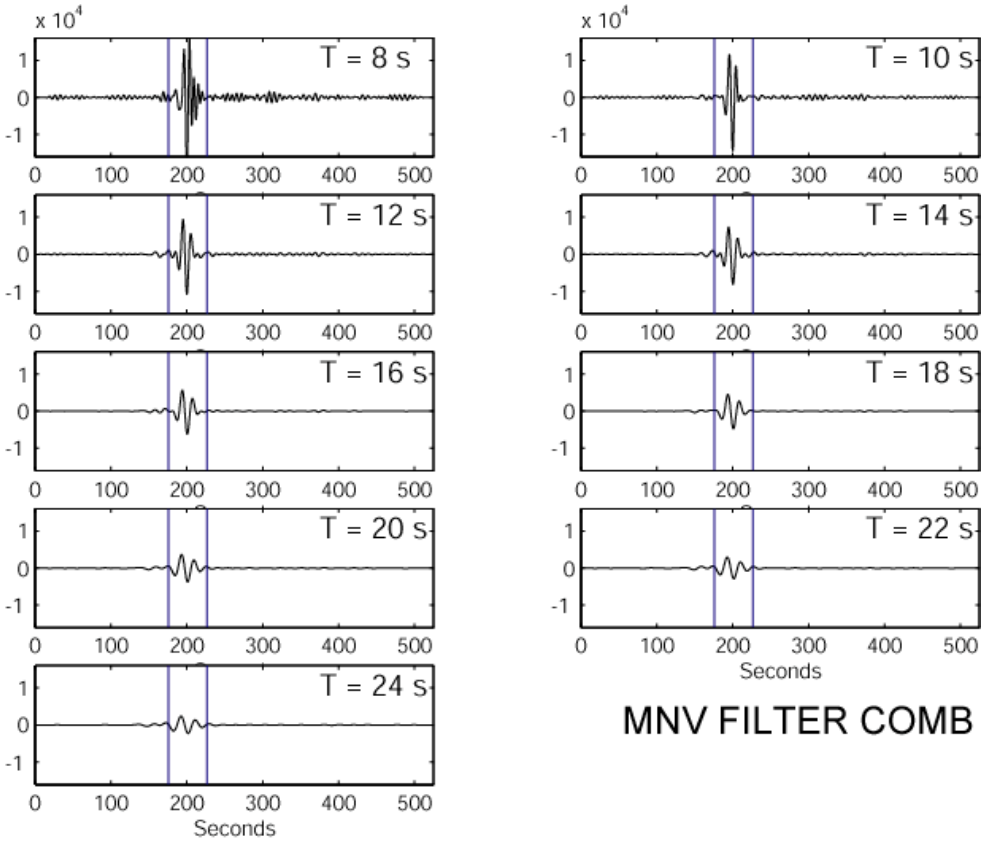


Figure 1. Filter combs through explosion seismograms recorded at station MNV for the m_b=5.26 Serpa explosion. The vertical lines represent group velocity windows of 4.0 and 2.0 km/sec. Amplitudes are in nm. We filter the data between periods of 5 and 25 seconds at 1-second intervals; however, only the periods between 8 and 25 seconds are used for magnitude estimation due to the values used for G_{min} in Equation 2.

Amplitude Corrections. The final step in calculating the M_s(VMAX) magnitude requires the application of an amplitude correction based on the excitation differences for shallow earthquakes and explosions at shorter periods. These corrections are relative to 20-seconds period and will account for the larger, shorter-period amplitudes generated from shallow earthquakes and explosions. This method is similar to the methodology of Stevens and McLaughlin (2001) for path-corrected spectral magnitudes. The correction does not create problems for deeper events (mid- to lower-crust events), because we use the period of maximum magnitude (VMAX) when estimating the final M_s. We calculated these corrections using simple regionalized simulations. For example, we used the Stevens et al., (2001) velocity models for the NTS to MNV, ELK, KNB, and LAC paths and generated fundamental-mode, Rayleigh-wave synthetics (Herrmann, 2002). We did not consider attenuation in the synthesis of these corrections, because variable-period attenuation is considered in Equation 1. We then used the same Butterworth filtering techniques discussed earlier to compare the log amplitude of the variable-period filter combs to the log amplitude of the filter at 20 seconds. At the periods and distances considered in this study, we used the mean of the corrections shown in Figure 2 as our period-dependent amplitude corrections. It is important to note that this correction, based on synthetic signals, replaces the final term in Equation 1 for our analyses because the correction values shown in Figure 2 are approximated by -0.66 log (20/T).

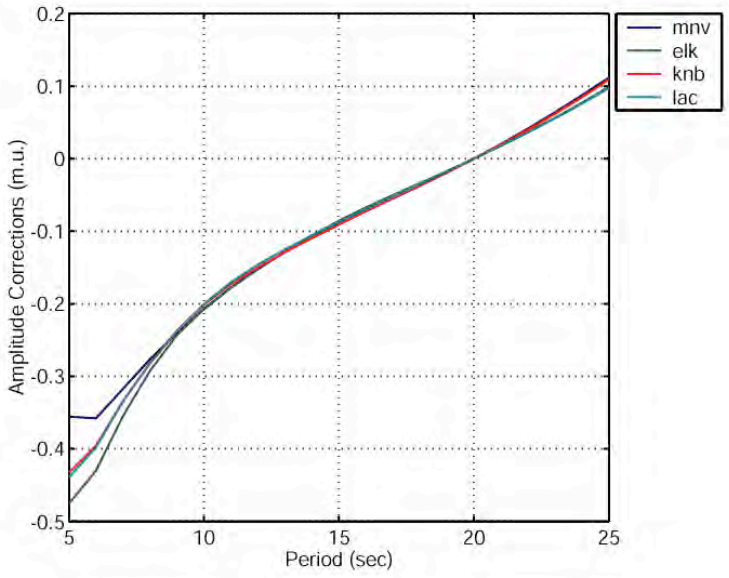


Figure 2. Amplitude corrections for a simulated 1-km deep explosion relative to 20-seconds period. The corrections were estimated using the same Butterworth filters as used on the real data.

VMAX. To obtain a final M_s(VMAX) value for each explosion or earthquake, we average the maximum magnitude at variable periods between 8 and 25 seconds over multiple stations and determine the standard deviation of the observations. Examples of the VMAX methodology applied to four earthquakes and explosions in the western U.S. are shown in Figures 3 and 4. Given in each explosion subplot, the 7-second magnitude estimate (M_s(7)) determined from Bonner et al., (2003) using a regionally-calibrated Marshall and Basham (1972) equation is given. The behavior of the noise (dashed lines in Figure 3) is a motivating factor behind this study. As the events become smaller, the noise and signal-based M_s estimates begin to overlap. For example, for the m_b=4.54 event DEPHINIUM, the noise and signal overlap at periods greater than 15 seconds. Therefore, for small events, we restrict the M_s(VMAX) analysis to periods where the signal is above the background noise levels (e.g., 8-14 seconds for this event). By allowing for the variable-period estimates, we can estimate surface wave magnitudes for smaller events than previous techniques would allow.

Testing the VMAX Methodology in the Western United States

Database. We developed a test dataset consisting of explosions and earthquakes in the western United States. The explosion data are vertical-component, digital broadband seismograms from NTS explosions recorded on two or more stations of the Lawrence Livermore Regional Seismic network (LNN). The LNN network consists of seismic stations at Landers, California (LAC); Mina, Nevada (MNV); Elko, Nevada (ELK); and Kanab, Utah (KNB). The network has been in operation since the 1960s (Figure 1).

M_s (VMAX) for NTS explosions that occurred between December 1968 and September 1992 were estimated. The primary research focus was on the 198 NTS explosions that were detonated after August 1979, for which digital data are available from the LNN stations. Sixty-five (65) of these events have no LNN data available, are plagued by untimely data dropouts and glitches, or are too small for measurable surface wave energy. We also analyzed 21 events prior to July 1979 that were digitized from analog records so that we could compare our new results with previous M_s studies completed by Yacoub (1983), Woods and Harkrider (1995), Marshall et al., (1979), and Stevens and Murphy (2001). We also estimated the M_s and m_b magnitudes for 69 earthquakes whose locations are shown in Figure 5. These events were recorded on various networks in the region; however, we required that at least one LNN station recorded the event so that an unbiased m_b could be measured using the Denny et al., (1987) *Pn* magnitude scale.

***M*$_s$(VMAX) vs *M*$_s$(7).** The M_s (VMAX) measurements for 154 explosions were compared, using the new Russell (2004) time-domain procedure and our variable-period measurement techniques, to the single 7-second period measurements from our previous research (Bonner *et al*., 2003). Figure 6 shows that VMAX explosion magnitudes are approximately 0.25 magnitude units (m.u.) larger than the Marshall and Basham M_s(7) estimates. The slope of the best fit line between the two datasets is approximately equal to 1. The VMAX methodology resulted in a 33%

reduction of the variance for both earthquakes and explosions over the previous single-period techniques based on Marshall and Basham regionally-calibrated $M_s(7)$ estimates. The VMAX techniques offered 47% reduction over the 7-second estimates based on the Rezapour and Pearce (1998) formula.

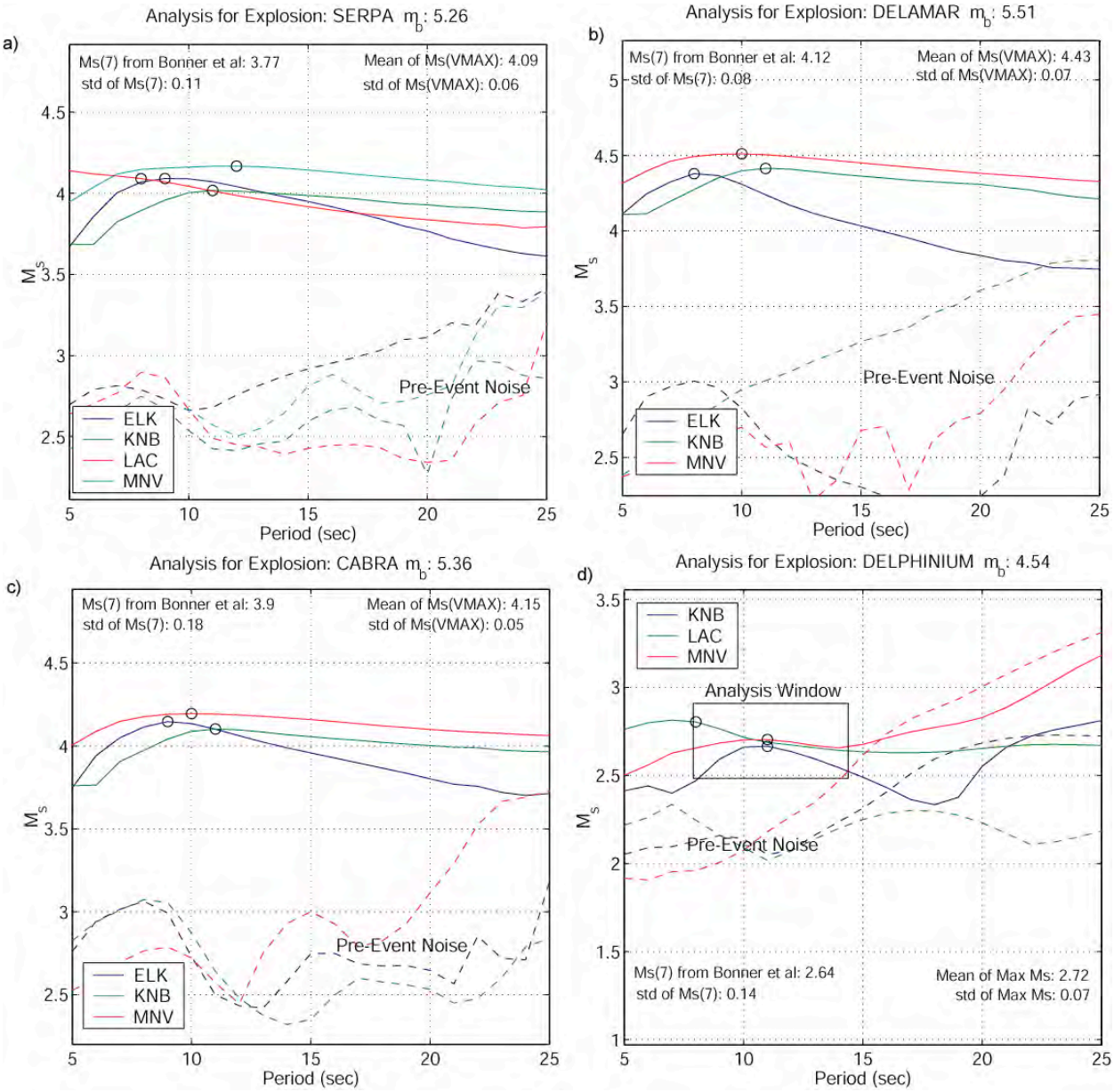


Figure 3. VMAX surface-wave magnitude estimation for NTS explosions (a) SERPA, (b) DELAMAR, (c) CABRA, and (d) DELPHINIUM. Solid lines represent time domain M_s estimates for the surface-wave data plotted as a function of the center period, whereas dashed lines represent similar estimates on pre-event noise data. For the smaller event DELPHINIUM, the noise levels begin to intersect the signal at periods great than 15 seconds, thus we restrict the analysis to 8 to 14 seconds for this event. For comparison, the $M_s(7)$ from Bonner et al. (2003) is listed in each subplot.

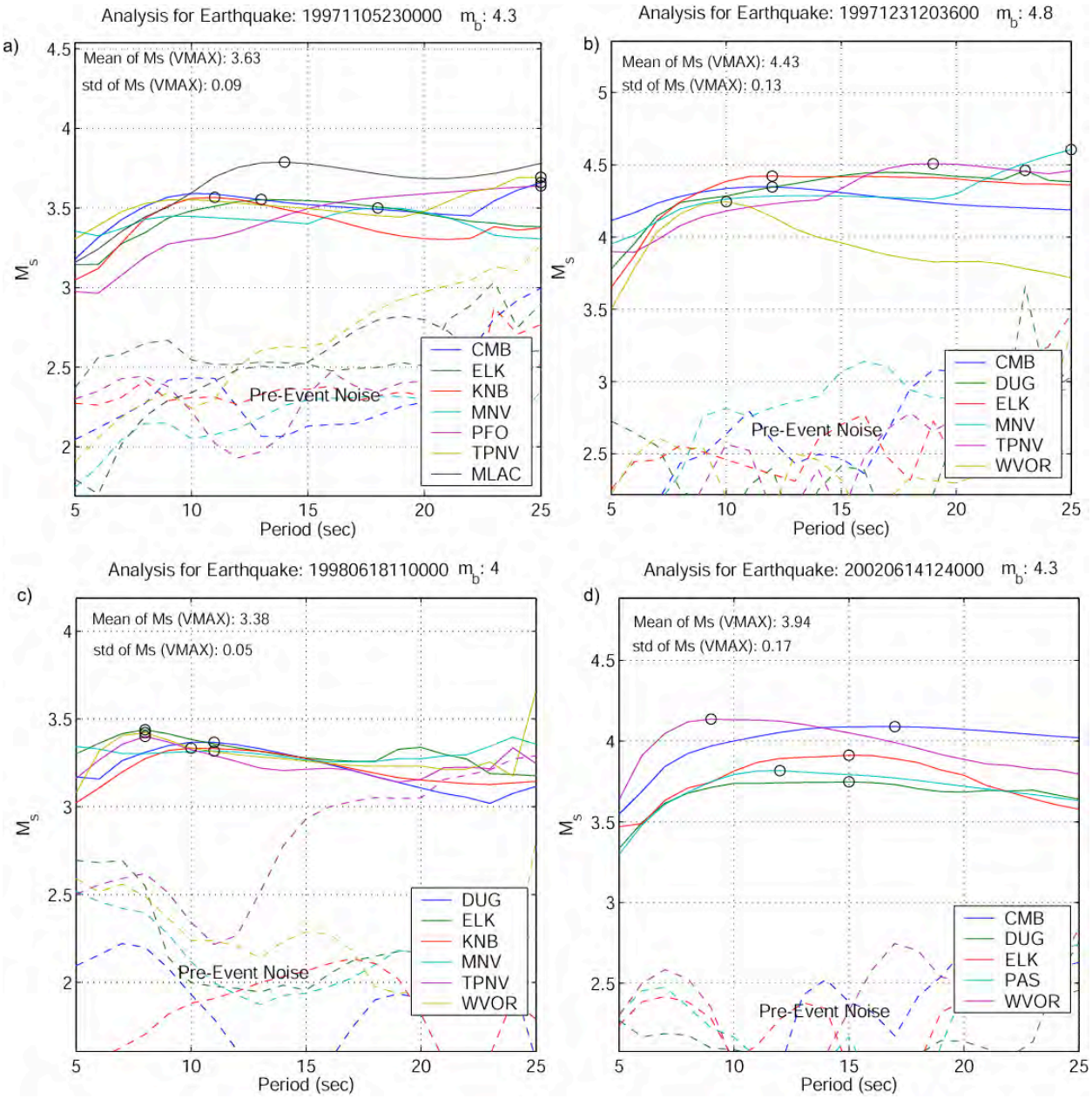


Figure 4. VMAX surface-wave magnitude estimation for four western United States earthquakes. Solid lines represent time domain M_s estimates for the surface-wave data plotted as a function of the center period, whereas dashed lines represent similar estimates on pre-event noise data.

***M_s*(VMAX) vs. Previous Regional/Teleseismic Studies.** Estimating near-regional M_s values for NTS events that can be calibrated to conventional M_s scales is of primary importance to our research. Figure 7 shows the comparison between our M_s(VMAX) estimates taken directly from the regional surface waves with the M_s measurements obtained from a modeling technique derived by Woods and Harkrider (1995), in addition to far-regional/teleseismic data (Yacoub, 1983; Marshall et al., 1979; and Stevens and Murphy, 2001). We note very good agreement to the Woods and Harkrider indirect method of estimating M_s. Woods and Harkrider modeled the surface waves recorded at regional distances, and then propagated the regional synthetics to distances of 40 degrees. At 40 degrees, their synthetics showed significant 20-second surface wave energy, and the authors used a modified von Seggern (1977) formula to measure M_s from the synthetics. We performed a fixed-slope (slope=1) linear regression to compare the M_s(VMAX) values with the Woods and Harkrider (1995) values and found a strong correlation.

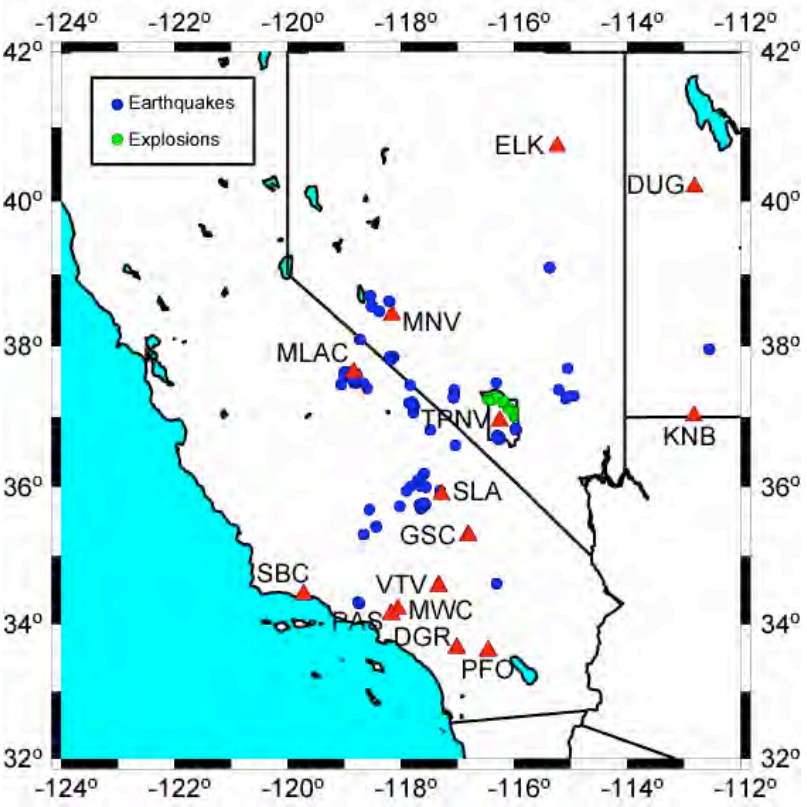


Figure 5. This test dataset consists of NTS explosions recorded on the LNN dataset together with western United States earthquakes recorded on at least one LNN station and other regional networks.

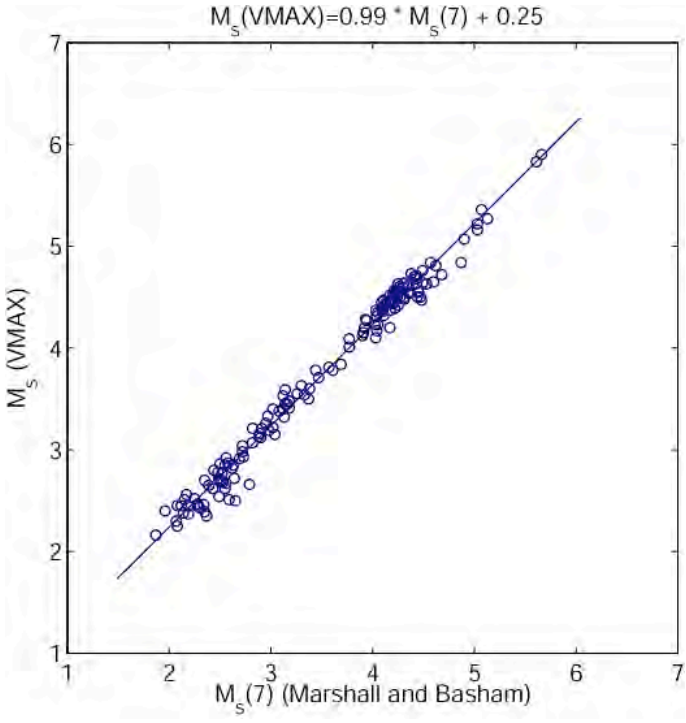


Figure 6. M_s(VMAX) magnitude estimates compared to 7-second estimates based on a regionally-calibrated Marshall and Basham formula. The VMAX estimates result in a 33% reduction in variance as compared to the 7-second estimates and are 0.25 m.u. larger.

The offset shows that the M_s(VMAX) estimates are -0.04 m.u. lower than the Woods and Harkrider (1995) estimates. We also compared the performance of M_s(VMAX) with teleseismic estimates from Yacoub (1983). The results for the comparison with Yacoub (1983) are shown in Figure 7 and indicate similar scaling relationships based on fixed-slope regression analysis. In this case, our M_s(VMAX) is offset from Yacoub's (1983) estimates by approximately +0.1 m.u. M_s(VMAX), which is +0.48 m.u. larger than teleseismic estimates from Marshall et al. (1979; based on the Marshall and Basham formula) and +0.4 m.u. larger than teleseismic/far-regional estimates from Stevens and Murphy (2001; based on the Rezapour and Pearce formula). Differences in these absolute estimates result from the use of different M_s definitions, especially in the attenuation factors. However, these comparisons do show that our estimates scale similarly to other measurements of NTS surface wave magnitudes. For a future study, we hope to further determine the differences in the absolute values of these scales by measuring M_s(VMAX) on the same datasets as used in the previous studies.

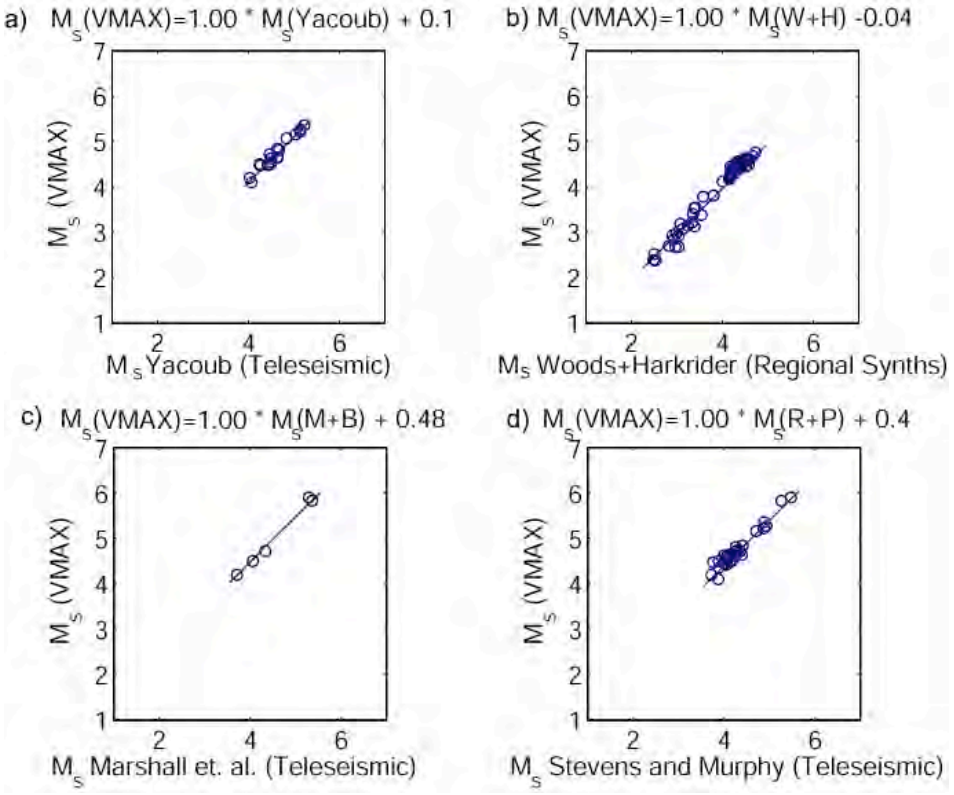


Figure 7. Fixed slope=1 regressions of M_s (VMAX) versus a) Yacoub (1983), b) Woods and Harkrider (1995), c) Marshall *et al*., (1979), and d) Stevens and Murphy (2001). The best-fitting regression line, with a fixed slope = 1.0, is given by the solid line running through the data points. The offset is referenced in the equation above each plot.

***M_s*(VMAX) vs *m_b*.** In Figure 8a, we regressed the M_s (VMAX) versus the Denny et al. (1988) m_b for both populations in our test dataset. The best-fitting regression lines are plotted and labeled in the figure and ± 1 standard deviation (σ) is plotted around the average M_s (VMAX). The final objective of this paper is to examine the performance of the M_s(VMAX)-m_b discriminants for earthquakes and explosions. The populations plotted in Figure 8a suggest that M_s and m_b will be fitted well by linear regressions, with approximately equal slopes assumed for the earthquake and explosion populations. Although, we did observe slightly different slopes in the regression analyses for the two populations, we believe that this is caused by inadequate sampling of earthquakes at m_b magnitudes greater than 5.2. Our dataset does not present any evidence that the two populations are converging at smaller magnitudes, although other M_s-m_b studies (Stevens and McLaughlin, 2001) suggest that convergence does occur. The classification equation based on the parallel-slope assumption becomes

$$d = M_s(\text{VMAX}) - 1.3m_b, \tag{3}$$

where d is the decision value. If d < -2.45, the event will reside in the explosion population. This does not require the event to be a nuclear explosion, as noted, and additional testing is needed to ensure the event is shallow enough to be a candidate explosion. If d > 2.45, the event falls into the earthquake classification. We note that no explosions were misclassified as earthquakes using the VMAX magnitude estimation technique with the Russell (2004) surface-wave magnitude scale. One earthquake was misclassified in the explosion population. In our previous studies based on 7-second data, four earthquakes were misclassified as explosions and two explosions as earthquakes.

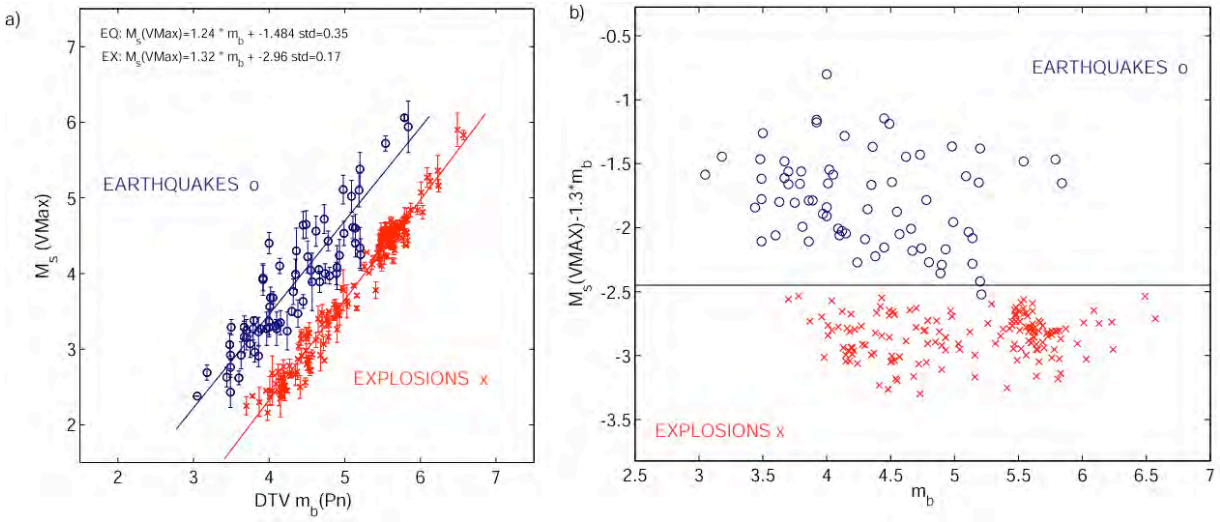


Figure 8. Discrimination results for M_s (VMAX). a) M_s (VMAX) vs. m_b for western United States earthquakes and nuclear explosions. b) Linear discrimination of the two datasets showing the decision line for classifying an event as a possible nuclear explosion. If d=M_s (VMAX) – 1.3m_b is less than -2.45, the event may be an explosion, and as a result may require additional analysis to prove the event is not a deep and/or anomalous earthquake.

Regional vs. Teleseismic. In future work, we will analyze whether there are biases in the M_s(VMAX) measurement technique when regional and teleseismic data are combined. Equation 1 should theoretically have no regional to telseseismic biases, unless there are changes to the attenuation models at greater distances. In these cases, a variant of Equation 1 has been defined by Russell (2004) so that a known frequency-dependent attenuation model can be applied. In the current study, we are using Equation 1 to determine if regional and teleseismic magnitudes estimated using the VMAX technique are equivalent. An example of the analysis to be completed is shown in Figure 9. In this example the regional and near-teleseismic magnitudes agree to within 0.1 m.u. However, we note that the period of the maximum magnitudes may be distance dependent. Additional analyses, including data at epicentral distances of 60 degrees and less, will be completed to quantify possible biases and better understand the behavior of our method.

CONCLUSIONS AND RECOMMENDATIONS

The results presented in this paper suggest that the 33% decrease in variance offered by the new Russell surface-wave magnitude formula, combined with the VMAX estimation technique, offers improved discriminant performance at the NTS over our previous 7-second magnitude estimation techniques. Additionally, using the Russell equations and the variable-period VMAX technique will allow flexibility when we examine the transportability of this method at other test sites, particularly in regions where the events may be deeper than the earthquakes near NTS. During the next two years, we will continue extensive testing of these techniques using a dataset of Eurasian explosions and earthquakes as part of a joint project with LLNL.

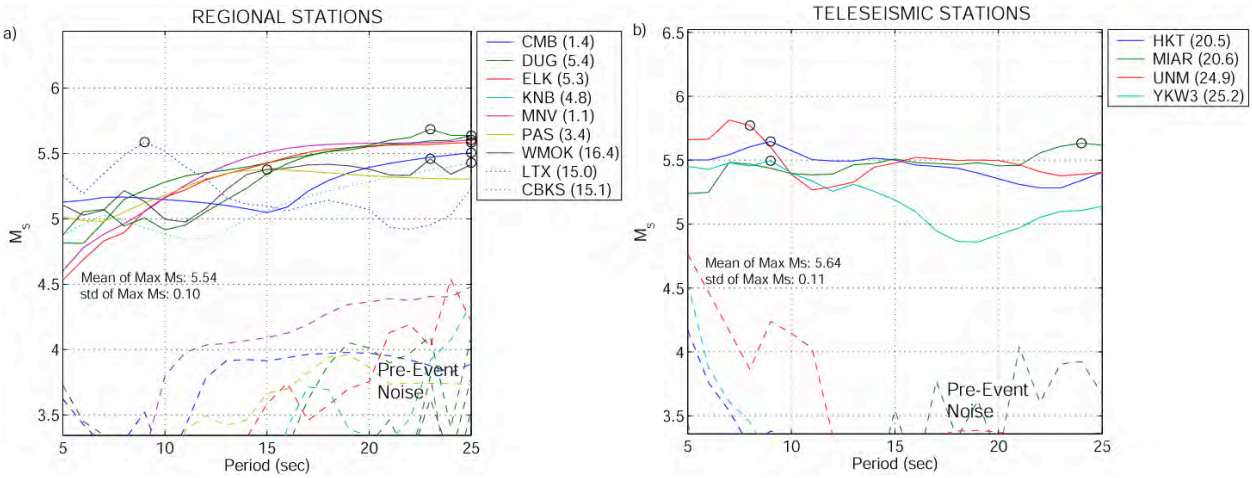


Figure 9. ***M*$_s$(VMAX) comparison for regional and near-teleseismic data. a) *M*$_s$(VMAX)=5.54 (σ=0.1) for a nine-station regional network recording of an *m*$_b$=5.1 western United States earthquake. b) *M*$_s$ (VMAX)=5.64 (σ=0.11) determined from four near-teleseismic records of the same event. Epicentral distance (in degrees) is provided next to each station name in the legend.**

REFERENCES

Denny, M.D., S. R. Taylor, and E.S. Vergino (1987). Investigation of m_b and M_s formulas for the western United States and their impact on the M_s/m_b discriminant, *Bull. Seism. Soc. Am.,* 77, 987-995.

Dziewonski, A.M., J. Bloch, and M. Landisman (1969). A new technique for the analysis of transient seismic signals, *Bull. Seism. Soc. Am.,* 59, 427-444.

Herrin, E.T. and T. Goforth (1977). Phase-match filtering: application to the study of Rayleigh waves, *Bull. Seism. Soc. Am.,* 67, 1259-1275.

Herrmann, R. B. (2002). Computer Programs in Seismology Version 3.15, St. Louis University.

Marshall, P.D. and P.W. Basham (1972). Discrimination between earthquakes and underground explosions employing an improved M_s scale, *Geophys. J. R. Astr. Soc*., 29, 431-458.

Marshall, P.D., Springer, D.L, and Rodean, H.C. (1979). Magnitude corrections for attenuation in the upper mantle, *Geophys. J. R. Astr. Soc.,* 57, 609-638.

Rezapour, M., and R.G. Pearce (1998). Bias in surface-wave magnitude M_s due to inadequate distance correction, *Bull. Seism. Soc. Am.,* 88, 43-61.

Russell, D.R. (2004). Theoretical analysis of narrow-band surface wave magnitudes, AFTAC Technical Report AFTAC-TR-04-004., 36 pp.

von Seggern, D. (1977). Amplitude distance relation for 20-Second Rayleigh waves, *Bull. Seism. Soc. Am.,* 67, 405-411.

Stevens, J.L., D.A. Adams, and E. Baker (2001). Surface wave detection and measurement using a one-degree global dispersion grid, *SAIC Final Report SAIC-01/1085*.

Stevens, J. L. and K.L. McLaughlin (2001). Optimization of surface wave identification and measurement, in *Monitoring the Comprehensive Nuclear Test Ban Treaty: Surface Waves*, eds. Levshin, A. and M.H. Ritzwoller, *Pure Appl. Geophys*., 158, 1547-1582.

Stevens, J. L. and J.R. Murphy (2001). Yield Estimation from Surface-wave Amplitudes, in *Monitoring the Comprehensive Nuclear Test Ban Treaty: Surface Waves*: *Source Processes and Explosion Yield Determination*, eds. Ekstrom, G., M. Denny, and J.R. Murphy, *Pure Appl. Geophys*., 158, 2227-2251.

Wessel, P. and W.H.F. Smith (1998). New, improved version of the Generic Mapping Tools Released, *EOS. Trans. Am. Geophys. Un., 79, 579.*

Woods, B. and D.G. Harkrider (1995). Determining surface-wave magnitudes from regional Nevada Test Site data, *Geophys. J. Int.,* 120, 474.

Yacoub, N.K. (1983). Instantaneous amplitudes: a new method to measure seismic magnitude, *Bull. Seism. Soc. Am.,* 73, 1345-1355.

ENERGY PARTITIONING FOR SEISMIC EVENTS IN FENNOSCANDIA AND NW RUSSIA

Hilmar Bungum[1], Tormod Kvaerna[1], Svein Mykkeltveit[1], Michael Roth[1], Volker Oye[1], Ketil Aastebol[1], David B. Harris[2], and Shawn C. Larsen[2]

NORSAR[1], Lawrence Livermore National Laboratory[2]

Sponsored by National Nuclear Security Administration
Office of Nonproliferation Research and Engineering
Office of Defense Nuclear Nonproliferation

Contract No. DE-FC03-02SF22636/A000[1] and W-7405-ENG-48[2]

ABSTRACT

Close cooperation has been maintained with the operators of the Pyhäsalmi mine in central Finland, where an in-mine network of 16 sensors (4 three-component and 12 vertical-component geophones) has been operational since January 2003. Up to the end of April 2004, waveforms for more than 18,000 rockbursts and mining blasts have been collected.

Using data processing software, developed at NORSAR, we have automatically estimated the seismic moment and corner frequency for all events from the shear wave signal and its coda. The results show some scattering, but also three distinct clusters. One cluster is found at frequencies between 100 and 800 Hz with a seismic moment between 10^{10} and 10^{8} Nm (corresponding to moment magnitudes between M_w 0.6 and -0.73). Most of the events within this cluster could be identified as daily production ripple-fired blasts at around 10 p.m. local time. A second cluster has corner frequencies between 100 and 400 Hz and seismic moments between 10^{7} and 10^{9} (M_w 0 to -1.4). The associated events are mainly microseismic events and small rockbursts that occur at random times during the day. A third small cluster is found at corner frequencies between 20 and 40 Hz and having seismic moments similar to the production blasts. Most of these events occurred prior to, and in the same area as, the largest rockburst (M_W 1.1) that occurred on 26 January 2003. This suggests that these events may be associated with a gradual failure of the pillar involved.

In order to assess the source contribution to the observed shear wave energy, we have calculated S/P ratios for both production blasts and rockbursts. A data set of about 2,000 well-located events with recordings at a minimum of 3 three-component stations has been selected. As expected, the rockbursts show generally larger S/P ratios, and we are continuing to investigate the effect of signal frequency and source location on the estimated ratios. However, significant shear energy is clearly observed within 100 meters of the source for both microearthquakes (rockbursts) and mine blasts.

Based on detailed information on the geometry of the 1,500 m deep Pyhäsalmi mine, we have constructed a three-dimensional (3-D) gridded model that includes the velocity and density characteristics of the ore bodies, mined-out voids, access tunnels, and surrounding rocks. Using the E3D finite difference code developed at Lawrence Livermore National Laboratory, extensive simulations of the wave propagation have been made in the mine model.

The modeling experiments have shown that we are able to model observed data at the Pyhäsalmi mine with a reasonable level of fit. Our favorable comparisons between synthetic and observed data lend a certain degree of confidence to our modeling techniques and our 3-D geologic model of the mine, which has been sampled with grid spacings of both 4 and 2 meters. Through simulations of the response to explosive sources, we have shown that significant shear energy can be generated in a 10-20 meter region around the source. This mode-converted energy can be of a similar amplitude to the incident compressional phase. Both the geologic heterogeneity and the structural influences of the mine appear to be contributors to the near-source generation of shear energy.

OBJECTIVE

The main objective of this project is to increase nuclear explosion monitoring effectiveness through improved understanding of basic earthquake and explosion phenomenology. What this entails in essence is detailed characterization and understanding of how the seismic energy is generated from these phenomena (including simple and complex explosions, rockbursts, i.e. stress release in mines, and ordinary tectonic earthquakes, all at different depths and in different geological environments) and how this energy is partitioned between P and S waves. Specific questions are:

- How is the generation and partitioning of seismic energy affected by properties such as source region medium and overburden, the local structure, and the surrounding tectonic structure?
- What are the significant measurable effects of the partitioning of the seismic energy into various regional P and S phases, especially at higher frequencies?
- What is the physical basis for a measurable property, such as magnitude, that can be directly related to the yield of a fully coupled explosion, and how can emplacement conditions affect the observations?

RESEARCH ACCOMPLISHED

Introduction

This project is a three-year effort that started on 30 September 2002, and is a collaboration between NORSAR (as the lead organization) and Lawrence Livermore National Laboratory (LLNL). The work addresses the generation of seismic shear waves by explosions. During the last year we have focused on two main activities related to the Pyhäsalmi mine in central Finland (see Figure 1). The first activity has been concerned with analysis of data from the 16 sensor in-mine network. Up to the end of April 2004 waveforms for more than 18,000 rockbursts and mining blasts were collected, and both automatic and manual analyses has been conducted on this data set. The second main activity has been concerned with three-dimensional finite-difference calculations of the wavefield in a detailed model of the mine, using the E3D code developed at LLNL (Larsen & Schultz, 1995). Based on a the model obtained from the mine operator, the NORSAR 3-D Model Builder (Vinje *et. al.*, 1999) has been used for building 3-D gridded velocity cubes that have been used by E3D. Velocity models with grid spacings of both 4 and 2 meters have been constructed.

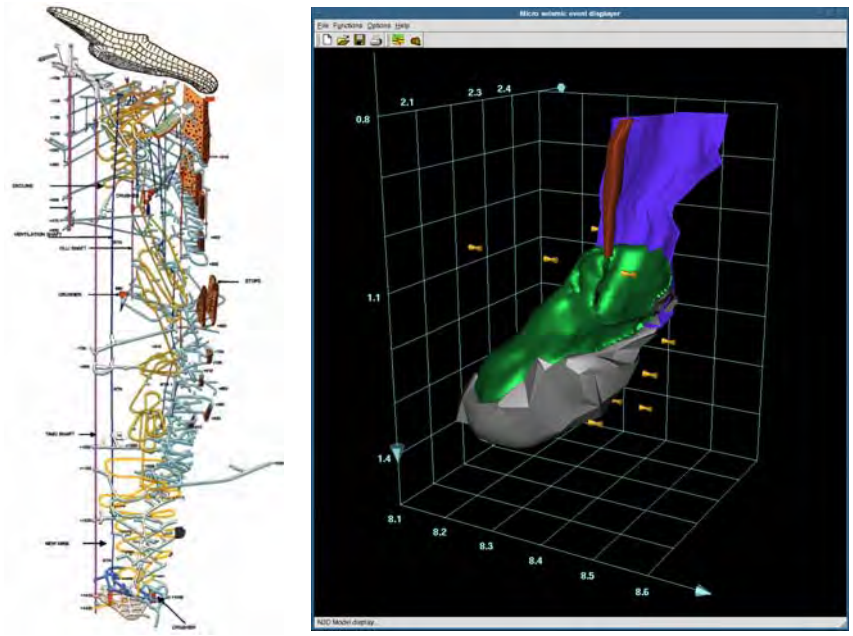


Figure 1. The left-hand part of the figure shows the shafts and access tunnels of the Pyhäsalmi mine from the surface down to a depth of 1,500 meters. The right-hand part of the figure shows a 3-dimensional model of the mine, for the depth range 800-1,500 meters. Green represents copper ore, grey represents zinc ore, and purple and red represent backfilled material. The locations of the in-mine monitoring network are indicated by the yellow symbols.

Estimation of source parameters for events in the Pyhäsalmi mine

An automatic estimation of source parameters was conducted for the entire Pyhäsalmi data set that now comprises about 18,000 seismic events (rockbursts and blasts). For each event we analyzed the seismogram section containing the shear wave signal and its coda. Typically we chose a time window of 0.1 to 0.2 second duration which started at the automatically picked S-wave arrival. The geophones of the in-mine network have a natural frequency of 4.5 Hz, and we assume that the instrument response is flat to velocity for frequencies above 10 Hz. The seismogram segments were fourier-transformed to obtain the signal amplitude spectrum.

The observed signal spectra for a given seismic event depend on the source spectrum, the source radiation pattern, the receiver site effects, and propagation effects such as geometrical spreading and intrinsic attenuation. We multiplied the signal spectra by the source-receiver distance and compensated for the intrinsic attenuation. This procedure ideally provides the signal spectra at unit distance. We assumed a quality factor Q=800, which is a reasonable choice for the hard-rock conditions. In order to obtain a representative source spectrum, these spectra were averaged to eliminate the station effects and the source radiation pattern. One method of determining the basic source parameters, i.e. seismic moment and corner frequency, from the displacement spectra is to fit a Brune-type spectrum. Alternatively the corner frequency and seismic moment can be estimated by numerical integration of the displacement and velocity power spectrum (Andrews, 1986; Richardson & Jordan, 2002). For automatic processing of the entire data set, we applied the robust numerical integration method.

Figure 2 shows the seismic moment as a function of corner frequency for about 4,000 explosions and about 1,000 rockbursts. The event localization as well as the spectral analyses were done fully automatically, this time using the spectral fit method, but for this data set both the data and the processing results were quality-checked by visual inspection. The results show some scattering, but also three distinct clusters. One cluster (green symbols) is at frequencies between 100 and 800 Hz with a seismic moment between 10^{8} and 10^{10} Nm (corresponding to moment magnitudes of about M_w = -0.73 and 0.6, respectively). Most of the events within this cluster could be identified as daily production ripple-fired blasts at around 10 p.m. local time. The typical charge of an individual detonation is about 80 to 120 kg of explosives.

A second cluster (blue symbols) has corner frequencies between 100 and 400 Hz and a seismic moments between 10^{7} and 10^{9} Nm (M_w = -1.4 and 0, respectively). The associated events are mainly microseismic events and small rockbursts that occur at times randomly during the day. The source parameters were determined by the spectral fit method, but they are also consistent with the integration method, conducted previously.

A third small cluster (red symbols) has corner frequencies between 20 and 40 Hz and seismic moments between 10^{8} and 10^{9} Nm. These events also occur at times randomly through the day. About 90% of these events were recorded in January 2003, the first month of the network installation. Later on they can be found only sporadically in the data set. It is not yet clear if the high number of occurrence in January 2003 is related to the 26 January, 2003 M_w=1.1 rockbursts or, if the low number of occurrence later on is due to event-filter settings of the in-mine network processing routines. However, most of these low-frequency events are located within 100 meters of the large rockburst. Since the corner frequencies determined here are very low, the plateau part of the spectra is short and an accurate fit of the spectrum was not possible. Hence an underestimation of seismic moments and an overestimation of corner frequencies might be the case for this third cluster.

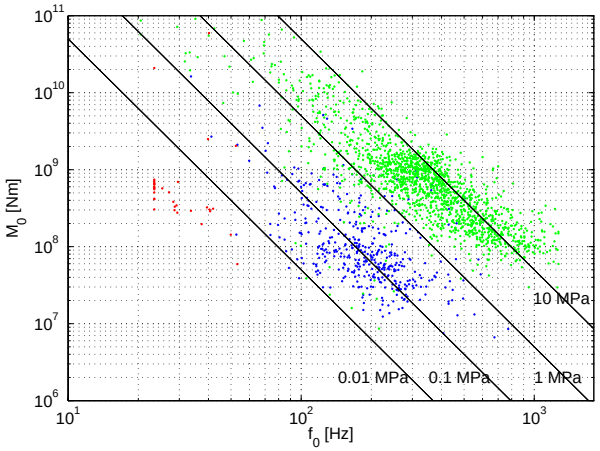


Figure 2. Relation between corner frequency and seismic moment for about 5,000 seismic events from the Pyhäsalmi mine. Blue indicates mining induced (stress release) events and green indicates delay-fired explosions. Red shows a small group of low-frequency events potentially associated with a large (M_w 1.1) rockburst. Black lines indicate values of constant stress drop.

S/P ratios

Clear S waves are observed at the Pyhäsalmi in-mine network for both rockbursts and regular blasts. Figure 3 shows a typical seismic section for the first shot of a ripple-fired production blast, and we see that shear energy is clearly observed as close as 100 meters from the source.

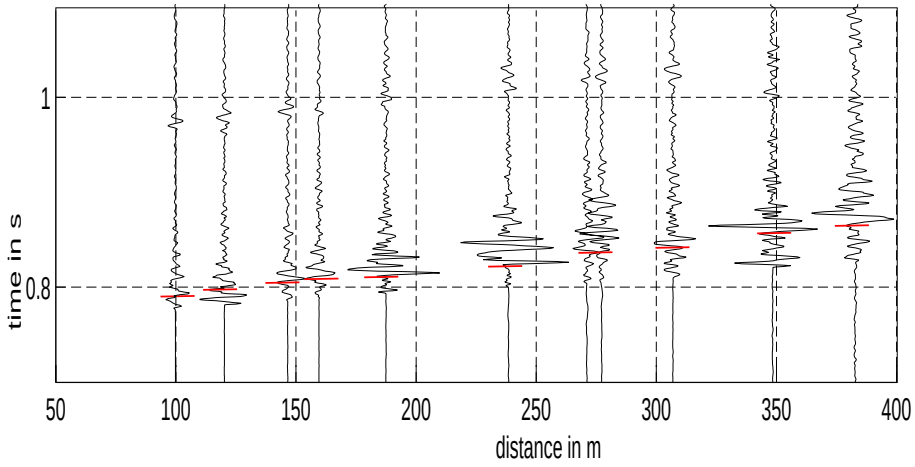


Figure 3. Observed seismograms from a production blast in the Pyhäsalmi mine showing how shear energy is observed as a function of distance from the source. The S arrival is indicated with red arrows. For the three-component sensors we show only the component having the largest S amplitude.

In order to assess the source contribution to the observed shear wave energy, we have calculated S/P ratios for both production blasts and rockbursts. A data set of about 2,000 well-located events with recordings at a minimum of 3 three-component stations was selected. The quality of the automatic processing results (i.e., phase picks, polarization estimates and event location) was checked by visual inspection of the three-component data, as shown in Figure 4. Events with erroneous time picks, polarization angles or location estimates were rejected.

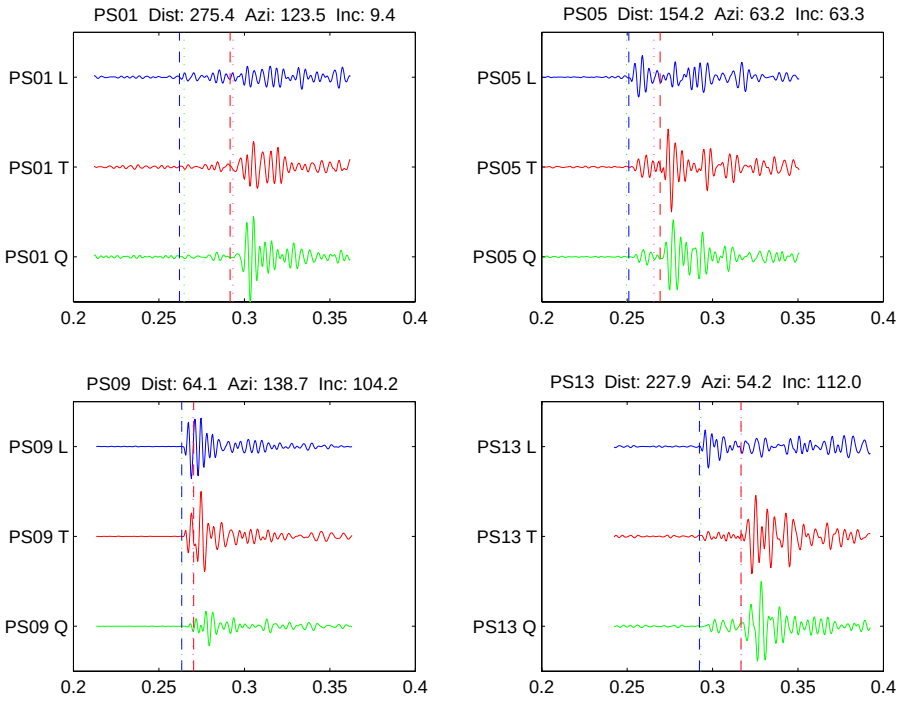


Figure 4. Panels showing observations and automatic processing results for a rockburst in the Pyhäsalmi mine. The data are filtered between 150 and 300 Hz. For each of the 4 three-component sensors we show the ray-oriented L, T and Q components (blue, red, green). The rotation is based on the automatically estimated polarization angles of the P-phase, given above each panel. The automatic P- and S-picks are shown by blue and red dashed lines, respectively. The corresponding theoretical arrival times calculated from the automatic event location are shown by green and magenta dotted lines. The distance to the event (in meters) is given above each panel.

About 1,300 events remained after the quality control, and for these we measured the maximum P and S amplitudes in a series of one octave passbands. The list of passbands are given in Table 1

Table 1: Passbands (in Hz) used for measurement of P and S amplitudes

20-40	30-60	40-80	50-100	60-120
70-140	80-160	90-180	100-200	120-240
140-280	160-320	180-360	200-400	250-500
300-600	350-700			

The P amplitude was taken to be the maximum amplitude on the L-component. The S amplitude was taken to be the maximum of total S-wave amplitude in the orthogonal TQ plane. Due to the proximity of the sensors to the events, there is little time separation between the P and S-phases. For example, at a distance of 150 meters, the P and S-phases are separated by only 0.02 s, corresponding to a cycle with a frequency of 50 Hz. From inspection of the data filtered in the passbands given in Table 1, we have found that P and S do not separate sufficiently unless the lower cut-off of the passband is greater than approximately $1.5/(S_{onset}\text{-}P_{onset})$, which in this case is 75 Hz. This implied that we could not obtain interpretable P and S amplitudes for the lowest passbands for recordings at the sensors closest to the events.

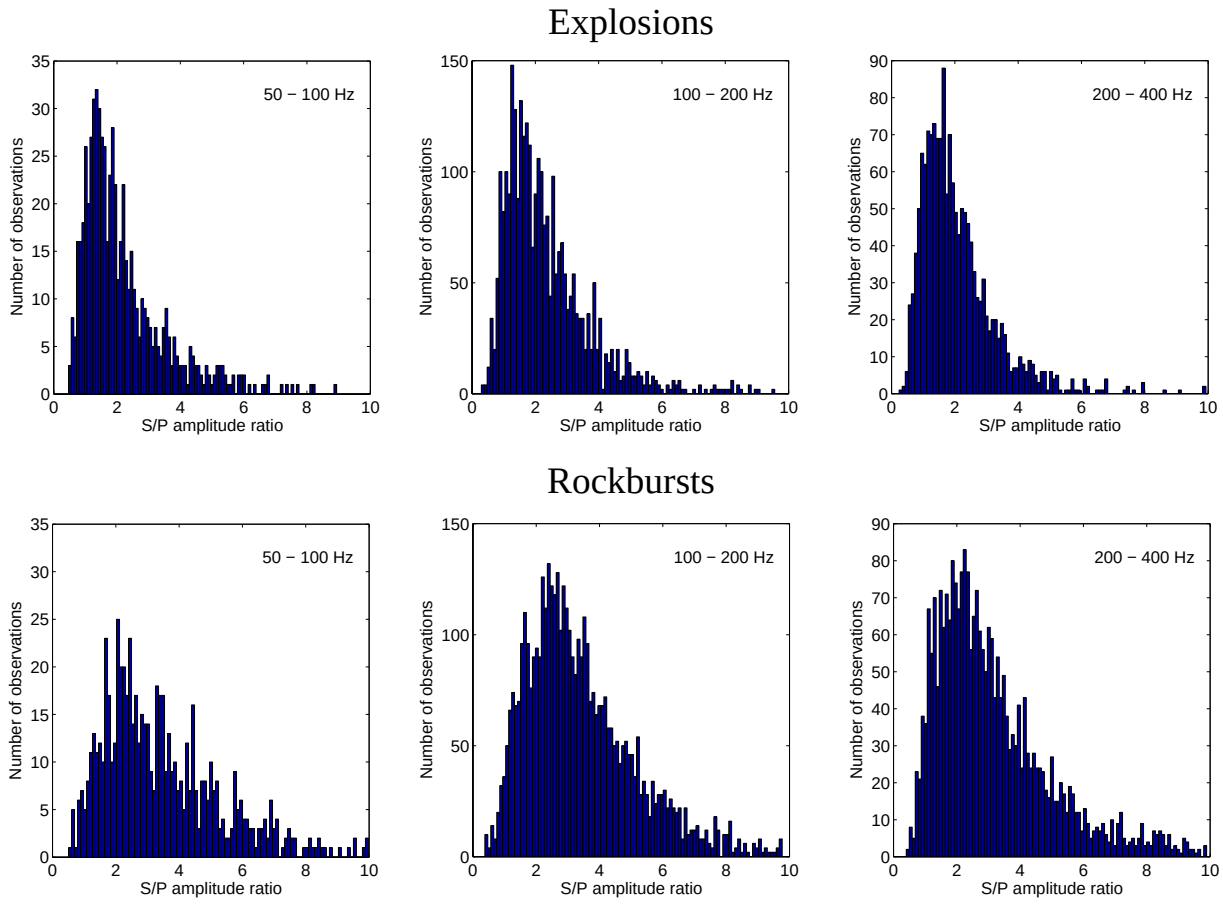


Figure 5. The three upper panels show the distribution of S/P ratios for all observations in the explosion data set for three frequency bands, 50-100 Hz, 100-200 Hz and 200-400 Hz. The three lower panels show the corresponding S/P ratios for the rockbursts.

The production blasting in the Pyhäsalmi mine takes place between 21:50 and 22:00 local time, so we labelled the events occurring within this time interval “the explosion data set”. This data set probably also includes a few rockbursts, but these will not significantly influence the overall statistical characteristics of the explosions. In order to avoid effects like signals from rockfall and interference from previous detonations, we only considered the first detonation of ripple-fired blasts. Events occurring outside the time window 21:45 to 22:05 were denoted the “rockburst data set”.

Figure 5 shows the distribution of S/P ratios for all observations of explosions and rockbursts for three frequency bands, 50-100 Hz, 100-200 Hz and 200-400 Hz. As expected, the explosions have generally lower S/P ratios for all frequency bands, but the difference is far too small to be significant for classification purposes. The maxima for the explosion distributions are all below 2, whereas they are all above 2 for the rockbursts. The rockbursts also have a wider distribution of S/P ratios, which can be explained by the variability of the radiation patterns from the rockburst sources. In addition, the rockbursts are more widely distributed within the mine volume, whereas the explosions only occur in the active parts of the mine.

The observed S/P ratios, for both explosions and rockbursts, do not show any significant dependency on the distance to the events. However, as discussed above, there is a lower distance limit below which the P and S-phases do not separate sufficiently in time to permit an estimation of the amplitudes. Example, for the 200-400 Hz passband this lower distance limit is about 50 meters. We have therefore no information in the distance dependency of the S/P ratios within the first tens of meters from the source.

In order to investigate S/P ratios for similar propagation paths within the mine, we have analyzed explosions and rockbursts occurring within a 100x100x100 meter volume, recorded at sensor PS01, at a distance of about 350 meters from the events. The distributions for this subset of the data set are very similar to those shown for the full data set in Figure 5. This indicates that the observed differences in S/P ratios between explosions and rockbursts are due to differences in the source characteristics, and not due to propagation effects along paths in the mine.

Wavefield modeling

We have investigated the physical mechanisms that partition seismic energy in the near source region by conducting modeling studies of the Pyhäsalmi mine. Our efforts have centered around two main activities: 1) comparison of observed data from seismic events at the Pyhäsalmi mine with synthetic data generated using a 3-D finite-difference wave propagation code and a 3-D geologic model of the mine; and 2) conducting synthetic sensitivity tests to determine the cause and characteristics of shear energy generated in the near source region.

The E3D finite-difference code and the 3-D geologic model of the mine have been described in more detail in previous papers (e.g., Larsen & Schultz, 1995; Bungum *et al.*, 2003). In summary, the wave propagation code solves the elasto-dynamic formulation of the wave equation on a staggered grid. As a full physics seismic simulation code, compressional, shear, and mode-converted energy is modeled. Viscoelastic attenuation capabilities are included. The code is computationally robust, and runs on a variety of high performance computing platforms. This makes it possible to simulate large problems. For this project, the E3D code utilizes a 3-D geologic model of the Pyhäsalmi mine. This model parameterizes the different geologic components of the mine (e.g., the ore bodies), as well as tunnels, voids, and back filled material produced by mine activity. The 3-D model is 500 m in all three dimensions. To date, the 3-D model has been discretized onto uniformly spaced grids of two and four meter grid spacings.

Figure 6 shows observed data at the Pyhäsalmi mine following a February 28, 2003 rockburst. These data are compared with synthetic data using the E3D code and the 3-D Pyhäsalmi geologic model discretized on the four meter grid. An explosive source was used for the simulation, with a frequency range up to 50 Hz. For comparison, the data have been low-pass filtered at 50 Hz. The rockburst event was located near the outer boundary of the mine ore body. The agreement between data and simulation is quite good. The synthetic data match the amplitude and overall character of the observed waveforms. There are a few discrepancies, which may be due to the simplicity of the source function, inaccuracies in the geologic model, and mislocated receiver (and source) positions.

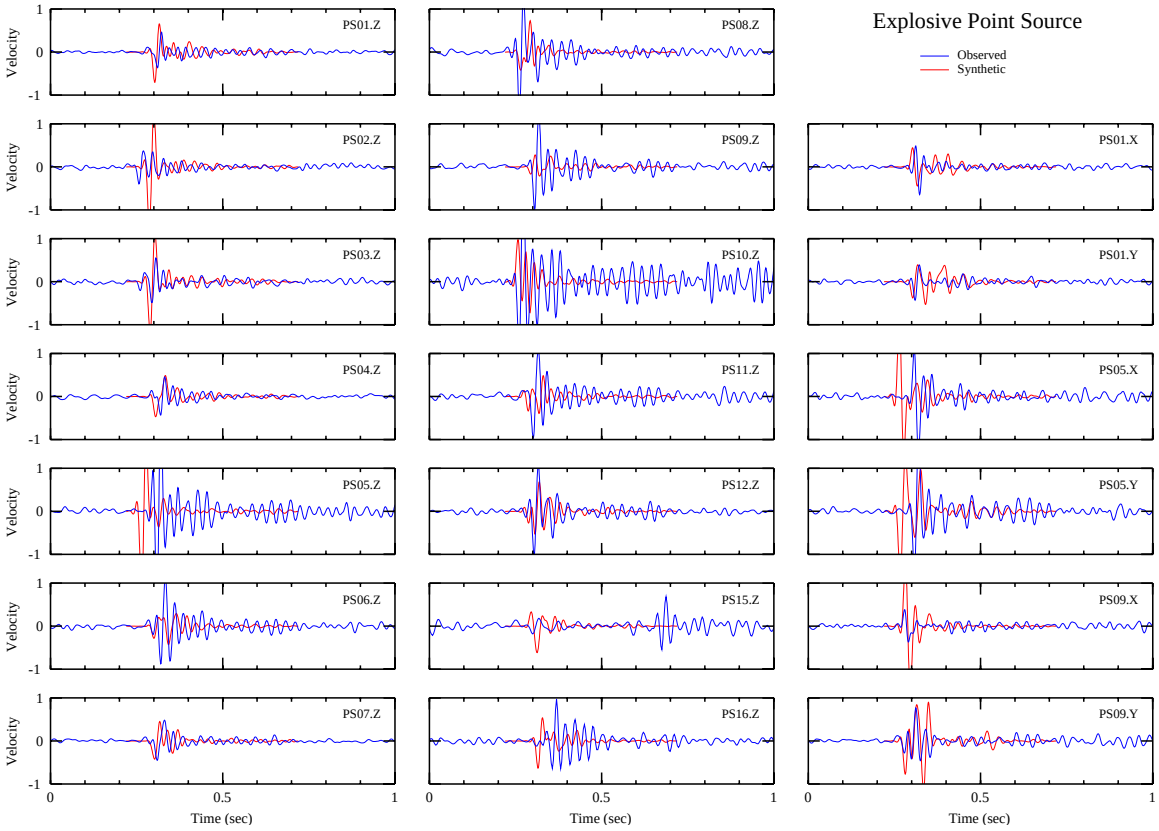


Figure 6. The blue seismograms show in-mine recordings in the Pyhäsalmi mine from a rockburst located near the outer boundary of the mine ore body. The data have been low-pass filtered at 50 Hz. Synthetic seismograms from an explosive source calculated in the Pyhäsalmi geologic model (4 m grid) using the E3D code are shown in red.

A similar comparison but one that incorporates seismic frequencies up to 100 Hz has also been made. In this case, the 2 meter discretized mine model was used. Although the agreement between model and observation was not quite as good as with the 50 Hz simulation, the comparison is still fair, especially considering the simplicity of the model. In addition to source and site effects, it may be more difficult to accurately characterize the Pyhäsalmi mine at these higher frequencies. Still, our results suggest that we can model real seismic events at the Pyhäsalmi mine, as well as perform synthetic sensitivity tests, at reasonably high levels of confidence.

To assess the sensitivity of the synthetic data to the source location, a simulation where the source position was modestly shifted from the rockburst location modeled above was performed. In this case, we moved the modeled source by 35 meters relative to its original location. The results of this simulation are shown in Figure 7. While a few stations indicate waveforms that are moderately different, in general, the agreement is very good. This suggests that a precise source location (i.e., less than 35 meters) is not required to model observed data from an event at the mine.

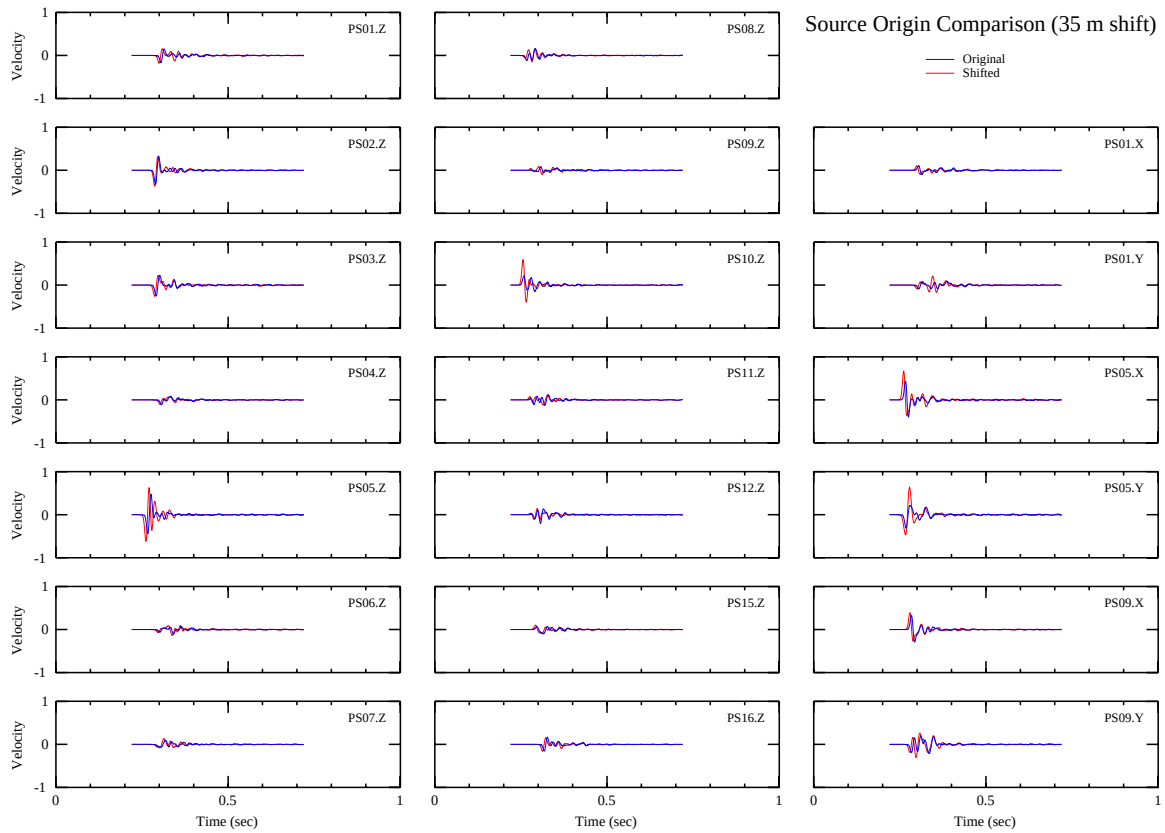


Figure 7. The seismograms shown in red are results from simulations after shifting the source location by 35 meters relative to its original location. The modeled seismograms using the original source location are shown in blue.

In addition to modeling the February 28, 2003 rockburst, several synthetic finite-difference simulations to investigate the character and cause of shear energy generation from the Pyhäsalmi mine were performed. In one series of simulations, we placed an explosive source at three locations in the mine region. One source was located at the boundary of the mine, in close proximity to the ore body. (In fact, this source was placed at the same location as that of the rockburst event discussed above). Another source was located near the center of the mine, while the third source was located relatively far from the mine boundary near the edge of our finite-difference numerical grid. The compressional nature of the explosive source (diagonal moment tensor components) means that all shear energy must be generated by mode converted P energy interacting with either the ore body or the structural components of the mine (e.g., tunnels, mined out regions). We investigated the amplitude and the near-source proximity of this shear energy generation. In each case, the geologic model discretized on the 4 meter grid was used.

Figure 8 shows the P and S potential amplitudes, and the P/S ratio, on the four horizontal and two vertical lines that extend outward from a source located at the rockburst location, near the boundary of the mine. The figure shows that shear energy is generated essentially in the immediate vicinity of the source. Both the P and S potentials fall off with distance due to geometrical spreading. The plot of P/S ratios indicates that most of the shear energy is generated within about 10 meters from the source, and that the shear energy is of comparable amplitude to the compressional energy.

For the source located at the center of the mine, we found that high amplitude shear energy is also generated in the immediate vicinity of the source. In this case, the modeled waveforms for both compressional and shear profiles are more complex than for a source at the rockburst location (in the outer part of the mine). This is likely due to the complexity of the mine (geologic heterogeneity, tunnels, voids).

For the source located some distance (over 100 meters) away from the mine, the modeling shows that little shear energy is generated. In fact, a good fraction of the shear energy that is observed may be numerical artifacts caused by unabsorbed reflections from the boundary of the finite-difference grid, as the source is relatively close to the grid boundary.

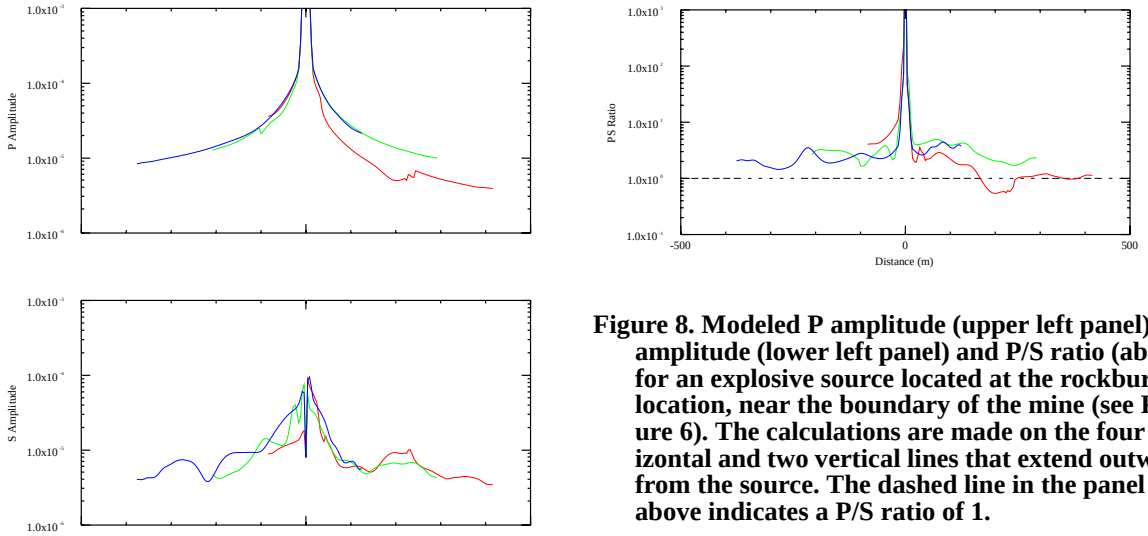


Figure 8. Modeled P amplitude (upper left panel), S amplitude (lower left panel) and P/S ratio (above) for an explosive source located at the rockburst location, near the boundary of the mine (see Figure 6). The calculations are made on the four horizontal and two vertical lines that extend outward from the source. The dashed line in the panel above indicates a P/S ratio of 1.

The Pyhäsalmi mine was also decomposed into its two main components to investigate the mechanism that generates shear energy. That is, we constructed one model that includes only the ore bodies, and another model that includes only the structural components of the mine (i.e., tunnels, mined regions). The second model is referred to as the "void" model. We ran simulations through both models using the 4 meter discretized grid. Close examination of the results from these simulations suggests that both the geologic inhomogeneity from the ore body and the structural voids may have similar influence on the mine-perturbed seismograms. It may be that the geologic inhomogeneity has a more pronounced effect early in the waveforms, whereas the voids are more influential and likely to produce scatter in the later portions of the seismograms. However, this may be due to the placement of the source near the ore body boundary, and further study is therefore needed to place more confidence in such a conclusion.

CONCLUSIONS AND RECOMMENDATIONS

We have continued our close cooperation with the operators of the Pyhäsalmi mine in central Finland. In late spring 2004, the in-mine network was extended by two triaxial sensors. Up to the end of April 2004, waveforms for more than 18,000 rockbursts and mining blasts were collected, and all of these events have been reprocessed using NORSAR's in-house microseismic monitoring software package (Oye & Roth, 2003). The automatic reprocessing has included phase onset picking, polarization analysis, phase association, event location, and estimation of seismic moment and corner frequencies for the located events. In addition, we have quality-checked the data and processing results for subsets of the 18,000 events, and created databases of high-quality events that have been used for both estimation of source parameters and measurements of S/P ratios.

The estimated seismic moments and corner frequencies for a database of high-quality events (about 4,000 explosions and about 1,000 rockbursts) show some scattering, but also three distinct clusters. The mining blasts have generally higher seismic moments than the rockbursts, and they also have generally higher corner frequencies. A third type of low-frequency rockburst is found with corner frequencies between 20 and 40 Hz and seismic moments similar to the production blasts. Most of these events occurred prior to, and in the same area as, a large rockburst (M_W 1.1) that occurred on 26 January 2003, which suggests that these events may be associated with a gradual failure of the pillar involved.

In order to assess the source contribution to the observed shear wave energy, we have calculated S/P ratios for both production blasts and rockbursts. A data set of about 2,000 well-located events with recordings at a minimum of 3 three-component stations has been selected. As expected, the rockbursts show generally larger S/P ratios for all fre-

quencies, but the difference is far too small to be significant for classification purposes. Significant shear energy is clearly observed within 50-100 meters of the source for both microearthquakes (rockbursts) and mine blasts. Due to the small time separation between the P- and S-phases, we were unable to measure S/P ratios for the very close distances (up to 30-50 meters). For distances above this range, no distance dependency could be observed for any type of events.

The modeling experiments have shown that we are able to model observed data at the Pyhäsalmi mine with a reasonable level of fit. The good match between synthetic and observed data lend a certain degree of confidence to our modeling techniques and our 3-D geologic model of the mine, which has been sampled with grid spacings of both 4 and 2 meters. Through simulations of the response to explosive sources, we have shown that significant shear energy can be generated in a 10-20 meter region around the source. This mode-converted energy can be of a similar amplitude to the incident compressional phase. This is consistent with the results obtained from analysis of events recorded at the in-mine network, where we find distance independent S/P ratios for distances larger than 30-50 meters. Both the geologic heterogeneity and the structural influences of the mine appear to be contributors to the near-source generation of shear energy.

Based on updated information from the Pyhäsalmi mine operators, we plan to build a new model of the Pyhäsalmi mine, now with a grid spacing of 1 meter. With a 1 meter grid spacing we will have to include the smaller structures of the mine and its infrastructure, and the building of this model will thus require quite large efforts. With this model at hand, we plan to make more wavefield simulations using the E3D code, and again compare with shot data. We also plan to investigate the possibility of making a source moment tensor inversion of the events. The two new triaxial sensors of the in-mine network may be important for the success of such an effort.

A near-term objective is to characterize quantitatively the generation of shear energy due to seismic events located in and near the Pyhäsalmi mine. Specifically, we will perform a large number of E3D simulations to parameterize the generation of shear energy as a function of source distance, mine heterogeneity, and seismic frequency. Our preliminary results indicate that significant shear energy is created in a region that is well within a seismic wavelength from explosive sources located near mine heterogeneities. We will compare synthetically computed estimates of S/P ratio's with those observed from the mine data. This will serve both as a validation step and as a means to determine the fraction of shear energy that can be attributed to the source radiation pattern versus the fraction that can be attributed to mode converted energy at mine heterogeneities.

REFERENCES

Andrews, D. J. (1986). Objective determination of source parameters and similarity of earthquakes of different size. *Geophysical Monograph #37, Earthquake source mechanics*. Vol. 6, AGU. Editors: Shamita Das, John Boatwright, Christopher H. Scholz

Bungum, H., T. Kvaerna, S. Mykkeltveit, M. Roth, K. Astebol, D.B. Harris and S. Larsen (2003). Energy Partitioning for Seismic Events in Fennoscandia and NW Russia. "*Proceedings of the 25th Seismic Research Review - Nuclear Explosion Monitoring: Building the Knowledge Base*", Los Alamos National Laboratory, LA-UR-03-6029, Tucson, AZ, Sept. 23-25, 2003.

Larsen, S. C. and C. A. Schultz (1995): ELAS3D: 2D/3D elastic finite-difference wave propagation code. *UCRL-MA-121792*, 18 p.

Oye, V, and M. Roth (2003): Automated seismic event location for hydrocarbon reservoirs. *Comp. and Geoscience*, 29, 851-863.

Richardson, E. and T.H. Jordan (2002): Seismicity in deep gold mines of South Africa: Implications for tectonic earthquakes. *Bull. Seism. Soc. Am.*, 92(5), 1766-1782.

Vinje V., Åstebøl K., Iversen E., and Gjøystdal H. (1999). 3-D ray modeling by wavefront construction in open models. *Geophysics*, 64, 1912-1919.

A SEISMIC EVENT DISCRIMINATION SYSTEM BASED ON IMPROVED UNDERSTANDING OF Lg FROM EXPLOSIONS – PRELIMINARY RESULTS

Indra Gupta[1], Steve Taylor[2], Robert Wagner[1], and Wilmer Rivers[1]

Multimax, Inc.[1], Los Alamos National Laboratory[2]

Sponsored by National Nuclear Security Administration
Office of Nonproliferation Research and Engineering
Office of Defense Nuclear Nonproliferation

Contract No. DE-FG02-03ER83720[1] and FIA-03-032[2]

ABSTRACT

Nuclear monitoring requires identification of small events observed at regional distances for which Lg is generally the largest and sometimes the only well-recorded seismic phase. Recent research, including ours, has provided significantly better understanding of the generation of Lg from explosions, but the new concepts have not yet been fully exploited for improving discrimination between low magnitude explosions and earthquakes in geologically distinct regions. Our analysis of regional data from nuclear explosions from both Nevada and Kazakh test sites and nearby earthquakes indicates several significant differences in the characteristics of the seismic phase, Lg. Spectrograms of underground nuclear explosions and earthquakes recorded at regional distances show the Lg wavetrain only from the explosions to consist of several distinct low-frequency arrivals with progressively lower frequency content and diminishing strength or amplitude. Comparisons of the spectral ratios of Lg based on ratio of spectral amplitudes within the low-frequency range of 0.5 to 2.0 Hz to those within a higher frequency range, such as 3.0 to 7.0 Hz, and of the mean spectral slopes of Lg over a fairly large range of frequencies, such as 0.5 to 7.0 Hz, show significant differences for the two types of seismic sources. Frequency-domain skewness – a measure of spectral shape – over a broad range of frequencies, such as 0.5 to 7.0 Hz, of the Lg spectra is also significantly different for the explosion and earthquake sources. These results suggest several source discrimination methods based on the use of only the Lg phase, including (a) amplitude-frequency-time analysis of spectrograms, (b) Lg spectral ratios, (c) Lg spectral slopes, and (d) skewness of Lg spectra. Remarkable similarity of discrimination results from the two geologically different regions suggests that these results should be applicable for identifying small seismic events in other regions of the world as well.

OBJECTIVE

Lg is generally the largest seismic phase from both explosion and earthquake sources recorded at regional distances. For small events, Lg may sometimes be the only well-recorded seismic phase. It is therefore important to develop a reliable source identification method based on the use of only the Lg phase, enabling discrimination of smaller events. Gupta et al. (1992) provided observations and theoretical model suggesting that near-source scattering of explosion-generated Rg into S makes a significant contribution to the low-frequency (less than 2 Hz) Lg. Observational support for this mechanism has grown in recent years (Patton and Taylor, 1995; Gupta et al., 1997; Myers et al., 1999; Patton, 2001). Several more recent studies, such as Bonner et al. (2003), Myers et al. (2003), and Wu et al. (2003), also provide strong evidence in favor of the Rg-to-S scattering mechanism for the generation of the low frequency S and Lg. It is important to make use of these new concepts regarding the generation of Lg from explosions for exploring the possibility of significant improvements in source discrimination.

RESEARCH ACCOMPLISHED

Discrimination Based on Analysis of Spectrograms

Spectrograms of underground nuclear explosions recorded at regional distances generally show the Lg wavetrain to consist of several distinct low-frequency arrivals with progressively lower frequency content and diminishing strength or amplitude. The most probable reasons for this are: the scattering of explosion-generated Rg into S occurs at several discrete near-source locations at different distances from the source, Rg has a significantly lower propagation velocity as compared to that of Lg, and Rg suffers considerably larger attenuation with distance than Lg. On the other hand, Lg wavetrains on earthquake spectrograms do not show such characteristics.

A spectrogram may be considered as a three-dimensional matrix of numbers providing amplitude and frequency information for each point in the time series. Instead of relying on subjective visual examination, we need to evaluate the most effective discriminants by making the required measurements within the spectrograms. Accurate measurements must be made of the sought-after patterns such as discrete Lg energy arrivals with decreasing frequency content and decreasing amplitudes. For this purpose, we first normalized the Lg wavetrain from events at various recording distances so that the number of time windows used for spectrograms is the same for all events. Lg from seismic events at regional distances is known to have a fairly constant velocity of 3.5 km/sec. The term Lg coda generally refers to seismic arrivals at travel times greater than about twice the direct Lg (e.g., Hartse et al., 1995). Our selection of Lg wavetrain represents a time window starting at Lg (i.e., at velocity of about 3.5 km/sec) and ending at a travel time no greater than about twice the direct Lg time. Henceforth, we will refer to this Lg window as Lg "wavetrain", since it does not contain any usual Lg "coda."

We tried to quantify the two features (i.e., decreasing frequency content and decreasing amplitudes with time) of Lg wavetrain on spectrograms by first selecting the Lg wavetrain starting at a velocity of 3.3 km/sec (instead of 3.5 km/sec) because the scattered arrivals are expected to be somewhat delayed as compared to the direct Lg. The Lg wavetrain used for analysis was taken to be from t_1 to t_2 (= t_2-t_1), where t_1 = D/(3.3 km/sec) and t_2 = D/(1.65 km/sec). Thus, t_2-t_1=D/(3.3 km/sec). The moving time window, w, for spectrograms was selected to be 1/10 of the selected Lg wavetrain, i.e., w = (t_2-t_1)/10 and the slice interval (time shift) was one-fourth of the moving window length. With these parameters, each spectrogram contained results from approximately 40 time windows within t_2-t_1.

Several measurements on both explosion and earthquake spectrograms were made, but most of these did not look promising for source discrimination. However, the following measurement that combines both temporal features (i.e., decreasing frequency and decreasing amplitudes) for explosions provided encouraging results.

For each time slice, a mean weighted frequency, f(mean) is defined as

$$f(\text{mean}) = (f_1A_1 + f_2A_2 + f_3A_3 + \ldots\ldots)/(A_1 + A_2 + A_3 + \ldots\ldots) \quad (1)$$

where A_1, A_2, A_3, ... are amplitudes associated with frequencies of f_1, f_2, f_3, ... The frequency range is generally selected to be 0.3 to 2.0 Hz for which the short-period Rg is generally dominant.

When these f(mean) values are plotted versus time within t_1 and t_2, a series of peaks representing prominent low-frequency arrivals are observed. For explosions, the frequency values corresponding to these peaks may be expected to decrease more systematically than for earthquakes. A linear regression of these peak frequency values versus time should therefore indicate much smaller variance for explosions than for earthquakes. The above statement is of course based on several simplifying assumptions, including (i) a single dominant source of explosion Rg, (ii) several near-source discrete sources of scattering generate similar scattered S waves (i.e., similar scattering functions), and (iii) attenuation of Rg with distance is strong and not much dependent on epicenter-to-scatterer azimuthal direction. If these assumptions are valid, all prominent spectral peaks in the Lg wavetrain should be due to Rg-to-S arrivals and they should progressively decrease with arrival time in both frequency content and amplitude. Most of the contribution to f(mean) for a given value of arrival time comes from the peak frequency and amplitude associated with the distinct Rg-to-S scattered arrival.

Our objective is to examine the variance associated with linear regression between f(mean) versus time based on the use of only prominent large-amplitude arrivals. For this purpose, we need to (1) correct for the general decrease in wavetrain amplitude with time and (2) remove the influence of low-amplitude arrivals filling the gaps between adjacent spectral peaks. For (1), all spectral amplitudes within the 0.3-2.0 Hz frequency band and within the selected Lg wavetrain (i.e. from time t_1 to t_2) were plotted versus travel time, t. A linear regression is carried out and the mean slope, s, is determined. This slope, s is almost always negative for both explosions and earthquakes because of attenuation with distance and time. In order to include the later arriving spectral peaks with generally lower amplitudes into our analysis, an attenuation with time correction was applied to all amplitude values by increasing the amplitudes at a given travel time, t, by the positive amount $-s(t-t_1)$. In this way, the mean slope for the selected amplitude values became 0. In order to correct for (2), we retained only those amplitude points that were within the top 25% values. These amplitude and associated frequency values are used for the linear regression in equation (1) and the corresponding standard deviation is determined. A correction for amplitude differences between various seismic events because of their magnitudes is applied by using normalized standard deviation values based on division by the average value of all mean weighted frequency values within t_2-t_1.

We carried out the above analysis on 10 Yucca Flat (Nevada Test Site, NTS) explosions and 10 nearby earthquakes recorded at the Lawrence Livermore National Laboratories (LLNL) broadband station, Mina, Nevada (MNV). As examples, spectrograms and linear regression results from the Yucca Flat explosion, Starwort (26 April 1973) and the Massachusetts Mountain earthquake (5 August 1971), both recorded at MNV, are shown in Figures 1 and 2. The Lg wavetrain on the Starwort spectrogram (Figure 1) shows several prominent peaks with progressively decreasing frequency content, combined with generally decreasing amplitudes. On the other hand, the spectral peaks on the earthquake spectrogram (Figure 2) indicate significantly different characteristics. The linear regression plots of f(mean) versus travel time for the Lg wavetrain for the two events (bottom plots in Figures 1 and 2) indicate significant difference in their normalized standard deviation values. The results for all 20 events are shown in Figure 3a. The mean value for the earthquake population is about 55% higher than for the explosion population. Considering that results from only one recording station are shown, it seems that the observed differences in normalized standard deviation values should be useful for source discrimination.

We performed analysis similar to that for the U.S. events for 10 Kazakh Test Site (KTS) explosions and 10 earthquakes recorded at the broadband digital station Wulumuchi, China (WMQ). However, because of the much larger epicentral dstances, the Lg wavetrain used for analysis was considered to be the interval within group velocities of 3.4 and (2/3)x3.4=2.27 km/sec. Thus t2-t1= D/(2.27)-D/(3.4)=D/(6.8 km/sec). The moving time window, w, for spectrograms was selected to be 1/20 of t2-t1 and the slice interval was one-half of the moving window length. With these parameters, each spectrogram contained results from approximately 40 time windows within t2-t1, the same number as for the U.S. data. Similar to Figures 1 and 2, the explosion and earthquake spectrograms generally indicated significantly different characteristics and the linear regression plots of f(mean) versus travel time for the Lg wavetrain also showed significant difference in their normalized standard deviation values. The results for all 20 events, shown in Figure 3b, indicate the mean value for the earthquake population to be about 52% higher than that for the explosion population. These results, similar to those for the U.S. data (Figure 3a), suggest that observed differences in the normalized standard deviation values could be useful for source discrimination based on the use of only Lg. It should be noted that, unlike the U.S. events, the available earthquakes (located in Russia and China) used for comparison with KTS nuclear explosions (which are clustered together) are at significantly different locations. This means that the differences in propagation paths and source-receiver distances for the two types of events are likely to significantly

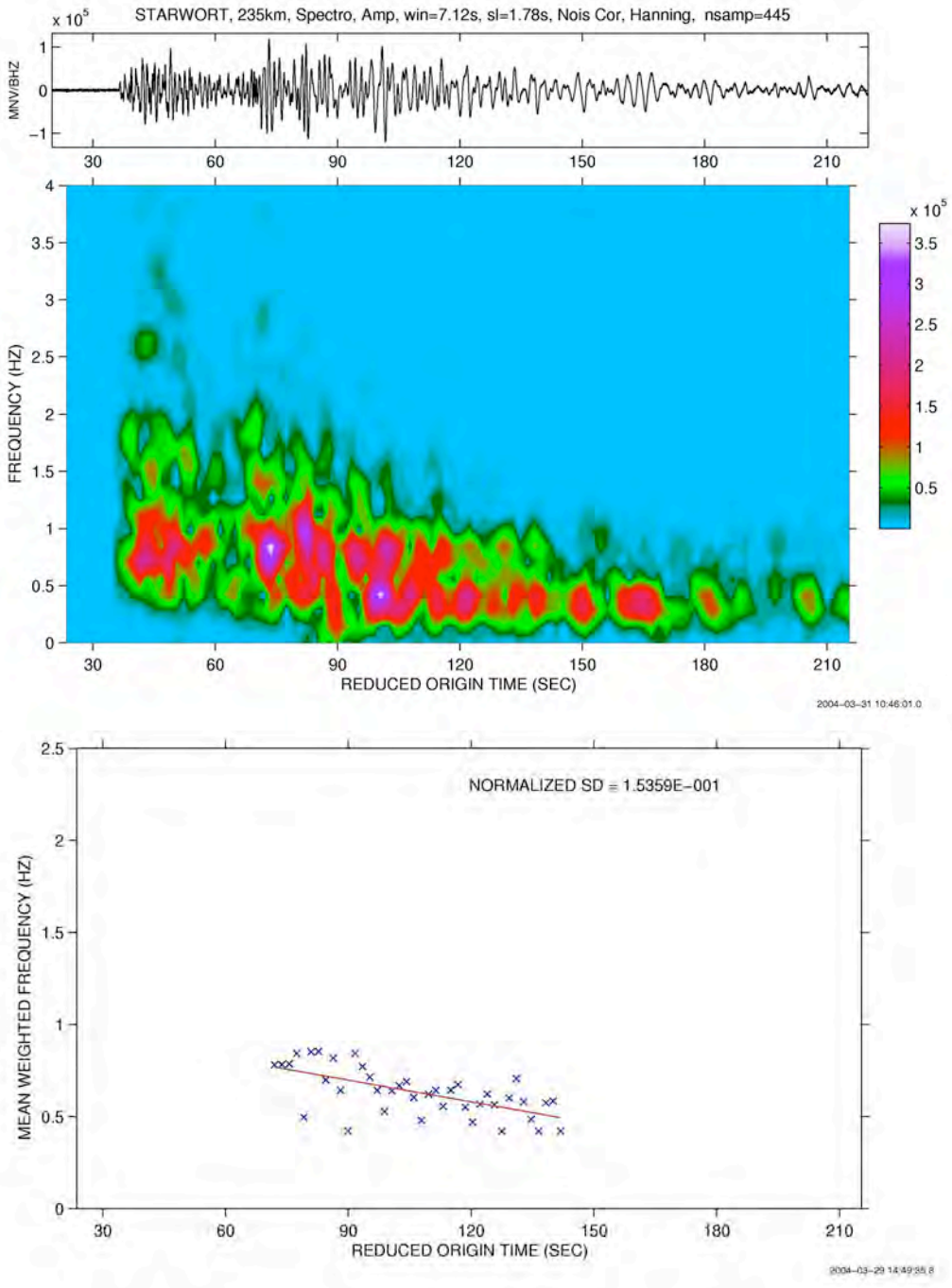


Figure 1. Seismogram (top) and spectrogram of Starwort recorded at MNV. The Lg wavetrain on the explosion spectrogram, starting at about 71 sec, shows several prominent peaks with progressively decreasing frequency content and amplitude. Bottom figure shows the mean weighted frequency versus travel time, within the time window D/(3.3km/sec) and D/(1.65 km/sec), where D is the epicentral distance; linear regression (red line) and the associated normalized standard deviation are indicated.

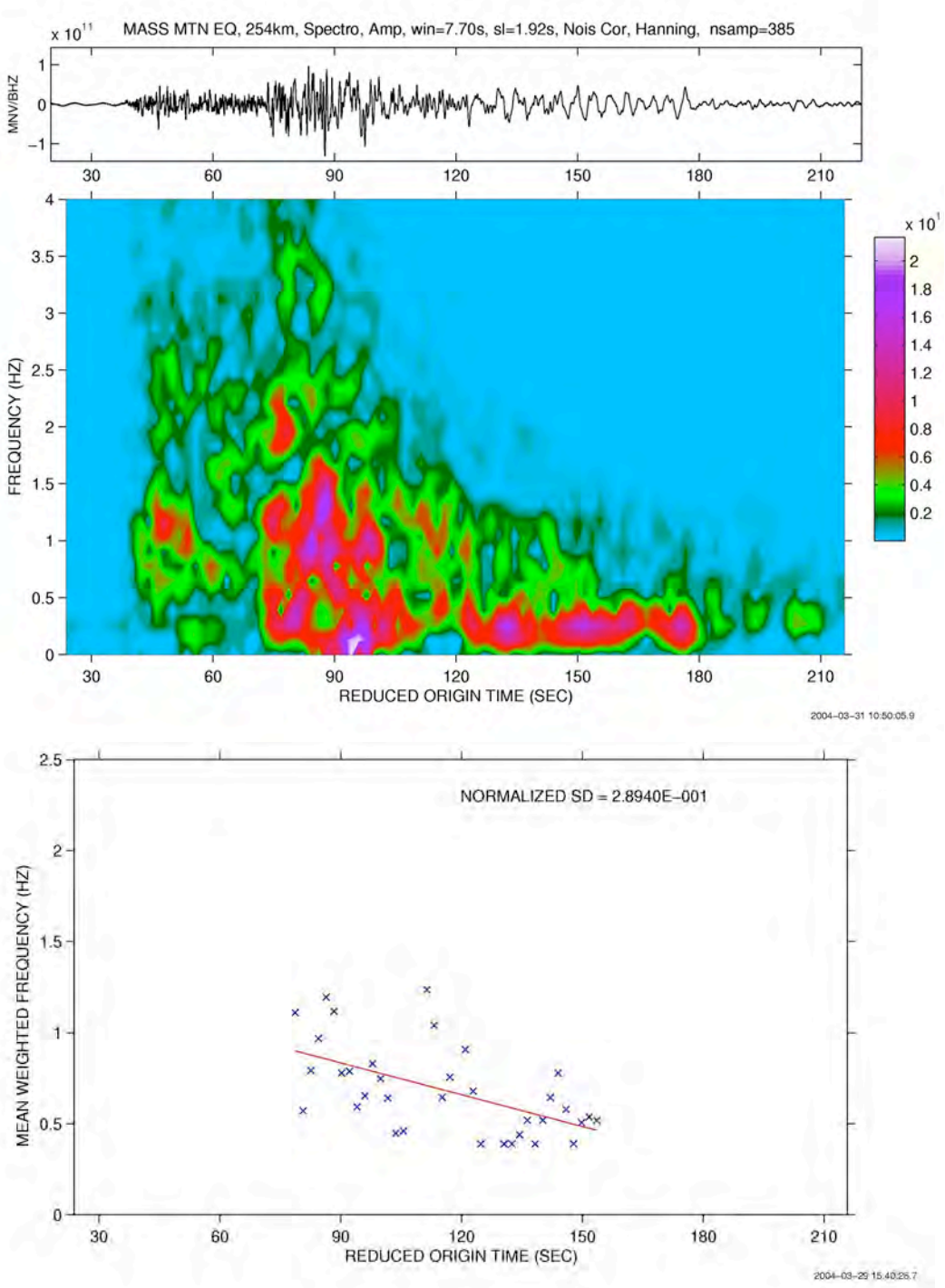


Figure 2. Seismogram (top) and spectrogram of the Massachusetts Mountain earthquake recorded at MNV. The Lg wavetrain, on the earthquake spectrogram, starting at about 77 sec, shows several prominent peaks but these peaks are not as systematically decreasing in frequency content and amplitude as those for the explosion in Figure 1. Bottom figure shows the mean weighted frequency versus travel time, within the time window D/(3.3km/sec) and D/(1.65 km/sec); linear regression (red line) and the associated normalized standard deviation are indicated.

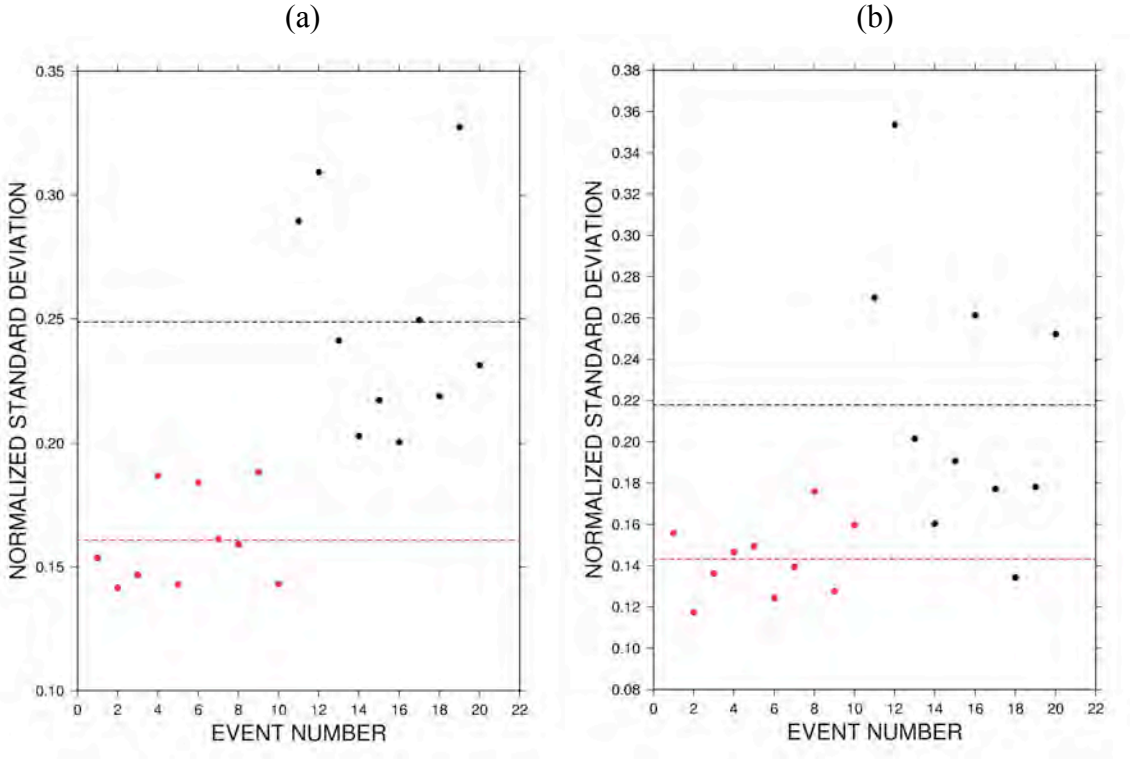


Figure 3. (a) Normalized standard deviation for 10 NTS explosions (red circles) and 10 nearby earthquakes (black circles) recorded at MNV. The earthquake and explosion populations are fairly well separated. The mean value for the earthquake population is about 55% higher than for the explosion population, suggesting that differences in standard deviation values should be useful for source discrimination. (b) Normalized standard deviation for 10 KTS explosions (red circles) and 10 earthquakes (black circles) recorded at WMQ. The earthquake and explosion populations are separated such that the mean value for the earthquake population is about 52% higher than for the explosion population. Considering large differences in propagation paths to WMQ, these results should be useful for source discrimination.

influence the source discrimination results much more than for the U.S. data. This provides a possible explanation for the Soviet discrimination results (Figure 3b) to be not as satisfactory as for the U. S. events (Figure 3a).

Discrimination Based on Lg Spectral Ratios and Spectral Slopes

Several investigators (e.g. Taylor et al., 1988; Gupta and Wagner, 1998) have used Lg spectral ratios for regional discrimination with limited success. There have also been a few studies of spectral slope as a discriminant but with ambiguous results. For example, by analyzing high frequency data, Chael (1988) found the spectral slope of Pg to be a good discriminant for NTS explosions and southwestern earthquakes. Gupta and Wagner (1998) were probably the first to successfully use the spectral slope of Sg and Lg as a source discriminant.

By using the same dataset of 10 NTS explosions and 10 U.S. earthquakes, we obtained spectra of Lg wavetrain starting at a velocity of 3.5 km/sec. Multitapered spectra, corrected for noise, for 25.6 sec long windows were used to obtain mean log amplitudes within several frequency bands. Results for Lg(0.5-2 Hz)/(3-7 Hz) are shown in Figure 4a (open symbols). All ten explosions are at nearly the same distance (within 234 to 246 km), whereas the epicentral distances for earthquakes vary from 179 to 300 km. A source-receiver distance correction was therefore computed by assuming linear dependence with distance for the ten earthquake spectral ratios, as by Taylor et al. (1988). Normalizing all data to the mean distance of the ten explosions (i.e. 238 km), the corrected results for all 20 events are also shown in Figure 4a (filled symbols), in which the mean values for the explosion and earthquake populations differ by 0.69 log units.

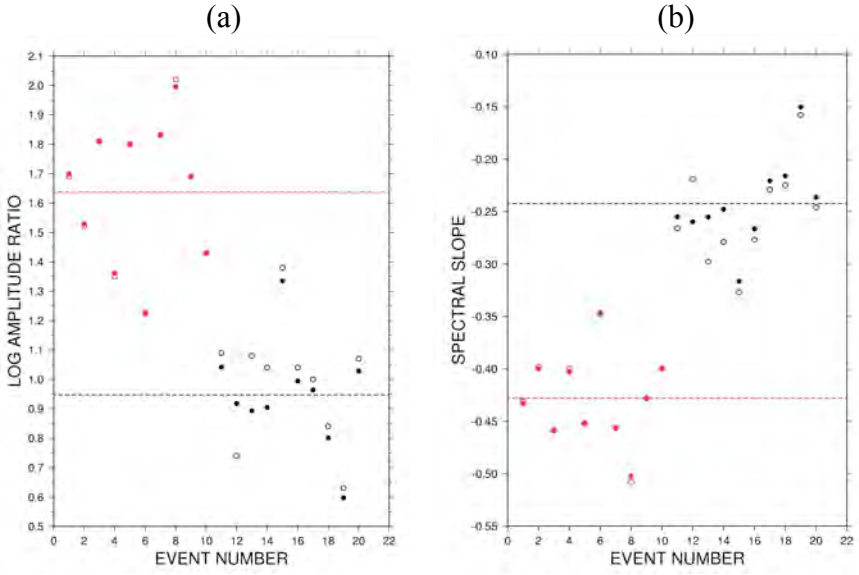


Figure 4. (a) Mean spectral ratio Lg(0.5-2 Hz)/(3-7 Hz) for 10 NTS explosions (red circles) and 10 nearby earthquakes (black circles) recorded at MNV. (b) Mean spectral slope of Lg over 0.5-7.0 Hz for the same dataset. In both figures, results without (open symbols) and with distance correction (filled symbols) are shown; the latter show the earthquake and explosion populations to be well separated by (a) 0.69 log units and (b) 0.19 log units. Differences in both (a) Lg spectral ratios and (b) Lg spectral slopes appear to be useful for source discrimination.

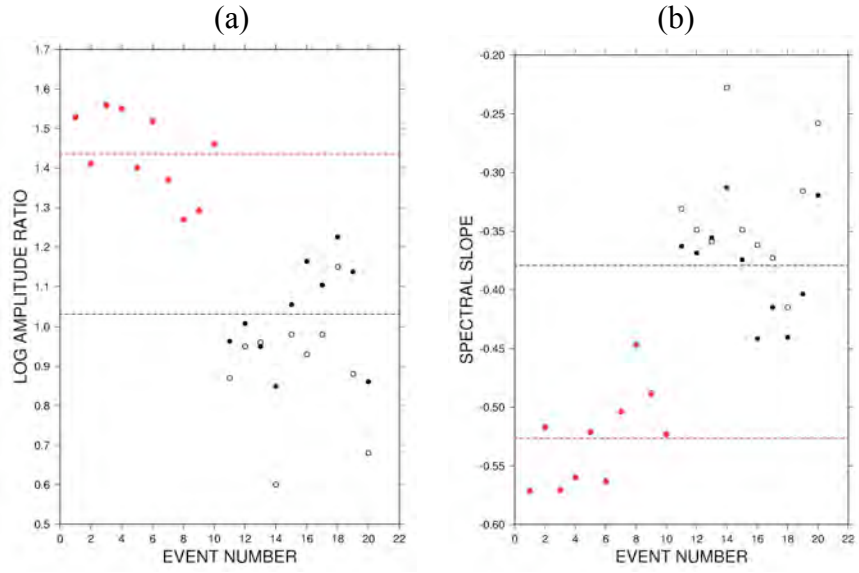


Figure 5. (a) Mean spectral ratio Lg(0.5-2 Hz)/(3-5 Hz) for 10 KTS explosions (red circles) and 10 earthquakes (black circles) recorded at WMQ. (b) Mean spectral slope of Lg over 0.5-5.0 Hz for the same dataset. In both figures, results without (open symbols) and with distance correction (filled symbols) are shown; the latter show the earthquake and explosion populations to be well separated by (a) 0.41 log units and (b) 0.15 log units. Differences in both (a) Lg spectral ratios and (b) Lg spectral slopes appear to be useful for source discrimination.

The mean spectral slopes over the frequency range of 0.5 to 7.0 Hz for all events are shown in Figure 4b, which shows results for both without and with distance correction. The explosion and earthquake populations are well separated (about 0.19 log units). Considering that results in Figures 4a and 4b are from only one recording station, it seems that the observed differences in the Lg spectral ratios and spectral slopes may serve as powerful regional discriminants based on the use of only the Lg phase.

By using the same dataset of 10 KTS explosions and ten earthquakes recorded at WMQ as used earlier, we obtained Lg spectra of 25.6 sec long windows by following the same procedure as for the United States data. Similar to the NTS shots, all ten explosions are at nearly the same distance (within 948 to 963 km). However, the epicentral distances for earthquakes vary from 476 to 975 km. Results for Lg(0.5-2 Hz)/(3-5 Hz), both without and with distance correction, are shown in Figure 5a, after normalizing all data to the mean distance of the ten explosions (about 956 km). The explosion and earthquake populations, with their mean values differing by 0.41 log units, are fairly well separated. The mean spectral slopes over the frequency range of 0.5 to 5.0 Hz for all events are shown in Figure 5b, which also shows results for both without and with distance correction. The explosion and earthquake populations are well separated (about 0.15 log units). Considering that results in Figures 5a and 5b are also from only one recording station, it seems that the observed differences in the Lg spectral ratios and spectral slopes may serve as powerful regional discriminants, similar to the findings for the U.S. data. It is also interesting to note that, although the available Russian and Chinese earthquakes are at significantly different locations as compared to the KTS explosions (unlike the U.S. events), the Lg spectral ratios and spectral slopes are still as effective regional discriminants as for the U.S. data.

Discrimination Based on Skewness and Kurtosis of Lg Spectra

A recent study by Ortiz et al. (2002) found statistical measures such as skewness and kurtosis to be useful for source discrimination at regional distances. Their approach, based on the use of time-series analysis of various regional phases, provided effective discrimination between nuclear explosions and earthquakes. We modified their procedure to frequency domain measurements and applied it to the spectra of Lg from both types of seismic events recorded at a common station.

Following Ortiz et al. (2002), skewness for signal S(t) may be expressed as

$$W(t) = \frac{\sum_i (t_i - t_0)^3 \left| S(t_i) \right|}{\left[\sum_i (t_i - t_0)^2 \left| S(t_i) \right| \right]^{3/2}} \qquad (2)$$

We used the following similar frequency-domain relationship for skewness

$$W(f) = \frac{\sum_i (f_i - f_0)^3 A_i}{\left[\sum_i (f_i - f_0)^2 A_i \right]^{3/2}} \qquad (3)$$

The above relationship provides results that vary with the absolute value of the amplitudes, A_i, which, in this study, are in log units. In order to obtain results that only depend on the shape of the spectra (rather than absolute values), all mean amplitudes within a specified frequency range are scaled by assigning the same fixed value for all events. This required all A_i values (in log units) for a given event to be adjusted by the same normalizing amount, which was of course different for different events.

Lg spectra for 25.6 sec long Lg windows, corrected for noise, were obtained for all 20 U.S. seismic events recorded at MNV. For the frequency range of 0.5-7.0 Hz, skewness was computed by using equation (3). Mean values of A_i for 0.5-7.0 Hz for most events were close to 3 so that a normalizing amount of 3.0 was used for all 20 events. Actually, skewness based on the use of equation (3) yielded negative values for all 20 seismic events and Figure 6a shows the absolute (positive) values. The explosion and earthquake populations are remarkably well separated. However, the

results for kurtosis showed no significant discrimination between the two types of seismic events. A source-receiver distance correction was applied to the skewness and the results are also included in Figure 6a. Furthermore, we also derived the skewness and kurtosis by using a normalizing amount of 5.0 but the results remained almost the same; indicating that the choice of the normalizing amount is not important. Considering that the skewness results in Figure 6a are from only one recording station, it seems that the observed differences in the skewness of Lg spectra serve as an effective regional discriminant.

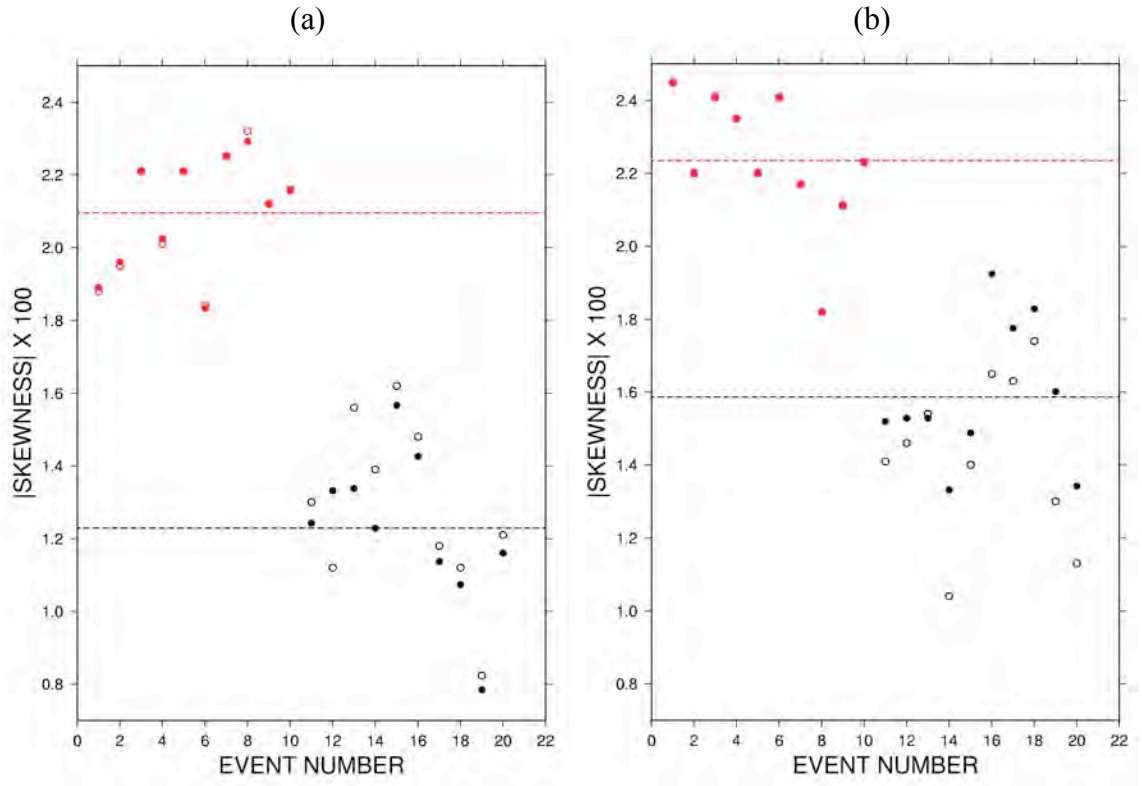


Figure 6. Skewness for (a) 10 NTS explosions (red circles) and 10 nearby earthquakes (black circles) recorded at MNV for the frequency range of 0.5-7.0 Hz and (b) 10 KTS explosions (red circles) and 10 earthquakes (black circles) recorded at WMQ. In both figures, results without (open symbols) and with distance correction (filled symbols) are shown; the latter show the earthquake and explosion populations to be well separated. Differences in skewness appear to provide an effective regional discriminant.

As for the U.S. data, Lg spectra for 25.6 sec long Lg windows, corrected for noise, were also obtained for 10 KTS explosions and 10 nearby earthquakes recorded at WMQ. For most events, mean values of A_i for 0.5-5.0 Hz were close to 3 so that a normalizing amount of 3.0 was used for all 20 events. As for the NTS data, skewness based on the use of equation (3) yielded negative values for all 20 seismic events and Figure 6b shows the absolute (positive) values. The explosion and earthquake populations are well separated. However, the results for kurtosis showed no significant discrimination between the two types of seismic events. A source-receiver distance correction was applied to the skewness and the results are also included in Figure 6b. Considering again that the skewness results in Figure 6b are from only one recording station, it seems that the observed differences in the skewness of Lg spectra serve as an additional regional discriminant, similar to the result for U.S. explosion and earthquake data (Figure 6a).

CONCLUSIONS AND RECOMMENDATIONS

Our analysis of regional data from nuclear explosions from both NTS and KTS and nearby earthquakes suggests the following conclusions: (1) There are several reliable source discrimination methods based on the use of the single seismic phase Lg recorded at regional distances. These should be especially useful for small magnitude seismic events

for which Lg may be the only well recorded seismic phase. (2) Our preliminary analysis of both NTS and KTS nuclear explosions and nearby earthquakes indicates four possible regional discriminants: (a) normalized standard deviation derived from spectrograms, (b) Lg spectral ratios, (c) Lg spectral slopes, and (d) skewness of Lg spectra. (3) Remarkable similarity of discrimination results from both NTS and KTS nuclear explosions and nearby earthquakes, with entirely different geological settings, indicates that our results should be applicable to other regions of the world. These regional discriminants should be tested and improved by analyzing significantly larger datasets from several regions of the world so that the most effective of these may be incorporated into an automated software system providing identification of small seismic events.

REFERENCES

Bonner, J. L., H. J. Patton, A. C. Rosca, H. Hooper, J. Orrey, M. Leidig, and I. Gupta (2003). Aspects of Rg and Lg Generation from the Shagan Depth of Burial explosions, *Proceedings 25th Seismic Research Review*, 384-393.

Chael, E. P. (1988). Spectral Discrimination of NTS Explosions and Earthquakes in the Southwestern United States Using High-Frequency Regional Data, *Geophys. Res. Lett.* 15, 625-628.

Gupta, I. N., W. Chan, and R. Wagner (1992). A Comparison of Regional Phases from Underground Nuclear Explosions at East Kazakh and Nevada Test Sites, *Bull. Seismol. Soc. Am*., 82, 352-382.

Gupta, I. N. and R. A. Wagner (1998). Study of Low and High Frequency Lg from Explosions and its Application to Seismic Monitoring of the CTBT, *AFRL-VS-HA-TR-98-0038*, Air Force Research Laboratory, Hanscom Air Force Base, Massachusetts.

Gupta, I. N., T. Zhang, and R. Wagner (1997). Low-Frequency Lg from NTS and Kazakh Nuclear Explosions—Observations and Interpretation, *Bull. Seismol. Soc. Am*., 87, 1115-1125.

Hartse, H. E., W. S. Phillips, M. C. Fehler, and L. S. House (1995). Single-Station Spectral Discrimination Using Coda Waves, *Bull. Seism. Soc. Am*. 85, 1464-1474.

Myers, S. C., J. Wagoner, S. Larsen, A. Rodgers, K. Myeda, K. Smith, and W. Walter (2003). Simulation of Regional Explosion S-phases (SIRES) project, *Proceedings 25th Seismic Research Review*, 117-124.

Myers, S. C., W. Walter. K. Mayeda, and L. Glenn (1999). Observations in Support of Rg Scattering as a Source for Explosion S waves: Regional and Local Recordings of the 1997 Kazakhstan Depth of Burial Experiment, *Bull. Seism. Soc. Am*. 89, 544-549.

Ortiz, A. M., S. R. Taylor, T. J. Fitzgerald, and T. Wallace (2002). Rediscovering Signal Complexity Discriminants: a Preliminary Study for Application to Regional Seismic and Radio Frequency Signatures, *LA-UR-02-7657*, Los Alamos National Laboratory, Los Alamos, NM.

Patton, H. J. (2001). Regional Magnitude Scaling, Transportability, and Ms : mb Discrimination at Small Magnitudes, *Pure appl. geophys*., 158, 1951-2015.

Patton, H. J., and S. R. Taylor (1995). Analysis of Lg Spectral Ratios from NTS Explosions: Implications for the Source Mechanisms of Spall and the Generation of Lg waves, *Bull. Seismol. Soc. Am*., 85, 220-236.

Taylor, S. R., N. W. Sherman, and M. D. Denny (1988). Spectral Discrimination between NTS Explosions and Western United States Earthquakes at Regional Distances, *Bull. Seism. Soc. Am.* 78, 1563-1579.

Wu, R. S., X. B. Xie, Z. Ge, X. Wu, and T. Lay (2003). Quantifying Source Excitation and Path Effects for High Frequency Regional Waves, *Proceedings 25th Seismic Research Review*, 172-181.

A COMPARATIVE TEST OF SEISMIC DISCRIMINANTS FOR MINING EXPLOSIONS

Michael A. Hedlin[1], Brian W. Stump[2], Stephen Arrowsmith[1], and Marie D. Renwald[2]

University of California at San Diego[1], Southern Methodist University[2]

Sponsored by National Nuclear Security Administration
Office of Nonproliferation Research and Engineering
Office of Defense Nuclear Nonproliferation

Contract No. DE-FC52-03NA99511[1], DE-FC52-03NA99510[2]

ABSTRACT

Seismic event identification can be viewed as a task to separate a collection of events into classes that could include earthquakes, single-fired explosions (nuclear or chemical), mining explosions, and underground mining collapses or rock bursts. Historical event identification based upon teleseismic data focused upon the simpler task of separating earthquakes and explosions. This approach was adequate for large events observed at teleseismic distances because there are few mining explosions, mining collapses and rock bursts large enough to be observed. The development of a robust seismic monitoring network, including high performance regional arrays has provided the opportunity to observe small-to-moderate size events that include many manmade sources. This transition in instrumentation and monitoring interest motivates this study to quantify event identification procedures focused upon mining explosions as separate from contained, single-fired explosions. A recent review of mining explosion tools has illustrated the vast array of tools available for this task (Stump *et al.,* 2002). The tools developed for this identification task should ideally be applicable to mining regions around the world. Broad application of tools requires an assessment of regional propagation path effects and a linkage of the identification procedures to the physical processes that accompany the mining explosion. We are studying mining explosions and their accompanying regional seismic waves in two regions in order to accomplish these goals. The first region is the continental United States (U.S.). We believe that this region is critical to the study because (1) significant ground truth information already exists; (2) a mixture of delay-fired and contained single-fired explosions either already exist or are planned; (3) multiple, high-performance regional arrays (PDAR, NVAR, TXAR) already exist; and (4) the U.S. can be divided into two distinct regions of propagation path — high attenuation in the west and low attenuation in the east. The second region of study is another area of significant mining activity, the Altai-Sayan in Russia. Ground truth information in this region is not as robust but is being expanded under this study. The tools developed in the U.S. will then be applied to data obtained for the numerous large-scale explosions in this region. A preliminary assessment of blasting in this region accompanied by seismograms has already been completed.

OBJECTIVES

To reach our primary goal of testing an integrated suite of discriminants in mining regions in the United States and Russia, we have a number of objectives each year. In the first year our objectives are as follows:

- Assembly and delivery of U.S. database.
- Identification of foreign region for study. Identify mine clusters in the foreign region.
- Develop contacts in foreign region for ground truth. Initiate communication with local seismologists, mining officials, and Russian authorities before a site visit. Develop a collaborative relationship with members of the nuclear monitoring and mining communities in Russia.
- Code development.

Objectives for the second year are as follows:

- Test integrated suite of discriminants on data from U.S. mining regions.
- Assembly and delivery of foreign database. We plan an initial dataset of 500 events recorded by five stations in the International Monitoring System (IMS) and the Ground Station Network (GSN), with detailed ground truth data on several mine blasts.
- Assessment of the U.S. results and modification of the tools based on initial testing.

Objectives for the third year are as follows:

- Test integrated suite of discriminants on foreign database.
- Assessment of testing of foreign database.
- Delivery of techniques and software.

We are currently in year 1. As will be described in the next section, we are ahead of schedule in some areas and are now working on some tasks originally planned for year 2. We believe that code development, originally to be completed in year 1, will not be completed until the first quarter of the second year of our contract.

HISTORICAL PERSPECTIVE

There is an unprecedented need to reliably discriminate mining explosions from nuclear tests, earthquakes and other mining related events. The crux of our effort is to determine if regional seismic data can reliably characterize mine blasts and reliably separate them from these other event types. Mining explosions are the most enigmatic among the large number of low magnitude-events. All mining events occur at shallow depths, and therefore a simple depth discriminant will never separate these events from nuclear tests. Like nuclear tests, mining blasts are detonated at a chosen time and place. It has been well documented that single-fired chemical explosions cannot be distinguished from nuclear explosions using seismic observations (Denny, 1994; Stump *et al.,* 1999). Fortunately, large-scale, single-fired chemical explosions are rare. Large-scale chemical explosions are used in the mining industry but most often with delay-firing thus introducing a spatial and temporal difference from concentrated, single-fired explosions. Because this latter type of explosion is very common, it will be necessary to identify the unique characteristics of seismic waves associated with this event type.

Although numerous mine-blast discriminants have been tested, some with notable successes (e.g., Baumgardt and Ziegler, 1988; Harris, 1991), so far no single technique has been globally reliable or transportable. Given the high cost of misidentification, no one technique is satisfactory. If there is a panacea for this problem, it may lie in the use of an integrated package of discriminants, particularly if the physical reasons for the failure of a single discriminant can be documented and understood. We have seen that the complexity of the mining explosions themselves and further complexity introduced by seismic wave propagation to the receivers cause the performance of generic discriminants to be regionally dependent. To date, there has been no operational test of an integrated discriminant package for identifying mine blasts. There is a clear need to develop, implement, test, and interpret such a discriminant package, possibly regionally tuned. The physical basis of these discriminants must be understood in order to interpret their performance under different conditions. This effort is built around extensive experience in blasting supported with ground truth information intended to provide these physical interpretations. For instance, L_g blockage along certain paths can move earthquakes into explosion populations, or long source durations from some

types of mining explosions may provide efficient excitation of intermediate period surface waves, unlike a concentrated charge.

Technical Issues

The review by Stump et al. (2002) illustrates that there are a number of questions that remain to be solved for effective identification of mining explosions around the world. These questions have played an important role in both motivating this effort and influencing the design of the research we will carry out.

What is the linkage between the physical effects accompanying mining explosions and the observed regional waveforms? A number of physical processes are important in how mining explosions generate seismic energy and include both the spatial extent of the multiple boreholes and the complex detonation pattern in time of these boreholes. These characteristics have been related to complex spectral interference patterns as well as the relative generation of long- and short-period energy. These physical contributions to the waveforms are in some sense dependent upon the style of blasting employed at a particular mine. Ultimately, this understanding of the relationship between blasting practices and regional discriminants will provide a basis for assessing discriminant performance in other regions of the world if some information is available on mine-blasting style.

Why are individual discriminants that are successful in one region subject to failure in another? Separation of physical processes accompanying mining explosions and regional propagation path effects will be critical to the assessment of this question. This problem can only be approached through a physical understanding of the source, possibly supported by empirical observations and ground truth, and an assessment of regional path effects. We will focus on the physical understanding of the source and the collection of ground truth and rely upon the National Nuclear Security Administration (NNSA) regional characterization effort to help assess path effects.

Can a set of integrated regional discriminants provide the basis for identifying or classifying mining explosions at regional distances? The review of techniques for identifying mining explosions at regional distances has illustrated the failure of individual discriminants either because of source or propagation path variations. We intend to test the proposition that a suite of tools properly applied and physically interpreted can provide robust identification.

Can regional seismic data, including array data, beyond 5^o be used to reliably discriminate mining explosions? In four of the world's major mining regions, the Altai-Sayan, the Powder River Basin, Morenci in Arizona, and Minntac in Minnesota, there is one seismic station within 2^o–4^o of the mines with additional stations at considerably farther distances. This means that many of the regional observations for these small events may be at great regional distances with the accompanying reduced amplitudes and limited bandwidth. The practical test of the proposed discriminants in a number of mining regions will provide experience with the effects of such station coverage on identification performance.

How important are anomalous blasts in the identification process? Mining blasts that do not detonate as planned can produce regional waveforms that are impulse as when a large number of the explosive boreholes detonate simultaneously. This type of blast is rare but has been observed and thus with the observed equivalence of seismograms from single-fired chemical and nuclear explosions could be problematic. The systematic analysis of a large number of mining explosions in a number of different parts of the world will allow us to assess the importance of this problem.

RESEARCH ACCOMPLISHED

In this section we describe our preliminary work to develop an integrated suite of discriminants. We use the United States as a control because we have experience in monitoring in this area, can readily obtain ground truth information, and can include data from contained single-fired explosions. Ground-truth data are an essential for any study of seismic discriminants. This dataset will prove invaluable to test the operational effectiveness of an integrated identification package in Russia where less is known about the sources and the paths to the stations.

Assembly of U.S. Database

We see the U.S. as a logical test-bed for the suite of discriminants because of the high quality of ground truth in this area. Our initial focus is in three areas for which ground truth is under development. The first is the area surrounding the Powder River Basin in northeast Wyoming. This region has active surface coal mining activities. Contact with local mines is providing ground truth information on recent cast blasting. We have gathered data for approximately 300 mining explosions recorded at the seismic and infrasound arrays in Pinedale, Wyoming (PDAR/PDIAR). The mining explosion database is being supplemented with earthquakes in Utah, Wyoming, Montana, and Idaho also recorded at PDAR/PDIAR. Future plans include expanding the database to include data from other regional stations. A companion study (Zhou et al., 2004) has analyzed the intermediate period surface waves generated by blasts in this region and applied a variant of the M_S:m_b discriminant to the data with some success. A series of contained, single-fired explosions (Stump et al. 2004), will provide an additional comparison.

The second focus area of our U.S. study is the porphyry copper mines of southeast Arizona where mining explosions are used to fracture rock for copper extraction. A database of mining explosions is being developed for this region as well. We intend to incorporate seismic and infrasound measurements from within one of the mines in the region to supplement the ground truth database. This database currently consists of 229 events for which ground truth information, including in-mine seismic and acoustic observations are available. A summary of this in-mine database is given in Figure 1a, which shows the peak ground motion and acoustic measurements and Figure 1b, which illustrates one of the shot patterns. A trip to the mine during January provided the opportunity to retrieve data from the in-mine recording system. The data-acquisition systems were placed in trigger mode so that additional ground truth could be recorded.

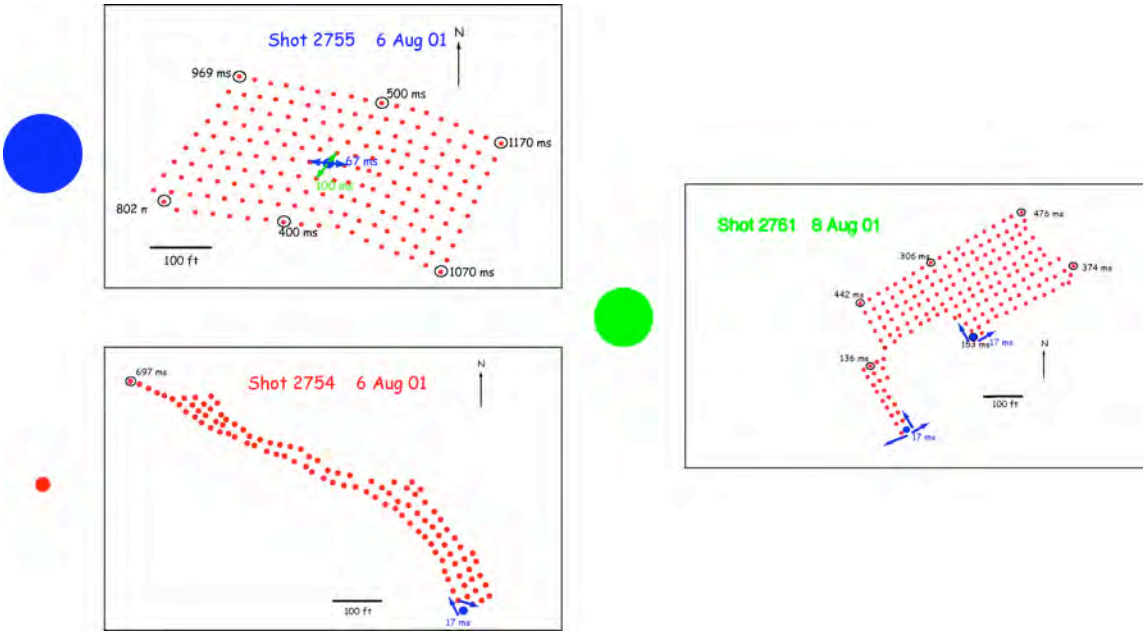


Figure 1a: Three example shot patterns from the southeastern Arizona ground truth database. The radius of the circle next to each pattern is proportional to the size of the blast with the largest, 348,070 lb. As noted in the figure, the largest shot (blue) uses much longer delay times than the other two shots.

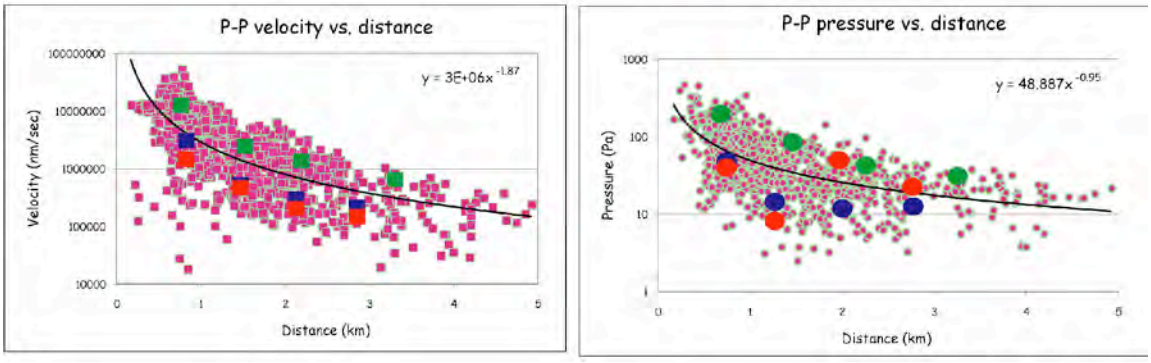


Figure 1b: Summary of the southeastern Arizona mining ground truth database. In-mine seismic and acoustic measurements from 229 explosions are summarized. The measurements for the three shots diagramed in Figure 1a are superimposed. The largest shot (blue) does not have the largest amplitudes either in-mine or at regional distances as a result of the longer delay times between individual shots. This information will be valuable in assessing the discriminants.

This area is the location of one of the two sites of a series of single-fired explosions conducted as part of the Source Phenomenology Experiment (Leidig et al., 2004). Data from these single-fired explosions and delay-fired explosions conducted during the experiments will be critical to our understanding of mining-explosion performance. Two record sections comparing a single-fired and delay-fired explosion are reproduced in Figure 2.

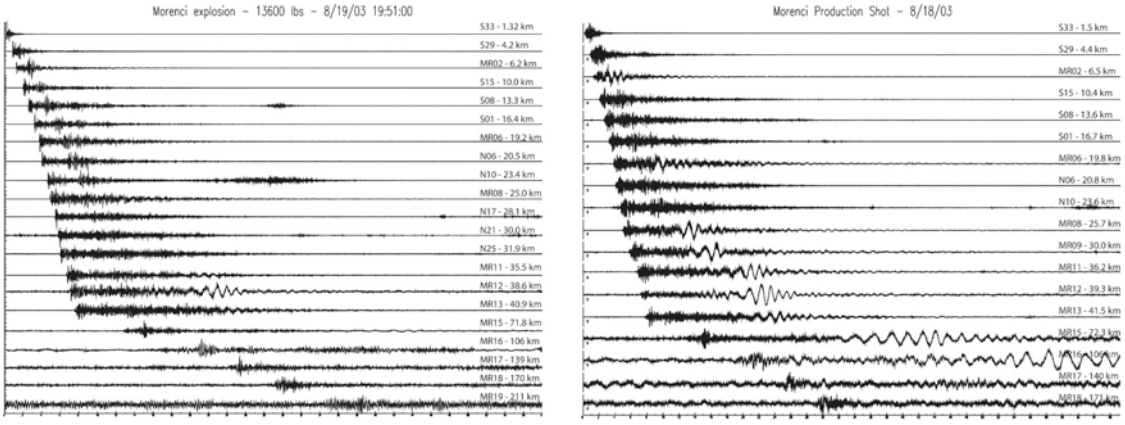


Figure 2: Regional record sections from a single-fired (left) and delay-fired (right) explosion detonated at one the southeastern Arizona copper mines.

The third area of focus is the Taconite Mines in Minnesota. Cooperation with one of the mines in the area provides shot information on each of the shots. The ground truth database currently consists of 472 events. The information provided includes the details of the shots in terms of the total amount of explosives, the number of shot holes, and the environmental conditions. The environmental conditions include the local wind speed and direction at shot time that may be important in understanding the accompanying infrasound signals. Figure 3 illustrates the type of data that is being gathered and the relatively large size of these blasts in Minnesota. We intend to visit the mine this summer for additional ground truth information.

In order to begin building the U.S. database of relevant seismic data, we contacted Dr. William Walter at Lawrence Livermore National Laboratory. Dr. Walter and his colleagues have assembled a database of seismic events featuring nuclear and mining explosions, as well as earthquakes, for the western U.S. (Walter et al., 2003). Dr. Walter agreed to distribute to us a copy of this database once his research team had finished making arrival onset picks and performing waveform quality control. He will be in contact with us once this occurs so that we may make arrangements for transferring the data.

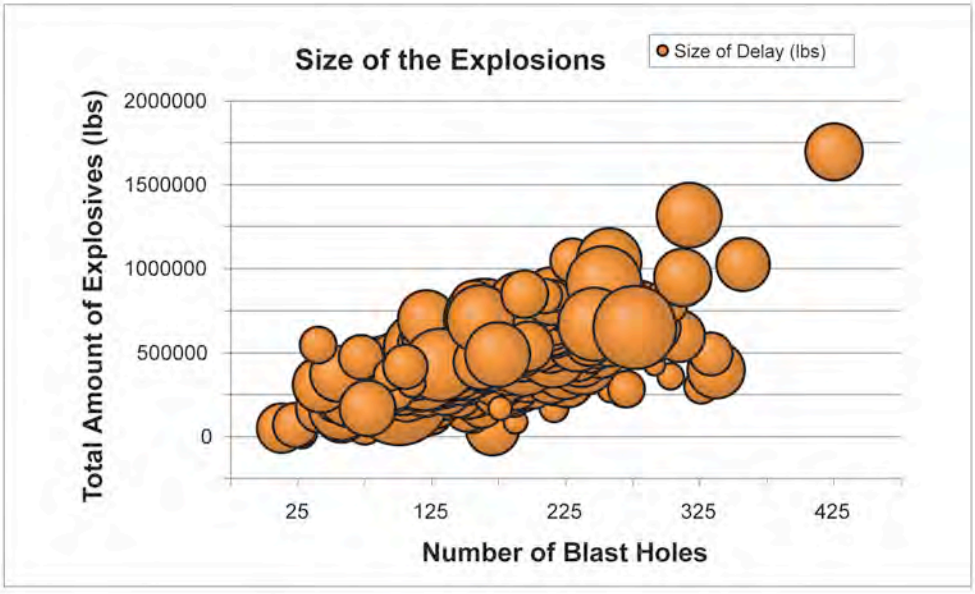


Figure 3. Summary of the Minnesota ground truth database. The largest explosion exceeds 1,500,000 lbs and consists of 425 individual blast holes.

Identification of foreign region

One of our primary goals for the first year was to identify a foreign region for study. We have selected the Altai-Sayan (A-S) mining trend near Novosibirsk, Russia. The A-S mining region is one of the largest and most active in the world. The 500 km long Altai-Sayan mining trend is located in a Paleozoic folded terrain just north of the Mongolian Altai and the Tien Shan. This is clearly a key area for monitoring research. This active mining trend is monitored by single stations and arrays in the IMS and the GSN as well as stations in the regional Altai-Sayan Seismological Expedition (ASSE) network (Figures 4 and 5) and offers a great range of mine blasts (e.g., explosive yield, shot patterns). Some ground-truth data was obtained from this region in the past, and we expect more detailed information in the future. One key to this analysis is identification of mine clusters in the Altai-Sayan trend. We have identified 8 clusters of mines in this trend (Figure 5). The clusters have been defined using event locations obtained by the ASSE network. We will seek more information about the mines in these clusters during our site visit (next section).

Development of contacts in Russia — Site Visit

With the target region selected, we have arranged for a site visit to Novosibirsk, Russia, and a mine in the Altai-Sayan mining trend in August, 2004. We believe that significant progress in this area will come with us working directly with experts from the Novosibirsk area. Dr. Khalturin has discussed the site visit with Dr. Vladimir Pergament, Head of the Mining Blasts Seismic Effects Laboratory of Magnitogorsk State Technical University. Dr. Pergament has agreed to work with the U.S. team during their site visit. Hedlin, working with Vitaly Khalturin, has contacted Dr. Alexander Fedorovoch Emanov, Head of the Altay-Sayans Experimental Methodological Seismic Expedition and Dr. Victor Sergeevich Seleznev, Head of the Siberian Geophysical Survey about this visit.

In August of this year, the entire team from Southern Methodist University (SMU) and the University of California at San Diego (UCSD) will travel to Novosibirsk for meetings with local seismologists and mining experts. We have several objectives in making this trip. First, we intend to establish a collaborative relationship with our counterparts in this area. Extensive discussions to date indicate that there are many areas of mutual interest relating to the monitoring of mining activity. Once common ground has been discussed in detail, our goal is to prepare for a detailed study of mine blasts in the A-S trend for the next 2 years. Historically, there has been limited ground truth data from this region. The information we have had access to in the past is typically lacking in detail. When detailed information about a blast is provided, it hasn't been possible to authenticate it. We will seek detailed

ground-truth data for several large mine blasts that will occur during the next 12 months. We also seek general information about mining along the A-S trend—the types of mining techniques, the types of material recovered, etc. We will also visit a coal mine in the Kuzbass region to observe a mine blast and to prepare to record a ground truth blast in that mine in 2005. We will inquire about gaining access to data from the 17-station ASSE Network (Figure 5).

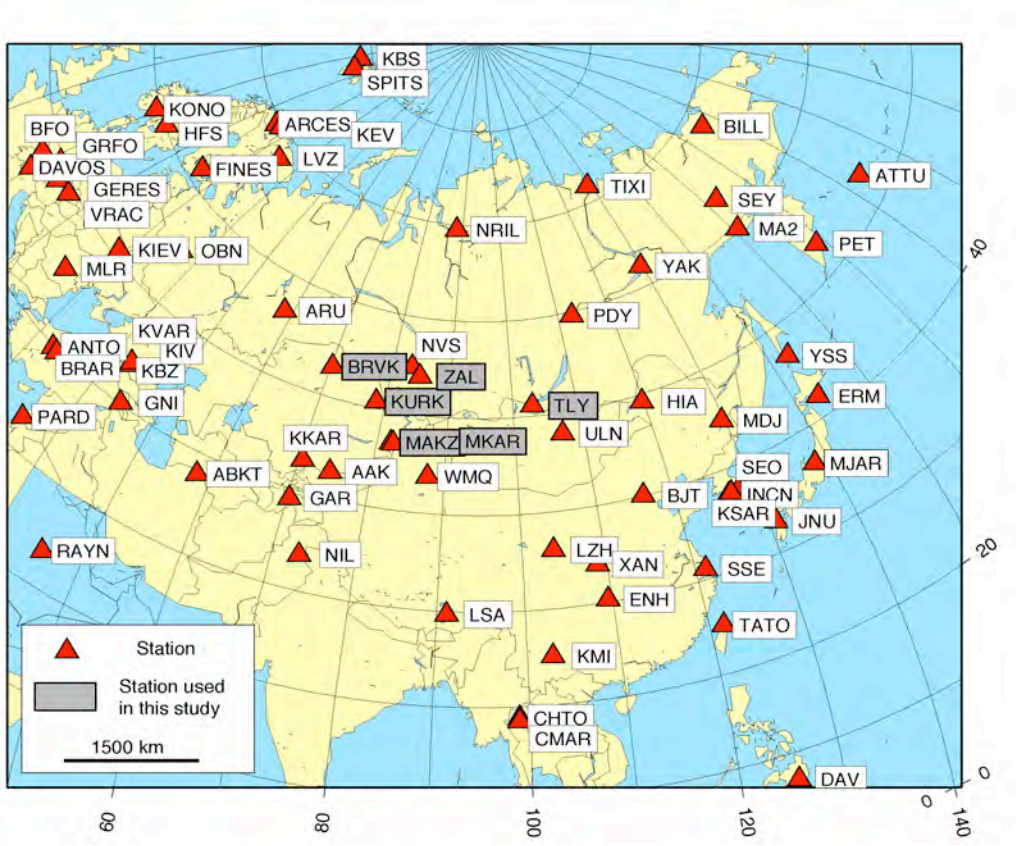


Figure 4. Seismic station coverage in Asia. The stations included in this study are highlighted.

Assembly of Russian Database

The Altai-Sayan trend is a natural laboratory for the study of mine blast identification tools. The trend includes several significant clusters of mines (Figure 5). Seismic-station coverage in the Altai-Sayan mining trend and surrounding region is indicated by Figures 4 and 5. The 3-component IMS station ZAL is located between ~100 km and 500 km from these clusters. This site has been recording data since day 346, 1991. The IMS array (MKAR) lies ~6° from most mines in the trend, and began delivering data on day 319, 2000, in a test phase; MKAR was certified as a primary IMS array in January 2002, and subsequent data are available through the International Data Center (IDC). Other IMS stations, KURK, TLY, BRVK, are not yet established; however, the Incorporated Research Institutions for Seismology (IRIS) GSN stations are operating at these sites and providing data for this study. Additional 3-component data from GSN station MAKZ , located southwest of the mining trend, serves as a surrogate for MKAR for the time prior to certification as an IMS array. All stations lie to the west, east, and south within ~1,000 km of the trend. We are presently developing a database of 500 mining events recorded at these stations in the IMS and the GSN.

The large numbers of events in each cluster identified in Figure 5 should prove useful in testing event correlation techniques (e.g., Harris, 1991) and in testing any other discriminant evaluating the performance of the event identification tools as a function of event location.

An essential component of this database will be ground truth data. A key goal of our site visit is to arrange for the collection of detailed ground-truth data from the mines in the A-S region. We have limited ground truth information for several thousand mine blasts that occurred between 1997 and 2001.

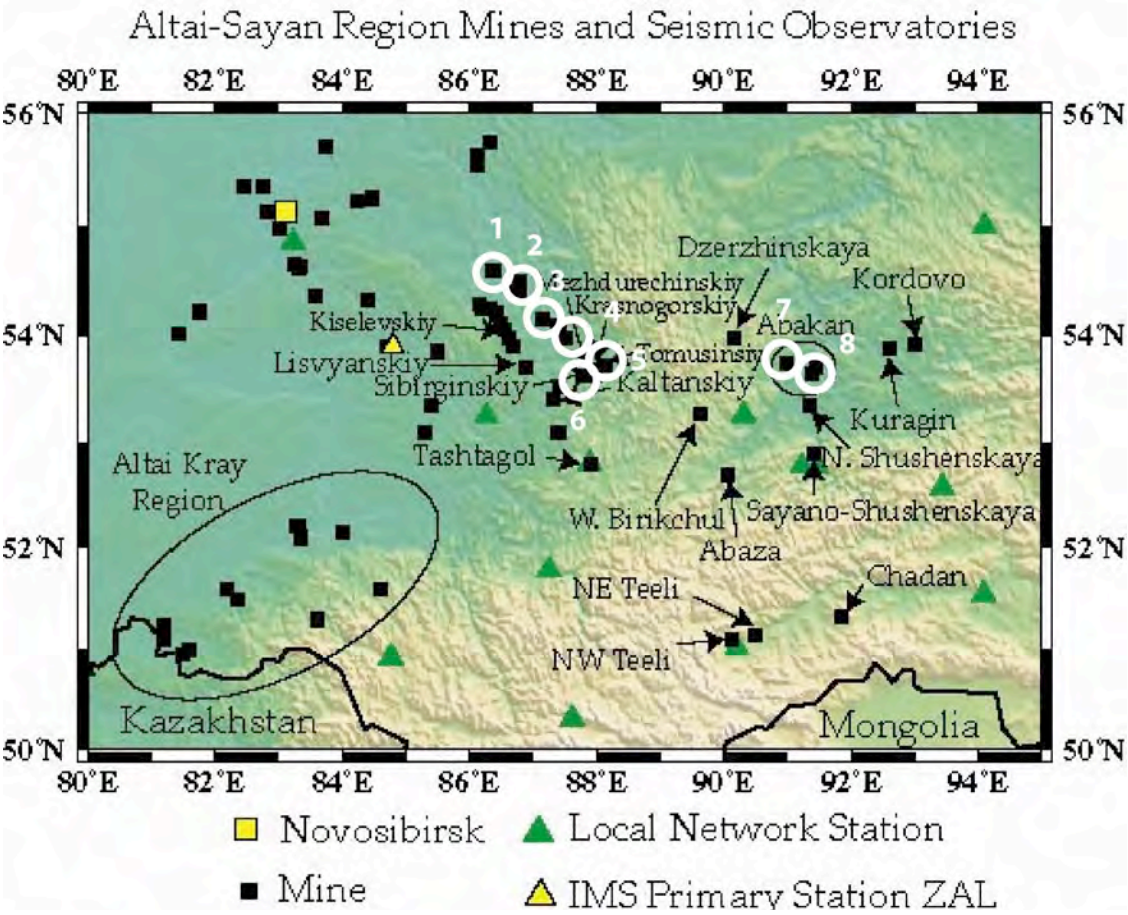


Figure 5. Mines in the Altai-Sayan region, stations in the Altai-Sayan Seismological Expedition regional network and the IMS (station ZAL). Eight clusters of mines/mining events are outlined.

Code development

Successful event identification employs analysis techniques using regional seismic data that identify characteristics for mining explosions that are distinct from those produced by contained, single-fired explosions and earthquakes. Special consideration is given to techniques that separate single-fired, contained explosions from delay-fired explosions typical of mining operations (Baumgardt and Ziegler, 1988; Smith, 1989; Hedlin et al.,1989; Chapman et al., 1992; Hedlin et al., 2002*)*. Procedures must minimize false alarms, the misidentification of a mining explosion as a contained, single-fired, possible nuclear explosion. A broad suite of discriminants has already been developed. Discriminants that we will include in our suite include the following:

- P/L_g at high and low frequency
- Surface Wave to Body Wave Amplitudes
- Time-varying spectral estimates
- Low-frequency modulations
- Correlation analysis
- Time-space clustering
- Acoustic and seismic signals

Our focus is to consistently test the complete list of identification tools and to judge the ultimate joint ability of these tools to separate mining explosions from single-fired explosions and earthquakes. Establishing the underlying physical basis of the tools is critical to developing a complete set of useable, portable, and extendable discriminants. Ground truth information is used to link the performance of individual identification tools to the physical processes accompanying the mining explosion. This information can be as simple as the source time and location but preferably includes details such as the individual borehole blast timing and explosive weight.

The application of multiple discriminants to single events means that some consideration of methods for combining the individual estimates must be considered. In our case, the use of ground truth information will be used to assess each discriminant and assess its contributions to the identification process. This will be based around the development of a physical understanding of discriminant performance with specific consideration of path and source contributions.

Through collaboration with Los Alamos National Laboratory (LANL), we intend to use regional discrimination methodology as described in Hartse *et al.* (1997) and associated computer codes developed by the Ground-based Nuclear Explosion Monitoring (GNEM) team at LANL. For example, the MDAC2 procedure removes magnitude and distance trends in regional phase amplitudes, allowing for maximum flexibility in the later construction of discriminants (Walter and Taylor, 2002). LANL also has developed feature selection codes that use the Mahalanobis distance metric as a measure for combining the best phase and spectral discriminants. We plan to tailor the discrimination work already accomplished at LANL for use on both the U.S. and Russian datasets.

Regional Ms:mb discriminant: Rong-mao Zhou (2004) has been developing a regional equivalent of the M_s:m_b discriminant. The procedure includes the determination of dispersion relations for intermediate period surface waves so that region-specific path corrections can be made to the observed surface waves. Preliminary application of the procedure to mining explosions in Wyoming and NE China suggest that large-scale, long-duration mining explosion may be identified as earthquakes.

Infrasound data: If techniques based solely on seismic data cannot provide an unambiguous classification of an event, infrasound data might be particularly useful. Surface blasts are known to generate large infrasonic waves, and propagation of these waves is particularly efficient downwind. Seasonal changes in stratospheric winds are well understood. As a result, it is known when IMS infrasound stations will be sensitive to mining activity. One example comes from the 8-element infrasound array at Pinon Flat in southern California. The array is ~400 km downwind of mines in eastern Arizona. The array at Pinon detects signals from mine blasts in Arizona during the summer season when the zonal stratospheric winds are to the west. We have detections from mines in the Kayenta and Morenci regions.

Integration: Ultimately rigorous methodologies for combining discriminants must be proposed and refined. We do not intend to develop such approaches as part of our research but take advantage of developments in this area by others. Specifically, we are interested in the preliminary work of Anderson and Taylor in this area. We have spoken to Dale Anderson at Pacific Northwest National Laboratory about coordinating our regional discrimination study of mining explosions with his development of methodologies for combining discriminants. He has expressed interest in communication and cooperation in this area. We feel that this cooperation will be critically important to the implementation of results developed during this research project.

CONCLUSION(S) AND RECOMMENDATION(S)

A key objective in nuclear monitoring is to find seismic-signal processing methods that have the potential to lower the thresholds at which detection, location, and identification functions can be performed without increasing false alarm rates to unacceptable levels. New techniques for discrimination, which make “significant improvement over current techniques” are of interest. We seek to address these issues as they relate to the monitoring of mining activity. It is well known that individual discriminants that have been found to be useful in some areas are often prone to failure in others and that one reason the discriminants fail is because the physics of signal generation at the source and propagation to the receiver are not yet well enough understood. We believe the solution to the problem posed by global mining activity lies in using all of these discriminants as an integrated package. We are developing this package, and will improve our understanding under what conditions the individual modules within the package will sometimes fail and use the package in a significant mining region in Russia. We have chosen to study the Altai-

Sayan mining in Russia under this second phase of our analysis because of the need to improve the U.S.'s ability to effectively monitor in this region.

ACKNOWLEDGEMENTS

Vitaly Khalturin (Lamont Doherty Earth Observatory) and Anna Titova (Siberian Geophysical Survey) for assistance with our work in Russia. Additionally, we wish to thank Steve Beil of Black Thunder Mine for providing shot times; Steve Taylor of LANL for facilitating access to codes; and Bill Walter of LLNL for sharing the Western U.S. dataset upon its completion.

REFERENCES

Baumgardt, D.R. & K.A. Ziegler, (1988), Spectral Evidence for Source Multiplicity in Explosions: Application to Regional Discrimination of Earthquakes and Explosions, *Bull. Seism. Soc. A., 78*, 1773-1795.

Chapman, M.C., G.A. Bollinger, & M.S. Sibol, 1992, Modeling Delay-Fired Explosion Spectra at Regional Distances, Bull. *Seism. Soc. A.,* 82*,* 2430-2447.

Denny, M. P., Editor, 1994, Proceedings of the Symposium on the Non-Proliferation Experiment (NPE): Results and Implications for the Test Ban Treaties, April 19-21, 1994, Rockville, Maryland, CONF 9404100, LLNL.

Harris, D.B., 1991, A Waveform Correlation Method for Identifying Quarry Explosions, *Bull. Seism. Soc. A.,* 81, 2395-2418.

Hartse, H., S. Taylor, W. Phillips, and G. Randall (1997), Regional Event Discrimination in Central Asia with Emphasis on Western China, *Bull. Seism. Soc. A.*, 87, 551-568.

Hedlin, M.A.H., J-B Minster, & J.A.O. Orcutt, (1989), The Time-Frequency Characteristics of Quarry Blasts and Calibration Explosions Recorded in Kazakhstan, USSR, *Geophys. J. Int.,* 99, 109-121.

Hedlin, M. A. H., B.W. Stump, D.C. Pearson & X. Yang, (2002), Identification of Mining Blasts at Mid- to Far-Regional Distances Using Low Frequency Seismic Signals, *PAGEOPH,* 159, 831-864.

Leidig, M. R., B. W. Stump, J. L. Bonner, C. T. Hayward, A. A. Velasco, D. F. Baker, H. Hooper, W. R. Walter, X. Yang, R.-M. Zhou, C. L. Edwards, M. D. Renwald, T.-S. Kim, M. McKenna and J. F. Lewkowicz, (2004), "Source Phenomenology Experiments in Arizona", in *Proceedings of the 26th Seismic Research Review: Trends in Nuclear Explosion Monitoring*, Orlando, FL (Sept. 21-23, 2004).

Smith, A.T., (1989), High-Frequency Seismic Observations and Models of Chemical Explosions: Implications for Discrimination of Ripple-Fired Mining Blasts, *Bull. Seism. Soc. A.,* 79*,* 1089-1110.

Stump, B. W., D. C. Pearson and R. E. Reinke, (1999), Source Comparisons Between Nuclear and Chemical Explosions Detonated at Rainier Mesa, Nevada Test Site, *Bull. Seism. Soc. A. 89,* 409-422.

Stump, B., M.A.H. Hedlin, D.C. Pearson, and V. Hsu, (2002), Characterization of Mining Explosions at Regional Distances, *Reviews of Geophysics, 40(4), 1011, doi:10.1029/1998RG000048.*

Taylor, S.R., A.A. Velasco, H.E. Hartse, W. S. Phillips, W.R. Walter, and A.J. Rodgers, (2002), Amplitude Corrections for Regional Seismic Discriminants, *PAGEOPH*, 159, 623-650.

Walter, W., K. Smith, J. O'Boyle, T. Hauk, F. Ryall, S. Ruppert, S. Myers, M. Anderson, and D. Dodge, (2003), *"*Improving the Fundamental Understanding of Regional Seismic Signal Processing with a Unique Western United States Dataset", in *Proceedings of the 25th Seismic Research Review - Nuclear Explosion Monitoring: Building the Knowledge Base*, LA-UR-03-6029, Vol. 1, pp. 486-494.

Zhou, R.-M., B. W. Stump and C. T. Hayward, (2004), "*M*s:*m*b Discrimination Study of Mining Explosions in Wyoming, USA and Qianan, China", in *Proceedings of the 26th Seismic Research Review: Trends in Nuclear Explosion Monitoring*, Orlando, FL (Sept. 21-23, 2004).

USING SHORT-PERIOD SURFACE WAVES TO MODEL SOURCE PHENOMENA

Heather Hooper[1], Howard J. Patton[2], Jessie L. Bonner[1], and Mark Leidig[1]

Weston Geophysical Corporation[1], Los Alamos National Laboratory[2]

Sponsored by National Nuclear Security Administration
Office of Nonproliferation Research and Engineering
Office of Defense Nuclear Nonproliferation

Contract No. DE-FG02-00ER83123

ABSTRACT

Nearfield and local seismograms of chemical explosions from 1) the Balapan depth of burial (DOB) experiment and 2) the Arizona source phenomenology experiment (SPE) provide an excellent opportunity to study the excitation of *Rg* waves for source effects. For the DOB experiment, *Rg* waves were identified using particle motion analysis and isolated from other arrivals using group velocity filtering. Fourier spectra were estimated, amplitude and phase information were processed, and path effects were removed. An *Rg* Q model and path-specific velocity models for phase corrections were developed for removal of path effects. Using a grid-search method, network-averaged source spectra were inverted to obtain source parameters for an axisymmetric source consisting of a monopole plus a compensated linear vector dipole (CLVD) or a horizontal tensile crack. The suite of observations, including ground-zero accelerograms and borehole logs, are best satisfied by models involving a CLVD with non-zero static moment. The CLVD source is related to tensile failure occurring at depths above the shot point, but a non-zero moment distinguishes this source from classical spallation source models. It appears to be more closely related to a conical source of block motions like the faulting source envisaged by Masse (1981). *Rg* source amplitudes are consistent with m_b(*Lg*) measurements at MAK, as would be expected if nearfield *Rg*-to-*S* scattering plays a role in generating *S*-waves seen at regional distances.

A new dataset recorded in September 2003 at a coal mine near Black Mesa, Arizona has allowed us to further examine the excitation of *Rg* from explosions in and below a topographic bench at the mine. A frequency-dependent attenuation model was developed and used to isolate source spectra and to generate radiation patterns. The source spectra for a set of nine explosions show that the one fully confined explosion scaled similarly to a Mueller-Murphy explosion with equivalent yield and depth of burial at most *Rg* frequencies. However, shots detonated at shallow depths that were not confined have frequency-dependent decoupling factors that vary from 2 to 10 at frequencies between 0.5 and 4 Hz when compared to theoretical scaling from a Mueller-Murphy source. Radiation patterns and spectral ratios from the explosions show increased energies and spectral ratios (factor of 1.5 increase) at azimuths behind the bench. Finally, spectral ratio plots show that detonating explosions with equivalent radiation patterns is a difficult task in the highly-fractured Black Mesa source medium.

OBJECTIVE

The objective of this research project is to improve nuclear monitoring efforts by developing an improved understanding of short-period surface waves generated by explosions. To accomplish this objective, we have created physically realistic models of short-period (0.2 to 12 second) surface wave generation from small chemical explosions and mine blast analogues. Additionally, we have worked to understand the propagation characteristics of these surface waves, possibly leading to an improved understanding of the physical mechanisms leading to the excitation of explosion-generated *Lg*.

RESEARCH ACCOMPLISHED

Rg Excitation by Underground Explosions: Insights from the Balapan DOB Experiment (Patton)

It has long been recognized that shallow sources excite *Rg* waves efficiently, but little is known about the mechanism(s) of *Rg* excitation by underground explosions. The excitation of *Rg* waves is of interest because of the role it may play in the generation of *Lg* waves and *Lg* coda from underground explosions. Gupta *et al.* (1992) proposed nearfield *Rg*-to-*S* scattering as a "transfer function" for converting energy radiated by underground explosions into *S* waves that become trapped in the crust and propagate to regional distances. Experimental support for this hypothesis comes from empirical studies (Gupta *et al.*, 1992; Myers *et al.*, 1999) and modeling studies (Patton and Taylor, 1995; Gupta *et al.*, 1997). A current limitation of modeling studies is that the source mechanism for *Rg* waves has to be assumed. Obtaining an improved understanding of the source of *Rg* waves is an important step towards building models of nearfield *Rg*-to-S scattering that can be tested against regional observations on a quantitative basis.

Explosions in the field are not simple monopole sources; rather, they are distributed in time and space, and emit non-spherical wave fields. Patton and Taylor (1995) proposed that the *Rg* excitation mechanism might involve a compensated linear vector dipole (Knopoff and Randall, 1970), where the CLVD is the elastodynamic equivalent of an inverted conical volume source with its apex at the detonation point. The medium inside the cone deforms and fails as a result of tensile stresses set up by the passage of the downgoing shock wave reflected off the free surface. Spallation, which usually involves shallow, poorly-coupling strata that open and close with no net displacement, is an example of such failure. Another example is that of driven block motions at depth, as envisioned by Masse (1981), which may have more significance for seismic wave generation, since it should allow for better coupling into the surrounding rock, and may involve permanent deformations.

Nearfield recordings of the 25-ton chemical explosions making up the DOB experiment at the Balapan test site, Semipalatinsk (Pearson *et al.*, 1997), offer a unique opportunity to investigate the excitation of *Rg* waves. Usable data were obtained from four nearfield stations for three of the depth of burial explosions.

Nearfield *Rg* Analysis

1) *Rg* waves were identified by (a) examining particle motions and (b) comparing observed arrival times with predictions based on the velocity models of Bonner *et al.* (2001).
2) *Rg* was extracted from the waveforms using the group-velocity filtering method of Landisman *et al.* (1969). This was necessary because the frequency content of the *P*, *S*, and *Rg* waves overlapped, and there wasn't enough time separation between the phases to do Fourier analysis on just the *Rg* signal.
3) The extracted *Rg* signals were Fourier transformed, and displacement spectra were calculated by dividing the amplitude and unwrapped phase spectra by *iw*. Noise spectra were also taken on a segment of coda the same length as the signal. Signal levels were usually well above the noise in the frequency band of interest.
4) Source spectra were calculated by correcting for the effects of amplitude attenuation and propagation phase delay using an *Rg* Q model and path-specific phase velocity models developed for that purpose.

Network spectra for three DOB explosions are shown in Figure 1, along with synthetic *Rg* spectra for a pure monopole source. The synthetic spectra were computed using the normal mode method of Saito (1967) for seismic moment M_o, determined using the scaling relationships for cavity radius and scalar moment of Denny and Johnson (1991; eqs. 39 and 41). For additional details of this study, both background and technical, see our extended abstract from the 25th Seismic Research Review (Bonner *et al*., 2003).

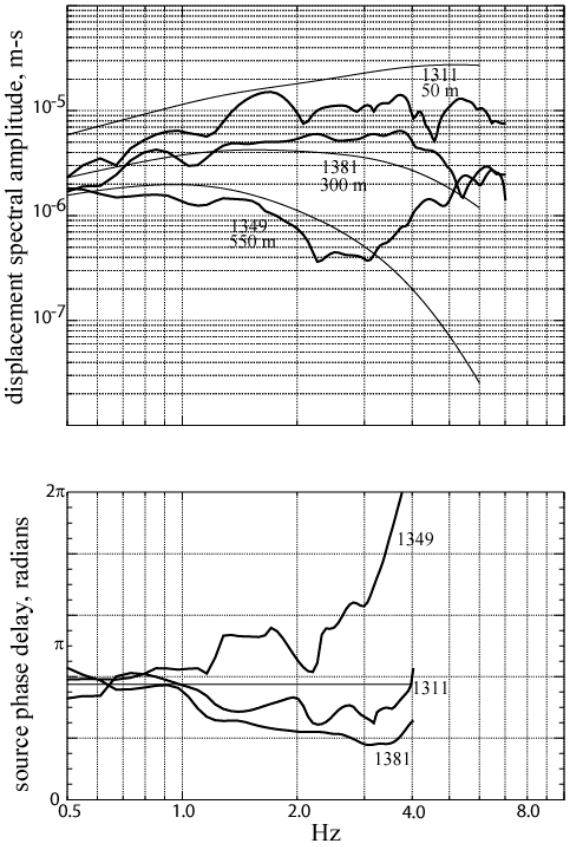


Figure 1. Network averaged *Rg* source spectra. (Top) Observed amplitude spectra (thick lines) and calculated amplitude spectra (thin lines) are for an equalization distance of 10 km. (Bottom) Observed phase delay spectra (thick lines) and the calculated spectrum (thin line) which applies to all three explosions.

Modelling Nearfield *Rg* Spectra

The next step was to model the nearfield *Rg* spectra for source effects using composite, axisymmetric sources. These sources consisted of a pure monopole linearly superposed with one of two secondary sources: either a CLVD or a horizontally-opening tensile crack. For practical and theoretical reasons, we chose to model network mean amplitude and phase spectra for each explosion. The model specifications included: (1) the centroid depth of the secondary source, (2) the source function of the secondary source, and (3) the M_o ratio between the secondary source and the monopole. The monopole M_o was determined by scaling the synthetic spectrum of the composite source to the observed amplitudes at low frequencies. The depth of the monopole was fixed to the centroid depth of the explosive package, and the source spectrum was assumed to be flat for the range of frequencies modeled based on the corner frequencies reported by Denny (1998).

The inversion was conducted by trial and error parameter search as follows:

1) The time history of the secondary source was fixed at a trial specification; we employed a von-Seggern-Blandford (1972) time history with two independent parameters: K (rise time) and B (overshoot);
2) A systematic search was conducted over centroid depth and M_o ratio on a 2-D grid;
3) At each grid point, the synthetic spectrum was scaled to match the observed amplitudes by least squares for frequencies of 0.5 - 1.5 Hz (0.8 - 1.5 Hz in the case of 1349); in doing so, the monopole M_o was determined;
4) Log amplitude and phase residuals were computed over specified frequency ranges: 0.8 - 6 Hz for amplitudes and 0.8 - 4 Hz for phase;
5) Residuals were contoured; the solution was taken to be the grid point with the minimum residual;
6) K and B were varied systematically and steps 2-5 were repeated.

The secondary source was delayed with respect to the explosion origin, where the delay was computed using the total transit time of a *P* wave emitted by the monopole source, reflected off the free surface with vertical incidence, and propagated down to the centroid depth of the secondary source. Thus the delay is solely a function of the

centroid depths and the Earth structure. The overall best solution was determined from the residuals as a function of K and B, using information from borehole logs and ground-zero (GZ) acceleration records for context.

Before discussing the results, we briefly review the salient features of *Rg* excitation by axisymmetric sources. The spectra in Figure 2 were computed keeping source function and source strength fixed while varying centroid depth. Each source type displays a unique *Rg* excitation. For a monopole, high frequency excitation systematically falls off as source depth increases. For a tensile crack, long-period excitation is weak in the upper 400 m. CLVD source spectra are more complicated due to the presence of spectral nulls related to source depth. Generally speaking, *Rg* excitation by the CLVD source can be as efficient as the monopole at low frequencies and less or more efficient at high frequencies depending on the respective source depths.

Phase spectra are identical for monopole and tensile crack sources and do not vary as a function of depth. On the other hand, *Rg* waves for a CLVD are 180° out of phase with respect to a monopole for frequencies less than the spectral null. Frequencies higher than the spectral null are in phase. Note that these results pertain to simultaneous sources with step function time history. The phasing will change for a secondary source delayed in time and with a different time history. Under those circumstances, superposition of monopole and secondary sources can lead to complicated interference patterns as a function of frequency.

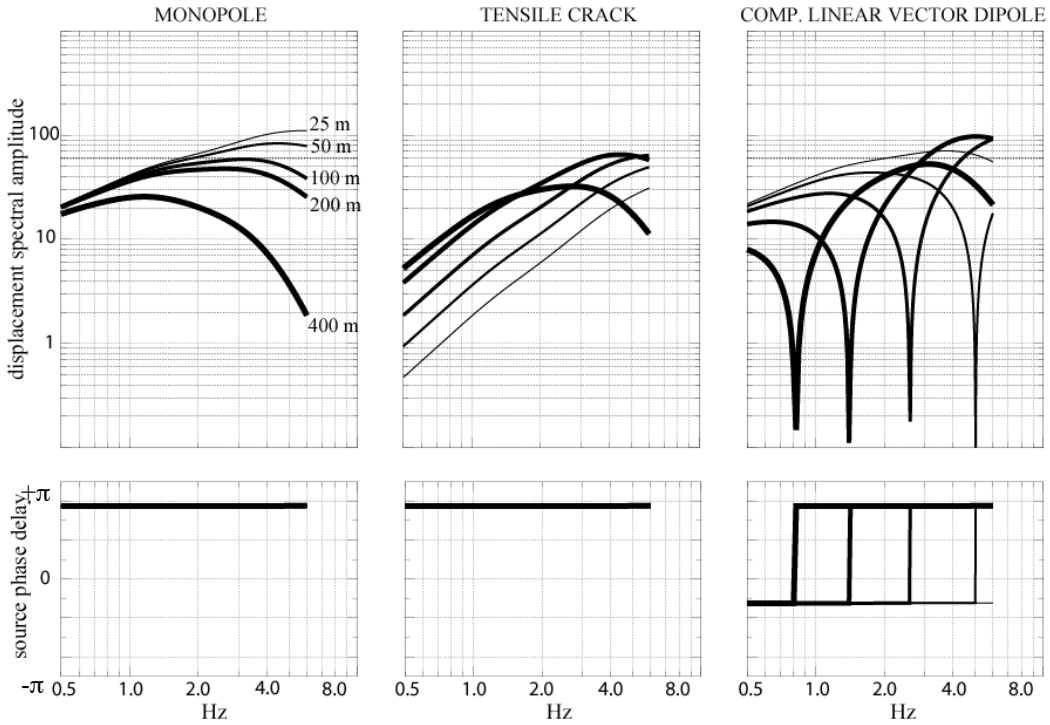


Figure 2. Synthetic *Rg* spectra for three sources with vertical axes of symmetry. All spectra were computed with a step function source time history. The vertical dipole moment Mzz was held fixed. (Left) The source description of a monopole explosion has equal moments along the diagonal of the moment tensor (M_{xx}, M_{yy}, M_{zz})=(1.0, 1.0, 1.0). (Center) The source description of a horizontal tensile crack is ($\lambda/(\lambda+2\mu)$, $\lambda/(\lambda+2\mu)$, 1.0). (Right) The source description of a CLVD with vertical axis of symmetry is (-0.5, -0.5, 1.0). Calculations are for centroid depths of 25, 50, 100, 200 and 400 m, where line thickness on the graph increases as depth increases. λ and μ are elastic constants.

Inversion results for 1349. The explosion in hole 1349 had a centroid depth of 535 m and a scaled depth of burial (SDOB) of ~1450 m/kt$^{1/3}$. Despite its depth, the free-surface acceleration records show that the medium over ground zero (GZ) spalled in response to the downgoing tensile wave. The depth of spall inferred from the time delay of the spall signal after the first arrival is remarkably deep, ~300 m or more, and borehole logs confirm the presence of layering with weak tensile strength at depths of ~340 m. The inversion results also favor an unusually deep secondary source of *Rg* waves. The solution with the overall minimum residual for a CLVD source is 250 m

deep with (K,B) of (100,10), while for a tensile crack source, it is 80 m deep with (K,B) of (100,1). The tensile crack centroid moves deeper as B increases. (Time history parameters were sampled at K = 1, 10, 100, 1000, 10000 and B = 1, 10, 100.) Both CLVD and tensile crack models fit the spectra well, and it is not possible to say which is in fact the true mechanism. Nevertheless, the behavior of the residuals for both models strongly suggests a link between the occurrence of tensile failure at depth and the excitation of *Rg* waves by a secondary source.

Inversion results for 1381. The explosion in hole 1381 had a centroid depth of 285 m and an SDOB of ~770 m/kt$^{1/3}$. Free-surface acceleration records show that the medium over GZ spalled, but in this case the spall occurred at shallow depths, which is more commonly the case for buried explosions. The time delay gives a depth of ~40 m, and borehole logs show a contact between overlying shales and basement rock at 41 m. The inversion results yield a centroid depth for a CLVD source consistent with a depth of 40 m and (K,B) of (1000,10). There are no physically meaningful solutions for a tensile crack. The rejection of all reasonable composite models involving a tensile crack model is due to the inability to match the spectral phase observations, which show phase advance relative to the phase spectrum predicted for a pure monopole (see Figure 2). Composite models involving a CLVD can predict phase advance because the source phase for a 40 m centroid depth is 180° out of phase with respect to a monopole for frequencies less than 7 Hz, and in addition there is a phase delay coming from the delayed origin time of the CLVD. Thus, the *Rg* observations for 1381 (and 1311) rule out a tensile crack mechanism, and we favor a CLVD mechanism for 1349 as well.

Inversion results for 1311. The explosion in hole 1311 had a centroid depth of 35 m and an SDOB of ~95 m/kt$^{1/3}$. It created a crater 40 m wide and roughly 5-10 m deep. The residuals for a CLVD source favor a very shallow centroid depth, and K greater than or equal to 100. The B value is not well resolved, however as B increases, the M_o ratio and the monopole M_o decrease, and almost all models with B greater than or equal to 10 have monopole M_o less than or equal to the monopole M_o estimated for 1381. These models contradict theoretical predictions that cavity size (hence M_o) should increase as rock strength diminishes due to lower overburden pressures (Glenn and Myers, 1997). Thus theory, coupled with the shallow depth of burial for 1311, argues for a larger M_o, hence a small value for B. A cratering source might be better modelled by time histories with little or no overshoot (B = 0) because there is no slap down (compaction) or gravitational reloading over GZ, as occurs in explosions with spall. (K,B) of the favored model is (100,1).

Summary Figure 3 shows time histories of the monopole and CLVD sources, as determined by Denny (1998) and the results of this study. Of significance are the static displacements associated with the CLVD source. The presence of statics may not be surprising for 1311 since cratering ejected material, and this could have resulted in elastic rebound over GZ. But 1381 and 1349 were spalling events, and the results for 1381 indicate statics associated in some way with tensile failure in the medium over the explosion. This finding contradicts conventional spall models (Stump, 1985; Day and McLaughlin, 1991) since they do not predict static M_o. Inversions assuming an impulse function gave large residuals for 1381, and all such models can be rejected; in the case of 1349, the results are equivocal, but favor a non-zero static M_o.

A CLVD force system with net M_o fits the source model proposed by Masse (1981) and could have important implications for the explosion source. While classical spall can be dismissed as a source of long-period Rayleigh waves (Day and McLaughlin, 1991), a CLVD source will radiate such waves with significant amplitudes if the static M_o is large enough (M_o ratio > 0.3). Long-period Rayleigh waves from monopole and CLVD sources will destructively interfere, canceling the amplitudes of waves emitted by the explosion. Such cancellation could affect measurements of explosion M_s, and, under extreme circumstances, the polarity of the resultant Rayleigh wave.

Finally, Figure 4 compares relative *Lg* amplitudes based on m_b(*Lg*) measured at station MAK with synthetic *Rg* spectra calculated for the preferred source models. The comparisons show very good agreement between the *Lg* amplitudes and the *Rg* source spectra for the composite monopole + CLVD source. Neither a monopole nor a CLVD source alone match the relative amplitudes. Thus, the composite source models are consistent with *Lg* waves generated by *Rg*-to-S scattering.

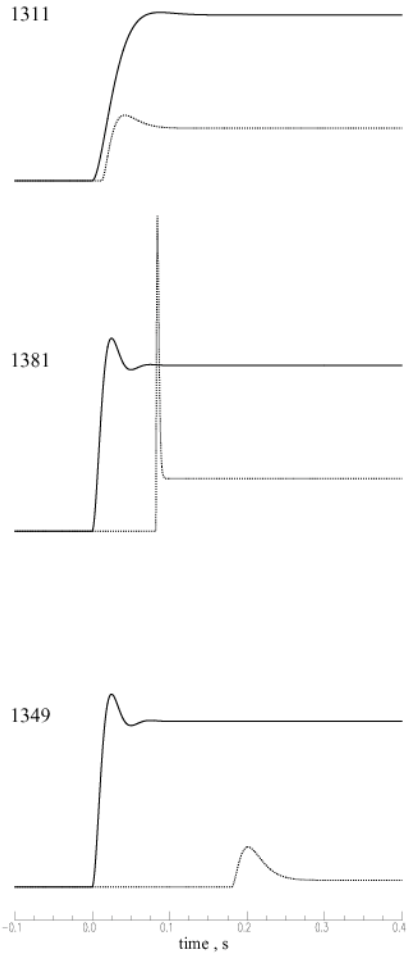


Figure 3. Displacement source functions for the monopole (solid line; after Denny, 1998)) and CLVD (dotted). The CLVD time histories are delayed and their static levels scaled relative to those of the monopole based on the results of this study.

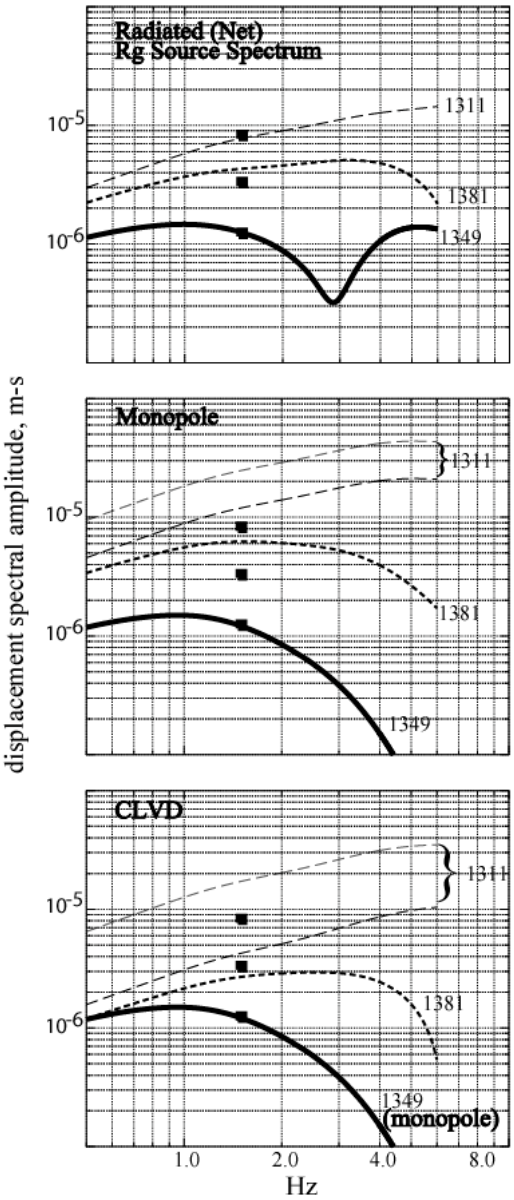


Figure 4. Synthetic *Rg* amplitude spectra for (Top) the final source models, (Middle) monopole sources and (Bottom) CLVD sources. Two spectra are shown for 1311 in the Middle and Bottom panels, one for K=1000 (gray dashed line) and the other for K=100 (black dashed line). Black squares are relative amplitudes based on m_b(*Lg*) values. *Lg* amplitudes were normalized to the *Rg* source spectrum for 1349 at 1.5 Hz (the frequency used to measure the magnitude).

Quantifying the Effects of Confinement on Explosion-Generated *Rg*: Preliminary Results from a New Dataset (Hooper, Bonner, and Leidig)

During the summer of 2003, the Source Phenomenology Experiment was conducted to investigate the differences between confined single-fired chemical explosions (surrogates for nuclear tests) and unconfined delay-fired mining explosions. As part of this experiment, nine single-fired chemical shots were designed, detonated, and recorded in an active pit at a mine in Arizona. The data acquired during the experiment have allowed us to further examine the excitation of *Rg* from explosions, specifically in and below a topographic bench at the mine.

Only four of the above-mentioned shots (Shots 6–9) are considered in this paper. All four shots were loaded similarly to typical production shots at the mine. Their source characteristics are tabulated in Table 1. Shots 6 and 7 were detonated in the pit below the bench, while Shots 8 and 9 were detonated in the bench and experienced the effects of the free face. The data used in this study were recorded on a network of 130 vertical single-component seismic stations (Texans), which were set up along roads in the mine at varying azimuths from the SPE shots, and at distances ranging from 1.5 to approximately 13 km. See Leidig *et al*. (2004) in these proceedings for a summary.

Table 1. Origin data for a subset of the Black Mesa SPE shots

Name	Latitude	Longitude	Elev (m)	# Boreholes	Yield (lbs)	Depth (m)	Confinement
SHOT6	36.4583	-110.3053	2046	6	5708	15	Unconfined (in pit below bench)
SHOT7	36.4585	-110.3051	2046	3	3590	15	Unconfined (in pit below bench)
SHOT8	36.4581	-110.3051	2062	6	6094	15	Unconfined (in bench beside free face)
SHOT9	36.4584	-110.3049	2059	3	3290	15	Unconfined (in bench beside free face)

Figure 5 presents video captures of Shots 6 and 8, and demonstrates the surficial effects of detonating an explosion in the bench near the free face (Shot 8, lower plots) as compared with detonating an explosion in the test pit without a free face (Shot 6, upper plots). Both shots had yields of approximately 3 tons, and the video captures show that the vertical movement of the material for both shots is similar. However, we note that there is an additional component of horizontal movement for the explosion on the free face (Shot 8). Similar effects were noted for Shots 7 and 9, which were designed similarly to the blasts shown in Figure 6, but with approximately half the yield (see Table 1). The videographic data for Shot 7 were difficult to interpret due to obstruction of the camera.

Data Analysis The Texan data were processed as follows:

1) *Rg* was extracted from the Texan data using phase match filtering;
2) The data were corrected for geometric spreading and for attenuation to a normalization distance of 6 km, using 1-D velocity and attenuation models;
3) Spectral energies were estimated for both the corrected and uncorrected *Rg* waveforms for 0.5-1 Hz, 1-2 Hz, and 2-4 Hz,
4) Radiation patterns were plotted using both the attenuation-corrected data and uncorrected spectral energy ratios.

Figure 6 shows comparative radiation patterns for Shots 6 and 8 (top) and Shots 7 and 9 (bottom) using corrected spectral energies. The idea was to compare the shots in the bench to the shots in the test pit in order to tease out the effects of the free face. We computed moving averages of the energies and plotted them as solid lines to aid in the radiation pattern interpretation. The data have been corrected for attenuation and geometric spreading. Similar results were obtained using uncorrected data plotted as spectral ratios (Figure 7).

In the upper subplot of Figure 6, we show the comparison of the two ~3 ton explosions, with Shot 6 (gray) detonated in the pit and Shot 8 (black) detonated in the bench next to the free face. All three frequency ranges show the same phenomena. We observe that at azimuths in front of the face (i.e. in the direction of the test pit – the white area) the energies for Shot 8 (bench with free face) are equivalent to the energies of Shot 6 (pit). However, at azimuths behind the face (the gray area), we see a large increase in the energies for Shot 8 (by a factor of 1.5 at azimuths near the bench normal). This is most evident at 0.66 Hz, since the effects of variable attenuation to the east skew the analysis for 1.5 and 3 Hz. However, even with the attenuation model problems at these higher frequencies, it is obvious that the energies are greatly enhanced behind the free face for Shot 8 (bench with free face) at all three frequencies.

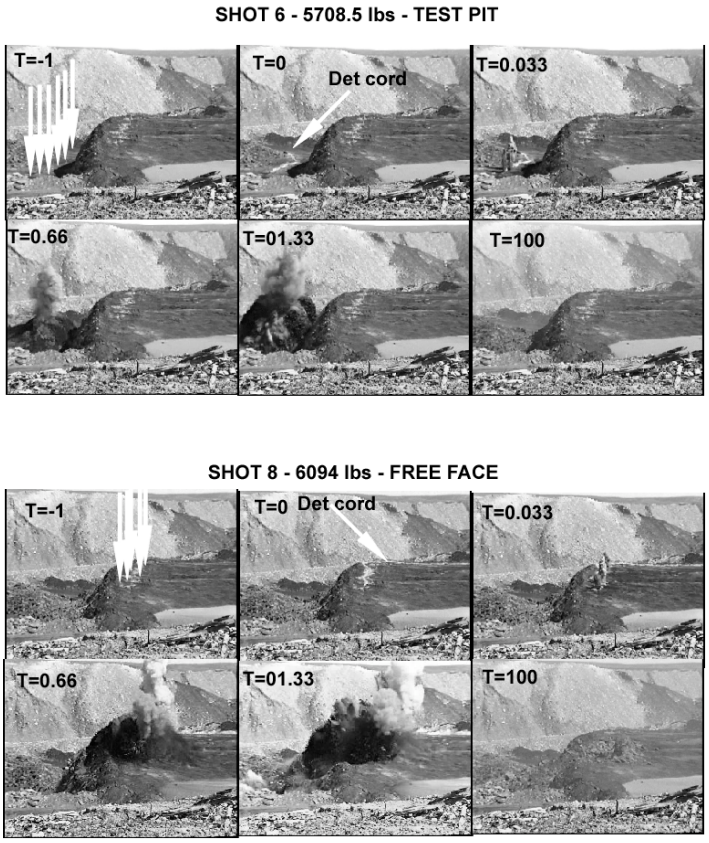


Figure 5. Video capture comparison of Shot 6 (in test pit) and Shot 8 (in bench / on free face).

A similar conclusion can be drawn from the comparison of Shot 7 (pit) and Shot 9 (bench with free face) shown in the lower subplot of Figure 6. In this case, the shots were both ~1.5 tons, detonated at the same depths as Shots 6 and 8. We see a bipolar radiation pattern for Shot 7, which is different from all of the other shots studied. We observe increased energy generation to the SW in this radiation pattern. As mentioned previously, our videographic data for this shot were difficult to interpret due to blockage by the free face and debris from previous blasts. It is possible that this shot did not detonate as designed, given that the alignment of the radiation pattern is parallel to the line of boreholes. When these problems with Shot 7 are taken into account, we see that Shot 9 and Shot 7 had similar energies in front of the free face; however the Shot 9 energies behind the free face are again 1.5 times larger than the energies in front of the free face.

Figure 6 also shows that the radiation patterns change as a function of frequency. This suggests that the explosion sources at Black Mesa (and probably elsewhere) were not simple isotropic explosions. We also note that the scatter in the energies is increased at higher frequencies. This is due to small-scale heterogeneities, and it invalidates the assumption that a 1-D velocity and attenuation model is appropriate at Black Mesa. This is not unexpected, given the geologic setting; however there isn't enough data to develop a 2-D or 3-D attenuation model.

Figure 7 shows plots similar to Figure 6, but using uncorrected data plotted as spectral ratios. The solid lines represent the theoretical Mueller-Murphy spectral ratios for these shots. The left plot presents ratios between the two shots in the pit (Shot 7 / Shot 6), and the two shots on the bench (Shot 9 / Shot 8). Both spectral ratio patterns are close to circular, indicating that the energies of the compared shots are similar. We also see evidence of increased energy generation in the SW quadrant for Shot 7, as discussed earlier. The right plot presents ratios between the shots in the pit and the shots on the bench (Shot 8 / Shot 6 and Shot 9 / Shot 7). These ratios are decidedly not circular, indicating that the energies of the compared shots are not similar. For azimuths in the SW and NW quadrants, the observed ratios are very close to the theoretical ratios (~1). However, for azimuths in the NE and SE quadrants, the observed ratios are increased to greater than 1.5. Given that the approximate bench azimuth is NNE-SSW, the changes in these ratio patterns suggest that the free face is playing an important role in determining the *Rg* radiation patterns for these shots. These results, combined with the results shown in Figure 6, suggest that the *Rg* energies from shots fired on the bench are increased at azimuths behind the free face.

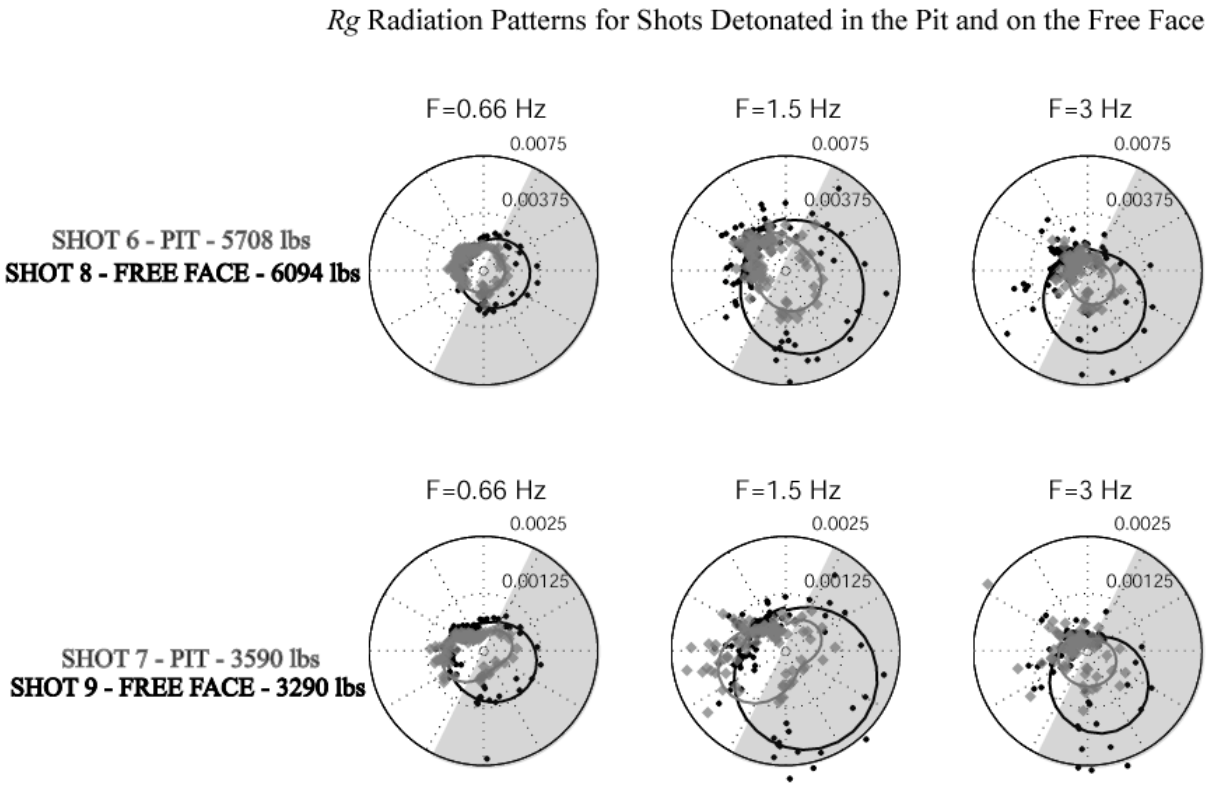


Figure 6. Azimuthal variations in *Rg* energy at 0.66 Hz (left), 1.5 Hz (middle) and 3 Hz (right) for Shots 6 and 8 (top) and Shots 7 and 9 (bottom). The white side of the circle is the pit, while the gray side is the bench. The line between white and gray shows the orientation of the free face.

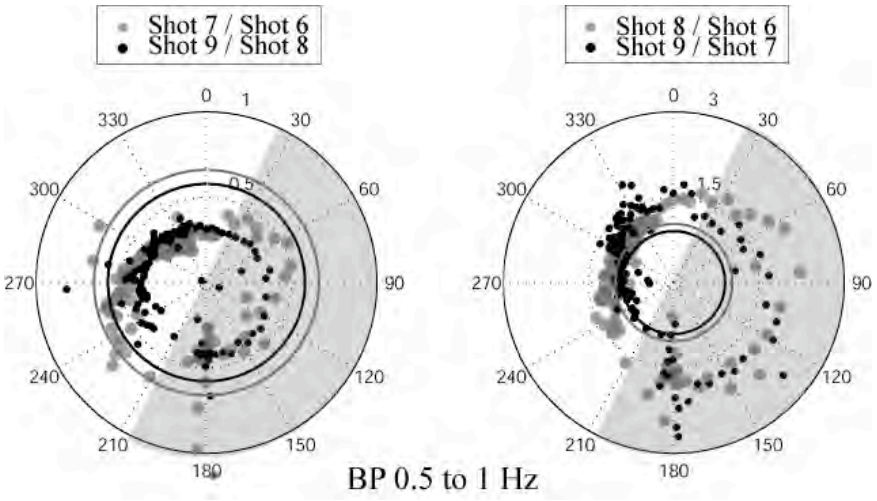


Figure 7. Station-based spectral ratios for combinations of Shots 6-9 in the bandwidth of 0.5 to 1 Hz. The gray and black circles represent the theoretical ratios based on Mueller and Murphy (1971) sources. The white side of the circle is the pit, while the gray side is the bench. The line between white and gray shows the orientation of the free face.

CONCLUSIONS AND RECOMMENDATIONS

Short-period surface waves generated by explosions contain important information about the properties of seismic sources. In the two research projects presented here, we show that a pure monopole source cannot model observed surface waves from chemical explosions at the Shagan Test Site and an Arizona coal mine. For the former, a combined monopole and CLVD source is required to model the surface wave phase and energy data, while for the latter, the effects of lack of confinement, horizontal spall, and non-linear free-face effects contribute to the observed anisotropic radiation patterns. In future research, we will seek to create more complicated models for these sources, in the hope of improving our understanding of the physical phenomena associated with small explosions.

REFERENCES

Bonner, J. L., D. C. Pearson, W. S. Phillips, and S. R. Taylor (2001), Shallow Velocity Structure at the Shagan River Test Site in Kazakhstan, *Pure Appl. Geophys*. 158, 2017-2039.

Bonner, J. L., H. Patton, A. Rosca, H. Hooper, J. Orrey, M. Leidig, and I. Gupta (2003), Aspects of *Rg* and *Lg* Generation from the Shagan Depth of Burial Explosions, in *Proceedings of the 25th Seismic Research Review - Nuclear Explosion Monitoring: Building the Knowledge Base*, LA-UR-03-6029, Vol. 1, 384-393.

Day, S. M. and K. McLaughlin (1991), Seismic Source Representation for Spall, *Bull. Seism. Soc. Am*. 81,191-201.

Denny, M. D. (1998), Seismic-source Corner Frequencies from the Depth of Burial Experiment, University of California, *LLNL Report No. UCRL-ID-132296*.

Denny, M. D. and L. R. Johnson (1991), The Explosion Seismic Source Function: Models and Scaling Laws Reviewed, in *Explosion Source Phenomenology*, Am. Geophys. Monograph 65, 1-24.

Dziewonski, A., S. Bloch and M. Landisman (1969), A Technique for the Analysis of Transient Seismic Signals,

Glenn, L. A. and S. C. Myers (1997), Depth of Burial Experiments at Balapan, University of California, *LLNL Report No. UCRL-ID- 128313*.

Gupta, I. N., W. W. Chan, and R. A. Wagner (1992), A Comparison of Regional Phases from Underground Nuclear Explosions at East Kazakh and Nevada Test Site, *Bull. Seismol. Soc. Am*. 82, 352-382.

Gupta, I. N., T. R. Zhang, and R. A. Wagner (1997), Low-frequency *Lg* from NTS and Kazakh Nuclear Explosions - Observations and Interpretation, *Bull. Seism. Soc. Am.* 87, 1115-1125.

Knopoff, L. and M. J. Randall (1970), The Compensated Linear-Vector Dipole: A Possible Mechanism for Deep Earthquakes, *J. Geophys. Res*. 75, 4957-4963.

Landisman, M., A. Dziewonski, and Y. Sato (1969), Recent Improvements in the Analysis of Surface Wave Observations, *Geophys. J. R. Astron. Soc*. 17, 369-403.

Leidig, M., J. Bonner, and H. Hooper (2004), Development of Velocity and Attenuation Models for Black Mesa and Eastern Arizona. *Weston Geophysical Corporation Technical Report, 29p.*

Masse, R. P. (1981), Review of Seismic Source Models for Underground Nuclear Explosions, *Bull. Seism. Soc. Am.* 71, 1249-1268.

Mueller, R.A. and J.R. Murphy (1971), Seismic Characteristics of Underground Nuclear Detonations, *Bull. Seism. Soc. Am.*, 61, 1675-1692.

Myers, S. C., W. R. Walter, K. Mayeda, and L. Glenn (1999), Observations in Support of *Rg* Scattering as a Source for Explosion *S W*aves: Regional and Local Recordings of the 1997 Kazakhstan Depth of Burial Experiment, *Bull. Seism. Soc. Am.* 89, 544-549.

Patton, H. J. and S. R. Taylor (1995), Analysis of *Lg S*pectral Ratios from NTS Explosions: Implications for the Source Mechanism of Spall and the Generation of *Lg* Waves, *Bull. Seism. Soc. Am.* 85, 220-236.

Patton, H. (2004), *Rg* Excitation by Underground Explosions: Insights from the Balapan DOB Experiment. *Weston Geophysical Corporation Final Report. DE-FG02-00ER83123.*

Pearson, D. C., L. A. Glenn, M. D. Denny, and W. S. Phillips (1997), The Source Depth of Burial Experiment at Shagan River, Kazakhstan, Ext. Abstr., University of California, *LLNL Report No. UCRL-JC-131190*.

Saito, M. (1967), Excitation of Free Oscillations and Surface Waves by a Point Source in a Vertically Heterogeneous Earth, *J. Geophys. Res*. 72, 3689-3699.

Stump, B. W. (1985), Constraints on Explosive Sources with Spall from Near-Source Waveforms, *Bull. Seism. Soc. Am.* 75, 361-377.

von Seggern, D. and R. Blandford (1972), Source Time Functions and Spectra for Underground Nuclear Explosions, *Geophys. J. R. Astron. Soc*. 31, 83-97.

SOURCE PHENOMENOLOGY EXPERIMENTS IN ARIZONA

Mark R. Leidig[1], Brian W. Stump[2], Jessie L. Bonner[1], Christopher T. Hayward[2], Aaron A. Velasco[3], Diane F. Baker[4], Heather Hooper[1], William R. Walter[5], Xiaoning (David) Yang[4], Rongmao Zhou[2], CL Edwards[4], Marie D. Renwald[2], and James F. Lewkowicz[1]

Weston Geophysical Corporation[1], Southern Methodist University[2], University of Texas at El Paso[3], Los Alamos National Laboratory[4], and Lawrence Livermore National Laboratory[5]

Sponsored by National Nuclear Security Administration
Office of Nonproliferation Research and Engineering
Office of Defense Nuclear Nonproliferation

Contract No. DE-FC03-02SF22638[1], 021364[2], 26-8210-14[3], FIA 02-048-A001[4], L-9783[5]

ABSTRACT

During the summer of 2003, Weston Geophysical, Southern Methodist University, the University of Texas at El Paso, Los Alamos National Laboratory, and Lawrence Livermore National Laboratory formed a consortium to quantify the differences between contained single-fired chemical explosions (a surrogate for nuclear tests) and delay-fired mining explosions. We designed, detonated, and recorded ten single-fired explosions at a copper mine in southeastern Arizona and nine single-fired explosions in the northeastern Arizona coal mining district. Delay-fired mining explosions at each mine were also recorded. The single-fired explosions ranged in size from 91 to 15,000 kg. The purpose of these experiments was to examine the source functions of single- and delay-fired explosions and to quantify near-source phenomenology and its role in the generation of shear waves observed at regional distances. A diverse set of instruments were deployed including high-g accelerometers within the nonlinear zone, high-frequency velocity instruments to document the transition from near source to regional, and broadband portable instruments to supplement permanent regional seismic stations. In addition, detailed refraction surveys were conducted in and around the source region to constrain local material properties. The refraction data document the effects of weathering in both the granitic (copper) and sedimentary (coal) rocks in and around the sources. Accelerometer data characterize the failure of the near-source materials in spall. High-frequency velocity instruments in the 1 to 100 km range capture the generation of strong shear arrivals, in addition to *P* waves, and their development into surface waves. The near-source and local data have extensive azimuthal coverage and have allowed the development of velocity and attenuation models for both test sites, as well as moment tensor inversions, which are being completed. The broadband instruments record the regional propagation of the *P*, *S* (*Lg*), and *Rg* phases and allow examination of *S/P* discriminants for single-fired and mining explosions. Differences between the single-fired and delay-fired explosions are noted and linked to the extended source duration of the production mining explosions.

OBJECTIVES

During the summer of 2003, Weston Geophysical, Southern Methodist University, the University of Texas at El Paso, Los Alamos National Laboratory, and Lawrence Livermore National Laboratory formed a consortium to quantify the differences between contained single-fired chemical explosions (a surrogate for nuclear tests) and delay-fired mining explosions. The objectives of our project include: 1) defining the fundamental source physics that govern energy partitioning among regional seismic phases, 2) identifying possible sources of *S*-wave generation for different types of explosions, 3) determining the effects of depth of burial, yield, and containment on the source function for contained chemical explosions, 4) completing moment tensor inversions for source properties, 5) performing discrimination between nuclear explosions, mining explosions, and earthquakes, and 6) determining whether regional signals from routine delay-fired explosions can be used to gauge anticipated signals from small nuclear explosions. We conducted the SPE at a coal (soft-rock) and copper (hard-rock) mine in Eastern Arizona because it allowed us to examine different propagation paths and geologic setting.

RESEARCH ACCOMPLISHED

Experiment Location and Design

We designed, detonated, and recorded ten single-fired explosions at a copper mine in southeastern Arizona and nine single-fired explosions in a northern Arizona coal mine. The single-fired explosions ranged in size from 91 to 15,000 kg. Delay-fired mining explosions at each mine were also recorded. We deployed a large range of instruments including high-g accelerometers within the nonlinear zone, high-frequency velocity instruments to document the transition from near-source to regional, and broadband portable instruments to supplement permanent regional seismic stations. We carried out detailed refraction surveys in and around the source region to constrain local material properties. Accelerometer data characterize the failure of the near-source materials in spall. High-frequency velocity instruments in the 1 to 100 km range capture the generation of strong shear arrivals, in addition to *P* waves, and their development into surface waves. Short-period, near-source, vertical-component sensors ("Texans") provide complete azimuthal coverage of the shots. Figure 1 shows the mine locations and stations deployed to record the explosions.

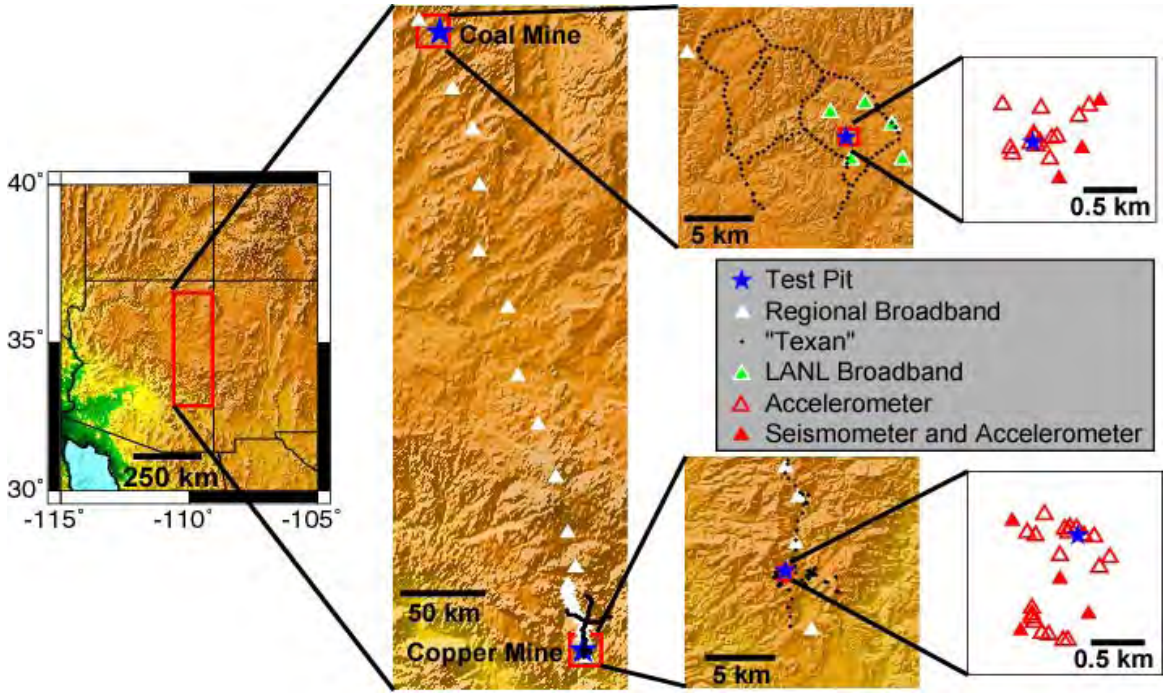


Figure 1. Location map for the SPE mines and stations deployed.

Source Phenomenology Experiments at a Coal Mine in Northern Arizona

The explosions at the coal mine in northern Arizona consisted of two fully confined and seven unconfined single-fired chemical explosions recorded on many of the stations shown in Figure 1. Additionally, a database of 18 mining production shots was also recorded by the broadband stations in the mine and at regional distances. Two of the unconfined shots were detonated in a topographic bench next to a free face. An example of an unconfined ~ 7-ton explosion detonated at a depth of 20 meters is shown in Figure 2. Our research on this important dataset has focused on the following areas:

1. Developing velocity and attenuation models of the Black Mesa basin and Colorado Plateau for moment tensor inversion,
2. Quantifying shear-wave generation from the single-fired explosions,
3. Examining the effects of confinement on explosion amplitudes and radiation patterns, and
4. Developing discriminants based on the observed differences between single-fired chemical and delay-fired mining explosions.

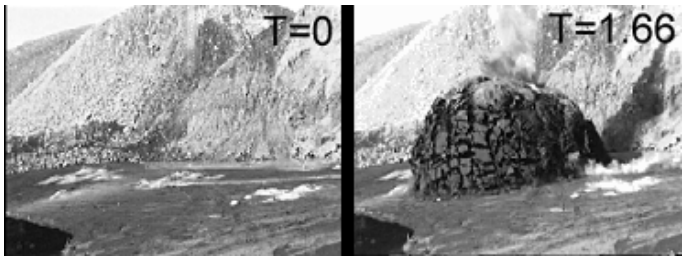


Figure 2. Images from northern Arizona SPE shot 4 taken just before detonation and 1.66 seconds after. This underburied shot lifted a dome of shattered rock more than 10 meters high.

Velocity and Attenuation Structure. We developed a detailed velocity and attenuation structure in order to complete moment tensor inversions and waveform modeling. For the northern Arizona coal mine, we used shallow refraction data to resolve the explosion test bed *P*-wave velocity and layer thicknesses. We also used 130 "Texans" at distances less than 15 km and the regional broadband stations to study the *P*-wave velocity structure of the upper crust (Figures 3a and 3b). Moment tensor studies also rely heavily on an adequate description of the shear-wave velocity structure, thus we considered ground roll (Figures 3c and 3d) and *Rg* inversion studies (Figures 3e and 3f) for *S*-wave velocity structure of the test pit region and upper crust. We also performed a joint inversion of surface wave dispersion and receiver functions using the software of Herrmann (2002) to constrain the structure in the middle and lower crust. Finally, a Q_β model for the upper crust was developed from observed *Rg* attenuation on the Texan and broadband datasets (Bonner *et al*., 2004).

Shear-Wave Generation. One of the research objectives of this study was to quantify the possible sources of explosion-generated shear waves. Our preliminary studies aimed at accomplishing this goal have been in identifying *S*-waves on our datasets and examining the spectral ratios for the *S*-waves for the various blasts. The northern Arizona SPE shots generated significant shear-wave motion as evidenced in Figures 4a and 4b. On the vertical-component Texan recordings (Figure 4a), the *P*-wave and *Rg* arrivals are easily identified and are traveling at apparent velocities of 2.7 km/sec and 1 km/sec, respectively. There are additional arrivals that we delineate on the figure as possible *S*-wave arrivals. The apparent velocity for the phase is approximately 1.8 km/sec; however, we note that tracing the arrival times of this phase back to the origin results in ~1 second of offset in the origin time of this phase. Some may want to attribute this delay to near-source scattering while others may argue the delay is caused by secondary source effects (e.g., spall or CLVD). It may take a detailed analysis of the prominent Love waves (Figure 4b); including an examination of any Love-wave phase delay, to determine the source of the SPE shear-wave arrivals. It is interesting to note that the largest amplitude Love waves are not associated with the largest yield explosions, but instead are observed on the blasts in the topographic bench next to an unconfined free face.

Local Comparisons of Delay-Fired Mining Explosions vs. Single-Fired Chemical Explosions. There are numerous physical and chemical differences between nuclear and mining explosions. Perhaps the most obvious difference is that one involves a nuclear reaction and the other is a chemical reaction, which for our study involved Ammonium Nitrate Fuel Oil (ANFO) explosives. The 1993 NPE chemical kiloton explosion at NTS established that single-fired contained chemical explosions could be used directly as surrogate nuclear tests for the purposes of calibrating regional discriminants (e.g. Walter et al., 1995), and that it would be very difficult to differentiate

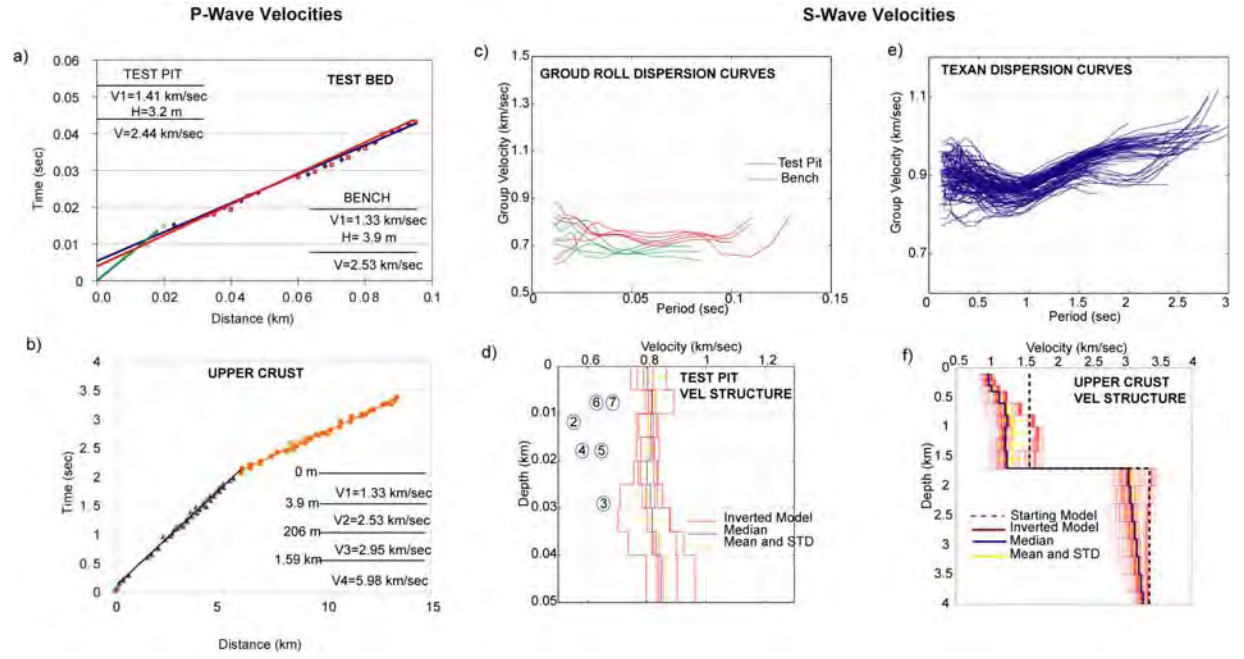


Figure 3. Data and models used to constrain the SPE test bed in northern Arizona. a). First arrival data from a 20-channel seismic refraction profile completed in the test bed and topographic bench. b). First arrival data for 130 "Texan" recordings used to develop a velocity model of the upper crust. c). Group velocity dispersion curves from ground roll observed on the 20-channel seismograph system. d). Inversion of ground roll dispersion curves for test bed shear-wave velocity structure. The explosion depth is indicated by the respective shot number on the plot. e) Short-period, fundamental-mode Rayleigh wave (*Rg*) group velocity dispersion curves for 130 Texan recordings. f). Inversion results for the *Rg* dispersion curves.

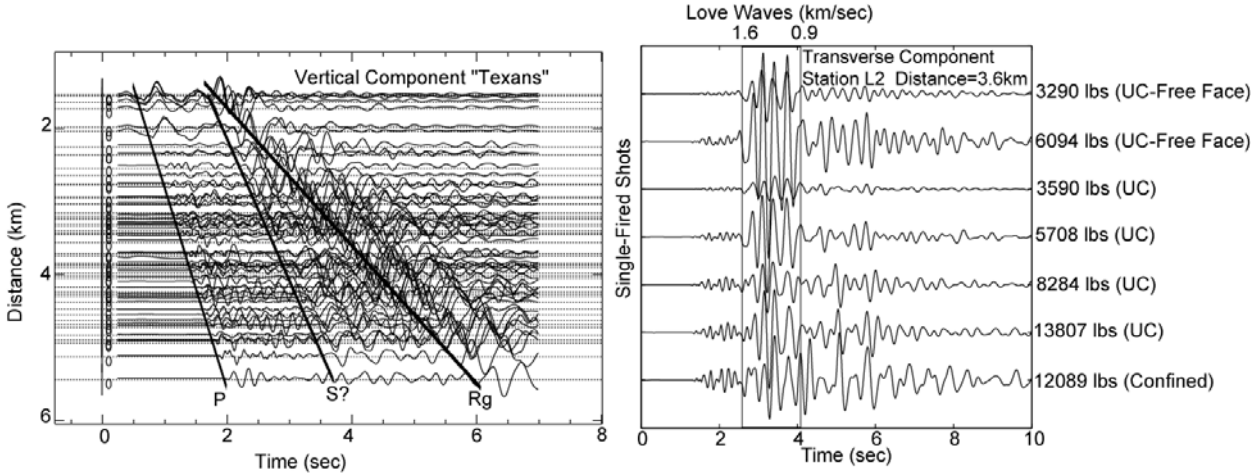


Figure 4. Shear-wave arrivals from the SPE shots in northern Arizona. a). Record section of "Texan" recordings showing *P*, *Rg*, and a possible *S*-wave arrival. b). Transverse component recordings of 7 SPE explosions at a single broadband station showing large amplitude Love-wave arrivals.

between the two types of explosions based on seismic data alone. Another important difference between nuclear and mining explosions is that mining explosions are rarely detonated simultaneously. For example, a typical mining explosion observed at regional distances may contain over 400,000 lbs. of ANFO; however, it may be detonated over a period of 2-4 seconds. The effect of this "delay-firing" technique is to fracture the rock as required for the

mining operations while limiting ground vibrations in order to prevent damage to nearby structures. A final difference between the two explosions involves confinement. Underground nuclear explosions are often buried beneath several hundred meters of rock to ensure that the explosion is fully confined (e.g., minimal surficial effects from the explosion) and fully contained (no leakage of radioactive gases). Most mining explosions are detonated next to both vertical and horizontal free surfaces, resulting in significant surficial damage to the rocks, thus they are unconfined and uncontained.

The effects of delay-firing on local recordings of production shots are evidenced in Figure 5. The median velocity spectrum of five production shots (delay-fired yields ranging from 6.5 to 280 tons) recorded at local distances of 3.6±0.6 km show increased 0.3 to 2 Hz energy in both the vertical and transverse components when compared to the median spectrum for the seven SPE shots (single-fired yields ranging from 1.5 to 7 tons) recorded at a distance of 4 km. We note that the peak magnitude of the ground motion for the SPE and production shots are very similar; however, at this distance the peak ground motion for the SPE shots is a *P*-wave, while it is *Rg* and Love-waves for the production shots.

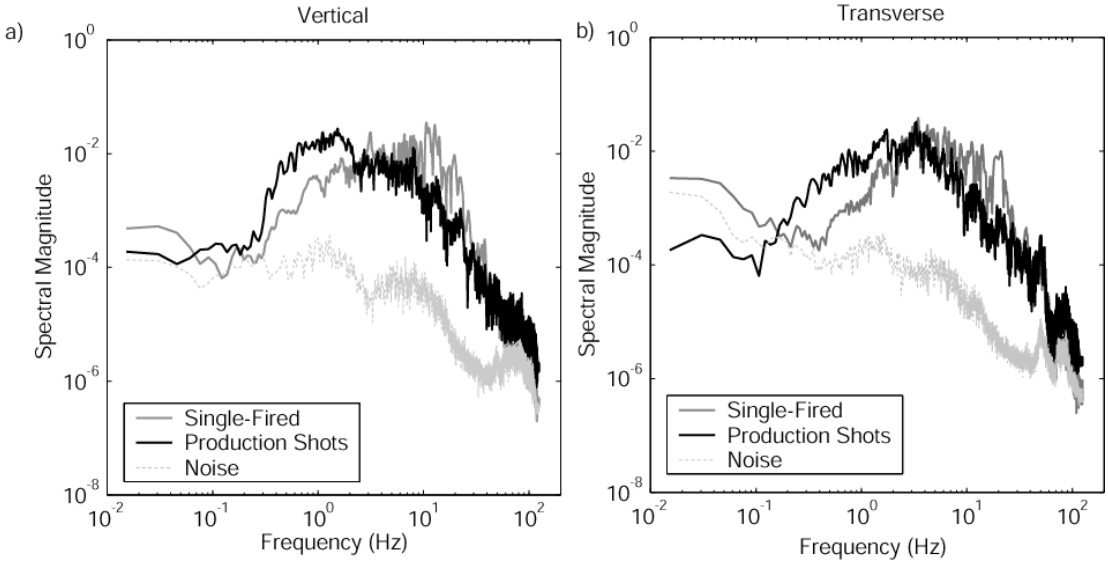


Figure 5. Spectral comparisons of delay-fired mining explosions and single-fired SPE shots. a). Median vertical component spectra for 5 production shots (black), 7 SPE shots (medium gray), and 7 pre-event noise estimates (light gray). b). Median transverse component spectra for same series of explosions and noise.

We have also examined the effects of confinement on the amplitudes recorded from the SPE experiment. As an example of this analysis, Figure 6 presents spectral ratios of Shot 3 to Shot 4 as recorded on the inner ring of the Texan network (see Figure 1). Shot 3 was a ~ 6-ton explosion detonated at 30 meters depth that was fully confined while Shot 4 was a ~ 7-ton explosion at 20 meters depth that was unconfined (see Figure 2). We used the Mueller and Murphy (1971) source to account for the differences in yield and depth of burial, and then simulated explosion synthetics in the velocity model described earlier. We formed the Shot 3/Shot 4 synthetic spectral ratio of the *P*-waves in five different frequency bands. The synthetic spectral ratios are plotted as solid black lines in the center of each plot in Figure 6. The observed spectral data in the same frequency bands are plotted as dots. The results show that at 1-2 Hz, 2-4 Hz, and 4-8 Hz, the observed *P*-wave ratios for Shot 3/Shot 4 are much larger than those predicted by the Mueller-Murphy sources. This is caused by lack of confinement (which videographic data confirms), improper shot detonation, or both. The degree to which the observed ratios differ from the theoretical ratios is dependent upon corner frequency effects, as by 8-15 Hz, the observed and theoretical ratios are similar. It is also interesting to note that the ratios are generally not circular (although the 8-15 Hz plot comes close), demonstrating that the unconfined Shot 4 and confined Shot 3 sources are different. Further analysis of the northern Arizona SPE data allowed us to calculate a set of “decoupling” factors, which quantify the amplitude decrease caused by lack of confinement. These decoupling factors vary widely over all frequency bands, and are frequency-

dependent with the largest decoupling factors occurring in the lower frequency bands (0.5 to 4 Hz). The decoupling factors are 1.1 to 4.8 for *P*, 1.1 to 4.3 for *S*, and 1.2 to 10.1 for *Rg*.

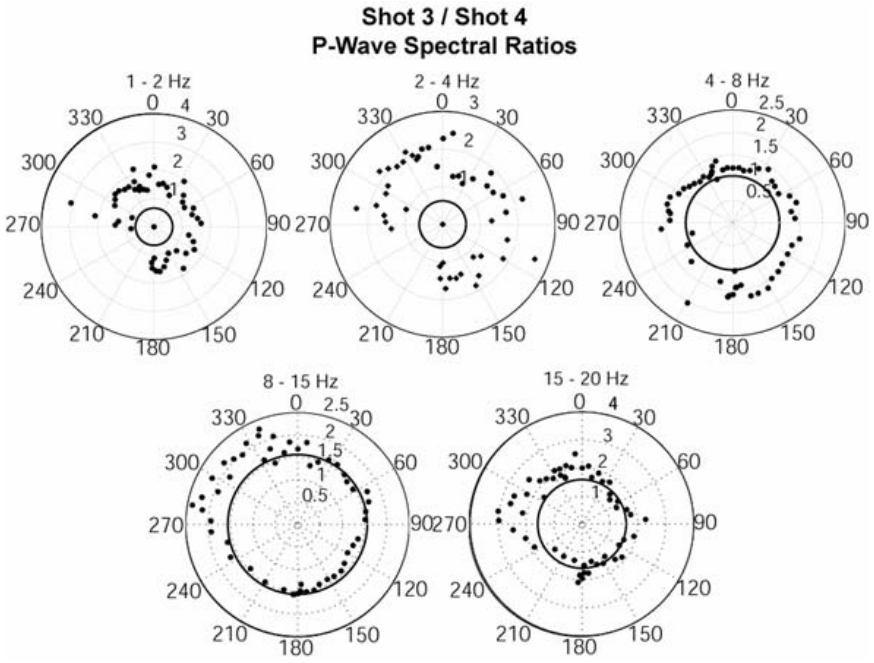


Figure 6. Shot 3 / Shot 4 plots showing theoretical (circles) and observed (dots) spectral ratios for *P*-waves in 5 frequency bands. Energy increases radially outward.

Single-Fired vs. Mining Explosion Spectral Amplitude Discriminant. We developed a regional station technique to discriminate between SPE single-fired chemical explosions and normal delay-fired mining explosions using spectral amplitude ratios of the *P* and *Lg* phases. The discriminant utilizes the equation:

$$D = \left[\frac{P(h) * Lg(h)}{P(l) * Lg(l)} \right]^2$$

where *P*(h) and *Lg*(h) are the average *P* and *Lg* amplitudes, respectively, between 4 and 8 Hz, and *P*(l) and *Lg*(l) are the average *P* and *Lg* amplitudes, respectively, between 0.5 and 1 Hz. Figures 7 and 8 plot the spectral amplitude of the *P* and *Lg* phases, respectively, of the SPE single-fired explosions and a closely located delay-fired mining explosion. The other delay-fired explosions have very similar spectra to the shown delay-fired explosion. The high frequency spectra have larger amplitudes than the low frequency spectra for the single-fired explosions, while the delay-fired explosions have the opposite relationship. The results of applying the above discriminant to explosions from the coal mine are shown in Figure 9. There is a clear separation between the two types of explosions. Initial results indicate the discriminant does not work for very large single-fired explosions such as nuclear explosions and the NPE due to the increased surface wave energy below 3 Hz.

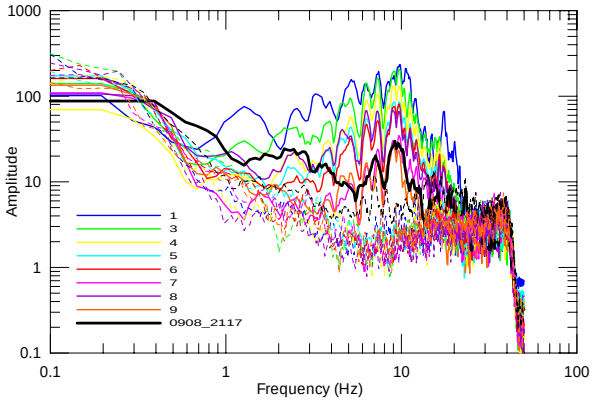


Figure 7. Vertical component *P* spectra of the single-fired shots and delay-fired production shot near the SPE test pit (heavy black line). Solid lines are the event spectra and dashed lines are pre-event noise spectra. Event and noise spectra have a 4-point smoothing applied.

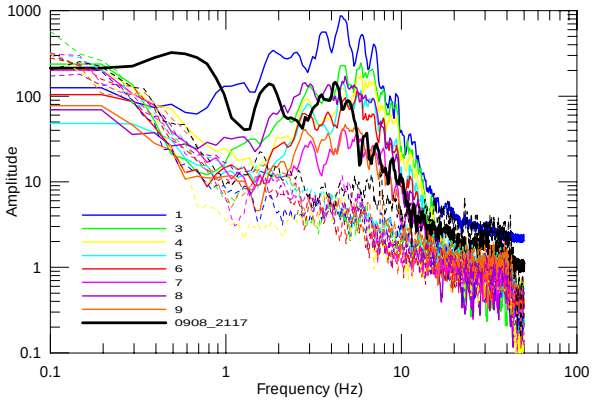


Figure 8. Transverse component *Lg* spectra of the single-fired shots and delay-fired production shot near the SPE test pit (heavy black line). Solid lines are the event spectra and dashed lines are pre-event noise spectra. Event and noise spectra have a 4-point smoothing applied.

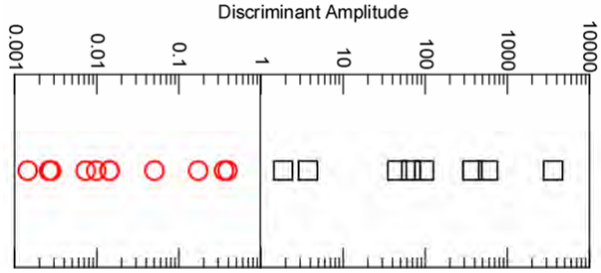


Figure 9. Single-fired (black boxes) vs. delay-fired (red circles) explosion discriminant results for the coal mine recorded at a regional station. A discriminant amplitude of 1 separates a single-fired from a delay-fired mining explosion.

Earthquake and Explosion (Chemical and Nuclear) Discrimination. Many seismic stations of monitoring interest have never recorded a regional distance nuclear test. Such tests were limited geographically mainly to the former test sites and temporally to the last century. Under the current global moratorium, the challenge to regional discriminant calibration is how to most effectively calibrate stations without nuclear test records. Many of these stations do record mining explosions and if clear physically based relationships between production mining explosions and nuclear tests were available, these events could be used to help calibrate regional discriminants.

We have started to examine the regional discrimination behavior of the SPE shots relative to normal production mining explosions, to natural earthquakes, and to previous nuclear tests at the Nevada Test Site. The analysis includes identifying and picking the onset arrivals of the regional phases *Pn*, *Pg*, and *Lg*, making amplitude measurements in a variety of passbands and then normalizing those measurements for the effects of source and path using the MDAC methodology (Walter and Taylor, 2002). LLNL has recently developed a sophisticated database oriented tool called RBAP (Regional Body-wave Amplitude Processor) that we use to complete the analysis. The tool allows interactive seismogram filtering, picking and phase window control needed for this analysis. We show in Figure 10 the results at KNB for six of the northern Arizona SPE shots (green diamonds) compared to a set of nuclear tests (red stars) and western U.S. earthquakes (blue circles). We find that the MDAC corrected SPE shots fall in the middle of the nuclear explosion population with very little variation due to the differing shot conditions. Thus for this particular discriminant at this station, the shots are good surrogates for nuclear explosions and the differences in depth of burial and single versus multiple shot have only a small effect on the discriminant measures. We are extending this analysis to other regional stations (e.g. ANMO, TUC, WUAZ) and other discriminants to more completely examine the discrimination relationship of these shots to production shots, earthquakes and nuclear tests.

Source Phenomenology Experiments at a Copper Mine in Southeastern Arizona

The explosions at the copper mine in southeastern Arizona consisted of four fully confined and six unconfined, single-fired chemical explosions recorded on many of the stations shown in Figure 1. Seven mining production shots were recorded by the stations. Many of the production shots consisted of multiple explosive arrays detonated over an extended time interval. Three of the unconfined shots were detonated in a topographic bench next to a free face. Our research to date on this important dataset has focused on the following areas:

1. Empirical determination of velocity models in the mine and their spatial variation,
2. Examination of the effects of confinement and yield on explosion amplitudes at close-in, near-source, and regional distances, and
3. Quantification of shear-wave generation and propagation from the single-fired explosions using a mixed set of instrumentation.

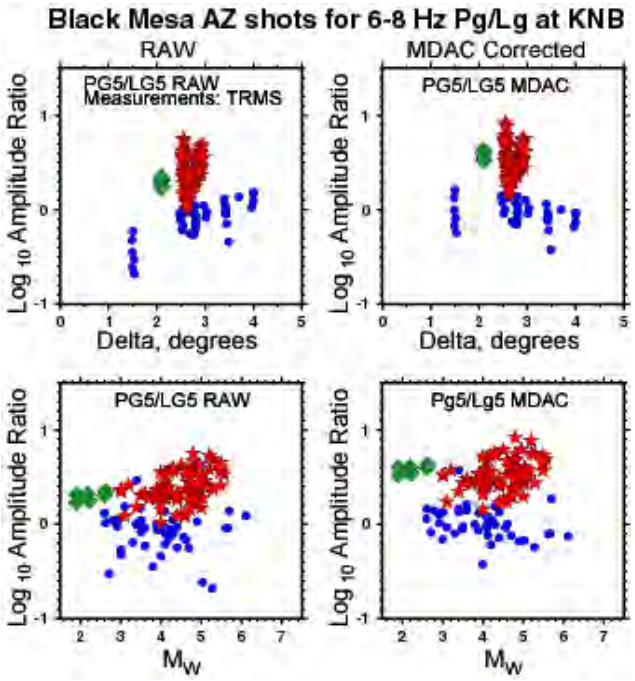


Figure 10. An example of six northern Arizona SPE shots (green diamonds) compared to Western U.S. earthquakes (blue circles) and NTS nuclear tests (red stars) at station KNB. Left-hand side shows the raw measurements as a function of distance (top) and magnitude (bottom). Right-hand side shows MDAC corrected measurements where magnitude and distance trends have been corrected, and earthquake data has near zero mean value. The MDAC values are based on the earthquake data only and then applied to the explosion data. Note that the SPE explosions fall right near the middle of the nuclear explosion values, indicating for this discriminant, they are reasonable surrogates for nuclear tests.

Development of a Velocity Model. A series of refraction surveys were conducted at the copper mine. The goals of the in-mine refraction study included: (1) Testing of procedures to gather shallow seismic survey data in a noisy mine environment; (2) Assessment of shallow (~ top 30 meters) velocity structure within the mine; (3) Determination of the variability of this structure both within an SPE test site and between different locations within the mine; (4) Determination of the relationship between the seismic structure and the test site geology. The test site where the SPE tests were conducted was one of those characterized.

Two orthogonal 300 foot lines of 40 Hz geophones were deployed at each site so that they crossed at the center. This geometry was employed to assess the three dimensional variation at each site. Sources were placed at each end of 30-geophone line. A Betsy seisgun was used as a set of sources at the surface for shallow structure, and a small explosive source at approximately 10-foot depth to resolve the deeper structure. Two benches of material have been removed between the time of the SPE and the refraction survey. The depth of the deepest blast conducted during the SPE was at 120 feet, close to the level of the refraction survey. The results from all the refraction surveys at North Coronado are summarized in Figure 11.

The north to south surveys produced a model with a very low velocity (1,900-2,200 ft/s) shallow layer (13-18 ft), an intermediate layer (~60 feet) with degraded velocity (8,000-10,000 ft/s) and finally the competent granite velocity (~15,000 ft/s). The length of the line and the size of the Betsy source made the imaging of the deepest layer difficult and so the estimate of its depth and velocity is the most uncertain. The structure along the west to east line is more complex,

possibly reflecting the effect of a high-wall to the east. As indicated in Figure 11, the west end of the line produced a structure similar to the north-south line. As one moves towards the east the travel time indicates a significant decrease in the second layer velocity at the 180 foot offset. As indicated in the summary results in Figure 11, the Betsy source at the center of the east to west lines produced quite different models to the west and east of the center point with the model to east producing the much slower intermediate layer velocity, possibly showing the effects of the free face.

Refraction surveys from four sites across the copper mine, including the SPE location, have been analyzed. The models at all the sites produce evidence for a very thin, low velocity zone, possibly reflecting damage from explosions conducted in the bench above the surface. A second layer of greater thickness was also imaged with reduced velocities from competent granite. The fastest material, with velocities between 15,000 to 17,500 ft/s, was found at depths from 60 to 80 feet. All refraction surveys that were conducted away from the bench free face produced nearly plane layer models. Dips of 0.5 to 1.5^{o} were observed. The refraction survey at North Coronado approached the free face along the bench. This refraction survey produced evidence of lateral velocity changes with the velocity slowing as the line approached the free face.

These velocity models will be the starting place for the development of propagation path models for the source inversion. They illustrate the range of materials and strengths in which the single-fired shots were detonated. These effects will have to be taken into account in assessing coupling and source characterization as a function of source depth and proximity to the free face. The next step is the utilization of the high-frequency surface waves for constraining the complementary shear structure.

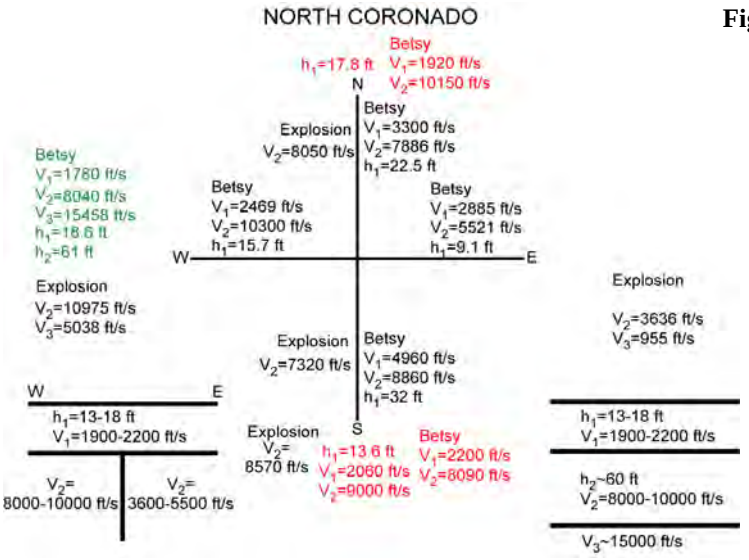


Figure 11. Summary of the refraction survey at North Coronado. The data suggests that there is some asymmetry in the structure. It also suggests that there is a lateral change in structure as one moves from west to east and approaches the free face where the velocity decreases in the intermediate layer as indicated in the model to the left. The model to the right is more representative of the structure away from the free face.

Effect of Yield and Confinement. The effect of yield and coupling on the close-in accelerations (S1 ~0.5 km, Figure 12), near-source Texan seismograms (M1A8 ~ 1.5 km, Figure 13), and regional broadband seismograms (MR12 ~ 40 km, Figure 14) are documented. The left panel in each figure compares the effect of yield using the shots at twice normal depth of burial, including shots B4 (6800 lbs.), B6 (1700 lbs) and B10 (13600 lbs). There is a strong amplitude variation from the three shots, which is also reflected in the spectra. Close-in, near-source, and regional observations document similar scaling. Spectral comparisons illustrate the differences in the close-in accelerometers, Texan geophones (4.5 Hz corner), and broadband regional instruments. The close-in data for all three shots peak at 10 Hz or above, indicative of the source corner frequency. This source corner is obscured by propagation path effects at greater distances and motivates the determination of the path effects, in particular, attenuation effects in order to interpret the waveforms.

The right panel in each figure compares the effect of confinement on the seismic waveforms. All the shots contained 6800 lbs. of explosives. The data displayed include Shot B2 (shot at the free face), B4 (twice normal burial depth) and B5 (twice burden but normal burial depth). The detonation of B2 resulted in a significant amount of material at the free face being moved into the mine pit. B4 created a large crater. There was little permanent displacement at the surface following the detonation of B5. These significant free surface differences are not reflected in the seismic observations. As the three figures document, the waveforms are very similar for the three shots. The shot with the greatest depth does have the highest amplitudes with about a factor of two variations in peak amplitudes.

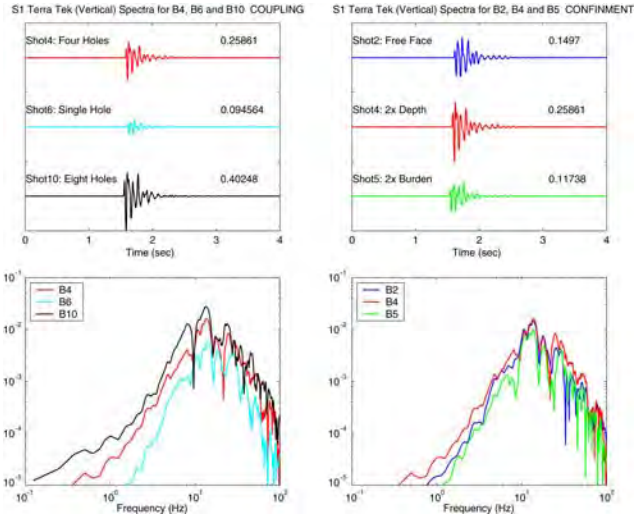


Figure 12. Close-in accelerograms from B4, B6, and B10 (left) and B2, B4, and B5 (right). Effect of yield is illustrated to the left and effect of confinement on the right.

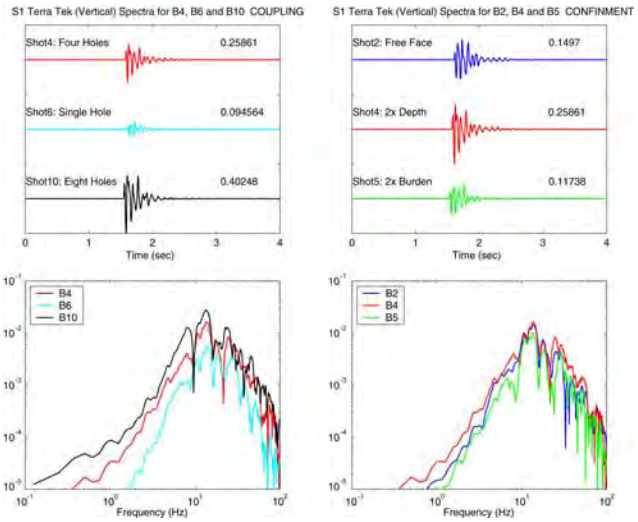


Figure 13. Near source Texan data from B4, B6, and B10 (left) and B2, B4, and B5 (right). Effect of yield is illustrated to the left and effect of confinement on the right.

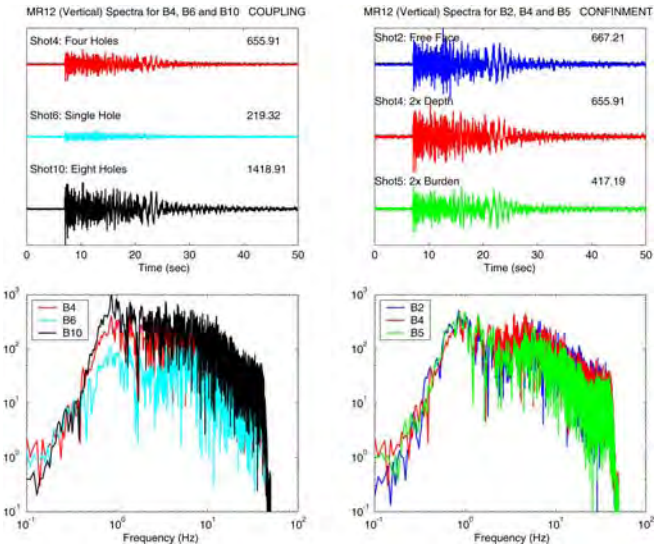


Figure 14. Regional broadband data from B4, B6, and B10 (left) and B2, B4, and B5 (right). Effect of yield is illustrated to the left and effect of confinement on the right.

Shear Generation and Propagation. One of the goals of these experiments was the quantification of generation and propagation of shear energy from the single-fired and delay-fired explosions. The shear energy includes both the direct shear arrivals and surface waves, R_g, at near-regional distances. In order to quantify these effects, a combination of Texans and broadband seismometers were deployed around the mine and along a profile to the north of the mine (Figure 1). The first step in the study was to assess the two types of instruments. Along the profiles to the north, there were co-located Texans (4.5 Hz nominal corner) and broadband Guralp seismometers (40T). The vertical component of broadband seismometers (Guralp 40T) was compared with collocated "Texans" to quantify the signal bandwidth. The broadband sensor has a 30 seconds natural period, 800V/m/s sensitivity and the short period Texans' sensor has a 4.5 Hz low cut corner and 91V/m/s sensitivity. The instrument responses of these sensors were removed from the raw data. A Hanning window was applied for the noise and signal data segments followed by spectral estimation (Figure 15). It is found that the noise level of the broadband seismometer is greater at high frequency (> 7 Hz) than that of the short period sensor in some cases. Therefore, the data quality of short period sensors is better at high frequency.

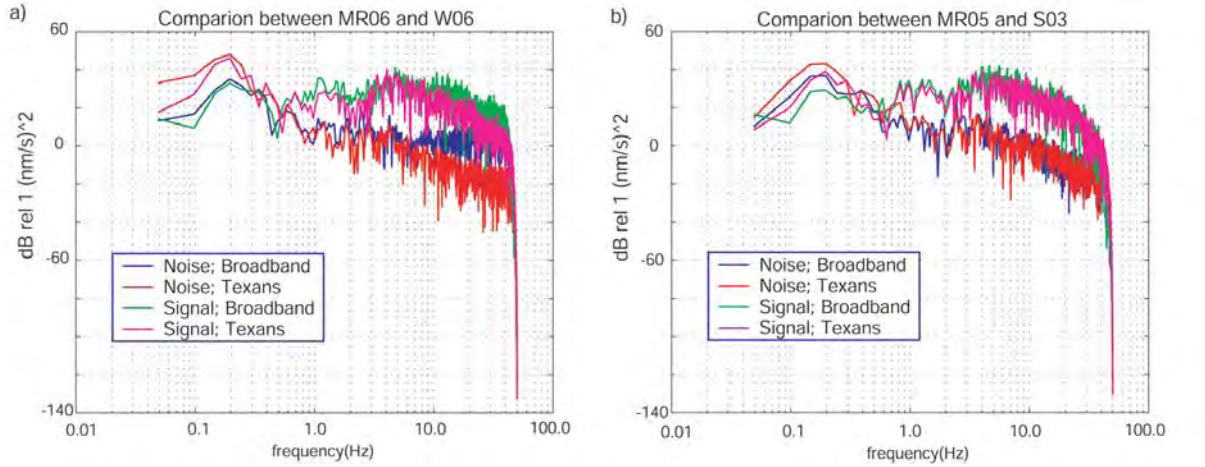


Figure 15. Spectral comparison between broadband CMG-40T and Texans after instrument correction. a). The noise level of the broadband (MR06) is higher than that of the collocated Texan (W06) at high frequency. b). The spectrum of the broadband (MR05) is identical with Texan (S03).

Based on this assessment, all the observational data along the line to the north of the mine was instrument corrected and a record section formed to assess shear wave generation and propagation path effects (Figure 16). Strong *P*, *S* and R_g phases are traceable back to the source. The R_g energy is strongest at the lowest frequencies (0.5 to 3 Hz). The *P* wave amplitudes are much larger than the shear amplitudes at high frequency, although, there is significant shear energy that is traceable back to the source. This data was used to estimate average *P*, *S*, and R_g velocities of 5.4 km/s, 3.0 km/s and 1.9 km/s respectively. Careful inspection of Figure 16 reveals that there is a break in the travel-time curve for *P* around 20 km, possibly indicative of upper crust structure.

These results illustrate the value of the Texans in both source and propagation studies from modest-sized explosions. The high-frequency content from the single-fired sources (> 0.5 Hz) and the increased high-frequency noise on some CMG-40T's makes the instrument-corrected Texan data very useful. Analysis of the delay-fired explosions may indicate the importance of the CMG-40T's since the longer duration source is expected to boost energy at the lower frequencies. The next step in this analysis is to explore the azimuthal radiation from these sources as was done at the northern Arizona coal mine. We also plan to explore the signals from the delay-fired shots using a similar analysis.

CONCLUSIONS AND RECOMMENDATIONS

The Arizona SPE experiments have resulted in an important dataset for the nuclear monitoring community. The 19 dedicated single-fired explosions together with multiple delay-fired mining explosions were recorded by one of the most densely instrumented accelerometer and seismometer arrays ever fielded, and the data have already proven useful in quantifying confinement and excitation effects for the sources. The results so far suggest that the single-fired explosions are surrogates for nuclear explosions in higher frequency bands (e.g., 6-8 Hz Pg/Lg discriminants). The datasets have also allowed us to develop a new discriminant to help separate small single-fired chemical and

delay-fired mining explosions based on the decreased 0.5 to 1.5 Hz energy in the small explosions. And finally, we have shown that the SPE shots, together with the mining explosions, are efficient sources of *S*-wave energy, and our next research stage is to postulate the possible sources contributing to the shear-wave energy. This will be completed through moment tensor inversions that make use of the detailed velocity structure obtained for the two SPE test sites.

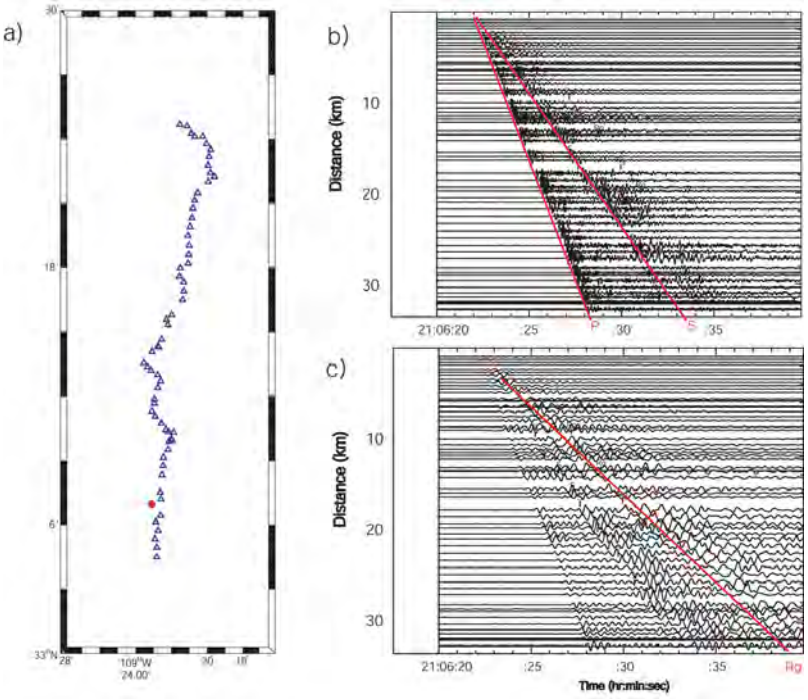


Figure 16. Texan record section from the fully confined single shot B10 (13,600 lb). The source (red dot) and station locations (blue triangles) are to the left. The record section in the upper right is filtered 0.7 to 20 Hz while that in lower right is filtered 0.5 to 3 Hz.

ACKNOWLEDGEMENTS

We would like to thank Bob Greshke, Steve Azevedo, and Glenn Gettemy (IRIS PASSCAL) who provided tremendous support in the field and helped process the Texan data correctly. James Britton (Weston Geophysical) helped to deploy the sensors. We would also like to thank the mine personnel for helping make this project as successful as it was.

REFERENCES

Bonner, J. L., H. Hooper, M. Leidig, D. Reiter, S. Azevedo, G. Gettemy, B. Stump, and J. Lewkowicz (2004), Getting the most out of a Texan, *Proceedings of the 20th Annual IRIS Meeting*, Tucson, AZ (June 10-12, 2004).

Herrmann, R. B. (2002), Computer Programs in Seismology Version 3.15, St. Louis University.

Mueller, R.A., and J.R. Murphy (1971), Seismic characteristics of underground nuclear detonations, *Bull. Seism. Soc. Am.*, 61, 1675-1692.

Walter, W. R., K. M. Mayeda, and H. J. Patton (1995), Phase and Spectral Ratio Discrimination Between NTS Earthquakes and Explosions, part I: Empirical Observations, *Bull. Seism. Soc. Am.*, 85, 1050-1067.

Walter, W. R. and S. R. Taylor (2002), A Revised Magnitude and Distance Amplitude Correction (MDAC2) Procedure for Regional Seismic Discriminants, Lawrence Livermore National Laboratory UCRL-ID-146882.

INTRAPLATE SEISMICITY AND THE DISCRIMINATION OF NUCLEAR TEST EVENTS USING AN UPDATED GLOBAL EARTHQUAKE CATALOG

Walter D. Mooney, Saskia M. Schulte, and Shane T. Detweiler

United States Geological Survey

Sponsored by National Nuclear Security Administration
Office of Nonproliferation Research and Engineering
Office of Defense Nuclear Nonproliferation

Contract No. DE-AT04-2000AL66517

ABSTRACT

In order to accurately discriminate the signatures of nuclear explosions from naturally-occurring seismic events, it is necessary to understand the frequency of earthquake occurrence, the stresses and mechanisms behind earthquakes in the regions of interest, as well as the properties of the crust in those regions. Areas of particular interest include many stable continental interiors such as the Gujarat Province of India, the Lop Nor test site in China, and the Semipalatinsk site in Kazahkstan. Such areas are often associated with intraplate seismicity. This seismicity must be identified and understood to discriminate suspect events and to serve as an accurate measure of ground truth. In this paper we present an updated earthquake catalog for Stable Continental Regions to examine the possible mechanisms of seismicity in these continental interiors. The last major global study of intraplate seismicity was the 1994 Electric Power Research Institute (EPRI) study, which included events up to 1990. Earthquake activity over the last 14 years therefore could not have been taken into account, a relatively long period considering that high-quality worldwide seismic monitoring only began in 1964. It is only from this year (1964) onwards that most M ≥ 4.5 events have well constrained locations, magnitudes and focal mechanisms.

We present an updated global catalog for Stable Continental Region (SCR) earthquakes that contains information on location, magnitude, seismic moment and focal mechanisms of 1373 M ≥ 4.5 crustal events from the year 495 to 2003. This is an increase of ~58% with respect to the last global study. This updated earthquake catalog, together with the recent publication of a catalog of rifts of the world provides an excellent opportunity to re-evaluate the correlation of earthquake activity and rifts on a global scale. This in turn will help us to further discriminate continental interior events that may be suspected nuclear events.

After removal of earthquakes that are considered to be non-tectonic, 1221 tectonic events were used for statistical analysis to re-evaluate the correlation of earthquakes with ancient rifts on a global scale. Earthquakes were then put into one of the following categories: interior rifts/ taphrogens (if located within ~20 km of identified ancient rift), rifted continental margins (if located within ~20 km of these rifted margins), or non-rifted crust (if located further than ~50 km of any of the above).

Our results are similar to those of previous studies, which found that 56% of all SCR earthquakes are associated with rifted crust. It is very important to note, however, that within continental interiors (i.e. excluding the rifted continental margins), more events in fact may be located within non-rifted crust. Of the 118 documented **M** ≥ 6.0 earthquakes, 30% are associated with interior rifts, 35% with rifted continental margins and 29% with non-rifted crust. However, the relative number of **M** ≥ 6.0 earthquakes in non-rifted crust increases from 29% to 32% and even 42% if we restrict the dataset to the instrumental or "complete" catalog events. Our earthquake database contains fourteen **M** ≥ 7.0 events, seven of which have occurred within interior rifts/taphrogens, six within rifted continental margins, and only one within non-rifted crust. Of these fourteen events, eight have been recorded instrumentally and are included in the "complete" catalog subset. Considering these eight events, two were located within interior rifts/ taphrogens and five within rifted margins. Due to the low number of samples, the statistics can be expected to change as more earthquakes occur.

OBJECTIVE

In order to accurately discriminate the signatures of nuclear explosions from naturally-occurring seismic events, it is necessary to understand the frequency of earthquake occurrence, the stresses and mechanisms behind earthquakes in regions of interest, as well as the properties of the crust in those regions. These study areas include many stable continental interiors where governments have been able to conceal their nuclear testing in relative secrecy, such as the Gujarat Province of India, the Lop Nor test site in China, and the Semipalatinsk site in Kazahkstan. Such areas are often associated with intraplate seismicity, and this seismicity must be understood both to discriminate suspect events, and to serve as an accurate measure of ground truth.

RESEARCH ACCOMPLISHED

In 1994, the Electric Power Research Institute (EPRI, 1994) published a benchmark global study on the seismicity in Stable Continental Regions. Stable Continental Regions (further referred to as SCRs) were defined as regions of continental crust that have not experienced any major tectonism, magmatism, basement metamorphism or anorogenic intrusion since the early Cretaceous, and no rifting or major extension or transtension since the Paleogene. The definition therefore is based on geology rather than seismic activity and uses the geological setting of the crust of the central and eastern United States as a reference. Although earthquakes are rare in SCRs, they have the potential to be large, thus making them excellent ground truth events.

Models that have been suggested to explain the occurrence of seismicity within continental interiors include localized stress concentration around weakened intrusions (Campbell, 1978), intersecting faults (Talwani, 1988, 1999) and ductile shear zones in the lower crust (Zoback, 1983). Fluids still present in the lower crust of ancient rift zones (Vinnik, 1989), and a weak zone in the lower crust (Kenner and Segall, 2000) have also been suggested. Liu and Zoback (1997) proposed the hypothesis that seismicity is related to elevated temperatures at depth. In their model plate-driving forces are largely supported by the (seismogenic) upper crust; the lower crust is weakened due to higher temperatures, and the cumulative strength of the lithosphere is reduced. Long (1988) suggested that intraplate seismicity is a transient phenomenon arising from a perturbation in crustal strength due to a disturbance in the hydraulic or thermal properties of the lower crust. Other models call for a perturbation of the regional stress field by forces associated with lithospheric flexure after deglaciation (Stein et al., 1979; Quinlan, 1984; Grollimund and Zoback, 2001), gravitational forces at structural boundaries (Goodacre and Hasegawa, 1980; Chandrasekhar and Mishra, 2002) or sediment loading (Talwani and Rajendran, 1991).

Many of the models for SCR seismicity listed above require features that are often found in ancient rifts: numerous large faults and intrusions, an anomalous crustal structure compared to the surrounding crust, rift pillows, and possibly remnant fluids. Thus the spatial correlation of some earthquakes with ancient rifts might be explained by the presence of these features. However, SCR seismicity is not unique to rift zones. Most of the models proposed have been based on case studies and have not been evaluated on a global scale, though a few that have show a correlation with ancient rifts (e.g. Sykes 1978; Johnston and Kanter, 1990; EPRI, 1994).

In this paper we use an updated earthquake catalog for Stable Continental Regions to examine the possible mechanisms of seismicity in these continental interiors. The EPRI (1994) study only included events up to 1990. Earthquake activity over the last 14 years therefore was not taken into account, a sizeable omission when considering that high-quality worldwide seismic monitoring only began in 1964, and that it is only from 1964 onwards that most $M \geq 4.5$ events have well constrained locations, magnitudes and focal mechanisms. This updated earthquake catalog, together with the recent publication of a catalog of rifts of the world (Sengör and Natal'in, 2001), provides an excellent opportunity to re-evaluate the correlation of earthquake activity and rifts on a global scale.

Figure 1 shows the seven main SCRs in the world: North America, South America, Africa (including the Arabian Peninsula), India, Eurasia, China (which consists of three smaller SCRs), and Australia. The Eurasian SCR has been subdivided into two regions. The region west of 20^{o} E will be referred to as Europe, whereas the region east of 20^{o} E will be referred to as Russia (Figure 1). In this paper we will discuss only the Indian, Eurasian and Chinese SCRs.

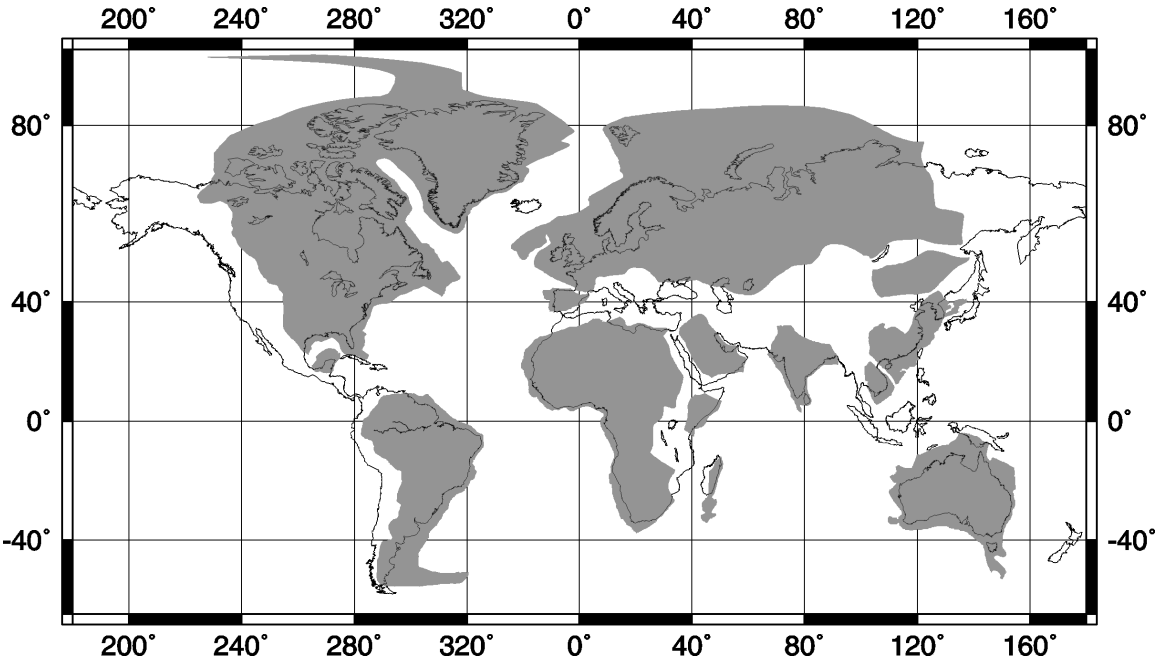


Figure 1. Stable Continental Regions (SCRs: light gray). Though there are seven large SCRs shown: North America, South America, Eurasia (subdivided into Europe; west of 20°E, and Russia, east of 20°E), Africa (including the Arabian peninsula), India, China (consisting of three separate SCRs) and Australia, we discuss only the Indian, Eurasian and Chinese SCRs here.

The earthquake catalog compiled for this study is available online at: http://earthquake.usgs.gov/scitech/scr_catalog.html. It contains crustal (maximum depth ≤ 45 km) events with Moment Magnitudes M ≥ 4.5 within SCRs. We chose not to restrict the catalog to the instrumental era (approximately from the beginning of the 20th Century), as, due to the relatively infrequent occurrence of large earthquakes in SCRs, such a restriction would severely limit the number of events to be included in the study. The catalog therefore includes documented historic events and instrumentally recorded events up to November, 2003. For each event, the epicenter, depth, Moment Magnitude, other reported magnitudes, and focal mechanism parameters (if available) are listed. The database contains 1373 events, which is an increase of approximately 58% with respect to the database developed for the EPRI (1994) report.

In order to have a sufficiently large dataset we did not restrict the study to the "complete" subsets of the earthquake catalog (Table 1). Magnitudes and locations of historic events, however, are often poorly determined. In addition, the time span over which events have been recorded varies greatly between, and in some cases even within, the different SCRs. The latter poses a problem with searching for spatial patterns in earthquake distribution, since these patterns may in fact reflect a difference in the time span of earthquake documentation and not in true seismic activity. In the analysis that follows we have therefore separately considered: (1) the entire earthquake dataset; (2) only instrumentally recorded events; and (3) events from the "complete" catalog (Table 1). The earthquakes for the various SCRs are presented in Figure 2.

Table 1. Subsets of the Compiled Earthquake Catalog that are considered "complete."

Period	*Magnitudes*
1900 – 2002	**M** ≥ 7.0
1964 – 2002	**M** ≥ 5.0

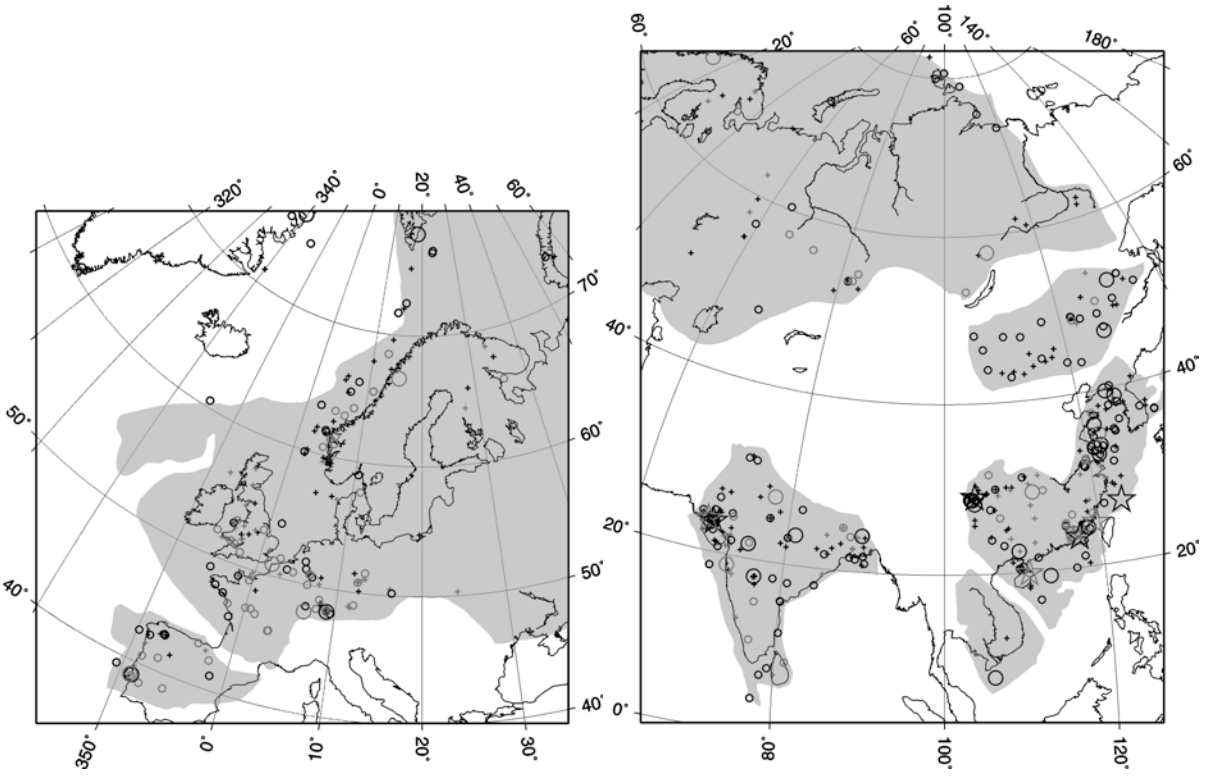


Figure 2: Earthquakes in the updated global database for different Eurasian SCRs. Events with an instrumentally-determined location and magnitude are denoted by circles, while historical events are denoted by crosses.

Taphrogens consist of a linked system of individual rifts and grabens. Interior rifts are sometimes referred to as "failed rifts", as stretching did not lead to sea floor spreading and therefore they are still surrounded by continental crust. Rifted continental margins are the regions of extended crust that form the transition from continental to oceanic crust. They are formed when extension leads to sea floor spreading.

The catalog of "Rifts of the World" (Sengör and Natal'in, 2001) is the most complete global listing of rifts and contains information on a rift's location, size, orientation, and age, as well as its placement among Sengör's (1995) hierarchical classification of geometry and dynamics. It was used in combination with the Exxon Tectonic Map of the World (Exxon, 1985) to determine a rift's exact location and extent. The Exxon (1985) map (eighteen sheets, each approximately 66 cm by 83 cm) is an unusually large-scale (1:10,000,000) map with a highly-detailed tectonic interpretation.

The inland boundaries of the extended margin regions were set at the most inland normal faulting identified at the edge of the continents. In regions where these could not be identified, the inland boundaries were based on interpolation, sudden transition on land from basement outcrop to sediment cover, gradients of sediment thickness, or the proximity of the boundary between SCR and oceanic crust. Interior rifts and their bounding faults were usually easily identified on the Exxon Tectonic Maps (Exxon, 1985). However, for some rifts in the Sengör and Natal'in (2001) catalog, it was difficult to establish the exact extent, or even to identify the rift at all on the Exxon (1985) maps.

The earthquakes of the compiled database were plotted onto individual sheets of the Exxon Tectonic Map of the World (Exxon, 1985). Based on their location, events were placed into one of five categories: (1) interior rifts/ taphrogens (within ~ 20 km from the bounding faults), (2) rifted continental margins (within ~ 20 km of rifted margins), (3) non-rifted crust, (4) possible interior rifts, and (5) possible rifted margins. In Figure 3 we have plotted the distribution of events over these five categories. In addition to considering the geographic distribution of the entire dataset, we also looked at the distribution of only the instrumentally recorded events (since they have much

better-determined estimates of location and magnitude) and the distribution of all events within subsets of the "complete" catalog (see section 2). Our tectonic analysis showed 27% of all earthquakes in the catalog being incorporated in the interior rifts/taphrogens category, 25% in the rifted continental margins and 36% in non-rifted crust categories (Figure 3a). 12% of the earthquakes were included in the possibly interior rifts category, 2% of which are earthquakes located in central west Europe that, as evidenced by extensive faulting and a very thin (≤ 30 km) crust, might actually be considered rifted (extended) crust.

Our results are similar to those of previous studies (Johnston and Kanter, 1990; EPRI, 1994), which found that 56% of all SCR earthquakes are associated with rifted crust. It is very important to note, however, that within continental interiors (i.e. excluding the rifted continental margins), more events in fact may be located within non-rifted crust (36% vs. 27%-37%). The numbers remain fairly constant if instrumental or only "complete" catalog earthquakes are considered (Figure 3b and 3c). Of the 118 documented **M** ≥ 6.0 earthquakes (Figure 3d), 30% are associated with interior rifts, 35% with rifted continental margins and 29% with non-rifted crust. However, the relative number of **M** ≥ 6.0 earthquakes in non-rifted crust increases from 29% to 32% and even 42% if we restrict the dataset to the instrumental or "complete" catalog events (Figure 3e, 3f). Our earthquake database contains fourteen **M** ≥ 7.0 events, seven of which (50%, Figure 3g) have occurred within interior rifts/taphrogens, six (43%, Figure 3g) within rifted continental margins, and only one (7%, Figure 3g) within non-rifted crust. Of these fourteen events, eight have been recorded instrumentally and are included in the "complete" catalog subset. Considering these eight events, two were located within interior rifts/ taphrogens (25%, Figure 3h/i) and five within rifted margins (62%). Due to the low number of samples, the statistics can be expected to change as more earthquakes occur.

Naturally, total seismic energy release is dominated by the largest events. Thus of the total seismic moment in SCRs included in the earthquake catalog, 67% is associated with interior rifts/ taphrogens, 24% with rifted continental margins, and 9% with non-rifted crust (Figure 3j). There is however a large uncertainty in these numbers, as the seismic moment of historic earthquakes is poorly determined. Of the seismic moment release from instrumentally recorded earthquakes (Figure 3k) 34% is associated with interior rifts, 45% with rifted continental margins, and 20% within non-rifted crust (36%, 47%, 16% respectively for the "complete" catalog subsets, Figure 3l).

In Figures 4a-c we have plotted all earthquakes according to tectonic category. It is evident that seismicity is not distributed evenly, but rather within each category certain regions exist in which seismicity is strongly concentrated. It should be noted that the active regions differ greatly in size. Concentration of seismicity is particularly strong for earthquakes that are associated with interior rifts and taphrogens, including the Kutch rift, India and the East China Taphrogen, for which several **M** ≥ 7 events have been documented (Figure 4b). We shall examine these in greater detail below.

It should be noted that the East China Taphrogen is a very extensive structure: it comprises a large part of the China SCR. Within non-rifted continental crust seismicity is more diffuse. There are however several regions that seem to show a higher level of seismic activity with respect to their surroundings (Figure 4c). These regions account for 70% of the total seismic moment release, but comprise only 26% of the total events in the category.

Unfortunately, a large part (24% of all **M** ≥ 4.5, 31% of all **M** ≥ 6.0, and 43% of all **M** ≥ 7.0 events) of the earthquake database used for analysis consists of historical earthquakes. If we restrict the dataset to the instrumental era or to the "complete" catalog subsets, the majority of the regions considered to be relatively seismically active no longer have a much higher seismicity than their surroundings. Therefore, the lack of seismicity within apparently aseismic interior rifts, and also within rifted margins and non-rifted continental interiors, may in fact be due to lack of documentation throughout history and not a lack of actual seismicity. Due to the large recurrence interval of SCR seismicity, the available global earthquake dataset is almost certainly a "snapshot", rather than a true representation of the distribution of SCR earthquakes. We note that for the non-rifted category, the majority of the regions have experienced higher magnitude earthquakes (**M** ≥ 6.0) in the instrumental era, whereas for the interior rifts/ taphrogens, the largest events are dominantly historical.

Figure 5a shows the Kutch rift in northwestern India. It is the locus of two of the largest events within the compiled earthquake database: the 1819 **M** = 7.8 and the 2001 **M** = 7.7 events. Apart from the East China rift system, it is the only rift that has experienced an **M** > 7 event that was instrumentally recorded, and therefore, has a very well-determined epicenter and magnitude. The Kutch rift proper is Mesozoic in age. However, active faulting has also

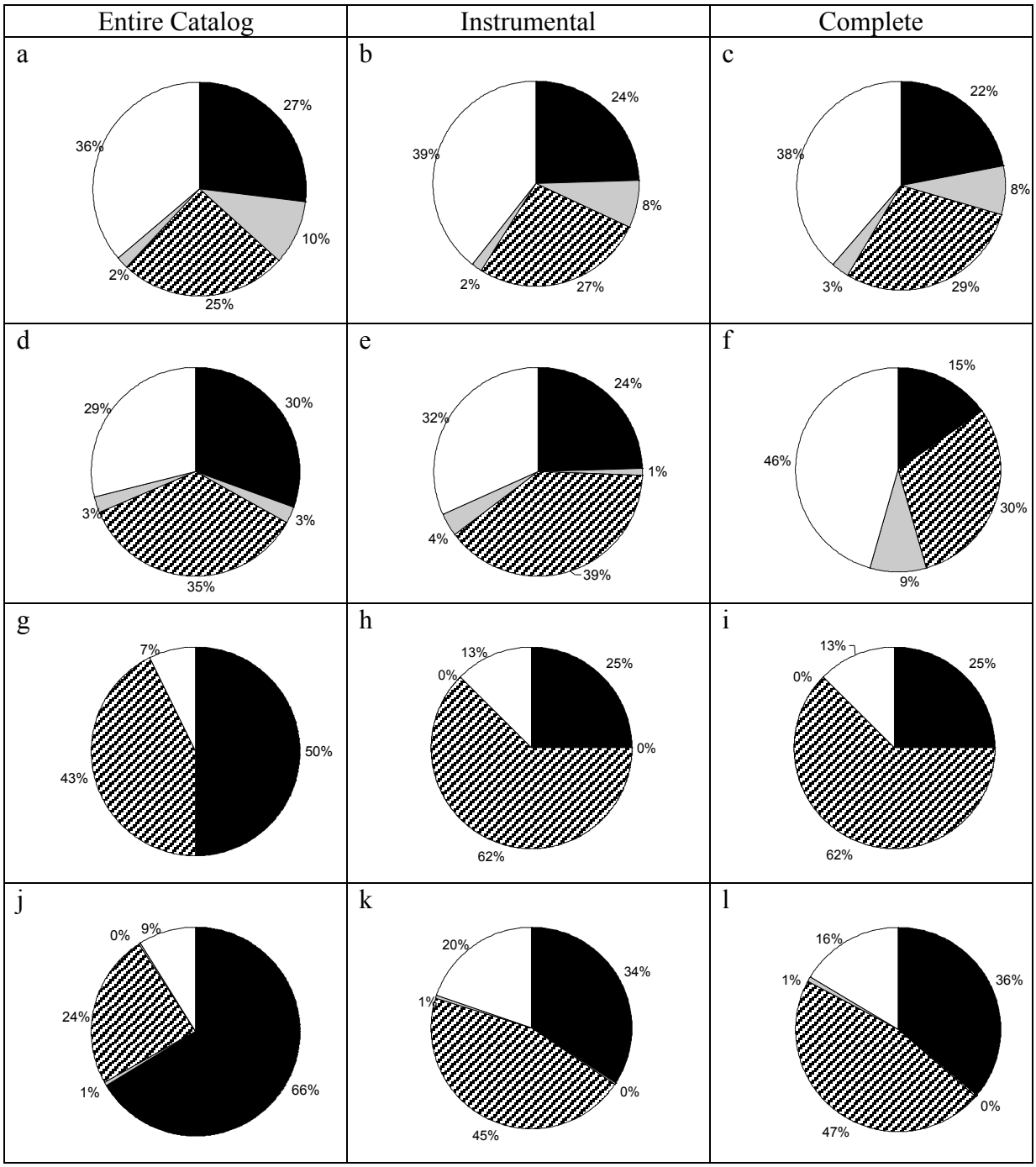


Figure 3: Distribution of seismicity over the five different categories for the entire database of instrumentally recorded events and "complete subset" events: Rifts (black), possible rifts (stippled), rifted margins (striped), possible rifted margins (gray), non-rifted crust (white). a-c) M ≥ 4.5 events, d-f) M ≥ 6.0, g-i) M ≥ 7.0 events and j-l) seismic moment release.

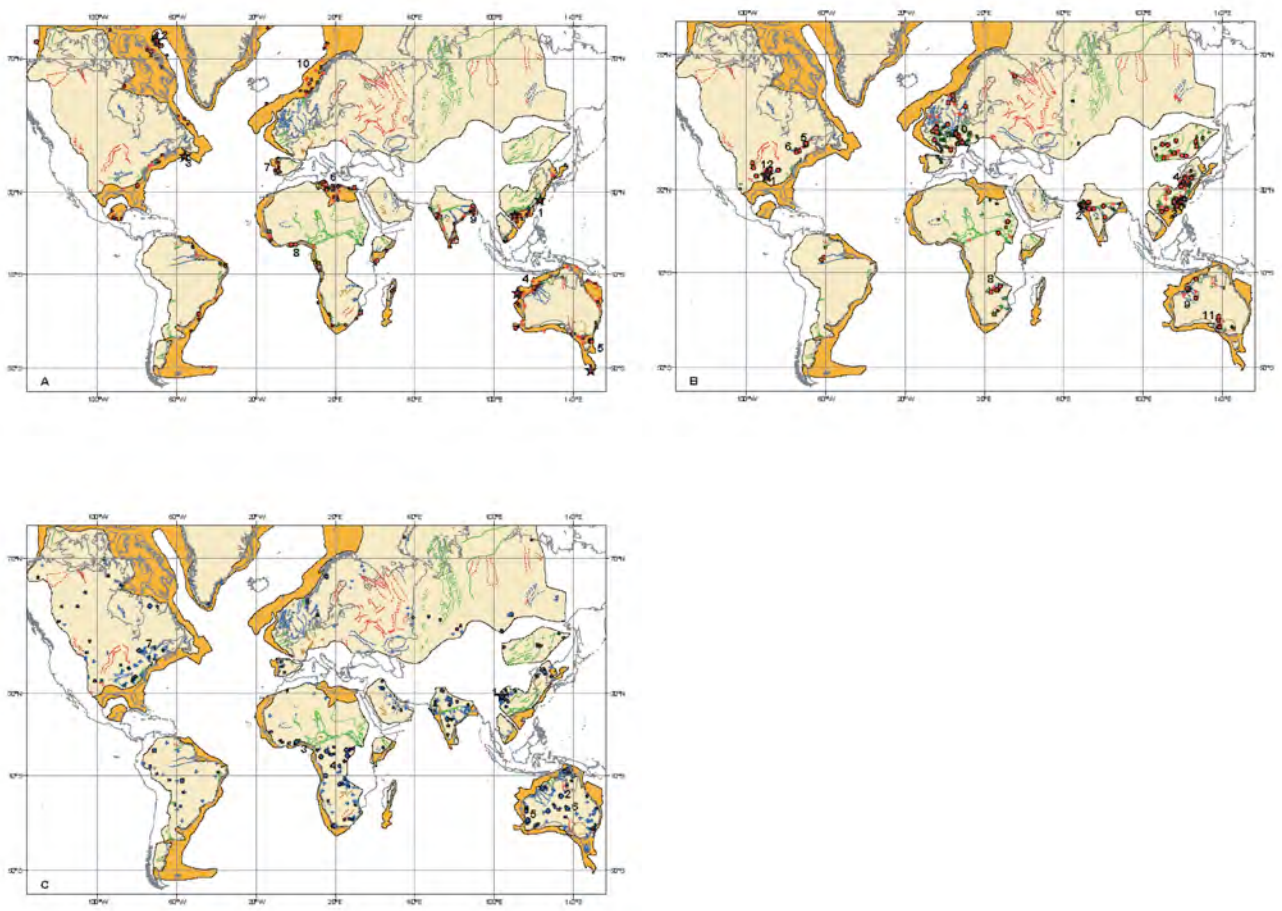


Figure 4: Earthquakes from the database for: a) rifted continental margins; b) interior rifts/ taphrogens; and c) non-extended continental crust. Extended margins are colored orange, continental interiors light gray. Rifts and taphrogens are indicated with solid (boundaries are well determined) or dashed (boundaries are poorly determined) lines. Precambrian rifts are indicated in red, Paleozoic in blue, Mesozoic in green and Cenozoic in brown. Red circles denote events that are and green circles events that might possibly be associated with rifted continental margins or interior rifts, blue circles denote events that are occur in non-rifted crust. Numbers indicate regions of concentrated seismicity.

been recognized (Stein et al., 2001). Furthermore, the Kutch rift is located relatively close (400 km) to the triple junction between the Eurasian, Indian and Arabian plate (Figure 5a). Thus, it has been suggested (Stein et al., 2001) that the Kutch area might in fact be an extension to the Indian diffuse western plate boundary described by Gordon (1998).

The East China Rift System comprises the largest part of the southeastern China SCR (Figure 5b). Though we do not distinguish the individual grabens, there are two regions within the East China Rift System that account for the majority of the events. The first is the Yellow Sea, with nineteen earthquakes, six of which (5 instrumentally recorded) were **M** > 6 events. The second is the region directly opposite the Ryuku trench at Taiwan with thirteen earthquakes, seven of which have **M** > 6.0. The two largest events located within the East China Rift System are: the historical 1604 **M** = 7.7 and the instrumentally recorded 1918 **M** = 7.3 events, both of which are located directly opposite the trench. Further inland, the East China Rift System does not show a significantly higher level of seismic activity than the non-rifted region west of it. Therefore, seismicity within the southeastern China SCR seems more likely to be related to the proximity to the plate boundary rather than to ancient rifting.

The strong concentration of events in the non-rifted SCR at the westernmost parts of Tibet, which has been categorized as non-rifted crust, has experienced four instrumentally recorded **M** > 6.5 events, including the 1917 **M** = 7.4 earthquake. The region shows large-scale intrusions and faulting, and directly borders the ACR (as defined by EPRI (1994)) of the Himalayas and Tibetan Plateau in the west. Seismicity might therefore be related to diffuse plate boundary processes of the Himalayas, such as the extrusion of the Tibetan Plateau, and may in fact lie in active continental crust.

For 209 events, focal mechanisms are available. Analysis of these focal mechanisms confirm results from earlier studies (Zoback, 1992; Reinecker et al., 2003) that compressive stress regimes dominate within the continental interiors, with maximum compressive stresses predominantly in accordance with absolute plate motion.

CONCLUSIONS AND RECOMMENDATIONS

We present an updated global catalog for Stable Continental Region (SCR) earthquakes that contains information on location, magnitude, seismic moment and focal mechanisms of 1373 M ≥ 4.5 crustal events from the year 495 to 2003. This is an increase of ~58% with respect to the last global study (EPRI, 1994). After removal of earthquakes that are considered to be non-tectonic, 1221 tectonic events were used for statistical analysis to re-evaluate the correlation of earthquakes with ancient rifts on a global scale. Earthquakes were then put into one of the following categories: interior rifts/ taphrogens (if located within ~20 km of identified ancient rift), rifted continental margins (if located within ~20 km of these rifted margins), or non-rifted crust (if located further than ~50 km of any of the above).

We found that 27% of the earthquakes fell in the interior rifts/ taphrogens category, 25% were rifted continental margins, 36% were non-rifted crust, and 12% remained uncertain. These numbers are similar to those of earlier studies (e.g. Johnston and Kanter, 1990; EPRI, 1994), who found that 56% of all SCR earthquakes are associated with extended crust (interior rifts/ taphrogens + rifted continental margins). However, if we consider continental interiors only (i.e. if the rifted continental margins are not taken into consideration), non-rifted crust has experienced more earthquakes compared with interior rifts/ taphrogens (27% interior rifts/ taphrogens vs. 36% non-rifted crust).

The percentages of earthquakes by tectonic affinity remain relatively constant if we consider only earthquakes from the instrumental era, for which magnitudes and locations are much better determined. The percentages remain fairly constant if only larger (**M** ≥ 6.0) events are considered, although for the largest events (**M** ≥7, N = 14), interior rifts/ taphrogens (50%) and rifted continental margins (43%) strongly dominate. Seismicity is not distributed evenly, however. For the interior rifts/ taphrogens category, only twelve rifts account for 74% of all events and 98% of the total moment release. The majority of interior rifts, in fact, show little or no seismicity. Several regions that have experienced multiple large (**M** ≥ 6.0) exist within apparently non-rifted crust.

The most seismically active rifts are the Kutch rift, India, (1819 **M** = 7.8 and 2001 **M** = 7.6 events) and the East China taphrogen (1604 **M** = 7.7 and 1918 M = 7.3). However, the Kutch rift is located relatively close to the triple junction between the Arabian, Indian and Eurasian plate. There is also evidence of active faulting, thus it has been suggested that the region is in fact part of the diffuse western Indian plate boundary (Stein et al., 2001). In addition, the majority of seismic energy that has been released within the East China rift/ taphrogen is located directly opposite the Ryuku trench at Taiwan. Plate boundary processes may therefore play an important role in these two regions and seismicity may not in fact be related to the presence of the ancient rift. The majority of the regions that are historically seismically active hardly show greater seismic activity than their surroundings if only the instrumental era is taken into account.

As these two regions are of particular interest for the nuclear test monitoring community, it is important that we consider future studies of these intraplate events. Although many earthquakes have occurred within rifted crust, the potential of seismicity within rifts should not be over-emphasized. Several regions within non-rifted crust have also shown strong seismic activity, and therefore a shift in focus of models for SCR seismicity from mainly rift-associated to a combination of rift-associated and non-rift-associated earthquakes is warranted. If a region of interest is seismically active, that makes discrimination somewhat more difficult, and this needs to be addressed.

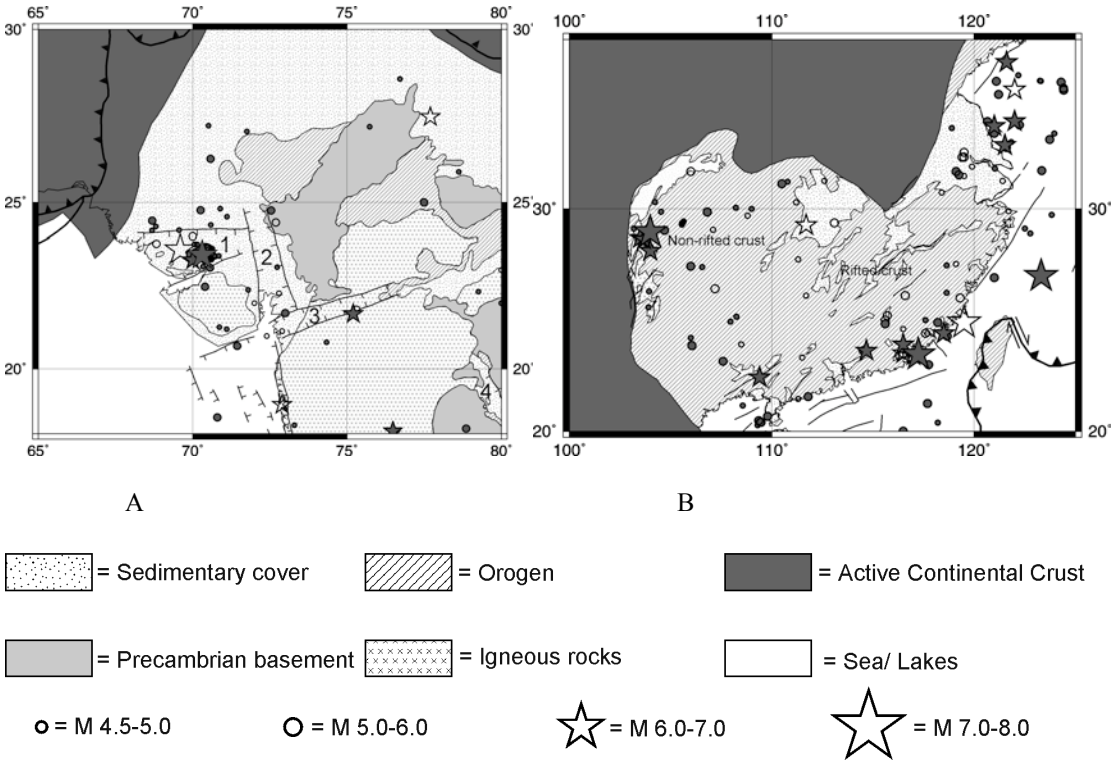


Figure 5: Simplified tectonic maps for different regions within Stable Continental crust, and earthquakes from the database. Events that were recorded instrumentally are colored dark gray, historic events are denoted by open symbols. a) India, with 1) Kutch Rift, 2) Cambay rift, 3) Narmada Son rift and 4) Pranhita-Godovari rift. b) Southern China, with the East China Rift system.

ACKNOWLEDGEMENTS

We would like to thank Allison Bent, Bill Bakun, Celal Sengör and Boris Natal'in for making their original datasets on seismicity and rifts available to us. We would also want to thank Luke Blair, Scott Haefner, Greg Allen, and Bart Schulte for their help in digitizing data. We are very grateful to Hanneke Paulssen, Art McGarr, Bill Bakun, Karl Fuchs, Mary Lou Zoback, Roger White, and Joe Fletcher for their critical reviews, encouragement, and suggestions.

REFERENCES

Campbell, D. L. (1978) Investigation of the Stress-concentration Mechanism for Intraplate Earthquakes, *Geoph. Res. Lett*. 5, 477-479.

Chandrasekhar, D. V. and D. C. Mishra (2002) Some Geodynamic Aspects of Kutch Basin and Seismicity: An Insight from Gravity Studies, *Curr. Sci.* 83, 13-34.

Electric Power Research Institute (EPRI), A.C. Johnston, K.J. Coppersmith, L.R. Kanter, and C.A. Cornell (1994) *The Earthquakes of Stable Continental Regions*, vol. 1-5, J.F. Schneider (Ed.), Palo Alto, California.

Exxon Production Research Company (1985) *Tectonic Map of the World*, 18 sheets, scale 1: 10,000,000, prepared by the World Mapping Project as part of the tectonic map series of the world.

Goodacre, A. K. and H. S. Hasegawa (1980) Gravitationally Induced Stresses at Structural Boundaries, *Can. J. Earth Sci*. 17, 1286-1291.

Grollimund, B. and M. D. Zoback (2001) Did Deglaciation Trigger Intraplate Seismicity in the New Madrid Seismic Zone?, *Geology* 29, 175-178.

Johnston, A. C. and L. R. Kanter (1990) Earthquakes in Stable Continental Crust, *Sci. Am.* 262, 68-75.

Kenner S.J. and P. Segall (2000) A Mechanical Model for Intraplate Earthquakes: Application to the New Madrid Seismic Zone, *Science* 289, 2329-2332.

Liu L. and M.D. Zoback (1997) Lithospheric Strength and Intraplate Seismicity in the New Madrid Seismic Zone, *Tectonics* 16, 585-595.

Long L.T. (1988) A Model for Major Intraplate Continental Earthquakes, *Seis. Res. Lett.* 59, 273-278.

Quinlan, G. (1984) Postglacial Rebound and the Focal Mechanisms of eastern Canadian Earthquakes, *Can. J. Earth Sci*. 21, 1018-1023.

Reinecker, J., O. Heidbach, and B. Mueller, (2003) The 2003 Release of the World Stress Map (available online at www.world-stress-map.org).

Sengör, A.M.C. (1995) Sedimentation and Tectonics of Fossil Rifts, in Busby, C.J. and R.V. Ingersoll, (eds.) *Tectonics of Sedimentary Basins:* Oxford, Blackwell, p 53-117.

Sengör, A. M. C., and B. A. Natal'in (2001) Rifts of the World, in Ernst, R. E., and K. L. Buchan (eds.) Mantle Plumes: Their Identification Through Time, *Geol. Soc. Am., Special paper* 352, 389-482.

Stein , S., N. Sleep, R. J. Geller, S. C. Wang, and G. C. Kroeger (1979) Earthquakes along the Passive Margin of eastern Canada, *Geoph. Res. Lett.* 6, 537-540.

Stein, S., M. Schoonover, G. Sella, and E. Okal, Bhuj (2001) A Diffuse Plate Boundary Zone Earthquake? GSA Annual meeting *http://gsa.confex.com/gsa/2001AM/finalprogram/abstract_24251.htm*.

Sykes, L. R. (1978) Intraplate Seismicity, Reactivation of Preexisting Zones of Weakness, Alkaline Magmatism, and Other Tectonism Postdating Continental Fragmentation, *Rev. of Geoph*. 16, 621-688.

Talwani, P. (1988) The Intersection Model for Intraplate Earthquakes, *Seism. Res. Lett*. 59, 305-310.

Talwani, P. (1999) Fault Geometry and Earthquakes in Continental Interiors, *Tectonophys*. 305, 371-379.

Talwani, P. and K. Rajendran (1991) Some Seismological and Geometric Features of Intraplate Earthquakes, *Tectonophys*. 186, 19-41.

Vinnik, L.P. (1989) The Origin of Strong Intraplate Earthquakes, *translated from O Prirode Sil'nykh Vnutrilplitovykh Zemletyaseniy, Doklady Akademii Nauk SSSR* 309, 824-827.

Zoback, M. L. (1992) First- and Second-order Patterns of Stress in the Lithosphere: The World Stress Map Project, *J. Geophys. Res.*97, 11703-11728.

Zoback, M. D. (1983) Intraplate Earthquakes, Crustal Deformation and In-Situ Stress, in Hays, W.W. and P.L. Gori (eds.), A Workshop on "The 1886 Charleston, South Carolina, Earthquake and its Implications for Today", Proceedings of Conference XX: *U.S. Geol. Surv. Open-file Rep*. *83-843*, 169-178.

CALIBRATION FOR CODA BASED MAGNITUDE AND YIELD

W. Scott Phillips, Howard J. Patton, Steven R. Taylor, Hans E. Hartse, and George E. Randall

Los Alamos National Laboratory

Sponsored by National Nuclear Security Administration
Office of Nonproliferation Research and Engineering
Office of Defense Nuclear Nonproliferation

Contract No. W-7405-ENG-36

ABSTRACT

The stability of local (<100 km) earthquake coda has been well established through observations that have shown coda amplitudes to be independent of distance, path details, and azimuth with respect to the focal mechanism. This behavior is consistent with scattered energy models of coda and allows accurate measurement of relative amplitudes. Furthermore, relative coda amplitudes can be measured to a high precision because of the redundant information in adjacent time windows. These properties have been employed to produce absolute source spectra from the relative coda measurements by applying empirical Green's function analysis followed by ties to independently determined moments, allowing comparison of scaling behavior worldwide. Recently, Mayeda (2003) extended these coda measurement techniques from local to regional scales by employing models of coda shape that contain up to six parameters to describe distance effects. The limited number of parameters will smooth through some coda shape variations over broad areas. We mitigate this limitation by employing the typecurve method of coda analysis. The typecurve is an empirically derived coda shape that does not rely on model assumptions. Typecurves are impractical for use over broad areas, but provide high precision measurements at local distances and for regional distance data that share a common path, such as earthquake clusters and test site explosions. Typecurve results can be combined with broad area results by correcting for the offset between the typecurve and the broad area coda shape model. This correction gives a precision that remains high within event clusters, but reverts to broad area levels between or outside clusters. We apply the combined coda method to over 6,500 events in China and central Asia, generating typecurve coda shapes for Semipalatinsk and Lop Nor explosions. The typecurve approach is especially appropriate for Borovoye archive data, as saturation forces the use of late time segments for many events, and effects of elapsed time, commonly observed for model fits to coda data, are avoided. Spectral results from this analysis are critical for studying amplitude-yield behavior for underground tests in central Asia.

OBJECTIVE

We have upgraded coda wave calibration procedures, in particular the calibration of coda shape variations, for application to Borovoye archive explosion data. This is achieved using a typecurve technique (e.g. Hartse *et al.*, 1995) that delivers extremely precise relative amplitudes for clustered events. These results can be used to constrain relationships between coda source factors and yield.

RESEARCH ACCOMPLISHED

Background material for this study has been published elsewhere, but will be repeated here for purposes of completeness. The stability of coda waves has been well established through observations that have shown coda amplitudes to be independent of distance, path details and azimuth with respect to the focal mechanism (Aki, 1969). This behavior is consistent with the generation of coda by scattering and allows accurate measurement of relative amplitudes for use in source scaling (e.g. Aki and Chouet, 1975) or site effect (Phillips and Aki, 1986) studies. Furthermore, coda amplitudes can be measured to high precision because of the redundant information in adjacent time windows. This makes coda ideal for monitoring small, sparsely recorded events for purposes of discrimination (Hartse *et al.*, 1995) and magnitude or yield estimation (Rautian *et al.*, 1979; Mayeda, 1993) as the measurement stability is equivalent to that available from a multi-station network.

The methods developed by Mayeda *et al.* (2003) are applied to obtain regional coda calibration parameters for China and central Asia stations. Records were processed from underground nuclear tests, chemical explosions and earthquakes recorded across China and central Asia (Figure 1) for purposes of calibrating coda wave behavior. Including duplicate and surrogate stations in the list, these are: AAK, BJI, BJT, BRV, BRVK, CHTO, ENH, HIA, KMI, KKAR, KK31 KUR, KURK, LSA, LZH, MAK, MAKZ, MKAR, MK31, MDJ, NIL, NVS, PDY, QIZ, SSE, TKM2, TLG, TLY, ULHL, ULN, WMQ, WUS, XAN and ZAL, as well as Borovoye archive STsR-TSG instruments KS, KSM and KSVM (Richards *et al.*, 1992; Kim and Ekstrom, 1996) and PASSCAL Tibetan Plateau Experiment stations AMDO, BUDO, ERDO, GANZ, LHSA, MAQI, SANG, TUNL, USHU, WNDO and XIGA (Owen *et al.*, 1993).

Following instrument correction, data were reduced by band-passing in 13 bands, from 0.03-0.05 to 6.0-8.0 Hz, followed by Hilbert transform envelope and smoothing operations. Final envelopes were formed by averaging the two horizontal component envelopes. Exceptions are the vertical components at short-period arrays and Borovoye archive KSVM. MKAR and KKAR array envelopes were stacked without shifting, which reduced the scatter that typically rides on top of the envelope, allowing better detection of low signal-to-noise (SNR) coda, especially in the higher frequency bands.

Coda analysis windows were determined by manual inspection for a subset of the China and central Asia envelope data that included all BRV(K), KKAR, MAK(Z), MKAR, NIL (BH), ULN, WMQ and Tibet Experiment records, all explosions, both nuclear and chemical, as well as all records of 44 earthquakes for which independently derived moments exist. The remaining data were analyzed using an automatic procedure to identify the coda window.

After manual review, we calibrated coda peak and shape parameters following the regional calibration procedure of Mayeda *et al*. (2003). First, coda peaks were determined by inspection of WMQ and NIL (BH) envelope data. In many cases, especially for low *Q* paths and high frequencies, peaks did not stand out; however a break in slope could be identified near the predicted Lg arrival. In some low *Q* path cases, the peak envelope occurred near the Sn arrival and no peak or break in slope could be identified near the Lg. Sn peaks were more commonly observed at NIL than at WMQ. Sn coda were used in the analysis if signal-to-noise were sufficient following the predicted Lg peak. The group velocities of the envelope peaks were calibrated by fitting (L_1) a flat Lg velocity along with a hyperbola with three adjustable parameters to describe the Sn velocity as a function of distance:

$$\mathbf{v_g} = \mathbf{v}_0 - \frac{\mathbf{v}_1}{\mathbf{v}_2 + \Delta}$$

where v_g is group velocity of the peak; v_0, v_1 and v_2 are adjustable parameters and Δ is distance in kilometers. Within scatter, Sn and Lg group velocities were the same for WMQ and NIL, so we applied the these calibration curves to all stations.

Coda shape was obtained by fitting the coda decay using:

$$\mathbf{a(t)} = \mathbf{a_0} \cdot \mathbf{t}^{-\alpha} \cdot \mathbf{e}^{\beta \cdot \mathbf{t}}$$

where *a(t)* is coda amplitude, *t* is time from the coda peak (taken as the smaller of the Lg and Sn velocities, see above), a_0 is the coda source factor, α is a spreading factor, and β is the coda decay parameter. The spreading factor and a distance dependent decay parameter were then fit to envelope data using direct search techniques in an L1 sense. The distance dependence of the decay parameter is described by fitted hyperbola parameters b_0, b_1 and b_2:

$$\beta = \mathbf{b}_0 - \frac{\mathbf{b}_1}{\mathbf{b}_2 + \Delta}$$

The coda shape parameters were determined for various station groups. Well sampled stations, such as WMQ, were calibrated alone. Closely located stations, such as MAK, MAKZ, MKAR and MK31, or Kirgiz network stations, were grouped together. Poorly sampled stations were grouped by regional propagation characteristics (based on two-dimensional (2D) amplitude tomography results, described below).

This coda shape method relies on four free parameters (spreading and the three hyperbola parameters that combine to represent the distance dependence of the decay parameter). The spreading can also be represented in hyperbola form, which gives six fit parameters. Even with six free parameters, we cannot expect to represent all the variations in regional coda shape. In particular, coda shape has been observed to vary laterally, and we can expect to see azimuthally dependent coda shapes in geologically heterogeneous regions. Furthermore, careful observation of coda shapes shows that various phases arrive in different bands at different times following the dominant phase in each band (see Rautian *et al.*, these proceedings). Thus, coda decay is not always uniform and ripple behavior can be superposed on an otherwise monotonically decreasing envelope. Finally, we wish to include Borovoye archive data in our study because of the rich collection of explosions recorded there. These data are often saturated and the coda measurement windows can start very late in the seismogram. Our procedures, based on using modern digital data, restrict coda windows to the early coda in order to calibrate portions of the coda that would be observable for small events. This procedure is incompatible with the Borovoye data as the early coda is often off scale. We can apply one model over the entire time interval, but this is known to be poor practice as the coda decay rates always decrease with time, due to multiple scattering or increased sampling of high *Q* materials at depth and this effect will not be captured by our parameterization.

Our solution to the coda shape problem outlined above is to use typecurve analysis (Hartse *et al.*, 1995). This technique is a variation on early coda techniques described by Aki (1969), and the common shape technique of Phillips and Aki (1986). These techniques were used to analyze local earthquake coda, where coda shapes could be expected to be similar for a wide range of event locations as long as the late coda was used, defined to start at twice the direct wave arrival time. Because we include early coda in regional work, we can only assume coda shapes similar if events are closely located relative to the path length. This holds for test site events recorded at regional distances, as well as for naturally occurring clusters of earthquakes. Assuming a constant shape for such coda envelopes, we invert for that shape without reference to a restrictive model by defining the model parameters to be the coda amplitudes over the entire range of times that are continuously sampled by the records. Typecurve results for Borovoye archive recordings of Semipalatinsk events are shown in Figure 2.

Of course, the typecurve offset is not resolvable and is set such that the mean is zero. Relative coda amplitudes are then measured by directly comparing with the typecurve, accounting for time varying error on the typecurve model terms in the calculation. This can be repeated for other stations for the same event cluster. The typecurve amplitudes are then made compatible with amplitudes measured using the four-parameter model fits, by fitting the typecurve with the appropriate shape model, and using the difference to adjust for the effect of the arbitrary typecurve level. In this way, the high precision of the typecurve measurement within clusters of events is retained, and fall back to the lower precision of the model fits over broad areas, analogous to advantages of the cross-correlation traveltime methods used in relative earthquake location. Clearly, the high precision, the lack of reliance on restrictive models and the ability to overcome problems with saturated Borovoye archive records of a large number of Soviet underground tests will greatly advance our ability to constrain amplitude-yield models for use in explosion monitoring.

We obtain raw coda source factors, a_0,using the calibrated envelope peak group velocity and coda shape factors, or the typecurve method described above. These values must be corrected for path and site effects. One-dimensional (1D) and 2D methods were used to do this. The 1D method follows Mayeda *et al*. (2003). We obtain initial path terms using a rough source correction based on mb (Taylor and Hartse, 1998) and fit (L_1) a spreading-attenuation model:

$$\mathbf{a}(\Delta) = \mathbf{s}_0 \cdot \Delta^{-\alpha} \cdot \mathbf{e}^{\frac{-\pi \mathbf{f} \Delta}{\mathbf{Q c}}}$$

where a is mb-corrected amplitude, s_0 represents the site effect, but contains other effects such as coda generation (media scattering strength), α is spreading, f is frequency, Q is the quality factor and v is velocity, to which we assign the nominal Lg velocity of 3.5 km/s. Spreading is set based on mb-corrected coda amplitudes at distances under 100 km. These values are zero at low frequencies and increase (0.7 for the 6 - 8 Hz band) with frequency. These values reflect the shrinking range over which coda amplitude is observed to be independent of distance as frequency increases. Site and Q terms are varied to obtain the best fit. While appearing physical, this equation is only used for empirical fitting and fit parameters must not be overinterpreted. These site and Q values are used as the starting point for a second refinement step.

The site and Q terms are further refined using data only from events recorded at more than one station. This is done by adjusting the site and Q models simultaneously for all stations in order to fit station-to-station amplitude ratios. This removes the influence of a possibly biased mb, which was used in the initial step to remove source effects (Mayeda *et al.*, 2003). This procedure was implemented using an L_1 criterion with direct search techniques (Press *et al.*, 2001). We note that the heterogeneous seismicity pattern results in sampling over limited distance ranges for many stations, which makes extrapolation risky using the 1D results.

Our preferred path correction method employs tomography techniques to invert for a laterally varying (2D) Q and relative site terms (Phillips *et al.*, 2000; Phillips *et al.*, 2001; Phillips and Hartse, 2002). The inversion equations are the same as for the 1D case above, with the addition of a sum over discretized path terms in place of $1/Q$. Only data from multiple recorded events, similar to the second, 1D path step, is used in order to eliminate source effects by fitting station-to-station amplitude ratios. We remove a small number of outliers (less than 1% of the data) based on the 1D results and use L_2 techniques in the inversion. Spreading is set as in the 1D calculations. Currently, the tomography treats the coda as a direct path, rather than an ellipsoidal area. This is most appropriate for short codas, and misfits are low as the root mean square (RMS) residuals fall below 0.1 log10 amplitude units for all bands. For data from 2,250 multiple recorded events in the band 0.7 to 1 Hz, for example, residual variance is reduced 86% relative to the best fit, uniform Q model. Q results follow regional geology well. We are confident to extrapolate path corrections into aseismic, but well resolved areas because of the more physical nature of the tomography model.

The 2D path correction technique was applied to Berkeley Seismic Stations data that had been analyzed by Lawrence Livermore National Laboratory (LLNL) scientists using a 1D model, and a comparison of the results can be found in Mayeda *et al.*, in these proceedings.

The final calibration steps adjust measurements between bands and shift to absolute units based on independently determined moments. Adjustments between bands are calculated in order to flatten the earthquake spectra below their corners. Corner frequencies are estimated using scaling based on mb (Taylor and Hartse, 1998). We start with earthquake data from bands less than 1/4 of the corner frequency in an L_1 simplex inversion to obtain the band corrections. For our data set, this gives corrections for bands below 1 Hz. We assume an ω^2 model and allow data less than 1/2 the corner, and so on, to obtain corrections for the higher bands, which are spliced to the low frequency results. This approach was suggested by results of synthetic tests that showed that high frequency spectra can drift high by 0.1 to 0.2 $\log_{10}$ units, likely due to a slight curvature of earthquake spectra when using a liberal corner frequency cut-off.

We are fortunate to have data from 44 earthquakes for which moments have been independently determined using waveform matching techniques (Zhu *et al.*, 1997; Patton, 1998; Ghose *et al.*, 1998). An overall shift is obtained such that spectral data from bands less than 1/4 of the corner frequency, calculated as above, match the appropriate moment in a median sense. Spectra then carry units of Newton-meter (N-m). Earthquake results become moment rate

spectra and we refer to explosion results as “apparent coda source spectra” the term “apparent” indicating possible near source effects, including near source path, on the spectra.

After correction, the scatter between coda and independently derived moments is 0.18 $\log_{10}$ units. We do not use the Harvard Centroid Moment Tensor (CMT) solutions in this step because of bias due to unaccounted for crustal thickness in this area (Patton, 1998). Additional independent moments will be needed in the future to further validate our results. A broad geographical distribution would help validate the broad area path calibration. Moments for small events, perhaps obtained by applying spectral techniques to local network data, would help validate the results in higher bands.

Apparent source spectra for a well recorded Lop Nor nuclear event show good correspondence between stations (Figure 3). These spectra match especially well in the higher bands. Low frequency coda are less well studied, but direct waves are known to exhibit multipathing effects in these bands (Patton *et al.*, 1985).

The earthquake results can be summarized by fitting a two-parameter ω^2 source model. Mw and stress drop using standard formulae are calculated. Stress drop for the highest quality network spectral fits show striking regional variation in China and central Asia (Figure 4). The patterns include low stress drop events (0.1 MPa) in areas of north-central Tibet and the North China Basin. A marked gradient in stress drop can be seen starting at the Tarim Basin-Tien Shan boundary where stress drops are uniformly about 1 MPa, then moving north into the Tien Shan where stress drops increase to above 10 MPa and finally approach 100 MPa. The stress drop patterns tend to be similar from station to station. Furthermore, for station WMQ and others, the low stress Tibet events lie along similar paths as more distant, higher stress events. This indicates unaccounted for path effects are not the cause of the variations. Such variations in scaling could be included in amplitude calibration efforts for event identification (MDAC) work. We use these regional patterns to limit the events used in the spectral flattening correction to the high stress drop regions. The stress drops can also be used to constrain spectral fits and Mw in cases when the frequency band is not well sampled due to signal-to-noise or other effects.

CONCLUSIONS AND RECOMMENDATIONS

Typecurve analysis provides high precision measures of relative amplitudes of clustered events, including test site explosions. This method allowed the inclusion of saturated explosion data from Borovoye archive records, which greatly enhances our ability to calibrate coda source factors with respect to yield. We plan to further enhance our collection of central Asia, regional explosion data with pre-digital era, multispectral (ChISS) measurements, as described in Rautian et al., these proceedings.

Broad area calibration using tomographic imaging for path and site effects allows coda spectra to be displayed on a common basis throughout China and central Asia, for both earthquakes and explosions. Residuals from the tomographic inversions are remarkably low, on the order of 0.1 $\log_{10}$ units, demonstrating the internal consistency and precision of the amplitude data. Similar, two-dimensional patterns should be investigated in other coda calibration steps, including the group velocity of the peak envelope and coda shape effects.

Following 2D path corrections, the coda results show interesting scaling for earthquake sources. Earthquakes show systematic, regional variations in scaling through stress drop patterns, which could be included in event identification work (MDAC) to reduce scatter in earthquake populations of discriminants. Kriged stress drop maps have been implemented in coda calibration procedures, where emphasis on high stress drop events is useful in obtaining spectral flattening corrections and knowledge of the stress drop provides a useful constraint in fitting narrow band spectra to obtain Mw.

REFERENCES

Aki, K. (1969), Analysis of the seismic coda of local earthquakes as scattered waves, J. Geophys. Res., 74, 615-631.

Aki, K. and B. Chouet (1975), Origin of coda waves: attenuation, and scattering effects. J.Geophys.Res. 80, 3322-3342.

Ghose, S., M.W. Hamburger and C.J. Ammon (1998), Source parameters of moderate sized earthquakes in the Tien Shan, central Asia from regional moment tensor inversion, Geophys. Res. Lett., 25, 3181-3184.

Hartse, H.E., W.S. Phillips, M.C. Fehler and L.S. House (1995), Single-station spectral discrimination using coda waves, Bull. Seism. Soc. Am., 85, 1464-1474.

Kim, W-Y. and G. Ekstrom (1996), Instruments responses of digital seismographs at Borovoye, Kazakhstan, by inversion of transient calibration pulses. Bull. Seism. Soc. Am. 86, 191-203.

Mayeda, K.M. (1993), mb (Lg Coda): A stable single station estimator of magnitude, Bull. Seism. Soc. Am., 83, 851-861.

Mayeda, K.M., W.R. Walter (1996), Moment, energy, stress drop and source spectra of western United States earthquakes from regional coda envelopes, J. Geophys. Res., 101, 11195-11208.

Mayeda, K.M., A. Hofstetter, J.L. O'Boyle, W.R. Walter (2003), Stable and transportable regional magnitudes based on coda-derived moment-rate spectra, Bull. Seism. Soc. Am., 93, 224-239.

Owens, T.J., G.E. Randall, F.T. Wu and R. Zeng (1993), PASCAL instrument performance during the Tibetan Plateau Passive Seismic Experiment, Bull. Seism. Soc. Am., 83, 1959-1970.

Patton, H.J., S.R. Taylor, D.B. Harris and J.M. Mills (1985), The utility of regional Chinese seismograms for source and path studies in central Asia, Geophys. J. Royal Astr. Soc., 81, 469-478.

Patton, H.J. (1998), Bias in the centroid moment tensor for central Asian earthquakes: Evidence from regional surface wave data, J. Geophys. Res., 103, 26963-26974.

Phillips, W.S. and K. Aki (1986), Site amplification of coda waves from local earthquakes in central California, Bull. Seism. Soc. Am., 76, 627-648.

Phillips, W.S., H.E. Hartse, S.R. Taylor and G.E. Randall (2000), 1 Hz Lg Q tomography in central Asia, Geophys. Res. Lett., 27, 3425-3428.

Phillips, W.S., H.E. Hartse, S.R. Taylor, A.A. Velasco and G.E. Randall (2001), Application of regional phase amplitude tomography to seismic verification, Pure Appl. Geophys., 158, 1189-1206.

Phillips, W.S. and H.E. Hartse (2002), Regional path calibration using multiple station amplitude tomography, Seism. Res. Lett., 73, 228.

Press, W.H., S.A. Teukolsky, W.T. Vetterling and B.P. Flannery (2001), Numerical Recipes in Fortran 77: The Art of Scientific Computing, Cambridge University Press, Cambridge, U.K.

Rautian, T.G., V.I. Khalturin, I.S. Shengelia, (1979), The coda envelopes and the determination of the magnitudes of Caucasus earthquakes, The Physics of the Earth, Acad. Sci. USSR, N6 22-29 (English translation of Russian original).

Richards, P.G., W.Y. Kim and G. Ekstrom (1992), The Borovoye Geophysical Observatory, Kazakhstan, EOS, 73, 201-206.

Taylor, S.R. and H.E. Hartse (1998), A procedure for estimation of source and propagation amplitude corrections for regional seismic discriminants, J. Geophys. Res., 103, 2781-2789.

Zhu, L.P. , D. Helmberger, C.K. Saikia, B.B. Woods (1997), Regional waveform calibration in the Pamir-Hindu Kush region, J. Geophys. Res. 102, 22799-22813.

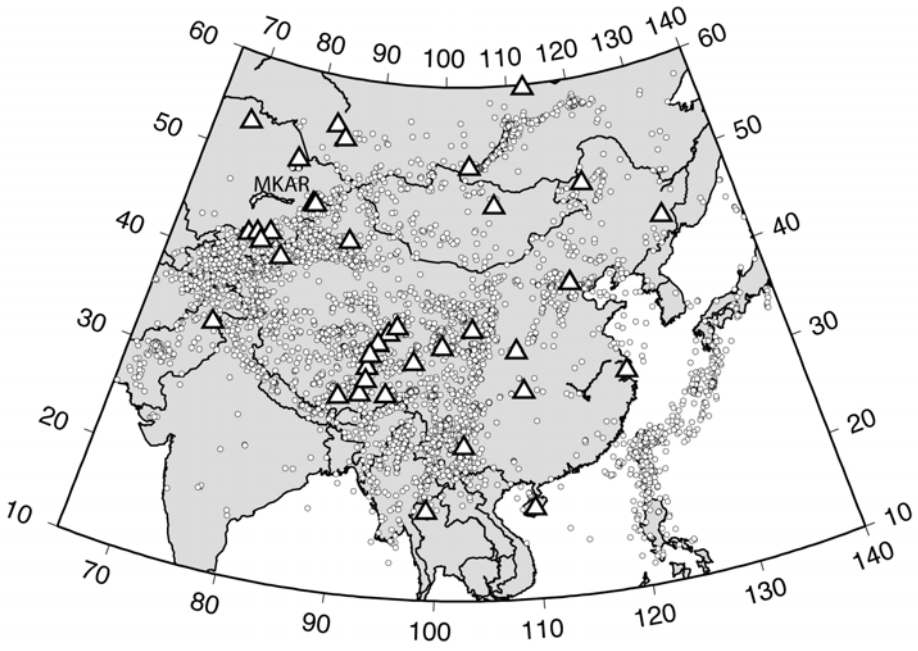


Figure 1. **Stations and events used in the coda wave study.**

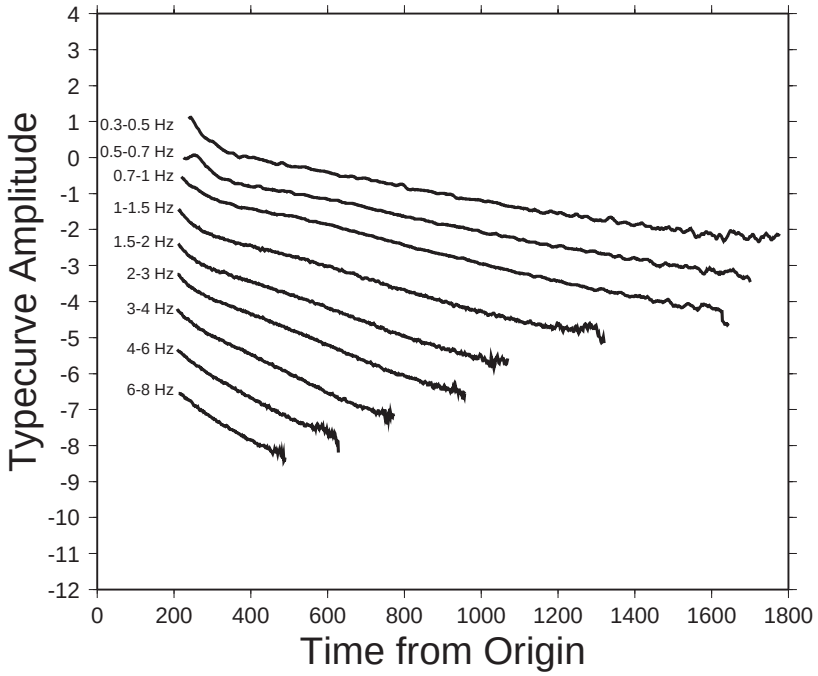


Figure 2. **Typecurves for Semipalatinsk explosions from the Borovoye archive. Balapan and Degelen results are nearly identical and all sub-areas of the Semipalatinsk test site are have been included together in these results. Typecurve levels have been shifted for plotting purposes.**

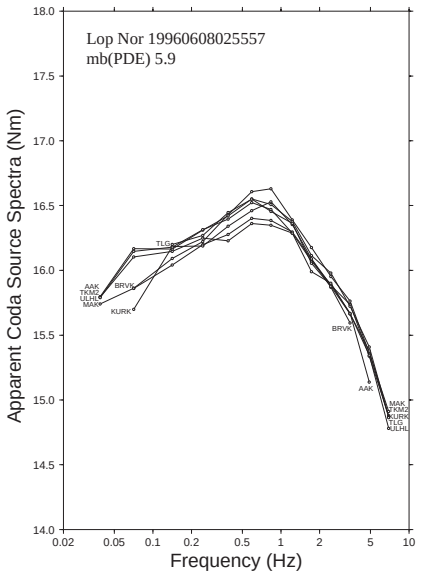


Figure 3. Apparent source spectra determined using coda wave data from seven stations for a Lop Nor test. Stations are indicated as spectra endpoints. The inter-station consistency is especially good for bands above 1 Hz.

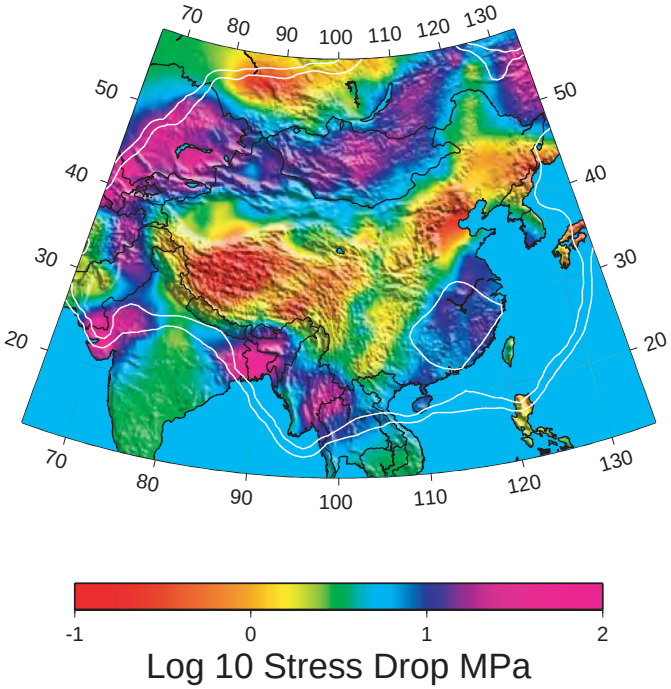


Figure 4. Kriged stress drop and error contours based on network fits of coda spectra to standard, omega-squared source model formulae. Events were restricted by requiring spectral coverage on both sides of the fitted corner frequency

EXPLOSION SOURCE PHENOMENA USING SOVIET TEST ERA WAVEFORM DATA

Tatyana G. Rautian[1], Vitaly I. Khalturin[1], W. Scott Phillips[2], and Paul G. Richards[1]

Columbia University[1], Los Alamos National Laboratory[2]

Sponsored by National Nuclear Security Administration
Office of Nonproliferation Research and Engineering
Office of Defense Nuclear Nonproliferation

Contract No. DE-FC52-03NA99513[1], W-7405-ENG-36[2]

ABSTRACT

During the nuclear testing era, the former Soviet Union carried out extensive observations of underground nuclear explosions, recording both their own shots and those of foreign nuclear states. Between 1961 and 1989, the Soviet "Complex Seismological Expedition" deployed seismometers at time-varying subsets of over 150 sites to record explosions at regional distances from the Semipalatinsk and Lop Nor test sites and from the shot points of peaceful nuclear explosions. This data set included recordings from broadband, multi-channel ChISS[1] seismometers that produced a series of narrow band outputs, which could then be measured to perform spectral studies. Quantitative, pre-digital era investigations of high-frequency source scaling relied on this type of data (e.g., Aki and Chouet, 1975; Rautian and Khalturin, 1978; Tsujiura, 1978). To augment data sets of Central Asia explosions, we have measured and compiled 537 ChISS coda envelopes for 124 events recorded at Talgar, Kazakhstan, at a distance of about 750 km from Semipalatinsk. Envelopes and calibration levels were measured manually from photo paper records for seven bands between 0.08 and 5 Hz. We obtained from 2 to 10 coda envelope measurements per event, depending on the event size and instrument magnification. Coda lengths varied from 250 to 1400 s. For small events, only bands between 0.6 and 2.5 Hz could be measured. Envelope levels were interpolated or extrapolated to 500 s and we have obtained the dependence of this quantity on magnitude. Coda Q was estimated and found to increase from 232 at 0.08 Hz to 1270 at 5 Hz. These relationships were used to construct an average scaling law of coda spectra for Semipalatinsk explosions. Significant differences from average scaling are observed and may result from variations in emplacement conditions. The ChISS envelope data will be integrated into coda processing at Los Alamos National Laboratory (LANL) by applying ChISS filter bands to modern, digital data from Central Asia, for purposes of magnitude and yield calibration.

[1] ChISS is the Russian abbreviation for multichannel spectral seismometer. In this instrument the signal from the seismometer is passed through a system of narrow bandpass filters and recorded on photo paper. ChISS instruments have from 8 to 16 channels in the frequency range from 100 sec to 40 Hz. We used data mostly from 7 channels, ranging from 0.08 to 5 Hz.

OBJECTIVE

Our objective is to augment the collection of seismic recordings of Central Asia underground nuclear tests and test-site earthquakes using ChISS data collected at Talgar, Kazakhstan, between 1961 and 1989; and to integrate these data into coda wave processing schemes currently in use with modern digital data. This will greatly increase the numbers of events used in explosion source scaling and yield estimation studies for the Semipalatinsk Test Site. Furthermore, data from rare earthquakes on and near the Semipalatinsk Test Site will be useful to test calibration parameters currently applied to amplitude data from that test site.

RESEARCH ACCOMPLISHED

The ChISS Instrument

The ChISS instrument is a real-time, spectral-analyzing seismic recording system, created by K.K. Zapolsky in the early 1950s. It produced band-passed traces in several (usually 7-10) frequency channels over a broad band from 100 seconds to 40 Hz. The components of a ChISS system are the seismometer, calibration device, amplifier, filter bank, and galvanometers with a photo-paper recording device. Instrument calibration was achieved by each seismometer having an excitation coil with a separate magnet to input the calibration signal. The frequency of the calibration electric signal was slowly decreased in time from the high end of the highest frequency filter to the low end of the lowest frequency filter. The shape of the response to this signal on the seismogram exactly corresponds to the frequency response of the seismometer-filter-galvanometer system. The impulse response consists of 1.5-2 periods (3-4 extrema). Such a short period of transition guarantees minimal distortion of the initial seismic signal and stabilizes the envelope shape. Filters used in ChISS systems are characterized by the low and high band limits (at 0.7 maximum magnification), f1 and f2; the central frequency, fc; the absolute bandwidth, df = f2 - f1; and the relative bandwidth, (f2 - f1)/fc.

The ChISS filter parameters at the Talgar station used in this study are shown in Tables 1 and 2. Parameters were changed in September 1971 when the system was improved to include two sets of filters for independent short-period (ShP) and long-period (LP) seismometers, as well as independent systems of calibration and recording. The LP and ShP ChISS instruments employ Soviet SKD and SKM seismometers, respectively. Two identical ChISS filters, with central frequency 0.62 Hz, are output from both systems. The calibration signal was recorded daily on each short period ChISS seismogram and once a week on long period ChISS seismograms.

Table 1. Early ChISS parameters (Sep 1961 – Aug 1971)

f1 - f2 (Hz)	0.27-0.4	0.54-0.84	1.1-1.7	2.3-3.6	4.6-7.1
fc (Hz)	0.32	0.67	1.36	2.9	5.7
Width	0.40	0.45	0.45	0.45	0.45

Table 2. Standard ChISS parameters (Sep 1971 – Oct 1990)

LP or ShP	LP	LP	LP	LP	ShP	ShP	ShP	ShP
f1 - f2 (Hz)	0.05-0.1	0.1-0.2	0.2-0.4	0.5-0.8	0.5-0.8	1.0-1.6	2.0-3.2	4-6.4
fc (Hz)	0.08	0.14	0.28	0.62	0.62	1.25	2.5	5.0
Width	0.7	0.7	0.7	0.5	0.5	0.5	0.5	0.5

Talgar Explosion Data

The Talgar ChISS station began operating in September 1961. It recorded almost all Soviet underground nuclear tests (UNTs) from the Semipalatinsk test site (STS), including the first two STS UNTs on Oct 11, 1961 and Feb 2, 1962 until the final test of Oct 19, 1989. Many small magnitude UNTs, which were not recognized by western stations, have been recorded by ChISS station TLG (Khalturin et al., 2001).

For this study, we manually measured coda envelopes of 178 Talgar ChISS records of 124 UNTs and entered the data into the computer. More than 500 coda envelopes were analyzed from channels between 0.08 Hz and 5 Hz.

For measurable channels, the number of coda amplitudes obtained varied from 3-5 to 10-12, depending on the intensity of event and magnification of instrumentation. For small events only two or three channels had records with coda large enough to be measured, generally 0.62, 1.25 and 2.5 Hz. For large events five, six and up to eight channels were measurable. Elapsed time relative to the event origin varied from 250 seconds to as much as 1,400 seconds in some cases.

Observed Direct and Coda Phases

We consider the coda as consisting of two parts. The first portion is the tail of the dominant direct wave, originating from scattering in the vicinity of the ray path. The second portion is the "late coda" or "coda" originating from scattering throughout a large volume of the Earth, of a dimension greater than the epicentral distance. Excitation of the late coda is insensitive to path variations, but depends on variations in spectral content radiated by each individual event. For this reason, we rely on the late coda to study spectral scaling and explosion emplacement conditions.

We must define the time at which the late coda begins, which entails detailed investigation of the dominant direct waves preceding the coda. We observe three intensive waves along the STS-Talgar path: 1) the ***Lg*** wave train, arriving at Talgar at 210-215 seconds, reaching maximum intensity at about 220-240 seconds and remaining intense until 250-270 sec; 2) the ***Rg***, arriving at 240 sec, with maximum at 260-270 sec and intense until 300 sec; and 3) the ***Lo***, which is a wave group observed in the 340-450 second time interval, perhaps a short-period surface wave train with group velocity 1.9-2.2 km/sec, observed on the 0.28 - 1.25 Hz channels with amplitude just above the coda. The ***Lo*** group is weaker than ***Rg*** on long-period channels, and weaker than ***Lg*** on short-period channels. At mid-period channels, 0.28 and 0.32 Hz, ***Lg***, ***Rg*** and ***Lo*** have roughly equal amplitudes. Each of these waves produces its own coda, which overlaps with coda of the other phases.

Aki's "rule of thumb" for coda measurement defines the beginning of the late coda as twice the travel time of the associated direct wave. In reality the factor of two can vary. We find the critical time empirically for our study. This is done based on observations of the envelope shapes, including both early and late coda. We began to measure the envelope soon after the passage of ***Lg*** or ***Rg*** waves.

To manually obtain the coda envelope from a photo paper record, one must choose each individual moment of time to measure. We chose measurement times such that monotonically decreasing amplitudes are obtained. Strict adherence to this rule enhances repeatability, which we have verified by comparing measurements obtained independently by two analysts. Further testing has shown that measurements from the short and long period recording in the common, 0.62 Hz, band are the same.

The accuracy of manual measurements of ChISS envelopes depends on amplitude. The accuracy is lower for small amplitudes (below 1-2 mm) and large amplitudes (over 70-100 mm). Our estimate is that amplitudes less than 1 mm can be measured with error on the order of the amplitude itself. Therefore we eliminate all data below this level. The difficulty with large amplitudes is that waveforms from neighboring channels can overlap. Channels are recorded side by side and are separated by 70 mm; thus, peak-peak amplitudes larger than 70-100 mm overlap. From our experience, measurement quality depends on brightness of the record.

Occasionally, errors result from mistakes in measuring calibration levels. In such cases, both coda and direct wave amplitudes have the same discrepancy for that channel. This cannot be seen in individual envelopes, but is revealed in the spectra of individual events and in correlations between amplitude and magnitude. Such comparisons have been made to control the quality of the Talgar data set.

We summarize observations of the coda envelopes by band in the following. All the individual envelopes were normalized to the level 1 at lapse time 500 seconds. The bands of f = 0.62 Hz from the LP and ShP ChISS systems were combined together. The envelopes (Figures 1a,b,c,d,e,f) are corrected for geometrical spreading, assumed to be $\sim t^{-0.5}$ for 0.08 and 0.14 Hz channels and $\sim t^{-1}$ for channels 0.28 and higher.

0.08 and 0.14 Hz: Envelopes from the two long period channels are similar, showing a dramatic decrease between 250 and 300-320 seconds (the Rg wave tail, Figure 1a). We observe a small increase between 350 and 450 seconds. This is a long-period ***Lo*** wave. The ***Rg*** tail for the 0.14 Hz channel is weaker than that observed on the 0.08 Hz channel. The increase at 400-450 sec is nearly invisible. The ***Lo*** wave is visible itself, but its coda is not, because of strong attenuation in the upper crust. The uniformly decaying envelope begins at lapse times of 500-550 seconds.

0.28 and 0.32 Hz: Envelopes from these bands differ from those of the long period channels (Figure 1b). ***Rg*** is very weak at these frequencies and no tails are observed. All the wave groups, ***Lg***, ***Rg*** and ***Lo*** are of similar amplitude and little exceed the irregular oscillations before and after them. A very smooth maximum is observed between 270 and 350 seconds, corresponding to a velocity interval from 2.1 to 2.8 km/sec, likely the result of a short-period surface wave ***Lo***, propagating in the upper crust. This wave is usually seen clearly at distances of 200 to 250 km. But because of strong scattering in the upper crust the ***Lo*** waves produce intense coda, then decrease and almost disappear at 750 km. At this distance, the ***Lo*** wave train does not dominate its own coda. This happens owing to strong loss of ***Lo*** energy by both scattering and attenuation processes. This produces a relatively intense coda that attenuates faster than ***Lg*** coda. That is because ***Lg*** travels throughout the entire crust, including the less attenuating lower crust. We conclude that the ***Lo*** coda dominates at lapse-time 400-550 seconds. But then it decreases and after 500-550 seconds the ***Lg*** coda begins to dominate. This conclusion is based on the coda slopes, which differ between 350-500 and 500-1,000 second time ranges. Therefore, we considered two separate codas based on these time limits in this study.

0.62 and 0.67 Hz: At this frequency ***Lg*** is much more intense than ***Lo*** and the coda is associated with the ***Lg*** (Figure 1c). But between 350 and 430 second envelopes flatten, indicating an additional source of scattered waves. This flat portion is, likely, a peak of the ***Lo*** wave, nearly hidden within its own coda. The corresponding arrival time gives a velocity of 1.8-2.1 km/sec. The envelope decay rate between 450 and 1,200 seconds corresponds to a coda Q of 525, which is too high for upper crust propagation. We conclude that at 0.62 Hz the observed coda originated mostly from ***Lg***; only the peak shows above the coda. The coda created from ***Lo*** is mixed with the ***Lg*** coda at times between 350 and 450 seconds.

1.25 and 1.36 Hz: The features we observe in these bands are the similar to those of the 0.62 Hz channel (Figure 1d).

2.5 and 2.9 Hz: These envelopes show a uniform linear decrease from nearly the beginning (300 sec, Figure 1e). The initial part of the envelope, 250 to 300 seconds, consists of a direct ***Lg*** tail. No sign of ***Lo*** exists. We conclude that 2.5 Hz coda originated from high-frequency ***Lg***. Decay slopes differ slightly between 2.5 and 2.9 Hz envelopes.

5 and 5.7 Hz: This high-frequency coda is short and straight, only a few measurements exist beyond 500 seconds, none are recorded at times greater than 550 seconds (Figure 1f).

We summarize our observations as follows: 1) the dominant wave is ***Rg*** at 0.08 and 0.14 Hz, ***Lg*** dominates at 0.62-2.5 Hz and displays a short tail, ***Lo*** dominates at 0.28 Hz and ***Lg*** is nearly invisible and no tail exists at 5 Hz; and 2) the short-period surface wave, ***Lo***, exists on almost all channels from 0.08 to 2.5 Hz, and is seen as a wide weak maximum, exceeding the straight coda envelope by a factor of only 1.2 to 1.7, and we define the beginning of late coda at 500-550 for 0.08 Hz, 450-500 seconds for 0.14-0.28 Hz, 400-450 seconds for 1.25 Hz and 300 seconds for 2.5 and 5 Hz.

We chose the logarithm of the coda envelope at lapse time 500 seconds as a standard measure of coda intensity. These values will be used to construct coda spectra.

Coda Attenuation

We estimate coda Q based on the standard equation (Aki and Chouet, 1975) and results are shown in Table 3. Coda Q was measured separately for earlier and later lapse time intervals for the 0.28 Hz band, as defined above. We believe that these two intervals represent ***Lo*** and ***Lg*** coda, scattered in the upper crust (***Lo*** coda) and in the whole crust, or, alternatively, in the crust and lithosphere (***Lg*** coda).

Raw Coda Spectra

The coda spectra means the logarithm of the value of coda envelope at lapse time 500 seconds, measured in nm/sec. The spectra were found in a wide frequency band, from 0.08 or 0.14 Hz up to 5.0 Hz, only for large events. For small events the coda exists on only three channels: 0.62-2.5 Hz.

The coda raw spectra of Balapan and Degelen tests are shown in Figures 2a and 2b. The events have a spectral peak with position varying between 0.62 and 1.25 Hz.

In general the Degelen and Balapan spectra are similar, but there are some systematic differences between these two groups. Degelen spectra are a little bit wider than those of Balapan, and have more high frequency energy. These differences are not a result of wave propagation (the volume of scattering media is the same), but are caused by various conditions at the source, and rock properties in these two areas of the Semipalatinsk Nuclear Test Site (STS). The smallest events (down to m = 4.5), with three points of spectrum only, show variable peak positions, either about 1 Hz or less than 0.6 Hz. This indicates a variation in source scaling that might originate with differences in emplacement conditions and that will cause scatter in the observed relationships between high frequency coda amplitude and event magnitude (see below). Generalizing all the spectra into a common scaling law allows us to use deviations of individual spectra from the standard spectra as an indication of source condition.

Table 3. Values of coda Q

Channel, f (Hz)	Qc	in t (sec) interval
0.08	232	550-1400
0.14	252	500-1200
0.28	200	300- 500
0.28	323	500-1400
0.32	180	350- 500
0.32	346	500-1000
0.62	520	450-1100
0.67	525	400-1000
1.25	685	400-950
1.36	625	350- 900
2.5	920	300- 750
2.9	980	300- 600
5	1270	300- 500
5.7	1400	270- 400

Coda Amplitude vs. Magnitude

The relationship between coda amplitudes and magnitude was obtained for each frequency channel. Figure 3 shows examples of such relationships (0.28, 0.62, 1.25 and 2.5 Hz). The magnitudes were taken mostly from AWRE[2] estimates. If AWRE data were not available, we used the mb obtained from energy class values estimated from records of local seismic stations (as described by Khalturin et al. 2001). For each frequency the slope is higher for small events and became lower for large ones. The slope of the relationship decreased with event size, reflecting saturation of the 1-Hz magnitude scale for larger events. At high frequencies (> 1 Hz) the high slope of small events is about 1.33 and the low slope for large events is about 1.0. At low frequencies (f < 1 Hz) the high slope is about 1.0 and the low slope is about 0.65. The change of slope takes place at magnitude about 5.6-5.8 (Figure 4). These relationships can be used to create a scaling law for STS explosions.

[2] AWRE = Atomic Weapons Research Establishment, which includes the British group also known as Blacknest.

Scaling Law of Coda Spectra

To create a scaling law we first estimate the spectrum for a fixed magnitude and then use the set of slopes, dependent on frequency and magnitude, to extrapolate the spectra for several magnitude values. We chose to use m = 5.8 ± 0.25 to obtain the basic spectrum. Events of this size are numerous and their spectra cover our entire frequency range (0.08-5.0 Hz). It is at this magnitude that the slope of coda amplitude vs. magnitude changes. The scaling law obtained was created for all bins of magnitude and frequency for which observed data are available (Figure 5). The scaling law obtained is just a smoothed picture. The most important observations are the individual deviations of real spectra from this averaged one and these remain a focus of our work. We build a common scaling of coda spectra for both Degelen and Balapan events. The individual deviation from this scaling law will be an indication of source conditions of the underground nuclear test.

CONCLUSIONS AND RECOMMENDATIONS

We have manually measured coda envelopes from Talgar ChISS analog records for 124 Semipalatinsk Nuclear Test Site explosions that occurred between 1961 and 1988. These data have been used to study the composition of the coda for the STS-Talgar path, to define coda limits, to estimate coda attenuation, and to construct a scaling law of explosion spectra. Deviations of the coda spectra from the average scaling law could depend on emplacement conditions and will be important to study further. The coda data will be integrated into a coda calibration procedure constructed for use with modern digital data. The ChISS data will be tested for consistency with existing Borovoye digital data from events recorded in common. We anticipate that an adjustment for manual against. Hilbert transform methods of envelope construction will be added to the site correction for these data. If verified, the data will then be useful for yield estimation. The ChISS data set also contains early Lop Nor explosions that are otherwise unavailable and rare, together with STS earthquakes, which will be used to test calibration parameters.

REFERENCES

Aki, K. and B. Chouet (1975). Origin of Coda Waves: Attenuation, and Scattering Effects. *J.Geophys.Res*., 80, 3322-3342.

Khalturin V.I., T.G. Rautian, P.G. Richards (2001). A Study of Small Magnitude Seismic Events During 1961-1989 On and Near the Semipalatinsk Test Site, Kazakhstan, *Pure and Appl. Geoph.*, 158, 143-172.

Rautian, T.G and V.I. Khalturin (1978). The Use of the Coda for Determination of the Earthquake Source Spectrum. *Bull. Seism. Soc. Am*., 68, 923-948.

Tsujiura, M. (1978). Spectral Analysis of the Coda Waves from Local Earthquakes. *Bull. Earthquake Res. Inst*., 53, 1-48.

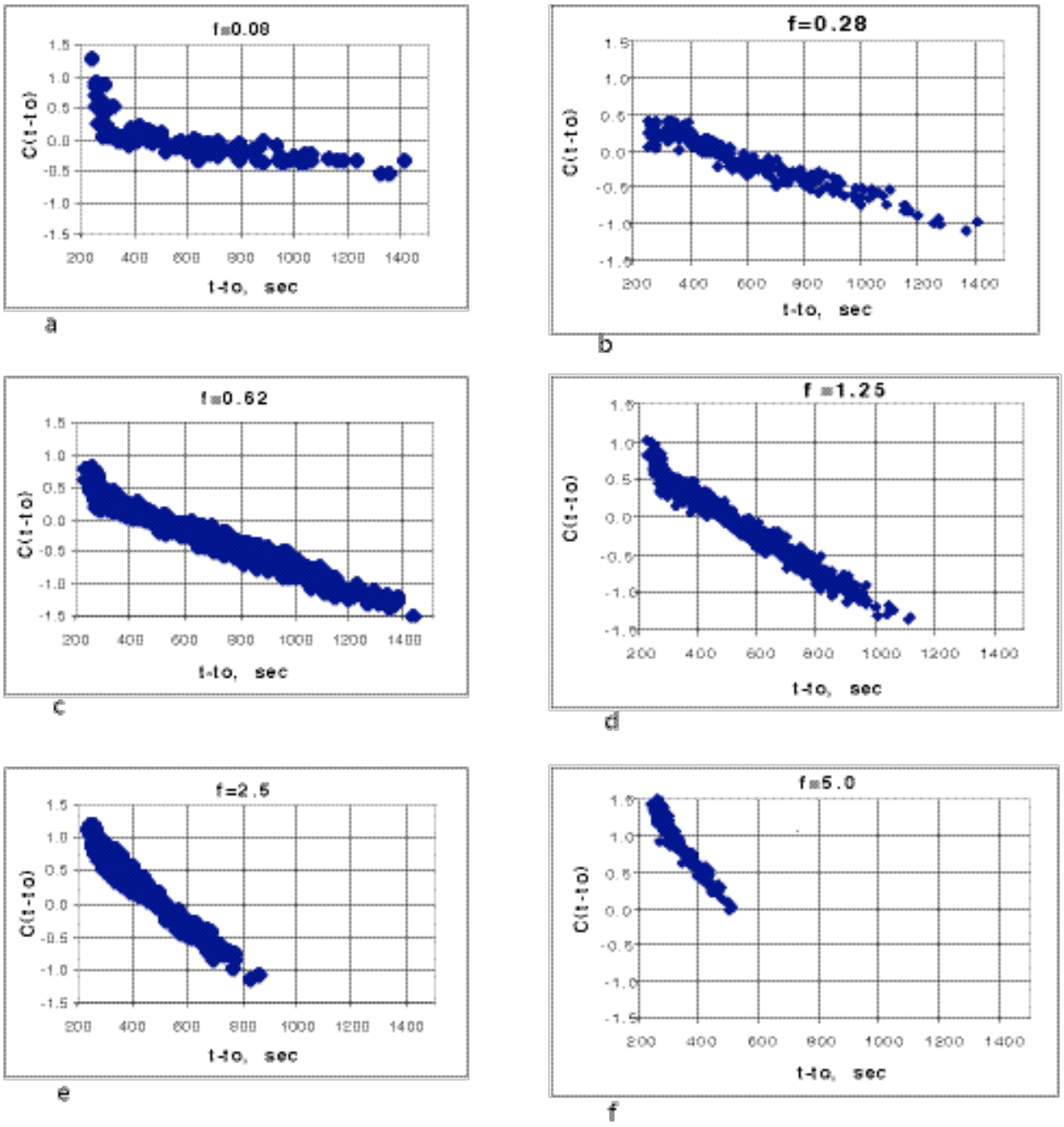
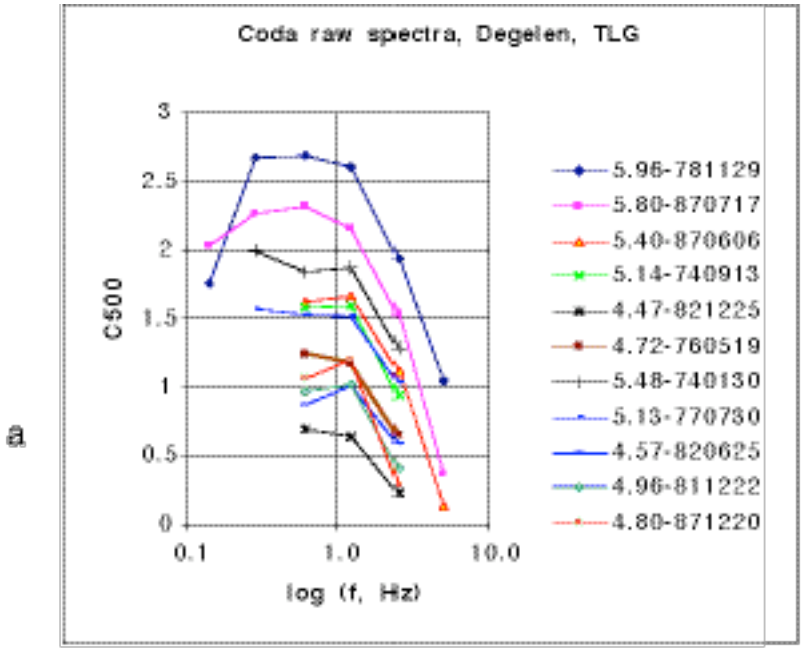
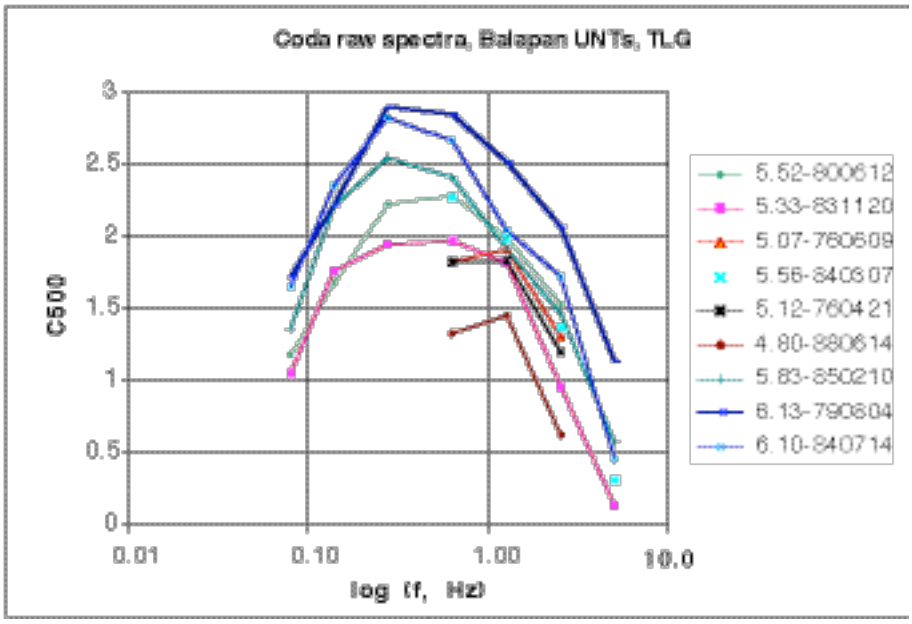


Figure 1. Normalized coda envelopes six channels. (a) 0.08 Hz channel, (b) 0.28 Hz channel, (c) 0.62 Hz channel, (d) 1.25 Hz channel, (e) 2.5 Hz channel, and (f) 5 Hz channel



a



b

Figure 2. Raw coda spectra, (a) Degelen explosions, and (b) Balapan explosions

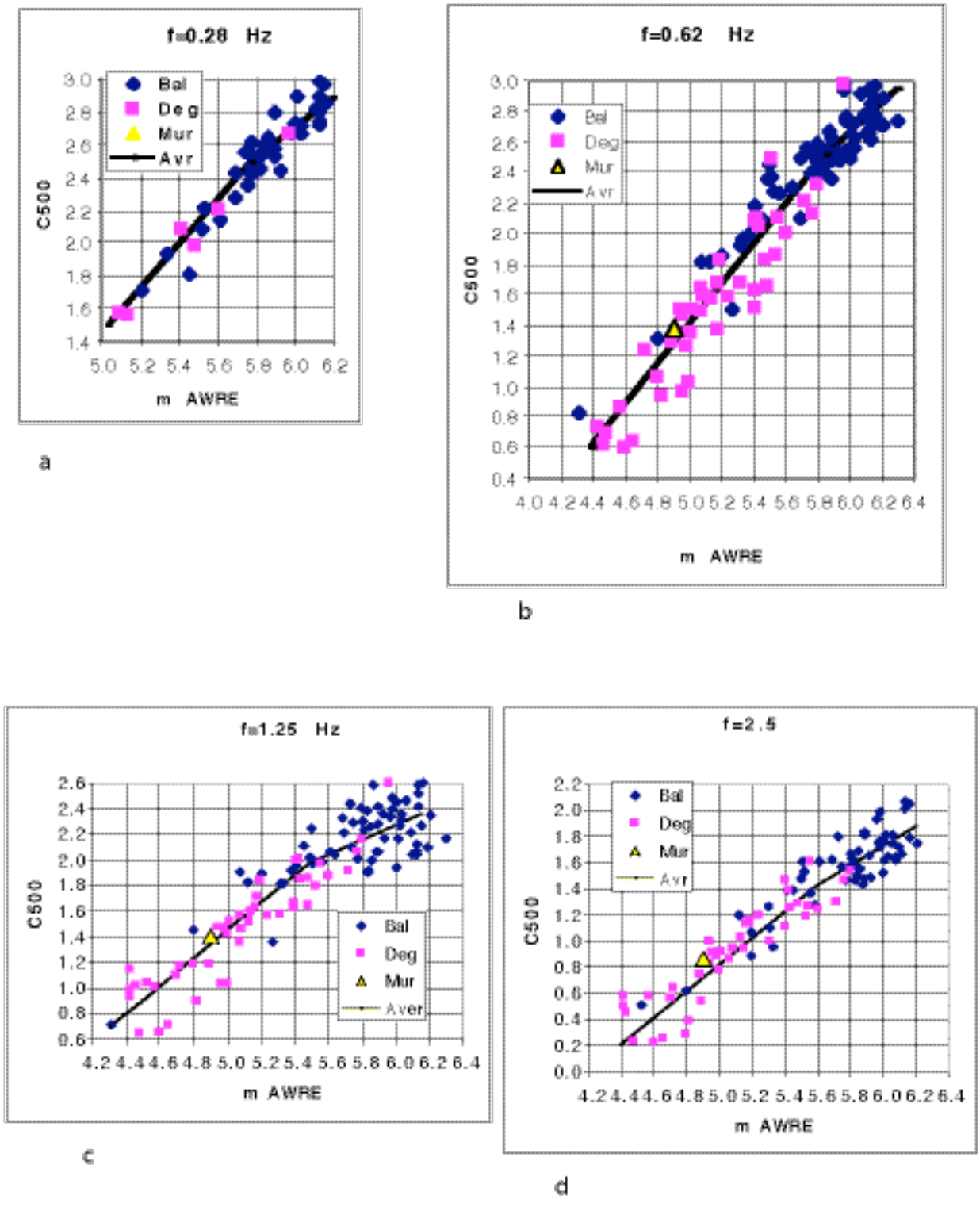


Figure 3. Coda – magnitude relations, (a) f = 0.28 Hz, (b) f = 0.62 Hz, (c) f = 1.25 Hz, and (d) f = 2.5 Hz

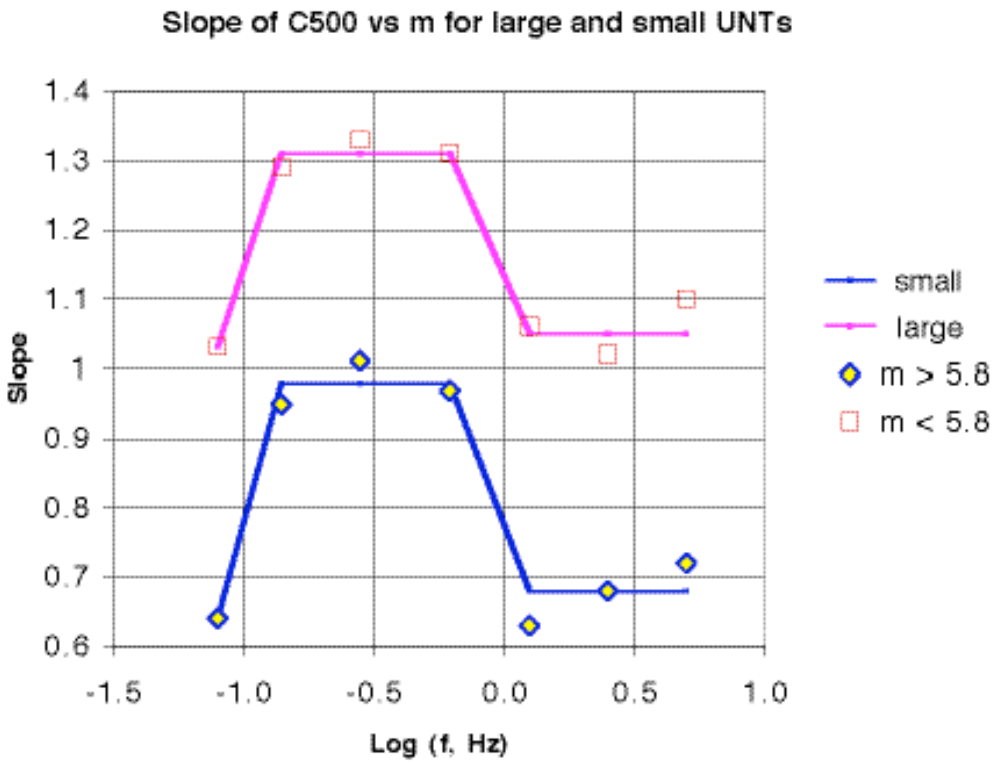


Figure 4. The coda-magnitude slope dependence on magnitude and frequency

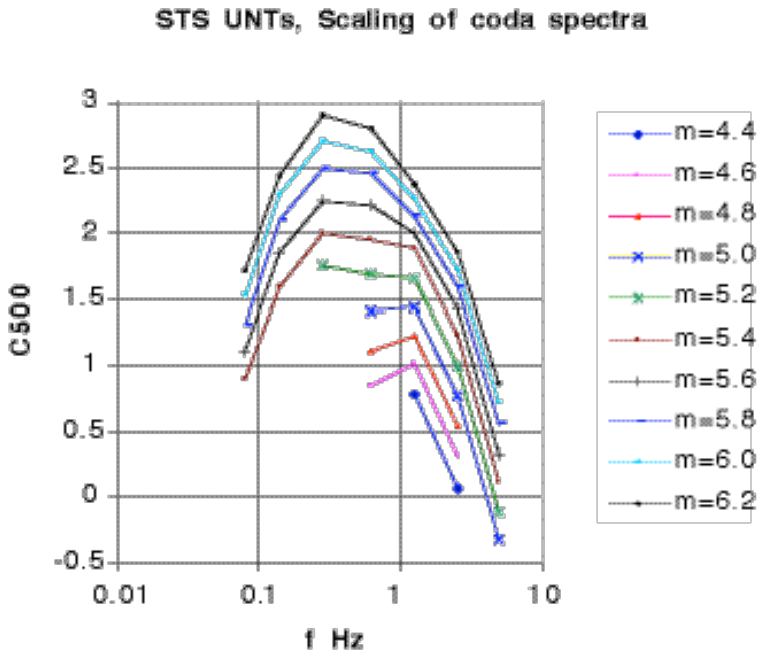


Figure 5. Average scaling of STS UNT coda spectra from Talgar ChISS records

SEISMIC SOURCE CHARACTERIZATION AND ENERGY PARTITIONING FROM IN-MINE AND REGIONAL BROADBAND DATA IN SOUTH AFRICA

Eliza B. Richardson[1], Andrew A. Nyblade[1], William R. Walter[2], and Arthur J. Rodgers[2]

Penn State University[1],
Lawrence Livermore National Laboratory[2]

Sponsored by National Nuclear Security Administration
Office of Nonproliferation Research and Engineering
Office of Defense Nuclear Nonproliferation

Contract No. DE-FC03-02SF22673[1] and W-7405-ENG-48[2]

ABSTRACT

Mining-induced seismicity provides an important link between man-made and natural tectonic processes because it includes both fresh-fracturing events that are directly triggered by excavation and blasting, as well as events dominated by frictional slip which are analogous to tectonic earthquakes. These two types of events have distinguishable characteristics, such as different spatio-temporal clustering patterns, as well as different spectral signatures. Some previous studies using local in-mine data indicated that the fresh-fracturing events often have isotropic (explosional) moment tensors. Being able to differentiate the two types of events at regional and teleseismic distances is important for seismic verification studies.

We are studying a dataset of M > 2.5 mining-induced events that occurred between 1997 and 1999 in the Far West Rand gold-mining region of South Africa, approximately 80 km southwest of Johannesburg. The depth range of these events is 1.5 - 4 km; they were recorded locally by five networks of 109 three-component geophones installed at depth throughout the active mining environment. These events were also recorded at regional distances by a two-year PASSCAL deployment of 80 broadband stations.

Using a spectral method, we have calculated source parameters for these events from the in-mine recordings, including seismic moment, stress drop, corner frequency and energy. Larger stress drops are found than for frictional events, although the latter generally have larger seismic moments. S/P wave amplitude ratios are lower for fracturing events as well, which can be an indication of isotropic components of the source. From spectral analysis, scaling relations, and statistical analysis of the characteristic length scales between sequential frictional events, we confirm earlier estimates of the critical slip length (D_c ~ 100 microns) and critical patch size (R_c ~ 10 m). We believe these dimensions represent the nucleation size of events in this hard-rock mine environment.

We have inverted for the moment tensors of 15 events from the Far West Rand gold-mining region of South Africa that range in size from 1.0 < M < 3.2. These events occurred at 1-4 km depth and were recorded locally by four networks of 102 three-component geophones installed at depth throughout the active mining region as well as by a two-year PASSCAL deployment of 80 broadband seismometers. The moment tensors of the 15 events are consistent with purely double-couple solutions. In addition, we studied several events in the range 1 < M < 2 whose poor signal-to-noise ratio on the regional recordings prevented reliable moment tensor inversions. We presume that these events also have double-couple mechanisms based on their similar P/S amplitude ratios in comparison to the 15 well-characterized events. Therefore, we find little evidence in our data of seismic events with isotropic (explosional) mechanisms, at least down to the M = 1 level.

OBJECTIVES

Mining-induced seismicity not only occurs at scales between those in the laboratory and those on tectonic faults, but also can be recorded at the depth of seismic nucleation using in-mine seismometers, thus creating an excellent "natural laboratory" in which to study the physics of earthquake rupture. At present most gold mines in the Witwatersrand basin of South Africa use sophisticated underground arrays of geophones and accelerometers to record over 1,000 events per day. The extensive seismicity recorded at moment magnitude $M_w > 2$ provides a unique dataset to develop and test methods of discrimination between natural seismicity, mining tremors, and other industrially-related events such as chemical explosions. These $M_w > 2$ mining-induced events are large enough to be recorded on the in-mine arrays, as well as regionally by broadband seismometers. Therefore, locations, magnitudes, and focal mechanisms may be accurately determined from the high-frequency local data while regional phase propagation and energy partitioning may be studied via regional recordings. Another feature of this dataset is the variety of focal mechanisms as some mine events are purely double-couple shearing events whereas, other have significant isotropic components (McGarr, 1992).

As the mines develop the technology to remove ore from deeper and deeper within the crust, larger stresses accumulate, producing higher rates of seismicity. Characterization of these events in terms of comparisons to other types of seismicity, both natural and man-made is important for building a comprehensive knowledge base of crustal seismic activity as well as for the pure science of earthquake physics and nucleation. In this study we seek to determine seismic source characteristics as well as moment tensors for a variety of mining-induced events in order to construct a catalog of "typical" large mining-induced events that can be used for source discrimination purposes as well as energy partitioning studies of the southern African crust.

RESEARCH ACCOMPLISHED

Source parameters

We have assembled a dataset of large ($M_w > 1.4$) mining-induced events from four gold mines in the Far West Rand region. The locations of these events were determined by operators at the mines via a ray-tracing algorithm based on body wave arrival times (Mendecki, 1993, 1997). This method incorporates a layered velocity model based on geologic units that have been determined by underground surveying and mapping as well as surface-based refraction profiles and borehole log data. The wavespeeds and location procedures have been verified by test blasting, so location uncertainties are typically on the order of 10-20 m for events of $M_w > 2$.

Using the spectral method developed by Andrews (1986) and adapted by Richardson & Jordan (2002) for use with in-mine seismic recordings, we have calculated source parameters for fourteen events that occurred in 1999, and 23 events from 1998 (see Table 1). Each of the events in this study was recorded by at least ten stations. In order to determine source parameters, we median-stacked each event's spectra and integrated the results up to the Nyquist frequency to determine S_D, the integral of the displacement power spectra (see Equation 6 of Andrews, 1986}), S_V, the integral of the velocity power spectra (see Equation 7 of Andrews, 1986), and A^2, the acceleration power spectral level (see Equation 19 of Andrews, 1986). These are used to determine the source parameters radiated energy (E), seismic moment (M_0), and static stress drop ($\Delta\sigma$) as follows:

$$E = 4\pi\rho v S_V$$

$$M_0 = \frac{8\pi\rho v^3 S_D^{(3/4)}}{\Re S_V^{(1/4)}}$$

$$\Delta\sigma = \frac{2\pi f_0 \rho A^2}{C\Re}$$

in which the corner frequency is found by

$$f_0 = \left(\sqrt{S_V / S_D}\right) / 2\pi.$$

In the previous equations, ρ is the rock density, which has been determined experimentally at the mines, v is wavespeed, $\Re$ is a constant based radiation pattern, and C is also a small constant. An advantage of this method is that the exponent of the spectral roll off is not a fixed parameter as in the case of fitting spectra with a Brune-type curve. Because our data is band-limited, there is an upper limit to the radiated energy we can determine (Ide & Beroza, 2001). However, in practice the underestimation of energy for this dataset is very small (approximately 5%) since typical corner frequencies for the events in this study are generally 1/5 to 1/10 of the Nyquist frequency (Richardson & Jordan, 2002).

In the following table, event dates and times are listed as yyyymmddhhmmss (The event times are local to the mines. Subtract two hours to get GMT time). Event locations are given by their latitude (°N), longitude (°E), and depth (meters below datum). It should be noted that event depths are referenced to the origin or "datum" of the Z axis of the local mine coordinates. This datum is a reference point in Johannesburg, and is 250 m above ground level and about 1800 m above sea level in the Carletonville Mining District where these events occurred. Seismic moment M_0 is in Nm, magnitude M_w is moment magnitude (Hanks & Kanamori, 1979), energy E is given in Joules, corner frequency f_0 is in Hz, and static stress drop Δσ is in MPa.

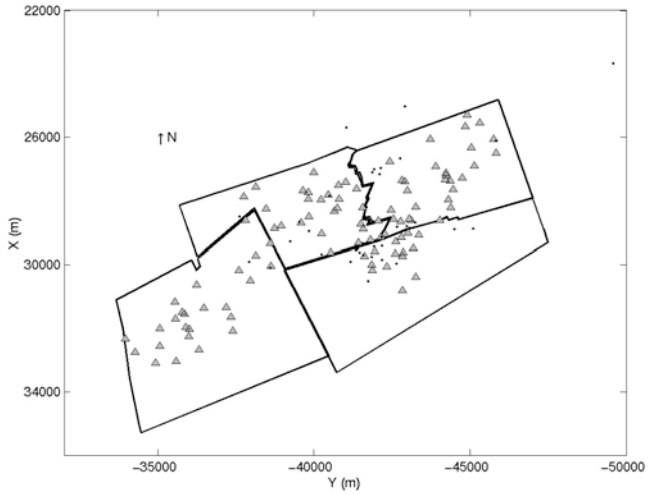


Figure 1. Map view of the lease areas of four mines in the Carletonville district (in mine coordinates). There are 102 three-component stations installed at depth (triangles). Dots represent the epicenters of large mining-induced events for which spectral source parameters were calculated (see Table 1) in this study.

Table 1. Source parameters of mining-induced events determined by in-mine array data. Events in bold are those for which moment tensors have been determined.

Event	Lat	Lon	Depth	M_0	M_w	E	f_0	Δσ
19980111144841	-26.401	27.411	2338	1.4e13	2.7	5.5e8	15.8	5.87
19980220050356	-26.429	27.430	3694	7.8e13	3.2	1.0e10	12.9	20.00
19980328134551	-26.437	27.417	2729	1.2e13	2.7	2.8e8	16.6	3.65
19980329051801	-26.435	27.422	2587	2.2e13	2.8	4.9e8	16.3	3.46
19980331135629	-26.439	27.380	2053	2.2e13	2.8	2.1e8	9.3	1.47
19980404190603	-26.430	27.399	2047	1.1e13	2.7	1.8e8	14.6	2.51
19980420170707	-26.395	27.430	2273	2.8e13	2.9	1.6e9	13.8	8.76
19980420194749	-26.412	27.422	1925	2.5e13	2.9	9.1e8	14.8	5.72
19980502123739	-26.414	27.419	1955	2.2e13	2.8	4.9e8	11.9	3.43
19980508103233	-26.440	27.427	2661	1.1e13	2.6	1.8e8	12.1	2.46
19980622162025	-26.439	27.423	2588	1.3e13	2.7	3.4e8	15.2	4.01
19980708212049	-26.434	27.416	2553	1.2e13	2.7	3.9e8	14.8	4.83

19980727135740	-26.427	27.419	2409	2.5e13	2.9	4.3e8	9.5	2.73
19981002194336	-26.432	27.423	2569	1.0e13	2.6	1.3e8	10.2	1.90
19981007192539	-26.420	27.406	3123	2.0e13	2.8	1.3e9	16.9	10.30
19981019200410	-26.436	27.416	2505	1.3e13	2.7	2.0e8	10.5	2.40
19981021044841	-26.434	27.420	2613	1.0e13	2.6	1.3e8	11.5	2.00
19981023160058	-26.437	27.420	2745	3.1e13	2.9	7.1e8	8.7	3.50
19981027090946	-26.426	27.377	2989	1.2e13	2.7	3.6e8	15.2	4.72
19981102163835	-26.427	27.434	2552	2.5e13	2.9	6.2e8	10.4	3.90
19981110172424	-26.404	27.459	2770	1.2e13	2.7	3.1e8	15.0	4.10
19981119170822	-26.414	27.422	2268	1.1e13	2.6	3.0e8	13.3	4.20
19981223093859	-26.433	27.393	3375	2.8e13	2.9	1.1e9	12.8	5.94
19990103155836	**-26.412**	**27.420**	**1748**	**1.1e13**	**2.6**	**1.2e7**	**12.1**	**0.87**
19990118102526	**-26.420**	**27.446**	**3422**	**9.0e11**	**1.9**	**9.4e6**	**27.3**	**0.80**
19990118112405	**-26.420**	**27.446**	**3443**	**2.0e11**	**1.4**	**1.1e6**	**36.1**	**0.68**
19990118200717	**-26.415**	**27.422**	**2039**	**2.9e12**	**2.2**	**1.9e7**	**15.9**	**0.51**
19990118213352	**-26.409**	**27.429**	**2879**	**9.1e12**	**2.6**	**1.6e7**	**15.0**	**1.00**
19990201194832	**-26.428**	**27.406**	**3137**	**4.8e12**	**2.4**	**3.4e7**	**13.6**	**0.53**
19990202123021	**-26.435**	**27.415**	**2582**	**1.2e13**	**2.7**	**3.2e7**	**13.6**	**3.00**
19990203221201	**-26.423**	**27.363**	**2638**	**1.4e12**	**2.0**	**1.5e7**	**23.4**	**1.98**
19990205025535	**-26.420**	**27.417**	**2991**	**4.3e12**	**2.3**	**5.8e7**	**17.6**	**1.37**
19990205175933	**-26.420**	**27.363**	**2686**	**3.1e11**	**1.6**	**5.0e6**	**44.3**	**3.07**
19990205205457	**-26.463**	**27.362**	**2558**	**2.9e12**	**2.2**	**3.1e7**	**18.5**	**0.96**
19990209154922	-26.477	27.329	2738	6.6e11	1.8	3.1e5	10.7	0.19
19990209195821	**-26.401**	**27.418**	**1618**	**4.2e13**	**3.0**	**9.2e8**	**9.3**	**3.20**
19990216053511	**-26.429**	**27.432**	**3761**	**1.2e13**	**2.7**	**9.2e6**	**10.4**	**0.56**
19990226143150	**-26.397**	**27.387**	**1981**	**4.5e12**	**2.4**	**2.2e6**	**12.3**	**0.53**
19990309161938	-26.435	27.415	2464	1.1e13	2.6	6.8e7	8.1	0.99
19990310023001	-26.429	27.428	2651	1.0e13	2.6	1.7e8	14.9	2.50
19990318193538	-26.428	27.396	395	4.6e13	3.1	1.5e9	11.5	5.20
19990703111216	-26.169	27.497	3099	2.2e13	2.9	1.8e8	18.5	10.60
19990709200228	-26.395	27.413	7235	5.5e13	3.1	9.7e8	8.7	4.00
19990718173016	-26.393	27.403	3823	7.0e13	3.2	1.2e9	8.6	4.80
19990907150924	-26.386	27.446	3634	4.0e13	3.0	2.7e9	13.0	10.90
19990923132820	-26.386	27.452	4028	4.1e13	3.0	1.5e9	13.3	10.30

Moment tensors of selected events

We determined moment tensors for events that covered a range of magnitudes, depths, and locations to provide as much variation as possible in composing a catalog of "typical" large mining-induced events. Some events are also part of foreshock-mainshock-aftershock sequences. We followed the method outlined in Ammon et al. (1998) and calculated regional Green's functions, then inverted for the moment tensors using broadband data from the Kaapvaal PASSCAL deployment. Since we used the PASSCAL data alone, we obtained independent measurements from those of the in-mine array data previously used to determine the source parameters (see Table 1). A comparison of event magnitudes as calculated by the spectral method using only the in-mine array data with magnitudes determined as part of the moment-tensor inversion is shown in Figure 3. By only using eight nearby stations for the inversions (see Figure 2), we will be able to use the more distant stations for regional phase amplitude analysis; therefore, the results of the two studies will not be dependent upon each other.

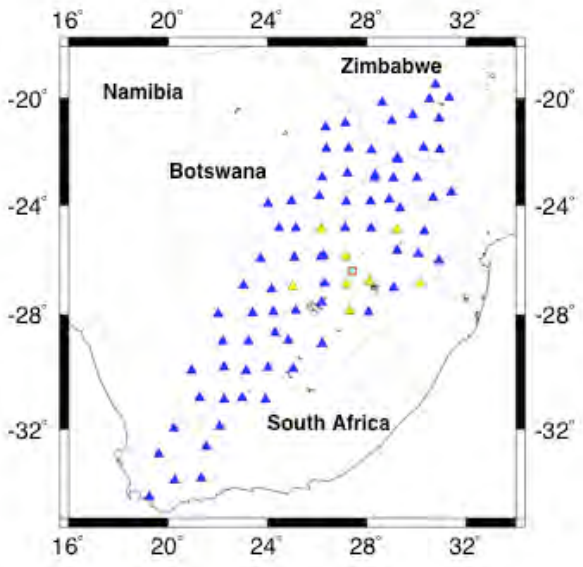


Figure 2. Map of southern Africa showing locations of the Kaapvaal Craton PASSCAL deployment (triangles). Yellow triangles are the stations used in the moment tensor inversions. The small red box is the area shown in detail in Figure 4.

To compute regional Green's functions, we used a simple 45-km thick crustal half-space for the velocity model based on the results of receiver function analysis of the crustal structure of the Archean craton by Nguuri et al. (2001). This study determined that crustal thickness ranged from approximately 41-50 km across the area covered by the stations used in our moment tensor inversions. We used wavespeed and density values determined experimentally by the mines (P = 6.1 km/s, S = 3.65 km/s, $\rho = 2.7 g/cm^3$).

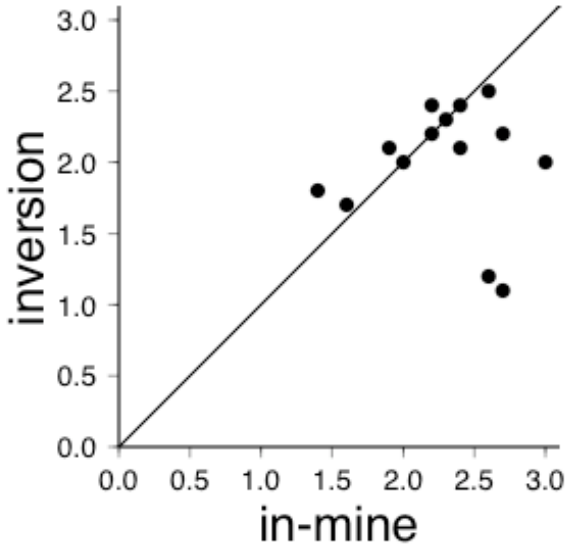


Figure 3. Comparison between moment magnitude as determined by the spectral analysis using in-mine seismic data and that determined through the moment tensor inversion using the broadband data. The 1:1 line is drawn for reference.

The results of the moment tensor inversions are given in Table 2. These are fully deviatoric tensors. We allowed the moment tensors to have some isotropic component in the inversion, but none were significantly isotropic. It has been shown that S/P-wave amplitude ratios of mining-induced events are often smaller for events with significant isotropic components when compared with purely double-couple events of approximately the same moment (Cichowicz et al., 1990, Gibowicz et al., 1991). Therefore, we calculated the S/P-wave amplitude ratios of several other events between $1< M_w < 2$ whose signal-to-noise ratios were not good enough to perform moment tensor inversions using broadband data. The S/P-wave amplitude ratios were not significantly different than those of the double-couple events for which we determined moment tensors, and therefore we do not expect significant isotropic components of the source down to at least $M_w = 1$. It should be noted that the previous studies involving S/P-wave amplitude ratios were conducted with events of $M_w < 0$.

The fourteen events for which we determined moment tensors ranged in size from $1.4 < M_w < 3.0$ and ranged in depth from 1.6 km to 3.8 km. This depth range is typical of the larger mining-induced events in the Carletonville district. We do not observe any significant trend in type of faulting with either depth or event size (see Figure 4). The events in this study so far show two major modes of failure: normal faulting and strike-slip faulting. It is surprising to find such a large population of strike-slip events in this group, as the vast majority of faults observed underground have measurable offsets consistent with normal motion alone. There are several possibilities for this apparent discrepancy. Not all seismogenic faults are directly visible underground, therefore there may be an historical bias in favor of normal faults because of observational limitations. In addition, the faults observed underground have yet to be studied in detail to determine whether all fault offset is due to seismic activity, or whether there is some creep. For example, do faults creep in a normal sense, but release seismic energy in a strike-slip or dip-slip pattern? Strike-slip motion is inherently difficult to discern when there is only limited visible access and when the displacement is not large enough to juxtapose different formations. There has been little in the way of detailed analysis of fault cores taken from depth; therefore sense of motion has been assumed, but may in fact be a relic of ancient fault activity that predates the active mining. It may also be that these moment tensors, which were determined by surface broadband data alone are not accurate, although the waveform fits are generally good. An obvious next step in this analysis will be to perform a joint inversion using in-mine data for moment tensor analysis. In addition, S-wave data could be included in the moment-tensor inversions.

Table 2. Moment tensors of mining-induced events

Event	M_{xx}	M_{xy}	M_{xz}	M_{yy}	M_{yz}	M_{zz}
19990103155836	-0.273E-03	-0.268E-02	0.230E-02	-0.583E-02	0.222E-02	0.611E-02
19990118102526	0.623E+00	-0.121E+01	0.179E-01	-0.152E+01	0.552E+00	0.896E+00
19990118112405	0.832E+00	-0.275E+01	-0.352E-02	-0.166E+01	-0.306E+00	0.828E+00
19990118200717	-0.132E+01	-0.169E+01	0.256E -01	0.239E+01	-0.965E -01	-0.107E+01
19990118213352	-0.382E+00	-0.185E+00	-0.166E-01	0.616E+00	-0.406E+00	-0.233E+00
19990201194832	0.186E -01	0.151E+00	-0.140E+00	0.112E+00	-0.273E+00	-0.131E+00
19990202123021	-0.118E+00	-0.320E-01	-0.143E-01	0.275E+00	-0.193E-01	-0.157E+00

Event	M_{xx}	M_{xy}	M_{xz}	M_{yy}	M_{yz}	M_{zz}
19990203221201	-0.188E+01	-0.154E+01	-0.125E-01	0.363E+01	0.884E-01	-0.175E+01
19990205025535	0.135E+01	0.194E+01	-0.961E-01	-0.240E+01	0.309E+00	0.106E+01
19990205175933	0.738E+00	-0.674E+00	-0.229E-01	-0.123E+01	0.135E+00	0.496E+00
19990205205457	0.408E+00	0.895E+00	-0.760E-01	-0.965E+00	0.318E+00	0.557E+00
19990209154922	-0.610E+00	-0.143E+01	0.560E-01	0.121E+01	-0.242E+00	-0.603E+00
19990216053511	0.353E-02	-0.130E-02	-0.270E-02	-0.360E-02	0.155E-02	0.738E-04
19990226143150	0.406E-02	-0.919E+00	-0.456E-01	0.190E+00	0.275E+00	-0.194E+00

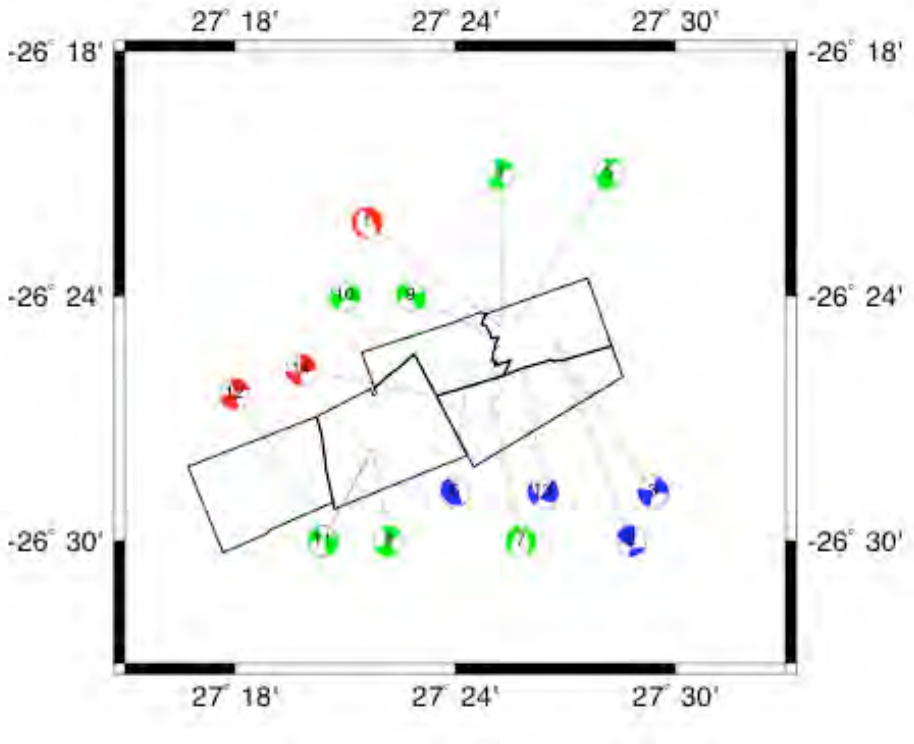


Figure 4. Map view of the lease areas of five mines in the Carletonville district with locations and beach ball diagrams of the events for which moment tensors have been determined. Events are labeled in chronological order (The beach ball labeled "1" is 19990103155836, and the beach ball labeled "14" is 19990226143150, etc.). Red beach balls denote events whose depths are between 1-2 km, green beach balls are for events between 2-3 km and blue beach balls show events whose depths are between 3-4 km.

CONCLUSIONS AND RECOMMENDATIONS

We have calculated source parameters for 46 mining-induced events of $M_w > 1$ and inverted for the best-fitting moment tensors for 14 of these events. We do not find any significant isotropic components of the source for any of the events studied. This supports the hypothesis that large mining-induced failures occur by shearing of pre-existing planes of weakness under frictionally-controlled conditions (i.e. high normal stress) and that these events are physically analogous to natural tectonic earthquakes. A surprising number of strike-slip mechanisms were determined, rather than all normal faulting, which was expected. There have been few thorough studies of the source characteristics of these events to date with which to compare our results. Therefore we must continue to determine more moment tensors, and we must incorporate the in-mine data in a joint inversion for the moment tensors. The next step in the characterization of these mining-induced events is to determine regional energy partitioning and propagation. The results of this work should allow further comparison between these events and naturally occurring tectonic events.

ACKNOWLEDGEMENTS

We thank Chuck Ammon for lending us his expertise in calculating local and regional Green's functions.

REFERENCES

Ammon, C. J., R. B. Herrmann, C. A. Langston and H. Benz, Source parameters of the January 16, 1994 Wyomissing Hills, Pennsylvania earthquakes, *Seism. Res. Letters*, 69, 261-269,1998.

Andrews, D. J., Objective determination of seismic source parameters and similarity of earthquakes of different size, in *Earthquake Source Mechanics*, S. Das, J. Boatwright, C.H. Scholz, eds, vol. 6 of Geophysical Monograph 37, pp. 259-267, Am. Geophys., Union, 1986.

Cichowicz, A., R. W. E. Green, A. van Zyl Brink, P. Grobler and P. I. Mountfort, The space and time variation of micro-event parameters occurring in front of an active stope, in *Rockbursts and Seismicity in Mines*, ed. C. Fairhurst, vol. 2, pp. 171-175, 1990.

Gibowicz, S. J., R. P. Young, S. Talebi, and D. J. Rawlence, Source parameters of seismic events at the Underground Research Laboratory in Manitoba, Canada: Scaling relations for events with moment magnitude smaller than –2, *Bull. Seism. Soc. Am.*, 81, pp. 1157-1182, 1991.

Hanks, T.C. and H. Kanamori, A moment magnitude scale, *J. Geophys. Res*., 84, pp. 2348-2350, 1979.

Ide, S. and G. C. Beroza, Does apparent stress vary with earthquake size?, *Geophys. Res. Lett.,* 28, pp. 3349-3352, 2001.

Mendecki, A. J., ed., *Seismic Monitoring in Mines*, Chapman and Hall, 1997.

Mendecki, A. J., Real time quantitative seismology in mines, Keynote lecture in *Proc. 3rd Intl. Symp. on Rockbursts and Seismicity in Mines*, ed. By R. P. Young, Balkema, Rotterdam, pp. 1141-1144, 1993.

McGarr, A., Moment tensors of ten Witwatersrand mine tremors, *Pure Appl. Geophys.,*139, pp. 781-800, 1992.

Nguuri, T. K., J. Gore, D. E. James, S. J. Webb, C. Wright, T. G. Zengeni, O. Gwavava, J. A. Snoke, and Kaapvaal Seismic Group, Crustal structure beneath southern Africa and its implications for the formation and evolution of the Kaapvaal and Zimbabwe cratons, *Geophys. Res. Lett*., 28, pp. 2501-2504.

Richardson, E. and T.H. Jordan, Seismicity in deep gold mines of South Africa: Implications for tectonic earthquakes, *Bull. Seism. Soc. Am*., 92, pp. 1766-1782, 2002.

MECHANICS OF STRENGTHENING IN CRYSTALLINE ROCK AT LOW TEMPERATURES: A PRELIMINARY ASSESSMENT

Charles G. Sammis and Ronald L. Biegel

University of Southern California

Sponsored by Air Force Research Laboratory

Contract No. DTRA01-01-C-0086

ABSTRACT

Mellor (1973) measured the uniaxial compressive and tensile strengths of granite, limestone, and sandstone over a range of temperatures from 20°C to –197°C. For each of the three rock types, he tested both air-dry and water-saturated samples. These data were modeled using the micromechanical damage model. This model was formulated by Ashby and Sammis (1990) by assuming that the primary role of the frozen water in the cracks is to increase the coefficient of friction through the formation of crack-bridging "ice asperities", in addition to the usual rock asperities. The rock asperities are far below their melting temperature and deform by dislocation glide, which is only weakly temperature dependent. The ice asperities, however, form at their melting temperature and therefore deform initially by diffusion-limited creep mechanisms, which are strongly temperature dependent. The strengthening of the ice asperities with falling temperature explains the observed monotonic increase in compressive and tensile strengths at progressively lower temperatures. It also explains the leveling off of strength at very low temperatures where ice is sufficiently below its melting temperature that it deforms by glide, just like the rock asperities. The model is most suitable for low porosity crystalline rock-like granite where Mellor (1973) observed a 35% increase in compressive and a 55% increase in tensile strength between 0 and -120°C. One important implication of our model is that the effective coefficient of friction, and hence the compressive strength, is both temperature and strain-rate dependent. At the high strain rates in an explosive source, the 35% increase in strength should occur over a much smaller range of temperatures close to 0°C. The observed strengthening in granite is the same for both the air-dry and saturated samples, whereas, in both limestone and sandstone the saturated samples strengthen much more than do the air-dry samples. This is probably due to the fact that the starter flaws in granite are very thin cracks which are effectively saturated by adhered water films in the air-dry state, while the filling of the more spherical pores in the sandstone and, to a lesser extent, the limestone preferentially increases their mechanical strength in the saturated frozen state. The damage mechanics model is able to qualitatively and quantitatively explain all observed differences between the low temperature behavior of the three rock types and between the dry and saturated states in each. This preliminary assessment of the mechanisms responsible for strengthening rock at low temperature should help guide the design of future low-temperature experiments, and suggests that low-temperature triaxial strength testing should be supplemented with low-temperature friction experiments.

OBJECTIVES

The objectives of this research program are as follows:

1. Build the micromechanical damage mechanics developed by Ashby and Sammis (1990) into source models for underground explosions.
2. Use this model to explore the influence of site effects such as rock type, ground water saturation, permafrost, and depth of burial on the seismic signature generated by the explosion.
3. Use this model to help interpret laboratory measurements and field experiments.
4. Explore the possibility that secondary radiation generated by the damage contributes to the regional seismic phases.

RESEARCH ACCOMPLISHED

Introduction

The Soviet test site at Novaya Zemlya at 73° north latitude lies well above the Arctic Circle. Rock at this site is probably below the freezing point of water to considerable depth. Permafrost thickness is greatest in non-glaciated polar regions like Siberia, where a record depth of 4,900 feet to the permafrost base has been reported. Permafrost thickness in arctic Canada has been estimated to exceed 3,000 feet and in arctic Alaska it may exceed 2,000 feet. The question has therefore arisen as to how frozen water in cracks and pores might affect the seismic signature of an underground explosion.

Uniaxial compressive and tensile tests at a low temperature have shown that freezing can increase rock strength by a factor of four in porous rock and by a factor of 1.8 in crystalline rock (Mellor, 1973). In this paper, we interpret these data using the micromechanical damage model (Ashby and Sammis, 1990) in which sliding on preexisting cracks in rock induces additional fracture damage and ultimate failure. The effect of ice in this model is to increase the effective coefficient of sliding friction on the preexisting cracks thus inhibiting the generation of new damage and strengthening the rock. In addition to strengthening, the damage model is also able to explain some of the more subtle phenomenology in the ice data such as the differences between porous and crystalline rock and the progressive strengthening observed to occur as the temperature is lowered from $0°\,C$ to $-150°\,C$.

The strengthening associated with low temperatures can be expected to significantly reduce the apparent radius of an explosion by suppressing crack growth in the non-linear damage zone, thus producing a higher frequency seismic signature than that from an equivalent explosion in rock above $0°\,C$. Also, the "pulse broadening" phenomena observed for shots in crystalline rock, which has been associated with dynamical weakening of the damage zone, should be suppressed in frozen crystalline rock. These effects can be assessed quantitatively using the source model developed by Johnson and Sammis (2001), which incorporates the Ashby and Sammis (1990) damage mechanics.

The Uniaxial Strength of Frozen Rock

Mellor (1973) measured the uniaxial compressive and tensile strength of granite, limestone, and sandstone over a temperature range from $20°\,C$ to $-197°\,C$ for both water saturated and air-dry samples. Results from the compressive tests are shown in Figure1 and those from the tensile tests in Figure 2. We first make a few observations about these results and offer a qualitative explanation of each in terms of the damage mechanics model. A more quantitative model for the granite data is given in the next section.

Observation 1: In compression, the saturated samples for all three rock-types show a strong increase in strength beginning at $0°\,C$ and continuing to $-120°\,C$. The air-dry limestone and sandstone samples do not show a comparable increase in strength at low temperatures. However, both the air-dry and saturated granite samples strengthen at approximately the same rate with decreasing temperature.

Damage Mechanics Explanation: In the saturated samples for all three rock-types, frozen water inhibits sliding on the preexisting flaws, suppressing damage and strengthening the samples. The flow strength of ice increases as the temperature falls below the freezing point thus increasing the apparent coefficient of friction and strengthening the samples. For the air-dry limestone and sandstone specimens, there is not enough adsorbed water in the pores to

provide this strengthening. However, for granite the preexisting microcracks are much narrower. The adsorbed water in the air-dry samples effectively saturates these cracks, and hence there is little difference between the low temperature compressive strength of saturated and air-dry granite. Note that the saturated granite is significantly weaker at 20°. This may be due to hydrolytic weakening which is suppressed below 0°C.

Observation 2: In tension, the saturated samples again all show an increase in strength beginning at 0°C and increasing to lower temperatures. However, in tension, none of the air-dry samples showed a comparable increase in strength. Even the air-dry granite samples remain significantly weaker than the saturated ones at low temperature.

Damage Mechanics Explanation: Failure in tension is nucleated at the largest most dangerously oriented flaw, which grows unstably to produce macroscopic failure. Failure in compression is a cooperative phenomenon involving structures created by the interaction of a myriad of smaller flaws. The reason that the tensile strength in air-dry granite does not track that of the saturated granite, is that the largest crack (the one responsible for the tensile failure) is too large to be saturated by the films of adsorbed water that saturate the myriad of smaller microcracks responsible for compressive failure.

We now quantify these observations by including the effect of frozen water in the Ashby and Sammis (1990) damage mechanics model for granite.

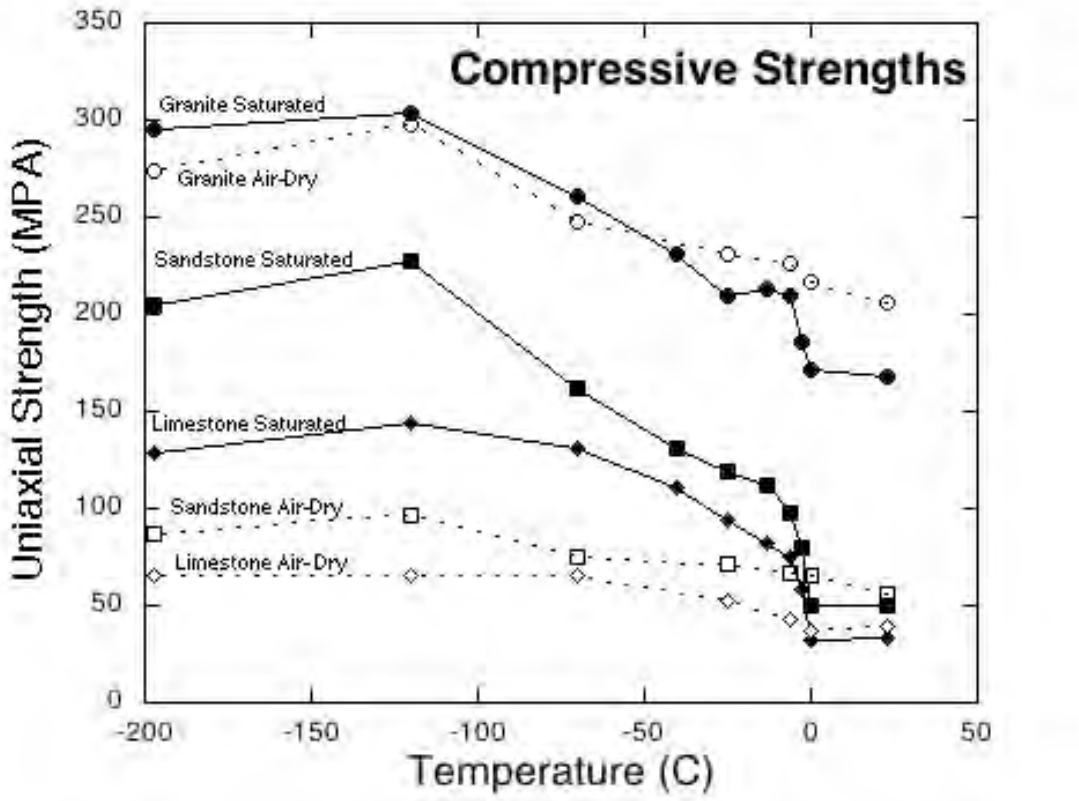


Figure 1. Strength of granite, limestone, and sandstone in uniaxial compression at low temperatures from Mellor (1973). Note that only in granite are the strengths of saturated and air-dry samples nearly the same at all temperatures.

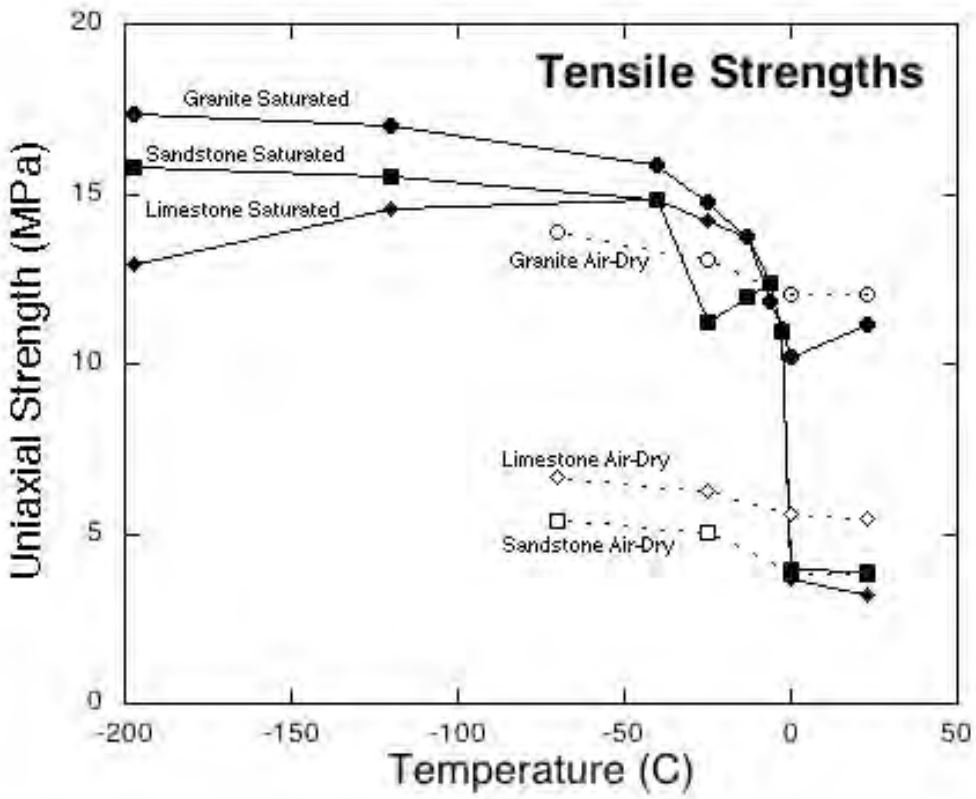


Figure 2. Strength of granite, limestone, and sandstone in uniaxial tension at low temperatures from Mellor (1973). Note that the saturated samples for all three rock-types show more strengthening at low temperatures than do the air-dry samples.

A Damage Mechanics Model for the Strength of Frozen Granite

Ashby and Sammis (1990) show that an initial inclined crack will nucleate tensile wing cracks (as illustrated in Figure 3) when

$$S_1 = C_1 S_3 + S_o \tag{1}$$

where

$$S_1 = \frac{\sigma_1 \sqrt{\pi a}}{K_{Ic}} \qquad C_1 = \frac{\left(1+\mu^2\right)^{1/2} + \mu}{\left(1+\mu^2\right)^{1/2} - \mu}$$

$$S_3 = \frac{\sigma_3 \sqrt{\pi a}}{K_{Ic}} \qquad S_o = \frac{\sqrt{3}}{\left(1+\mu^2\right)^{1/2} - \mu}$$

Using the published value for the critical stress intensity factor $K_{Ic} = 1$ MPa m$^{1/2}$, Ashby and Sammis (1990) fit equation. (1) to data for the initiation of microcrack damage in granite to determine μ in the range 0.55 to 0.65 and a crack length 2*a* near 1 mm. The assumption is that the cracks do not interact during nucleation so that equation. (1) is independent of the initial crack density.

The failure curve is sensitive to the initial crack density, which (in 3D) is expressed by the initial damage defined as

$$D_0 = \tfrac{4}{3}\pi\left(a\cos\chi\right)^3 N_V\,, \tag{2}$$

where χ is angle describing the orientation of the cracks (see Figure. 3) and N_V is the number of cracks per unit volume. In response to loading above the nucleation stress, wing cracks of length l grow at opposite edges of the initial crack thereby increasing the damage to

$$D = \tfrac{4}{3}\pi\left(l + a\cos\chi\right)^3 N_V\,. \tag{3}$$

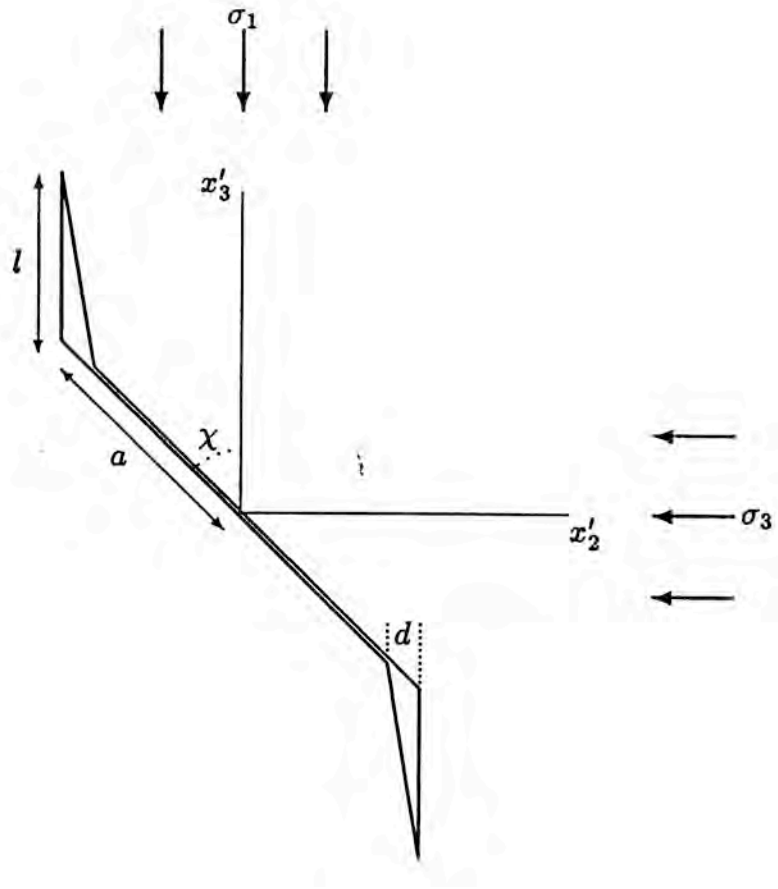


Figure 3. Geometry of a penny-shaped crack of radius *a,* that is extended by wing cracks of length *l*.

The value of l is determined by letting the wing cracks grow until the stress intensity factor at the tip decreases to the fracture toughness of the medium. The equation that relates the equilibrium damage to the initial damage and the dimensionless principal stresses is (Ashby and Sammis, 1990)

$$S_1 = -\frac{C_2\left(\left(\frac{D}{D_0}\right)^{1/3} - 1 + \frac{\beta}{\cos\chi}\right)^{3/2} - S_3\left[C_1\left(1 + \left(\frac{C_3 D_0^{2/3}}{1-D^{2/3}}\right)\left(\left(\frac{D}{D_0}\right)^{1/3} - 1\right)^2\right) + C_4\left(\left(\frac{D}{D_0}\right)^{1/3} - 1\right)^2\right]}{1 + \frac{C_3 D_0^{2/3}}{1-D^{2/3}}\left(\left(\frac{D}{D_0}\right)^{1/3} - 1\right)^2} \tag{4}$$

Where S_1 and S_3 are the maximum and minimum normalized principal compressive stresses defined above. The constants in (4) are

$$\begin{aligned} C_1 &= \frac{\left(1+\mu^2\right)^{1/2} + \mu}{\left(1+\mu^2\right)^{1/2} - \mu} \\ C_2 &= \pi\left(\cos\chi\right)^{3/2}\sqrt{3/\beta}\,\frac{1}{\left(1+\mu^2\right)^{1/2} - \mu} \\ C_3 &= 2 \\ C_4 &= 2\pi\left(\cos\chi\right)^{2}\sqrt{3/\beta}\,\frac{1}{\left(1+\mu^2\right)^{1/2} - \mu} \end{aligned} \tag{5}$$

In equations (5), β is a correction factor for the effective length of the crack, typically 0.45, introduced by Ashby and Sammis (1990) to bring their approximate analytical model into agreement with numerical simulations in the limit of small *l*. Also, crack orientation χ is assumed here to be 45°.

When equation. (4) is used to plot S_1 as a function of *D* (for fixed values of D_o, S_3 and the other parameters), S_1 has a maximum value which Ashby and Sammis (1990) interpret as the failure stress. For larger values of *D* beyond this peak, S_1 decreases. This weakening rheology leads to shear localization and macroscopic failure. Fitting the uniaxial strength of dry granite at $20°\mathrm{C}$ using the values of *a* and μ deduced above from the nucleation gives an initial damage of $D_o = 0.1$.

We now ask how much of an increase in μ is required to produce the compressive strengthening at low temperatures observed in Figure (1). Holding all the other parameters constant, we increased μ to get the uniaxial strength measured by Mellor (Figure1). Figure 4 shows the value of μ as a function of temperature required by this damage mechanics interpretation of Mellors data.

The Apparent Coefficient of Friction of Frozen Cracks

The coefficient of friction μ is defined by Amonton's Law that relates the shear stress τ required to initiate sliding between two surfaces that are supporting a normal stress σ.

$$\tau = \mu\sigma \tag{6}$$

In the case where the boundary contains a fluid with pressure *P*, friction is described by the apparent friction law

$$\tau = \mu(\sigma - P) \tag{7}$$

The coefficient of friction shows the smallest variation of any mechanical parameter across different rock types. Known as "Byerlee's Law", $\mu \approx 0.6$ for virtually all rock surfaces independent of hardness.

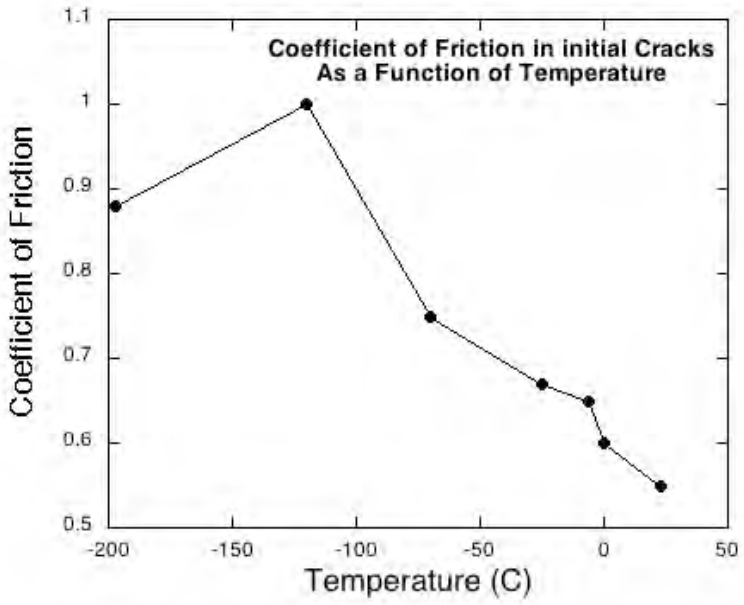


Figure 4. Coefficient of friction on starter cracks required if the damage mechanics model is to explain the increase in compressive strength at low temperatures in Figure 1.

The asperity model for friction, initially formulated by Bowden and Tabor (1950, 1964) offers a simple physical explanation for the constancy of μ. This model recognizes that all surfaces are rough at some scale, and that actual contact occurs at a limited number of high points called asperities. Under a normal load σ the asperities flow thereby increasing the true area of contact, A_c, until the stress on the asperities falls to the normal yield stress, σ_y, of the rock. If the apparent area of the contacting surfaces is *A*, we have

$$\sigma A = \sigma_y A_c \tag{8}$$

The shear stress τ required to initiate sliding is determined by the shear yield stress τ_y at which the asperities fail in shear, which gives:

$$\tau A = \tau_y A_c \tag{9}$$

Equations (8) and (9) may be combined to write

$$\tau = \left(\frac{\tau_y}{\sigma_y}\right)\sigma \tag{10}$$

which is just Amonton's law where $\mu = \tau_y / \sigma_y$. To see why the ratio τ_y / σ_y is nearly independent of rock type, consider the strength of a single asperity with cross-section A_c that is loaded to the compressive yield stress σ_y. This asperity will fail when the maximum shear stress reaches τ_y. As illustrated by the Mohr Circle in Fig 5 the normal yield stress is related to the shear yield stress by $\tau_y / \sigma_y = 0.5$, independent of the material.

If the area between the asperities is saturated with water, this will have no direct effect on μ, as long as $P<<0$. However, if this water freezes, the shear resistance will increase to

$$\tau = \tau_{y_{rock}} \frac{A_{c_{rock}}}{A} + \tau_{y_{ice}} \frac{A_{c_{ice}}}{A} \tag{11}$$

Assuming that the normal load is supported entirely by the rock asperities such that

$$\sigma = \sigma_{y_{rock}} \frac{A_{c_{rock}}}{A} \tag{12}$$

we can express the ice strengthening by an apparent coefficient of friction μ' as

$$\mu' = \frac{\tau}{\sigma} = \frac{\tau_{y_{rock}} A_{c_{rock}} + \tau_{y_{ice}} A_{c_{ice}}}{\sigma_{y_{rock}} A_{c_{rock}}} = \mu + \frac{\tau_{y_{ice}}}{\sigma_{y_{rock}}} \frac{A_{c_{ice}}}{A_{c_{rock}}} \tag{13}$$

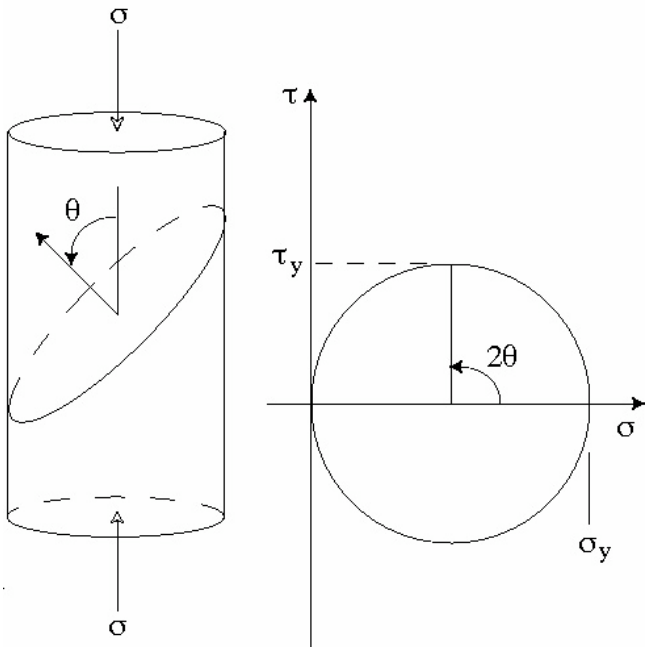


Figure 5. Stress state for a cylindrical asperity loaded to its compressive yield stress σ_y. Note that $\tau_y = 0.5\sigma_y$ where τ_y is the shear strength.

Direct observation of asperities in transparent silicates has shown that they deform by plastic flow (Dieterich and Kilgore, 1996). At the high stresses and low homologous temperature (T/T_m where T_m is the melting temperature) in the rock asperities, the flow stress is nearly independent of strain-rate or temperature. However, the flow stress in ice near its melting temperature is determined by thermally activated diffusion limited creep mechanisms that are very sensitive to both temperature and strain-rate. This is why μ rises rapidly just below $0°\text{C}$ in Figure 1. In equation (13), this behavior is caused by the rapid increase in $\tau_{y_{ice}}$ with falling temperature below $0°\text{C}$. At very low temperatures, flow in the ice will also be controlled by glide and μ' will be almost independent of temperature and strain-rate.

Flow in ice near its melting point is more complicated than high temperature flow in rock. There is a poorly understood change in activation energy at about $-10°\text{C}$ thought to be associated with the suppression of pressure melting at grain boundaries below this temperature (Goodman et al., 1981; Duval et al., 1983). We will take the analysis in this paper one step further by assuming a generic form for this high temperature power-law flow in ice:

$$\dot{\varepsilon} = B\tau^n \exp\left(-Q/RT\right) \tag{14}$$

Solving for the flow stress gives

$$\tau_{y_{ice}} = \left(\frac{\dot{\varepsilon}}{B}\right)^{1/n} \exp\left(Q/nRT\right) \tag{15}$$

Using this in equation. (13) and combining constants gives

$$\mu' = \mu + D\exp\left(Q/nRT\right) \tag{16}$$

or, equivalently,

$$\ln(\mu' - \mu) = \ln D + Q/nRT \tag{17}$$

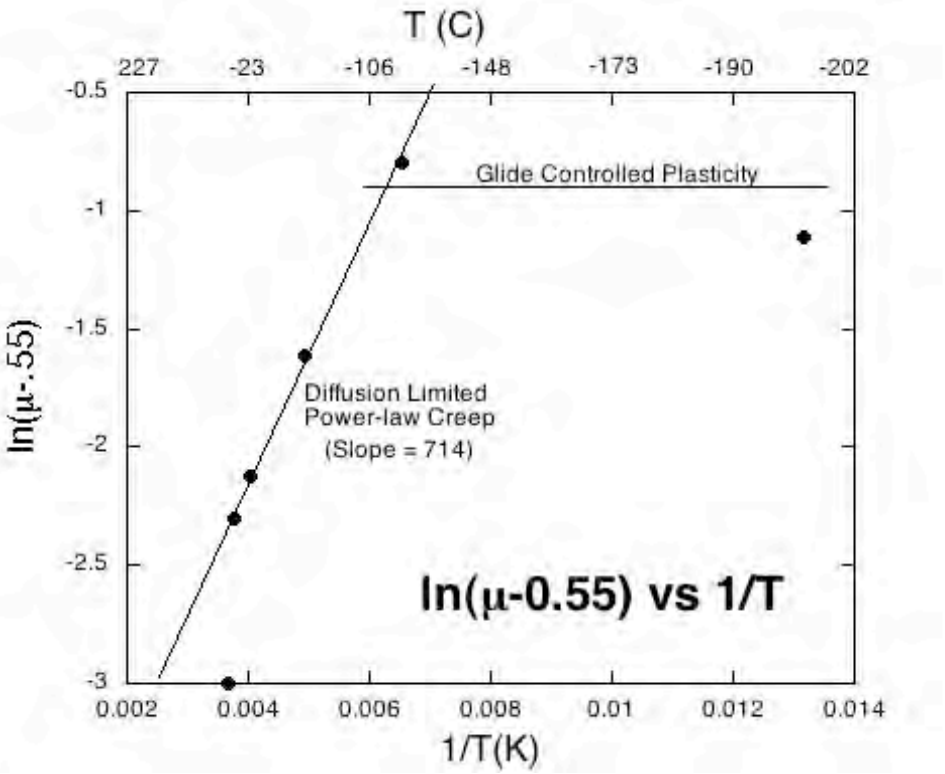


Figure 6. Plot of equation (17) in the text. The slope in the thermally activate region gives $Q/nR \approx 714$. At temperatures below about 110°C the mechanisms changes to glide controlled plasticity.

In Figure6, $\ln(\mu' - \mu)$ is plotted as a function of 1/T. The linear portion has a slope of $Q/nR = 714$. Below 8.3° C, the activation energy for power law creep is $Q \approx 80$ KJ mole^{-1}(Goodman et al., 1981). This implies a creep power of

$$n = \frac{8x10^4}{(714)(8.3)} = 13.5 \tag{18}$$

This is significantly higher than $n \approx 3$ observed at stresses below 1MPa. However, n for ice is observed to rise rapidly at stresses above one MPa (Goodman et al., 1981), so this may simply reflect a higher flow stress on the asperities.

CONCLUSIONS AND RECOMMENDATIONS

The preliminary analysis of rock strength at low temperatures has led to the following conclusions:

1. The basic characteristics of the low temperature uniaxial strength data from Mellor (1973) can be explained by ice in the initial pores and cracks.

2. For uniaxial compression in granite, the observed strengthening at low temperature can be quantitatively modeled using the micromechanical damage model formulated by Ashby and Sammis (1990). In this model the role of the ice is to increase the apparent coefficient of sliding friction on the initial cracks. The temperature dependence of power law creep in the ice asperities near their melting temperature explains the progressive strengthening observed in granite between $0°C$ and $-150°$.
3. The strengthening at low temperatures should also be strain-rate dependent. At high loading rates, as in an underground explosion, the full strengthening should occur over a limited range of temperatures near $0°C$.
4. The effect of frozen rock on the seismic signature of an underground explosion can be investigated using source models that include the micromechanical damage model such as that formulated by Johnson and Sammis (2001).

The following recommendations are based on the preliminary analysis in this paper:

1. The uniaxial data from Mellor (1973) should be supplemented with a full set of triaxial data in granite at low temperatures. Uniaxial data typically shows large experimental scatter, mostly because the strength is extremely sensitive to the initial flaw distribution in the absence of confining stress. A set of triaxial data would allow a more comprehensive assessment of the extent to which the damage model can represent the strength of rock at low temperatures.
2. The triaxial data set should be supplemented with measurements of the coefficient of friction as a function of temperature under saturated and air-dry conditions. These measurements can be made either on saw-cut samples as part of the triaxial set of experiments, or in Jim Dieterich's double-shear apparatus at the United States Geological Survey laboratory in Menlo Park, California.
3. Both the triaxial measurements and friction measurements should be performed at different strain-rates to further test the hypothesis that the strengthening is associated with ice asperities.
4. The Johnson and Sammis (2001) model for explosions in granite should be rerun with larger friction coefficients to assess the changes in seismic radiation caused by frozen rock.

REFERENCES

Ashby, M. F., S. and C. G. Sammis (1990), The damage mechanics of brittle solids in compression, *Pure appl. Geophys,* 133, 489-521.

Bowden, F.P., and Tabor D. (1950) *The Friction and Lubrication of Solids. Part I,* Clarenden Press, Oxford.

Bowden, F.P., and Tabor D. (1964) *The Friction and Lubrication of Solids. Part II,* Clarenden Press, Oxford.

Dieterich, J.H., and B.D. Kilgore, Imaging surface contacts: Power law contact distributions and contact stresses in quartz, calcite, glass, and acrylic plastic, *Tectonophysics*, *256*, 219-239, 1996.

Duval, P., M. F. Ashby, and I. Anderman (1983), Rate controlling processes in the creep of polycrystalline ice, *J. Phys. Chem.,* 87, 4066-4074.

Goodman, D. J., H. J. Frost, and M. F. Ashby (1981), The plasticity of polycrystalline ice, *Phil. Mag. A*, 43, 665-695.

Johnson, L. R. and C. G. Sammis (2001), Effects of rock damage on seismic waves generated by explosions, *Pure Appl. Geophys,* 158, 1869-1908.

Mellor, M. (1973), Mechanical properties of rocks at low temperatures, Second International Conference on Permafrost, National Academy of Sciences, Washington, D.C., 334-343.

THE PHYSICAL BASIS OF Lg GENERATION BY EXPLOSION SOURCES

Jeffry L. Stevens[1], G. Eli Baker[1], Heming Xu[1], Theron J. Bennett[1], Norton Rimer[1], and Steven M. Day[2]

Science Applications International Corporation[1], San Diego State University[2]

Sponsored by National Nuclear Security Administration
Office of Nonproliferation Research and Engineering
Office of Defense Nuclear Nonproliferation

Contract No. DE-FC03-02SF22676[1, 2]

ABSTRACT

The goal of the project is to develop a quantitative predictive capability for explosion-generated Lg phases with a sound and unambiguous physical basis. The research program consists of a theoretical investigation of explosion-generated Lg combined with an observational study. The specific question addressed by this research program is how the Lg phase is generated by underground nuclear explosions. This question is fundamental to how Lg phases are interpreted for use in explosion yield estimation and earthquake/explosion discrimination.

A simple point explosion in an infinite medium generates no shear waves, so the Lg phase is generated entirely by nonspherical components of the source and conversions through reflections and scattering. We find that the most important contributors to the Lg phase are (1) P to S conversion at the free surface and other near source interfaces; (2) S waves generated directly by a realistic distributed explosion source, including nonlinear effects resulting from the free surface and gravity; and (3) Rg scattering to Lg. Additional effects that contribute to Lg are the scattering of converted S phases that traps more of the converted P to S in the crust, and randomization of the components of Lg.

We analyze several explosion data sets: (1) Degelen Mountain explosions recorded at distances less than 100 km and corresponding recordings at Borovoye (BOR) at 650 km; (2) recordings from Russian deep seismic sounding experiments; (3) Nevada Test Site (NTS) explosion sources including the Nonproliferation Experiment (NPE) and nuclear tests covering a range of source depths and media properties. Using the NTS data, we are investigating the dependence of three-component Lg amplitudes and spectra on source depth and media attributes (including gas porosity), to complement the model predictions.

We model the overburied NPE, and underburied and overburied Degelen explosions, using point sources and two-dimensional nonlinear finite-difference calculations to quantify the source effects. Finite-difference calculations indicate that the topography at Degelen much more effectively scatters P and Rg to Lg, and traps more of the surface P-to-S converted phase in the crust, than do crustal heterogeneities. We use energy conservation to determine an upper bound on Rg to Lg scattering. Rg to Lg scattering may contribute to Lg and Lg coda at frequencies less than 1 Hz, but contributes less at higher frequencies than Lg generated directly by the explosion or by surface P-to-S conversion.

OBJECTIVES

The goal of the project is to develop a quantitative predictive capability for explosion-generated Lg phases with a sound and unambiguous physical basis. The research program consists of a theoretical investigation of explosion-generated Lg combined with an observational study. The specific question addressed by this research program is how the Lg phase is generated by underground nuclear explosions. This question is fundamental to how Lg phases are interpreted for use in explosion yield estimation and earthquake/explosion discrimination.

RESEARCH ACCOMPLISHED

A simple point explosion in an infinite medium generates no shear waves, so the Lg phase is generated entirely by nonspherical components of the source and conversions through reflections and scattering. The most important contributors to the Lg phase are (1) P-to-S conversion at the free surface and other near-source interfaces, (2) S waves generated directly by a realistic distributed explosion source including nonlinear effects as a result of the free surface and gravity, and (3) Rg scattering to Lg. In addition to source and near source effects, Lg is affected by scattering and conversion along the travel path. The most important effects are S-to-S scattering that changes the orientation and direction of the near source P-to-S converted waves, affecting the extent to which they are trapped in the crust and randomization of the components of Lg, although the calculations presented in this study suggest that topographic scattering of P-to-S converted waves may be more important. The focus of the project is to quantify through data analysis and simulations the dependence of these various mechanisms on source conditions. We have made considerable progress in understanding explosion-generated shear waves by quantifying and numerically reproducing features of observations of shear waves generated under different source conditions.

In the proceedings paper for the first year of this project (Stevens et al., 2003), we described the data sets collected, their analysis, and the results of nonlinear finite difference simulations of explosion sources under different source conditions. We briefly review those results, adding some new results to the observations.

Table 1 lists the data sets, which provide waveforms from explosions ranging from 100s of meters from the source to regional distances. Table 2 lists the most important new observations from the project. There are three principal conclusions that can be drawn from the observations: (1) There is strong evidence for shear waves generated directly by the source that are observable at regional distances; (2) there is strong evidence for transverse Lg generated directly by or very close to the source that cannot be explained by a spherically symmetric explosion, a vertically oriented Compensated Linear Vector Dipole (CLVD), or any other axisymmetric source; and (3) the Rg phase persists to great distances in some earth structures, notably Central Asia.

These observations show that S is generated directly by the source and is observable in local records and that the explosion generates an impulsive Sn phase and will therefore also generate Lg. Lg due to Rg scattering may be superimposed on this signal. A major objective of our project is to determine the relative sizes of these components of Lg. The persistence of Rg in Eurasia suggests that the scattering rate there may be quite different from the western United States.

Table 1. Data Collected and Used in the Current Project.

Source	No. Events	Yield, Depth, or mb range	Recording Range
Degelen	7	1.5–78 Kt	7-50 km & 650 km
Deep Seismic Soundings (DSS)	4	8.5–22 Kt	every 10–15 km for 1000s of km in two directions
NTS	155	111–701 m depth	190–400 km
NPE	1	1 Kt 400 m depth	65 near source (100s of m), 3 local, 60 regional (10s-100s of km)
Khirgizia (decoupling)	4	1–6 tons 292 m depth	5–10 km
Lop-Nor	10	4.7–6.4 mb	250–1900 km
Balapan	21	4.8–6.1 mb	950–1500 km

Table 2. Summary of Observations and Their Implications.

Observations	Implications
Sg (tangential and radial) is observed very near the source for the NPE, Deep Seismic Sounding (DSS) profiles, and Degelen explosions.	Some shear waves, both SH and SV, must be generated at or very near (within 100s of meters of) the source.
Rg persists to hundreds of km in the DSS data.	The rate of Rg scattering and attenuation in Eurasia are very different from the Western U.S. and this may reduce Lg generated by Rg scattering.
Distinct impulsive Sg and Rg are clearly separate at a few km to 100s of km from Degelen and DSS explosions.	Temporally compact shear waves are generated independent of Rg scattering for many of the data sets.
Shear wave phases are usually larger on horizontal than vertical seismograms.	Additional relevant information about the explosion source is contained in the horizontal component of Lg.
Sn is prominent, short duration, and sharp for Degelen explosions recorded at BOR.	Sharp Sn is consistent with generation at or very near the source and inconsistent with a distributed scattering process.

Stevens et al. (2003) focused on observations and source calculations. In this paper we focus on further source calculations and two types of scattering calculations. These calculations provide a means of investigating the relative importance of the proposed mechanisms under different source and near-source conditions. Finite-difference scattering calculations show the effects of topography and heterogeneity on P-to-S and Rg-to-S scattering and trapping of the scattered S in the crust. A modal method is used to place an upper bound on Rg-to-Lg scattering and characterize the frequency and temporal dependence of its contribution.

Nonlinear finite-difference source calculations: Figure 1 shows Lagrangian finite-difference near source calculations of a 62 kt explosion in a high-velocity medium at depths of 300 and 1,000 meters (75 and 252 m/kt$^{1/3}$), which are underburied and overburied, respectively, compared to a standard containment depth of approximately 120 m/kt$^{1/3}$. For the shallow explosion, the region of nonlinear deformation is more conical than spherical, but for the deep explosion, the primary region of deformation around the explosion is approximately spherical, but there is an additional region of spall and similar nonlinear behavior near the free surface. The deeper explosion therefore generates a smaller direct-S phase and smaller Lg. These differences suggest that this effect could be observable in Lg from deep explosions in high-velocity media; however, none of the Degelen explosions were this deep.

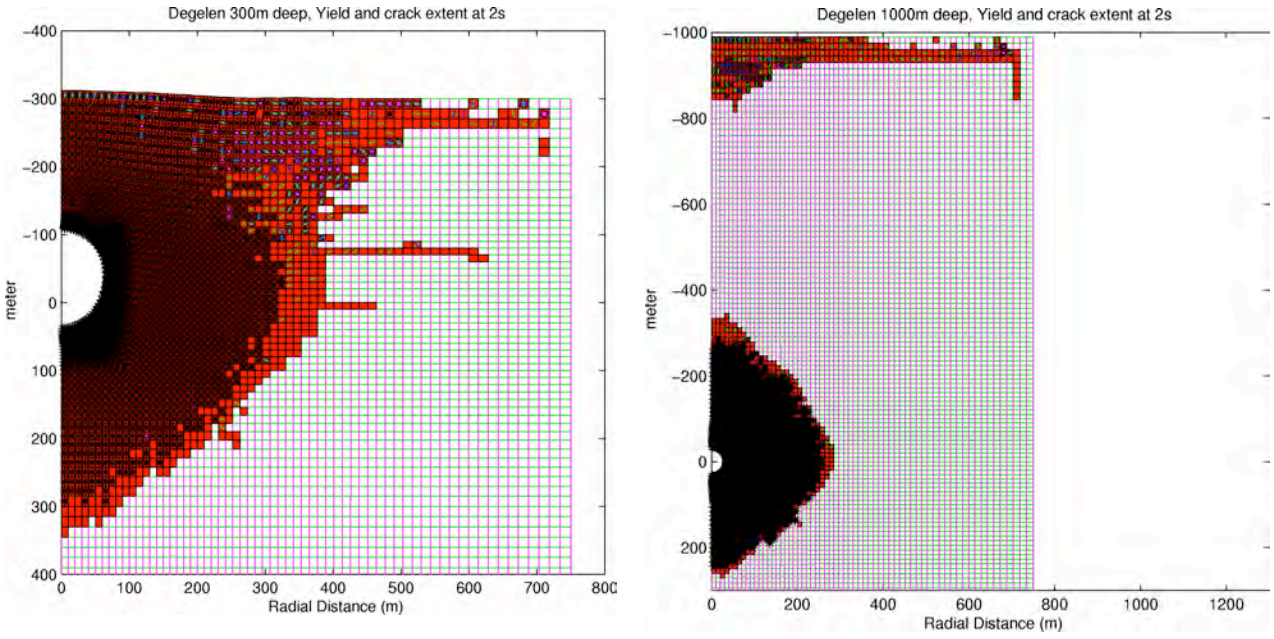


Figure 1. Regions of nonlinear yielding and cracking from an explosion in a high-velocity structure similar to the Degelen test site. Left – 62 kt at 300 meters depth. Right – 62 kt at 1,000 meters depth.

Effects of topography and heterogeneity on free-surface P-to-S scattering: To investigate P-to-S and Rg-to-Lg scattering, we compare results of finite-difference calculations for 5 models, using a point-explosion source at 325 m depth. The first is a homogeneous, horizontally layered velocity model appropriate for Degelen Mt (Figure 2, left side). The second model is that base model plus the topography at Degelen Mt. (Figure 2, second from left). It uses a topographic profile along an east-west line through Degelen, while maintaining the average upper layer thickness. The third model is the base model plus zeroth order Von Karman-distributed P- and S-wave velocity variations with a 5% standard deviation, an aspect ratio of 1, and a correlation length of 1 km in the upper 1.5 km (Figure 2, center). The correlation length corresponds to the Rg wavelength in the passbands of interest and so should effectively scatter it. The fourth model combines the topography and upper layer heterogeneity (Figure 2, second from right). The fifth model adds heterogeneity throughout the crust to the fourth model. The heterogeneities below the surface layer also have a 5% standard deviation, but are asymmetric with a 5:1 horizontal-to-vertical aspect ratio. This last model is intended to test whether additional, surface-converted, P-to-S wave energy can be trapped by scattering induced changes in incidence.

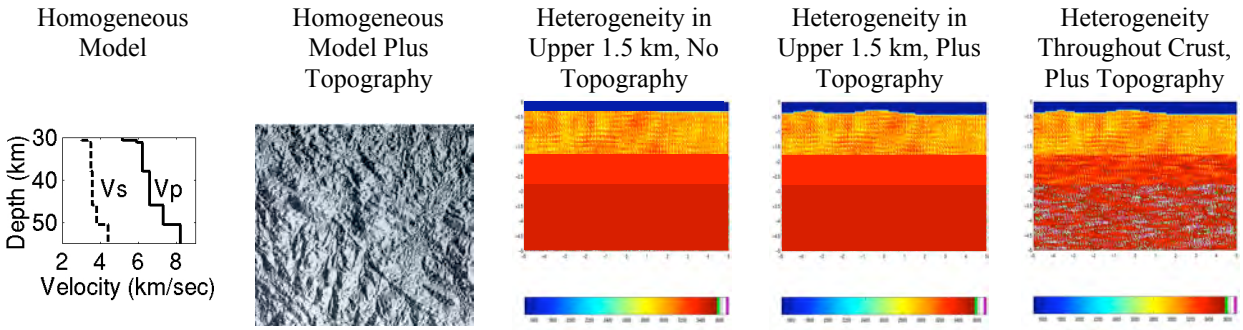


Figure 2. Models used in the scattering calculations. The far left plot shows the 1D homogenous base model. The second plot shows a 200 x 200 km shaded relief image centered on Degelen Mt. The next 3 plots show 5 km deep by 10 km wide slices of the heterogeneous models described in the text. The source is always 325 m deep, and its position for the models with topography is in the center (horizontally) of the snapshots shown.

Figure 3 shows the effects of topography and heterogeneity on the seismograms. Each record section's position corresponds to the position in Figure 2 of the model used to generate the data. The source P-wave velocity is greater than the upper mantle S-wave velocity, so in the base model where there is no scattering that will change the wavenumber, the energy in pS (the free surface P-to-S converted phase) is expected to propagate into the mantle. There is some Sg or Lg seen in the base model record section, however (Figure 3, left side), caused primarily by the non-geometric P-to-S scattered phase S* (e.g., Vogsfjord, 1997), which we address in the discussion of Figure 6. For the model with topography, the Sg or Lg phase is more prominent, indicating that the incidence of pS is sufficiently randomized by the irregular free surface so that some is now trapped in the crust (Figure 3, second from left). Adding heterogeneity to just the surface layer makes little difference to pS (Figure 3, center). The record section for the fourth model also looks much like that of the second. That is, adding surface layer heterogeneities to the model with topography changes little in the records. The addition of heterogeneity throughout the crust causes an increase in coda throughout the records but does not appear to amplify Lg.

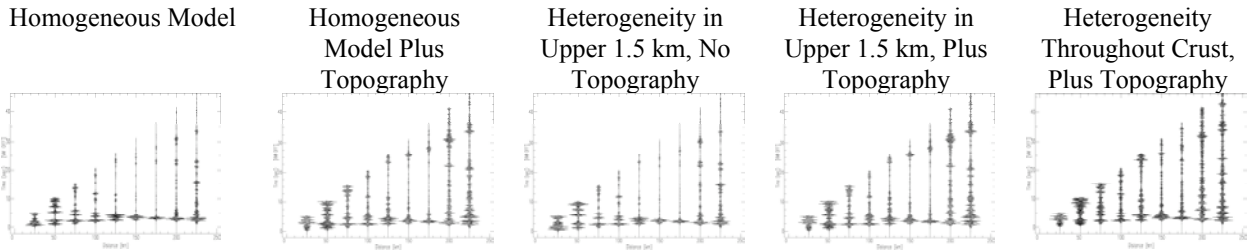


Figure 3. Radial record sections for a 325-m depth point explosion filtered from 3 to 5 Hz, from 25 to 225 km.

Figure 4 shows just the Lg windows at 225 km, filtered from 3 to 5 Hz, for each model. These are the most distant traces of each record section in Figure 3. The rms amplitudes of the Lg phases corrected for pre-Lg noise levels,

listed to the left of the radial traces and right of the vertical traces, are given as a percent of the rms Lg amplitude for the homogeneous model with topography added. The rms Lg amplitude is larger for the models with topography, and topography appears to be the most important factor in trapping pS in the crust.

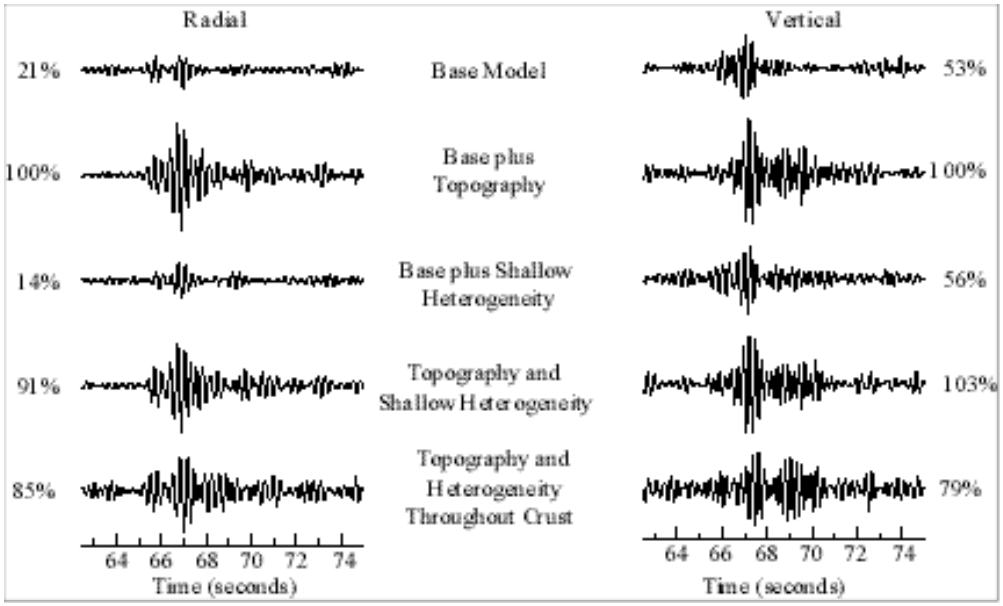


Figure 4. Radial (left) and vertical (right) component Lg (3.6 to 3.0 km/s) at 225 km for each of the models. All 5 traces are plotted at the same scale. Percentages to the left of each radial and right of each vertical trace are rms amplitudes as a percent of the radial and vertical records' rms amplitudes respectively for the homogeneous base model with topography added.

Figure 5 illustrates how broken up the pS wavefront is in the model with topography (lower row), compared with the flat-layered base model (upper row). It shows snapshots of the curl of the velocity, which isolates the shear waves, specifically the pS phase, shortly after the explosion. The source is at 325 meters below the free surface, in the horizontal center of the snapshots.

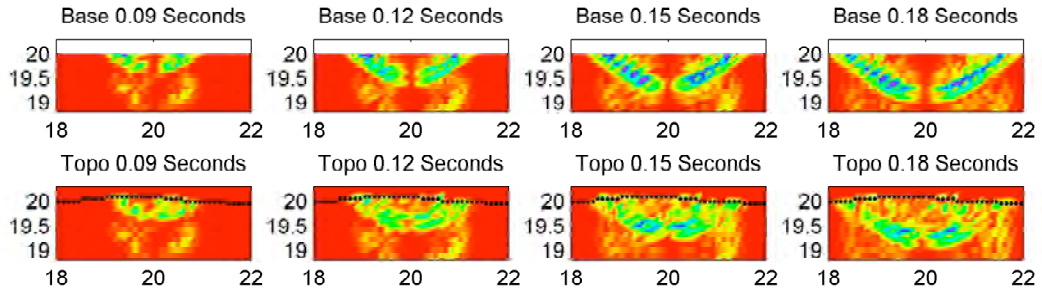


Figure 5. Snapshots of the curl of the velocity just after the explosion, for the homogeneous base model (top row) and model with topography (bottom row) illustrate the effect of topography on pS. The black line in the lower row shows the free surface.

The S* mechanism predicts conversion of P to S waves from sources within a small fraction of the wavelength from the surface as a result of curvature of the P wavefront (e.g., Vogfjord, 1997). Degelen sources were largely between 100 and 300 m depth. The source depth for all the synthetics shown in Figures 3 and 4 is 325 m. Figure 6 shows the dependence of S-phase amplitudes on source depth relative to wavelength, using wavenumber synthetics. They show large S amplitudes, arriving at approximately 64 seconds, for source depths less than 20% of the wavelength, and virtually no S for source depths near the wavelength. The record for the 300-m source depth, filtered from 3–5 Hz, has a small but clear S phase. This suggests that some, or perhaps most, of the Lg in the base model synthetics of Figures 3 and 4 is a result of S*.

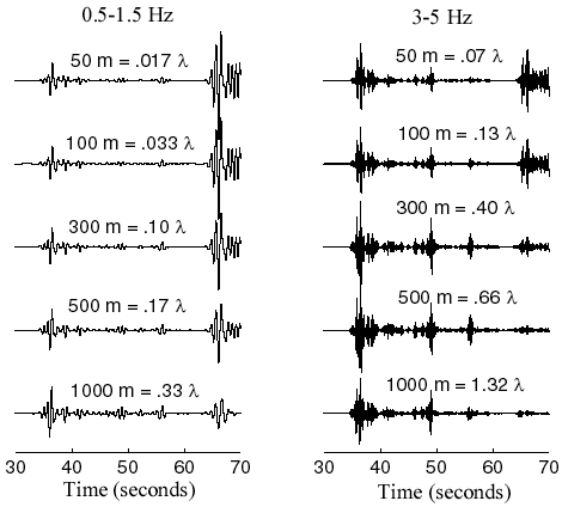


Figure 6. Wavenumber synthetics, at 225 km, for the homogeneous model at 1 (left) and 4 Hz (right), for sources at 50, 100, 300, 500, and 1,000 m. S* arrives at approximately 64 seconds.

Although S* appears to be a significant source of Lg, it predicts a strong depth dependence which has not been observed in Lg from explosions. It could, however, contribute to the relative increase in low frequency Lg, which has been observed in explosion-generated Lg. The scattering results shown in Figures 3-6 indicate that even in a high-velocity source medium where pS should not contribute to Lg, topographic scattering can trap more Lg than is produced by S*, at least at high frequency. One set of future finite-difference source calculations will use deeper point-explosion sources to eliminate the S* phase and so isolate just the scattering effects. A second set of calculations will use a CLVD source in the different models as a proxy for the nonspherical source effects, which will permit estimation of the Lg contribution from direct source generation.

Effects of topography and heterogeneity on Rg-to-Lg scattering: The finite-difference scattering calculations described above were also used to analyze Rg-to-Lg scattering. As with pS, the most significant scattering effect among the models is due to topography, and we focus on the difference in Rg scattering between the homogeneous plane-layered model and that same model plus the topography at Degelen.

Figure 7 shows the seismograms filtered in different passbands at 10 (left) and 30 (right) km from the source for the two plane-layered homogeneous models, flat and with topography. Each pair is plotted on the same scale. All records are plotted from 7.5 to 1.67 km/s group velocity. There is little effect below 1 Hz, the greatest difference being in amplitude, with the topographic model producing larger Rg. At 1–2 Hz, there are differences in arrival time, decay, and initial amplitude. The record for the topographic model is delayed, initially larger, and decays faster. There is also more P coda, which is most apparent at 30 km. At 2–4 Hz, there is practically no overlap in time between the well-defined Rg of the flat model, and the scattered Rg of the topographic model, even at 10 km. At 10 km, the topographic model Rg is larger, but by 30 km the Rg has slightly smaller maximum amplitude than that of the flat model, although it persists for much longer. At 4–8 Hz, Rg is not clearly distinguishable from coda in the topographic model.

To examine further what Rg scatters to, we look at cross sections of the vertical velocity and the curl, centered on the Rg phase near the source (Figure 8). This provides insight into the potential contribution of topographically scattered Rg to Lg. The vertical velocities (Figure 8, left half) show a compact Rg phase in the model without topography, but in the model with topography, the Rg energy has been spread out all along the surface. The downgoing phase in the cross sections at 1 second is P-to-S scattered energy. The curl of the velocities (Figure 8, right half), which isolates the shear waves, shows a similar result. At least during the first three seconds shown here, the main effect of topography on Rg is to cause strong dispersion of the phase rather than scattering into downgoing S.

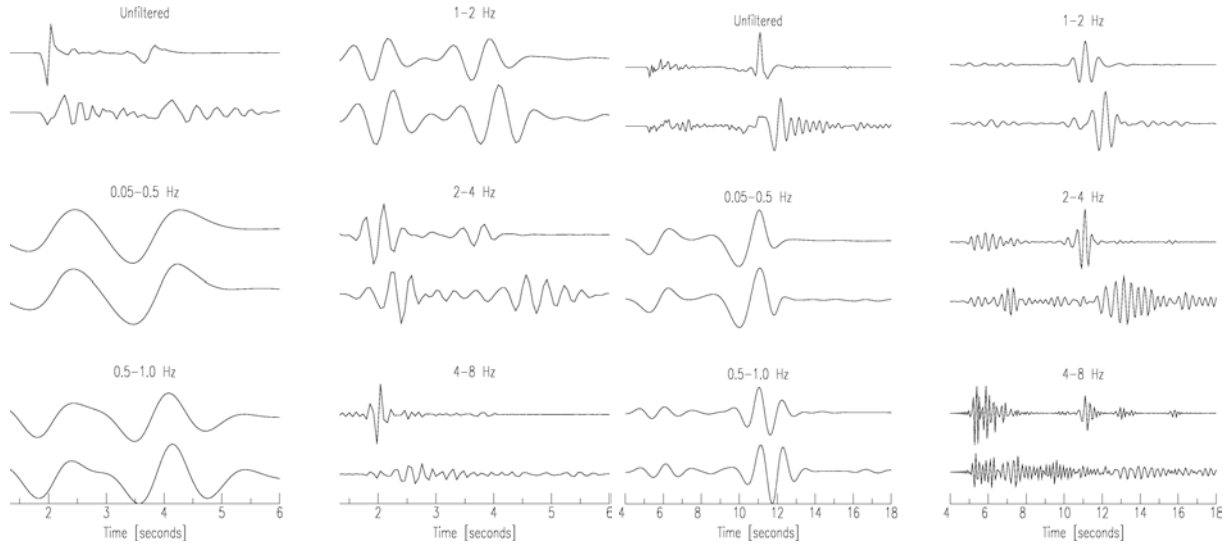


Figure 7. Synthetic seismograms, in various passbands, 10 (left half) and 30 (right half) km from the source, for the homogeneous model without (upper trace of pairs) and with (lower traces) topography.

To further quantify the effect of topography on Rg, we estimate Q as a function of frequency for the homogeneous model with a flat free surface and for the similar model with topography. A decrease in Q in the second model can be attributed to topographic scattering. The left side of Figure 9 shows frequency vs the estimated intrinsic Q values. The Q values determined for the base model are consistent with those of the original model structure (the frequency dependence is caused by the particular implementation of attenuation in the finite-difference calculation). Attenuation is greater for the model with topography (Figure 9, left side, and Table 3). The effect of dispersion is less than the measurement error for the model without topography but is dramatic for the model with topography. There the Rg is slowed at all frequencies, considerably at higher frequencies. This 2D analysis predicts that around 3 to 4 Hz, the scattering Q for Rg as a result of the topography at the Degelen test site is approximately 300. Around 1 Hz it is close to 1,000. A preliminary analysis of local Rg records from Degelen explosions indicates a significantly lower Q value. We cannot determine the partition between intrinsic Q and scattering Q in the observations, but the observations suggest that the scattering calculations probably underestimate the attenuation because of scattering. In the next section of this paper, we use a modal approach to determine an upper bound on Lg scattered from Rg.

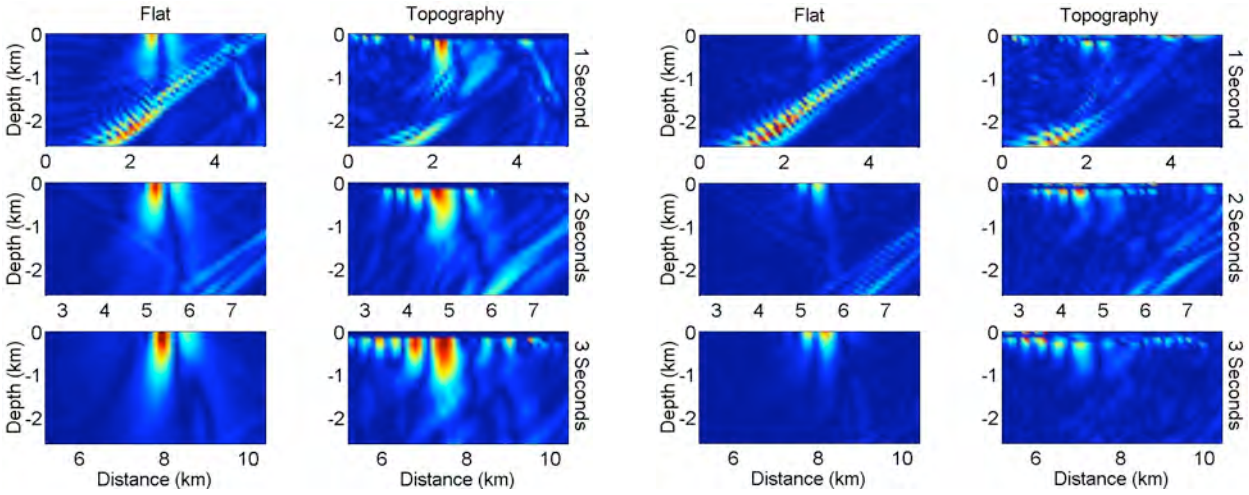


Figure 8. Cross sections of vertical velocity (left) and curl (right) centered on Rg at 1, 2, and 3 seconds for the homogeneous base model with a flat free surface (left column in each set of plots) and the same model plus topography (right column in each set of plots). Each pair (same time, different models) is plotted with the same color axis.

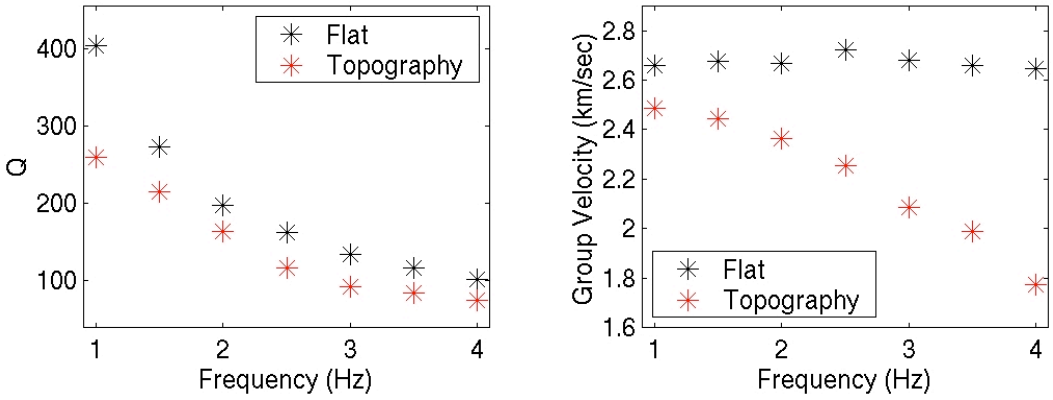


Figure 9. Q vs frequency (left) and group velocity vs frequency (right) for the flat (black) and topographic (red) models.

Table 3. Theoretical (subscript "model") and measured attenuation, Q, and group velocity, U, for the models without (Q_{flat} and U_{flat}) and with topography (Q_{topo} and U_{topo}). Scattering Q, Q_s, is determined by the difference in Q between models.

Passband (Hz)	Q_{model}	Q_{flat}	Q_{topo}	Q_s	U_{model}	U_{flat}	U_{topo}
0.5 - 1.5	502	404	260	730	2.66	2.66	2.49
1.0 – 2.0	294	274	215	1007	2.72	2.67	2.44
1.5 - 2.5	219	198	164	956	2.76	2.67	2.36
2.0 – 3.0	174	163	117	417	2.77	2.72	2.25
2.5 – 3.5	145	134	92	292	2.77	2.68	2.09
3.0 – 4.0	124	117	84	294	2.77	2.66	1.99
3.5 – 4.5	108	101	75	287	2.78	2.65	1.77

A modal method for calculating an upper bound on Rg-to-Lg scattering: To make a seismogram that approximates Lg generated by Rg scattering, we use energy conservation and the distribution of energy in each mode, derived from a similar analysis by Bennett et al. (1997). Rg is the fundamental mode surface wave generated by the explosion source. As discussed earlier, the explosion source can be complex, but can be represented to first order as a point explosion source plus a CLVD. For deeply overburied or decoupled explosions, the point source may be a very good approximation, but for shallower sources, the nonspherical components are important. We can make an approximate, but fairly realistic, calculation of the Lg generated by Rg by considering the Lg to be generated by scatterers at the earth's surface distributed over the region through which Rg propagates and assuming that all Rg converts to Lg. For this estimate, we make the following assumptions:

1) The explosion is a simple point explosion source. The same technique will work for a more complex explosion source.

2) Scattering occurs quickly enough that we can model the scattering duration as instantaneous. Under this assumption, we can also neglect intrinsic attenuation of the fundamental mode prior to scattering.

3) No energy is lost in scattering, and all scattering is forward scattering.

4) All scattering is from Rg to higher modes. We neglect secondary scattering and scattering to leaky phases.

5) The scattered energy has the modal distribution of a vertical point force. This is reasonable because the strongest Rg scattering occurs at the earth's surface.

We therefore consider that the scattered Rg consists of waves from a cylindrical distribution of point forces at the location of the propagating Rg phase, and that the scattered Rg goes into higher modes. These are very optimistic assumptions and should be regarded as providing an upper bound on Lg generated by Rg scattering. Forward

scattering is a better approximation than it may seem because scattering from a vertical point force in another direction simply adds to the outgoing wave in that direction with a small time delay.

Seismograms for Lg generated by the point explosion source, and by Rg scattering made under the assumptions listed above are shown in Figure 10 (left) for an 80-kiloton explosion at 500 meters depth in an earth model for NTS. The corresponding spectra are shown in Figure 10 (right). Figure 11 shows the spectra of the two time windows, 3.6 to 3.0 km/s and 3.0 to 2.5 km/s. The Lg from scattered Rg, at least in this optimal case, is comparable to Lg from the point explosion for frequencies of about 0.6 to 1 Hz, larger for lower frequencies, and smaller for higher frequencies. The Lg produced by scattered Rg has stronger excitation of the first higher mode than the Lg generated by the point explosion, which causes the higher spectral amplitudes at low frequencies and the late arriving higher-amplitude waves in the time series.

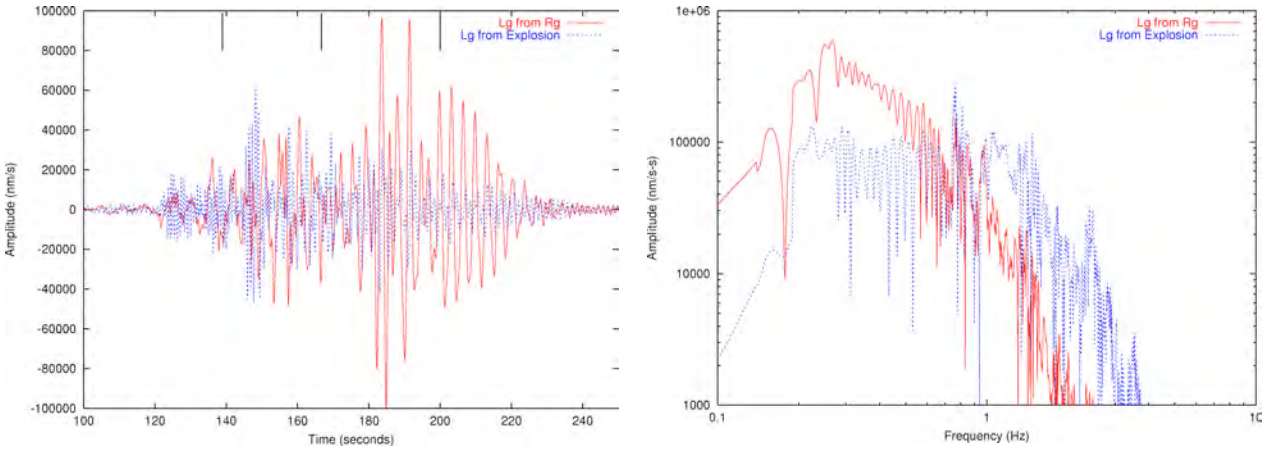


Figure 10. Left: Lg velocity seismograms calculated for a point explosion at 500 meters depth (blue) and for Lg generated by Rg scattered from the same explosion (red). Marks at the top show arrival times for 3.6, 3.0, and 2.5 km/s. Right: Lg spectra calculated from these two waveforms. The Lg calculated for the point explosion and that scattered from Rg have similar amplitudes within the 3.6 to 3.0 km/s group velocity window, but Rg scattering contributes more to the late Lg.

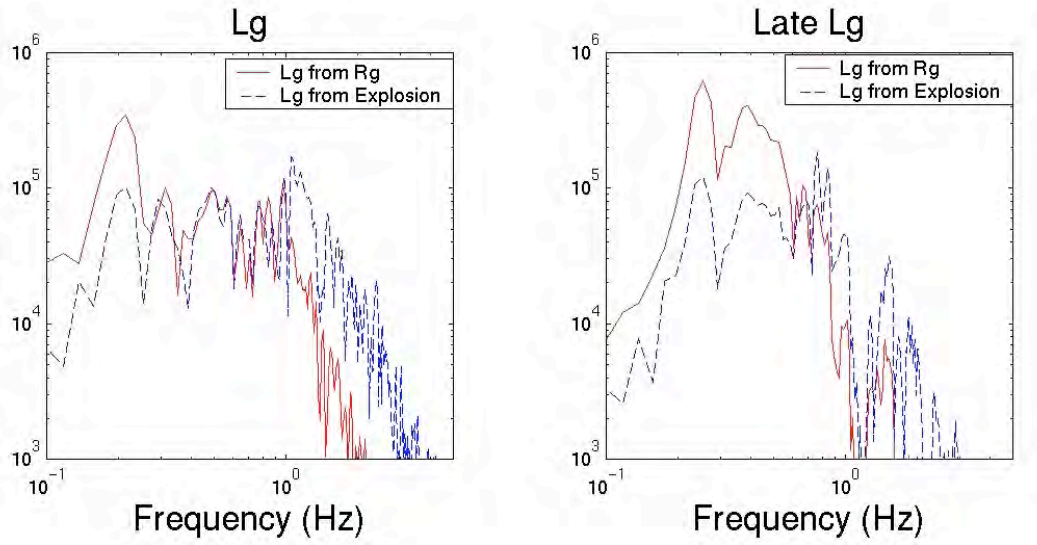


Figure 11. Spectra derived from the time series of Figure 10 using time windows of 3.6 to 3.0 km/s (left) and 3.0 to 2.5 km/s (right). In the Lg window, spectral amplitudes below 1 Hz are similar, but the spectra of the Rg-to-Lg scattered Lg begins to drop off at a lower frequency than the spectra of Lg calculated for the point explosion source. Spectra of both share the same spectral nulls.

These results suggest that Lg observed from overburied explosions is likely to consist of a superposition of Lg generated by the point-explosion source and by Rg scattering, that each source may dominate in a different frequency band, and that the two sources may interfere with each other, particularly near 1 Hz, complicating the use of the Lg waveform in discrimination. Explosions that are normally buried or underburied may have additional Lg as a result of direct generation of shear waves by nonspherical components of the source. Those components of the source will also generate more Rg. Future work will include more complex sources than a point explosion.

CONCLUSIONS AND RECOMMENDATIONS

We have investigated the most significant mechanisms for generating shear waves from explosions; P-to-S scattering, particularly from the free surface, Rg-to-Lg scattering, and direct generation of shear waves by nonspherical components of the explosion source. We have performed calculations capable of quantifying the contribution of each mechanism under different source and near-source propagation conditions, including depth, scaled depth, material properties, velocity structure, and topography. Nonlinear source calculations quantify the direct generation of shear waves. Finite-difference calculations provide insight into how scattering may trap P-to-S converted energy, particularly in high-velocity source media. They also provide insight into the nature of Rg scattering. A modal method of simulating Rg-to-Lg scattering places bounds on the Lg amplitude and characterizes its nature.

Specific results include the prediction of vertical and radial Lg and Sn for Degelen explosions by direct generation of S-waves by nonspherical components of the source and the prediction of vertical and radial Lg for the NPE explosion by free surface P-to-S-scattered waves. Topography at Degelen has a much stronger effect than 5% standard-deviation velocity heterogeneities on pS, randomizing its incidence so that more pS is trapped in the crust as Lg. Topography also more strongly scatters and disperses Rg than do the crustal heterogeneities tested. The scattered and dispersed Rg energy appears to remain concentrated along the surface. Modal calculations indicate that if all Rg scatters to Lg, its contribution is predominantly to late Lg and lower frequencies.

Recommended future work should include further comparison of simulations with data from the extensive data set summarized in Table 2. For example, we intend to perform further nonlinear finite difference simulations of the explosion source to predict near regional and regional data from Degelen and Balapan explosions to isolate the direct contribution of the source to the regional waveforms, distinct from near-source and path-scattering effects. We also intend to model the Rg-to-Lg scattering mechanism using the time-dependent modal energy transfer technique for several realistic structures, including Central Asia and NTS, and make a quantitative estimate of the contribution of Rg scattering to Lg. We will compare characteristics of jointly observed Lg and Rg in Eurasian explosions and NTS to determine whether predictions and observations are consistent. This will include the comparison of spectral characteristics of near-regional and regional Lg with predictions based on source calculations and Rg scattering calculations, taking into account the source-region structure, near-regional path characteristics, source depth, scaled depth, and yield.

Future data analysis and calculations with the methods presented will also focus on subsets of events for which only one parameter, such as depth, changes. Future work must also address the question of tangential Lg and Sn, which is not well explained by current mechanisms. We will extend the scattering calculations to 3D, both to more realistically quantify the effects of topography and heterogeneity and to investigate the randomization of shear-wave polarization.

REFERENCES

Bennett, T. J., K. L. McLaughlin, M. Marshall, and J. L. Stevens (1997), "The Physical Basis for the Lg/P Discriminant: General Properties and Preliminary Modeling," PL-TR-97-2044, MFD-FR-97-15727

Vogfjord, K. (1997), "Effects of Explosion Depth and Earth Structure on the Excitation of Lg Waves: S* Revisited," *Bull. Seism. Soc. Am.*, 87, 1100–1114

ANALYSIS AND SIMULATION OF CAVITY-DECOUPLED CHEMICAL EXPLOSIONS

Jeffry L. Stevens[1], Norton Rimer[1], Heming Xu[1], John R. Murphy[1], Brian W. Barker[1],
Steven J. Gibbons[2], Conrad Lindholm[2], Frode Ringdal[2], Tormod Kvaerna[2], and Ivan Kitov[3]

Science Applications International Corporation[1], NORSAR[2], Institute for the Dynamics of the Geospheres[3]

Sponsored by Air Force Research Laboratory

Contract No. DTRA01-01-C-0069[1, 2, 3]

ABSTRACT

The objective of this project is to improve our capability to quantitatively predict the decoupling effectiveness of underground cavities in a variety of realistic configurations. This is being accomplished by expanding the existing decoupling data set with data that have recently become available from Russian and Swedish decoupled chemical explosions, and by performing data analysis and numerical modeling of this data set. This is a joint project of Science Application International Corporation (SAIC), the Russian Institute for the Dynamics of the Geospheres (IDG), and NORSAR.

We have previously reported on the analysis of data from seven decoupled chemical explosions conducted from 1986-2002 in Älvdalen, Sweden. The last four explosions were conducted in a cavity approximately 4 meters high by 8 m wide by 30 m long (1,000 m^3). The first three explosions were in two smaller chambers approximately 3 meters high by 4 meters wide with lengths of 17 meters (200 m^3) and 25 meters (300 m^3). Explosive yields ranged from 2,500 kg to 10,000 kg, with charges consisting of TNT, ANFO, and ammunition shells. The smallest explosion in the largest chamber appears to be fully decoupled, while the other explosions are partially coupled. Several 1,000 kg explosions were also conducted in the two smaller chambers, but we do not have times for these events, and they were not identified in seismic bulletins. We have applied a waveform correlation procedure to the NORSAR data for the approximate time period of the explosions using data from one of the larger events as a matched filter and have identified the data for some of the smaller explosions, allowing us to expand the data set further. For the more recent explosions, near field data were recorded on pressure gauges in the chamber and adjacent tunnel, and on velocity gauges in boreholes at several locations near the chamber. We have modeled these data using three-dimensional finite difference calculations. The calculations show enhanced signals in the direction along the small axis of the chamber and reduced signals near the long end of the tunnel. Although we do not have free field data from all directions, the data for the available locations are consistent with these calculations.

OBJECTIVE

The objective of this project is to improve our capability to predict quantitatively the decoupling effectiveness of underground cavities in a variety of realistic configurations. This will be accomplished by 1) expanding the existing decoupling data set using data that have recently become available from Russian and Swedish decoupled chemical explosions; 2) performing numerical simulations of these data and other decoupled data and then using the results to refine the material models used in the simulations; 3) performing numerical modeling of decoupled chemical explosions in nonspherical cavities for a variety of realistic material models and cavity geometries. This is a joint project between SAIC, the Russian Institute for the Dynamics of the Geospheres, and NORSAR.

RESEARCH ACCOMPLISHED

Swedish Decoupled Chemical Explosions

At a site within Älvdalen Skjutfält in central Sweden, a number of decoupled chemical explosions have been carried out within three underground chambers at a depth of approximately 100 meters (Gronsten and Krest, 2002; Gronsten, 2000). Figure 1 shows the location of the site together with the locations of the seismic arrays HFS (Hagfors, Sweden), NRS (NORES, Norway), and the wide aperture NORSAR array. Stevens et al. (2003) described preliminary data analysis using data from seven decoupled explosions at the Älvdalen site. This data set has now been expanded by searching the NORSAR archives for additional data from smaller (1000 kg) explosions that were not previously detected. Table 1 lists all events for which some seismic data has been identified.

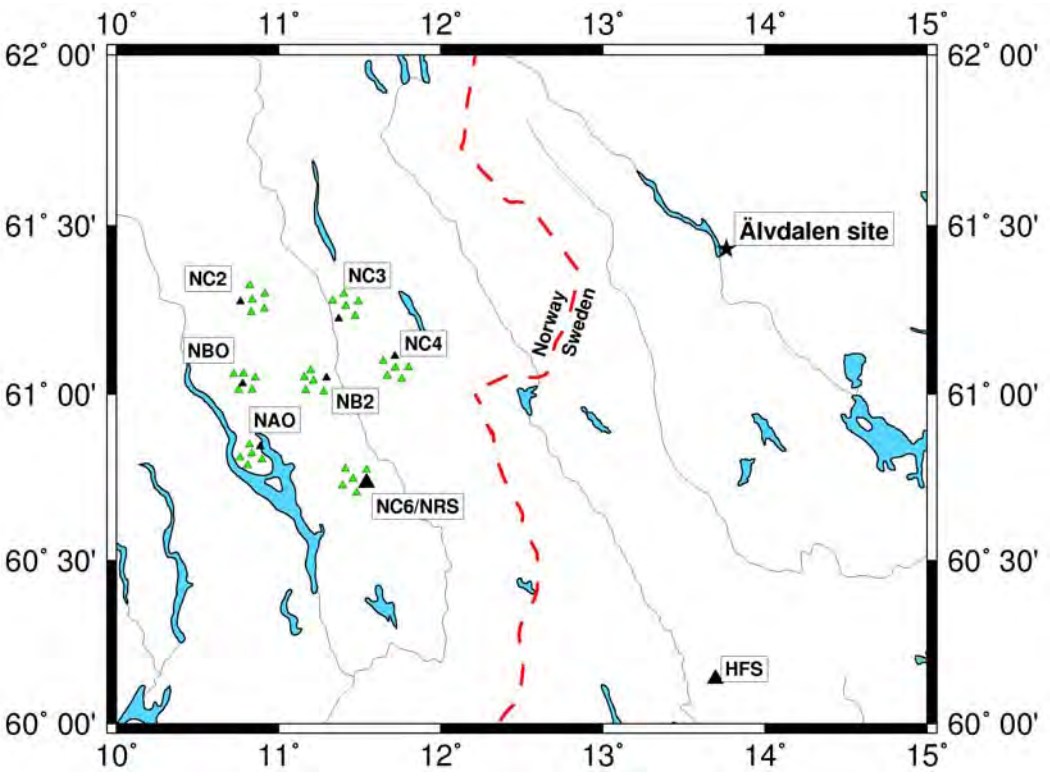


Figure 1. The location of the explosion site relative to the HFS and NRS arrays and the NORSAR (NOA) sub-arrays. The dashed line is the Norway/Sweden national boundary.

Table 1 Cavity decoupled chemical explosions at the Älvdalen site. Origin times of the 1986-89 events were derived from waveform cross-correlation measurements. Origin times of the 2000-2002 events were determined from a station at the explosion site.

Origin ID	Explosion origin time	Explosion charge (kg)	Explosive	Chamber Volume (m^3)	Charge/Volume (kg/m^3)
1986C168	1986-168:10.06.15.9	1000	TNT	300	3.3
1986C177	1986-177:09.14.06.6	1000	TNT	200	5.0
1986C260	1986-260:11.34.17.4	1000	Ammunition Shells	300	3.3
1986C246	1986-246:11.50.45.1	1000	Ammunition Shells	200	5.0
1987C141	1987-141:10.16.08.3	1000	ANFO	300	3.3
1987C146	1987-146:10.47.38.2	5000	ANFO	300	16.7
1987C259	1987-259:10.36.13.0	5000	ANFO	200	25.0
1989C242	1989-242:10.12.21.0	1000	Ammunition Shells	300	3.3
1989C263	1989-263:10.06.03.5	5000	ANFO	300	16.7
2000C348	2000-348:10.03.02.0	10000	TNT	1000	10
2001C150	2001-150:10.03.56.2	2500	TNT	1000	2.5
2001C186	2001-186:10.41.23.5	10000	Ammunition Shells	1000	10
2002C164	2002-164:08.59.25.1	10000	TNT/powder	1000	10

The 1000 kg events did not appear in any seismic bulletin and a visual search of the records for the corresponding day (the time was not available) identified only one probable signal. We therefore developed a waveform correlation technique using the event with the largest signal (1987C259) as a master event. The data from this event was cross-correlated with the data for the known day of each event. Arrivals from all six of the 1000 kg events were identified using this technique. Figure 2 shows an example for event 1986C177.

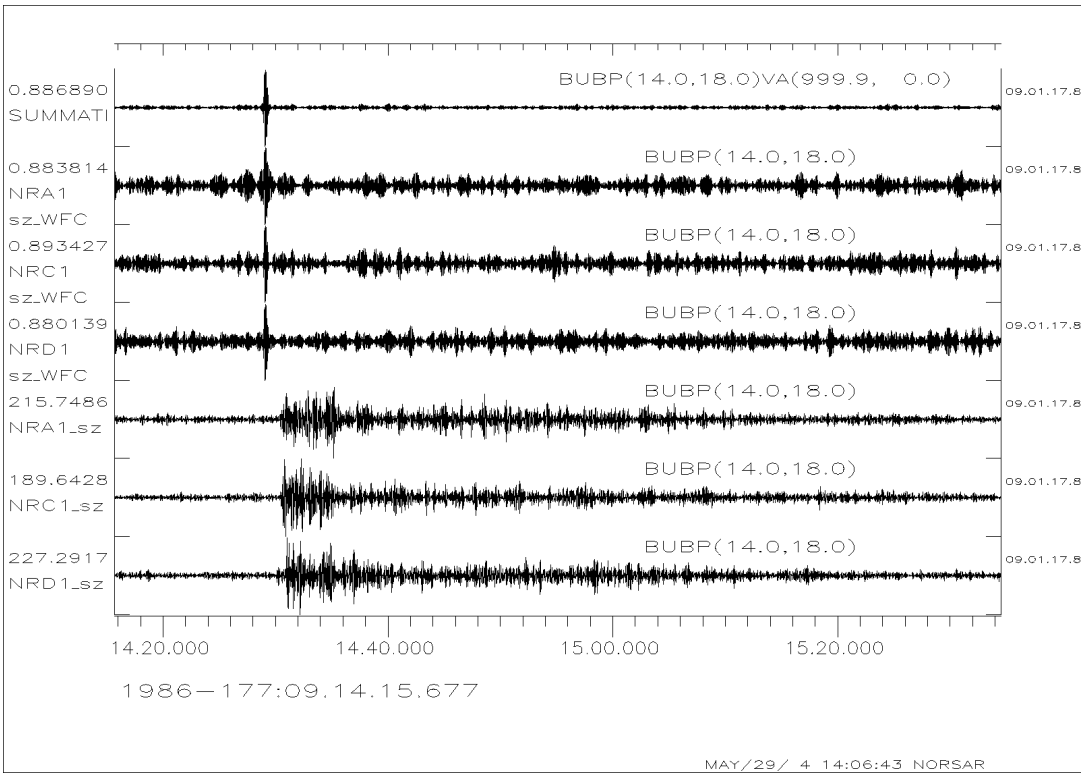


Figure 2. Results of waveform correlation between the filtered master event waveforms and NORES data, which includes the hypothesized Älvdalen event. The lowermost three traces indicate the filtered data, the traces labeled WFC, the corresponding correlation coefficient traces and the upper trace gives the summation of all NORES waveform correlation traces.

NORES P-wave spectra are shown in Figure 3 for all of the explosions, with the exception of 2002C164 which was conducted after NORES was destroyed by a lightning strike, and the 1986C246 event which occurred at a time the station was not operating. Each line is the arithmetic mean of a spectrum calculated by the Thomson Multitaper Method (Thomson, 1982) from each of the available NRS short period channels in an 8.0 second time window beginning at the first P-arrival. Spectra are corrected to Hagfors response for the sake of comparison with the figures in Stevens et al. (2003). The spectra clearly show the decoupling effectiveness of the cavities, as well as the relatively enhanced coupling of the larger explosions in the smaller chambers. The largest signals are from the 5000 kg explosions in the 200 and 300 m^3 chambers, and these signals are approximately twice as large as the signals from the 10,000 kg explosions in the larger 1000 m^3 chamber.

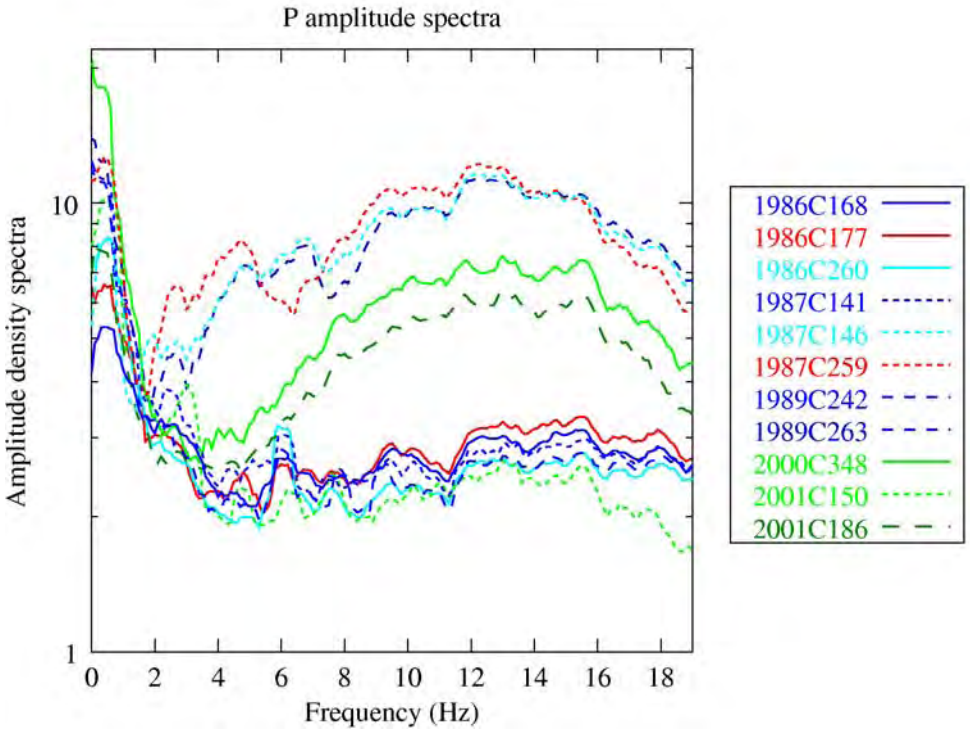


Figure 3. Amplitude spectra from the Älvdalen explosions for which NORES data exists. Green lines are events which took place in the 1000m^3 chamber, blue lines are events which took place in Chamber A (300m^3), and red lines are events which took place in Chamber B (200m^3).

The spectra of the five 1000 kg and the 2500 kg explosions are substantially lower than the spectra of any of the larger events. Somewhat surprising is that the spectrum of the 2500 kg explosion is lower than any of the 1000 kg explosions, suggesting that there was more nonlinear coupling from these 1000 kg events than from the 2500 kg explosion. This is possible since the 2500 kg explosion was in the larger 1000 m^3 chamber, but is inconsistent with the predictions obtained from an equivalent volume spherical cavity.

The criterion for full decoupling is usually expressed in terms of a requirement that the late-time, equilibrium pressure in the cavity be less than or equal to some constant, k, times the overburden pressure (Herbst et al, 1961):

$$\frac{(\gamma - 1)W}{V} \leq k\rho gh \qquad (1)$$

where k is between 0.5 (Latter) and 1.0 (Patterson), ρgh is the overburden pressure at depth h, γ is the adiabatic expansion constant, which is approximately 1.2 for air and 1.3 for chemical explosion products, and V is the cavity volume. The Swedish chamber explosions are all at approximately 100 meters depth in granite. Figure 4 shows the Latter criterion for full decoupling together with the actual parameters calculated from the known depth and volume for each of these explosions. All of the explosions exceed the Latter threshold, although the 2500 kg explosion as well as the 1000 kg explosions in the 300 m^3 cavity are close to fully decoupled.

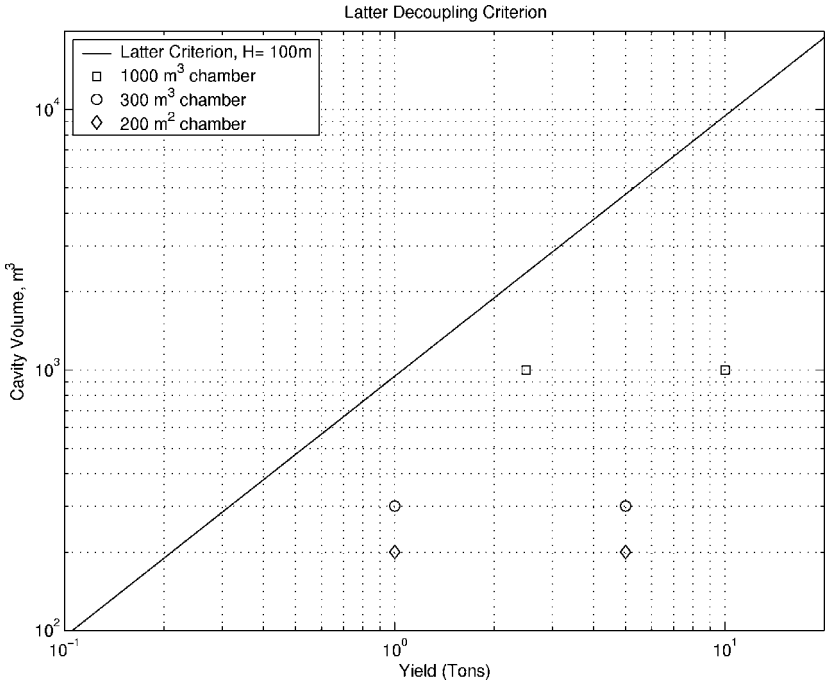


Figure 4. Latter decoupling criterion calculated for the conditions of the Swedish chamber explosions. The actual values for the Swedish chamber explosions are marked.

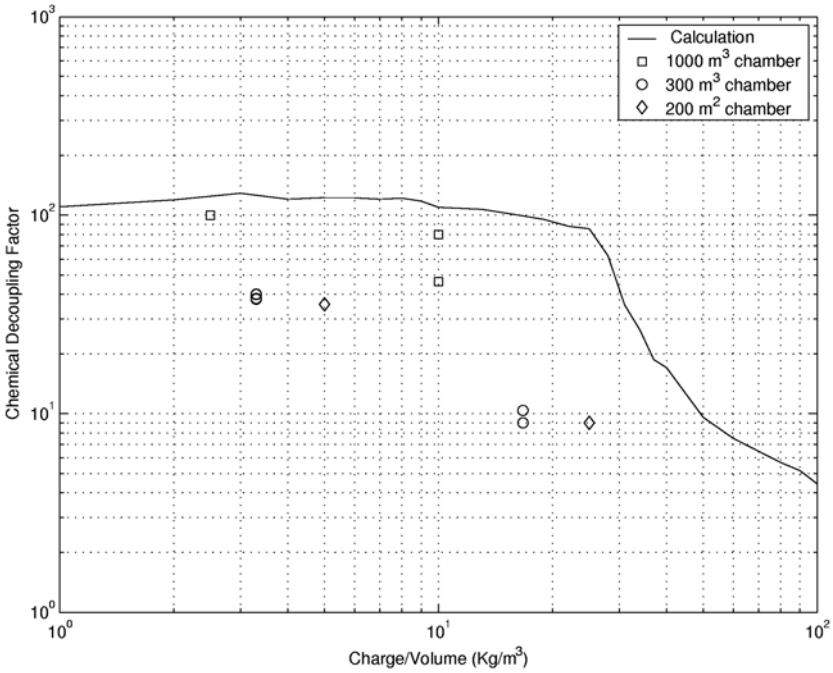


Figure 5. Observed and predicted decoupling factor for Swedish explosions. The Swedish explosions were in rectangular chambers in granite with volumes of 200 m^3, 300 m^3 and 1000 m^3. The calculations were for a chemical explosion in a 6.3 meter spherical cavity in granite (1000 m^3).

Figure 5 shows the observed and predicted decoupling factor for Swedish explosions. The calculations were for a chemical explosion in a 6.3 meter spherical cavity in hard (non-weakening) granite. The decoupling factor contains an unknown scale factor since we do not have data for a tamped explosion, so the smallest signal was arbitrarily scaled to have a decoupling factor of 100. The horizontal axis corresponds approximately to the overdrive factor above full decoupling. There are two things to notice from this figure. First, the calculations predict that decoupling

will be nearly complete up to more than a factor of 10 above the Latter threshold. This is because the chamber is in a material (granite) with considerable strength, while the Latter criterion assumes that it is only necessary for the explosion to overcome overburden pressure. Second, the decoupling factor is generally less than predicted. Although decoupling is nearly complete for events up to 10 times the Latter threshold, as mentioned above there is significantly more coupling observed for the 1000 kg events in the smaller chambers than for the 2500 kg event in the larger chamber. Also, the explosions with the largest signals show that coupling increases substantially at yields above 10xLatter at lower charge/volume than the calculations predict.

The differences between the observed and calculated decoupling factors shown in Figure 5 are likely due to the fact that the calculations were performed for a spherical cavity while the actual explosions were in a rectangular chamber. To improve our understanding of these geometrical effects, several three-dimensional finite difference calculations were performed using the "Stellar" code. Stellar is a second-order accurate Eulerian two- and three-dimensional stress wave propagation code with the same constitutive models that were used for the spherically symmetric calculations. The chamber was modeled as an air-filled chamber with dimensions 4.8m high, 30m long, and 7.2m wide. The near field results are sensitive to the layout of the explosive in the chamber, so several layouts were used in the simulations. Figure 6 shows the regions of nonlinear deformation (corresponding to non-zero plastic work) for the calculation of the 2500 kg explosion. Note that this is the most decoupled of any of the explosions. The calculations show that while the region of nonlinear deformation is limited to the part of the chamber near the explosion, there is a significant amount of nonlinear deformation and this will lead to enhanced coupling relative to a fully decoupled explosion.

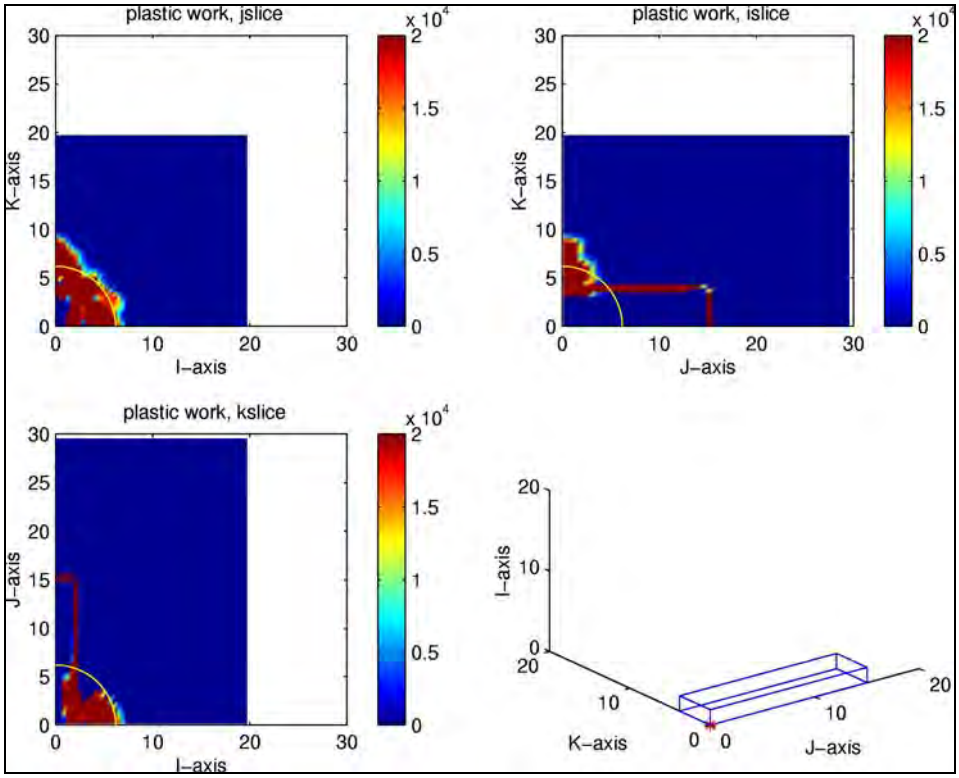


Figure 6. Regions of nonlinear deformation for 2500 kg chamber calculation. The three figures show the nonlinear deformation around each of the three axes. The yellow line shows the size of an equivalent volume sphere.

Figure 7 shows the calculated waveforms at the locations of recording stations V1 and V2 drillholes for one of the 10,000 kg calculations, together with the horizontal and vertical components of the recorded waveforms at the same locations. The chamber reverberations are stronger than the observations, however the peak amplitudes and general shape and duration of the waveforms are reproduced fairly well. The calculations predict a strong radiation pattern

to the waveforms, with stronger amplitudes above and below the chamber and reduced amplitudes along the long axis of the chamber near the recording points V1 and V2.

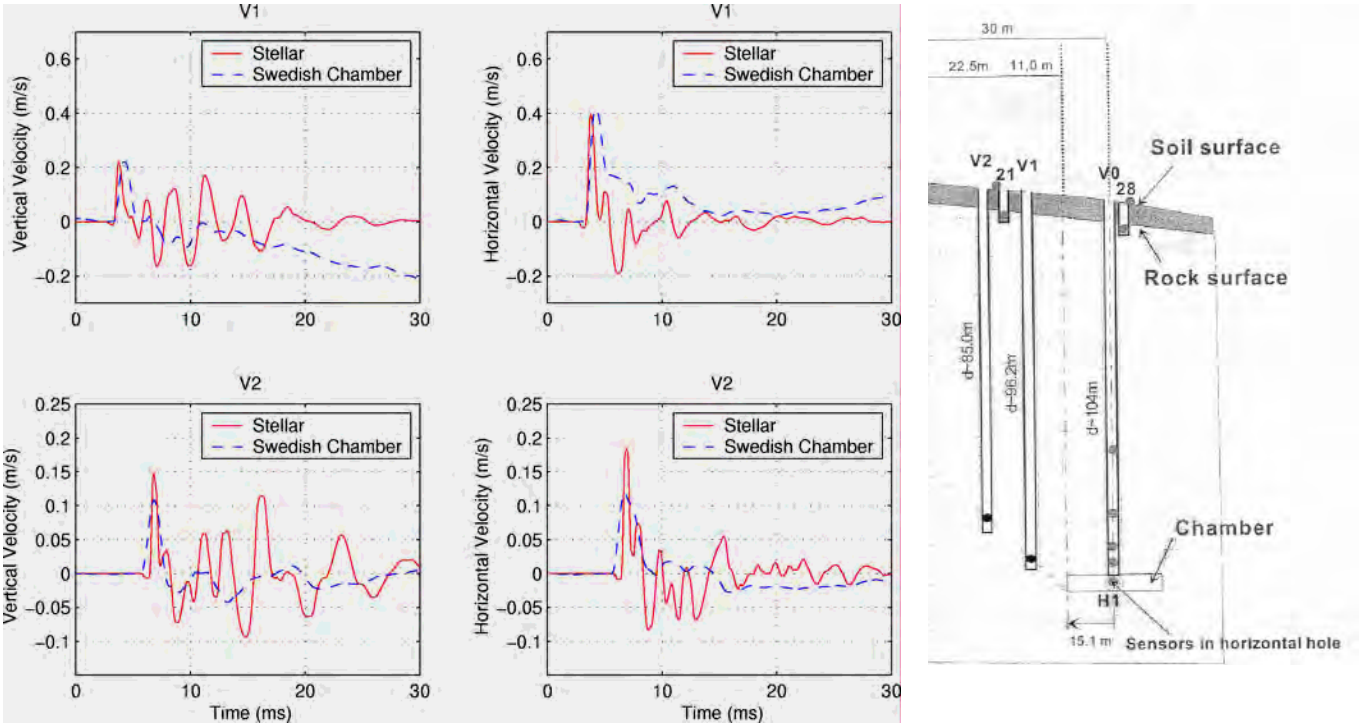


Figure 7. Data and calculated waveforms at stations V1 and V2. The station geometry relative to the chamber is shown on the right.

CONCLUSIONS AND RECOMMENDATIONS

The following conclusions are derived from analysis of the Swedish chamber explosions:

- A fully decoupled chemical 2.5 ton explosion is detectable at NORSAR at a distance of 140 km. 1.0 ton decoupled explosions are also detected, however the signals from these events, which were in smaller chambers, are larger than that of the 2.5 ton explosion so they appear to be partially coupled.
- This data set covers a range of yields overdriven beyond full decoupling by factors of approximately 2-25.
- Decoupling remains approximately complete for yields less than 10 times the Latter decoupling criterion, and there is more variation in coupling than predicted by a spherical cavity model for explosions with small overdrive.
- At yields higher than 10 times the Latter criterion coupling increases rapidly, increasing by an order of magnitude for a factor of 2 increase in yield/volume.
- 3D nonlinear calculations of the chamber explosions show strong nonlinearity at the points closest to the explosion. This leads to enhanced coupling relative to the equivalent volume sphere.

ACKNOWLEDGEMENTS

The Swedish chamber explosions discussed in this paper were conducted in a cooperative effort between the Norwegian Defense Building and Infrastructure Agency (Forsvarsbygg), Defense Science & Technology Agency (DSTA) of Singapore and the Swedish Defense Research Agency. The lead agency of the large-scale tests, DSTA, and the other participants, kindly provided the data. We thank them for their support and for the use of their data.

REFERENCES

Gronsten, G. A. (2000), “The Älvdalen Large Scale Tests”, Data report from the Norwegian measurements, Fortifikatorisk notat nr. 286/01, Forsvarets Bygningstjeneste, Oslo, Norway, 2000.

Gronsten, G. A. and Krest, O. (2002), “The Älvdalen Large Scale Tests”, Data report from the Norwegian measurements, Fortifikatorisk notat nr. 297/01, Forsvarets Bygningstjeneste, Oslo, Norway, 2001.

Herbst, R. F., G. C., Werth and D. L. Springer (1961), "Use of Large Cavities to Reduce Seismic Waves From Underground Explosions," J. Geophys. Res., 66, p. 959.

Stevens, J. L., Rimer, N., Xu, H., Baker, G. E., Murphy, J. R., Barker, B.W., Lindholm, C., Ringdal, F., Gibbons, S., Kværna, T., and Kitov, I. (2003). “Analysis and Simulation of Cavity-Decoupled Chemical Explosions”, in *Proceedings of the 25th Seismic Research Review- Nuclear Explosion Monitoring: Building the Knowledge Base*, LA-UR-03-6029, Vol. I, pp. 466-475.

Thomson, D. J. (1982): Spectrum Estimation and Harmonic Analysis. Proc. IEEE, 70(9), 1055-1096.

CHARACTERIZATION OF AN EXPLOSION SOURCE IN A COMPLEX MEDIUM BY MODELING AND WAVELET DOMAIN INVERSION

M. Nafi Toksöz, Xu Li, Mary Krasovec, and Shihong Chi

Massachusetts Institute of Technology

Sponsored by Air Force Research Laboratory

Contract No. F19628-03-C-0126

ABSTRACT

Explosions are often conducted in complexes with chambers, tunnels, and shafts used for access and instrumentation. These structures can act as strong scatterers of seismic waves and complicate the radiation patterns from explosions. The objectives of this project are (1) to study the effects of these near-source scatterers on seismic waves radiated from explosions, and (2) to use a wavelet domain based moment-tensor inversion scheme to determine "explosive" and "multicouple" components of the source.

During the first phase of the project, emphasis has been on forward modeling. A three-dimensional (3-D) variable grid finite-difference code was used to model the effects of cylindrical cavities located near an explosion source. The presence of a cylinder results in strong scattering into P and S waves, and the reverberation of energy in the cylinder. Waves going around the cylinder and those reverberating inside continue to radiate long after the initial explosion. The observed wave trains are longer than those of the explosion alone. A cylinder near an explosive source scatters energy into P, SV, and SH waves. The P and S waves are separated by calculating the divergence and curl of the displacement fields. The relative significance of factors contributing to scattering (e.g., size, proximity to explosion, orientation, etc.) is investigated. Synthetic seismograms are used to test the performance of moment-tensor inversion and its ability to separate the volumetric and shear components of the source. With good azimuthal coverage, the moment-tensor shows significant shear components in the presence of a scatterer.

OBJECTIVE

An explosive source in a laterally homogeneous layered half-space generates P, SV, and Rayleigh waves, but not SH or Love waves. However, seismograms from a large number of explosions show nonisotropic radiation patterns for P and Rayleigh waves, and prominent SH and Love waves. The near-source contribution to nonisotropic radiation of P, Rayleigh and SH waves generated by an explosion can be attributed to three mechanisms. First is the tectonic strain energy released by the explosion, resulting in a composite source consisting of an explosion and a double couple (e.g., Archambeau and Sammis, 1970; Toksoz et al., 1965; Toksoz and Kehrer, 1972; Wallace et al., 1983, 1985; Priestley et al., 1990; Schlittenhardt, 1991; Stump et al., 1994; Patton and Taylor, 1995). The second factor that contributes to the nonisotropic seismic radiation pattern from explosive sources is the shape of the explosion cavity and the location of the explosive source in that cavity (Rial and Moran, 1986; Stevens et al., 1991; Zhao and Harkrider, 1992; Ben-Menahem and Mikhailov, 1995; Gibson et al., 1996; Ben-Menahem, 1997; Imhof and Toksöz, 2002). The third mechanism contributing to complex seismic radiation from an explosion is the near-source scattering (Gupta et al., 1990; Johnson, 1997; Ben-Menahem, 1997; Imhof and Toksöz, 2000, 2002). This mechanism could be significant when strong scatterers are present near the source.

The objective of this research is to study the role of scattering from near-source structures such as tunnels, shafts, adits, and surface topography in the generation of complicated radiation patterns and SH waves from explosions. In addition, the study will test the performance of moment-tensor inversion to separate the isotropic (i.e., explosion) and multicouple components of the source as an aid to seismic discrimination.

RESEARCH ACCOMPLISHED

A three-dimensional (3-D) finite-difference (FDTD) program was developed to model wave propagation and scattering in heterogeneous media. The program utilizes a variable grid implemented through a grid-stretching technique. The code is parallelized to be run on a computer cluster. Initial calculations were directed to 3-D forward modeling with an explosive source and a finite-length tunnel in a homogeneous medium. The calculations show strong P to P and P to S scattering and a complicated radiation pattern. A simple moment-tensor inversion using the calculated seismograms shows that there is a double couple component, but the isotropic component is still dominant over the double couple. The radiation pattern at high frequencies (40 Hz) is too complicated to be represented by a first-order moment-tensor.

Forward Modeling by the Finite Difference Approach

The time domain finite-difference method has been one of the most widely used tools to simulate wave propagation in 2-D and 3-D elastic media with spatial variations of elastic properties. Computational efficiency can be achieved by sampling the physical space adaptively with a variable grid. However, the variable grid can introduce wave distortion or numerical reflections due to phase change at the interface of two grids of different sizes (Browning et al., 1973). Numerical reflections can be eliminated by taking extra averages of solutions at the grid interface. However, wave distortion cannot always be avoided. Introducing a change in grid spacing may also adversely affect the formal truncation error and the stability of the system (Crowder and Dalton, 1971). In our finite difference algorithm, we apply a coordinate transformation, or stretching, to achieve effective variable grids in the physical domain and uniform grids in the transformed domain (Huang, 2003). Because the computation is carried out on a uniform grid, the formal truncation error and the stability properties of the finite-difference computation are preserved.

Strong scattering from a near-source tunnel is simulated with the FDTD algorithm described above. Figure 1 shows the 3-D geometry of the simulation model including a cylindrical tunnel. Simulations are also conducted with the tunnel absent. The infinite formation is modeled by a finite volume of 3000 m by 3000 m by 1100 m in the x, y, and z directions. Absorbing boundaries are placed at all six sides of the model to eliminate wave reflection. An explosion source with a center frequency of 40 Hz is excited in the center of the model. The length and radius of the cylindrical tunnel are 50 m and 15 m, respectively. The axis of the tunnel is parallel to the y axis of the Cartesian coordinate. The distance between the source and the tunnel is 30 m. The formation is a perfect Poisson medium, with compressional and shear wave velocities and density of 4000 m/s, 2300 m/s, and 2500 kg/m^3, respectively. Inside the tunnel, we assume a sound velocity of 340 m/s and a compressed air density of 200 kg/m^3. The grid size increases from 1 m near the source and cylinder tunnel to 10 m away from the source region. Examples of

calculated seismograms are shown in Figure 2. The receiver plane is in the xy plane and 200 m above the source. The seismograms are along a line parallel to the x axis. Computations are made for an explosion alone (without a tunnel) and an explosion with a tunnel present.

The top row of Figure 2 shows the x and z components of the motion (velocity fields) when the tunnel is absent. As expected, only P waves are generated. When the tunnel is present near the explosion source, strong scattering occurs. The seismograms in the middle row of Figure 2 show that the strong shear waves are scattered from the tunnel. To demonstrate the effect of scattering, we subtract the explosion only seismograms from those with the explosion plus the tunnel. The bottom row of Figure 2 shows these strong scattered waves. These are both P and S scattering, and scattered S waves are larger than P waves. SH waves are also observed, but their amplitudes are much smaller than the x and z components.

The divergence and curl of the wavefield separate the compressional and shear components of the wavefield, respectively. Figure 3 shows snapshots of the divergence and curl of the velocity field at 60 ms on the xz, yz and xy planes passing through the origin of the coordinate system. One can clearly see the complex pattern of the scattering. The curl is zero inside the tunnel. The snapshots of the xz plane and xy plane reveal the vertical and horizontal cross section of the tunnel. The snapshot along the yz plane, parallel to the tunnel, shows the complexity introduced by the finite length of the tunnel.

Understanding the patterns of scattered waves will help us choose appropriate models for inversion of the source mechanism. In the xz plane, the shear wave energy is divided into four quadrants, and the shear waves are in-phase in the diagonal quadrants. Shear waves in the half-space above and below the xy plane are 180^{o} out of phase. The disturbance to the P wavefield, caused by scattering, can also be seen in the divergence field, but the scattering patterns are not as clear as those of the shear waves.

The presence of several tunnels creates very complicated scattered waves. Figure 4 shows one example of such a model, where there are six intersecting tunnels 30 meters below the surface. Two components of the seismic motion are shown.

Moment Tensor Inversion

We used synthetic seismograms with an explosion and a strong scatterer near the source to test the performance of the first-order moment-tensor inversion. A simple frequency-domain inversion method was used (Stump and Johnson, 1997; Li and Chen, 1996).

We used three sets of seismograms: explosion alone, explosion plus a tunnel, and a scattered field only. The scattered signals were obtained by subtracting the pure explosion seismograms from the explosion plus tunnel seismograms, as shown in the bottom row of Figure 2.

Figure 5 shows the results of the first-order moment-tensor inversion. For an explosion without a tunnel, only the diagonal components of the moment-tensor (m11, m22, and m33) are nonzero. For an explosive source and a nearby tunnel, the nondiagonal components appear, but the explosion term still dominates. Even with purely scattered waves, the diagonal components of the moment-tensor are larger than the off-diagonal components. This suggests the need of a more realistic representation of the source with the inclusion of a higher-order tensor (Knopoff and Randall, 1970; Aki and Richards, 1980).

CONCLUSIONS AND RECOMMENDATIONS

Time domain finite-difference modeling of seismic waves from an explosion source in the presence of a nearby tunnel shows a complex scattering pattern. The tunnel acts as a scatterer and a secondary source radiating both P and S waves.

The results shown in this paper are for a high frequency source (40 Hz center frequency) in a relatively high-velocity medium (Vp = 4000 m/s; Vs = 2300 m/s). A high-frequency source was chosen to test the stability of the variable grid code. In addition, the high-frequency source provided high-resolution examples of the scattering phenomena. New models are being computed in the 1–10 Hz frequency range to generate representative seismograms.

Seismic waves generated by an explosion plus a strong scatter cannot be represented adequately by a single first-order moment tensor. The performance of the first-order moment-tensor representation at low frequencies needs to be tested.

REFERENCES

Aki, K., and P.G. Richards (1980), *Quantitative Seismology*, *Vol. 1,* Freeman and Company, New York.

Archambeau, C.B., and C. Sammis (1970) Seismic Radiation from Explosions in Prestressed Media and the Measurement of Tectonic Stress in the Earth, *Rev. Geophys*., 8, 473-499.

Ben-Menahem, A. (1997), Seismic Source Functions for Explosions in a Non-Spherical Cavity Embedded in a Scattering Environment: Application to the Regional Discrimination of Nuclear Explosion and Earthquakes. *Geophys. J. Int*., 128, 97-124.

Ben-Menahem, A., and O. Mikhailov (1995), Multiple Radiation of Seismic Waves from Explosions in Non-Spherical Cavities and its Application to Signal Identification, *J. Acoust. Soc. Am*., 97, 2675-2698.

Browning, G., H.O. Kreiss, and J. Oliger (1973), Mesh Refinement, *Mathematics of Computation,* 27, 29-39.

Crowder, H.J., and C. Dalton, C. (1971), Errors in the use of Nonuniform Mesh Systems, *J. Computational Physics,* 7, 32-45.

Gibson, R. L., M. N. Toksöz, and W. Dong (1996), Seismic Radiation from Explosively Loaded Cavities in Isotropic and Transversely Isotropic Media, *Bull. Seism. Soc. Am.,* 86, 1910-1924.

Gupta, I. N., C. S. Lynnes, T. W. McElfresh, and R. A. Wagner (1990), F-K Analysis of NORESS Array and Single Station Data to Identify Sources of Near-Receiver and Near-Source Scattering, *Bull. Seism. Soc. Am.*, 80, 2227-2241.

Huang, X (2003), Effects of Tool Positions on Borehole Acoustic Measurements: A Stretched Grid Finite Difference Approach, Ph.D. Thesis, Massachusetts Institute of Technology.

Imhof, M.G. and M.N. Toksöz (2000), Scattering from Tunnels Near Sources and their Effects on Seismic Signatures of Explosions. *Bull. Seism. Soc. Am*., 90, 229-242.

Imhof , M. G. and M. N. Toksöz (2002), The Effects of Synchronized Multiple-Cavity Sources on Seismic Radiation. *Bull. Seism. Soc. Am*., 92, 2381-2390.

Johnson, L. R. (1997), Generation of S Waves by Explosion, in *Proceedings of 19th Annual Seismic Research Symposium on Monitoring a Comprehensive Test Bay Treaty (CTBT),* M. J. Shore, R. S. Jih, A. Dainty, and Erwin (eds.), Defense Special Weapons Agency, 625-631.

Knopoff, L., and M. Randall, M. (1970), The Compensated Linear-Vector Dipole: A Possible Mechanism for Deep Earthquakes, *J. Geophys. Res.,* 75, 4957-4963.

Li, X. and Y.T. Chen (1996), Inversion of Long-Period Body-Wave Data for the Source Process of the Gonghe, Qinghai, China Earthquake, *Acta Seismologica Sinica*, 9, 361~369.

Patton, H.J. and S.R. Taylor (1995), Analysis of Lg Spectral Ratios from NTS Explosions: Implications for the Source Mechanisms of Spall and the Generation of Lg Waves, *Bull. Seism. Soc. Am*., 85, 220-236.

Priestley, K.F., W.R. Walter, V. Martynov, and M.V. Rozhkov (1990). Regional Seismic Recordings of the Soviet Nuclear Explosion of the Joint Verification Experiment, *Geophys. Res. Lett*., *17*, 179-182.

Rial, J.A., and B. Moran (1986). Radiation Patterns for Explosive-Loaded Axisymmetric Cavities in an Elastic Medium: Analytic Approximations and Numeric Results. *Geophys. J. R. Astr. Soc*., *86*, 855-862.

Schlittenhardt, J. (1991). The Effects of Spall on Teleseismic P-Waves: an Investigation with Theoretical Seismograms, in *Explosion Source phenomenology*, S. Taylor, H. Patton, and P. Richards (eds.), American Geophysical Union, Washington, D.C., 141-150.

Stevens, J.L, J.R. Murphy, and N. Rimer (1991). Seismic Source Characteristics of Cavity Decoupled Explosions in Salt and Tuff, *Bull. Seism. Soc. Am*., *81*, 4, 1272-1291.

Stump, B.W., and Johnson, L.R. (1977). The Determination of Source Properties by the Linear Inversion of Seismograms, *Bull. Seism. Soc. Am.*, *67*, 1489–1502.

Stump, B.W., R.E. Reinke, K.H. Olson, and L.R. Johnson (1994). Isotropic and Deviatoric Characterization of the Coalora Nuclear Explosion in Yucca Flats, *Geophys. J. Int*., *116*, 538-552.

Toksöz, M.N., D.G. Harkrider, and A. Ben-Menahem (1965). Determination of Source Parameters by Amplitude Equalization of Seismic Surface Waves: Part 2, Release of Tectonic Strain by Underground Nuclear Explosions and Mechanisms of Earthquakes*, J. Geophys. Res*., *70*, 907-922.

Toksöz, M.N., and H.H. Kehrer (1972). Tectonic Strain Release by Underground Nuclear Explosions and its Effect on Seismic Discrimination, *Geophys. J. R. Astr. Soc*., *31*, 141-161.

Wallace, T.C., D.V. Helmberger, and G.R. Engen (1983). Evidence of Tectonic Release from Underground Nuclear Explosions in Long-Period P-Waves, *Bull. Seism. Soc., Am*., *73*, 593-613.

Wallace, T.C., D.V. Helmberger, and G.R. Engen (1985). Evidence of Tectonic Release from Underground Nuclear Explosions in Long-Period S-Waves, *Bull. Seism. Soc. Am.*, *75*, 157-174.

Zhao, L. and D.G. Harkrider (1992). Wavefield from an Off-Center Explosion in an Embedded Solid Sphere, *Bull. Seism. Soc. Am., 82*, 1927-1955.

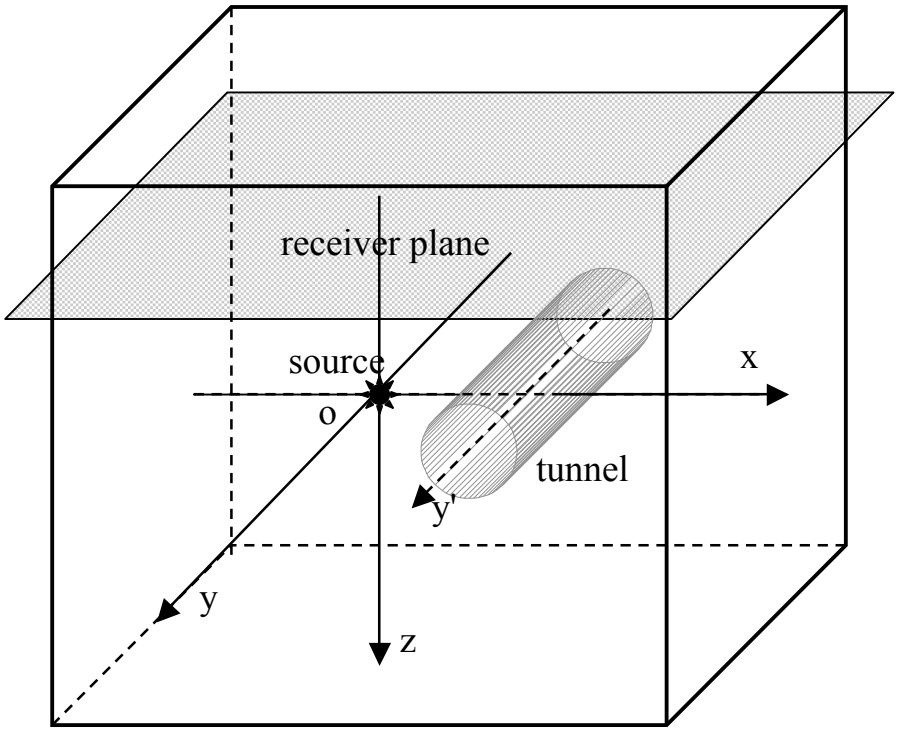


Figure 1. The geometry skeleton diagram of the model discussed in this paper. The explosion source is set in the middle of the model, coincident with the origin of the coordinates. A cylindrical tunnel is set 30 m away from the source, with radius of 15 m and length of 50 m. Its symmetric axis is parallel to the y axis. The receivers are set in the plane 200 m above the source. The distance between the neighbor receivers is 100 m. The medium parameters can refer to the context.

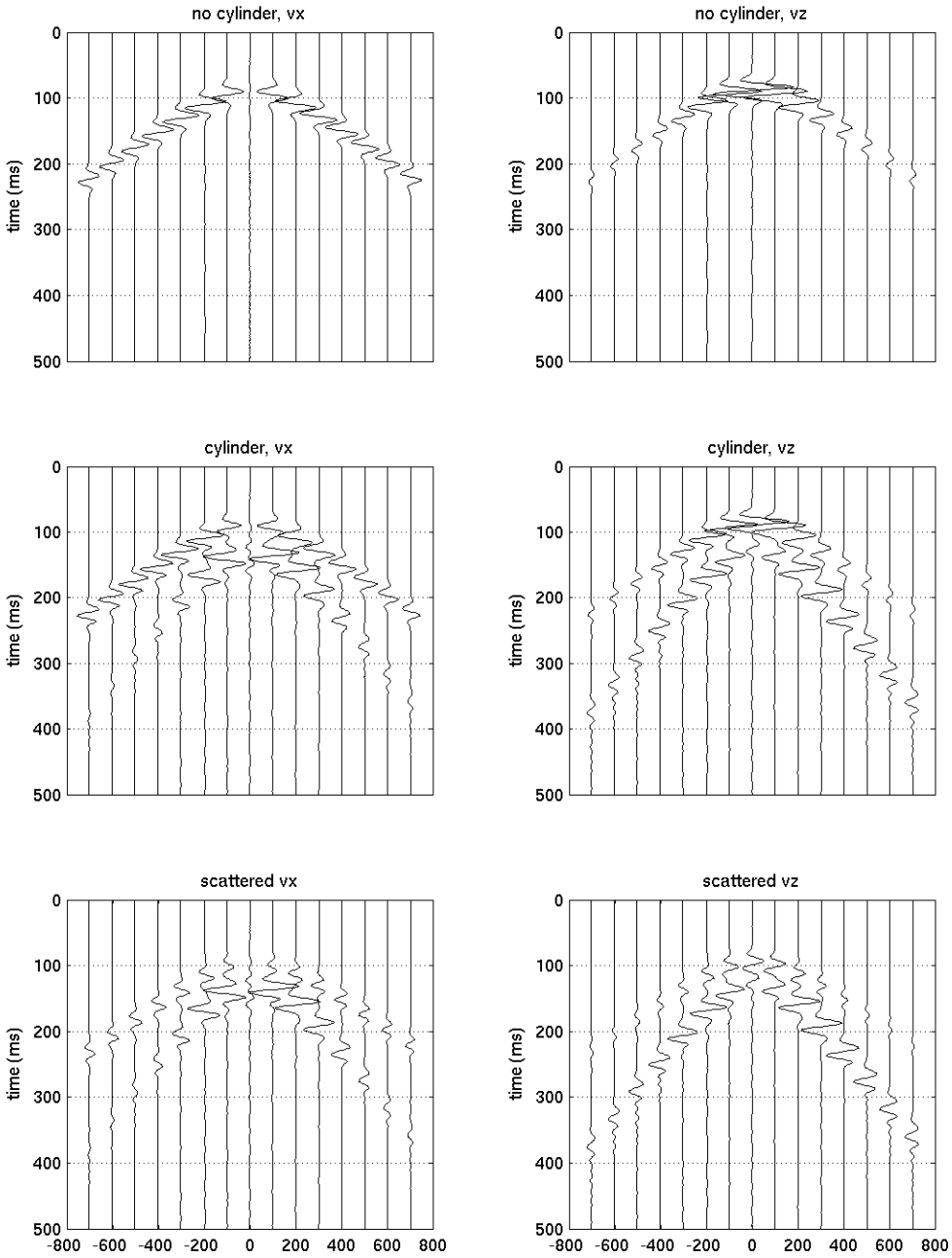


Figure 2. Comparison of the x and z components of the velocity fields at the receiver plane in the absence and the presence of the tunnel. Respective scattered velocity fields of the x and z components are also shown in the bottom row of this figure.

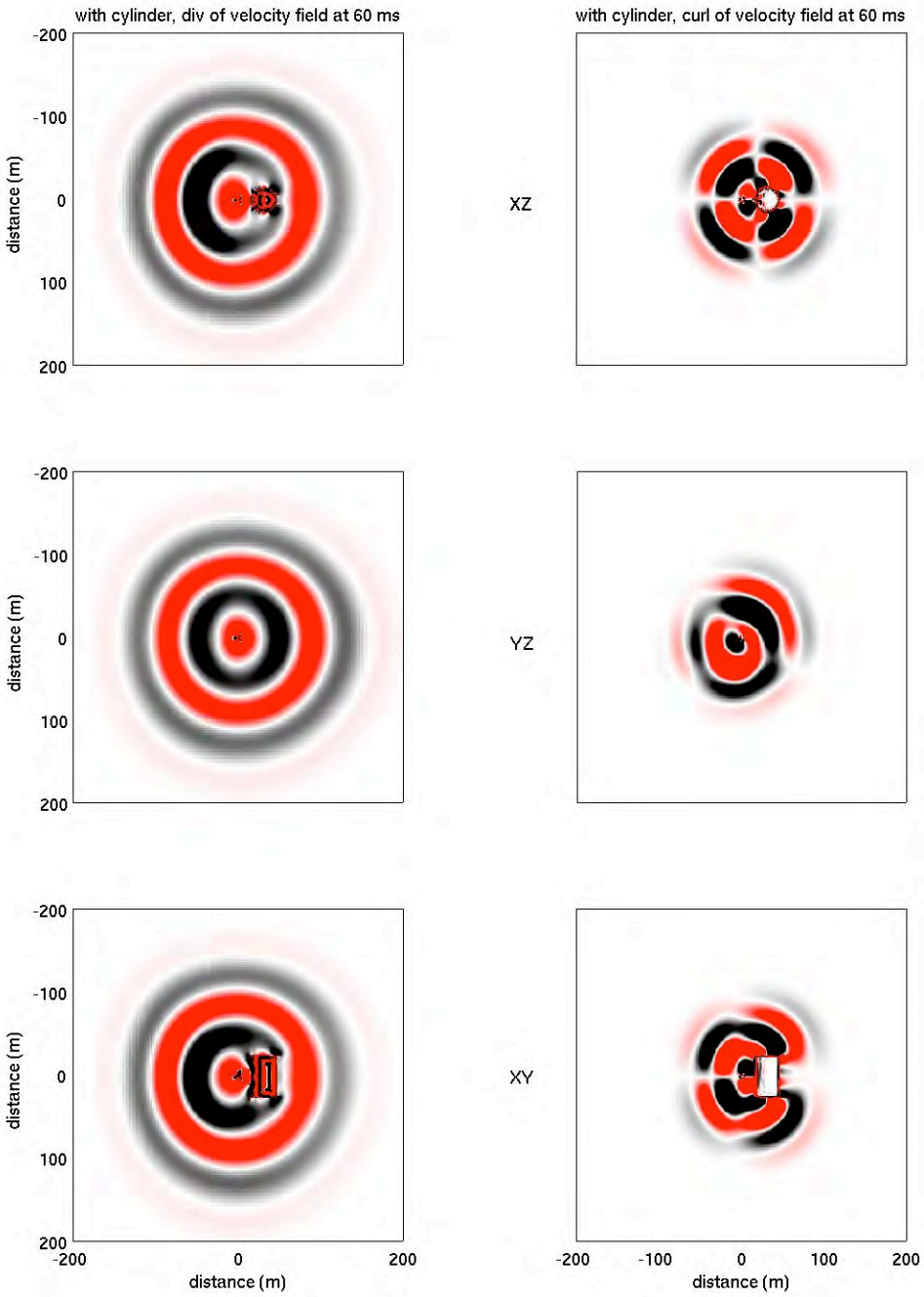


Figure 3. Snapshots of the divergence and curl of the velocity field from an explosion in the presence of a near-source tunnel. The snapshots were taken at 60 ms after the explosion.

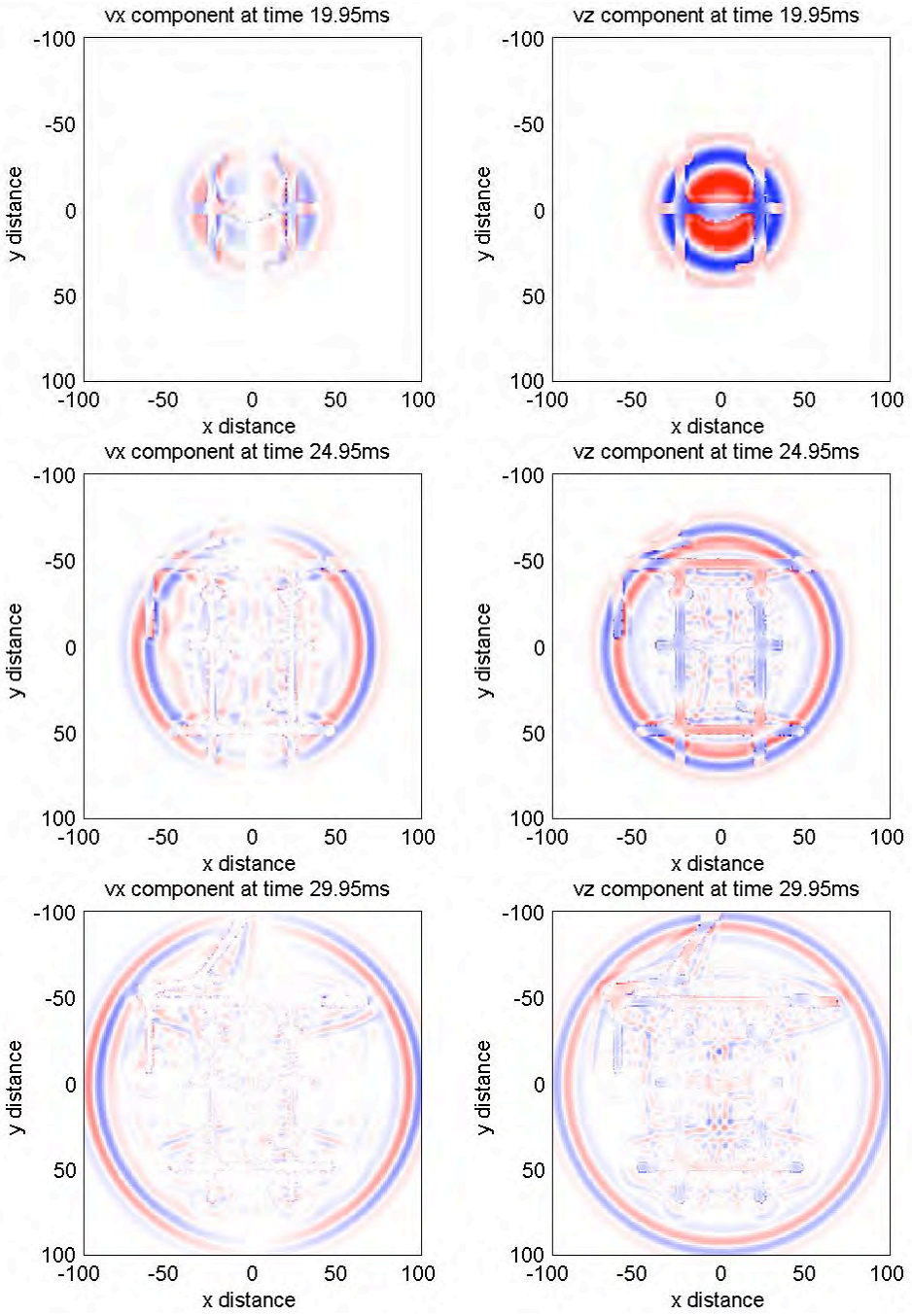


Figure 4. An example of the scattered wave propagating in a complex tunnel structure. There are six intersecting tunnels. Snapshots of Vx and Vz were taken above the model.

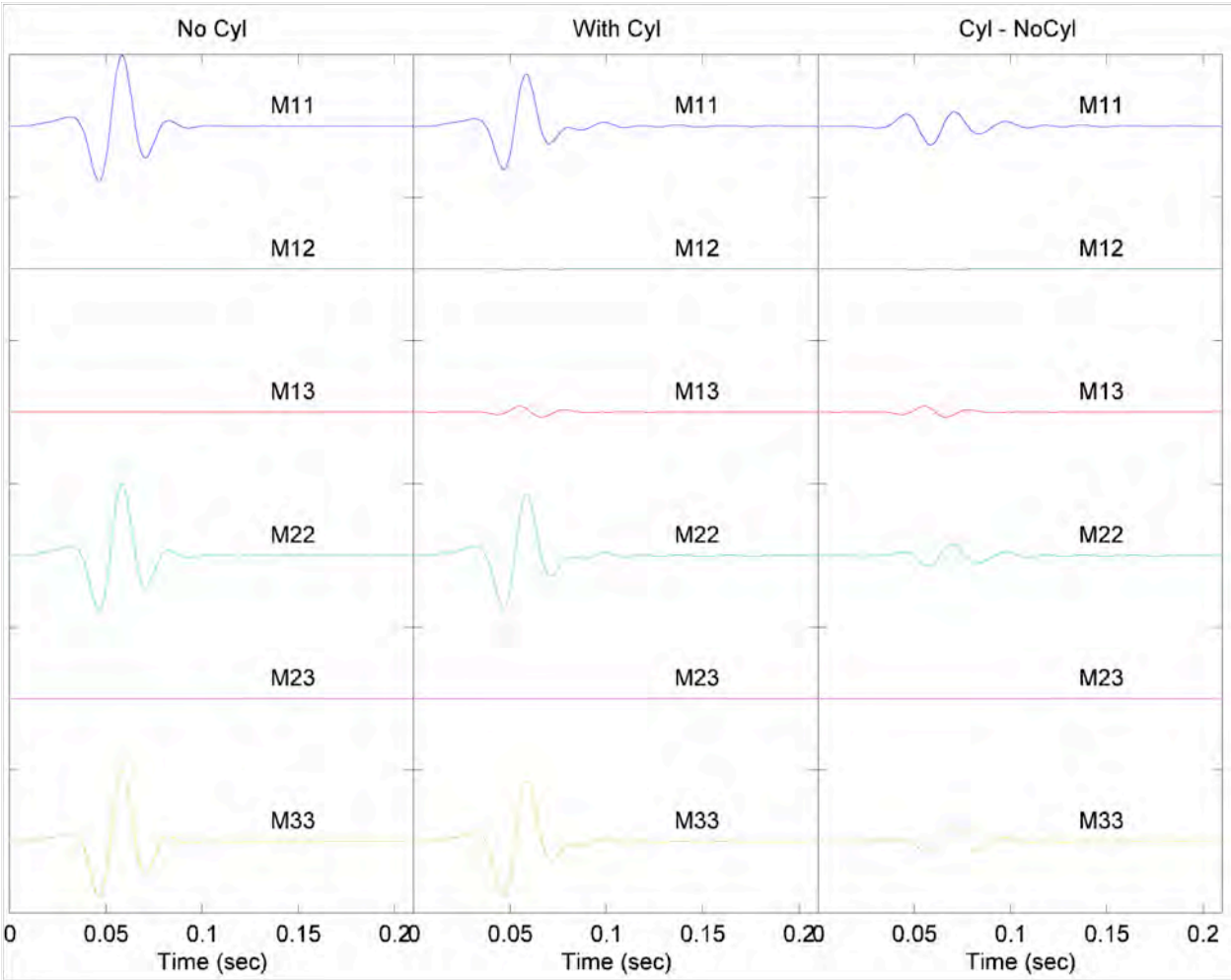


Figure 5. The results of moment-tensor inversion for an explosion alone (left), an explosion with a nearby cylindrical tunnel (middle), and pure scattered signals (right). Even for pure scattered signals, the isotropic component is still dominant. The large amplitude of M13, relative to other two deviatoric components M12 and M23, suggests that the radiation pattern could be related to the geometry property of the tunnel.

REGIONAL SEISMIC IDENTIFICATION RESEARCH: PROCESSING, TRANSPORTABILITY AND SOURCE MODELS

William R. Walter[1], Kevin M. Mayeda[1], Arthur J. Rodgers[1], Steven R. Taylor[2], Douglas A. Dodge[1], Eric Matzel[1] and Michael D. Ganzberger[1]

Lawrence Livermore National Laboratory[1], Los Alamos National Laboratory[2]

Sponsored by National Nuclear Security Administration
Office of Nonproliferation Research and Engineering
Office of Defense Nuclear Nonproliferation

Contract No. W-7405-ENG-48[1] and W-7405-ENG-36[2]

ABSTRACT

Our identification research for the past several years has focused on the problem of correctly discriminating small-magnitude explosions from a background of earthquakes, mining tremors, and other events. Small magnitudes lead to an emphasis on regional waveforms. It has been shown that at each test site where earthquake and explosions are in close proximity and recorded at the same station, clear differences in the regional body waves, such as the relative high frequency amplitudes of P and S waves, can be used to discriminate between event types. However, path and source effects can also induce such differences; therefore these must be quantified and accounted for. We have been using a specific technique called Magnitude and Distance Amplitude Correction (MDAC), (Walter and Taylor, 2002) with some success to account for some of these effects.

Here we briefly present highlights from three aspects of our recent work:

1) *Efficient Processing* – In order to calibrate the source and path behavior of a particular region we need to be able to quickly and efficiently measure hundreds to thousands of prior events. We have developed processing software called Regional Body-wave Amplitude Processor (RBAP) that is optimized for quickly selecting data, reviewing seismograms and making amplitude measures for the four major regional phases Pn, Pg, Sn and Lg. The code includes an MDAC modeling module. The code works with a database so that changes to parameters (e.g. locations, magnitudes, MDAC values, etc.) are traced and results can easily be updated to reflect the changes.

2) *Transportability* – We have been re-examining the large database of the western United States (U.S.) underground nuclear tests and earthquakes assembled under a prior agreement. This western U.S. data covers a wide range of depths and material properties and has excellent ground truth information. We define the MDAC parameters based on fitting the earthquakes alone. We are comparing and contrasting how well MDAC corrected events discriminate in the western U.S. compared to MDAC-corrected events in other regions such as Eurasia. Two issues are important: first, how effectively can an earthquake-based MDAC model remove gross path and source effects. Second, how large is the variability in the MDAC-corrected explosion source spectra from region to region. This addresses the issue of whether a particular discriminant such as high frequency P/S works everywhere or only under certain circumstances.

3) *Source Models* – The MDAC procedure uses a new generalized Brune (1970) style earthquake model to predict expected earthquake spectra. One of its parameters is the apparent stress, a ratio of seismic energy to moment. Currently the geophysical community is split on whether apparent stress is constant or increasing with the size of the earthquake. Here we briefly present some research results examining the scaling of earthquake apparent stress. Another factor in addressing the transportability is the explosion source model. We have started to investigate how effectively the existing explosion models can be incorporated into MDAC using path parameters determined from earthquakes. We present some preliminary results here where we have tested some basic explosion source models on western U.S. explosions.

OBJECTIVE(S)

Monitoring the world for potential nuclear explosions requires characterizing seismic events and discriminating between natural and man-made seismic events, such as earthquakes and mining activities, and nuclear weapons testing. We continue developing, testing, and refining size-, distance-, and location-based regional seismic amplitude corrections to facilitate the comparison of all events that are recorded at a particular seismic station. These corrections, calibrated for each station, reduce amplitude measurement scatter and improve discrimination performance. We test the methods on well-known (ground truth) datasets in the U.S. and then apply them to the uncalibrated stations in Eurasia, Africa, and other regions of interest to improve underground nuclear test monitoring capability.

RESEARCH ACCOMPLISHED

As part of the overall National Nuclear Security Administration Ground-based Nuclear Explosion Monitoring (GNEM) Research and Engineering program, we continue to pursue a comprehensive research effort to improve our capabilities to seismically characterize and discriminate underground nuclear tests from other natural and man-made sources of seismicity. To reduce the monitoring magnitude threshold, we make use of regional body and surface wave data to calibrate each seismic station. Our goals are to reduce the variance and improve the separation between earthquakes and explosion populations by accounting for the effects of propagation and differential source size.

Efficient Processing

Effective earthquake-explosion discrimination has been demonstrated in a broad variety of studies using ratios of regional amplitudes in high-frequency (primarily 1-to 20-Hz) bands (e.g., Walter et al., 1995, Taylor, 1996, Rodgers and Walter, 2002, Taylor et al., 2002 and many others). When similar-sized earthquakes and explosions are nearly co-located, we can understand the observed seismic contrasts, such as the relative P-to-S wave excitation, in terms of depth, material property, focal mechanism and source time function differences. However it is well known that path propagation effects (e.g., attenuation, blockage) and source scaling effects (e.g., corner frequency scaling with magnitude) can make earthquakes look like explosions and vice versa. We have developed a technique called MDAC (Magnitude and Distance Amplitude Corrections, Walter and Taylor, 2002) that can account for these effects with proper calibration. Such calibration is most effective if a very large number of earthquakes can be used.

To efficiently process larger data sets we have recently developed a database tool call RBAP (Regional Body-wave Amplitude Processor). RBAP provides a organized way to do the necessary processing, including the ability to add new events as they become available in the database, recalculate results based on new information (e.g., better location, magnitude, velocity model, MDAC parameters) and store the results for analysis or future use in the database. The RBAP capability includes the user's ability to select data, review traces for quality, mark arrivals, control the location of phase (and noise) windows, make amplitude measures, estimate MDAC parameters and calculate MDAC values (using coda based Mw's and database locations). The processing is organized by station-centric projects controlled by authorship. The tool is quite sophisticated, providing multiple GUI interfaces, depending on a particular configuration of the database and containing more than 100,000 lines of JAVA and 10,000 lines of PL/SQL. It was developed over the past year with close coordination between the users and the developers and we are now working on fine-tuning it.

Given the limited space in this paper, we show just two screen shots from an RBAP project of western US earthquakes at ELK. In Figure 1 we show the initial setup window and map and in Figure 2 we show the interactive picking module for an example event. In the initial window the user can select the dataset from the database by placing restrictions on date, time, magnitude, depth, and event type. Alternatively the user can input a specific list of events, as was done here. The user can also draw a polygon on the map (or import one) to select data based on geographic region. The user can also restrict the waveform retrieval to particular channels. After data selection is committed the data is retrieved and events plotted on the map and labeled by database evid (event ID). The data is then ready for analysis in the picking module.

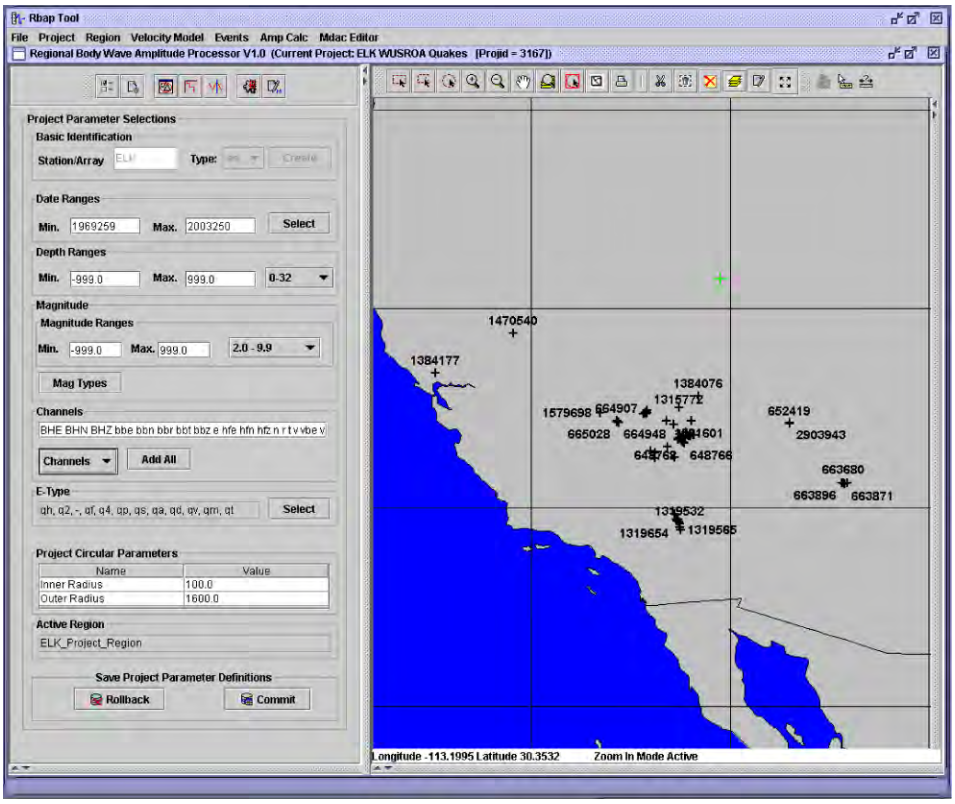


Figure 1. RBAP screen shot of initial set up window and map.

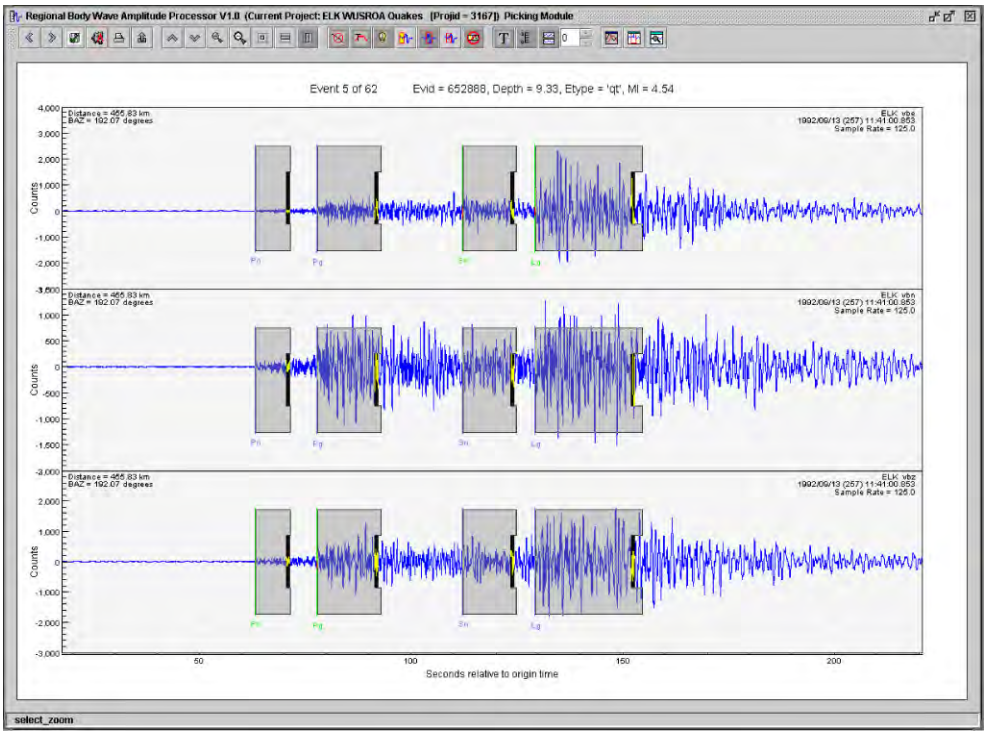


Figure 2. Screen shot of RBAP interactive picking module for an example earthquake at ELK.

Next we show an example of the interactive picking and window control portion of the tool in Figure 2. In this example of a western U.S. earthquake, part of an earthquake project at station ELK, the tool has imported LLNL analyst Flori Ryall's picks for Pn, Pg, Sn and Lg (green). If the tool user had re-picked a phase it would be labeled black (black) and the grey-blue picks are nominal based on a velocity model and automatically migrated to other components (or array elements). Window ends are also controlled by a user settable velocity model or user hand-picked times. The interactive tool allows filtering, zooming and marking of bad trace portions and is designed to allow the user to work through a data list picking arrivals and setting windows and then calculating all the amplitudes in a batch processing mode. Other parts of the tool (not shown) allow MDAC parameter determination and calculation.

Transportability

We have been re-examining the large database of the western United States (U.S.) underground nuclear tests and earthquakes assembled under a prior year BAA. This western U.S. data covers a wide range of depths and material properties and has excellent ground truth information. We define the MDAC parameters based on fitting the earthquakes alone. A longstanding problem in monitoring research is how best to transport discriminant measures to other stations in different parts of the world where we may not have any prior nuclear test data. We can illustrate some of the problems just by transporting results between stations within the western U.S. Figure 3 shows the raw and MDAC-corrected measurements of 6-8 Hz Pn/Lg at stations KNB and ELK as a function of distance and magnitude. For ratios of phase ratios of P/S in the same frequency band the magnitude trends are minmal, but there is a clear trend with distance that is removed by the MDAC process. For the raw data it is clear that the mean values of the populations are different at each station. After the MDAC correction the earthquakes have similar mean values near zero (clear distance trends have been removed), but the KNB explosions have a higher values than ELK. This 6-8 Hz Pn/Lg discriminant simply works better at KNB than ELK. These stations are in the same gross tectonic region and this difference appears to be due to subtle differences in propagation and energy partitioning in the regional phases. This example points to the need to do detailed calibration, station-by-station for regional discriminants. We do not believe there are any easy shortcuts to this process if true and optimal discrimination performance is to be assessed.

An additional issue for optimal discrimination is to make use of multiple discriminant measures, some of which may work only in that region. For example in Figure 4 we show three different discriminant measures that have been shown to work well in the western U.S. (e.g., Walter et al., 1995). One of them (6-8 Hz Pg/Lg) does better than the other two, but still there are events that do not discriminate well. We highlight one such event of each type (earthquake and explosion) in the figure. Note that they discriminate better using the other measures. Optimal combinations of measurements can give a better overall performance than any individual measure as shown in the combined measure plot. Here we made use of a low to high frequency spectral ratio in Lg. It is well known that this discriminant does not work as well in central Asia as it does in the western U.S. (e.g., Hartse et al. 1997). However, if we used only discrimiants that are highly effective globally, such as high frequency P/S ratios, we would hobble our potential discrimination capability in the western U.S. and elsewhere. Again we believe that detailed calibration studies to calibrate with a large set of prior earthquakes, mapping out structure using kriging (e.g., Schultz et al, 1998) and/or attenuation tomography, and determining optimal discriminant measures and their combinations can dramatically improve performance.

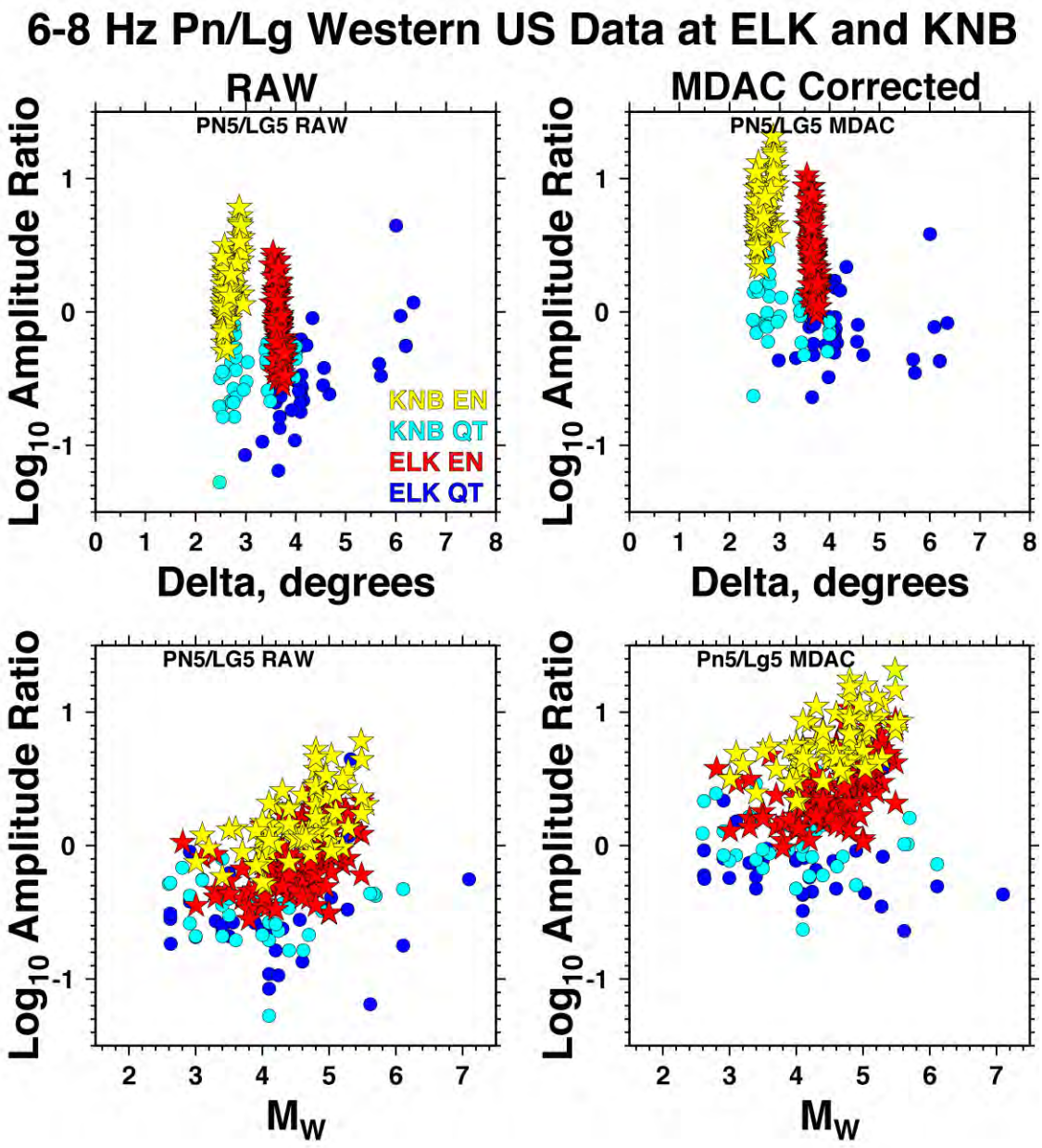


Figure 3. Western U.S earthquakes (circles) and nuclear explosions (stars) for the discriminant phase ratio 6-8 Hz (our frequency band 5) Pn/Lg at stations KNB and ELK. Left-hand side shows raw data as a function of distance (top) and magnitude (bottom). Right-hand side shows MDAC corrected data. Note that strong distance trends apparent in the raw data especially at ELK are removed by MDAC, improving discrimination. Even after MDAC correction it is clear this discriminant works better at KNB than ELK. Thus we show that transportability even between stations in the western U.S. is challenging, and there is no substitute for detailed regional calibration.

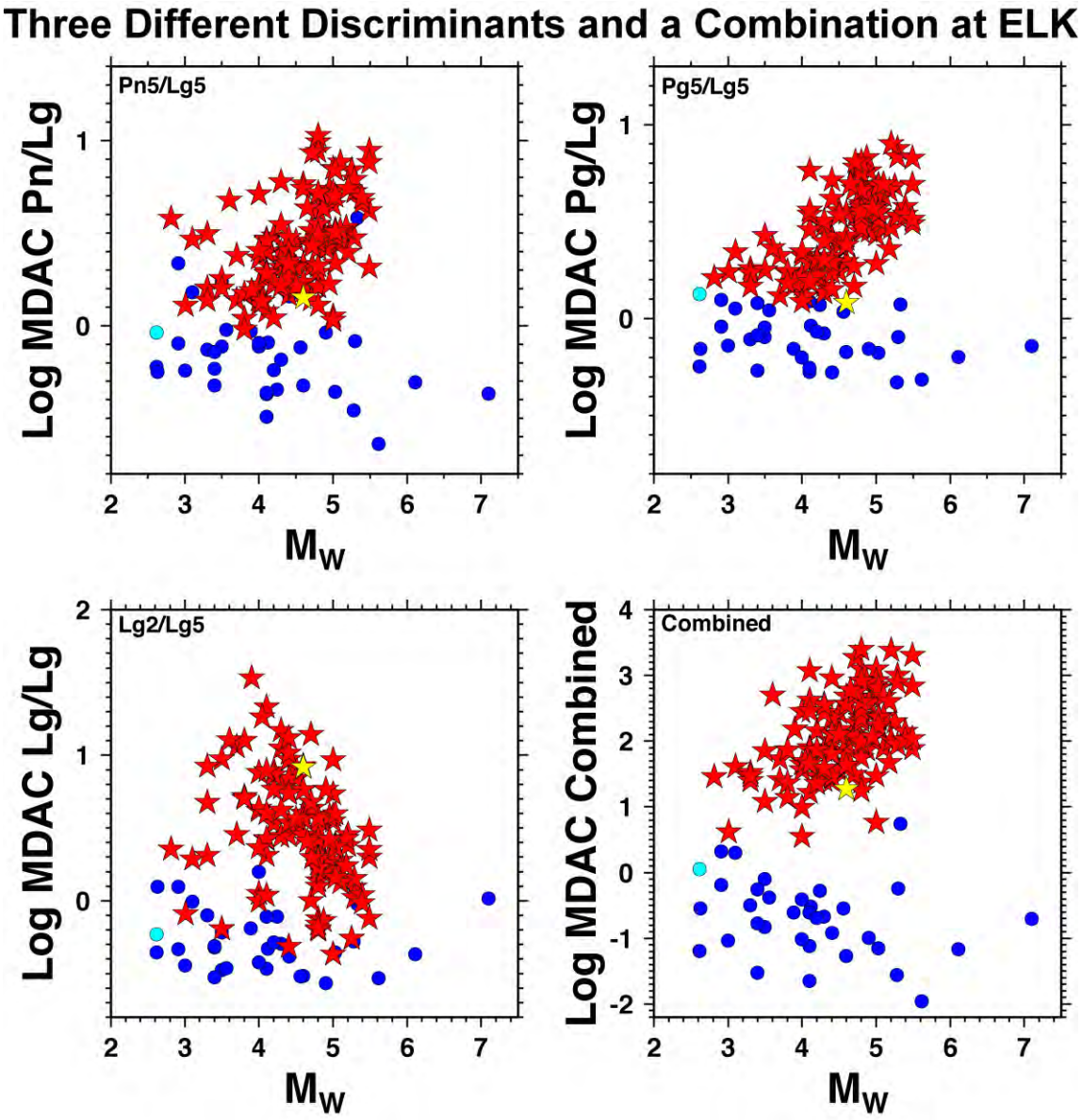


Figure 4. Examples of three different discriminant measures and an optimal combination of all of them at station ELK. The data are the same western U.S. earthquakes and nuclear tests shown in Figure 3. The measures are 6-8 Hz (our band 5) Pn/Lg, 6-8 Hz Pg/Lg and 1-2 Hz (our band 2) Lg to 6-8 Hz Lg. The data have all been MDAC corrected. The best individual discriminant for this station is 6-8 Hz Pg/Lg, but even here there is some overlap. We highlighted two events that do not discriminate well for Pg/Lg, one southern NTS earthquake on 1/19/02 and one NTS Yucca flat explosion Roquefort on 10/18/85. Note that these events discriminate better for the other measures particularly the Lg spectral ratio. Each event varies on which measure works best for them. Thus, when we combine all 3 measures we get a much better overall discrimination performance.

Source Models

The MDAC procedure uses a new generalized Brune (1970) style earthquake model to predict expected earthquake spectra. One of its parameters is the apparent stress, a ratio of seismic energy to moment. Currently the geophysical community is split on whether apparent stress is constant or increasing with the size of the earthquake (for example see http://earthscience.llnl.gov/scaling-workshop/). We have recently completed an LDRD funded study to look at the apparent stress scaling. In Figure 5, we shown an example using the 1999 Mw 7.1 Hector Mine mainshock and afterhocks recorded on scale at four regional stations. We integrated the energy in the Lg spectra to obtain energy and used regional coda envelope techniques to obtain moments. We show results for three different attenuation models: model A is based on Anu Venkatamaran's (written comm.) estimate of the mainshock energy, Model B is based on Jack Boatwright estimate (Boatwright et al., 2002) and Model C is based on lowering the attenuation to the point where the apparent stress scaling starts to become nearly constant. The attenuation in model C is lower than what other Basin and Range studies have found, which is closer to that of Model B. Although we have not resolved this issue, we have shown it is important to include the appropriate amount of apparent stress scaling for the attenuation model you are using in a region in order to optimally fit spectra. We do this as part of our MDAC parameter estimation process.

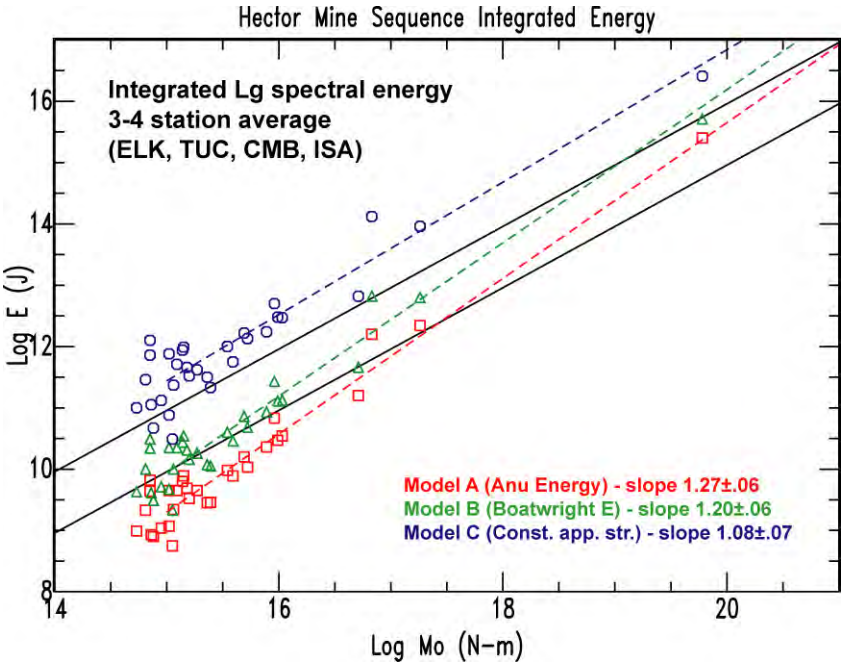


Figure 5. A plot of apparent stress scaling for the 1999 southern California Hector Mine mainshock and aftershocks for three different attenuation station specific attenuation models. These events were recorded on scale at four regional stations. Because the paths are very similar we can examine the scaling of the sequence as a whole by looking at the slope of the best fit line. Note that for typical western U.S attenuation (Model B) the data show that apparent stress increases with magnitude (slope > 1).

Another factor in addressing the transportability is the explosion source model. We have demonstrated in prior work (Walter et al., 1995) that nuclear tests at NTS in porous, gas-filled material are deficient in high frequencies compared to tests done in saturated material. We show an example in Figure 6 for two tests that have similar coda magnitudes recorded at the same station. It is clear that at frequencies above 4 Hz there is a significant loss in high frequency energy in the high gas porosity event relative the low-gas porosity explosion. Most current used explosion source spectral models have a constant falloff with high frequency like f^2 and do not account for this behavior.

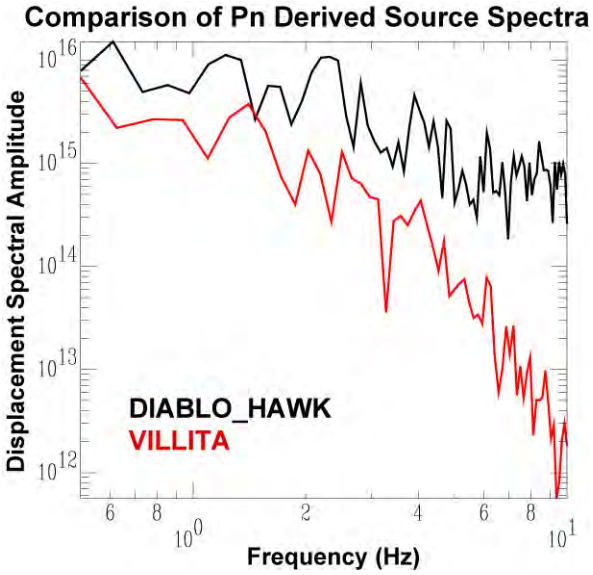


Figure 6. Comparison of path-corrected Pn spectra of two similar size (Mlcoda 4.30-4.39) and depth (373-388m) events at station KNB. DIABLO_HAWK has gas porosity of only 1.8% while VILLITA has a gas porosity of 20%. This plot clearly shows that source spectra are strongly dependent on media properties.

We have started to investigate how effectively the existing explosion models can be incorporated into MDAC using path parameters determined from earthquakes. We present some preliminary results testing some basic explosion source models on western U.S. explosions in Figure 7 at station ELK. The earthquake spectra are well fit by the model for all three phases out to 15 Hz. Using the same path parameters (geometrical spreading, frequency dependent attenuation) we use the Mueller-Murphy (1971) model and the announced narrow yield range to try and fit the US JVE explosion Kearsarge. The fits below 6 Hz or so are quite good but at higher frequencies the model predicts more energy than is observed. There are three possibilities: 1) the explosion model spectra need to fall off faster at frequencies above about 6 Hz than the f^{-2} of the model and/or 2) that the attenuation model is not right (which would need to be compensated by a corresponding change in the earthquake apparent stress and/or 3) that the path corrections are different at high frequencies for earthquakes and explosions due to the depth difference of the sources. Currently we are researching this issue. Finally, there is the well-known problem of the lack of a good explosion S-wave model to use in this kind of evaluation. While there are many ideas and studies supporting particular methods of generating S-waves from explosions (e.g., Rg-to-S and P-to-S conversion, cracking, block motions, spall, tectonic release) there are no good analytical models available to generate synthetic spectra of the kinds that are available for P-waves.

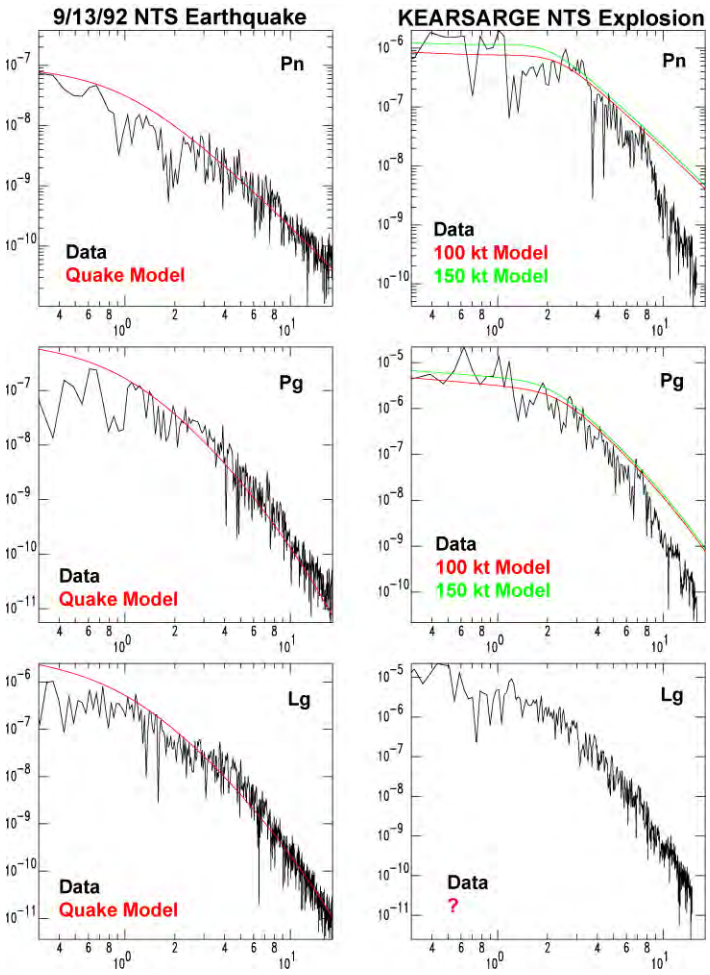


Figure 7. Regional Pn, Pg and Lg spectral fits of an NTS earthquake (left hand side) and an NTS explosion using MDAC. The data were recorded at station ELK. The earthquake model is based on Mw=4.32 and apparent stress of 0.15 Mpa from Mayeda and Walter (1996). The explosion is fit using the Mueller-Murphy (1971) tuff model with a depth and yield range of 100-150 from Springer et al. (2002). We currently lack a good theoretical explosion S-wave model to try and fit the Lg data.

CONCLUSION(S) AND RECOMMENDATION(S)

Regional discrimination algorithms require calibration at each seismic station to be used for nuclear explosion monitoring. We have developed a revised Magnitude and Distance Amplitude Correction procedure to remove source size and path effects from regional body-wave phases. This allows the comparison of any new regional events recorded at a calibrated station with all available reference data and models. This also facilitates the combination of individual measures to form multivariate discriminants that can have significantly better performance.

ACKNOWLEDGEMENTS

We thank Veronica Parker who helped process data with RBAP while a summer student at LLNL. We thank Stan Ruppert, Terri Hauk and Jennifer O'Boyle for loading and maintaining the LLNL database.

REFERENCES

Brune, J. N. (1970), Tectonic Stress and Seismic Shear Waves from Earthquakes , *J. Geophys. Res.* 75, 4997-5009.

Boatwright, J., G. L. Choy and L. C. Seekins, (2002), Regional Estimates of Radiated energy, *Bull. Seism. Soc. Am*, 92, 1241-1255.

Hartse, H., S. R. Taylor, W. S. Phillips, and G. E. Randall (1997), A Preliminary Study of Regional Seismic Discrimination in Central Asia with an Emphasis on Western China, *Bull. Seism. Soc. Am*. 87, 551-568.

Mayeda, K. M. and W. R. Walter, (1996), Moment, Energy, Stress Drop and Source Spectra of Western U.S. Earthquakes from Regional Coda Envelopes, *J. Geophys. Res*. 101, 11,195-11, 208.

Mueller, R.A., and J. R. Murphy, (1971), Seismic Characteristics of Underground Nuclear Detonations. Part I. Seismic Scaling Law of Underground Detonations, *Bull. Seismol. Soc. Am*. 61, 1675-1692.

Rodgers, A. J. and W. R. Walter, (2002), Seismic Discrimination of the May 11, 1998 Indian Nuclear Test with Short-Period Regional Data From Station NIL (Nilore, Pakistan), *Pure Appl. Geophys.* 159, 679-700.

Schultz, C, S. Myers, J. Hipp, and C. Young (1998), Nonstationary Bayesian Kriging: a Predictive Technique to Generate Corrections for Detection, Location and Discrimination, *Bull. Seism. Soc. Am., 88* 1275-1288.

Springer, D. L., G. A. Pawlowski, J. L. Ricca, R. F. Rohrer and D. K. Smith, (2002), Seismic Source Summary for all U.S. Below-Surface Nuclear Explosions, *Bull. Seism. Soc. Am.* 92, 1806-

Taylor, S., (1996), Analysis of High-Frequency Pg/Lg Ratios from NTS Explosions and Western U.S. Earthquakes, *Bull. Seism. Soc. Am.*, 86, 1042-1053.

Taylor, S., A. Velasco, H. Hartse, W. S. Philips, W. R. Walter, and A. Rodgers, (2002). Amplitude corrections for regional discrimination, *Pure. App. Geophys*. 159, 623-650.

Walter, W. R., K. Mayeda, and H. J. Patton (1995), Phase and Spectral Ratio Discrimination between NTS Earthquakes and Explosions Part 1: Empirical Observations, *Bull. Seism. Soc. Am.*, 85, 1050-1067.

Walter, W. R. and S. R. Taylor (2002), A Revised Magnitude and Distance Amplitude Correction (MDAC2) Procedure for Regional Seismic Discriminants, Lawrence Livermore National Laboratory UCRL-ID-146882.

A STUDY OF REGIONAL WAVE EXCITATION BY CLUSTERED UNDERGROUND EXPLOSIONS USING A RECIPROCAL THEOREM

Jiakang Xie, Anyi Li, Jian Zhang, and Tae-Kyung Hong

Columbia University

Sponsored by National Nuclear Security Administration
Office of Nonproliferation Research and Engineering
Office of Defense Nuclear Nonproliferation

Contract No. DE-FC52-03NA99514

ABSTRACT

Hundreds of clustered underground nuclear explosions (UNE) in central Asia and Nevada between 1970 and 1990 were recorded at common regional stations. Under a reciprocal theorem, these waveforms provide a dense time-space domain sampling of the wavefield in the near source region. We propose a three-stage study of the waveforms. In the first stage we shall use the source array to conduct a frequency-slowness power spectra (FSPS) analysis to determine the plane-wave composition of regional P and S waves as they leave the sources. In each frequency band we shall estimate the powers of various wavelets, including the direct, “diving” body wavelets and the scattered/multipathed waves, such as the lower frequency Rg waves. In the second and third stages we shall examine the compatibility between the observed FSPS and each of the previously proposed physical mechanisms for regional wave excitations by explosions. We will then attempt to improve the best-fit source model and develop better explosion discriminants.

Our efforts have been focused on three tasks. First we have been collecting data from the Borovoye Digital Seismogram Archive (1964-1989). Waveforms were recorded with older, narrow band, low dynamic range systems. Certain critical channels were very often contaminated by random spurious spikes. We have developed and applied a simple algorithm to rapidly, and reliably remove the spikes, resulting in a large number of cleaned waveforms. Second, we have been collecting information on accurate source locations, depths and origin times of the Balapan explosions. This information is critical to a successful reciprocal analysis. Third, we have been developing and implementing the FSPS algorithm. We plan to obtain the FSPS of the Balapan regional waves in the next several months.

OBJECTIVE

The primary objective of this research project is to better understand how regional P (Pn, Pg) and S waves (Sn, Lg) are generated by underground nuclear explosions (UNE) of various sizes, with various depths and testing styles, in various frequency bands and geological environments. This understanding will be achieved by using clustered historical UNEs, recorded by regional single-stations, as source arrays in a reciprocal geometry. A frequency-slowness power spectral (FSPS) analysis will be applied to the array recordings of the regional waves in the reciprocal geometry.

Research prior to this project already show that for UNE in central Asia, the source corner frequencies (fc) of regional P and S waves are very different. This difference explains why there has been an observed, statistical trend for the Pn/Lg ratios to be dependent on the frequency and explosions' magnitudes. To explore why there is such a difference in fc values of regional P and S waves, we shall conduct a comprehensive study to understand different excitation processes of the regional P and S waves from UNEs. Hundreds of clustered UNEs in central Asia and Nevada between the 1970s and 1990s were recorded at common regional stations. Under a reciprocal theorem, these waveforms provide dense time-space domain sampling of the wavefields in the near source region. We shall conduct a three-stage study of the waveforms. Firstly we shall use the source array to conduct a frequency-slowness power spectra (FSPS) analysis to determine the plane-wave composition of regional P and S waves as they leave the sources. In each frequency band we shall estimate the powers of various wavelets, including the direct, "diving" body wavelets and the scattered/multipathed waves, such as the lower frequency Rg waves. A bi-product of this stage will consist of improved depth estimates of the UNEs in central Asia.

In the second stage we shall examine the compatibility between the observed FSPS and each of the previously proposed physical mechanisms for regional wave excitations. The best-fit mechanism will be found for each phase, in each frequency band and test site.

In the third stage we shall replace our simplified mathematical model of explosion sources by better models corresponding to the best excitation mechanisms determined in the second stage. We shall use the improved model to estimate source spectral parameters, including seismic moments and corner frequencies. We shall develop scalings of these parameters with event magnitudes and depths, and explore the dynamic relations among all these parameters and testing styles, local structures, and geological environments. Accordingly, dynamic correction procedures will be developed for transporting the P/S spectral ratio discriminant across different frequencies, magnitudes and testing conditions.

RESEARCH ACCOMPLISHED

We are only in the beginning stage of this research project. In the following paragraphs, we summarize the developments in the first few months.

Algorithm development on the reciprocal theorem and f-k spectra

In this research we collect regional waveforms from multiple clustered UNEs conducted between 1970s and 1990s. If the source locations can be determined with a theoretically tolerable precision, then we can apply a reciprocal theorem, in which the physical UNE sources become fictitious sites of "array stations", and the physical recording station becomes a fictitious "source". We can then form frequency-wavenumber (f-k) spectra in an array analysis in the reciprocal geometry and examine the frequency-slowness composition of the fictitious "incoming" regional waves. Physically, in the true geometry, the latter examination is roughly equivalent to an examination of the frequency-slowness composition of the regional waves as they leave the explosion sources. Below we give a more rigorous description of the reciprocal theorem and formation of the f-k spectra.

The reciprocal property of path Green's functions involving ground motions from double couple sources is developed by Spudich and Bostwick (1987); that involving motions from explosions is derived by Nowack and Chen (1999). There is some subtlety about which wavefields (e.g., divergence or strain of motion) are theoretically involved, but the plane-wave decomposition can be conducted directly to ground displacement or velocity (Spudich and Bostwick, 1987). We re-write and slightly modify the method of slowness power spectral analysis developed by Spudich and Bostwick (1987) below.

Assume that a number, N_e, of clustered explosions generated ground motion (e.g., velocity) seismograms at a station. We will denote a component (e.g., vertical) of the ground motion from the *i*th source as $v(\xi_i, t_i)$, where ξ_i and t_i are the location of, and travel time from, the *i*th source ($i=1,2,...,N_e$). These seismograms can be translated into the frequency-wave number domain by simple Fourier Transforms to obtain the spectra (also cf., Aki and Richards, 1980)

$$v(\xi_i, t_i) \rightarrow \text{FT from time to } \omega \rightarrow \text{FT from location to } \mathbf{k} \rightarrow V(\mathbf{k}, \omega),$$

where ω and $\mathbf{k}$ are angular frequency and wave number vectors, respectively, and $V(\mathbf{k}, \omega)$ is the ground motion spectra in the frequency-wave number domain. We can replace the wave number vector $\mathbf{k}$ by $\omega\mathbf{s}$, where $\mathbf{s}$ is the slowness vector, and form power spectrum from $V(\mathbf{k}, \omega)$:

$$P(\omega\mathbf{s}, \omega) = V^2(\mathbf{k}, \omega).$$

The frequency-slowness power spectrum (FSPS), $P(\omega\mathbf{s}, \omega)$, thus formed is directly calculated from data. In practice, weighting of slowness power spectra is usually applied. There is an abundant literature on various weighting procedures and we will not discuss the issue of weighting here.

In the past few months we have modified some previous software developed by Xie et al. (1996) for forming the f-k spectra under the reciprocal theorem. The modified software is nearly ready to be used for the current project.

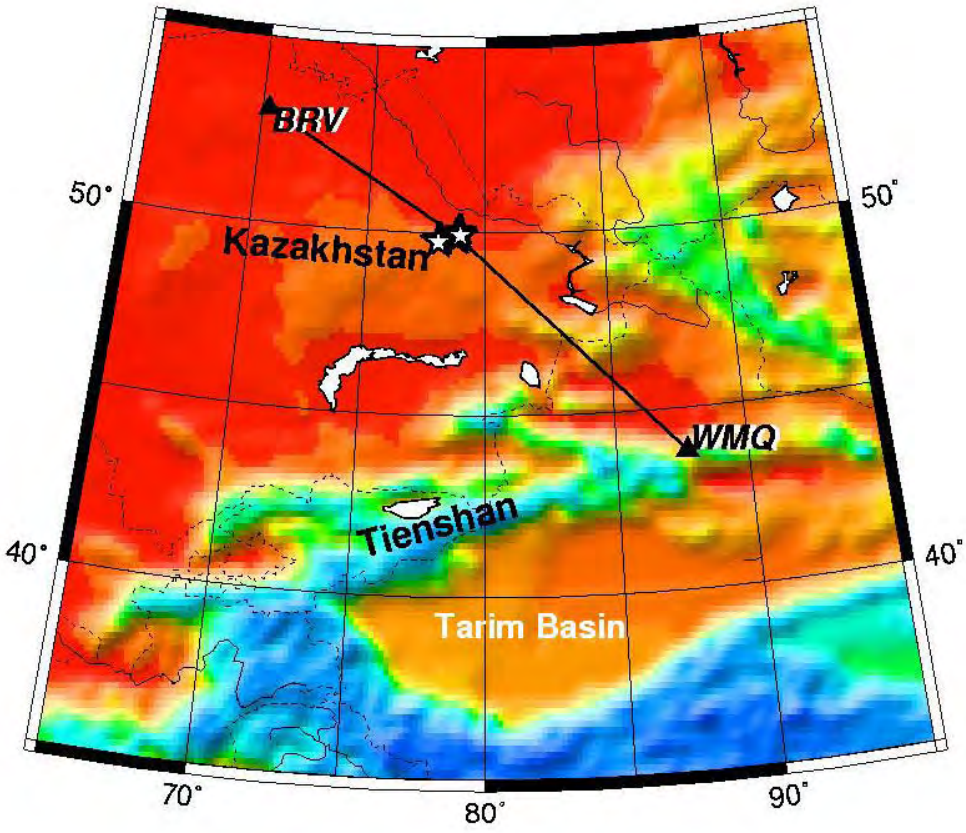


Figure 1. Map showing locations of the Borovaye observatory (BRV) station WMQ (triangles), and explosions in the Balapan and Degelen Mountain Test Sites. Also shown are representative, regional-distance paths from Balapan to BRV and WMQ. Topography is color-coded with blue represent elevations larger than 5000 M (those in the regions of Tienshan and Tibetan Plateau).

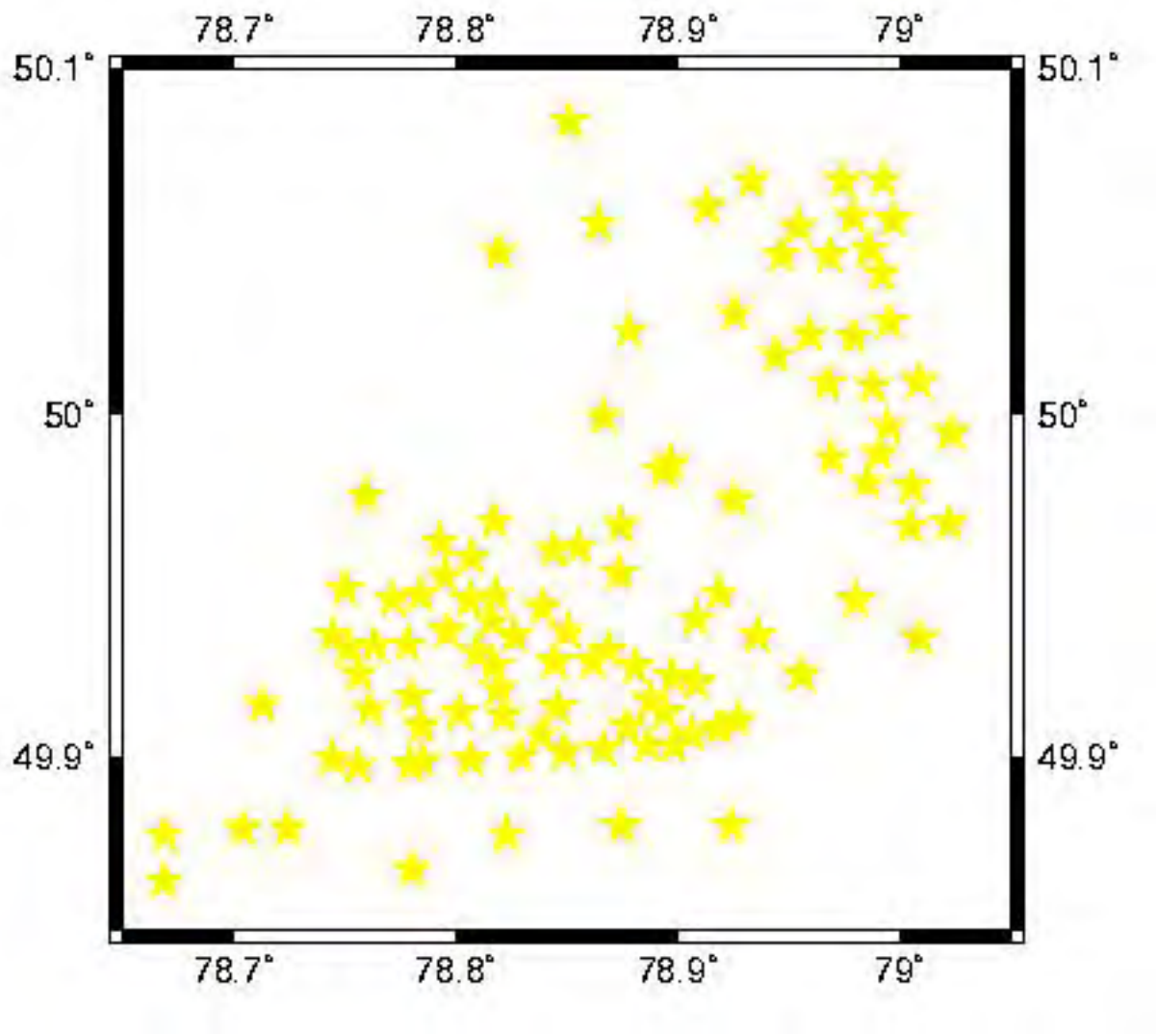


Figure 2. Map showing locations of the vertical shafts in the Balapan region of the Semipalatinsk Test Site. Between 1964 and 1989, 106 underground nuclear explosions were conducted in these shafts. The locations were determined using GPS survey.

Collection of ground truth information of UNEs from the Semepalitinsk test site

The first data set we will use consists of regional wave seismograms from the historic Soviet UNEs contained in the Borovoye Digital Seismogram Archive (Kim et al., 2001; available at the LDEO's ftp site). There are two groups of STS explosions (Figure 1). The first group consists of Balapan explosions in shafts. Figure 2 shows detailed locations of 106 tests of in the Balapan region of the Semipalatinsk Test Site. The tests were conducted between 1964 and 1989 in vertical shafts, which were located by GPS surveys (personal communication between Vitali Khalturin at LDEO and Prof. Natalya N. Mikhaylova, Director of Kazakh National Data Center, Kurchatov, Kazakhstan; December, 2002). We believe that the locations of the shafts are within 200 m of the actual tests. Thurber et al. (2001) provided joint relocations of these events using ground truth information of hypocenters and some origin times, as well as teleseismic time picks. They provided a set of the original time estimates, at a precision of 0.1 s or better. These estimates of origin times are considered as the best, or one of the best, estimates openly available (Vitally Khalturin, personal communication, April, 2004). Many of these explosions were recorded by the Borovoye Digital Seismogram Archive at regional distances. About ten of these explosions between 1987 and 1989 were also recorded at the CDSN station WMQ (Xie, 2002).

The second group of explosions consists of those from the Degelen Mountain region in tunnels. Between Oct. 1961 and Oct. 1989, 209 explosions are detonated in 181 tunnels. Owing to the tunnel testing style the locations are subject to larger (up to ~1 km) uncertainties. The estimates of the origin time estimates of these explosions by Trabant et al. (2002) are probably the best, or close to the best, estimates that are openly available.

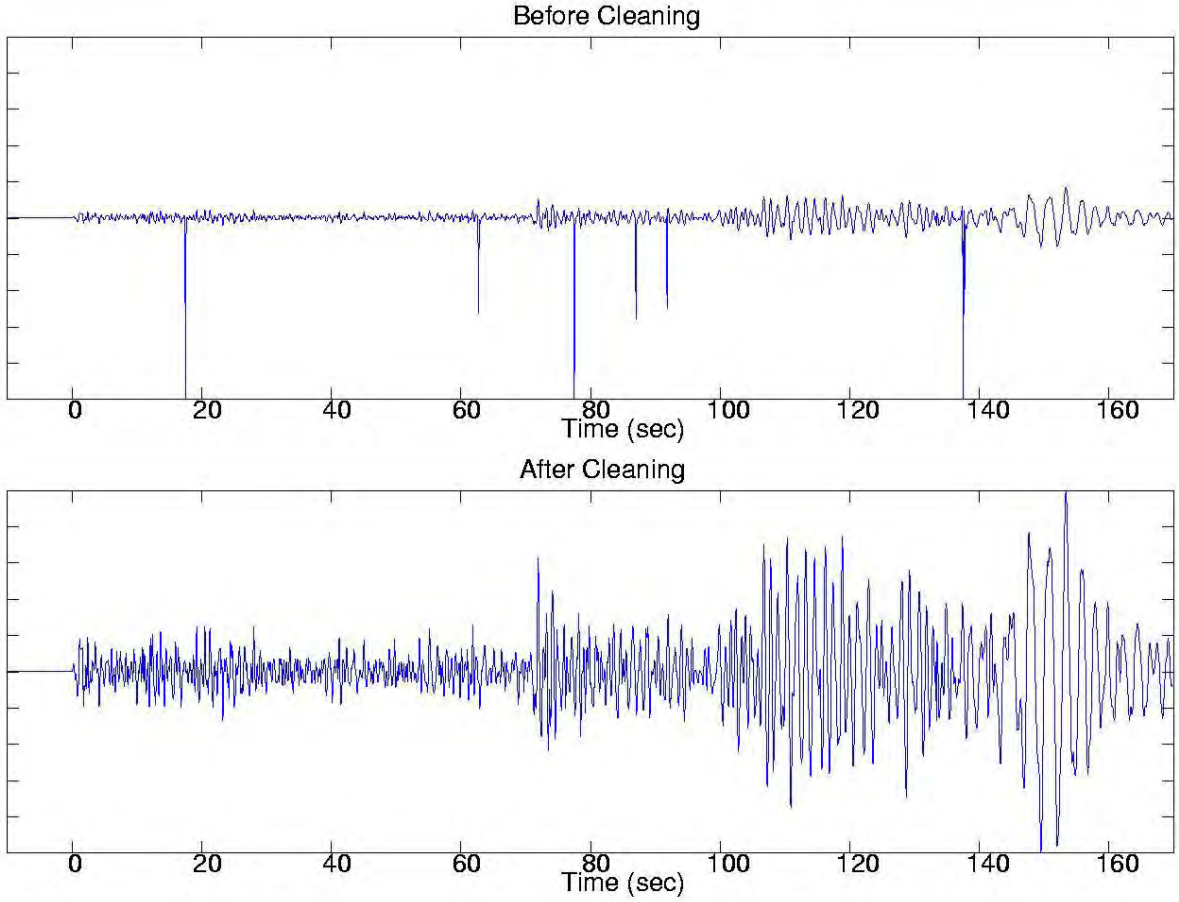


Figure 3. An example of the Borovoye regional waveforms from Balapan explosions before (top panel) and after (bottom panel) being processed with our cleaning procedure for spike-removal.

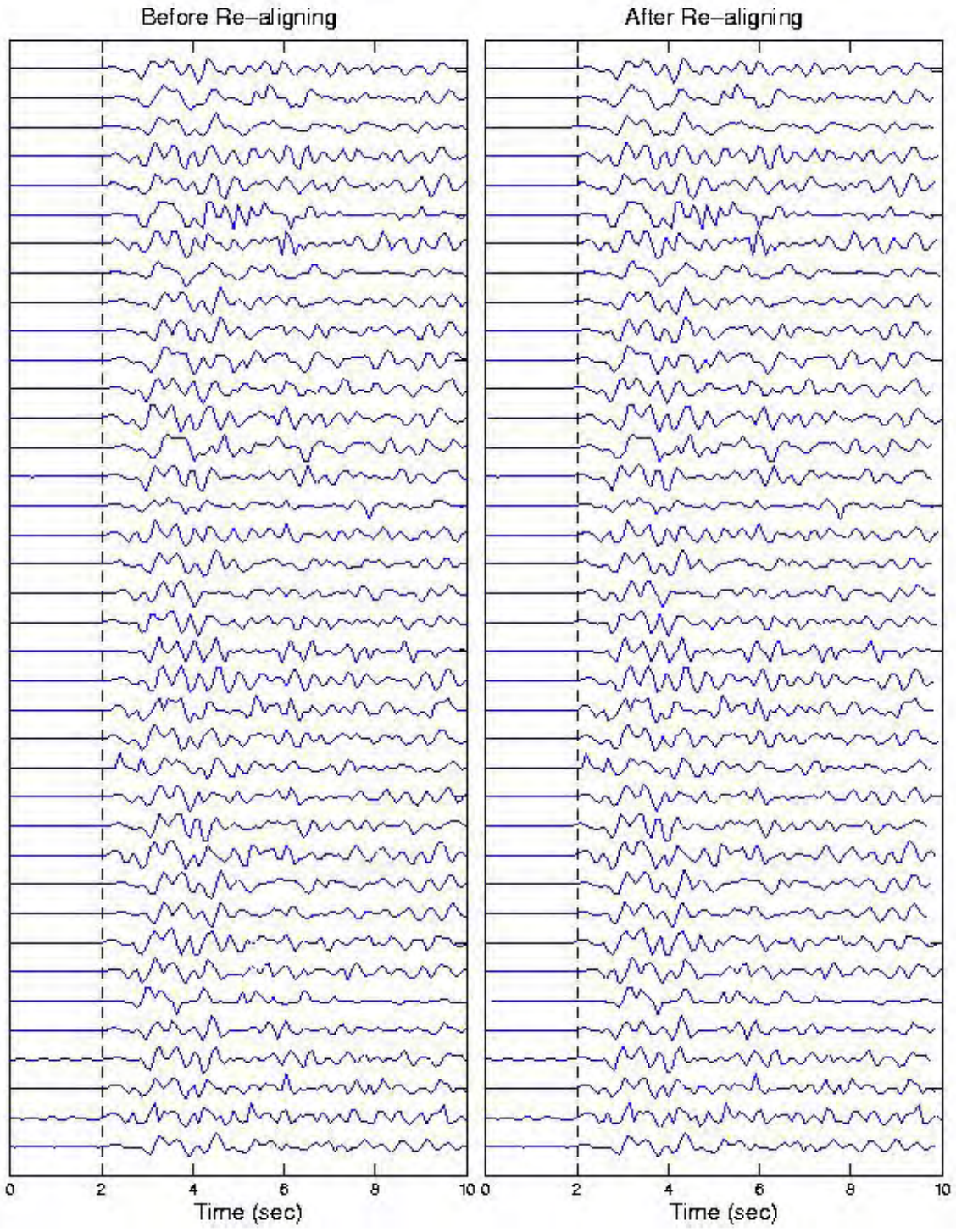


Figure 4. (Left panel) A record section that contains Pn waves from 38 Balapan explosions recorded between 1982 and 1989 by sensor S06Z of the BRV multi-sensor recording system. (Right) Same as left but with Pn wave re-aligned using a cross-correlation procedure.

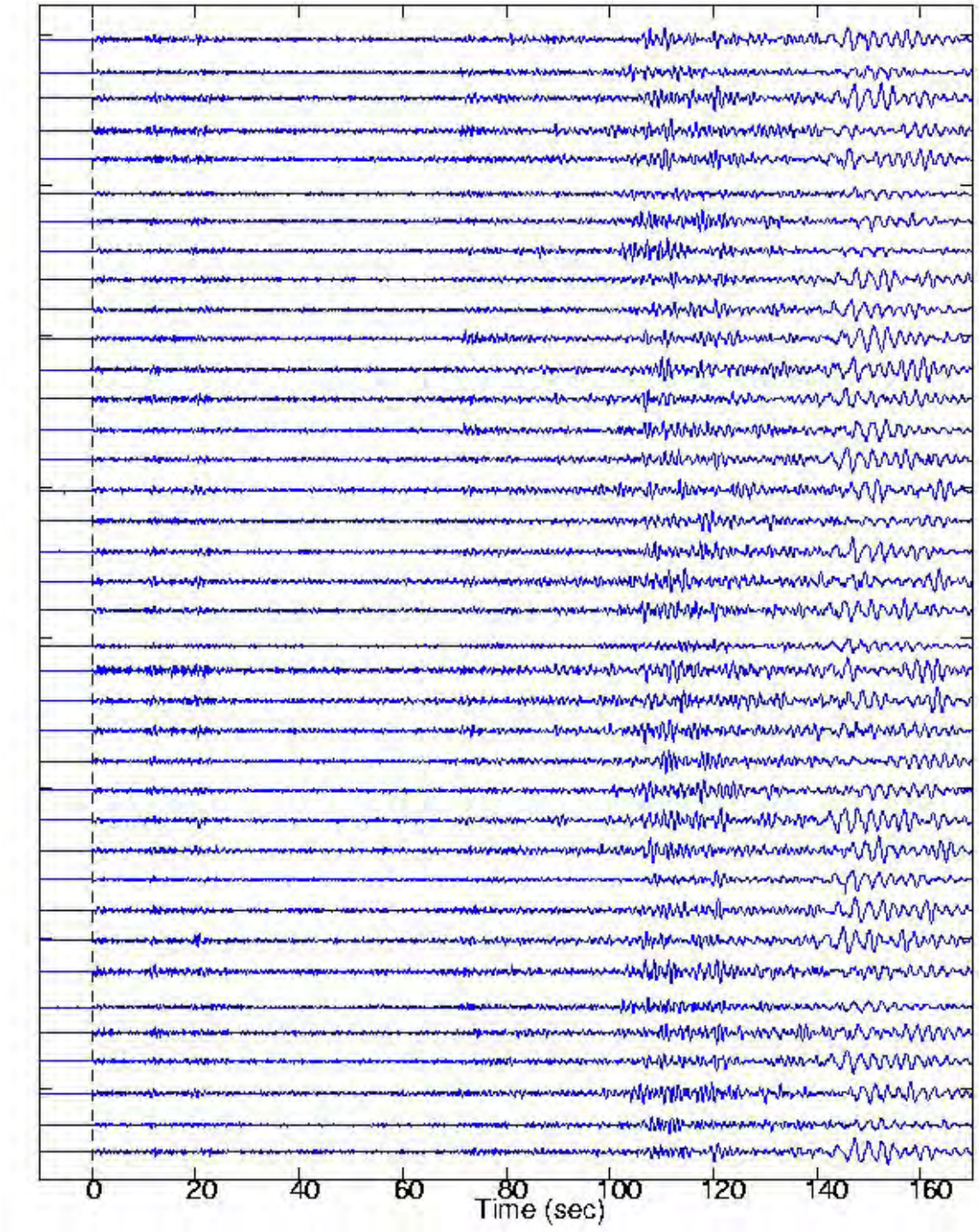


Figure 5. Same as the right panel of Figure 4, except a longer time duration is shown so that more phases, such as short-period surface waves, can be seen.

Processing of regional seismograms from the Borovoye historical archives

We have been collecting waveform data from the Borovoye Digital Seismogram Archive (1964-1989) from the LDEO website (Kim et al., 2001). These waveforms were recorded with older, narrow band, low dynamic range systems. Certain critical channels were very often contaminated by random spurious spikes. We have developed and applied a simple algorithm to rapidly, and reliably, remove the spikes, resulting in a large number of cleaned waveforms. The algorithm is designed to first detect triangularly, or trapezoidly, shaped spikes by defining these spikes as "peaks" or "troughs" that exceeds a specified height. Once detected, the value of the spurious peak or trough is replaced by a value found by interpolating those of the neighboring points. Figure 3 shows an example of the short-period Borovoye waveforms former Soviet UNEs between 1982 and 1989, collected from one of the several Borovoye sensors, before and after the spike removals. We have started cross-correlating the Pn waveforms to re-align the seismograms recorded by this sensor (S06Z), as shown in Figures 4 and 5.

CONCLUSIONS AND RECOMMENDATIONS

The past few months mark an initial phase of this research. During this time period, we have been implementing the frequency-slowness power spectral algorithm under a reciprocal theorem. This algorithm will soon be used to study regional wave excitation by clustered underground nuclear explosions. We have also been collecting information on precise source locations, depths and origin times of the historic Soviet explosions (1964-1989) at Balapan, which generated regional waves at the Borovoye Observatory. Finally, we have developed and applied a simple algorithm to rapidly and reliably remove spikes contained in the Borovoye Digital Seismogram Archive (1964-1989). We have started to re-align the Pn waves of the Borovoye seismograms using a cross-correlation method.

ACKNOWLEDGEMENTS

We thank Drs. Vitali Khalturin, W.Y. Kim and Paul Richards for their assistance on finding the Balapan source information, and on various aspects of the BRV historical data.

REFERENCE

Aki, K. and P.G. Richards (1980), *Quantitative Seismology: Theory and Methods*, W.H. Freeman, New York.

Kim, W.Y., P.G. Richards., V. Adushkin, and V. Ovtchinnikov (2001), Borovoye Digital Seismogram Archive for Underground Nuclear Tests during 1966-1996. *REPORT*, April 2001, Palisades, NY.

Nowack R.L. and W.P. Chen (1999), Source-Receiver Reciprocity and Empirical Green's Functions from Chemical Blasts, *Bull. Seism. Soc. Am*., 89, 538-543.

Spudich, P. and T. Bostwick (1987), Studies of Seismic Coda using an Earthquake Cluster as a Deeply Buried Seismograph Array, *J. Geophys. Res.* 92, 10,526-10,546.

Thurber, C., C. Trabant, F. Haslinger, and R. Hartog (2001), Nuclear Explosion Locations at the Balapan, Kazakhstan, Nuclear Test Site: the Effects of High-Precision Arrival Times and Three-Dimensional structure, *Phys. Earth Planet. Inter.* 123, 283-301.

Trabant, C, C. Thurber, and W. Leith (2002), Ground Truth Seismic Events and Location Capability at Degelen Mountain, Kazakhstan, *Phys. Earth Planet. Inter.* 131, 155-171.

Xie, J., L. Cong, B.J. Mitchell and J.M. Chiu (1996), Complexities in High-Frequency Seismic Waveforms due to Three-Dimensional Structure in the New Madrid Seismic Zone, *J. Geophys. Res*. 101, 5751-5778.

Xie, J. (2002), Source Scaling of Pn, Lg Spectra and their Ratios from Explosions in Central Asia: Implications on Identification of Small Seismic Events at Regional Distances, *J. Geophys. Res*. 107, 10.1029/2001JB000509.

REGIONAL EVENT IDENTIFICATION RESEARCH IN EASTERN ASIA

Xiaoning (David) Yang, Steven R. Taylor, Monica Maceira, Howard J. Patton, James T. Rutledge, George E. Randall and Marie D. Renwald

Los Alamos National Laboratory

Sponsored by National Nuclear Security Administration
Office of Nonproliferation Research and Engineering
Office of Defense Nuclear Nonproliferation

Contract No. W-7405-ENG-36

ABSTRACT

We describe ongoing studies of broad-area, regional-event identification in eastern Asia. The goal of our work is to provide a framework that allows for accurate identification, operational transparency, and clear reporting to nontechnical decision makers. The underlying methodologies need to have a clear physical basis packaged in a sound statistical framework having proper uncertainty estimates.

We are developing regional surface-wave discriminants (e.g., m_b - M_s) through a suite of focused studies. One of these studies is the development of surface-wave attenuation tomographic maps for central and southeast Asia. These maps can be used in the reformulation of regional M_s calculations with two-dimensional (2-D) path corrections to reduce station-magnitude scatter and network-magnitude bias. We have developed the 20-sec Rayleigh-wave attenuation map using a Bayesian inversion approach. *A priori* tomographic maps were constructed using two-station amplitude-ratio measurements. Single-station amplitude measurements were then inverted for higher resolution maps. In order to isolate and enhance the surface-wave signal, we applied phase-matched filters to the data before making spectral-amplitude measurements. The filtering proved to be effective in reducing the amplitude bias caused by multipathing and focusing. The average Q of the region estimated from the measurements is about 220, lower than most global estimates. The resultant tomographic map shows general correlation between the surface-wave attenuation pattern and the geology and tectonics of the region. Compared with one-dimensional (1-D) distance corrections, the use of 2-D attenuation model for path corrections in M_s calculations reduced the station-magnitude scatter by an average of 16 to 18 percent.

Another component of these studies involved evaluation and refinement of existing surface-wave slowness tomographic models. Slowness models at shorter periods (6 seconds and above) have been developed for central Asia. The development of these models is useful in lowering detection thresholds and allowing for discrimination at smaller magnitudes. Rayleigh-wave group-velocity dispersion curves were used to compute high-resolution, 0.5-degree cell size, slowness tomographic maps. We used a declustering technique to minimize the effect of event clusters on the inversion results. Patterns of the tomographic maps correlate well with known geologic and tectonic features in the area. Residual analysis with an independent set of group-velocity measurements showed significant improvement by the refined model compared with the *a priori* model especially at shorter periods. The refined model also showed a 15% improvement in the detection of surfaces waves with respect to previous 1-D models.

The Magnitude and Distance Amplitude Correction (MDAC) methodology is used to correct regional seismic amplitudes for propagation effects and earthquake source scaling. We correct amplitudes rather than predefining various phase ratios because all information is retained from which to construct discriminants. Because signals from explosions are highly dependent on near-source material properties and emplacement conditions, it is difficult to *a priori* select discriminants for uncalibrated regions. The MDAC approach adds much flexibility to the problem and allows for construction of numerous combinations of discriminants in a multivariate setting using Gaussian statistics. Recent research results involving analysis of the Borovoye Archive and associated processing challenges will be presented. Additionally, preliminary work on optimal amplitude measurements from regional arrays for regional discriminants and on developing discriminant transfer functions between newly operational stations and historic stations will be presented.

OBJECTIVE

The objective of this work is to provide methodologies and calibration parameters for robust regional-event identification at reduced magnitude thresholds.

RESEARCH ACCOMPLISHED

20-sec Rayleigh-Wave Attenuation Tomography

The $m_b - M_s$ relationship has proven to be an effective teleseismic discriminant. Extending its application to regional distances requires the extension of the M_s definition and regionalized path and station calibration. Inclusion of two-dimensional (2-D) path correction in regional M_s calculations has the potential to reduce the station-magnitude scatter and network-magnitude bias. To test the concept, we developed 20-sec Rayleigh-wave attenuation models for central and southeast Asia (15° - 65° N; 70° - 130° E). The following two steps were used in developing the attenuation model. First, two-station amplitude-ratio measurements, which were less affected by source-parameter error than single-station amplitude measurements, to obtain a coarse-grid (5° cell) model through a tomographic inversion. Second, we inverted for the final model (2° cell) with single-station amplitude measurements, which had much better path coverage. The coarse-grid model was used as the *a priori* model in the final inversion in a Bayesian approach (Tarantola, 1987).

The instrument-corrected surface-wave spectra can be expressed as

$$A_o(\omega, R) = S(\omega)G(R)P(\omega)B(\omega, R), \tag{1}$$

where $S(\omega)$ is the source spectrum; $G(R)$ is the geometrical spreading; $P(\omega)$ is the site-response effect and $B(\omega, R)$ is the apparent attenuation. ω is the angular frequency and R is the distance. The attenuation term $B(\omega, R)$ can be written as $B(\omega, R) = \exp(-\gamma(\omega)R)$, where γ is the attenuation coefficient. Equation (1) is linearized by taking natural logarithms of both sides of the equation. After the geometrical-spreading correction, the linearized version of equation (1) becomes

$$\ln A(\omega, R) = \ln S(\omega) + \ln P(\omega) - \gamma(\omega)R. \tag{2}$$

If two seismic stations lie on the same great-circle path that goes through a seismic source, the geometrical-spreading corrected amplitude ratio between the two stations is

$$\frac{A(\omega, R_1)}{A(\omega, R_2)} = \frac{P_1(\omega)}{P_2(\omega)} e^{\gamma(\omega)(R_2 - R_1)},$$

or in the logarithm domain as

$$\ln \frac{A(\omega, R_1)}{A(\omega, R_2)} = \ln P_1(\omega) - \ln P_2(\omega) + \gamma(\omega)(R_2 - R_1). \tag{3}$$

In the tomographic inversion, we discretized the last term in Equations (2) and (3) and grouped multiple observations together. In a matrix form, the problem is expressed as

$$\mathbf{d} = \mathbf{G}\mathbf{m}. \tag{4}$$

Using 20-sec Rayleigh-wave spectral amplitudes, we solve for the model $\mathbf{m}$, which contains discretized attenuation coefficients, site-response and source terms, with a maximum-likelihood method (Menke, 1989) as

$$\mathbf{m} = \mathbf{m}_0 + (\mathbf{G}^T\mathbf{C}_d^{-1}\mathbf{G} + \mathbf{C}_{m0}^{-1})^{-1}\mathbf{G}^T\mathbf{C}_d^{-1}(\mathbf{d} - \mathbf{G}\mathbf{m}_0), \tag{5}$$

where $\mathbf{m}_0$ is the *a priori* model, and $\mathbf{C}_d$ and $\mathbf{C}_{m0}$ are the data and *a priori* model covariance matrices respectively. Within this Bayesian framework, statistical characteristics of the data and the *a priori* information are utilized in the inversion to constrain the results and their uncertainty.

Surface-wave generation and propagation are affected by many factors such as source mechanism and location, path heterogeneity and site response (e.g., Mitchell, 1995). To make reliable attenuation estimation, it is critical to separate attenuation effects from source effects and elastic path effects to the maximum extent possible. To accomplish this, we employed the phase-match filtering technique (Herrin and Goforth, 1977) and incorporated available source and path information in the amplitude-measurement procedure. The process involved correlating the surface-wave data with the phase-matched filter, identifying and windowing the primary surface-wave arrival on the resulting crosscorrelation, convolving the windowed crosscorrelation with the phase-matched filter to obtain the cleaned data and Fourier transforming the cleaned data into the frequency domain. This technique effectively reduced the bias caused by multipathing and focusing. Other background noise was also reduced. An added benefit of the filtering process was that it smoothed the data spectrum so that no arbitrary smoothing, such as autocorrelation or moving average, was needed before making the measurement.

With the procedure described above, we made 4,398 single-station amplitude measurements from 324 events that occurred in the study region. Figure 1a shows the path coverage of the measurements and Figure 1b plots the Harvard Centroid Moment Tensor (CMT) and geometrical-spreading corrected amplitudes as a function of source-receiver distance. The linear trend of the data in Figure 1b reflects the effects of the medium attenuation. Straight-line fit of the trend yielded an average Q of about 221. This value is similar to the Q estimate from two-station amplitude ratios. The value is smaller than most global estimates, which range from 400 to 700 (cf. Rezapour and Pearce, 1998). The amount of offset from unity of the intersection between the y-axis and the fitted line, about 0.19 $\log_{10}$ unit, is comparable with the amount of systematic bias of the CMT moments found by Patton (1998) for central Asia.

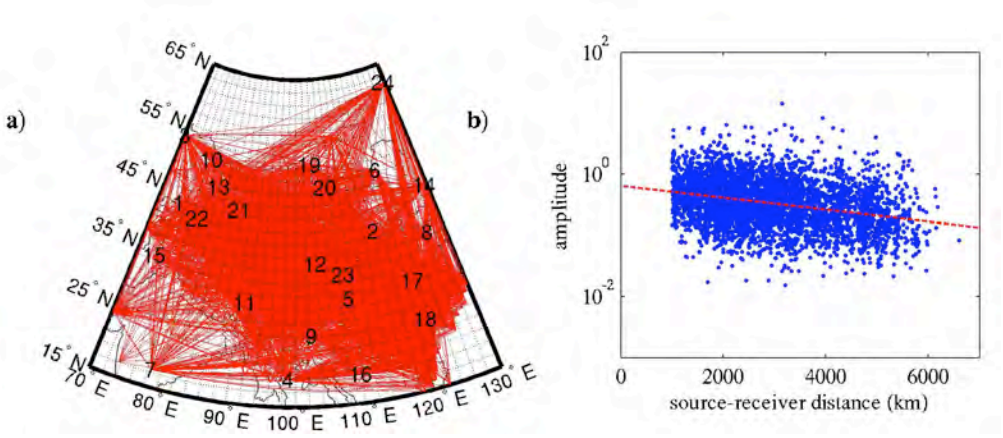


Figure 1. a) Path coverage of the single-station amplitude measurements. Station locations are marked by numbers. Grid lines define the discretization of the region for the final-model inversion. b) Source and geometrical-spreading corrected amplitudes as a function of source-receiver distance. Straight-line fit (dashed line) yielded an average Q of about 221.

With the results from the two-station amplitude-ratio inversion (Taylor *et al*., 2003) as the *a priori* model, we inverted the single-station spectral amplitudes using Equation 5 to obtain the final high-resolution 20-second Rayleigh-wave attenuation model together with site-response and source terms. Figure 2 presents the final model from the inversion. There is a broad correlation between the attenuation map and geologic and tectonic features of the region with low attenuation in cratonic regions (the Yangtze Craton, the Sino-Korean Craton and the Tarim Craton) and high attenuation in tectonically active regions (e.g., Tibetan Plateau). In Figure 2, the moment-magnitude data follow the line of linear correlation closely until the CMT magnitudes reach about 7.5. The CMT magnitudes then become larger than the corresponding magnitudes from the inversion, signaling magnitude saturation. The largest positive site-response term is for station BJT in northern China and the largest negative term is for station HYB in India.

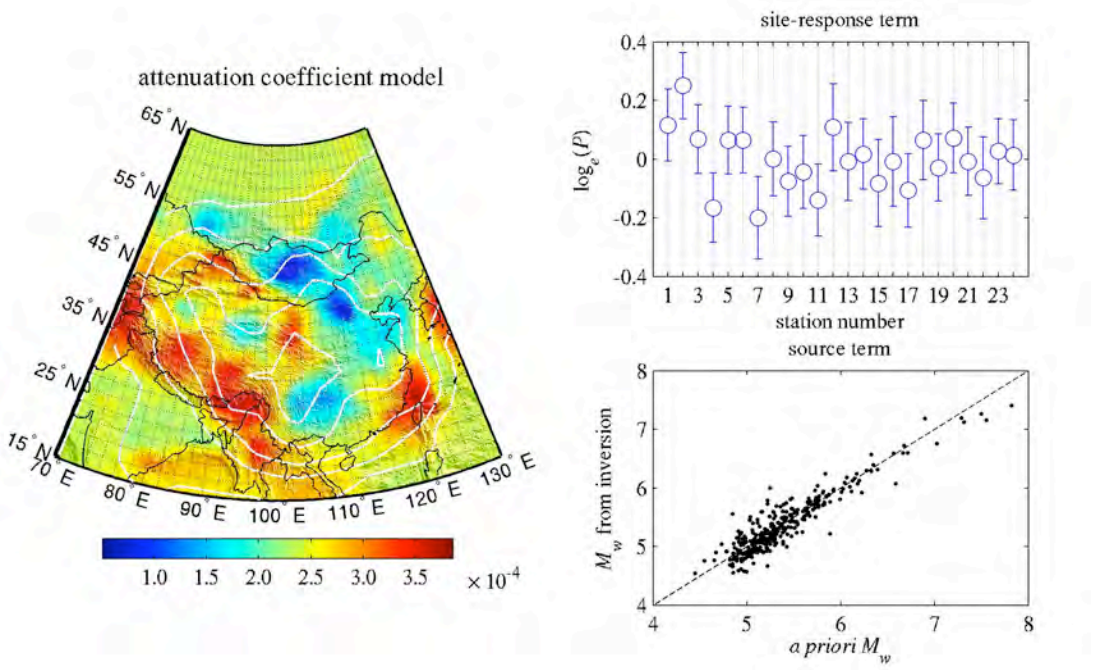


Figure 2. 20-second Rayleigh-wave attenuation-coefficient map, site-response and source terms from the single-station amplitude inversion. White contours in the attenuation map are isolines of one standard deviation of the map with smaller values in the middle of the map where path coverage was better. Site-response terms are displayed along with the error estimates. Station numbers correspond to those in Figure 1a. Source terms of the model are plotted as corresponding moment magnitudes against those from CMT.

One potential application of 2-D surface-wave attenuation maps is to make accurate distance corrections to amplitudes measured for M_s calculations. Current M_s formulae were defined for earthquakes at teleseismic distances (Gutenberg, 1945; Vanek et al., 1962; Rezapour and Pearce, 1998). A common feature of these formulae is the use of one-dimensional distance corrections. Because of the ever-improving station coverage of the Earth, surface-waves from smaller earthquakes are being recorded by an increasing number of regional stations, rendering the reliable regional M_s calculation possible. The use of regional 2-D attenuation models for distance corrections in regional M_s calculations is expected to reduce the scatter of the station magnitudes for an event and the network M_s bias.

In order to test the effectiveness of our model in reducing the station-magnitude scatter, an independent set of broadband data from 104 events was collected. We corrected the data for instrument response and band-pass filtered the data between 17 and 23 seconds. Then we measured the peak-to-zero amplitudes within the surface-wave window. By using Rezapour and Pearce's (1998) M_s formula, the average attenuation coefficient that we estimated from straight-line fitting of the spectral-amplitude data and the 2-D attenuation model from the inversion to apply different path-corrections to the amplitudes and estimated the station-magnitude variance reduction of the 2-D attenuation model. The maximum-likelihood value of the variance reduction is 32% when compared with Rezapour and Pearce's (1998) M_s formula and is 25% when compared with the constant attenuation model. The mean values of the variance reduction are 18% and 16% respectively. Considering the fact that another important cause of data scatter — the source radiation patterns, were not compensated for, we believe the amount of the variance reduction is significant.

Short-Period Rayleigh-Wave Slowness Tomography

Slowness models at short periods (6 seconds and above) have been developed for a region in central Asia. The development of these models is useful in lowering surface-wave detection thresholds and allowing for discrimination at smaller magnitudes.

We focus on the region of central Asia between 69°-108° E longitude and 29°-54° N latitude. Broadband waveform data from more than 1,100 events that occurred in the area between January 1997 and May 2002 was retrieved. Using multiple-filter analysis (Dziewonski *et al*., 1969; Herrmann, 1973) and phase-matched filter (Herrin and Goforth, 1977) techniques, we measured the dispersion characteristics of the signals. These Rayleigh-wave group velocity dispersion curves were used to compute high-resolution, 0.5° cell size, slowness tomographic maps for periods of 6, 8, 10, 12, 15, 18, 20, 22, 25, and 30 seconds.

A Bayesian tomography method (Tarantola, 1987) was adopted to solve the equation that relates the travel-time data with the velocity structure (Equation 4). Data and model parameters are considered independent and their covariance matrices are set to be diagonal. One of the advantages of using a Bayesian approach is that large-scale and well-accepted tomographic models from previous studies can be used as *a priori* background model. Global and regional 1° group-velocity maps were requested from different research groups (Levshin *et al*., 2001; Ritzwoller and Levshin, 1998; Stevens *et al*., 2001) and used as our background model.

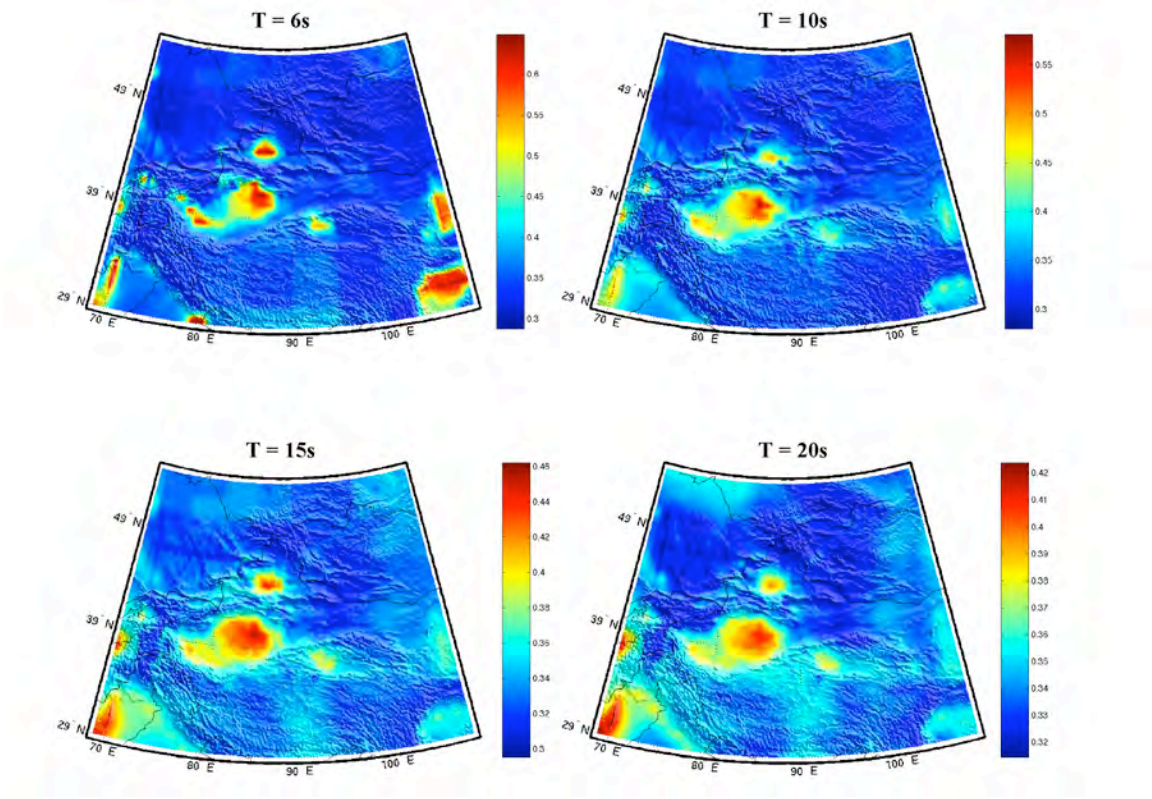


Figure 3. Rayleigh wave slowness maps for different periods. The slowness values are expressed in s/km and they are superimposed in a topographic map to ease the identification of plains and basins from mountains. Note that the color scale is different for each map.

We used a cell declustering technique (Isaaks and Srivastava, 1989) to remove the effect of event clusters. The cell declustering method uses the moving window concept to calculate how many measurements fall within particular regions or cells. Each measurement in a cell receives a weight that is inversely proportional to the number of events that fall within that cell.

Figure 3 gives some examples of the short-period slowness maps from the inversion. Patterns in our model correlate well with known geologic and tectonic features in the area. The short-period maps reflect the shallow part of the crust. The maps display low velocities associated with major sedimentary basins – Tarim, Junggar and Quaidam basins - in the area of central Asia under study. Higher velocities are associated with mountainous tectonic features such as the Tian Shan.

In order to test the effectiveness of our model, we collected an independent set of data that was not used in the computation of the slowness models, and measured the dispersion curves from the new data. Residual-analysis results for our slowness model and for the *a priori* model are shown in Figure 4. The overall map predictions are very good and, in general, better than the performance of the *a priori* model (plots a and c). The difference in performance is obvious at shorter periods (up to 15 seconds). Plots b and d include data for all periods, but the analysis of individual-period data yielded similar distributions. Their residual distributions are Gaussian-like with a mean close to zero (from –0.0219 km/s to +0.0202 km/s depending on the period) and with standard deviations ranging from 0.1810 to 0.2277 km/s. Considering all the periods together, most of the residuals have values between –0.5 and +0.5 km/s.

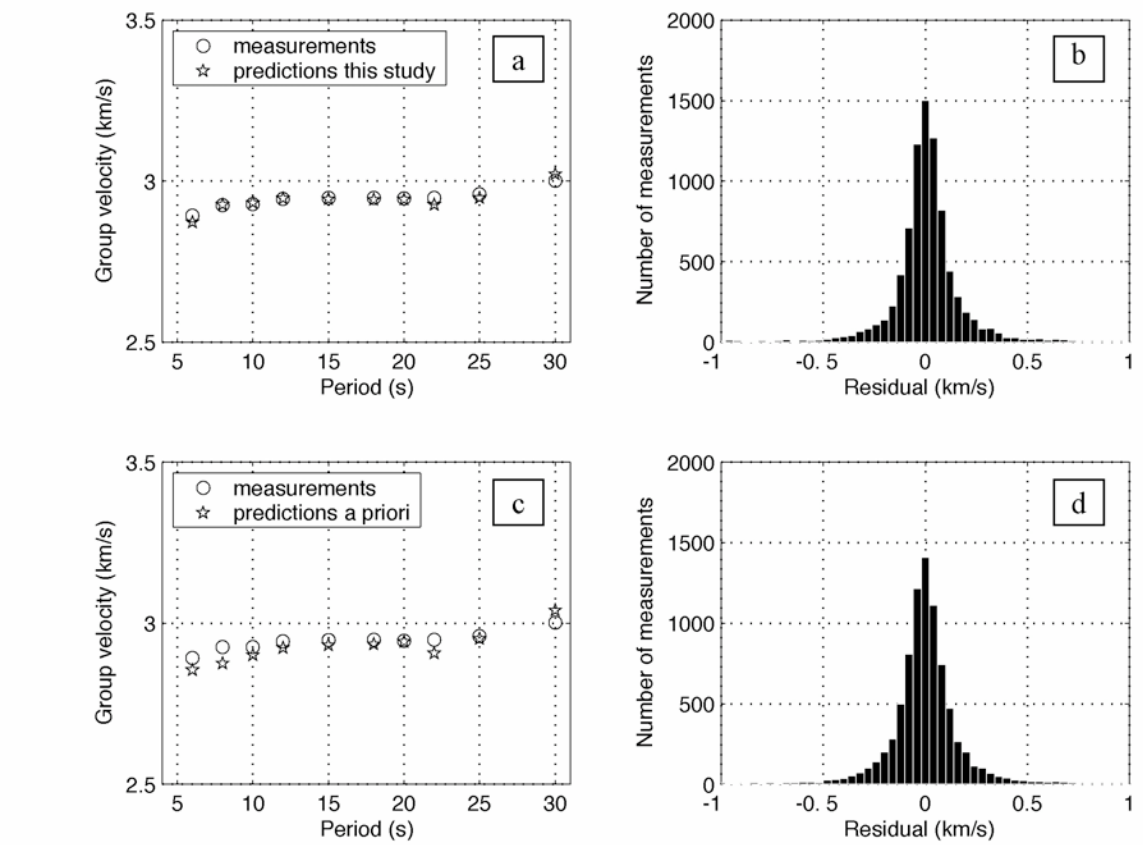


Figure 4. Residual analysis results. a) Average group velocities from the measurements and from slowness-model predictions. b) Distribution of the residuals obtained by subtracting the measurements from our model predictions. c) Average group velocities from the measurements and from the *a priori* model predictions. d) The same as b) with the predictions from the *a priori* model.

To evaluate the performance of our slowness model in detecting surface waves, we used Stevens and McLaughlin's (2001) surface-wave detection method and tested the improvement of our model against a one-dimensional (1D) China model (Jih, 1998) and the Preliminary Reference Earth Model (PREM from Dziewonski and Anderson, 1981). Figure 5 shows the number of surface wave detections using different velocity models. PREM and China 1D are the detection results using group velocity predictions calculated from the PRE, and from Jih's (1998) China crustal model. The use of our group velocity maps increased the number of surface wave detections by 15% with respect to using the China model.

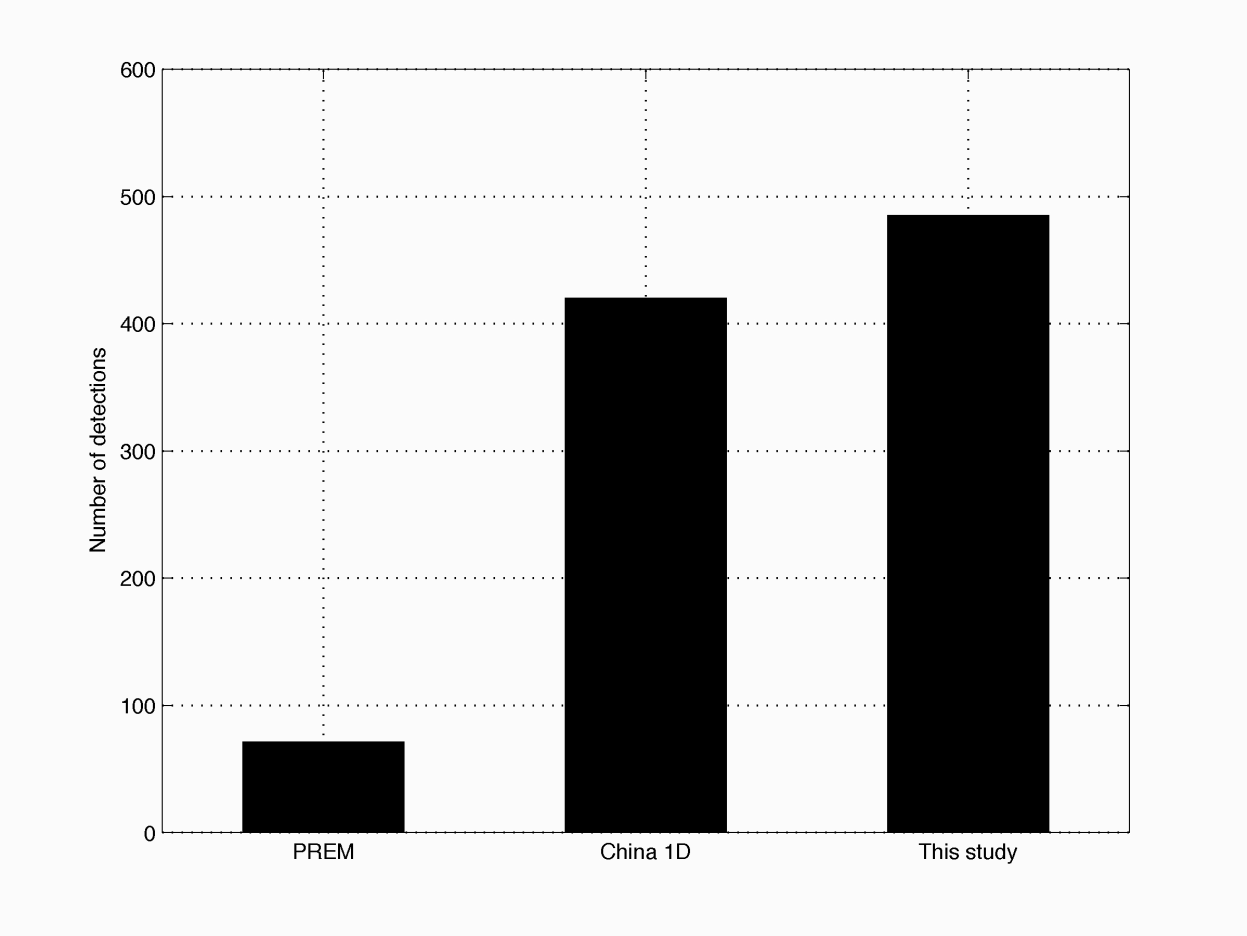


Figure 5. Number of surface wave detections using different group velocity models.

Magnitude and Amplitude Distance Corrections (MDAC)

A fundamental problem associated with event identification lies in deriving corrections that remove path and earthquake source effects on regional phase amplitudes used to construct discriminants. Our goal is to derive a set of physically based corrections that are independent of magnitude and distance, and amenable to multivariate discrimination by extending the technique described in Taylor and Hartse (1998) and Taylor *et al.* (2002). The MDAC procedure for correcting regional seismic amplitudes for seismic event identification has been modified to include more realistic earthquake source models and source scaling (MDAC2; Walter and Taylor, 2002).

The MDAC2 prediction of the observed, instrument-corrected spectra is similar to Equation 1:

$$A_m(\omega, R) = S(\omega)G(R)P(\omega)B(\omega, R). \tag{6}$$

We linearize both Equation 1 and Equation 6 by taking the logarithm of both sides and correct the observed spectrum by subtracting the log of MDAC2 spectrum

$$\log A_c(\omega, R) = \log A_o(\omega, R) - \log A_m(\omega, R). \tag{7}$$

These corrected spectra or residuals can then be kriged to further reduce un-modeled path effects (e.g., Schultz *et al.,* 1998).

For a given station and source region, a number of well-recorded earthquakes are used to estimate source and path corrections. In the MDAC2 formulation, the Brune (1970) earthquake source model is generalized with a more

physical apparent-stress model that can represent non-constant stress-drop scaling. We include a parameter that allows for variable P-wave and S-wave corner frequency scaling. The discrimination power in using corrected amplitudes lies in the assumption that the earthquake model will provide a poor fit to the signals from an explosion. The propagation model consists of a frequency-independent geometrical spreading and frequency-dependent power-law Q. Regional phase attenuation tomographic models are incorporated to replace a constant Q_0 model (Phillips *et al.,* 2000; Taylor *et al.,* 2003).

A grid search is performed simultaneously at each station for all recorded regional phases over stress-drop, geometrical spreading, and frequency-dependent Q to find a suite of good-fitting models that remove the dependence on M_w and distance. Very stable moment magnitude measures from regional coda wave envelopes that have been tied to independently derived regional seismic moments are incorporated. We also solve for frequency-dependent site/phase excitation terms. Once a set of corrections is derived, effects of source scaling and distance as a function of frequency are applied to amplitudes from new events prior to forming discrimination ratios. Thus, all the corrections are tied to M_w and distance and can be applied very rapidly in an operational setting. Moreover, phase-amplitude residuals as a function of frequency can be spatially interpolated (e.g., using kriging) and used to construct a correction surface for each phase and frequency. The spatial corrections from the correction surfaces can then be applied to the corrected amplitudes based only on the event location. The correction parameters and correction surfaces can be developed offline and entered into an online database for pipeline processing providing multivariate-normal corrected amplitudes for event identification illustrated in Figure 6.

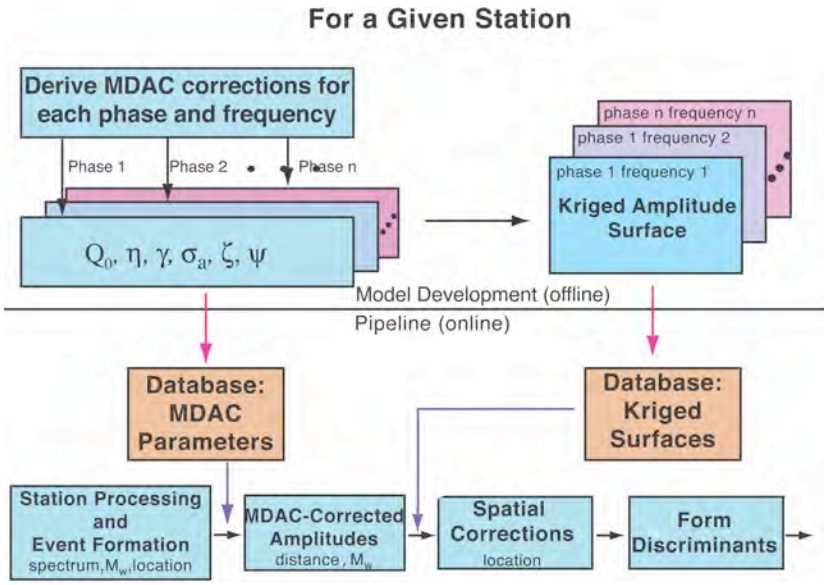


Figure 6. Example flowchart illustrating how the MDAC method can be combined with spatial interpolation (e.g., kriging) to develop database parameters to provide amplitude corrections for regional event identification in near-real time. These parameters can easily be incorporated into an operational pipeline to correct amplitudes from a new event for identification purposes.

CONCLUSIONS AND RECOMMENDATIONS

Event identification studies in Eastern Asia involve development of algorithms for constructing discriminants as well as applying the algorithms for station calibration. Our research, outlined in this paper, has focused on regional seismic discrimination using regional $m_b - M_s$ discriminants and MDAC corrected amplitudes. Ongoing work in the development of regional $m_b - M_s$ discriminants will build upon the surface-wave attenuation model and short-period surface-save slowness maps that we have developed.

ACKNOWLEDGEMENTS

We thank Anatoli Levshin and Michael Ritzwoller at the University of Colorado at Boulder, and Jeffry Stevens of Science Applications International Corporation (SAIC) for providing us with their surface-wave group-velocity models.

REFERENCES

Brune, J. N. (1970), Tectonic stress and spectra of seismic shear waves from earthquakes, *J. Geophys. Res.,* 75, 4997-5009.

Dziewonski, A. M., S. Bloch, and M. Landisman (1969), A technique for the analysis of transient seismic signals, *Bull. Seism. Soc. Am*., 59, 427-444.

Dziewonski, A. M. and D. L. Anderson (1981), Preliminary reference Earth model, *Phys. Earth Planet. Inter*., 25, 297-356.

Gutenberg, B. (1945), Amplitudes of surface waves and magnitudes of shallow earthquakes, *Bull. Seism. Soc. Am.*, 35, 3-12.

Herrmann, R. B. (1973), Some aspects of band-pass filtering of surface waves, *Bull. Seism. Soc. Am*., 63, 663-671.

Herrin, E. T. and T. T. Goforth (1977), Phase matched filters: application to the study of Rayleigh waves, *Bull. Seism. Soc. Am.*, 67, 1259-1275.

Isaaks, E. H. and R. M. Srivastava (1989), *An Introduction to Applied Geostatistics*, Oxford University Press, New York, 561 pp.

Jih, R. S. (1998), "Location Calibration Efforts in China", in *20th Annual Seismic Research Symposium on Monitoring a Comprehensive Test Ban Treaty (CTBT)*, pp. 44-55.

Levshin, A.L., M. H. Ritzwoller, M. P. Barmin, and J. L. Stevens (2001), "Short Period Group Velocity Measurements and Maps in Central Asia", in *Proceedings of the 23rd Seismic Research Review: Worldwide Monitoring of Nuclear Explosions*, pp. 258-269.

Menke, W. (1989), *Geophysical Data Analysis: Discrete Inverse Theory*, Academic Press, San Diego, California.

Mitchell, B. J. (1995), Anelastic structure and evolution of the continental crust and upper mantle from seismic surface wave attenuation, *Rev. of Geophys.*, 33, 441-462.

Patton, H. J. (1998), Bias in the centroid moment tensor for central Asian earthquakes: evidence from regional surface wave data, *J. Geophys. Res.*, 103, 26963-26974.

Phillips, W. S, H. E. Hartse, S. R. Taylor (2000), 1 Hz Lg Q tomography in central Asia, *Geophys. Res. Lett.,* 20, 3425-3428.

Rezapour, M. and R. G. Pearce (1998), Bias in surface-wave magnitude M_s due to inadequate distance corrections, *Bull. Seismol. Soc. Am.*, 88, 43-61.

Ritzwoller, M. H. and A. L. Levshin (1998), Eurasian Surface Wave Tomography: Group Velocities, *J. Geophys. Res.* 103, 4839-4878.

Schultz, C. A., S. C. Myers, J. Hipp, and C. Young (1998), Nonstationary Bayesian Kriging: A predictive technique to generate spatial corrections for seismic detection, location, and identification, *Bull. Seism. Soc. Am.,* 88, 1275-1288.

Stevens, J. L., D. A. Adams, and G. E. Baker (2001), Improved Surface Wave Detection and Measurement using Phase-Matched Filtering with a Global One-Degree Dispersion Model, in *Proceedings of the 23rd Seismic Research Review: Worldwide Monitoring of Nuclear Explosions*, pp. 420-430.

Stevens, J. L. and K. L. McLaughlin (2001), Optimization of Surface Wave Identification and Measurement, *Pure Appl. Geophys*., 158, 1547-1582.

Tarantola, A. (1987), *Inverse Problem Theory*, Elsevier Science, Amsterdam, The Netherlands, 630 pp.

Taylor, S. R. and H. E. Hartse (1998), A procedure for estimation of source and propagation amplitude corrections for regional seismic discriminants, *J. Geophys. Res.,* 103, 2781-2789.

Taylor, S. R., A. A. Velasco, H. E. Hartse, W. S. Phillips, W. R. Walter, and A. J. Rodgers (2002), Amplitude corrections for regional seismic discriminants, *Pure. App. Geophys*. 159, 623-650, 2002.

Taylor, S. R., X. Yang, W. S. Phillips, H. J. Patton, M. Maceira, H. E. Hartse, and G. E. Randall (2003), Regional event identification research in Eastern Asia, in *Proceedings of the 25th Seismic Research Review - Nuclear Explosion Monitoring: Building the Knowledge Base*, LA-UR-03-5017, Vol. 1, pp. 476-485.

Taylor, S. R., X. Yang, and W. S. Phillips (2003), Bayesian Lg attenuation tomography applied to eastern Asia, *Bull. Seism. Soc. Am.*, 93 795-803.

Vanek, J., A. Zatopek, V. Karnik, N. V. Kondorskaya, Y. V. Riznichenko, E. F. Savarensky, S. L. Solov'ev, and N. V. Shebalin (1962), Standardization of magnitude scales, *Bull. Acad. Sci. USSR, Geophys. Ser.*, no. 2, 108-111 (in English).

Walter, W. R. and S. R. Taylor (2002), A revised Magnitude and Distance Amplitude Correction (MDAC2) procedure for regional seismic discriminants: Theory and testing at NTS, *Los Alamos National Laboratory*, LA-UR-02-1008, 15pp.

M_s:m_b DISCRIMINATION STUDY OF MINING EXPLOSIONS IN WYOMING, USA AND QIANAN, CHINA

Rong-Mao Zhou, Brian W. Stump, and Christopher T. Hayward

Southern Methodist University

Sponsored by Air Force Research Laboratory

Contract No. DTRA01-02-C-0003

ABSTRACT

Regional networks often record many mining explosions. The relative excitation of regional body and surface waves is useful in identifying these mining events. We investigate the use of intermediate period surface wave magnitude, M_S, and high frequency body wave magnitude, m_b, from regional mining explosions for event discrimination using techniques originally intended for teleseismic observations. Data for this study are taken from a portable broadband deployment in Wyoming recording mining explosions in the Powder River Basin and a broadband network currently deployed in northeast China. The magnitudes, M_s and m_b were estimated for five, kiloton-size mining explosions, four in Wyoming and one in QianAn, China.

These kiloton-size mining explosions, used to remove overburden or to fragment rocks, are conducted with delays between an array of individual charges resulting in source durations up to several seconds. The total size of the explosion, its time duration and spatial characteristics generate short- to intermediate-period (1 ~ 20 s) surface waves. These surface waves provide an opportunity to constrain upper crustal shear structure and attenuation. The fundamental mode Rayleigh wave dispersion curves were estimated using multiple filter analysis and refined by phase matched filtering. The associated dispersion curves were used to make path corrections to the observed surface wave amplitudes so that intermediate period surface wave magnitude, M_s, estimates could be made for each mining explosion. Multiple surface wave observations along different paths for each event provided a measure of the importance of the path corrections. In Wyoming, the path corrections vary significantly from station to station reflecting the heterogeneous structure in the area. In China, all but one of the corrections are similar reflecting common paths across the Yanshan Uplift. Despite differences in the path corrections, the final M_S estimates in China and Wyoming produce similar values for common events as illustrated by the small standard deviation values. Regional body wave magnitudes, m_b, were estimated for these events as well. The body wave magnitudes are similar (m_b 2.9 to 3.4) sized for all the explosions except one of the Wyoming mining explosions.

The resulting network M_S:m_b data were compared to data from a previous study that included earthquakes and contained, single-fired explosions (Stevens and Day, 1985). Although the previous study examined mostly larger events than those in this study, the Wyoming and China mining events plot in or near the earthquake population. Data from one Wyoming event, an anomalous blast in which a failure of the timing system caused a large portion of the blast pattern to simultaneously detonate, plots within the explosion population with m_b 4.39. The simultaneous detonation increased the body wave magnitude but had little effect on surface wave amplitudes. This study illustrates a possible approach to the inclusion of intermediate period surface waves for discrimination. The range in amplitudes associated with the raw intermediate period surface waves illustrates that path corrections are critical. The application of path corrections based upon dispersion analysis was found to significantly reduce the scatter. The actual values of M_S and m_b suggest that the surface waves generated by long duration mining explosions can make them appear earthquake like. The data from a single anomalous shot indicates that if a significant part of the total explosives is simultaneously detonated the event will fall into the explosion population.

OBJECTIVES

Large-scale chemical blasts are routinely conducted by the mining and quarrying industries to remove overburden or to fragment rocks. Large mining explosions are conducted with delays between individual charges in an array, resulting in source durations as great as several seconds. The total size of the explosion, its time duration, and spatial characteristics can generate short- to intermediate-period (1-20 s) surface waves (Hedlin *et al.*, 2002; Zhou *et al.*, 2003; Zhou and Stump, 2004). Analysis of surface wave dispersion provides a method for determining the shear-wave velocity distribution in the Earth.

Characterization of propagation path effects provides for further study of source induced differences in the regional waveforms. Data from Wyoming and Northeast China blasts are used to study the generation of regional seismic signals from mining explosions. We focus on both the body waves and intermediate period surface waves from these sources. A physical understanding of mining explosions as sources of regional seismic waves would provide a basis for the development of seismic discriminants for the different source types. The existence of regional body waves and intermediate period surface waves from these sources suggests that a modification of the successful M_s:m_b teleseismic discriminant (Stevens and Day, 1985) might be worth examination.

Marshall and Basham (1972) have suggested that M_s estimation can be extended to smaller events and shorter periods. It is recognized that regional observations hold the key to better monitoring at low magnitudes. There is therefore high interest in extending M_s:m_b applicability to regional data (Patton, 2001; Bonner, *et al.*, 2003). Characterization of short-period propagation path effects on regional surface waves will be critical to such applications. To understand the applicability of this discriminant the relative surface wave excitation difference between contained possibly nuclear single-fired explosions and delay-fired mining explosions must also be assessed (Myers *et al.*, 1999). The data and propagation models from Wyoming and northeast China provide the basis for the study of some of these effects. Path specific models for both northeast China and Wyoming will be used to investigate a possible broadband regional discriminant, M_s: m_b.

RESEARCH ACCOMPLISHED

Study Areas and Data

Data for this study are taken from a portable broadband deployment in Wyoming recording mining explosions in the Powder River Basin (Figure 1a and 1b) and a broadband network currently deployed in northeast China (Figure 1c).

The Wyoming events (Figure 1b) are four kiloton size (2.07, 1.12, 1.26 and 2.70 kiloton for event 96201, 96214, 96215 and 97226, respectively) cast blasts from the Black Thunder Mine, the largest producer of coal in North America. Four temporary broadband seismic stations were deployed in a ring at 200 km range from the mine. To examine the range dependence of the waveforms station KRET was deployed about 100 km north of the mine along the azimuth to CUST. The Powder River Basin is outlined in white in Figure 1a. The total explosive of the QianAn event is 1.3 kiloton from an iron mine in China, the largest open-pit iron mine in Asia. Stations AYPU, BAKOU, MJPU and YFANG are four broadband seismic stations operated by Southern Methodist University (SMU) and Institute of Geophysics, China Seismological Bureau (IGCSB) (Figure 1c). Station BJT is a China Digital Seismic Network (CDSN) station. The raw observed vertical component seismic data from these five events are presented in Figure 2.

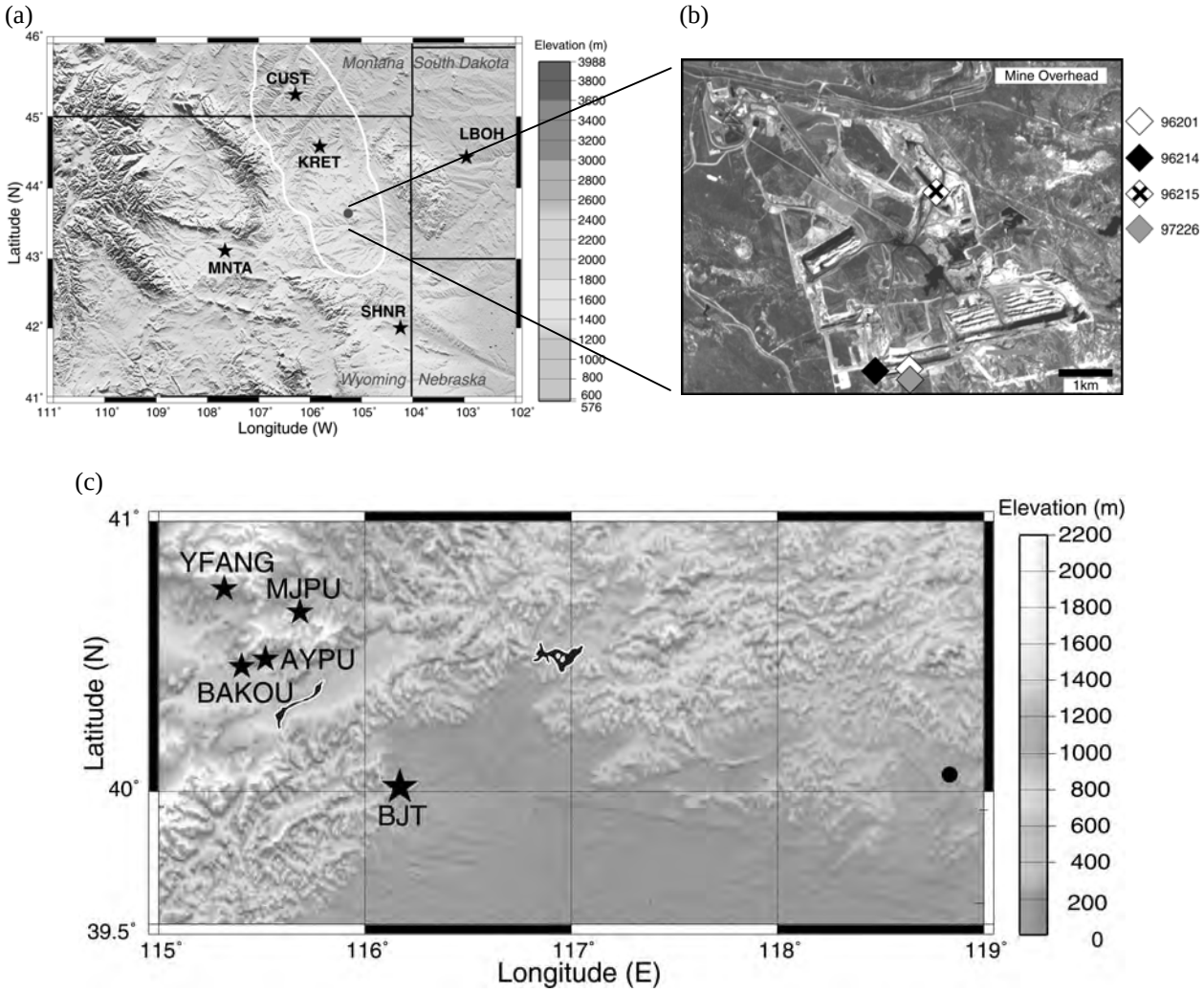


Figure 1. Study areas (a: Wyoming, USA; c: QianAn, China) with the locations of stations (stars) and events (dots). b is the locations of four events at Wyoming superposed on a satellite photo of the Black Thunder coal mine at Powder River Basin outlined by white line in (a), Wyoming.

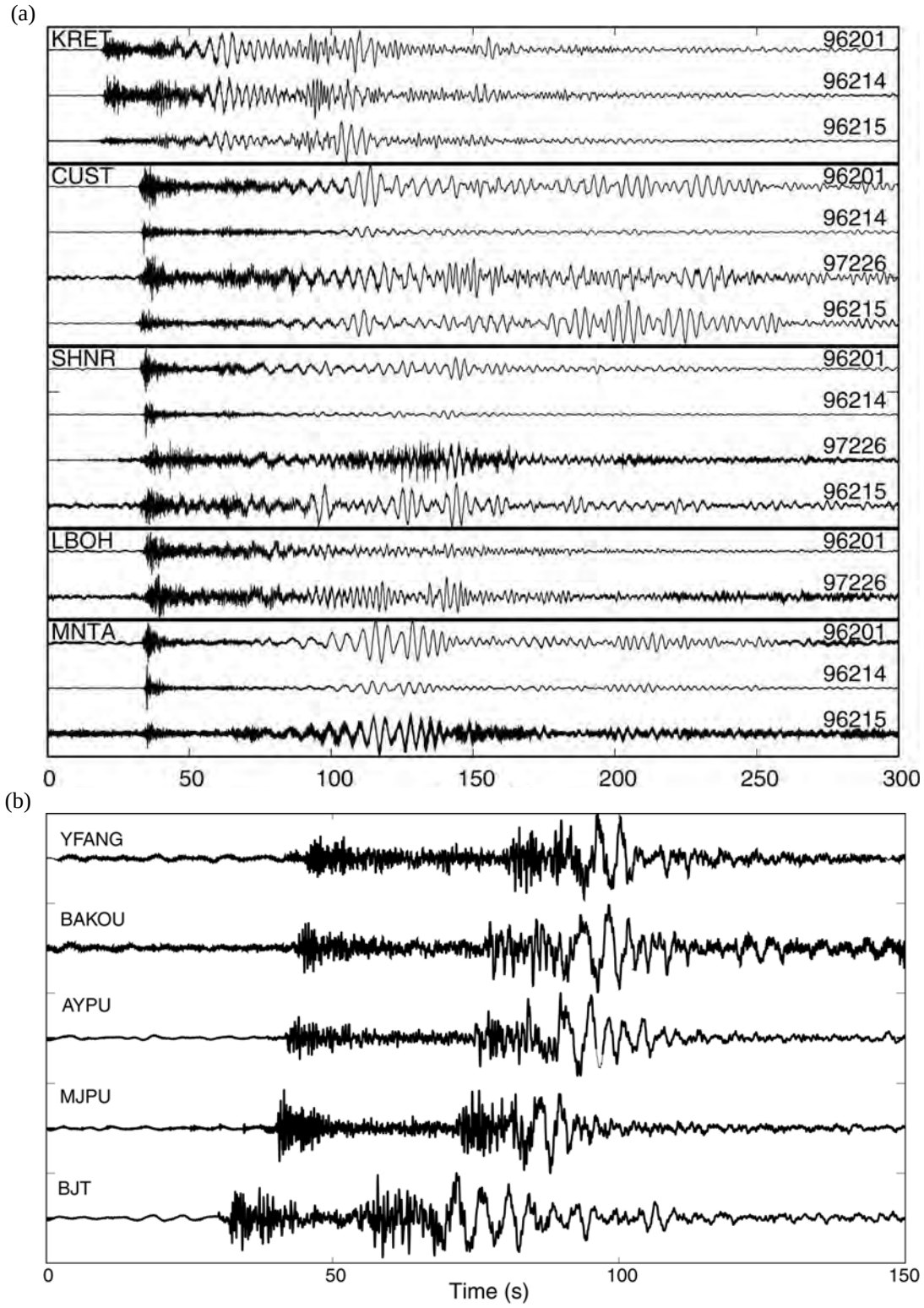


Figure 2. Vertical-component seismograms at all stations for the four events at Wyoming (a) and the event in QianAn, China (b).

M_s Estimation

Quantification of dispersion curves and the inferred velocity model for intermediate period surface waves opens the opportunity to estimate surface wave magnitudes at intermediate periods. Application of such estimates to the explosion waveforms and determination of body wave magnitudes provides for the investigation of such measures as discriminants between earthquakes and explosions.

Comparing M_s and m_b values for earthquakes and nuclear explosions has proven to be a successful teleseismic discriminant (Stevens and Day, 1985) since for a common body wave magnitude, earthquakes are more efficient in generating surface waves than are explosions. The theoretical understanding of this relationship is related to the source function of the two event types, the materials surrounding the source, and the source depth.

M_s in these teleseismic studies was defined for Rayleigh waves by Gutenberg (1945) with periods near 20 s for events recorded at epicentral distances greater than 20°. Marshall and Basham (1972) have suggested that M_s determination can be extended to smaller events and shorter periods. Regional observations hold the key to better monitoring at low magnitudes and it is therefore of interest to extend M_s:m_b applicability to regional data (Patton, 2001; Bonner, *et al.*, 2003). The mining explosion data from China (Zhou *et al.*, 2003) and similar data from mining explosions in Wyoming (Zhou and Stump, 2004) provide regional data for exploring this set of discriminants.

Following the suggestion of Marshal and Basham (1972) the regional M_s is defined as:

$$M_s = \log_{10}(A) + B'(\Delta) + P(T) \quad (1)$$

Where A is the Rayleigh wave amplitude (zero-to-peak in nanometers), $B'(\Delta)$ is an attenuation correction as a function of distance (Δ) in degrees, and P(T) is a path correction as a function of period T. The distance correction, $B'(\Delta)$, is particularly important at regional distances. Basham (1971) suggested $0.8 \cdot \log_{10}(\Delta)$ as an appropriate distance correction for both earthquakes and explosions in the period range 8-14 s. If one knows the group velocity dispersion curve then the path correction P(T) can be estimated as (Marshall and Basham, 1972; Denny *et al.*, 1987; Bonner *et al.*, 2003):

$$P(T) = \frac{U}{T^{3/2}\sqrt{\frac{dU}{dT}}} \quad (2)$$

The P(T) corrections are normalized to 20 s period in order to compare the short-period results with conventional M_s measurements.

Group velocities of fundamental mode Rayleigh waves were estimated using the Multiple Filter Analysis (MFA) technique (Dziewonski *et al.*, 1969) and refined with Phase Matched Filtering (PMF) (Herrin and Goforth, 1977). A set of programs written by Herrmann (1988) has been run for MFA and PMF. A program written by David Harkrider (personal communication) at Weston Geophysical has been used to calculate P(T) using equation 2 and the empirically derived group velocity curves for the regions of interest. To calculate the P(T) correction, we averaged the dispersion curves for each path obtained after PMF (Figure 3). Although the period range of the surface waves from those mining explosions are from 1 to 20 s, the periods of the maximum amplitudes of Rayleigh waves recorded at these near regional distances fall at about 4~5 s for both regions (Figure 10 in Zhou and Stump, 2004 for Wyoming, and Figure 6 in Zhou *et al.*, 2003 for China). Based on these observations, we decided to make our surface wave measurements at period of 4.5 s. The P(T) corrections for Wyoming and China are listed in Table 1. The amplitudes of surface waves are measured from the fundamental Rayleigh waves after PMF. The average M_s of all stations for all events with the standard deviations (σ) are listed in Table 2.

For the Wyoming data, the path corrections (Table 1) vary significantly from station to station reflecting the heterogeneous structure in the area. For the China data, all but one of the corrections are similar reflecting common paths across the Yanshan Uplift. In China, the station BJT has a quite different path correction because the path from the explosion to this station is dominated by the Hebei Plain. Despite differences in the path corrections, in both China and Wyoming the final M_S estimates produced similar values at the different stations for common events

as illustrated by the small standard deviation values in Table 2. This result suggests that the intermediate period surface wave estimation procedure used here is a consistent measure.

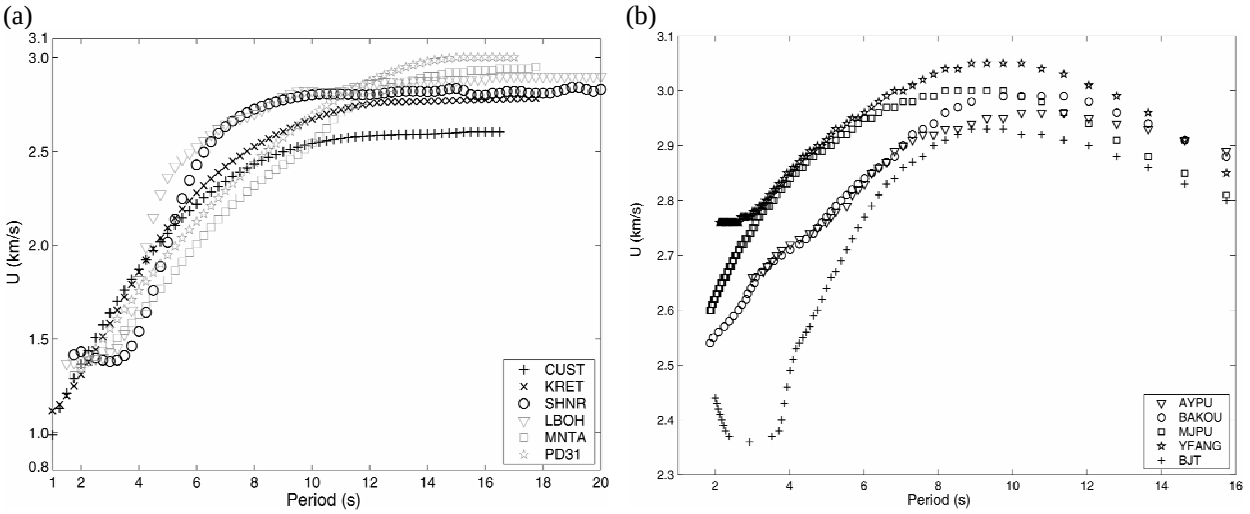


Figure 3. Averaged dispersion curves from Wyoming events (a) and QianAn event (b)

Table 1. P(T) corrections for Wyoming, USA and QianAn, China

Region	Station	P(T)
Wyoming, USA	CUST	-0.69
	KRET	-0.63
	LBOH	0.23
	MNTA	-0.35
	SHNR	-0.24
QianAn, China	AYPU	-0.63
	BAKOU	-0.54
	BJT	-0.17
	MJPU	-0.49
	YFANG	-0.54

Table 2. Averaged M_s of events

Event Code	Yield (kg)	M_s	σ
96201	2065412	3.04	0.14
96214	1117171	2.94	0.10
96215	1264181	3.02	0.20
97226	2704937	2.94	0.35
02363	1301000	2.86	0.26

m_b Estimation

For the events in Wyoming, we use the Denny *et al.* (1987) body wave magnitude formula, which was specifically developed for the western United States from an extensive database of earthquakes and nuclear explosions at or near the Nevada Test Site. It is:

$$m_b = \log_{10}(A) + 2.4 \cdot \log(\Delta) - 3.95 + c_i \quad (3)$$

Where A is the peak-to-peak amplitude in nanometers of the P_n wave, Δ is the distance in km and c_i is the site correction.

In order to measure the amplitude of P_n phases from the Wyoming events, we integrated the original velocity seismograms into displacement after removing the instrument response. The displacement seismograms with a 0.5 Hz 3rd-order Butterworth high pass filter applied are presented in Figure 4. The same procedure has been applied to the QianAn data (Figure 4). Between epicentral distance of about 2° and 12.5°, P_n is the first-arriving phase. As an emergent phase, sometimes P_n is difficult to pick. To estimate the magnitude m_b we followed Vergino and Mensing (1990) and picked the maximum peak-to-peak amplitude of the first 3-5 cycles of the seismograms.

Evernden (1967) has shown that the patterns of P_n amplitudes versus Δ in the western and eastern United States are markedly different. The differences in the two regions are related to crustal origin and age. The velocity structures of northeast China are more similar to the eastern United States than the western United States. Based on this comparison, we use Evernden's (1967) formula to estimate m_b for QianAn:

$$m_b = -3.27 + \log_{10}(A/T) + 2\log_{10}\Delta, \quad (4)$$

where A is the zero-to-peak amplitude in nanometers (nm), T is the period in s and Δ is distance in kilometers.

Table 3 lists the average m_b values estimated for all events with accompanying standard deviations. The standard deviations of the estimates indicate the similarity of the P_n measurements among the broadband instruments in China and Wyoming. The body wave magnitudes for all but one of the mining explosions in both regions range from 2.9 to 3.38.

The one anomalous event from Wyoming, 96214, with a m_b 4.39 is almost an order of magnitude larger than the others. Near-source observations of this blast documented that the delay firing of this explosion failed resulting in the nearly simultaneous detonation of the last half of the explosion. This simultaneous detonation resulted in a very impulsive source that is reflected in the m_b values observed at regional distances.

Stevens and Day (1985) presented an analysis of m_b versus M_s for earthquakes and explosions using 1,260 earthquakes for which m_b and M_s were recorded by National Earthquake Information Service (NEIS) during 1980 and 1981 and explosion data through 1982 for which m_b and M_s were available. They found that above approximately m_b 5.5, the earthquake and explosion populations are well separated, and for smaller events there is a small amount of mixing. We reproduce their figures here as Figure 5 superposing our m_b: M_S data for the four events in Wyoming and one in China. All of our events fall at the very smallest range of Stevens and Day study. Since the events are small, all of the estimates are based upon regional observations, whereas the Stevens and Day (1985) observations are primarily teleseismic. Despite these significant differences it is interesting to compare the two results. Except for the anomalous event (96214), all our mining blasts plot in the earthquake population, a result consistent with the robust intermediate period surface waves generated from these events.

The one anomalous event (96214) had about the same surface wave magnitude of the other events but the body wave magnitude is almost one full magnitude unit higher moving it into the explosion population. The only difference between this event and the other four is the time over which the explosion was detonated with the anomaly being nearly simultaneously detonated. This comparison suggests that the time function of mining and single-fired explosion may play a critical role in the performance of this discriminant.

Table 3. Averaged m_b of events

Event Code	Yield (kg)	m_b	σ
96201	2065412	3.38	0.09
96214	1117171	4.39	0.09
96215	1264181	3.28	0.17
97226	2704937	3.32	0.13
02363	1301000	2.90	0.09

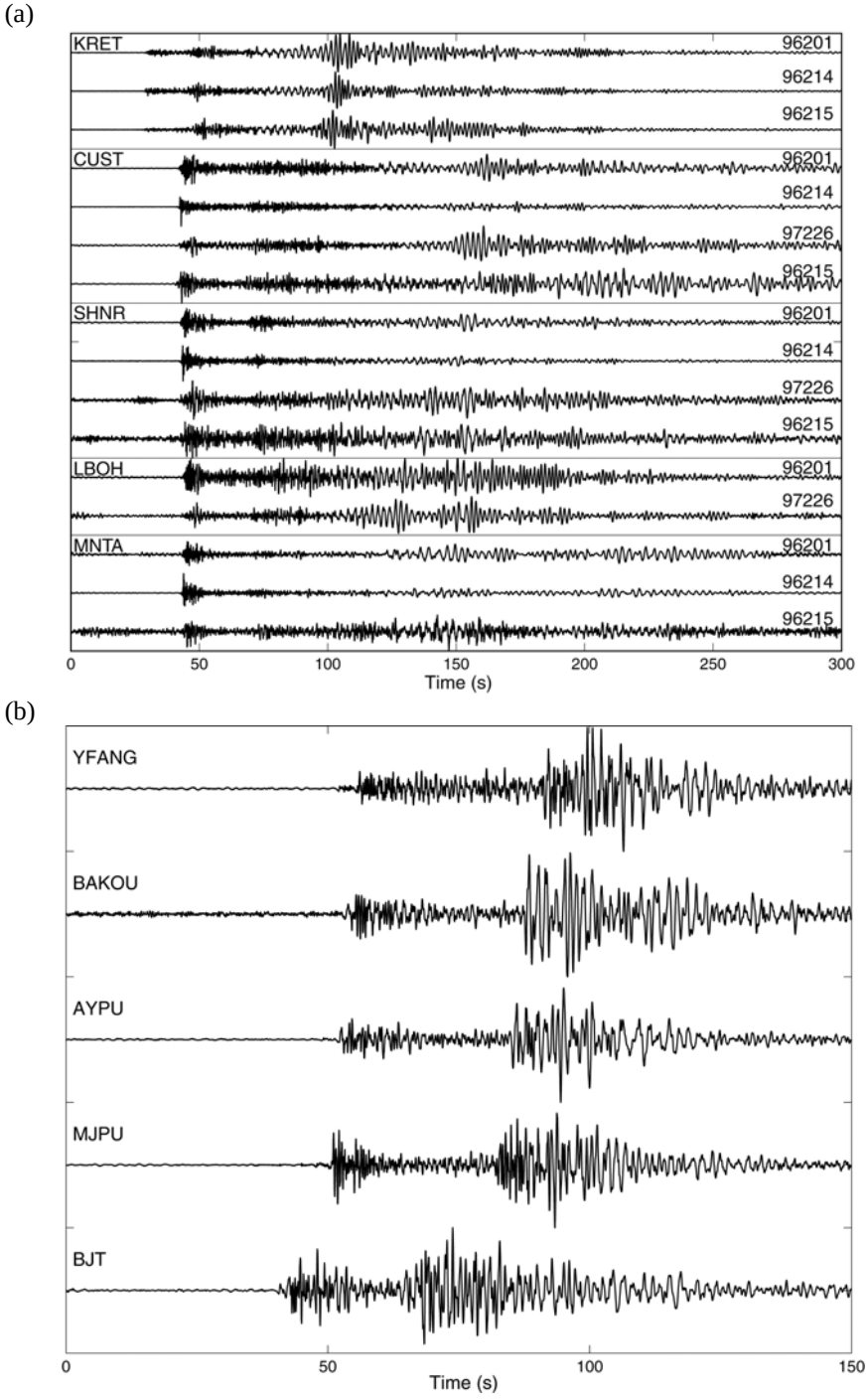


Figure 4. Displacement seismograms for all events in Wyoming (a) and QianAn (b) after removing the instrument response (STS-2) and applying a 3rd-order Butterworth high pass filter with corner frequency of 0.5 Hz.

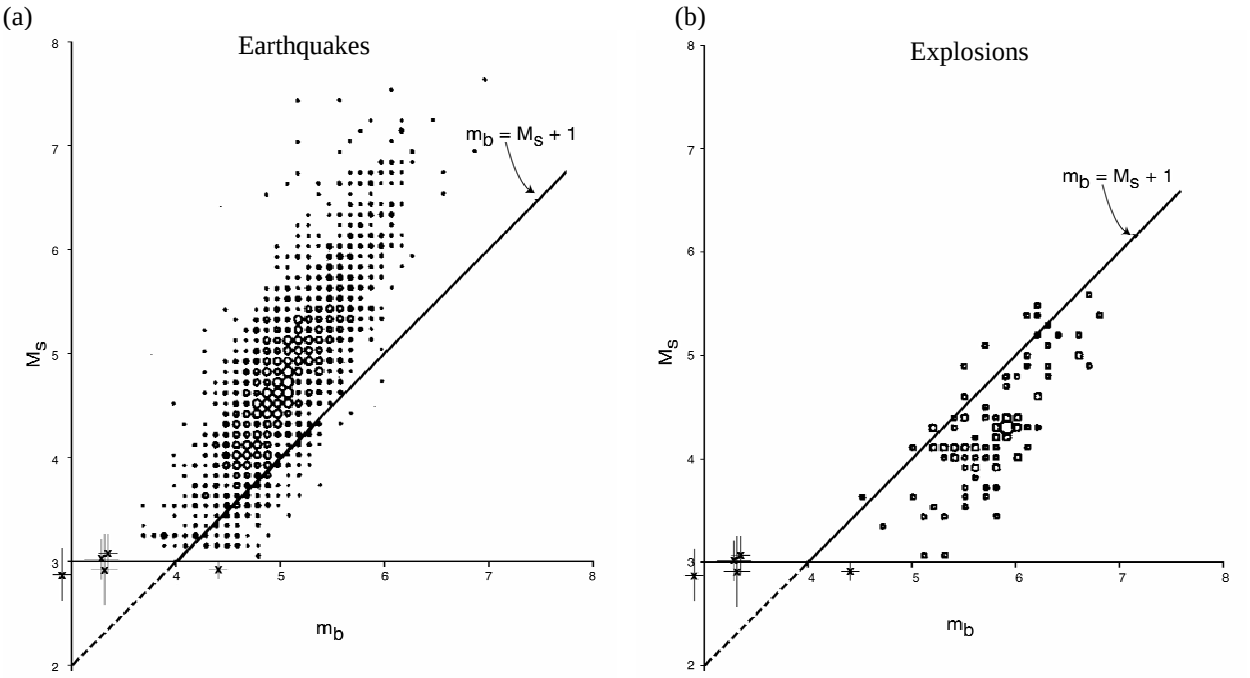


Figure 5. The m_b:M_s plots for earthquakes (a) and explosions (b). The figures were from Stevens and Day (1985) superposed with our results (x-mark) and the standard deviations.

CONCLUSIONS AND RECOMMENDATIONS

The mining explosion data in China has been used to estimate m_b and intermediate period M_S for purposes of investigating an intermediate period discriminant. We also analyzed a similar data set of large scale mining explosions from Wyoming where the surface wave dispersion is well characterized at intermediate periods. These two data sets suggest that mining explosions with long time durations produce larger intermediate period surface waves than single-fired explosions. The enhanced surface waves can make these events look earthquake-like. An anomalous mining explosion in which the delay timing failed resulted in the simultaneous detonation of a large portion of the blast and resulted in significantly enhanced P waves that put the event into the explosion population. A synthetic modeling exercise to quantify the relationship between the timing of the mining explosion, the components of the source model and the resulting body and surface waves is needed to better understand these effects.

ACKNOWLEDGEMENTS

The authors would like to thank Craig Pearson at Los Alamos National Laboratory, Michael Hedlin at the University of California San Diego, and Vindell Hsu at the Air Force Technical Applications Center for their collaboration in conducting experiments in Wyoming. David Blackwell, Robert Gregory, Eugene Herrin at Southern Methodist University, John Ferguson at the University of Texas at Dallas, and Jessie Bonner at Weston Geophysical Corporation who provided critical comments on this study. Robert Herrmann provided programs for multiple filter analysis and phase matched filter. The explosion data from QianAn mine was from the cooperative project between Southern Methodist University and the Institute of Geophysics, China Seismological Bureau. We would like to thank Yun-tai Chen and his research group and Mary Templeton at Incorporated Research Institutions for Seismology (IRIS/PASSCAL) Instrument Center for their help with network installation and data collection.

REFERENCES

Basham, P. W. (1971), A new magnitude formula for short period continental Rayleigh waves, Geophys. *J. R. Astr. Soc.* 23, 255-265.

Bonner, J. L., D. G. Harkrider, E. T. Herrin, R. H. Shumway, S. A. Russell, and I. M. Tibuleac (2003), Evaluation of short-period, near-regional M_s scale for the Nevada Test Site. *Bull. Seism. Soc. Am.* 93, 1773-1791.

Denny, M. D., S. R. Taylor, and E. S. Vergino (1987), Investigation of m_b and M_s formulas for the Western United States and their impact on the M_s/m_b discriminant, *Bull. Seism. Soc. Am.* 77, 987-995.

Dziewonski, A., S. Bloch, and M. Landisman (1969), A technique for the analysis of transient seismic signals. *Bull. Seism. Soc. Am.* 59, 427-444**.**

Evernden, J. F. (1967), Magnitude determination at regional and near-regional distances in the United States, *Bull. Seism. Soc. Am.* 57, 591-639.

Gutenberg, B. (1945), Amplitudes of surface waves and magnitudes of shallow earthquakes, *Bull. Seism. Soc. Am.* 35, 3-12.

Hedlin, M. A. H., B. W. Stump, D. C. Pearson, and X. Yang (2002), Identification of mining blasts at mid- to far-regional distances using low frequency seismic signals. *Pure Appl. Geophys* 159, 831-863.

Herrin, E. and T. Goforth (1977), Phase-matched filters: Application to the study of Rayleigh waves, *Bull. Seism. Soc. Am.* 67, 1259-1275.

Herrmann, R. (1988), Surface wave inversion program. *Computer programs in seismology*, Vol. IV. Saint Louis University. St. Louis, Missouri.

Marshall, P. D. and P. W. Basham (1972), Discrimination between earthquakes and underground explosions employing an improved M_s scale, *Geophys. J. R. Astr. Soc.* 28, 431-458.

Myers, S. C., W. R. Walter, K. M. Mayeda, and L. Glenn (1999), Observations in support of R_g scattering as a source of S waves: regional and local recordings of the 1997 Kazakhstan depth of burial experiment, *Bull. Seism. Soc. Am.* 89, 544-549.

Patton, H. J. (2001), Regional magnitude scaling, transportability, and M_s:m_b discrimination at small magnitudes, *Pure Appl. Geophys.* 158, 1951-2015.

Stevens, J. L. and S. M. Day (1985), The physical basis of m_b:M_s and variable frequency magnitude methods for earthquake/explosion discrimination, *J. Geophys. Res.* 90, 3009-3020.

Vergino, F. S. and R. W. Mensing (1990), Yield estimation using regional $m_b(P_n)$, *Bull. Seism. Soc. Am.* 80, 656-674.

Zhou, R.-M., B. W. Stump, and Y.-T. Chen (2003), A comparative study of intermediate-period surface waves from kiloton-size mining explosion in Northeast China and Western United States, poster for the *AGU Fall Meeting*, San Francisco, CA.

Zhou, R.-M. and B. W. Stump (2004), Rayleigh waves generated by mining explosions and upper crustal structure around the Powder River Basin, Wyoming. *Bull. Seism. Soc. Am.* to appear Vol. 94, No. 4.

2004

Proceedings of the 26th Seismic Research Review:
Trends in Nuclear Explosion Monitoring

Vol. II

To view these Proceedings online, visit
https://www.nemre.nnsa.doe.gov/review2004

Proceedings of the 26th Seismic Research Review: Trends in Nuclear Explosion Monitoring

September 21-23, 2004

Orlando, Florida

Volume II

Hydroacoustic Monitoring
Radionuclide Monitoring
Infrasound Monitoring
Data Processing and Analysis

Approved for Public Release; further dissemination unlimited.

National Nuclear Security Administration

LA-UR-04-5801

AIR FORCE RESEARCH LABORATORY

Table of Contents - Volume II

5. Hydroacoustic Monitoring 551

5-01 **Harben, P., E. Matzel, D. Blackman, and D. Clarke**
Hydroacoustic Blockage Calibration for Discrimination: Results from 2003 Indian Ocean Cruise, and Imploding Sphere Calibration Source Development 553

5-02 **Pulli, J., Z. Upton, and J. Bhattacharyya**
Insights Into Blockage, Reverberation and Direction Finding Using Array Processing of Hydroacoustic Signals in the Indian Ocean 560

5-03 **Tolstoy, M., D. Bohnenstiehl, and E. Chapp**
Long Range Acoustic Propagation of High Frequency Energy in the Indian Ocean from Icebergs and Earthquakes 568

6. Radionuclide Monitoring 579

6-01 **McIntyre, J., C. Aalseth, T. Bowyer, J. Hayes, T. Heimbigner, S. Morris, and P. Reeder**
Triple Coincidence Radioxenon Detector 581

6-02 **Rynes, J., D. Penn, and P. Donohoe**
Research and Development of Radioxenon Monitoring Systems 588

7. Infrasound Monitoring 599

7-01 **Bass, H. and F. Shields**
The Use of Arrays of Electronic Sensors to Separate Infrasound from Wind Noise 601

7-02 **Bowman, J., G. Baker, and M. Bahavar**
Infrasound Station Ambient Noise Estimates 608

7-03 **Chael, E. and R. Whitaker**
Infrasound Signal Library 618

7-04 **Garces, M., M. Willis, C. Hetzer, and S. Businger**
The Hunt for Leaky Elevated Infrasonic Waveguides 624

7-05 **Gibson, R. and D. Norris**
Integration of Infrasound Propagation Models and Near-Real-Time Atmospheric Characterizations 635

7-06 **Herrin, E., P. Golden, P. Negraru, H. Bass, G. Hunter, W. Andre, J. Olson, D. Osborne, M. Garces, M. Hedlin, and K. Hoffmann**
Infrasound Calibration Experiments at White Sands Missile Range: Planning and Preparations 645

7-07 **Norris, D.**
Time-Domain Modeling Techniques and the Study of Infrasonic Propagation 654

7-08 **O'Brien , M. and G. Shields**
Infrasound Source Location Using Time-Varying Atmospheric Models 660

7-09 **ReVelle, D., R. Whitaker, J. Mutschlecner, and M. Renwald**
Discrimination of Earthquakes and Mining Blasts Using Infrasound 670

7-10 **Walker, K., S. Arrowsmith, J. Berger, M. Hedlin, and M. Zumberge**
Resolving Infrasound Signal Back Azimuths with Arrays of Optical Fiber Sensors 680

8. Data Processing and Analysis 689

8-01 **Aguilar-Chang, J., R. Stead, and M. Begnaud**
Advances in Applying Data Warehouses to Seismic Calibration Research 691

8-02 **Ballard, S. and J. Lewis**
DBTools: A Suite of Tools for Manipulating Information in a Relational Database 700

8-03 **Heimbigner, T., T. Bowyer, J. Hayes, C. Hubbard, J. McIntyre, M. Panisko, M. Ripplinger, and R. Suarez**
State-of-Health Software for the Automated Radioxenon Sampler/Analyzer 710

8-04 **Kerr, J. and D. McClung**
Low-Noise Borehole Triaxial Seismometer 719

8-05 **Kohl, B., T. Bennett, I. Bondar, B. Barker, W. Nagy, C. Reasoner, and J. Hanson**
Development of a Network Data Set for Evaluating Detection and Network Processing Performance 725

8-06 **Kromer, R. and T. Townsend**
Seismic Sensor Component Evaluation 735

8-07 **Kvaerna, T., S. Gibbons, F. Ringdal, and D. Harris**
Integrated Seismic Event Detection and Location by Advanced Array Processing 742

8-08 **Langston, C., I. Rabak, C. Chiu, and C. Liang**
Working With and Around the NNSA Database Schema 752

8-09 **Merchant, B., D. Hart, E. Chael, M. Chown, and J. Hampton**
Knowledge Base Navigator Facilitating Regional Analysis Inter-Tool Communication 760

8-10 **Rivers, W., R. Wagner, J. Chen, E. Siu, C. Schultz, D. Dodge, and G. Pope**
Efficient Integration of Old and New Research Tools for Automating the Identification and Analysis of Seismic Reference Events 770

8-11 **Ruppert, S., D. Dodge, A. Elliott, M. Ganzberger, T. Hauk, E. Matzel, and F. Ryall**
Enhancing Seismic Calibration Research Through Software Automation 780

8-12 **Woodward, R., M. Bahavar, and R. North**
Data Resources to Support Nuclear Explosion Monitoring Research and Development 790

Acronyms, etc. 801

Hydroacoustic Monitoring

HYDROACOUSTIC BLOCKAGE CALIBRATION FOR DISCRIMINATION: RESULTS FROM 2003 INDIAN OCEAN CRUISE, AND IMPLODING SPHERE CALIBRATION SOURCE DEVELOPMENT

Philip E. Harben[1], Eric Matzel[1], Donna K. Blackman[2], and Doug Clarke[1]

Lawrence Livermore National Laboratory[1], University of California at San Diego[2]

Sponsored by National Nuclear Security Administration
Office of Nonproliferation Research and Engineering
Office of Defense Nuclear Nonproliferation

Contract No. W-7405-ENG-48[1], DE-FC03-01SF22356[2]

ABSTRACT

The central focus of research in FY04 was to develop a tool to assess hydroacoustic blockage that could easily be used by analysts to predict which hydroacoustic monitoring stations can be used in discrimination analysis for any particular event. The research involves two approaches (1) model-based assessment of blockage, and (2) ground-truth data-based assessment of blockage. The goal is to reliably determine all hydroacoustic stations that can support a discrimination analysis from any event location in the world's oceans. An important aspect of this capability is to eventually include reflected T-phases where they reliably occur. This year a prototype analyst tool was developed using model-based blockage assessment with provision for future inclusion of databased assessment. The tool presents the analyst with a map of the world, and plots raypath blockages from stations to sources. The analyst inputs source locations and blockage criteria, and the tool returns a list of blockage status from all source locations to all hydroacoustic stations. The model-based blockage tool assessment reliability is currently limited by the coarse bathymetry of existing databases. In collaboration with BBN Inc., the Hydroacoustic Coverage Assessment Model (HydroCAM) that generates the blockage grid files that serve as input to the prototype analyst tool, is being extended to include high-resolution bathymetry databases in key areas that increase model-based blockage assessment reliability.

The 2003 Indian Ocean (IO) cruise sources were analyzed at all IO stations for frequency content, signal-to-noise, and blockage. The 2003 and 2001 cruises together provide a 17-event database of ground-truth explosive sources that are widely distributed within the IO basin. This will be added to the earthquake event database to provide the basis for extension of the analyst tool to databased blockage assessment. The 2003 cruise also provided the data to compare sphere and signals underwater sound (SUS) small explosive sources. The SUS source provides larger amplitude signals at long range. Both sources provide energy above background noise in the 20 – 100 Hz bandwidth.

The sphere source was modeled using a hydrodynamic code. Peak pressures increased as the sphere internal air pressure decreased, and the bubble pulse period and amplitude decreased with decreasing internal pressure. Relatively small variations in the internal pressure from one sphere to the next accounts for the observed variation in the bubble pulse period. By including a shell of fluid with the density and mass of the glass sphere in the model, some complex waveform features observed in the field tests were reproduced in the models. The model differs notably from test results in the shock-wave pulse width and the bubble pulse period, possibly because glass crushing effects could not be included in the model. Poor repeatability in the clustered 5-sphere source design gave rise to a line-sphere system that should result in an azimuth independent waveform, enhanced survivability, and modularity.

OBJECTIVE

The objective of this research is to enhance discrimination capabilities for events located in the world's oceans. Two research and development efforts are needed to achieve the stated objective: 1) improvement in discrimination algorithms and their joint statistical application to events, and 2) development of an automated and accurate blockage prediction capability that will identify all stations and phases (direct and reflected) from a given event that will have adequate signal to be used in a discrimination analysis. More emphasis will be put on the first R&D need in the future. This paper will focus on the progress made on the second R&D need.

The strategy for improving blockage prediction in the world's oceans is to improve model-based prediction of blockage and to develop a ground-truth database of reference events to assess blockage. This two-pronged approach emulates the approach taken in seismic monitoring. As much as possible, seismic tools and know-how will be utilized in hydroacoustic blockage assessment. Improving model-based blockage prediction entails, first and foremost, improving resolution of the bathymetry databases used in blockage calculations. The BBN Inc. developed code HydroCAM is the basis for all model-based grid file calculations. Improving HydroCAM's blockage modeling capability starts with improving the bathymetry databases the blockage calculations are based on. Research has focused on developing the capability in HydroCAM to utilize variable resolution bathymetry data and hence incorporate high-resolution "spotlight" bathymetry databases into the overall bathymetry data utilized in blockage calculations.

Research has also focused on the development of a blockage assessment software tool. The software tool is envisioned to develop into a sophisticated and unifying package that optimally and automatically assesses both model-based and databased blockage predictions in all ocean basins, for all NDC stations, and accounting for reflected phases (Pulli *et al*., 2000). A prototype blockage assessment tool has been developed. The model-based software tool effort focuses on the Diego Garcia station in the Indian Ocean and uses a suite of blockage grids produced by HydroCAM to assess blockage.

The ground-truth element of blockage assessment began with the assembly and delivery of an earthquake event database recorded at Diego Garcia and Cape Leeuwin stations in the Indian Ocean and implementation of an automated event-loading schema. A database rich in high-frequency ground-truth events is important; consequently the database is being augmented with explosive events whenever possible. The Indian Ocean cruises in 2001 and 2003 have supplied 17 high-frequency ground-truth events that are widely distributed over the Indian Ocean basin. Further development of the sphere source, particularly an improved multi-sphere source, offers a relatively inexpensive way to assess high-frequency blockage through ground-truth experiments on ships of opportunity. Future plans call for integration of the database element with the blockage assessment software tool and the eventual addition of reflected phases in the analysis. In the immediate future, based on analyst input, the tool will be improved to provide ease-of-use and integrated with waveform databases.

RESEARCH ACCOMPLISHED

The primary research and development accomplished in FY04 was the development of a prototype analyst tool that employs a model-based approach to assess blockage from event(s) to all hydroacoustic monitoring stations. Analysis of the Indian Ocean cruises and source recordings was accomplished as well as advanced modeling and system design of the imploding sphere source.

The model-based research and development has focused on utilizing the modeling capability of HydroCAM to develop a basic software tool that can be used to access a suite of blockage grid files (based on different blockage criteria) calculated by HydroCAM. The critical shortcoming in current HydroCAM blockage modeling is due to present-day worldwide bathymetry databases. The nominal wavelengths in the hydroacoustic monitoring band are about 15 m to 1.5 km, whereas the current average resolution of the ocean surface slope and topography with satellite altimetry is 24 km (Smith and Sandwell, 1997). The vast majority of the world's ocean basin area is deeper than the sound channel depth, and consequently, poor bathymetry resolution is not a factor in blockage prediction. Instead, accurate blockage prediction hinges on augmenting the worldwide database with high resolution (nominally 200 m from ship soundings) bathymetry in "spotlight regions," particularly near monitoring stations. Collaboration

with BBN Inc. to develop and enhance HydroCAM modeling and supporting bathymetry databases is tightly coupled to improvements in the model-based analyst tool accuracy.

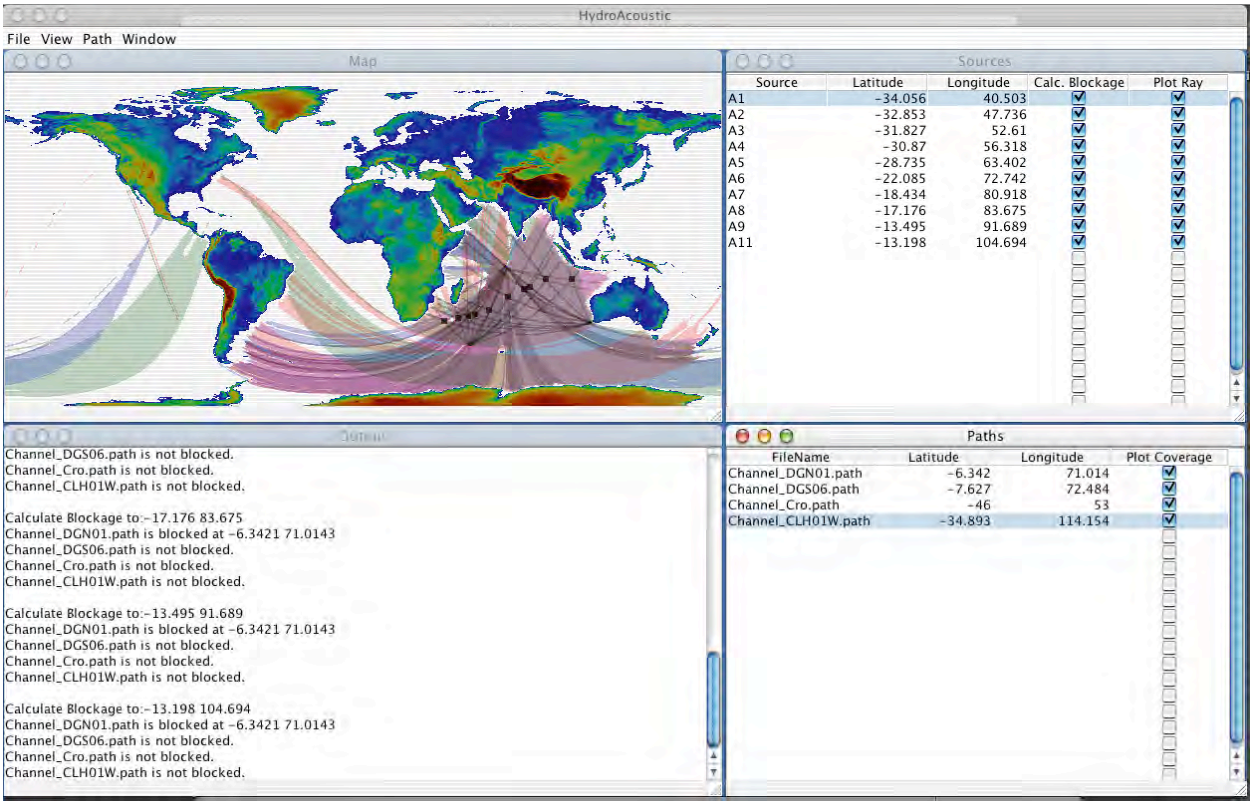


Figure 1. The user interface to the blockage assessment tool plots station coverage and unblocked paths to specific sources in the upper left panel. The user defines source locations in the top right panel, and stations in the lower right panel, and is provided a list of path blockage assessment to each source in the bottom left panel.

The user interface to the blockage assessment tool is shown in Figure 1. The tool is divided into four panels, the top left panel providing a scalable map of all input sources and monitoring stations with optional plotting of station coverage. In the example below, all eleven of the 2003 Indian Ocean cruise source locations are plotted, as are the three Indian Ocean station coverage (Diego Garcia, Cape Leeuwin, and Crozet Is.) maps and unblocked paths from stations to sources (black lines). The panel below the map shows an assessment of blockage to each station from a given source in list format. The rightmost panels are editable lists of source locations (top) and station/path locations (bottom). The tool provides an analysis for specific user-specified blockage criteria given in depth cutoff criteria. A 1,000 m cutoff criteria, for example, means that a specific source-receiver path is considered blocked if bathymetry above 1,000 m is encountered anywhere along the path. Grid files produced by HydroCAM were based on a number of cutoff criteria from 1,000 m to sea level. The user cutoff criteria specify the grid file the analyst tool uses. In general, more blocked paths are predicted with deeper cutoff criteria.

Features of the prototype model-based blockage assessment tool include:

- Platform independent JAVA tool.
- Does not require other software (such as MATLAB or HydroCAM) to run.
- Does not require specialized graphics tools or capability.
- Reads HydroCAM “path” files and plots the coverage defined by the outer contour.
- Coverage for multiple “paths” and stop criteria can be read in, plotted and manipulated simultaneously.

• User defined "source" locations can be input manually or read in as a list and edited directly within the tool.
• Blockage identifications can be made simultaneously for multiple source-receiver pairs.
• Multiple blockage criteria can be tested simultaneously.
• Path coverage and source-receiver raypath plots can be toggled on and off for individual elements.
• Blockage identification can be toggled on and off for individual sources.
• The Map figure can be scaled up and down to allow focus on particular areas of the globe.

Future development of the blockage assessment tool will focus on implementing a parallel ground-truth data-driven assessment capability based on a database of ground-truth event. Although many explosive or other high-frequency events that are identified will be included in the database, most of the database content will consist of earthquake events. The tool will also be linked to waveform databases so that on unblocked paths the tool can deliver the event waveforms recorded during a time window containing the predicted arrival time.

The second Indian Ocean cruise took place in 2003, sailing from Cape Town, South Africa, to Port Hedland, Australia. The ship tracks of both the 2001 and 2003 cruises are shown in Figure 2. The cruises resulted in 17 high-frequency ground-truth events within the Indian Ocean basin that will become part of the databased blockage assessment database. Imploding spheres, an airgun array, SUS charges and an electro-acoustic source (HX-554 by University of Washington's Applied Physics Lab) were investigated as possible calibration sources. The airguns required shallow depths for firing; consequently, energy entered the sound channel primarily by scattering off the sea floor. Detailed, and currently unavailable, bathymetry data are required to accurately model near-source scattering at frequencies above 20 Hz. The HX-554 is now operational and provides a well-calibrated signal, however use of this system is significantly more challenging, logistically, than the other sources.

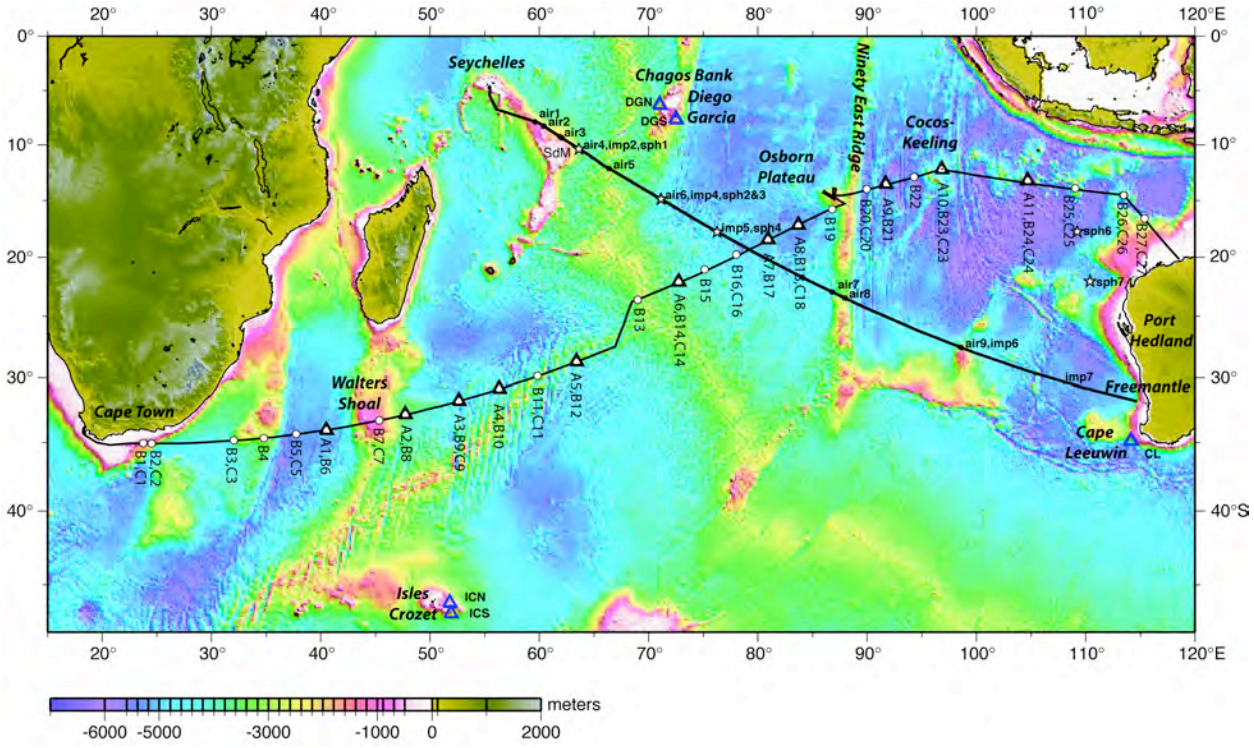


Figure 2. The Indian Ocean basin map shows the ship track of the 2001 cruise (Seychelles –Freemantle) and the 2003 cruise (Cape Town – Port Hedland) and the locations of all SUS, sphere, and airgun sources.

The SUS charges and 5-sphere implosion systems were both fired at several station locations so that a comparison of long-range propagation characteristics could be made. Such a comparison is shown in Figure 3. The recordings are at Cape Leeuwin from station A7, a range of 3,752 km. The top left waveform (high passed at 40 Hz) shows the

arrival from the sphere source, and the bottom left waveform (high passed at 40 Hz) shows the SUS arrival at each hydrophone of the triad. Clearly, the SUS source has better signal-to-noise at long range than has the sphere source. Although the two sources have about the same peak pressure at 1 m from the source, the longer signal duration and relatively lower frequency content of the SUS source makes for superior long-range propagation at the depths of these tests (nominally 700 m). The spectra on the right plot signal amplitude (red) and pre-event background noise (blue) for the sphere source (top) and the SUS source (bottom). Both source types have no appreciable energy below about 20 Hz but do span the monitoring band between 20 Hz and 100 Hz.

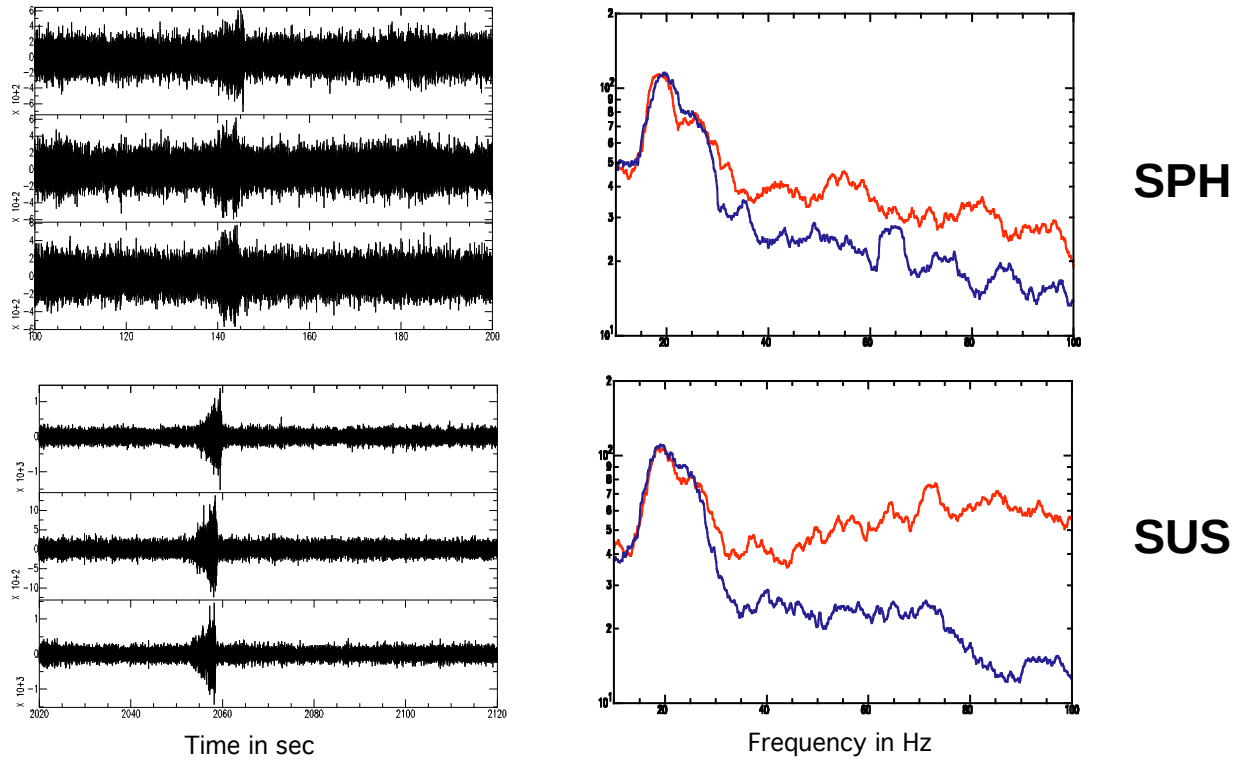


Figure 3. The sphere source waveform (top left) and spectra (top right) are compared to the SUS source waveform (bottom left) and spectra (bottom right) as recorded at Cape Leeuwin, 3,752 km from the source. Note that the spectra plots event amplitude (red/upper) and pre-event background noise amplitude (blue/lower).

The sphere source (Harben *et al*., 2000) signal was modeled using the hydrodynamic code CALE (C-code, Arbitrary Lagrangian, Eulerian) to predict overpressures at 1 m from the source (R. T. Barton, 1985; J. Hagelberg, 2003). Several models were run varying only the internal pressure of the sphere. Peak pressures increased as the sphere internal air pressure decreased, and the bubble pulse period and amplitude decreased with decreasing internal pressure. When the internal pressure was a sixth of standard atmospheric pressure, the peak pressure matched field tests. We found that the temperatures reached in blowing and sealing the glass spheres would result in internal pressures very close to one-sixth standard atmospheric pressure. In addition, relatively small variations in the internal pressure from one sphere to another accounts for the observed variation in the bubble pulse period. Figure 4 shows the modeled signal waveform of the source (top plot). The model included a shell of fluid with the density and mass of the glass sphere. Including a glass like fluid in the model gave rise to the trailing shock peak and high-frequency hash, and it resulted in a sharper or pointed bubble pulse. The field tests shown in the bottom plot have those same features; consequently, we can conclude that the density contrast of the glass compared to seawater plays

wave pulse width and the bubble pulse period. Both differences may be the result of the crushing of the solid glass that must be occurring, but that is not captured in the simplified model.

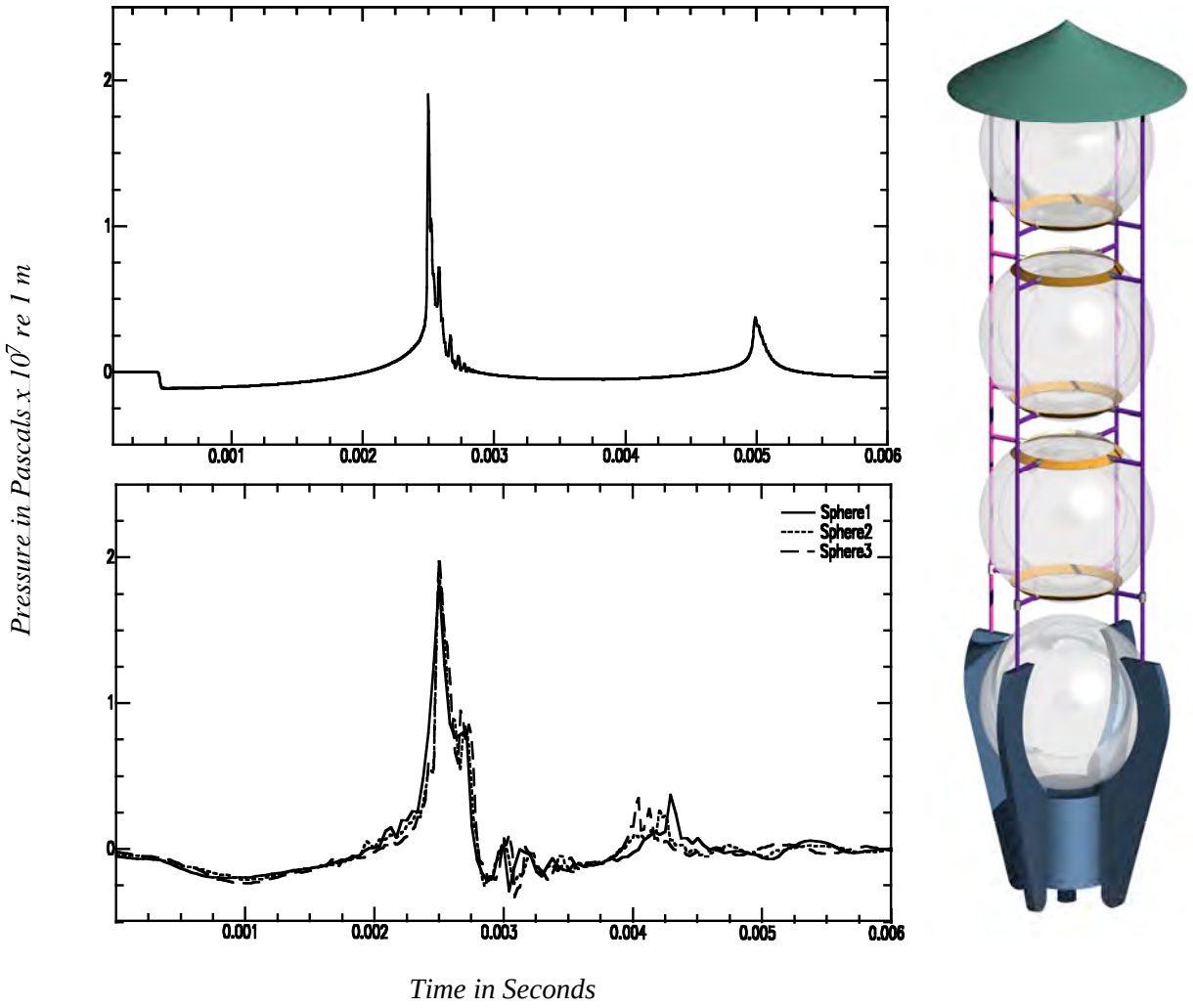


Figure 4. The modeled sphere implosion source signal (top plot) compared to three field tests at 680 m depth (bottom plot). An artist's conception of a linear and modular multi-sphere system is shown on the right.

Although the single sphere-source is highly repeatable, the clustered 5-sphere source showed poor repeatability. This is because the 5-sphere source is not cylindrically symmetric; consequently, source waveform features show a dependence on azimuth. The 5-sphere system also was lacking in ruggedness and exhibited damage after repeated firings on the 2003 cruise. An improved design is shown on the right of Figure 4. The in-line system should result in an azimuth independent waveform and be rugged. An added feature of the design is that any number of spheres can be utilized as source needs dictate.

CONCLUSIONS AND RECOMMENDATIONS

A prototype model-based blockage assessment tool has been developed and is undergoing analyst evaluation. The tool makes use of blockage grid files produced by HydroCAM; consequently, improvement in model-based blockage assessment reliability of the tool is tightly coupled to improvement in HydroCAM, particularly in the resolution of the bathymetry databases used by HydroCAM to create the blockage grid files. The blockage assessment tool had been developed with provision for including a ground-truth databased assessment component. This will be added in the near future and, depending on the density of ground-truth data, should increase reliability of overall blockage assessment in spotlight regions. In addition, future blockage assessment tool development will focus on interfacing to waveform databases, and will thereby automatically provide the analyst with the raw waveforms from all unblocked stations.

The 2001 and 2003 Indian Ocean cruises have shown that 1.8 lb SUS charges and 5-sphere implosion sources can be used for ocean basin calibration of travel time and blockage provided the sources are at SOund Fixing and Ranging (SOFAR) channel depths. In all, the cruises have contributed 17 widely distributed Indian Ocean events to the ground-truth database. Since these sources are small and are recorded at relatively low signal-to-noise, there is little hope that they could be useful in understanding reflected T-phases at high frequency (above 30 Hz). A larger explosion (30 – 300 lbs) in the SOFAR at a strategic location from a known reflecting coastline would be needed to determine the signal-to-noise reduction from reflection as a function of frequency.

The imploding sphere source was studied via field tests as well as by hydrodynamic modeling. The field tests have shown highly repeatable signal waveforms from single spheres but poor repeatability from the 5-sphere design. The 5-sphere design also proved mechanically vulnerable after repeated uses. A new linear multi-sphere design promises to produce a repeatable, multi-sphere source waveform and high survivability as well as to offer flexibility in the number of spheres employed. Hydrodynamic modeling has provided insight on the source waveform. The role of internal pressure and the glass density contrast explains many specific waveform features and variations. Modeling has not correctly predicted the pulse width of the implosion. This may be because the phenomenon of glass fracturing and the resulting crushing during implosion was not accounted for in the models.

REFERENCES

Barton, R. T. (1985), "The CALE Computer Code," *Numerical Astrophysics*. Boston, Jones and Bartlett.

Hagelberg, J., (2003), CALE Implementation Guide, Lawrence Livermore National Laboratory, Livermore, California, UCRL-ID-155540, September 2003.

Harben, P. E., C. . Boro, L. . Dorman, and J. . Pulli (2000), Use of Imploding Spheres: An Alternative to Explosives as Acoustic Sources at Mid-Latitude SOFAR Channel Depths, UCRL-ID-139032.

Pulli, J. J., Z. . Upton, R. . Gibson, J. . Angell, T. . Farrell, and R. . Nadel (2000), Characterization of Reflected Arrivals and Implications for Hydroacoustic Test-Ban-Treaty Monitoring, BBN Tech. . Memor. . W1380.

Smith, W. H. F. . and D.T. . Sandwell (1997), Global Seafloor Topography from Satellite Altimetry and Ship Soundings, *Science*, 277, 1956-1962.

INSIGHTS INTO BLOCKAGE, REVERBERATION AND DIRECTION FINDING USING ARRAY PROCESSING OF HYDROACOUSTIC SIGNALS IN THE INDIAN OCEAN

Jay J. Pulli, Zachary M. Upton, and Joydeep Bhattacharyya

BBN Technologies

Sponsored by National Nuclear Security Administration
Office of Nonproliferation Research and Engineering
Office of Defense Nuclear Nonproliferation

Contract No. DE-AC03-02SF22560

ABSTRACT

BBN Technologies is currently tasked to improve the ability of the hydroacoustic community to model network performance using HydroCAM, the Hydroacoustic Coverage Assessment Model. Recent station installations in the Indian Ocean have yielded excellent data that allow us to evaluate and improve the models in HydroCAM. One of the resulting issues is that ray-based model predictions of hydroacoustic blockage do not always match what is seen in the data.

This year, BBN has focused on understanding blockage and developing a HydroCAM model that predicts blockage with greater accuracy. To achieve this goal, BBN is searching for very high-resolution bathymetry in areas near hydroacoustic stations, investigating model calculations of blockage to be integrated into HydroCAM, and leveraging its database of ground-truth events in the Indian Ocean to study blockage. We have obtained and integrated a 15-second bathymetry database near the site of the future station at Wake Island. We are still searching for high-resolution bathymetry databases near the active Indian Ocean stations at Diego Garcia and Cape Leeuwin.

To understand the effects of bathymetry on the received signals, we examined signals recorded by the International Monitoring System (IMS) arrays at Diego Garcia and Cape Leeuwin using array-processing techniques. Signals examined include seismic phases (*P* and *S* waves converted to acoustic energy below the arrays) and *T* waves from a number of earthquakes along the major tectonic features of the Indian Ocean. We used a modified version of the HydroTool component of MatSeis to compute both scrolling cross-correlations and frequency-wavenumber spectra for each event studied.

One of the events analyzed was the M_w 7.6 event on the Carlsberg Ridge on 15 July 2003. This event occurred on a nearly 200-km long fault break that was roughly perpendicular to the great circle path to Diego Garcia. Array analysis of the signals from this event indicate that the back-azimuth of the converted P and S waves point to the published epicenter, but the back-azimuth of the *T* wave points to the event centroid, 100 km from the epicenter, which is larger than the location error (as published by the Harvard Centroid Moment Tensor [CMT] project). This observation, confirmed by the analysis of a number of large events in our database, suggests that presumed back-azimuth biases of *T* waves might actually be attributed to the location differences between epicenter and centroid.

Array analysis of the *T* waves generated by the M_w 4.8 earthquake just west of the Chagos Archipelago on 25 July 2002 provides insight into the effect of back-scattering and reverberation on the back-azimuth calculations. This event produced *T* waves with a signal-to-noise ratio of 55 dB at the north array of Diego Garcia. However, only the first 10 percent of the *T* wave signal is coherent across the array. We attribute the incoherence of the remaining 90 percent of the *T* wave signal to backscatter from the Chagos Archipelago near the array. Ray-based blockage predictions for Diego Garcia indicate that the *T* waves from this event are blocked from reaching the south array. However, the *T* wave signal can be seen at amplitude that is 30 dB below that of the north array. Coherence and back-azimuth estimates for this smaller *T wave* signal are stable over a longer time-duration than for the larger signal at the north array. We attribute this stability to a lack of reverberation and back-scatter, since there are no significant bathymetric features behind the south array.

The array analysis of *T*-wave arrivals at Diego Garcia has yielded a better understanding of the capabilities and limitations of the array characteristics, *T*-wave generation, and the effects of blockage and reverberation on observed waveforms. Furthermore, the analysis of the 25 July 2002 event demonstrates the value of using signals that might appear to be blocked but that are, most probably, attenuated as the signals diffract around bathymetric features. In some cases, high amplitude arrivals do not demonstrate strong coherence across the array, but attenuated and diffracted signals may produce very coherent arrivals that can be used in back-azimuth calculations.

OBJECTIVES

The primary objective of this work is to support the Department of Energy (DOE) and the Air Force Technical Applications Center (AFTAC) in the use of the acoustic modeling program the Hydroacoustic Coverage Assessment Model (HydroCAM). Our previous work has shown that our predictions of hydroacoustic blockage using HydroCAM were inadequate to reflect the observations made at the hydrophone arrays in the Indian Ocean at Diego Garcia. Specifically, some paths that are predicted to be blocked are merely attenuated, with signals that are recorded and can be verified with travel-time calculations. In order to improve the model predictions, we have focused on two areas. First is the identification and integration into HydroCAM of high-resolution (<1-min grid) bathymetric data near the hydrophone stations. Second, we have been analyzing our Ground Truth Database of events in the Indian Ocean using array signal processing techniques in order to better understand the acoustic field around the receivers, especially the effects of refraction, diffraction, and reverberation.

Hydroacoustic blockage and diffraction of hydroacoustic energy around islands and seamounts is important to the evaluation of potential station locations and in the identification and classification of hydroacoustic arrivals. An improved modeling capability in HydroCAM will allow station planners and data analysts to better assess the detection and localization potential of the hydroacoustic network.

RESEARCH ACCOMPLISHED

High-Resolution Bathymetry

To better understand the effects of blockage, diffraction, and reverberation, BBN has been searching for high-resolution bathymetry data near the sites of International Monitoring System (IMS) hydroacoustic sensors. In prior modeling efforts (Pulli and Upton, 2001) the best resolution bathymetry available was the 2-min Sandwell and Smith bathymetry (Smith and Sandwell, 1997). This 2-min bathymetry represents a grid spacing of approximately 4 km. For smaller islands, atolls and seamounts, this resolution makes blockage prediction difficult. Also, even at the low frequency of 10 Hz, the wavelengths of acoustic energy are approximately 100 m, making a detailed study of blockage and diffraction difficult with these bathymetric data. While bathymetric data may never be collected near IMS hydroacoustic stations at a resolution less than 100 m, the research community will need greater resolution bathymetry in order to study its effects on hydroacoustic propagation in close proximity to the sensors.

The HydroCAM has been modified to use high-resolution bathymetric datasets near IMS stations in its hydroacoustic raypath calculations. The model uses these local datasets in conjunction with global, lower-resolution datasets to predict propagation and blockage on the ocean basin scale.

Bathymetric data at less than 1 arc-min resolution has been difficult to find, but we have had a few recent successes. During the site survey for the Wake Island IMS station, a 15sresolution grid was collected in a 3x3 degree area near the proposed station installation. These data have been integrated into HydroCAM. Figure 1 shows a cross section of the 15-second data compared to the same cross section using the Sandwell and Smith 2-min bathymetry.

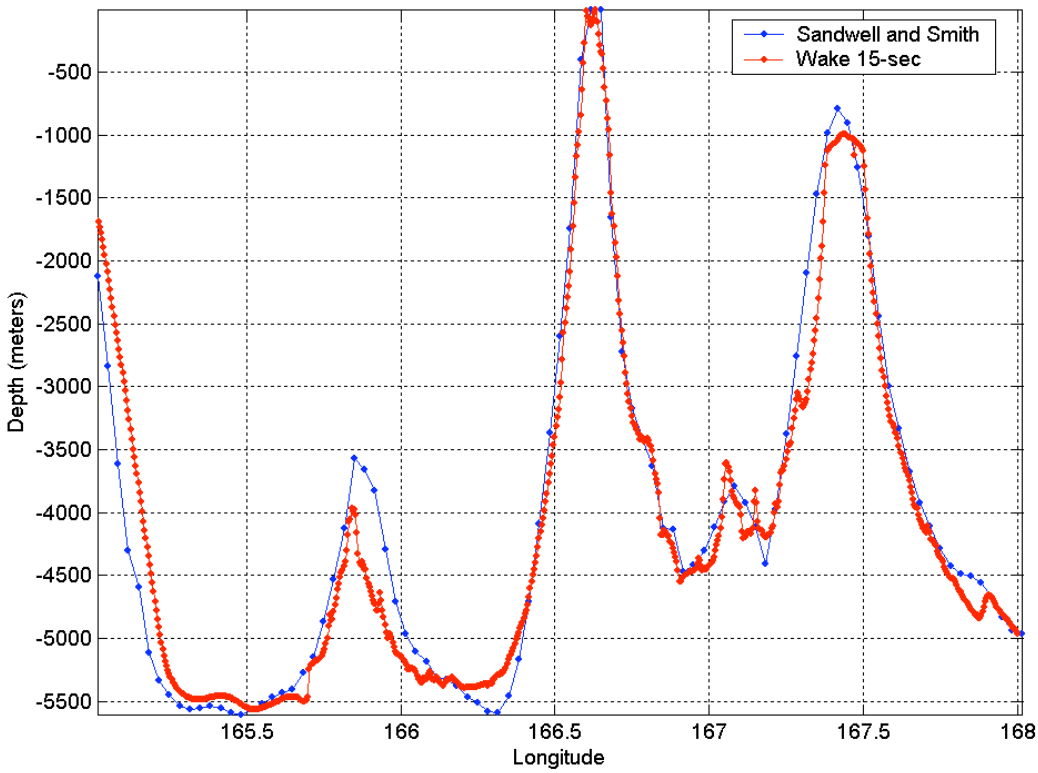


Figure 1. Bathymetric cross sections at 19.3° N Latitude. The red plot is at a 15-second resolution. The blue plot is at 2-min resolution

The IMS hydrophone station has not yet been installed at Wake Island. Therefore, we have delayed using these data in a detailed study of blockage. However, these data have been integrated into HydroCAM. As stated above, HydroCAM can now use the local high-resolution bathymetry in conjunction with global lower-resolution bathymetry in order to predict hydroacoustic raypaths.

We have also obtained a 36-second resolution bathymetric/topographic database of Australia and the surrounding waters, including the Cape Leeuwin (HA01) station location. These data are bounded by the coordinates: 8^{O} S, 52^{O} S, 102^{O} E, 172^{O}E and are a product of Geoscience Australia (Petkovic and Buchanan, 2002). The database represents over 900 surveys acquired since 1963 by Geoscience Australia, the Australian Hydrographic Service, oil exploration companies, and foreign institutions.

The Cape Leeuwin station has been receiving data since 2002. This bathymetric dataset could provide some valuable insight into local hydroacoustic propagation. Figure 2 shows the entire database. Figure 3 shows a subset of the data around the Cape Leeuwin station location. Figure 4 is a cross section comparison of the 9-second Geoscience Australia data and the 2-min Sandwell and Smith data. Of particular interest are the differences in the datasets. For example, note the areas in Figure 4 between -37.5 and –38 ° latitude or between –35 and –36 ° latitude.

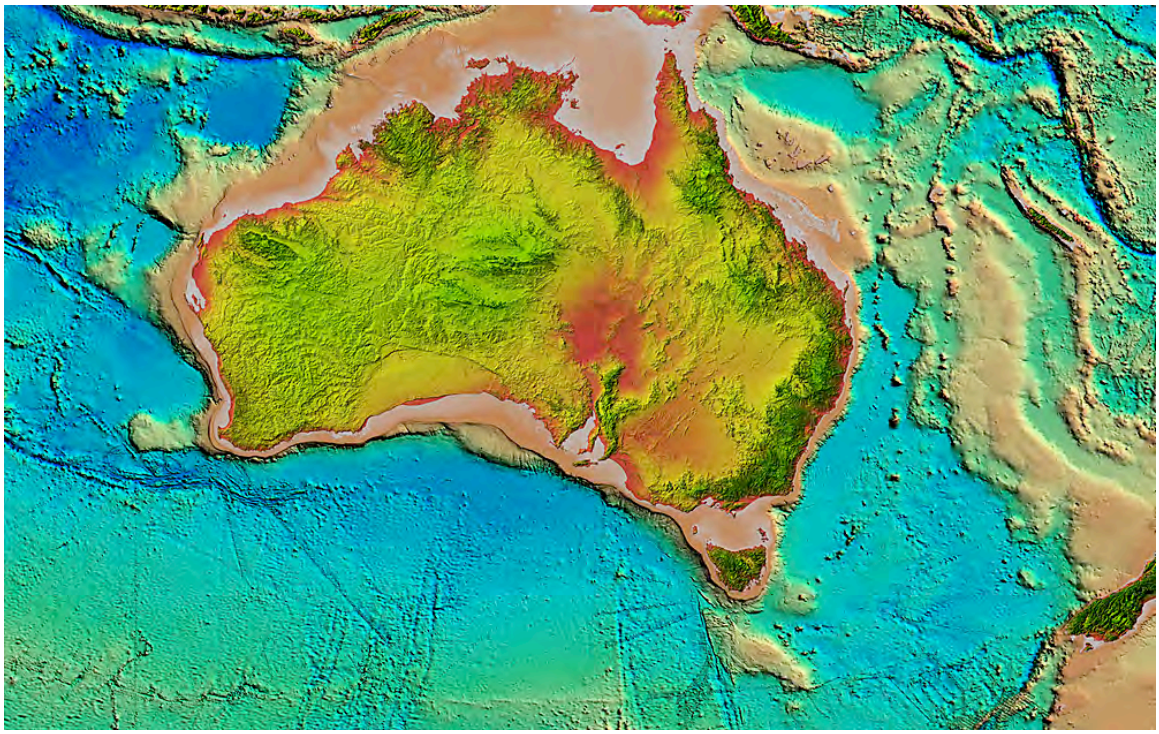


Figure 2. Geoscience Australia 36-second Bathymetry/Topography dataset

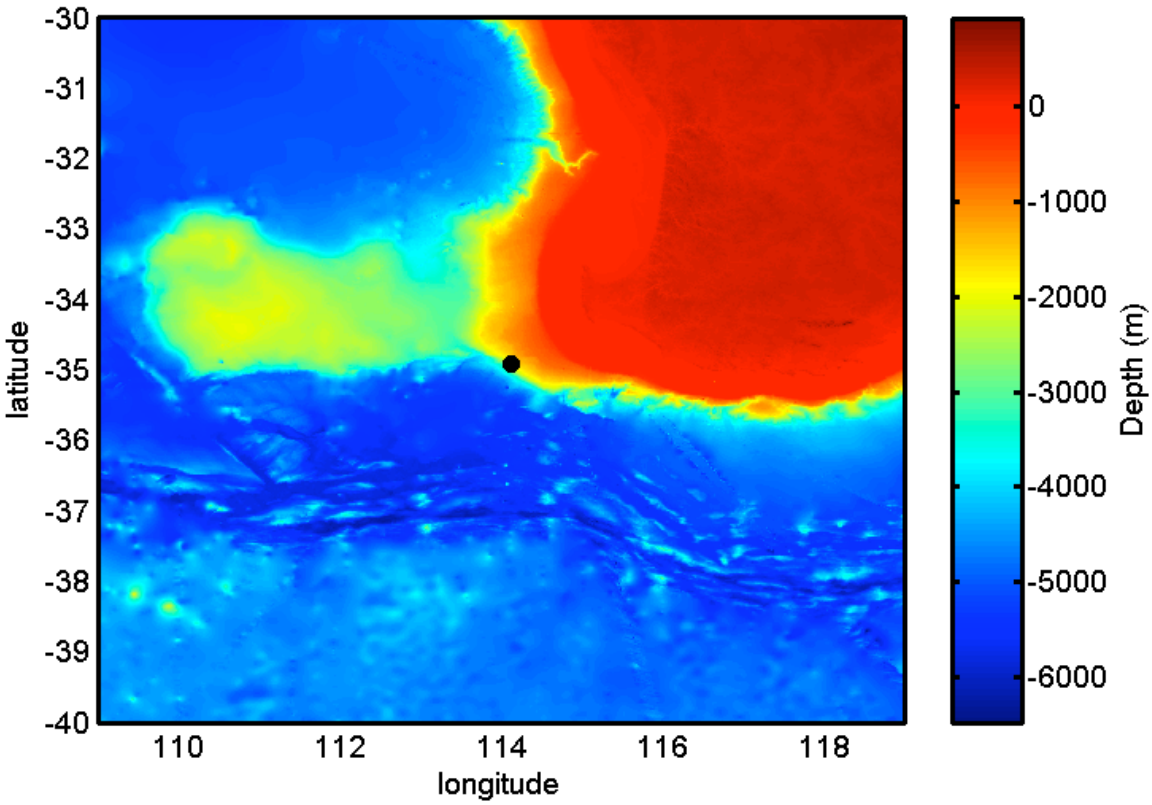


Figure 3. Geoscience Australia 36-second Bathymetry/Topography near Cape Leeuwin (HA01), which is represented by the black dot

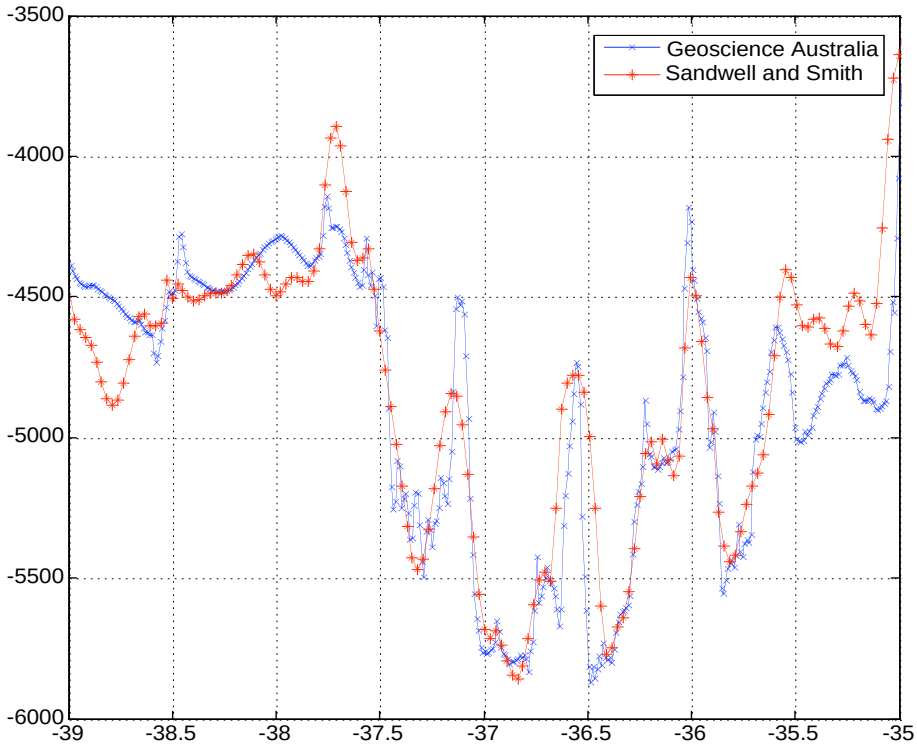


Figure 4. Bathymetric cross-sections at 114^{o} East Longitude. The blue plot is of the Geoscience Australia 36-second data; the red plot is of the 2-min Sandwell and Smith data.

The Geoscience Australia database is being integrated into HydroCAM as part of the HydroCAM 4.2 release. The HydroCAM 4.2 release will also include compatibility with Matlab version 7.0, a complete set of HTML-based tutorials, and many bug fixes and interface improvements.

Array Processing of Hydroacoustic Signals

Our ability to accurately predict hydroacoustic blockage will ultimately depend not only on the availability of high-resolution bathymetry near the source and receiver, but also on an understanding of actual propagation effects, including diffraction, refraction, and reverberation. This is best accomplished with an array of sensors, from which information about the propagating wavefield can be derived using array signal processing techniques. Although we are limited by the three-element configuration of the hydroacoustic arrays, we can derive information about signal coherence and propagation direction versus time in the *T* wave signal.

To accomplish this, we have used the hydroacoustic toolkit recently added to the program MatSeis (Merchant, et al., 2003). We processed the *T* wave signals, including the higher modes leading up to the Mode-1 peak of the *T*-wave and post Mode-1 *T*-wave coda, for approximately 25 Indian Ocean events recorded at Diego Garcia and Cape Leeuwin. The accompanying poster illustrates the analytical results for a number of these events, but here we will concentrate on the results of processing the *T*-wave data for two events located near the Diego Garcia arrays. These events occurred on 15 July 2003 on the Carlsberg Ridge, and on 25 July 2002 off the Carlsberg Ridge near the Chagos Archipelago. A map of these epicenters is shown in Figure 5.

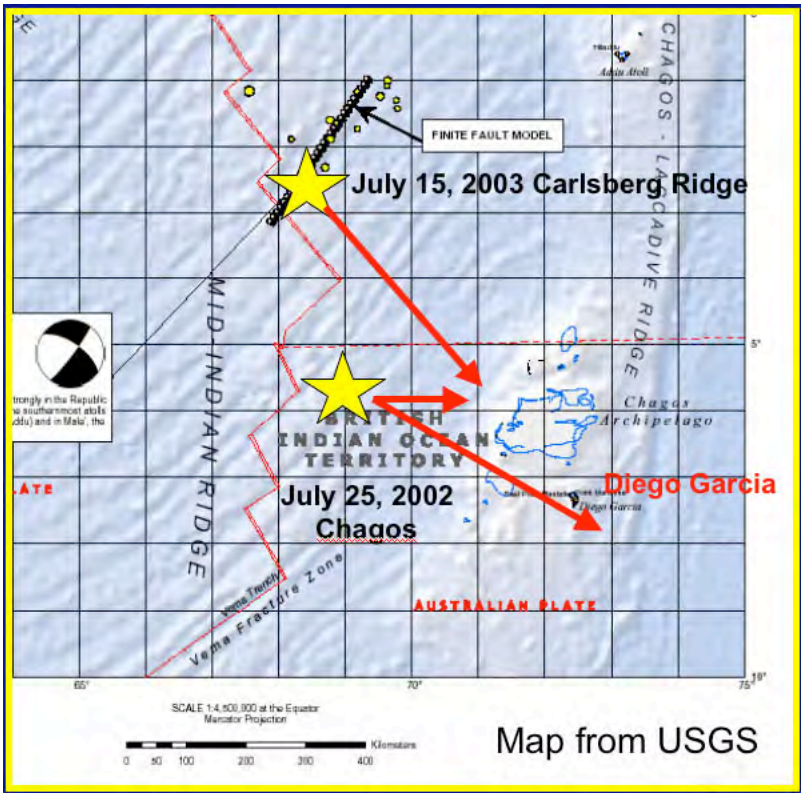


Figure 5. Epicentral map, adapted from a USGS map, illustrating the locations of the Carlsberg Ridge and Chagos Arch earthquakes, as well as the locations of the north and south hydroacoustic arrays at Diego Garcia.

For our analysis, we pre-filtered the data to a band of 3-50 Hz at each element. Scrolling cross-correlations were performed for 10-second windows with a 50% overlap. Figure 6 illustrates the result of this processing for the 15 July 2003 event on the Carlsberg Ridge, recorded on the north array at Diego Garcia. This event had a moment magnitude of 7.6, and the *T* wave signal had a peak signal-to-noise ratio at DGN of approximately 80 dB. Prior to the Mode-1 peak *T*-wave arrival at a travel time of 450s, the array processing indicates a stable back azimuth and apparent velocity estimate consistent with the actual back azimuth (330°) and acoustic velocity (1.5 km/sec). The only exceptions to this are the short windows around 325 and 375s, where the signal back azimuth is around zero degrees and the apparent velocity is unrealistically slow at 1 km/sec. After the Mode-1 arrival (> 450s), the signal-to-noise ratio is still high but signal coherence decreases, as indicated by the unstable back azimuth and apparent velocity. If we look at the map in Figure 5, we see that the Chagos Arch is approximately 100 km behind the DGN array, and back-scatter from this feature should begin to arrive at DGN at a two-way travel time of approximately 130s. This means that back scattered signals originating from near the start of our analysis window (320s) can interfere with the *T* wave signal after 450s.

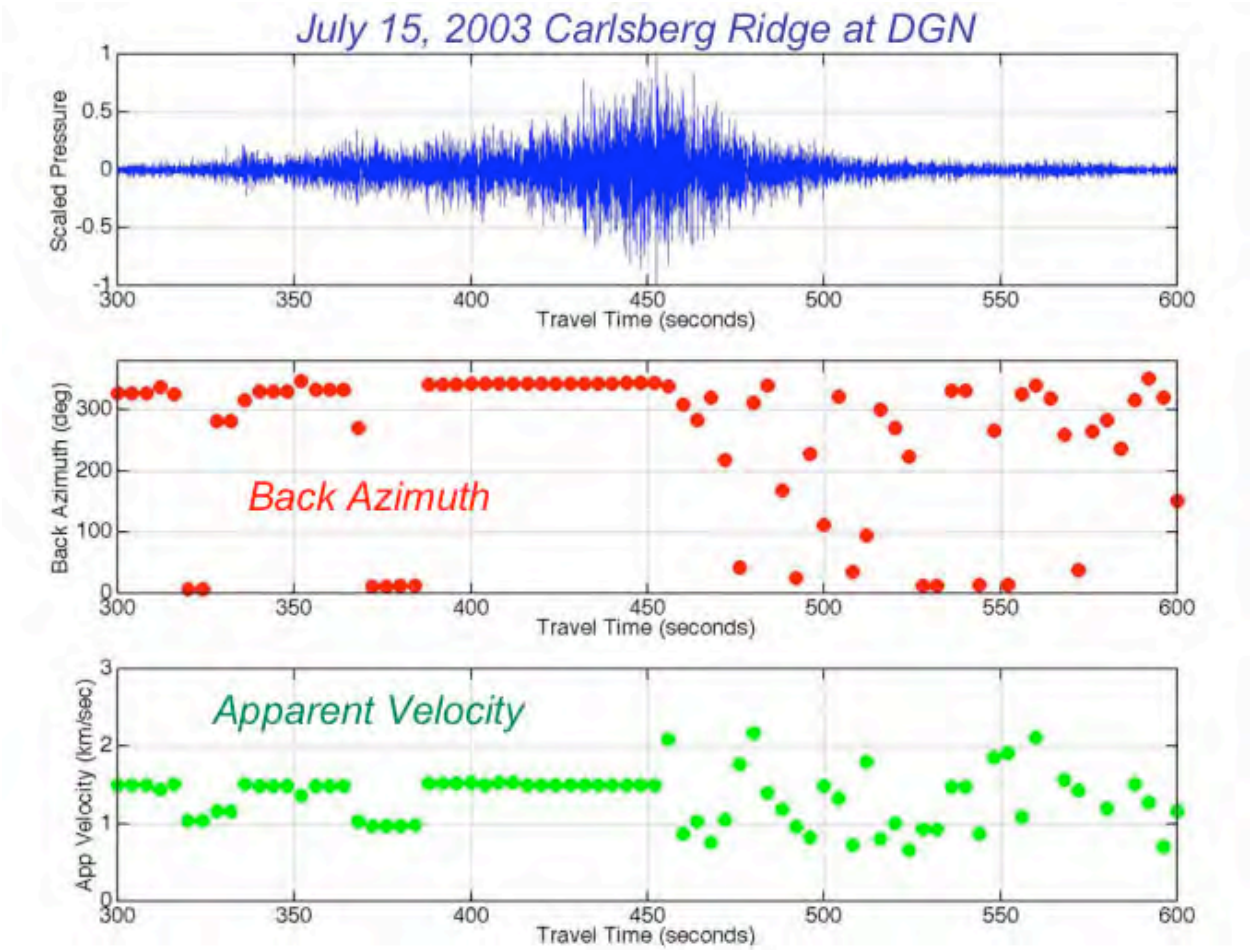


Figure 6. Array processing of the *T* wave signal for the 15 July 2003 earthquake on the Carlsberg Ridge recorded at Diego Garcia north. Three hundred seconds of data are included in the analysis. The Mode-1 peak arrives at the station at a travel time of 450s.

Our second example is that from the 25 July 2002 event off the Carlsberg Ridge near the Chagos Archipelago, shown in Figure 7. This was a smaller event, m_b=4.8, but closer to both Diego Garcia arrays. The *T* wave signal was well recorded at the north array, but is partially blocked on the south array. Array analysis of the data indicates that although the signal-to-noise ratio is high on the north array, the stability of the back azimuth is low, except for an approximately 25-second window just before the Mode-1 *T*-wave arrival at 225-seconds. Contrast this result with the observation at the south array, where the signal-to-noise ratio is much lower for the partially blocked signal. The back azimuth stability is significantly higher at the south station due to increased signal coherence. We hypothesize that this high coherence is due to the lack of back-scattered signals at the south array. Looking at the map in Figure 5, we see that there are no significant bathymetric features behind the south array to produce a back-scattered acoustic field. The back azimuth estimate is thus stable at 300° for nearly 140-seconds of recorded time, giving us robust signal detection.

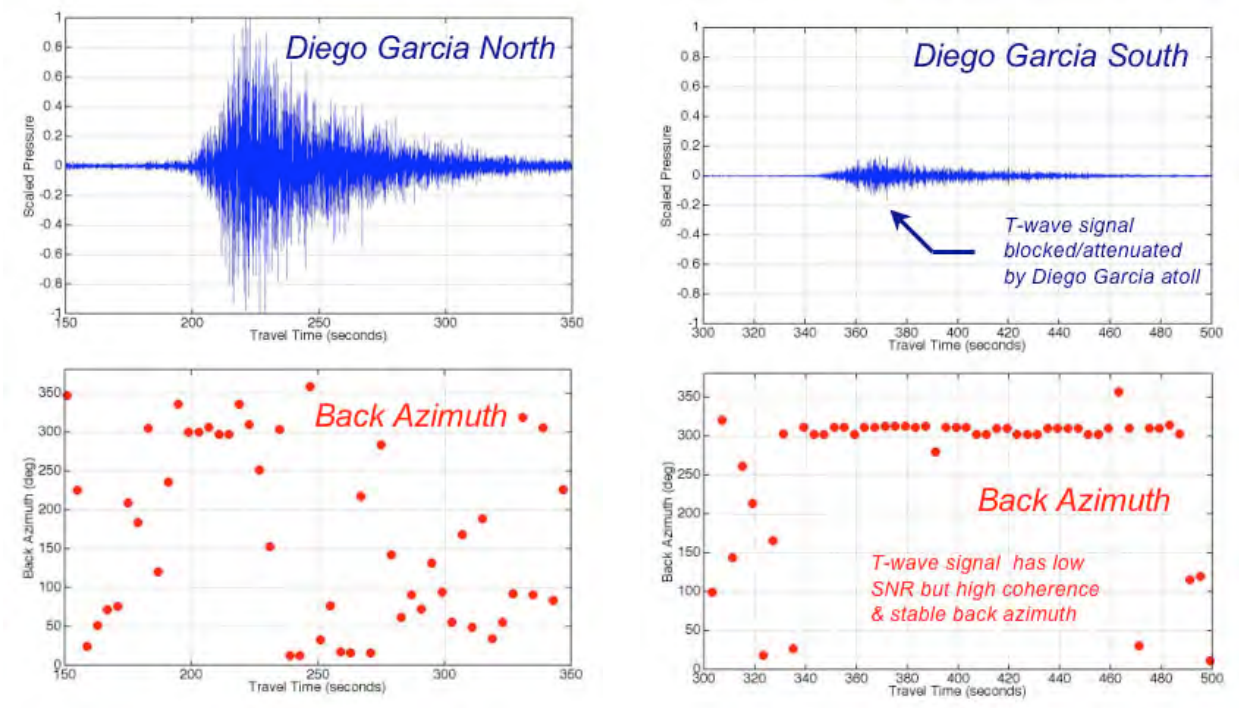


Figure 7. Array analysis at Diego Garcia north and south for the 25 July 2002 event off the Carlsberg Ridge. Although the signal level is high on the north array, the back azimuth estimate is unstable, due to the apparent interference effects of the back-scattered acoustic field from the Chagos Arch. The partially blocked signal on the south array is not affected by back-scatter interference, since there are no significant bathymetric features behind the array.

CONCLUSIONS AND RECOMMENDATIONS

We have identified and integrated two high-resolution bathymetric databases into HydroCAM. These data will allow researchers to better assess the effects of refraction, diffraction, and reverberation on the detection and localization capability of the hydroacoustic network. In addition, we have analyzed a number of hydroacoustic events from our Indian Ocean Ground Truth Database using array processing techniques. Our results illustrate the importance of backscatter and reverberation to the hydroacoustic field around the receivers, especially with respect to signal coherence and the determination of back azimuth.

Further study of these events will allow us to gain more insight into the nature of hydroacoustic blockage, diffraction and its prediction. A complete study, coupling the high-resolution bathymetry to the detailed data analysis is necessary to fully understand these effects on the acoustic field around the arrays.

REFERENCES

Petkovic, P. and C. Buchanan, (2002), *Australian bathymetry and topography grid*. Canberra: Geoscience Australia.

Pulli, J. J. and Z. M. Upton, (2001) "Hydroacoustic Blockage at Diego Garcia: Models and Observations," *Proceedings of the 23rd Seismic Research Review: Worldwide Monitoring of Nuclear Explosions*, pp. 45-54.

Smith, W. H. F. and D. T. Sandwell, (1997), Global Seafloor Topography from Satellite Altimetry and Ship Soundings, *Science*, 277, 1956-1962.

Merchant, B., E. Chael, C. Young (2003) "MatSeis and the GNEM R&E Regional Analysis Tools" in *Proceedings of the 25th Seismic Research Review – Nuclear Explosion Monitoring: Building the Knowledge Base,* Vol. II, pp. 721-728.

LONG RANGE ACOUSTIC PROPAGATION OF HIGH FREQUENCY ENERGY IN THE INDIAN OCEAN FROM ICEBERGS AND EARTHQUAKES

Maya Tolstoy, DelWayne R. Bohnenstiehl and Emily Chapp

Columbia University

Sponsored by Air Force Research Laboratory

Contract No. DTRA01-01-C-0070

ABSTRACT

Naturally occurring sound sources are used to investigate the hydroacoustic propagation of high-frequency energy within the Indian Ocean Basin. These sources include tremor associated with ice movement along coastal Antarctica and moderate-to-large earthquakes associated with tectonic events adjacent to the Central Indian Ridge.

Ice-related signals, with variable spectral characteristics, are recorded throughout the year. The loudest of these ice events can be seen at both the Cape Leeuwin and Diego Garcia South hydroacoustic stations, with the arrivals at Diego Garcia South being attenuated at all frequency bands relative to Cape Leeuwin. The long-range propagation of these signals suggests that energy up to 90 Hz is coupling well through the convergence zone and into the SOFAR channel.

A specific type of ice-related signal, referred to as a 'cusped-pulsed', has been associated spatially with ice streams, which are rapidly flowing ice conduits that drain parts of the shelf into the sea. This identification was achieved through azimuthal and travel time calculations, and comparison of these location estimates with satellite imagery of the area. In addition, a more continuous harmonically-banded signal has been associated with a specific drifting iceberg (B-15D). The accuracy of these locations, as confirmed through satellite ground-truth data, suggests that ice-generated signals may yield a useful high-frequency acoustic source for future studies.

An extremely large (7.6 Mw) earthquake in the northwest Indian Ocean on July 15, 2003 [Bohnenstiehl *et al.*, 2004] has provided very intriguing data with regard to T-wave generation and long-range hydroacoustic propagation. Comparison of arrivals at Diego Garcia North, Diego Garcia South and Cape Leeuwin stations show a strong T-wave arrival at Diego Garcia North, a barely visible lower-frequency T-wave arrival at Diego Garcia South and a strong high-frequency arrival at Cape Leeuwin, despite apparent blockage along the direct path from much of the rupture plane to this station. Travel-time and azimuthal analysis suggests that the earliest T-wave arrival at Cape Leeuwin consists of converted P- and S-wave energy sourced from the eastern scarp of the Chagos and Maldives Archipelagos, at distances of several hundred kilometers from the earthquake rupture. The highest-frequency and highest-amplitude component of the Cape Leeuwin T-wave signal packet exhibits an arrival time consistent with a dominantly hydroacoustic path that may be partially refracted through a bathymetric low to the north of Diego Garcia or represent T-wave energy scattered in the near-field from the region adjacent and to the north of the main rupture. Reflections from bathymetric highs to the north and east of the rupture zone are evident within the T-wave coda.

OBJECTIVES

Propagation of high-frequency energy through the Antarctic Convergence Zone (ACZ) is a poorly understood problem. However, understanding this process is an important problem in signal discrimination. In particular, the high-latitude regions of the southern ocean lack a SOund Fixing And Ranging (SOFAR) channel, and so there has been considerable concern that energy generated in these areas would not be readily detectable using IMS hydrophone stations. Our objectives were to look for signals that could be used to study propagation through the ACZ, as well as studying high-frequency blockage associated with shallow bathymetric features.

Utilizing primarily hydroacoustic data from Diego Garcia South and Cape Leeuwin we have studied the origin of ice-related signals with high-frequency energy and their propagation through the ACZ and over thousands of kilometers through the Indian Ocean SOFAR channel. Utilizing hydroacoustic data from the Diego Garcia North, Diego Garcia South and Cape Leeuwin hydroacoustic stations (Figure 1) we have studied the high-frequency blockage of a particularly large (7.6 Mw) earthquake that showed unusual propagation of low and high frequency energy through areas where significant blockage would have been expected.

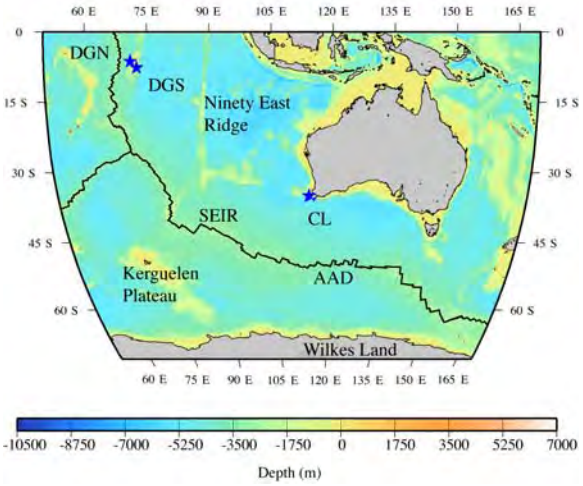


Figure 1. Map of Indian Ocean Basin study area. Blue stars indicate hydrophone triad locations labeled as CL (Cape Leeuwin), DGS (Diego Garcia South) and DGN (Diego Garcia North. Mid-ocean ridges shown as black lines with the following geographic location labels: Southeast Indian Ridge (SEIR), Australian-Antarctic Discordance (AAD), Ninety East Ridge, Kerguelen Plateau, Wilkes Land section of Antarctica. Color bar indicates sea floor bathymetry in meters relative to sea level.

RESEARCH ACCOMPLISHED

Propagation of Ice-Related Signals through the Convergence Zone

Variable Harmonic Tremor (VHT)

The dominant tremor type observed at the DGS and CL stations consists of multiple harmonic bands with spectral peaks that fluctuate in frequency through time, hereinafter referred to as Variable Harmonic Tremor (VHT) (Figure 2). These tremors are comparable to the iceberg-related signals observed by Talandier *et al.* [2002] at lower-frequencies (< 25 Hz) using Pacific Seismic Network (PSN) seismic stations. Our sound-channel based observations indicate a fundamental frequency that is typically within the 4-10 Hz range (Figure 2a,b panel 5), but can reach as high of 30 Hz in some instances (Figure 2c, panel v). As many as eight spectral bands can be seen in some tremor packets, with significant power above 80 Hz (Figure 2b). VHT signal packets can persist from ~ 1-30 min, but their occurrence is spatially clustered with periods of activity lasting from hours to days.

As illustrated in Figure 2 (panels i and ii), VHT signals commonly exhibit abrupt starts and stops, and in some instances these polychromatic signals evolve from or into a continuous monotonic signal (Figure 2b) or broadband noise (Figure 2a,b,c). Within a signal packet, azimuth estimates do not change significantly through time, despite changes in the spectral character of the signal (Figure 2a,b,c, panel 3). This suggests that these various portions of the signal packet likely originate from the same source region or within a narrow source zone. The received signal strengths of the VHTs at DGS range from 119-133 dB re 1μPa and those at CL range from 126-142 dB re 1μPa (peak-to-peak). Signals were seen throughout the year; however, many of the loudest and longest duration signals were observed during the Austral fall and winter.

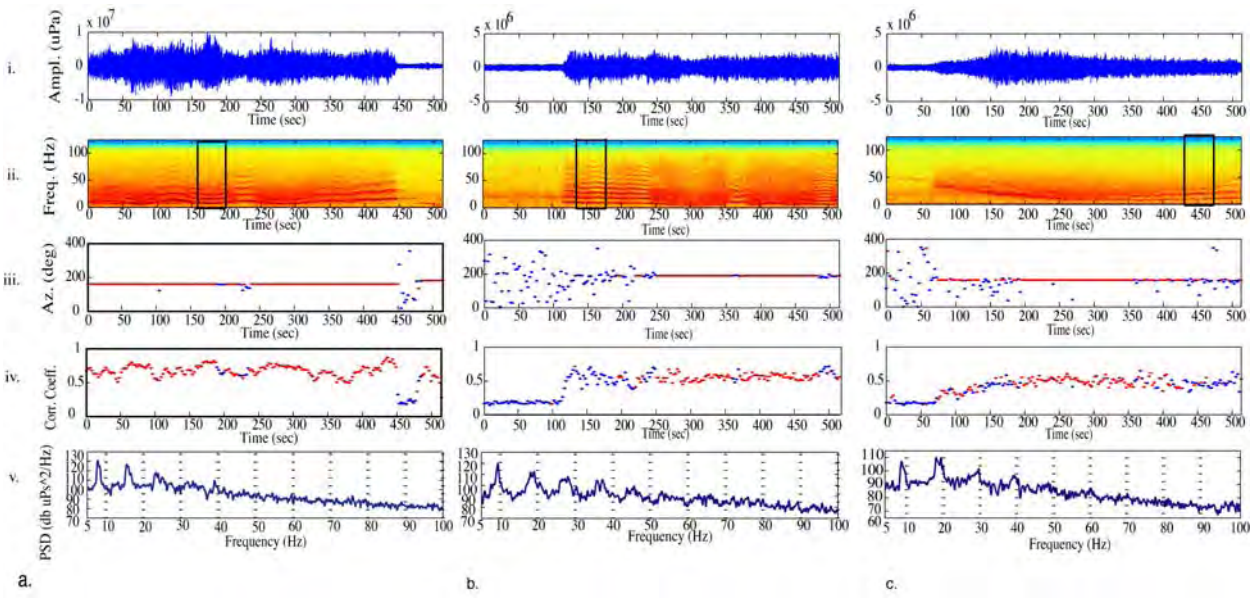


Figure 2. (a, b, c) Signal (i), spectrogram (ii), azimuth (iii), correlation coefficient of azimuth calculation (iv), and power spectral density plots (v) of three different VHT signals recorded on CL hydrophones in 2002, Julian Day (JD) 113 at 12:36; 2003, JD 128 at 23:31; and 2002, JD 208 at 04:19, respectively. Note the harmonic bands of energy with fundamental frequency at ~ 7, ~ 9, and ~ 8 Hz, respectively and the variation in spectral content as each signal progresses with time. Red dots on the azimuth and correlation coefficient panels represent points where the slowness velocity was 1.485 ± 0.03 km/sec. The abrupt onset and termination of these signals are typical of VHTs. Azimuth calculations used a bandpass filtered (5 to 35 Hz) signal using 5 second windows with 50% overlap, and power spectral density plots used the boxed portion of the spectrogram (45 second window) using zero padding and a Hanning window.

In keeping with the observations of Talandier *et al.* [2002], a subset of the loudest VHT episodes can be correlated spatially and temporally with a large (~8 x 27 km) iceberg that migrated westward along the eastern Antarctic coast during 2002 and early 2003 (Figure 3). This iceberg, B-15D, was originally calved from the same ice mass that spawned the B-15B iceberg tracked by Talandier *et al.* [2002] within the Ross Sea. The azimuths for six pairs of VHT signals that were recorded at both the CL and DGS stations are shown in Figure 3a, with shaded areas representing error bounds for each signal. Satellite-derived iceberg locations, color-coded in time, show the westward migrating iceberg B-15D. As iceberg positions are not updated daily, we have used iceberg locations within three days of the VHT arrivals. For each episode, B-15D locations fall within the error bounds of our azimuthal locations.

The set of possible locations that satisfy the differential arrival time (Δt) data for stations CL and DGS are shown in Figure 3b. These curves also show reasonable agreement with the B-15D locations that are temporally closest to the time of the VHT observations. A constant velocity medium of 1.475 km/s provided the best agreement between the locations derived from the intersection of the azimuth pairs (Figure 3a) and the differential arrival time locations, with the absolute value of the residuals being between 1 and 29 seconds.

Most of the VHT azimuths, however, do not align with drifting icebergs. Figure 4 shows azimuthal paths and locations calculated for the VHT signals from 2002 through mid-2003, with green and red lines representing azimuths calculated from CL and DGS, respectively. The prevalence of these signals suggests that VHT noises may be generated by smaller icebergs, which are not being tracked, but litter the Antarctic shelf region, or that VHT signals can be generated also by coastal ice sources. The Wilkes Land region, for example, is populated by a number of outlet glaciers and ice streams, which are distributed throughout the region where azimuthal data indicate the VHT signals originate (Figure 4). As the ice scrapes over the bedrock, harmonic signals could be generated in a manner analogous to an iceberg scraping the shelf. Consistent with this idea, Talandier *et al.* [2002] have identified

at least two tremor episodes not associated with drifting icebergs in January 2001 and November 2000 that appear to originate from the Mertz Glacier (~68°S, 145° E) and the Tucker Glacier (~72°S, 170° E), respectively. Our data shows the area near the Mertz glacier to be very active in 2002 and 2003 with several VHT azimuths aligning with this section of the coast. A direct hydroacoustic acoustic path does not exist, however, between the hydrophone stations and the Tucker glacier within the Ross Sea region.

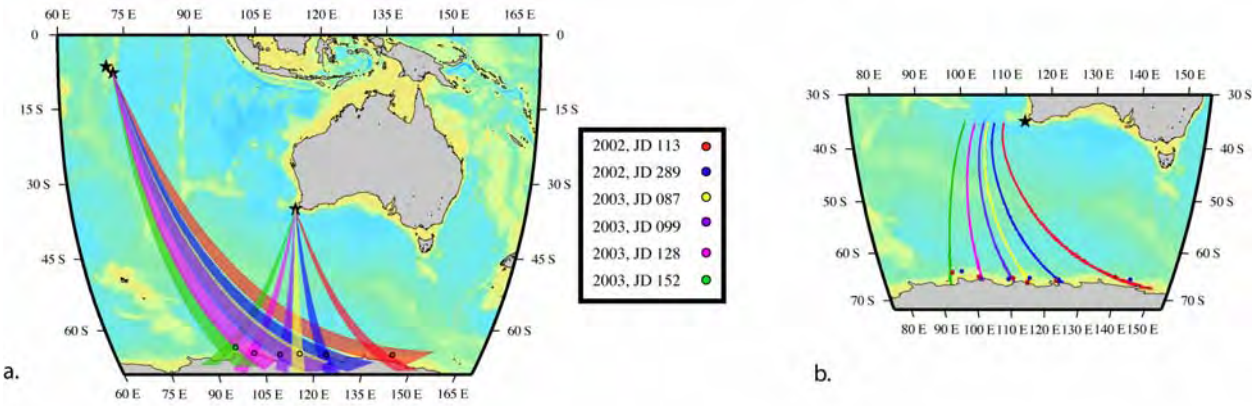


Figure 3. a.) Azimuths of six VHT signals from CL and DGS hydrophones along with iceberg locations. Each colored circle represents the National Snow and Ice Data Center (NSIDC) location of iceberg B-15D at various times throughout 2002 and 2003 (steady westerly migration). Each colored path corresponds to the azimuth and error bounds (±1.26 degrees for CL and ±1.51 for DGS derived from known earthquake locations) calculated from signals arriving at CL and DGS hydrophones within 3 days of the NSIDC reported locations. Black stars represent hydrophone locations. b.) Differential travel time curves for each of the six VHT signals. Each curve represents a set of locations yielding the calculated arrival time differences using a 2 km by 2 km spaced grid and a sound velocity of 1.475 km/sec. Red dots indicate our iceberg locations derived from azimuths, and dark blue dots indicate NSIDC locations.

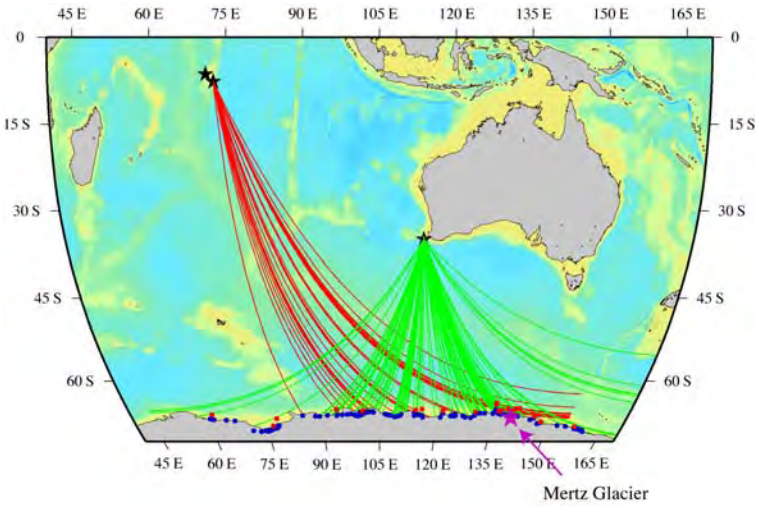


Figure 4. Azimuth traces for VHT signals recorded on CL hydrophones (green) and DGS hydrophones (red) in 2002 and 2003. Blue dots indicate USGS named glaciers, red dots indicate locations for glacial tongues, and black stars represent hydrophone locations. Note the gaps between azimuth paths where no glaciers and ice streams are present. The deficiency in azimuths falling west of 90°E are a result of partial blockage from the geography of the Antarctic coast and the Kerguelen Plateau, and an absence of azimuths east of 160°E may reflect the limits of our detection capabilities. There are a small number of easterly CL azimuths (>150 degrees) that appear to originate from lower latitudes for which we have no explanation.

Cusped-Pulsed Tremor (CPT)

A second signal, a cusped-pulsed tremor (CPT) signal, is characterized by curved harmonic bands of energy in the 4-100 Hz frequency range with fundamental frequencies ranging from 4-10 Hz (Figure 5). The CPT signals were only seen on 31 days in 2002 and on 7 days in 2003 (up to May 2003), occurring primarily in the Austral fall and winter. The received levels of these signals range from 126-139 dB re 1 μPa at CL and 120-131 dB re 1 μPa at DGS. There appearance is very similar to some hydroacoustically-observed volcanic tremor [e.g., Dziak and Fox, 2002], with the duration of a single pulse ranging from 25-60 sec and the interval between pulses ranging from 30-90 sec. Pulsed signal trains can last anywhere from 10 min to over 1 hr. They usually exhibit a near regular pulse spacing (Figure 5a); however, some series have pulses at variable intervals (Figure 5b).

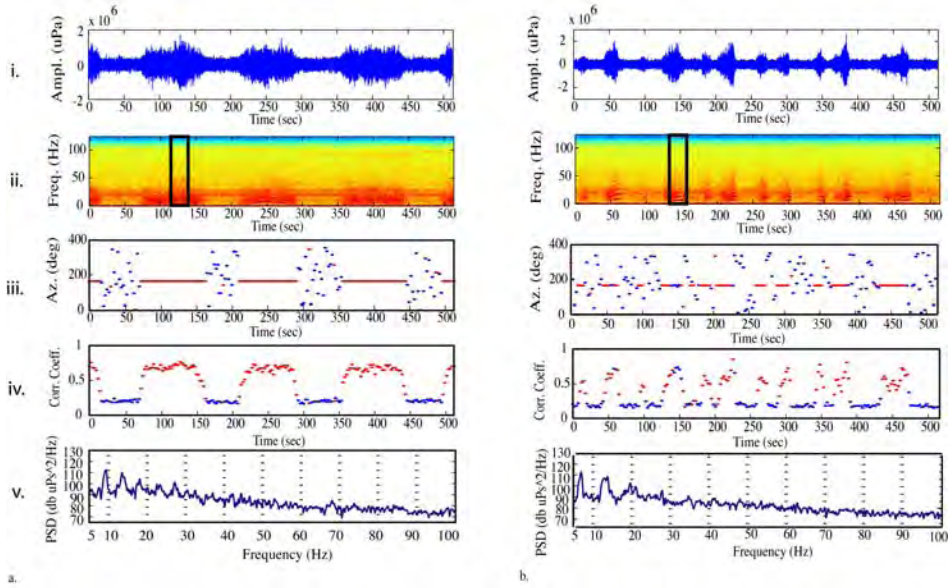


Figure 5. (a and b). Signal (i), spectrogram (ii), azimuth (iii), correlation coefficients of azimuth (iv), and power spectral density plot (v) of pulses in a regularly spaced CPT series (a.) and an irregularly spaced CPT series (b.) recorded on CL hydrophones starting at 2002, JD 160 at 11:07 and 2002, JD 177 at 20:43 respectively. The fundamental frequencies of the series are ~ 9 and ~ 6 Hz with harmonics up to at least 35 Hz. Red dots on the azimuth and correlation coefficient panels represent points where the slowness velocity was 1.485 ± 0.03 km/sec. Azimuth calculations used a bandpass filtered (5 to 35 Hz) signal using 5 second windows with 50% overlap, and power spectral density plots used the boxed portion of the spectrogram (20 second window) using zero padding and a Hanning window.

Azimuth calculations show fixed azimuths throughout each pulse, as well as the entire pulse series (Figure 5, panel iii), with pulses exhibiting high correlations coefficients. Unlike the more continuous VHT signals there is no coherent energy between the pulses (Figure 5, panel iv).

CPT azimuthal locations were checked against iceberg locations from the NSIDC. While icebergs were present within the error bounds of a few signals, the majority of the signals did not originate from known iceberg locations. Moreover, those CPT signals that did have icebergs near their azimuth track were observed later in the year originating from the same location after the iceberg had drifted out of the error bounds—suggesting that the sources for the CPT signals remain fixed.

Unlike the VHT azimuths that included most of the Antarctic coast from 90°E to 160°E, CPT signals only originate from five geographic areas. CPT azimuths are shown in Figure 6a with green and red lines representing azimuths calculated from both CL and DGS, respectively. RADARSAT imagery from the source regions, as estimated from intersecting azimuth pairs, show small ice streams in each of these areas. Free floating ice blocks are observed trailing off some of these ice streams, perhaps indicative of ongoing activity. Figure 6b shows sets of possible CPT

source locations based on the arrival time differences between the CL and DGS stations. Each curve falls within the errors of our azimuth calculated source locations, with the absolute values of Δt residuals ranging from 0.6-47 sec.

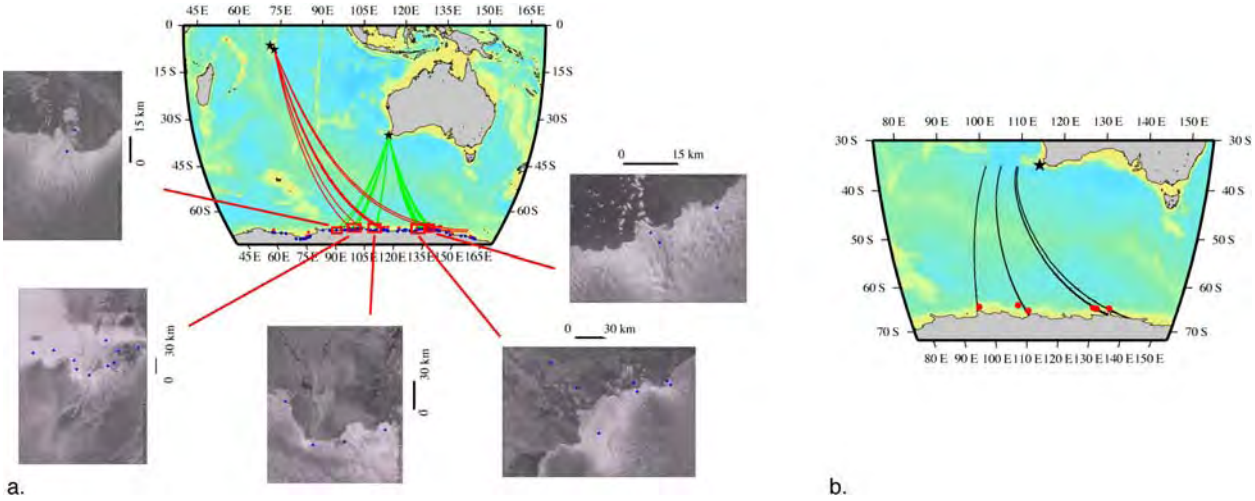


Figure 6. a.) Azimuth traces for CPT signals recorded on CL hydrophones (green) and DGS hydrophones (red) in 2002 and 2003. Blue dots indicate USGS named glaciers, red dots represent glacier tongue locations, and black stars represent hydrophone locations. The red squares show areas where RADARSAT images are taken and the figures around the map are the corresponding satellite images. Blue dots on the images are the same glacier locations as those on the map. Note the presence of several different ice streams connecting the glaciers to the ocean, some with floating blocks of ice trailing from the ends of the streams, which may be indicative of on-going activity. b.) Differential travel time curves for the CPT series where DGS data produced reasonable azimuths. Each curve represents a set of locations yielding the calculated arrival time differences using a 2 km by 2 km spaced grid and a sound velocity of 1.475 km/sec. Red dots indicate the CPT locations for each travel time curve. Note some curves overlap for different CPT locations.

Discussion

The spatial and temporal correlations outlined above argue that the observed tremors are generated in association with drifting icebergs and coastal ice sources, such as outlet glaciers and ice streams. Similarities between the VHT signals described here and ice-related signals reported by Talandier et al. [2002] argue strongly for a common source mechanism. Talandier et al. [2002] have suggested that harmonic nature of the Ross Sea tremors results from resonance with a drifting iceberg or fluid filled cavity within the iceberg. As seafloor scours appear to be common within many polar shelf regions and the icebergs became acoustically quiet after leaving the shelf, they argued that this resonance is excited as the iceberg scrapes the seafloor.

The dominant 4-10 Hz fundamental observed within the VHT signals is consistent with the observations of Talandier et al. [2002]; however, in some instances, these hydroacoustic data show fundamental frequencies exceeding 30 Hz (Figure 2). If similar high-frequency energy was generated during the Ross Sea tremor events, those signals would have been aliased by the PSN seismic sensors—as would many of the high-order overtones in Figure 2. Talandier et al. [2002] have discussed possible types of resonators in some detail. As they point out, the lowest frequency ~3 Hz fundamentals would corresponded to the eigenfrequency of a vertical shear mode within a ~300 m thick ice layer (assuming β=1.8 km/s). This thickness is consistent with that predicted for iceberg B-15, and sufficient to allow the ice mass to scrape across portions of the shelf. Higher-frequency fundamentals (~10-30 Hz) would suggest resonance within an ice layer having a thickness of only a few tens of meters. Other possible resonator scenarios include the excitation of a fluid (water and air) filled cavities within the ice, making the eigenfrequency a complex function of the cavity's shape and size, as well as the impedance contrast between the fluid and surrounding ice mass. Changes in these parameters during ice movement could help to explain spectral fluctuations during the tremor events [Talandier et al., 2002].

Despite the correlation of some VHT signals with a large iceberg being tracked by the NSIDC, our observations suggest that tremor signals also may be linked to the movement of smaller icebergs and/or coastal ice sources along eastern Antarctica. The land-based portion of glacial ice masses and their glacial tongues are known to be active in many areas. These ice tongues extend over the water where they can break up into smaller blocks of ice that could become mobile due to the influence of wind and waves [Menzies et al., 1995]. As with larger drifting icebergs, acoustic signals generated within or near these tongues could radiate energy into the water column.

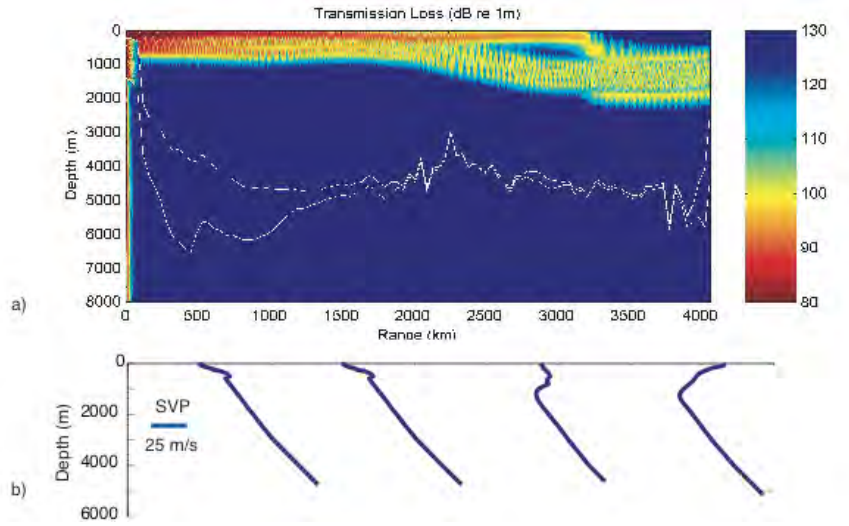


Figure 7. a) Transmission loss model for a 40-Hz source at a depth of 100 m near the Mertz Glacier (~86 S, 145 E). The Cape Leeuwin receiver is located at a depth of 1100 m at a range of ~4100 m. Range dependant sediment thickness is derived from a NOAA sediment thickness database and range dependant sound velocity profiles are taken from the US Navy's Generalized Digital Environmental Model (GDEM) for the month of July (30 minute resolution). Sediment properties: 1600 m/s sound speed, density 1.5 g/cm^3,compressional attenuation of 0.15 dB/m/kHz. Bottom properties: 2300 m/s sound speed, density 2.21 g/cm^3, compressional attenuation of 0.05 dB/m/kHz. The PE code UMPE2DBB was used in this calculation [Smith, 2001]. b) Sample sound velocity profiles along the transect.

The abrupt onset and termination of many of the VHT signals (Figure 2) suggests the ice is moving in stick-slip manner, and there is mounting evidence for such behavior in within Antarctic glaciers and ice streams. For example, a continuous GPS study recently demonstrated tidally influenced stick-slip motion within a Siple Coast ice stream in western Antarctica. Individual slip events lasted from 10 to 30 minutes with an average slip velocity of ~1 m/hr [Bindschadler *et al.*, 2003]. This duration is similar to the VHT signals observed in the IMS hydroacoustic data, and the surging nature of the ice movement could act to excite these tremor signals. Similarly, Ekstrom *et al.* [2003] have identified a series of unusual long-period surface wave events (equivalent to a > 4.5 M earthquake) located in glacial regions, including tectonically stable areas such as Greenland and coastal Antarctica. As opposed to a standard double-couple earthquake source model, the radiation pattern of these events could be modeled as a single force couple, as previously applied to landslides. This led the authors to suggest that these events were generated by stick-slip glacial quakes.

Although CPT signals are observed to originate from a subset of the active ice streams within the Wilkesland region, the environmental conditions necessary to generate these signals are not well constrained. The near uniform spacing of CPT signals is reminiscent of a geyser-like process, as observed within subareal volcanic systems. Consequently, we speculate that the process may be hydrologically driven, with a periodic recharge that allows the glacier to slip in a repeating manner. It is not clear why some ice streams generate CPT signals and others do not.

In high latitude regions, colder oceanic temperature profiles do not facilitate the existence of a deep sound channel. Acoustic energy from a shallow depth source along the Wilkesland shelf must initially propagate as a surface reflected phase, crossing the Antarctic convergence zone, and later becoming coupled within the mid-latitude sound

channel. In Figure 7, a parabolic equation (PE) code [Smith, 2001] is used to investigate propagation from a source near the Mertz Glacier. This model confirms that sound propagation from Antarctica is still possible in the absence of a SOFAR channel and that energy can be transferred efficiently into the sound channel, where the IMS hydrophones are moored. Transmission loss estimates using this model for a path to CL are ~100 dB, implying maximum source levels of more than 240 dB re 1μPa @ 1 m.

Blockage of High Frequency energy from Earthquake Sources

On July 15, 2003, an extremely large (7.6 Mw) earthquake occurred in the northwest Indian Ocean [Bohnenstiehl *et al.*, 2004]. Comparison of arrivals at Diego Garcia North, Diego Garcia South and Cape Leeuwin stations shows a strong T-wave arrival at Diego Garcia North, a barely visible lower-frequency T-wave arrival at Diego Garcia South and a strong high-frequency arrival at Cape Leeuwin (Figure 8), despite apparent blockage along the direct path from much of the rupture plane to this station. This large event, along with its well-located aftershocks, allows some interesting observations to be made regarding blockage.

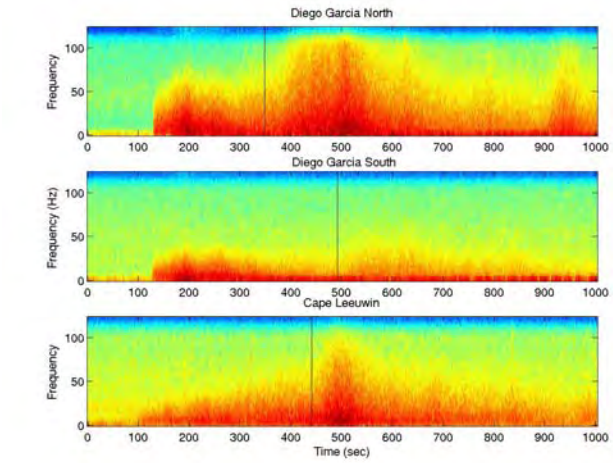


Figure 8. Spectrogram for earthquake arrival at Diego Garcia North (top), Diego Garcia South (middle), and Cape Leeuwin (bottom). Thin vertical black line indicates predicted start time of T-wave arrival. Abrupt P-wave arrivals are evident at both Diego Garcia stations. Cape Leeuwin shows a prolonged build up of energy before the primary T-wave.

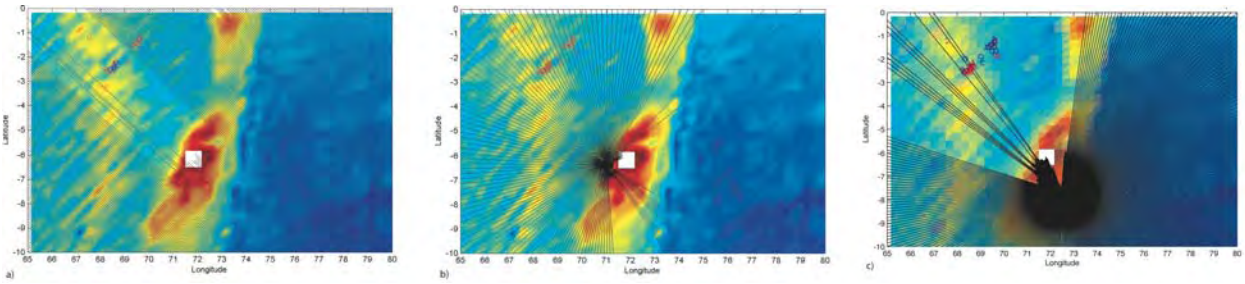


Figure 9. Blockage maps with 50 m stop criteria and 1 degree rays for Cape Leeuwin (a), Diego Garcia North (b) and Diego Garcia South (c). Red circles – detected aftershocks. Blue circles – not detected aftershocks. White square – Diego Garcia.

Figure 9 shows blockage maps for all three stations with a 50-m cut off, and earthquake locations color coded to indicate if they were observed (red) or not (blue) at the given station. The maps show that the 50-m cut off is a fairly good indication of when signals will be blocked. However, those observed signals that traveled over relatively shallow areas were quite weak and lacking in high-frequency energy.

The strike-slip mainshock event ruptured ~ 210 km of crust, with an estimated rupture duration of ~ 65 seconds. T-wave azimuths from arrivals at Diego Garcia North indicate that the bulk of the T-wave energy was generated at the moment centroid location, which is consistent with that being the location of the maximum earthquake energy release.

Arrivals at Cape Leeuwin, particularly for the mainshock provide some surprising results. Travel-time and azimuthal analysis suggest that the earliest T-wave arrival at Cape Leeuwin consists of converted P- and S-wave energy

originating from the eastern scarp of the Chagos and Maldives Archipelagos, at distances of several hundred kilometers from the earthquake rupture. Figure 10 shows the varying azimuth associated with the long T-wave arrival at Cape Leeuwin, along with predicted arrival azimuths and times for P-wave and S-wave energy from the epicenter, moment centroid and end of rupture for a variety of bathymetric features (Figure 11).

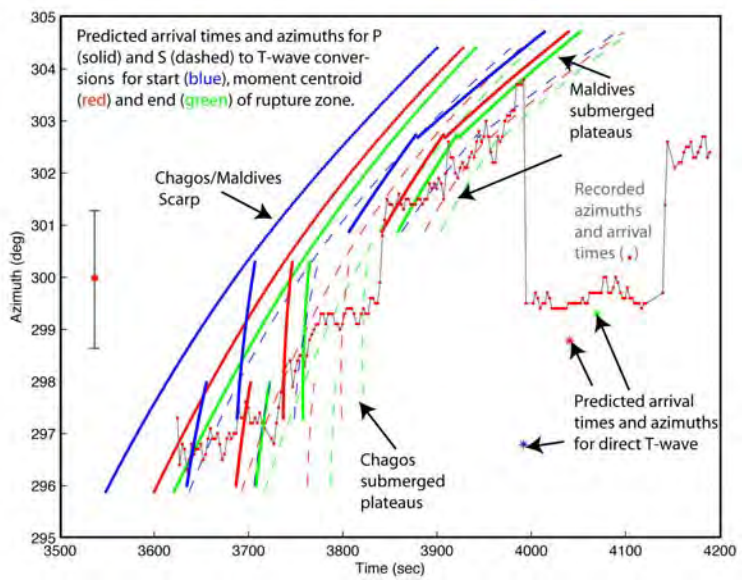


Figure 10. Calculated azimuths (red dots) for the T-wave arrival at Cape Leeuwin (see Figure 8 – bottom) compared with predicted arrival times and azimuths for P-wave (solid lines) and S-wave (dashed lines) that converted to T-waves on various bathymetric features of the Chagos and Maldives Archipelagos (see Figure 11). Predictions are made for energy coming from the start of the rupture (blue), the centroid moment (red) and the end of the rupture (green). Also shown are predicted arrival times and azimuths for the direct T-wave arrival (*). Note last set of azimuths (~4150-4200 seconds) may indicate a reflected arrival from the more northern features on the Maldives Archipelago.

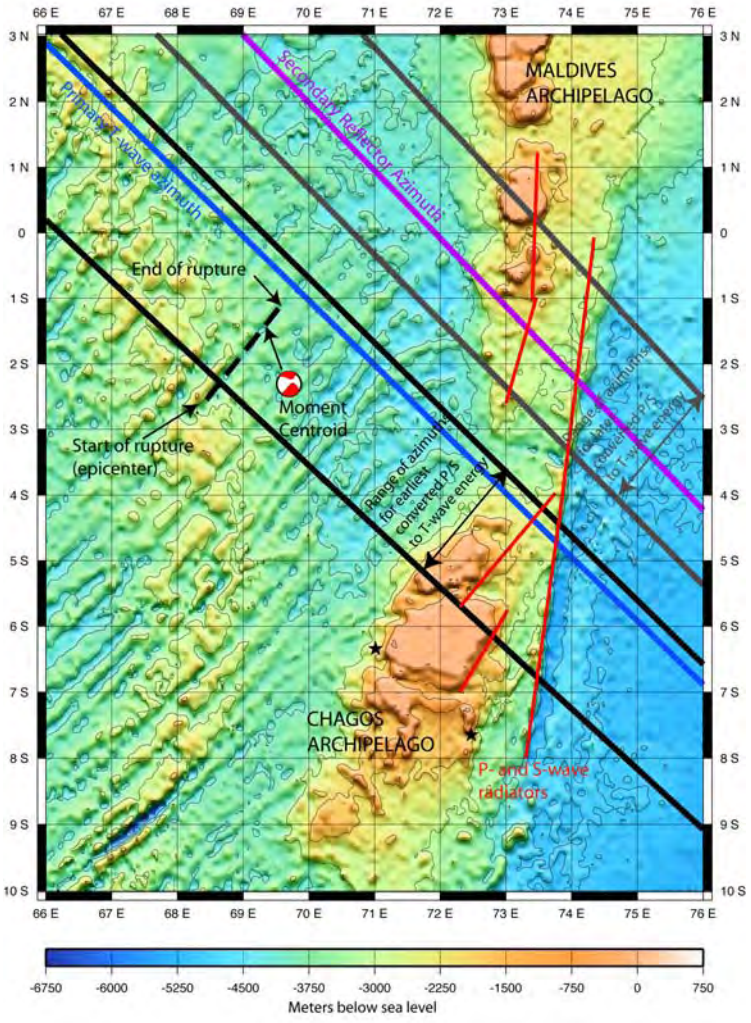


Figure 11. Primary bathymetric features associated with Cape Leeuwin T-wave arrival from July 15th, 2003 7.6 Mw earthquake. Earthquake rupture area is indicated by the dashed black line with the start, moment centroid, and end positions noted. Black and gray lines indicate the range of azimuths for converted P/S-wave to T-wave energy observed for the earlier and later arrivals respectively (see Figure 10). Red lines indicate likely radiators, with arrival times modeled in Figure 10. The blue and purple lines indicate azimuths for the primary high frequency direct T-wave arrival and a later reflected arrival respectively.

The direct T-wave energy, which arrives at a time consistent with an exclusively water-borne pathway, comes in at an azimuth a little to the north of the end of the rupture, and aligned with a deeper area between the Chagos and Maldives Archipelagos. It appears therefore that the energy was either refraction around the northern area of the Chagos bathymetric highs, or that it represents significant excitation of the seafloor north of the actual rupture zone. The latter is reasonable given the magnitude of the earthquake and the relative roughness of the seafloor adjacent to this slow spreading ridge segment. This arrival is the only portion of the T-wave train that contains significant high-frequency energy. Lower energy reflections from Maldives bathymetric highs to the north and east of the rupture zone are evident within the T-wave coda and show azimuths consistent with the Maldives submerged plateaus.

CONCLUSIONS AND RECOMMENDATIONS

We have characterized two hydroacoustic sources capable of exciting high-frequency energy that propagates over 8000 km through the Indian Ocean. From hydroacoustic data, azimuth calculations and satellite imagery, we have defined surging ice streams and drifting icebergs as the dominant signal generators along the coastal sections of Wilkesland, eastern Antarctica. The harmonic nature of these signals supports the idea of resonating ice masses, and the calculated azimuths allow specific areas of active ice movement to be located. These naturally occurring sources provide excellent tools for more details studies of long-range propagation of high-frequency energy through the ACZ.

To better utilize these natural sources, ground-truthing of source locations and near field characterization of the signals should be accomplished through hydrophone measurements made within 10-100's of km of the source, well within the ACZ. Utilizing such tools would allow individual sources to be well located, and provide an improved source model for use in investigating propagation across the ACZ.

Our studies of hydroacoustic blockage support the idea that T-wave energy can be generated from multiple scatters. It also appears that high frequency energy generated by near-field scattering from the seafloor may be detected, even though the direct path may be partially or completely blocked. This scattered energy represents the highest frequency, highest amplitude portion of the arrival for the July 15, 2003 mainshock. While blockage appears fairly complete for smaller events when bathymetry of < 50 m is encountered, some energy is still transmitted at relatively shallow depths > 50 m. Further rigorous analysis of large earthquake sources of opportunity would help confirm these observations, and provide more detailed understanding of the processes.

REFERENCES

Bindschadler, R.A., M.A. King, R. B. Alley, S. Anandakrishnan, and L. Padman, (2003) Tidally controlled stick-slip discharge of a West Antarctic ice stream, *Science*, 301, 1087-1089.

Bohnenstiehl, D.R., M. Tolstoy, and E. Chapp (2004), Breaking into the Plate: A 7.6 Mw Fracture Zone Earthquake Adjacent to the Central Indian Ridge, *Geophys. Res. Lett.*, 31, doi:10.1029/2003GL018981.

Dziak, R.P., and C.G. Fox (2002), Evidence of harmonic tremor from a submarine volcano detected across the Pacific Ocean basin, *J. Geophy. Res.*, 107, 10,1029-10,1044.

Ekstrom, G., M. Nettles, and G.A. Abers (2003), Glacial earthquakes, *Science*, 302, 662-624.

Menzies, J. (1995),The dynamics of ice flow, in: J. Menzies (Ed.), Modern Glacial Environments: Processes, Dynamics and Sediments, Buterworth Heinemann Ltd., Oxford, 139-196.

Smith, K.B. (2001), Convergence, stability, and variability of shallow water acoustic predictions using a split-step Fourier parabolic equation model, *J. Comp. Acoust.*, 9, 243-285.

Talandier J., O. Hyvernaud, E.A. Okal, and P.-F. Piserchia (2002), Long range detection of hydroacoustic signals from large Icebergs in the Ross Sea, Antarctica, *Earth and Planet. Sci. Let.*, 203, 519-534.

Radionuclide Monitoring

TRIPLE COINCIDENCE RADIOXENON DETECTOR

Justin I. McIntyre, Craig E. Aalseth, Theodore W. Bowyer, James C. Hayes, Tom R. Heimbigner, Scott Morris, and Paul L. Reeder

Pacific Northwest National Laboratory

Sponsored by National Nuclear Security Administration
Office of Nonproliferation Research and Engineering
Office of Defense Nuclear Nonproliferation

Contract No. DE-AC06-76RLO 1830

ABSTRACT

The Automated Radioxenon Sampler/Analyzer (ARSA) built by Pacific Northwest National Laboratory (PNNL) is one of the world's most sensitive systems for monitoring the four radioxenon isotopes ^{133}Xe, ^{133m}Xe, ^{131m}Xe, and ^{135}Xe. However, due to size, weight, and power specifications appropriate to meet treaty-monitoring requirements, the ARSA is unsuitable for rapid deployment using modest transportation means. To transition this technology to a portable unit that can be easily and rapidly deployed can be achieved by significant reductions in size, weight and power consumption if concentration were not required. As part of an exploratory effort to reduce both the size of the air sample and the gas processing requirements PNNL has developed an experimental nuclear detector to test and quantify the use of triple coincidence signatures (beta, conversion electron, x-ray) from two of the radioxenon isotopes (^{135}Xe and ^{133}Xe) as well as the more traditional beta-gamma coincidence signatures used by the ARSA system. The additional coincidence requirement allows for reduced passive shielding, and makes it possible for unambiguous detection of ^{133}Xe and ^{135}Xe in the presence of high ^{222}Rn backgrounds. This paper will discuss the experimental setup and the results obtained for a ^{133}Xe sample with and without ^{222}Rn as an interference signature.

OBJECTIVE

There are currently four automated platforms that have been developed to detect the four radioxenon isotopes, ^{133}Xe, ^{133m}Xe, ^{131m}Xe and ^{135}Xe. These systems primary mission is to monitor for clandestine underground nuclear explosions, and several publications discuss both the IMS and the radioxenon systems; CTBT/WGB/TL-11/5/Rev. 4 (1999); Auer et al. (2004); and L. E. DeGeer (1995). The Automated Radioxenon Sampler/Analyzer (ARSA) is one such system that is currently under commercial development, see Bowyer (2002). All of these systems sample large volumes of air and have low minimum-detectable-concentrations (MDC). These requirements have by necessity, led to large, heavy systems that are loud, consume large amounts of power and make them inappropriate for man-cartable equipment that can be easily and rapidly deployed, or deployed on moving platforms.

The current technology uses a "brute force" method to separate the ambient xenon from the air (ambient xenon accounts for less than 1 ppm of air). Current technology typically uses a series of chemical adsorbent materials (charcoal and mole sieve in the case of the ARSA) to collect and concentrate the xenon so that it can be counted in a small volume beta-gamma coincidence detector (see Reeder *et al* (2004) for a detailed description of the coincidence spectrometer). The collection method is very efficient at collecting ambient radon and with the large volumes of air collected the interference from the radon daughters would easily obscure all but the largest concentrations of radioxenon. To remove the radon, requires additional separation columns and traps and thus increases the size and power consumption of the system. Significant reductions in size, weight and power consumption can be achieved if preconcentration were not required and the removal of radon was no longer a necessity.

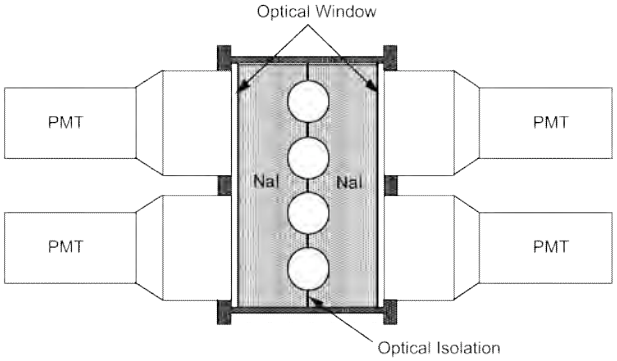


Figure 1. Diagram of the Nai (Tl) saddle detector for the ARSA system.

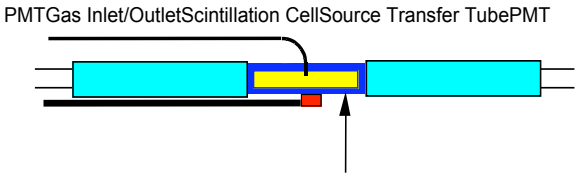


Figure 2. Schematic representation of plastic scintillation beta cell with photo-multiplier tubes, gas transfer line and calibration source transfer tube.

The ARSA nuclear detector (see figures 1 and 2) uses a beta-gamma (β, γ) coincidence to detect ^{133}Xe and ^{135}Xe. The two metastable xenon isotopes, ^{131m}Xe and ^{133m}Xe, emit only a conversion electrons (CE) and x-ray (for more detail see McIntyre (2000)). The x-rays and gammas are detected in the two NaI(Tl) saddle detectors (figure 1) and plastic scintillator beta cells occupy the four holes in the detector. The beta and (CE) are detected in the 6 cc plastic scintillation cell shown in figure 2 along with the two photomultiplier tubes (PMT), gas transfer tube and the calibration source transfer tube. The geometry provides nearly complete coverage for the decay process making the ARSA detector very efficient with greater than 60% efficiency for gammas and x-rays and greater than 80% efficiency for beta and CE.

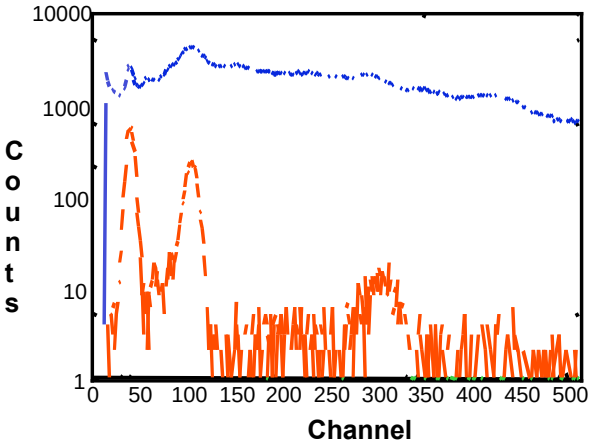


Figure 3. A beta-gated gamma-ray spectrum showing the significant reduction in the background when a beta-gamma coincidence is used.

The coincidence nature of the physics decay process allows for a dramatic reduction in the ambient background caused by cosmic rays and terrestrial gammas and x-rays. Figure 3 shows the difference in the between the gamma singles spectrum, the top blue curve and the beta-gated gamma spectrum, the lower red curve. The beta-gated spectrum clearly shows the

30-keV x-ray and 80-keV gamma-ray of ^{133}Xe as well as the 250-keV gamma-ray of ^{135}Xe. The reduction in the dominant Compton background in the ungated gamma spectrum is dropped by three orders of magnitude when a coincidence is required.

Figure 4 shows the beta-gated, x-ray/gamma response of ^{133}Xe (green circles) and ^{214}Pb plus ^{214}Bi (blue triangles). The ^{214}Pb and ^{214}Bi are daughter products of ^{222}Rn and are a significant source of interference. Note that ^{135}Xe is not present in this sample but it would appear at 250-keV and also has a significant interference problem caused by ^{214}Pb.

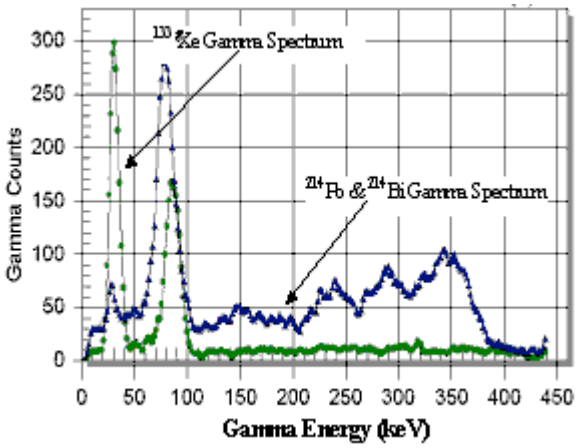


Figure 4. A beta-gated spectrum of a ^{133}Xe sample (green circles) and a beta-gated radon daughter spectrum, ^{214}Pb, (blue triangles).

In addition to (β, γ) and (CE, x-ray) coincidences ^{133}Xe and ^{135}Xe have a triple coincidence (β, CE, x-ray) that can be exploited. Requiring three detectors to register something simultaneously would further reduce the background and reduce the interference from the dominant 80-keV ^{214}Pb and ^{214}Bi peak. This triple coincidence detection can be achieved by using a highly segmented detector. Such a detector could achieve Compton scattering background rates approaching zero and be able to dramatically suppress the radon interference. For long enough count times ^{133}Xe and ^{135}Xe could be detected without any sample purification or preconcentration. A radioxenon measurement device could be designed that could be carried to the field with similar sensitivity as the current state-of-the-art.

RESEARCH ACCOMPLISHED

The goal of this project was to build and test a new radiation detector for radioxenon that could eliminate the need for chemical separations altogether by measuring all of particles emitted from ^{133}Xe and ^{135}Xe simultaneously. This is a major step in the evolution of radioxenon detection techniques and represents the only conceivable approach to drastically changing this type of monitoring. It will allow real-time radioxenon detection from several platforms that are currently too restrictive for existing equipment because of weight, size and power requirements.

The major research of this project was to develop a segmented detector for CE and betas and an appropriate detector for x-rays. Figures 5 shows the test detector that was built. It consists of a 60 cc gas cell made up of two paddles of 1.0 mm thick scintillating plastic to detect the beta particles in one paddle and the CE in the other. A thin aluminized Mylar sheet has been stretched between the two paddles to prevent the scattering of scintillation light between the two paddles. Each paddle is viewed by four PMT's and crude position sensitivity is possible with very little post data acquisition processing. The scintillator planes are 2 cm apart to create a 60 cc gas cell (beta-cell). To prevent the scintillation light from one plane of the scintillator from being seen by the other the two planes are separated by a thin sheet of aluminized Mylar. The two scintillator paddles are 2 cm apart and a gas tight inlet tube is located at the top of the assembly for the introduction of gas samples. Two 5"x2" NaI detectors can be placed against each of the scintillator paddles to provide gamma and x-ray detection. These detectors have good energy resolution and high stopping power for the low energy gamma/x-rays from the

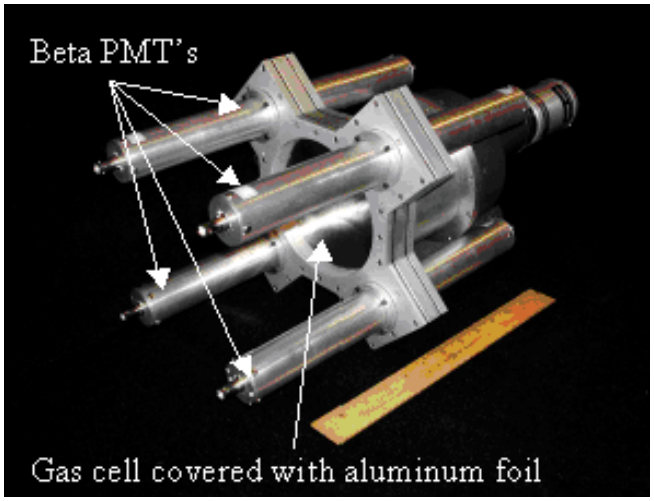


Figure 5. Pictures of the SSXD test detector (note 12" ruler for scale).

radioxenon isotopes. The detectors are also easy to calibrate and integrate into data acquisition systems. The detector assembly was energy calibrated with several sealed gamma-ray line sources and ^{133}Xe and radon gas sources. Modeling of the detector clearly indicated that the ambient background from a triple coincidence would be low and most of the events would be cosmic rays and have very high-energy deposition in the plastic and NaI.

Each PMT had to be gain matched so that nonlinear response was minimized. With each PMT for a single paddle giving the same response it was possible to sum the PMT signals together to give a total signal that was proportional to the total energy deposition in each paddle. Figure 6 show a histogram of the response of paddle 1 vs. paddle 2. The counts in the histogram require signals from both paddles and indicated either a (β, CE) coincidence or a high energy cosmic ray going through both paddles. The triangular low-energy region was the region where (β, CE) coincidence from the ^{133}Xe were most likely to occur and the triangular high-energy region was where cosmic rays were most likely to occur and could be rejected from further analysis.

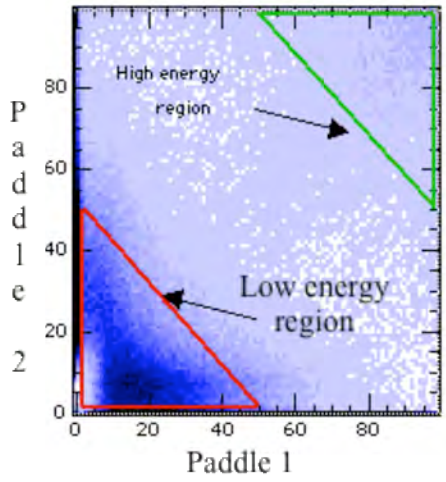


Figure 6. This 2-dimensional histogram is the summed response of all four PMT's on beta-cell paddle 1 vs. the summed response of all four PMT's on paddle 2.

An additional analysis parameter was calculated to give a crude position of the events in a given paddle. This parameter used the response from all four PMT's of a single paddle and is plotted in figure 7. The green indicates no counts and the white indicates high counts. The highlighted lines indicate saturation of the amplifier-ADC channel for one of the PMT's. For future detectors the ability to accurately determine event position would allow an additional method to reduce the interference of radon. Radon gas particles after the first alpha decay will bind strongly to the detector walls and hence emit subsequent alphas and betas from decays in the same location.

Additional studies indicated that the detector would be sensitive to the levels of stable xenon that were injected into the gas cell because xenon is a high-density gas. The detector has the greatest efficiency when there are small volumes of Xe gas. The other constituents of ambient air, O_2, N_2, etc. play a much smaller role in γ/x-ray attenuation and β/CE energy loss than xenon. Modeling also indicated that the solid angle would be sufficient for the test detector (~20%), but it is anticipated that later models for an early proto-type would attempt to achieve 50% or better. The current ARSA beta cell has a solid angle of ~80%.

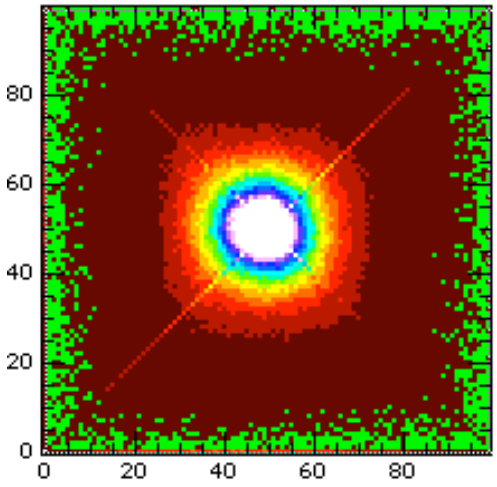


Figure 7. A 2-dimensional histogram that gives a crude position plot of events for one of the beta-cell scintillating paddles.

After the gain matching of the PMT's was completed data was taken using a high- level ^{133}Xe spike (~100 Bq). The ^{133}Xe spike was injected into the cell and the double coincidence response was measured (see figure 8, red curve). The 30-keV x-ray and 80-keV gamma-ray lines are both present and the ratio between the two peaks is well within the range of the current ARSA beta-gamma detector. This indicates that the efficiency for both detectors is comparable for the low energy gamma and x-ray. Only the low energy gamma-ray region (0-150 keV) is shown, as this is the region of most interest. The detector electronics were than modified to accept only triple coincidence events (both scintillator paddles and one of the NaI detectors) and the results are presented in figure 8 as well (green curve). The 30-keV peak is clearly present while the 80-keV is suppressed. It is not clear why there were any events in the 80-keV peak as these events are not triple coincidence events and it is felt that some sort of cross talk in

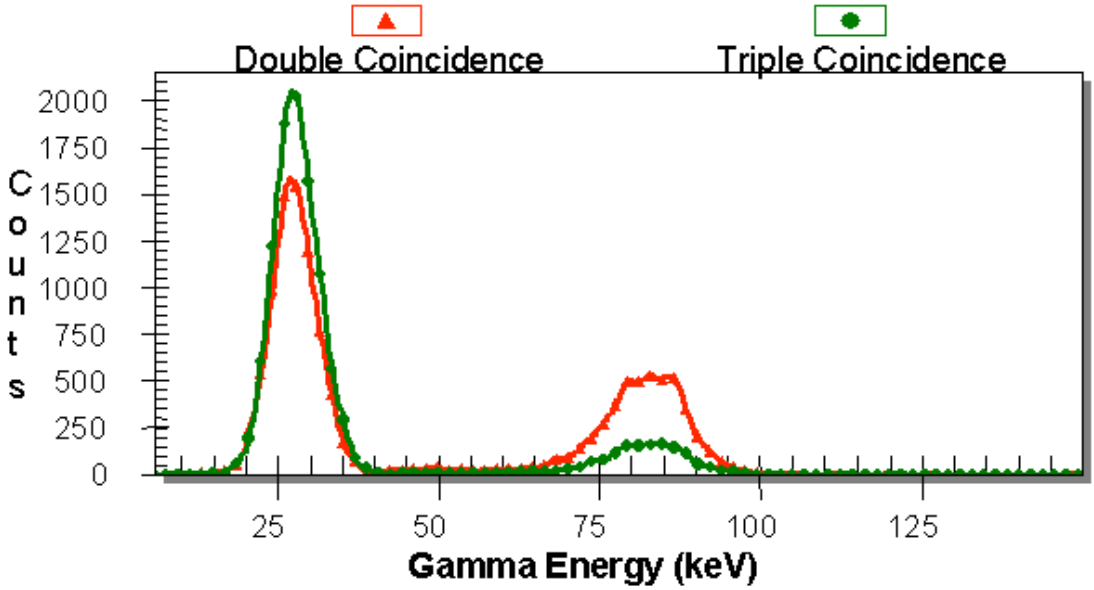


Figure 8. Histogram showing beta gated gamma spectrum with beta only gating (red triangles) and beta plus CE gating (green circles).

the electronics must be occurring. In an ideal detector there would be no counts in the 80-keV region and further optimization of the detector geometry and the readout electronics is necessary to achieve this result.

The next test was to add a spike of comparable strength of radon and measure the double and triple coincidence events. The results of this test are shown in figure 9. As in figure 8 the green curve represents the double coincidence gated gamma-ray spectrum and the red curve is the triple coincidence gated gamma spectrum. A significant reduction in the Compton scattered background is apparent in the triple coincidence data. A cut on high energy beta plus CE shows that the radon interference is reduced dramatically and it will now become possible to measure much lower levels of radioxenon concentrations in the presence of high radon backgrounds. As in figure 8 the green curve is a double coincidence and it is clear that the radon daughter ^{214}Pb x-ray at 80-keV is a significant interference term for the 80-keV gamma ray of ^{133}Xe. For lower concentrations of ^{133}Xe even the 30-keV line will be completely obscured by the radon interference. A significant reduction of the Compton scattering interference is seen and much lower (2-3 orders of magnitude) concentrations of ^{133}Xe can now be measured with a high radon background.

Using the solid angle, efficiency and the ambient background that the detector registered an MDC of ~7 Bq/m^3 of air was determined for the current test detector. This result is very high in comparison to the state of the art by approximately 4 orders of magnitude and is driven by the small quantity of gas that is sampled (1 liter in this case). Crude concentration techniques would dramatically decrease this MDC. The MDC falls linearly with an increase in sampled gas. Such concentration methods would increase the size and power consumption of a unit with a trade off in much lower MDC's (2-3 orders of magnitude).

Additional improvements can be made in the overall detector design and potentially the readout electronics. For instance using a segmented phoswich style detector as outlined in Ely (2003). Phoswich detectors are a set of two or more scintillating detectors that give a different response depending on the particle detected. This would have the effect of having both the gamma and beta detectors viewed by half the total number of PMT's that would normally be used, reduce the overall detector size, and provide superior beta and CE separation.

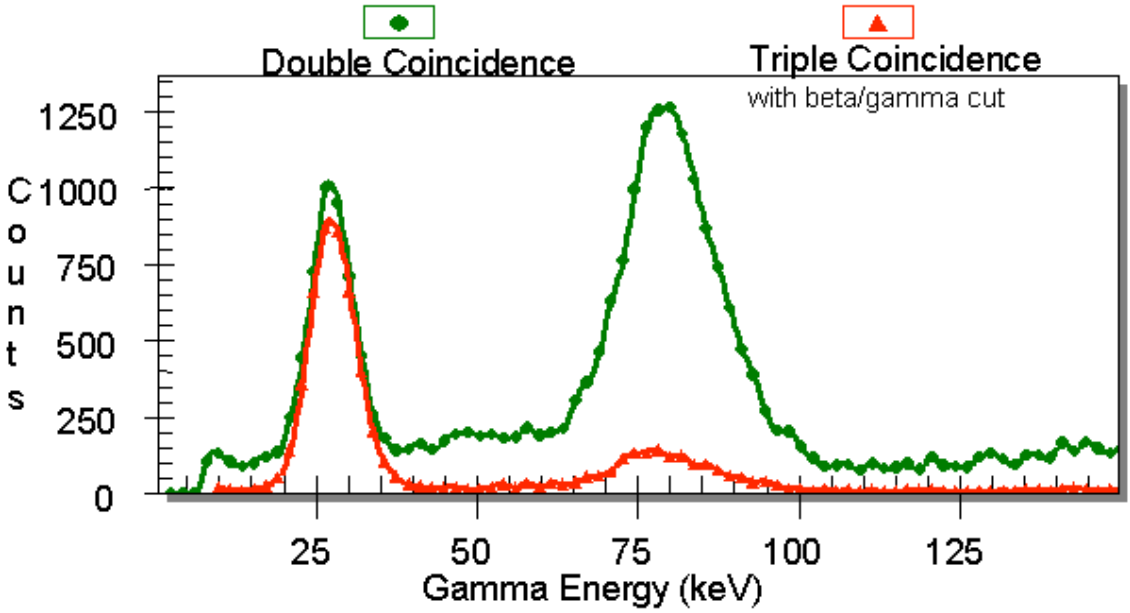


Figure 9. This histogram shows the beta-gated gamma spectrum of a mixed ^{133}Xe and radon spike with equal source strengths of both isotopes.

CONCLUSIONS

From data taken from the test detector it is clear that is possible to detect ^{133}Xe with little to no radon separation and little to no lead shielding. This significant detection enhancement opens the possibility of developing portable systems that can be automated for remote site deployment. Additional R&D will be required to optimize and shrink the current test detector but the fundamental nuclear signatures are present and measurable.

It is important to note that with a properly designed detector, data acquisition system gamma-ray singles, beta singles, (β, γ) coincidences, and (β, CE, x-ray) triple coincidence signals can be detected simultaneously. This increases the ability of the system to detect other radioxenon isotopes (^{131m}Xe and ^{133m}Xe).

Further research to find methods and processes to reduce the current chemical separation systems in size and power consumption would further increase the sensitivity of remotely deployed systems. In this scenario most of the noble gases would be collected to some degree and all would be counted in the nuclear detection system. It is envisioned that such as system would be deployed remotely and not be a hand carried device. Modification to the current test detector to provide a more compact and portable detector would be useful to measure high level radioxenon levels such as above ground nuclear explosions and reactor or criticality accidents.

REFERENCES

Operational Manual for Radionuclide and the International Exchange of Radionuclide Data, Preparatory Commission for Comprehensive Nuclear-Test-Ban-Treaty Organization, CTBT/WGB/TL-11/5/Rev. 4, (1999).

Auer, M., A. Axelsson, X. Blanchard, T.W. Bowyer, G. Brachet, I. Bulowski, Y. Dubasov, K. Elmgren, J.P. Fontaine, W. Harms, J.C. Hayes, T.R. Heimbigner, J.I. McIntyre, M.E. Panisko, Y. Popov, A. Ringbom, H. Sartorius, S. Schmid, J. Schulze, C. Schlosser, T. Taffary, W. Weiss, and B. Wernsperger, (2004) Intercomparison experiments of systems for the measurement of xenon radionuclides in the atmosphere, Applied Radiation and Isotopes 60 863–877.

Bowyer, T.W., C. Schlosser, K.H. Abel, M. Auer, J.C. Hayes, T.R. Heimbigner, J.I. McIntyre, M.E. Panisko, P.L. Reeder, H. Satorius, J. Schulze, and W. Weiss (2002), Detection and Analysis of Xenon Isotopes for the Comprehensive Nuclear-Test-Ban Treaty International Monitoring System, , *J. of Environmental Radioactivity* 59 139 151.

DeGeer, L. E. (1995). Atmospheric radionuclide monitoring: A Swedish Perspective. In: E. Husebye, A. Dainty (Eds.), Monitoring a Comprehensive Test Ban Treaty. NATO ASI Series E: 303,Boston: Applied Sciences, Boston: Lower Academic Publishers 157-177.

Ely, James H., Craig E. Aalseth, James C. Hayes, Tom R. Heimbigner, Justin I. McIntyre, Harry S. Miley, Mark E. Panisko, Mike Ripplinger, (2003), Novel beta-gamma coincidence measurements using phoswich detectors. Assembling the NNSA Knowledge Base, 25th Seismic Research Review - *Nuclear Explosion Monitoring: Building the Knowledge Base*.

McIntyre, Justin I. KH Abel, TW Bowyer, JC Hayes, TR Heimbigner, ME Panisko, PL Reeder, and RC Thompson, (2001). Measurement of Ambient Radioxenon Levels Using The Automated Radioxenon Analyzer/Sampler (ARSA), J. Radioanal. Nucl. Chem., 248 629-637

Reeder, P.L., T.W. Bowyer, J.I. McIntyre, W.K. Pitts, A. Ringbom, C. Johansson, (2004), Gain calibration of a b/g coincidence spectrometer for automated radioxenon analysis, *Nuclear Instruments and Methods in Physics Research A* 521 586–599.

RESEARCH AND DEVELOPENT OF RADIOXENON MONITORING SYSTEMS

Joel C. Rynes, David Penn, and Patrick Donohoe

General Dynamics Advanced Information Systems

Sponsored by Army Space and Missile Defense Command

Contract No. DTRA01-99-C-0031

ABSTRACT

General Dynamics Advanced Information Systems (GDAIS) through its contract with the United States (U.S.) Army Space and Missile Defense Command (SMDC) is engaged in research and development, and deployment of a manufacturing prototype Automated Radioxenon Sampler / Analyzer (ARSA). A summary of the work performed this past year on the manufacturing prototype and on the U.S. participation in the International Noble Gas Experiment (INGE) will be presented.

An engineering prototype is deployed in Guangzhou, China as part of INGE. A more advanced manufacturing prototype ARSA is currently in the System Development and Demonstration phase and the design readiness review has been completed in accordance with the Department of Defense (DoD) 5000 acquisition model Technical Program Plan. Based on an initial Pacific Northwest National Laboratory (PNNL) design, the field version of the ARSA is being manufactured through a joint effort between Advanced Measurement and Technology (AMETEK) and GDAIS. By early June 2004, the manufacturing prototype ARSA build was approximately ninety-five percent complete. The mechanical assembly of the system is complete but remaining issues including the beta-gamma detector pulse processing electronics and xenon collection efficiency are being addressed. The system is scheduled to complete Factory Acceptance Testing and be installed at the RN75 monitoring station in Charlottesville, Virginia in August 2004. After installation at RN75, the ARSA will be subject to the Test and Evaluation Master Plan to be performed under the supervision of Sandia National Laboratories.

In addition to the development of ARSA hardware, GDAIS has developed advanced software to process and analyze the ARSA data. Most notably, GDAIS integrated the Multiple Isotope Component Analysis (MICA) algorithm into the Radionuclide Monitoring System (RMS) software. The enhanced RMS software will be installed at the U.S. National Data Center (USNDC) located at the Air Force Technical Application Center (AFTAC) during the fall of 2004.

OBJECTIVE

The primary objective of this research is to enhance the U.S. capability to detect nuclear detonations through the detection of radioxenon gases. The research performed by GDAIS centered on advancing both the hardware and software related to the Automated Radioxenon Sampler / Analyzer (ARSA) detection system. The primary objective was obtained through three program elements:

- Develop and deploy a manufacturing prototype ARSA based off the engineering prototype design;
- Continue to gain operational experience of the ARSA through participation in the INGE; and
- Advance the data processing algorithms used to analyze data from the ARSA and other radioxenon sensors.

Each program element will be described separately in the "Research Accomplished" section below.

HISTORIC PERSPECTIVE

The ARSA was originally designed by PNNL (Bowyer et al., 1998). This design was transitioned to DME Corporation who built the ARSA engineering prototype (ARSA001). ARSA001 along with system documentation and schematics was delivered and installed in a GDAIS facility in Charlottesville, Virginia in 2001. At this facility, GDAIS tested and evaluated the ARSA001 to assess its readiness for field deployment, to assess its ability to meet certification requirements, and to develop a manufacturing plan for future units. After several design modifications, ARSA001 was delivered to Guangzhou, China as part of the INGE in 2002 (Penn et al., 2002 and 2003). GDAIS was contracted by SMDC in 2003 to build the ARSA manufacturing prototype (ARSA002). After a competitive bid process, GDAIS selected the ORTEC division of Advanced Measurement Technology, Inc. (AMETEK) as its manufacturing partner.

RESEARCH ACCOMPLISHED

ARSA Manufacturing Prototype

During June 2003, the ARSA research and development task was reviewed by a joint audience representing DoD and the Department of Energy (DOE). GDAIS presented a Technical Program Plan (TPP) developed jointly with SMDC in accordance with DoD acquisition policy, directive 5000. The TPP outlines the execution strategy to build and install the ARSA manufacturing prototype in Charlottesville, Virginia. The ARSA system is currently in the System Development and Demonstration phase and has successfully passed the design readiness review. After the design readiness review was completed, the system was cleared to continue with the build of a manufacturing prototype.

The ARSA manufacturing prototype task is aimed at the production, installation, and performance validation of automated radioxenon detection equipment. The task leverages GDAIS experience along with operational experience of the engineering prototype (currently installed in Guangzhou, China) to produce a reliable design that meets all requirements identified in the TPP. The most notable requirement is the minimum detectable concentration of 1mBq of XE-133 per cubic meter (m^3) of air at standard temperature and pressure (STP).

The ARSA manufacturing prototype (ARSA002) build is a joint effort between GDAIS and AMETEK. The joint effort takes advantage of each company's strengths to produce an end product that will be commercially available. GDAIS provides scientific and software support and AMETEK brings manufacturing and design expertise to the program. Both companies work together to provide documentation and configuration control.

ARSA002 construction began in August 2003. Figure 1 shows the ARSA frame during the initial construction period. The production of the manufacturing prototype has gone well except for a few schedule setbacks. The majority of the setbacks were due to issues identified as program risks early on and ended up becoming more difficult to resolve than originally anticipated. The three issues that most notably affected the ARSA002 production were the state of the engineering prototype documentation, communications between the control computer and the process control hardware, and the need to have the system nearly complete before software testing could commence.



Figure 1: ARSA Manufacturing Prototype under Construction

The engineering prototype documentation received from DME that was to be used for the ARSA002 build was extensive; however, it contained many errors and was incomplete in several key areas. For the mechanical assembly, although the documentation was complete, it contained multiple errors. For example, the documentation would have incorrect placement of holes for fabricated parts so that after fabrication the part could not be assembled and would have to be reworked or replaced. Also, many errors were found in the layout of the wiring harness that resulted in wires crossing either rendering the component inoperative or destroy it. As the build continued, the drawings were marked for correction and the appropriate level of detail added so that after completion, the drawing set can be updated to reflect the current design.

The greatest issue associated with the drawing package was the state of the documentation for the radiation detector pulse processing electronics. The detector electronics package is composed of two custom electronic boards with analog and digital circuitry. The analog component was fairly well documented and even included data for commercial production of the printed circuit board. The digital component had major portions undocumented and was not consistent with a 75% complete prototype board that was delivered with the documentation. Once work began on the detector electronics, it was clear that the task required significantly more time than originally scheduled. It was not clear from the documentation and previous experience with the engineering prototype how some of the circuitry was operated. A team of experts was assembled to asses the electronics and determine a path forward. The team of experts evaluated the electronics for two weeks and came to the conclusion that the design had enough merit to continue with development and not start over. The board was then delivered to the AMETEK research and development (R&D) experts who have nearly completed the board design and fabrication. The board currently is connected to the detector and produces coincidence spectra but has a high dead time (~25%). The dead time is the time spent processing a pulse before a new pulse can be accepted. The issue of dead time is currently under investigation. The most likely cause is ground loop problems or a possible intermittent failing component on the electronics board. Figure 2 shows a picture of the completed electronics board and CS-137 spectrum used for calibration.

The communication issues between the control computer and the process hardware were numerous and sometimes difficult to diagnose. The process of solving the problem was taken in steps and first uncovered several infant failures in the hardware. The majority of hardware used in the ARSA002 build was spare parts from the ARSA001 build. The control computer talks to approximately 120 pieces of instrumentation for control and monitoring of the system. Each of the 120 pieces of instrumentation are connected to one of seven electronic backplanes that has an electronic brain (OPTO22 SNAP B3000) that interprets the signals and communicates directly with the control computer through an RS485 serial circuit. When the system was first initialized, it would automatically shut down within seconds due to a watchdog circuit built into each brain. If a brain did not receive a command within a set period of time, the watchdog circuit would shut down the brain and not allow further commands to be processed.

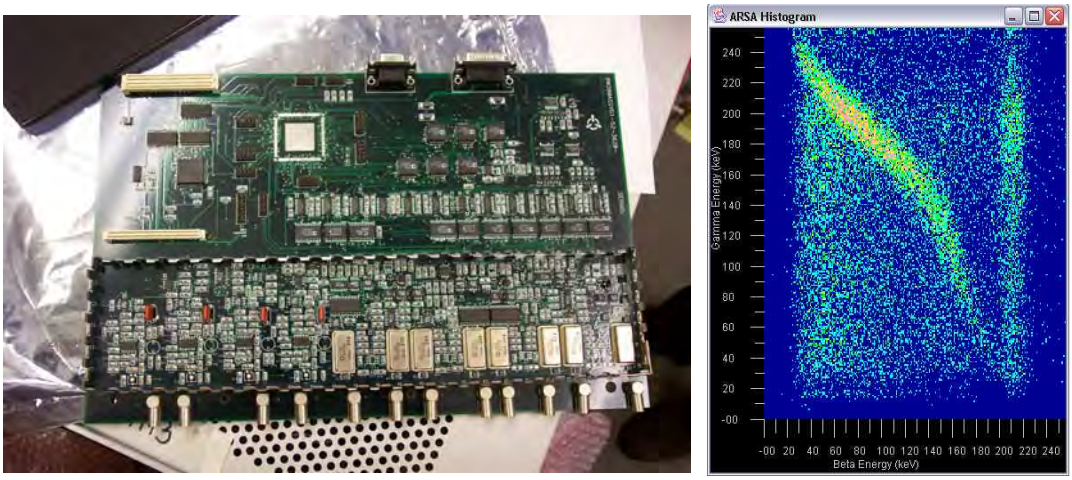


Figure 2: Detector Electronics Board and Calibration Spectrum

The infant failure experienced was determined to be an internal issue with the SNAP brain that shut off the receive buffers in the brain and tripped the watchdog circuit. Two brains were replaced because of this problem.

The next issue with the communication circuit was a very high level of error generation. Much time was spent seeking technical support from the hardware manufacturers and eventually all options were exhausted. Finally, a consultant was brought in to diagnose the system. The consultant determined the problem was a bad printed circuit board on one backplane that was disturbing communications to all of the backplanes. The board would not go into a fault state long enough to be picked up until it had pressure applied to a certain point as was done when the connection was being made.

The last problem with the communications was very elusive to find due to its intermittent nature. The system would lose communications for approximately 10 seconds causing the system to shut down with a frequency of occurrence ranging from hours to days. Technical support for the hardware vendors recommended testing different configurations of the hardware to resolve the issue. When this was unsuccessful, we developed a test that logged each command the system sent both internally by the control computer and externally through a computer placed on the circuit. The logs from the two computers were compared and it was determined that for a brief period of time the control computer would think it sent a command but it was never seen on the communication line. This showed that the problem was in either the control computer or the communications (RS485) circuit. A call was then placed to the operating system (OS) vendor, QNX, and after quite a bit of discussion they admitted that there is a problem with the new QNX OS serial driver and that a new driver was going to be formally released soon. In the interim, we were given a beta version of a fixed driver and this resolved the problem. Unfortunately there was no documentation of this problem in the public domain and it appeared that many of the QNX technical support personnel were not aware of it either.

Once the mechanical and communication issues were resolved, the system software was tested and several bugs were identified and repaired. Currently the system is running well and is producing approximately 1.5 cm^3 of xenon per 8 hour sampling period, exceeding the requirement of 1.0 cm^3. The only major remaining issue to be resolved is the dead time of the detector electronics.

Once complete the system will be tested as outlined in the Test and Evaluation Master Plan (TEMP) that was generated as part of the TPP. The TEMP consists of a Factory Acceptance Test (FAT) and a Requirements Verification Test (RVT). The FAT will be performed by GDAIS at the AMETEK facility with oversight from SMDC and Sandia National Laboratory (SNL). Testing is scheduled to begin in the second week of August. Upon successful completion of the FAT, the ARSA will be shipped to Charlottesville, Virginia where it will be installed at the RN75 monitoring station. An installation plan has been developed and is currently being evaluated by the U.S. station Configuration Control Board (CCB). Figure 3 shows the proposed configuration of RN75 after installation of the ARSA.

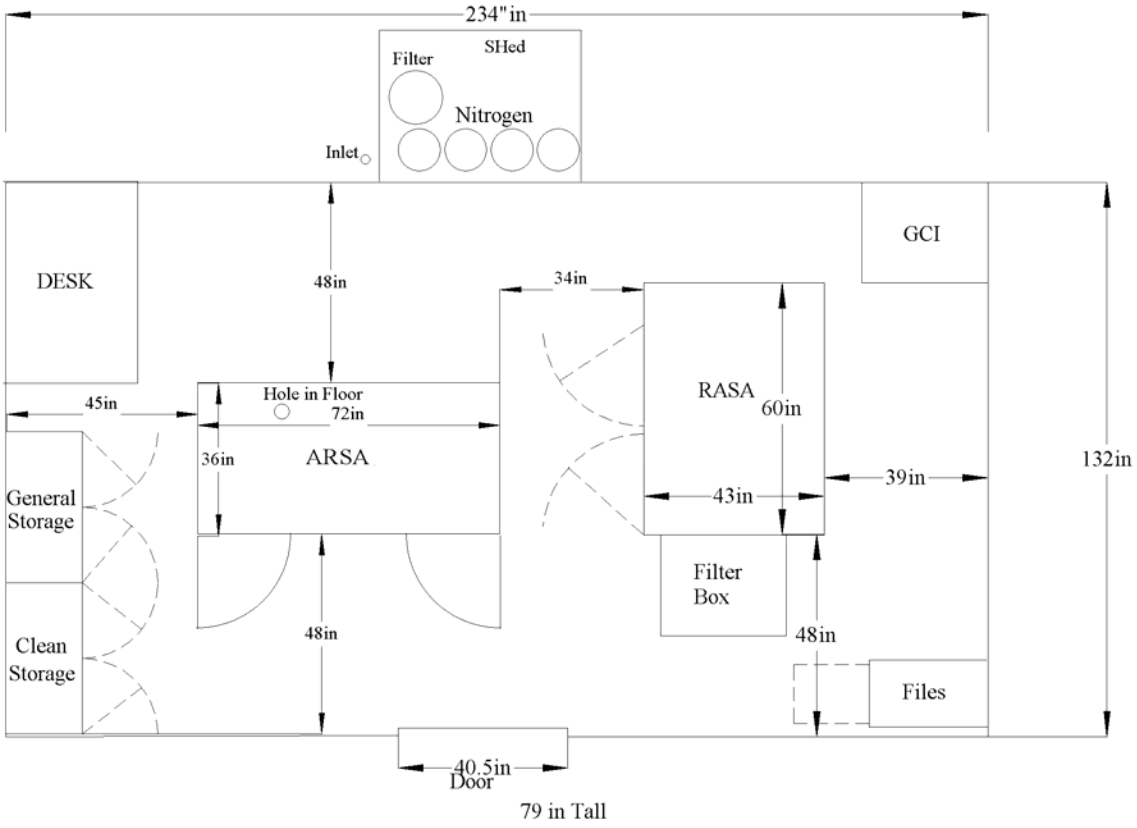


Figure 3: Proposed RN75 Layout after ARSA Installation

Once the unit is operational at RN75, SNL will conduct the RVT under the direction of SMDC to ensure that the system meets all design requirements. Once the system passes the RVT, the drawing and documentation package will be updated to reflect the final configuration and the system will be ready to be transferred to production. The RVT is tentatively scheduled for December 2004.

INGE Participation

ARSA001 was installed in Guangzhou, China in November 2002 (see Figure 4) and entered the International Noble Gas Experiment (INGE) Phase IIIA. The objective of Phase IIIA is to tune the system and have the vendors provide oversight to the local operators for operations and maintenance of the equipment. Phase IIIA lasted approximately nine months and the system experienced several issues that required intervention for the system to continue operation. These issues resulted in a total downtime of 80 days. The majority of the downtime was attributed to sensors monitoring the temperature of an activated charcoal bed. The sensors would fail intermittently causing the system to read an out of range temperature. This caused the safety systems to shut the system down automatically. The out of range temperature measurement and system shutdown occurred unexpectedly and too quickly for the system to record the fault at the preset data logging interval. Once the fault was diagnosed, the system was repaired and the system returned to normal operation. After resuming normal operation, the xenon collection was near zero. It was determined that during the diagnosis of the temperature sensors, the local operators had operated one of the collection traps without first evacuating oxygen from the trap. This caused the entire active element in the trap to burn making the trap ineffective. A new trap was fabricated and delivered to the local operators for installation in August 2003. Once the new trap was installed, the system returned to its original performance levels and the system entered into the International Noble Gas Experiment Phase IIIB.



Figure 4: ARSA Installed in Guangzhou, China

The INGE Phase IIIB utilizes the same equipment and personnel as Phase IIIA, but the level of effort from the vendors is greatly reduced. The vendors are required to perform regular scheduled maintenance of the systems. The local operators are required to perform all operations and unscheduled maintenance to the system including any diagnostics that need to be performed. The vendors have direct access to the system and can support the local operators only at the request of the INGE staff.

The last quarter of 2003 was uneventful with the ARSA performing well; the online time was approximately 83%. The downtime was primarily due to a faulty compressor. In December 2003, a scheduled maintenance trip was to be performed to replace system consumables and to check the system calibration. Approximately one week before our team left for China, the trip was cancelled by the local operators due to a schedule conflict. Due to additional schedule conflicts, it was decided that the local operators would have to perform the scheduled maintenance. The maintenance itself is a simple task of replacing filters, gaskets, and the air compressor as well as performing a thorough system leak test. The maintenance was performed by the local operators in early March 2004. After the scheduled maintenance, the system appeared to run well except that little xenon was being collected. The local operators continued to let the system operate without being able to correctly make a diagnosis. In addition, the system pressure began to drop slowly, and after a short power outage, the compressor was unable to maintain the required pressure and flow rate. The local operators then shut the system down. The INGE staff then contacted GDAIS to support the local operators.

Remotely, GDAIS was able to operate the ARSA and perform some limited testing on the system. It was determined that the air compressor capacity had degraded and that one of the xenon collection traps had been damaged. A new collection trap and a compressor rebuild kit were sent to China. Also, during remote testing the beta gamma coincidence detector electronics were found not to be responding. The beta gamma coincidence detector system is composed of a custom pulse processing electronics coupled to a multi piece scintillation detector. Several tests indicated the fault was either in the RS232 communications channel between the control computer and the electronics board or the electronics board itself. The only way we could diagnose the fault would be to travel to China.

In May 2004, GDAIS traveled to China to perform the repairs on the system. After the planned maintenance tasks were completed, the detector electronics board was examined. The communications and power to the board were found to be in working order. The fault appeared to be directly related to the electronics board; therefore, it was removed from the system and brought back to the U.S. for repair. The electronics board has been returned to manufacturer for repair and the exact fault has yet to be determined. The system is currently offline awaiting the

repair and return of the electronics board. Because the electronics board is a custom part, no spare units are available.

From the last two years of operating the ARSA, it is evident that the system provides very sensitive measurements of atmospheric radioxenon, but maintenance and reliability are an issue for full time operation. Figure 5 shows the failures the ARSA has experienced in the last two years along with the associated number of days of downtime.

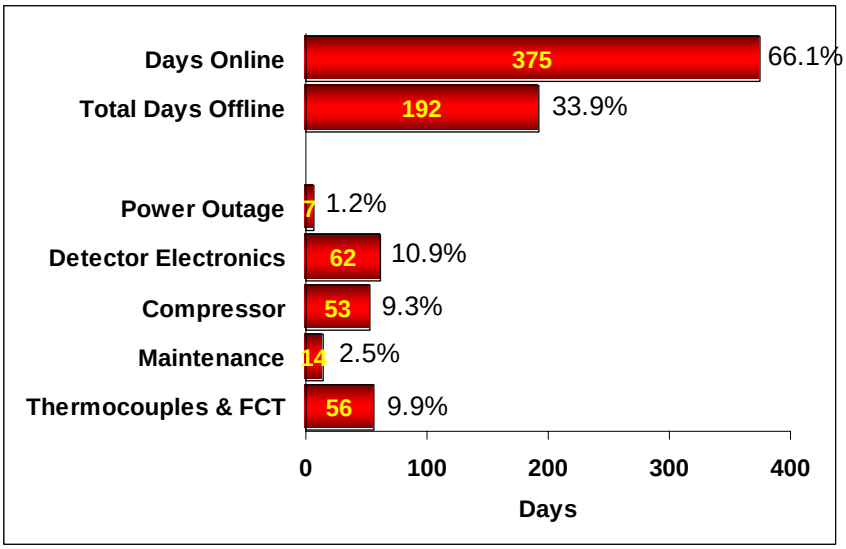


Figure 5: ARSA Reasons for Downtime

The data availability for the past two years is 66%. Much of this time was due to having no replacement parts at the site as well as local operators who are hesitant to work on the system because of its complexity. The solution to increasing the online time would be to carry a more significant level of spare parts on site as well as more extensive training for the local operators. Also, the local operators are not always aware when there is an imminent problem with the system such as a failing pressure from the compressor. Therefore, both an alert system that notifies the operator immediately after a failure has occurred and routinely inspecting the system data would significantly reduce the offline time of the system. Taking the proposed solution into consideration it is possible to reduce the offline time from the compressor, detector electronics, and thermocouples to 2 days each, one for diagnosis and one for repair. This would reduce the offline number of days to 27 and provide an online time of 95%.

Data Processing Algorithms

In addition to the development of ARSA hardware, GDAIS has developed advanced software to process and analyze the ARSA data. Most notably, GDAIS integrated the Multiple Isotope Component Analysis (MICA) algorithm into the Radionuclide Monitoring System (RMS) software. The development of the MICA algorithm was reported last year (Biegalski 2003). An overview of the MICA algorithm and a description of how it is integrated into the RMS software are presented here.

The current RMS component software used to analyze data from beta-gamma coincidence radioxenon sensors, such as the ARSA, is the program *rms_xanalyze* (Rynes 2002). This algorithm is based on a Region of Interest (ROI) approach not dissimilar from most high-resolution gamma spectroscopy algorithms, but applied in two dimensions. The main problem arising with the *rms_xanalyze* algorithm is that not all the physics of the problem are taken into account (such as XE-135 contributions in the E = 30 keV region), which can result in negative net counts or higher than necessary false positive detection rates for some radioxenons. The MICA algorithm was developed to improve

the data processing for such beta-gamma coincidence data by accounting for all known physics and reduces the uncertainties involved in the results.

MICA involves the deconvolution of a sample signal into the contributions from each isotope (see Figure 6). MICA uses the entire isotopic signatures and not just ROIs; therefore, it is theoretically possible to obtain better minimal detectable concentration levels. Detector-specific responses for each possible isotope are used in the deconvolution. The responses can be generated using actual radioisotope sources counted on the detector, or they can be created using modeling techniques like the Monte Carlo N-Particle Extended (MCNPX) code. The geometry and materials of the detector must be known to produce good response files. Because only a small number of isotopes are detected in xenon samples, deconvolving a sample is not highly complex. Deconvolution of nuclear spectroscopy data is not a new concept. MICA is unique in that this methodology is applied to three-dimensional beta-gamma coincidence data. The MICA software contains activity concentration and minimal detectable concentration (MDC) calculations as well as nuclide identification methodology.

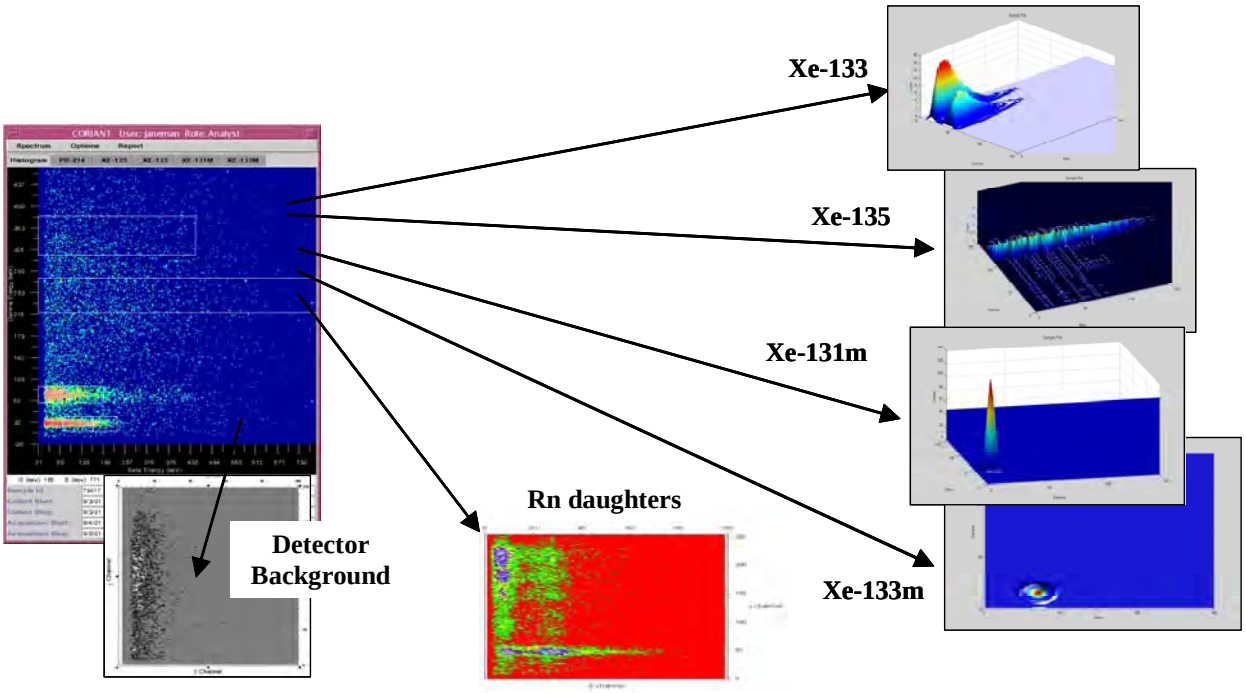


Figure 6: MICA Involve the Deconvolution of Sample Signals

The objective was to integrate the MICA algorithm into *rms_xanalyze* so that either the ROI algorithm or the MICA algorithm could be used from a single software application. The first step of this integration was to modularize *rms_xanalyze*. The new *rms_xanalyze* program flow is shown in Figure 7. It contains six modules that are executed sequentially. The functions of these modules are initialization, calibration, count calculation, concentration calculation, MDC calculation, and finalization. A major component of this work was the creation of a single data structure that contained all relevant variables and that could be passed between the modules. This modularity facilitates simple insertion of the MICA algorithm as well as the insertion of other algorithms into the baseline software at a later time. The new modular code was developed and tested against the RMS Validation Test. The new *rms_xanalyze* software produced the same validation test results as the old software.

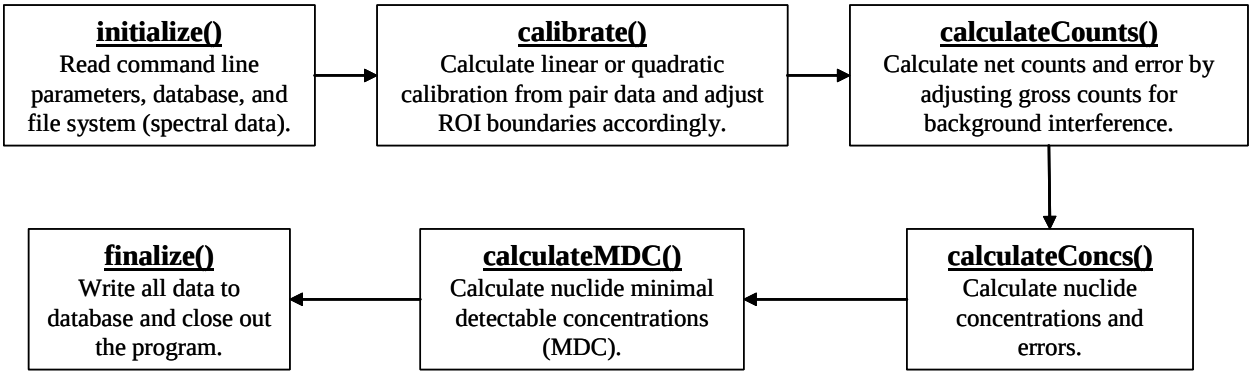


Figure 7: Processing Flow of Noble Gas Automatic Processing Software

The original MICA algorithm was developed in MATLAB, whereas *rms_xanalyze* is written in JAVA. The MATLAB algorithms that performed calibration, count calculation, concentration calculation, and MDC calculation were ported to JAVA and inserted into *rms_xanalyze*. The existing *rms_xanalyze* initialization and finalization algorithms were sufficient. The new *rms_xanalyze* with the integrated MICA algorithm was tested and it produced the same results as the MATLAB software. It should be noted that the MICA software (both MATLAB and JAVA) were tested with simulated detector response functions. Although the algorithm appears to work well using the simulated detector response functions, these functions have not yet been evaluated with a real detector system. This evaluation will most likely take place after the ARSA002 is installed in Charlottesville.

CONCLUSIONS AND RECOMMENDATIONS

The fabrication of the ARSA manufacturing prototype is near completion. The FAT is scheduled for early August and it should be installed and operating at the RN75 site by the end of September. The system is expected to meet or exceed all requirements. The delay in fabrication was caused predominately by inadequate documentation for the engineering prototype resulting in the redesign of several key components and by communication problems between the control computer and the process control hardware. The later problem was the result of faulty hardware and problems with the new QNX OS. It is recommended that the entire drawing packet be updated as soon as possible and that the drawing packet be updated on a regular basis so that these problems do not reappear in the next ARSA build.

The ARSA deployed in Guangzhou, China entered Phase IIIB of the INGE in September 2003. The system worked well from September through February when the gas processing system failed as part of scheduled maintenance by the local operator. During repair of the gas processing system, it was determined that the detector electronics board was also damaged. This board was returned to the U.S. for repair. Because this electronics board was a custom part produced by a vendor that no longer supports it, there are no spare units available and it is unlikely that the board can be repaired. It is recommended that we build a new board after the ARSA manufacturing prototype passes the FAT and install this board in Guangzhou as soon as possible.

The MICA algorithm has been integrated in the RMS software. The software is working according to its design. However, before this algorithm is installed in an operational environment at the USNDC, the MICA detector response functions must be validated against real spectra data. The detector response histograms will be improved by a combination of enhanced MCNPX modeling and direct radioxenon calibration measurements on a beta-gamma coincidence detector. The algorithm will then be tested with a large quantity of real sample data. The ARSA, soon to be installed in Charlottesville, will be used in these tests.

REFERENCES

Biegalski, K. and S. Biegalski (2003), "Deconvolution of Three-Dimensional Beta-Gamma Coincidence Spectra from Xenon Sampling and Measurement Units," in *Proceedings of the 25th Seismic Research Review - Nuclear Explosion Monitoring: Building the Knowledge Base*, LA-UR-03-6029, Vol. II, pp. 542-551.

Bowyer, T.W. et al. (1998), "Xe Radionuclides, Atmospheric: Monitoring" in *Encyclopedia of Environmental Analysis and Remediation*, editor: R. A. Meyers, John Wiley & Sons, Inc.

Penn, D., S. Biegalski, and K. Biegalski (2002), "Status of thee Automated Radioxenon Sampler Analyzer and the IMS International Noble Gas Experiment," *Proceedings of the 24th Seismic Research Review -- Nuclear Explosion Monitoring: Innovation and Integration*, LA-UR-02-5048, Vol. II, pp. 701-710.

Penn, D. (2003), "Status of the United States International Monitoring System Radionuclide Monitoring Stations," in *Proceedings of the 25th Seismic Research Review - Nuclear Explosion Monitoring: Building the Knowledge Base*, LA-UR-03-6029, Vol. II, pp. 552-567

Rynes, J., K. Biegalski, P. Donohoe, and S. Biegalski (2000), "Automatic and Interactive Analysis Software for Beta-Gamma Coincidence Systems used in CTBT Monitoring," *Proceedings of the 22nd Annual DoD/DOE Seismic Research Symposium*.

Infrasound Monitoring

THE USE OF ARRAYS OF ELECTRONIC SENSORS TO SEPARATE INFRASOUND FROM WIND NOISE

Henry E. Bass and F. Douglas Shields

University of Mississippi and Miltec Research and Technology

Sponsored by Army Space and Missile Defense Command

Contract No. DASG60-00-C-0061

ABSTRACT

With current technology for near simultaneous detection of multiple signals it is possible to replace the pipes with arrays of individual sensors. With such arrays it is not only possible to average the pressure signals over an extended area, as is done with the pipe arrays, but to combine the signals in innovative ways to preferentially cancel the wind noise. A three axis orthogonal array with 10 sensors in each arm has been constructed and used to study the correlation of the wind noise as a function of distance in the vertical and two horizontal directions. The rugged all weather sensors are of original design and require no external power source. Measurements have been made for wind speeds from 4 to 7 meters per second and at three different sites.

The frequency dependent correlation of the wind noise over a range of wind velocities and atmospheric and environmental conditions in the downwind direction varies as exp (-3.2 x) cos (2π x), and the crosswind correlation varies as exp (-7.4y), where x and y are the sensor separations in wavelengths in the downwind and crosswind directions, respectively. The correlation of pressure signals from sensors in the vertical arm of the array decreased with sensor separation approximately twice as fast as those from the horizontal arms that were on the ground. For two of the sites studied, over a limited range of wave numbers, the spectra of the varying velocity as measured 3 meters off the ground demonstrated the characteristics of the inertial sub-range. Over the same range of wave numbers the pressure spectra obeyed the –7/3 power law.

OBJECTIVE

The objective of this research is to improve techniques for detecting infrasound in the presence of wind noise. Current wind noise filters generally use extensive pipe arrays with multiple ports to average pressure signals over an extended area.[1-3] Because sound travels approximately 100 times faster than wind, pressure ports in the pipe arrays can be separated far enough to get random signals from the wind and still get coherent signals from sound. If the pressure variations due to the wind are incoherent, the averaging process will reduce the noise pressure by a factor of $1/n^{1/2}$. If the pressure due to wind noise is not coherent, this averaging is not applicable. The goal of this research program is to replace the pipe arrays and ports with individual rugged sensors. Optimum spacing and numbers of sensors requires that correlation of pressure under different conditions is understood. To study correlation an array of rugged infrasound pressure sensors has been constructed and used to determine the spatial correlation of wind noise.

RESEARCH ACCOMPLISHED

The Infrasound Sensors

The infrasound sensing capsules are constructed by cementing piezoelectric bimorphs on each side of a metallic ring. A voltage is generated between the conducting coating of the ceramic and a metal backing plate that is proportional to the pressure bending the bimorphs and is independent of frequency from 0 Hz up to frequencies approaching the resonant frequency of the bimorph. For the 3.5 cm bimorphs used here the resonant frequency was 1.5 kHz.

These sensors are sensitive to changes in temperature as well as pressure. In order to compensate, two capsules have been constructed with the ceramic surface turned outward on one and inward on the other. When wired in series, the changes due to pressure add and the changes due to differential expansion cancel. The pair of capsules is then potted in polyurethane. To further insulate the sensors from temperature fluctuations in the atmosphere, the potted sensors have been wrapped in fiberglass and housed in capsules made of two inch, schedule forty, PVC pipe with end caps. Each of the end caps has 26 holes 1/16 inch in diameter. When temperature compensated and housed in this way, temperature fluctuations ordinarily encountered in the atmosphere produce a negligible signal for frequencies above 0.1 Hz. A total of thirty transducers were individually calibrated and the outputs corrected so that all had the same sensitivity to within + or- 3%. Their phase response was constant and uniform to + or - 0.1 radian between 0.1 Hz and 10 Hz.

Widely different results are reported for pressure spectrum measurements in turbulence [4]. One must always be concerned that intrinsic pressure fluctuations are being measured and not the interactions of the wind with the sensing element. To study this question further, the pressure sensors employed here have also been tested in the field and shown to be insensitive to orientation relative to wind direction over the frequency range of interest.

The site for the measurements

The sensors described above were used for five sets of field measurements from Sept., 2001 to Jan., 2003. For the first of these, the sensors were arranged along two directions at right angles to each other with 15 sensors in each arm 0.46 m apart. One of the arms was into the wind and one across wind. The sensors were placed on the ground in a plowed cotton field. The cotton had been harvested and the remaining cotton stalks were approximately 0.7 meters tall.

For the other four sets of measurements, 28 of the sensors were arranged in a three dimensional rectangular array. An ultrasonic anemometer was mounted 3 meters off of the ground about 0.5 meters from one of the pressure sensors on the vertical arm of the array. This anemometer and the three dimensional array was deployed at four different sites. The first was on a junction of service roads between 20-acre catfish ponds. The second was a sod field. Measurements were taken at this site on two different days. The third was a disked field in the Mississippi delta. The fourth site was at a different place in the same cotton field where the first measurements were made approximately one year earlier.

The average response of each arm in the array

The power spectral density of the pressure variations for each of the three arms of the array for each of sites 3, 4 and 5 is plotted in Fig. 1.

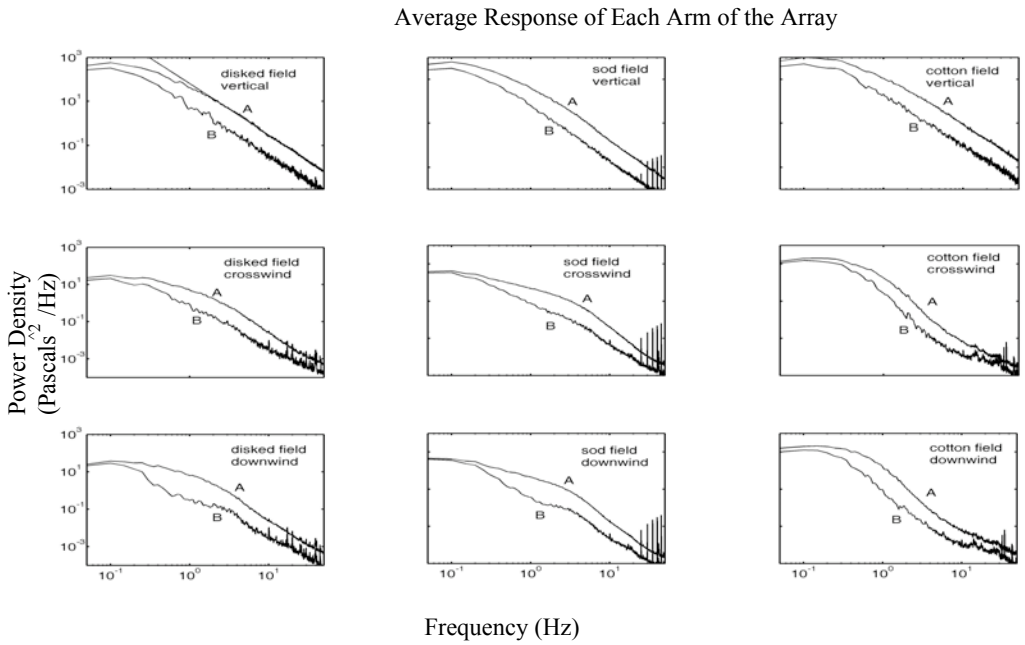


Figure 1. The power density spectra of the varying pressure as measured by each arm of the array at each of three sites. Curves A were obtained by averaging the spectra from nine sensors in each arm. Curves B were obtained by taking the spectra of the average signal from the same nine sensors.

The top curve (A) in each figure is obtained by calculating the spectrum of time signals from each of the nine sensors in the arm and then averaging these spectra. The lower curve (B) is obtained by averaging the time signals from the nine sensors and then calculating the spectrum of this average. For curves B, if the sensors are far enough apart so that their signals are uncorrelated, averaging the time signals should divide the noise power density by the number of sensors. This is seen to be the case for the vertical arm signals at all three sites for frequencies above approximately 1 Hz. For the two horizontal arms that are on the ground the wind noise at the higher wave numbers is reduced to where the spectra are influence by background sound. Since the sound is at least partially correlated over the arm of the array averaging the time signals reduces the power level by less than the 1/n factor.

The average spectrum for the nine sensors in the vertical arm that are from 2 feet to 18 feet off the ground has very nearly a –7/3 slope. This is illustrated by the straight line plotted through the data for vertical arm in the disked field. For the horizontal arms on the ground, the surface boundary reduces the turbulence and causes a deviation of the spectral slopes from –7/3. The spectra for the cotton field data differ significantly from the other two sites. The noise level in the vertical arm is greater and the shape of the spectra for the two arms on the ground is different. The pressure levels at frequencies in the neighborhood of 0.3 Hz are increased while those around 3 Hz are decreased.

For the disked field and sod field, averaging the signals from the downwind arm produces greater than 1/n noise reduction for wave frequencies between about 0.5 and 5 Hz. This can be explained by assuming that the turbulent pressure field has a periodicity. When the convection velocity carries this periodic field across the downwind arm of the array, for wavelengths comparable to the length of the array arm, signals from different parts of the array will be out of phase and cancel out in the averaging process.

Correlation studies

Fig. 2 A and B shows the correlation as a function of lag time for signals from 5 sensors in the downwind and

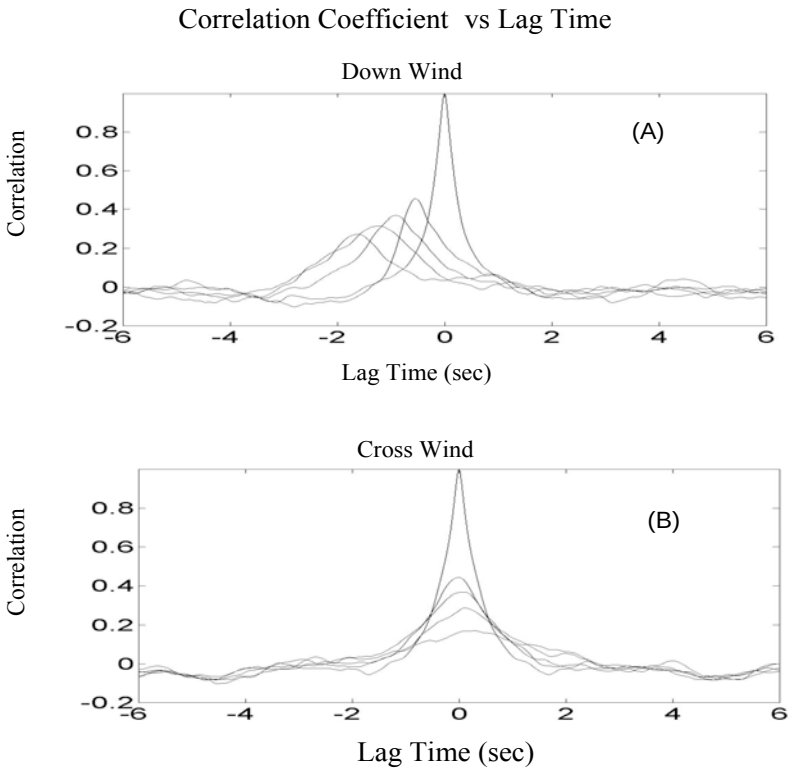


Figure 2. The Correlation coefficient versus the lag time for signals from 5 sensors in (A) the downwind arm of the array and (B) the crosswind arm of the array. For the crosswind arm the sensors are separated by 2 feet (61 cm.), and for the downwind arm, they are separated by 4 feet (122 cm.)

crosswind arms of the array respectively for the disked field data. Plotting the correlation at zero lag time versus sensor separation in these two figures gives the decrease in correlation with distance in the crosswind and downwind directions. Plotting the peak heights versus lag time for the downwind arm gives the decrease in correlation with time at a fixed position in the turbulent pressure pattern. As has been pointed out by Bass, Raspet and Messer[5], the average wind velocity should equal to the slope of the plot of the sensor separation versus lag time.

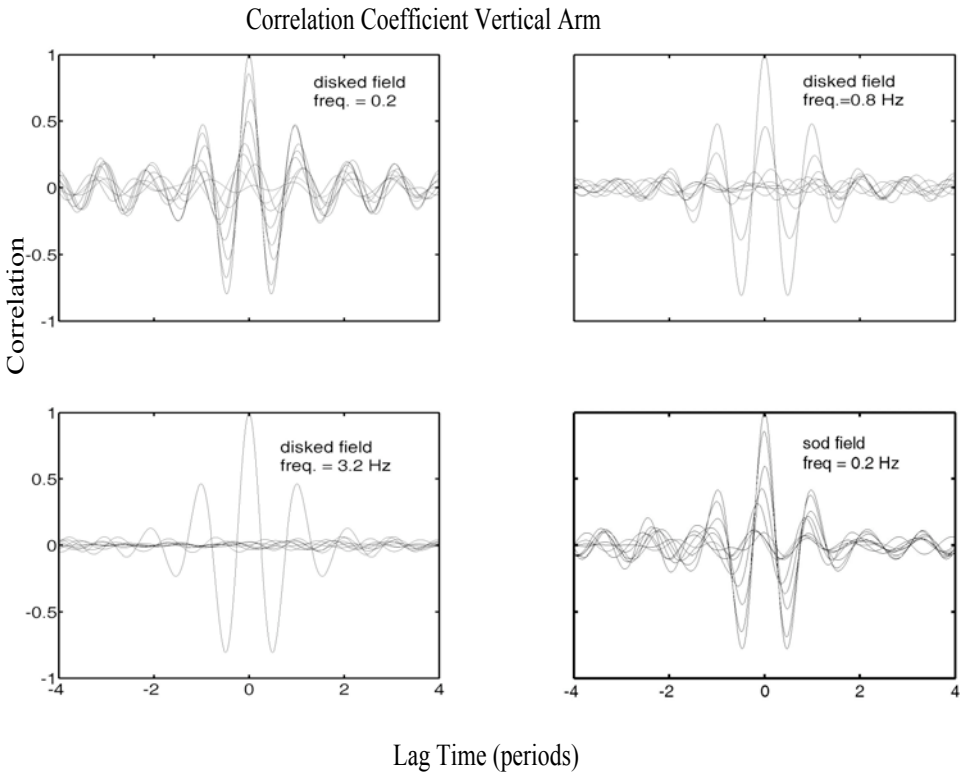


Figure 3. Single frequency correlation versus lag time in periods for varying pressure signals from eight sensors in the vertical arm of the array.

It is interesting to examine these correlation curves as a function of frequency. Figs. 3 A, B, and C show the correlation of the signals at three different frequencies from eight sensors in the vertical arm of the array for the disked field data. The sinc function shape of the correlation curves is characteristic of the correlation of narrow band of frequencies. The lag time has been normalized by dividing by the period of the filtered signal. This gives the same shape to curves at different frequencies. As the frequency is increased from 0.2 Hz in Fig 3A to 3.2 Hz in Fig 3C the rate of decrease in correlation with distance rapidly increases to where at 3.2 Hz there is negligible correlation even between the adjacent sensors separated by only 0.6 meters. Fig 3D gives the curve for the same sod field. The correlation at the two sites is very similar.

Nearly 40 years ago J. T. Priestley [6] made narrow band pressure correlation measurements in the frequency range 0.008 to 1 Hz. for wind speeds ranging from 2.1 to 7.2 m/sec. He used six pressure sensors to study the dependence of the correlation on the downwind and crosswind separation of the sensors. He determined, in agreement with earlier studies, that the narrow band correlation coefficients in the down wind and cross wind directions are given by

$$R(\text{downwind}) = e^{-\alpha x} \cos(k_1 x), \quad (1)$$

and

$$R(\text{crosswind}) = e^{-\beta y}, \quad (2)$$

with x and y the down wind and cross wind separations. Priestley found that, though the convection velocity given by (2π *F/k_1) was highly dependent upon meteorological variables, the functional relationships between alpha, beta and k_1 were remarkably independent of them. (F was the center frequency of his filtered signal and k_1 chosen to fit his data.) He obtained

$$\alpha = 0.33 * k_1^{1.28} \ m^{-1}, \quad \text{for } 0.5 < 1/k_1 < 50. \quad (3)$$

$$1/\beta = 0.84*(1/\alpha)^{0.74} \ m, \quad \text{for } 3 < (1/\alpha) < 500. \quad (4)$$

Fig 4 is a plot of the correlation at zero lag time between sensors in the downwind arm of the array versus the sensor

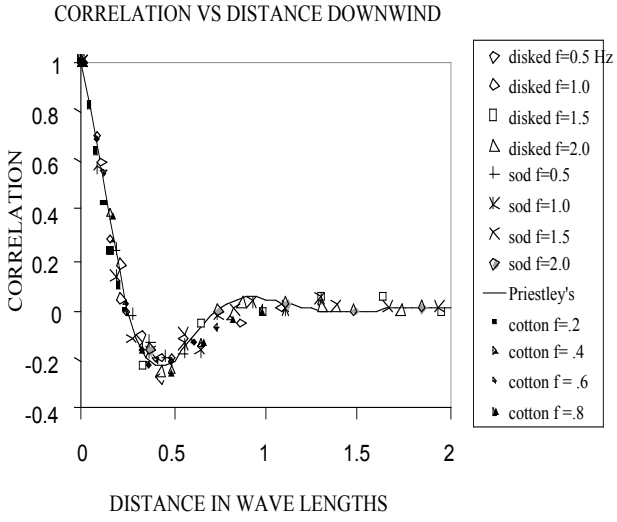


Figure 4. Correlation of the varying pressure signals versus the sensor separation in wavelengths in the downwind direction. The data are for four different frequencies and for three different sites as designated in the legend. The solid curve is the fit to Priestley's data taken at much lower frequencies in 1964.

separation in wavelengths. Data for the disked, sod, and cotton fields for a number of frequencies have been plotted on the same graph. The data for each site have been averaged not only for all runs at the site, but also for all pairs of sensors with the same separation. The wavelength was determined by dividing the convection velocity by the frequency of the filter. However, since the sensors are on the ground, the anemometer measurement of the velocity made 3 meters above the ground is inadequate. Instead the convection velocity for the three sites was adjusted to make the data fit Eq. 1. These velocities were 2.8, 3.3, and 3.0 m/s for the disked, sod, and cotton fields respectively. The velocities obtained in this way were approximately equal to those obtained from the plot of the sensor separation versus the lag times at which the maximum in the correlation occurs. The average velocities for the three sites measured with the anemometer 3 meters above the ground were 6.2, 6.7, and 5.9 m/s respectively.

To within experimental error, the correlation is seen to be a function of the separation divided by the wavelength independent of frequency, wind velocity (over the limited range of velocities measured) and even the terrain. frequency dependent. The α value used to draw the curve in Fig. 4 corresponds to Priestley's α as calculated from Eq 3 with a wave number of 4.7m $^{-1}$. This is the highest wave number for the data plotted in Fig. 4. approximately 2 m/sec. The distance in the direction of the wind is the time times the average wind velocity.

CONCLUSIONS AND RECOMMENDATIONS

The conclusions can be summarized as follows:

1) Noise power reduction produced by averaging signals from individual sensors varies as 1/(number of sensors) when the signals averaged are not correlated.
2) The frequency dependent correlation of the wind noise over a range of wind velocities and atmospheric and environmental conditions varies as exp(3.2x) cos(2π x), where x is the sensor separation in wave lengths in the down wind direction. This allows greater than 1/n noise reduction if the aperture of the array is greater than _ wavelength of the pressure variations in the wind. Use of multiple sensors rather than fixed separation ports allows one to take advantage of this cosine dependence to further reduce noise.
3) The correlation as a function of sensor separation for arrays in the crosswind and vertical directions is given approximately by exp(-7 x) for a range of wind velocities and atmospheric and environmental conditions.

ACKNOWLEDGEMENTS

The help of Chris Clark and Brandon Smith in taking data is gratefully acknowledged. Thanks also go to Drs. Ken Gilbert, Carrick Talmadge, Richard Raspet, and Garth Frazier, for helpful discussions.

REFERENCES

F. B. Daniels, "Noise-Reducing Line Microphone for Frequencies below 1 cps", J. Acoust. Soc. Am., 31, 529-531 (1959).

S. T. Tenny, B. T. Mays, and J. M. Noble, "A methodology for infrasonic detection and array signal processing," Army Research Laboratory , Security Office, 2800 Powder Mill RD. Adelphi, Md 20783, (1999).

M. A. Hedlin, B. Alcoverro, and G. D'Spain, "Evaluation of rosette infrasonic noise reducing spatial filters," J. Acoust. Soc. Am., 114, 1807-1820(2003).

W. K. George, P. D. Beuther, and R. E. A. Arndt, "Pressure spectra in turbulent free shear flows", J. Fluid Mech.," 148, 155-191(1948).

H. E. Bass, R. Raspet, and J. O. Messer, "Experimental determination of wind speed and direction using a three microphone array", J. Acous. Soc. Am., 97 (1) 695-696 (1995).

Joseph Tant Priestley, "Correlation Studies of Pressure Fluctuations on the Ground Beneath a Turbulent Boundary Layer", *National Bureau of Standards Report, No. 8942*, (1965), also M. S. Thesis, University of Maryland (1965). Joseph Tant Priestley, "Calculation of the Effectiveness of Infrasonic Line Microphones for Reducing Wind Noise", *National Bureau of Standards Report* 9380, (1966).

INFRASOUND STATION AMBIENT NOISE ESTIMATES

J. Roger Bowman, G. Eli Baker, and Manochehr Bahavar

Science Applications International Corporation

Sponsored by Army Space and Missile Defense Command

Contract No. DASG60-03-C-0009

ABSTRACT

The main objective of this study was to characterize, for the first time, the noise environment of all existing infrasound stations using a standard methodology to enable meaningful comparisons among stations and to provide noise estimates for use in network detection simulations. Spectral amplitudes were measured for the central site of all 21 infrasound arrays for which data were available. Of these stations, 16 were part of the International Monitoring System (IMS) and 5 were research stations in North America. Power Spectral Densities (PSDs) were estimated for 21 consecutive 3-minute segments of data taken four times daily, beginning at 06:00, 12:00, 18:00, and 24:00 local time from January 2003 through January 2004. Three-minute windows were used to minimize smoothing of the amplitude distributions while permitting estimation of the longest periods of interest. For stations that had both high- and low-frequency sites, spectra were estimated separately, one site for each type. Spectra were corrected for instrument responses contained in the station database of the Space Missile Defense Command (SMDC) monitoring research program. More than 614,000 spectra were calculated and displayed in 16 plots per station (four times a day for four seasons) for frequencies from 0.03 to 7 Hz. This effort utilized the spinning disk mass-store archive of the SMDC monitoring research program, a unique resource providing researchers with almost instantaneous access to more than 12 terabytes of IMS and other waveform data.

The ambient noise at infrasound stations is highly variable by season, time of day, sensor type and station. For example, noise spectra for individual stations may vary by more than four orders of magnitude at any given frequency across the frequency band analyzed. At station I07AU (central Australia) the median noise PSDs for 6-7 AM below 1 Hz are similar for winter, spring and autumn, but are about an order of magnitude lower for summer. At I07AU the median PSDs for summer are about an order of magnitude higher at noon than at dawn, dusk or midnight. The microbarom peak is generally not observable above the level of other noise at I07AU, but at the quietest time of day (midnight) for the quietest season (summer), the microbarom peak is seen clearly. Ambient noise can vary significantly for the high- and low-frequency sites at I57US (Piñon Flat, California). Noise recorded by the two site types is almost identical between 0.1 and 1 Hz at midnight in January, but is a factor of three times higher on the low-frequency sites in July.

Drawing conclusions from comparisons among stations is difficult because of the variation with time of day, season and frequency. With that caveat, we compared the median PSDs of high-frequency sites during the winter months from 6 to 7 AM and from noon to 1 PM. Noise levels vary among stations by 1 to 2 orders of magnitude. Noise levels are less variable among stations in the 0.1 to 1 Hz band than they are at lower or higher frequencies. The quietest stations in the 0.1 to 1 Hz band appear to be DLIAR (New Mexico), I17CI (Ivory Coast) and TXIAR (Texas), whereas the noisiest stations appear to be I07AU (Australia), I26DE (Germany) and I33MG (Madagascar).

Inspection of noise PSDs uncovered anomalies with instrument responses for 9 of the 21 stations studied. Quantitative analysis of infrasound data relies on accurate knowledge and representation of station instrument response characteristics. This study demonstrates the utility of examining noise to help identify incorrect instrument response descriptions.

OBJECTIVE

The objective of this study was to characterize, for the first time, the noise environment of all existing infrasound stations using a standard methodology. The results allow meaningful comparisons among stations and provide noise estimates for use in network detection simulations.

RESEARCH ACCOMPLISHED

The ambient noise at infrasound stations is highly variable over time and among stations. Ambient infrasound noise is dominated by pressure fluctuations due to local winds and by long-range pressure fluctuations generated over the oceans (microbaroms). Station-dependent factors that contribute to the ambient noise include climate, station latitude and position relative to oceans, local topography, local noise sources, vegetation or snow cover at the sensor sites, and sensor and wind noise suppression filter configurations. In order to characterize the ambient noise, spectral amplitudes were measured at one site of 21 arrays (Figure 1) using an approach similar to that of Bahavar and North (2002). Data were analyzed from January 20, 2003 through January 31, 2004, from 21 consecutive 3-minute segments of data taken four times daily, beginning at 06:00, 12:00, 18:00, and 24:00 local time. Three-minute windows were used to minimize smoothing of the amplitude distributions, while permitting estimation of the longest periods of interest. Some stations have high- and low-frequency sub-arrays with different noise suppression filters at high- and low-frequency sites; for these stations spectra were estimated separately for one site of each type. Spectra were calculated using *geotool* (Coyne and Henson, 1995) and applying a Hanning taper to the outer 10% of each data window. Spectra were corrected for instrument responses contained in the station database of the SMDC monitoring research program.

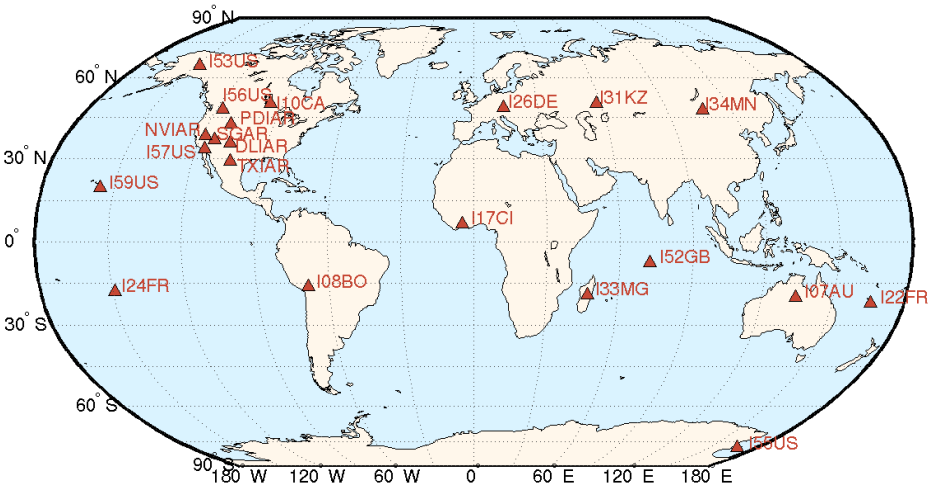


Figure 1. Infrasound stations for which noise was estimated.

Spectral Amplitudes of Noise

Plots of Power Spectral Density (PSD) for noise in four seasons and at four times of day are shown in Figure 2 for station I08BO in Bolivia. Southern hemisphere seasons are defined as summer: December 21-March 20; autumn: March 21-June 20; winter: June 21-September 20; and spring: September 21-December 20. Northern hemisphere seasons are reversed. All spectra calculated for each time and season interval are plotted as yellow lines, the median for each interval as a black line, and the 5th and 95th percentiles of the distribution as red lines. Green lines show the median of all spectra for all project stations, times and seasons (except those with anomalous instrument responses), and serve as a reference for comparison among time and season intervals and among stations. At all frequencies the amplitude varies among the I08BO spectra by 4 orders of magnitude. The median noise level is similar to the network median for some times, such as 6 PM in winter, but is almost 2 orders of magnitude higher than the median at others, such as noon in the spring. Plots similar to Figure 2 are provided for all 21 available stations in Bowman et al. (2004).

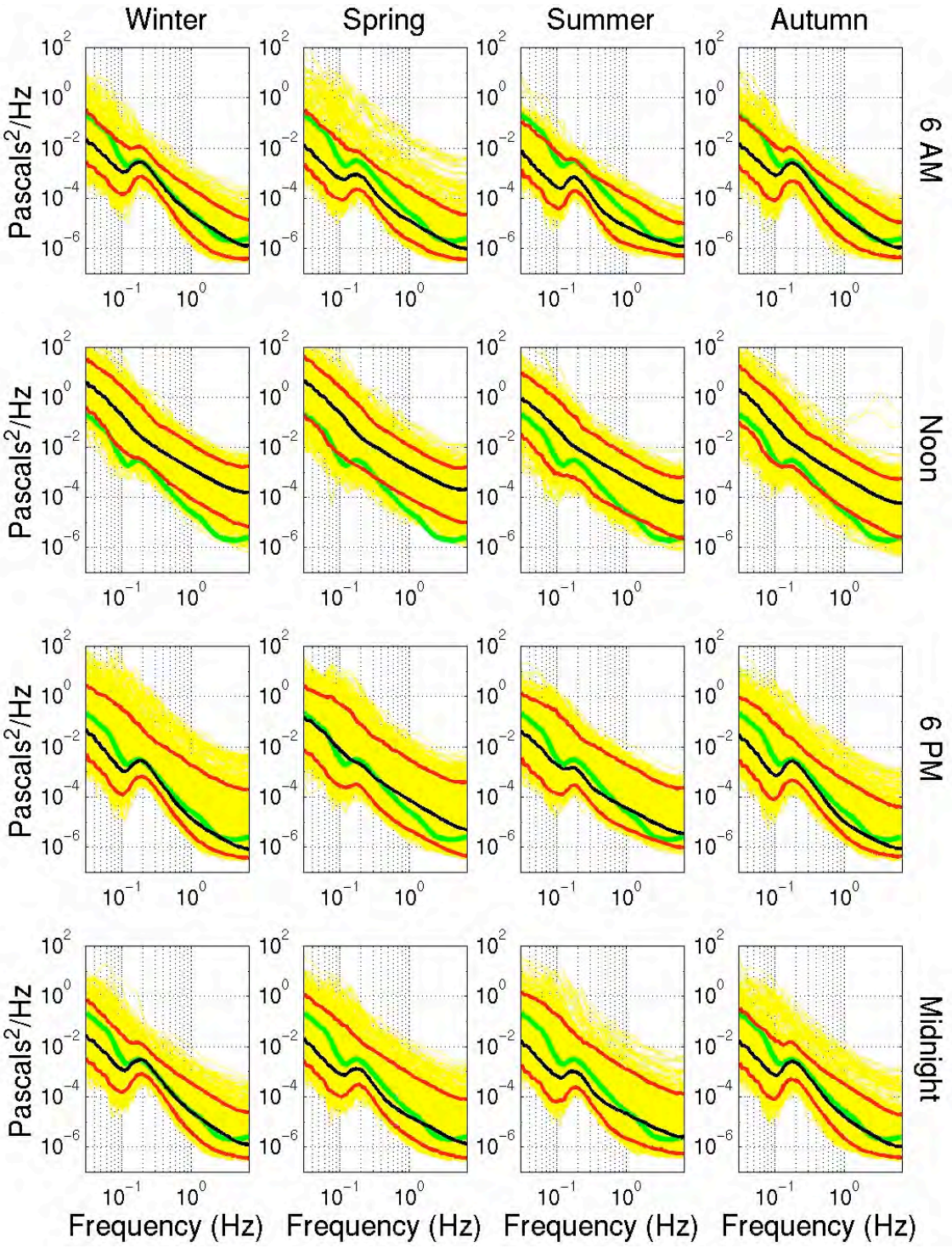


Figure 2. Power spectral density for I08BO, La Paz, Bolivia.

Plots are of power spectral density of individual time segments (yellow), the time and season specific station median (black) with 5th and 95th percentile confidence limits (red), and the all-time network median (green). The rows group plots by time intervals: 6 to 7 AM, 12 to 1 PM, 6 to 7 PM, and 12 to 1 AM local time. The columns group plots by seasons: winter, spring, summer, and autumn. Data were collected for I08BO from March 7, 2003 through January 31, 2004. Note that at any time, season and frequency the PSD varies by four orders of magnitude.

Several of the features seen in the noise spectra are highlighted here. Figure 3 shows the median power spectral densities recorded between 6 and 7 AM during each season at station I07AU in central Australia. The median PSDs vary seasonally by as much as an order of magnitude over most of the spectral range. The microbarom peak is only identifiable during summer, and then just barely, at this noisy station.

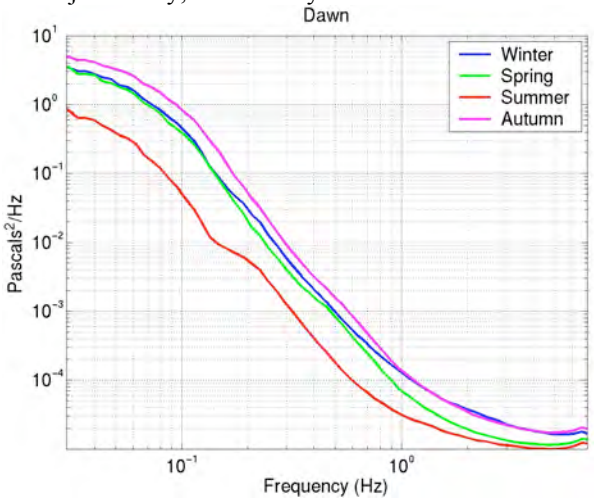


Figure 3. Median noise PSD from 6 to 7 AM during each season at I07AU, Warramunga, Australia. Noise levels are substantially lower in the summer than in the other seasons.

Figure 4 shows how the time of day can affect noise amplitudes at a single station. At I07AU the median power spectral density of noise at most frequencies is more than an order of magnitude larger around noon than at other times, although from 1 to 4 Hz, it drops dramatically to the quietest levels. The change in spectral slopes with time of day and frequency suggests that different processes may control the noise amplitudes at different frequencies, and those processes are most active at different times of day.

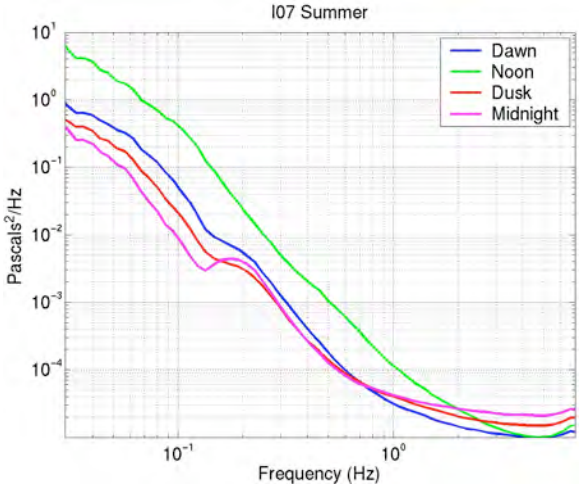


Figure 4: Median noise PSD during summer at four times of day at I07AU,Warramunga, Australia. Noise is substantially higher at noon than other times of day.

Figure 5 provides another example of seasonal variations in noise amplitudes and shows the effect of different spatial wind noise reduction filters on noise measurements at I57US, at Piñon Flat, California. It shows median pressure power spectral density recorded at midnight in January and July at nearby sites with high- (green) and low- (purple) frequency wind noise reduction filters. The filters are 18-m and 70-m pipe rosettes for the high- and low frequency sites, respectively (Hedlin et al., 2003) and were designed to suppress incoherent noise.

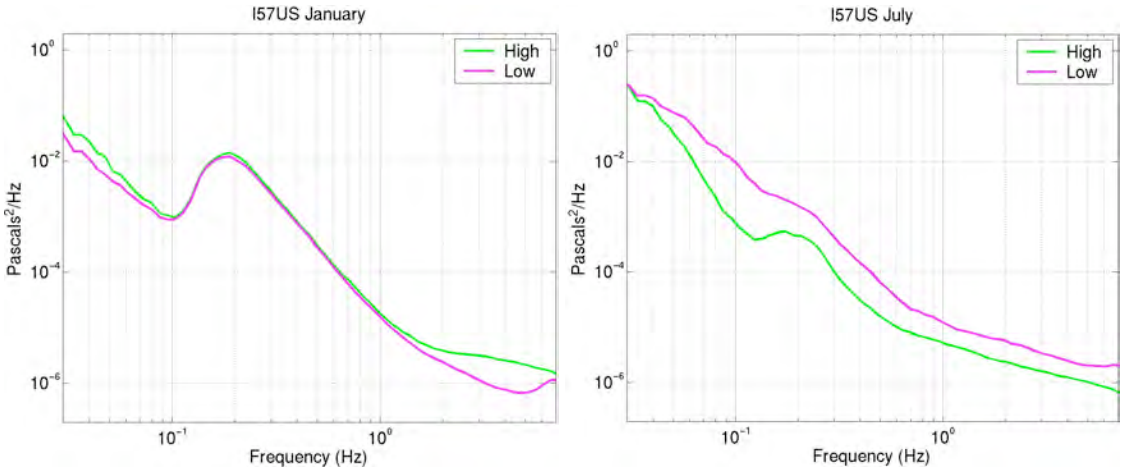


Figure 5. Median noise PSD at high- and low-frequency sites at I57US, Piñon Flat, California. Plots show noise from midnight to 1 AM during January (left) and July (right). Noise observed by the two nearby sensors with different spatial filters is almost identical between 0.1 and 1 Hz in January, but the noise observed at the site with the low-frequency filter is about a factor of 3 higher than the high in July.

Noise levels at the high- and low-frequency sites of I57US are similar in some passbands and seasons, and different in others. The left panel of Figure 5 shows noise for January. Microbaroms, centered at 0.2 Hz, are prominent at I57US during this winter month, because of the station's proximity to the ocean and its lower overall noise level compared to I07AU (Figure 3). Microbarom levels are nearly identical on the high- and low-frequency sites from 0.1 to 1.0 Hz, suggesting that they span both the high- and low-frequency sites. Microbaroms are acoustic waves, distinct from the pressure variations advecting past the sensors that are the likely sources of noise at other frequencies. We expect the high-frequency site's spatial noise filtering to perform worse at low frequencies, where noise may be coherent across all or most inlets, and this prediction appears to hold below 0.1 Hz in January. Noise amplitudes at the high-frequency site above 1.0 Hz are also higher than those at the low-frequency site, showing that the 70-m pipe rosette more completely suppresses uncorrelated noise.

The right panel of Figure 5 shows noise for July. The noise level above 0.03 Hz at the high-frequency site is much lower than that at the low-frequency site. The high-frequency site (I57H1) is surrounded by Piñon pine trees (Hedlin et al., 2003), which may reduce the wind velocity and therefore the noise compared to the low-frequency site (I57L1).

These observations provide an important reminder that the response of the noise reduction filters is not being taken into account, so the measurements recorded are not of pressure at the ground, but of pressure sampled at the many filter inlets and convolved with the filter response. The different responses of the noise reduction filters used at each installation may be responsible in part for the apparent differences in noise amplitudes and the falloff of noise with frequency.

The variability in noise levels at different stations and at different times of day is illustrated in Figure 6, which shows the median amplitude spectra of high-frequency sites at each station during the winter months, from 6 to 7 AM. PSDs are shown for 18 stations and are partitioned alphabetically. (Insufficient winter data were available for the other three stations.) A number of interesting observations can be made from these plots. One is that microbaroms, with a peak at 0.2 Hz, define a lower bound on the noise level at most stations and times of day. For stations where the microbaroms do not stand out, other sources of noise may be dominant. Second, although resonance within the pipe arrays typically peaks around 8 Hz, a broad pipe resonance may affect the background noise at lower frequencies for which we would like to detect signals of interest. For example, the noise level stops decaying at a rate of 1/f somewhere around 1 Hz at station I10CA in Canada and I26DE in Germany and by 4 Hz starts increasing towards the pipe resonance peak. In addition, the PDIAR station in Wyoming appears to have a reverberation peak at about 3 Hz.

At some stations, the noise level varies little with time of day, for example at I26DE and PDIAR. At others it varies considerably. For example, I24FR (Tahiti) is an order of magnitude noisier at noon than at dawn over all frequencies. It appears that diurnal wind noise intensity at many stations repeats from day to day. In contrast, noise levels at I55US (Windless Bight, Antarctica) do not exhibit diurnal variation, because of the station's extreme southern latitude.

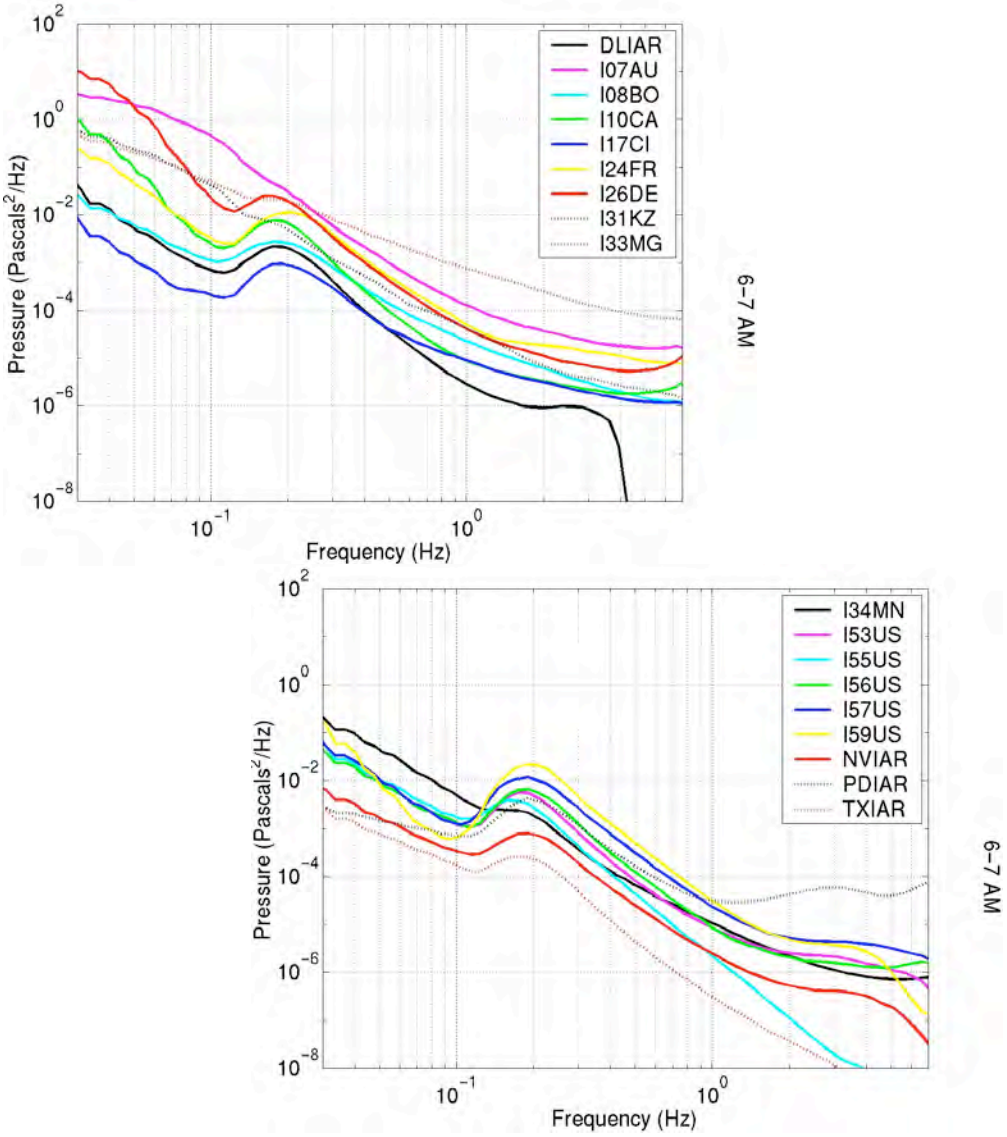


Figure 6. Comparison of wintertime power spectral density from 6 to 7 AM for project infrasound stations. Curves are median power spectral densities of noise between 6 and 7 AM during winter at high-frequency sites. Stations are divided alphabetically among the upper and lower plots for easier identification. The microbarom peak is clearly seen near 0.2 Hz at all stations except I33MG and I07AU. No winter data were available at I22FR, I52US, or SGAR.

From 6 to 7 AM, the noise level at I55US is in the middle of the range of spectral amplitudes at the microbarom frequencies and below, but falls off dramatically at high frequencies. The sharp drop may be due to generally low winds, the spatial filters, or the effect of snow cover that would filter wind noise when the snow is deep. Typically, the spatial filters must be extracted from under approximately 1.5 m of snow every year.

Instrument responses and electronic filters are also not consistent among stations. Some may be in error. The non-IMS stations SGAR (Utah) and PDIAR appear to be high-pass filtered, with much of the noise filtered out below 0.1 Hz. The high corner at the non-IMS station DLIAR seems to be at 3 Hz. Many of the stations appear to use low-pass, presumably anti-aliasing, filters with different high-frequency corners that are not properly represented in the station database. Furthermore, no correction has been made for spatial wind noise reduction filters, which may affect details of frequency response as well as the calibration value at the calibration period.

The seasonal variability of amplitudes at a single station, and the variation among stations, can be seen in Table 1, which lists the median amplitudes at 6 to 7 AM local time, for each season, at 0.2 and 1.0 Hz, for all high-frequency stations. The last row shows the ratio between the highest and lowest noise levels for stations in this season and passband. Dashes indicate times with no data or when gains were in doubt. Amplitudes at 0.2 Hz reflect the effect of microbaroms. The seasonal effect is generally stronger at 0.2 Hz than at 1 Hz. For example, at DLIAR the median amplitude at 0.2 Hz increases by a factor of 3 from summer to winter, while the 1 Hz noise is unchanged. PDIAR has by far the greatest change in 1 Hz median amplitude, dropping by a factor of 5.7 from autumn to winter, possibly due to snow cover. The corresponding drop at 0.2 Hz is by a factor of 3.5.

Table 1. Noise Amplitudes in Millipascals/Hz$^{1/2}$ by Season for High-Frequency Sites

Station	Spring		Summer		Autumn		Winter	
	0.2 Hz	1.0 Hz	0.2 Hz	1.0 Hz	0.2 Hz	1.0 Hz	0.2 Hz	1.0 Hz
DLIAR	–	–	15.5	1.7	37.9	1.8	44.6	1.7
I07AU	145.6	8.4	76.4	5.7	228.6	11.8	192.0	12.4
I08BO	27.5	3.7	24.2	2.7	48.8	4.4	48.7	4.8
I10CA	28.9	2.2	20.2	2.2	47.9	3.0	82.5	3.0
I17CI	21.4	1.8	30.2	3.0	20.3	1.3	15.5	1.3
I22FR	68.8	4.8	111.9	6.2	–	–	–	–
I24FR	80.4	6.5	102.6	5.7	121.4	6.5	109.2	8.8
I26DE	26.7	3.2	19.7	2.5	88.1	5.9	139.6	6.5
I31KZ	–	–	16.7	2.4	41.6	5.2	69.3	6.4
I33MG	71.6	14.0	89.8	11.6	100.6	14.5	130.3	26.5
I34MN	40.0	7.3	50.3	8.6	46.4	5.2	43.5	3.3
I52GB	–	–	–	–	43.6	4.4	–	–
I53US	22.5	1.5	15.4	1.5	61.2	3.0	69.7	3.0
I55US	33.4	0.8	36.8	0.8	67.0	1.6	49.9	1.3
I56US	18.8	1.8	15.0	1.4	50.4	3.0	79.6	3.0
I57US	–	–	25.6	2.5	109.5	5.3	104.8	4.9
I59US	48.0	2.9	30.0	2.9	94.8	4.4	145.3	5.7
NVIAR	16.2	2.3	8.8	1.2	23.7	1.6	27.4	1.6
TXIAR	13.2	1.2	11.9	1.1	16.3	0.7	15.3	0.6
PDIAR	120.1	24.5	123.0	31.7	217.7	31.7	63.0	5.6
SGAR	65.4	12.0	–	–	–	–	54.6	4.5
Ratio max/min	11.3	30.6	14.0	39.6	14.0	45.3	12.5	44.2

The maximum noise variations among stations range from 11 to 14 at 0.2 Hz and 30 to 45 at 1 Hz, depending on the season. The noise is generally higher in winter than summer by an average factor of 3 at 0.2 Hz and 2 at 1 Hz, although at I17CI, 134MN and PDIAR, the noise is higher in the summer at both frequencies.

In the course of this investigation, inspection of noise spectra uncovered a number of problems with instrument responses and gains, summarized in Table 2. This demonstrates the utility of examining noise to confirm proper operation of stations and to help to verify instrument response descriptions.

Table 2. Calibration Problems Identified at Network Stations

Station	Anomaly Identified	Resolution
DLIAR	Anomalous amplitudes for April 7 – June 3, 2003.	Excluded data from anomalous period from analysis.
I10CA	Unusual increase in noise spectral amplitude above 0.7 Hz.	Identified error in instrument response received from the International Data Centre (IDC) in 2001. Updated instrument response file with information from IDC database current in January 2004 and recalculated spectra.
I26DE	Same as for I10CA.	Same as for I10CA.
I52GB	Spectral amplitudes higher than observed by station operator.	Acquired new instrument response from station operator and recalculated spectra.
I57US	Anomalously high amplitudes by 10^4 for January -April 2003.	Excluded data from anomalous period from noise analysis. Identified and fixed problem with calibration value for anomalous period.
NVIAR	Spectral amplitudes are 6 orders of magnitude larger than other stations.	Acquired new calibration value from station operator and replotted spectra. Excluded station from network median noise.
PDIAR	Spectral falloff with frequency much flatter than other stations.	Made inquiries to station operator.
SGAR	Same as for PDIAR.	Same as for PDIAR.
TXIAR	Same as for NVIAR	Same as for NVIAR.

Transformation of Spectra to Probability Density Functions

A quantitative knowledge of the noise field at a given station is also essential for estimating that station's signal detection capability. However, infrasound detection is performed against time-domain measures, so the PSD is not the most useful form of noise information for that purpose. The ability of any time-domain detector to detect target signals is ultimately linked to the signal-to-noise ratio (SNR) so that the detection capability of a station is largely determined by the fraction of time that the SNR exceeds some detection threshold. The SNR is substantially controlled by the amplitude of the noise at any moment. Thus, we have converted the PSDs into time-domain noise amplitude Probability Density Functions (PDFs) at each station within each of several typical frequency bands used in infrasound detection processing, 0.1 to 0.5 Hz, 0.5 to 1.0 Hz, 1.0 to 1.5 Hz, 1.5 to 2.0 Hz, and 2.0 to 2.5 Hz. The conversion to root-mean-square time domain amplitude from the PSDs is straightforward. However, our infrasound detectors is based on mean-absolute amplitude, so we estimated a conversions between the two by evaluating both measures on random noise with a 1/f amplitude spectrum (an accurate first-order approximation in which noise is generated by shearing of eddies into ever smaller eddies) filtered to match each of the detection filter bands. PDFs were estimated for all 21 stations, the four seasons and four times of day, as for the PSDs, and can be found in Bowman et al. (2004).

The shapes and amplitudes of the noise PDFs at any given station vary substantially with time of day, seasons, and passband. Figure 7 illustrates some of this variation at I07AU. Noise amplitude histograms for the 0.5 to 1 Hz passband are displayed for January and February (summer) in the upper row for July and August (winter) in the lower row, at the four canonical times of day. Noon is the noisiest time of day in both seasons; dawn is also noisy in the winter. Dusk, especially in winter, and midnights during summer are the quietest times of day. At this station, the histograms have similar shape in all passbands, although the absolute amplitude decreases with frequency.

A noteworthy property of these histograms is their extreme skew to the right and heavy tails. In the past, noise amplitude has been approximated as log-normal in many estimations of station detection capability, but such extreme features may invalidate such approximations or at least complicate their application. Generally, we observe that the noise amplitude becomes more heavy-tailed than log-normal as the frequency increases. At I07AU the Kolmogorov-Smirnov test (e.g., Hogg and Tanis, 2000) indicates that the 0.1 to 0.5 Hz PDF has a probability of 0.61 of having been drawn from a log-normal distribution, and the 0.5 to 1 Hz PDD, a probability of 0.48. In the higher bands, that probability drops precipitously to 6.7×10^{-3}, 3×10^{-5}, and 4.2×10^{-7}, respectively. Even when diurnal and seasonal trends are accounted for, infrasound noise distributions cannot generally be described as log-normal.

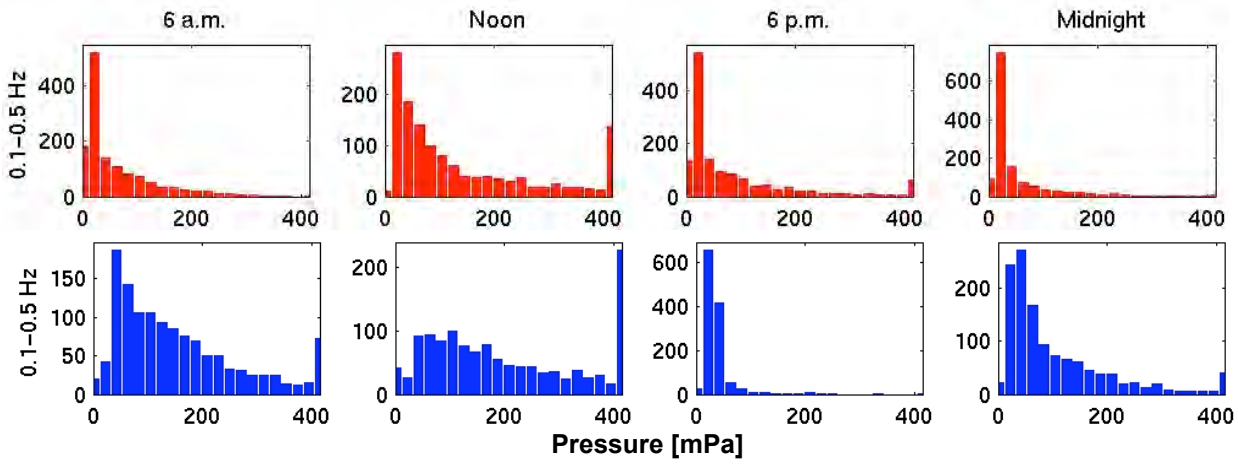


Figure 7. Noise amplitude histograms at I07AU, Australia.
Noise amplitude histograms for four different times of day during January and February (top row) compared with July and August (bottom row). Horizontal axis is noise amplitude in mPa. Maximum pressure plotted for each passband is that which includes 95% of the data for all times and months (the last 5% are included in the rightmost bins of the histograms for that passband). Bin widths are chosen to permit 20 bins.

Figure 8 shows empirical noise amplitude PDFs for station I59US, at Kona, Hawaii. I59US has generally lower noise levels than I07AU and, in contrast, the PDFs are quite different between summer and winter. Winter noise (January and February, bottom row) is higher and has heavier tails. Also unlike the I07AU observations, there is little difference due to time of day in either season. Again, the distributions are similar in different passbands for the same time of day and month.

The PDFs at I59US are closer to log-normally distributed than are those at I07AU, although all of the distributions still fail a Kolmogorov-Smirnov normality test. Specifically, they fail because they are heavier tailed than a Gaussian distribution. The deviation from log-normality of PDFs for I59US does not change systematically with passband.

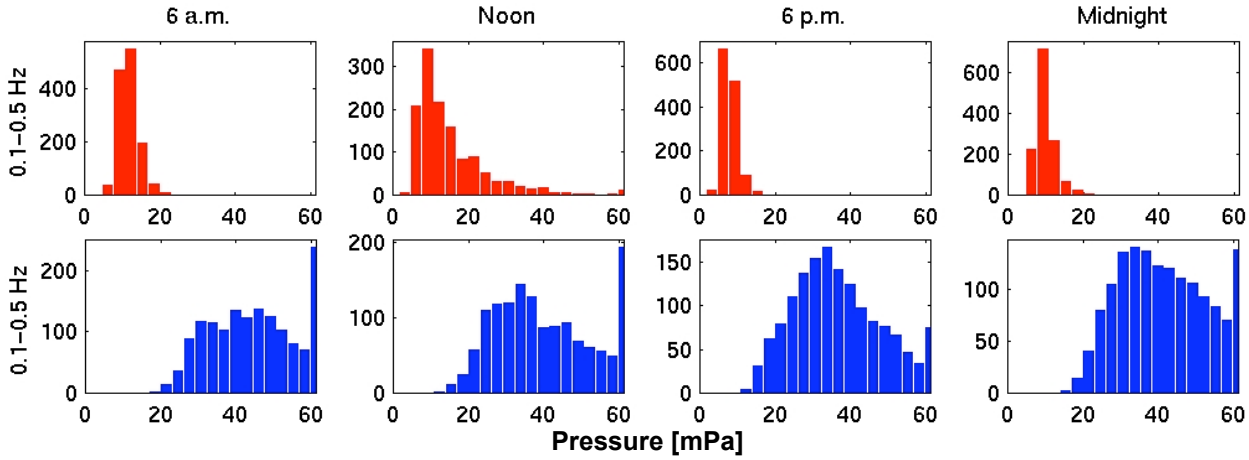


Figure 8. Noise amplitude histograms at I59US, Hawaii.
Details of the figure are the same as for Figure 7. Unlike the I07AU observations, there is little difference due to time of day in either season.

CONCLUSIONS AND RECOMMENDATIONS

Products and Accomplishments

- Summary statistics (power spectral densities and amplitude histograms) of infrasound background noise were tabulated versus season, time-of-day, and frequency at 21 existing infrasound stations.
- Instrument response or gain anomalies were uncovered during the noise survey and corrected for six stations (I10CA, I26DE I52GB, I57US, NVIAR and TXIAR) and documented for three others (DLIAR, PDIAR and SGAR).

Conclusions

- The median noise amplitude varies among the stations characterized by a factor of about 10 at 0.2 Hz and about 40 at 1 Hz.
- The median noise amplitude at a given station may vary by 2 orders of magnitude depending on time-of-day or season.
- The median noise amplitude at a given station is on average a factor of 2.5 higher during local winter than local summer.
- The frequency specific noise PDFs estimated for each station are not well approximated by a log-normal distribution as assumed in the past and, specifically, have longer than log-normal tails.

Recommendations

- Extend estimates of ambient noise to a full year for all current stations to fully quantify seasonal variations.
- Estimate ambient noise for new infrasound stations as they become available.
- Estimate the correlation between ambient noise and surface meteorological conditions for all infrasound stations.
- Estimate noise statistics at all station elements to capture site-to-site variations due to sensors, local topography, vegetation, etc.

ACKNOWLEDGMENTS

We thank Paul Piraino for calculating noise spectra, Bob North for identifying and helping to unravel errors in instrument responses, Dan Osborne for comments on an early draft, and Paul Golden for providing updated calibration values for two stations.

REFERENCES

Bahavar, M. and R. North, Estimation of background noise for International Monitoring System seismic stations, *Pure Applied Geophysics*, 159, 911-944, 2002.

Bowman, R., M. O'Brien, D. Adams, M. Bahavar, E. Baker, J. Bhattacharyya, D. Drob, M. Garces, C. Hetzer, H. Israelsson, D. Norris, C. Reasoner, G. Shields and J. Stevens, Methods for monitoring nuclear explosions using infrasound, SAIC technical report SAIC-04/3000, 2004.

Coyne, J. and I. Henson, Geotool Sourcebook: User's Manual, Teledyne Brown Engineering, Scientific report. no. 1, 01 Sep 1995.

Hedlin, M. A. H., B. Alcoverro, G. D'Spain, Evaluation of rosette infrasonic noise -reducing spatial filters, *J. Acoust. Soc. Amer*., 114, 1807-1820, 2003.

Hogg, R.V. and E.A. Tanis, Probability and Statistical Inference (6th Edition), Prentice Hall, 704 pp., 2000.

INFRASOUND SIGNAL LIBRARY

Eric P. Chael[1] and Rodney W. Whitaker[2]

Sandia National Laboratories[1] and Los Alamos National Laboratory[2]

Sponsored by National Nuclear Security Administration
Office of Nonproliferation Research and Engineering
Office of Defense Nuclear Nonproliferation

Contract No. DE-AC04-94AL85000[1] and W-7405-ENG-36[2]

ABSTRACT

We have been retrieving old infrasound recordings from the archives at Sandia National Laboratories (SNL) and Los Alamos National Laboratory (LANL). The archives at SNL hold many boxes of paper strip-chart records collected by the Blast Prediction Unit during the era of atmospheric nuclear testing at the Nevada Test Site (NTS), between 1953 and 1961. The NTS tests were typically recorded using either single or dual sensors, at about a dozen sites from the Control Point on NTS to as far away as Bishop, California. From the SNL holdings, we have selected events spanning a wide range in yields, from well below 1 kiloton to as high as 74 kilotons. Data from these tests should be valuable for studies of the scaling of infrasound signals with source size. In addition, we have selected the few available high-altitude tests, to address the variation of the signals with source altitude. We are digitizing all of the available signals for each selected test, using a continuous-feed scanner and a commercial software package designed for digitizing well logs. To date, we have recovered over 100 traces. Los Alamos has operated 4-element infrasound arrays in New Mexico and Utah since the early 1980s. These stations have recorded numerous underground NTS tests, as well as many chemical explosions, earthquakes, and a few bolides across the western United States (US). Most of the recordings prior to the mid-1990s were archived on 9-track magnetic tapes. The age of the tapes and the scarcity of the obsolete tape drives combine to make these data difficult to recover. We obtained a 9-track drive that we can operate from a Unix workstation. We have retrieved nearly 2 gigabytes of data from the old tapes, and expect to double this amount. Prior to completing this project later this year, we will enter many of the signals we have retrieved in the familiar National Nuclear Security Administration (NNSA) schema, including the origin, site, sitechan and wfdisc tables. These tables and the binary waveform files will then be made available to the monitoring research community, and some will be incorporated in the NNSA Knowledge Base (KB).

OBJECTIVES

Our objectives have been to recover valuable infrasound recordings of atmospheric and underground nuclear tests and other events from the archives at Sandia National Laboratories (SNL) and Los Alamos National Laboratory (LANL); to digitize the SNL strip-chart records and extract the files from the LANL 9-track tapes; to convert the signals we recover to the current NNSA schema; and to provide the resulting signal library to the infrasound monitoring research community. The collection will provide reference information on known events that should help to improve the analysis of data from the infrasound network under development for the International Monitoring System.

RESEARCH ACCOMPLISHED

Nuclear testing at the Nevada Test Site (NTS) began in 1951. Throughout the 1950s, most tests at NTS were detonated above ground. SNL established a Blast Prediction Unit (BPU) in 1951 to monitor the off-site pressure waves from these tests, primarily in order to minimize damaging overpressures in the surrounding communities, including Las Vegas, Nevada (Reed, 1974). The BPU designed an infrasound recording system that used commercial pressure sensors and strip-chart recorders. The recorders added a time code along the bottom of the chart; fiducial pulses were added to the pressure signals at the shot time and at 5-minute intervals thereafter. This system was typically deployed at 10—12 sites, mostly in Nevada, Utah, and California (Figure 1), for all subsequent atmospheric nuclear tests. In addition, many of the Project Plowshare cratering tests were recorded, as well as numerous underground tests. Nearly all of the original paper records have been preserved in SNL's archives.

Because of the renewed international interest in infrasound monitoring, we have been working to digitize some of the old records and make these data available to researchers.

The original paper records are 9 cm wide but can be many meters in length (see Fig.ure2 for a sample). As a result, they are not readily reproduced nor can they be conveniently handled on common digitizing tables. We procured a system developed for digitizing paper well logs, which are similar in shape. It employs a continuous-feed scanner that generates a scanned image file for each paper record and a software package for digitizing the traces from the image. Once the time and amplitude axes are defined for the software, it can automatically follow a trace with reasonable success. The operator monitors the progress to ensure that the program follows the desired trace and validates the fidelity of the end result. Finally, the software writes the digitized signal to a text file as a series of paired time and amplitude values.

Our initial emphasis has been to digitize signals from atmospheric tests spanning a wide range in yields to support studies of scaling relationships. For this, we began with the tests of Operation Teapot in the spring of 1955. This series included several events with yields from 1 kt to 43 kt, all detonated a few hundred feet above ground. For comparison, we have done a single record from the 13.5 Mt surface event Yankee in the Pacific, and signals from the cratering test Ess. We have also retrieved the signals from the test HA, detonated at an altitude of 11 km above sea level. Records from this and the few other high-altitude tests should be useful for studying the variation of the signals with source altitude and perhaps for improving the infrasound-based energy estimates for bolide events. Table 1 lists the tests whose signals we have digitized to date. We have extracted about 15 traces per test from the available stations, some of which used two sensors separated about 1 mile along the direction from NTS. We have at present over 100 digitized traces in hand and we hope to process a few more events under the current funding for this effort.

The last step in preparing these data for use in the Knowledge Base will be to convert the text output files to binary waveform files, and to generate the appropriate tables for capturing the necessary event, station and waveform information. The tables will follow the well-established NNSA schema, which will make the signals readily useable by a wide array of analysis programs.

Table 1. Tests for which SNL infrasound records have been digitized.

Date	Name	Location	Yield
May 4, 1954	Yankee	Bikini Atoll	13.5 Mt
Feb 18, 1955	Wasp	NTS	1 kt
Mar 7, 1955	Turk	NTS	43 kt
Mar 12, 1955	Hornet	NTS	4 kt
Mar 22, 1955	Bee	NTS	8 kt
Mar 23, 1955	Ess	NTS	1 kt
Mar 29, 1955	Wasp Prime	NTS	3 kt
Apr 6, 1955	HA	NTS	3 kt

Los Alamos National Laboratory has operated infrasound arrays in Nevada, New Mexico, and Utah since the early 1980s. These were mostly four-element arrays, with three sensors arranged in a triangle and the fourth at the center. In some cases, seismic data were also recorded at the same sites. Over the years, these arrays have recorded a variety of acoustic events, including underground nuclear tests at NTS and subsequent cavity collapses, conventional explosions both above and below ground, moderate-sized shallow earthquakes, space shuttle reentries, and possibly some bolides. The recordings also contain some unique events such as a boundary-layer turbulence experiment conducted in Boulder, Colorado by the National Oceanic and Atmospheric Administration (NOAA). Data from the LANL stations were written to 9-track magnetic tapes until the mid-1990s, and many boxes of these tapes have been preserved at LANL. However, the 9-track drives have since become obsolete, and it is now difficult to obtain a working unit. We were fortunate to find a drive in the property reapplication yard at SNL. Connected to a Unix workstation, this drive is again operational and can successfully read most of the LANL tapes, despite their advancing age. We began by selecting tapes most likely to contain interesting events and are currently reading them. So far, we have retrieved about 2 Gb of data from these tapes. A number of different formats were used for the files; we have definitions for most of the formats and expect to identify the remaining ones. Figure 3 shows the signals recorded by the four elements of the array in Los Alamos, New Mexico following the underground test Barnwell, detonated at NTS on December 8, 1989. As with the digitized SNL traces, the signals from these tapes will be converted to the formats used by the NNSA Knowledge Base, complete with tables of event, station, and waveform information.

The holdings at LANL contain two additional data sets of potential interest, both comprised of paper records that will require digitization. The first of these consists of select events from the infrasound network operated by the Air Force Technical Applications Center (AFTAC) from the 1950s to the 1970s. This set includes nearly 100 records from atmospheric explosions and bolides, which are the most important impulsive natural sources of infrasound. The second data set represents a series of large-scale explosions sponsored by the Defense Nuclear Agency and conducted at White Sands Missile Range. These tests had charge weights of 24 to 4,880 tons and were executed between 1981 and 1993. They were recorded at the LANL arrays and usually at 2 to 4 mobile stations. We do not anticipate digitizing any of these signals under the current project, but they could be retrieved if follow-on efforts are warranted.

CONCLUSIONS AND RECOMMENDATIONS

Because the nuclear powers have effectively discontinued testing, both above and below ground, the archived pressure signals at SNL and Los Alamos provide invaluable reference data for the future International Monitoring System (IMS) infrasound network. Though the recordings are now decades old (and some are over 50 years old), most can still be recovered and converted to current digital formats. Under this project, we have retrieved a significant number of the signals of highest interest, but these represent well below half of the available holdings. We will keep the digitizing platform and the 9-track tape drive while they remain serviceable. We recommend that the effort to recover the remaining infrasound signals be continued.

REFERENCES

Cox, E. F. and J. W. Reed (1957), Long-Distance Blast Predictions, Microbarometric Measurements, and Upper-Atmosphere Meteorological Observations for Operations Upshot-Knothole, Castle, and Teapot, *Report* WT-9003, Sandia Corporation, Albuquerque, NM.

Reed, J. W. (1974), Archiving Guide to Microbarograph Records of Nuclear and Chemical Explosion Tests, *Report* SLA-74-0210, Sandia Laboratories, Albuquerque, NM.

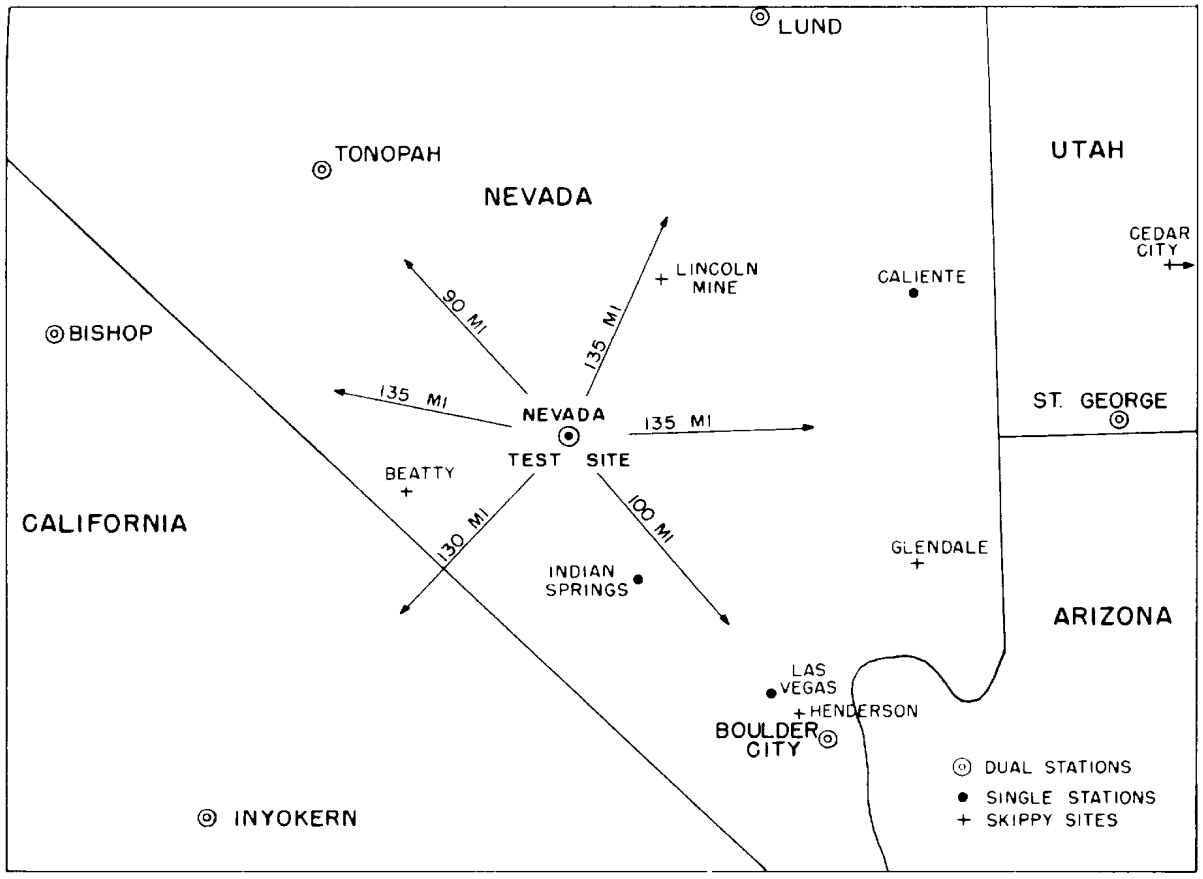


Figure 1. Map of microbarograph station locations used during 1955 (Cox and Reed, 1957).

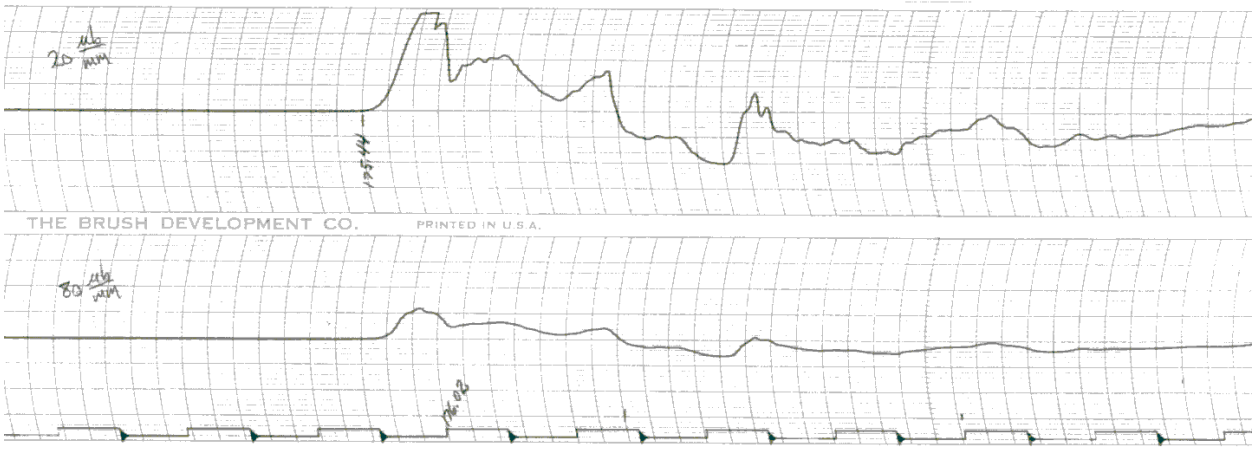


Figure 2. A portion of the strip chart from Indian Springs, NV for the NTS test HORNET, 3/12/1955.

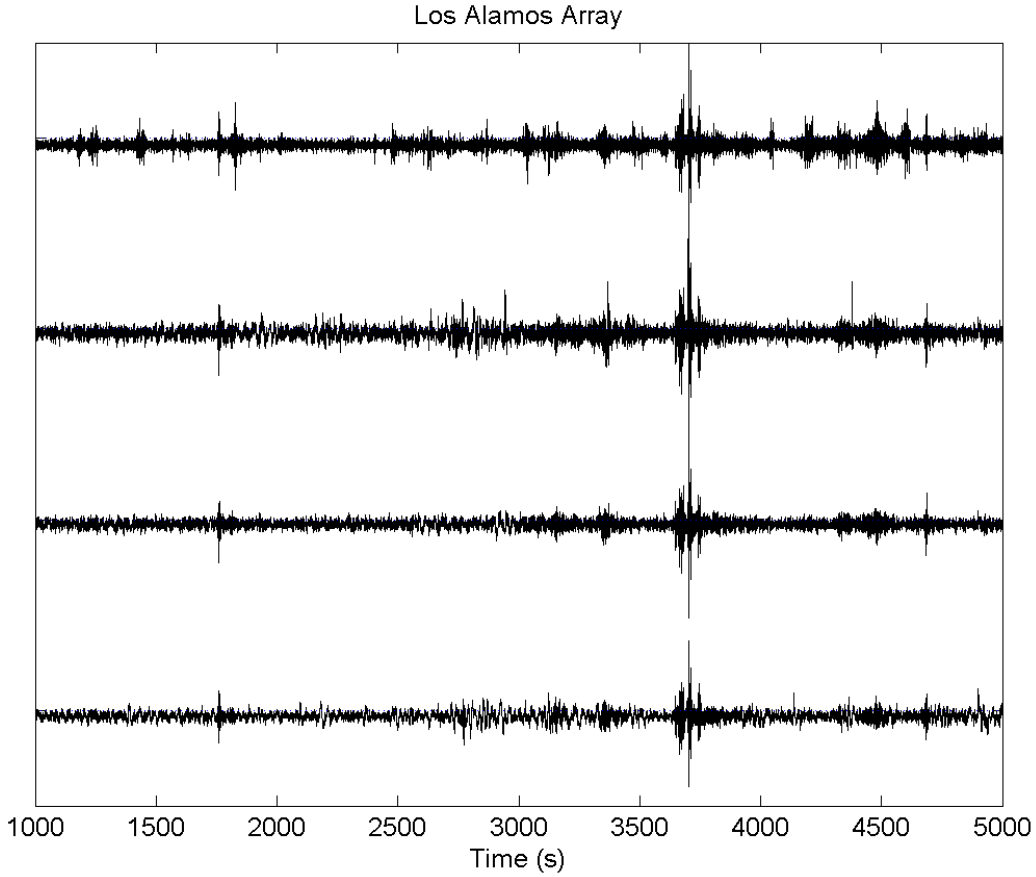


Figure 3. Los Alamos Array recordings for the NTS test BARNWELL, December 8, 1989.

THE HUNT FOR LEAKY ELEVATED INFRASONIC WAVEGUIDES

Milton A. Garcés, Mark Willis, Claus Hetzer, and S. Businger

University of Hawaii, Manoa

Sponsored by Army Space and Missile Defense Command

Contract No. DTRA01-01-C-0077

ABSTRACT

The ability to locate explosive events with infrasound pivots on our understanding of the temporal and spatial scales of atmospheric variability that define the propagation paths that sound waves may take from the source to the receiver. Source location analyses of bolide events suggest that high-altitude sources may efficiently ensonify elevated waveguides in the stratosphere, and that this acoustic energy may leak to the ground by diffraction and scattering. There is also a precedent for ground-based explosive sources that may yield stratospheric returns even when sound is propagating against the prevailing winds. Microbaroms are infrasonic waves generated by nonlinear interactions of ocean surface waves traveling in nearly opposite directions with similar frequencies. Such interactions commonly occur between ocean waves with approximately 10-second periods, which are abundant in the open oceans and correspond to the observed 0.2 Hz infrasonic spectral peak. Although microseisms and microbaroms share a common source, microseisms in the ground and oceans are generated by the vertical component and microbaroms are generated by the near horizontal component of the source radiation pattern. In contrast to microseisms, microbarom signals are also strongly influenced by the atmospheric winds. We compared microbarom signals observed at Hawaii in 2003 with the Wavewatch 3 ocean wave model and the Naval Research Laboratory (NRL) Ground-to-Space (G2S) atmospheric specification. The arrival azimuths of coherent microbarom signals observed in Hawaii are associated with high ocean wave activity in the Pacific Basin, the dominant wind directions in the troposphere, stratosphere, and mesosphere, and the thermal structure of the atmosphere. Some of the seasonal trends in the microbarom observations can be explained by the winds in the stratosphere and lower mesosphere, while some of the daily variability can be explained by the winds in the troposphere and lower stratosphere. However, coherent energy from powerful swells may overcome the wind-carried microbarom signals and arrive to the station through thermospheric ducting. Our observations suggest that either (1) the wind speeds in the troposphere, stratosphere and lower mesosphere may be underestimated in atmospheric models or (2) leaky elevated infrasonic waveguides are persistent propagation paths that should be investigated in more detail. Although ocean swells have been previously used as a natural source for continuous measurements of atmospheric winds over long horizontal ranges, recent advances in measurement and modeling techniques can provide new insight on this complex but tractable method for continuous, passive acoustic tomography of the atmosphere.

OBJECTIVE

The aim of this work is to characterize microbarom signals observed in the Pacific and model the source processes that generate these signals, with the aim of determining infrasonic detection thresholds in the microbarom frequency range. In the process of differentiating the effects of swells and winds on infrasonic wave generation and propagation, we also found that microbarom signals may be readily used to test and validate atmospheric winds and temperature specifications in the lower, middle and upper atmosphere. Such accurate atmospheric specifications are essential for the development of accurate infrasonic location algorithms.

RESEARCH ACCOMPLISHED

Introduction

A large fraction of the ambient infrasonic field observed at I59US, Hawaii, is related to pervasive signals known as microbaroms. Microbaroms are observed as a continuous atmospheric pressure oscillation with most of its energy between 0.1 and 0.5 Hz (Figure 1). Microbaroms are detected at the I59US arrays as coherent bursts with durations of minutes and have a root mean square (RMS) amplitude varying between approximately 10 mPa and 100 mPa. For infrasonic stations near the ocean, microbaroms comprise the low-wind noise floor. The microbarom peak is in the midst of the detection region for 1-kt nuclear explosion tests, and thus microbaroms can obscure an important signal of interest.

Microbaroms were first observed by Benioff and Gutenberg (1939) on an electromagnetic microbarograph at the Seismological Laboratory of the California Institute of Technology. At the time of their studies, there was no accepted hypothesis for microbaroms or their better-known seismic counterparts, microseisms. Longuet-Higgins (1950) was the first to recognize and develop a theory for the excitation of microseisms by ocean waves. Studies by Saxer (1945, 1954), Daniels (1952, 1962), Donn and Posmentier (1967), Donn and Naini (1973) and Rind (1980) confirmed that microbarom and microseism sources are related to strong storms over the ocean and the resulting high seas. The accepted physical mechanism for microbarom and microseism generation is the nonlinear interactions of ocean surface waves traveling in nearly opposite directions with similar frequencies (e.g. Arendt and Fritts, 2000). Microbaroms exhibit frequencies twice that of the individual ocean waves and amplitudes proportional to the product of the energy of the opposing wave trains. However, while microseisms propagate through the ground as a result of vertical excitation through the ocean, microbaroms propagate to infrasonic stations after horizontal propagation through the atmosphere (Tabulevich, 1995). Thus seismic and infrasonic measurements sample complementary portions of the total radiated source field. Yet microbaroms will be primarily affected by the dynamic temperature and wind structure of the atmosphere, whereas microseisms will be propagated through the relatively static geologic structure of the Earth. This paper seeks to explain in more detail the effects of atmospheric temperature and winds on the spatial, temporal, and spectral distribution of coherent and incoherent microbarom energy.

A typical power spectral density plot for I59US is shown in Figure 1. During the winter season, when surf is highest, the frequency band above 2 Hz is dominated by sound from breaking ocean waves (Garcés *et al.*, 2003). The large, broad peak between 0.1 and 1 Hz corresponds to coherent and incoherent microbarom energy arriving from all possible source regions in the Pacific. The microbarom peak usually has a maximum at 0.2 Hz, corresponding to the 10s periods common to open-ocean swells, but may have a secondary peak between approximately 0.12 and 0.15 Hz or the peak may appear to broaden to include this frequency band. As discussed in Willis (2004), the lower frequency component corresponds to large, long-period swells that can be sufficiently energetic to dominate the coherent infrasound field in the microbarom band. Previous work (Daniels, 1952; Donn and Rind, 1971; Rind, 1978) related microbarom amplitude variability to solar tide fluctuations in the thermosphere during winter and stratospheric wind strength during summer. Their studies concentrated on the results from an infrasound station in the eastern U.S. that was primarily exposed to microbaroms arriving from the North Atlantic. Le Pichon *et al.* (2003) showed a correlation between the prevailing direction of the stratospheric winds and microbarom arrival azimuths observed by southern hemisphere stations. These austral stations would primarily observe the ocean swells driven by southern hemisphere typhoons and the continuous circumpolar winds. In this study we investigate microbaroms arriving at Hawaii from anywhere in the Pacific Ocean, and we present a relationship between the arrival direction of coherent microbarom energy and the dominant wind direction in regions of the troposphere,

stratosphere, and lower mesosphere. In addition, we postulate that microbaroms generated by energetic swells may refract in the thermosphere to arrive at a station from any direction.

Microbarom observations at I59US during 2002–2003

The Progressive Multi-Channel Correlation (PMCC) algorithm of Cansi *et al.* (1995) is the primary detection system used at I59US. PMCC uses the cross-correlation between various groupings of three sensors to estimate the consistency of the lag-closure (Cansi and Klinger, 1997). A microbarom detection is only registered if the consistency is below 0.5s within the 0.1–0.5 Hz passband. The microbarom event processing scheme utilizes an analysis of overlapping windows of data (length–90s, overlap–70s). PMCC is used to detect coherent infrasonic energy across the array, which allows the apparent horizontal phase speed, arrival azimuth, and amplitude of the detected arrivals to be extracted. Infrasonic power spectral densities (Figure 1) are used to study the spectral structure in the microbarom frequency range. The power spectral densities were computed using the modified periodogram method (Madisetti and Williams, 1998) with a 102.4s Hanning window (2^{11} samples) and a 50% overlap. Power spectra include the combination of both coherent and incoherent microbarom contributions. Infrasonic power spectral densities at I59US exhibit a quasi-permanent peak around 0.2 Hz (Figure 1). This corresponds to the abundance of microbarom energy produced by opposing ocean waves containing periods of approximately 10s. Occasionally, the peak will broaden or split at slightly lower frequencies (approximately 0.12 to 0.15 Hz) when the conditions are just right to where strong storm systems are producing an abundance of interacting long period swell energy.

Strong microbarom signals tend to arrive from regions of marine storminess because they can produce high amplitude ocean waves converging from opposite directions. By using wave spectra output by the Wavewatch (WW3) model (Tolman et al., 2002) in conjunction with the infrasonic source formulation of Garcés et al. (2003), Willis (2004) confirmed that strong microbarom source regions in the Pacific often occur in the wake regions of both mid-latitude and tropical cyclones, where swell spectra are confused with multidirectional components created ahead of and behind the surface low center (Figure 2). This research also showed that strong signals can originate outside of storm wake regions (occasionally 1,000–3,000 km away from the wave producing winds), especially when multiple storms are present. The wake region microbarom generation theory is discussed in Ponomaryov et al. (1998) and converging wave trains of opposite directions were also observed in the wake of Hurricane Bonnie (Wright et al, 1998).

Coherent microbarom arrival azimuths and amplitudes at the I59US site during 2002–2003 show an annual cycle (Figure 3). During the months from June through September microbarom arrivals generally come from east (55°–130°) or south (160°–220°) directions. The concentration of east arrivals is much stronger than the south arrivals during this time. Months October through March show an abundance of arrivals from 230°–360° with a peak from northwesterly directions. Arrivals during April, May, late September and early October appear to arrive from a variety of different azimuths with no distinct peak noted. Annual arrivals correspond to dominant storm activity in the Pacific Basin but are also affected by topographic shadowing and zonal and meridional winds throughout the atmosphere.

A total of 21,459 coherent microbarom arrivals reached I59US in 2003. Of these arrivals 9,334 (43%), came from 270°–315°. The second highest 45 degree directional bin, 225°–270°, contained 4,211 (19.6%) microbarom arrivals during 2003. 2606 arrivals (12%) came from 45°–90°, 1605 (7.5%) from 315°–360°, 1599 (7.5%) from 180°–225°, 1,168 (5.4%) from 0°–45°, 549 from 90°–135°, while only 377 arrivals came from azimuths 135°–180°.

During the first quarter of 2003 (containing months December 2002, January and February 2003), 98% of the microbarom arrivals came from azimuths 225°–360°. The second quarter of 2003 (March, April, May) shows a similar directional dependence with 81% of the arrivals coming from 225°–360°. However, stronger signatures from 0°–90° (13%) and 180°–225° (4%) were evident in the second quarter, than in first quarter.

A very different pattern of microbarom arrival azimuths was observed during the boreal summer months. 70% of the arrivals during June, July, and August came from 0°–135° while 26% came from 135°–225°. Arrivals at I59US during the fall months of fourth quarter (September, October, November) show a very similar pattern to the springtime (second quarter) arrivals–with 72% coming from 225°–360°, 13% from 0°–90°, and 10% from 180°–225°.

The effect of temperature and wind on the reception of microbarom signals

The temperature and winds in the atmosphere determine where sound waves travel (e.g. Cox et al., 1954). Infrasound can propagate for long ranges in waveguides defined by the thermal and wind structure of the atmosphere. Along the downwind direction, infrasonic energy may be trapped between the ground and the troposphere and lower stratosphere (tropospheric ducting), and between the ground and the stratosphere and lower mesosphere (stratospheric ducting). However, if the winds are not sufficiently strong, these tropospheric and stratospheric waveguides do not reach the ground. From a ray theory perspective, such elevated waveguides would not be able to transfer energy to ground-based recording stations. But in practice, such waveguides may leak energy to the ground through diffraction and scattering (Garcés et al., 2002b). Due to the high temperatures at the thermosphere, infrasonic energy is always refracted back to the ground by the thermosphere (thermospheric ducting), although the attenuation is stronger for these paths.

In order to produce atmospheric specifications for infrasonic propagation studies, NRL G2S model (Drob et al, 2003) was run to produce a self-consistent dataset extending from January 1, 2003 to March 29, 2004. Global spectral coefficients of wind, temperature, and density were produced at 6-hour time intervals. These coefficients have a triangularly truncated spectral order of 72 (T–72) resulting in an effective output resolution of approximately 2.25 degrees.

From the Earth's surface to 10 mb (0 to 35 km), we use 1x1 degree operational global aviation weather forecasts from the National Oceanic and Atmospheric Administration (NOAA) National Centers for Environmental Predication (NCEP). From 1 to 0.4 mb (20 to 55 km), we use the 1.0 x 1.5 global assimilative analysis from the NASA Goddard Space Flight Center, Global Modeling and Assimilation Office (GSFC-GMAO). This data set is limited distribution but available for basic scientific research. The upper atmosphere conditions (50 to 170 km) are specified by the HWM/MSIS models, which use the 3-hour and daily geomagnetic activity (Ap) and solar EUV flux (F10.7) indices from the NOAA space environment center (SEC). The trade winds typical of the tropical regions are generally limited to the lower 4 km of the atmosphere, and may be excessively averaged by the 1 km grid of the G2S specifications.

In order to investigate the effect of atmospheric winds on microbarom propagation, the wind speed and wind arrival azimuth (Figure 4) were extracted from the G2S global grids at a vertical profile above the Hawaii infrasound station. We evaluated Figures 1 and 2 at a fixed time (18 h GMT) to eliminate the variability induced in the thermosphere by the solar tides (Garcés et al., 2000). Although most of the tropospheric variability appears to be governed by storms, it is possible to observe clear seasonal patterns above 15 km. As will be discussed in the next section, the detection of coherent microbarom energy appears to be primarily dictated by the proximity of the source, the swell extent and size, and the predominant wind direction in specific regions of the atmosphere.

Microbaroms determined by swell size, wind strength, and source proximity

Modeling the radiation of infrasonic waves from the nonlinear interaction of ocean waves is far from trivial. Willis (2004) used the output of the WW3 model to produce a frequency-dependent synoptic plot of the microbarom source regions in the Pacific. His results show that microbarom sources with a frequency of 0.2 Hz form predominantly between two storms or in the lee of a storm, and are abundant in the Pacific. Thus a listening post in the midst of the ocean will be continuously bombarded by microbarom signals originating from multiple azimuths and ranges. When these signals arrive at an infrasonic array and are processed to find the most coherent arrivals, a competition ensues. Figure 5 shows as black dots all the coherent arrivals observed in Hawaii for 2003. These arrivals have an apparent horizontal phase velocity that is close to that of the sound speed at the ground, suggesting that the source energy was radiated very close to the horizontal. There is an obvious seasonal trend, with microbaroms arriving predominantly from the northwest in winter and south and northeast in summer. The prevailing wind directions between 50–70 kms are shown as red dots, and the winds between 10–20 kms are shown as blue dots in Figure 5. We can see that the seasonal pattern roughly coincides not only with the most energetic swell source regions but also with the prevailing wind directions in the selected layers. Microbaroms arriving from the south during summer, which would reach at the Hawaii array through multiple bounces between the thermosphere and the ground, would be affected by the solar tides in the upper atmosphere. As shown in Willis (2004), the summer arrivals appear to have a lower amplitude. During the shoulder periods of spring and fall,

arrivals are more evenly distributed along the compass (Willis et al., 2004), corresponding to the change in the wind patterns and a more equitable partition of swell energy between the northern and southern hemispheres. By using the G2S models to compute the wind-corrected effective sound speeds over Hawaii, the upper boundaries of the stratospheric ducts are predicted to reach as high as 70 km during winter, and as low as 60 km during summer. However, from April to May and September to October, stratospheric winds are light. and stratospheric waveguides are predicted to be elevated above the ground. Likewise, tropospheric winds at approximately 10 km are only sufficiently strong in January and February to consistently maintain a ground-reaching tropospheric waveguides. The lower panel of Figure 5 shows a close up of the upper panel for the months of January and February of 2003. These are often the most active swell months for the Hawaiian Islands. Some of the microbarom arrival azimuths in January and February track the tropospheric winds very well, corresponding to energy that would be refracted back to the ground between the 10–20 km height in the atmosphere, where there is very little attenuation. Likewise, energy ducted between the lower mesosphere and the ground would suffer very little attenuation and thereby retain a relatively large amplitude. However, some microbarom azimuths do not match the prevailing winds, as in the case of January 4–to 7, 2003. This case study corresponds to the largest swell event of 2003 (Garcés et al. 2003), is considered in detail by Willis (2004), and will be the subject of a separate paper. The marine storm responsible for this event produced high open ocean wave heights over a wide spectrum of frequencies between 0.05 and 0.1 Hz, and thus produced high microbarom source amplitudes between 0.1 and 0.2 Hz. High source amplitudes, coupled with lower attenuation and a larger correlation length at lower frequencies, would permit long-range propagation of this energy over large distances and preferential detection by an array.

Thus it is possible to explain the structure of ocean-related infrasound spectra observed in Hawaii (Figure 1) by attributing (1) a broad 2–5 Hz energy peak to breaking ocean waves (surf) in the littoral zone, (2) 0.2 Hz energy to the predominant 10s swell energy and (3) 0.1–0.2 Hz energy to 12s–20s period swells associated with powerful storms. The surf peak depends on the swell energy arriving near the array site, and in Hawaii surf sound appears to be propagated in the boundary layer and the troposphere. The coherent component of the main microbarom peak at 0.2 Hz depends on the prevailing winds and the amount of swell energy in the ocean. However, the energy of the main microbarom peak is the sum of coherent and incoherent components, and the amplitude of this peak may be related to the diurnal tides in the upper atmosphere (Rind, 1978). Coherent microbaroms in the approximately 0.12 to 0.2 frequency range may arrive from any direction where energetic long-period swells are interacting, and under certain circumstances may also be used to study the mesosphere and lower thermosphere (Garcés *et al.*, 2002a). Such thermospheric returns would explain southerly arrivals associated with the powerful southern hemisphere swells during the boreal summer.

CONCLUSIONS AND RECOMMENDATIONS

Microbaroms are generated wherever ocean surface waves traveling in nearly opposite directions with similar frequencies meet. This situation commonly occurs with ocean waves of periods near 10s, in particularly in storm wake regions. Thus, a quasi-permanent infrasonic spectral peak of 0.2 Hz is observed at I59US, as well as most infrasound stations in the world. In the case of an eastward-moving middle latitude storm, the south side of the storm will contain the strongest fetch lengths, durations, and intensities and thus higher wave heights and periods can be expected on the south of the center. It is rare for an eastward moving storm to produce long wave periods of 13s or more on the north side of the center unless the storm is a slow mover, large in diameter, and quite strong. Furthermore, since long period swells exhibit higher group velocities than short period swells, unless a storm is very large, symmetrical, and fast moving, the long period energy created ahead of a low center will often be dispersed and not have time to interact with any longer period energy that may be created behind the low center. This is especially true when the storm is moving slower than the group velocities of the long period ocean waves it produces. Steep, short period swells (< 8s) often dissipate within a few wavelengths due to whitecapping and angular spreading effects. This can prevent opposing wave trains of short periods from interacting. On the other hand, opposing wave trains of medium periods (8s–12s) are very likely in wake of both middle latitude and tropical cyclones, giving credence to the commonly observed infrasonic peak at 0.2 Hz. If there are long period swells created on the north side of the center, the amplitudes are normally small and thus the resulting infrasonic wave will also have small amplitude. Similarly, dissipating shorter period swells that may interact will also produce smaller amplitude infrasonic waves. This also helps explain the persistent infrasonic spectral peak at 0.2 Hz.

Coherent microbarom arrivals at I59US during 2003 suggest a relationship between microbarom arrival azimuth and dominant storm activity in the Pacific Basin (Figure 2). Boreal winter-time arrivals at I59US come from west and

northwest directions, while summer arrivals come primarily from east and south azimuths. Arrivals during the shoulder seasons are more evenly distributed around the compass. Microbaroms observed at I59US come primarily from regions where storm and wave activity are the strongest throughout the year, and the seasonal trend roughly coincides with the stratospheric wind patterns. The seasonal pattern of coherent microbarom amplitudes may be due to the closer distance of the source to the receiver during winter. Propagation path effects may also play a role, and will be addressed in a separate study. Figure 4 also shows evidence for acoustic shadowing by adjacent Mauna Loa and Hualalai volcanoes, which shelter the array from the trade winds. Reflections from the coastline may also contribute to a portion of the arrivals from 45° to 95° at I59US, especially during summer months when trade winds are present 80–90% of the time near the Hawaiian Islands (Sanderson, 1993).

Infrasound generated by the ocean waves can be used to continuously study the temperature and wind structure of the atmospheric boundary layer, troposphere, stratosphere, mesosphere, and lower thermosphere. Ocean-surface winds generate swells, which may interact nonlinearly to generate infrasound, which in turn may propagate for thousands of kilometers along the lower, middle, and upper atmosphere. Once these ocean swells reach a coastline, waves break and generate infrasound that may propagate along the boundary layer and lower atmosphere. Our studies suggest that a large portion of coherent microbarom arrivals observed in Hawaii are strongly affected by advection from the atmospheric winds in the 10–20 and 50–70 km height ranges. However, energetic swells can generate strong microbarom signals that may arrive from any direction, and may be refracted back to the ground at the thermosphere. By comparing the predicted atmospheric waveguide boundaries with the observed microbarom arrivals, we conclude that either (1) the wind speeds in the troposphere, stratosphere and mesosphere may be underestimated in atmospheric models or (2) elevated leaky infrasonic waveguides are persistent propagation paths that should be investigated in more detail. In particular, it would be valuable to study diffraction and scattering of infrasonic energy into and out of these postulated elevated waveguides.

Although in general the continuous microbarom noise is uncorrelated at I59US, distinct coherent microbarom packets can be routinely detected in the Hawaii array. When designing an array it may be useful to retain the coherence of microbaroms, as then it may then be possible to remove this contribution from a signal of interest and lower the background noise levels around the 0.2 Hz band. In principle, it may be also possible to individually extract coherent arrivals associated with open-ocean sources to yield signals refracted from different layers of the atmosphere and source regions. This may permit the identification of interesting transient reflection and refraction layers in the atmosphere as well as facilitate the recognition of microbarom signals produced by reflections from coastlines. Microbarom amplitude studies may yield further information on the variability of the atmospheric wind structure. There is also potential for using microbaroms to monitor ocean wave activity, since microbaroms contain information about the wave periods and amplitudes of the generating open ocean waves.

Although ocean swells have been previously used as a natural source for continuous measurements of atmospheric winds over long horizontal ranges, recent advances in measurement and modeling techniques can provide new insight on this complex but tractable method for continuous, passive acoustic tomography of the atmosphere.

ACKNOWLEDGEMENTS

Many thanks to Douglas Drob, NRL, and Alexis Le Pichon, CEA/DASE, for their collaboration on the study of the wind effects. Paul Wittmann (FNMOC) provided the guidance in getting WW3 operational for this research.

REFERENCES

Arendt, S., and D. Fritts, (2000) Acoustic radiation by ocean surface waves. *J. Fluid Mech*., 415, 1-21,

Benioff, H. and B. Gutenberg, (1939) Waves and currents recorded by electromagnetic barographs. *Bull. Am. Met. Soc*., 20, 421.

Cansi, Y, (1995) An automatic seismic event processing for detection and location: The P.M.C.C. method, *Geophys. Res. Lett., 22*, 1021-1024.

Cox, E., H Plagge, and J. Reed, (1954) Meteorology directs where blast will strike, *Bull. Amer. Meteorol. Soc*., 35.

Daniels, F. B., (1952) Acoustical energy generated by the ocean waves. *J. Acoust. Soc. Am*., 24, 83.

Daniels, F. B., (1942) Generation of infrasound by ocean waves. *J. Acoust. Soc. Am.*, 34, 352-353.

Donn, W. L. and B. Naini, (1973) Sea wave origin of microbaroms and microseisms. *J. Geophys. Res.,* 78, 4482-4488.

Donn, W. L. and E. S. Posmentier (1967) Infrasonic waves from the marine storm of April 7, 1966. *J. Geophys. Res.*, 72**,** 2053-2061.

Donn W. and D. Rind, (1971) Natural infrasound as an atmospheric probe, *Geophys, J. R. Astr. Soc*., 26, 111-133.

Drob, D., M. Picone, and M. Garcés, (2003) The Global Morphology of Infrasound Path Partitioning, *J. Geophys. Res*., 108, 4680.

Garcés, M., C. Hetzer, M. Merrifield, M. Willis, and J. Aucan. (2003) Observations of surf infrasound in Hawaii, *Geophys. Res. Letts.*, **30**(24), 2264.

Garcés, M., D. Drob, and M. Picone, (2002a) A theoretical study of the effect of geomagnetic fluctuations and solar tides on the propagation of infrasonic waves in the atmosphere. *Geophys. J. International*, 148, 77-87.

Garcés, M., C. Hetzer, K. Lindquist, and D. Drob. (2002b) Source Location Algorithm for Infrasonic Monitoring, *Proceedings of the 24th Seismic Research Review–Nuclear Explosion Monitoring*. 745-754.

Garcés, M., C. Hetzer, M. Willis, and S. Businger, (2003) Integration of infrasonic models with ocean wave spectra and atmospheric specifications to produce global estimates of microbarom signal levels. *Proceedings of the 25th Seismic Research Review–Nuclear Explosion Monitoring: Building the Knowledge Base,* 617-627.

Le Pichon, A., J. L. Plantet, Y. Cansi, J. Guilbert, P. Herry, S. Lambotte, (2003) Recent developments on infrasound data processing at the French NDC, *Proceedings of the Infrasound Technology Workshop*, San Diego, CA, 27–30 October 2003.

Madisetti, V. K. and D. B. Williams, (1998) *The Digital Processing Handbook.* CRC Press, Florida. 14-7pp..

Longuet-Higgins, H. C. (1950) A theory of the origin of microseisms, *Philos. Trans. Roy. Soc*., London Ser. A243, 1-35.

Ponomaryov E. A., A. G. Sorokin, and V. N. Tabulevich, (1998) Microseisms and infrasound: a kind of remote sensing. *Physics of the Earth and Planetary Interiors*, 108, 339-346.

Rind, D., (1980) Microseisms at Palisades 3. Microseisms and microbaroms, *J. Geophys. Res.*, 85, 4854-4862.

Sanderson, M. (Editor), (1993) *Prevailing Trade Winds*. Univ. of Hawaii Press, 12-36.

Saxer, L., (1945) Electrische Messung kleiner atmospharischer Druckshwankingen, *Helv. Phys. Acta.*, 18, 527.

Saxer, L., (1954) Über Entstehung und Ausbreitung quasiperiodischer Luftdruckschwankungen. *Arch. Meteorol. Geophys. Bioklum*., A6, 451-457.

Rind, D., (1978) Investigation of the lower thermosphere results of ten years of continuous observations with natural infrasound, J. of Atmospheric and Terrestrial Physics, 40, 1199-1209.

Tolman, H., B. Balasubramaniyan, L. Burroughs, D. Chalikov, Y. Chao, H. Chen, and V. Gerald, (2002) Development and implementation of ocean surface wave models at NCEP, *Weather and Forecasting*, 17, 311-333.

Tabulevich, V., (1995) On recordings of global microseismic vibrations and observations of microseisms in shore zones of oceans, *Physics of the Earth and Planetary Interiors*, 91, 299-305.

Willis, M., (2004) Observations and source modeling of microbaroms in the Pacific. Masters Thesis, Dept. of Meteorology, University of Hawaii at Manoa, 65 pp.

Wright, C. W., E. J. Walsh, D. Vandemark, W. B. Krabill, A. W. Garcia, S. H. Houston, M. D. Powell, P. G. Black, and F. D. Marks, (1998) Hurricane Directional Wave Spectrum Variation in the Open Ocean. *J. Phys. Oceanogr.*, 31, 2472-2488.

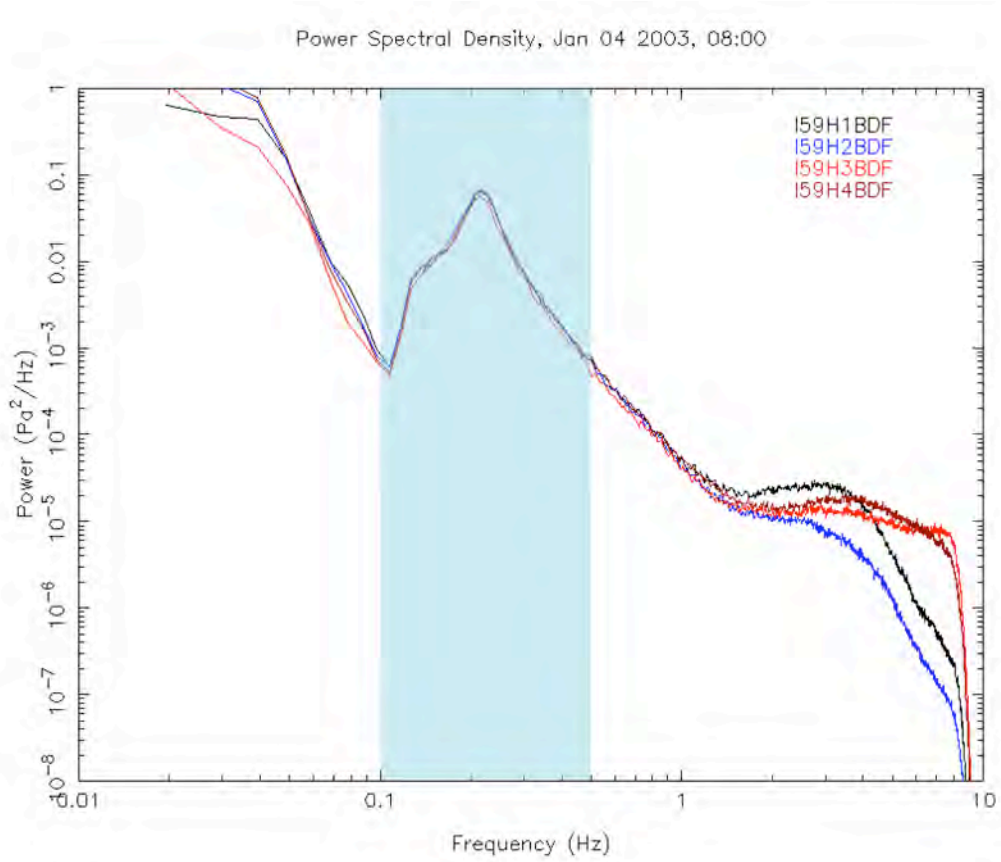


Figure 1. Infrasonic power spectral density observed at I59US site on January 4, 2003 18 UTC (8 AM local). Colored lines represent power observed by the four components of the infrasonic array. Power (Pa^2/Hz) is on the vertical axis, frequency (Hz) is on the horizontal axis. The blue-shaded region represents the microbarom-frequency range. The approximately 0.2-Hz peak is common throughout the year at I59US, which theoretically corresponds to ocean waves of 10 seconds.

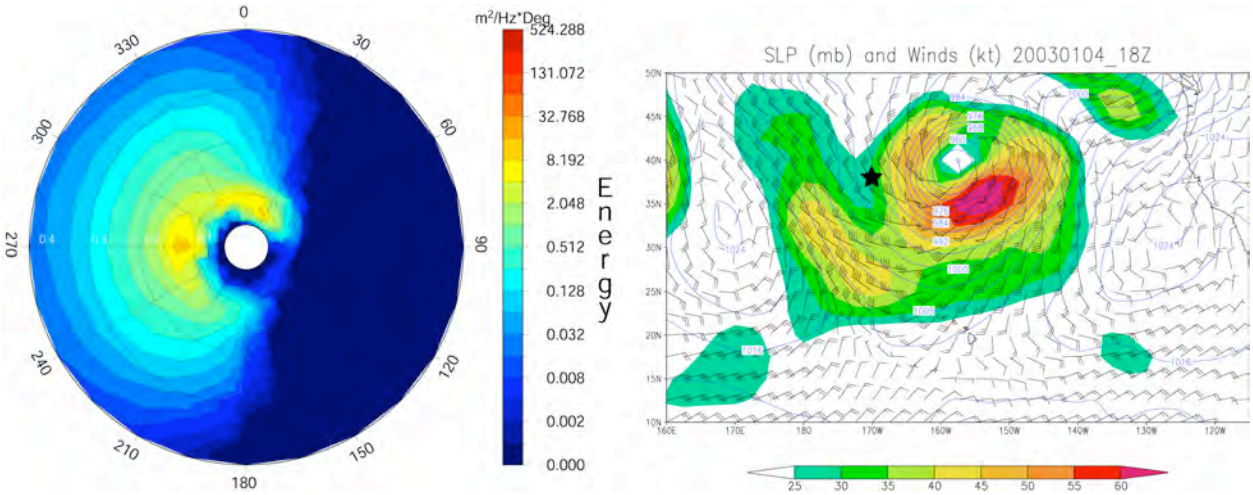


Figure 2. Polar plot (left) represents the directional ocean-wave spectrum for a grid point (38.00N, 170.00W) at 18 UTC on January 4, 2003 in the wake region of a strong marine storm shown in adjacent plot of sea-level pressure. Frequency (Hz) decreases towards the center, wave energy scale (m^2/Hz*deg) on the right hand side. This ocean-wave spectrum contains energy arriving from several directions and thus, microbarom generation is expected. The black star on the sea-level-pressure map represents the point of the wave spectrum. The wave spectrum was plotted using WW3 hindcast data. NCEP/NCAR Reanalysis data was used to generate the surface weather plot.

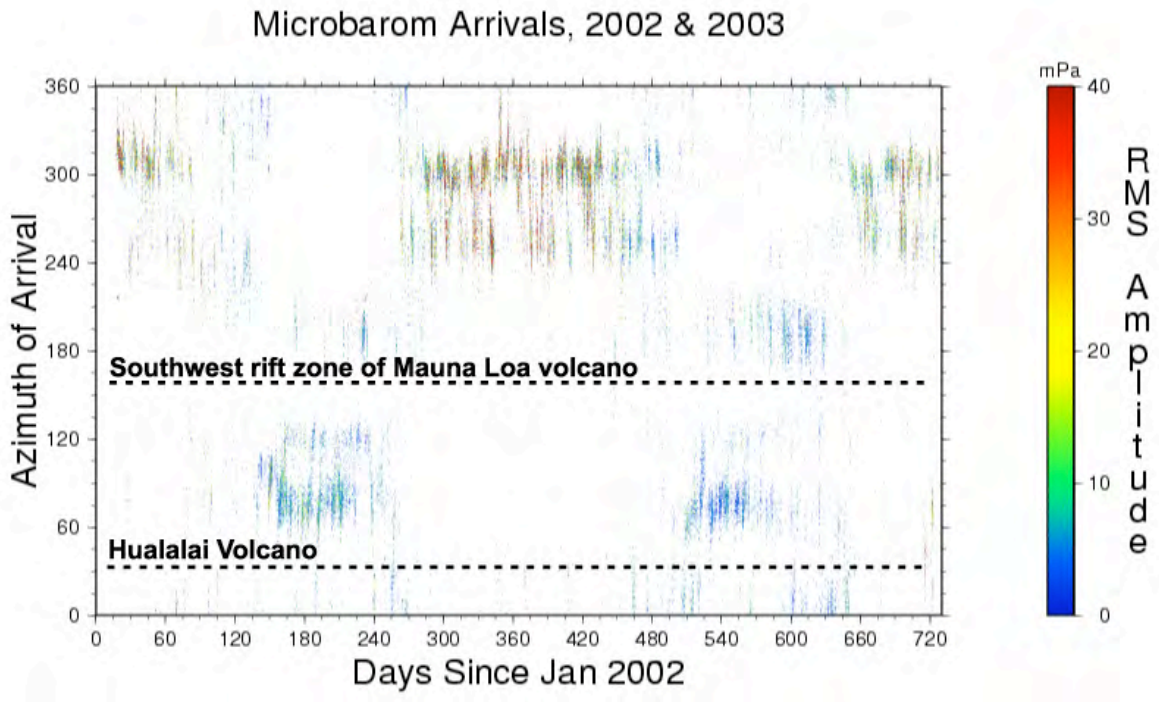


Figure 3. Infrasonic wave arrival azimuth and amplitude of coherent microbarom arrivals at I59US during 2003. Arrival azimuth at the array is measured clockwise from north (0° to 360°).

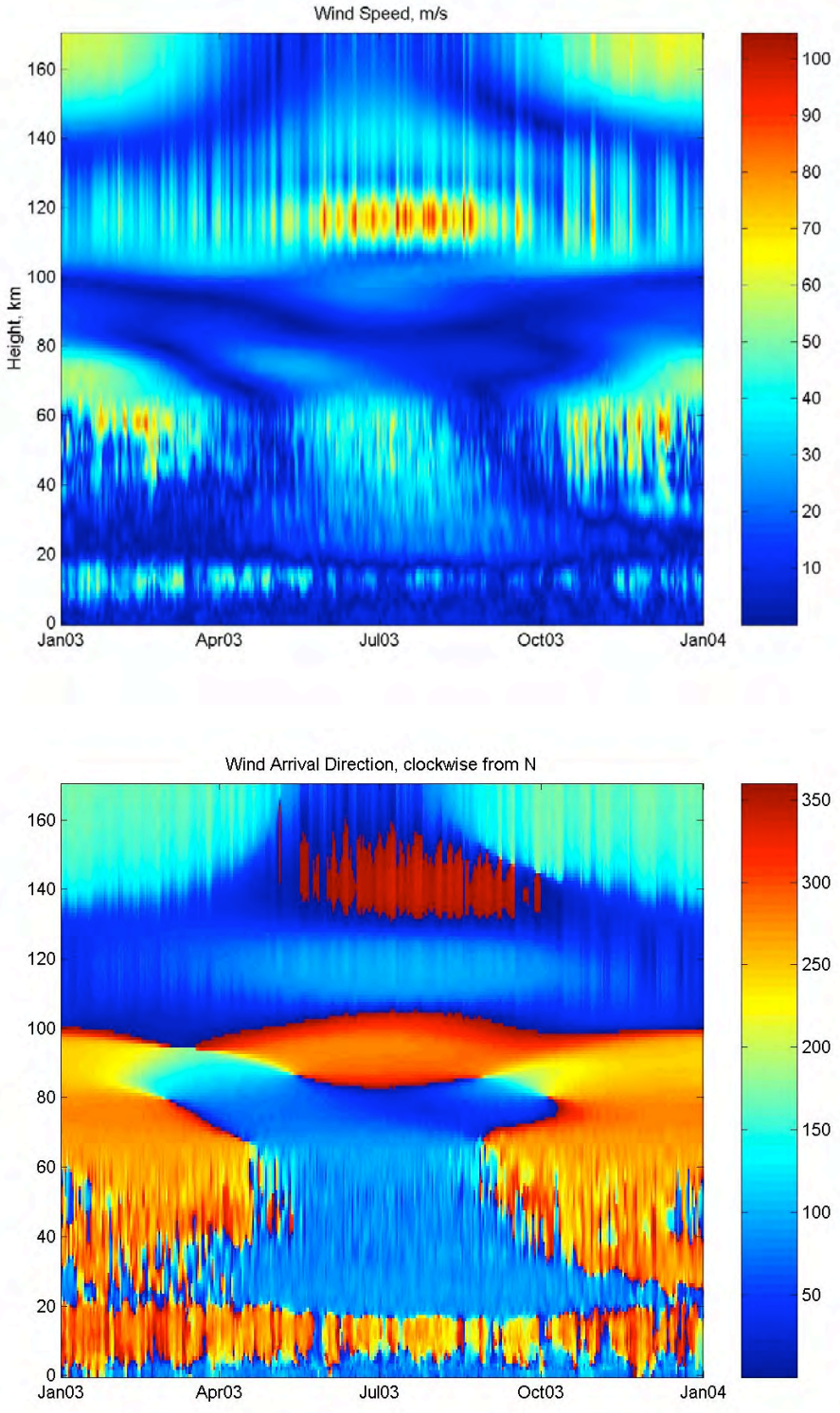


Figure 4. Wind-speed and direction as provided by the G2S atmospheric specifications over Hawaii for 2003 at 18 UTC.

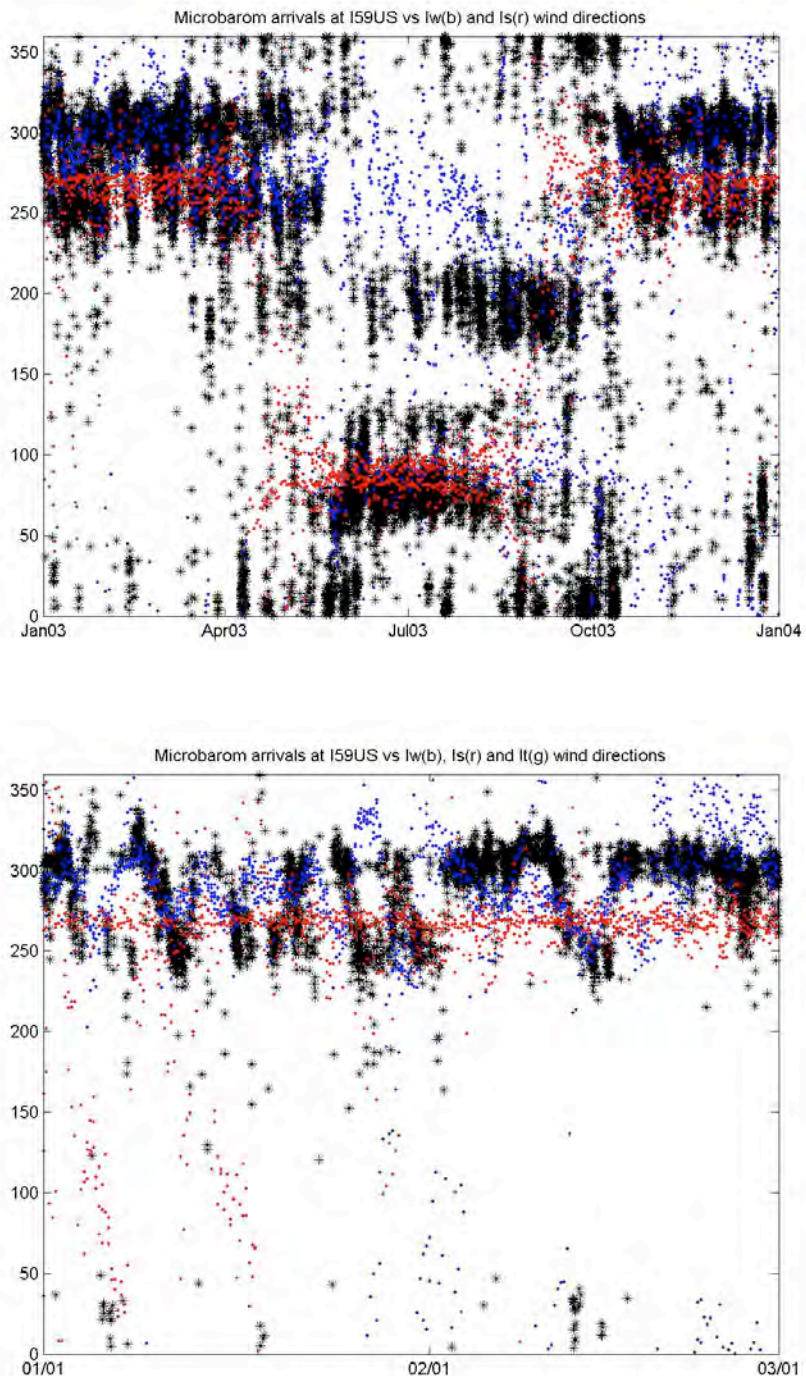


Figure 5. Coherent microbarom arrival and wind arrival azimuths, clockwise from north, at the Hawaii array. The red dots represent the winds between 50–70 km and the blue dots represent the winds between 10–20 kms. The dominant wind directions match the seasonal variability for some of the arrivals, except for the arrivals from the southern hemisphere during the Austral winter. These swells are large, consistent, and powerful, and may overwhelm the 10 second period swell energy.

INTEGRATION OF INFRASOUND PROPAGATION MODELS AND NEAR-REAL-TIME ATMOSPHERIC CHARACTERIZATIONS

Robert G. Gibson and David E. Norris

BBN Technologies

Sponsored by Air Force Research Laboratory

Contract No. DTRA01-01-C-0084

ABSTRACT

Numerical modeling of infrasound propagation directly supports infrasound source location and phase identification. Predicting the details of infrasound propagation relies on characterization of the propagation medium, namely the global atmosphere from the ground to altitudes above 100 km, and the accuracy of propagation modeling depends on the fidelity of the atmospheric characterization. The analysis tool kit InfraMAP (*Infra*sound *M*odeling of *A*tmospheric *P*ropagation) has been upgraded to offer new options for specifying the propagation environment. Near-real-time atmospheric updates, such as the output from numerical weather prediction models, supplement the baseline climatological characterization of temperature, wind and air composition.

InfraMAP integrates advanced infrasound propagation models (ray-tracing, parabolic equation, normal mode) and environmental representations. It also incorporates algorithms for assessing propagation variability and for localizing infrasound sources based on both observations and model calculations. New InfraMAP modules enable integration of propagation models with two near-real-time atmospheric characterizations. Output from the NRL-G2S (Naval Research Laboratory Ground to Space) specification can be imported and used to characterize the entire propagation environment. Naval Research Laboratory's NRL-G2S is a semi-empirical spectral model that fuses climatological models with output from operational numerical weather prediction models. Alternatively, output from the Navy's synoptic model NOGAPS (Navy Operational Global Atmospheric Prediction System) can be imported into InfraMAP and merged with the baseline climatological models, horizontal wind model HWM-93 and NRL-MSISE-00 (or the mass spectrometer 1/N incoherent scatter radar extended model). NOGAPS generates global grids of temperature and wind, several times per day, on a one-degree grid over 27 isobaric surfaces. The corresponding altitudes are not sufficiently high to characterize the entire region of interest for infrasound propagation; therefore, NOGAPS output is merged with climatology within InfraMAP at the higher altitudes to cover the full propagation domain. These new capabilities extend the ability of infrasound researchers to investigate critical propagation phenomena, conduct sensitivity studies, and compare results of numerical modeling with observed signals.

Validation efforts are essential to build confidence in the modeling procedures and are used to assess the value of potential improvements to the atmospheric specification. Observed infrasound events with known ground truth represent valuable sources of opportunity for use in validating propagation modeling techniques. InfraMAP has been used to model long-range propagation of infrasound originating from the space shuttle, bolides, and other sources. Model predictions of infrasound arrival times and azimuths resulting from use of various environmental characterizations are compared with observed data.

OBJECTIVES

The primary objective of this research effort is development of a software tool kit with capabilities for higher-fidelity infrasound propagation modeling by the incorporation of near-real-time atmospheric characterizations. This effort is intended to support improved event localization, and phase identification. A validation effort has also been undertaken, using a diverse set of observations and ground truth, in order to improve confidence in the modeling techniques and provide calibration in support of operational needs. Anticipated uses of the software include: in-depth analysis of events and scenarios of particular monitoring interest, sensitivity analyses, and detailed infrasound localization and detection studies.

RESEARCH ACCOMPLISHED

Near-Real-Time Environmental Updates to InfraMAP

The InfraMAP software tool kit is composed of research-grade infrasound propagation models (3-D ray tracing, parabolic equation and normal modes) and upper-atmospheric characterizations, integrated to allow for user-friendly model execution and data visualization. InfraMAP was developed to enable the efficient application of advanced computational models, in support of the nuclear explosion monitoring research and development community. InfraMAP can be applied to predict travel times, bearings, and amplitudes from potential event locations worldwide. Such predictions can be used to identify infrasound phases and to define travel-time and bearing corrections, which can improve localization performance (Gibson and Norris, 2002a). Recent enhancements to the InfraMAP suite of computational tools enable analysis of propagation variability due to environmental effects, calculation of source location using measurements and model predictions, and prediction of network localization performance (Norris and Gibson, 2002).

Global characterizations of temperature, wind, and air composition are incorporated into the propagation models to account for temporal and spatial variability of the atmosphere. Modeling of spatial variability enables range-dependent propagation modeling to be performed. The baseline atmospheric characterizations in InfraMAP are two empirical models: the horizontal wind model, HWM-93 (Hedin *et al.*, 1996), and the mass spectrometer-incoherent scatter radar extended model, NRLMSISE-00 [Picone *et al.*, 2002]), which provides temperature and air composition. (Note: NRLMSISE-00 is a recent upgrade from the earlier baseline temperature model, MSISE-90 (Picone *et al.*, 1997)). Using these characterizations, wind, temperature, and molecular densities are modeled from the surface into the thermosphere and include spatial, diurnal, and seasonal effects. The models are climatological in that they predict the mean environmental state based on assimilation of multiple years of data.

The HWM and MSISE models were chosen for use in InfraMAP due to their high fidelity over a wide range of altitudes and temporal scales, their global domain, and the relative ease of software integration. However, global climatological models such as HWM and MSISE that are based solely on historical data do not capture fine-scale atmospheric structure that evolves over time. This research addresses the use of appropriate near-real-time sources of atmospheric information to improve the estimate of the infrasound propagation environment.

During this effort, new InfraMAP modules have been developed to incorporate output from physics-based synoptic models that assimilate observations from a number of sources. Range-dependent propagation modeling is now possible using these updated global atmospheric characterizations. Previously, updated atmospheric profiles could be used, but only in range-independent propagation modeling scenarios. In addition, a number of other enhancements have been introduced in InfraMAP to improve the fidelity of the environmental characterization. They include:

- Integration of an archive of solar flux and geomagnetic disturbance parameters (F10.7, F10.7A, and A_p) from the National Geophysical Data Center;
- Incorporation of variable molecular weight in sound velocity calculations;
- Incorporation of variable specific heat ratio in sound velocity calculations.

These new features are primarily intended to improve fidelity of the modeling of thermospheric infrasound at little or no computational cost, as discussed previously (Gibson and Norris, 2003).

The near-real-time global atmospheric characterizations that have been integrated with infrasound models are:

- The Naval Research Laboratory Ground to Space (NRL-G2S) specification; and
- The Navy Operational Global Atmospheric Prediction System (NOGAPS).

Output from the NRL-G2S specification (Drob, 2003) can be used to characterize the entire propagation environment. NRL-G2S is a semi-empirical spectral model that fuses climatological models with output from operational numerical weather prediction models from the National Oceanic and Atmospheric Administration (NOAA), the National Aeronautics and Space Administration (NASA), and other sources. The G2S atmospheric characterizations from the surface to approximately 55 km utilize the output of multiple numerical weather prediction systems and other relevant global data sets. Above this region, upper atmospheric characterizations are based on the NRLMSISE-00 and HWM-93 climatologies. NRL-G2S employs spherical and vector spherical harmonics in the data assimilation process to produce a set of model coefficients for each day and time of interest. Coefficient sets can then be used to reconstruct fields of each atmospheric state variable as well as spatial derivatives.

An InfraMAP user can access NRL-G2S coefficient sets from a data repository, import the coefficients, and utilize the resulting specifications within InfraMAP to define a propagation environment. InfraMAP incorporates "client-side" routines (Drob, 2003) that perform inverse transforms necessary to determine vertical atmospheric profiles over the entire globe using the NRL-G2S coefficients. The NRL-G2S system is configured to produce coefficient sets autonomously every six hours, and also for special events of interest.

NOGAPS provides near-real-time global grids of temperature and wind, several times per day, over three spatial dimensions (Bayler and Lewit, 1992). NOGAPS, originated by the Navy's Fleet Numerical Meteorology and Oceanography Center (FNMOC), is a numerical weather prediction system that utilizes not only profiles measured by radiosondes, but also an extensive data set of ship-based, land-based, and satellite measurements. Output data from NOGAPS are readily available from the ground up to the 10 mb pressure surface (approx. 30-35 km). As shown previously, there is considerably more fine-scale structure in the NOGAPS characterization than in the climatology at altitudes below 35 km (Gibson and Norris, 2003). However, because infrasound propagation modeling requires atmospheric information above the NOGAPS domain, climatological models remain an essential tool for estimating the environment, particularly at high altitudes.

Techniques have been developed within InfraMAP to merge NOGAPS grids at lower altitudes with climatological models at higher altitudes. InfraMAP modules import and decode NOGAPS grid files. A user then selects a subset of the global grid (i.e., a range of latitude and longitude cells) for use in a propagation scenario of interest. Within the region of interest, NOGAPS output is used in conjunction with the HWM and MSISE characterizations to define the propagation environment. A user specifies the thickness of the transition layer above NOGAPS. A cubic interpolation algorithm that matches the values and their derivatives at the boundaries is employed to join NOGAPS temperatures, zonal winds, and meridional winds with the climatologies.

The global temperature and wind profiles from both the NRL-G2S and the NOGAPS characterizations can be viewed using InfraMAP's environmental menu. Furthermore, either near-real-time characterization can be used in range-dependent infrasound propagation modeling using ray-tracing or parabolic equation techniques or, alternatively, in range-independent propagation modeling using ray-tracing, parabolic equation, or normal modes. This flexibility allows the direct comparison of the results of calculations using climatology or user-defined profiles with predictions using the near-real-time enhancements. It also allows the user to choose between computationally fast range-independent modeling and slower, higher-fidelity range-dependent modeling. Supplementing the baseline climatological models with available near-real-time updates is anticipated to yield improved infrasound predictions, particularly for propagation paths that dwell primarily in the lower and middle atmosphere, where updated data are more readily available.

A beta version of the software, including graphical user interfaces, was provided to selected users, and feedback received from the testers was used to prioritize research and development activities. Recent development efforts have focused on improving calculation speed and efficiency of range-dependent propagation modeling. The near-real-time update capabilities and other environmental enhancements have been integrated into the InfraMAP software tool kit, and an updated user manual has been developed. The most recent software release, InfraMAP 4.0, produced during this effort, provides the near-real-time atmospheric functionality described herein.

Examples of Infrasound Modeling using Near-Real-Time Characterizations

This section provides an example of the use of climatology, NRL-G2S and NOGAPS in a range-dependent propagation modeling study for an event of interest.

A bolide was observed over the state of Washington on 3 June 2004. A video camera in Vancouver Island, Canada observed the fireball at 09:40:12 UTC, according to a news bulletin report from the Dutch Meteor Society (http://www.xs4all.nl/~dmsweb/fireballs/20040603_US_fireball.html). The Pacific Northwest Seismograph Network localized the event at 47.9717N, 121.9782W, with an estimated altitude of 43.45 km, according to a press release (http://www.pnsn.org/NEWS/PRESS_RELEASES/June3_2004_meteor.html) and accompanying analysis (http://www.pnsn.org/WEBICORDER/INTERESTING/bolide040603.gif).

The event was observed infrasonically by the I56US array at Newport, Washington, and the I57US array at Pinon Flat, California. Preliminary analyses of the infrasound observations were reported by Stephen Arrowsmith and Michael Hedlin of UCSD (http://mabu.ucsd.edu/~arrowsmith/bolide.htm). At I56US, detections (Progressive Multichannel Cross-Correlations {PMCC]) were reported from 09:59:05 to 10:07:35 UTC, with an apparent main arrival at approximately 10:05 UTC. At I57US, detections (using PMCC) were reported from 11:11:55 to 11:19:25 UTC.

In this study, propagation modeling was conducted with InfraMAP using the seismically determined latitude, longitude and altitude and the visually determined origin time. The resulting range to I56US is 363 km (with a back azimuth of 266.7 degrees) and to I57US is 1661 km (with a back azimuth of 345.5 degrees). Modeling with the HWM and MSISE climatology used atmospheric profiles that were range-dependent as well as time-evolving (i.e., stepping forward from the event origin time as calculations progressed). Modeling with NRL-G2S used a coefficient set calculated for 10:00 UTC. Modeling with NOGAPS used a grid calculated for 12:00 UTC.

Using the ray-tracing model, with the bolide modeled as an omnidirectional point source, eigenrays were identified if they came within 5 km of the I56US array or within 10 km of the I57US array. (This rather loose eigenray constraint is intended to identify elevated rays as well as those that reach the ground at the receiver range. Energy from elevated rays may reach the ground through diffraction.)

A summary of ray-tracing model results for I56US using the three atmospheric representations is shown in Table 1. In each case, two thermospheric eigenrays were identified, one with an upward launch elevation angle and one with a downward launch elevation angle. Travel times vary by 1% or less across the three model scenarios. Azimuth deviation results vary by 0.5 degrees or less across the three scenarios. The predicted arrival times (approximately 10:04 and 10:06 UTC) are within 1 minute of the apparent main arrival in the observed data. Arrivals as early as 09:59 UTC were not predicted using any of the atmospheric characterizations.

Table 1. Ray-tracing parameters for eigenrays identified to I56US using three atmospheric characterizations

	Elev. Ang.	Az. Dev.	Time	Arr. Time	Arr. Vel.
HWM/MSISE	23.9	0.1	1427	10:03:59	0.254
	-33.8	0.5	1541	10:05:53	0.235
NRL-G2S	27.7	0.3	1415	10:03:47	0.256
	-36.0	1.0	1550	10:06:02	0.234
NOGAPS	21.4	0.1	1410	10:03:42	0.257
	-33.0	0.6	1542	10:05:54	0.235

Amplitude fields calculated using the parabolic equation model for the path to I56US are shown in Figure 1 for both the NRL-G2S and the NOGAPS atmospheric characterizations. The modeled frequency is 0.1 Hz. The two plots show generally similar predictions of energy distribution, although the prediction using NOGAPS shows a somewhat higher concentration of energy in the stratospheric duct.

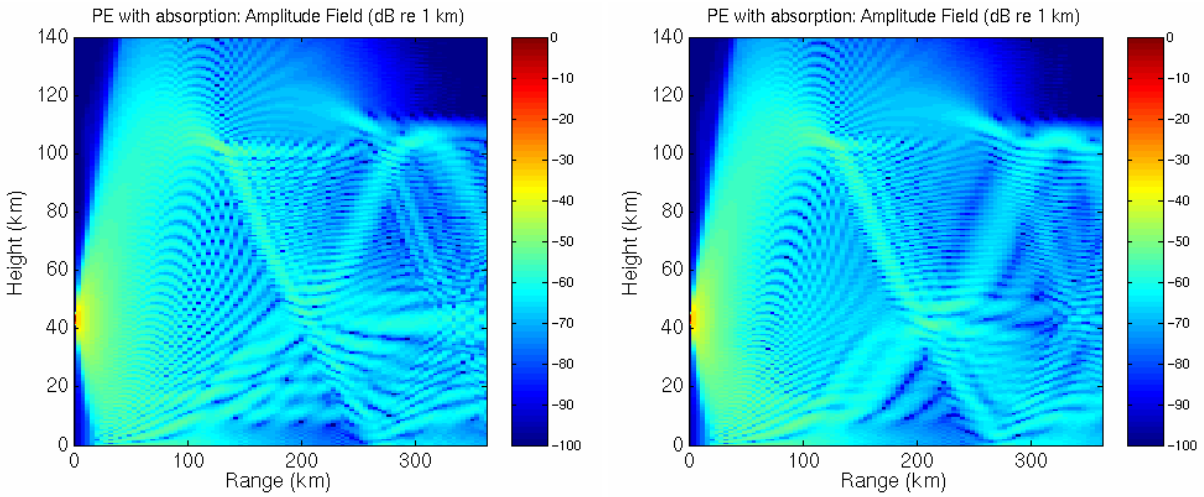


Figure 1. Amplitude fields at 0.1 Hz calculated using parabolic equation modeling to I56US for NRL-G2S atmospheric characterization (left) and NOGAPS characterization (right).

A summary of ray-tracing model results for I57US using the three atmospheric representations is shown in Table 2. The rays shown are limited to those with launch elevation angles of up to 35 degrees from the horizontal. In each case, six or seven thermospheric eigenrays were identified. Using the HWM and MSISE climatology, two stratospheric rays were also identified. Considering only the thermospheric rays, the travel time of the earliest arrival varies by up to 1.5% across the three model scenarios. The stratospheric rays identified using HWM and MSISE are predicted to arrive approximately 7 to 8 minutes earlier than the earliest thermospheric rays. Azimuth deviation results vary by less than 1 degree across the three scenarios.

Table 2. Ray-tracing parameters for eigenrays identified to I57US using three atmospheric characterizations

	Elev. Ang.	Az. Dev.	Time	Arr. Time	Arr. Vel.
HWM/MSISE	2.0	-0.8	5568	11:13:00	0.298
	-1.9	-0.8	5588	11:13:20	0.297
	7.8	-2.1	6031	11:20:43	0.275
	-11.2	-1.7	6117	11:22:09	0.272
	21.0	-1.5	6349	11:26:01	0.262
	-24.0	-1.3	6492	11:28:24	0.256
	29.3	-1.2	6784	11:33:15	0.245
	-33.0	-1.0	6947	11:35:59	0.239
NRL-G2S	11.6	-2.9	6091	11:21:43	0.273
	-15.1	-2.3	6185	11:23:16	0.269
	26.0	-1.9	6404	11:26:56	0.259
	23.0	-2.1	6420	11:27:12	0.259
	-28.0	-1.7	6558	11:29:30	0.253
	32.9	-1.6	6815	11:33:47	0.244
	-35.2	-1.4	6980	11:36:32	0.238
NOGAPS	5.5	-2.2	6004	11:20:16	0.277
	-7.9	-1.8	6105	11:21:57	0.272
	16.2	-1.8	6342	11:25:54	0.262
	17.0	-1.9	6343	11:25:55	0.262
	-22.5	-1.5	6468	11:28:00	0.257
	28.4	-1.4	6730	11:32:22	0.247
	-32.0	-1.2	6893	11:35:05	0.241

The predicted thermospheric arrival times (approximately 10:20 UTC and later) are somewhat late compared to the arrivals detected in the observed data. The predicted stratospheric arrival times are consistent with the beginning of the main coherent cluster detected in the observed data.

Synthetic waveform envelopes, determined by convolving the train of arrival times with a Gaussian that is weighted by the calculated absorption along the propagation path, are shown in Figure 2 for the modeled ray-tracing results using the three atmospheric characterizations. The spread in travel times can be seen. The source strength in the model was chosen arbitrarily, so only the relative amplitudes are of interest. The differences in relative amplitudes among the three modeled cases is primarily due to differences in the predicted upper turning height of the rays.

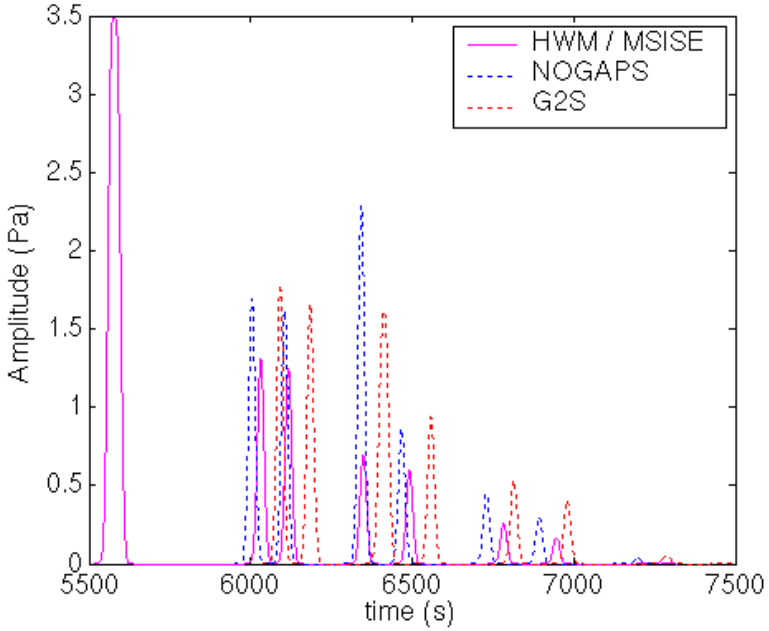


Figure 2. Synthetic waveform envelope determined from calculations using ray-tracing modeling to I57US for three atmospheric characterizations. Since source strength is unknown, the absolute signal amplitudes are not calibrated in the model results.

Plots of effective sound speed profiles at 100 km increments along the great circle azimuth in the direction from the source location to I57US are shown in Figure 3 for the three environmental characterizations. Significant differences among the characterizations can be seen at altitudes between approximately 30 and 50 km, and these features determine the presence or absence of a stratospheric duct in this model scenario. For this event time and region, NRL-G2S predicts lower temperatures at these altitudes than MSISE, which results in the weaker stratospheric duct when using NRL-G2S, as evidenced by Figures 1 and 2. At lower altitudes, the NOGAPS profiles have more fine-scale structure than the other characterizations. The subtle differences among the sets of profiles at thermospheric altitudes result from the slightly different time of day used in the climatological representations in the three cases.

Although it is tempting to draw conclusions about the fidelity of the atmospheric characterizations based on comparisons between propagation modeling results and infrasound ground truth, it should be noted that bolides are complex sources that are challenging to model and that are not necessarily well represented by impulsive point sources. Various source mechanisms and regions may exist for a bolide event, as discussed by Brown *et al.* (2002), for example. These complexities result in modeling challenges, as shown in previous studies, e.g., Norris and Gibson (2001). Nevertheless, the sensitivity study presented here points out some of the important effects that the detailed atmospheric characterization can have on propagation model predictions. Accurate near-real-time specification of temperature and wind will ultimately improve on climatology and result in higher-fidelity infrasound predictions. Further side-by-side comparisons among the atmospheric characterizations for a larger set of observed events will be essential. It will also be important to investigate the fidelity of infrasound predictions using time-domain propagation models such as those discussed by Norris (2004), when used in conjunction with near-real-time specifications such as NRL-G2S and NOGAPS.

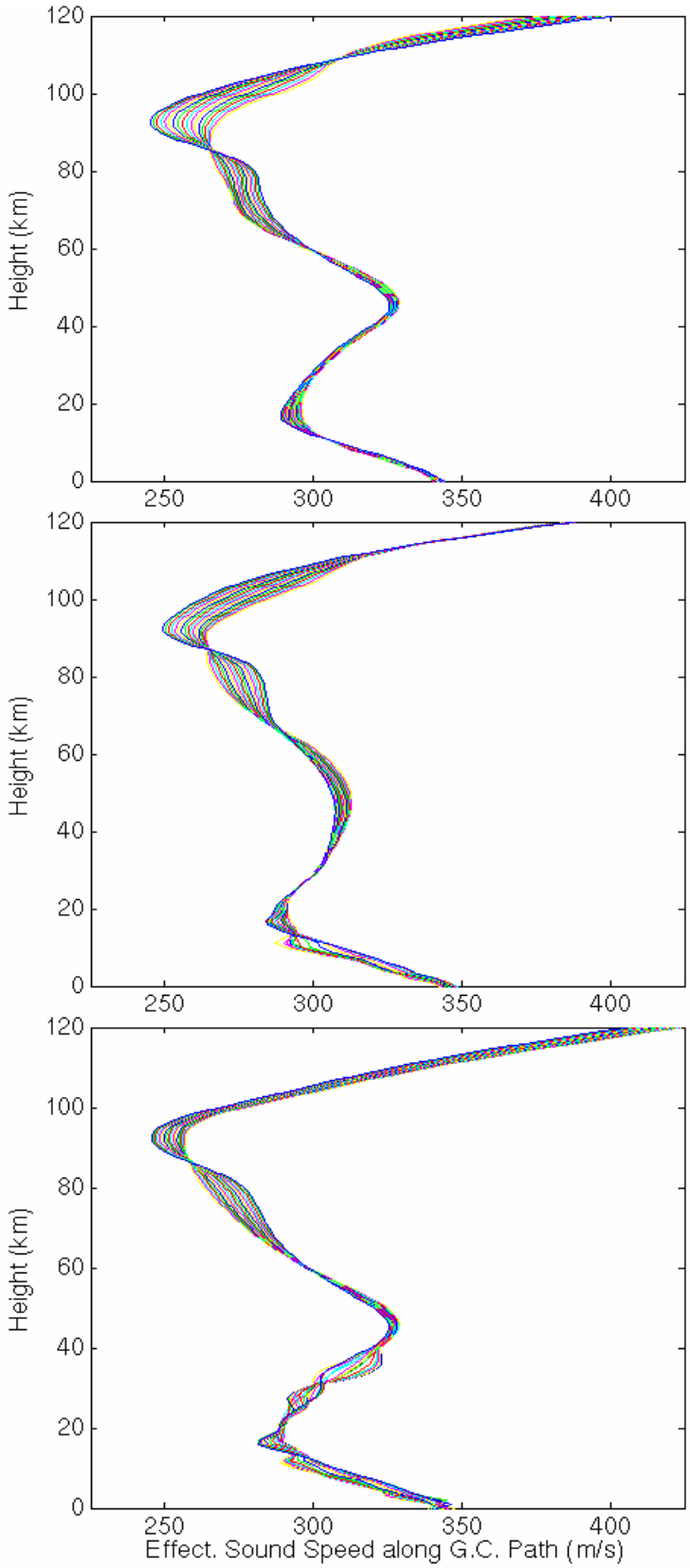


Figure 3. Effective sound speed profiles along the great circle azimuth from the source location to I57US, determined using HWM and MSISE (top), NRL-G2S (middle), and NOGAPS (bottom).

Other Model Validation Efforts

As the database of ground truth infrasound events grows and as additional NRL-G2S coefficient sets become available for both recent and historical events, further validation of modeling techniques will be enabled. Earlier validation activities conducted as part of this effort focused on infrasound from space shuttle launches, as discussed by Gibson and Norris (2002b). Components of infrasound signals have been associated with both the ascending orbiter and the descending solid rocket boosters. Reasonably good agreement in both travel time and azimuth has been obtained between ray tracing model results and observed infrasound, and analyses have been conducted of annual trends in observability, travel time and azimuth. Modeling of these events primarily used climatology.

The authors also participated in the Department of Defense Columbia Investigation Support Team Infrasound Working Group, the work of which was presented in the *Report to the Department of Defense on Infrasonic Re-Entry Signals from the Space Shuttle Columbia (STS-107)* (Bass, 2003). InfraMAP was used to model infrasound from the reentry and approach of the space shuttle Columbia (STS-107) up to the point of its untimely breakup. During this investigation, the NRL-G2S specifications were used to characterize the propagation environment. Range-independent propagation modeling was conducted from a large number of points along the reentry trajectory to the locations of those infrasound arrays in the western US and Canada that observed the event. Ray tracing model predictions of arrival time, azimuth, and elevation angle were generally in good agreement with the observations. One example is presented here to illustrate the model fidelity. Figure 4 shows a comparison of ray-tracing results with detections at I57US as computed using MatSeis and Infratool (Young, *et al*., 2002). The analysis passband is 1-8 Hz. The observed trends in azimuth and travel time from the moving source are generally well predicted. The results can be used to determine what portion of the reentry trajectory contributed to infrasound signals received at a given time of interest.

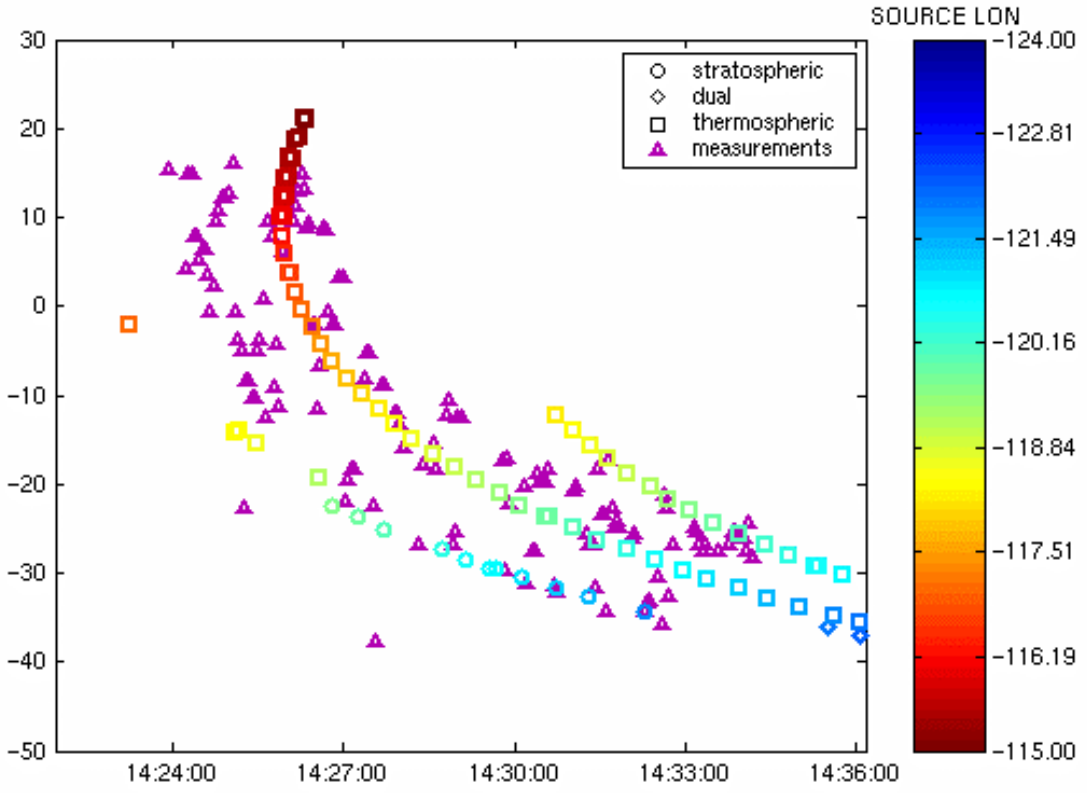


Figure 4. Predicted infrasound arrivals at I57US using ray-tracing (circles, diamonds and squares) compared to observations (triangles) from the reentry of Columbia (STS-107). Vertical axis shows azimuth (degrees) and horizontal axis shows arrival time (UTC). Color bar indicates the longitude of the orbiter at the origin time of each modeled ray arrival.

CONCLUSIONS AND RECOMMENDATIONS

The InfraMAP tool kit is used to predict the critical propagation characteristics that affect infrasound localization and detection. Adequate atmospheric characterization is necessary to correct for biases in travel time and azimuth that result from the propagation environment in order to avoid phase misidentification or large location errors.

The NRL-G2S atmospheric specifications and the output from the NOGAPS numerical weather prediction model have been integrated with range-dependent propagation models. The integrated set of models will allow for higher fidelity propagation modeling than has previously been available to the infrasound monitoring community.

Efforts should continue on the development of time-domain propagation modeling techniques, including the consideration of non-linear effects. Although ray-tracing is a powerful technique for predicting travel time and azimuth deviation, it is not always sufficient for predicting the detailed features of infrasound observations from ground-truth events. The integration of time-domain models with near-real-time atmospheric characterizations should be undertaken in order to conduct model comparison studies and to model infrasound propagation from observed events.

Other high-fidelity environmental characterizations should be considered for integration into an enhanced version of the InfraMAP software, particularly mesoscale models for use in studying short-range events of interest.

Rocket events and bolides generate infrasound signals for use in model validation studies. Further modeling of a large set of observed ground truth events, using updated atmospheric characterizations, should continue in order to quantify the improvements in travel time and azimuth predictions that are achievable. These investigations should focus on first establishing a baseline and then documenting the modeling improvements achievable with near-real-time updates as compared to climatology. The results may also be useful for identifying improvements that could be made to the atmospheric specifications.

ACKNOWLEDGMENTS

Doug Drob provided NRL-G2S client software, advised us on the use of the G2S specifications, and produced the G2S coefficient sets. Dean Clauter and Rod Whitaker provided useful feedback on modeling requirements and software functionality. Michael Hedlin and Stephen Arrowsmith provided analysis of the 03-June-2004 bolide via a link from the *inframatics.org* website.

REFERENCES

Bayler, G. and H. Lewit (1992), The Navy Operational Global and Regional Atmospheric Prediction System at the Fleet Numerical Oceanography Center, *Weather and Forecasting*, 7(2).

Brown, P. G., R. W. Whitaker, D. O. ReVelle, and E. Tagliaferri (2002), Multi-station infrasonic observations of two large bolides: signal interpretation and implications for monitoring of atmospheric explosions, *Geophys. Res. Lett*., 29(13), 14-1 – 14-4.

Drob, D. P. (2003), Detailed specifications of the atmosphere for infrasound propagation modeling, *Proceedings of the 25th Seismic Research Review – Nuclear Explosion Monitoring: Building the Knowledge Base*, pp. 605-616.

Gibson, R. and D. Norris (2002a), Development of an Infrasound Propagation Modeling Tool Kit, DTRA-TR-99-47.

Gibson, R. G. and D. E. Norris (2002b) "Integration of near-real-time atmospheric models with InfraMAP and applications to modeling infrasound from rockets," *Proceedings of the 24th Seismic Research Review – Nuclear Explosion Monitoring: Innovation and Integration*, pp. 775-782.

Gibson, R. G. and D. E. Norris (2003) "Integration of InfraMAP with near-real-time atmospheric characterizations and applications to infrasound modeling," *Proceedings of the 25th Seismic Research Review – Nuclear Explosion Monitoring: Building the Knowledge Base*, pp. 638-645.

Hedin, A. E, E. L. Fleming, A. H. Manson, F. J. Schmidlin, S. K. Avery, R. R. Clark, S. J. Franke, G. J. Fraser, T. Tsuda, F. Vial, and R. A. Vincent (1996), Empirical wind model for the upper, middle, and lower atmosphere, *J. Atmos. Terr. Phys*., 58, 1421-1447.

Norris, D.E. (2004), Time-domain modeling techniques and the study of infrasound propagation, in this volume.

Norris, D. E. and R. G. Gibson (2002) "InfraMAP enhancements: environmental/propagation variability and localization accuracy of infrasonic networks," *Proceedings of the 24th Seismic Research Review – Nuclear Explosion Monitoring: Innovation and Integration,* pp. 809-813.

Norris, D. E. and R. G. Gibson (2001), "InfraMAP propagation modeling enhancements and the study of recent bolide events," *Proceedings of the 23rd Seismic Research Review – Worldwide Monitoring of Nuclear Explosions,* pp. 150-159.

Picone, J. M., A. E. Hedin, S. L. Coffey, J. Lean, D. P. Drob, H. Neal, D. J. Melendez-Alvira, R. R. Meier, and J. T. Mariska (1997), The Naval Research Laboratory program on empirical models of the neutral upper atmosphere, in *Astrodynamics: Advances in the Astronautical Sciences,* 97, F. R. Hoots, B. Kaufman, P. J. Cefola, and D. B. Spencer, (Editors) American Astronautical Society, San Diego, Ca.

Picone, J. M., A. E. Hedin, D. P. Drob and A.C. Aikin (2002), NRLMSISE-00 Empirical model of the atmosphere: statistical comparisons and scientific issues, *J. Geophys. Res*., 107 (A12): article no. 1468.

Report to the Department of Defense on Infrasonic Re-Entry Signals from the Space Shuttle Columbia (STS-107) (2003), H. Bass (Editor), National Center of Physical Acoustics, University of Mississippi.

Young, C. J., E. P. Chael, and B. J. Merchant, (2002) "Version 1.7 of MatSeis and the GNEM R&E Regional Seismic Analysis Tools," *Proceedings of the 24th Seismic Research Review – Nuclear Explosion Monitoring: Innovation and Integration*, LA-UR-02-5048, II, 915-924.

INFRASOUND CALIBRATION EXPERIMENTS AT WHITE SANDS MISSILE RANGE: PLANNING AND PREPARATIONS

Eugene T. Herrin,[1] Paul W. Golden,[1] Petru Negraru,[1] Henry E. Bass,[2] Gary S. Hunter[3], William L. Andre[3], John V. Olson[4], Daniel L. Osborne[4], Milton A. Garces[5], Michael A. H. Hedlin[6] Kathie Hoffman,[7]

Southern Methodist University,[1] University of Mississippi,[2] U.S. Army Space and Missile Defense Command,[3] University of Alaska at Fairbanks,[4] University of Hawaii,[5] University of California San Diego,[6] Naval Surface Warfare Center White Sands,[7]

Sponsored by Army Space and Missile Defense Command

Contract No. DASG60-99-C-0018

ABSTRACT

There are now a number of permanent infrasound arrays in place in the United States, and several portable or temporary arrays can be deployed. The calibration of this combined network and a test of predictions of infrasound travel times in the atmosphere can be accomplished using explosive shots with active radar tracking and exact positioning. Currently there are plans for firing rocket launches with explosive charges at the White Sands Missile Range. This will serve as an accurate calibration experiment for infrasound arrays. A good first choice for test parameters is a 50 lb. charge on the downward leg of a rocket trajectory at a height of 50 km.

These tests will expand on information acquired from the Columbia disaster. Eight impulsive signals recorded at the Lajitas infrasound array in far west Texas on 1 February 2003 were found to originate from the Space Shuttle Columbia. These signals all had essentially the same back azimuth and so were considered to be multipath arrivals from a single explosion. Using a method employed at Los Alamos National Laboratory (LANL) in the study of bolides, it was determined that based on a peak period of about 1 second for the signals, the explosion had a yield of approximately 2 lbs. of TNT. The explosion occurred about 50 seconds before the Columbia broke up. The impulsive arrivals had signal-to-noise ratios of 3 to 10 at the Lajitas station, located about 600 km from the source. The altitude of the source was 63 km.

This observation reminded the authors of a set of rocket grenade explosions in 1961-1965 that produced similar signals. An explosion of 2 lbs. of TNT at an altitude of 67 km produced a signal at ground level with a peak period of about 0.8 seconds.

The calibration experiments will be discussed and plans provided for testing by the end of the 2004 calendar year.

OBJECTIVE

We are planning an experiment to explode at least one 50 lb. charge in the atmosphere at a height of 50 KM from a rocket launch with active radar tracking and exact positioning over the White Sands Missile Range (WSMR) in New Mexico. Signals from the explosion should be recorded at many permanent and temporary infrasound arrays in North America. Calibration of the network of arrays, including various noise reducing methods, and a test of predictions of infrasound travel times in the atmosphere can be accomplished. Validation of existing software for atmospheric and wave-form modeling should be possible as well.

RESEARCH ACCOMPLISHED

Low frequency acoustic signals are seen at the TXAR infrasound array in far west Texas for shuttle landing tracts across Northern Mexico and Texas. Figure 1 shows the tract for STS 107 (Columbia) on 01 Feb 2003 that is essentially the same as for STS 78. Figure 2 shows the signal from STS 78 that consists of "noise like" infrasound from the decaying shock wave. As seen in Figure 3, the signal from Columbia is clearly different in that impulsive arrivals are superimposed on the expected "noise like" background.

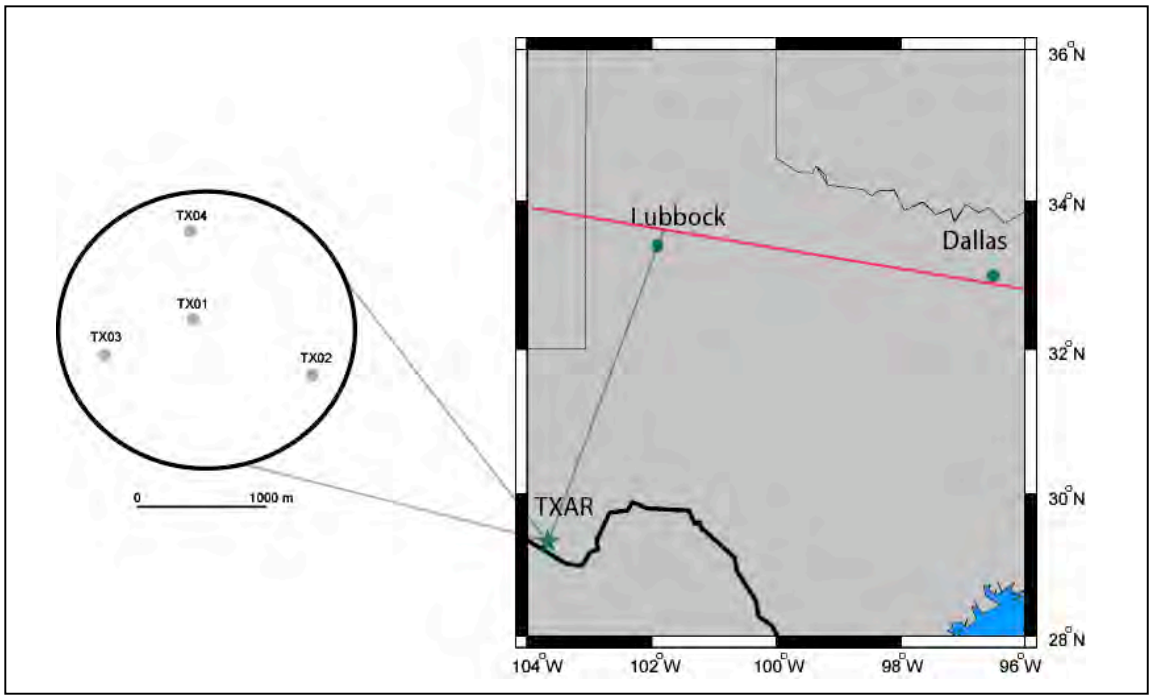


Figure 1. The re-entry path for STS 107 (Columbia) on 01 Feb 2003 from NASA. The path is similar to that of a previous mission, STS 78.

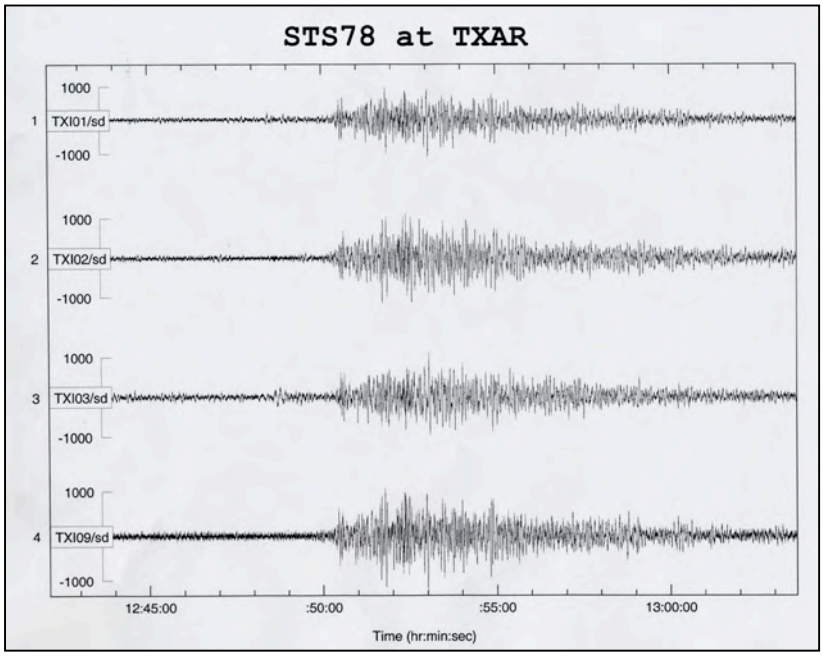


Figure 2. The signal from the normal re-entry of STS 78 consisting of "noise like" infrasound from the decaying shock wave.

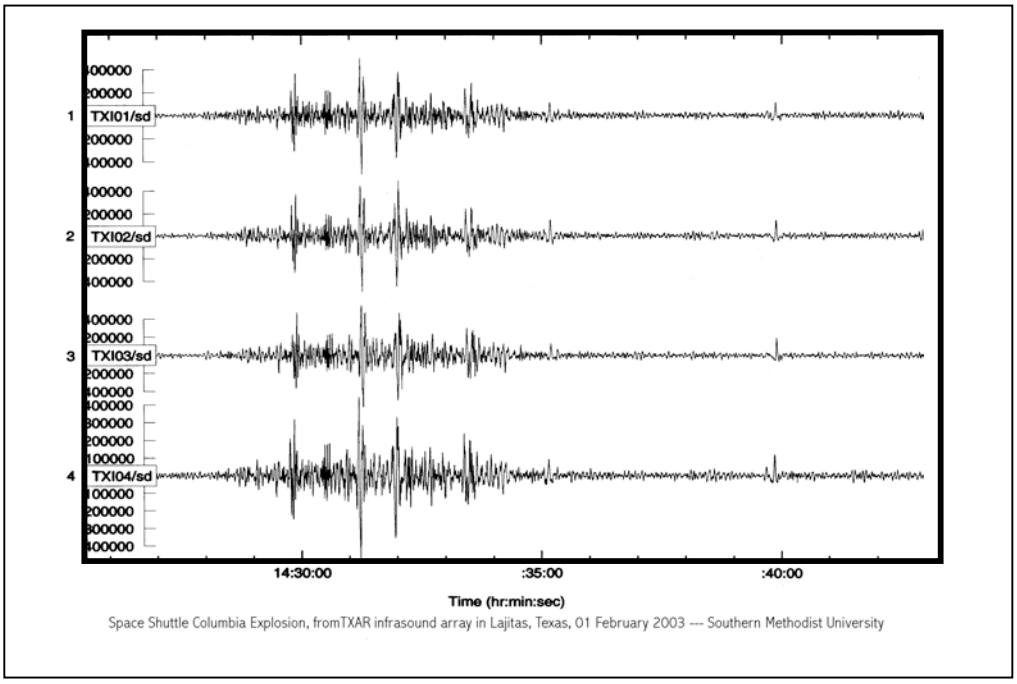


Figure 3. The signal from Columbia showing differences from STS 78 with impulsive arrivals superimposed on the "noise like" background.

Array analysis of the impulsive signals as summarized in Figure 4 show that the back azimuths of these arrivals are essentially the same within the expected analysis error. We conclude that the signals are multipath arrivals from a single event because the shuttle was traveling at a speed greater than Mach 19 at that time.

Arrival	Azimuth	Phase
14:28:13	18.11	0.312
14:29:44	19.01	0.311
14:30:26	19.01	0.311
14:31:08	20.31	0.312
14:31:51	19.01	0.311
14:33:22	19.41	0.313
14:35:05	18.65	0.307
14:39:40	17.34	0.307

Figure 4. Array analysis of the impulsive signals showing the back azimuths of all arrivals essentially the same.

Synthetic wave forms were computed using Inframap software based on the atmospheric model shown in Figure 5 using the time and location of an assumed explosion aboard the shuttle found by crossing the mean back azimuth from TXAR with the GPS shuttle tract data provided by NASA. The synthetic waveforms shown in Figure 6 show impulsive multipath arrivals, several of which agree in travel time with that of the observed arrivals at TXAR, within a few seconds. We consider this to be an excellent result for a travel path of over 600km. Parameters of the assumed explosion are shown in Figure 7. In order to estimate the size of the explosion we used an empirical formula based on atmospheric nuclear explosions. This formula was corrected for the known, factor of two difference between the effects of conventional vs. nuclear explosions, but was based entirely upon surface or low altitude events. We determined that the Columbia event occurred at a height of just over 63 Km. Correction of the predominant period – yield relation for altitude is made using the relation by Armstrong shown in Figure 8. Based upon this analysis the size of the shuttle explosion was between 2 and 3 lbs. of TNT equivalent.

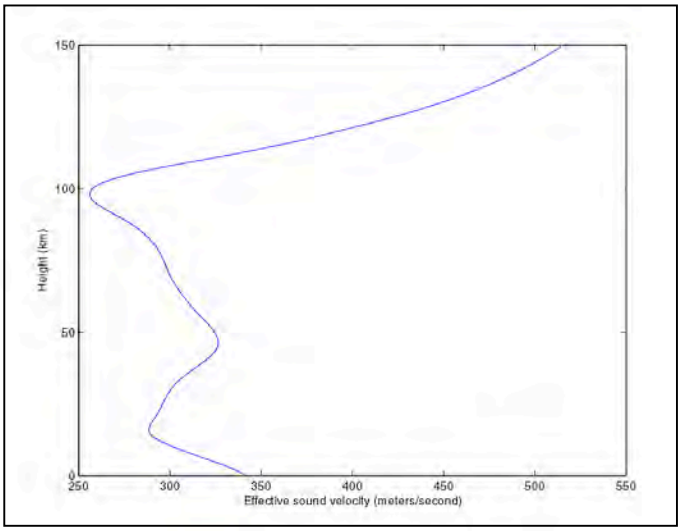


Figure 5. The atmospheric model used for computing synthetic wave forms using Inframap software.

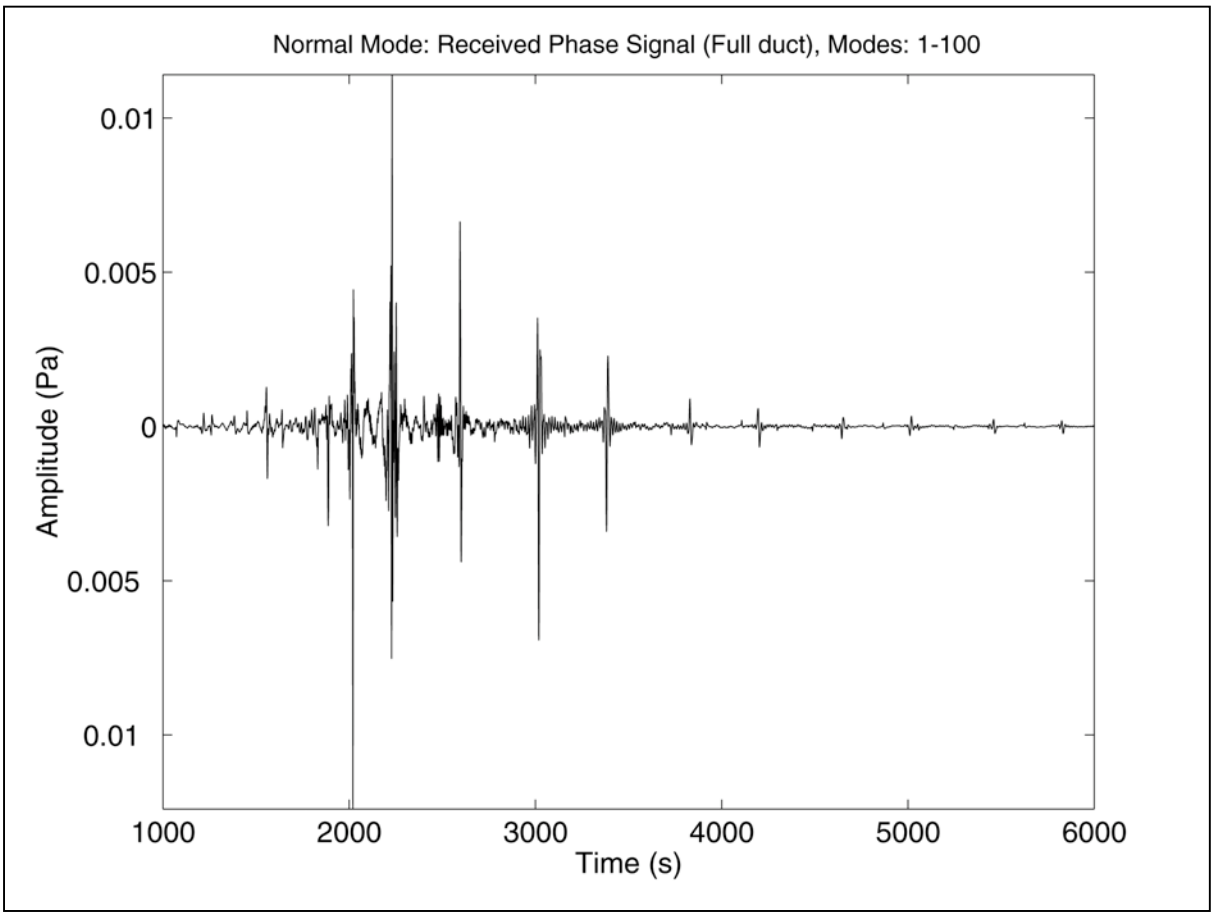


Figure 6. Synthetic waveforms from Inframap showing impulsive multipath arrivals, several of which agree in travel time with the observed arrivals at TXAR.

Our best estimate of the parameter of the explosion

On 1 February 2003

Location:	33.85 N	101.92 ± 20 km
Time:	13 56.65 Z ± 0.1 min	
Height:	63.3 km	
Speed:	Mach 16.2	

Figure 7. Parameters of the assumed explosion.

Empirical formula for estimating yield of atmospheric Explosions modified for HE instead of nuclear source

Point source at low altitude

$$Y \approx (2) \times 2.63 \times T^{3.34}$$

Where Y is the yield in tons

T is dominant period of infrasound signal

Correction for altitude Z (from W. T. Armstrong (1998)
20th Seismic Research Symposium, p. 554
For constant period yield estimate is proportional to ambient pressure where

$$P(z) = P_o \, e^{-Z/H}$$

Where H is pressure scale height of atmosphere (about 7 km)

Figure 8. The period-yield relation of Armstrong.

HISTORICAL PESRPECTIVE

The results above reminded the authors of "grenade" experiments concluded four decades ago. From 1960 to the early 1970's, NASA conducted a series of rocket grenade experiments to produce infrasound as a means to study the mesosphere. The experiments were comprised of rocket launches at four latitudes, four times per year, for 12 years. In the initial experiment 28 sounding rockets were launched from 1960 to 1963. Temperature, pressure, density and wind measurements were derived from the received infrasound signals. During this early period the grenades were the equivalent of 1 or 2 pounds of high explosives. The charges were ejected and exploded at 4 to 6 km intervals to profile the atmosphere from ~30 to ~90 km. Radar and other ranging systems were used to measure the location of the explosions. The time of the explosions was recorded by photocells on the payload. Later, charges from 1/4 pound to 1/2 pound were used up to 50 km, and 2 to 3 pound grenades from 50 to 90 km.

The frequency of infrasound signals received varied with altitude of the explosion; signals less than 1 Hz were received from the higher explosions. These experiments were all reported in a series of NASA Technical Reports from 1963 onward. We propose to explode high altitude small charges to produce infrasonic waves for confirmation of the performance and calibration of infrasound arrays. The signals from a known charge, when exploded, can be used to characterize the performance of an infrasound array. Charges exploded near the earth's surface can be complicated due to reflections, damping, and multi-path problems. Low altitude explosions require very large charges to generate infrasound waves. However, small charges exploded at high altitudes can produce infrasound very well. Furthermore detonation of explosives in the mesosphere and lower ionosphere can produce acoustic waves that can be used for diagnostic measurements of the atmosphere.

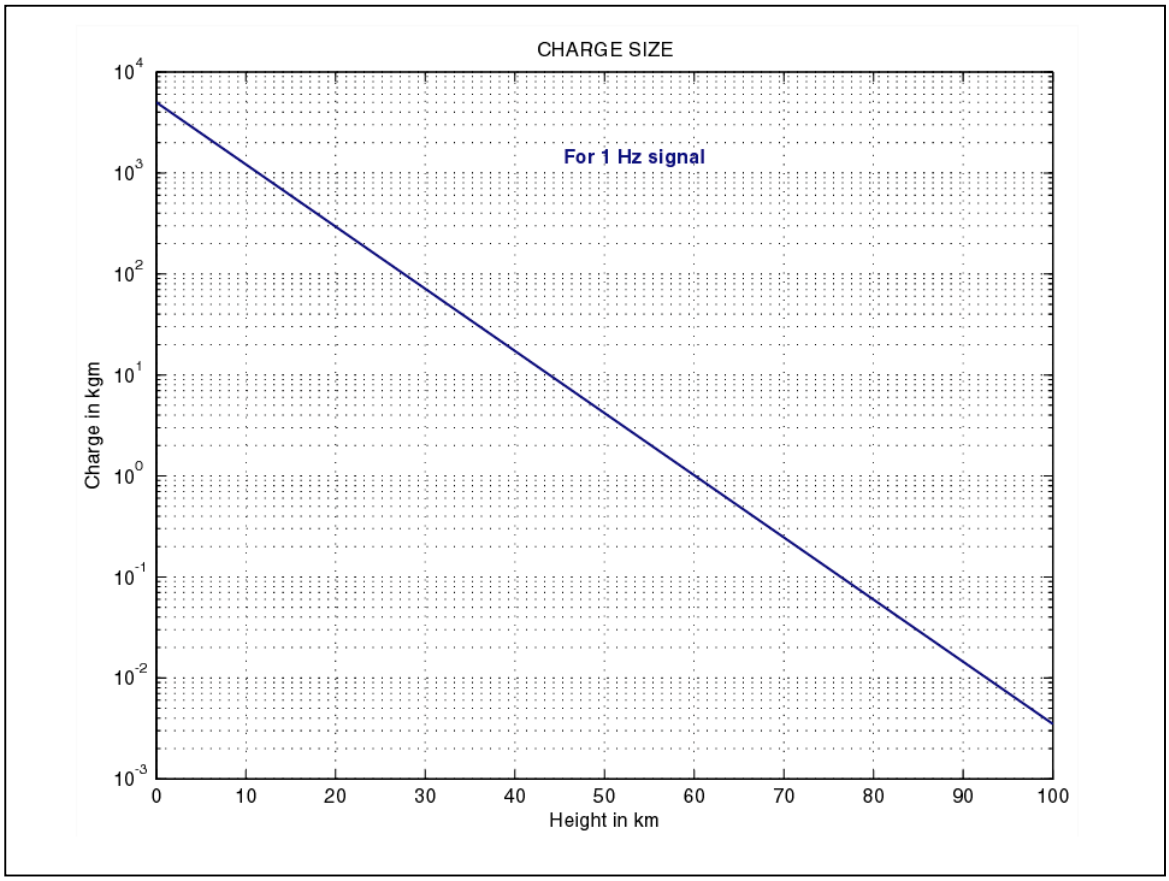


Figure 9. The scaling relation between yield and height of burst that is expected to produce infrasound waves with a predominant period of about 1 second.

CONCLUSIONS AND RECOMMENDATIONS

Explosion experiments can be conducted at White Sands Missile Range using rockets capable of reaching heights of many tens of kilometers. Figure 9 shows the scaling relation between yield and height of burst that is expected to produce infrasound waves with a predominant period of about 1 second. Signals of this period are expected to be observed at many permanent and temporary infrasound arrays in North America provided the timing of the experiment is designed to minimize the effect of atmospheric global winds. We believe that the signals produced will be useful for calibrating the existing infrasound arrays and for validating synthetic data based upon Inframap calculations. Our preliminary design, on the first of the experiments, was to fire a charge of 50 lbs. of TNT equivalent, on the downward leg of a rocket trajectory at a height of 50 km. This was carried out near the autumnal or vernal equinoxes, when the zonal winds are at a minimum. Figure 10 shows typical performance characteristics for a single stage Orion depending on the maximum payload. We include our proposed performance for the 50 lb. explosion at 50 km. Current plans to use the Orion rocket are driven partially by cost, since it is less expensive than the smaller Lance missile due to required up front costs for certifying Lance rounds. Figure 11 shows the planned configuration of the single stage Orion vehicle proposed for the experiment. Figure 11 illustrates one possible flight path for the first of the experiments indicating the launch, apogee and impact site of the rocket.

Plans are in process to order 10 explosive charges in FY 2004 for future missions. In addition to the first experiment described previously, future funding may allow additional missions firing up to 3 explosions a day, at two hour intervals, and possibly two or three missions scheduled over a year. Multiple missions could provide experiments at an equinox and at times when the zonal winds are at maximum from the east and/or west. We have requested a meeting at WSMR in October for planning purposes to set dates and schedules for the missions.

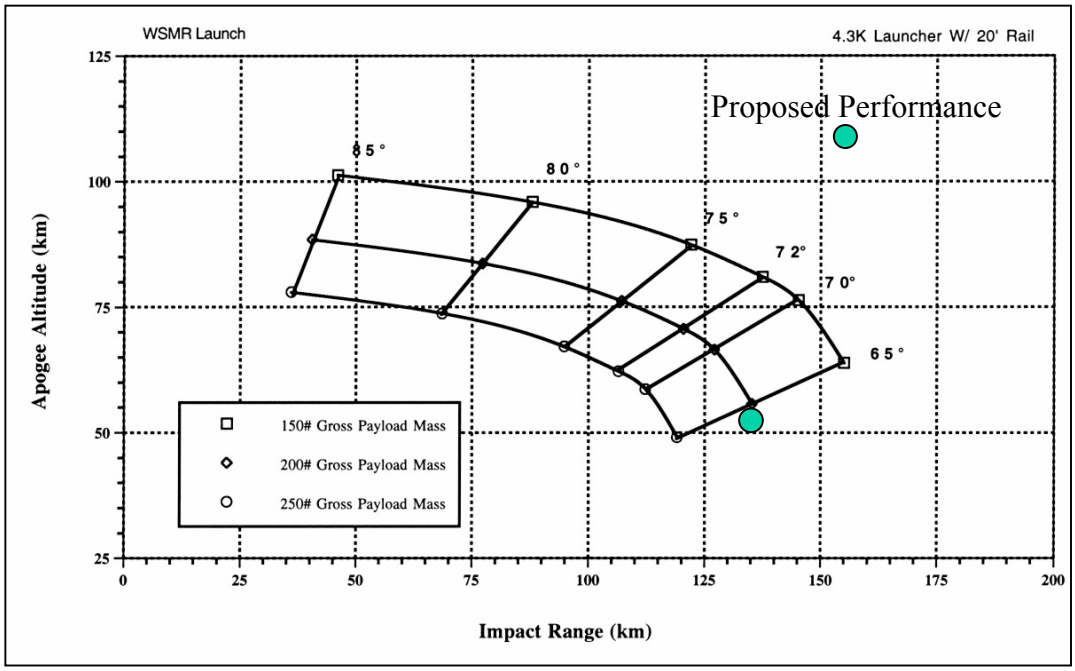


Figure 10. Typical performance characteristics for a single stage Orion rocket depending on payload.

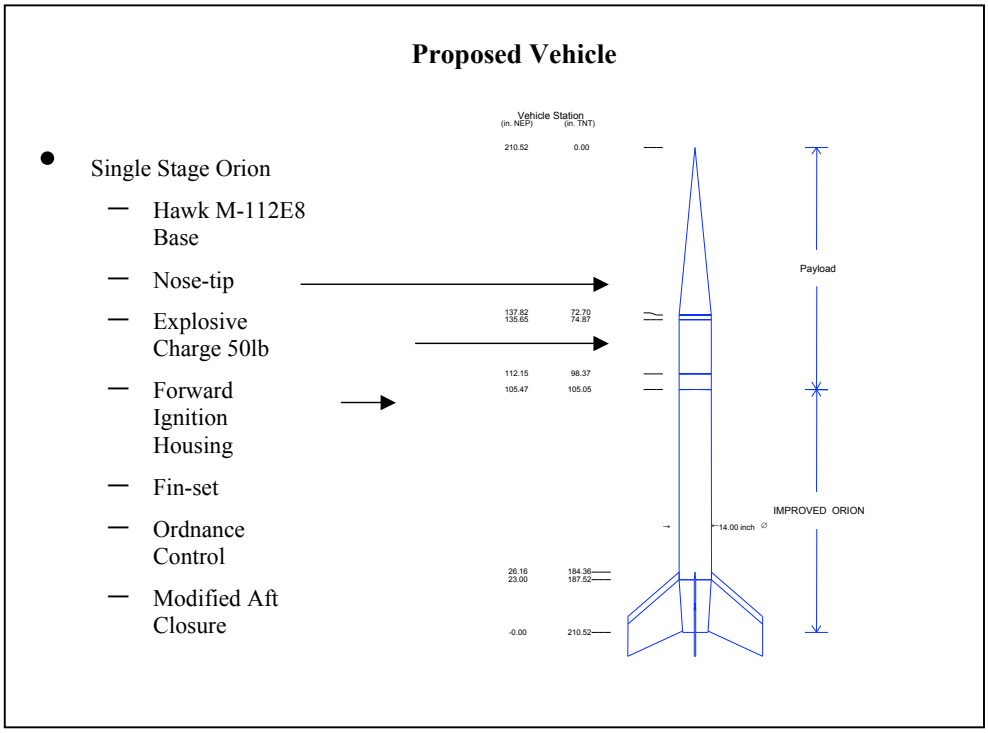


Figure 11. Planned configuration of the single stage Orion vehicle proposed for the experiment.

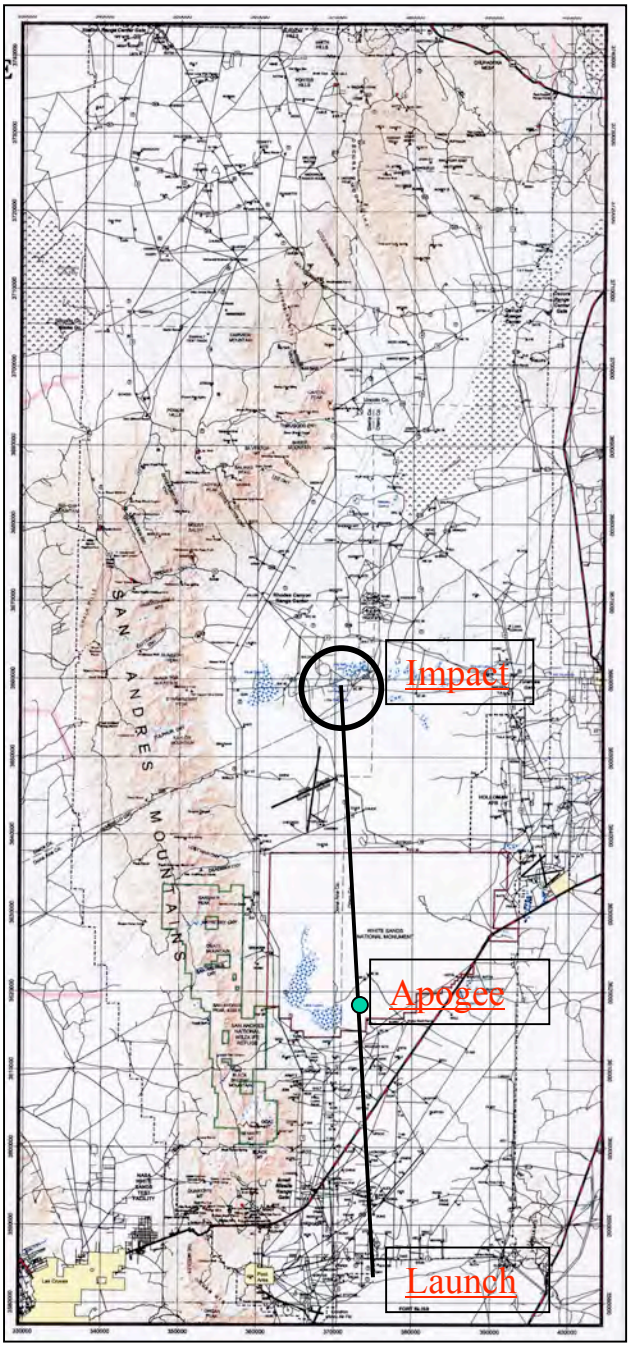


Figure 12. A proposed flight path for the first of the experiments.

REFERENCES

Armstrong W.T., (1998), Comparison of infrasound correlation over differing array baselines in Proceedings of the *20th Annual Seismic Research Symposium on Monitoring a Comprehensive Test Ban Treaty (CTBT)*, p. 554.

Osborne D.L, H. Nielsen, M. Conde, J.V. Olson and C. R. Wilson, (2003), Infrasound Generating Rocket Grenade Experiment for Investigations of Infrasound Array Capability and Diagnostic Tool to Study the Mesosphere and Lower Ionosphere, White Paper, University of Alaska.

TIME-DOMAIN MODELING TECHNIQUES AND THE STUDY OF INFRASONIC PROPAGATION

David E. Norris

BBN Technologies

Sponsored by Army Space and Missile Defense Command

Contract No. DASG60-99-C-0018

ABSTRACT

Numerous propagation models, including ray tracing, normal mode, and Parabolic Equation (PE), are available for the study of infrasound. This paper will focus on time-domain (TD) modeling techniques. PE and nonlinear implementations are reviewed, and comparisons are made between Fourier synthesis TD PE predictions and infrasonic measurements. The atmosphere is defined using climatologic wind (HWM-93) and temperature (MSIS-90) models that capture the dominant seasonal and diurnal features. Normal mode predictions are also included in the comparisons.

OBJECTIVE

Over the last several years, modeling capabilities in the study of infrasound propagation have improved significantly. Atmospheric characterizations have moved beyond climatological models and can now leverage synoptic nowcasts that capture fine-scale features in the wind and temperature fields (Gibson and Norris, 2002). Propagation modeling has mainly focused on application of ray trace, normal mode, and PE formulations, with the latter limited to continuous-wave propagation. Studies comparing modeling predictions and measurements have shown limited agreement in some cases (e.g., Norris and Gibson, 2001).

Despite these successes, state-of-the-art propagation models have failed to consistently predict many of the features of measured infrasonic waveforms, including

- Spectral content
- Arrival times and amplitudes
- Waveform shape and associated parametric descriptors.

Modeling waveform features is critical to advancing our infrasonic capabilities. With improved models, waveform synthetics can be generated and used to evaluate and improve infrasound station detection algorithms. Predictions of received waveforms for different source mechanisms can be used to develop association and classification algorithms. In addition, improved amplitude and travel-time predictions over multiple phase arrivals will reduce event localization uncertainty and provide more robust network performance models.

As a result of these issues, time-domain propagation modeling techniques have experienced renewed interest within the infrasound research and analyst community. Previous time-domain models have been limited to normal mode formulations (Dighe et al., 1998; Pierce and Kinney, 1976). These models can only be used with a range-independent realization of the atmosphere. In addition, they cannot account for atmospheric absorption or complex boundaries. Newer approaches are based upon the PE model. PE-based models have the advantage of being able to accommodate complex boundaries, absorption, and a range-dependent atmosphere.

In this study, a summary is given of the time-domain Parabolic Equation (TDPE) approach. Example predictions are shown from a TDPE model developed for infrasound (Norris and Gibson, 2003a). Finally, comparisons between the TDPE predictions and measurements from the 1996 El Paso bolide are presented.

REASEARCH ACCOMPLISHED

TDPE Model

The Parabolic Equation approach is based upon solving the wave equation in spherical coordinates. Azimuth symmetry is assumed, and the problem is reduced to solving an equation in range vs. height coordinates. In the continuous-wave PE, a single frequency is assumed, and the wave equation is transformed into the Helmholtz equation.

Time-domain PE implementations fall in one of two categories: Fourier synthesis and finite difference. Fourier synthesis involves running a continuous wave model at each frequency bin that defines the source waveform. An inverse Fourier transform of the synthesized spectrum is then computed to derive the received waveform (Tappert et al., 1995). The main advantage of Fourier synthesis is that all capabilities of the continuous-wave model are maintained. The main disadvantage is the high computational loading, especially for large frequency bandwidths and for acoustic arrivals that are widely dispersed in time.

The second approach uses finite-difference methods to solve the propagation equations directly in the time domain (Collins, 1988). The main advantage is a (potentially) significant reduction in computational loading. Additional properties such as nonconstant density gradients and nonlinear effects can also be more easily incorporated into the characterizations. The main disadvantage is that the formulation must be carefully examined for numerical stability. Boundary condition specification can also be more complicated.

A large variety of PE numerical solutions exist for both the Fourier synthesis and finite-difference approaches. As a baseline model, we have implemented a Fourier synthesis approach (Nghiem-Phu and Tappert, 1985) based on the continuous-wave, split-step algorithm (Jensen et al., 1994). This implementation provides predictions of

propagation waveforms in a Lagrangian, or wave-following, reference frame that moves with the propagating waveform at a reference sound speed, usually taken to be 0.34 m/s. Figure 1 is an example of a TDPE waveform prediction. A consequence of this "wave-following" reference frame is that the predictions are given in reduced time, which starts at the beginning of the Lagrangian time window. To compute absolute travel time, the reduced time must be added to the reference time (range divided by the reference sound speed). This computed travel time is only an estimate since it depends on choice of reference sound speed. Versions of the TDPE that are not based on a reference sound speed are currently being evaluated for application to infrasound.

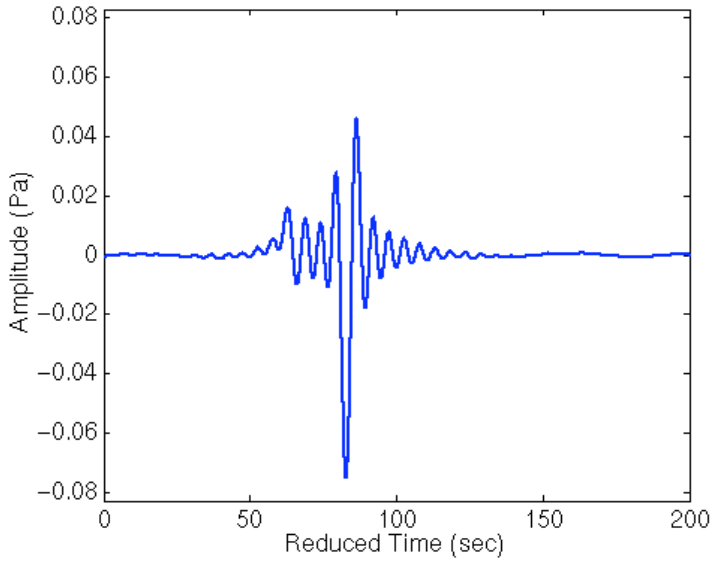


Figure 1. Example of TDPE predictions in wave-following reference frame.

Comparison Studies

Comparison studies with observations are critical to assess the performance of the models. To date, large-scale validation exercises for infrasound have been few (e.g., Whitaker at al., 2003; O'Brien et al., 2003). In this study, we focus on comparing TDPE predictions to a bolide observation that includes ground truth.

On 9 Oct 1997, a large bolide traveled above Texas near El Paso. The height of the bolide, as determined from satellite observations, was 29 km. This bolide was detected at both the Los Alamos DLIAR array (range 445 km) and the Southern Methodist University TXIAR array (range 359 km). In a previous study, eigenrays were computed over a range of source heights from 0 to 50 to evaluate the ability to verify or refine the source height estimate (Norris and Gibson, 2003a). Synthetic waveforms were next computed for each source height and mapped into an image as a function of arrival time and source height (bottom of Figure 2). The eigenrays were compared to the measured waveform (top of Figure 2), and a source height estimate was made by correlating the measured arrival times with the predicted amplitudes. The three measured arrivals matched the predictions at source heights of 33, 26, and 23 km, respectively. Although there is a spread in these heights, they are in general agreement with the satellite-determined source height of 29 km.

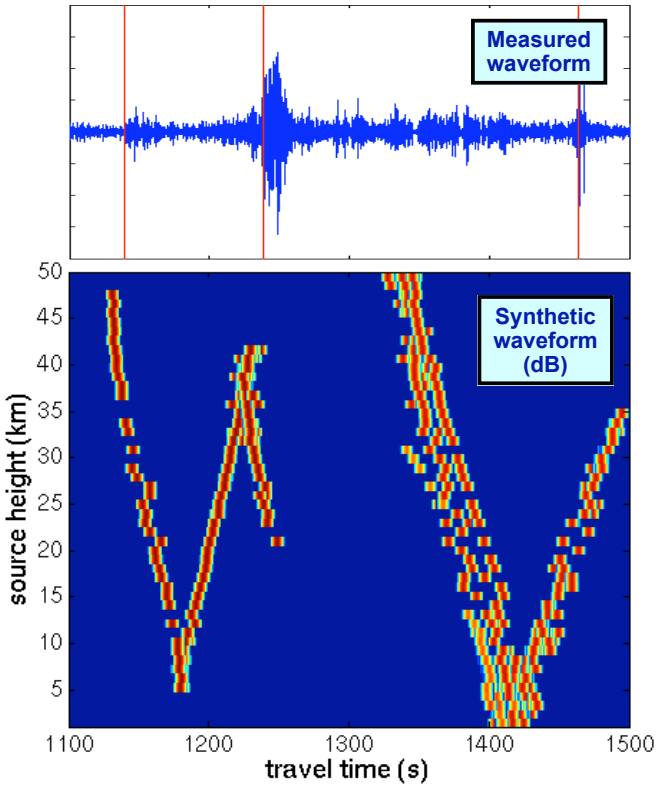


Figure 2. Comparisons between measured waveform and ray synthetic waveforms over a span of source heights.

In this study, initial broadband predictions are made using the Fourier synthesis TDPE. At the writing of this paper, predictions have only been made at the ground truth source height of 29 km, although predictions over the entire height range are in process. Figure 3 shows the waveform structure at the receiver over a range of receiver heights. A waveform time series is generated by taking a slice at a given height. At the ground, stratospheric energy is observed at reduced times of 75 and 150 s. Thermospheric energy is seen arriving at 300 s.

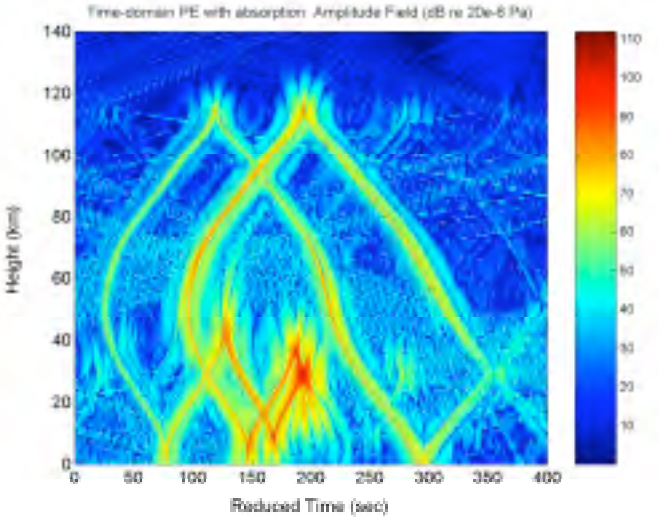


Figure 3. TDPE waveform arrival structure at receiver.

To compare the TDPE predictions with the observations, a reference sound speed of 0.34 km/s is assumed. The results are shown in Figure 4. Three observations are seen both the observations and predictions. The time-of-arrival difference between the first two arrivals is similar, but the third predicted arrival is approximately 70 s earlier than that observed.

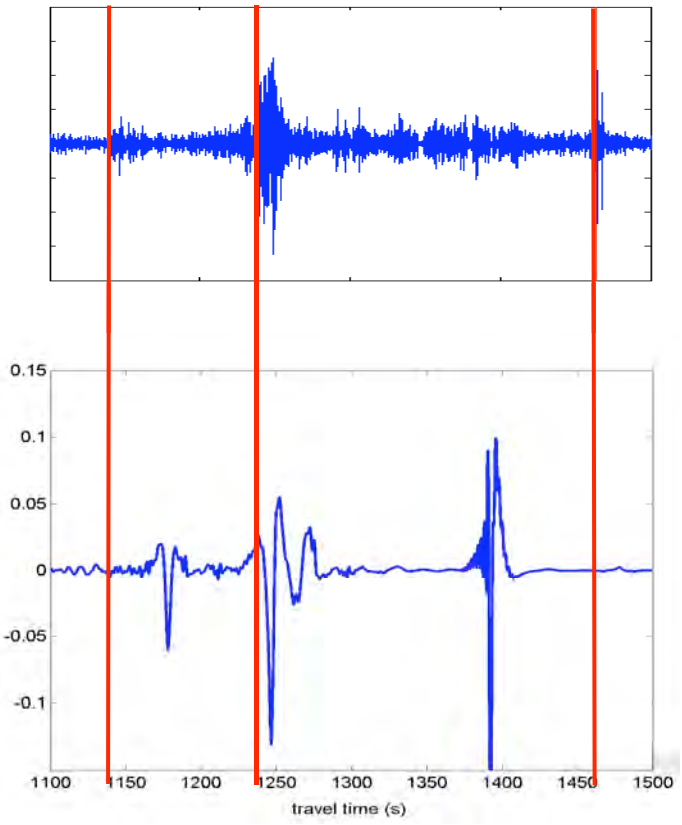


Figure 4. Comparison between measured waveform and TDPE prediction at 30 km source height.

CONCLUSIONS RECOMMENDATIONS

A baseline TDPE model has been implemented using the continuous-wave split step algorithm and Fourier synthesis. Initial comparison studies have yielded some limited agreement with observations, although more comparisons are needed over a variety of infrasonic sources and atmospheric conditions.

One source of the modeling limitations may be the neglect of nonlinear effects. By including nonlinear terms in the model formulations, predictions that account for some of the dominant nonlinear effects can be made. Evaluation of nonlinear models applied to infrasound is currently in progress. It is anticipated that the nonlinear modeling efforts will help identify more of the relevant physics affecting the propagation and thus contribute to better predictions of travel time, amplitude, and other waveform characteristics.

REFERENCES

Collins, M. D. (1988), The Time-Domain Solution of the Wide-Angle Parabolic Equation including the Effects of Sediment Dispersion, *J. Acoust. Soc. Am*. 84, 2114–2125.

Dighe, K. A., R. W. Whitaker, and W. T. Armstrong (1998), "Modeling Study of Infrasonic Detection of a 1 kT Atmospheric Blast", in proceedings of the *20th Annual Seismic Research Symposium on Monitoring a Comprehensive Test Ban Treaty (CTBT)*, Santa Fe, NM.

Gibson, R. and D. Norris (2002), Infrasound Propagation Modeling: Near-Real-Time Environmental Characterization and Variability Studies*, Infrasound Technology Workshop,* De Bilt, The Netherlands.

Jensen, F. B., W. A. Kuperman, M. B. Porter, and H. Schmidt (1994), *Computational Ocean Acoustics*, AIP Press, New York.

Nghiem-Phu, L. and F. Tappert (1985), Parabolic Equation Modeling of the Effects of Ocean Currents on Sound Transmission and Reciprocity in the Time Domain, *J. Acoust. Soc. Am.* 78, 642-648.

Norris, D. and R. Gibson (2003a), InfraMAP: Status and Recent Activities*, U.S. Infrasound Team Meeting,* La Jolla, CA.

Norris, D. and R. Gibson (2001), "InfraMAP Propagation Modeling Enhancements and the Study of Recent Bolide Events*,"* in *Proceedings of the 23rd Seismic Research Review: Worldwide Monitoring of Nuclear Explosions*, LA-UR-01-4454, Vol. 2, pp. 150-159.

O'Brien, M., M. Bahavar, E. Baker, M. Garcés, C. Hetzer, H. Israelsson, C. Katz, C. Reasoner, and J. Stevens (2003), Detection of Infrasonic Events using a Sparse Global Network of Infrasound Stations, *Infrasound Technology Workshop*, La Jolla, CA.

Pierce, A. D., and W. A. Kinney (1976), *Computational Techniques for the Study of Infrasound Propagation in the Atmosphere*, Technical Report AFGL-TR-76-56, Air Force Geophysics Laboratories, Hanscom AFB, MA.

Tappert, F., J. L. Spiesberger, and L. Boden (1995), New Full-Wave Approximation for Ocean Acoustic Travel Time Predictions, *J. Acoust. Soc. Am*. 97, 2771–2782.

Whitaker, R., T. Sandoval, and J. Mutschlecner (2003), "Recent Infrasound Analysis", in *Proceedings of the 25th Seismic Research Review - Nuclear Explosion Monitoring: Building the Knowledge Base*, LA-UR-03-6029, Vol. 2, pp. 646-654.

INFRASOUND SOURCE LOCATION USING TIME-VARYING ATMOSPHERIC MODELS

Michael O'Brien and Gordon Shields

Science Applications International Corporation

Sponsored by Army Space and Missile Defense Command

Contract No. DASG60-03-C-0009

ABSTRACT

Advancement of global infrasound event location capabilities for nuclear monitoring has been limited until recently because there were few permanent infrasound stations. The recent completion of several International Monitoring System (IMS) infrasound stations, together with advances in atmospheric propagation modeling, motivated the re-examination of the use of modern atmospheric models in infrasound event signal association, location and analysis.

The first objective of this study was to address known deficiencies in the existing infrasound travel time (TT) tables of Brown (2000) and to generate new tables for all current infrasound stations. The existing tables embody a number of approximations that severely limit their location prediction accuracy. They model only one possible infrasonic arrival as a function of distance, whereas it is well known that infrasound may propagate between the same source and receiver by many paths through effective ducts in the thermosphere, stratosphere and troposphere, each producing different transit times. In addition, the TTs were estimated by ray tracing through the HWM/MSISE climatological atmospheric model (Hedin *et al.*, 1996) but only for four seasons of the year; the diurnal and sub-seasonal variations were not captured. We generated a new tabulation of TTs also based on HWM/MSISE. The Tau9.1 one-dimensional (1-D) ray tracer (Garces *et al.*, 1998) was used to compute TTs from monthly samples of HWM/MSISE at four times of the day. Separate arrival phases were modeled for the two principal atmospheric ducts, thermospheric and stratospheric, but all TTs resulting from multiple-skip paths within each were collapsed to a single TT curve. Uncertainties were estimated from the TT variations calculated in the same manner from time-specific Ground-to-Space (G2S) atmospheric models (Drob, 2003) spanning eight months. Tables were constructed for a total of 19 stations, including 12 recently activated IMS stations. In all over 50 million TTs with uncertainties were computed and arranged into 1704 tables.

The second objective of the study was to evaluate the relative merits of different atmospheric models and approaches to representing them (we refer to this combination as a propagation model) for estimating infrasound event locations in global nuclear monitoring and analysis. We compared the seasonal HWM/MSISE based Brown (2000) model, the new monthly HWM/MSISE based model, a similarly computed but event-specific G2S based model, a constant two-celerity model of 245 and 320 m/s, and the best *a posteriori* fit single-celerity model of 282 m/s. A major difficulty in evaluating location accuracy is the paucity of usable ground-truth events, that is, low atmospheric events for which waveform data, station metadata and well constrained space-time location are available. In this study we compiled data for 21 atmospheric events, from chemical explosions, mining explosions, gas pipe explosions, rocket motor tests and rocket launches, against which to evaluate the predictions of the propagation models. Of these only seven were detected at multiple stations (required for computing an actual location), so we also formulated accuracy measures in terms of predicted TTs and back azimuths.

Overall, the new monthly HWM/MSISE based model performed the best against the data set, followed by the two-celerity model, the event-specific G2S model, the best celerity model, and, finally, the seasonal Brown (2000) model. Counter to expectation, the two-celerity model predicted TTs the best of all models, while the most timely event-specific model was fourth in this respect. In contrast, back azimuth prediction was not very different among the models although all the time-varying models did improve locations and back azimuth residuals over the constant celerity models. We attribute the relatively strong performance of the constant celerity models to the fact that the evaluation dataset is far too small to representatively sample the unmodeled variations related to atmospheric change; thus, our initial results are not likely reflective of the overall predictive abilities of these models. In addition, the TT and back azimuth residuals suggest that collapsing the multiple-skip paths into a single TT curve may be a significant source of error; explicitly modeling them may improve the travel times and back azimuths predicted using HWMS/MSISE and G2S. Further studies are underway to more fully explore these sources of variability.

OBJECTIVES

The first objective of this study was to generate new infrasound travel-time tables for all current infrasound stations based on the HWM/MSISE climatological atmospheric model to address known deficiencies in the existing tables. These travel times are used for locating infrasound events.

The second objective of the study was to evaluate the relative merits of travel times based on different atmospheric models for estimating infrasound event locations in global nuclear monitoring and analysis.

RESEARCH ACCOMPLISHED

Locating events using infrasound arrivals is challenging because wave propagation in the atmosphere is highly variable in both space and time; this is mainly the result of variations in wind and temperature that change the local sound velocity field. Propagation paths, times, and amplitudes are all observed to vary strongly with each of geographic position, direction of propagation, time of day, time of year, and current weather conditions. Moreover, for any source-receiver combination there are almost always multiple propagation paths by which energy may reach the receiver. Thus, there are several elements that contribute to errors in predictions of the infrasound observables (travel time and back azimuth) and source locations computed from them: 1) the atmospheric sound velocity model, 2) the way that model is sampled, 3) approximations in representing the observables from multiple propagation paths, and 4) the method of numerical propagation used to convert sound velocity into infrasound observables. We refer to a single specification of the set of these elements as a “propagation model”.

The difficulties are compounded when using infrasound in systematic global signal association and event location because the association of measured signals with hypothesized events is ultimately inferred from consistency with the hypothesized event location and time. As a result, the consistency of virtually all possible event locations and times must be evaluated. In the U.S. National Data Center association software this is done as an exhaustive global search. It is computationally expensive and, practically, requires that knowledge of the propagation medium be rendered in advance into predicted travel times and deviations between observed and source-receiver back azimuths at each receiver location for energy traveling via all possible paths from all possible source locations. The more dynamic the propagation medium, the more frequently it must be sampled and the less manageable the tabulation becomes. For infrasound in particular, there is an unavoidable trade-off among accuracy, timeliness and computational cost and complexity that affects the choice of each element of a propagation model.

In this paper we present a new tabulation of infrasound travel times, intended for use in global association and location, that improves upon the prediction capabilities of the existing Brown (2000) travel times without affecting timeliness of results or unacceptably increasing computational or logistical cost. First we discuss the trade-offs relating to each propagation model element and present the rationale behind our choices for creating the new travel-time tables. We then present a comparison of predictive capabilities of this propagation model to four others of lesser and greater complexity, including that of the Brown (2000) travel times, to assess the achieved and potential improvements associated with adopting more complexity. We did not tabulate back azimuth information but did include predicted corrections in the evaluation.

Propagation of Infrasound and Atmospheric Sound Velocity Models

The most important element of a propagation model is the atmospheric velocity model. The left panel of Figure 1a illustrates typical atmospheric velocity profiles with zones of increasing velocity that create propagation ducts. Typical propagation paths in the right panel illustrate the most prominent thermospheric and stratospheric ducts. The thermospheric duct exists between all source-receiver combinations at all times; the stratospheric duct exists only under the right wind conditions, which depend on time of day, time of year, propagation direction, and current weather. Tropospheric ducts are much less commonly predicted and occasionally are inferred from observations.

Until recently, the best global atmospheric characterization was provided by HWM/MSISE, a combination of the Horizontal Wind Model (HWM-93) (Hedin et al., 1996) and the Extended Mass Spectrometer - Incoherent Scatter Radar (Picone et al., 2002). This model estimates atmospheric state properties globally up to about 200 km altitude for all times of the year, obtained from averaging across many years of atmospheric observations. For infrasound propagation HWM/MSISE can provide an estimate of the vector sound speed anywhere for any time. However, it predicts only long-term averages of sub-annual trends (diurnal to seasonal), so it has inherent inaccuracy with

respect to the velocity field at any specific time. HWM/MSISE was employed by Brown (2000) at which time it was the only velocity model available. More recently the Naval Research Laboratory (NRL) began generating the Ground to Space (G2S) atmospheric models (Drob, 2000) that fuse lower atmospheric numerical weather prediction results for a specific epoch in the lower 50 km of the atmosphere at (Figure 1b, panel A) with the average trends predicted by HWM/MSISE in the upper atmosphere (Figure 1b, panel B) to produce a single time-specific model of the atmosphere (Figure 1b, panel C). In principle, each G2S model provides more accurate stratospheric propagation velocities at its epoch than HWM/MSISE, and should lead to better prediction of the stratospheric duct and of infrasound observables in general. However, G2S is inherently limited with respect to timeliness of availability for the near-real-time data processing and analyses done in a global monitoring system. For this reason we based the propagation model for the new tabulation of global travel times on HWM/MSISE.

Other velocity models were used to assess their relative potential in an infrasound monitoring system. We based one propagation model on the G2S models because they are presumed to be the most accurate. We also based a propagation model on constant celerities (average horizontal propagation speed) of 245 and 320 m/s for thermospheric and stratospheric arrivals, respectively; this is the simplest model that accounts explicitly for two principal propagation ducts. Finally, we based a propagation model on the single celerity (282 m/s) that best fit the evaluation data set to assess how much of the observations require the complexity in other models to be explained.

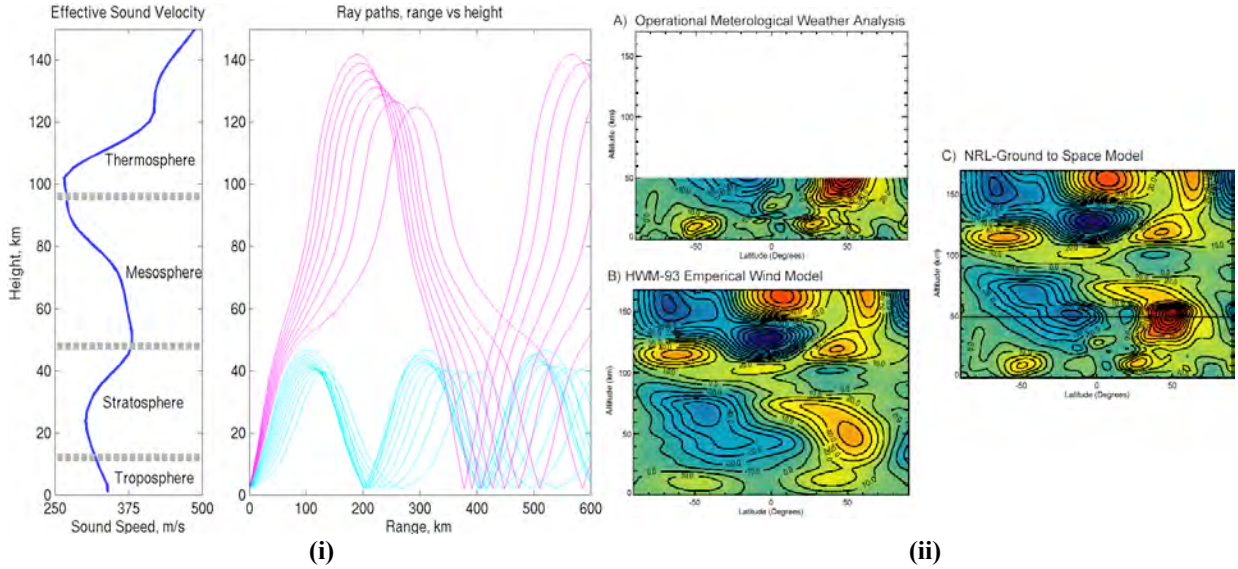


Figure 1. Features and predictions of atmospheric models.

(i) A typical velocity profile in the left pane and predicted ray paths for stratospheric (blue) and thermospheric (purple) arrivals in the right; note the multiple return paths for distance >400 km. (ii) Zonal sound velocities (figure from Drob (2003)) illustrating the construction of G2S models (panel C) from the Operational Weather Analysis data (panel A) and the HWM-93 climatological model (panel B); note the low altitude detail provided by weather data, which can significantly affect stratospheric paths and travel times.

Sampling Atmospheric Models

The innate spatial and temporal limitations of the atmospheric model are compounded by a further sampling performed in its exploitation. Brown (2000) chose to represent travel times at only four times of the year in his seasonal tables, computing travel times from HWM/MSISE sampled once in each season. This misses the important diurnal and sub-seasonal variations altogether, so we chose to sample HWM/MSISE each month at four times of the day (48 averages) to better capture these variations in the new global travel times. This is not an issue for G2S models, which are time specific, or for the constant celerity models, which have no spatial or temporal variations.

Spatial variability is accounted for in a propagation model by predicting travel times and back azimuth deviations at discrete azimuths and ranges from each station. For the global tables, we computed the travel times at azimuths every 1° and ranges every 1.5° from the station out to 120° to accommodate arrivals from large, distant sources. The range discretization was finer for the other propagation models, depending on the event and station.

Approximating Observables from Multiple Propagation Paths

There are almost always multiple paths by which infrasound may propagate from source to receiver with different travel times. This is apparent in Figure 1a at ranges beyond 400 km. The most significant travel-time differences are between stratospheric and thermospheric paths in general. Travel times are typically 10 to 20% smaller for stratospheric paths, due simply to the relative heights and thicknesses of the two ducts. When the stratospheric duct exists, its arrivals are typically stronger than thermospheric arrivals, leading Brown (2000) to a representation of travel times that uses the average stratospheric travel time if predicted for a given azimuth and range, and the average thermospheric travel time otherwise. Thus, where the stratospheric duct is erroneously predicted, travel times for the wrong duct are assigned. We represented times for the two ducts separately in the new HWM/MSISE and G2S propagation models, to allow the more consistent time to be chosen where the duct is predicted.

Skipping within each duct also produces multiple propagation paths with different travel times at a given distance. The effect is illustrated in Figure 2a for thermospheric arrivals. Accounting for each of these separately would multiply the tabulation volume – the spatial and temporal resolution described above for 19 existing stations implies ~25 million travel times per phase which pushes the limitations of existing software, so we opted to represent all the possible travel times within each duct by a single average phase, determined by linear fit to predicted travel times, similar to that shown in the figure. Thus, we represented travel time for each station, time, azimuth and range by two possible phases, "It" for thermospheric paths and "Is" for stratospheric paths where that duct is predicted to exist.

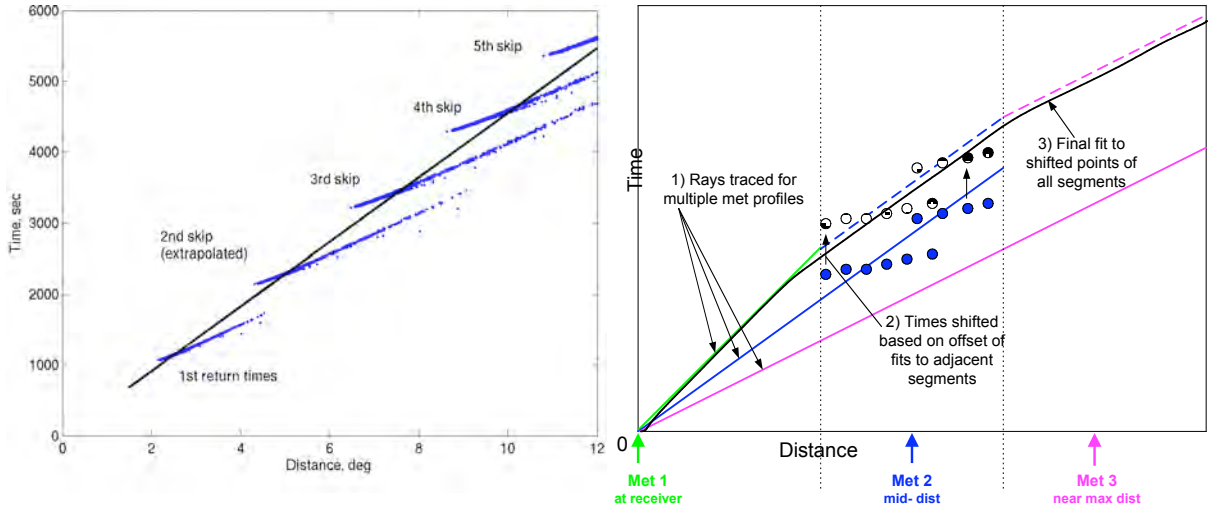


Figure 2. Computation of HWM/MSISE and G2S travel times.

(a) Approximating travel times for multiple skip paths within the thermosphere by a single travel-time curve and (b) accounting for range dependence using Tau9.1 (Garces et al., 1998). The large number of potential skip phases motivated our approximation of a single phase per duct; the large distance range desired in the travel-time tables motivated our approach to accommodate range dependence in the meteorological model.

Methods for Numerical Propagation of Infrasound

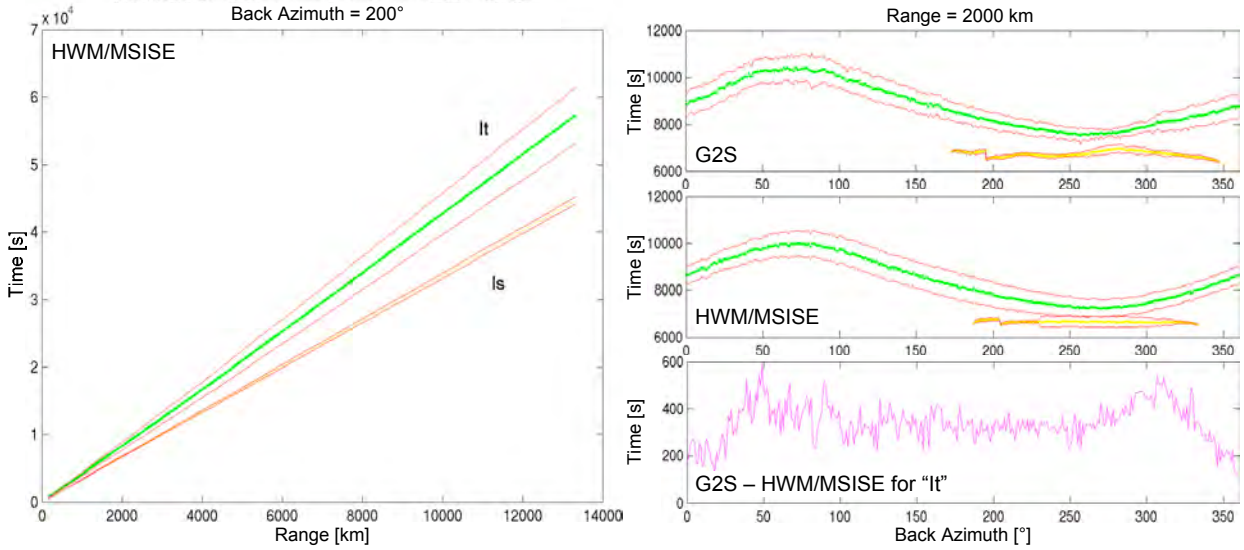
There are several methods for numerically propagating infrasound in a non-uniform medium to predict travel times and back azimuths, ranging in complexity from one-dimensional ray tracing to full wave field propagation. Most of these are computationally intensive and were impractical for computing the 50 million travel times of the new global tables – we estimated several months of CPU time to compute them via the HARPA three-dimensional ray tracer of Jones (1986). To make the computation practical we used the Tau9.1 one-dimensional ray tracer, developed at the Infrasound Laboratory at the University of Hawaii (Garces et al., 1998, Hetzer and Garces, 2002), to compute all HWM/MSISE and G2S travel times and back azimuth deviations. Based on the Tau-P method, Tau9.1 solves for the turning points of rays as a function of their takeoff angle assuming a laterally invariant velocity profile; it sums the contributions of each vertical layer to yield time, distance and lateral path offset (azimuth deviation) from translation of the wave front by cross winds. Times for skips through a duct are multiples of the first ground-to-ground traverse. Tau-P does not model time and azimuth effects of wave front bending or accumulated along-path velocity variation.

Along-path velocity invariance is a more serious limitation because it inherently limits the range within which predicted travel times are usefully accurate. To compensate for this we applied Tau9.1 in a crude but computationally cheap approximation of 2-D propagation, as illustrated in Figure 2b. The full 120° distance range was divided into three or four sub-ranges (green, blue and magenta in the figure) and selected a single velocity profile to represent each sub-range. Within each range, travel times were computed (filled circles) using the corresponding velocity profile and a straight line fit to them (dashed lines). The slopes were then spliced together (solid lines) and the resulting curve anchored at zero distance and zero time. The raw travel times were then shifted as were the straight lines (open circles). A fourth order polynomial was fit (not shown) to these over the full distance range and sampled to produce all the HWM/MSIS and G2S travel times. This procedure was performed separately for thermospheric and stratospheric ducts to yield travel-time curves for "It" and "Is" phases respectively. Examples are illustrated in Figure 3. Panel (a) illustrates the typically minor perturbation of our 2-D approach on the constant-slope 1-D results. Figure 3b illustrates typical differences between G2S and HWM/MSISE predicted travel times (G2S predictions are often systematically slower) and back azimuths at which a stratospheric duct is predicted.

To obtain back azimuth deviations, we averaged the first-skip back azimuths predicted for all three profiles. Thus, we estimated only one correction per back azimuth.

Travel-Time Uncertainties

Uncertainties on travel times are necessary for computing confidence limits on source locations. We estimated uncertainties for the global travel times for a given month and time of day as the spread in the travel times predicted by all the available G2S models from the same month and time of day, essentially a superposition of many sets of travel times like that in Figure 2a. In all we used 556 G2S (6-hour) epochs spanning about eight months. For months in which G2S models were not available, we used the spread over the other eight months at the same time of day. The uncertainties thus reflect errors relating to unmodeled temporal variations and to approximations we made in representing multiple skip paths with a single travel time. In contrast, we assumed the skip-path approximations to be the primary source of error in G2S-based travel times and computed the uncertainties for each epoch as the spread among its predicted multiple skip paths, essentially a single set of travel times similar to that in Figure 2a. Note in Figure 3b that the two estimates are almost the same, indicating that more uncertainty relates to averaging the multiple skip times into a single phase, than to unmodeled temporal variations.



(a) **(b)**

Figure 3. New HWM/MSISE and G2S travel times at station DLIAR, New Mexico.
Travel times predicted for an event on January 23, 2003 20:00 at DLIAR as function of (a) range at back azimuth 200º and (b) back azimuth at range 2000 km. Stratospheric times are yellow, thermospheric times are green, and 1_ confidence limits are red. The stratospheric duct producing "Is" is predicted only within a finite back azimuth range that is roughly downwind. Note the differences between G2S and HWM/MSISE predictions of travel time and range of back azimuths at which stratospheric arrivals are predicted.

Summary of Propagation Models

The five propagation models for which we computed travel times and back azimuth deviations are summarized in Table 1. Global tables were constructed only for the Monthly/TOD (time-of-day) model, although as a consequence of their trivial nature, travel times for the Two-Celerity and Best-Celerity models are time, station and azimuth independent. The event-specific travel times were tabulated only for epochs, ranges, and stations relevant to the data set.

Table 1. Propagation Models Used to Generate Travel Times Sets

Propagation Model	Velocity Model	Sampling			Phases	Propagation Method
		Time	Azimuth	Distance		
Event-Specific	G2S	event times	as needed	as needed	Is, It	Tau9.1 + linear fit
Monthly/TOD	HWM/MSISE	1 per month / 4 per day	1°	1.5°	Is, It	Tau9.1 + linear fit
Seasonal	HWM/MSISE	4 per year	1°	1.5°	I	as in Brown (2000)
Two-celerity	245, 320 m/s	1 for all time	N/A	N/A	Is, It	N/A
Best celerity	282 m/s	1 for all time	N/A	N/A	I	N/A

Evaluation Data Set

We compiled a data set against which to evaluate and compare the predictive capabilities of the propagation models investigated here. The set consists of 21 events, including 32 arrivals, listed in Table 2, for which independent ground truth locations and times are known. The "GT" column indicates uncertainty on the true location. Prior to the evaluation, arrival times and back azimuths were carefully estimated for all 32 detections.

Table 2. Evaluation Data Set

Event	Date	Time	Latitude [°]	Longitude [°]	GT [km]	Detecting Stations
WSMR chemical explosion, New Mexico	11/19/97	18:00:00	33.621	-106.480	1	2
Titan IVB rocket launch, VAFB, California	05/22/99	9:36:00	34.7	-120.6	100	2
Atlas II AS rocket launch, VAFB, California	12/18/99	18:57:00	34.7	-120.6	100	2
Space Shuttle rocket launch, KSC, Florida	10/11/00	23:17:00	28.49	-80.58	100	2
Watusi chemical explosion, NTS, Nevada	09/28/02	21:25:17	37.099	-116.092	1	5
Thiokol plant rocket motor test, Utah	01/23/03	20:00:20	41.626	-112.392	2	3
Chemical explosion, Billy-Berclau, France	03/27/03	5:15:00	50.511	2.881	1	2
Argyle mine explosion, Australia	09/22/96	7:07:29	-16.987	128.357	15	1
WSMR chemical explosion, New Mexico	11/12/97	17:47:00	33.621	-106.450	1	1
Gas pipe explosion, New Mexico	12/12/98	12:55:00	35.4	-108.4	5	1
WSMR chemical explosion, New Mexico	02/25/99	18:20:00	33.679	-106.523	1	1
Hector Mine earthquake, California	10/16/99	9:46:46	34.541	-116.361	100	1
NTS chemical explosion, Nevada	12/08/99	19:29:58	37.012	-116.196	1	1
WSMR chemical explosion, New Mexico	12/09/99	19:00:00	33.681	-106.523	1	1
Gas pipe explosion, New Mexico	08/19/00	11:26:19	32.038	-104.029	1	1
Seattle earthquake, Washington	02/28/01	18:54:34	47.234	-122.521	100	1
Chemical explosion, Toulouse, France	09/21/01	8:17:57	43.62	1.37	20	1
Argyle mine explosion, Australia	04/16/02	9:08:58	-16.751	128.426	10	1
Powder River Basin mine explosion, Wyoming	08/27/02	20:06:53	43.52	-105.27	10	1
Powder River Basin mine explosion, Wyoming	02/12/03	18:59:28	43.75	-105.37	10	1
Powder River Basin mine explosion, Wyoming	03/13/03	19:10:35	43.618	-105.196	10	1

Comparison of Model Predictions

The mean absolute residuals between the predictions of five propagation models in Table 1 and the ground-truth events in Table 2 are listed in Table 3. Locations were computed for the 7 multiply detected events (18 arrivals) using arrival times and observed back azimuths, uncorrected and corrected. The travel-time and back azimuth residuals were averaged over all 32 arrivals. Arrivals were assigned the phase, "It" or "Is", with the best matching travel time for each propagation model that distinguished between them, the Two-Celerity, Monthly/TOD and Event-Specific models. For the Best-Celerity model, arrivals were assigned the Event-Specific phase designations. Travel-time residuals were normalized by the ground-truth travel times to compensate for their distance dependence. Counter to expectation, the Two-Celerity model was the best predictor of locations and travel times, and the most complex Event-Specific model was almost the worst. The expected improvement with model complexity is seen only in back azimuth residuals and locations using corrected back azimuths. However, in any sense, varying the complexity of the propagation model resulted in no more than 20% reduction in the residuals.

Table 3. Mean Absolute Residuals from the Evaluation Data Set

Propagation Model	Location Residuals [km]		Travel-Time Residuals [%]	Back azimuth Residuals [deg]
	Back Azimuth Uncorrected	Back Azimuth Corrected		
Event-Specific (G2S)	170	161	8.9	5.7
Monthly/TOD (HWM/MSISE)	142	139	8.3	5.8
Seasonal (HWM/MSISE)	161	155	9.5	5.7
Two-Celerity (245 / 320 m/s)	129	129	7.7	6.9
Best-Celerity (282 m/s)	178	178	8.1	6.9

Assessment of overall prediction capability is difficult from Table 1 because the four statistics are based on different subsets and kinds of the data. As a result, the significance of the differences between models is unclear. To put all the data on equal footing, to allow all the data to be combined together, and to estimate the significance of differences between model predictions, we constructed the following travel-time and back azimuth statistics:

$$F_t = \frac{\sum_{k=1}^{N}\left(\frac{\Delta t_{ik}}{T_k}\right)^2}{\sum_{k=1}^{N}\left(\frac{\Delta t_{jk}}{T_k}\right)^2} \sim F_{N,N} \qquad F_a = \frac{\sum_{k=1}^{N}\Delta a_{ik}{}^2}{\sum_{k=1}^{N}\Delta a_{jk}{}^2} \sim F_{N,N} \qquad F_{ta} = \frac{\sum_{k=1}^{N}\left\{\left(\frac{\Delta t_{ik}}{T_k}\right)^2 + \Delta a_{ik}{}^2\right\}}{\sum_{k=1}^{N}\left\{\left(\frac{\Delta t_{jk}}{T_k}\right)^2 + \Delta a_{jk}{}^2\right\}} \sim F_{2N,2N}$$

Here, i and j denote any two of the five propagation models, k sums over the N=32 arrivals, Δt_{jk} and Δa_{jk} are the travel-time and back azimuth residuals predicted by the j^{th} model for the k^{th} arrival, and T_k. is the ground-truth travel time for the k^{th} arrival. If the unsquared elements in each denominator and numerator are independently drawn from the same standardized normal distribution then F_t, F_a, and F_{ta} have the indicated F distributions. We can evaluate each statistic, as computed from our limited data sample, against percentage points of F to evaluate the confidence at which one model is indeed a better predictor than another of travel time, back azimuth, or both. To first order we expect Δt_{jk} to linearly increase with distance so that the $\Delta t_{jk}/T_k$ (the fractional along-path errors) should be similarly distributed for a given model j. Also, small Δa_{jk} approximate the fractional cross-path location errors, since, for source-receiver distance d_k, $d_k \sin(a_{jk})/d_k \cong \Delta a_{jk}$. Thus, we expect the Δa_{jk} and $\Delta t_{jk}/T_k$ to be distributed similarly to one another. Table 3 confirms that they have similar size. We assume *a priori* that each population is normally distributed and that the errors in ground truth locations are small compared to those resulting from the propagation model. Confidence limits so obtained will at least have the correct sense and approximately indicate relative ability.

The confidence levels at which one propagation model is a generally better predictor than another of travel times, back azimuths, and both are listed in Table 4. Each cell contains the confidence level at which the row model is a better predictor of the indicated quantity than the column model. Confidence in the converse is given by 100% minus the stated value. The row models are ordered most to least complex and the columns least to most complex, so that for each cell the row model is expected to be a better predictor than the column model, based on that complexity, and, thus to have a value greater than 50%. To highlight results versus expectation, cells are colored green where the expectation is clearly upheld (confidence of 70% or higher), yellow where the result is ambiguous (confidence between 30 and 70%) and red where the expectation is clearly violated (confidence 30% or lower).

Table 4. Confidence Level (%) at which the Row Model is a Better Predictor than the Column Model

Row Model \ Column Model	Best-Celerity 282 m/s	Two-Celerity 245, 320 m/s	Seasonal HWM/MSISE	Monthly/TOD HWM/MSISE
Travel Time				
Event-Specific (G2S)	24	7	42	14
Monthly/TOD (HWM/MSISE)	64	35	81	
Seasonal (HWM/MSISE)	30	10		
Two-Celerity (245, 320 m/s)	77			
Back Azimuth				
Event-Specific (G2S)	70	70	55	56
Monthly/TOD (HWM/MSISE)	65	65	49	
Seasonal (HWM/MSISE)	66	66		
Two-Celerity (245, 320 m/s)	50			
Travel Time + Back Azimuth				
Event-Specific (G2S)	51	38	52	31
Monthly/TOD (HWM/MSISE)	70	58	71	
Seasonal (HWM/MSISE)	49	35		
Two-Celerity (245, 320 m/s)	64			

Table 4 reinforces the indications of Table 3. The new Monthly/TOD propagation is a better overall predictor than the Best-Celerity, Seasonal, and Event-Specific models but at a confidence of only ~70%; it is not much different than the Two-Celerity model. The existing seasonal model of Brown (2000) is the worst. However, most results are not dramatic and some are ambiguous. The most advanced Event-Specific model is consistently the best predictor of back azimuth at confidences up to 70% but is significantly a worse predictor of travel times at confidences as high as 93%. Each time-varying model is better than the static models at estimating back azimuth but only marginally at confidence of 60 to 70%. Some insight into these results can be obtained from examination of the fractional travel-time and azimuth residuals in Figure 4. Residuals are color coded by the phase, “Is” or “It”, assigned to them.

First, it must be noted that the evaluation data set is quite small (32 arrivals) relative to the amount of spatial and temporal variability inherent in infrasound propagation. Thus, the population of arrival data as a whole may not be well represented by this data set and pathological behavior with respect to one or more of the models may be the result. If true, simple, constant celerity propagation models might be expected to perform comparatively well on this data sample but to break down as the sample size increases and becomes more representative of the population. For example, the Event-Specific model predicted travel times very well for a large group of arrivals (the spike of small residuals), but substantially underpredicted another. This could be a fortuitous result of the composition of the data set. However, it may also be result of systematic biases inherent in the propagation models, discussed next.

The most significant approximation we made in computing travel times and back azimuths, was averaging the arrival curves from multiple skip paths into a single curve, as in Figure 2a. It is possible that, in doing so, we have introduced a significant source of error into the thermospheric predictions, by averaging away significant, resolvable detail. This conjecture is supported by features of the travel-time and, to a lesser extent, the back azimuth residuals. First, the inferred “Is” and “It” residuals (blue and red, respectively) have distinctly different distributions for all five models; in each case the “Is” residuals are more compactly and simply distributed. This is consistent with model predictions for significantly more variation among thermospheric than stratospheric travel times and back azimuths of multiple skip paths, as illustrated in Figure 3 – the predicted spread among “It” skip travel times is typically about 10 to 15%, which is about the size of the “It” residuals in Figure 4. In fact, if the “It” residuals are dominated by this source of error, then their uneven distributions are also expected since only a few discrete arrival times are predicted for any source-receiver scenario. The observed biases in the “It” residuals further support this. Since no formal accounting was made for the predicted amplitudes of the skip arrivals, hence their likelihood of being detected, a bias proportional to the spread among the skip travel times is inevitable in fitting as we did. The widely spread “It” yield produce large biases, while the tightly confined “Is” skips yield almost none. This suggests simply replacing the duct-averaged phases we chose to use with skip-specific phases. However, the validity of such a representation hinges on being able to accurately estimate amplitudes of these arrivals to determine the likelihoods of observing them. A particular skip arrival may be predicted but so weakly that it cannot be detected; thus, its inclusion in the travel-time tabulation would add a modeling degree of freedom that does not practically represent the physical system, leading to reduced location residuals but not improved location accuracy.

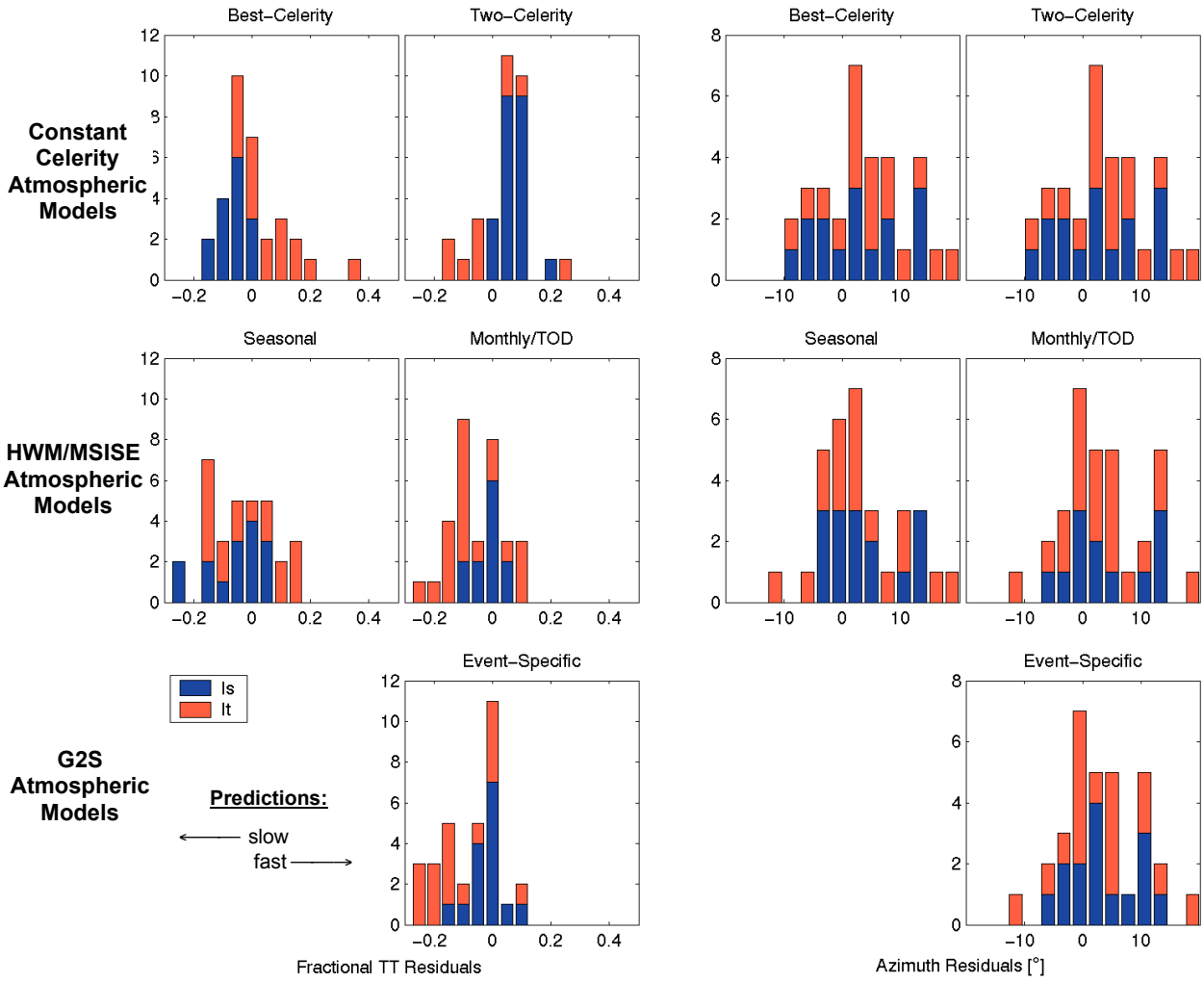


Figure 4. Back azimuth residuals and fractional travel-time residuals.
(a) Fractional travel-time residuals, (ground-truth – observed) / (ground-truth) and (b) back azimuth residuals computed from the propagation models in Table 1. Counterclockwise from the top left, frames in each panel correspond to the following propagation models: the Two-Celerity (245, 320 m/s), the Best-Celerity (282 m/s), the Monthly/TOD, the Event-Specific model, and the Seasonal models. Inferred "Is" and "It" residuals are blue and red, respectively. Predictions that are faster than observed have positive residuals. The distinctly different shapes, spreads and biases of the distributions of "Is" and "It" residuals suggests that significant error may result from averaging multiple skip paths within each propagation duct.

There are other possible sources of the observed residuals. There is some error in the manually determined "ground truth" arrival times and azimuths despite close examination – arrivals from the Thiokol static rocket motor test and the three rocket-launch events have low signal-to-noise, so those picks have lower confidence associated with them. In addition, our ground-truth locations have some uncertainty for events such as the three rocket launches, which are moving sources. Ground-truth errors will be manifest in the residuals from all models but somewhat unpredictably, possibly in a uniform manner introducing an overall residual water level, possibly introducing or even countering model-specific biases. It is also possible that the Tau-P based ray-tracing approach we used make too many approximations to obtain accurate travel times. We have only crudely accounted for along-path velocity variations, and not at all for changes in the direction of the wave front as is possible with other methods.

CONCLUSIONS AND RECOMMENDATIONS

We computed a new set of global infrasound travel-time tables based on a monthly and time-of-day sampling of HWM/MSISE to replace the tables of Brown (2000). The new tables produced more accurate estimates of travel times and back azimuths than the old tables at the 70% confidence level. We compared the predictive capabilities of five atmospheric propagation models of varied complexity on the same set of ground-truth events. The performance of these from best to worst as follows: the new Monthly/TOD model based on HWM/MSISE, the Two-Celerity model of 245 and 320 m/s, the new Event-Specific model based on G2S models, the best fitting constant celerity of 282 m/s, and the Seasonal HWM/MSISE model of Brown (2000). However none is better than any other with confidence of more than 71%. The significance of these results is limited due to the small size of the evaluation data set, particularly with respect to the amount of variability inherent in infrasound propagation. We recommend that more ground truth data be sought and compiled for the purpose of evaluating the predictive abilities of propagation models.

We suspect that a significant amount of the total residual from the new HWM/MSISE and G2S based travel times is the result of approximating of the multiple skip paths within each atmospheric duct by one infrasonic phase, and that this partly obscures the accuracy inherent in the atmospheric velocity models. We recommend investigating location improvement by independently representing travel time and back azimuth corrections for each skip path and studying predicted arrival amplitude to identify the paths with high probability of detection.

We also suspect that approximations in the method we employed for propagating infrasound through a spatially variant atmosphere contributes significantly to the observed residual with respect to ground-truth. We recommend investigation of prediction improvement through the application of more sophisticated propagation methods.

ACKNOWLEDGEMENTS

We thank Doug Drob of the Naval Research Laboratory for generating the G2S atmospheric models used in this work and Milton Garces for comments on an early draft.

REFERENCES

Brown, D.J. (2000), PIDC 7.0 – Station specific, 2-D infrasound travel-time tables, *Center for Monitoring Research*, CCB-PRO-00/19Rev. 1.

Drob, D.P. (2003), Detailed specification of the atmosphere for infrasound propagation modeling, *Proceedings of the 25th Annual Seismic Research Review – Nuclear Explosion Monitoring: Building the Knowledge Base*, LA-UR-03-6029, Vol. II, pp. 605-616.

Garces, M.A., R.A., Hansen, and K.G. Lindquist (1998), Traveltimes for infrasonic waves propagating in a stratified atmosphere, *Geophys. J. Int*., 135, 255-263.

Hedin, A. E, E. L. Fleming, A. H. Manson, F. J. Schmidlin, S. K. Avery, R. R. Clark, S. J. Franke, G. J. Fraser, T. Tsuda, F. Vial, and R. A. Vincent (1996), Empirical wind model for the upper, middle, and lower atmosphere, *J. Atmos. Terr. Phys*., 58, 1421-1447.

Hetzer, C. and M. Garces (2002), Tau 9.1 Users Manual, Infrasound Laboratory, University of Hawaii, Manoa, October 21.

Jones, R. M., J. P. Riley, and T. M. Georges, (1986), HARPA -- A versatile three-dimensional Hamiltonian ray-tracing program for acoustic waves in the atmosphere above irregular terrain*, NOAA Special Report*, 410.

Picone, J.M., A.E. Hedin, D.P. Drob, and A.C. Aikin, (2002) NRLMSISE-00 Empirical model of the atmosphere statistical comparisons and scientific issues, *J. Geophys. Res*., 107, no. 1468, doi:10.1029/2002JA009430.

DISCRIMINATION OF EARTHQUAKES AND MINING BLASTS USING INFRASOUND

Douglas O. ReVelle, Rodney W. Whitaker, J. Paul Mutschlecner, and Marie D. Renwald

Los Alamos National Laboratory

Sponsored by National Nuclear Security Administration
Office of Nonproliferation Research and Engineering
Office of Defense Nuclear Nonproliferation

Contract No. W-7405-ENG-36

ABSTRACT

Infrasonic signals from 31 large earthquakes have been observed by arrays of microphones operated by the Los Alamos National Laboratory (LANL) over the period of 1983 to 2003. Signal amplitudes, corrected for propagation and distance, have been used to determine a relationship with seismic magnitude. The variance in the relationship can be understood primarily in terms of the uncertainties in the ground motion, deduced from an independent data set, and the middle atmospheric winds, which strongly influence signal propagation. Signal durations can extend over many minutes, and a relationship was also found between signal duration and magnitude. To understand this relation, we have proposed a model in which regions distant from the epicenter are excited by seismic surface waves. The surface motion of these regions in turn, produce signals that precede or follow signals from the epicenter. Standard signal processing analysis failed to detect signals from 56 earthquakes during the observation period. The predicted signal-to-noise ratios (SNR) for these earthquakes generally indicated that signals would have been too weak to be detected.

During the past year we have also systematically and independently investigated infrasonic detection of small earthquakes and mining blasts in the Western USA, and have found that small mining blasts were routinely easier to detect. Part of the reason for this relative efficiency of mining-blast detection is that earthquakes must shake the earth's surface to create a significant amplitude infrasonic signal, and yet earthquakes can deposit most of their energy at great depths below the surface. In addition, there are at least three earthquake-faulting mechanisms and only for the up-down type is significant infrasonic emission expected. Lastly, not all earthquakes have infrasonic waves emanating from their epicenter. These facts not withstanding, we have still managed to detect 13 earthquakes from some 90 events that were examined, In the case of small mining blasts, we detected 13 of 40 events that were searched. All events generally had local seismic magnitudes between 3 and 4. In all detections, we have found a repetition of source locations either from the same sets of mines (for example, Morenci in Arizona and Wyoming's Powder River Basin) or the same sets of geologically active regions, i.e., the southern California/Baja region, etc.

The goal of this latter research is to be able to reliably distinguish between earthquakes and small mining blasts using discriminants established through either infrasound signals alone or in conjunction with seismic data. We have already suggested several possible discriminants, and are presently in the process of evaluating them along with continuing to search our database for additional infrasonic detections of earthquake and mining blasts. The earthquake and mining-blast discriminants currently being examined include: 1) the amplitude of infrasound as corrected for range and stratospheric wind effects, but not for winds in the case of thermospheric arrivals, 2) FFT (Fast Fourier Transform) power spectral analysis differences, 3) seismic R_g phases for separating earthquake signals from mining blasts, i.e., as a fundamental depth discriminant concept and finally, 4) the separation of signals by types of arriving infrasonic returns (phases) as a function of their source type.

OBJECTIVE

We will present the results of our analyses of earthquake generated infrasound and mining explosions. We start with a summary of results for the larger events in order to gain confidence in our analysis techniques and subsequently focus attention on only ***regional*** detections of small earthquakes and mining blasts (with local seismic magnitudes generally < 4 at ranges < 1500 km). The goal in this work is to establish reliable discriminants for distinguishing earthquakes from mining blasts over ***regional*** propagation distances.

RESEARCH ACCOMPLISHED

We analyzed large-event observations from 1983 through 2003, but emphasized the period through 1992. At LANL we have a very long history of processing and analysis of such earthquake infrasound records (Mutschlecner *et al*, 1985; Mutschlecner and Whitaker, 1994; Mutschlecner *et al*, 1999). A total of 31 earthquakes were detected through 2003 of which 13 were detected by two or more infrasound arrays, for a total of 47 recorded signals. All, but nine of the earthquakes were in California. Station to event distances ranged from 165 kilometers to 4100 kilometers. All magnitudes were obtained from the National Earthquake Information Center and placed on a common M_L scale by the use of transformations given by Utsu (2003) with additional information given in the review by Lay and Wallace (1995).

The data from the larger earthquakes were recorded at arrays operated by LANL. These data included infrasonic detections at Los Alamos, New Mexico at both the small baseline research arrays as well as at DLIAR (DOE LANL Prototype array), and at two other small baseline arrays, namely at St. George, Utah and Mercury, Nevada (NTS). We have searched for detections of small earthquakes and mining blasts only at the LANL, DLIAR array so far in this work that is a research in progress. The LANL research arrays have four very low frequency microphones spaced at distances of about 100 m from a central point and cover an overall distance of about 300 m. The microphones are Globe 100C or Chaparral Physics Model II. Wind noise reducers consisting of porous hoses are attached to each microphone in a radial pattern with a diameter of about 30 m. Two of the earthquakes were also observed at the DLIAR prototype array at Los Alamos with an overall diameter of 1.2 km. Data were sampled 20 times/sec except for the prototype array for which the rate was 10 times/sec. The Chaparral microphone frequency band pass is ~0.1-10 Hz, while the corresponding band pass for DLIAR is 0.1-4 Hz.

Data were processed by using a Fourier-domain correlation beam-former that employs frequency-slowness plane variables. For the smaller events, Matseis software was used for the routine data processing (available from Sandia National Laboratories [SNL], Albuquerque). For the larger events, the standard Matseis data-analysis software with enhancements from the work of Young and Hoyle (1975) were also included. Time windows were generally 20 sec with 50 % overlap. The most frequent noise sources were local winds or microbaroms (sea-storm generated infrasound), which typically have a peak power near 0.2 Hz. The frequency pass band used for most analysis was 0.5 to 3.0 Hz to reduce the effects of the microbaroms and local wind noise while still including most of the earthquake signal. In a few cases this band pass was altered to give a greater SNR. The larger events generally had semi-automatic detections within the Matseis software whereas the smaller events were almost always detected manually by varying either the data-window size or the degree of overlap or by varying the allowed band-passed frequency range, etc.

The results of the processing are: average pair-wise channel cross-correlations, azimuth of the correlated energy, trace velocity, frequency of the peak power determined from a power spectrum, and power. An example of the processing is given in Figure 1 for the earthquake of 2 February 2002 that occurred in the Southern California/Baja California region.

Peak-to-peak amplitudes were determined as averages over major correlated signal features and averaged over all microphone channels. Amplitudes were converted from microphone output voltage to pressure in microbars (1 μb = 0.1 Pascal) using calibrations determined for each microphone at reasonably frequent intervals and have an estimated accuracy of 15% (Mutschlecner and Whitaker, 1997).

The observed amplitudes, $A_{O,}$ have been normalized for the effects of distance and stratospheric wind effects by the use of the relation:

$$A_n = A_o 10^{-kv_d} \left(\frac{R}{R_s}\right)^S \quad (1)$$

where A_n is the normalized amplitude, R is the great-circle distance to the epicenter, R_S is an arbitrary standard distance, and v_d is the stratospheric wind component directed from source to array. S and k are empirically curve-fitted parameters. Mutschlecner et al. (1999) discuss the background for this normalization process and determinations of S and k. Based upon analysis of signals from numerous atmospheric nuclear explosions and large high-explosive tests, we have adopted S = 1.45, k = 0.018 s/m and R_S = 1000 km which is approximately the average of the distances for the larger earthquakes.

Stratospheric wind data are needed to normalize the signals as indicated in (1). These data were taken from National Climate Data Center records of high altitude winds observed by rocketsonde flights. Rocketsonde stations included Point Mugu, California; White Sands, New Mexico; Wallops Island, Virginia; and Cape Canaveral, Florida. We employed data from all stations that were available and close to the required date, but we emphasized data from Point Mugu and White Sands for the California earthquakes. Zonal and meridional components of the wind were averaged from the records for altitudes between 45 and 55 km. This procedure is in agreement with the protocol used for the Stratospheric Circulation Index described by Webb (1969), and closely represents the region of the stratosphere involved in the return of signals to earth where the wind velocity is critical. Because wind data for a specific earthquake date were usually not available, data were interpolated for the zonal and meridional components from nearby dates. If no at all wind were available, values were taken from statistical models as given in Mutschlecner et al. *(*1999).

In addition to the infrasound detections described here, signals from 56 earthquakes were searched for but not found; 32 of these earthquakes were located in California. In 14 instances two or more arrays were employed for a total of 71 non-detections (NDs). For several of the NDs the causes are rather obvious: either all epicenters are at very large distances or there was very high wind noise or both possibilities occurred.

Additional earthquake studies performed during the past year include the following:

i) The normalized relationship between infrasonic amplitude and seismic magnitude was developed.
ii) The relationship between the peak vertical ground motion near the source and the seismic magnitude was developed.
iii) The most important parameters producing the large variance found for the relationship between the normalized infrasonic amplitude and the seismic magnitude were identified using Monte Carlo statistical simulations.
iv) The relationship between the total infrasonic signal duration and the seismic magnitude was developed.
v) The relationship between the limiting infrasonic observation distance from the earthquake epicenter and the seismic magnitude was developed.
vi) The minimum, near-field, peak ground acceleration necessary for infrasound detection from earthquakes was developed.
vii) Reasons for the non-detections of an additional 56 earthquakes within the database were examined.
viii) Two new infrasonic signal-processing detectors to be used in Matseis/Infra_tool were developed with SNL.

In addition to the study described above that has only been partially presented here, an additional independent study of small earthquakes and small mining blasts was also undertaken. The latter study is still a work in progress, but will be described briefly. Data for the location and times of small earthquakes and mining blasts in the western United States from 2000-2002 were assembled with the help of Dr. B. Stump (Southern Methodist University, Dallas, Texas) and from a United States Geological Survey (USGS) website. Over 300 earthquakes and over 425 mining blasts were assembled as a list for a subsequent infrasonic search for coherent signals with the requisite great circle back azimuth, signal velocity and amplitude to be designated as a single station detection. For mining blasts we demanded a much closer back azimuth between observations and processed data than we did for the small earthquakes. Because other researchers have shown that the epicenter need not be the source of the strongest

infrasonic waves, we chose to use a weaker azimuth constraint on the deduced infrasound back azimuth from earthquakes (Le Pichon et al, 2003).

The new study emphasized ***regional*** scale detection of small earthquakes and mining blasts whereas the earlier study emphasized regional and teleseismic detection of much larger earthquakes. In order to proceed with the domain of very small sources we wanted to establish a set of reasonable search criteria. Thus our new emphasis was to use the larger earthquakes as a guide for the successful detection of smaller events. The approach used in our semi-automatic "nominal" data processing analysis for small vents was as follows:

i) A minimum cross-correlation threshold for three or more consecutive data windows was set
ii) A specific limit of allowable array trace speed was established
iii) A specific limit of allowable observed signal velocities was established
iv) A maximum allowable deviation from the great circle back azimuth was set. This value was much smaller for mining blasts than for earthquakes
v) Observed microbarom back azimuths in the time region of interest were determined in order to be confident that the observed signals were not microbarom related "bursts" (Less than 10 % of the final detections were deleted because of this constraint).
vi) Comparisons between the Matseis/Infra_tool back azimuth and the f-k (frequency-wavenumber) slowness plane approach were made in order to confirm the detections made in Infra_tool. In addition, examination of Matseis spectrograms often allowed confirmation of the infrasonic detections at least as long as the time period of the signal was no too "noisy".

After a semi-automatic detection was established for the searched events, either the data window size or the upper and lower band-pass frequency limits were systematically varied in order to refine the search. This approach however took substantial amounts of time and needs to be further automated.

So far in our data processing search we have examined ~ 100 earthquakes and ~50 mining blasts using only a single array (DLIAR). The full details of this continuing search will be reported on at a later date. The distributions of the number of events versus local seismic magnitude and the number of events versus source-observer range for both earthquakes and mining blasts (from an earlier search encompassing only ~90 earthquakes with local seismic magnitudes between 3 and 5.8, and ~40 mining blasts with local seismic magnitudes between 3 and 3.6) is shown in Figure 2a and 2b. Of these 90 earthquakes, only 13 infrasonic detections were made with a high degree of certainty, whereas for the mining blasts a total of 13 high quality detections were made from a search of only 40 events in a similar local seismic magnitude range. A geographic summary of these infrasonic detections is given in Figure 3 where it is noted that for both source types, a repetition of source locations is clearly evident. In Figure 3, we have plotted the locations of both types of sources in the Western USA (for events during 2000 to 2002) including the locations of both detections and non-detections at DLIAR. A detailed, albeit brief summary of detections of small earthquakes and small mining lasts is also listed in the Tables 1 and 2.

Part of the reason for our success in detecting small mining blasts relative to earthquakes is a result of the source ground-coupling factor, and also the fact that the mining-blast source is very near ground level. Only earthquakes that have vertical ground motion are expected to generate significant infrasonic signals. In addition however, earthquake sources can also be at great depths. Since the generation of infrasound is fundamentally related to the up-down ground motion sustained near the source, deeper earthquakes are generally not expected to generate significant infrasound. For our study all earthquakes were shallow sources in a geophysical sense because all earthquakes events that we studied were within 25 km of the surface. The deepest source that was detected using infrasound so far was 13.8 km; the shallowest source was right at the earth's surface.

We also examined our detections in terms of establishing possible discriminants between small mining blast and earthquakes. We are currently examining earlier predictions of normalized infrasonic amplitude versus local seismic magnitudes that were developed for larger sources at generally longer ranges to determine if we can establish a

similar regression curve for use in the small source-size range. Additional discriminants currently being investigated include the following:

i) Amplitude of infrasound as corrected for range and stratospheric wind effects, but not for winds in the case of thermospheric arrivals.

ii) FFT (Fast Fourier Transform) power spectral analysis differences between the two source types.

iii) Seismic R_g phases for separating earthquake signals from mining blasts over short-range shallow propagation paths, i.e., as a fundamental depth discriminant concept.

iv) The separation of signals by the types of arriving infrasonic returns (phases) as a function of their source type.

Finally, we have also examined sources of error and additional uncertainties in our observed and analyzed source and infrasonic detection and propagation parameters. These results will also be presented at a later date.

CONCLUSIONS AND RECOMMENDATIONS

We have examined a fairly wide range of earthquake and mining-blast magnitudes and distances. For large earthquakes, we determined that a relationship exits between the normalized infrasonic amplitude and local seismic magnitude. Within our new search for the infrasonic detection of much smaller sources that is currently under examination, we wish to determine if this relationship is still applicable. In any event, if a similar regression line can be established for such small sources over regional detection distances, a possible discriminant can be developed for separating mining-blast shots from earthquakes. This discrimination tool will be a very important development since a very large number of both types of sources occur annually worldwide.

ACKNOWLEDGEMENTS

We are grateful to Masha Davidson, Susan Noll and the late Susan Bunker for their careful work in the processing of the data.

REFERENCES

Lay, T. and T. C. Wallace (1995), *Modern Global Seismology,* Academic Press, San Diego, 379-383.

Le Pichon, A., M. Aupetit, E. Blanc, Y. Cansi, J. Guilbert, S. Lambotte. and J. Plantet (2003), Six-years review of infrasound monitoring at the French NDC, Invited Abstract U32C-01, AGU Annual Fall Meeting.

Mutschlecner, J. P. and R. W. Whitaker (1994), Infrasonic observations of the Northridge, California earthquake, *6th Int. Symp. on Long-Range Sound Propagation*, 498-513.

Mutschlecner, J. P. and R. W. Whitaker (1997), The design and operation of infrasound microphones, Los Alamos Nat. Lab. Tech Rep. LA-13257, UC-706.

Mutschlecner, J. P., R. W. Whitaker, S. S. Bunker, and C. A. Painter (1985) , Infrasonic observation of the Coalinga and Bishop earthquakes, *abstract, J. Acous. Soc. of Am.* April, 8-12.

Mutschlecner, J. P., R. W. Whitaker, and L. H. Auer, (1999), An empirical study of infrasound propagation, Los Alamos Nat. Lab. Tech Rep. LA-13620-MS.

Utsu, T.(2003), Relation between magnitude scales, in *International Handbook of Earthquake Engineering Seismology*, (William H. K. Lee, Hiroo Kanamori, Paul C. Jennings, and Carl Kisslinger, Editors,), Academic Press, Amsterdam, 733-746,

Young, J. M. and W. A. Hoyle (1975), Computer programs for multidimensional spectra array processing, NOAA Tech. Rep., ERL 345-WPL43.

Webb, W. L., (1966), *Structure of the Stratosphere and Mesosphere*, Academic Press, New York, NY, 141-145

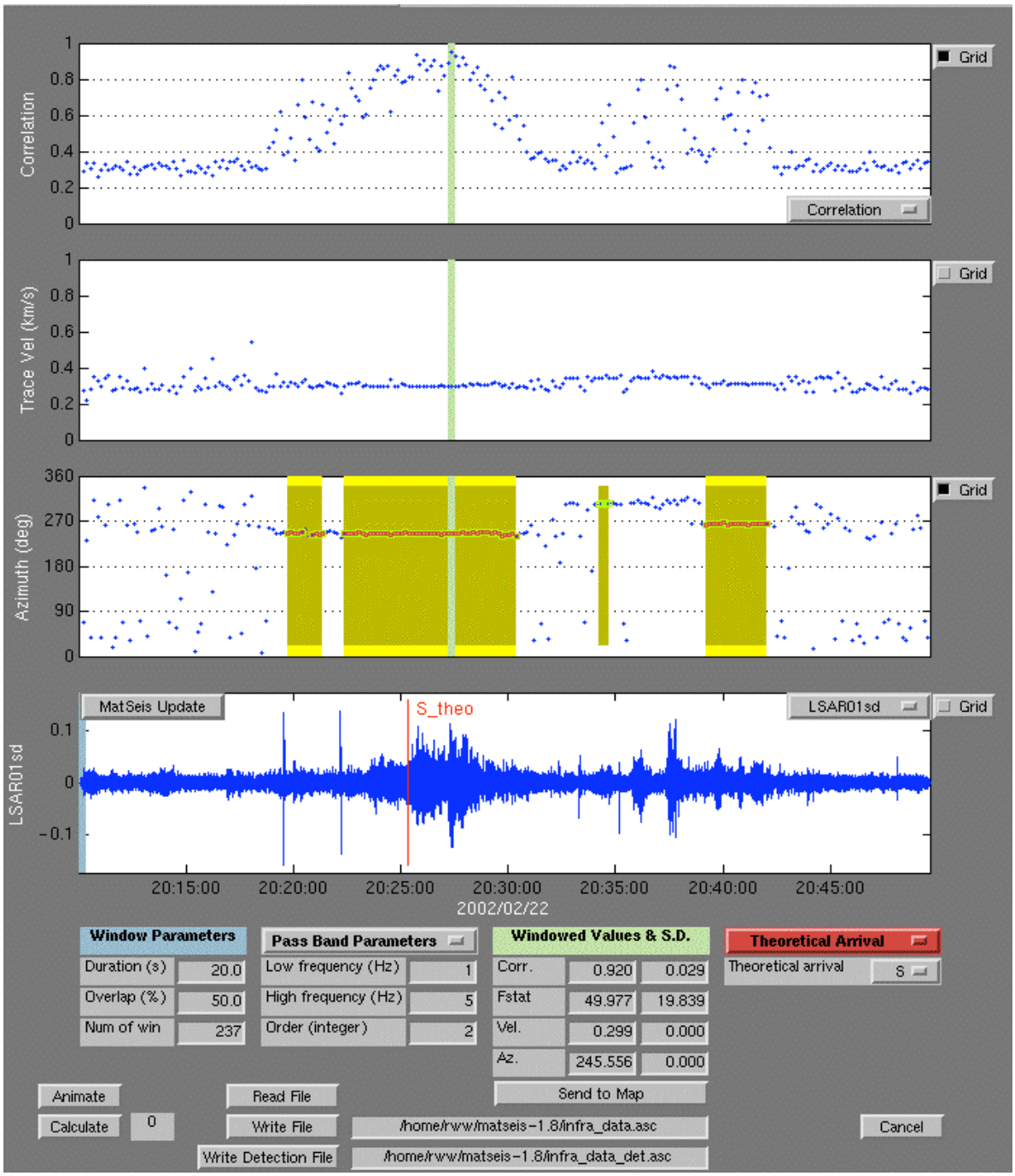


Figure 1: Matseis signal processing and analysis: Infrasonic earthquake detection of 2/22/2002- Averaged pair-wise cross-correlation, trace velocity, back azimuth and a single channel time series.

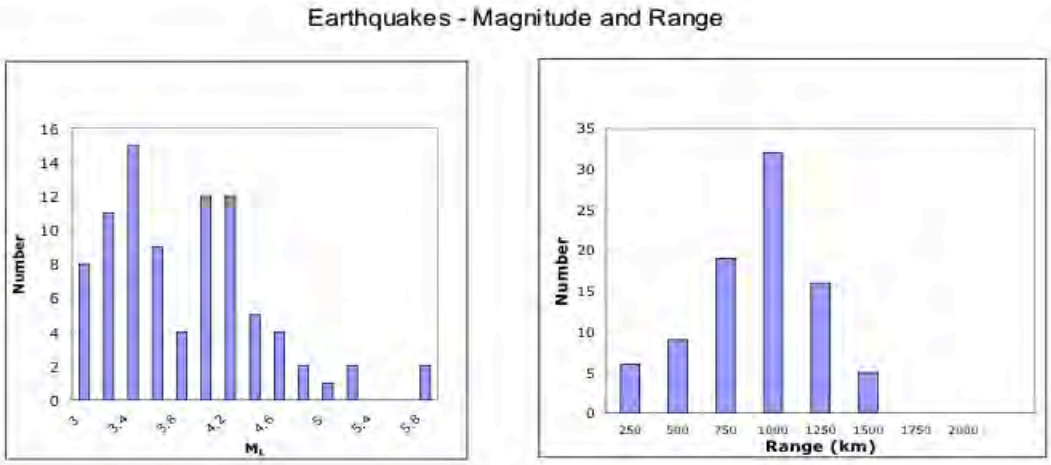


Figure 2a: Number of earthquakes versus local seismic magnitude and versus source-observer range.

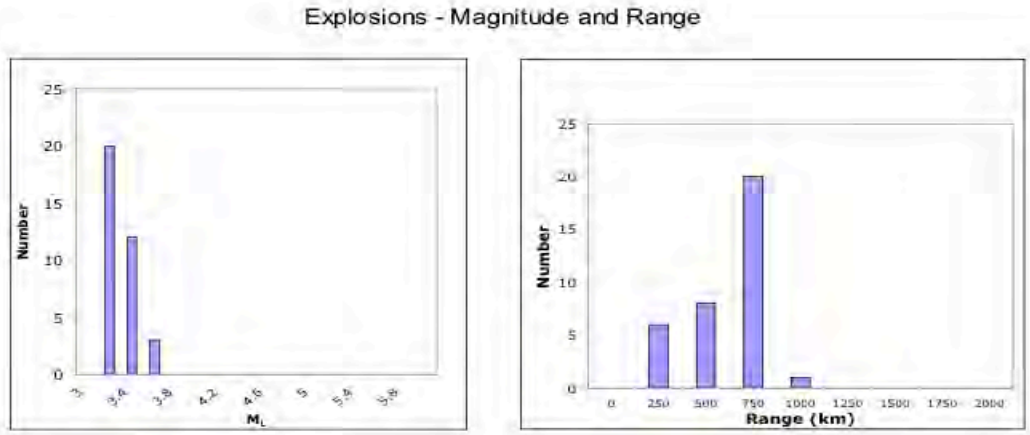


Figure 2a: Number of earthquakes versus local seismic magnitude and versus source-observer range.

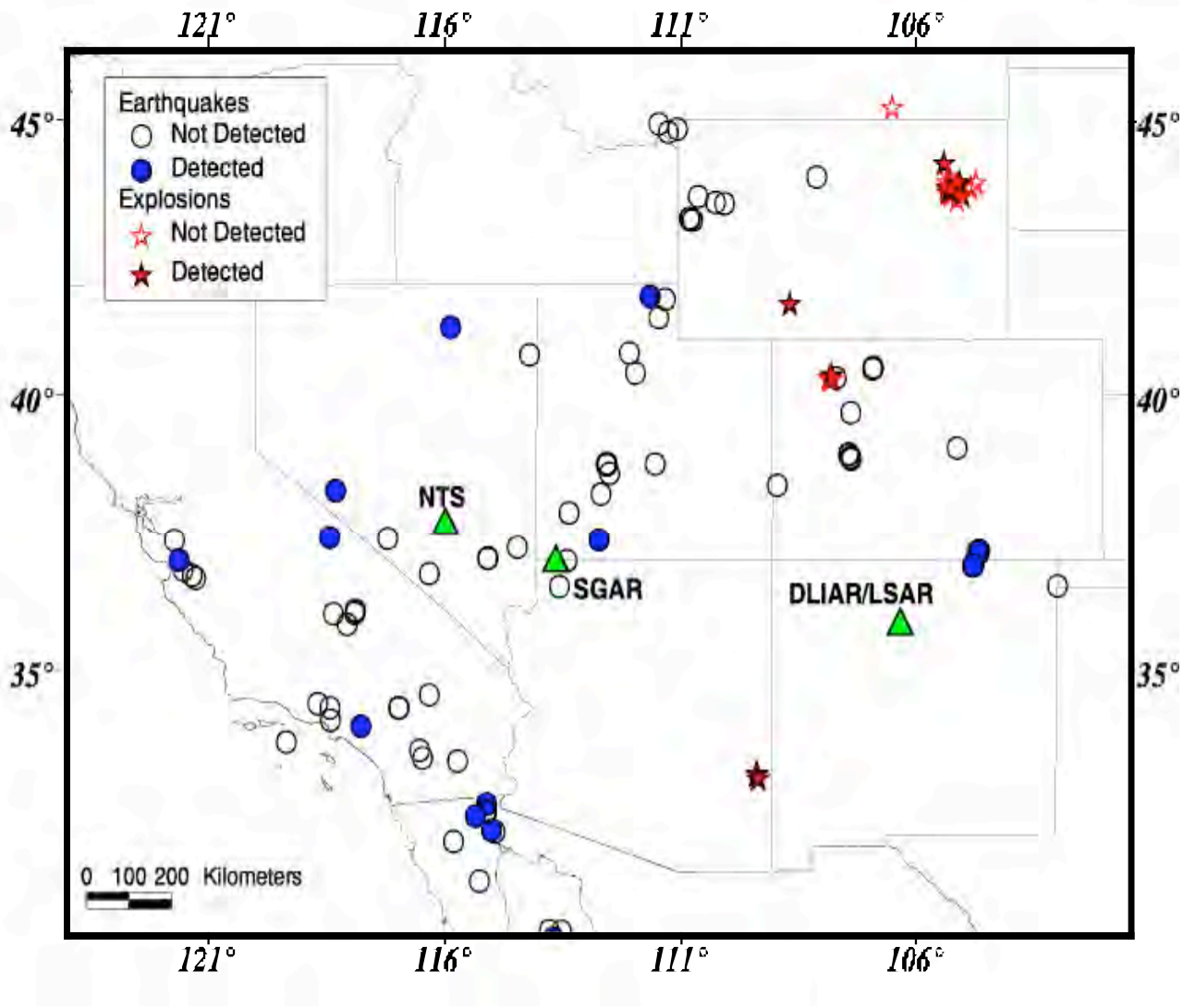


Figure 3: Geographic summary of infrasonic detections of small earthquakes and mining blasts.

Table 1: Infrasonic earthquake detections at DLIAR

Earth-quake	Date	Location	Time: UT	Magnitude and Depth	Range km	Azimuth ●	Raw ampl. Pa	Signal velocity: km/s
# 133	2/17/01	CA-NV	22:54	4.1,12.4km	1092.6	280.4	0.037	0.17
# 177	9/04/01	CO	12:45	4.0, 5 km	206.9	47.2	0.030	0.29
# 192	10/08/01	NV	05:37	4.6, 0 km	1018.4	302.7	0.010	0.22
# 206	12/09/01	W. AZ - Sonora	01:42	4.5, 10 km	901.8	239.7	0.031	0.26
# 209	12/14/01	S. CA	12:01	4, 13.8 km	1061.4	255.2	0.012	0.25
# 217	1/04/02	CA-Baja	19:38	3.1, 7 km	885.4	242.9	0.100	0.26
# 225	1/08/02	UT	17:26	3.2,8.2 km	592.1	281.1	0.050	0.22
# 239	2/22/02	CA-Baja	19:32	5.5, 7 km	916.3	242.0	0.087	0.29
# 242	3/19/02	Gulf CA	22:14	4.1, 10 km	935.3	225.0	0.113	0.28
# 264	5/11/02	UT	06:30	3.0, 9.2 km	800.5	323.4	0.128	0.24
# 265	5/14/02	Cntl CA	05:00	4.9, 7.7 km	1370.0	270.5	0.052	0.14
# 273	6/18/02	NM	09:12	3.5, 5.0 km	179.2	51.5	0.032	0.07 (●)
# 278	7/15/02	CA-NV	20:18	4.1, 13 km	1089.7	275.3	0.050 0.075	0.16, 0.34

(*): This event is still under study because the earthquake fault type is strike-slip and since the resulting signal velocity arrival is so low. This type of earthquake faulting mechanism is not expected to produce significant infrasonic amplitude at either local or great ranges (personal communication, T. Wallace, 2004).

Table 2: Infrasonic Mining Blasts at DLIAR

Mining blast	Date	Time: UT	Magnitude	Range: km	Azimuth: °	Amplitude: Pa	Signal velocity: km/s
Gillette, WY	21901	18:59	3.3	880.5	6.5	0.037	0.16
Newcastle, WY	22601	21:09	3.5	871.0	7.9	0.035	0.28
Craig, CO	22801	23:06	3.3	510.7	344.8	0.032	0.27
Safford, AZ	32201	19:19	3.2	417.2	221.2	0.05 0.05	0.30 0.15
Gillette, WY	32701	21:17	3.1	880.5	6.5	0.13	0.35
Gillette, WY	40101	20:10	3.1	880.5	6.5	0.13	0.32
Craig, CO	40401	22:02	3.1	510.7	344.8	0.025	0.27
Gillette, WY	42001a	19:02	3.4	880.5	6.5	0.25 1.875	0.28 0.13
Rock Springs, WY	42001b	20:58	3.1	674.9	341.9	1.50	0.19
Gillette, WY	42501a	20:04	3.2	880.5	6.5	0.25	0.31
Safford, AZ	42501b	22:13	3.4	417.2	221.5	0.017	0.28
Safford, AZ	43001	18:50	3.1	417.2	221.5	0.35 0.045	0.25 0.17
Gillette, WY	51201	20:02	3.3	880.5	6.5	0.25	0.14

RESOLVING INFRASOUND SIGNAL BACK AZIMUTHS WITH ARRAYS OF OPTICAL FIBER SENSORS

Kristoffer Walker, Stephen Arrowsmith, Jonathan Berger, Michael Hedlin, and Mark Zumberge

University of California, San Diego

Sponsored by Army Space and Missile Defense Command

Contract No. DTRA01-00-C-0085

ABSTRACT

Optical Fiber Infrasound Sensors (OFIS) are long compliant tubes wrapped with two optical fibers that interferometrically measure the differential pressure variation along the length of the tube. Because each sensor averages spatially along the path of the tube, the frequency response of the recorded pressure variation is a function of the orientation of the OFIS sensor relative to the back azimuth and incidence angle of the incoming wave. We have exploited this property to investigate the ability of various OFIS array geometries to determine the back azimuth of infrasound signals. We have found that an array comprised of two orthogonal 89-m-long OFIS having their centers separated by 63 m can resolve the back azimuth of most arrivals having good signal-to-noise ratio. We find a good match between the back azimuths determined from our technique and those determined from the same signals recorded on the co-located pipe array I57US using the Progressive Multichannel Cross-Correlation technique. Based on our results, we are proposing to build an OFIS array that will be able to resolve signals from all directions and with smaller signal-to-noise ratios.

OBJECTIVES

Optical Fiber Infrasound Sensors (OFIS) are a unique way to detect acoustic signals, in particular, signals in the infrasound band (below 20 Hz), which propagate approximately in the horizontal plane. We defer a detailed instrument description to Zumberge et al. (2003). In general, a 1310-nm laser illuminates a single-mode fiber, which is split into two (Figure 1). A lock-in amplifier is then used to generate a $\pi/2$ phase lag in one of the fibers while modulating the length difference by a small fraction of a wavelength at several hundred kHz with a piezoelectric crystal (PZT Modulator). The two fibers are then helically wrapped around a sealed, compliant tube, one with twice as many wraps as the other. At the end, the two fibers are recombined and yield an interference pattern that is recorded by a photo detector. For an ambient pressure variation, the tube expands and/or contracts, changing the difference in the optical-fiber path length each laser must travel. This difference is measured by the number of fringes counted in the interference pattern, and related to pressure by an empirically determined calibration factor of 2.52 Pa m rad^{-1}.

An OFIS has several advantages over other infrasound sensors such as pipe and hose arrays. It is relatively inexpensive to build, deploy, and maintain. It is also easy to deploy, and requires much less space, making it highly portable. There is also evidence that in low-wind conditions, the noise floor of the OFIS is lower than the pipe and hose arrays for frequencies down to 1 Hz. However, pipe and hose arrays are more intuitive, and have led to the development of various techniques for determining the signal characteristics (back azimuth and incidence angle), characteristics that are important for determining the source and location of infrasound signals. Finally, the OFIS appears to be highly responsive to high frequencies (up to at least 100 Hz), which makes it ideal for detecting signals in both the infrasound and low-frequency audible sound band.

The objectives of this research are to (1) determine the number and configuration of OFIS that is necessary to resolve the back azimuth of infrasound signals, (2) develop a generic technique for estimating back azimuths using an *n*-OFIS array, and (3) test the technique by comparing back azimuths estimated from synthetic signals and real signals recorded at Piñon Flat Observatory (PFO, I57US) in the southern California high desert.

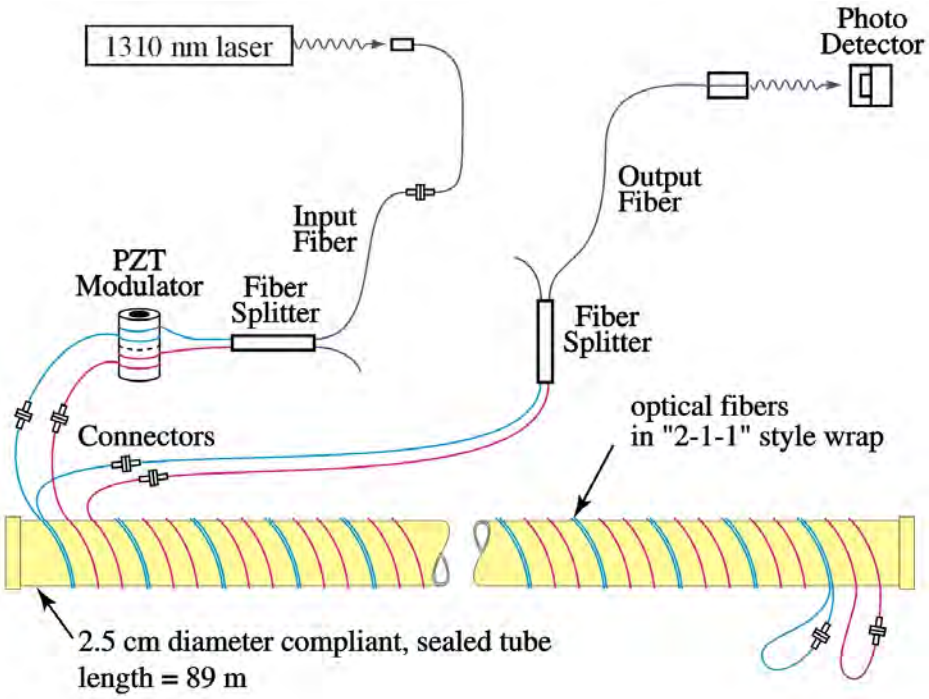


Figure 1. Schematic of the Optical Fiber Infrasound Sensor (OFIS) design that is being implemented at PFO (I57US).

RESEARCH ACCOMPLISHED

Sensor Directivity

The response, *R*, of an OFIS relative to a point detector is a function of the orientation of the signal propagation with respect to the length of the OFIS:

$$R = \left| \mathrm{sinc}\left(\frac{L\pi f}{V_a}\cos(\theta)\right) \right| \quad (1)$$

where f is frequency, L is the length of the OFIS, V_a is the sound speed at the Earth's surface, and θ is the angle between the incident ray path and the OFIS

$$\theta = \cos^{-1}(\cos(\theta_b)\sin(\theta_i)) \quad (2)$$

where θ_b is the back azimuth, and θ_i is the incidence angle. For typical infrasound signals, θ_i is approximately 90° (horizontal), and $\theta = \theta_b$. Figure 2a shows a polar plot of *R* as a function of angle from the long axis of the OFIS for three typical infrasound signal frequencies.

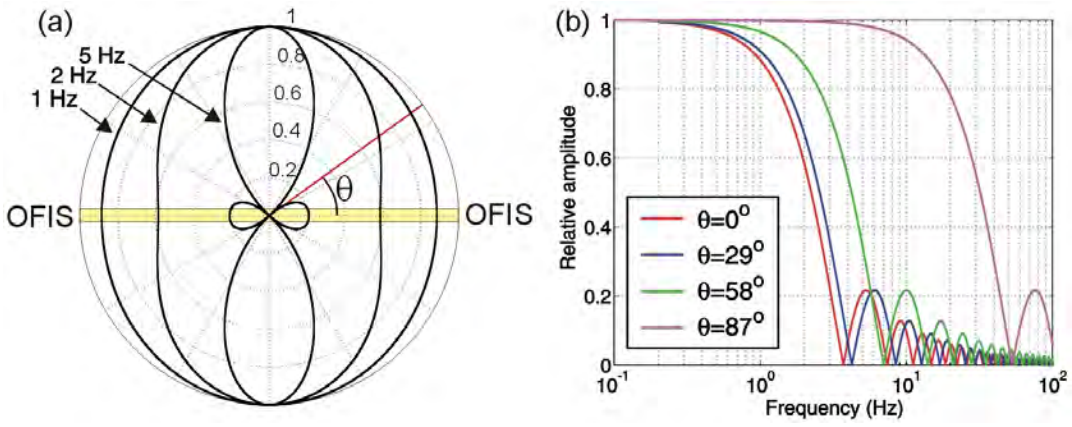


Figure 2. Frequency response *R* for an 89-m long OFIS as a function of frequency and angle θ (equations. 1-2).

The response *R* varies remarkably as a function of frequency (Figure 2b). Therefore, if the back azimuth for a signal with a significant bandwidth is known, one can deconvolve *R* from the recorded signal S_r to determine the actual signal waveform $S_w = S_r / R$.

Two-OFIS Array

We exploit the dependence of the frequency response on the back azimuth (θ_b) and test the capabilities of a two-OFIS array in resolving θ_b for synthetic and real infrasound signals recorded at PFO.

Algorithm

The recorded OFIS signal $S_r = f(S_w, \theta, L)$, where only S_w and θ are the unknowns. One can therefore estimate S_w and θ if one records the signal on two OFIS with different orientations (Figure 3)

$$S_{r1} = f(S_w, \theta_1, L) \quad (3)$$

$$S_{r2} = f(S_w, \theta_2, L)$$

where θ_1 and θ_2 are related by the array configuration. We do this by substitution, i.e., using S_{r1} to predict $S_w{}^p$, and then $S_{r2}{}^p$

$$S_{r2}{}^p = S_w{}^p R_2 = S_{r1} R_2 / R_1 \tag{4}$$

We make the assumption that the incidence angle θ_i=90°, and perform a grid search over trial θ_b (between 0-90° from the OFIS1 azimuth in 1° increments) to minimize the L2 misfit between S_{r2} and $S_{r2}{}^p$. We currently perform the deconvolution in the frequency domain by using the water-level technique to avoid numerical instability, i.e., we raise all near-zero amplitudes in the denominator frequency spectrum to a "water level" of 1% of the maximum amplitude (e.g., Langston, 1979). We also calculate formal 2σ error bars using the technique of Silver and Chan (1991), which assumes the misfit function is the sum of squares of a random chi-squared noise process.

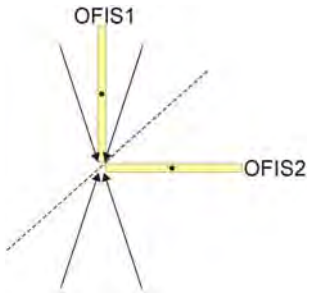


Figure 3. Layout of the two-OFIS array with centers separated by 63 m.

Because an OFIS integrates the change in pressure, a scalar field, along the length of the tube, one cannot determine the quadrant from which a signal originates (Figure 3). Any angle from OFIS1 is part of a complementary set of four angles from which an incoming signal has identically recorded shapes on both OFIS. To get around this ambiguity, we exploit the fact that the two OFIS are separated by 63 m, and perform a cross-correlation during each trial θ_b to find the optimum time separation between S_{r2} and $S_{r2}{}^p$ before calculating the misfit. Then for the optimum θ_b, we check the corresponding *dt*, which determines from which of the four angles it originated assuming θ_i=45-90°. The resulting misfit function contains misfits from the optimally time-shifted S_{r2} and $S_{r2}{}^p$. Some improvement would come from incorporating the predicted *dt* from each trial θ_b to time shift the signals before the misfit is calculated. This should only require a slight increase in the computation time required for the calculation since the number of Fourier transforms does not change, but it may increase the ratio between the maximum and minimum misfit for most signals.

The angle halfway between both OFIS is an angle for which the recorded signals on both OFIS should be identical (Figure 3). We term this special angle the angle of ambiguity because one cannot resolve between it, its 180° complement, or a signal with a low incidence angle.

This two-OFIS technique is completely generic, and could be applied to an *n*-OFIS array. However, such an approach requires the deconvolution of *n* functions with holes in the amplitude spectra. If water-level deconvolution is performed, it invariably introduces noise into the resulting waveforms, the magnitude of this noise depending on the recorded signal bandwidths. We believe the above technique could be made more stable by using all recorded OFIS signals to estimate the predicted waveform signal for each trial θ_b and θ_i, then predict the recorded signals for each OFIS

$$S_{rk}{}^p = S_w{}^p R_k = \frac{\sum_i^n S_{ri}}{\sum_j^n R_j} R_k \tag{5}$$

where $S_{rk}{}^{p}$ is the predicted recorded signal for the kth OFIS and *n* is the number of OFIS in the array. The larger *n* is, the greater the chance of resolving the properties of signals with a low signal-to-noise ratio.

Testing the Two-OFIS Algorithm on Synthetic Data

We generated synthetic data based on the infrasound signal from a Vandenberg Delta II rocket launch (8 September 2001), which was recorded by an OFIS oriented perpendicular to the signal back azimuth (θ_b) at PFO. We use equations 3a-b to calculate what would be recorded by the OFIS sensors for θ_b =290° and θ_i =90°, time shift the signals appropriately, add white noise, frequency filter the signals between 0.2-5 Hz, and apply the grid-search technique described above to these waveforms. Figure 4 shows the result of this experiment for noise levels ranging linearly between 0.01-100% as determined on S_{r1}. The misfit as a function of trial θ_b is shown at the top, and the waveforms for S_{r2} (recorded) and $S_{r2}{}^{p}$ (optimum) are shown below.

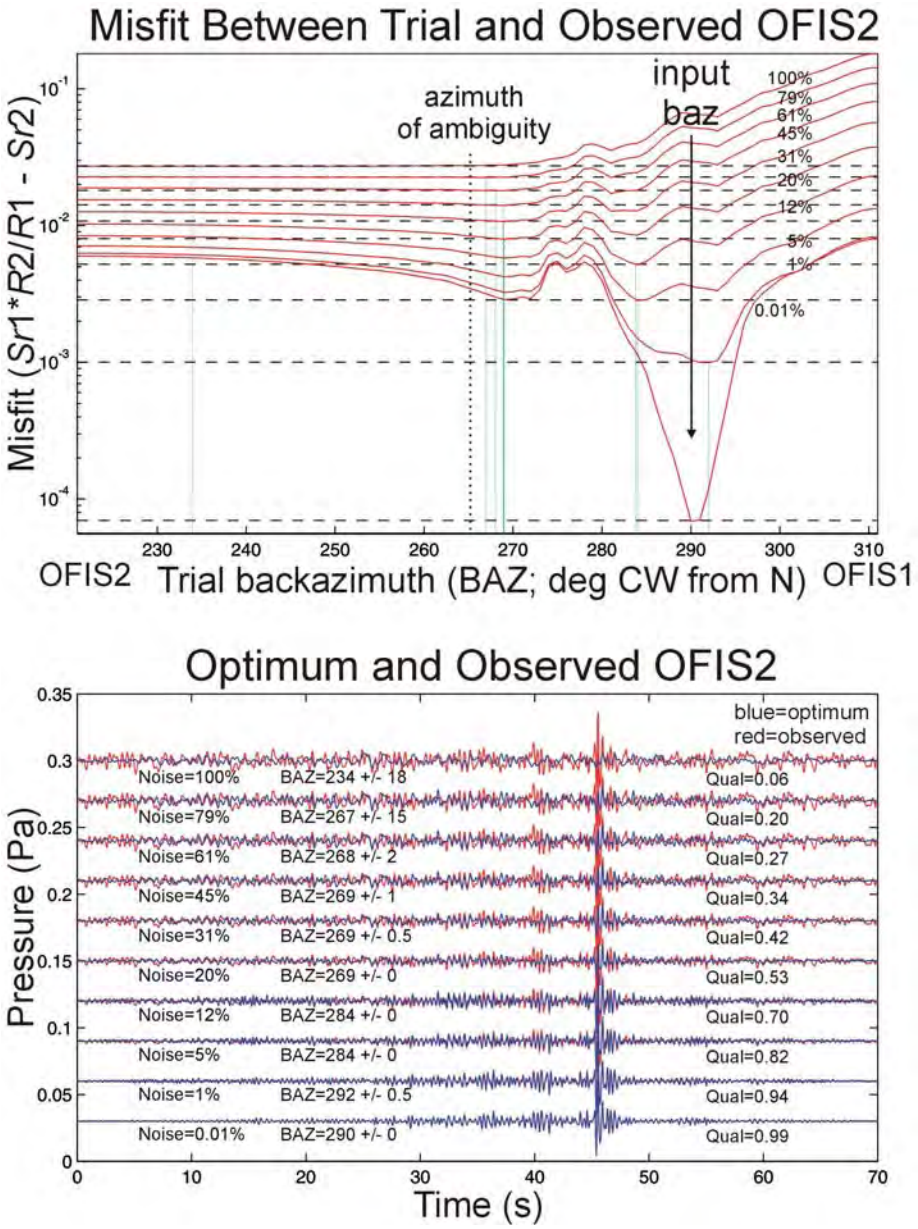


Figure 4. Testing technique with synthetic data for an assumed 290° back azimuth (BAZ).

We find that the algorithm approximately identifies the input θ_b for noise levels up to ~10%, which leads to correlation coefficients (qual) between S_{r2} and $S_{r2}{}^{p}$ of 0.75-1.0. As the noise level increases, the global minimum (indicated by green vertical lines) moves progressively toward the azimuth of ambiguity, and then toward the azimuth of OFIS2. This behavior is not surprising. As the noise increases, the signal-to-noise ratio (SNR) on S_{r1} decreases much faster than that on S_{r2} (see Figure 2b). At trial θ_b near the azimuth of OFIS1, the noise is being amplified because R_1 is only flat for low frequencies (equation. 4), which results in a very noisy $S_w{}^{p}$ and $S_{r2}{}^{p}$. As trial θ_b goes to the azimuth of OFIS2, the predicted $S_w{}^{p}$ gets smaller in amplitude because R_1 gets flatter. The subsequent convolution with R_2 yields a much lower amplitude $S_{r2}{}^{p}$. So the misfit-curve trend at high noise levels simply represents the decrease in $S_{r2}{}^{p}$ RMS amplitude, and has nothing to do with the coherence between S_{r2} and $S_{r2}{}^{p}$. The toward-OFIS2 global-minimum trend represents the gradual loss of signal resolution and reversion to this state. The same basic conclusion is reached for different signal bandwidths and deconvolution water-level parameters.

We also find that our formal error bars are too optimistic, and do not accurately account for the deviation between the optimum and actual θ_b. With a multi-element OFIS array however, one could perform a bootstrap procedure to determine the error bars, although this would make the technique much more computationally intensive. Error bars could also be crudely estimated by performing the technique along a running window across the signal, and measuring the standard deviation of all the θ_b estimates at the end (this is what the PMCC code does).

The most important conclusion of the synthetic tests is that the algorithm should work for real signals (see next section) with good SNR. We also tested this method by performing a 2-D grid search over θ_b and θ_i, and found that one can also determine θ_i for θ_i = 45-90° if θ_b is a significant distance from the azimuth of ambiguity (the distance depending on the SNR). But we focus on the assumption that θ_i = 90° because most infrasound signals of interest obey this assumption and the 1-D grid search is computationally less intensive by about two orders of magnitude.

Testing the Algorithm on Real Data

We also tested the method on 93 real infrasound signals of good signal-to-noise ratio recorded on a two-OFIS array during the first quarter of 2004 at PFO. To determine if the estimated OFIS θ_b are accurate and to distinguish between horizontally traveling and near-vertically traveling infrasound signals, using the Progressive Multichannel Cross-Correlation algorithm (Cansi, 1995), we also analyzed the same signals that were recorded by the co-located IMS pipe-array consisting of four 18-m and four 70-m diameter rosettes spread over a 1,400 m region (Hedlin et al., 2003).

Figure 5 compares θ_b calculated from both methods, and shows the residual deviation after the error bars are used to explain as much of the misfit as possible. We find that for most of the signals, there is a very good correlation (Figure 5b). For the other signals, there is a significant deviation of up to 30° and greater than 30° for θ_b =105-125°, 215-225°, and 280-330°. These OFIS estimates deviate from the PMCC estimates in the counterclockwise direction. It may be significant that the first and last problem region are ~180° apart, and the deviation of the OFIS θ_b is toward OFIS2, suggesting noise may be the responsible for the deviation (see Figure 4). If this is the case, the middle problem region, which is only 10° wide, originates from a different source.

We used several methods to determine the orientation of each OFIS to within 0.3°. We also performed an analysis on the pipe-array orientation by using PMCC to analyze the signals of 16 known regional mine-blast events from θ_b = 280-340°, and found that the theoretical θ_b matched those from PMCC within 10°. Ignoring the possibility that there are θ_b (and θ_i) outside 280-340° for which PMCC does not yield reliable estimates, it tentatively appears that the above technique has a difficult time resolving the correct θ_b in those problem regions.

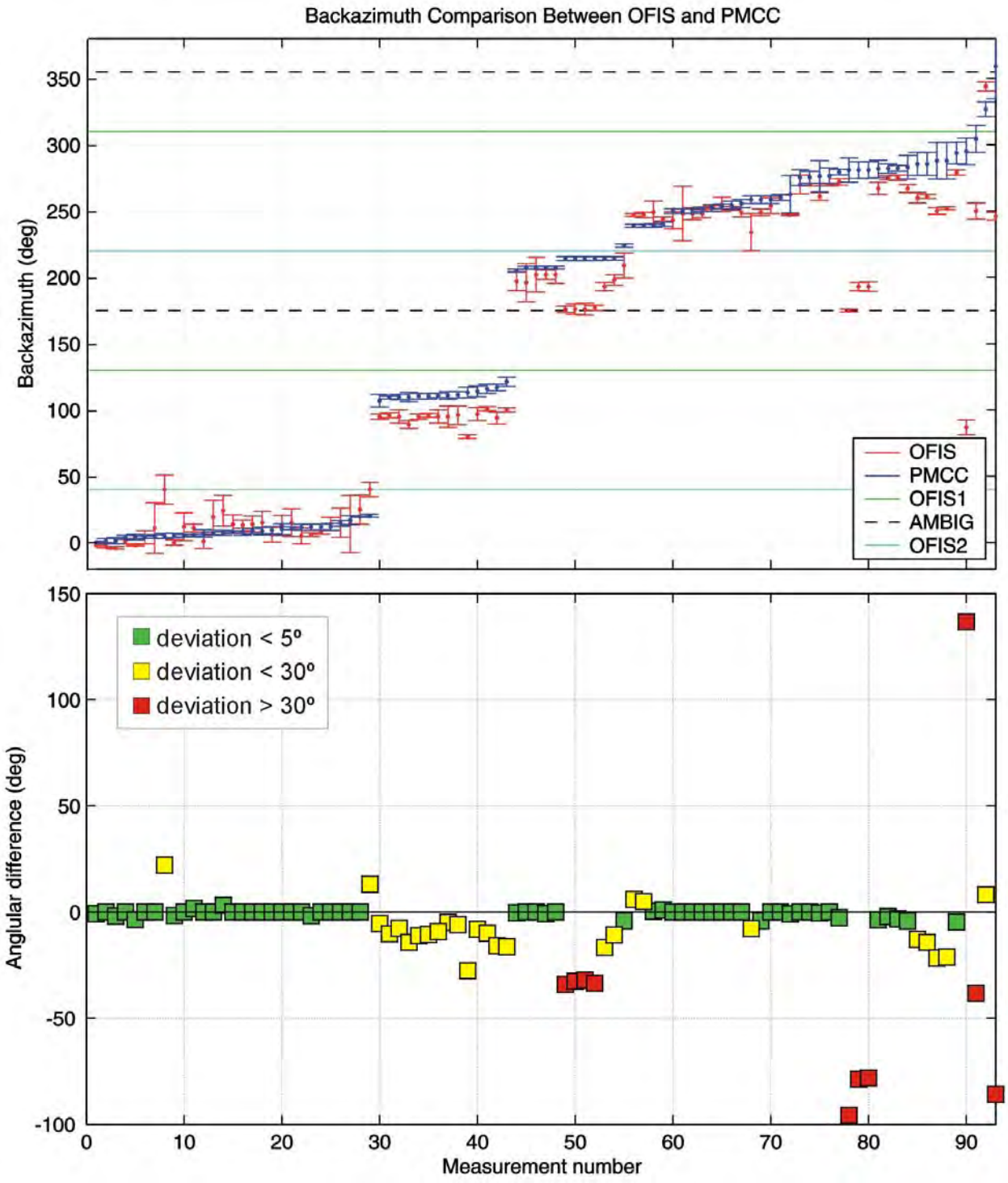


Figure 5. Comparison of back azimuths calculated from signals recorded on a two-OFIS array using the technique described in this paper and a more traditional pipe array using the PMCC code.

CONCLUSIONS AND RECOMMENDATIONS

Synthetic and recorded infrasound signals at PFO (I57US) suggest that a two-OFIS array with centers separated by 63 m is generally capable of resolving the back azimuth of signals that have a good signal-to-noise ratio with the generic technique we present above (Figures 4 and 5). Based on these encouraging results, we suggest that the above technique, when combined with a few enhancements and applied to a multi-element OFIS array, should be capable of resolving the properties of signals with various signal-to-noise ratios from all possible orientations. Specifically, we are proposing to design a six-arm OFIS array oriented in a radial pattern with each OFIS separated by an angle of 60° (although a three-arm OFIS array is enough to alleviate the problems associated with the azimuth of ambiguity, the six-arm OFIS would provide redundancy, which is important when analyzing signals of low signal-to-noise ratio). Enhancements to the generic technique we present above include: (1) using the predicted *dt* during the grid search rather than at the end, (2) using all OFIS signals for a trial θ_b and θ_i to directly calculate S_w, which avoids numerical instability (see equation. 5), and/or (3) using a better deconvolution technique in lieu of the water-level method.

These results are significant because they indicate that an OFIS array, acting as a directional antenna, is capable of providing the same directional information as an array of conventional rosette filters while covering much less space. Conventional arrays rely on time delays between elements to determine θ_b and θ_i, requiring significant separation between elements (hundreds of meters) to produce time differences. The OFIS reliance on directional frequency response should provide the same information within a more localized area -- a significant advantage when space is at a premium (e.g., on island sites).

ACKNOWLEDGEMENTS

We are indebted to Matt Dzieciuch for his time and effort in developing the software used to record the OFIS infrasound signals at PFO.

REFERENCES

Cansi, Y. (1995), An automatic seismic event processing for detection and location: the P.M.C.C. method, *Geophys. Res. Lett*., 22, 1021.

Hedlin, M.A.H., B. Alcoverro, and G. D'Spain (2003), Evaluation of rosette infrasonic noise-reducing spatial filters, *J. Acoustic. Soc. Am.*, 114, 1807.

Langston, C.A. (1979), Structure under Mount Rainer, Washington, inferred from teleseismic body waves, *J. Geophys. Res.*, 84, 4749.

Silver, P.G., and W.W. Chan (1991), Shear-wave splitting and subcontinental mantle deformation, *J. Geophys. Res.*, 96, 16,429.

Zumberge, M.A., J. Berger, M.A.H. Hedlin, E. Husmann, and S. Nooner (2003), An optical fiber infrasound sensor: A new lower limit on atmospheric pressure noise between 1 and 10 Hz, *J. Acoust. Soc. Am.*, 113, 2474.

Data Processing and Analysis

ADVANCES IN APPLYING DATA WAREHOUSES TO SEISMIC CALIBRATION RESEARCH

Julio C. Aguilar-Chang, Richard J. Stead, and Michael L. Begnaud

Los Alamos National Laboratory

Sponsored by National Nuclear Security Administration
Office of Nonproliferation Research and Engineering
Office of Defense Nuclear Nonproliferation

Contract No. W-7405-ENG-36

ABSTRACT

The Ground-based Nuclear Explosion Monitoring Research & Engineering (GNEM R&E) program has made recent advances in applying data warehouses to seismic calibration research. Some of the most challenging tasks of maintaining functional data warehouses are the development of software to automate the continuous population of the database, the quality control needed to resolve data conflicts, the synchronization of database tables between unclassified and classified warehouses, and the integration of all data sources into a cohesive database for delivery to the Knowledge Base.

Calibration efforts by Los Alamos National Laboratory (LANL) researchers require working with three separate data warehouses: unclassified at LANL, classified at LANL, and classified at the Air Force Technical Applications Center (AFTAC). It is therefore necessary to maintain three data warehouses that are physically unable to communicate with each other. Unclassified data are common to all the data warehouses, and some classified data are common only between the two classified warehouses. While it is relatively simple to add new data to all warehouses, it is difficult to capture changes made in one and then propagate them to the other two. We have recently developed a procedure based on database triggers to capture these changes. These triggers capture all update, insert, and delete operations against a predefined set of tables. Periodically, the information captured by these triggers is moved to the other environments and executed, thus keeping the warehouses synchronized.

One important challenge in using these large data warehouses is the simple and efficient access to the vast holdings in them. Web-based tools are important assets that address this problem. We have developed new web-based tools that enable researchers to do tasks such as track the progress of seismic analysis, access information about stations, handle logistical tasks (i.e., assignment of unique identifiers, and tracking the description and resolution of data problems identified through quality controls), and fast access to database metadata (e.g., schema descriptions).

Advances in easy access to metadata are supporting many of the higher-level efforts in quality control, automation, and web access. The first of these is the documentation of the seismic calibration schema using a database schema. This schema is designed to represent all of the detailed table and field information that, up until recently, has been available only in text-based documents. Such information in database form has immediate application to a wide variety of efforts involving the database, including those mentioned above, as well as future applications (see presentation at this meeting by Ballard, *et al*., on the subject of DBTools). Another advance in using metadata, with a more narrow application, has been the creation of bulletin descriptive tables. These tables describe the sources of bulletin data that have been imported into the data warehouse, as well as providing a means to track individual data elements to the corresponding lines of text in the original document.

As data become more voluminous and complex, quality control (QC) has become an increasingly visible and difficult issue regarding the Knowledge Base. Improvements in QC procedures are helping researchers and data managers to more readily identify complex quality problems. The outcome is improved research products resulting from improved data upon which those products are based. The improvements GNEM R&E has made in this area have even had modest impact outside the program; for example, in helping the International Seismological Centre (ISC) identify some problems with their data products. As we understand the QC problem in more detail, we have begun to automate the process of applying QC to large datasets.

OBJECTIVE

The Ground-based Nuclear Explosion Monitoring Research & Engineering (GNEM R&E) program has made recent advances in applying data warehouses to seismic calibration research. Some of the most challenging tasks of maintaining functional data warehouses are the development of software to easily access the contents of the data warehouse, the quality control needed to resolve data conflicts, the synchronization of database tables between unclassified and classified warehouses, and the integration of all data sources into a cohesive database for delivery to the Knowledge Base. This paper is a brief introduction to the wide range of data management technical issues that we face everyday, the progress we have made so far, and the future work needed to fully address all aspects of managing and handling vast amounts of data in a data warehouse that is used in explosion monitoring research.

RESEARCH ACCOMPLISHED

Database synchronization - capturing data changes

Calibration efforts by Los Alamos National Laboratory (LANL) researchers require working with three separate data warehouses: unclassified at LANL, classified at LANL, and classified at the Air Force Technical Applications Center (AFTAC). It is therefore necessary to maintain three data warehouses that are physically unable to communicate with each other. Unclassified data are common to all the data warehouses, and some classified data are common only between the two classified warehouses. While it is relatively simple to add new data to all warehouses, it is difficult to capture changes made in one and then propagate them to the other two.
We have recently developed a procedure based on database triggers to capture certain changes made to registered database tables. This procedure has been implemented at the beta-testing level and is currently being used in our production database. Results to-date have been satisfactory.

The changes currently being monitored on a pre-defined set of tables are data inserts, updates, and deletes. This process is referred to as Capture Data Changes (CDC). The acronym, as well as the fundamental idea, is similar to Oracle's Change Data Capture method of implementing the incremental recording of data changes. The main difference between Oracle's implementation and ours is that our method does not depend on a particular version of the Oracle Relational Database Management System (RDBMS). Oracle's CDC method is directly tied to a specific application that must be installed, configured, and run against an Oracle 9i database. Our procedure is entirely based on database triggers that are available on any version of the Oracle RDBMS, thus our implementation is not tied to any particular version of the Oracle database.

The concept is simple. A database table called SYNC_TABLES is created with the list of tables to be monitored. This table contains the schema the table belongs to and the table name. A pre-defined set of SQL scripts is run once at the beginning of the set-up process to create several objects. The first set of objects are the insert/update and the delete triggers on the monitored tables defined in the table SYNC_TABLES. These triggers capture unique information about a row being inserted, deleted, or updated. Another SQL script reads from the SYNC_TABLES table to create tables called CDC_*tablename*_DELETES. These tables record unique information about the rows that are being deleted from the corresponding monitored source table. For example, the unique information needed to identify which row has been deleted from an ORIGIN table is different than that needed to identify a row being deleted from an ARRIVAL table. We are not saving the entire row being deleted, but rather only its unique information is stored in the database, which will later be used during the synchronization operation to identify the row to be deleted from the database being updated. The space savings are significant with our implementation. As an example, the average row length in the CDC_ARRIVAL_DELETES table is 24 bytes, while the average length of an entire deleted row from a typical ARRIVAL table is 110 bytes.

A table called CDC_UPSERTS is also created only once during the set-up process. This table contains basic information such as the schema name, the table name, and the *rowid* for each row that has been either inserted or updated in the monitored table. The *rowid* is a built-in Oracle identifier that uniquely identifies a row in a table. With this information we know exactly which rows have changed over the monitoring time period, allowing us to recreate and apply those changes to the target tables being synchronized.

It is important to note that both types of tables, the CDC_UPSERTS and CDC_*tablename*_DELETES, also capture the modification date and the name of the database user who made the modification to the monitored tables. This

information, together with the standard database auditing capabilities that can be enabled at the table level, can serve a second purpose of providing a security audit trail to be able to answer questions regarding changes made to critical production data.

The synchronization operation between the unclassified (source) database and the classified (target) databases is a manual process at this time. The synchronization operation starts after a pre-determined number of changes have occurred in the source database tables. The source tables are put in read-only mode for a brief period of time, usually around 15 to 30 minutes. A group of tables called CDC_*tablename*_UPSERTS are created during this time period. The term **upsert** is commonly used among Oracle users to refer to **up**date and in**sert** operations together. These are the tables that contain the actual table structure and changed rows of data from the source tables that will be used to replace the out-dated data in the target database. The CDC_*tablename*_UPSERTS and CDC_*tablename*_ DELETES tables are moved from the unclassified system to the classified environment and used to synchronize the databases. At this point in time, the CDC_UPSERTS and CDC_*tablename*_ DELETES tables in the source database are truncated (i.e. their contents deleted) so that they can be reused, and the CDC_*tablename*_UPSERTS tables are dropped from the source database in order to reclaim valuable disk space.

The final step of the synchronization process is done in the classified environment, where the target database resides. There are only two steps involved here: first we delete rows from the target tables, and then we insert rows into the target tables. Information about the rows to be deleted comes from the CDC_*tablename*_ DELETES and CDC_*tablename*_UPSERTS tables. The CDC_*tablename*_ DELETES contains unique information about the rows that were deleted from the source tables, thus the same rows need to be deleted from the target tables. The CDC_*tablename*_UPSERTS tables contain the rows that have been inserted as new rows, or rows whose data have been updated. In either case, the procedure is to delete the rows from the target tables containing out-dated data, and then inserting the entire contents of the CDC_*tablename*_UPSERTS into the target tables. In this step, the decision was made to replace the entire row of data where an update occurred, rather than try to make a column-by-column comparison to update only a specific column. The latter choice is costlier in terms of computer resources.
The steps defined above to synchronize the unclassified and classified databases at LANL are repeated to synchronize the LANL classified database and the classified LANL research database at AFTAC.

Web access to data

One important challenge in using these large data warehouses is the simple and efficient access to the vast holdings in them. Web-based tools are important assets that address this problem. We have developed a web interface that allows researchers to do tasks such as track the progress of seismic analysis, access information about stations, handle logistical tasks (i.e., assignment of unique identifiers, and tracking the description and resolution of data problems identified through quality controls), and fast access to database metadata (e.g., schema descriptions).

The new web interface being used in LANL's GNEM R&E program has been in operations only a few months, but it has already proven to be an extremely efficient tool that researchers and computer technicians involved in the management of our vast data holdings are using more each day.

This web interface is used to manage two types of information: static and dynamic information. Both the static and dynamic pages can be accessed by anyone authorized to do so from anywhere inside or outside of LANL through the use of an internet connection and a LANL-issued crypto card. All pages are protected through password and the HTTPS protocol.

Static information consists of reference documents that rarely change. Examples of such documents are: database schema descriptions, coordination schedules for upcoming Knowledge Base (KB) deliveries, and general database usage instructions. These documents are generally presented in PDF format in order to eliminate operating system platform dependencies.
Dynamic information is generated by generally issuing queries to our data warehouse to retrieve the most up-to-date information. Below is a brief summary of the different types of data that can be accessed by our researchers.

Database Operational-Health System (DOHS
The primary purpose of this application is to give database users an easy and flexible way to report problems found in the data. This application is a recent implementation and will most likely become the back bone of the data

warehouse quality control procedures being developed in our program. Users reporting a problem have the choice to enter both a short and a free-format detailed description of the problem. Information such as the date the problem was reported and who reported the problem is automatically generated by the application. LANL GNEM R&E personnel involved in data management are alerted of new problems, and, as problems are resolved, the status of the reported issue is changed to reflect the current status of resolution. The information shown in the web page is stored in and retrieved as needed from custom database tables. Storing this information in tables in the data warehouse has many advantages. We use the daily backup routines employed to backup research data to save this information. The optimization features implemented in the database that allow fast access to these data are also employed.

Lastid table

This application was designed to help researchers coordinate updating the CSS3.0 database table LASTID, which keeps track of the maximum value assigned to a unique column identifier (such as *evid, orid, arid, magid*, etc.). The LASTID table is a critical table in the data warehouse, since unique column identifiers in tables such as CSS3.0-style EVENT, ORIGIN, ARRIVAL, and others, are required for every record that are used in our daily research activities. This application allows two or more researchers generating new data to see quickly the maximum identifier value for a particular column, but more importantly the application shows them if the identifier that they are interested in is currently being updated by another user, thus avoiding the common and extremely damaging problem of producing duplicate identifiers for the same table. This application is a critical tool in the quality control effort currently underway in LANL's GNEM R&E research data warehouse.

Picking status

Through this application researchers have instant access to view the current status of phase picking at LANL. At any one time, there can be several researchers and computer technicians making phase picks on different stations and creating arrival information for given events. Researchers who need the phase arrival information use this application to see the status of the stations and events of interest, and also view general comments and warnings noted while making the phase picks. This information is of high value to researchers involved in location and event identification efforts, to name a few. Two of many examples of highly valuable information available on this page are: "Station X very low S/N" – valuable information to know when making amplitude measurements for event identification; and "Station Y timing error, phase appears 4 mins before predicted" – valuable data for event relocation purposes. These comments are presented to the researcher in a clear and easy to read format, and each comment is tied to a specific event, thus giving the researcher the information needed to manually access the data warehouse and mine the necessary information to look at the problem first-hand.

Station location information

A quick interface was created to allow users to search for station location information easily. Users can enter a station or reference station into the query page and receive full CSS3.0 site information (i.e., latitude/longitude, elevation, ondate/offdate, dnorth/deast) about that station or station that belongs to the entered reference station (e.g. array elements).

Schema information

This page was designed to show all of the detailed table and column information that, up until recently, has been available only in text-based documents. This information has been compiled in custom database tables and is updated when necessary, thus giving the user dynamic access to the most up-to-date information about table design and column definition (Fig. 1). This tool eliminates the need for a researcher to keep bulky paper copies of potentially out-dated material. The specific use of this application is detailed below, in the **Metadata** section.

Metadata

A major new effort in making database metadata available is the documentation of the seismic calibration schema using a database schema. This schema is designed to represent all of the detailed table and field information that, up until recently, has been available only in text-based documents. These documents include various versions of the NNSA Knowledge Base (KB) core schema, NNSA KB custom schema, and the United States National Data Center (USNDC) schema documents. The portions that are most needed as readily available metadata are also the portions most amenable to adaptation into database tables themselves: the table descriptions and the column description. The schema designed for this purpose is still preliminary at the time of this writing. It includes four tables. The first is also the simplest, the table description table, TABDESCRIPT (see Table 1).

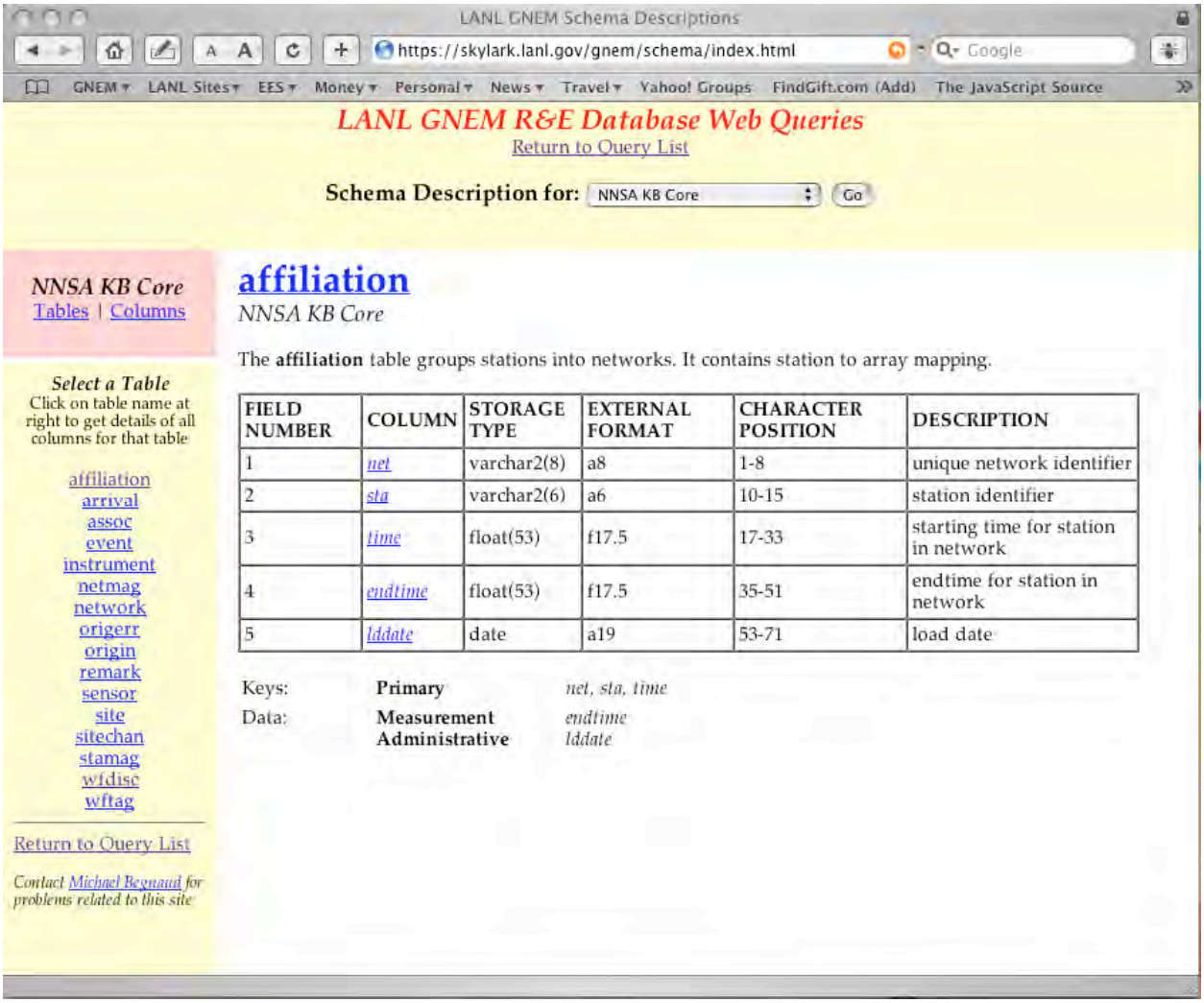


Figure 1. View of web tool view of the NNSA KB Core table AFFILIATION. Users may navigate between table or column view for a particular schema.

Table 1. TABDESCRIPT

field number	column	storage type	description
1	table_name	varchar2(30)	name of table
2	descript	varchar2(1024)	full text description of table
3	schema	varchar2(30)	name of schema
4	auth	varchar2(15)	author
5	lddate	date	date of entry

TABDESCRIPT provides a basic description of the table, identifies that table with a particular documented schema, and provides a reference in the database to connect the fields that may be associated with the table.

The second table is the COLDESCRIPT table (see Table2). This table is where most of the practical information is stored, and thus it is a somewhat more complicated table.

Table 2. COLDESCRIPT

field number	column	storage type	description
1	column_name	varchar2(30)	name of column
2	internal_format	varchar2(30)	format within relational database (same as storage type above)
3	external_format	varchar2(30)	format for programmatic reads and writes
4	external_width	number(8)	width of external text format in characters
5	na_value	varchar2(80)	value to use when field is not set
6	units	varchar2(80)	physical units, if any
7	range	varchar2(80)	full text description of range
8	rangetype	varchar2(30)	range type (numeric, defined, finite set, reference set, any integer, any float, any string, etc.)
9	nmin	number(53)	minimum for numeric rangetypes, if any
10	nminop	varchar2(2)	operator corresponding to nmin
11	nmax	number(53)	maximum for numeric rangetypes, if any
12	nmaxop	varchar2(2)	operator corresponding to nmax
13	reftab	varchar2(30)	reference table name for rangetype='reference set'
14	short_descript	varchar2(80)	one-line brief description of column
15	long_descript	varchar2(1024)	full text description of column
16	schema	varchar2(30)	name of schema
17	auth	varchar2(15)	author
18	lddate	date	date of entry

The COLDESCRIPT table not only provides the description of a column, but also provides metadata such as NA values, units and ranges in useful forms. In fact, it is planned that the "range" column will eventually be retired, when the information contained in this column is fully represented. Currently, "range" stands as a go-between to bring the text information on range from the documents into the database. Similarly, units and na_value may change somewhat when the information is properly distilled. Currently most NA values are just a single value represented as a text string, which is the goal for all entries in this column. Most numeric ranges have been properly translated into *nmin*, *nminop*, *nmax*, and *nmaxop*. Each operation is relative to the value in the column; that is, 'column *nminop nmin'* and 'column *nmaxop nmax'*. If both are set, then both must apply (implied 'and'). In general, one is a minimum and the other a maximum. To represent it as a range, the sense of *nminop* must be reversed, '*nmin* reverse(*nminop*) column *nmaxop nmax'*. A range type of 'defined' means the value of the column is limited to a short set of pre-defined values. A 'finite set' is a limited but long or not pre-defined set of values. A 'reference set' is limited to the values in a particular table (as given in *reftab*). Using these fields properly can completely and precisely define the various field ranges.

The next table is COLASSOC (see Table 3). This table provides the necessary links between TABDESCRIPT and COLDESCRIPT.

Table 3. COLASSOC

field number	column	storage type	description
1	table_name	varchar2(30)	name of table
2	column_name	varchar2(30)	name of column
3	column_type	varchar2(30)	function of column
4	column_position	number(8)	column ordering position within table
5	na_allowed	varchar2(1)	is NA allowed for the column
6	key	varchar2(30)	type of key, if column is a key
7	keyschema	varchar2(30)	schema to which key's reference table belongs
8	schema	varchar2(30)	name of schema
9	auth	varchar2(15)	author
10	lddate	date	date of entry

Each table will have multiple columns (column positions 1 through the total number, in order), and columns can appear in multiple tables. The column type will define the basic function of the field in the database (i.e. primary key, unique key, descriptive data, measurement data, administrative data). An NA value should always be given for a column in COLDESCRIPT, but na_allowed will indicate if that NA value can be used in a particular table or not. Key allows key columns to be identified with respect to the table: the reference table for the key, or a table in which the key is foreign. These keys are primarily numerical identifiers. Keyschema is used when the reference table is part of a separate schema.

The remaining table is the GLOSSARY table (see Table 4). This table serves two purposes: the first is to simply define generic strings used in various description fields, primarily acronyms and abbreviations. The second is to serve as the reference table for 'defined' range types and 'finite set' range types.

Table 4. GLOSSARY

field number	column	storage type	description
1	glossid	number(8)	unique numerical identifier
2	lineno	number(8)	numerical order if definition is multiple lines
3	name	varchar2(30)	name to be defined
4	column_name	varchar2(30)	column name if specific to a subset of columns
5	table_name	varchar2(30)	table name, if specific to a subset of tables
6	owner	varchar2(30)	owner of table in database, if specific to a subset of owners
7	definition	varchar2(80)	full text definition of name
16	schema	varchar2(30)	name of schema, if specific to a subset of schemas
17	auth	varchar2(15)	author
18	lddate	date	date of entry

A given definition can apply in all circumstances (column_name, table_name, owner and schema are all not set), which is a generic definition, or it can apply to increasingly selective subsets of columns, tables, owners and schemas. For 'defined' and 'reference set' range types in COLDESCRIPT, the complete permitted set of values will be found in GLOSSARY, one entry for each value (values are found in the name column), and column_name will always be set for these.

As with any other new application, there are issues associated with our implementation of capturing metadata information and making it readily available through the power of a relational database. These issues have appeared as more people use the tables we have designed. We are working successfully with application developers at Sandia National Laboratories in identifying areas where improvements to this process can be made. To-date, we consider this approach to be in beta-testing mode, but will work hard to elevate it to full production mode within one year. Having such information in database form has immediate application to a wide variety of efforts involving the database, both specific to Los Alamos, and across NNSA (see presentation at this meeting by Ballard, et al., on the subject of DBTools). This schema for table description metadata is a key contribution to the web-based database documentation discussed in this paper. It is also the foundation for an automated quality control (QC) effort at LANL. As a rather fundamental tool, it is foreseeable that a wide variety of other uses may arise with time. It is hoped, for example, that this schema can contribute to the maintenance of the schema descriptions, such that they are maintained in the database, where they can be easily checked for errors, quality, and completeness, and that the corresponding section of the documents could be generated automatically, directly from the database.

Another advance in using metadata, with a more narrow application, has been the creation of bulletin descriptive tables. These tables describe the sources of bulletin data that have been imported into the data warehouse, as well as providing a means to track individual data elements to the corresponding lines of text in the original document. There are two tables involved: BULLETIN and BULLASSOC. The BULLETIN table contains one entry for each individual bulletin, with columns *dir* and *dfile* pointing to the text file on the system that contains the bulletin. It also has a *bullid* column that is unique to each bulletin. The other information in the table describes the bulletin, including format. The BULLASSOC table has one line for each data object extracted from the bulletin (origins, arrivals, magnitudes, etc.) It links the *bullid* and the *id* of the extracted object and provides the line number in the

bulletin corresponding to the object. These tables have two immediate uses. The first is to help in QC – problematic objects can be directly traced to the corresponding file and line number. The second is user interaction – an application can be created that allows the user to automatically view the source line and context for any bulletin-derived data in the database, which it is hoped will be helpful in understanding the nature of some bulletin data.

Quality control

As data become more voluminous and complex, quality control (QC) has become a challenging and extremely interesting issue to consider when developing content for the Knowledge Base (KB). In particular, because of recent advances in tools that access KB data, researchers have been able to make more efficient use of this large volume of data, but have also found problems in applying the data to their research efforts. Improvements in QC procedures are helping researchers and data managers to more readily identify complex quality problems. The outcome is improved research products resulting from improved data upon which those products are based. QC is handled in a wide variety of ways at the present, and much effort is being made to better structure this procedure and automate as much of it as is practical to do so. There are three main categories of QC: manual, tool-assisted, and automated. Improvements in manual QC are occurring constantly as a wider variety of issues are captured and understood. But this kind of QC is the least transportable and repeatable. The next step is to capture the tracking and resolution of QC problems in various simple tools, usually case-specific scripts. Tool-assisted QC is more transportable and repeatable, since the script serves as documentation of procedures, but it still requires case-by-case modification and application. Automated QC is preferred and cannot happen without there first being a fairly comprehensive understanding of the problem. The best approach is to document exactly what the database should be and reject anything that does not conform. This approach is why the database descriptive schema discussed above will be a valuable tool in automated QC of database data. However, not all QC issues are in the database. QC must be applied to all data from raw waveforms to final calibration parameters.

The improvements GNEM R&E has made in this area have even had modest impact outside the program; for example, in helping the International Seismological Centre (ISC) identify some problems with their data products. This opportunity arose during QC investigations into unusual problems linking origins and events. Using tool-assisted QC of the problem, we were able to identify problems in the original data files where duplicate information was being reported as different events. We could completely characterize the problem and send detailed descriptions to the ISC, which then worked to correct the problems we reported. Considering that the problems were unreported and dated back to bulletins that were released as many as five years earlier, and that the ISC produces a widely-used bulletin recognized by the seismological community as the final global bulletin, it is apparent that these errors are difficult to find in any research or operation context. In other words, QC is a hard problem and GNEM R&E is making new and unique contributions toward resolving the problem.

Applying data warehouses to event location research

Merged global and regional phase arrival and ground-truth source data are available in our research data warehouse to assist researchers in their event location efforts. The location effort has, in fact, created its own database tables by combining all available phase arrival information and manipulating it to create consistent arrivals and improve event relocations that lead to better correction surfaces. Researchers use the reconciled database tables that contain global and regional bulletin information, as well as LANL-generated phase arrival and waveform data, to create new tables specific for relocation purposes.

LANL researchers have created Arrival Sorter (ARsorter), a Perl-based program whose primary objective is to reconcile similar phases reported from many organizations, including our internal phase picks. The reconciliation of many reported similar phases recorded by different sources for a particular seismic station for a given event requires some phases to be renamed. The phase renaming process is necessary to provide the best distinct phase arrival times to the programs used in location. By doing this process, we are compiling a database with the best distinct seismic phase arrivals, so that for a given event at a given station there is only one particular phase (e.g., only one Pg, Pn, Sn).

Applying data warehouses to event discrimination and yield research

The event discrimination and yield research conducted at LANL benefits directly and indirectly from the data warehouse. The event discrimination work uses data stored in database tables directly as input for processing, while

event yield work uses the data warehouse indirectly by extracting the data contained in the headers of the SAC-format waveform files, which are populated using data from the database. The final products of the event discrimination work are MDAC (Magnitude and Distance Amplitude Corrections) parameters for given event/station paths and amplitude corrections for raw amplitude measurements. These data are also stored in the data warehouse in NNSA custom tables, which are used by tools such as EventID and CodaMag developed at Sandia National Laboratories (SNL). The final products of the yield research work are the computation of network and station coda moment magnitudes, also stored in CSS-style database tables.

CONCLUSIONS AND RECOMMENDATIONS

The newly created process of capturing data changes (CDC) shows great promise. It is expected that we have not encountered all possible use cases, where modifications to the process will need to be made and perhaps auxiliary tables or triggers will need to be created. This process has been in place for several months and it appears to get the work done. As mentioned earlier, many of the steps involved are manual and human intervention is needed throughout. The next step of this process is to automate many of the synchronization steps, and also incorporate appropriate quality control checks to ensure that the synchronization between databases was successful and that the data being inserted does not create internal conflicts and errors in the target database.

The use of web-based database querying/population tools has shown to be an efficient method to access database table information and track important research steps on any computer platform with a web browser. We are continually finding new reasons and ways to access the database through the web, including determination of outdated information based on newly loaded data (e.g., new/updated arrival picks) and quality control checks.

The newly acquired ability to parse and store in the database the contents of core documents such as the KB database table and column descriptions is proving to be extremely valuable. Having such information in database form has already had immediate impact on a wide variety of efforts. One specific example can be viewed at this meeting on the subject of DBTools, paper and poster by Ballard, et al. It is also the foundation for an automated QC effort at LANL that has recently started this summer. It is hoped, for example, that this schema can contribute to the maintenance of the schema descriptions, such that they are maintained in the database, where they can be easily checked for errors, quality, and completeness. Our vision for the future is that the corresponding section of the documents could be generated automatically, directly from the database.

Quality control (QC) has become an increasingly visible and difficult issue regarding the Knowledge Base (KB), as data have become more voluminous and complex. Improvements in QC procedures currently under way will help researchers and data managers to more readily identify complex quality problems. The outcome is improved research products resulting from improved data upon which those products are based. The improvements GNEM R&E has made in this area have even had modest impact outside the program; for example, in helping the International Seismological Centre (ISC) identify some problems with their data products. We hope that present and future quality control efforts will lead to continued collaboration with external organizations to benefit the entire seismic community.

ACKNOWLEDGEMENTS

The authors wish to acknowledge LANL personnel (below) who have made important contributions in the past, and those who continue to make vital contributions to the development and maintenance of the LANL research data warehouse:

Hans E. Hartse, Diane F. Baker, George E. Randall, James T. Rutledge, Steven R. Taylor, W. Scott Phillips, Marian D. Peters, and Thomas L. Riggs.

REFERENCES

Carr, D. (07/04), *National Nuclear Security Administration Knowledge Base Core Table Schema Document*, Sandia National Laboratories report SAND2002-3055, available at: https://www.nemre.nnsa.doe.gov/prod/nemre/fileshare/coretables.pdf

DBTOOLS: A SUITE OF TOOLS FOR MANIPULATING INFORMATION IN A RELATIONAL DATABASE

Sanford Ballard and Jennifer Lewis

Sandia National Laboratories

Sponsored by National Nuclear Security Administration
Office of Nonproliferation Research and Engineering
Office of Defense Nuclear Nonproliferation

Contract No. DE-AC04-94AL85000

ABSTRACT

While loading data into a database is a simple operation, doing so *intelligently* is deceptively difficult. Intelligent loading means loading data in a manner that, at a minimum, (1) does not duplicate information already in the database, (2) links new information to related information already in the database, and (3) remaps identification numbers in the input data to prevent conflict with identification numbers already in the database. In this paper, we present a suite of tools that we have developed to help users intelligently manipulate database information.

- EvLoader – This tool merges one or more rows from a source EVENT table into a target EVENT table. All information in the database that is linked to the source event row(s) is also merged (the user specifies what information is related to the source event in the parameter file). The code operates in two modes. In the first, origins in the source event are merged with origins in the target event based on EVID number. In the second mode of operation, source events are merged with target events based on spatial/temporal correlation. Origins that are members of the same Event in the source tables will remain members of the same Event in the target tables.

- Unloader – This tool deletes one or more specified rows from the database and also deletes all rows that are connected to the specified row(s) according to relationships specified in the Entity Relationship Diagram. Rows are only deleted if doing so will not violate any foreign key relationships in the database.

- FileInterface – This tool recognizes three information storage formats: a set of database tables, a set of ASCII flatfiles, and XML. The tool can convert information from any one of these formats into any of the others. For the XML format, we have designed an XML schema document that completely captures all of the information in a data set.

- Remap – Given two sets of similar database tables, this tool will generate a remap table which will relate the identification numbers in the source tables to the identification numbers in the target tables.

All of these tools depend on a library of utilities called DBToolBox. DBToolBox is written in a completely generic manner in the sense that it does not have hard-coded within it any information about any particular set of tables, column descriptions, or entity relationship diagram. All such schema-specific information is supplied by the user via parameter files and Table Definition Tables. This approach makes the tools that use DBToolBox immune to most schema changes such as addition/deletion of columns from a table or changes in the size of a particular data element (i8 to i9, for example).

OBJECTIVES

Many of the custom software tools that have been developed to support nuclear-explosion monitoring do not insert the results of the calculations that they perform back into the relational database where data are stored. This is due primarily to concern that the new data will be inserted incorrectly, which might not only make the new data inaccessible, but may also corrupt data that already reside in the database. To remedy this situation, we have developed a library of software tools, called DBToolBox, that facilitates proper insertion of new information into a relational database. DBToolBox, which is written in the Java programming language, can be included in software applications and allow those applications to insert, update and delete rows of information in the database while ensuring that new identification numbers (IDs) do not conflict with existing IDs, that foreign key relationships are obeyed (even without having foreign key constraints turned on in the database) and that unique keys are honored.

Besides the DBToolBox library itself (a Java package), we have developed a number of applications built on DBToolBox. Each of these applications will be described below.

RESEARCH ACCOMPLISHED

DBToolBox uses graph theory (Sedgewick, 2004) extensively in its implementation. A graph is a mathematical concept involving a collection of vertexes and another collection of edges, which are connections between pairs of vertexes. A directed graph is a special type of graph in which all of the edges have a direction, i.e., they originate in one vertex and terminate in another. A set of tables in a database constitute a directed graph, which we will refer to as a TableGraph, where the tables are the vertexes and the foreign key relationships are the edges. An entity relationship diagram of the tables in a relational database is a representation of a TableGraph. Consider Figure 1, which illustrates the entity relationship diagram for the core tables of the NNSA schema (Carr, 2002). Each box in the diagram represents a table (vertex) in the TableGraph and each line connecting two tables represents two edges in the TableGraph, one going in each direction. The edges can be expressed as SQL select statements that include where clauses involving foreign keys. For example, consider the line between the Origin Table and the Event table that is labeled orid-prefor. Given a row from the Origin table (which will have a unique orid value), one can represent the edge in the TableGraph that extends from the Origin table to the Event table with the select statement "select * from Event where prefor=#orid#' where #orid# represents the actual value of the orid field in the current row of the Origin table. The select statement 'select * from Origin where orid=#prefor#' represents an edge in the TableGraph that originates in the Event table and terminates in the Origin table.

There is another, even more useful graph in a database which we will call a RowGraph. A RowGraph is a directed graph in which the vertexes are rows from the database and edges emanate from a row that produced another row to the row that was produced. A RowGraph is constructed by starting from one or more rows in the database and executing all the edges in the TableGraph that emanate from the table of which the row is a member (execution of an edge in a TableGraph means execution of the SQL statement that the edge represents). All of the rows produced by the execution of the edge are added to the RowGraph, provided that the RowGraph does not already contain that row. For each row that is added to the RowGraph an edge is added that originates in the row that produced the new row and terminates in the new row. When each new row is added to the RowGraph, all of the edges in the TableGraph to which the row belongs are executed and the new rows produced are also added to the RowGraph. This process continues until no more rows are added to the RowGraph. Note that it is critical that rows only be added to the RowGraph once. If this precaution is not adhered to, it is possible to enter an infinite loop.

From the point of view of application development, a RowGraph is an extremely useful construct. Once a set of database tables has been identified and the relationships between those tables defined, one may specify some initial row in the database and extract all the other rows in all the other tables in the database which are related to the initial row by one or more of the defined relationships. If the tables and relationships are properly defined, then the application will have in memory all the rows that it needs to do its work, and no more. Not only that, it will also have the information needed to efficiently traverse the data set and visit the rows with which it needs to interact. At the most abstract level, the role that DBToolBox performs is to manage the assembly, traversal, modification and input/output of RowGraphs.

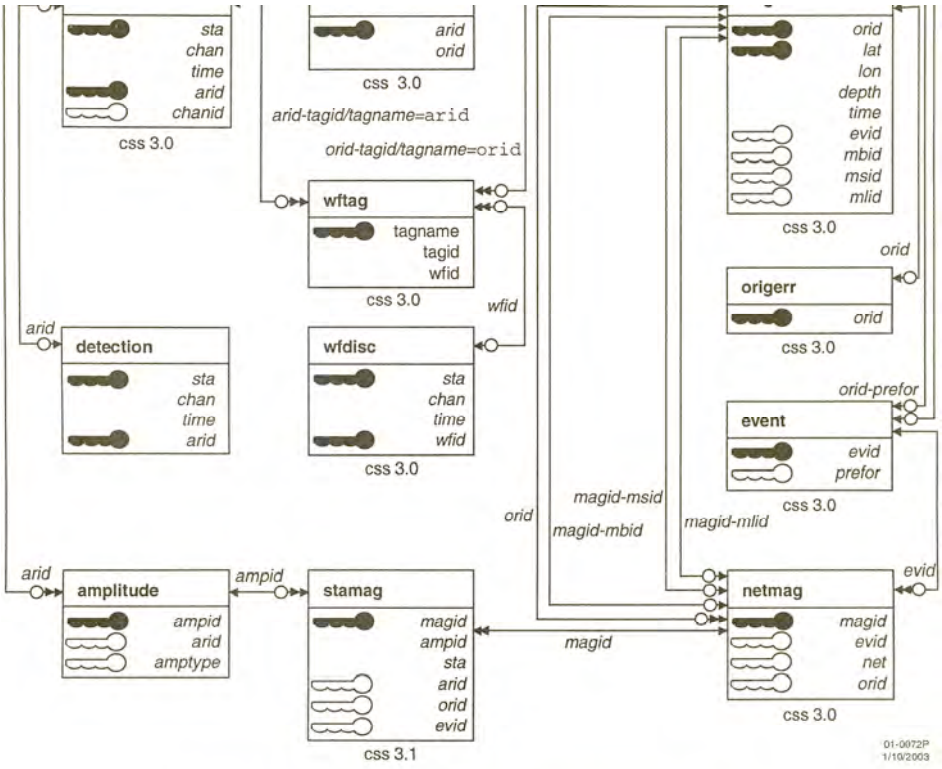


Figure 1. TableGraph of the tables and relationships in the NNSA core schema.

System Architecture

DBToolBox is a Java package that instantiates objects from a number of classes. The primary classes can be divided into two major categories: those that encapsulate specific features or properties of the database system and those that implement specific functions that operate on the system.

The major property-type classes managed by DBToolBox are organized as illustrated in Figure 2. At the top of the structure is the RowGraph object, of which there is generally only a single instance in a DBToolBox session. The RowGraph object contains one or more Schema objects, each of which encapsulates the features of a TableGraph as described in the previous section. A Schema object has a collection of Table objects, which are the vertexes of the TableGraph, and a collection of Relationship objects, which are the edges of the TableGraph. Relationship objects manage the execution of SQL select statements between an origination table and a termination table.

Each Table object knows its name (the name of the table in the database), and what type of table it is (as defined in the database schema documentation). Each Table maintains a collection of Column objects, each of which knows the name of the column in the database table, its SQL type, NAValue, foreign key status, etc. Note that Schema, Table and Column objects do not contain any data from the database, per se, but rather serve to manage all the metadata that describes the actual data.

Actual data are contained within Row objects, each of which has a collection of data values and a reference to the Table object that contains the Row. The architecture was designed this way because typical applications will likely only have to deal with a limited number of Schema, Table and Column objects but may have to instantiate a very large number of Row objects. Given this consideration, Rows are designed to have the smallest memory size possible while all the metadata describing the data in a Row object is accessible through a single reference to a Table object. A Row object also has a unique identifier, called a RowID, which is used to identify the Row in the RowGraph of which it is a member. The RowID is computed as the MD5 hash (Rivest, 1992) of a string

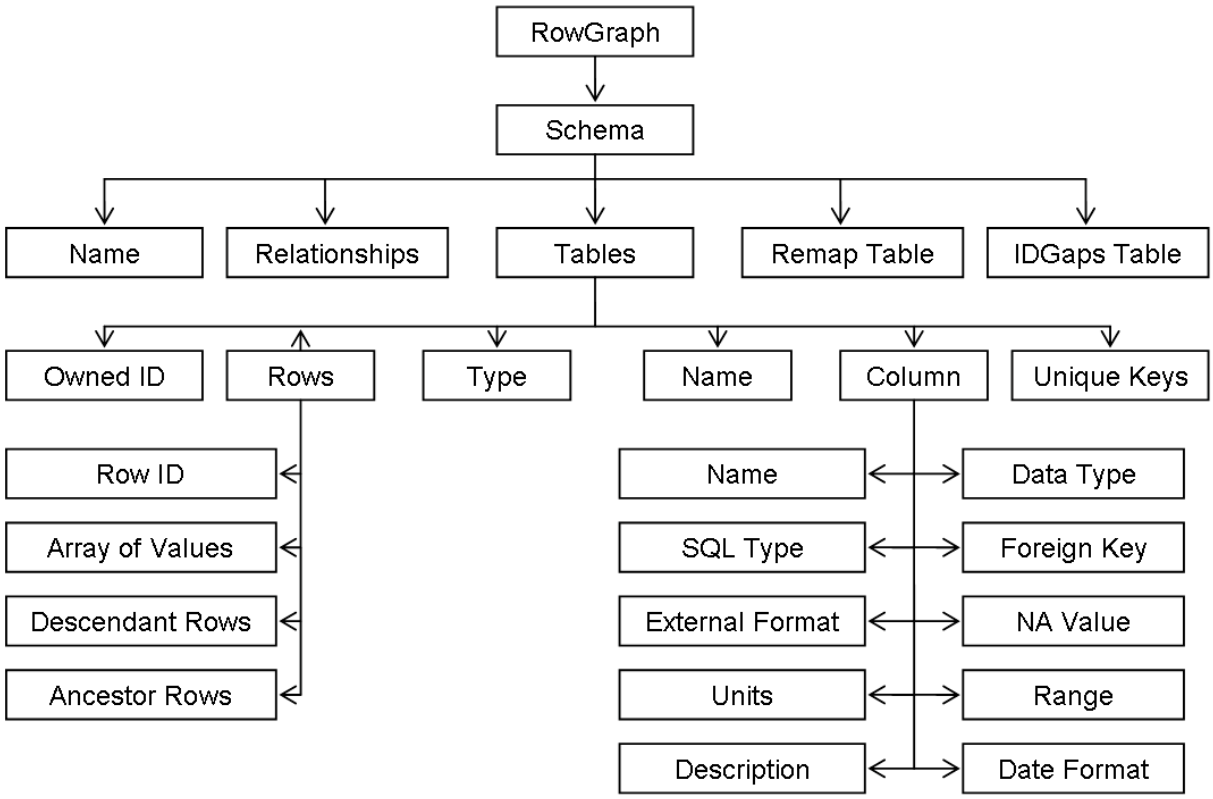


Figure 2. DBToolBox system architecture.

constructed from the following values: the name of the Schema object that the Row is a member of, the type of the Table object that the Row is a member of, and string representations of all the data values in the Row, with the exception of LDDATE (the date that the information was loaded into the database). It is imperative that the RowID be unique so that the same row of information will not be added to the same RowGraph more than once.

The only object in the system that contains a collection of Row objects is the RowGraph object. In addition to the Row objects, a RowGraph keeps track of all the edges in the RowGraph. A RowGraph is designed so that it can efficiently retrieve all the Row objects that come from a particular Schema or Table object, all the direct descendents of a particular Row, all the direct ancestors of a particular Row, and more. RowGraph implements the Java Set interface, so it has iterators and all of the other features of a Set that Java developers are familiar with.

Several classes in DBToolBox manage functional behaviors rather than object features and properties. To describe how these operators work, it is necessary to clearly define a number of terms as they are used in the context of DBToolBox operations:

ID owner table – DBToolBox distinguishes between two fundamental types of tables, those that ‘own’ an ID and those that do not. Each ID must be ‘owned’ by one and only one table. ID owner tables tend to be tables that represent some fundamental quantity that is of interest to the users of the database. In the NNSA core schema, the tables that are ID owners include Event, which owns evid, Origin (orid), Arrival (arid), and Netmag (magid). Non ID owner tables tend to be tables that contain supporting information (Origerr for example), or tables that serve as a bridge between two ID owner tables (Assoc for example). Non ID owner tables contain fields that relate to fields in ID owner tables, forming foreign key relationships with those tables.

Unique keys – these are fields in a row of a table that, taken as a group, should not be duplicated in the table. An important corollary is that two rows that come from different tables of the same type and which have equal unique keys, are considered equal, regardless of the values in the other fields of the two Rows. This means that if a source row is to be added to a target table but a row already exists in the target table with equal unique keys, then the source row need not be added to the target table but all other source rows which are related to the discarded source row by foreign key relationships may be linked to the target row that has unique keys equal to the discarded source row. As used in DBToolBox, unique keys may include only data fields and must not include any IDs. In the NNSA schema, many of the fields defined as primary keys are used in DBToolBox as unique keys. For example, the NNSA schema defines the Origin table to have primary keys LAT, LON, DEPTH, TIME and AUTH. In DBToolBox, these would constitute a set of unique keys.

The most important of the functional type classes is the Merge class, which implements methods to merge a collection of Rows (which are linked together in a RowGraph), into a set of target Tables where the target Tables are not the same tables as the ones from which the Rows originated. Merging information from one set of tables into another set presents a number of challenges. The first is that the IDs in the source Rows may conflict with IDs in the target Tables. To overcome this difficulty, the IDs in the source Rows are renumbered using new ID values that do not currently exist in the target Tables. DBToolBox has an IDGaps class to facilitate this renumbering (IDGaps keeps track of used id values in a set of tables, including gaps in the ID values). Another challenge when merging Rows into a different schema is that duplication of unique keys in the target table is to be avoided. Before inserting a Row from the source RowGraph into the target Table, Merge checks to see if a Row with equal unique keys already exists in the target Table. If one or more such Rows are found, Merge will refrain from duplicating the information in the target Table and will renumber IDs in the source Rows so as to preserve the necessary foreign key relationships.

The Merge operation executes three passes through the collection of source Rows that are to be merged into the target tables. During the first pass, only Rows that come from Tables that own an ID are visited. Each Row from an ID owner Table is examined to see if a Row exists in the corresponding target Table that has equal unique keys. If such a Row is found then an entry is made in the Remap Table that relates the value of the owned ID in the source Row to the value of that ID in the target Row, and the source row is labeled in such a way that it will not be copied into the target tables. If no target Row with equal unique keys is found, a new value for the owned ID is retrieved from the target IDGaps Table, an entry is made in the Remap table that relates the value of the ID in the source Row to the new value obtained from the IDGaps table, and the Row is labeled such that it will be copied into the target tables. Other than the labels, the source Row is not modified during this first pass.

During the second pass, Merge visits only Rows from non-ID owner tables. All the IDs are renumbered using the remap relations established during the first pass of the Merge operation. Then the target Tables are searched for a Row that has equal ID values. If none are found, the non-ID owner source Row is labeled for insertion into the target Tables. If one is found, it must be true that all the ID owner source rows with which the non-ID owner source row shares foreign key relationships found target rows with equal unique keys and were labeled such that they would not be copied into the target tables. In this case, if unique keys were defined for this non-ID owner table, the non-ID target row is checked to see if it has unique keys that are equal to those in the source Row. If unique keys were defined, and the unique keys in the target Row are not equal to those in the source Row, there is a conflict. The ID owner rows that the non-ID owner Row is related to are not to be copied into the target table but will have their IDs remapped to ID values that already exist in the target table. In order to avoid duplication of the primary keys in the non-ID owner Row, the non-ID owner source Row should not be copied into the target tables either. But, since the unique keys have unequal values, critical information will be lost (it is assumed that unique keys contain critical information). We are confronted with a dilemma. On the one hand, we do not want to duplicate unique keys in the ID owner Rows but on the other hand we do not want to lose critical information contained in the non-ID owner Row. The DBToolBox Merge function will always choose to duplicate information in one of the ID owner tables rather than lose critical information in the non-ID owner table. When confronted with this situation, it will reverse a decision made during the first pass through the RowGraph where it decided to not copy a Row of information to the target Tables.

During the third pass through the RowGraph, all Rows that were labeled for insertion into the target tables are visited. A new Row is created that honors the target Schema. ID fields in the source Row are renumbered using the Remap information generated during the first two passes through the RowGraph and copied into the target Rows. Then all the data fields are copied from the source to the target Row and the new target Row is inserted into the target Table.

Applications

The DBToolBox library of utilities described in the previous section can serve as the basis for a variety of applications that need to interact with a database. So far, we have written four applications that perform system management activities. These applications are described below. In addition to these applications, DBToolBox is used by the Peer to Peer Tool Communication (Merchant et al., 2004). RowGraphs serve as the fundamental objects that are passed around during interprocess tool communication. While DBToolBox is written in a completely generic manner in that no specific schema information such as table names or column definitions are hard-coded into the library itself, that is not true of the applications described below.

EvLoader

This tool merges one or more rows from a source EVENT table into a target EVENT table. All information in the database that is linked to the source event row(s) is also merged (the user specifies what information is related to the source event in the parameter file). EvLoader uses DBToolBox to build a RowGraph starting from the initial EVENT rows specified by the user. It then invokes the Merge function in DBToolBox to merge the source rows into the target tables in such a way that primary keys, foreign keys and unique keys are properly managed.

The code operates in two modes. In the first, origins in the source event are merged with origins in the target event based on EVID number. In this mode, EVID numbers in source rows are not renumbered but are inserted into the target tables without modification. This mode of operation is used by AFTAC to merge data from the various pipeline database accounts (SOCPRO, AL1, AL2, EVAL), into the AFTAC global account.

In the second mode of operation, source events are merged with target events based on spatial/temporal correlation. The code is used in this mode to merge global and regional seismic event catalogs into a single database. The goal is to combine origins from disparate sources into coherent events based on the spatial-temporal proximity of the origins in the events.

A precise description of the algorithm used by EvLoader is provided below, using set notation.

Given:

1. a single source event consisting of 1 or more origins
2. a target event table where each row represents an event consisting of 1 or more origins,
3. no two origins that are members of the same event may have the same author. This must be true for the source event and must be true for all events in the target event table, both before and after merging of the source event.
4. Source origins which are ‘equal’ to a target origin that already exists in the target origin table are not duplicated in the target origin table. Origin equality is defined as:

```
where source.auth=target.auth
and abs(source.lat-target.lat)<1e-3
and abs(source.lon-target.lon)<1e-3
and abs(source.depth-target.depth)<1e-2
and abs(source.time-target.time)<1e-3.
```

5. Source origins that were all members of the same source event prior to the merge will all be members of the same target event after merging. Integrity of target events is not guaranteed, however. Target origins which were ‘equal’ to source origins will be repointed from the target event of which they were a member before merging to the target event into which the source origins are being inserted.

Variables

The following variables are defined:

EventEqualityTest: A SQL WHERE clause that defines what it means for two events to be 'equal'. Examples might include 'WHERE EVID=#EVID#' or 'WHERE EVENT_NAME=#EVENT_NAME#'. To evaluate the EventEqualityTest, EvLoader will, for a given row from the source EVENT table, replace the field names enclosed in '#' characters with the value of those fields from the source EVENT row and execute the select statement against the target EVENT table. If one target EVENT row is returned, the test returns the event that that row represents. If no rows are returned, the test returns ∅. If two or more rows are returned an error condition is asserted. The EventEqualityTest may be undefined.

E_t: The set of target events that are each a potential recipient of the source origins. The set is defined by a SQL select statement based on the contents of the preferred origin of the source event. The following example will select all target events whose preferred origin is within 30 seconds in time and 100 km in horizontal distance from the preferred origin of the source event:

```
select * from target_event_table where prefor in (select orid from
target_origin_table where abs(time-#time#)<30 and distance(lat, lon, #lat#,
#lon#) < 100)
```

The field names enclosed in '#' characters are replaced with the values of those fields extracted from the preferred origin of the source event.

e_t : a single target event, which is defined in the algorithm. At the conclusion of the algorithm, e_t is the target event to which source origins will be added.

T : the set of origins in e_t.

T_{eq}: a subset of T such that for each origin in T_{eq} there exists an origin in S with the same author, lat, lon, depth and time. The subscript *eq* denotes 'equality'.

T_a: a subset of T such that for each origin in T_a there exists an origin in S with the same author but with a different lat, lon, depth or time. The subscript *a* denotes 'author'.

T_u: a subset of T such that for each origin in T_u there are no origins in S with the same author. The subscript *u* denotes 'unique'.

t_p : the origin in T_u that has the highest author ranking. If T_u is empty, $t_p = \varnothing$. t_p is only guaranteed to be the preferred origin in e_t if $T_a \bigcup T_{eq} = \varnothing$, or stated another way, $T_u = T$.

S: the set of origins in the source event, with the constraint that $S \neq \varnothing$.

S_a: a subset of S such that for each origin in S_a there exists an origin in T with the same author but with a different lat, lon, depth or time. The subscript *a* denotes 'author'.

s_p: the preferred origin in the source event.

S_g: the origins in S for which there exists an origin in the target ORIGIN table which is 'equal' to the source origin. The subscript *g* denotes 'global'.

T_g: the origins in the target ORIGIN table for which there exists an origin in S which is 'equal' to the target origin. The subscript *g* denotes 'global'.

E_g: the subset of all target events in the target EVENT table such that each event in E_g contains only origins in T_g. These events contain only origins that are equal to origins in the source event.

e_{best}: the event in E_g that contains the maximum number of origins. If more than one event in E_g contains the maximum number of origins, e_{best} can be any one.

Observations

$(T_u \cap T_{eq}) \cup (T_{eq} \cap T_a) \cup (T_a \cap T_u) = \varnothing$. This says that T_u, T_a and T_{eq} are each mutually distinct (they don't overlap).

$T_{eq} \cup T_a \cup T_u = T$ *which indicates that* T *does not contain any target origin that is not a member of either* T_u, T_a *or* T_{eq}.
S_g and T_g are the same size but may both be empty.
S_a and T_a are the same size but may both be empty.

Given the definitions above:
$(T_g - T_{eq})$ will include all target origins that are 'equal' to a source origin but which are not already members of the target event, e_t. These are origins in the target ORIGIN table which should be repointed to e_t.
$(S - S_g)$ will include all the origins in the source event, except those which are 'equal' to an origin that already exists in the target ORIGIN table. These are the source origins that need to be added to e_t.

Algorithm

1. If the EventEqualityTest is not defined proceed to step 2. Otherwise, define e_t to be the target event returned when the EventEqualityTest is evaluated.
    a. If $e_t \neq \varnothing$, goto 4.
    b. If the EventEqualityTest is "`where evid=#evid#`", define e_t to be a new target event with the same evid value as the source event. Goto 4.
    c. Goto 2.
2. If $T_u \neq \varnothing$ for any $e_t \in E_t$, find $e_t \in E_t$ such that t_p is closest to s_p
    a. If $T_a = \varnothing$, goto 4.
    b. If the separation between the centroid of S_a and the centroid of T_u is greater than the separation between the centroid of T_a and the centroid of T_u, goto 3.
    c. If the separation between the centroid of S_a and the centroid of T_u is less than the separation between the centroid of T_a and the centroid of T_u, create a new target event with a new evid from the ID_GAPS table and repoint the elements of T_a to it. Goto 4.
3. If $E_g \neq \varnothing$, set $e_t = e_{best}$. Otherwise, define e_t to be a new target event with a new evid from the ID_GAPS table. Goto 4.
4. Repoint $(T_g - T_{eq})$ to e_t and add $(S - S_g)$ to e_t. Terminate the algorithm.

Unloader

Deletion of a row from a database is a deceptively simple operation to execute in major database applications such as Oracle, but, when foreign key constraints are turned off in the database, as they frequently are, the unintended consequences of row deletion can be profound. Row deletion can break numerous foreign key relationships, which can severely compromise the integrity of the data in the database. With Unloader, the user specifies one or more rows from a single table that are to be deleted and also specifies a series of relationships that lead to more rows in other tables in the database. The intention is to delete all of these rows. Unloader takes this information and constructs a RowGraph based on the tables, relationships and starting rows specified by the user. It then analyzes the RowGraph to ensure that deletion of all these rows will not break any foreign key relationships. Finally, Unloader

deletes from the database only the rows in the RowGraph that will not violate the integrity of other data in the database.

The operations performed by Unloader are perhaps best illustrated with an example. Consider an Event with two Origins, each of which is related to 5 Arrival rows through 5 Assoc rows (a total of 10 Assocs and 5 Arrivals). The user requests that one of the Origins be deleted (the one that is the preferred origin of the Event row), and specifies relationships from the Origin table to the Assoc and Arrival tables. Unloader constructs a RowGraph with the Origin that is to be deleted, the 5 Assocs that are related to the Origin and the 5 Arrivals that are related to the Assocs. It analyzes all the foreign key relationships involving these rows in the RowGraph. For the Origin row, it will consider the orid-prefor relationship with the row in the Event table and will modify the Event row since the Origin that is to be deleted is the preferred Origin of the event. If the Origin to be deleted was the only Origin in the Event, it would have deleted the Event as well. Next, it considers all of the Assoc rows and determines that all the rows with which the Assoc rows have foreign key relationships are themselves members of the RowGraph and that the Assoc rows can therefore be safely deleted. At that point it moves on to the Arrival rows where it finds that there are other Assoc rows, which are not members of the RowGraph to be deleted, that have relationships with the Arrival rows. It concludes that the Arrival rows may not be deleted. Finally, Unloader deletes the Origin row, the 5 Assoc Rows and modifies the Event row, but leaves the Arrivals intact.

FileInterface

Not all of the data that researchers must deal with are stored in the database. Data must frequently be imported from flatfiles, or must be exported to flatfiles so that it can be transferred to other users. Also, as mentioned earlier, some applications used by researchers write their output to flatfiles rather than to the database because of the difficulty of implementing database interactions. FileInterface facilitates the transfer of data between the database and flatfiles. It recognizes three information storage formats: a set of database tables, a set of ASCII flatfiles, and XML. The tool can merge information from any one of these formats into any of the others, using the DBToolBox Merge functions described earlier.

For the XML format, we have designed an XML schema that completely captures all of the information in a data set, including both the data itself and the metadata that describes the data. The schema closely mimics the architecture of the DBToolBox system illustrated in Figure 2.

Remap

The Remap utility generates a new remap table between two tables that purportedly contain the same data but with different ID values. This allows researchers to discover the identification numbers in the merged database that equate to their original identification numbers, even in the case where the Remap tables generated during merge operations are lost.

Remap operates as follows: For each ID for which remap information is to be generated, the user specifies a source table, a target table, and a SQL select statement that defines equality of rows in the source and target table. The specified tables should be the ones that ‘own’ the ID under considerations. For every row in the source table, the select statement is executed against the target table, and, if a single row is returned, an entry in the remap table is generated that relates the value of the owned ID in the source table to the value in the target table. If no row is retrieved, no entry is made. If more than one entry is retrieved, an error condition is asserted.

CONCLUSIONS AND RECOMMENDATIONS

We have developed a library of software modules called DBToolBox that facilitates interaction between software tools and data stored in a relational database. The modules are totally generic in that the specifics of the schema that describes the relational database that the code operates on are not hard-coded into the software but rather are stored externally in database tables or XML files. Schema modifications, additions and enhancements can be made to the external data structures and implemented without requiring modification to the DBToolBox library.

To date, we have developed four applications based on DBToolBox. These applications merge information from disparate databases into a single set of tables, safely delete information from a set of tables without compromising the integrity of the data that remains, convert data stored in database tables, flatfiles and XML files to and from each

of these formats, and generate ID remap tables between compatible sets of database tables. In addition, DBToolBox RowGraphs serve as the fundamental data objects that are passed between software tools in the Peer to Peer Tool Communication System (Merchant et. al., 2004).

ACKNOWLEDGEMENTS

Many thanks to Chris Young for support and guidance during development of this code and for reviewing the manuscript.

REFERENCES

Carr, D. (2004), National Nuclear Security Administration Knowledge Base Core Table Schema Document, Sandia National Laboratories, SAND2002-3005, available at https://www.nemre.nnsa.doe.gov/prod/nemre/fileshare/coretables_062104.pdf.

Merchant, B. J., D. Hart, E. Chael, M. Chown, J. Hampton (2004), Proceedings of the 26th Seismic Research Review: Knowledge Base Navigator Facilitating Regional Analysis Inter-Tool Communication, Orlando, FL (Sept. 21-23, 2004).

Rivest, R. (1992), "The MD5 Message-Digest Algorithm," http://theory.lcs.mit.edu/~rivest/Rivest-MD5.txt.

Sedgewick, R. (2004), Algorithms in Java, Part 5, Graph Algorithms, 3rd Edition, Addison-Wesley.

STATE-OF-HEALTH SOFTWARE FOR THE AUTOMATED RADIOXENON SAMPLER/ANALYZER

Tom R. Heimbigner, Theodore W. Bowyer, James C. Hayes, Charles W. Hubbard, Justin I. McIntyre, Mark E. Panisko, Michael D. Ripplinger, and Reynold Suarez

Pacific Northwest National Laboratory

Sponsored by National Nuclear Security Administration
Office of Nonproliferation Research and Engineering
Office of Defense Nuclear Nonproliferation

Contract No. DE-AC06-76RLO 1830

ABSTRACT

The Automated Radioxenon Analyzer/Sampler (ARSA) is a complex gas-collection and analysis system that requires constant online monitoring of system operations and overall system health. The software-control system records and monitors and over 100 different system sensors (temperature, pressures, voltages, etc.). A real-time record of the system state allows the system to monitor for unsafe conditions and maintain the system in a safe state regardless of external or internal failures (vacuum pump, valve or power failures, and runaway temperatures are a few examples). Another function of real-time monitoring allows the user to troubleshoot the system when a problem arises, should a minor sensor or a major system failure occur. This paper will outline the general scheme used by the state-of-health program to monitor and assess the system, the graphical user interface programs, and the alert message system, and give specific examples of proper system performance and some systems failures.

OBJECTIVE

In this paper we describe the development and application of a state-of-health monitoring system. This paper is directed primarily toward the ARSA described by Hayes et al (1999). However, the concepts presented are applicable to nearly any automated system, as outlined in CTBT/WGB/TL-11/5/Rev. 4 (1999), where verification of proper operation, recognition of system failure, identification of a failed component, adjustment of critical timing, and safety-related issues are a concern. A complete description of international noble gas testing can be found in Auer et al., (2004). We have found that the capability of easily monitoring a system's state-of-health is as critical in the development phase as it is once the system has been deployed. The ARSA state-of-health monitoring system is made up of three main components (1) sensor information, (2) event log data, and (3) alerts.

RESEARCH ACCOMPLISHED

Description of the ARSA system

The ARSA is a relatively complicated instrument operating autonomously under computer control. It uses Opto22 hardware to perform the necessary I/O. There are an excess of 80 digital outputs used to control valves, apply power to various pumps and compressors, reset various components, and shuttle calibration sources in and out of the system's nuclear detector. Approximately 17 digital input signals are used to monitor source transfer and safety-related sensors such as heater over-temperature signals. The 10 analog output signals are used to adjust three mass-flow controllers as well as to control the system's seven heaters. Finally, there are an additional 44 input signals used to monitor dew points, CO_2 readings, mass flow, pressures, temperatures, current, voltages, and a thermo conductivity detector (TCD).

The ARSA system includes an uninterruptible power supply (UPS) that provides power to critical components. This particular UPS can be interrogated to obtain additional information that is critical to proper system operation (input/output power, battery status, load power, and temperature). Early detection of an input power failure is crucial to allow time for critical operations to be performed and the execution of an orderly shutdown to mitigate unsafe operating conditions.

Components of the ARSA State-of-Health Monitoring System

1. Locally Maintained State-of-Health File

One of the primary goals of any state-of-health monitoring system is to be able assess the "state" of the system at any given time. This provides a historical perspective of the system, allowing a user to review in detail how the system was performing over some previously defined time interval. Furthermore, it allows the user to form comparisons between the day-to-day operations to see if performance is degrading with time. More importantly, however, is having the ability to diagnose the root cause for any decrease in performance that may have been recognized. With a system as complicated as the ARSA, this is not a trivial task. Software solutions providing automated analysis or predictive failure can be extremely complicated. Typically, the analysis of a state-of-health file is performed manually by an experienced operator who is intimately familiar with the system.

The ARSA software architecture implements a client/server model with each server having a responsibility for maintaining one dedicated task. The ARSA state-of-health server's sole responsibly is to interrogate the other servers in the system for the necessary sensor information and write this information to a local binary file. We refer to the ARSA state-of-health file as a "ringfile". The implication here is that after some predetermined time, the sensor data will be overwritten as more and more state-of-health records are accumulated. The ARSA "ringfile" will normally only maintain the previous 13 days of sensor data, sampled at two-minute intervals. Each state-of-health record in the file is time stamped. Because all normal operations performed during the ARSA process control are usually separated by many minutes, or even hours, the 2 minute sampling interval is usually more that sufficient. However, in the development stages of the system, some timing critical information is not yet known and it is important that the developers have the ability to increase the sampling interval to say, 10 seconds, therefore, a finer-grained history is available. This is easily accomplished by a simple command to the state-of-health server.

2. Locally Maintained Event Log

Although the state-of-health file conveys a wealth of information about all sensors in the system, additional information is sometimes required in order to fully understand a particular reading. During system development and testing, the users will often override the normal control system. Although it is true that the state-of-health sensor readings will reflect any changes the user had made, it may not be obvious from the sensor data alone what actually occurred. Similarly, a condition may have existed on an unattended ARSA that forced it to take some action that is outside the norm of everyday operation. Here again, it may not be obvious from the sensor data alone exactly what transpired up to that time. Consequently, the ARSA employs a second software server whose sole responsibility is to maintain a binary Event Log. Whenever any change is made to the system or the control process changes state, an event record is written to this file. Each event record message includes a timestamp, the originator of the message, a priority that was assigned to the message, and a brief description of the message. The ability to review this Event Log is invaluable in assessing the total state-of-health of the system.

3. The ARSA Safety Server

The real-time analysis component of the ARSA state-of-health monitoring software is provided by an additional server called the safety server. This server, unlike the state-of-health and Event Log servers, regularly performs an analysis of the system's health. The sole purpose of this server is ensuring that the system is protected should an unsafe condition arise. It is the only server that has the capability of terminating all other servers. Unlike the state-of-health server, the safety server only interrogates those sensors that are involved in maintaining the safety of the system.

The ARSA must adhere to some very rigid operating parameters in order to preclude any unsafe condition from occurring. To further complicate the problem, many of these parameters are continually changing as the ARSA sequences through the collection, separation, and archiving processes. A few of these parameters are referred to as "global" parameters and are not dependent on the state of the system. Global parameters are always checked. Other conditions, such as the temperatures of the seven charcoal traps, are very dependent on the state of the control system. Traps that are being regenerated or eluted can safely maintain higher temperatures than if they were in the active phase. One final condition, the loss of primary AC power, is also considered. Another unique feature of these parameters is that they have a time-variable condition associated with them. Various perturbations in the system, such as valves opening and closing, can occasionally cause momentary spikes in the sensor data. These spikes are normal and do not necessarily reflect an unsafe condition. The time variable condition ensures that no action is taken unless the condition being tested is out of bounds for the duration of the variable.

If the safety server ever detects an unsafe condition, it will immediately take the required action to ensure that the system is brought back to a safe condition. All servers will be terminated and an alert message placed in the e-mail queue. Additionally, a DO.NOT.RUN file is generated. If for some reason the system is rebooted after a safety shutdown, the ARSA will not start until the condition is corrected and this file has been deleted.

4. The E-mail Interface

Many of the ARSA systems will run unattended. Although there are mechanisms for remotely accessing the system directly (TELNET, FTP, Phindows, or the GUI), this is not the norm. In normal operation, eight files are routinely e-mailed to addresses defined in a configuration file each day. These files include six detector files, an abbreviated state-of-health file, and all records in the Event log that were entered that day. In addition to these files, alert messages may also be e-mailed.

The e-mailed state-of-health file contains only a subset of all the sensors in the normal file. Additionally, this file has been converted to ASCII format that is more suitable for parsing by database applications and Excel. Normally, only the most important analog sensors are included. If analysis of this file determines there is a problem with the system, the entire binary file can be retrieved for a more complete analysis. The e-mailed event log file is also converted to ASCII format.

Whenever a major event occurs on the ARSA, an alert message is e-mailed to the recipients listed in a configuration file. The ARSA will always e-mail an alert message during startup. Once the ARSA system has started, alerts are

only sent if the safety server detects a problem with the system. In most cases, these alerts are severe enough that a shutdown of the system is required. The following is an alert message sent by the safety server indicating that a pressure sensor (PS-6) has exceeded its allowable range. Note that the severity of the error is FATAL, indicating that normal operations can no longer continue and that the system will be shut down. Additionally, the alert message contains the date and time that the failure was identified. At this point, we only know that there was a problem with this particular system (USX99). A more thorough analysis of the state-of-health file would have to be performed to determine the root cause of the problem (Figure 1).

```
BEGIN     IMS1.0
MSG_TYPE  DATA
MSG_ID    6859  USX99
DATA_TYPE ALERT
USX99 SYSTEM     2003/06/26 03:41:40
FATAL           (2003/06/26 03:41:40)
a-PS-6 out of range(-40.0-105.0),
value: 115.1, Global


2003/06/26 03:41:40
STOP
```

Figure 1. Example Alert Message from the ARSA.

The System Data Viewer

A Visual Basic application, the System Data Viewer, was developed by Pacific Northwest National Laboratory (PNNL) to aid in the analysis of the binary files generated by the ARSA systems. This application has provisions for viewing the binary state-of-health and Event Log files. The state-of-health viewer and the Event Log viewer are both structured in a way that allows the user to easily navigate through the files.

When viewing state-of-health data, the user can select any combination of analog and digital sensors for simultaneous display. It is this capability that allows a user, who is familiar with the operations of the ARSA, to evaluate the health of the system. With the inherent zoom capability, the user can examine specific regions of the data in more detail (Figure 2).

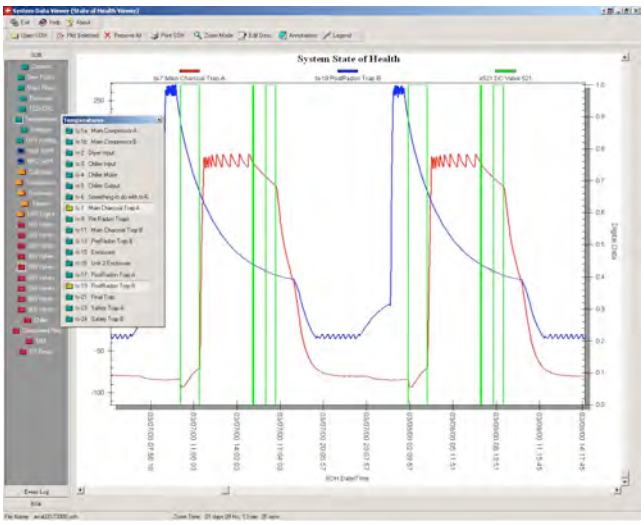


Figure 2. State-of-Health Viewer Sensor Selection.

The Event Log viewer displays all the associated records in the file. When displayed, each record is color coded according to the priority of the message. Additional options allow the user to display only messages matching a specific priority. A limited search capability allows users to easily find records such as those that may have been generated by the ARSA safety server (Figure 3).

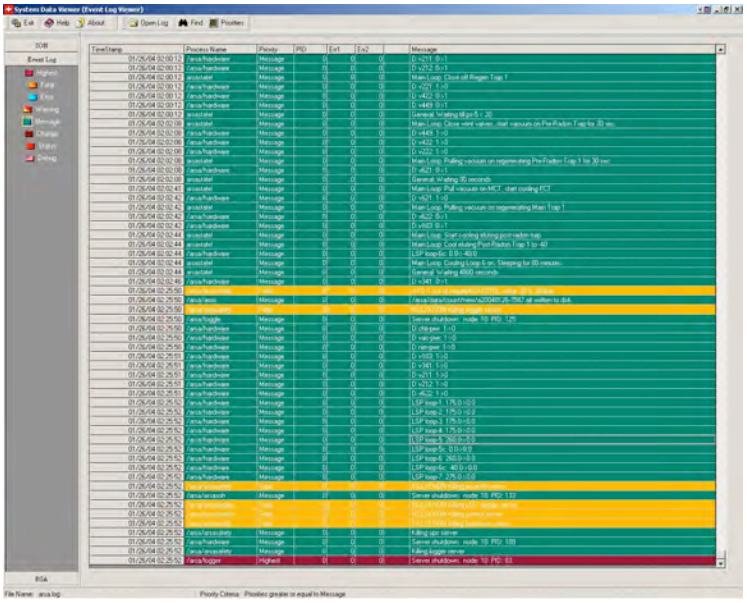


Figure 3. Event Log View with Priority Highlighting.

Examples of Normal Operation

In most instances, when the ARSA is operating normally, state-of-health data are used primarily to verify that system performance is not degrading with time. In many cases, the operator simply may want to obtain a baseline for future comparisons. This is particularly important after the system is initially installed. The ARSA is designed with two distinct processing chains. These are typically referred to as the A and B sides. The purpose of having the two sides is to allow one side to be regenerated while the other side is actively collecting Radioxenon. Ideally, both sides would exhibit the same characteristics. Unfortunately, this is not always the case. There are many reasons why this may not be the case. Subtle differences in the sensors, sensor location, or small details in the manufacturing can all have an affect.

The importance of obtaining a baseline is demonstrated in the Figure 4 below. The temperatures and pressures for both of the main charcoal traps are graphed simultaneously. We recognize immediately that there is very good agreement between the temperature readings for trap A (TS-11, cyan) and trap B (TS-11, green). Both have approximately the same maximum and minimum value and behave similarly over the same time interval. However, when examining the corresponding pressures for the two traps over the same time interval, we notice a distinct difference in the profiles. There is a peak in pressure sensor PS-5 (blue) that does not appear in pressure sensor PS-4 (red). It turns out that this difference in pressure sensors readings has always existed and does not present a problem. If we had not recognized that this peak was present initially, we might suspect that something had occurred on the system and would unnecessarily investigate this anomaly in further detail.

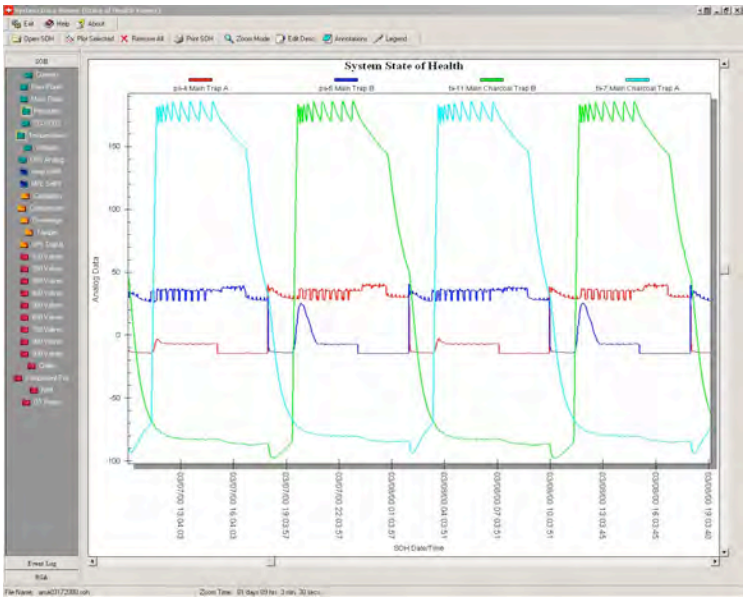


Figure 4. Normal Sensor Readings with Baseline Requirement.

Abnormal Event Resulting in a System Shutdown

While the ARSA system was deployed in Frieburg, Germany, the 24-V power to all the DC valves would occasionally drop out for brief periods of time. Normally, the ARSA would survive these momentary dropouts without incident. The dropouts occurred infrequently, and the nature of the process was such that many of these dropouts occurred at a time when there was minimal impact on the system. On occasion, however, the dropout would coincide with a time in the process when the effects of the dropout were much more pronounced.

In Figure 5 we see multiple dropouts in the 24-V valve supply (red) but see very little perturbation of the dry process pressure sensor, PS-6, shown in blue. The duration of these dropouts is on the order of 1 to 4 minutes. The ARSA survives these dropouts without any problem, and no more dropouts occur for another 9 days.

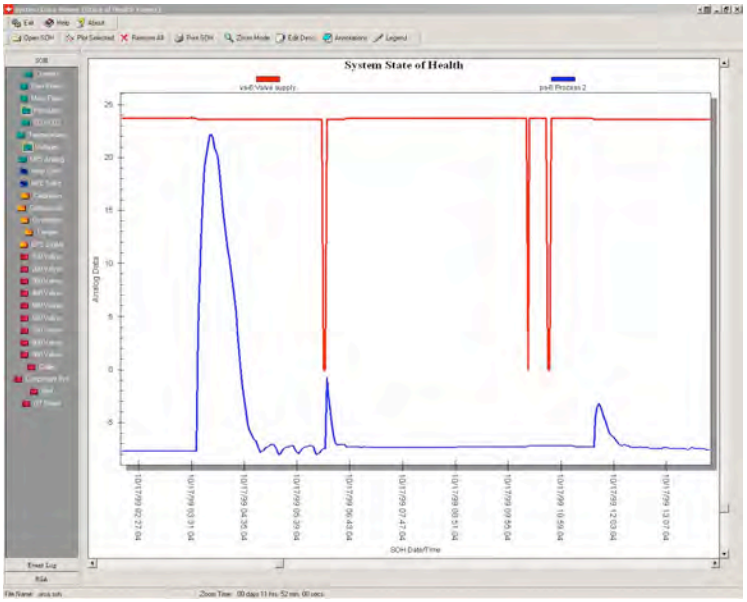


Figure 5. Valve Power Dropouts Unrecognized by the ARSA

Nine days later, another dropout in the valve power supply occurs and remains for many minutes. This time the effect is far more dramatic. In Figure 6 below we see that as soon as the dropout occurred, PS-6 immediately rises, and the sensor reading saturates at its maximum valve. The dropout does not recover this time, and the pressure reading remains high for many minutes. The ARSA safety server, recognizing that PS-6 has exceeded its maximum allowable value for the allowable time defined in the configuration file, will initiate the sending of an e-mail alert message and execute an orderly shutdown of the system.

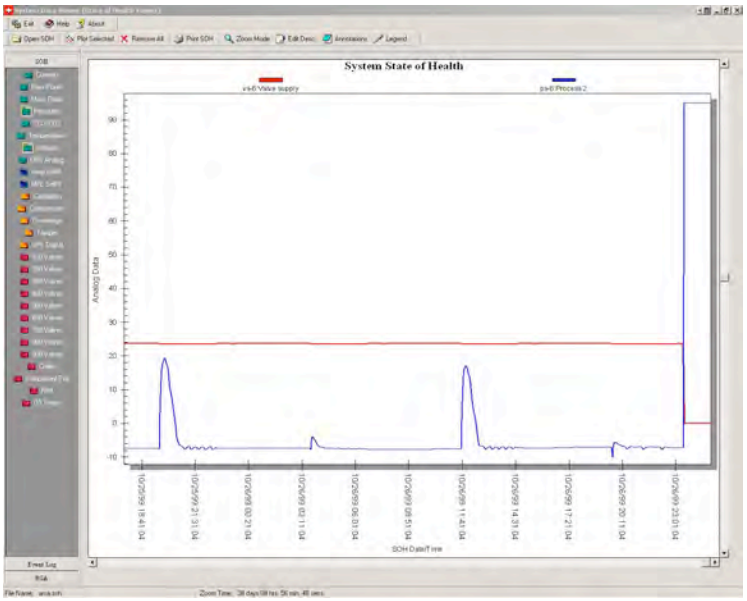


Figure 6. Valve Power Dropout Resulting in System Shutdown.

Sample of an Orderly System Shutdown

When a condition is recognized by the safety server that requires a shutdown of the system, a series of very ordered actions occur. Each action taken is recorded in the Event Log. Figure 7 displays the actions of a typical safety shutdown.

The first line highlighted in orange demonstrates that the safety server has recognized that PS-1 is out of range and has determined that the severity of this message should be FATAL. The following line shows that an alert file (.alt) has been written to the disk. It is this file that will ultimately be emailed by the system. After the alert message is written, the safety server first kills the toggle server so that it is no longer able to cycle the dryer valves. As the toggle server closes, it writes its own message to the log file. The safety server then closes all open valves in the system through an interface to the hardware server. Additionally, the safety server ensures that all heater-control loops have been turned off and that the outputs to the heaters are set to zero. Safety then terminates all other servers and writes the DONOT.RUN file (Figure 7).

01/26/04 02:02:46	/arsa/hardware	Message	0	0	0	D v341: 0->1
01/26/04 02:25:50	/arsa/arsasafety	Fatal	0	0	0	a-P5-T out of range(40.0-125.0), value: 20.6, Global
01/26/04 02:25:50	/arsa/arms	Message	0	0	0	/arsa/data/count/new/a20040126-7587.alt written to disk
01/26/04 02:25:50	/arsa/arsasafety	Fatal	0	0	0	KILL-XENON-Killing toggle server
01/26/04 02:25:50	/arsa/toggle	Message	0	0	0	Server shutdown: node: 10 PID: 125
01/26/04 02:25:50	/arsa/hardware	Message	0	0	0	D chlr-pwr: 1->0
01/26/04 02:25:50	/arsa/hardware	Message	0	0	0	D vac-pwr: 1->0
01/26/04 02:25:50	/arsa/hardware	Message	0	0	0	D nim-pwr: 1->0
01/26/04 02:25:51	/arsa/hardware	Message	0	0	0	D v103: 1->0
01/26/04 02:25:51	/arsa/hardware	Message	0	0	0	D v341: 1->0
01/26/04 02:25:51	/arsa/hardware	Message	0	0	0	D v211: 1->0
01/26/04 02:25:51	/arsa/hardware	Message	0	0	0	D v212: 1->0
01/26/04 02:25:51	/arsa/hardware	Message	0	0	0	D v622: 1->0
01/26/04 02:25:52	/arsa/hardware	Message	0	0	0	LSP loop-1: 175.0->0.0
01/26/04 02:25:52	/arsa/hardware	Message	0	0	0	LSP loop-2: 175.0->0.0
01/26/04 02:25:52	/arsa/hardware	Message	0	0	0	LSP loop-3: 175.0->0.0
01/26/04 02:25:52	/arsa/hardware	Message	0	0	0	LSP loop-4: 175.0->0.0
01/26/04 02:25:52	/arsa/hardware	Message	0	0	0	LSP loop-5: 260.0->0.0
01/26/04 02:25:52	/arsa/hardware	Message	0	0	0	LSP loop-5c: 0.0->0.0
01/26/04 02:25:52	/arsa/hardware	Message	0	0	0	LSP loop-6: 260.0->0.0
01/26/04 02:25:52	/arsa/hardware	Message	0	0	0	LSP loop-6c: -40.0->0.0
01/26/04 02:25:52	/arsa/hardware	Message	0	0	0	LSP loop-7: 275.0->0.0
01/26/04 02:25:52	/arsa/arsasafety	Fatal	0	0	0	KILL-XENON-Killing arsasoh server
01/26/04 02:25:52	/arsa/arsasoh	Message	0	0	0	Server shutdown: node: 10 PID: 133
01/26/04 02:25:52	/arsa/arsadisplay	Fatal	0	0	0	KILL-XENON-Killing LCD display server
01/26/04 02:25:52	/arsa/arsacontrol	Fatal	0	0	0	KILL-XENON-Killing control server
01/26/04 02:25:52	/arsa/arsasafety	Fatal	0	0	0	KILL-XENON-Killing hardware server
01/26/04 02:25:52	/arsa/arsasafety	Message	0	0	0	Killing ups server
01/26/04 02:25:52	/arsa/hardware	Message	0	0	0	Server shutdown: node: 10 PID: 109
01/26/04 02:25:52	/arsa/arsasafety	Message	0	0	0	Killing logger server
01/26/04 02:25:52	/arsa/logger	Highest	0	0	0	Server shutdown: node: 10 PID: 83

Figure 7. Sequence of Safety Server Initiated Shutdown.

Recognizing Long-Term Component Degradation

Historically, most component failures in the ARSA have been sudden, catastrophic failures. Compressors suddenly failed to start, heaters have burned out, valves have quit operating, and temperature sensors have failed. For these types of failures, there is very little, if any, warning of an impending failure. Even though current sensors and temperature sensors were attached to the compressors, these sensors did not exhibit abnormal readings before their failure.

There have been some instances, however, where the state-of-health sensor data could have forewarned of an impending failure had it been interpreted correctly. Initially, the state-of-health data from the ARSA was not being stored in a database. The normal access to state-of-health data was through the e-mailed files (daily files that represented only a subset of all sensors) or the binary state-of-health file that had to be manually (by way of FTP) from the system. Because these files represented a relatively short time interval and could only be interpreted accurately by an experienced user, it was very easy to overlook slowly varying changes in a sensor.

The ARSA diaphragm vacuum pumps were a common failure point. Usually, the diaphragm in the pump would first develop a very small tear. This tear would cause a very small, almost imperceptible, rise in the baseline of the vacuum pressure sensor. As the tear continued to develop, the vacuum baseline would continue to increase. At some point, a catastrophic failure in the diaphragm would occur. This very slow rise in the baseline reading was certainly not evident when a single e-mailed file was plotted. The time frame was just too short. In order to effectively examine this data, many emailed files would have to be concatenated together to produce a much longer time span.

A Unique Problem

While the ARSA was in Germany, a unique problem began occurring on the system. For no apparent reason, the system would simply reboot. Our first inclination was to examine the state-of-health data coming from the UPS, surmising that we may periodically be losing primary AC power and that the UPS was failing during the switch to battery power. However, up to the point of the reboot, all UPS indicators were well within normal operating ranges. The UPS indicated that its battery was fully charged and that it had in excess of 10 minutes of reserve at the current power draw. Additionally, both the line input power and the line output power were operating in normal ranges. Conversations with the personnel at the Institute for Atmospheric Research (IAR) in Frieburg verified that there was not a power failure at the times these problems surfaced. Examination of the event log initially did not help in diagnosing the problem. At the point of failure, there were absolutely no records in the event log that would indicate

a problem. After the reboot, the messages immediately before the "System Started" message were normal, everyday messages. Basically, the system was behaving as if it didn't have a UPS at all and as if someone had just disconnected the primary AC from the wall.

Compounding the problem was the fact that it happened infrequently. What we hadn't initially noticed was that although the shutdown was infrequent, it was happening regularly. Although we were receiving e-mailed alert messages that the system had restarted, there was no reason to suspect that these message were related in time. Finally, someone happened to recognize that these alert startup messages were occurring at almost exactly a two-week interval. We wondered what possible component of the system would do anything on a two-week interval. The ARSA control process was fully understood and could not be the problem because it operated strictly on eight-hour cycles. The only conclusion that could be drawn was that the UPS was the source of the problem even though there had never been a loss of primary AC power.

Closer examination of the UPS manual indicated that it was configured to perform a self-test at two-week intervals. When this test is performed, the UPS will switch to battery power even though line input power is available. Although all indicators of the battery status were good, the battery had obviously failed. When current was demanded from the battery, the output AC voltage could not be sustained and the computer would reboot. Although it took a great deal of time to diagnose this problem, it could not have been done without using the combined capabilities of the state-of-health viewer, the Event Log viewer, and the alert messaging system.

CONCLUSIONS AND RECOMMENDATIONS

The suite of applications and programs developed for the ARSA state-of-health monitoring system has proven to be invaluable in both the development and deployment phases of the project. With few exceptions, problems that have developed on the system are easily diagnosed by a careful examination of the files and alert messages generated by the system. The full implementation of a state-of-health database and the development of automated analysis routines (with predictive capabilities) would fully complete the ARSA state-of-health monitoring system.

REFERENCES

Auer, M., A. Axelsso, X. Blanchard, T.W. Bowyer, G. Brachet, I. Bulowski, Y. Dubasov, K. Elmgren, J.P. Fontaine, W. Harms, J.C. Hayes, T.R. Heimbigner, J.I. McIntyre, M.E. Panisko, Y. Popov, A. Ringbom, H. Sartorius, S. Schmid, J. Schulze, C. Schlosser, T. Taffary, W. Weiss, and B. Wernsperger, (2004); Intercomparison experiments of systems for the measurement of xenon radionuclides in the atmosphere, Applied Radiation and Isotopes 60 863–877.

Hayes, James C., Keith H. Abel, Theodore W. Bowyer, Tom R. Heimbigner, Mark E. Panisko, Paul L. Reeder, Justin I. McIntyre, Robert C. Thompson, Lindsay C. Todd, and Ray A. Warner, (1999), in *Proceedings of the 21st Seismic Research Symposium: Technologies for Monitoring the Comprehensive Nuclear-Test-Ban Treaty*, LA-UR-99-4700, Vol. I, p. 249.

Operational Manual for Radionuclide and the International Exchange of Radionuclide Data (1999), Preparatory Commission for the Comprehensive Nuclear-Test-Ban-Treaty Organization, CTBT/WGB/TL-11/5/Rev. 4.

LOW-NOISE BOREHOLE TRIAXIAL SEISMOMETER

James D. Kerr and David W. McClung

Geotech Instruments, LLC

Sponsored by National Nuclear Security Administration
Office of Nonproliferation Research and Engineering
Office of Defense Nuclear Nonproliferation

Contract No. DE-FG02-03ER83667

ABSTRACT

This report describes the preliminary design of a Low Noise Borehole Triaxial Seismometer for use in networks of seismic stations for monitoring underground nuclear explosions. The design assumes the use of the latest technology of broadband seismic instrumentation. Each parameter of the seismometer is defined in terms of the known physical limits of the parameter. These limits are defined by the commercially available components, and the physical size constraints. A theoretical design is proposed, and a solid model of the proposed instrument is included to verify the ability to meet the size constraints.

OBJECTIVES

The goal of this Small Business Innovation Research (SBIR) award is to design a Low Noise Borehole Triaxial Seismometer for use in networks of seismic stations for monitoring underground nuclear explosions. The design assumes the use of the latest technology of broadband seismic instrumentation. Each parameter of the seismometer is defined in terms of the known physical limits of the parameter. These limits are defined by the commercially available components, and the physical size constraints. A theoretical design is proposed, and a computer assisted design (CAD) model of the proposed instrument is included to verify the ability to meet the size constraints.

The design goals set out for the SBIR are for a triaxial seismometer that can be deployed in 7-inch boreholes at a depth of 100 meters. The instrument must operate over a bandwidth of 0.2 to 16 Hz with a response flat to velocity or acceleration. Two instruments may be used to meet the requirements. The self-noise of the instrument(s) must 6 dB below the United States Geological Survey (USGS) low-noise model over the full bandwidth and have a dynamic range of 120 dB. Self-calibration within 5 percent of amplitude and within five degrees for phase over the bandwidth is a requirement. The instrument must have low power requirements and a high reliability when operated unattended in harsh environments.

RESEARCH ACCOMPLISHED

For Phase I, seven parameters of a broadband instrument were analyzed to define the requirements needed to meet the design goals for response, low-noise, and dynamic range and the requirement to fit into a 7-inch diameter or less borehole. Phase I looked at the suspension, the minimum mass requirements, and maximizing the sensitivity of the suspension to acceleration. Detecting the mass motion of the sensor relative to the reference frame, the mass motion transducer, and the control loop requirements are described. A noise analysis of the control loop was done, and a CAD feasibility model was made to verify a fit into the borehole.

In the analysis, comparison is made to the characteristics of existing and historical seismometers such as the KS36000, KS54000, and KS2000 instruments in order to verify the validity of some of the calculations and characteristics of the proposed design.

A pendulous suspension was chosen for the response analysis and a natural frequency of approximately 10 Hz was used. This natural frequency will allow a simple seismometer design that does not require a mass lock. It is assumed that the suspension is not in a vacuum to further simplify the design. The mass size is set according to the well-known MPQ criteria.

The ratio of the distances from the pivot point to the center of mass ($\bar{r}$) and to the center of percussion (q) is set to maximize the angular sensitivity of the suspension within the constraints of the borehole diameter requirements. Figure 1 shows this relationship and the historical characteristics of existing designs. The maximum sensitivity occurs at a ratio $q/\bar{r}$ of 2.

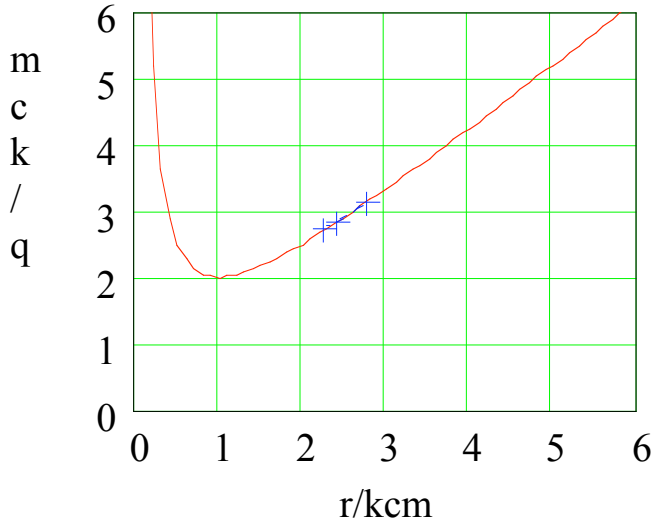


Figure 1. Relationship of q, $\bar{r}$, and $\hat{e}_{cm}$ for maximizing angular sensitivity of the suspension. Blue '+' symbols show ratios (from left to right) of the KS2000, KS54000 (vertical) and KS54000 (horizontal).

Figure 2 shows the relationship if the goal is to maximize power delivered by the suspension, and the historical data of previous designs.

There must a compromise between these to extremes. When the minimum mass is computed from the MPQ thermal noise criteria, it is found that maximizing angular sensitivity requires that the mass be twice the size that is required for maximizing power. But, maximizing power requires the mass to be located as far as possible from the suspension pivot point. The design must fit into the borehole and doubling the mass to increase sensitivity is not desirable, but the borehole diameter places a limit on $\bar{r}$. Basically it is the size of the mass and the configuration of the mass that is important.

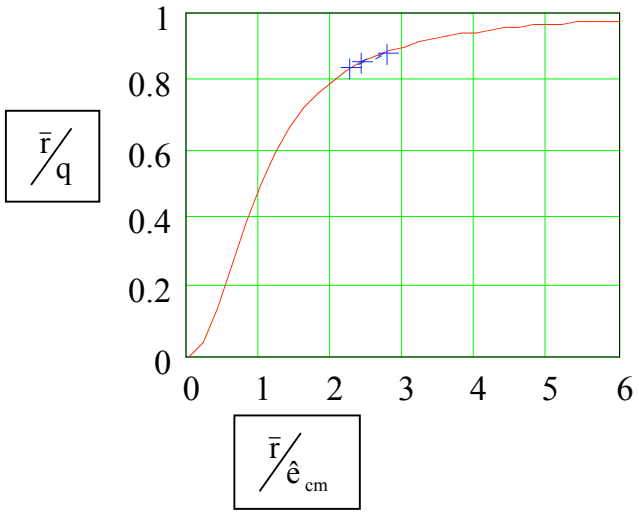


Figure 2. Relationship of q, $\bar{r}$, and $\hat{e}_{cm}$ for maximizing power sensitivity of the suspension.

Once the suspension has been designed to have a threshold signal greater than the thermal noise, the next step is to convert the angular output of the suspension into a useable electrical or digital signal.

For an analog design assume the amplifier at the output of the detector has a noise spectra referred to its input of E_{pa} volts^2/Hz, and that the noise is white noise without 1/f noise. Also assume the detector has a sensitivity of K_B and that the suspension has a natural frequency of f_m. Figure 3 shows the affect on noise threshold referred to the input of the suspension when f_m is varied and K_B is held constant. Figure 4 shows the variation when K_B is varied and f_m is held constant.

It should be restated that Figure 3 and Figure 4 assume the ideal theoretical situation of no 1/f noise and possibly K_B values that may not be realistic.

Figure 5 shows the theoretical E_{pa} noise thresholds of the KS54000 and KS2000 suspensions. Other noise sources in the system will generally keep the design from seeing these thresholds. In particular, the thermal noise threshold of the KS54000 is -200 dB worst case, and typically it is -204 dB. The typical thermal noise threshold of the KS2000 is -195 dB. It is obvious that the KS54000 suspension has much more sensitivity at the low frequencies than is required, and that the KS2000 suspension has far better potential at the higher frequencies.

Also shown in Figure 5 is a theoretical model of a suspension plus detector that could have a noise level 15 dB below the Albuquerque Low Noise Model (ALNM) over the frequency from dc to 16 Hz. Again the assumption of no additional noise added by other elements of the system applies. The design goal is to be 6 dB below the ALNM, so there is considerable margin for other noise sources.

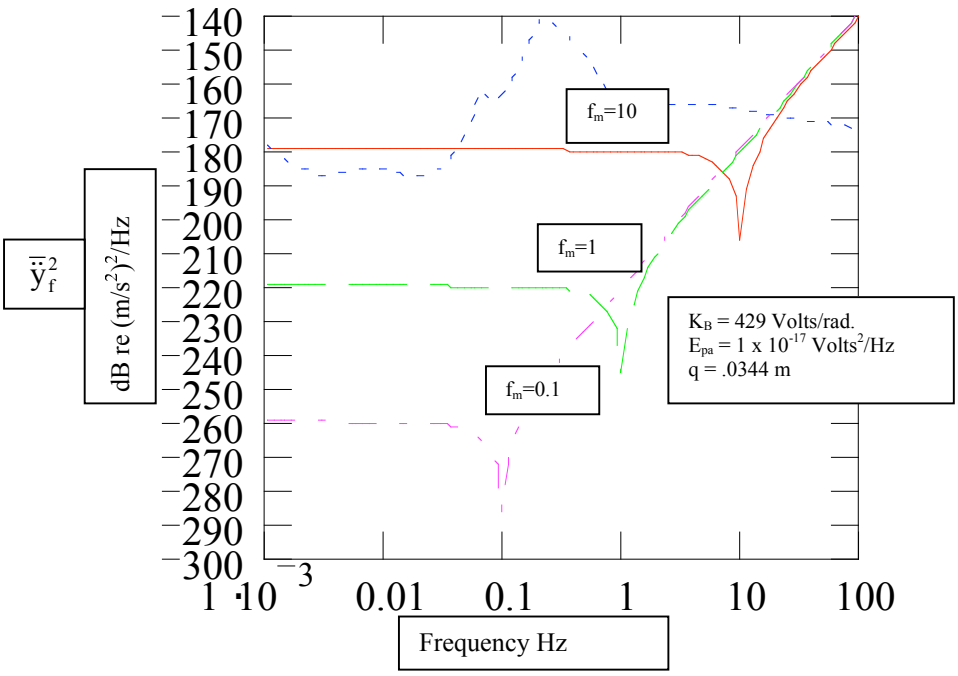


Figure 3. E_{pa} noise threshold versus f_m.

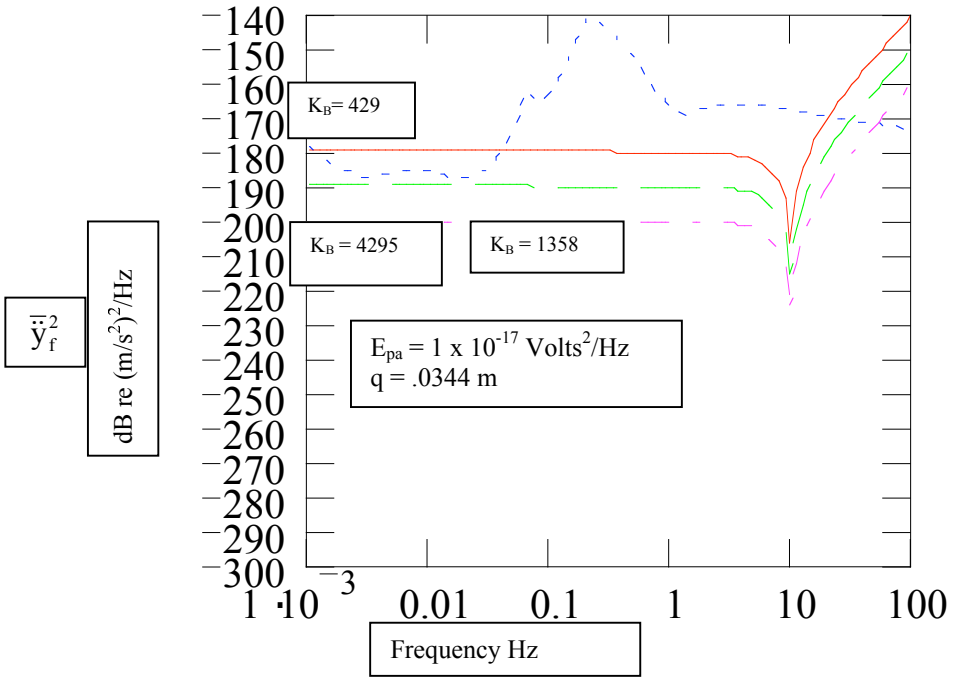


Figure 4. Epa noise threshold vs. K_B.

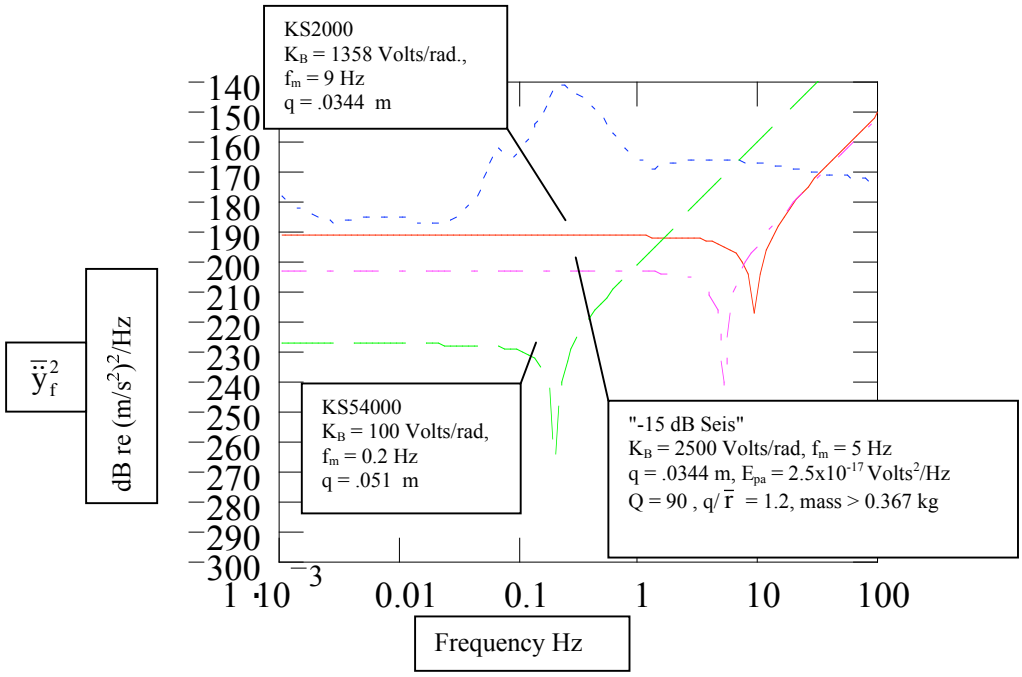


Figure 5. Theoretical E_{pa} noise threshold of KS54000 and KS2000 suspensions.

Based on the equations underlying the above figures, a CAD feasibility model indicates that the instrument can be housed in a 4-inch diameter housing that is approximately 48-inches long. This concept is shown in Figure 6.

One of the requirements may be to install this new seismometer into existing KS54000 boreholes. The larger diameter accessories that are shown at either end will allow installation in larger boreholes. Without these accessories the seismometer will fit into a 6-inch casing or possibly a 5 3/4 inch casing.

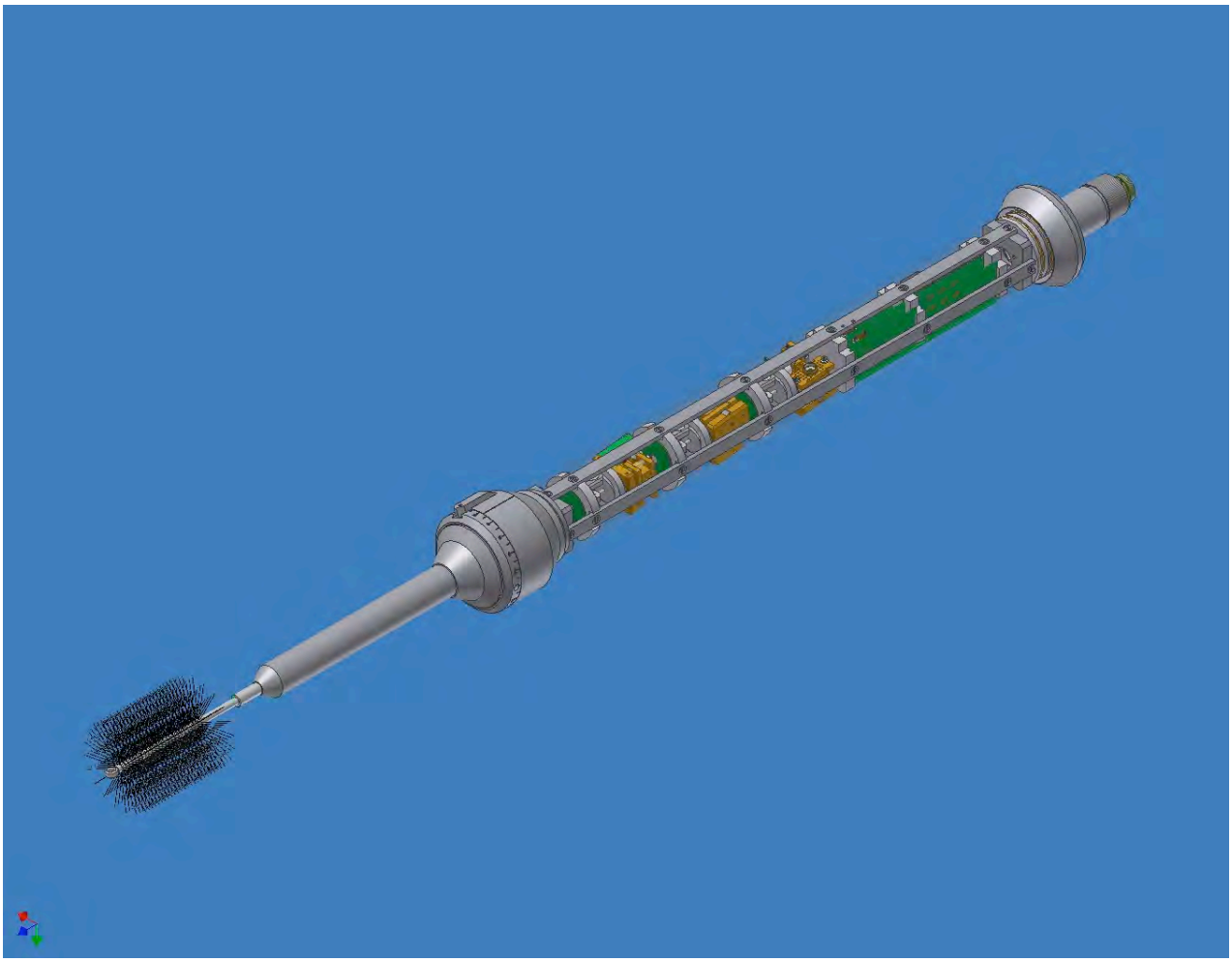


Figure 6. Model for estimating size and configuration.

CONCLUSIONS AND RECOMMENDATIONS

One of the questions to be considered in this preliminary study was to determine if it was feasible to achieve a seismometer self noise level at least 6 dB below the USGS low noise model over the frequency range of 0.2 to 16 Hz. A second question was could it be done with one instrument or would two instruments be required. Based on this preliminary theoretical study, only one instrument will be required. The requirements for the electronics, suspension, and basic sensors can be achieved with current technology based on the experience with and the history of the KS36000, KS54000 and similar designs.

It is recommended that Phase II of the SBIR proceed with the development and testing of prototypes.

DEVELOPMENT OF A NETWORK DATA SET FOR EVALUATING DETECTION AND NETWORK PROCESSING PERFORMANCE

Benjamin C. Kohl, Theron J. Bennett, István K. Bondár, Brian W. Barker, Walter C. Nagy, Colin Reasoner, Jeffrey A. Hanson

Science Applications International Corporation

Sponsored by Army Space and Missile Defense Command

Contract No. DASG60-03-C-0009

ABSTRACT

The assessment of signal detectors and/or network based event detection, association and characterization algorithms is typically quantified in terms of probability of detection and false alarm rates or other similar metrics. This relies on the use of a data set in which both the desired "actual" signals and presumed false "noise" detections have been identified and characterized.

We have been developing a framework for constructing a data set comprised of waveforms from well-recorded high signal-to-noise ratio (SNR) events, scaled down to various sizes and embedded in clean background noise. The noise is being carefully constructed to be devoid of signals, based on the execution of standard signal detectors and by excluding time-windows of phase arrivals predicted from global, regional and local bulletins. Available noise segments are being merged into continuous blocks of several days of noise data while maintaining the basic attributes of target time period (overall noise level, seasonal, weekly and diurnal variations) and consistency with historically established noise characteristics for each station. The construction of the noise data set is iterative with interactive review of the resulting waveforms.

To provide a utility for assessing the performance of algorithms to properly detect and characterize low SNR signals and small events (e.g. sub-kiloton tamped explosions or fully decoupled cavity explosions), we are theoretically scaling data observed from a variety of large events to approximate the signals expected from smaller events. We are using a frequency-dependent scaling methodology based on the spectral ratio of the source function of the small event divided by the large event. For explosions the source spectral ratio is initially based on the Mueller/Murphy explosion source model. For earthquakes, we are developing similar methods utilizing simplified earthquake scaling models and regionally varying empirically derived sets of source spectral ratios, based on observations from earthquake mainshock/aftershock sequences. We are embedding the scaled earthquake and explosion signals into the clean background noise with distributions of local, regional and teleseismic earthquakes designed to simulate the overall detection rate observed at each of the stations. The framework we have developed allows for the embedding of events in a customizable manner to allow for the construction of various scenarios, e.g., the detection of a small explosion during an earthquake aftershock sequence. Initially we are emphasizing the construction of data sets of events and stations in southern Asia. The resulting data sets are expected to provide a valuable resource for testing and quantifying sensitiveness of signal detection and network processing at low magnitude levels and for evaluating monitoring scenarios that cannot be assessed using currently available network data.

OBJECTIVE

Practical implementations of new or improved monitoring technologies such as signal detectors, network phase association algorithms, location and event identification methods rely on quantitative assessments of performance such as probabilities of detection and false alarm rates. These types of performance metrics are typically obtained through experiments using data sets constructed from archival data records. Such experimental data sets implicitly contain signal and event recordings from numerous unknown sources (e.g. small earthquakes not listed in published local, regional or teleseismic bulletins), potentially contaminating the data set and complicating the interpretation of processing results. Furthermore, they are only representative of the event characteristics and network and station configurations in use at the time of archival data recordings. In particular, nuclear explosions from only a few isolated locations have been recorded on historical sensor networks.

Our objective is to develop an experimental network data set in which target signal and event detections are known, as well as having realistic distributions of false or "clutter" detections and background noise characteristics. We are utilizing a variety of actual nuclear explosion recordings and developing scaling and transformation algorithms to yield surrogate data for nuclear explosions originating at new locations in southern Asia. This will allow for experiments involving low threshold nuclear explosion waveform records under realistic background noise and seismicity conditions.

RESEARCH ACCOMPLISHED

The basic framework for the comprehensive network data set is depicted in Figure 1. It depends upon taking waveforms from well-recorded high signal-to-noise ratio (SNR), scaling them down to various sizes and embedding them in clean background noise. We are embedding scaled earthquake signals with distributions of local, regional and teleseismic earthquakes designed to simulate the overall seismicity and detection rates observed at each of the stations. To facilitate realistic assessments of new or improved monitoring technologies we are scaling and embedding nuclear explosion waveform recordings at low thresholds.

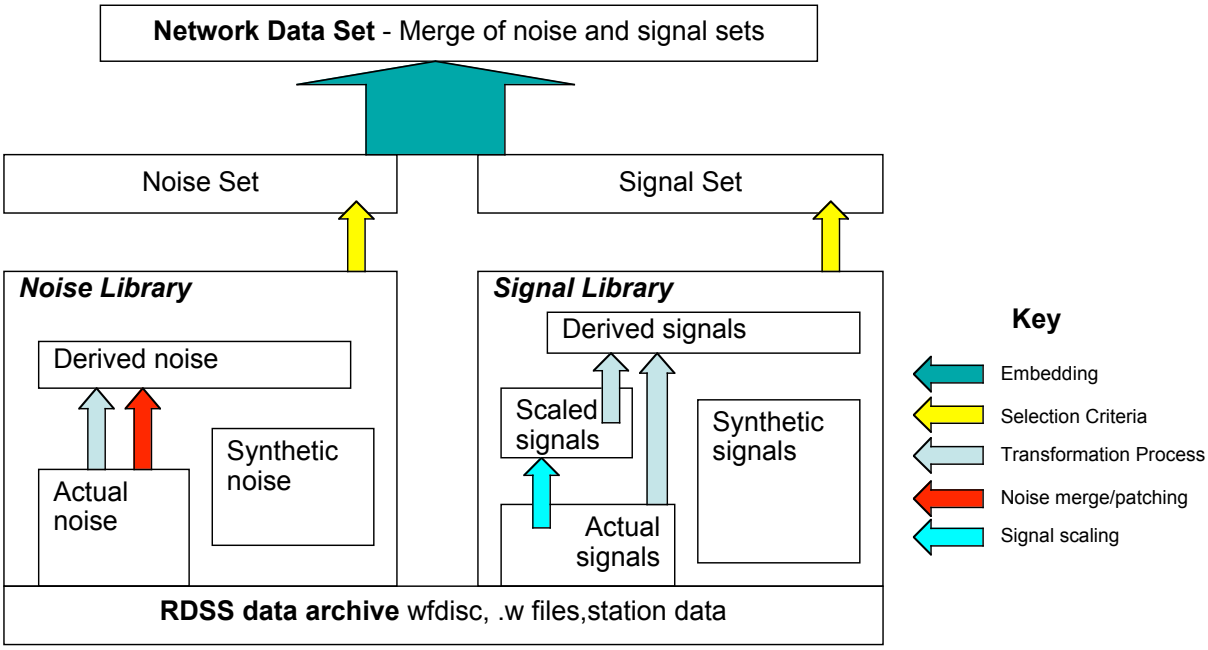


Figure 1. Basic framework for constructing a network data set suitable for systematic testing and evaluation of new or improved monitoring technologies. The data set builds upon the extensive archive of waveform data available through SMDC's Research and Development Support Services (RDSS) database. Scaled signals from a variety of sources (potentially including synthetics) are being embedded into clean background noise to construct a data set in which target and clutter detections have been characterized.

Initially we are emphasizing the construction of a data set of events and stations in southern Asia. Figure 2 shows the target area and key regional stations. To provide utility for assessing the performance of algorithms to properly detect and characterize low-SNR signal and small events, we are scaling and embedding nuclear explosion waveform data to simulate low-yield explosions from four sites in southern Asia marked in Figure 2 with blue squares. Two of the sites are known nuclear test sites (the Indian test site, and Lop Nor China) while the remaining two sites are illustrative locations for assembling surrogate nuclear explosion events. The basic methodology being used for constructing the low-yield explosion surrogate data at the sites marked in Figure 2 is readily applicable to other sites or regions.

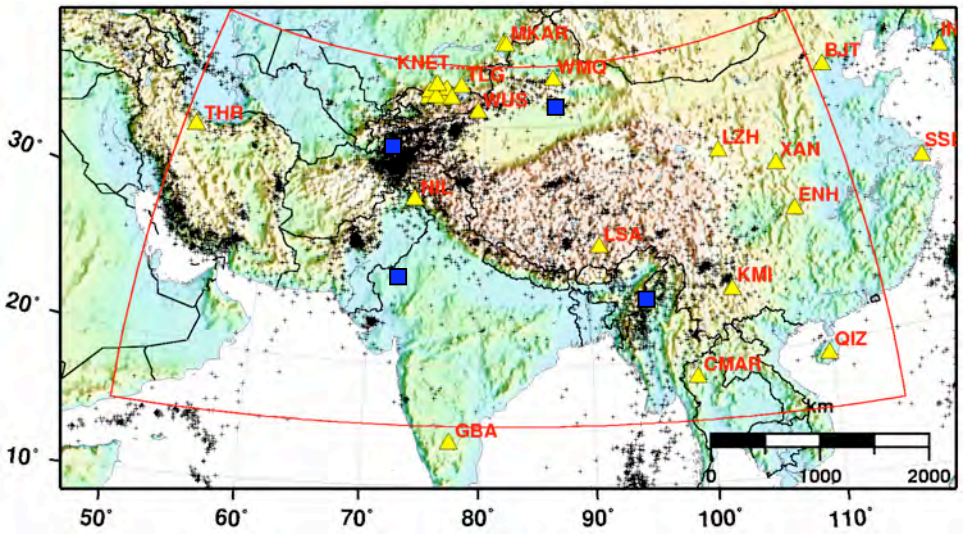


Figure 2. Area and stations in represented in network data set. While the framework we are developing is applicable to other areas, to date we have focused on southern Asia. The background seismicity is shown with "+" symbols, while the locations of hypothetical scaled low yield nuclear explosions are marked with blue squares.

Background Noise Library

The simulation of scenarios of nuclear monitoring interest requires relatively long, continuous noise waveforms spanning several days. However, because of the background seismicity of the earth, such long quiet periods do not normally occur. Figure 3 shows that for an 8-day period in 1998, detection-free intervals rarely exceeded 10 minutes at the CMAR array.

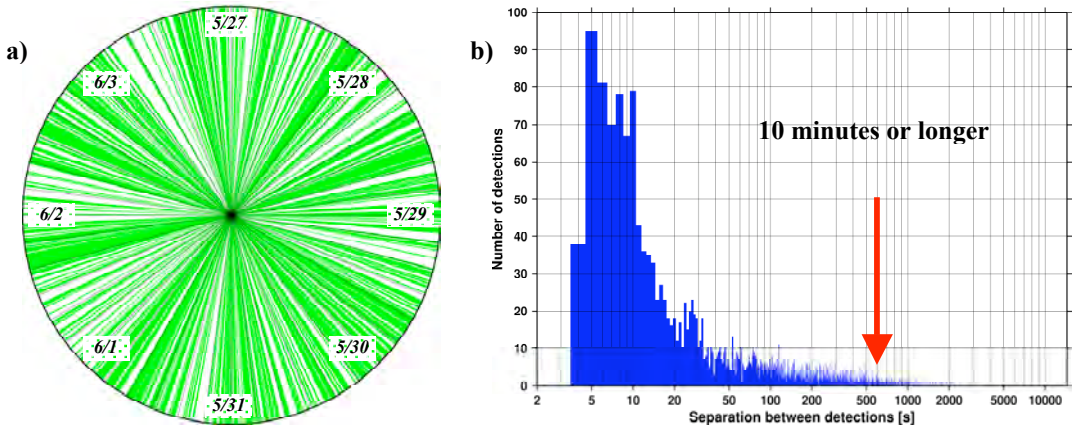


Figure 3. a) Detection-free segments (green) of 10 minutes or longer at CMAR between 5/27/1998 and 6/4/1998. b) Distribution of the lengths of detection-free waveform segments. Long continuous blocks of detection free segments are not readily available; hence we are developing a merging technique that allows numerous detection free segments to be combined into a single continuous trace.

Figure 4 illustrates the procedure of merging noise segments to produce a continuous waveform, devoid of any signals. The interpolation and tapering between the noise segments is carried out in the frequency domain to avoid abrupt changes in the frequency content of the resulting waveform. The final derived waveform is subject to further quality assurance procedures (e.g. no spurious detections are generated at segment boundaries, the spectrogram does not show discontinuities, etc.) before it is used as background noise for embedding events

To provide a realistic background for the embedding of scaled signal data, the merging approach must accommodate the variability of noise conditions observed at each station. We are currently engaged in a number of complementary efforts to characterize seismic and infrasonic noise conditions (e.g. Bowman et al., 2004). Figure 5 illustrates that noise conditions at a station can dramatically change from season to season. The waveform merging procedures ensure the preservation of seasonal and diurnal characteristics in the target, derived noise waveform, as well as the noise levels relative to high and low noise conditions. The low, high and average noise models for a given station build upon the noise characterization efforts of Bahavar and North (2002).

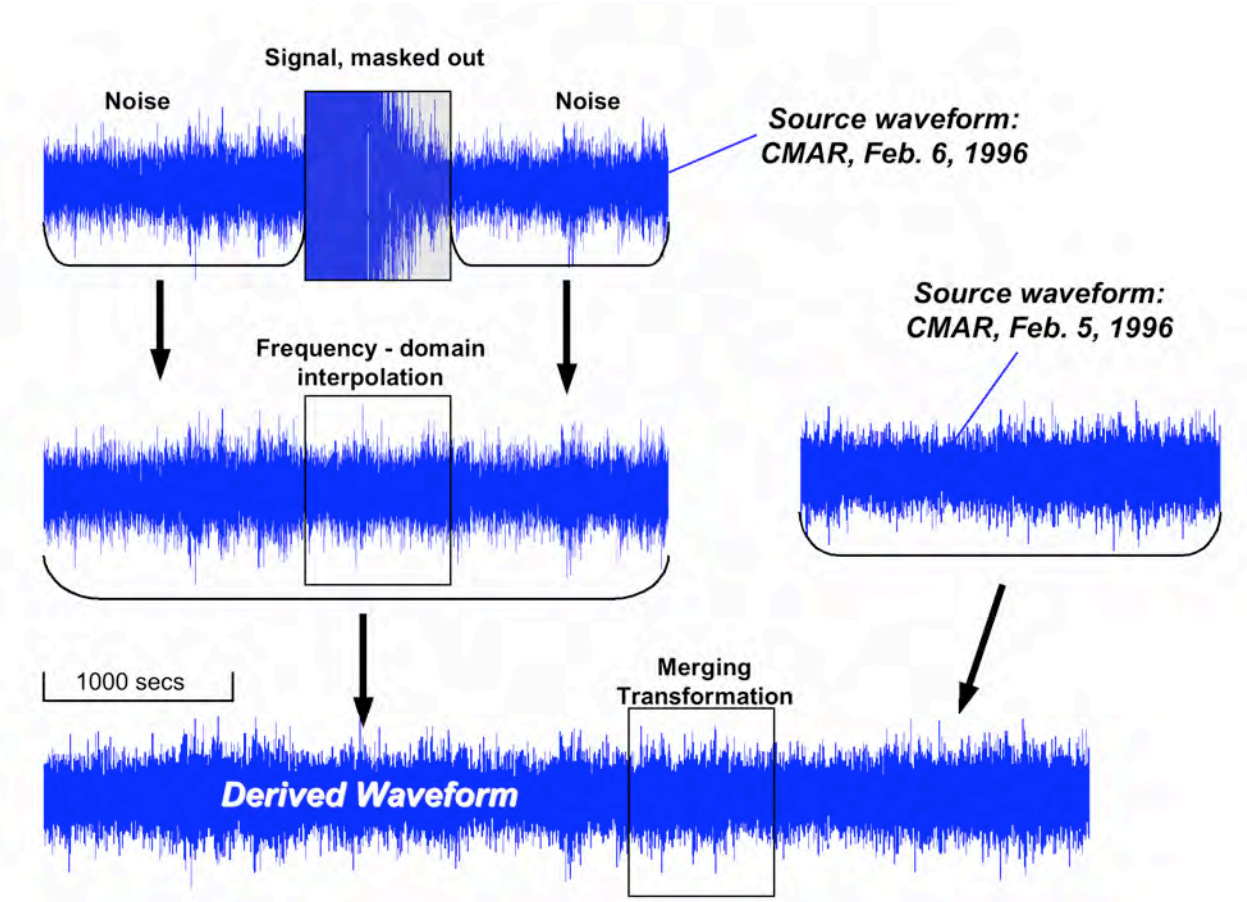


Figure 4. Illustration of the procedure of merging noise segment to produce detection free continuous background noise waveforms. In this example, two waveforms segments and two transformation operators are utilized to form a single continuous waveform trace devoid of signals. In the first waveform (upper-left) an observed signal is first masked and then replaced with a noise segment interpolated from the neighboring noise records. A second segment (upper-right), from a different day but with compatible spectral characteristics is merged with the main segment to extend the resulting derived waveform. These types of operators are repeatedly utilized to form a detection free background noise data set, suitable for embedding scaled signals.

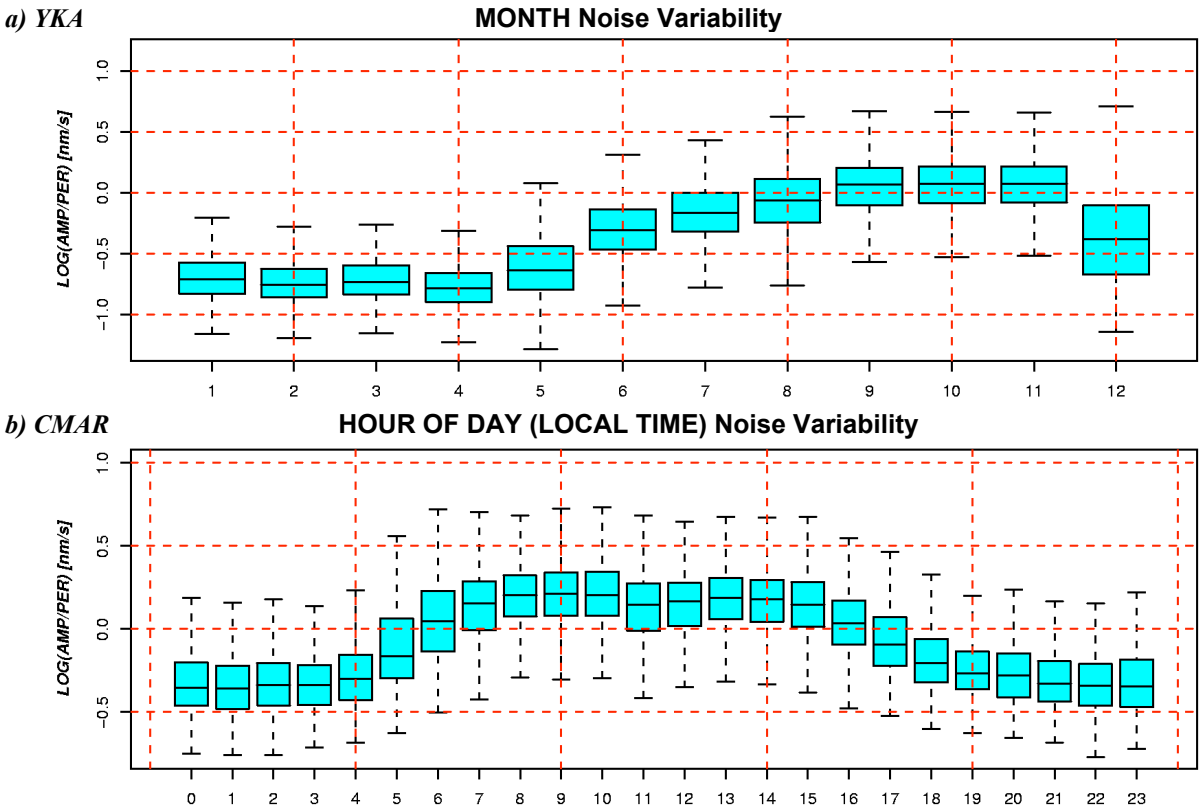


Figure 5. Seasonal variations of noise levels at YKA and diurnal variations at CMAR. The boxes show the median (horizontal line) and outline the upper and lower quartiles of the noise levels. The whiskers extend about 2.5 times the standard deviation. The noise level at YKA (panel a) dramatically decreases during the winter months. Noise levels at CMAR (panel b) show increased levels during the day and decreased levels at night. The construction of the clean background noise set retains these basic features for all stations.

Explosion Sources and Scaling

The expected ground motion time history for a small explosion can be determined from the observed ground motion from a large explosion at the same station if the spectral ratio of the two seismic source functions can be estimated. This approach was successfully applied to scale a number of large nuclear explosions at Lop Nor (Kohl et al. 2002), where we approximated the source spectral ratio using the well-documented Mueller/Murphy explosion source model (Mueller and Murphy, 1971). As a test of the applicability of this methodology, we first theoretically scaled selected observed regional data from the larger of two reference explosions (i.e. May 15, 1995, m_b(REB) = 5.73) to the source conditions of the smaller reference explosion (i.e. July 29, 1996, m_b(REB) = 4.71) and compared the resulting synthetics with the corresponding observed data from the smaller explosion. The results for station MAK ($\Delta \approx 7°$) are shown in Figure 6, where it can be seen that the theoretical scaling very accurately accounts for the observed frequency dependent changes in waveform characteristics, as evidenced by the pronounced change in the L_g/P amplitude ratio between the larger and smaller explosions.

Our ability to quantify network monitoring capability in the region of interest is limited because past nuclear explosions have occurred at only a few sites and have been recorded at just a few regional monitoring stations. In order to develop a more representative data set for the region, we are investigating the possibility of using "surrogate" explosions and associated "surrogate" regional recordings to simulate what might be expected if an explosion occurred at a new, uncalibrated source location and was recorded by existing, or possibly future, regional recording stations. For example, if a nuclear explosion were to occur in the Pamir/Hindu Kush region and was recorded by stations at regional distances, it might be expected that the characteristics of those recordings would be

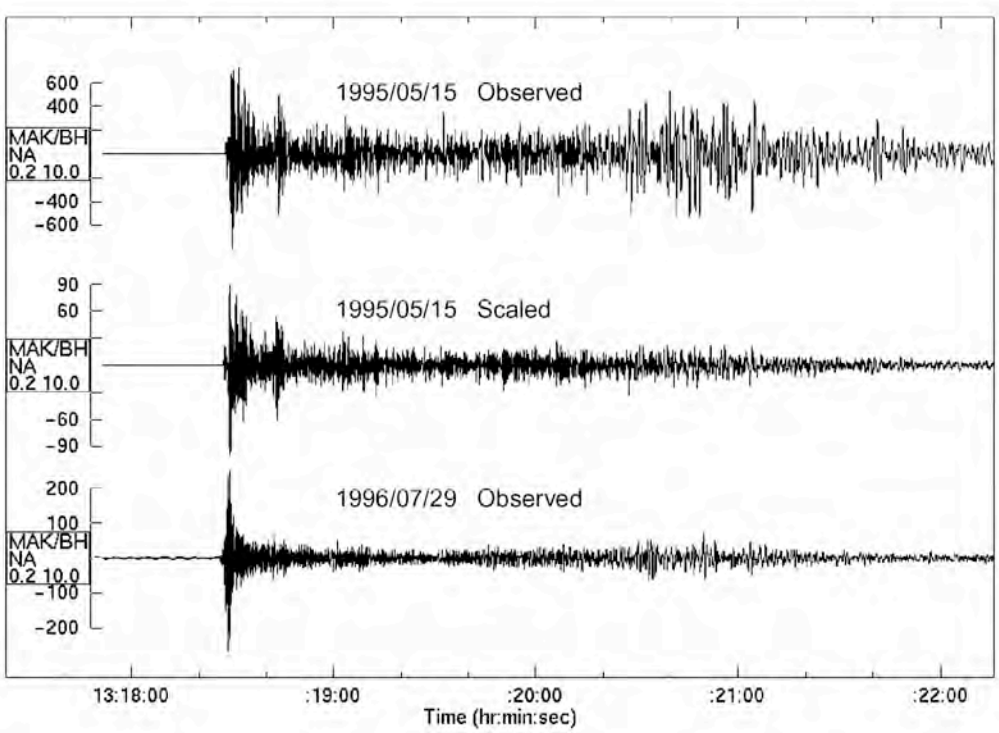


Figure 6. Comparison of the station MAK seismogram obtained by scaling the observed data from the larger May 1, 1995 (m_b= 5.73) reference Lop Nor explosion (top) to the source conditions of the smaller July 29, 1996 (m_b= 4.71) reference Lop Nor explosion (center) with the corresponding observed July 29, 1996 data (bottom).

similar in some ways to the regional signals that have been recorded from previous explosions that have occurred in the region (i.e. explosions at the Lop Nor, India and Pakistan test sites or Soviet PNE's). If we accept some uncertainty, then we can use these prior regional explosion recordings to assess the detection, location and identification performance of a regional network in monitoring a hypothetical future explosion.

Figure 7 shows a sample of recorded regional and far-regional signals from 5 previous explosions of similar magnitude that have occurred in the region, plotted in order of increasing distance. These waveforms represent the general characteristics to be expected at these distances from explosions occurring in the region. At the closer stations, there is abundant broadband S-wave energy which in some cases is equal in size to the P-wave energy. At greater distances, the P-wave energy begins to dominate until the point where the broadband S-wave energy disappears. In a general sense there does not seem to be any particular dependence of these characteristics on the individual source regions. So, if we place our surrogate explosion of an assumed yield at a given location, we can select from this list of recordings, scale the waveforms according to our explosion scaling laws, and "create" the network that we want to have record this simulated explosion.

We are also exploring ways of simulating small station distance changes by applying time and frequency corrections, in order to produce waveforms at distances where none currently exist. If we can accept even more uncertainty, the library of regional explosion signals could be expanded to include explosions recorded from other, more diverse test sites (e.g. STS, NZ, NTS...). It should be noted that other researchers (e.g. Fisk et al., 2000) have, in the course of developing regionalized discriminants, compared nuclear explosion waveform data from a variety of test sites. Clear differences due to variability in attenuation models and other factors have been observed. This suggests that the development of surrogate waveform explosion data at new sites can at best be considered representative of an event recorded in an uncalibrated region. It should not be considered a simulation of precisely what would be expected to be recorded from that site.

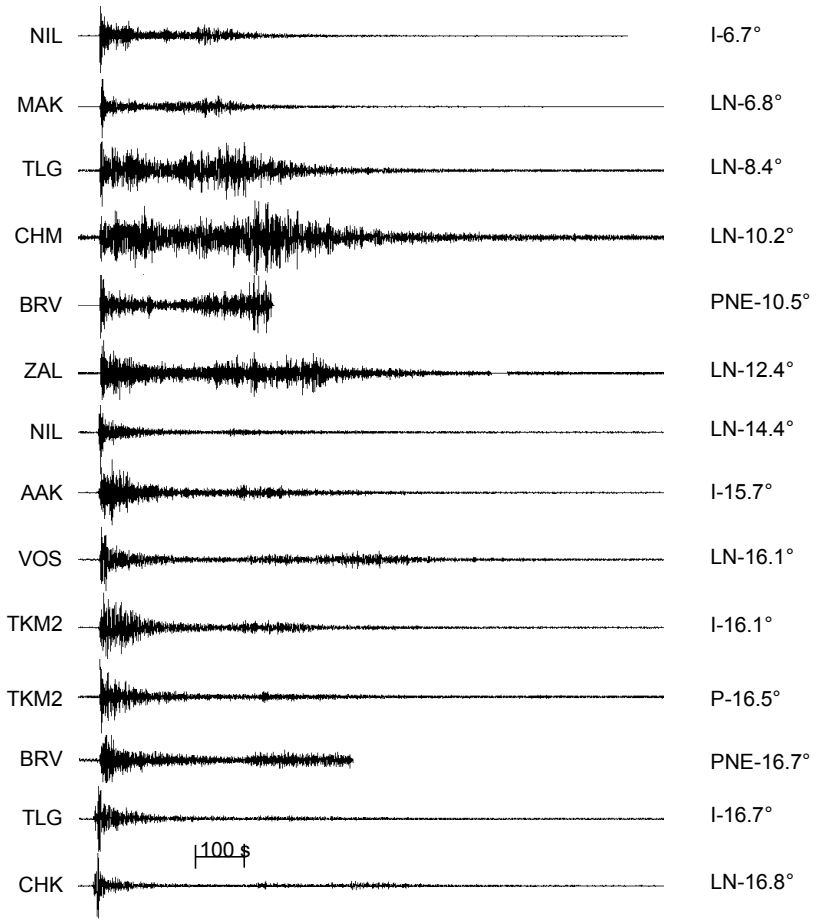


Figure 7. Regional recordings from the Pakistan explosion of 5/28/98 ('P', REB m_b = 4.8), the Indian explosion of 5/11/98 ('I', REB mb = 5.2), the Soviet PNEs of 8/15/73 and 4/11/72 ('PNE', m_b = 5.3, 4.9 respectively) and the Lop Nor explosion of 7/29/96 ('LN', m_b = 4.8).

Earthquake Sources and Scaling

To provide realistic conditions for testing and evaluating new monitoring technologies, the network data set is being constructed to retain a reasonable representation of background clutter signals originating from earthquakes. To this end, we have been reviewing the natural seismicity of the region with the intent of abstracting a representation of the relative level and frequency of natural earthquake activity that will affect seismic monitoring.

The region encompasses several rather active zones including (1) the Pamir-Hindu Kush area, (2) India-Bangladesh-Myanmar border area, (3) Yunan-Szechwan China area, (4) southern Iran, (5) southwest India (Bhuj), and (6) Turkmenistan, as well as several intervening relatively quiet areas. To analyze the natural seismicity, we binned the overall region into a series of 5°-x-5° blocks and used a combination of the Reviewed Event Bulletin (REB) results for the time period 1994/10/19-2001/09/01 as well as published information on earthquake recurrence rates for Flinn-Engdahl (FE) seismic areas (Kagan, 1997). For each bin in our regional grid, we assigned an FE designation and used the published recurrence rates to determine the slope (b) and the REB results to set the level of activity (a) for cumulative earthquake recurrence relations represented by

$$\text{Log } N = a - b\, m$$

where N is the number of earthquakes per year exceeding magnitude m. Figure 8 shows the number of earthquakes ($m_b \geq 3$) expected per year for each element in our grid covering southern Asia. The predicted seismicity levels generally agree with historical activity and published information for the region, i.e. high levels of activity in bins corresponding to most active zones.

The recurrence relations define distribution functions for natural seismicity in southern Asia. We are using these distributions to define expected event magnitudes from earthquakes in the region. That is, for each zone in Figure 8 we have identified a representative large high-SNR "designated" earthquake and have derived the projected number of events at a particular magnitude expected to occur in that zone within a given time period of interest (e.g. 2 weeks). We are constructing the network data set by scaling and embedding the representative earthquake to the projected magnitudes and distribution applicable to that zone, and repeating this for all relevant zones in Figure 8. By tracking the precise embedding times of the signals, the network data set implicitly includes a full inventory of a realistic distribution of real and clutter (e.g. small earthquake) signals. This will facilitate signal detection and network processing experiments resulting in rigorous estimates of probabilities of detection and false alarm rates.

Latitude Range \ Longitude Range	50-55	55-60	60-65	65-70	70-75	75-80	80-85	85-90	90-95	95-100	100-105	105-110	110-115
40-45	14.7	0.38	4.16	9.54	18.6	44.6	35.4	23.9	2.95	1.62	2.57	3.63	14.4
35-40	25.1	24.5	5.37	120.	645.	281.	19.4	53.7	17.3	23.9	12.3	5.37	4.67
30-35	30.1	32.3	26.3	199.	169.	77.6	34.6	120.	51.2	41.6	24.5	5.37	0.93
25-30	158.	87.0	11.7	371.	11.4	10.7	33.8	79.4	70.7	85.1	107.	10	0.93
20-25	0.	1.14	4.16	10.7	43.6	2.18	3.80	3.80	125.	75.8	21.3	3.31	2.18
15-20	1.69	6.76	0.56	0.	5.88	2.69	0.	1.62	13.4	16.9	3.63	1.81	1.20

Figure 8. Number of events per year of $m_b \geq 3.0$ for 5°-x-5° blocks in southern Asia, based on recurrence relations. This distribution function is being used to define the target magnitudes, and how often representative earthquakes are scaled and embedded in the background noise for each zone.

Key to this approach is the scaling of earthquake data. For source scaling we are using, amongst others, a Brune ω^2 source model (Brune, 1970; 1971) with some modifications including those of Hanks and Kanamori (1979) and source dimension relations determined by Wells and Coppersmith (1994) for continental earthquakes. Figure 9 (left) shows the P-wave displacement amplitude spectra predicted by these scaling models over the magnitude range from 4.8 to 2.8, and we show on the right the relative spectral amplitudes as a function of frequency for scaling 4.8 magnitude earthquakes to the lower magnitudes based on this model. Over this magnitude range, the model predicts significant differences over frequency bands from just below 1 Hz to frequencies in the range 10-20 Hz, with the two corners in the right figure representative of the magnitudes of the two earthquakes (i.e. in scaling larger events the lower corner would be shifted to the left).

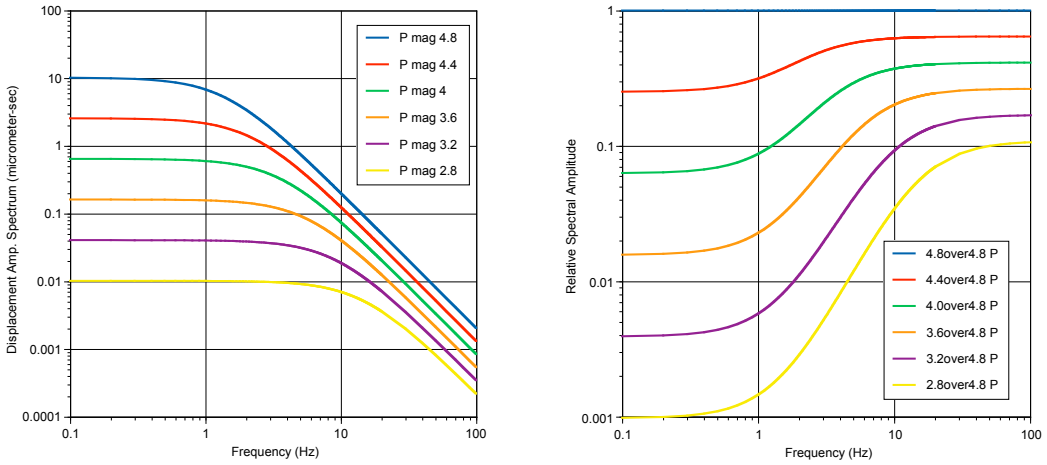


Figure 9. Frequency-dependent earthquake source scaling relationships based on Brune model and Wells-Coppersmith relations for source dimensions of continental earthquakes

Our quasi-empirical approach involves developing relative spectral amplitude scaling relations from the theoretical models and validating their applicably by comparing with empirical spectral ratios derived from sequences of well-recorded events (e.g. large aftershock/mainshock pairs). Recognizing that the detailed earthquake source characteristics depend on variables such as fault plane geometry and dynamic stress drop, in addition to the long-period source size, which is usually quantified as the earthquake moment, we expect different models to be applicable under different conditions. Hence we maintain flexibility and employ a quasi-empirical approach, including models first demonstrated for earthquakes in the Lop Nor region (Kohl et al. 2002).

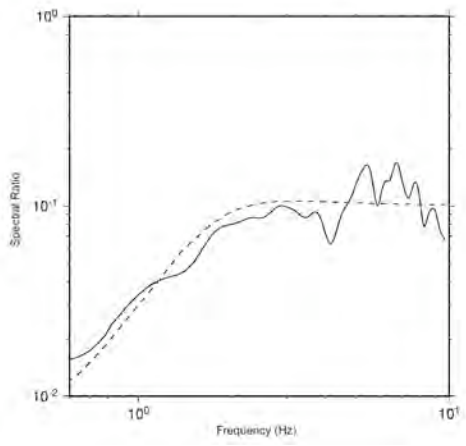


Figure 10. Average observed and model predicted source spectral ratios for the Lop Nor earthquakes of 1999/01/27 and 1999/01/30.

For example, we computed the average P-wave spectral ratio between two reference earthquakes at Lop Nor (i.e. 1999/01/30, m_b(REB) = 5.34 and 1999/01/27, m_b(REB) = 3.93) using data recorded at a number of regional stations. We then fit the average P-wave spectral ratio to a simplified one-dimensional explosion source model. The resulting fit to the average source spectral ratio for the 1999/01/27 and 1999/01/30 earthquakes is shown in Figure 10, where it has been assumed that the ratio of the source corner frequencies scales as the cube-root of the ratio of the two earthquake moments. The simple source model fits the observed spectral ratio quite well over the frequency range extending from about 0.5 to 10 Hz.

The scaling model was evaluated by scaling the observed data from the larger earthquake (1999/01/30) to the source conditions of the smaller earthquake (1999/01/27) and then comparing the results with corresponding observed broadband data at selected regional stations. The results for station MAK are shown in Figure 11 where it can be seen that the adopted scaling model accurately accounts for the observed frequency-dependent changes in waveform characteristics, as evidenced by the pronounced change in the Pn/Lg amplitude ratio between the larger and smaller earthquakes. In this case, where the range in amplitude scaling is about a factor of 50, the broadband amplitude level of the theoretical synthetic matches that of the corresponding observed seismogram to within about a factor of 1.5 at this station. We conclude that this model adequately accounts for frequency-dependent effects of source size on the seismic data observed from these Lop Nor earthquakes.

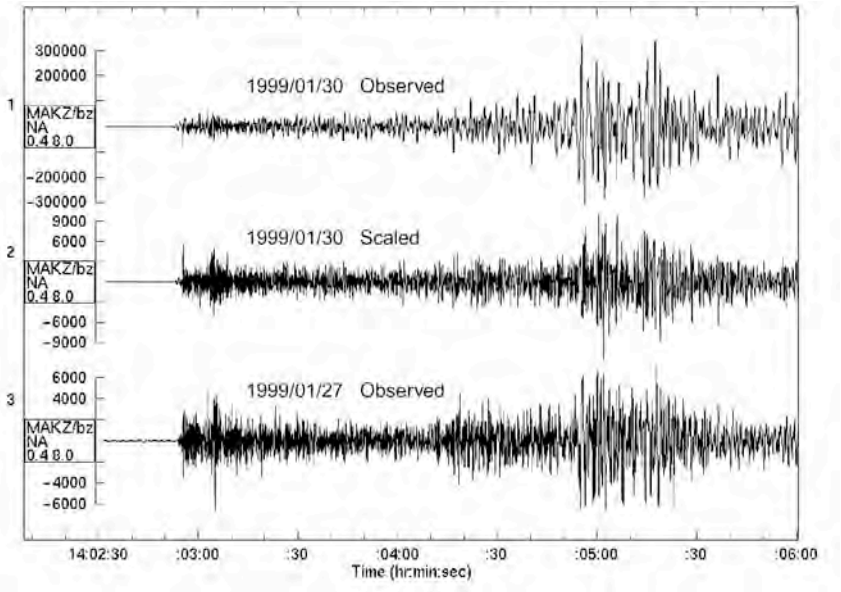


Figure 11. Observed MAK data from a 1999/01/30 (m_b = 5.34) Lop Nor earthquake (top) compared to the earthquake scaled to m_b = 3.93 (center), and compared to observed MAK recording from the 1999/01/27 (m_b = 3.93) event (bottom).

CONCLUSIONS AND RECOMMENDATIONS

We are developing a network data set comprised of actual and surrogate nuclear explosion waveform data to simulate the realistic monitoring conditions expected for southern Asia. By using an approach that involves embedding scaled nuclear explosion waveform data, as well as scaled earthquakes, the data set includes a complete inventory of event and signal attributes over a wide range of magnitude thresholds. Through the incorporation of surrogate nuclear explosion waveform data, the data set will be useful for evaluating monitoring scenarios involving new locations and the latest sensor systems, independent of the availability of historical nuclear explosion data records.

This data set will support a variety of experiments of monitoring technologies focused on improved signal detection, network association and identification capabilities. Through the use of the network data set, with its controlled content including only known scaled explosions and earthquake signals embedded in detection-free clean background noise, rigorous performance metrics will be readily measured. Thus the resulting data sets are expected to be a valuable resource for testing and quantifying the performance of signal detection and network processing at low magnitude levels and for evaluating monitoring scenarios that cannot be assessed using currently available network data.

REFERENCES

Bahavar, M. and R. North (2002), Estimation of background noise for International Monitoring System seismic stations, *Pure Appl. Geophys.,* 159, 911-944.

Bowman, R., E. Baker and M. Bahavar (2004), Infrasound station ambient noise estimates, *in Proceedings of the 26th Seismic Research Review: Trends in Nuclear Explosion Monitoring*, Orlando, FL (Sep. 21-23, 2004).

Brune, J. (1970), Tectonic stress and the spectra of seismic shear waves from earthquakes, *J. Geophys. Res.* 75, 4997-5009.

Brune, J. (1971), Correction*, J. Geophys. Res.* 76, 5002.

Fisk, M., S. Bottone, R. Carlson, H. Gray and G. McCartor (2000), Event Characterization Development and Analysis at the Prototype IDC, *DTRA Technical Report*, DTRA-TR-99-5.

Hanks, T. C., and H. Kanamori (1979). A moment magnitude scale, *J. Geophys. Res*. 84, 2348-2350.

Kagan, Y. Y. (1997). Seismic moment-frequency relation for shallow earthquakes: Regional comparison, *J. Geophys. Res.* 102, 2835-2852.

Kohl, B., R. North, J. R. Murphy, M. Fisk and G. Beall (2002), "Demonstration of Advanced Concepts of Nuclear Test Monitoring Applied to the Nuclear Test Site at Lop Nor, China", *in Proceedings of the 24th Seismic Research Review – Nuclear Explosion Monitoring: Innovation and Integration,* LA-UR-02-5048, Vol. 1, pp 302 – 312.

Mueller, R. A. and J. R. Murphy (1971), Seismic characteristics of underground nuclear detonations. Part I. Seismic spectral scaling, *Bull. Seism. Soc. Am*. 61, 1975.

Wells, D. L., and K. J. Coppersmith (1994), New empirical relationships among magnitude, rupture length, rupture width, rupture area, and surface displacement, *Bull. Seism. Soc. Am*. 84, 974-1002.

SEISMIC SENSOR COMPONENT EVALUATION

Richard P. Kromer and Toby O. Townsend

Sandia National Laboratories

Sponsored by National Nuclear Security Administration
Office of Nonproliferation Research and Engineering
Office of Defense Nuclear Nonproliferation

Contract No. DE-AC04-94AL85000

ABSTRACT

Sandia National Laboratories tested and evaluated seismic sensors from Geotech Instruments, LLC (Garland, Texas) and Güralp Systems Limited (GSL) (Aldermaston, United Kingdom). The sensors evaluated were Geotech model GS21A, a single component short-period vertical borehole seismometer and GSL model CMG-3V, also a single component short-period vertical borehole seismometer.

Both the Geotech GS21A and the Güralp CMG-3V tests included side-by-side testing to determine:

- Sensor self noise
- Seismometer response
- Seismometer sensitivity
- Calibration capability

Response and self-noise mathematical models were developed.

OBJECTIVE

Introduction

Sandia National Laboratories tested and evaluated seismic sensors from Geotech Instruments, LLC (Garland, Texas) and Güralp Systems Limited (GSL) (Aldermaston, United Kingdom) for possible use in the United States Atomic Energy Detection System (USAEDS). Testing was performed using the system requirements for the USAEDS. Since some USAEDS seismic stations may be included in the International Monitoring System (IMS), some testing was performed using IMS requirements. The sensors evaluated were Geotech model GS21A, a single component short-period vertical borehole seismometer and GSL model CMG-3V, also a single component short-period vertical borehole seismometer.

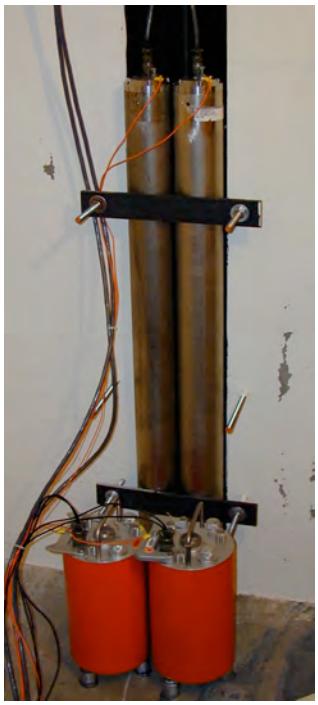
Evaluations Performed

Tests included side-by-side coherence analysis to determine sensor self noise, seismometer response, seismometer sensitivity, and calibration capability. The results of these evaluations were compared to relevant AFTAC and IMS application requirements or specifications.

RESEARCH ACCOMPLISHED

Geotech GS21A Short-period Vertical Borehole Seismometer

Testing of the GS21As was performed during January-February 2004, at the Sandia National Laboratories Facility for Acceptance, Calibration and Testing (FACT) Site, Albuquerque, NM. Two GS21A seismometers were provided for testing; serial numbers 273 and 302. Two GS13 seismometers were positioned as references. Data were recorded on a Quanterra Q4128 data logger with external preamplifiers.



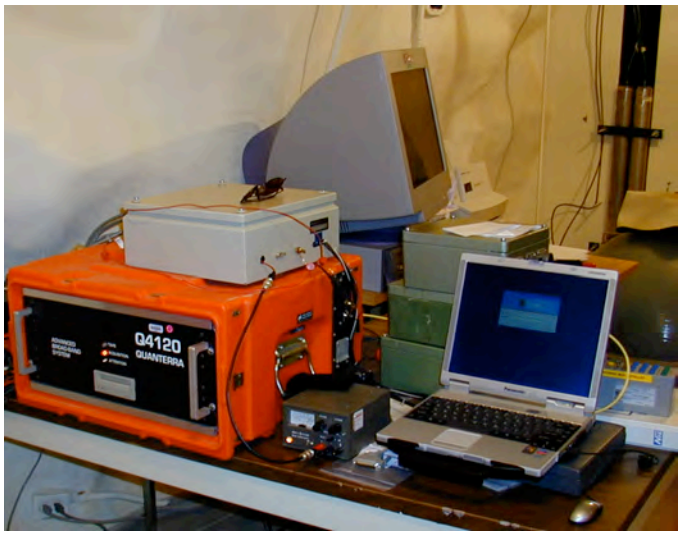


Figure 1. Geotech GS21A Installation

The GS21A seismometers were configured as single vertical axis, short-period borehole seismometers. The sensitivity of the GS21A's was 1311 v/m/s (1834.7 v/m) at 1 Hertz.

The following tests were conducted on the GS21As. This is the basic set of tests as outlined in the Sandia Ground-based Monitoring R and E Technology Report: *Test Plan for the Evaluation of Seismic Sensors for Ground-based Geophysical Monitoring, 3 March 2003*.

1. **Seismic Sensor Characterization**
   1.1 Response Model Development

2. **Seismic Sensor Signal Performance Tests**
   2.1 Seismic Sensor Self-Noise (SSSN)
   2.2 Seismic Sensor Response Verification (SSRV)

Geotech GS21A SP Seismometer Response Model Development

The GS21A response was developed using the GS21A response parameters measured by Geotech and the Sandia Seismometer Response Model software. The Geotech GS21A has the response indicated in the figures below.

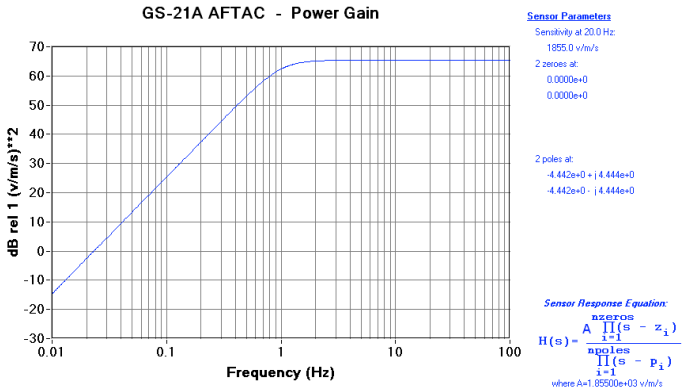


Figure 2. Geotech GS21A Gain Plot

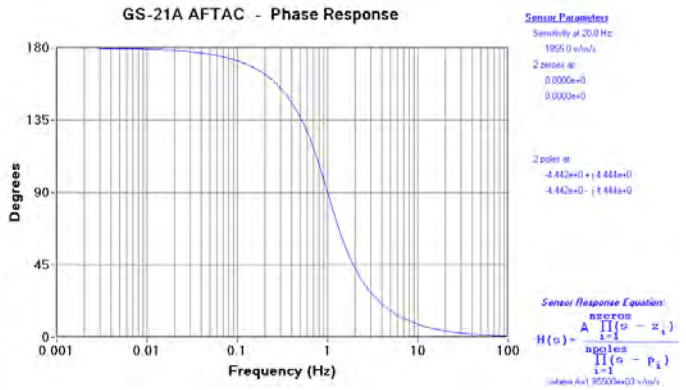


Figure 3. Geotech GS21A Phase Plot

A magnet-coil, spring-mass passive seismometer can be characterized by measuring specific seismometer parameters and calculating others. Characterization of a GS21 seismometer is outlined in the GS21 Operation and Maintenance Manual. Parameters that need to be determined include main coil resistance, spring-mass natural frequency, main coil generator constant, seismometer open circuit damping, main coil critical damping resistance and calibration coil motor constant.

Specific GS21A Seismometer Response

Purpose: The purpose of the seismometer response test was to characterize the overall response of the GS21A seismometer.

Configuration: Measure the GS21A response parameters using procedures from the GS21 Operation and Maintenance Manual or use the Geotech Seismometer Calibration data sheets.

Evaluation: A GS21A response model was developed using the response parameters measured by Geotech and the Sandia Seismometer Response Model software. A nominal GS21A response model was calculated. Damping resistance for 0.707 damping was calculated. Termination resistance for the DB24 ITN test was determined from the parallel combination of the coil resistance and 0.707 damping resistance.

Results: The calculated response for the two GS21As under test is shown in the figure below.

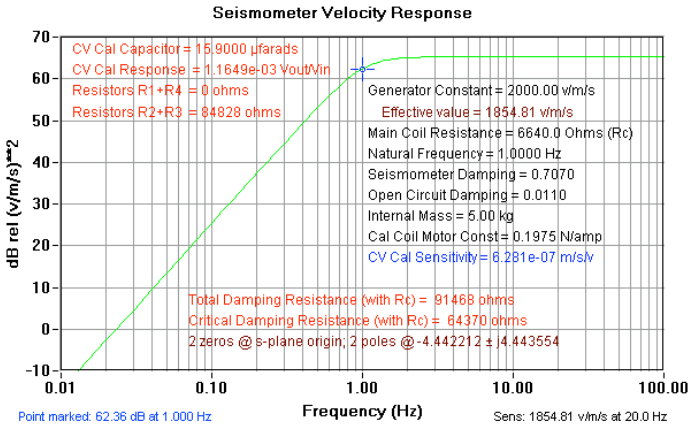


Figure 4. Geotech Specific GS21A Response Plot

GS21A Seismic Sensor Self-Noise (SSSN)

Purpose: The purpose of the seismometer self-noise test is to determine the seismometer self-noise in the presence of low seismic background signals.

Configuration: Two seismometers are installed side-by-side or stacked vertically in specially designed seismic vault fixtures. The seismometer outputs are connected to a data acquisition system that samples the data synchronously. Data are acquired during low seismic backgrounds.

Evaluation: A noise-power coherence analysis computation provides the noise-floor of the seismometer for a low seismic background stimulus.

Results: The GS21A's self-noise is plotted below. The theoretical noise floor was experimentally verified between 1 – 5Hz. The plot extends into the other areas of the passband of interest as verification of the worst possible case for seismometer noise. The DWR's self-noise limits the ability to record the seismometer noise in these areas. It is believed that the seismometer's theoretical noise model is a closer approximation in these frequency bands. This is shown in the figure below.

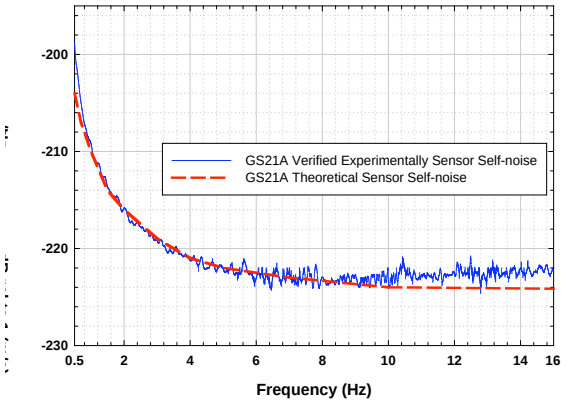


Figure 5. Geotech GS21A Self-noise Plot

GS21A Seismic Sensor Response Verification (SSRV)

Purpose: The purpose of the seismometer response verification test is to verify the seismometer response using seismic background signals and a reference seismometer.

Configuration: Two seismometers, (1) a characterized reference seismometer and (2) the seismometer under test, are installed side-by-side or stacked vertically in specially designed seismic vault test fixtures. The seismometer outputs are connected to a data acquisition system that samples the data synchronously. Data are acquired during moderate seismic backgrounds.

Evaluation: The data are converted from each seismometer to equivalent ground motion using the seismometers mathematical response model for each seismometer. If the seismometer response model is correct, the response calculations in earth-motion units will be identical.

Results: After converting the data to ground motion for both the reference and the GS21A the data were nearly identical (to within 0.2 dB). This result verifies that the sensor response model is accurate. The overlaying corrected data in earth units for each seismometer is shown below.

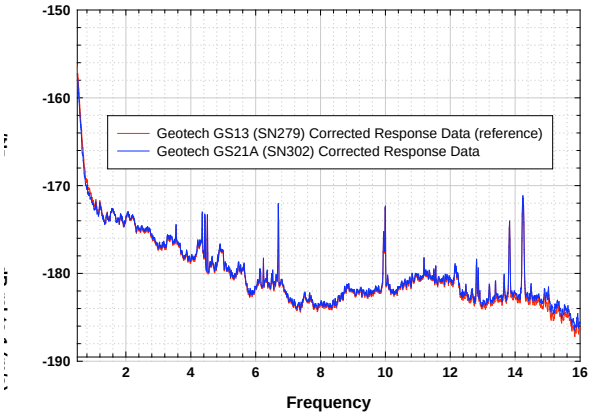


Figure 6. Geotech GS21A SSRV Plot

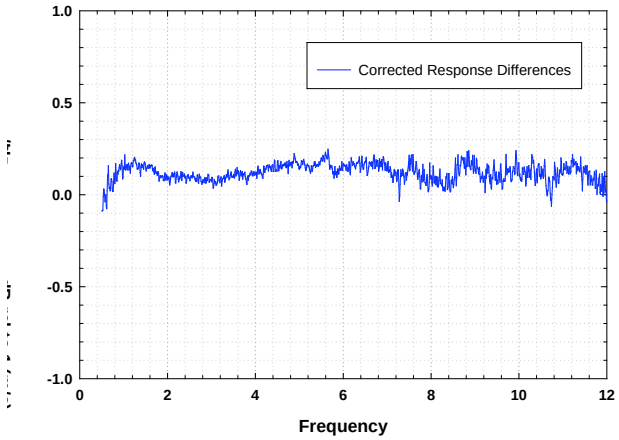


Figure 7. GS21A GS13 Corrected Response Difference Plot

***Güralp* CMG-3V Short-period Vertical Borehole Seismometer**

The GSL CMG-3V short-period vertical borehole seismometer was manufactured by Güralp Systems Limited (GSL) (Aldermaston, UK). The sensor has a flat response from 30 seconds to 50 Hertz. GSL provided two CMG-3V seismometers for evaluation.

Testing is being performed at the Sandia National Laboratories FACT site.



Figure 8. CMG-3V Testing at FACT site

Sandia will evaluate the overall technical performance of the GSL CMG-3V short-period vertical borehole seismometer component of the Güralp instrumentation. GSL CMG-3V tests include side-by-side testing to

determine sensor self noise, seismometer response, seismometer sensitivity, and calibration capability. The results of these evaluations will be compared to relevant AFTAC and IMS application requirements or specifications.

CONCLUSIONS AND RECOMMENDATIONS

GS21A Seismometer Response:
Utilizing the parameters that Geotech provided for the seismometers under test and the Sandia Seismometer Response Model software a determination of the GS21A seismometer responses was developed.

Seismic Sensor Self-noise (SSSN) Test:
The Geotech GS21A theoretical noise model was experimentally verified between 1 – 5Hz. Extensions into the other areas of the passband of interest were calculated as the worst possible case for seismometer noise. It is believed that the seismometer's theoretical noise model is a closer approximation in these frequency bands.

Seismic Sensor Response Verification (SSRV) Test:
The theoretical seismometer responses for the GS21A seismometers under test were verified. The GS21A responses where verified to a reference Geotech GS13 seismometer.

REFERENCES

Kromer, Richard P. Townsend, Toby O., Ground-based Monitoring R and E Technology Report, 'Test Plan for the Evaluation of Seismic Sensors for Ground-based Geophysical Monitoring', 3 March 2003.

Townsend, Toby O. Kromer, Richard P., Ground-based Monitoring R and E Technology Report, 'A Technique for Measuring the Self-noise of Ultra Low Noise Seismometers within Modern Seismic Systems', 15 February 2004.

INTEGRATED SEISMIC EVENT DETECTION AND LOCATION BY ADVANCED ARRAY PROCESSING

Tormod Kvaerna[1], Steven J. Gibbons[1], Frode Ringdal[1], and David B. Harris[2]

NORSAR[1], Lawrence Livermore National Laboratory[2]

Sponsored by National Nuclear Security Administration
Office of Nonproliferation Research and Engineering
Office of Defense Nuclear Nonproliferation

Contract No. DE-FC52-03NA99517[1] and W-7405-ENG-48[2]

ABSTRACT

The principal objective of this two-year study is to develop and test a new advanced, automatic approach to seismic detection and location using array processing. Our aim is to obtain significantly improved precision in the location of low-magnitude events compared with current automatic approaches, combined with a low false alarm rate. We plan to develop and evaluate a prototype automatic system which uses as a basis regional array processing with fixed, carefully calibrated, site-specific parameters in conjunction with improved automatic phase onset time estimation.

In the first part of this project, we have focussed upon regional events in Fennoscandia and NW Russia using the regional arrays operated by NORSAR and the Kola Regional Seismological Centre (KRSC) in Apatity, Russia. Through a collaboration with KRSC, we have acquired Ground Truth (GT) data for routine industrial mining blasts from four mining regions on the Kola Peninsula at distances between 200 and 410 km from the ARCES regional seismic array. From September 2001 to March 2004, 1977 explosions had been included in this database. The characteristics of signals resulting from events at each of the mines have been investigated in detail. Recordings of the blasts from the open-pit mines are often very complex and the signals from subsequent blasts at the same pit display great differences, indicating significant variation in the nature of the source and ripple-firing techniques.

We have focussed particularly upon the single array scenario since, in the context of explosion monitoring, many low-magnitude events of interest may only be recorded by a single array station. For a test period from October 1st 2001 to September 30th 2002, every detection at the ARCES array was subject to a two-stage reprocessing. Firstly, a careful re-estimation of onset time was performed using an autoregressive method and, secondly, the slowness and azimuth of each phase was estimated using broadband frequency-wavenumber analysis in each of ten fixed frequency bands with corresponding time-windows and array configurations. For GT events from each of the mines being studied, the statistics of the slowness estimates were investigated for each frequency band.

Almost all of the fixed frequency bands provided more stable slowness and azimuth estimates than those determined in a variable frequency band as used by the standard on-line detector (i.e. a frequency band maximizing the signal to noise ratio), although the variance of slowness estimates from known sources differed significantly between the different fixed frequency bands. As an example, slowness estimates for the initial P-phases from events at the Zapoljarni mines at a distance of approximately 200 km from ARCES displayed the most stable slowness estimates in the 2.0 - 4.0 Hz frequency band whereas initial P-phases for events from the more distant Olenegorsk and Khibiny mining regions displayed a far smaller variance in the 4.0 - 8.0 Hz band. In most fixed frequency bands, the slowness estimates from the four main mining regions fall into distinct clusters, which is not the case for the variable frequency bands.

OBJECTIVE

This two-year project is a collaboration between NORSAR (as the lead organization) and Lawrence Livermore National Laboratory (LLNL). The main objective of this study is to investigate new approaches and processing methods for the automatic detection and location of seismic events using arrays. A particular feature of this study will be the utilization of information from previous ground-truth events in the method implementation and parametrization of the processing sequences. A goal for this work will be to attribute, with a high degree of confidence, the automatically detected and located events to active mines or areas with known recurring seismicity.

We will evaluate the results from applying this approach for selected sites with recurring mining explosions in Fennoscandia and Kazakhstan, with emphasis on the one-array monitoring scenario. In addition, we plan to develop and test an initial framework for multi-array processing. In this study we will also investigate the potential of applying advanced new array-processing methods to obtain even further improvements. Specifically, we plan to develop and test a so-called “matched field processing” technique that aims at compensating for array processing loss due to refraction and scattering, and thus enhances array gain at high frequencies.

RESEARCH ACCOMPLISHED

Introduction

During the first year of this study we have focused on the development of algorithms for processing of mining events from the northern Fennoscandian region, using the ARCES array. As shown in Figure 1, there are several active mines in this region, which are used as targets for this study. Since September 2001, an extensive collection of ground truth (GT) information on mining explosions in the Kola Peninsula has been conducted on the DoE funded contract entitled “Ground-Truth Collection for Mining Explosions in Northern Fennoscandia and Russia” (Harris et al., 2003). Our plan has been to use the ground truth events for the one-year time period October 2001 - September 2002 for development and tuning of the algorithms, and to use events after September 2002 for evaluation.

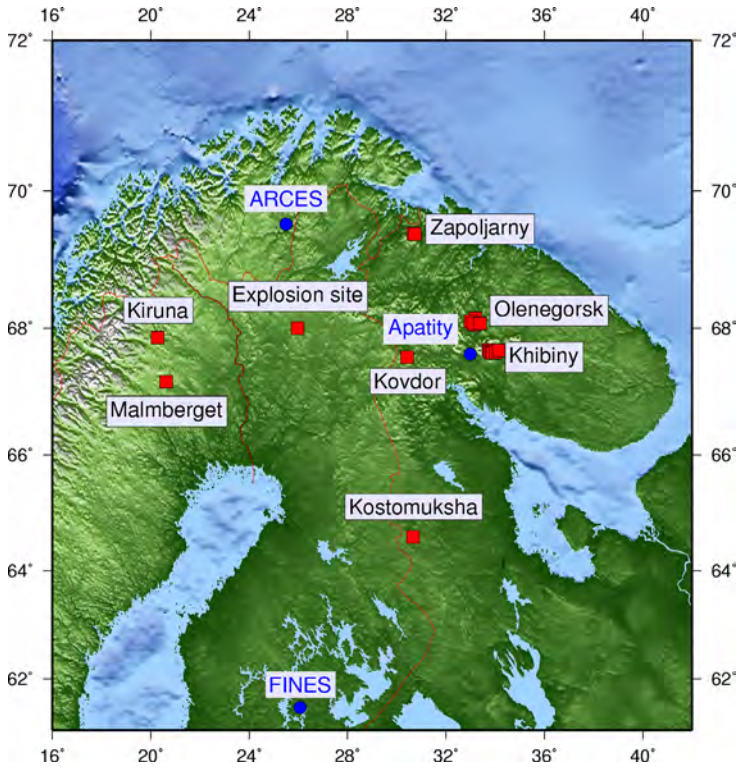


Figure 1. Locations of the main mining regions in NW Russia and Sweden, together with the location in Finland of a site regularly used by the Finnish military for destruction of ammunition. Also shown are the locations of the seismic arrays in the region (ARCES, Apatity and FINES).

Regional observations of underground and open-pit mine blasts

We have investigated in detail events from the Khibiny and the Olenegorsk mines (see Figure 2). Ground truth information (Harris et al., 2003) and earlier studies of mining events from this region (Gibbons and Kværna, 2002; Ringdal et al., 2003) have revealed that a wide range of source types are present at these mines. The blasts in the open-pit mines are usually large ripple-fired explosions, often detonated in several groups with some seconds delay. The regular blasts in the Khibiny Massif underground mines usually have yields between 120 and 240 tons with many delays of 20-35 milliseconds. So-called compact shots are also detonated in these underground mines. The compact shots have yields between 1 and up to a few tons, having only a few delays, and provide the simplest source type available in these mines. The main purpose of the compact shots is to remove smaller parts of rocks remaining after the regular underground blasts.

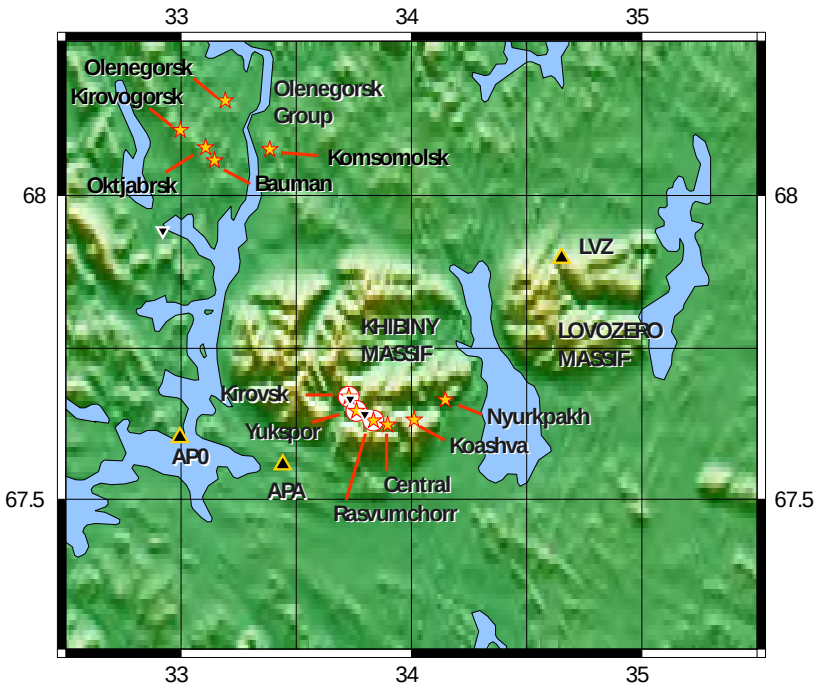


Figure 2. Locations of the mines (stars; circles indicate mines with both underground and surface facilities), permanent stations (triangles) and temporary stations (inverted triangles) in the vicinity of the Khibiny Massif. The five mines in the Olenegorsk group are all open-pit mines.

In order to get an overview of typical seismograms observed at the ARCES array from explosions in the Khibiny and Olenegorsk mines, we have taken a closer look at the compact shots from the underground Rasvumchorr mine in the Khibiny Massif. The distance from ARCES to the Rasvumchorr mine is approximately 400 km. For each of the 99 events in the ground truth database (October 2001 - September 2002), we have calculated the Pn beam and the corresponding semblance coefficient. In order to enhance the coherent parts of the wavetrain, we also calculated the Pn beam weighted with the semblance coefficient. The frequency band used for this analysis was 4 - 8 Hz. The Pn beam was formed using the ARCES center instrument (A0), the C- and D-ring instruments steered with an apparent velocity of 7.5 km/s and a back-azimuth of 121.0 degrees. The semblance coefficients were calculated for 0.5 second window lengths with a 40 Hz sampling rate.

The three upper panels of Figure 3 show the processing results for three selected compact shots in the underground Rasvumchorr mine. For these compact shots we know the total yield, but not the number of individual detonations (holes). However, we have information from the mine operators that the common 1 ton compact shots consist of one or two individual detonations. We can see that the first event has a relatively simple Pn signature, which most likely is the result of a single one-ton compact shot. The second event, with a total yield of 4 tons, has a Pn signature with a slightly longer duration, whereas five separate pulses can clearly be seen for the third event, having a total yield of 6 tons. From the observation of relatively simple Pn signatures at ARCES for the smallest compact shots, it is reasonable to assume that observed complex Pn signatures generally result from more complex source types.

Processing results for three blasts in the Khibiny Central open-pit mine are shown in the middle panel of Figure 3, whereas the three lower panels show results for three typical events at the open-pit mines in the Olenegorsk group. Detailed information obtained on the blasting technique used for some events (Harris et al., 2003; Ringdal et al., 2003), reveal that events in the open-pit mines can consist of up to 5 separate, ripple-fired explosions detonated in sequence in different parts of the mine with some seconds delay.

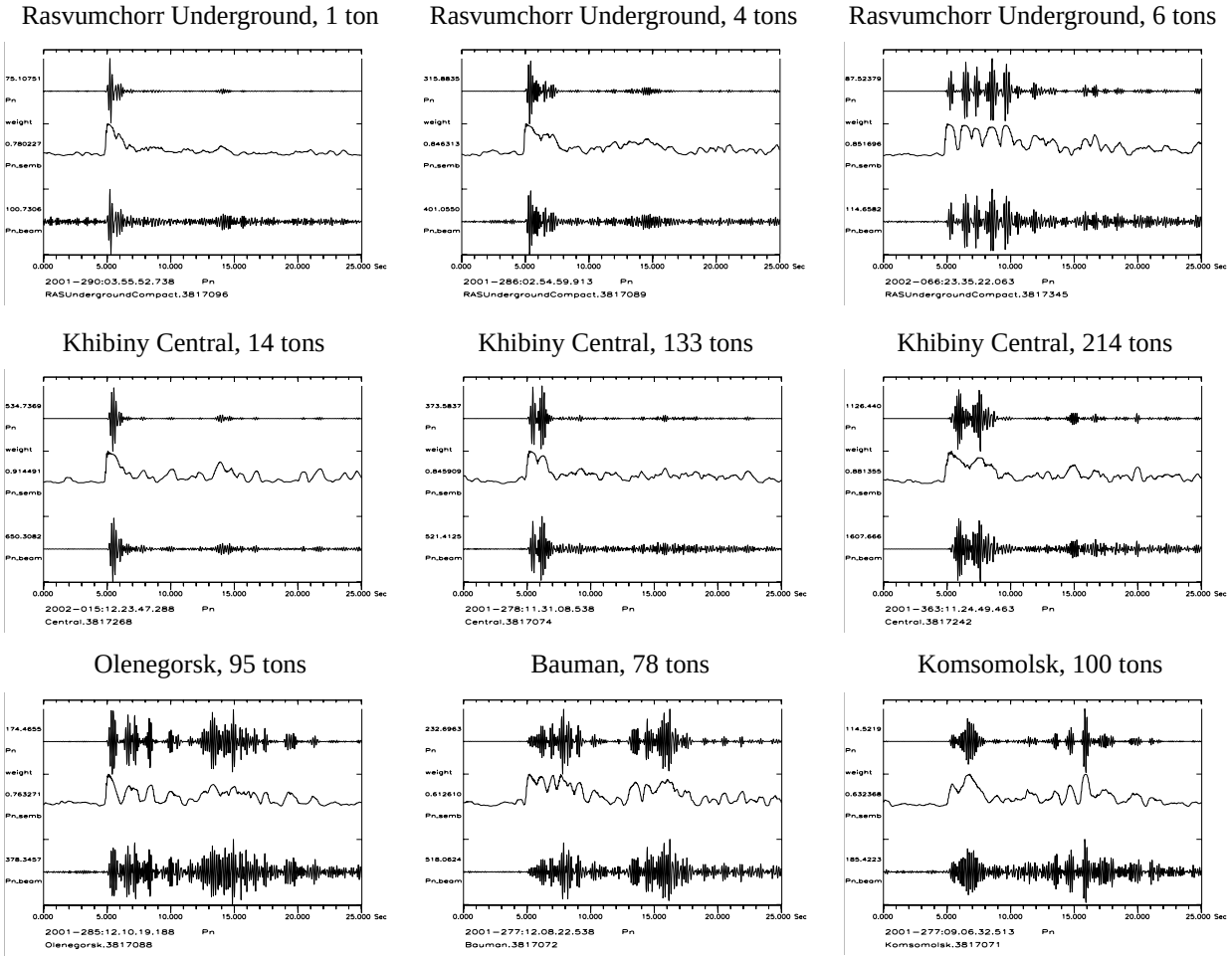


Figure 3. The upper three panels show ARCES recordings of 3 compact shots in the underground Rasvumchorr mine in the Khibiny Massif. In each panel we show the 4-8 Hz Pn beam (bottom), the semblance coefficient (middle) and the Pn beam weighted with the semblance coefficient. The total yields reported for each blast or blasting sequence are also given.
The three middle panels show similar traces for 3 events in the Khibiny Central open-pit mine, whereas the three lower panels show typical recordings of events at the open-pit mines in Olenegorsk group.

The semblance analysis (illustrated in Figure 3) conducted for 107 GT events in the Olenegorsk group shows that the vast majority of these blasts act as very complex seismic sources, having a duration often exceeding 10-15 seconds. Most of the 48 ground-truth events from the Khibiny Central open-pit mine also show complex Pn signatures at ARCES, but with generally shorter duration than the Olenegorsk events. However, some of the smaller events have a relatively simple Pn signature, indicating simpler sources. Out of the 99 ground-truth events from the underground Rasvumchorr mine, most of the 1 ton compact shots have Pn signatures similar to those shown in the upper left panel of Figure 3. The larger compact shots have generally slightly longer duration, and in some cases separate pulses can be observed.

To investigate further the source and propagation effects of events from the underground Rasvumchorr mine, we have stacked the ARCES Pn semblance coefficients of the 99 events in the ground truth database. The stacking is aimed at reducing random effects from the source, while retaining consistent propagation and source effects. The stacked semblance trace is shown by the red curve in the panels of Figure 4, and we note the close similarity between the stacked semblance trace and the "simple" waveform semblance trace shown in the upper left panel of Figure 3. The Khibiny Central mine is located within 1-3 km of the underground Rasvumchorr mine, and we find from the upper left panel of Figure 4 that, except for the first few seconds after Pn, the stacked semblance curves are quite similar to that of the Rasvumchorr mine events. The peak located 9 seconds after Pn corresponds to the Pg arrival. The mines in the Olenegorsk group are located 50-60 km closer to ARCES than the Khibiny mines, but, as seen from Figure 4, four of the stacked semblance traces are quite similar to those from the Khibiny mines. The only exception is the Oktjabrsk mine, but in this case only 14 GT events were available for stacking. Several of the Oktjabrsk events had a distinct signal arriving about 5 seconds after Pn, which is again seen in the corresponding panel of Figure 4.

Our comparisons of the stacked semblance traces for the different mines of the Khibiny and Olenegorsk groups have shown that the remaining, consistent features of the early part of the seismograms correspond to the first-arriving Pn and Pg arrivals. The remaining coherent energy pulses of the different events are due to the temporal and spatial distribution of the blasting sources within the mines.

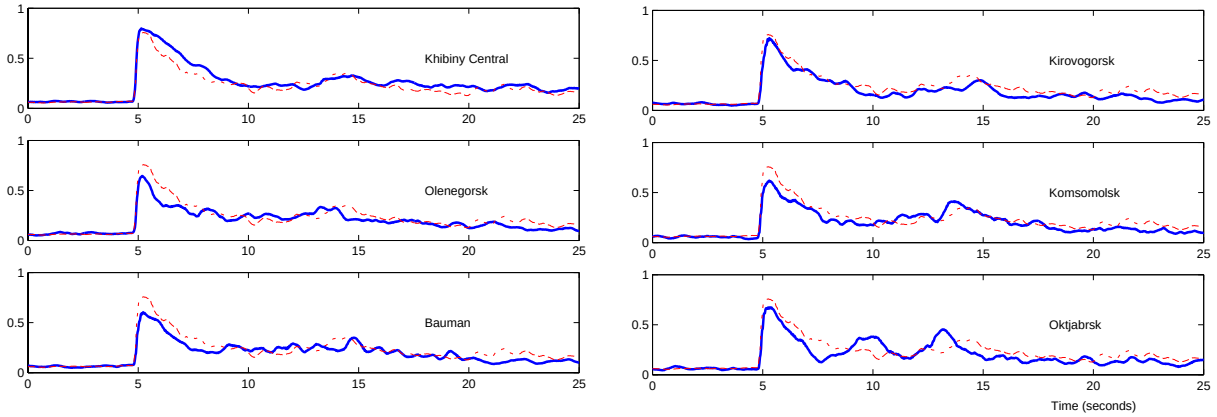


Figure 4. The blue curves show the stacked ARCES Pn semblance coefficients in the 4-8 Hz frequency band for the ground truth events in the Khibiny Central mine (upper left trace), and for the mines in the Olenegorsk group. The dashed red curve shows the stacked semblance coefficients for the compact underground shots in the Rasvumchorr mine.

Improvement of automatic onset time estimates

The widely used AR-AIC (Auto-regressive Akaike Information Criterion) method for automatic arrival time determination has proved to be highly successful when applied to the types of regional phases being studied here, which are often dominated by high frequency seismic energy. The method is most effective when the signal and preceding noise exhibit a good contrast both in amplitude and in the spectral content. For this reason, it is important to make the analysis frequency band as broad as possible without too great a reduction in the SNR. Using the trigger time on the detecting beam (which has often been filtered in a narrow frequency band in order to improve the SNR) as an initial condition, an algorithm is followed which calculates an optimal frequency band and repeatedly applies the AR-AIC process in progressively shorter time windows in order to determine the most accurate automatic arrival time estimate. A strict set of safety checks reduces the likelihood that a good arrival time estimate is replaced by a spurious estimate, using SNR measurements made on both the actual waveforms and error-prediction channels. An example of this procedure is illustrated in Figure 5, where we re-estimate the onset time for a detection of a weak Sn phase.

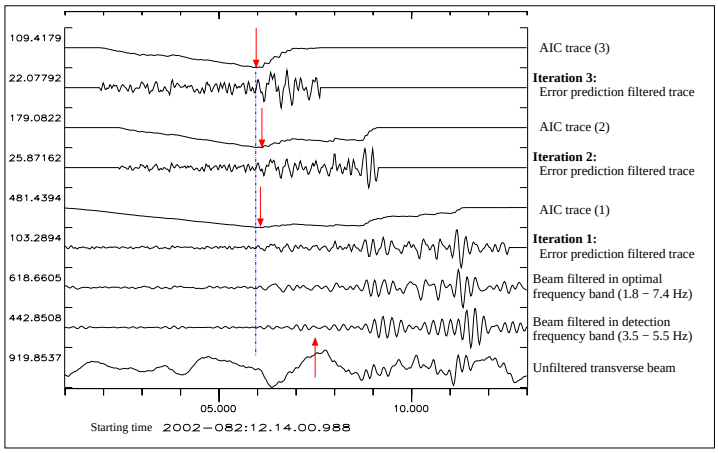


Figure 5. Re-estimation of onset time using the AR-AIC method for a phase detection at ARCES. The lowermost arrow indicates the initial onset time estimate and the remaining arrows indicate modified times from autoregressive estimates in three successive iterations. The detected phase is an Sn arrival from a mining event in northern Sweden and the modified arrival time is within 0.5 seconds of the Sn onset time predicted by the barey model, based on a network location.

For the purpose of site-specific monitoring, the most important phase onset time estimate is that of the initial P-arrival. The first stage of the single array monitoring process described by Gibbons, Kværna and Ringdal (2003) was the identification of detections which were likely to correspond to initial P-arrivals from the region being monitored. For all such phases, the onset time was re-estimated using an autoregressive method and all subsequent slowness and azimuth measurements were performed within time-windows fixed relative to this onset time. Starting values for secondary phase arrival time determinations are also based upon the initial P-arrival time.

Calibration of processing parameters for improved event location using Ground-Truth information from active mines in NW Russia.

Each detected arrival is subject to an estimation of the slowness and azimuth in order to classify and associate the phase. Inaccuracies in such estimates may lead to the exclusion of valid phases and/or the inclusion of spurious phases in the association process and a decrease in location accuracy. Accuracy in azimuth is of the greatest importance for single station locations.

It has been demonstrated (Kværna and Ringdal, 1986) that slowness estimates for phases from repeated events at a given site are far more stable when calculated in a fixed frequency band than in variable bands calculated to maximize the SNR. For the test-period October 1st 2001 to September 30th 2002, each phase detected by ARCES was subject to an auto-regressive arrival time re-estimation and subsequent slowness estimation by broadband f-k analysis in each of ten fixed frequency bands: (0.5-1.5 Hz), (1.5-3.5 Hz), (2.0-4.0 Hz), (2.0-5.0 Hz), (3.0-6.0 Hz), (3.0-8.0 Hz), (4.0-8.0 Hz), (5.0-10.0 Hz), (6.0-12.0 Hz), and (8.0-16.0 Hz). For each frequency band is associated a set of parameters defining the time window and an array configuration; for example, the D-ring instruments are not included in the f-k analysis for the highest frequencies in order to mitigate the effects of signal incoherence. Tapering is applied to the data segments to prevent edge effects in the Fourier transforms.

The extensive database of GT mining events provides an excellent natural laboratory for the testing of this re-processing. Figure 6 displays the slowness estimates for the initial P-arrivals for all the GT-events during the test-period in two of the fixed frequency bands, together with those from the existing variable band processing. The black, red, green, and blue symbols correspond to slowness estimates from P-arrivals from the four main Kola mining regions indicated in Figure 1 and it is clear that the estimates from the different sources show a far better separation and smaller variance for the fixed bands. One example of the problems with the variable band processing is the false interpretation of many of the P-arrivals from Kovdor events. The signals are dominated by frequencies over 10.0 Hz and so the existing procedure estimates slowness in high-frequency bands. Probably a result of the specific ripple-firing practices at this mine, compounded by poor signal coherence over the array, slowness estimates were consistently too low and azimuth estimates misleading. Such results were also observed for the reprocessing in the highest frequency bands, despite the absence of the more distant D-ring sensors.

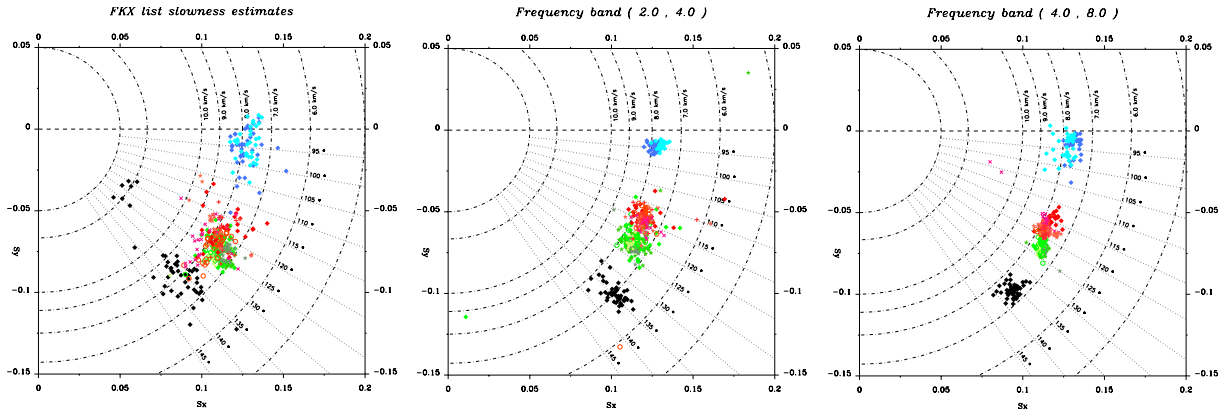


Figure 6. Slowness estimates for the initial P-phases from each of the Ground Truth events in the database between October 1st 2001 and September 30th 2002 in an optimal frequency band (ARCES online processing: left), the 2.0-4.0Hz frequency band (center) and the 4.0-8.0 Hz band (right). The mines are indicated by symbols as shown.

The slowness estimates in the band (4.0-8.0 Hz) are far more stable than those in the (2.0-4.0 Hz) band for the three more distant mining regions; the opposite is true for slowness estimates from the Zapoljarni mines. Many smaller events in the database have a very low SNR in the lower of these frequency bands which often leads to an fk-result dominated by coherent background noise.

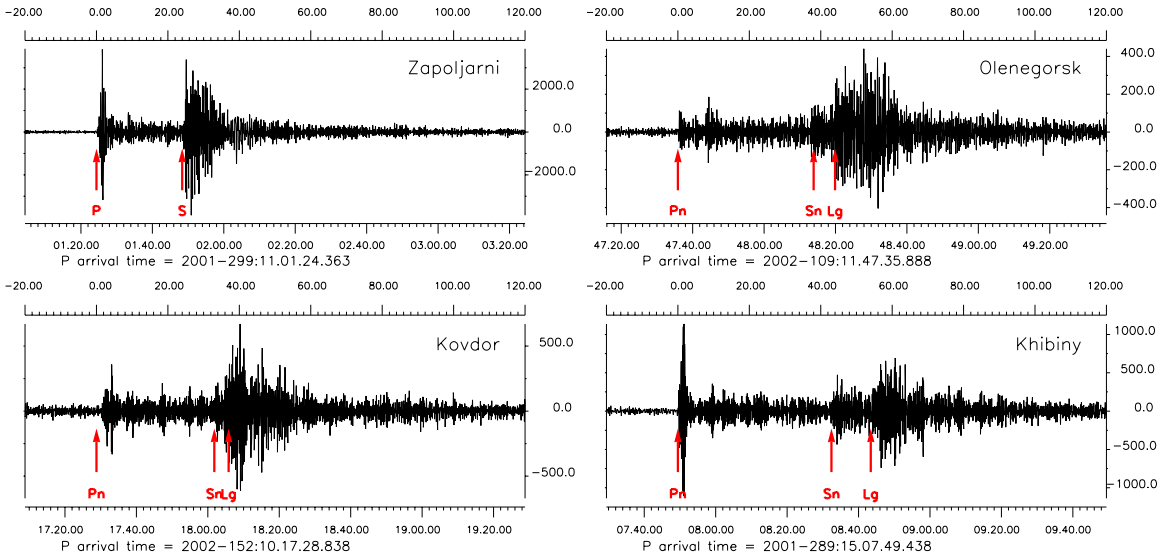


Figure 7. A typical event from each of the four mining areas studied. The ARA0_sz trace is displayed for each event, filtered in the frequency band 2.0-5.0 Hz. According to the "barey" velocity model, the Pb, Pg, and Pn phases all arrive within a second of each other for events from the Zapoljarni mines (distance 204 km from ARCES), as do the Sb, Sg, and Sn phases; we therefore simply denote first arrivals P and S. For the more distant mines at 298 km (Kovdor), 345 km (Olenegorsk), and 400 km (Rasvumchorr, Khibiny), Pn and Sn are the first arrivals and are indicated as predicted by "barey". The time for the Lg phase cannot be directly predicted from the barey model and is based upon group-velocity measurements from the Ground Truth events.

For the seismic monitoring of specific source locations, it is probably best to measure slowness and azimuth for the anticipated secondary phases in time-windows fixed relative to the initial P-arrival which almost certainly will have the most reliably determined onset time. We demonstrated in Figure 3 how, due to the complexity of the firing sequences for events from these mines, there were unpredictable pulses of coherent energy throughout the coda which compound the frequent problem of low SNR for the onset-time determination of weak secondary phase arrivals.

Figure 7 shows a selected seismogram for an event from each of the four main mining regions, together with phase onset times predicted by the "barey" model (Schweitzer and Kennett, 2002). For each event in the GT database, f-k analysis was performed for each of the indicated secondary phases with time-windows set at the appropriate delays following the P-onset. Slowness estimates in the 2.0-5.0 Hz frequency band for each phase for each GT event during the test period are displayed in Figure 8. The first observation is that the slowness estimates for the secondary phases are far less consistent than those for the first P-arrivals for all source regions considered. In this frequency band, it is almost possible to determine from which of the four regions a signal comes based on the P-phase slowness estimate alone. The Olenegorsk and Khibiny regions are poorly separated in azimuth from ARCES and this results in a small overlap in the slowness estimate populations; this overlap is greater in some frequency bands and smaller in others.

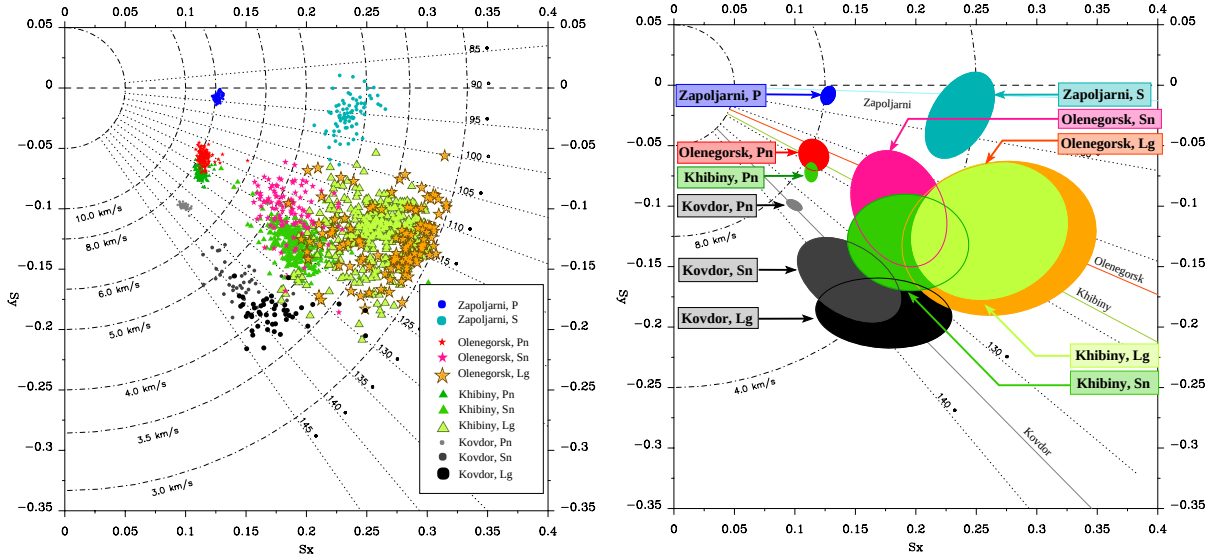


Figure 8. ARCES slowness estimates in the 2.0 - 5.0 Hz frequency band for phases as indicated for Ground Truth confirmed mining events between October 1st 2001 and September 30th 2002 (left) and 95% confidence error-ellipses for these populations (right) together with the geographically expected backazimuth values. Note the small spread of the slowness estimates for initial P-arrivals compared with that of the secondary phases from all of the mines considered. Other frequency bands lead to an improvement in the distribution of slowness estimates for some phases and a deterioration for others. A few outliers which were evidently the result of a low signal to noise ratio were omitted for the calculation of the error ellipses.

In calculating these confidence intervals, it was necessary to remove some data points for which slowness estimates had clearly been dominated by background noise, coda signals, or other unrelated events. As reported by Gibbons et al. (2003), many Kovdor Sn phases were attributed a slowness value consistent with a Kovdor Pn/Pg phase due to repeat blasting at the same site. Many of the underground explosions on the Khibiny massif have weak associated signals which are dominated by background noise in this frequency band.

The overlap between Sn and Lg slowness determinations from the Khibiny and Olenegorsk mines is very large. These measurements should correspond to different time-windows relative to the P-arrival although Sn-type slowness values can be anticipated long into the S-coda and fortuitous firing sequences may lead to Sn or Lg from delayed blasts being observed at unexpected times. Lg is not observed in higher frequency bands and slowness estimates in the Lg time-window only measure the S-coda.

In addition to useful information about the variance of these slowness estimates, we observe how these distributions relate to the anticipated azimuth values. Slowness estimates from the initial P-arrivals generally over-estimate the backazimuth, with the exception of the Kovdor events (although, in other frequency bands, the backazimuth is also overestimated for these events: Gibbons and Kvaerna, 2002). The large variance in slowness estimates is probably a consequence of the broad-band f-k analysis with the slowness corresponding to maximum coherence being determined according to the relative strength of high and low frequency energy within the given band.

Empirical Matched Field Processing

We are investigating the application of matched field processing to seismic array data. Matched field processing is a narrowband technique borrowed from underwater acoustics (Baggeroer et al., 1993) that generalizes the notion of beamforming to non-planar wave structure. Recall that narrowband beamforming and FK measurements may be interpreted as a spatial inner product operation with a vector of complex numbers (called a steering vector) representing phase delays at a given processing frequency under a plane-wave propagation assumption. Matched field processing most often substitutes theoretical predictions of the steering vector structure computed from a model of propagation in the medium. The complex components of the steering vector consequently may have non-planar phase structure and non-uniform amplitudes. An empirical approach to matched field processing measures the wavefield structure, rather than calculating it from a model (Fialkowski et al., 2000). In this approach, sample covariance matrices are measured from narrowband data for sources of known location, and empirical steering vectors are extracted as the eigenvectors corresponding to the largest eigenvalues. Steering vectors derived this way are tied to particular source locations. This approach may be adaptable to producing narrowband, aperture-level calibrations for seismic arrays. The quality of the calibrated steering vector is determined by the quality of the narrowband covariance matrix. In the seismic case, high-quality covariance matrices may be estimated by stacking many observations of a particular phase (especially from repeating sources, such as mines).

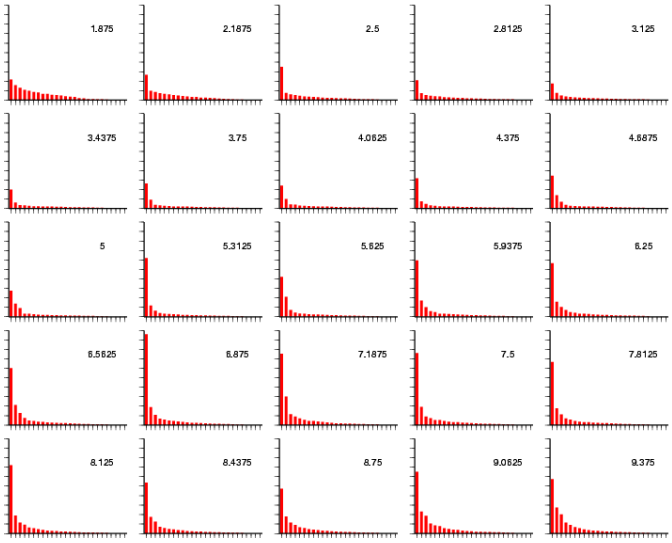


Figure 9. Eigenvalue structure (square-root scaling) of Pn spatial covariance matrices (ARCES array) made by averaging sample covariance matrices from 28 observations of events at the Olenegorsk mine.

In situations where a single incident wave is anticipated the quality of the covariance matrix may be assessed from the matrix eigenstructure, which should be dominated by a single large eigenvalue. An example of this situation is shown in Figure 9. These are results of preliminary covariance matrix estimates for Pn phases generated by explosions in the Olenogorsk mine and recorded by the ARCES array. In this example, Pn covariance matrices were averaged for 28 GT events in each of 25 narrow (0.3125 Hz bandwidth) frequency bands. The plot shows the square root (to compress dynamic range) of the eigenvalues in each frequency band, and demonstrates that a single eigenvalue does indeed predominate in most frequency bands. Generally this observation breaks down at the very low frequencies (where noise flattens the eigenstructure) and the very high frequencies (where scattering spreads signal energy over multiple wavenumbers and eigenvalues). To date, we have completed software to efficiently calculate average covariance matrices for a large number of events on a regular set of frequencies and extract eigenvalues and eigenvectors. We plan next to use the eigenvectors as empirical steering vectors in narrowband beamforming and FK operations.

CONCLUSIONS AND RECOMMENDATIONS

Our initial results have confirmed that application of a fixed frequency band for f-k analysis provides a greatly improved stability of slowness estimates of regional events, compared with the conventional procedure which uses a variable frequency band (i.e. the frequency band with the highest SNR). The application of broadband f-k analysis in parallel in a number of fixed frequency bands has been shown to provide a convenient method to select the best frequency band for a particular station-site configuration. From our initial studies of ARCES data for several mining sites in the Kola Peninsula, we have found that the "optimum" frequency band varies with site and phase type, and the selection of such a band for operational processing therefore requires careful calibration for each case. The stability for the slowness estimates for the first P-phase is much more stable than for secondary phases (S and Lg), and gives an azimuth estimate with a typical scatter as low as +/- 2 degrees for the events studied.

Semblance analysis of ARCES recordings from different mining sites has been investigated in detail, and has revealed significant variations even for signals from the same mine. Thus, it may be difficult to successfully apply waveform correlation techniques for these mining explosions in general, but some promise is seen for the simple "compact" explosions. Further progress will require detailed analysis by taking into account relative location of the explosions as well as the different firing practices.

Further work will focus on applying automatic one-array location processing to the mines in Fennoscandia, expanding upon the procedure introduced by Gibbons et al. (2003). We will also develop and apply an initial multi-array process for detecting and locating recurring mining explosions in Fennoscandia, and compare the results to the current experimental regional monitoring system in operation at NORSAR. Furthermore, in the second year of this project, we will apply the analysis procedures to selected mining sites in Kazakhstan. This work, which will include calibration of specific station-site configurations will be carried out in cooperation with the Kazakhstan NDC.

REFERENCES

Baggeroer, A. B., W. A. Kuperman, and P. N. Mikhalevsky (1993). An overview of matched field methods in ocean acoustics, *IEEE Journal of Oceanic Engineering*, 19 (4), 401-424.

Fialkowski, L. T., M. D. Collins, W. A. Kuperman, J. S. Perkins, L. J. Kelly, A. Larsson, J. A. Fawcett, and L. H. Hall (2000): Matched-field processing using measured replica fields, *Journal of the Acoustical Society of America*, 107 (2), 739-746.

Gibbons S. and T. Kværna (2002). Analysis and Processing of Events from the Kovdor Mine, NW Russia, NORSAR Contribution No. 793.

Gibbons, S. J., T. Kværna, and F. Ringdal (2003). Single array analysis and processing of events from the Kovdor mine, Kola, NW Russia. NORSAR Sci. Rep. No. 1-2003, Kjeller, Norway, p44-55.

Harris, D. B., F. Ringdal, E. O. Kremenetskaya, S. Mykkeltveit, J. Schweitzer, T. F. Hauk, V. E. Asming, D. W. Rock and J. P. Lewis (2003). Ground-truth Collection for Mining Explosions in Northern Fennoscandia and Russia. "*Proceedings of the 25th Seismic Research Review - Nuclear Explosion Monitoring: Building the Knowledge Base*", Los Alamos National Laboratory, LA-UR-03-6029, Tucson, AZ, Sept. 23-25, 2003.

Kværna, T. and F. Ringdal (1986). Stability of various f-k estimation techniques. NORSAR Sci. Rep. No. 1-1986/1987, Kjeller, Norway, p29-40.

Schweitzer, J. and B. L. N. Kennett (2002): Comparison of Location Procedures - the Kara Sea Event 16 August 1997, NORSAR Sci. Rep. 2-2001/2002, Kjeller, Norway, 97-114.

Ringdal, F., T. Kværna, E. O. Kremenetskaya, V. E. Asming, S. Mykkeltveit, S. J. Gibbons and J. Schweitzer (2003). Research in Regional Seismic Monitoring. "*Proceedings of the 25th Seismic Research Review - Nuclear Explosion Monitoring: Building the Knowledge Base*", Los Alamos National Laboratory, LA-UR-03-6029, Tucson, AZ, Sept. 23-25, 2003.

WORKING WITH AND AROUND THE NNSA DATABASE SCHEMA

Charles A. Langston, Ivan Rabak, Christy Chiu, Chuntao Liang

University of Memphis

Sponsored by National Nuclear Security Administration
Office of Nonproliferation Research and Engineering
Office of Defense Nuclear Nonproliferation

Contract No. DE-FC04-2002AL68280

ABSTRACT

We are implementing modifications of the National Nuclear Security Administration (NNSA) database schema and the Sandia National Laboratories (SNL) MatSeis program to handle waveform manipulation needed in modeling observed seismograms with synthetics. Functions include writing of windowed, processed data waveforms and waveform inversion for source and earth structure parameters. Our objective is to work within the existing NNSA schema in as far as possible without adding many additional tables or additional keys to relate the tables while preserving the original data within an event database. A modification of MatSeis allows writing of processed waveforms with a text file that describes the processing history. A single channel of data may have up to 99 “generations” of processed versions of itself that become input to other Matlab modules for modeling the processed data. Additional Matlab modules are constructed for earthquake focal mechanisms, moment tensor inversion, surface wave dispersion analysis and inversion, and regional waveform phase-time inversion. The ideal solution, which is beyond our work here, is to extend the NNSA database schema to add keys to the wfdisc table or to have additional wfdisc-type tables with keys for relations between waveforms.

OBJECTIVES

Objectives for this research include the following:

1) Determine waveform characteristics of earthquakes and explosions over a broad frequency band that can be used to locate and identify small seismic sources in central Asia
2) Construct a waveform and source parameter database to be used to understand local/regional wave propagation in central Asia and to identify sources
3) Construct an earth structure database for models of the crust and upper mantle that accurately predicts the waveforms for seismic sources in central Asia
4) Construct a knowledge base system that links data, data-derived source models, data-derived structure models, and educational tutorials for understanding sources, structure, and wave propagation in central Asia.

In this paper we report on problems encountered in our attempt to use the NNSA database schema as the basis of a seismic analysis processing system for treatment of global earthquake data. Our objective for this report is to suggest that some effort be made to fully incorporate relationships between data waveforms, derived processed waveforms, and synthetic waveforms in the NNSA database schema to fully integrate seismological waveform studies with previous parameter studies.

RESEARCH ACCOMPLISHED

Introduction

New tables for parameter data are continually being developed to extend the database schema as new data processing packages come online.

In conjunction with the use of the NNSA database schema, there have been ongoing software development efforts to incorporate seismic databases directly into seismic modeling codes. The Seismic Analysis Code (SAC), for example, can have the capability for making database queries and accessing waveforms if an Oracle database is available on the network. Of more interest to this work is the MatSeis system written at Sandia National Laboratories. This program has many of the attributes of SAC but with access to the functionality of the full Matlab system that it runs under.

Routinely handling waveform data from many events at many stations would seem to require a database system. Unfortunately, the industry standard, Oracle, is very expensive for a small research laboratory. MySQL is an alternative as are other open software systems, but it was decided that a simple flat file system based on the NNSA schema would be simplest. A flat file system consists of simple text files, can be constructed using a variety of programming languages and existing database systems, and can be easily accessed as well. Using the NNSA schema would also allow consistency with DOE laboratory efforts in seismic data handling.

The current practice in the graduate program at the University of Memphis is to encourage the use of the Matlab programming language in graduate courses and research. Matlab is a very extensive programming language with many useful mathematical, scientific, graphical, etc., software libraries. It also contains tools for building elaborate graphical user interfaces (GUIs). Thus, it seemed a straightforward decision to choose Sandia National Laboratories MatSeis system as the basis for modeling the seismic data in this project. MatSeis can be configured to query an Oracle database, an NNSA (CSS3.0) flat file system, or a “generic” database flat file system. Waveforms can be read into the system and then analyzed, modifying the existing event database, and a new database saved to disk. Once a database has been read into MatSeis, all information (waveforms, parameters) can be accessed by internal MatSeis routines and used in other applications run under Matlab but external to MatSeis. Thus, MatSeis seemed like the natural tool to use that would incorporate NNSA database flat file structures and serve as a software platform to build other waveform analysis tools not currently found in MatSeis through Matlab.

The Problem

The NNSA schema is good for storing derived parameter data like earthquake magnitudes, location, and the like but does not express relationships between waveforms. An ideal attribute for a seismological database is to collect pertinent information about the data (metadata) and the waveform data themselves and then to append all derived parameters, earth models, modeling methods, processed data seismograms, and synthetic seismograms. It should be unnecessary to duplicate database tables, for example, in a processing cycle of analysis.

For example, in a teleseismic moment tensor inversion, raw waveform data must be corrected for instrument response, filtered in some manner to avoid noise, time-windowed to obtain P or S wave body phases, possibly correlated with synthetic waveforms, time-shifted, and then modeled using a variety of assumptions about the source, the source-area earth structure, and choice of input waveform data. The NNSA schema has the facility for different source origins (orid) that can key into different moment tensor results, but it does not have appropriate keys to relate different waveform files to the raw data waveforms. In other words, a database key that relates many different processed waveforms back to the original data waveform is necessary. There also should be a key that relates many different synthetic waveforms back to processed waveforms and the data waveforms. In the current schema, this would mean being able to define many different “wfdisc” tables that relate to entries in other wfdisc tables. In addition to relations between wfdisc tables, it would be useful to have additional tables that define the processing steps that relate the tables together.

MatSeis and the present implementation of the NNSA schema allow a particular event database to be read in. Some processing can occur, and some database tables can be modified as a result of the processing. For example, first motions, times, and amplitudes can be picked using measuretool and the arrival table modified. MatSeis then has the facility to write a new set of database tables to disc. In effect, different processing steps on the data require a repetition of database tables and a need to manipulate the resulting multiple databases outside of MatSeis with other database software.

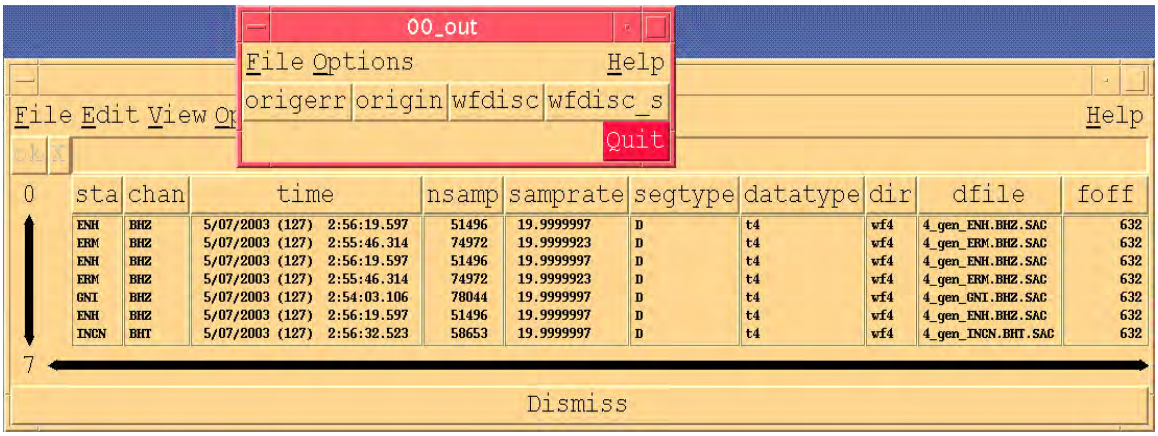
A larger problem, however, is that MatSeis does not allow a user to save processed waveforms to disc, and the NNSA database schema does not allow relations between waveforms, as discussed above. These two problems were not recognized at the beginning of the decision-making process for streamlining a waveform modeling system. The problems are significant enough and the possible solutions important enough for future database and seismic analysis work that we have spent considerable effort trying to come up with solutions that are most closely consistent with the idea of using a single-event database in and as part of the modeling process.

Approach

MatSeis is a software package intended to help process waveforms. It is GUI driven relying on Matlab to handle graphics. Furthermore, it is tied with Matlab in terms of a toolbox giving all the functionality of Matlab-based programs. This advantage is exploited to expand MatSeis capabilities by writing custom Matlab code.
One of the goals in expanding MatSeis is to allow saving processed waveforms.

The current version of MatSeis (1.7 devel), here at the University of Memphis, and the new version (1.8) coming from Sandia National Laboratories do not support writing waveforms. Myriads of seismic data formats are used by various geophysical groups, so choosing the right format for writing waveforms is somewhat a matter of institutional preference. The University of Memphis widely uses the SAC format so we decided to use it as the only supported format for writing waveforms at this time. Additional data formats can be bundled into the solution and implemented as Matlab function/scripts.

MatSeis allows access to Custom Menus through the main GUI. We use this option to build a set of scripts to perform various database related tasks. The database schema is a modified NNSA type. The modification includes creating additional tables to reflect the existence of processed and saved waveforms and accompanying information on the processing steps. Figure 1 shows a custom table *wfdisc_s* that contains saved waveform information.



sta	chan	time	nsamp	samprate	segtype	datatype	dir	dfile	foff
ENH	BHZ	5/07/2003 (127) 2:56:19.597	51496	19.9999997	D	t4	wf4	4_gen_ENH.BHZ.SAC	632
ERM	BHZ	5/07/2003 (127) 2:55:46.314	74972	19.9999923	D	t4	wf4	4_gen_ERM.BHZ.SAC	632
ENH	BHZ	5/07/2003 (127) 2:56:19.597	51496	19.9999997	D	t4	wf4	4_gen_ENH.BHZ.SAC	632
ERM	BHZ	5/07/2003 (127) 2:55:46.314	74972	19.9999923	D	t4	wf4	4_gen_ERM.BHZ.SAC	632
GNI	BHZ	5/07/2003 (127) 2:54:03.106	78044	19.9999997	D	t4	wf4	4_gen_GNI.BHZ.SAC	632
ENH	BHZ	5/07/2003 (127) 2:56:19.597	51496	19.9999997	D	t4	wf4	4_gen_ENH.BHZ.SAC	632
INCN	BHT	5/07/2003 (127) 2:56:32.523	58653	19.9999997	D	t4	wf4	4_gen_INCN.BHT.SAC	632

Figure 1. An example of a *wfdisc_s* table filled with the fourth generation of waveforms.

Method

In the pull-down 'Custom' menu in MatSeis, a new option allows saving of manipulated waveforms in up to 99 generations (Figure 2). It is possible to save all the manipulated waveforms (not affecting raw read-in data that already exists on disc) or the selected ones with a standard suite of interactive 'Are you sure?' dialog boxes. The new waveforms can be read in MatSeis, manipulated again, and saved as a new generation.

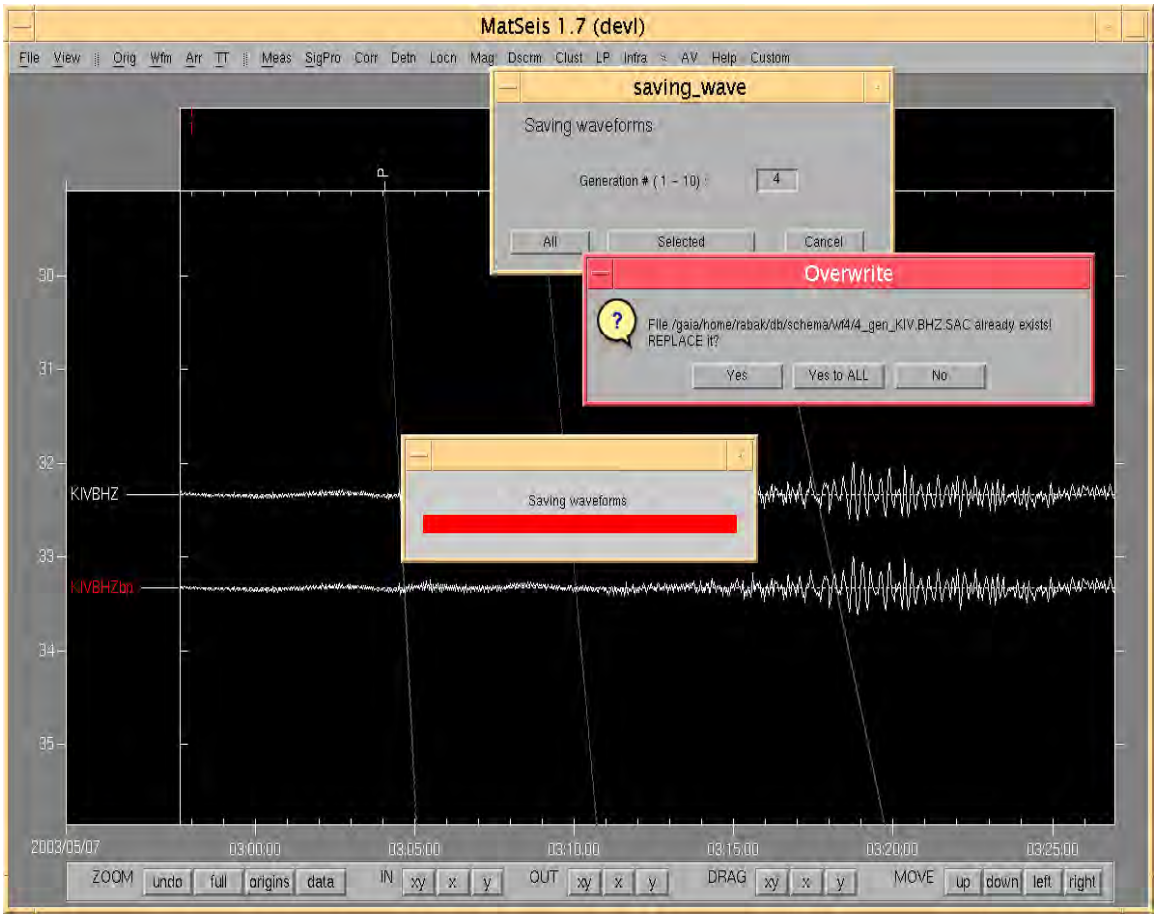


Figure 2. The 'saving waveforms' GUI, once custom -> write waveforms is selected from the pull-down menu.

Several Matlab scripts are being developed that deal in stages with the problem of saving waveforms. As much as possible, data are retrieved using existing MatSeis vocabulary, but at this stage, some hardwiring has been performed through editing of the original MatSeis function/scripts. The following scripts are called in the order shown. However, they are written as functions so they can be called by passing arguments listed through 'help *script_name'* command.

script 1 – the GUI that deals with the generation selection. It is created using a the Matlab GUI editor and saved as a Matlab figure. It is not created on-the-fly, with code, as most of MatSeis interactive windows are.

script 2 – retrieves all the information using existing MatSeis functions necessary to save waveforms such as current generation number, waveform station and channel names, directory locations, NNSA table fields, table formatting, currently selected waveforms, file name generation.

script 3 – writes SAC files. The algorithm uses the original SAC header for a processed waveform header because this information is not used by the NNSA schema once the tables are generated. This approach is subject to change.

script 4 – finally the existence of the new waveforms is reflected through a new *wfdisc*-like table. The existence of this table must be reflected in the NNSA schema text file. This step can be done automatically, but at the moment the change is done by editing the file with a text editor.

script 5 – makes sure that wfdisc_s table rows stay unique throughout other table updates.

The following diagrams give more detail about the scripts:

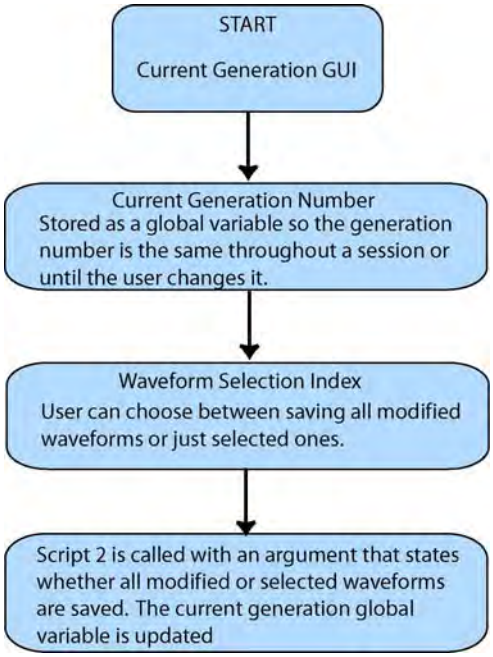


Figure 3. Flow chart of Script 1.

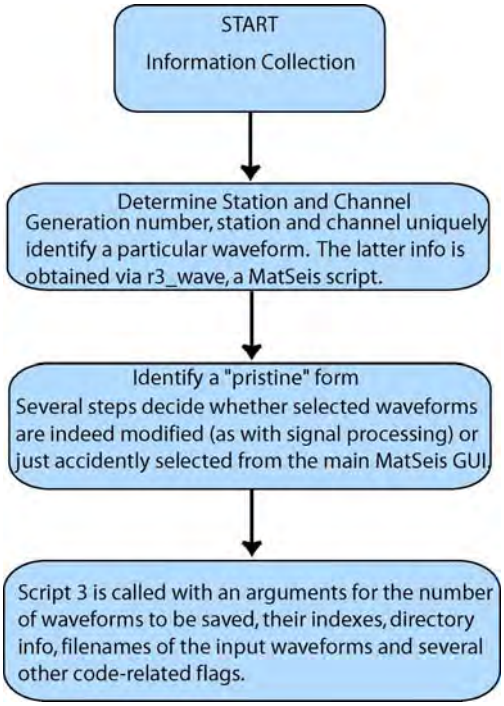


Figure 4. Flow chart of Script 2.

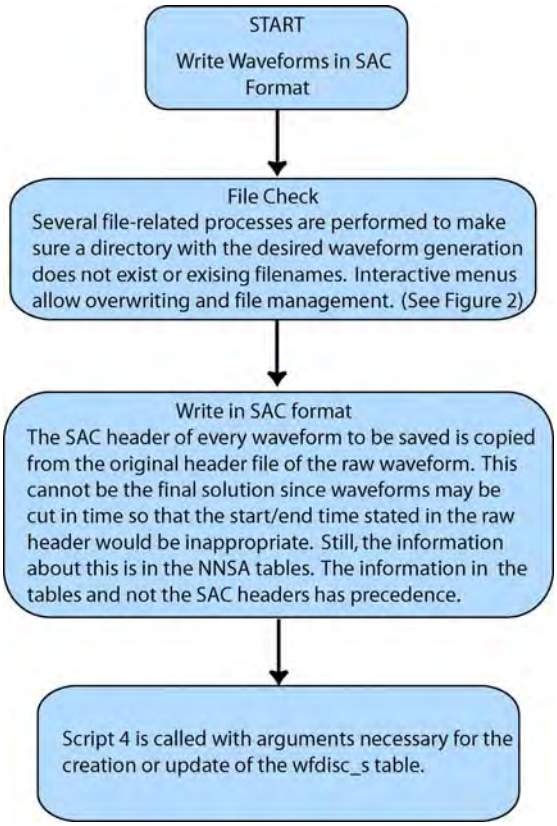


Figure 5. Flow chart of Script 3.

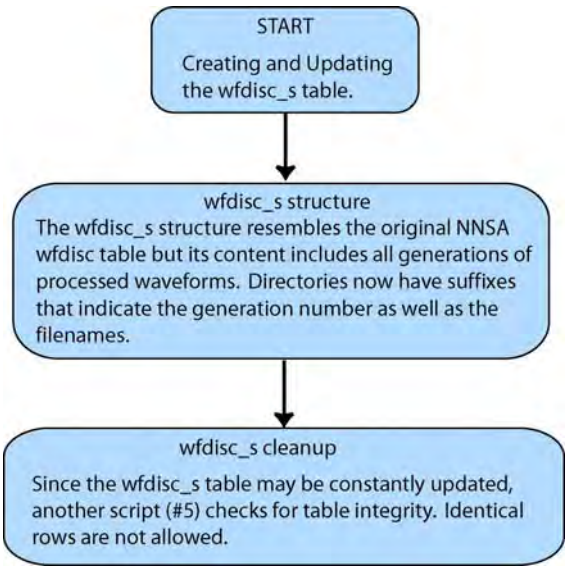


Figure 6. Flow chart of Scripts 4 & 5.

MatSeis obtains necessary information from its **.config* file for each event. Because processed waveforms can be read in and additionally processed and saved as another generation, a second *config* file must be generated. At this time, this must be done with a text editor by copying the raw *config* file and substituting the MS_IN_DB3_WFDISC variable with a new value: *wfdisc_s.*

Future steps should eliminate a need for hardwiring of the original MatSeis scripts. This will unfortunately duplicate tasks already performed by the original scripts, but it will create portability with future MatSeis releases. The lack of a MatSeis blueprint reduces the speed of building independent custom scripts to the programmer's ability to infer what and how various steps work by analyzing the Matlab and C code.

There are plans to develop an additional table and introduce it into the NNSA schema that would contain all the processing steps applied on a particular waveform, and would accelerate future processing because guesswork on what was done for a particular event would disappear.

An important additional step to complete the processing system is to include an additional wfdisc table for synthetic seismograms and a key to associate the synthetics with a particular generation of processed waveforms. Perhaps called wfdisc_aux, such a table would contain a variety of synthetic waveforms that include "complete" waveforms (constructed with all source and structure parameters) and Green's functions for computing complete waveforms.

CONCLUSIONS AND RECOMMENDATIONS

The global seismic data set of waveforms is constantly growing with the addition of new seismic stations and arrays. Considerable progress has been made on archiving these data and constructing catalogs of parameters derived from the waveform data. However, many modern seismological studies rely on waveform modeling to infer structure and source parameters. At the moment, no self-consistent database structure can incorporate either processed or synthetic data waveforms within the same database. Ideally, it is important to preserve processed and synthetic waveforms within an event database so future researchers can evaluate the accuracy of wave propagation codes used in constructing the synthetics in deriving parameters or to investigate other assumptions made in the modeling. Such a database structure would also help standardize seismogram modeling systems and software packages that incorporate it, improving collaboration between researchers.

Our principal recommendation is for the NNSA to develop an extension of the existing NNSA database schema to incorporate processed waveforms, synthetic waveforms, and processing history with the raw data waveforms.

Appropriate database keys should associate all tables. Such a modification would address an important need in the seismological community and could serve to standardize waveform data handling and modeling.

ACKNOWLEDGEMENTS

Work on these modifications and additions to MatSeis and issues with the database schema have benefited from suggestions and comments made by Darren Hart at Sandia National Laboratories.

KNOWLEDGE BASE NAVIGATOR FACILITATING REGIONAL ANALYSIS INTER-TOOL COMMUNICATION

B. John Merchant, Darren Hart, Eric P. Chael, Matthew N. Chown, and Jeff W. Hampton

Sandia National Laboratories

Sponsored by National Nuclear Security Administration
Office of Nonproliferation Research and Engineering
Office of Defense Nuclear Nonproliferation

Contract No. DE-AC04-94AL85000

ABSTRACT

To make use of some portions of the National Nuclear Security Administration (NNSA) Knowledge Base (KB) for which no current operational monitoring applications were available, Sandia National Laboratories have developed a set of prototype regional analysis tools (MatSeis, EventID Tool, CodaMag Tool, PhaseMatch Tool, Dendro Tool, Infra Tool, etc.), and we continue to maintain and improve these. Individually, these tools have proven effective in addressing specific monitoring tasks, but collectively their number and variety tend to overwhelm KB users, so we developed another application – the KB Navigator -- to launch the tools and facilitate their use for real monitoring tasks. The KB Navigator is a flexible, extensible java application that includes a browser for KB data content, as well as support to launch any of the regional analysis tools. In this paper, we will discuss the latest versions of KB Navigator and the regional analysis tools, with special emphasis on the new overarching inter-tool communication methodology that we have developed to make the KB Navigator and the tools function together seamlessly. We use a peer-to-peer communication model, which allows any tool to communicate with any other. The messages themselves are passed as serialized XML, and the conversion from Java to XML (and vice versa) is done using Java Architecture for XML Binding (JAXB).

OBJECTIVE

MatSeis and the regional analysis tools continue to provide an excellent prototyping environment in which promising seismic analysis techniques can be implemented and evaluated quickly with relatively little effort. These products are now all fairly mature, but development on them continues in response to the research results from our co-workers at LANL and LLNL.

The KB Navigator is a relatively recent addition to the suite of tools that Sandia has developed. The goal of the KB Navigator has been to provide a simple, consistent way to access the tools and content of the KB. Another part of using the KB that is being addressed is the level of interoperability between the diverse set of tools. The Peer to Peer Tool Communication provides a flexible framework in which applications can interact with one another.

RESEARCH ACCOMPLISHED

The following sections describe the latest versions of KB Navigator, MatSeis, the regional seismic analysis tools, and the new tool communication capabilities.

KB Navigator

The KB Navigator is a graphical interface into the KB that allows a user to find the research products, check geographic extents, access standard GIS datasets, view metadata and launch the research tools. An Oracle database schema was designed for the KB Navigator to hold all the pertinent information about the products.

Nodes in the KB Navigator are created for each dataset. There are two distinct kinds of nodes: folder nodes and dataset nodes. Folder nodes provide an organizational hierarchy and can contain other folder nodes as well as dataset nodes. Dataset nodes represent a variety of files, dataset types, database queries (SQL) and research tools - all the contents of the KB as best as can be captured with one tool. Each dataset node includes as much descriptive information as possible: proper name and version, location of the data on disk, dataset type, descriptive keyword information and the tools that can be used for access.

The new version of KB Navigator includes a streamlined database interface that simplifies the process of importing and exporting database content by allowing the user to drag and drop the pieces of the hierarchy. Double clicking on a dataset entry in the browser will automatically execute the default tool for that dataset. Keyword entry has also been simplified by allowing the user to drag and drop keywords, delete keywords, and select from existing keywords using a pulldown list.

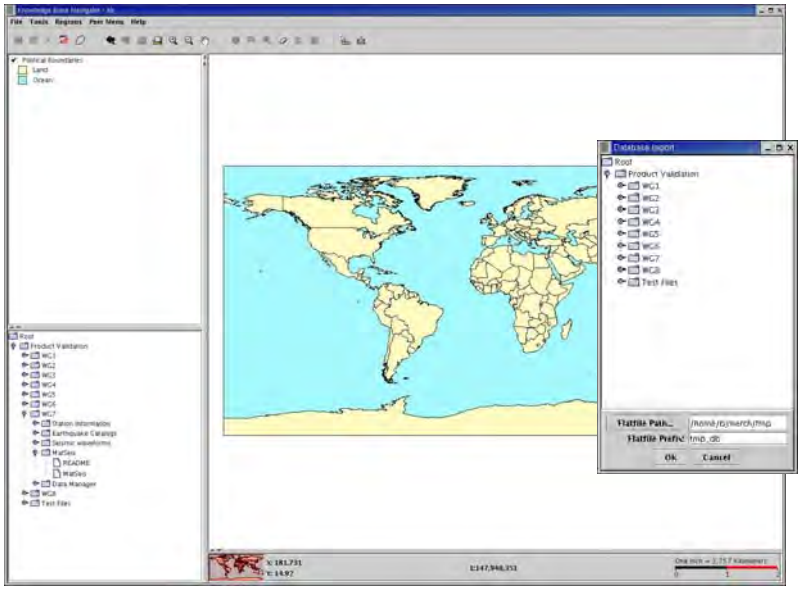


Figure 1. The KB Navigator and the Database Import interface

MatSeis 1.8

The main MatSeis graphical window is a standard time vs. epicentral distance plot that can display waveforms, arrivals, origins, and travel time curves. The user can interact with this display by clicking directly on the displayed objects, by using the buttons along the bottom, by using the menus along the top, or by typing commands at the Matlab prompt. MatSeis is predominantly written as Matlab m-file functions, which are organized in a set of directories according to the general purpose of each. However, the package also includes a set of compiled C functions and Java objects. Typically the compiled code is introduced where performance of an m-file is too slow (e.g. FK calculations) or cumbersome (e.g. managing the waveform, arrival, origin, and travel time objects). New features in MatSeis.1.8 are described below.

Support for System Environmental Variables
MatSeis 1.8 supports system environment variables within its configuration files. For example, in the following lines $MATSEIS_HOME will be replaced by the content of the environment variable MATSEIS_HOME:

setenv	MS_MAP_DATA	$MATSEIS_HOME/data/map
setenv	MS_MAP_FILE	$MATSEIS_HOME/data/map/world_15min.mf

Theoretical vs. Observed Travel Times
MatSeis 1.8 provides an interface for displaying actual arrival time versus theoretical arrival time. For a set of origins that have associated arrivals, we plot the relative arrival time versus epicentral distance, along with the theoretical travel time model data. Researchers can then see how their travel time model fits the observed arrival data.

Database Access
MatSeis was originally developed to read data from an Oracle SQL database using a command line utility to output the database results to a file on disk. This method of reading from a database was very inflexible and provided limited cross-database and cross-platform functionality. In order to make the software more generally useful and to provide access to any SQL Relational Database, for MatSeis 1.8 we have moved to using Java DataBase Connectivity (JDBC). This capability will allow MatSeis to access any type of database so long as a JDBC driver is available, and this makes it possible to read data from a remote database on the internet.

As part of our support for flatfile databases, CSS 3.0 and NNSA KB core table schema (Carr, 2002), we have added the ability to view flatfile database table contents by selecting from a menu within MatSeis (i.e. *View → CSS FF table Viewer → 'table name'*). The menu selection allows a user to choose from a subset of the available tables within the core schema. Current supported tables include affiliation, arrival, assoc, event, gregion,

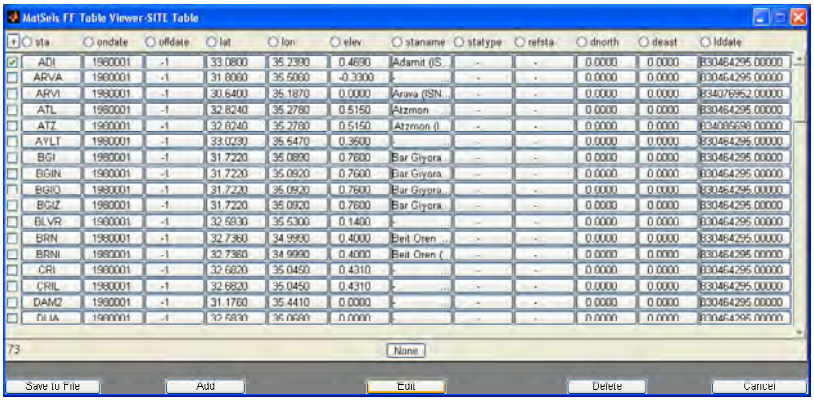


Figure 2. MatSeis Flatfile Table viewer

instrument, lastid, netmag, network, origerr, origin, remark, sensor, site, sitechan, sregion, stamag, and wfdisc. The viewing functionality was added to allow the user to verify the integrity of the flatfiles (error messages are displayed if the files have errors). In addition, the flatfile viewers provide the user with the ability to quickly read in select portions of a flatfile database.

In version 1.9 of MatSeis, users will also have the ability to add, edit or delete rows using this interface for their flatfile tables.

Signal Processing
MatSeis 1.8 contains several enhancements to simplify various signal processing operations. First, the FK interface now has the capability for the user to seamlessly transfer the azimuth and slowness information from the FK plot to the arrivals in MatSeis. Also, an interface has been added to allow the user to transfer arrivals from one element of an array to another by maintaining a time offset from the theoretical arrival time. Finally, the spectrogram and power spectral density plots can be animated to display the change in frequency content over time.

What's Coming in 1.9
MatSeis 1.9, due to be released in November 2004, will contain a number of useful feature enhancements. MatSeis will be able to write out wfdisc and binary waveforms data files. Two new MatSeis data types are being added for network and arrival magnitude association: netmag and stamag. These new data types are used in the same fashion as the existing MatSeis functions: arrival, origin, travtime and waveform. When reading in origins, if the netmag table exists and holds network magnitude values for the supplied origins, then those entries are read into netmag. In

a similar fashion, when arrivals are read into MatSeis, corresponding entries in the stamag table are read into stamag.

Phase Match Tool 1.8

PhaseMatch Tool is a waveform analysis interface launched from MatSeis that allows the user to calculate the predicted surface wave dispersion for a given source to receiver path by ray tracing through a model, and then use the model dispersion to generate and apply a matched filter (Herrin and Goforth, 1977). The tool allows the user to view the observed waveform, the model dispersion, the predicted waveform, the cross-correlation of the predicted and observed waveforms, and the match-filtered waveform. The user can control the frequency range of the model dispersion used, as well as the time limit of the portion of the cross-correlated waveform from which the match-filtered waveform is taken. Once a satisfactory filtering has been achieved, the user can send either the observed waveform or the filtered waveform to Measure Tool to measure surface wave amplitudes, which can then be used to determine event magnitude.

Phase Match Tool does not contain any new features for versions 1.8 or 1.9. However, beginning with MatSeis 1.9, Phase Match Tool will be included with the basic MatSeis package that is openly available on the GNEM R&E website.

Coda Magnitude Tool 1.8

CodaMag Tool is a waveform analysis interface launched from MatSeis that allows the user to calculate magnitudes and source spectra for an event of interest by fitting empirical decay functions to narrow-band coda envelopes of a given phase (currently Lg). The technique was developed by Mayeda and has been described in detail in several papers (Mayeda, 1993; Mayeda and Walter, 1996; Mayeda, et al., 1999). The tool consists of two displays. The main one shows the calculated moment spectrum and the derived magnitudes. The second display shows how the spectrum was derived. The user can adjust the Lg arrival window, examine the fit between the observed and synthetic envelopes, and control which frequency bands are used for the magnitude calculations. The various required parameters (frequency bands, groups velocity windows, decay curves, etc.) are read from parameter files unique to each station.

The only significant change for Version 1.8 is support for 2D tomographic Q models.

Event Identification Tool 1.8

EventID Tool is a waveform analysis interface launched from MatSeis that allows the user to identify an event of interest (i.e. explosion or earthquake) using spectral ratios of standard regional arrivals (see Hartse *et al*., 1997; Walter et al., 1999). The tool consists of three displays. The main display plots the phase ratio for the current event against a backdrop of the same ratio for archived events that have already been identified. The user can choose different phases and/or frequency bands to ratio to try to improve the separation of the earthquake and explosion populations, and the display will immediately update. A second display shows the user a plot of an "MDACogram" (i.e., the MDAC corrected measurements at all of the phase/frequency combinations) for the current event along with all of the archived events. This can be useful in deciding which ratio will yield the best separation. If there are questions about the amplitude measurements themselves, a third display can be brought up, and the user can easily examine group velocity windows for the

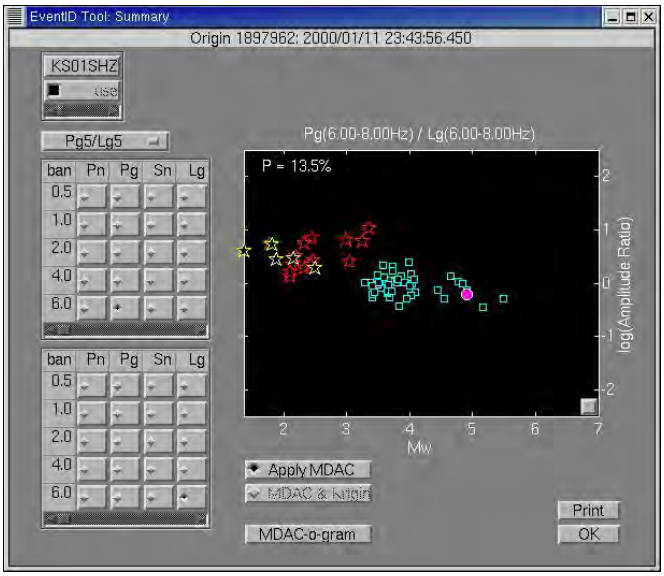


Figure 3. EventID Tool. Reference events are subclassified by event type.

phases and change them if necessary. If they are changed, the measurements will automatically be re-made and the ratios updated in the main display.

New features for Version 1.8 of EventID Tool include the ability to display a single measurement (i.e., not a ratio) and to change the scales on which the ratios/measurements are plotted.

Version 1.9 of EventID Tool will support the use of the origin event type to sub-classify the reference events. This will provide the ability to color code the reference events in order to distinguish between chemical and nuclear explosions.

Dendro Tool 1.8

Dendro Tool performs waveform correlation-based cluster analysis techniques on waveform data. The purpose of Dendro Tool is quite simple: to allow a user to quickly and efficiently determine whether a waveform of interest matches any in the available archives. By arranging the correlations in a hierarchical dendrogram, rather than just determining the most similar waveform, the user gets a much more complete picture of how the current event fits with the archived events. For example, in regions with repeated mining explosions, the mines are often easily identified as distinct clusters, and new mining events can be readily identified as such by association with those clusters.

Dendro Tool 1.8 includes the correlation matrix plot within the main display. This should assist the user in quickly determining the appropriate threshold level for selecting families. Dendro Tool also contains two options to help users attempting to process real-world data. The first option is to ignore channel name and just use the station name when determining which waveforms to cross-correlate (Dendro will still only correlate waveforms from the same station) and which arrivals to include. This option is useful for processing waveform data whose channel may have been renamed over time (i.e., 'sz' vs 'SHZ') or for associating arrivals that were picked on a channel other than the one the waveforms are on. The second option is to automatically transfer arrivals from the reference station of an array to an individual element. This option is to assist users who may want to use Dendro Tool to process a single element of an array and want to include the arrivals that where made on the reference station.

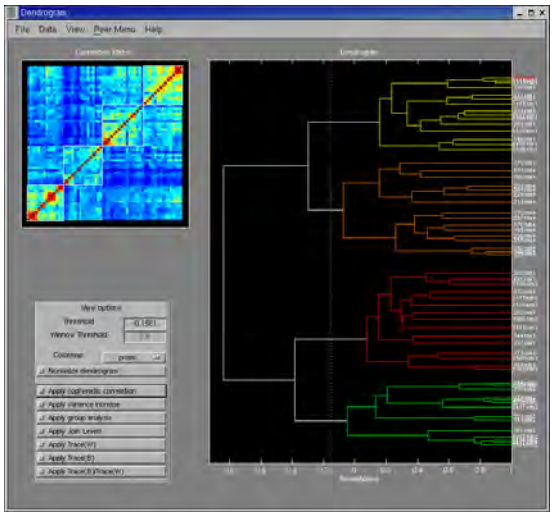


Figure 4. Dendro Tool with the correlation matrix

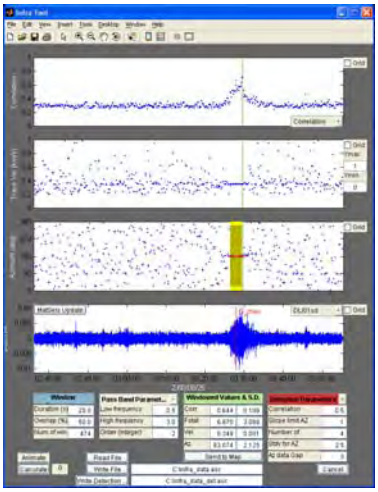


Figure 5. Infra Tool

Infra Tool 1.8

Infra Tool, included within the MatSeis release, has been expanded to support automatic detection of infrasound signals. Two routines were developed for the task of infrasound signal detection (Whitaker et al., 2002). Both methods are designed to use the results of frequency-slowness signal processing and a set of threshold parameters to determine when signals are detected (Hart, 2004). The detection threshold parameters are of four types: 1) number of point data considered, 2) correlation value to exceed, 3) slope limit bounds with standard deviation, and 4) detection gap points. The final detection parameter that will need to set is Number of Points. This fixes the number of data points used by the detection algorithms in determining the characteristic slope for the azimuth data being analyzed. Once processing is complete, detection results can also be written to a file.

Version 1.9 of Infra Tool will have the ability to add an arrival to MatSeis and set the arrival's azimuth and azimuth standard deviation based on the results from Infra Tool.

Hydro Tool 1.8

Hydro Tool employs the same array and frequency-slowness processing techniques as Infra Tool, except that the default parameter settings have been changed to values more appropriate for hydroacoustic data. It is also included in the standard MatSeis release. Hydro Tool is intended to provide a platform for future research and development in hydroacoustic processing. Subsequent versions will incorporate any feedback and suggestions that users may have.

Measure Tool 1.8

Measure Tool is the MatSeis utility for performing picking/re-timing arrivals and measuring amplitudes. There are three new features in Measure Tool 1.8: The addition of a spectrogram plot, the ability to set first-motion direction and quality for long-period and short-period signals, and the ability to compute regional event durations using a frequency spectrum analysis technique.

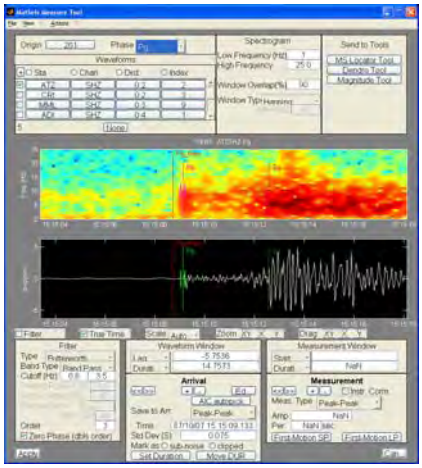


Figure 6. Measure Tool

Tool Communication

The rich suite of KB tools developed by NNSA has provided important new capability for monitoring, but without some sort of inter-tool communication, using the tools for daily monitoring is impractical. In general, each tool has been developed independently without any expectation that it would be able to interface with anything other than a small subset of the KB. Also, the evolutionary method by which the KB has grown has prevented any sort of standardization of practices across the software being developed. The effect of this manner of development has been that we are now faced with a set of tools that have little in common, other than the fact that they are all part of the KB. The tools are written in a variety of programming languages and were each custom developed to address a specific need.

Previous efforts to address this failing have met with mixed results. In the past, changes to the tools have been made to allow specific tools to communicate. This communication has always been point to point between the two tools in question (such as ArcView and MatSeis).

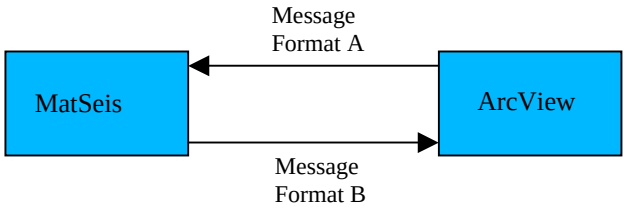


Figure 7. Previous style of tool communication

The messages passed between the tools were in a custom format that was very inflexible, and a new format had to be defined for each communication path. Also, it was necessary to manually implement all of the possible interactions between tools. The end result was a method of communicating that was difficult to create and even more difficult to extend.

The challenges experienced with previous attempts at tool communication have led to a set of requirements that should greatly improve the ability of tools to interact as well as reduce the burden on the individual tool developers. First, the design should allow any tool to communicate with any other tool without having to be modified specifically to implement that interaction. This implies that the set of allowable tool interactions have to be defined at run-time. Second, the design and implementation should require minimal effort on the part of the developer to make use of this communication. The developer should not have to be involved in any of the details relating to how

the communication is taking place. Third, the communication should not be platform-specific and a consistent message format should be used for all communication.

Towards this end, we have developed a common library that the tools can make use of in order for them to communicate. By using such a library, all the tools will be guaranteed to be making use of the same compatible communication mechanism. We chose to implement the tool communication in Java and use XML as the message format. This combination of language and message format will provide us with platform independent communication. However, we still have the fact that our set of tools was written in a variety of languages (Java, Matlab, C, C++). Fortunately, we have been able to work around this multiplicity of languages without too much trouble. Java tools can use the communication package directly, and so can the Matlab based tools thanks to Matlab's Java support. C/C++ applications we develop can make use of JNI to interface between the Java and C/C++ code.

The tool communication makes use of the Java Architecture for XML Binding (JAXB). Using JAXB, we are able to write a schema document that is then compiled into Java source code. These JAXB derived Java Objects are able to convert themselves to and from XML, freeing the developers from having to work directly with XML. The use of JAXB has greatly simplified the message handling within the tool communication.

The tool communication also makes use of an NNSA-developed library called DBTools (see Ballard and Lewis, 2004), which is used for intelligently managing database content. DBTools is a very rich library capable of managing any type of relational data that could be stored in a database. By using DBTools as the basis for passing data between applications, the tool communication also has the ability to pass any type of data.

The tool communication consists of two distinct parts. The first part of the communication allows the tools to advertise themselves to each other. The second part of the communication allows each tool to take advantage of the advertisements that it has received to interact with another application.

Peer to Peer Advertisement

In the advertisement portion of the communication, all of the tools connect to a multicast UDP socket. So, all of the KB tools are listening to a single common source. Any messages sent to the Multicast Socket are received by all of the tools.

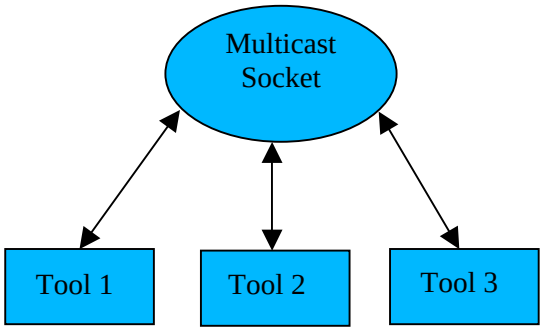


Figure 8. Peer-to-Peer Advertisement using a Multicast Socket

Advertisement messages are sent across the multicast socket. The advertisements contains information such as the name of the tool, the port and address at which the tool is maintaining a server on a TCP socket, and a list of functions that the tool provides. Each function advertisement defines some service that the tool can perform. The advertisement also defines the inputs that the function requires using a DBTools Schema object. The calling application will use the Schema object to determine the type of data to provide as input to the function. An example for MatSeis is shown below:

```
<advertisement>
       <name>MatSeis</name>
       <address>192.168.0.1</name>
       <port>4446</port>
```

```
        <id>2382382832</id>
        <timeout>340983482398</timeout>
        <functions>
               <name>gov.sandia.gnem.matseis.MatSeis</name>
               <method>function1</method>
               <label>Function One</label>
               <description>Perform Function One</description>
               <schema>
               …
               </schema>
        </functions>
        <functions>
               <name>gov.sandia.gnem.matseis.MatSeis</name>
               <method>function2</method>
               <label>Function Two</label>
               <description>Perform Function Two</description>
               <schema>
               …
               </schema>
        </functions>
</advertisement>
```

The advertisements also contain an ID to uniquely identify the tool and a timeout that represents the time when the advertisement expires. Each tool is responsible for periodically sending an updated advertisement to replace the expired advertisement. Each tool also maintains a list of the advertisements that it has received. This caching mechanism eliminates the need to implement any sort of centralized repository (e.g. Tuxedo). Since each tool retains a registry of the tools available and the functions that each provides, it is a trivial process to present the user with a menu detailing these functions.

These messages combine to form a dynamic peer to peer network of tools that are capable of registering themselves with each other. None of the tools need to be coded to specifically interact with any other tool since the introductions are handled at runtime. When a tool exits, it stops sending updated advertisements and so is removed from the registries when the existing advertisements expire.

Though we have not yet tried to implement our communication beyond the applications running on a given user's computer, this should be possible because multicast sockets are not limited to operating on a single host. Since the address of a multicast socket does not correspond to any physical machine address, applications on multiple hosts could all bind to the same socket and would then be included in this network of peer-to-peer tool communication. The messages sent on the multicast socket would propagate through the network as far as the network architecture allowed. This capability holds definite promise for possible future development involving distributed computing. For example, a computationally intensive function could be provided on a high-performance server and that function would be available to everyone on the network. Tools on the users desktop could then access this function as if it were just another application on the desktop.

Function Calls

In the second part of the communication, tools can call the functions that have been advertised. Each tool maintains a TCP socket on which it runs a server. Because the server port number will be communicated at run-time within the advertisement, the next available port on the system can be used. This eliminates the need to track the port numbers for each of the tools in the user environment or some configuration file.

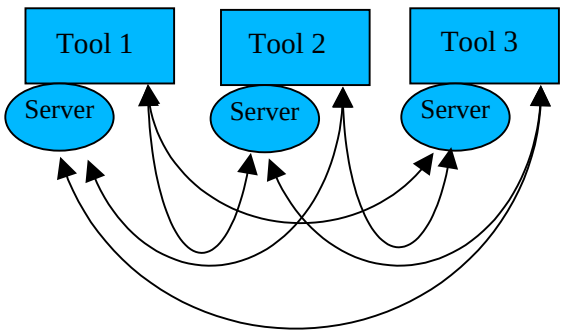


Figure 9. Function Calls between tools.

Using the function advertisement, a tool can assemble a Function Call message to pass to the server. The server then processes the function call by executing the indicated method with the supplied inputs. Once the method has completed, the server collects the outputs from the method and returns them to the calling tool. The inputs and outputs of the function calls are passed as DBTools RowGraph objects.

Although there is some complexity involved in managing the communication for the multicast socket and the server/client code, it is functionality that is common to all of the tool implementations. Therefore, this functionality has been implemented within the communication package and provides a simple interface for each of the tools to make use of. The goal has been to hide as much as possible of the details of the communication and messaging from the individual tool. This should allow the tool communication to develop and expand with minimal impact on the tools.

The Peer to Peer Tool Communication has been incorporated into KB Navigator, MatSeis, and Dendro. In each of these tools, there is a dynamic "Peer Menu" item at the top of the figure. Within the peer menu, there is a submenu for each tool, labeled with the name of the tool. Within each tool submenu is the list of functions that tool has advertised. Using these menus, a user can easily perform any of the functions provided, such as transferring origins between applications. More advanced functions are also available that will allow a user to select origins and stations within KB Navigator and have MatSeis automatically read in the corresponding waveforms.

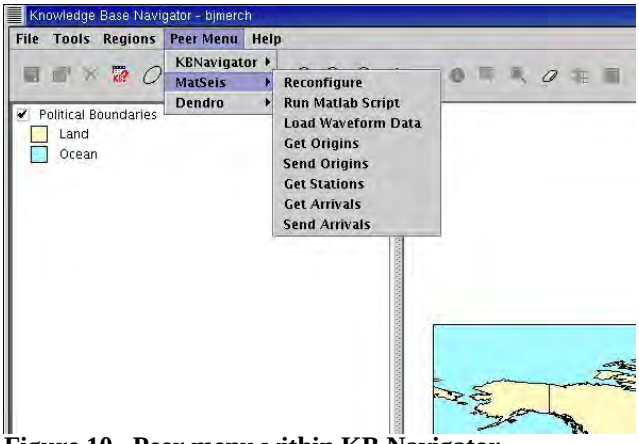


Figure 10. Peer menu within KB Navigator

The utility of the Peer to Peer Tool Communication is expected to increase dramatically as additional tools are incorporated and as the number of functions that each tool can perform increases.

CONCLUSIONS AND RECOMMENDATIONS

In this paper, we have highlighted some of the more significant changes in KB Navigator, MatSeis, and the MatSeis-based regional seismic analysis tools. We have also discussed the tool communication capabilities that are in the process of being incorporated into the various Knowledge Base tools. We expect that the continued development of the individual tools coupled with increasing interoperability between the tools will result in a very powerful and easily extensible regional analysis environment.

The official 1.8 version of the basic MatSeis package for Matlab 6.5 is available to all from the GNEM R&E web site: https://www.nemre.nnsa.doe.gov/cgi-bin/prod/nemre/matseis.cgi

MatSeis 1.9, which will support Matlab 6.5 and 7.0, will be available from the above website in November 2004.

Matlab and the Signal Processing Toolbox are required to run MatSeis. MatSeis will run on Sun workstations, Windows PC's, and Linux PC's. It should run on other supported Matlab platforms as well, but the C code will need to be re-compiled.

ACKNOWLEDGEMENTS

We thank all of the MatSeis users who have helped us to debug and improve the software, particularly our colleagues at LANL and LLNL.

REFERENCES

Ballard, S. and J. Lewis (2004), DBTools: "A Suite of Tools for Manipulating Information in a Relational Database," in Proceedings of the 26th Annual Seismic Research Review Symposium, Orlando, Florida, USA.

Carr, D. (2004), National Nuclear Security Administration Knowledge Base Core Table Schema Document, Sandia National Laboratories, SAND2002-3005 available at https://www.nemre.nnsa.doe.gov/prod/nemre/fileshare/coretables_062104.pdf.

Everitt, B. S. (2001), Cluster Analysis, Arnold, London.

Hart, D. H. (2004), Automated Infrasound Signal Detection Algorithms Implimented in MatSeis – Infra Tool, Sandia Technical Report SAND2004-1889.

Hart, D.H. and Chris J. Young (2002), MatSeis User Manual version 1.7, https://www.nemre.nnsa.doe.gov/cgi-bin/prod/nemre/matseis.cgi.

Hartse, H. E., Taylor, S. R., Phillips, W. S., and G. E. Randall (1997), A Preliminary Study of Regional Seismic Discrimination in Central Asia with Emphasis on Western China, *Bull. Seism. Soc. Am*. 87, 551-568.

Herrin, E. and T. Goforth (1977), Phase-Matched Filters: Application to the Study of Rayleigh Waves, *Bull. Seism. Soc. Am.* 67, 1259-1275.

Mayeda, K. (1993), Mb(LgCoda): a Stable Single Station Estimator of Magnitude, *Bull. Seism. Soc. Am*. 83, 851-861.

Mayeda, K. and W. R. Walter (1996). Moment, Energy, Stress Drop, and Source Spectra of Western United States Earthquakes from Regional Coda Envelopes, *J. Geophys. Res*. 101, 11,195-11,208.

Mayeda, K., R. Hofstetter, A. J. Rodgers and W. R. Walter (1999). Applying Coda Envelope Measurements to Local and Regional Waveforms for Stable Estimates of Magnitude, Source Spectra, and Energy, *21st Annual Seismic Research Symposium on Monitoring a CTBT*, Vol I, 527-533.

Walter, W. R., A. J. Rodgers, A. Sicherman, W. Hanley, K. Mayeda, S. C. Myers and M. Pasyanos (1999). LLNL's Regional Seismic Monitoring Research, *21st Annual Seismic Research Symposium on Monitoring a CTBT*, Vol I, 294-302.

Whitaker, W., Douglas ReVelle, and Tom Sandoval (2002), "On Infrasound Detection and Location Strategies," in Proceedings of the 24th Annual Seismic Research Review Symposium, Ponte Vedra Beach, Florida, USA.

EFFICIENT INTEGRATION OF OLD AND NEW RESEARCH TOOLS FOR AUTOMATING THE IDENTIFICATION AND ANALYSIS OF SEISMIC REFERENCE EVENTS

Wilmer Rivers[1], Robert A. Wagner[1], Joey Chen[1], Eric Siu[1], Craig A. Schultz[2], Douglas A. Dodge[2], and Gregory Pope[2]

Multimax, Inc.[1]; Lawrence Livermore National Laboratory[2]

Sponsored by National Nuclear Security Administration
Office of Nonproliferation Research and Engineering
Office of Defense Nuclear Nonproliferation

Contract No. DE-FG02-01ER83218[1] and W-7405-ENG-48[2]

ABSTRACT

The selection and study of reference events for inclusion in the National Nuclear Security Administration (NNSA) Knowledge Base (KB) require the application of a much broader suite of seismic analysis software than do either the routine production of a seismic bulletin or the subsequent preliminary screening of those bulletin events to conduct nuclear monitoring. For either of the latter applications, a large program designed explicitly for that single purpose can perform all the tasks that must be applied to the many events that will be processed daily, whereas all the different measurements and algorithms that a scientist may wish to apply to a candidate reference event cannot be anticipated in advance and incorporated into a single large program. A scientist studying candidate reference events is therefore more likely to need the capabilities found in many separate specialized programs, and it may in fact be necessary to develop new software to perform specific analyses that are modified or designed just for the particular events under examination. All these applications, including the developmental software that is still in the testing phase, must then be made to work in tandem so that they can be applied to the data set under examination.

To link together the different applications (which may be running in separate execution threads on a single computer or on separate computers, perhaps even under different operating systems), it is necessary to implement a middleware layer and then modify the applications so that they can communicate through it. There are two principal approaches to establishing the interprocess communications, and we have examined both of them. One is the tight coupling of one application to another through socket-based remote procedure calls that are implemented directly in code or within common object request broker architecture (CORBA) or Java remote method invocation (RMI) client-server software. The alternative approach is the loose coupling of a diffuse cluster of clients and servers employing a service-oriented architecture (SOA) for communications, especially across an intranet or internet, such as “Web services” that exchange both processing requests and data as XML-formatted simple object access protocol (SOAP) messages transmitted by HTTP.

In this project we have assumed that the familiar program *geotool,* for the interactive display and processing of seismic data, will be the cornerstone program in a reference event analysis system. Because *geotool* is built using an early 1990s architecture consisting of a single, large C-language program running within UNIX (or Linux) that invokes operations through callback functions from Motif widgets, it is a difficult program to modify without introducing unanticipated software “side effects” into parts of the code that were not themselves directly modified. We have met with mixed results in attempting to make *geotool* flexible enough to allow it to request services from other programs by acting as a so-called “fat client” (i.e., a program that does most of the data processing itself and relies on server programs only for specialized tasks). A preferable approach would be to employ a “thin client” program that serves mainly as a user interface (like a graphics terminal), but it would be better still to retain much of the client-side functionality of *geotool* by breaking it up into individual components that could be modified independently of one another, thereby minimizing the side effects introduced by those modifications. Modern software architectures as such J2EE and .NET rely on client and server programs that are developed using this approach. A promising future platform for building a reference event analysis system comprising individual software components for different seismic data processing tasks is the next version of the Windows operating system, which is built upon a middleware layer called “Indigo” that blurs the distinction between a tight client-server coupling and a loose coupling of Web services by employing SOAP messages for both types of interprocess communications.

OBJECTIVE

Scientists use a variety of stand-alone computer programs to analyze and identify seismic events for the monitoring of the nuclear test ban, and an especially wide selection of software tools is needed for the detection and intensive study of reference events that will be included in the NNSA KB for use in future event comparisons. Some of these stand-alone programs are large software packages that offer many tools for routine seismic analysis, but they are difficult to modify to include additional tools for specialized tasks. Others of these stand-alone programs offer the capability of performing only specific operations, and they must be used in conjunction with other programs such as interactive waveform graphics displays that offer more general analysis capabilities. In most cases neither the large software packages nor the specialized analysis programs can communicate adequately from one to another without the tedious creation and input of temporary data files and other awkward techniques. Since the stand-alone programs cannot exchange data easily, it is difficult to use them in a data-processing pipeline that could add new capabilities to those offered by the large software packages or that could allow the specialized analysis programs to rely on other software for tasks such as graphics displays.

A reference event analysis system should therefore be built by using a system architecture that facilitates data flow among these stand-alone programs, including any new programs that will be developed in the course of future research and that may be especially valuable for the identification and characterization of reference events. This new architecture should allow the results of one program to be sent easily to another one, as chosen on a case-by-case basis by the seismic analyst, without the creation of temporary files and database tables. Because many of the stand-alone seismic analysis programs that need to communicate with one another are written in different computer languages, and many are written for use under different operating systems, it will be important for this architecture to be as nearly platform-independent as possible. Furthermore, the communications among the separate programs should allow access to remote resources for data retrieval or specialized computations. Ideally, the reference event analysis system should therefore be constructed as a distributed system of individual software components rather than as a single, large software package. We have investigated the use of this architecture for the processing of seismic data, by using the large C-language program *geotool* (Henson, 1993; Coyne and Henson, 1995) as the primary tool for user interaction and by determining how difficult it is to add new functionality to *geotool* by using software architecture that is based on distributed processing.

RESEARCH ACCOMPLISHED

Use of CORBA for extending *geotool*

Figure 1 shows one manner in which a distributed architecture can be used in practice, and it is the method that we used in the first phase of our investigation (Rivers et al., 2002). In that phase we used CORBA (a client-server architecture commonly used in the 1990s for large-scale business systems) as the means for data communications between the seismic analysis program *geotool*, operating as a data server running under Linux, and a Java program called *WaveformViewer,* operating as a client application on a Windows computer. (*WaveformViewer* is a program that displays a waveform on the screen using Java "Swing" graphics but that also allows the operator to perform some signal-processing operations such as digital filtering on the data.) CORBA has a particular advantage for our purposes, in that because much business software in the 1990s was written in C under UNIX, CORBA can be made to interface with a program like *geotool*. As will be discussed below, much modern software for data communications is not suitable for that environment, which remains the most common one for software performing nuclear monitoring data processing, especially for legacy applications.

We wrote software called CORBA Center to specify that *geotool* on a Linux computer will operate as a data server and that the Java program *WaveformViewer* on a Windows computer will be a client. As is shown in the diagram in Figure 1, we modified *geotool* by adding new callback functions that allow it to communicate with an Object Request Broker (ORB). (Since *geotool* is running under Red Hat's distribution of Linux, we can make use of the open-source ORB known as ORBit that is bundled as a part of the distribution. For *geotool* running instead under Solaris, we could use one of a number of commercial ORBs for UNIX.) Using the X Resources file for *geotool* we can then add a new pull-down menu item that will allow the user to send data to *WaveformViewer* by invoking CORBA Center. The CORBA Center utility expedites the process of setting up the data connection by effectively acting as a switchboard for choosing a server side and a client side of the data flow. This utility registers the IP addresses with the CORBA naming service (to associate object references with symbolic names) so that the two

programs can exchange data across the LAN as easily as if they were both running on the same computer. CORBA's data communication across the LAN takes place using the Internet Inter-ORB Protocol (IIOP). This is an official Internet protocol (such as FTP and HTTP) that allows an ORB on one platform to communicate with one on another platform. Note that it is irrelevant that *geotool* is written in C and *WaveformViewer* is written in Java, since IIOP is platform-independent. We modified the *WaveformViewer* client application by adding callback functions that allow it to communicate with a new "Agent" Java class, which in turn handles the communication with the ORB that is included within the Java platform under release JDK 1.2. The data messages that are exchanged through this client-server communication consist of seismograms and the metadata that describe them, in conformance with the standard CSS data schema (Carter *et al.*, 2001). To allow this communication, we have translated the CSS-schema data structures such as *.wfdisc*, *.arrival*, *.origin*, etc., into CORBA's interface definition language (IDL). An IDL routine does not know whether the application with which it is communicating is written in C or Java (or one of several other languages). All it knows is that the application on the other side of the data stream expects to receive a message conforming to a particular IDL argument list, and we have therefore translated all the standard CSS data tables into a single IDL interface so that we can reuse that same interface for as many different *geotool* client-server applications as possible.

The architecture shown in Figure 1 may be a bit misleading, since *geotool* is shown operating as a data server and *WaveformViewer* as a client application. The goal of this investigation, however, is to use *geotool* as a graphical interface for user interaction (i.e., as a client), and to use external software as application servers delivering requested information and processing results to that client. For the CORBA architecture in Figure 1 this distinction is not critical, since CORBA establishes a socket connection that is actually being used in more nearly a peer-to-peer mode, with a scientist performing graphical operations on both the *geotool* and *WaveformViewer* sides by switching back and forth between working on the Linux workstation and the Windows PC (both of which must therefore be physically accessible to the scientist). In practice, this design would be implemented by running both *geotool* and the Java *WaveformViewer* within separate windows on the same Linux workstation, instead of running the Java *WaveformViewer* on a separate Windows computer. In the next section we shall examine a more typical scenario, wherein the distinction between client and server is sharper, and *geotool* does indeed operate as a graphical client of remote server applications.

Use of Web Services for Extending *geotool*

In the second phase of our investigation, we replaced the tight coupling of applications with a loose coupling architecture, namely Web services. In this configuration, application programs are treated as URLs that are accessed over an intranet or the Internet by sending XML messages over simple HTTP connections. The format of these XML messages includes the necessary data for the service to be performed and a remote procedure call, expressed in ASCII text rather than binary code, as specified by the SOAP standard. After the Web service application performs the data-processing (and/or data-retrieval) service for which it was invoked, it returns its results to the client application through another SOAP-formatted XML message over HTTP. The tight binary coupling of the client and server tiers that characterize CORBA is thus replaced by an ASCII-based messaging system. The concept is analogous to that of the World Wide Web: through the transmission of XML messages, the Internet can become not only a Web of information but also a Web of services. A particular benefit of using XML and SOAP to transmit messages between a client and (multiple) servers is that because the messages are ASCII, and the wire protocol is HTTP, they can pass through firewalls that would block attempts by remote systems to transmit binary messages and invoke operating system actions through CORBA. The trade-off for the flexibility of the loose coupling is that, by operating at a higher level of abstraction in the TCP/IP software stack, Web services are less efficient than a tight coupling architecture like CORBA. In particular, since the data transmitted to and received from the Web services are ASCII encoded, and since they are augmented with tags for XML markup, the messages that are sent over the intranet or Internet are considerably larger than the corresponding binary data would be. An example of a SOAP message for performing a signal-processing operation on a time-series array (such as a seismogram) is shown in Figure 2.

We have encountered difficulties in this project due to the paucity of satisfactory software for using SOAP with C or C++ programs on UNIX and Linux, and like much other geophysical analysis software (especially older code), *geotool* is in fact such a program. The Microsoft SOAP toolkit makes it possible, albeit not especially easy, to use SOAP with C/C++ software on Windows (a task that now has been made considerably easier under the .NET platform, as we discuss below), but there is no corresponding commercially supported off-the-shelf technology for C/C++ on Unix or Linux other than certain expensive products that have been developed for enterprise-scale

commercial applications. In our 2003 work we therefore used the academic software *gsoap* to enable *geotool* to communicate using SOAP, but the process was not so simple as we would like it to be. This is a significant problem, since ease of use will be an important consideration by a scientist who wishes to integrate new and legacy research software. By far the most popular UNIX and Linux Web server for utilizing SOAP is the Java-based software *Axis*, which is developed and maintained by the open-source software organization Apache. Throughout the duration of this project, we have waited for Apache to deliver the promised C++ version of *Axis*, but it was not released until the spring of 2004. Our attempts to use that C++ version of *Axis* have been unsatisfactory, and we are not alone in that experience, so we feel this version 1 software release needs further improvements before we can interface it to *geotool*. Fortunately, a new version of *gsoap* has now been released that generates header files that require less manual changing, so it is now a bit easier to use *gsoap* to implement C/C++ Web services on UNIX and Linux than it was previously. However, the process is still far from transparent, and many or most scientists will not want to make use of it for routine purposes.

Problems with Incorporating *geotool* into a Reference Event Analysis System

As is described above, we found adding functionality to *geotool* by modifying the program to send and receive SOAP messages to be a more complicated process than most scientists would be willing to do for routine modifications, and so the process needs to be simplified. Perhaps an even bigger problem, however, is that not only is it cumbersome to modify *geotool* to communicate with other applications, it is difficult to modify *geotool* to make use of the information that those other applications would send to it. This problem is a consequence of the program's architecture, namely an early, 1990s-style, large, C-language program with many internal interdependencies. Thus, changing the code to modify a feature or add a new one is liable to cause unanticipated "side effects" in a different feature. In a reference event system, it will be necessary to modify *geotool* by adding widgets that permit the user to manipulate the displayed data and select seismogram segments, make measurements, enter parameter data, and then dispatch those values to another application which will in turn send its results back to *geotool* for display, a process that will require further modification to add new widgets (or expand existing ones) to incorporate those results. Each of these modifications to the code is liable to cause problems and introduce bugs. In many cases it is possible to accomplish changes by editing a table of X Windows resources, and this process is certainly preferable since it requires changing only an ASCII file outside of *geotool* instead of the source code. However, most modifications require some reprogramming, and the architecture of *geotool* is not sufficiently robust for changes to be made easily.

Evidence of this problem can be seen in the host of changes we have made to *geotool* during this project simply to fix existing bugs in the code and to expand the functionality of many existing operations, since these changes were all internal to *geotool* and involved no communications with any other applications. An extensive list of bug fixes was generated by intensive testing of the existing code, and the mere fact that these bugs have persisted in a program that is well over a decade old shows how hard the code is to modify successfully. In spite of the problems in making changes to a large C program, we did correct those bugs, and we added many features that users have specified as being needed to enhance the utility of *geotool* and improve its ease of use. The process (illustrated by the addition of the Oracle interface shown in Figure 3) has been a tedious one, however, and it bodes ill for our intended use of *geotool* as a central application in a reference event system, since we would like it to serve as a graphical user interface and would thus require frequent modification to perform new data manipulation and display operations. We acknowledge that a preferable approach would be to use, at the very least, a program that runs within a modern software "platform" like Java or .NET that handles the low-level systems operations, instead of a legacy program like *geotool* that must make UNIX kernel calls and other systems-level operations. It would be better still to use a program running within that platform that is far more flexible than is a monolithic C code like *geotool*, such as an object-oriented program organized into independent components (such as Enterprise Java Beans) that can be swapped in and out just as hardware components can be. In this regard, *geotool* is significantly inferior to a modern seismic analysis program like *MatSeis* (Hart, 2004), which minimizes many of these difficulties because it is built upon a robust commercial software platform (MATLAB) that offers to the programmer an extensive suite of graphical and computational components that adhere to this architecture. In the long term it would be easier to build new "thin client" programs (i.e., small object-oriented codes that rely on an underlying software platform for systems-level operations and that have little functionality other than to serve as a user interface for server-side components and applications) to act as intermediaries in a seismic reference event system than to continually make major modifications to a large, fragile program like *geotool* every time that new functionality is required. In the following section we discuss modern trends in software development that should be exploited to construct the type of programs that would be better suited than *geotool* for use within a seismic reference event system.

Recent Developments in Service-Oriented Architecture for Commercial Software Systems

The need to integrate separate business processes, such as shipping products and submitting invoices, has long been a requirement in commerce, and large, complex management information systems have been sold for many years to address that need. More recently, these systems have evolved to a higher level by unifying all the separate "information stovepipes" within a corporation, for instance, by allowing the warehouse inventory system to initiate requisition processes in the purchasing system. Most of these enterprise resource management software systems make use of data warehouse systems, a specialized type of database for online analysis processing (OLAP) that used to be a separate technology but that is now being incorporated into conventional transactional processing relational database management systems, such as the latest versions of Oracle and SQL Server. These commercial software systems for integrating separate processes are conventionally implemented using a three-tier client-server architecture wherein desktop computers function as "thin clients" for graphical user interaction, a database server allows all applications to have access to the same data (to the extent allowed by security controls), and in the middle tier the actual business rules are carried out by programs running on an application server. The communications between the desktop clients and the application server, and between the application server and the database server, are carried out through tight coupling of the tiers. The inter-tier communications use socket connections directly or underneath remote procedure calls, CORBA, or Java remote method invocations (RMI), which is a Java-specific implementation of CORBA.

Currently, however, most enterprises are starting to implement, or at least to experiment with, a loosely coupled architecture for integrating separate processes, namely SOA. One of the principal motivations for using SOA is that it allows a still higher level of integration, not just within a department or throughout the enterprise but among separate enterprises. The concept underlying SOA is that a company can use a Web server tier to respond to requests for services from individual applications whether those applications are running locally or at another site. That way the purchasing system of one company can initiate a process by the order fulfillment system of another company, without the need for manually re-entering the data from the first company's purchase order (generated by that company's application server tier) into the back-end database of the other company so that the second company's application server can process it. Obviously, allowing data to flow directly from one company to another cannot be accomplished by a tight coupling of the two computer systems, due to security concerns. A nonintrusive data communications model is required for an SOA that uses an open protocol such as HTTP for transmitting data in ASCII format instead of in a binary format that can contain viruses or spyware. Such a model is provided by SOAP and XML, and in fact, the acronym "SOAP" is sometimes now re-interpreted to mean "service-oriented architecture protocol." Corporations are actively addressing methods to expose their business processes as Web services so that they can be utilized by both local and remote applications, and a large software industry is emerging to meet that demand. Our work in Phase II of this project began at about the same time as SOA became popular in industry, and in future work, we expect to be able to make use of forthcoming software products, both commercial and opensource, that will considerably expedite application integration using SOAP.

A large part of the problem in our use of SOAP has been that not only are programs such as *geotool* legacy software, but the fundamental architecture for developing software that runs at a level close to the operating system (in our case, Linux) is itself a legacy design. Modern software is for the most part written at a higher level, specifically one that targets a "platform" such as Java or .NET rather than the underlying operating system. The platform interposes a software layer that operates as a virtual machine to handle the low-level communications protocols. We hope that the available tools such as *gsoap* and Apache's *Axis* for C/C++ will become easier to use, but for now, it is considerably simpler to implement Web services within the Java and .NET platforms where much of the data communications is handled by the platform software instead of by the applications.

Furthermore, the ease of use of the platforms is escalating rapidly. Because Java has its own CORBA-style RMI software for performing Java-to-Java communications, and since it also supports CORBA directly, Java software used for SOAP communication has heretofore been provided only by packages external to the core language. With the release in July 2004 of Java 1.5 (now re-labeled Java 5), however, JAX-RPC (Java application programming interface [API] for XML-based remote procedure calls) has been incorporated into the client-side platform, and this same change will be made to the next release of the server-side platform. Moreover, in 2005 Sun will release new software development tools that will make the use of Web services easier, and the open-source Eclipse organization is doing the same. On the .NET platform, the implementation of Web services has always been made relatively easy (although still not transparent) by the use of ASP.NET (a technology that replaced Microsoft's Active Server Pages for its earlier COM platform), since much of the low-level coding of both the proxy client and the proxy server is generated

automatically in a fashion that requires no recoding by the programmer. This processing is becoming easier still, because on July 1, 2004, Microsoft released the first beta distribution of "Whibdey", its new integrated development environment for .NET programming (which will be released officially as *Visual Studio 2005* next year). "Whidbey" contains a new tool with the code name "Whitehorse" that expedites the design and construction of SOA software. Unlike the Java platform, the .NET platform supports multiple languages, and Web service clients and services can be constructed using the version of C++ that runs within .NET. (The syntax for C++ under .NET, and the scope and utility of that language for the .NET platform, will also be considerably enhanced under "Whidbey".) Web services can be implemented in .NET even by using Fortran 95 with selected Fortran 2003 object-oriented extensions, and the commercially available Lahey-Fujitsu v7.1 compiler accomplishes this. We anticipate that the introduction of JAX-RPC into the Java 1.5 platform, the introduction of "Whidbey" for the .Net platform, the release next year of new Java software development tools by Sun and by Eclipse, and the continued evolution of the lower-level *gsoap* and Apache *Axis* tools for C/C++ application on Unix and Linux will all make the implementation of Web services considerably more efficient within the next year or so than it has been heretofore.

Future Developments in System Architecture for Desktop Clients

As we have noted, most modern desktop applications, unlike legacy programs such as *geotool*, are written using an object-oriented design that permits them to be altered with less danger of introducing unanticipated side effects than is possible in a large C language program. An important trend is that the platforms on which these modern programs run, such as .NET and Java, are themselves object-oriented, so modern application development software readily enables desktop client programs to be constructed that are more nearly suitable for easy modification than *geotool*. We plan to continue development by migrating functionality from *geotool* to new client and server applications that will be sufficiently flexible for easy incorporation into a seismic analysis system that can be tailored for the needs of analyzing specific data sets.

A particular software platform that will likely be useful for constructing the sort of highly flexible distributed systems that will be needed for integrating seismic analysis applications is the next version of Microsoft Windows, which has the code name "Longhorn" and will likely be released as "Windows 2006." Although the software that is available to developers is still in its pre-alpha release, it is possible to begin investigating its utility for constructing new client and server applications that may eventually replace *geotool*, and we intend to pursue that investigation. "Longhorn" offers a particular benefit to the construction of distributed applications in that it incorporates a new data communications software system called "Indigo" that uses XML and SOAP messages not only for Web services but also for interprocess communication within the local environment. It will thus be transparent to the developer whether function calls are being made across threads or across computer systems. More importantly for the ease of use, and hence for the likelihood that scientists will write their code in a manner that allows its incorporation into a distributed system, the "Indigo" software will automate most of the coding required to perform data communications using SOAP. This will be an important change from the current situation with CORBA and Web services, and we feel it is important that work begin on building new programs using this new data communications software. Another significant feature of "Longhorn" is that the screen graphics for drawing windows, window controls (such as menus, buttons, etc.), and presentation graphics within windows (such as plots of seismograms, spectra, etc.) will be performed using a new API that is based on XML. Moving to XML-based displays and screen graphics from those built using Motif and Xlib on Linux and UNIX or using COM widgets or .NET Forms and GDI+ or Win32 low-level graphics on Windows, will be a significant change in the construction of seismic analysis software and is a potentially valuable feature. In particular, the use of XML graphics may make it possible for application servers to generate not only processed data, such as a seismogram that has been subjected to a particular filter, but also to generate presentation graphics displaying the results, and those graphics would be returned to the client program as an XML message. This would alleviate the client application from having to know how to display the processing results of the server application, so it could act as a true "thin client" for user interaction and not maintain the huge graphics and processing overhead that makes an application like *geotool* so difficult to modify. We intend to investigate this possibility actively before the anticipated 2006 release of "Longhorn."

CONCLUSIONS AND RECOMMENDATIONS

We believe that a distributed system of individual applications for seismic data analysis, all communicating to a client program acting as a graphical user interface, is the appropriate design for a software system to identify and study seismic reference events that are candidates for inclusion in the KB. However, the need for graphical interaction with each of the component programs means that they are perhaps better operated in a peer-to-peer mode than within a network of Web services. In either case, the requirement to use legacy C-language code in UNIX or Linux as major components of this system imposes significant limitations upon the ease with which components may be added to this system and modified. Whether these legacy components are wrapped within Java interfaces, so that they can communicate through RMI or JAX-RPC or whether they communicate directly through middleware such as CORBA or *gsoap* (or, after it becomes more nearly stable, through Apache *Axis* for C/C++), establishing the data communications software for these legacy applications and modifying them to use that communications software and to properly handle the data and processing results that will be transmitted to them remains a difficult task that most scientists would not undertake for routine software applications maintenance and modification. Newer data communications software such as ASP.NET and the inclusion of JAX-RPC in the core Java platform make the production of data communications software easier (for programs other than C-language applications running under Linux, which remain problematic), and future systems such as the "Indigo" software that will be part of the next version of Microsoft Windows will make much of this programming transparent to the developer. The problem will still remain, however, of modifying the component applications such as *geotool* to handle new data and perform new applications without having those modifications break existing features in the code. That problem can be solved only by migrating the functionality of large monolithic programs like *geotool* into object-based programs, preferably "thin clients" that handle user interaction but that do not carry the overhead of extensive computational code.

ACKNOWLEDGEMENTS

We are indebted to Floriana Ryall for her many extensive and insightful contributions to the evaluation of problems with the operation of *geotool* and the identification of useful and important extensions to its current capabilities.

REFERENCES

Carter, J., R. Bowman, K. Biegalski, J. Bohlin, M. Fisk, R. Carlson, W. Farrell, B. MacRitchie, and H. Magyar (2001), IDC Documentation Database Schema Revision 3, Center for Monitoring Research User Guide on-line document (available at http://www.pidc.org/librarybox/idcdocs/downloads/511r3ab.pdf).

Coyne, J. M. and I. Henson (1995), *Geotool* Sourcebook: User's Manual, Phillips Laboratory report PL-TR-96-2021.

Hart, D. (2004), *MatSeis* User's Manual, version 1.8, Sandia National Laboratories on-line document (available at https://www.nemre.nnsa.doe.gov/prod/nemre/fileshare/matseis-1.8_manual.pdf).

Henson, I. (1993), "The *Geotool* Seismic Analysis System," in Proceedings of the 15th Annual Seismic Research Symposium, September 8–10, 1993, Phillips Laboratory report PL-TR-93-2160.

Rivers, D. W., C. A. Schultz, and D.A. Dodge (2002) "Efficient Integration of Old and New Research Tools for Automating the Identification and Analysis of Seismic Reference Events", in *Proceedings of 24th Seismic Research Review - Nuclear Explosion Monitoring: Innovation and Integration*, LA-UR-02-5048, Vol. 2, pp. 882-891 (available at http://www.nemre.nnsa.doe.gov/srr/2002/screen/07-05.pdf).

Rivers, D. W., R. A. Wagner, E. Siu, C. Chen, C. A. Schultz, D. A. Dodge, and G. Pope (2003), "Efficient Integration of Old and New Research Tools for Automating the Identification and Analysis of Seismic Reference Events", in *25th Seismic Research Review - Nuclear Explosion Monitoring: Building the Knowledge Base*, LA-UR-03-6029, pp. 738-747 (available at http://www.nemre.nnsa.doe.gov/srr/2003/papers/08-10.pdf).

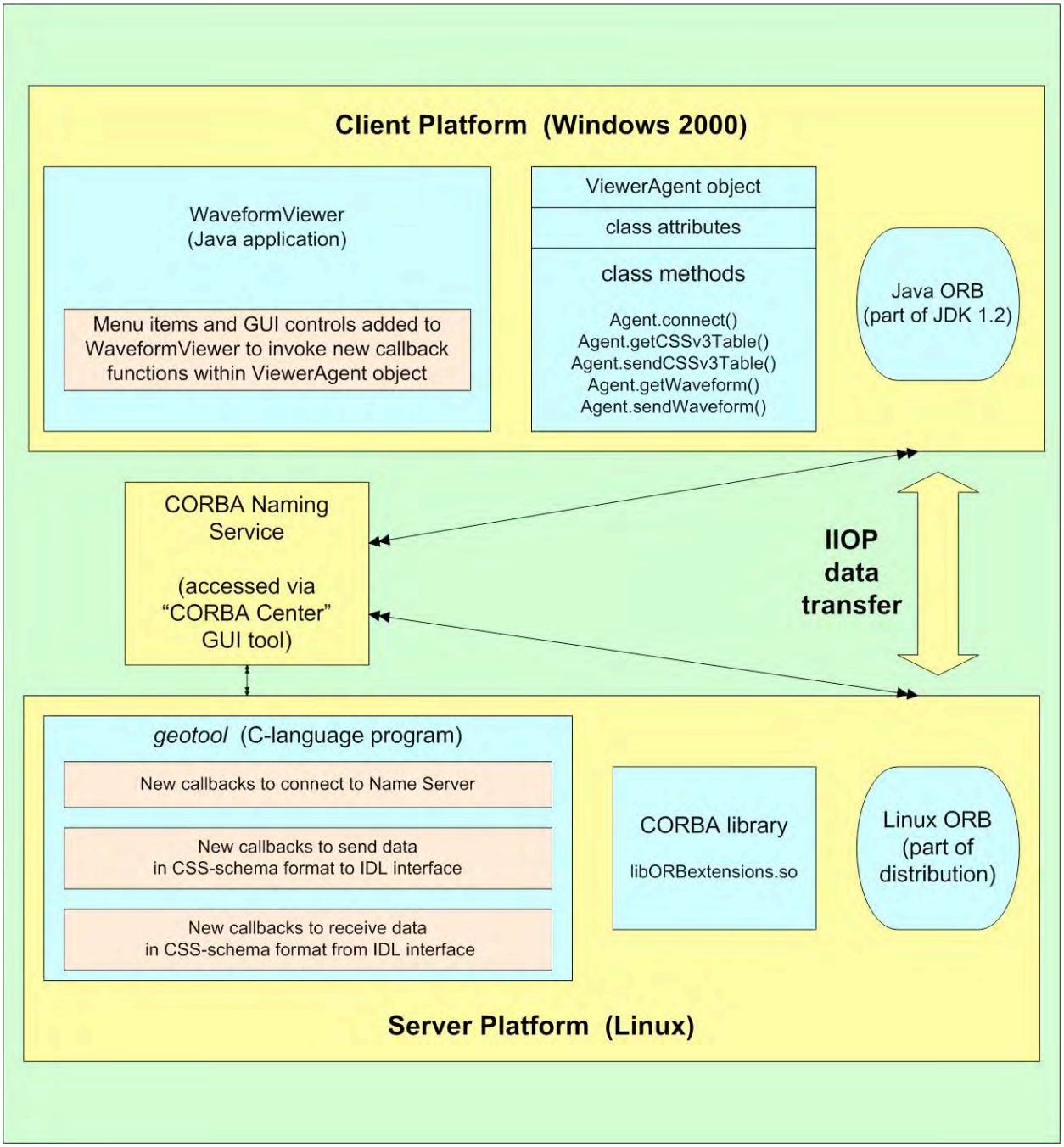


Figure 1 (From Rivers et al., 2002). Using CORBA to enable client/server data communications between the C-language program *geotool*, running as a data server under Linux, and the Java program *WaveformViewer*, running as a client application under Windows 2000. The data communication takes place between the ORBs on each platform via the IIOP, which is an Internet standard. We have modified the client code and the server code so that they link to CORBA, and that link can now be used to permit data communications between the server and additional client applications that are invoked by the user through items added to the *geotool* pull-down menus. The data that are exchanged between the client and server programs are translated from the standard CSS database table schema to CORBA IDL. We have written a utility called CORBA Center that makes it easier for the user to set up the client/server link (which requires the *geotool* server to register itself with the CORBA name server).

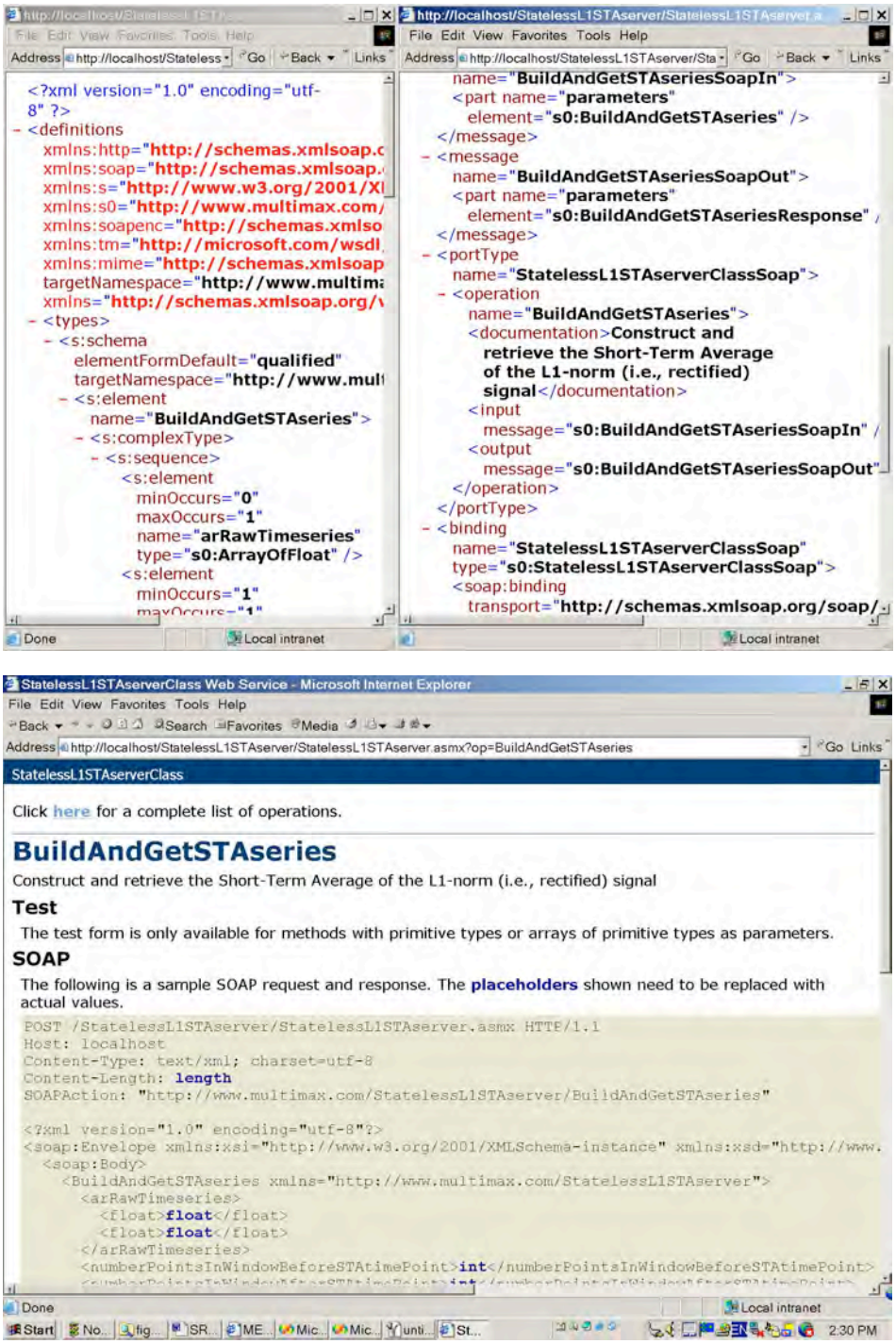


Figure 2 (After Rivers et al., 2003). (Top) Web services description language (WSDL) interface to a service application that accepts a waveform as an array of floating-point numbers and computes the short-term average of the rectified values. (Bottom) Sample code template (compiler generated) showing the format of a SOAP message that invokes this service. A client program such as *geotool* would dispatch a message in this format either through a manually written function or through machine-generated proxy code, and it will satisfy the WSDL interface shown in the top figure. The template also shows the format of the SOAP response message that is transmitting from the Web service to the client containing the XML-encoded processing results, and *geotool* would be modified to await that message (as the return value from a proxy function call) and then to parse it.

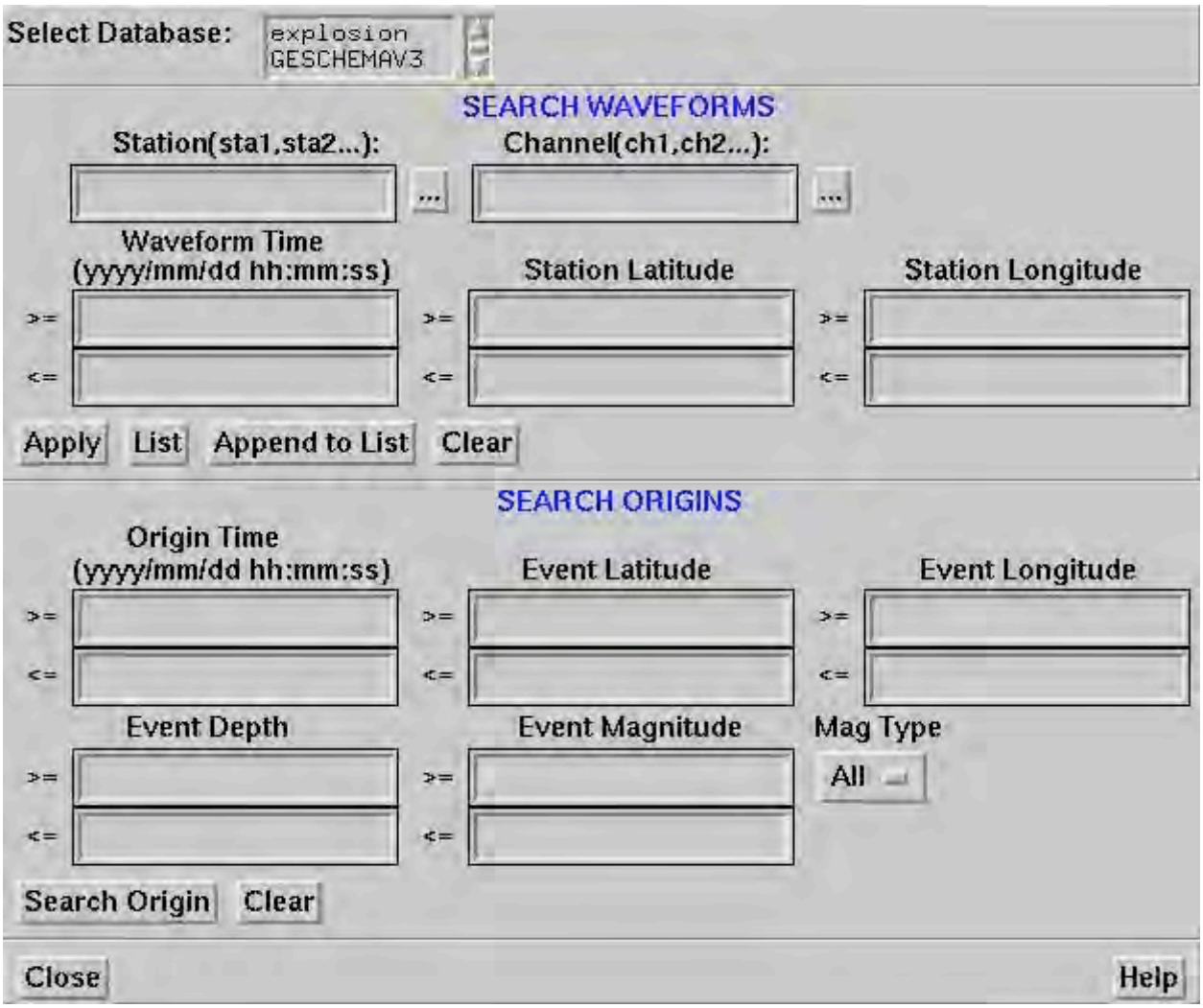


Figure 3. Among the bug fixes and enhancements that we have added to *geotool* during the last year is a graphical interface to the Oracle database that allows the user to query the database and retrieve waveforms of interest. This interface was added to *geotool* through conventional C-language Motif widget callback functions, and considerable difficulty was experienced in its implementation due to unanticipated "side effects" in parts of the program unrelated to the changes that were made in the code. This behavior is typical of large, monolithic C-language programs, and it points out the need for, at the very least, object-based software design or, preferably, a component-based architecture wherein separate features are completely encapsulated and run within individual threads of execution. A distributed software design (even if all the components are local to a single workstation) will make programs such as *geotool* more flexible and safer to modify, but in its current state, *geotool* operates poorly as a client for distributed service applications. A more flexible system for analyzing potential seismic reference events would use a "thin client" for graphical interactions as a user interface and do much of the actual analysis by invoking self-contained services. Implementing such a design is becoming easier with the introduction of software tools that hide most of the low-level data communications within proxy code that is generated automatically by the development system. Under forthcoming platforms such as Windows 2006, the implementation of interprocess communications will be made considerably more nearly straightforward than it currently is, and we expect platforms such as J2EE to follow a similar trend. In these environments XML will be used as the data format for most applications, including database interactions and presentation graphics. The distinction between local and distributed applications will become indistinct, since the same data communications protocols will be used in both circumstances.

ENHANCING SEISMIC CALIBRATION RESEARCH THROUGH SOFTWARE AUTOMATION

Stanley D. Ruppert, Douglas A. Dodge, Annie B. Elliott, Michael D. Ganzberger, Teresa F. Hauk, Eric M. Matzel, and Floriana Ryall

Lawrence Livermore National Laboratory

Sponsored by National Nuclear Security Administration
Office of Nonproliferation Research and Engineering
Office of Defense Nuclear Nonproliferation

Contract No. W-7405-ENG-48

ABSTRACT

The National Nuclear Security Administration (NNSA) Ground-Based Nuclear Explosion Monitoring Research and Engineering (GNEM R&E) Program has made significant progress enhancing the process of deriving seismic calibrations and performing scientific integration with automation tools. We present an overview of our software automation efforts and framework to address the problematic issues of very large datasets and varied formats utilized during seismic calibration research. The software and scientific automation initiatives directly support the rapid collection of raw and contextual seismic data used in research, provide efficient interfaces for researchers to measure/analyze data, and provide a framework for research dataset integration. The automation also improves the researcher's ability to assemble quality controlled research products for delivery into the NNSA Knowledge Base (KB). The software and scientific automation tasks provide the robust foundation upon which synergistic and efficient development of seismic calibration research may be built.

The task of constructing many seismic calibration products is labor intensive and complex, hence expensive. However, aspects of calibration product construction are susceptible to automation and future economies. We are applying software and scientific automation to problems within two distinct phases or "tiers" of the seismic calibration process. The first tier involves initial collection of waveform and parameter (bulletin) data that comprise the "raw materials" from which signal travel-time and amplitude correction surfaces are derived and is highly suited for software automation. The second tier in seismic research content development activities include development of correction surfaces and other calibrations. This second tier is less susceptible to complete automation, as these activities require the judgment of scientists skilled in the interpretation of often highly unpredictable event observations. Even partial automation of this second tier, through development of prototype tools to extract observations and make many thousands of scientific measurements, has significantly increased the efficiency of the scientists who construct and validate integrated calibration surfaces. This achieved gain in efficiency and quality control is likely to continue and even accelerate through continued application of information science and scientific automation.

Data volume and calibration research requirements have increased by several orders of magnitude over the past decade. Whereas it was possible for individual researchers to download individual waveforms and make time-consuming measurements event by event in the past, with the Terabytes of data available today, a software automation framework must exist to efficiently populate and deliver quality data to the researcher. This framework must also simultaneously provide the researcher with robust measurement and analysis tools that can handle and extract groups of events effectively and isolate the researcher from the now onerous task of database management and metadata collection necessary for validation and error analysis. We have succeeded in automating many of the collection, parsing, reconciliation and extraction tasks, individually. Several software automation prototypes have been produced and have resulted in demonstrated gains in efficiency of producing scientific data products. Future software automation tasks will continue to leverage database and information management technologies in addressing additional scientific calibration research tasks.

26th Seismic Research Review - Trends in Nuclear Explosion Monitoring

OBJECTIVES

The National Nuclear Security Administration Ground-Based Nuclear Explosion Monitoring Research and Engineering Program has made significant progress enhancing the process of deriving seismic calibrations and performing scientific integration with automation tools. We present an overview of our software automation efforts and framework to address the problematic issues of very large datasets and varied formats utilized during seismic calibration research and the attributes required to construct next generation data acquisition. The scientific automation engineering and research will need to provide the robust hardware, software, and data infrastructure foundation for synergistic GNEM R&E Program calibration efforts. The current task of constructing many seismic calibration products is labor intensive and complex, hence expensive. However, aspects of calibration product construction are susceptible to automation and future economies. Data volume and calibration research requirements have increased by several orders of magnitude over the past decade. We have succeeded in automating many of the collection, parsing, reconciliation and extraction tasks, individually. Several software automation prototypes have been produced and have resulted in demonstrated gains in efficiency of producing scientific data products. In order to fully exploit voluminous real-time data sources and support new requirements for time critical modeling, simulation, and analysis, a more scalable and extensible computational framework will be required.

RESEARCH ACCOMPLISHED

The primary objective of the Scientific Automation Software Framework (SASF) efforts are to facilitate development of information products for the Ground-Based Nuclear Explosion Monitoring Research and Engineering (GNEM R&E) regionalization program. The SASF provides efficient access to, and organization of, large volumes of raw and derived parameters, while also providing the framework to store, organize, integrate and disseminate information products for delivery into the National Nuclear Security Administration Knowledge Base (NNSA KB). The current framework supports integration, synthesis, and validation of the various different information types / formats required by each of the seismic calibration technologies (Figure 1). For example, the seismic location technology requires parameter data (site locations, bulletins), time-series data (waveforms), and produces parameter measurements in the form of arrivals, gridded geo-spatially registered corrections surfaces and uncertainty surfaces. Various tools and information processing frameworks (relational database (RDB), Geographical Information System (GIS), and associated product/data visualization and data management tools (e.g. RBAP, KBALAP, KBCIT, DM).

These information management and scientific automation tools are used together within specific seismic calibration processes to support production of tuning parameters for the United States Nuclear Seismic Monitoring System run by the Air Force (Figure 2). The calibration processes themselves appear linear (Figure 2) beginning with data acquisition extending through reconciliation, integration, measurement/simulation through to construction of calibration / run-time parameter products. Efficient production, however, of calibration products requires extensive synergy and synthesis between not only data-types (Figure 1), but also between measurements and results derived from the different calibration technologies (e.g. Location, Identification, Detection) (Figures 1 and 2). Even with successful implementation of automation within many of the individual steps, the current infrastructure will not scale to handle an order of magnitude additional data nor extend to handle time critical data acquisition or analysis. This lack of scalability and flexibility limits efficient production and delivery of run-time calibrations to the operational seismic monitoring pipeline (Figure 2 – Bottom) as a large manual effort is still required to acquire and integrate streaming (10 – 20 GB/day) signals with associated metadata. This synergy and synthesis between complex tools and very large datasets is critically dependent on having a scalable and extensible unifying framework. These requirements of handling large datasets in diverse formats and facilitating interaction and data exchange between tools supporting different calibration technologies led to an extensive scientific automation software engineering effort to develop an object oriented database centric framework (Figure 3) as an unifying foundation.

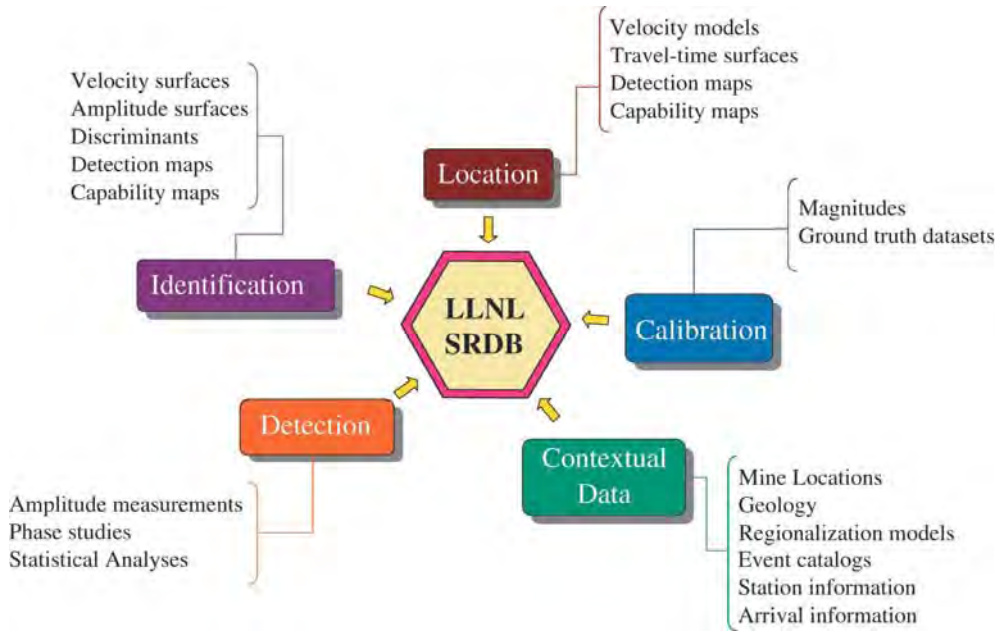


Figure 1. The Scientific Automation Software Framework provides a unifying framework for contextual/reference data and information products.

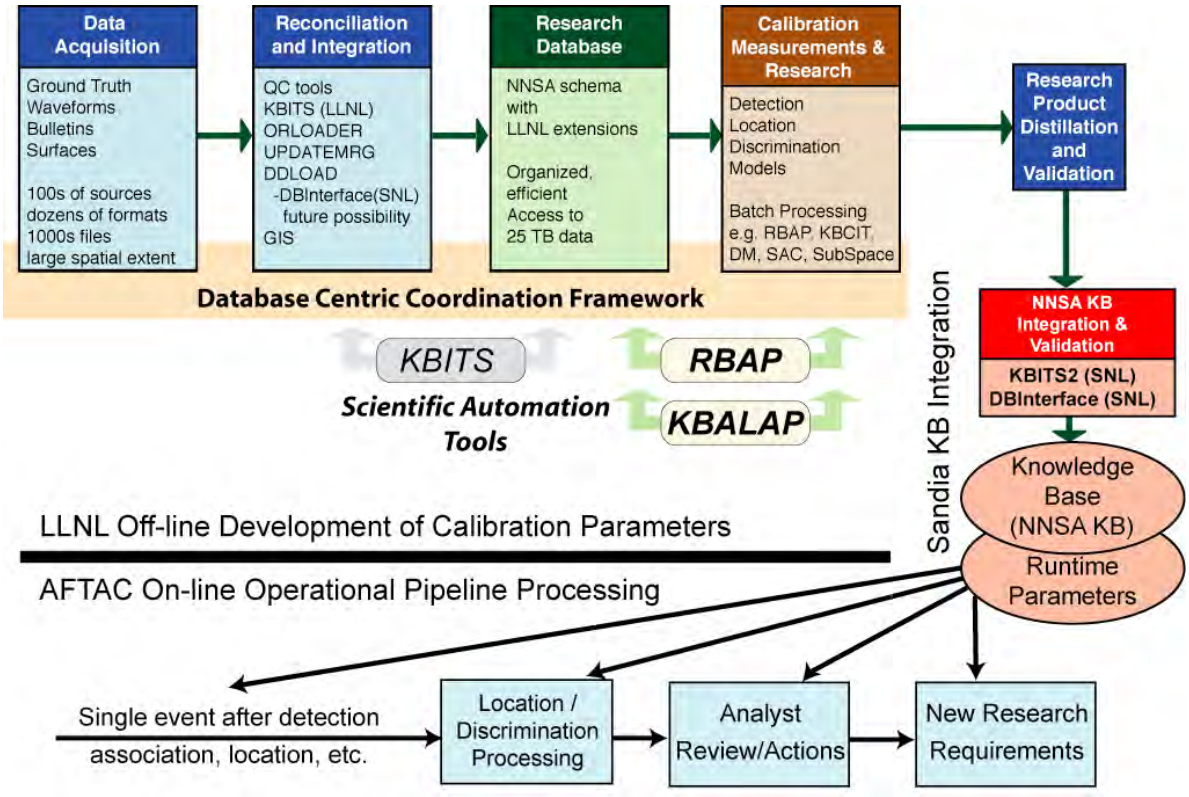


Figure 2: Summary of the processes of data collection, research and integration within the LLNL calibration process that result in contributions to the NNSA KB. The relationships of the current LLNL calibration tools, scientific automation tools, and database coordination framework to those involved in the assembly of the NNSA KB or within the AFTAC operational pipeline are delineated.

Scientific Automation Software Tools

Information products created using the LLNL SRDB may be grouped under two major categories or tiers: Tier 1 - primary data products and Tier 2 - derived products. In order to calibrate seismic monitoring stations, the LLNL SRDB must incorporate and organize the following categories of primary and derived measurements, data and metadata:

Tier 1: Contextual and Raw Data

- Station Parameters and Instrument Responses
- Global and Regional Earthquake Catalogs
- Selected Calibration Events
- Event Waveform Data
- Geologic/Geophysical Data sets
- Geophysical Background Model

Tier 2: Measurements and Research Results

- Phase Picks
- Travel-time and Velocity Models
- Rayleigh and Love Surface Wave Group Velocity Measurements
- Phase Amplitude Measurements and Magnitude Calibrations
- Detection and Discrimination Parameters

Automating Tier 1

Corrections and parameters distilled from the calibration database provide needed contributions to the NNSA KB for the WENA region and will improve capabilities for underground nuclear explosion monitoring. The contributions support critical functions in detection, location, feature extraction, discrimination, and analyst review. Figure 2 outlines the processes of data collection, research and integration within the LLNL calibration process that result in contributions to the NNSA KB and the relationship of the LLNL calibration tools to those involved in the assembly of the NNSA KB or within the AFTAC operational pipeline. Within the major process steps (Data Acquisition, Reconciliation/Integration, Calibration Research, Product Distillation) are many labor intensive and complex steps. The previous bottleneck in calibration process was in the reconciliation/Integration step (Figure 2). This bottleneck became acute in 1998 and the KBITS suite of automated parsing, reconciliation, and integration tools for both waveforms and bulletins (ORLOADER, DDLOAD, UpdateMrg) were developed. The KBITS suite provided the additional capability required to integrate data from many data sources and external collaborations. Data volumes grew from the 11,400 events / 1 million waveforms in 1998 to the 4 million events / 60 million waveforms today (e.g. Ruppert et al., 1998, O'Boyle et al. 2003).. This rapid increase in stored parameters soon led to two new bottlenecks hindering rapid development and delivery of calibration research

Automating Tier 2

As the number of data sources required for calibration increased in number and source location, it became clear that the manual and labor intensive process of humans transferring thousands of files and un-manageable metadata could not keep the KBITS software fed with data to integrate nor could the seismic research efficiently find, retrieve, validate, or analyze the raw parameters necessary to effectively produce seismic calibrations in an efficient manner,

Significant software engineering and development efforts were applied to address this critical need to produce software aids for the seismic researcher. Two scientific automation tool prototypes (RBAP, KBALAP) (Figure 2) are under development for Seismic Location and Seismic Identification calibration tasks.

Both of these prototypes include methods and aids for efficiently extracting groups of events and waveforms from the millions contained in the SRDB and making large numbers of measurements with metadata in a batch mode. The concept of event sets (groups of related seismic events or parameters that can be processed together, e.g. either station centric or event centric) was introduced as previous SAC scripts and macros could not scale to the task.

The KBALAP Program

The Knowledge Base Automated Location Assessment and Prioritization (KBALAP) program is a set of database services and a client application that combine to efficiently produce location ground truth data that can be used in the production of travel time correction surfaces and as part of the preferred event parameters used by other tools in our processing framework.

The part of KBALAP that runs as a database service is responsible for evaluating bulletin and pick information as it enters the system to identify origin solutions that meet pre-defined GT criteria with no further processing, and to identify events that would likely meet a pre-defined GT level if a new origin solution was produced using available arrivals. The database service is also responsible for identifying events that should have a high priority for picking based on their existing arrival distribution, and the availability of waveform data for stations at critical azimuths and distances.

The interactive portion of KBALAP has three principal functions. These are

- interactive production of GT origins through prioritized picking and location,
- interactive specification of GT-levels for epicenter, depth, origin time, etype, and
- batch-mode location of externally-produced GT information.

The first of these capabilities allows the user to view epicenters and GT information on a map based on selection criteria input by the user. The user can select any GT or potential GT event and observe the distribution of stations with picks and stations with available waveforms. The user can select any station with available waveforms and open a picker with any current picks displayed. There the user can adjust existing picks, add new picks, mark bulletin picks as unusable, and relocate the event. A new GT level is calculated, and the user can choose to accept that origin solution and GT level or continue working with other stations.

The interactive GT entry mode of KBALAP allows the user to retrieve information about a specific event and add or update that event's GT parameters. The program can also create a new event with a GT level for cases where epicenter, time, depth and magnitude GT data are available. Similarly, the batch mode part of the program allows specification of flat files containing GT data for events already in the database.

The RBAP Program

The Regional Body-wave Amplitude Processor (RBAP) is a software tool developed by the Ground-based Nuclear Explosion Monitoring (GNEM) group at Lawrence Livermore National Laboratory (LLNL). RBAP helps to automate the process of making amplitude measurements of regional seismic phases for the purpose of calibrating seismic discriminants at each station. RBAP generates station-centric raw and MDAC corrected Pn, Pg, Sn and Lg amplitudes along with their associated calibration parameters (e.g. phase windows, MDAC values, reference events, etc.) in database tables. It strictly follows the Working Group (WG) 2 standardized processing and it replaces the original collection of LLNL scripts described by Rodgers (2003). RBAP has a number of advantages over the previous scripts. It is much faster, significantly easier to use, scales more easily to a larger number of events and permits efficient project revision and updating through the database.

RBAP integrates the functions of the modules in the previous LLNL scripts into a single program that is designed to perform the amplitude measurement task efficiently and to require a minimum effort from the users for managing their data and measurements. For well-located events with pre-existing analyst phase picks, the user reviews for quality control and then generates all the amplitudes with just a few mouse clicks. For events needing more attention, the user has complete control over the process (e.g. window control, ability to mark bad data, define regions, define MDAC parameters and define the events to be used in the overall calibration process). RBAP shortens the time needed by the researcher to calibrate each station while simultaneously allowing an increase the number of events that can be efficiently included. RBAP is fully integrated with the LLNL research database. Data is always read directly from the appropriate tables in the research database rather than from a snapshot as was done in the previous system. All RBAP result tables have integrity constraints on the columns with dependencies on data in the LLNL research database. This design makes it very difficult for results produced by RBAP to be stale and also ensures that as the research database expands, RBAP automatically becomes aware of new data that should be processed.

Some RBAP Key Features as follows:

• *Based on WG 2 Standardized Algorithm*
- RBAP is built on the WG 2 standardized body-wave amplitude measurement algorithms.

• *Fast and Efficient Calibration*
- RBAP is self-contained and optimized for station-centric body-wave processing. "Good" events can be handled with just few mouse clicks. The researcher has direct control over key calibration parameters within the tool such as phase amplitude windows and migration, marking bad segments, defining distinct geophysical regions, event types to process, etc. We expect RBAP to provide roughly a factor of 5 increase in calibration speed compared with the original scripts, enabling us to calibrate more stations, with more events per station.

• *Project Management*
- RBAP is designed so that a calibration project can be put down for a day, month or a year, and easily picked up, by the same researcher or a new one. All processing metadata is saved and events are easily tracked as processed, unprocessed or outside the current project definitions. This allows a researcher to efficiently work through a huge data list without repetition and to easily identify and incorporate new events as they become available in the database.

• *Utilizes Database for Up-to-Date results*
- RBAP can draw on the latest calibration parameters being generated by other Working Groups, such as the most recent phase picks, re-locations, magnitudes, instrument response information, or event type ground truth.

• *Batch Processing*
- RBAP is designed to allow simple batch updating of the amplitude results, whether the change is small (e.g. one-event is re-located) or large (instrument response is changed affecting all events).

Database Centric Coordination Framework

Significant software engineering and development efforts have been applied successfully to construct an object-oriented database framework that provides database centric coordination between scientific tools, users, and data (Figure 3). A core capability this new framework provides is information exchange and management between different specific calibration technologies and their associated automation tools such as Seismic Location (e.g. KBALAP), seismic identification (e.g. RBAP), and data acquisition / validation (e.g. KBITS). A relational database (ORACLE) provides the current framework for organizing parameters key to the calibration process from both Tier 1 (raw parameters such as waveforms, station metadata, bulletins etc) and Tier 2 (derived measurements such as ground-truth, amplitude measurements, calibration and uncertainty surfaces etc). Efforts are underway to augment the current relational database structure with semantic graph theory structured queries for handling complex queries.

Seismic Calibration Technologies (Location, Identification, etc) are connected to parameters stored in the relational database by an extensive object-oriented multi-technology software framework (Figure 3 – middle) that include elements of schema design, Stored procedures, real-time transactional database triggers, constraints, as well as coupled Java and C++ software libraries to handle the information interchange and validation requirements. This software framework provides the foundation upon which current and future seismic calibration tools may be based.

Sharing of derived event parameters

We have long recognized the inadequacies of the CSS3.0 origin table to serve as a source of information about the "best" parameters for an event. One origin solution may have the best epicenter but poor information on other parameters.

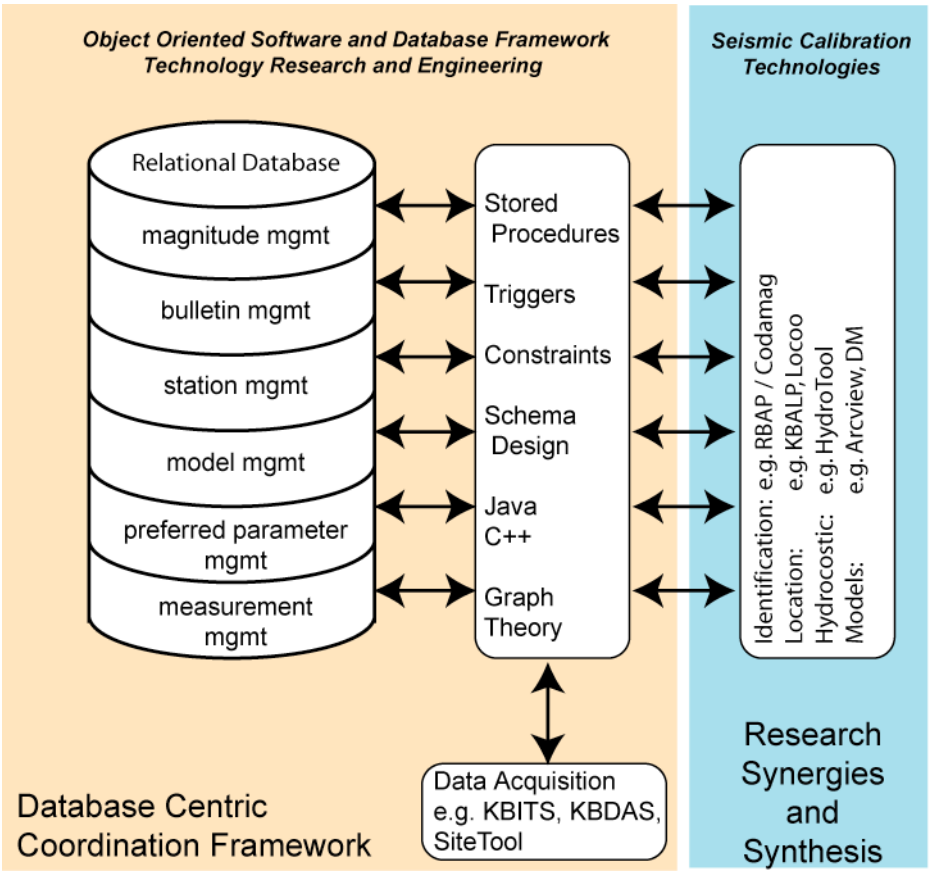


Figure 3. Overview of the Database Centric Coordination Framework that provides the enabling information technology to allow synergy and synthesis of data and calibration technologies for the efficient production of calibration deliverables.

Another may have the correct event type, but be poor in other respects, and so on. We had discussed producing origin table entries with our organization as the author, but that approach has difficulties. Different groups would have responsibility for different fields in the origin. Because their information would not be produced in synchronization we would either have to always be updating the preferred origin or else producing new preferred origins. Also, there would be difficulties in tracking the metadata associated with each field of the preferred origin. Our solution was to create a set of new tables and associated stored procedures and triggers that collectively maintain the “best” information about events. The tables involved are shown in Figure 4. Any tool that needs event parameters references the preferred origin table. It has five parameters of interest:

1) Event Epicenter
2) Event Time
3) Event Depth
4) Event Moment Magnitude
5) Event Type.

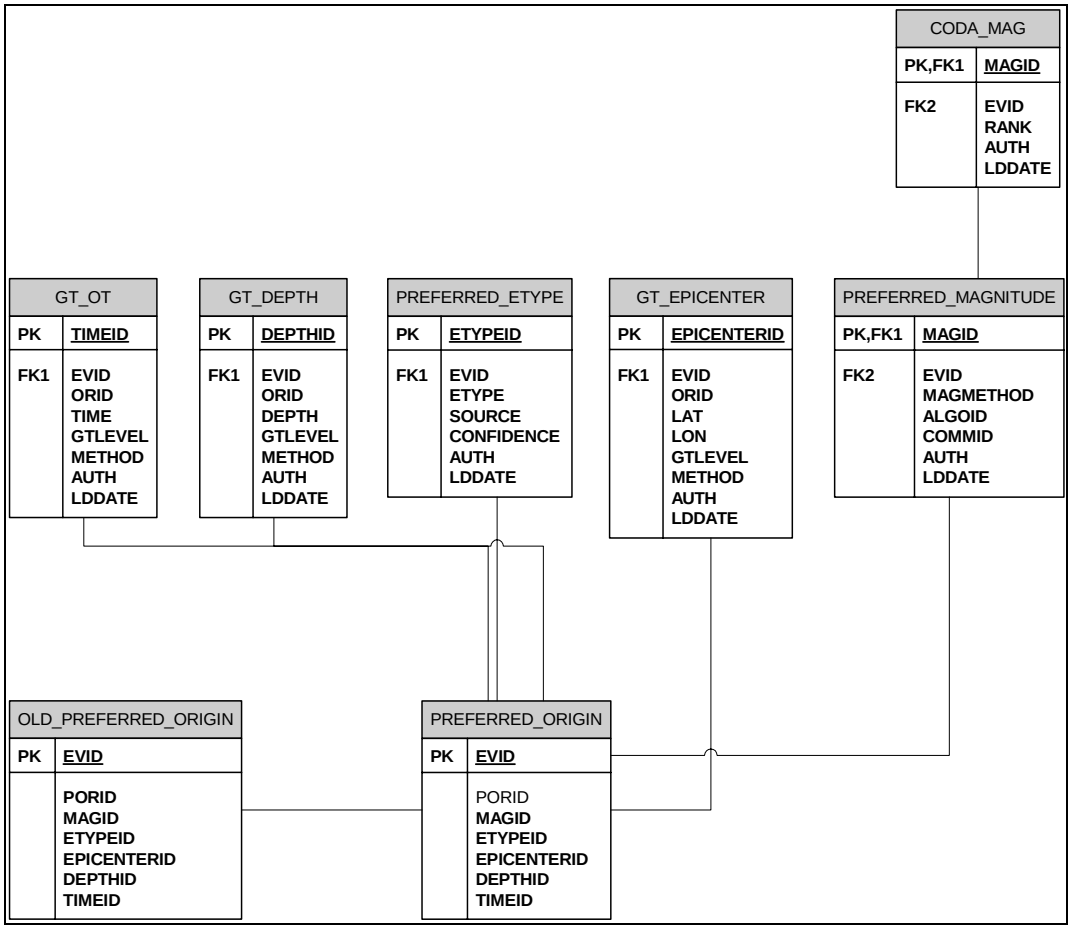


Figure 4. Tables involved in management of preferred event parameters.

Each of these parameters may be set either from the corresponding columns in the preferred origin from the main origin table or from a table containing the parameter value, confidence level, and other metadata. Rows can be added interactively or using software tools. Inserts, updates or deletes on the main origin table or on any of these tables trigger automatic updating of the preferred origin table. Thus the preferred origin table always has the most current “best” parameter estimates. Whenever a row in the preferred origin table is changed or deleted, a copy of that row is created in the old preferred origin table and the PORID key is updated in the preferred origin table. Thus measurements can always be referenced to the event parameters in existence when the measurements were made.

Currently, both magnitudes and epicenters are being updated automatically as origins enter the system. When the coda magnitude loading tool adds a new coda magnitude, that estimate is automatically ranked against pre-existing coda magnitude estimates, and if it outranks the others (or there are no others) that magnitude becomes the preferred origin magnitude. Whenever a NETMAG entry or an EQ_SOURCE_PARAMS entry occurs, a trigger executes that converts to Mw if necessary, ranks the entry against other Mw estimates for the event, and possibly makes the new estimate the preferred Mw for the event. Whenever a new origin with arrivals enters the system, a set of rules is applied that determine the GT-level (if applicable) of the new origin. If the origin has a GT-level that outranks the current epicenter GT-level, then the epicenter from the new origin solution becomes the preferred epicenter for the event. When the KBALAP tool is complete, it will allow managed changes to preferred origin time, epicenter, depth and etype fields. Currently, the RBAP tool is being modified to read from the PREFERRED_ORIGIN table and to be able to update GT_DEPTH, PREFERRED_ETYPE, and GT_EPICENTER under certain restrictions.

Sharing and Updating of Arrival Information

Although our program has long been using arrivals stored in our CSS3.0 ARRIVAL table, there have been a number of problems that prevented full utilization of those arrivals. These include:

1) Efficiently accumulating all arrivals associated with an event
2) Dealing with the many variations of phase names found in the global bulletins
3) Selecting a "best" pick when more than one author has picked a phase for the same event at some station
4) Associating appropriate site data with each phase pick
5) Where applicable, retrieving filter data associated with the pick
6) Avoiding retrieval of picks previously found to be erroneous.

Again, our solution was to create a set of new tables, stored procedures, functions, and triggers.

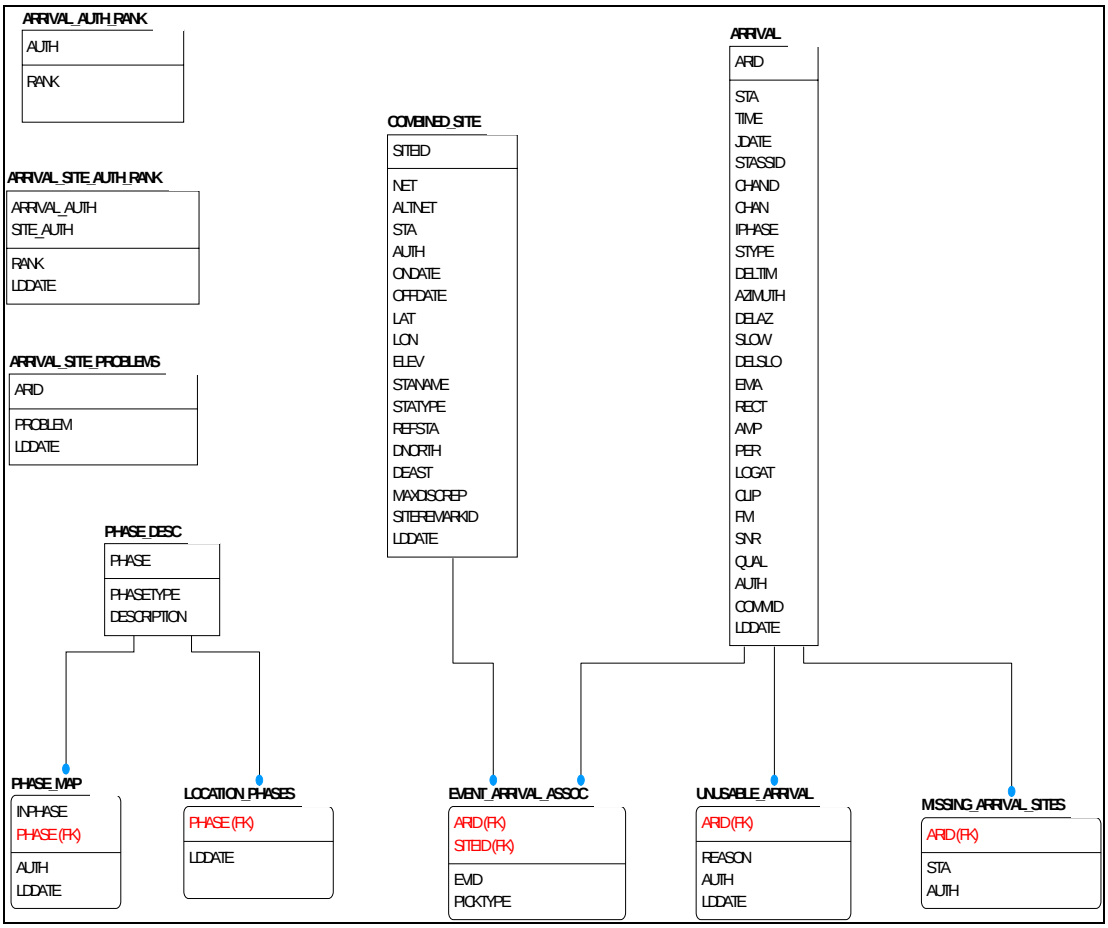


Figure 5. Tables involved in managing arrival information.

The EVENT_ARRIVAL_ASSOC table plays a central role in managing arrivals. In part, it is analogous to the CSS3.0 ASSOC table. But, instead of associating arrivals to origins, it associates arrivals to events. This saves doing a three-table join when selecting all arrivals for an event, an important factor when the arrival table is extremely large. Just as important as being able to easily select all arrivals for an event is the ability to associate the best available site information with each arrival. Arrivals in our system come from a number of different sources, and the associated site information may be inconsistent between authors. This is where the COMBINED_SITE table comes into play. It contains all the site information available to us along with the means to discriminate among sites provided by different authors and for different networks. During loading of arrivals or loading of sites, triggers execute that determine the "best" association between arrivals and sites. This is done using lookups into the ARRIVAL_SITE_AUTH_RANK table. The association is recorded in the EVENT_ARRIVAL_ASSOC table using the SITEID column.

Retrieval of a set of arrivals and associated sites is accomplished using a stored function returning a REF_CURSOR. This function

- maps phase names to a consistent set using the PHASE_MAP table,
- filters picks for phase suitability using the LOCATION_PHASES table,
- filters picks that have previously been found to be erroneous using the UNUSABLE_ARRIVAL table,
- returns the "best" pick when multiple authors have a pick for the same station-phase,
- and returns the "best" site for each station in the pick set.

The function also allows filtering on the MAXDISCREPANCY column in the COMBINED_SITE table. This, in effect allows rejection of phase picks from stations whose location is not agreed upon to within the user's requested tolerance.

Currently, the RBAP, KBALAP, and TOGEOTOOL programs use this stored function when requesting sets of arrivals. This summer, both KBALAP and RBAP will be given the capability of adding to the UNUSABLE_ARRIVALS table.

Two other tables not shown in Figure 5 are the APPLIED_FILTER and STORED_FILTER tables. The STORED_FILTER describes a particular filter and the APPLIED_FILTER relates an arrival to a stored filter. Currently, these tables are populated by the RTLOADER program when it loads picks made by the GEOTOOL program. This summer RBAP will be given the capability to both read and write these tables. This will allow easy reproduction of the state used to make a certain phase pick, and should be a time saver when reusing picks made by others.

Sharing of QC Information

We have made a start at sharing quality control information among processing tools. So far, the only tool that is writing QC information is RBAP. Users can identify bad segments in traces being processed and write the information into a BAD_SEGMENTS table. This table is visible to all other tools, so it could be used to filter waveforms if appropriate. RBAP also identifies instrument responses that failed, and station-channel-epochs without instrument responses. It is expected that we will write a site metadata tool soon that would, among its other capabilities, use these tables to resolve these problems. In a similar manner, RBAP populates a table of evids for which coda magnitudes need to be computed. At this time, there is still a manual step required in reading this table and using the information to drive the generation of coda magnitudes. When we complete the coda magnitude processing tool, that step should become automatic.

CONCLUSIONS

We present an overview of our software automation efforts and framework to address the problematic issues of very large datasets and varied formats utilized during seismic calibration research and the attributes required to construct next generation data acquisition. These new software and scientific automation initiatives could directly support our current mission including rapid collection of raw and contextual seismic data used in research, provide efficient interfaces for researchers to measure/analyze data, and provide a framework for research dataset integration. The initiatives would improve time critical data assimilation and coupled modeling / simulation capabilities necessary to efficiently complete seismic calibration tasks. The scientific automation engineering and research will need to provide the robust hardware, software, and data infrastructure foundation for synergistic GNEM R&E Program calibration efforts.

REFERENCES:

Ruppert, S., T. Hauk, J. O'Boyle, D. Dodge, M. Moore, Lawrence Livermore National Laboratory's Middle East and North Africa Research Database, in Proceedings of the 21st Seismic Research Symposium: Technologies for Monitoring The Comprehensive Nuclear-Test-Ban Treaty, September 1999.

O'Boyle, J., S. Ruppert, T. Hauk, D. Dodge, M. Ganzberger, F. Ryall, Middle East, North Africa and Western Eurasia Seismic Research Database, Proceedings of the 25th Seismic Research Symposium: Nuclear Explosion Monitoring – Building the Knowledge Base, September 2003.

DATA RESOURCES TO SUPPORT NUCLEAR EXPLOSION MONITORING RESEARCH AND DEVELOPMENT

Robert L. Woodward, Manochehr Bahavar, and Robert G. North

Science Applications International Corporation

Sponsored by Army Space and Missile Defense Command

Contract No. DASG60-03-C-0009

ABSTRACT

A wide range of raw data, unique research databases, and state-of-the-art data access tools are available to the nuclear explosion monitoring research and development (R&D) community through the Research and Development Support Services (RDSS) project operated by the United States (U.S.) Army Space and Missile Defense Command (SMDC) Monitoring Research Program (MRP).

The waveform data archive component of the RDSS has recently been re-engineered to facilitate a new class of computational experiments and to vastly improve data access. All waveforms in the archive (roughly 12 Tb of seismic, hydroacoustic and infrasound waveforms from over 300 locations world-wide) are stored in an analysis-ready format (CSS3.0) on a high-speed spinning disk mass-storage system. Every waveform in the archive can be directly and instantly accessed, making it possible to perform experiments on any desired cross-section of the archive, with no need to "stage" data or make special modifications to scientific software. Further, we have developed a new interactive, web-based tool which supports direct downloads of desired data. The web tool also supports browsing of event bulletins—when the desired event is found in a bulletin the user simply clicks through a simple on-line form to download data associated with the event. Traditional data request tools, such as the e-mail based *AutoDRM* software, not only provide backwards compatibility for users but also benefit from the new mass-storage system by providing greatly improved response times.

The RDSS provides a range of value-added R&D databases that are a significant resource for the U.S. R&D community. For example, the infrasound database draws on a unique collection of waveforms (many of which are not archived anywhere else) from infrasound arrays operated by the Department of Energy, the International Monitoring System, and other organizations. These data go back to 1995, and include data from sites on every continent. The database includes acoustic recordings of a variety of natural and man-made events, including atmospheric nuclear explosions. We are actively adding data from recent infrasound events to the database and we provide examples of a number of such events. The seismic R&D databases include: the Nuclear Explosion Database, an exhaustive collection of metadata and waveforms from nuclear tests; the Ground Truth Database, containing a wide range of carefully selected and quality-controlled events for ground truth levels of 0 to 15 km; and region-specific databases for the Lop Nor, China region, the arctic region, and the Korean Peninsula (currently in preparation). The region-specific databases are prime examples of value-added databases, as they bring together a wide range of open-source data into a single, well-organized package. All of the R&D databases are accessible through interactive web-based tools.

A multi-technology hypocenter location service (HLS) is also provided by the RDSS. This service will locate event hypocenters or epicenters based on any combination of seismic, hydroacoustic and infrasonic arrivals. The service supports both default and user-defined travel-time tables for each technology, and supports multiple input/output formats. The service is based on the *EvLoc* hypocenter location software (the software currently in operational use at the International Data Centre) and is accessed through an e-mail-based interface.

In this paper we provide a summary of the major RDSS data assets and resources. We provide examples and descriptions of the types of data and metadata in each database, and provide information on how these resources can be accessed.

OBJECTIVE

The objective of the RDSS is to support the nuclear explosion monitoring research and development community with a wide range of data, state-of-the-art data access tools, and value-added datasets.

RESEARCH ACCOMPLISHED

During the current contract we have pursued initiatives in three primary areas with the goal of extending existing resources or developing new resources which will provide direct benefit to the nuclear explosion monitoring R&D community. First, we have expanded and improved the waveform archive, concentrating especially on creating a high-speed archive and new access tools which fully exploit the capabilities of the new system. Second, we have improved our existing, value-added R&D databases and have created several new databases. Third, we have developed new tools, using an application service provider model, to provide remote users with access to sophisticated R&D software. In the following sections we describe these developments in greater detail.

Waveform Archive and Data Access

The RDSS maintains a large archive of waveform data from seismic, hydroacoustic, and infrasound stations. Data in the archive go back to 1995 (earlier for some stations) for stations distributed worldwide (Figure 1).

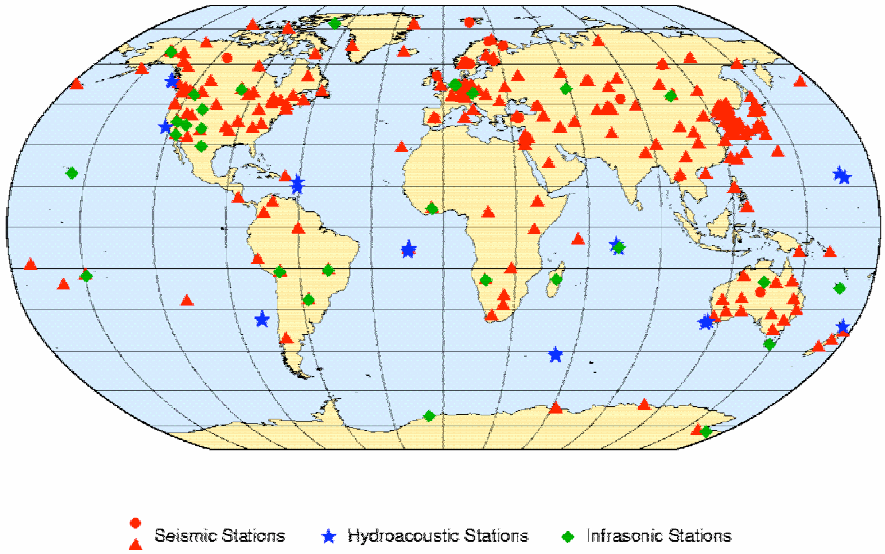


Figure 1. (right) Seismic arrays (circles) and three-component stations (triangles), and hydroacoustic and infrasonic arrays (stars and diamonds, respectively) for which waveform data are available from the RDSS archive. For many of these stations and arrays the data are continuous over periods of several years.

The archive currently contains over 12 Tb of data. To facilitate a new class of computational projects, we have migrated our data archive from a robotic mass-storage system to a system based on conventional spinning-disk technology (RAID disk farm). The current system (Figure 2) provides access to the entire archive that is at least two orders of magnitude faster than its predecessors, and makes very large scale experiments and data visualizations possible. Data on the mass-store are stored in an analysis ready format (CSS3.0) so that they may be accessed directly by application software -- making it possible to perform experiments on any desired cross-section of data in the archive, with no need to "stage" data or make special modifications to scientific software.



Figure 2. (left) This 15 Tb mass-storage system provides direct access to over 12 Tb of waveform data.

Figure 3 provides an example of the type of computations the new mass-storage system facilitates. We show the results of computing root-mean-square (RMS) pressure noise using an entire year of 20 samples per second data (~600 million samples per year per channel) from the Mongolian (I34MN) infrasound array. The results of these calculations show fluctuations in pressure noise on daily to seasonal time scales, with many of the shorter duration daily effects being directly related to wind. The software which computes the running RMS values accesses data directly from the mass-storage system on-the-fly as the computations proceed. These computations are only limited by the CPU requirements of the applications and the spinning-disk input/output speeds. Similarly, the same mass-storage system has been used for a large-scale project to compute ambient infrasonic noise for International Monitoring System (IMS) and other infrasound arrays. The noise computations are based on data samples from multiple time windows per day, for one year (or longer) time spans (Bowman et al, 2004). While the ambient noise computations are relatively straightforward, they require access to a massive quantity of data spread across both stations and time and would pose a significant challenge to traditional robotic mass-storage systems which cannot readily support direct, random access to data.

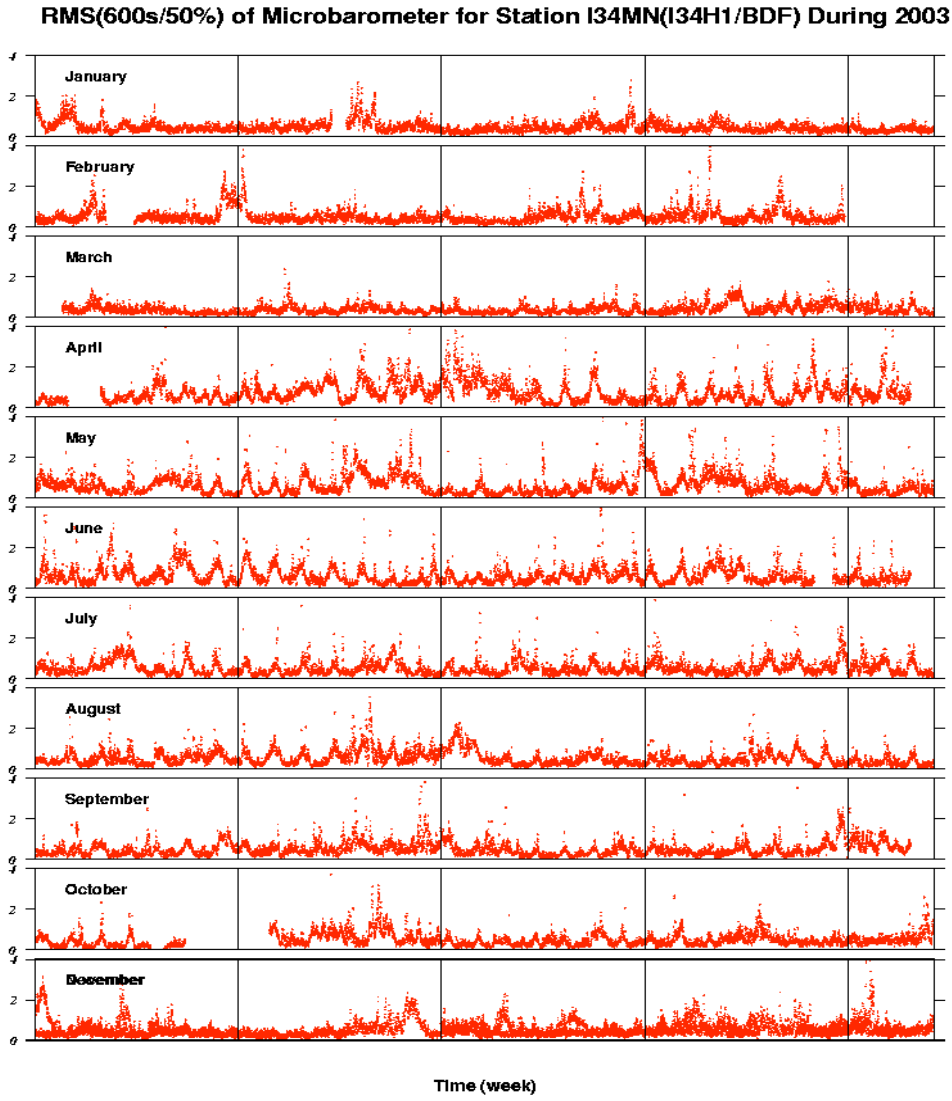


Figure 2. RMS pressure at station I34MN (Mongolia) during 2003 (from a single microbarograph channel). RMS pressure is calculated using a 600 s running window, with 50% window overlap. The pressure noise tracks wind speed fluctuations measured at the same site (and also available from the archive), with a few notable exceptions. An entire year's worth of data (600 million samples) was processed for this figure.

To enhance the value of the mass-store system for the research community we have initiated an effort to upgrade the data access tools. First, we have developed a new interactive, web-based tool which supports direct downloads of desired data. The web tool supports browsing of event bulletins—when the desired event is found in a bulletin the user simply clicks through a simple on-line form to obtain an immediate download of the data associated with the event (Figure 4). The data time windows can be of fixed length or can be adjusted relative to predicted phase arrival times or group velocities. This interactive tool also supports the download of custom data windows – based on arbitrary time windows or based on user-supplied event information. Data are downloaded immediately upon completion of the specification of the desired stations/channels/time windows and are in analysis ready formats (CSS3.0 is currently supported, SAC is being implemented). As a second major enhancement to the mass-store system, we are pre-rendering waveform plots for all events in the Reviewed Event Bulletins (REBs) produced by the Prototype International Data Center (1995-2000) and the International Data Centre (2000-present). These plots allow the user to review the waveforms utilized for each REB event, and can further assist the user in identifying waveforms which the user may want to download. Finally, we are actively developing a mechanism for users to dynamically view any waveform in the data archive, as a means of providing a "browse before you download" capability. Finally, traditional data request tools, such as the e-mail based *AutoDRM* software, provide backward compatibility for users and benefit from the new mass-storage system by providing greatly improved response times.

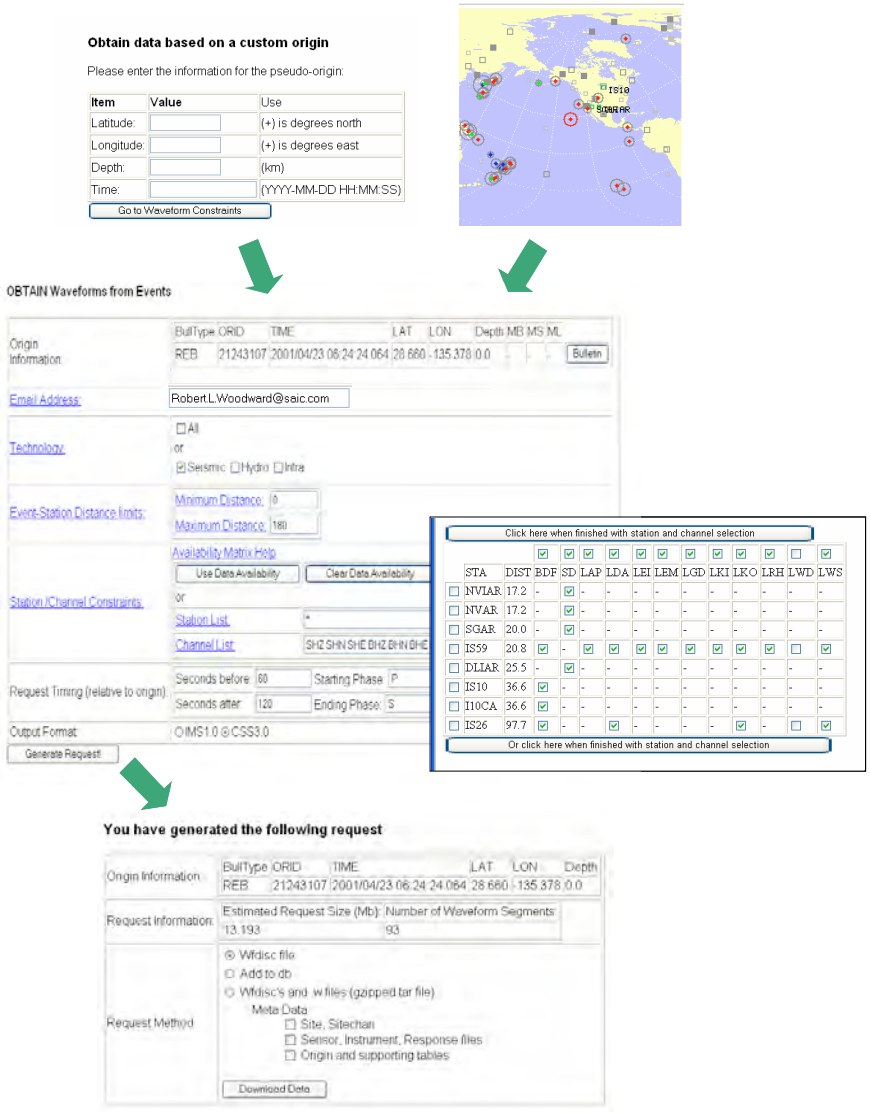


Figure 4. The web-based data access tool provides easy access to data, through both custom query and map-based interfaces. A station-channel selection matrix allows fine-tuning of the data request and data may be downloaded immediately.

Value Added Databases

The RDSS provides a range of value-added R&D databases that are a significant resource for the U.S. R&D community (Table 1). The data (waveforms and/or arrivals) which are included in these databases are extracted from the general RDSS waveform archive (described above) as well as from a wide variety of other open sources. The careful compilation of data, along with relevant metadata, is typically a challenging and time consuming task. However, the resultant data sets provide unique, value-added resources which can support studies in nuclear explosion detection, location, and identification. We describe several of the value added databases below.

Table 1. Summary of value-added research databases which are available as part of the RDSS.

Database	Description
Infrasound	A wide range of acoustic recordings from natural and man-made events, including atmospheric nuclear explosions. Data suitable for detection and source classification studies.
Nuclear Explosion	A vast compilation of seismic and infrasound recordings and arrival data from underground, underwater, and atmospheric nuclear explosions.
Ground Truth	Seismic phase arrival data for GT0 through GT15 events.
Lop Nor	Seismic waveforms (~100 GB) and phase arrival data for events and stations in the Lop Nor, China region. Includes recordings of larger nuclear explosions which have been scaled down to smaller yields and embedded in background noise. Provides multiple source location estimates obtained from different open sources. See Kohl et al (2002).
Arctic Region	Seismic waveforms and phase arrival data for events and stations in the Arctic region. Provides multiple source location estimates obtained from different open sources.
Korean Peninsula	Includes seismic waveforms, ground truth locations, and event characterization information for hundreds of events on and near the Korean Peninsula.

The infrasound database draws on a unique collection of waveforms (many of which are not archived anywhere else) from infrasound arrays operated by the Department of Energy, the International Monitoring System, and other organizations. The 27 infrasound arrays for which continuous data are currently in the database are shown in Figure 5. These data holdings go back to 1995, and include data from sites on every continent. The database includes acoustic recordings of a variety of natural and man-made events, including atmospheric nuclear explosions. We are actively adding data from recent infrasound events to the database. For example, Figure 6 shows the location of several recent events which occurred during a nine hour interval on a single day and which were recorded by the IMS infrasound station in Kazakhstan (I31KZ). The signals in the infrasound database are suitable for a variety of signal detection and source characterization studies, including the examination of such issues as seasonal propagation variability, etc.

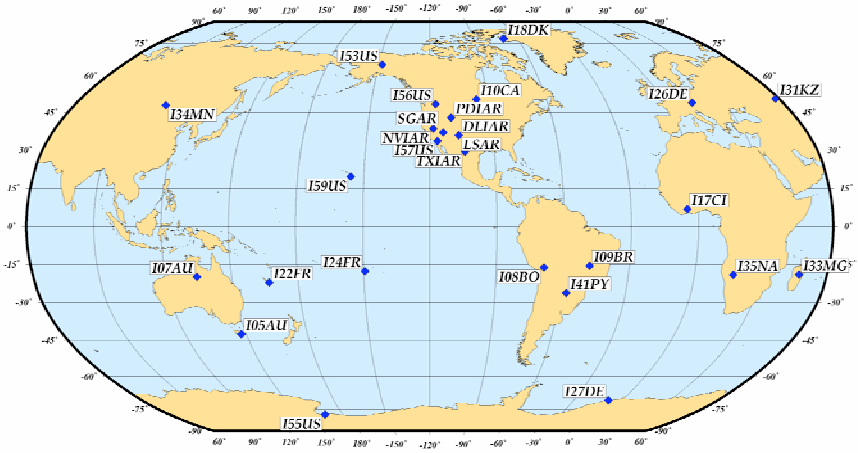


Figure 5. The infrasound database contains continuous data from the 27 infrasound arrays shown on this map.

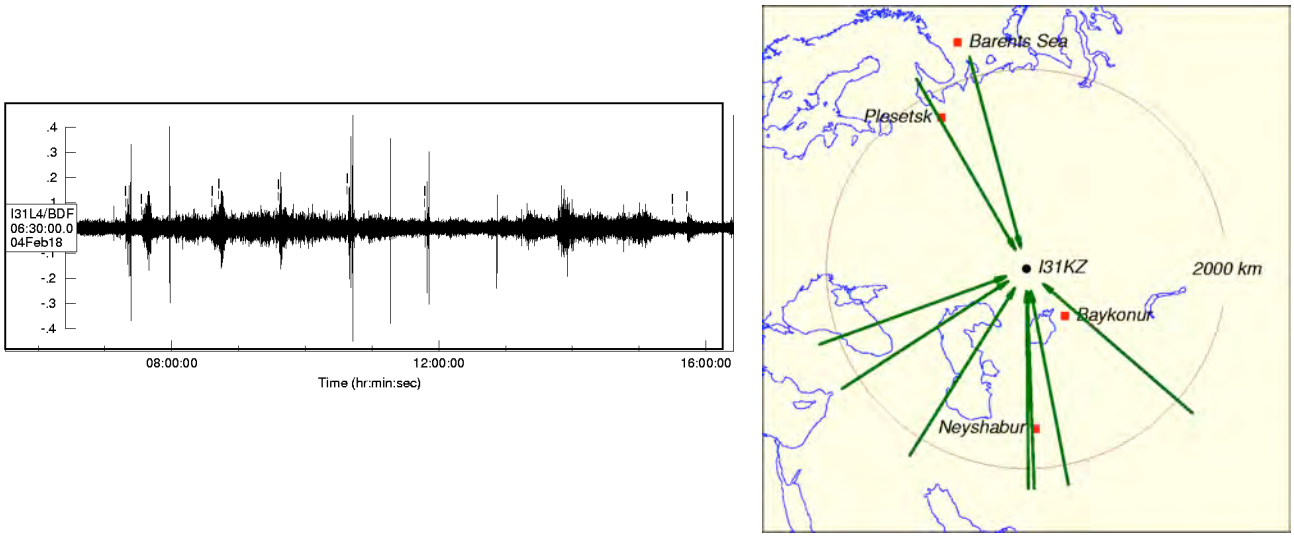


Figure 6. Multiple signals were observed at station I31KZ (Kazakhstan) during a nine hour period on February 18, 2004. The left panel shows a nine hour record recorded at I31KZ, with numerous clear signals. The right panel shows likely sources and azimuths for each of the observed signals. Signals were observed from missile launches at Baykonur, Kazakhstan and Plesetsk, Russia and the Barents Sea, as well as from a train explosion in Neyshabur, Iran.

The Nuclear Explosion Database contains information on all reported nuclear explosions in the atmosphere, underground and underwater since the first nuclear explosive device was set off in 1945 (Figure 7). The database gives the most accurate and complete unclassified information on time and place of both announced and presumed nuclear explosions and provides, whenever available, information on explosion yield, depth and shot medium (Table 2). In addition, the database contains a large archive of seismic (and some infrasound) recordings from about one third of the explosions (Figure 8).

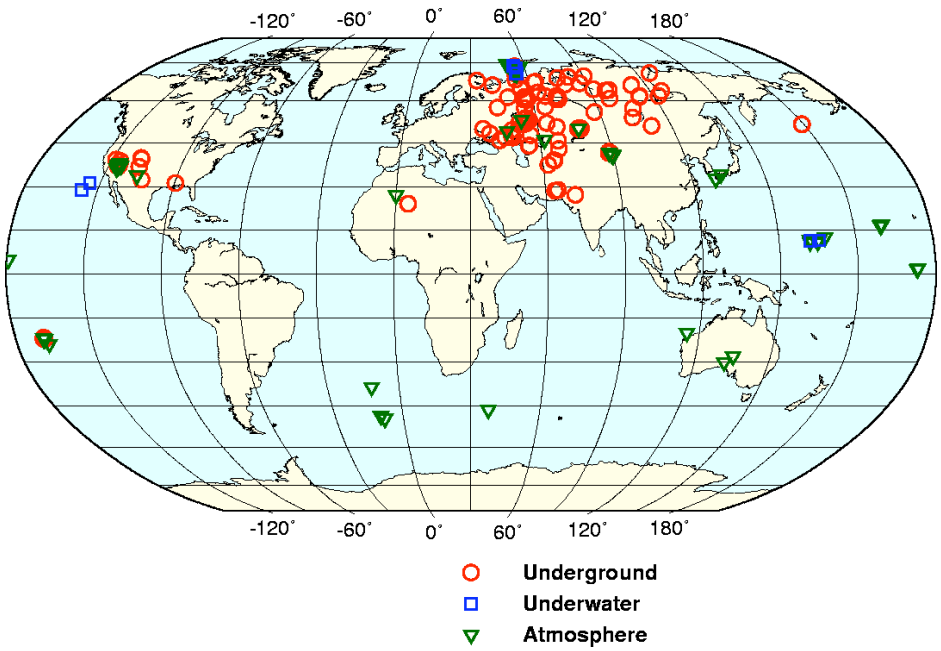


Figure 7. Locations of nuclear explosions for which information is included in the Nuclear Explosion Database.

The explosion database was originally compiled in 1997 and has subsequently been maintained and updated and it currently holds data for 2041 explosions. The list of explosions in the data base was derived from more than 40

different data sources with information reported by both official, such as Department of Energy (DOE/NV-209, 2000), and non-official organizations and appearing in a variety of publications. A detailed description of the database has been compiled by Yang et al. (2000, 2003) and Bondar et al. (2001).

Table 2. Locations of stations for which nuclear explosion waveforms (seismic or infrasound) or arrival data are included in the Nuclear Explosion Database.

Explosion Environment	Total Number of Explosions	Number of Explosions with:				
		Shot Depth/ Height	Yield	Shot Medium	Arrival data	Waveforms
Underground	1516	632	1035	457	608	739
Underwater	10	7	9			1
Atmosphere	515	110	452		7	25

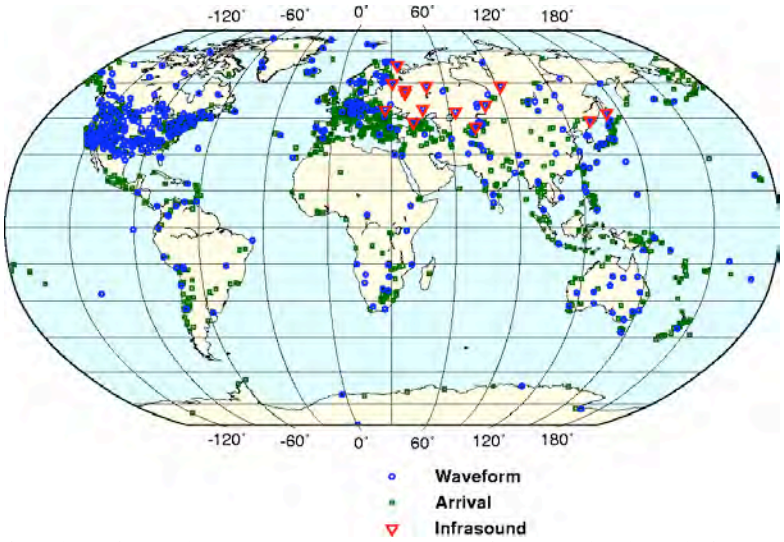


Figure 8. Locations of stations for which nuclear explosion waveforms (seismic or infrasound) or arrival data are included in the Nuclear Explosion Database.

The Ground Truth Database contains a collection of events of ground truth (GT) quality to support location calibration studies. The database includes nuclear and chemical explosions, mine blasts, rock bursts and earthquakes of global coverage. The earthquakes in the database all have shallow focus (less than 40 km focal depth), since deep earthquakes are of lesser interest from a nuclear monitoring point of view. Every event is accompanied with arrival data as well as references to document the source of information.

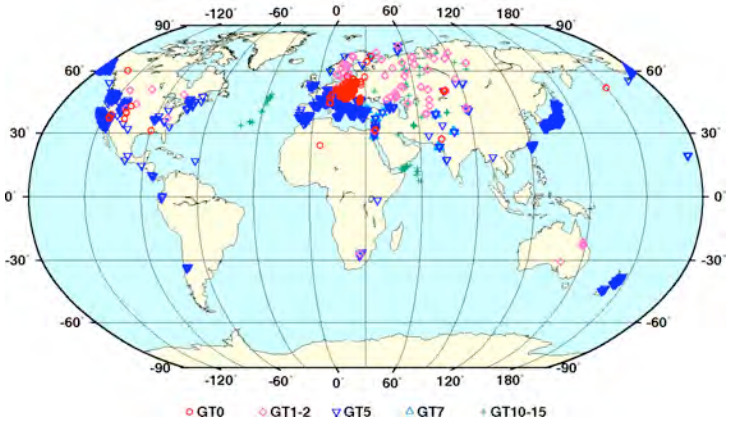


Figure 9. Locations of events in the Ground Truth Database.

The events in the Ground Truth Database are distributed globally, though they are dominantly in the northern hemisphere (Figure 9). The database currently holds 13,379 GT0-15 events (Table 3) with some 900,000 associated phases (of which some 810,000 are defining) recorded at 3,771 stations. Residuals in the bulletins refer to IASP91 (Kennett and Engdahl, 1991) predicted travel times with the source fixed to the GT locations. Note that the categories GT7 and GT11 stand for events promoted to ground truth status after performing

multiple event location on an event cluster. For details see Bondár et al. (2004), Engdahl and Bergman (2001), and Engdahl et al. (2002). The GT15 events (Pan et al., 2002) are only included to provide coverage on mid-oceanic ridge events in the mid-Atlantic ridge, the Carlsberg ridge and the Gulf of Aden.

Table 3. Summary of Ground Truth Database holdings, by source type and GT level.

Source	GT0	GT1-2	GT5	GT7	GT10	GT11	GT15	Total
Nuclear explosion	428	359	23	-	26	-	-	836
Chemical explosion	155	44	1	-	-	-	-	200
Mine blast, rock burst	-	141	58	-	-	-	-	199
Earthquake	-	-	11596	324	12	183	29	12144
Total	583	544	11678	324	38	183	29	13379

Hypocenter Location Server

The RDSS has developed the Hypocenter Location Server (HLS) to provide a remotely accessible interface to the powerful hypocenter location program *EvLoc*. The *EvLoc* software is the same software used by the International Data Centre (and by the former Prototype International Data Center) to produce Reviewed Event Bulletins. *EvLoc* is capable of using any combination of seismic, hydroacoustic, and infrasound arrivals to determine hypocenters and (seismic only) to compute magnitudes. The HLS is accessed by sending formatted e-mail messages to the server (in this sense it looks much like an *AutoDRM* server), as illustrated in Figure 10. The user provides data files, configuration files, and custom parameter files via FTP (using a flat-file structure or using XML). The HLS processes requests, with their associated input files, and then e-mails the results to the user.

EvLoc is a complex software component that relies heavily on a carefully configured database environment (e.g. Oracle) to function properly. As such, *EvLoc* is not readily portable. By providing access to *EvLoc* functionality through the Application Service Provider model as described here, researchers can readily use *EvLoc* in their analysis without worrying about software portability or configurability. Further, the capability provided by the HLS completely supercedes that provided by the stand-alone hypocenter determination program *LocSAT*. Note that the HLS is fully backward compatible with *LocSAT* input files.

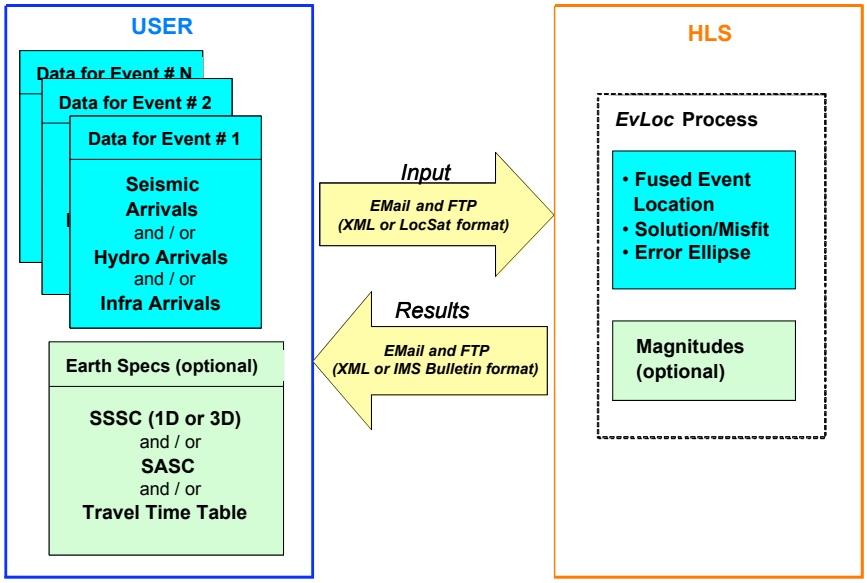


Figure 10. Illustration of the relationship between user provided inputs and HLS-produced processing results.

CONCLUSIONS AND RECOMMENDATIONS

We have described a variety of resources that are available to the U.S. nuclear explosion monitoring research and development community.

A new, state-of-the-art mass-storage system makes a vast quantity of data available for direct computations and rapid remote access. With this new system it is possible to perform computations in which data are accessed directly from the mass-store and to select and instantly access data across any combination of stations and time windows. Sophisticated new tools are provided to enable remote users to browse the data holdings and obtain instant downloads of data in analysis-ready formats.

A wide range of value added databases have been produced. These databases represent unique assemblies of waveform data, arrival and event data, and metadata. The databases are all available on-line, and provide valuable resources for use in detection, location, and identification studies.

To support remote users who require event location capability, we provide an application service provider interface to the powerful event location software *EvLoc*. *EvLoc* can provide fused event location solutions (using any combination of seismic, hydroacoustic, and infrasonic arrivals). The interface to *EvLoc* can support the user with either small, occasional event location requirements, or the user performing bulk relocations as part of a calibration project. In either case, there is no need for the user to install and configure the complex database environment that software like EvLoc requires.

We recommend that researchers in the nuclear explosion monitoring R&D community visit the MRP web sites to learn more about the MRP's RDSS resources. The MRP maintains an open web site and a restricted access web site, limited to U.S. government-authorized researchers. As an additional convenience to authorized users, the MRP web site may also be accessed using the SMDC channel of the *Army Knowledge Online* web portal at https://www.us.army.mil.

ACKNOWLEDGEMENTS

We thank Rod Whitaker of Los Alamos National Laboratory (LANL) for making available the data from the infrasound arrays that LANL has operated in the western U.S. for many years. We thank Hans Israelsson and Istvan Bondar for their contributions to this paper.

REFERENCES

Bowman, J.R., E. Baker, and M. Bahavar (2004), Infrasound Station Ambient Noise Estimates (2004), *Proceedings of the 26th Seismic Research Review: Trends in Nuclear Explosion Monitoring*, Orlando, FL (Sept. 21-23, 2004).

Bondár, I., E.R. Engdahl, X. Yang, H.A.A. Ghalib, A. Hofstetter, V. Kirichenko, R. Wagner, I. Gupta, G. Ekström, E. Bergman, H. Israelsson and K. McLaughlin, (2004), Collection of a reference event set for regional and teleseismic location calibration, *Bull. Seism. Soc. Am.*, in press.

Bondár, I., X. Yang, R.G. North and C. Romney (2001), Location Calibration Data for CTBT Monitoring at the Prototype International Data Center, *Pure Appl. Geophys*., 158, 19-34.

DOE/NV-209 (2000), United States nuclear tests, July 1945 through September 1992, Rev. 15.

Engdahl, E.R. and E.A. Bergman (2001), Validation and generation of reference events by cluster analysis, in *Proceedings of the 23rd Seismic Research Review: Worldwide Monitoring of Nuclear Explosions*, LA-UR-01-4454, Vol. I, pp. 205-214.

Engdahl, E., E. Bergman, M. Ritzwoller, N. Shapiro and A. Levshin (2002), A reference event data set for validating 3-D models, in *Proceedings of the 24th Seismic Research Review - Nuclear Explosion Monitoring: Innovation and Integration*, LA-UR-02-5048, Vol. I, pp. 261-270.

Kennett, B. and E.R. Engdahl (1991), Travel times for global earthquake location and phase identification, *Geophys. J. Int*., 105, 429-465.

Kohl, B., R. North, J.R. Murphy, M. Fisk, and G. Beall, (2002) Demonstration of Advanced Concepts For Nuclear Test Monitoring Applied to the Nuclear Test Site at Lop Nor, China, in *Proceedings of the 24th Seismic Research Review - Nuclear Explosion Monitoring: Innovation and Integration*, LA-UR-02-5048, Vol. I, pp. 302-312.

Pan, J., M. Antolik and A. Dziewonski (2002), Locations of mid-oceanic earthquakes constrained by sea- floor bathymetry, *J. Geophys. Res.*, 107, 2310, doi:10.1029/2001JB001588.

Yang, X., R. North, and C. Romney (2000), CMR Nuclear Explosion Database (Revision 3), *CMR Technical Report CMR-00/16*.

Yang, X., R. North, C. Romney, and P. Richards (2003), Worldwide nuclear explosions, in *International Handbook of Earthquake and Engineering Seismology*, Vol. 81B, eds. W.H. Lee, H. Kanamori, P. Jennings, and C. Kisslinger, *Academic Press*.

Acronyms, etc.

Acronyms, etc.

Acronym	Definition
2-D, 2D, 3-D, 3D	two-dimensional, three-dimensional, etc.
ABCE	Annual Bulletin of Chinese Earthquakes
ACD	Advanced Concept Demonstration
AFRL	Air Force Research Laboratory
AFTAC	Air Force Technical Applications Center
AK135	seismic travel time model
ANOVA3	analysis of variance code
ArcView	commercial GIS software (used in Knowledge Base)
ARSA	Automated Radioxenon Analyzer/Sampler
ASSE	Altai-Sayan Seismological Expedition
ATOC	Acoustic Thermometry of the Ocean Climate
BB	broad band
BDSN	Berkeley Digital Seismic Network
Be-7	beryllium-7
CANC	Correlated data Adaptive Noise Canceling
CauSIN	Caucasus Seismic Information Network
CDSN	Chinese Digital Seismic Network
CEA	Commissariat à l'Energie Atomique (French bulletin)
ChISS	Russian abbreviation for multichannel spectral seismometer
CLVD	Compensated Linear Vector Dipole
CMT	Harvard Centroid Moment Tensor
CodaMag	tool to implement magnitude calculations (Mayeda, 1993; Mayeda and Walter, 1996)
CORBA	Common Object Request Broker Architecture (data communications tool)
CRUST2.0	crustal model (Bassin et al., 2000)
CTBT	Comprehensive Nuclear-Test-Ban Treaty
CTBTO	Comprehensive Nuclear-Test-Ban Treaty Organization
CU	University of Colorado
CUB2.0	3D global models (Shapiro et al., 2002)
CU-Boulder	University of Colorado, Boulder
DB24	Geotech Remote Digitizer
DD	double-difference
DMC	Data Management Center
DOB	depth of burial
DoD	Department of Defense
DOE	Department of Energy
DOS	Department of State
DSS	deep seismic sounding
DTRA	Defense Threat Reduction Agency
EDR	Earthquake Data Reports
EHB	Engdahl, E.R., van der Hilst, R. & Buland, R., 1998. Global teleseismic earthquake relocation with improved travel times and procedures for depth determination, Bull. Seismol. Soc. Amer.,

Acronym	Definition
ESRI	Environmental Systems Research Institute
ESRI	Environmental Systems Research Institute (makers of ArcInfo, ArcIMS, ArcGIS, etc. [http://www.esri.com/company/about/history.html]
ETOPO5	terrain model
ETTC	Empirical Travel Time Corrections
EventID	tool to implement event discrimination (Hartse et al., 1997; Walter et al., 1999)
EvLoc	location software
FSPS	frequency-slowness power spectra
Fstat, F-stat	F-statistic
FSU	Former Soviet Union
GBF	generalized beamforming
GDAIS	General Dynamics Advanced Information Systems
GII	Geophysical Institute of Israel
GIS	Geographical Information System
GMEL	grid multiple-event location or multiple-event location algorithm
GSEL	grid single-event location or single-event location algorithm
GSN	ground station network
GT	ground-truth
GUI	graphic user interface
Guralp CMG-3T	3-component broadband seismometer
HDC	hypocentroidal (or hypocentral) decomposition
HIMNT	Himalayan Nepal Tibet Seismic Experiment
HPGe	High Purity Germanium
HydroCAM	Hydroacoustic Coverage Assessment Model
HypoDD	hypo double-difference
Hz	hertz
IASPEI	International Association of Seismology and Physics of the Earth's Interior
IASPEI91	standard earth model
IDC	International Data Center
IDG	Russian Institute for the Dynamics of the Geospheres
IKONOS	satellite-based imagery acquisition systems, 4m multispectral and 1m panchromatic
IMS	International Monitoring System
INDEPTH II, III	experiments
InfraMAP	Infrasound Modeling of Atmospheric Propagation
InSAR	Interferometric Synthetic Aperture Radar
IRIS	Incorporated Research Institutions for Seismology
ISC	International Seismological Centre
ISTC	International Science and Technology Center
JAXB	Java Architecture for XML Binding
JHD	Joint Hypocenter Determination
KACST	King Abdulaziz City for Science and Technology
KB	Knowledge Base
KBCIT	Knowledge Base Calibration Integration Tool
KIGAM	Korean Institute of Geology and Mining or Korea Institute of Geosciences and Mineral Resources
KLD	Karhunen-Loéve decomposition
KMA	Korean Meteorological Administration

Acronym	Definition
KOERI	Kandilli Observatory Earthquake Research Institute
KRSC	Kola Regional Seismological Centre
LANL	Los Alamos National Laboratory
LBNL	Lawrence Berkeley National Laboratory
Lg	regional seismic near surface shear phase
LLNL	Lawrence Livermore National Laboratory
LOCOO	LOCator Object Oriented (program code)
Matlab	commercial software application
MatSeis	seismic analysis package developed by SNL using Matlab
mb	body wave magnitude
MCMC	Markov Chain Monte Carlo
MDAC	magnitude and distance amplitude corrections
MDAC2	Magnitude and Distance Amplitude Correction procedure (Walter and Taylor, 2002)
ME/NA/WE	Middle East/North Africa/Western Europe
MFA	Multiple Filter Analysis
MIT	Massachusetts Institute of Technology
MOU	Memorandum of Understanding
Ms	surface wave magnitude
MSE	mean squared error
MSIS	thermospheric atmospheric model
MSISE	total atmospheric model
Mw	Moment Magnitude
NA-22	Office of Nonproliferation Research and Engineering
NCEDC	Northern California Earthquake Data Center
NEIC	National Earthquake Information Center
NEM R&E	Nuclear Explosion Monitoring Research and Engineering
NK ATD	North Korea Advanced Technology Demonstration
NNSA	National Nuclear Security Administration
NOAA	National Oceanic and Atmospheric Administration
NOGAPS	Navy Operational Global Atmospheric Prediction System
NRL	Naval Research Laboratory
NTS	Nevada Test Site
OFIS	Optical Fiber Infrasound Sensors
ORB	object request broker
ORLOADER	software package
PANDA	CERI's portable network - The PANDA stations were deployed in the central New Madrid seismic zone during October 1989 - August 1992.
PASSCAL	IRIS program that manages seismic equipment
PDE	Preliminary Determination of Epicenters
PDF	Portable Document Format
Pg	local and regional seismic phase
PGL	Parametric Grid Library
PhaseMatch	tool that implements match filtering to isolate surface waves (Herrin and Goforth, 1977)
PMCC	Progressive Multichannel Cross-Correlation
PMEL	Progressive Multiple Event Location or Pacific Marine Environmental Laboratory
PMF	Phase Matched Filtering
Pn	regional seismic compressional phase

Acronym	Definition
PNE	peaceful nuclear explosions
PNNL	Pacific Northwest National Laboratory
PPD	posterior probability distribution
PREM	Preliminary Reference Earth Model (Dziewonski and Anderson, 1981)
PrepCom	Preparatory Commission
PS362	3D global models (Antolik et al., 2002)
PSDs	Power Spectral Densities
PSU	Penn State University
P-wave	primary wave
Q	Q Factor
RASA	Radionuclide Aerosol Sampler Analyzer
RBAP	Regional Body-wave Amplitude Processor
RDB	relational database
RDSS	Research and Development Support Services
REB	Reviewed Event Bulletin
REFTEK or RefTek	72a 24-bit data recorder
RELOC	software
rftn96	program suite for determining crustal structure
RMS	root mean square (errors)
RUM	mantle velocity model
SA	seismic-acoustic or simulating annealing
SAC	Seismic Analysis Code
SAIC	Science Applications International Corporation
SAN2000B	SAIC Authenticator/Formatter
SASCs	Slowness-Azimuth Station Corrections
SBSO	Serialized Binary Stream Object
SDAS	Seismic Data Acquisition System
SDI	Spatial Data Interface (application)
SLU	Saint Louis University
SMDC	Space Missile Defense Command (Army)
Sn	regional seismic shear phase
SNR	signal-to-noise ratio
SNU	Seoul National University
SP	Short Period
SPOT	high-resolution imagery products are 10m panchromatic
SRD	System Requirement Document or Secret Restricted Data
SRDB	Seismic Research Database
SSS	Sensor Site Subsystem (AFTAC)
SSSCs	source-specific station corrections or site-specific station corrections
STS-2	Streckeisen seismometer model STS 2
surf96	program suite for determining crustal structure
SUS	stationary uncorrelated scattering or signals, underwater sound
SVD	singular value decomposition
S-wave	secondary wave
TM	threshold monitoring
T-phase	hydroacoustic phase

Acronym	Definition
UCB	University of California, Berkeley
UCSD	University of California, San Diego
UNE	underground nuclear explosions
UNR	University of Nevada, Reno
USGS	United States Geological Survey
USNDC	United States National Data Center
VELEST	software program
VEXTool	Viewing and EXtraction Tool
VMAX	Variable-Period, Maximum Magnitude Estimation
WCC	waveform cross-correlation
WG	working group
WINPAK3D	P-wave velocity model for India and Pakistan
WWSSN	World Wide Standard Seismograph Network
YSKP	Yellow Sea – Korean Peninsula

Station Code	Location and/or description
AAK	Ala-Archa (Kyrgyzstan)
AKTO	Aktyubinsk Auxiliary Seismic Station
ANMO	Albuquerque
APA	Apatity station (array)
ARCES	seismic array in northern Norway
ARS	Arshan
AS049	auxilliary seismic IMS station #49 on Mount Merron, Israel
BJI	Beijing (Baijiatuan; Peking)
BRAR	seismic array in Belbasi, Turkey
BRVK	Borovoye auxiliary seismic station
CHG	Chiang Mai
CHNAR	Chulwon (seismo-acoustic array)
CMB	Columbia College
DUG	Dugway
EIL	Elat (Eilat) (seismic)
ELK	Elko
FINES	seismic array in southern Finland
GEOFON	global seismic Broadband Digital Network; Potsdam; Germany
Geoscope	global Seismic broadband network; France
H01	Cape Leeuwin
H08	Diego Garcia
HFS	Hagfors
HLR	Highlands Ranch (closed)
ISP	Isparta
KAZ	Karuizawa
KEV	Kevo regional station
KMI	Kunming
KNB	Kanab
KNET	Kyrgyz Broadband Seismic Network
KSAR	seismic array in Wonju, Korea
KURK	Kurchatov Auxiliary Seismic Station

Station Code	Location and/or description
LAC	Landers
LSA	Lhasa (Tibet, China)
LVZ	Lovozero regional station
LZH	Lanzhou
MAG	Magadan
MAKZ	Maqanshy (Makanchi)
MALT	Malatya
MEDNET	MedNet digital seismic broadband network; Italy
MNA	Mina
MRNI	Mount Meron (old seismic station that has been replaced by AS049)
NEW	Newport
NIL	Nilore
NORES	seismic array in southern Norway
NRIS (NRI)	Noril'sk
NVAR	seismic array in Mina, Nevada
OBN	Obninsk seismic station
PDY	Peleduy seismic station
PFO	Pinon Flat Observatory
PS38	seismic array in central Saudi Arabia
SEY	Seymchan
SPITS	seismic array in Spitsbergen
SSE	Sheshan
TIXI (TIK)	Tiksi
TLY	Talaya seismic station
TUC	Tucson
ULN	Ulaanbaatar, (Mongolia)
WMQ	Urumqi (Wulumuchi) seismic station
XAN	Xi'an (Hsian)
YAK	Yakutsk
YKA	seismic array in Yellowknife, Canada
ZAL	Zalesovo